

1273  
5/3-79

Rev 2535

UCRL-50021-77

**MASTER**

# **Laser Program Annual Report — 1977**

## **Volume 2**

**Lawrence  
Livermore  
Laboratory**



**LAWRENCE LIVERMORE LABORATORY**  
*University of California Livermore, California 94550*

UCRL-50021-77

# **LASER PROGRAM ANNUAL REPORT — 1977**

## **Volume 2**

Scientific Editor: Charles F. Bender  
Publication Editor: Brian D. Jarman

MS date: July 1978

**NOTICE**

This report was prepared as an account of work sponsored by the United States Government. Neither the United States nor the United States Department of Energy, nor any of their employees, nor any of their contractors, subcontractors, or their employees, makes any warranty, express or implied, or assumes any legal liability or responsibility for the accuracy, completeness or usefulness of any information, apparatus, product or process disclosed, or represents that its use would not infringe privately owned rights.

*Handwritten signature*

## **FOREWORD**

This volume consists of Sections 4 through 9 of the 1977 Laser Program Annual Report. The remaining sections are published under separate cover in Volume 1 (Sections 1 through 3).

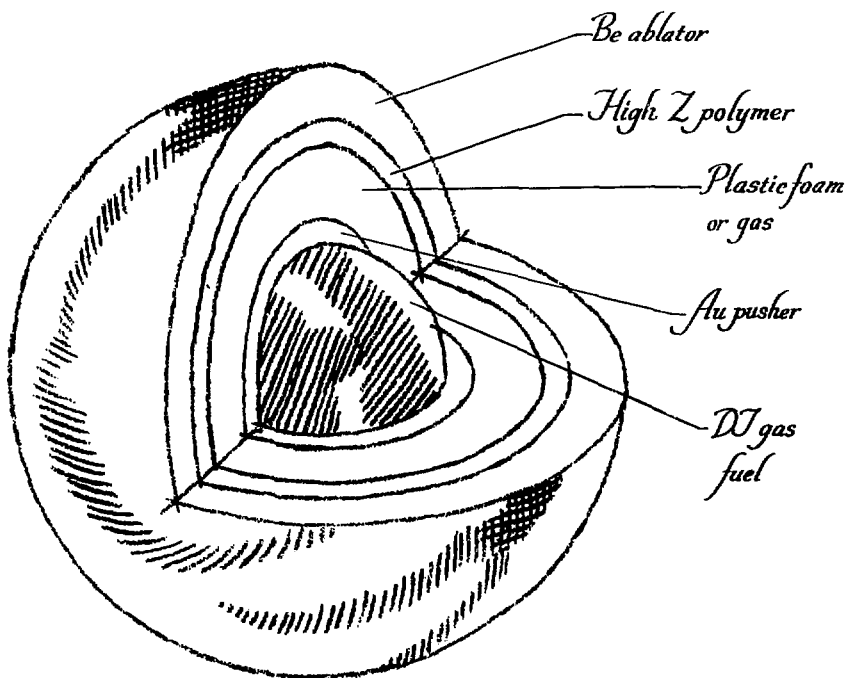
## CONTENTS

Section 4 – Fusion Target Design . . . . .	4-i
Section 5 – Target Fabrication . . . . .	5-i
Section 6 – Laser Fusion Experiments and Analysis . . . . .	6-i
Section 7 – Advanced Lasers . . . . .	7-i
Section 8 – Systems and Applications Studies . . . . .	8-i
Section 9 – Laser Isotope Separation Program . . . . .	9-i



# SECTION 4

## FUSION TARGET DESIGN



## SECTION 4

### CONTENTS

4.1	Overview . . . . .	4-1
4.2	Laser Target Design and Analysis . . . . .	4-1
4.2.1	Exploding-Pusher Targets at 30 TW . . . . .	4-1
4.2.2	Exploding-Pusher Target Performance: Theoretical Model . . . . .	4-6
	Temperature Calculation . . . . .	4-6
	Compression Calculation . . . . .	4-8
	Yield Calculations . . . . .	4-8
	Acknowledgments . . . . .	4-9
4.2.3	Using Inner-Shell X Rays Produced by Collisions between Charged Particles and Atoms to Diagnose Implosion Characteristics of Inertially Confined Fusion Targets . . . . .	4-9
	Two-Dimensional Image . . . . .	4-11
	Line Image . . . . .	4-12
	<i>Detecting the Number of <math>K_{\alpha}</math> X Rays Produced</i> . . . . .	4-12
4.2.4	Low-Aspect-Ratio Double Shells for High Density and High Gain . . . . .	4-12
4.2.5	High-Performance Inertial Confinement Fusion Targets . . . . .	4-15
	Theoretical Possibility of High Performance with Very Low Density Targets . . . . .	4-15
	Targets with Very Thin Shells . . . . .	4-17
	Targets with Central Ignitors . . . . .	4-18
	Targets with Magnetic Insulation . . . . .	4-18
	Nonablative Acceleration . . . . .	4-19
	Summary . . . . .	4-19
4.2.6	Acceleration of Solid Macroparticles by Laser-Produced Ablation . . . . .	4-20
4.2.7	Calculation of Actinide Burnup in ICF Pellets . . . . .	4-23
4.3	Electron- and Ion-Beam Target Design and Analysis . . . . .	4-24
4.3.1	Magnetically Insulated Charged-Particle Targets . . . . .	4-24
4.3.2	Maximum Ion Energies for Heavy-Ion Fusion . . . . .	4-27
4.4	LASNEX Overview . . . . .	4-29
4.4.1	New Ponderomotive Force Algorithm . . . . .	4-29
4.4.2	Improvements to XSN Atomic Physics . . . . .	4-31
4.4.3	X-Ray Lines as a Density Diagnostic in DT Plasmas near $100\times$ Solid Density . . . . .	4-33
	Line Intensity . . . . .	4-33
	Line Broadening . . . . .	4-33
	Experimental Design . . . . .	4-34
4.5	Laser Plasma Theory and Simulation . . . . .	4-35
4.5.1	Overview . . . . .	4-35
	Density-Profile Steepening . . . . .	4-35
	Laser Light Absorption . . . . .	4-36
	Heated-Electron Temperatures . . . . .	4-37
	Plasma Expansion . . . . .	4-38
	Stimulated Scattering . . . . .	4-38
	Energy-Transport Inhibition . . . . .	4-38
	Simulation Techniques . . . . .	4-39
	Summary . . . . .	4-39

4.6	Light Absorption . . . . .	4-40
4.6.1	Laser Light Absorption on a Steepened, Rippled Critical-Density Surface . . . . .	4-40
4.6.2	Properties of Resonantly Heated Electron Distributions . . . . .	4-43
4.6.3	Absorption of Focused Light Beams . . . . .	4-47
4.6.4	Linear Theory of the $2\omega_{pe}$ Instability in Inhomogeneous Plasmas . . . . .	4-49
4.6.5	Resonant Absorption of Laser Light by a Magnetized Plasma . . . . .	4-51
4.6.6	Three-Dimensional Simulations of Laser Light Absorption . . . . .	4-54
4.7	Profile Steepening and Plasma Expansions . . . . .	4-55
4.7.1	Effects of Flow on Density Profiles in Laser-Irradiated Plasmas . . . . .	4-55
	Jump Conditions across the Critical Surface . . . . .	4-56
	Shock-plus-D Fronts . . . . .	4-58
	Conditions for Supersonic Flow Relative to the Critical Surface . . . . .	4-59
	Discussion . . . . .	4-60
4.7.2	Self-Similar Solutions to Plasma Flow with Strong Collisional Heating . . . . .	4-61
4.8	Simulated Scatter . . . . .	4-63
4.8.1	The Competition between Inverse Bremsstrahlung and Brillouin Reflection . . . . .	4-63
4.8.2	Forward Raman Scatter in Laser Fusion Reactors . . . . .	4-65
4.9	Heat-Transport Inhibition . . . . .	4-67
4.9.1	Cross-Field Thermal Transport Caused by Ion-Acoustic Waves in Magnetized Laser Plasmas . . . . .	4-67
	Introduction . . . . .	4-67
	The Equilibrium . . . . .	4-67
	Linear Theory . . . . .	4-68
	Anomalous Thermal Conduction . . . . .	4-69
	Application to Target-Design Computer Codes . . . . .	4-70
4.9.2	Qualitative Aspects of Underdense Magnetic Fields . . . . .	4-71
4.10	Analysis of Numerical Models for Simulation of Plasmas . . . . .	4-74
4.11	Microwave-Simulation Experiments . . . . .	4-75
4.11.1	Resonant Absorption, Hot-Electron Production, and Energy Transport . . . . .	4-75
4.11.2	Electron Heating in a Plasma-Filled Capacitor . . . . .	4-76
4.11.3	Microwave Absorption and Hot-Electron Transport in a Weak Magnetic Field . . . . .	4-77

## SECTION 4

### FUSION TARGET DESIGN

#### 4.1 Overview

Target Design includes the Plasma Theory, LASNEX, and Design Groups. These groups develop the theory of laser plasma, implosion, and thermonuclear processes; build particle and fluid computer codes, including ZOHAR and LASNEX; and use these theoretical-computational tools to design targets and to simulate experiments.

In 1977 most of our effort concentrated on ablative targets that compress DT to 10-100 times liquid density for Argus experiments and on high-density targets capable of achieving gains of 1000 in reactors. In addition, we developed high-performance exploding-pusher targets for Shiva experiments.

Ablative high-density implosions are essential for practical thermonuclear microexplosions. Because of preheat, fluid instability, and entropy constraints, these implosions are far more difficult than exploding-pusher implosions. In 1977 we made important advances in identifying and understanding plasma and atomic physics critically important in laser-driven high-density ablative implosions, and in improving approximations to this physics in LASNEX. These physical processes include stimulated scattering, density-profile modification, collective and collisional absorption, suprathermal electron and x-ray spectra, inhibited thermal-electron transport, and nonlocal-thermodynamic-equilibrium atomic physics. By late 1977 we achieved good agreement between experiment and LASNEX calculations and were designing a sequence of targets for Argus experiments to demonstrate implosion of DT to 10-100 times liquid density.

An ultra-high-performance, multishell target design was developed for reactor applications. In this design a low-density, low-aspect-ratio ablator/fuel shell is used to drive a levitated central ignitor. This target appears capable of gains approaching 1000 with a 1-MJ/100-TW driver. With this target the laser and target requirements for a 1-GW<sub>e</sub> reactor are:

Laser efficiency	> 1%
Wavelength	≅ 1-2 μm
Energy	≅ 1 MJ
Peak power	≅ 100 TW
Pulse rate	4/s
Target surface finish	≅ 1000 Å
Target cost	≅ 30¢

Target designs with similar performance have been developed for implosion by relativistic electron beams, light ions, and heavy ions.

Advanced exploding-pusher targets were designed for Shiva experiments. When driven by a 30-TW/60-ps pulse, these targets have a calculated neutron yield of  $\approx 10^{12}$ , a target gain of  $\geq 10^{-3}$ , and a DT gain approaching breakeven ( $\geq 10^{-1}$ ). Compared to our record-breaking Argus exploding-pusher experiments in September 1976, this is nearly a 500-fold increase in neutron yield with a 10-fold increase in laser power. This extraordinary increase in calculated neutron yield with laser power was achieved by improving the implosion symmetry and laser-light absorption, and by using an unusually large radius/thickness ratio for the glass pusher. This capsule is optimally matched to Shiva.

In the following articles, the Design, LASNEX, and Plasma Theory Groups describe these results and other significant advances in somewhat greater detail.

#### Author

J. H. Nuckolls

#### 4.2 Laser Target Design and Analysis

##### 4.2.1 Exploding-Pusher Targets at 30 TW

In the 1976 laser program annual report we presented results of a parametric study of exploding-pusher targets.<sup>1</sup> That study was performed with the LASNEX computer code to determine the optimum combinations of target diameter, wall thickness, DT gas fill, and laser pulse duration for absorbed laser powers varying from 0.1 to 12 TW. Here we present the results of a detailed study of optimal parameters of exploding-pusher targets for Shiva.<sup>2</sup>

The Shiva peak laser power was assumed to be 30 TW. At this power the optimum pulse duration is between 50 and 100 ps, and the optimum initial density of the DT is approximately 0.002 g/cm<sup>3</sup>. The target diameter and wall thickness were varied to find the optimum target gain (ratio of the thermonuclear energy released to the incident laser energy). This quantity is related to the neutron yield by

$$\text{Gain} \approx \frac{2.66 \times 10^{-12} N_n}{P_L \tau_L}, \quad (1)$$

where  $N_n$  is the neutron yield,  $P_L$  is the peak laser power in TW, and  $\tau_L$  is the Gaussian pulse FWHM in picoseconds.

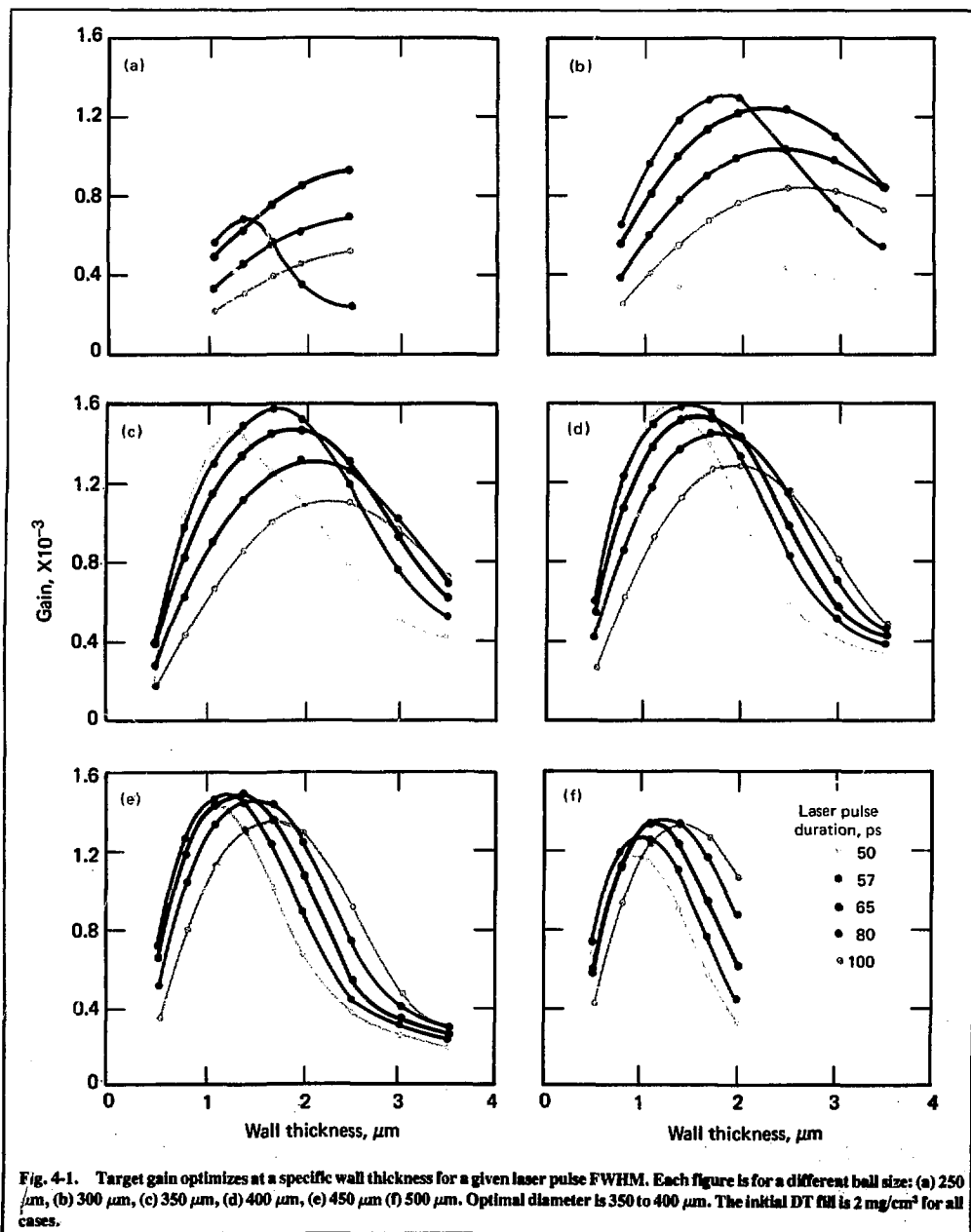


Fig. 4-1. Target gain optimizes at a specific wall thickness for a given laser pulse FWHM. Each figure is for a different ball size: (a) 250 μm, (b) 300 μm, (c) 350 μm, (d) 400 μm, (e) 450 μm (f) 500 μm. Optimal diameter is 350 to 400 μm. The initial DT fill is 2 mg/cm<sup>3</sup> for all cases.

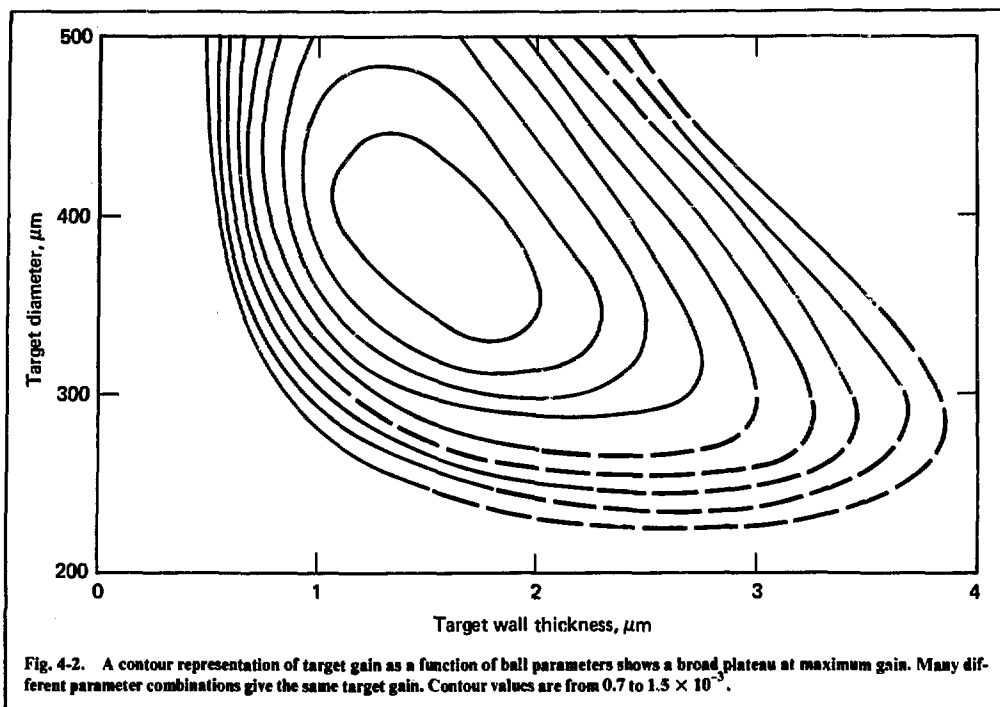


Fig. 4-2. A contour representation of target gain as a function of ball parameters shows a broad plateau at maximum gain. Many different parameter combinations give the same target gain. Contour values are from  $0.7$  to  $1.5 \times 10^{-3}$ .

These calculations assumed spherical symmetry, 40% laser light absorption by collective mechanisms, multigroup electron transport, and inhibition of thermal-electron transport by the electron-ion two-stream instability. The characteristic temperature of the laser-heated suprathermal electron distribution at the critical density was computed in LASNEX from Estabrook's equation:<sup>3</sup>

$$\theta_{\text{hot}} = \theta_{\text{AV}} + 4.48 \times 10^{-6} I_L^{0.42} \theta_{\text{AV}}^{0.03} \text{ keV}, \quad (2)$$

where  $\theta_{\text{AV}}$  is the average electron temperature and  $I_L$  is the laser intensity at the critical density in  $\text{W}/\text{cm}^2$ . Typically, the maximum laser intensity is  $10^{15}$ - $10^{16} \text{ W}/\text{cm}^2$ , and the hot temperature is 15-30 keV.

Results are shown in Fig. 4-1, where the target gain is plotted as a function of shell wall thickness for several laser pulse durations. Each figure is for a different target ball diameter.

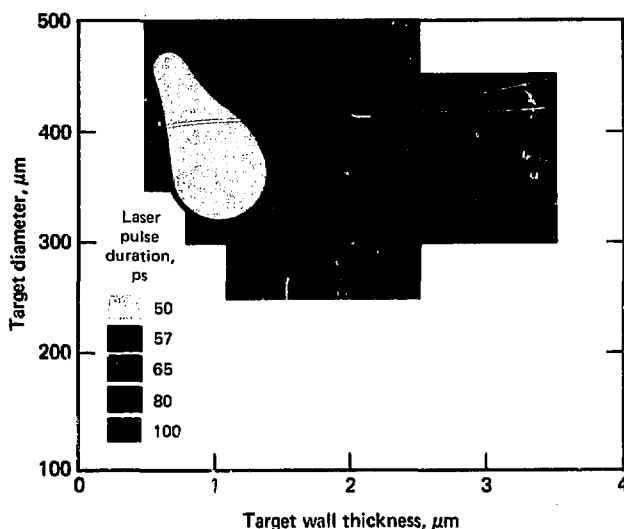
Figure 4-2 is constructed from the envelope of the curves in Fig. 4-1. Contours of constant target gain are shown as functions of capsule thickness and diameter. Each point on these contours corresponds to the maxi-

mum target gain achieved with the optimum pulse duration for the given capsule diameter and thickness. The maximum gain is about  $1.6 \times 10^{-3}$ . There is a broad range of target dimensions with near maximum gains. For example, gains greater than  $1.5 \times 10^{-3}$  may be achieved with diameters between 350 and 425  $\mu\text{m}$  and corresponding wall thicknesses in the range of 1.2-1.8  $\mu\text{m}$ . The pulse durations corresponding to these contours are shown in Fig. 4-3. For example, a target with a 400- $\mu\text{m}$  diameter, 1.5- $\mu\text{m}$  wall thickness, and ~57-ps pulse duration achieves a gain of  $1.5 \times 10^{-3}$ .

Table 4-1 shows LASNEX calculations of various important implosion fusion parameters for selected targets spanning the space of Figs. 4-2 and 4-3. The table shows that higher DT ion temperatures predominate for thinner shells with smaller diameters and that peak fuel densities are larger for smaller targets with thicker walls.

Finally, Figs. 4-4 and 4-5 show details of the implosion and burn of a near optimum target with a 400- $\mu\text{m}$  diameter, a 1.7- $\mu\text{m}$  wall thickness, and an 80-ps laser pulse FWHM. Figure 4-4 is a plot of the DT-glass interface trajectory, with  $t = 0$  at the peak of the laser pulse.

Fig. 4-3. Each combination of target parameters has a specific pulse-width requirement for optimal performances. This contour plot shows the approximate pulse width to be used for a given diameter and shell thickness for the largest target gain, which is found from Fig. 4-2.

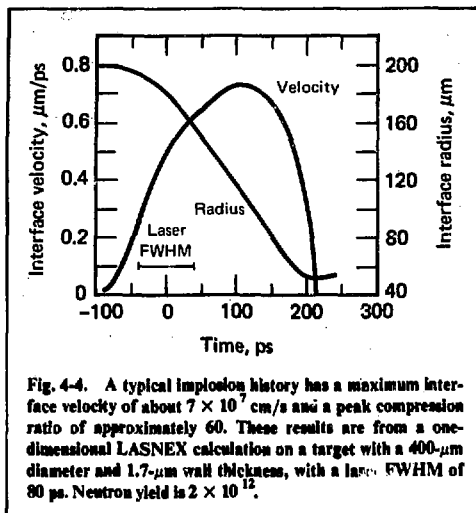


A maximum implosion velocity of  $7 \times 10^7$  cm/s is reached more than one  $\sigma$  (where  $\text{FWHM} = 2\sqrt{2 \ln 2} \sigma$ ) after the peak of the laser pulse, when the interface radius is slightly less than half its original value. Figure 4-5 shows the average DT temperature and density his-

stories. The DT reaction time, 10-90% of the yield, is approximately 95 ps. In this calculation and in general for this parameter study, maximum gain occurs with a DT ion temperature of about 15 keV and a peak fuel density of about 0.1 g/cm<sup>3</sup>.

Table 4-1. LASNEX calculations of some important implosion fusion parameters at 30-TW input power.

Target diameter, $\mu\text{m}$	Shell thickness, $\mu\text{m}$	Gaussian pulse FWHM, ps	Maximum interface velocity, $\mu\text{m}/\text{ps}$	Maximum fuel density, g/cm <sup>3</sup>	Peak fuel ion temperature, keV	DT reactions
500	0.5	57	0.84	0.03	10.6	$4.7 \times 10^{11}$
500	2.0	100	0.63	0.10	10.5	$1.2 \times 10^{12}$
400	0.5	57	0.97	0.05	13.4	$3.8 \times 10^{11}$
400	3.0	100	0.63	0.12	11.5	$9.1 \times 10^{11}$
300	0.8	57	1.13	0.14	20.3	$4.2 \times 10^{11}$
300	3.5	80	0.75	0.17	16.4	$7.8 \times 10^{11}$
200	2.0	65	1.07	0.35	25.5	$6.2 \times 10^{11}$
400	1.4	57	0.81	0.10	16.1	$1.0 \times 10^{12}$

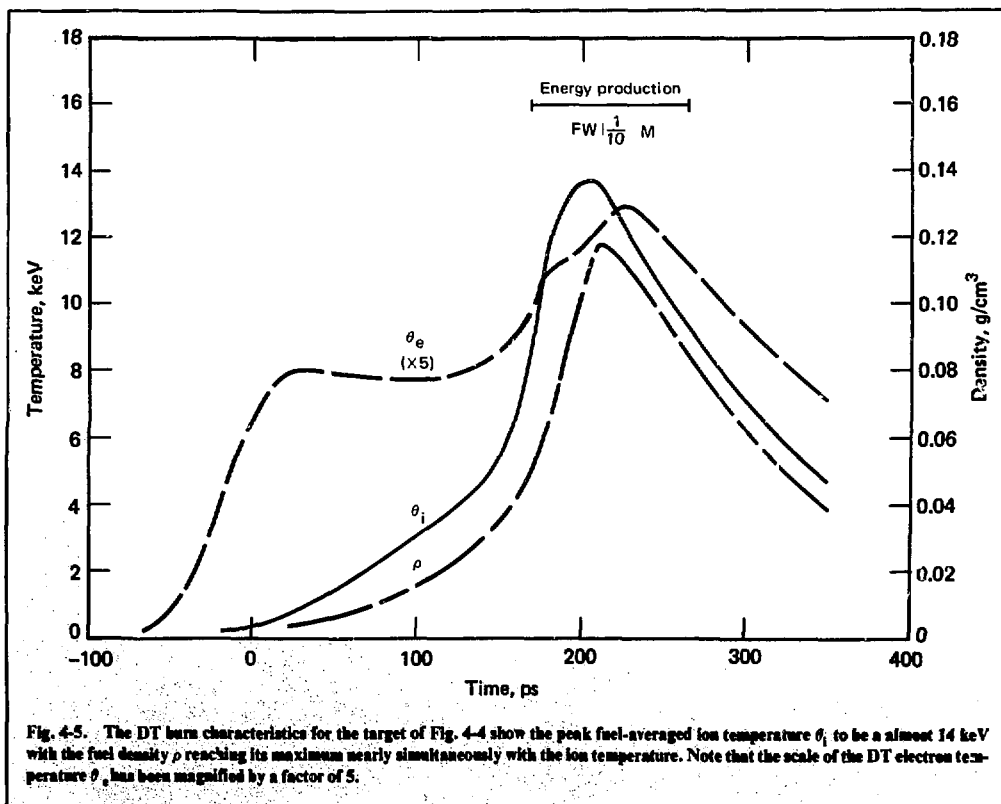


## References

1. J. T. Larsen, "Exploding Pusher Target Parameter Study," in *Laser Program Annual Report-1976*, Lawrence Livermore Laboratory, Rept. UCRL-50021-76 (1977), p. 4-6.
2. R. O. Godwin and J. A. Glaze, "Shiva," in *Laser Program Annual Report-1976*, Lawrence Livermore Laboratory, Rept. UCRL-50021-76 (1977), p. 2-54.
3. K. G. Estabrook and W. L. Kruer, "Properties of Resonantly Heated Electron Distributions," *Phys. Rev. Lett.* **40**, 42 (1978).

## Author

J. T. Larsen





## 4.2.2 Exploding-Pusher Target Performance: Theoretical Model

Exploding-pusher targets,<sup>4</sup> the most common targets in early laser fusion experiments, are the first targets to be shot on the 25-TW Shiva laser system at Lawrence Livermore Laboratory. Typically, they consist of glass microspheres of DT gas. For Shiva, microspheres are typically 200  $\mu\text{m}$  in radius, 2  $\mu\text{m}$  in thickness, and filled with low-density DT gas at 2  $\text{mg}/\text{cm}^3$ . DT microspheres are popular for many reasons. They are relatively easy to fabricate and diagnose; also, they require no special temporal laser pulse shaping other than the usual Gaussian. As explained below, their physics requirements are also less stringent than those of the usual high-compression, isentropic implosion targets that will lead ultimately to economical energy production.<sup>5</sup>

An exploding-pusher target heats the DT ions to thermonuclear temperatures (a few keV) in a three-step process. In the first step, an intense laser pulse rapidly heats the glass microsphere, preferentially heating the electrons. Because of its density, the electron-ion (e-i) coupling in the glass is good ( $\tau_{ei} \sim 1$  ps), producing an increase in glass ion temperature. In the second step, the electron thermal wave moves quickly through the glass and into the DT gas. Because of its low density, the electron-ion coupling in the DT is quite poor ( $\tau_{ei} \sim 1$  ns), and the DT ions are heated only slightly. Energy deposition in the glass occurs so quickly that the shell explodes: roughly half its mass outward and the remaining half inward. The imploding half of the shell acts as a piston, driving a shock through the DT that principally heats the ions. This is the second step of the ion-heating process. (At this stage,  $\lambda_{ii}/R$  is still  $\leq 1/10$ , so that a hydrodynamic description is quite accurate.) In the third step, the glass shell continues to move inward behind this shock front, isentropically compressing the postshock region of DT and further heating the ions to thermonuclear temperatures. The latter two hydrodynamic processes drive the ion temperature ( $\theta_i$ ) above the electron temperature ( $\theta_e$ ). The weak e-i coupling in the DT preserves this imbalance; thus, even by peak compression time,  $\theta_i \gg \theta_e$ . The DT thermal pressure builds up and eventually stops, reversing the inward moving glass. The fusion reactions occur until thermal conduction and expansion cool the DT.

High-compression, isentropic implosion targets are sensitive to electron preheat and to Rayleigh-Taylor instability. But exploding-pusher targets, because of their rapid thermal-wave early heating and their non-ablative implosion dynamics, are insensitive to such preheat and instability. However, the latter targets' preheat levels and exploding-pusher behavior limit their peak densities to a few times liquid density, falling

short of the densities that lead to propagating thermonuclear burn waves and concomitant high gains.

In this subsection, we present a simple model of the performance of exploding-pusher targets. To predict the neutron yield  $Y$  for given initial conditions, radius  $R$ , thickness  $\Delta R$ , DT fill  $\rho_0$ , peak absorbed laser power  $P$ , and pulse width  $\tau$ , note that

$$Y \sim M \rho_F \bar{\sigma} v \tau_c, \quad (3)$$

where  $M$  is the DT mass,  $\rho_F$  is its compressed density,  $\bar{\sigma} v$  is the product of velocity and fusion cross section averaged over a Maxwellian distribution, and  $\tau_c$  is the confinement time. Fokker-Planck calculations for the parameters of interest here show that the DT ion distribution is sufficiently Maxwellian to justify the use of  $\bar{\sigma} v$  in the yield formula.<sup>6</sup> The mass  $M \sim \rho_0 R^3$  and  $\rho_F = \eta \rho_0$ , where the compression ratio  $\eta$  also equals  $(R/R_F)^3$ , in which  $R_F$  is the final compressed radius; also  $\tau_c \sim R_F/c_s$ , where the sound speed  $c_s \sim \theta_i^{1/2}$ , in which  $\theta_i$  is the DT ion temperature at peak compression. Consequently, when the appropriate constants of proportionality are inserted, Eq. (3) becomes

$$Y_{(\text{neutrons})} = 2.4 \times 10^{10} \times \rho_0 (5 \text{ mg}/\text{cm}^3) R^4 (100 \mu\text{m}) \eta^{2/3} \times (\bar{\sigma} v / \theta^{1/2}) (10 \text{ keV}), \quad (4)$$

with quantities measured in the units appearing in the parentheses. Because  $\bar{\sigma} v$  is a well-known function of  $\theta_i$ , we need only calculate  $\theta_i$  and  $\eta$  to predict the yield  $Y$ . Below, we calculate  $\theta_i$  and  $\eta$ . Then we compare the subsequent yield calculations with simulations.

**Temperature Calculation.** To find  $\theta_i$ , recall that the ion heating is caused by a strong shock followed by isentropic compression. From the strong shock relations<sup>7</sup> for an ideal  $\gamma$ -law gas, it follows that in the postshock state the specific internal energy  $\epsilon = P/[(\gamma-1)\rho]$  is equal to the specific kinetic energy  $(1/2)u^2$ , and thus both are equal to one-half the specific energy of the system  $E/2M$ . Consider some time  $\tau_E$ , to be determined later, at which a shock driven by the exploding-pusher target is now propagating through the DT. If this shock has not undergone significant spherical convergences, the postshock (PS) DT velocity equals the velocity of the DT-pusher interface; thus,

$$\frac{1}{\gamma-1} \left( \frac{P_{\text{DT}}}{\rho_{\text{DT}}} \right)_{\text{PS}} \equiv \epsilon_{\text{DT}} = 1/2 v_{\text{DT}}^2 = 1/2 v_p^2 = a \frac{E(\tau_E)}{M_p}. \quad (5)$$

The parameter  $\alpha$  is a measure of (1) how the energy in the pusher is partitioned between internal and kinetic and (2) the velocity gradients across the pusher. If we consider the pusher explosion process in terms of shock-tube theory<sup>7</sup> for a gas of  $\gamma = 5/3$ , we obtain  $\alpha = 1/2$ . Let  $y \equiv V_p/3c$  with  $c$  the sound speed and  $x \equiv \rho_{DT}/\langle \rho_p \rangle$  in which  $\langle \rho_p \rangle$  is the time-averaged density of the pusher. Then, shock-tube theory yields the relation  $y = 1 - (20xy^2)^{1/5}$ . For typical cases,  $x = 0.005/0.4$ , which implies that  $y = 0.45$  and thus  $1/2 V_p^2 = \epsilon$  or  $\alpha = 1/2$ . Because of the  $1/5$  power dependence,  $y$  (and therefore  $\alpha$ ) is insensitive to  $x$ .

This treatment, using shock-tube theory, is only a first approximation because the exploding-pusher target is being strongly heated by the laser. However, as we show later, because of a self-correcting mechanism in this theory, the values of the initial DT temperature and the final DT temperature  $\theta_i$  (and therefore the value of the yield as well), are insensitive to the exact choice of  $\alpha$ . (Matching an isothermal rarefaction of the pusher to the DT shock also leads to values of  $\alpha$  near  $1/2$ .) Since  $\rho_{PS} = (\gamma + 1) \rho_0/(\gamma - 1) = 4\rho_0$  (by the strong shock relations), we obtain with  $\alpha = 1/2$ :

$$P_{PS} = 4\rho_0 E(\tau_E)/3M_p. \quad (6)$$

To determine the explosion time  $\tau_E$ , we require that this shock propagate until it has shocked the mass-averaged fluid element at the half-mass point, which is at  $0.8R$  [(0.8)<sup>3</sup> = 0.5]. The strong shock relation,  $v_{shock} = (\gamma + 1)v_{piston}/2 = (4/3)v_p$ , implies that the pusher is at  $0.85R$  at time  $\tau_E$ . The right side of Eq. (5) relates  $v_p$  to  $E(\tau_E)$ ; thus it can be integrated to yield

$$r(t) = R - M_p^{-1/2} \int_{\infty}^t \left[ \int_{\infty}^{t'} P(t'') dt'' \right]^{1/2} dt' \quad (7)$$

and  $r(\tau_E) \equiv 0.85R$ . With  $\tau_E$  known,  $E(\tau_E)$  is also known (the integral of  $P(t)$  from  $-\infty$  to  $\tau_E$ ).

The isentropic compression, which occurs after the shock, follows the law

$$\left( \frac{P_F}{P_{PS}} \right) = \left( \frac{\rho_F}{\rho_{PS}} \right)^{5/3} = (\eta/4)^{5/3}. \quad (8)$$

However,  $P_F = (\eta\rho_0)(\theta_e + \theta_i)/2.5 m_p$ , where  $2.5 m_p$  is the atomic mass of DT; thus, Eqs. (6) and (8) yield

$$(\theta_e + \theta_i) = E(\tau_E) m_p \eta^{2/3} / 3M_p. \quad (9)$$

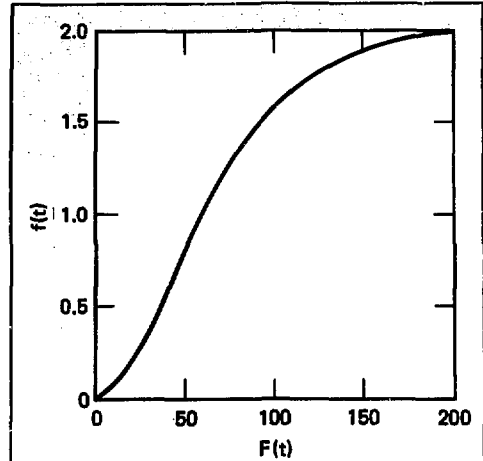


Fig. 4-6. The quantity  $f(t)$  [normalized energy under a Gaussian power pulse; see Eq. (11)] vs the quantity  $F(t)$  [normalized radius of pusher; see Eqs. (7) and (10)].

As noted earlier,  $\theta_e$  is small compared to  $\theta_i$ ; thus, Eq. (9) completes the  $\theta_i$  calculation ( $\eta$  is determined below). As a higher order correction, we can set  $\theta_e \approx m_p E(\tau^*)/3M_p$ , where  $r(\tau^*) = R_p$ , because the electrons heat up by conduction rather than by shock or compression.

For a practical application of this model we define two functions,  $F(t)$  and  $f(t)$ , plotted in Fig. 4-6 with  $t$  implicit. The function  $f(t)$  is simply a normalized integral of a Gaussian [ $f(t) = 1 + \text{erf}(0.017t - 5)$ ], which is clearly related to calculating  $E(\tau_E)$ . The function  $F(t)$  is proportional to  $\int t^{1/2} dt$  and is related to  $r = r(t)$  and, thus, to finding  $\tau_E$  [see Eq. (7)]. More precisely,  $\tau_E$  is found implicitly by

$$F(\tau_E) = 3.7 R^2 \Delta R^{1/2} \tau^{-3/2} \eta^{-1/2}, \quad (10)$$

with  $R$  and  $\Delta R$  in  $\mu\text{m}$ ,  $\tau$  in ps, and  $P$  in TW. Eq. (10) is derived from Eq. (7), with a Gaussian profile of FWHM  $\tau$  and peak absorbed power  $P$ . Thus,  $F(\tau_E)$  can be found from the initial conditions. Then Eq. (9) leads to

$$(\theta_e + \theta_i) = 60 P \tau R^{-2} \Delta R^{-1} \eta^{2/3} f(\tau_E) \text{ (keV)}, \quad (11)$$

where  $\eta$  is yet to be calculated, and  $f(\tau_E)$  can be read from Fig. 4-6 because  $F(\tau_E)$  is now known. The self-correcting aspect of this theory now becomes apparent. Suppose  $\alpha$  of Eq. (5) differs from  $1/2$  by a factor  $\beta$  (say  $\beta > 1$ ). Then,  $V_p$  will be  $\sqrt{\beta}$  greater and  $F(\tau_E)$  in

Eq. (10) will be  $1/\sqrt{\beta}$  smaller. In most cases of interest, we operate in the region of Fig. 4-6, where  $f \sim F^2$ ; as a result,  $f(\tau_E)$  will be  $1/\beta$  smaller and so will  $E(\tau_E)$ . But Eq. (5) leads to  $P_{ps} \sim \beta E(\tau_E) \sim \beta/\beta$ ; thus,  $P_{ps}$  remains unchanged and so does  $\theta_1 \sim P_{ps}$ .

From the discussion following Eq. (9), we set

$$\theta_e = 60 \text{ Pr} R^{-2} \Delta R^{-1} f(\tau^*)$$

$$F(\tau^*) \equiv 6.6 (1 - \eta^{-1/3}) F(\tau_E), \quad (12)$$

so that  $\theta_1$  can be determined unambiguously.

**Compression Calculation.** The compression- $\eta$  calculation is based on the conservation of mass, in which we equate the inner half of the pusher at time zero and at peak compression time. Thus,

$$(1/2) 4\pi R^2 (\Delta R) (2.5) = 4\pi \int_{R_f}^R \rho(r) r^2 dr, \quad (13)$$

where the 2.5 represents the initial glass density. We need to calculate  $\rho(r)$  at compression time. To a first approximation, we expect  $\rho(r) = \rho(R_f)(R_f/r)^2$ , which can be derived from the continuity equation  $(\partial \rho / \partial t) + r^{-2} \partial(\rho v_r r^2) / \partial r = 0$ . At peak compression time,  $(\partial \rho / \partial t) \approx v_r \approx 0$  at  $r = R_f$  and  $r = R$ ; consequently, by approximating  $v_r = \text{constant}$  for all  $R_f \leq r \leq R$ , we obtain  $\rho(r) \sim r^{-2}$ . Because at compression time the pressure at the glass-DT interface  $R_f$  is continuous, thermal conduction implies  $\rho(R_f)(\text{glass}) = \rho_r(DT) \equiv \eta \rho_0$ . Thus, performing the integral in Eq. (13) leads to

$$\eta = (1 + W)^3; W \equiv (1.25) \Delta R / R \rho_0 \quad (14)$$

Detailed studies of the one-dimensional LASNEX computer simulations show that for optimal targets, from 0.1 to 100 TW in absorbed powers, the glass density at peak compression time actually differs slightly from the first approximation  $(1/r^2)$  as derived above. We find that  $\rho(r) \approx \rho(R_f)(R_f/r)^{2/2}$ . This profile, applied to Eq. (13), gives

$$\eta = (1 + 1.5 W)^2 \quad (15)$$

**Yield Calculations.** With  $W$  from Eq. (14) and  $\eta$  from Eq. (15), we can now insert  $\eta^{2/3}$  into Eq. (11). After first finding  $\theta_e$  from Eq. (12), we can insert  $\theta_1$  from Eq. (11) into Eq. (4) along with  $\eta^{2/3}$  and thus calculate the yield. Figure 4-7 shows the comparison

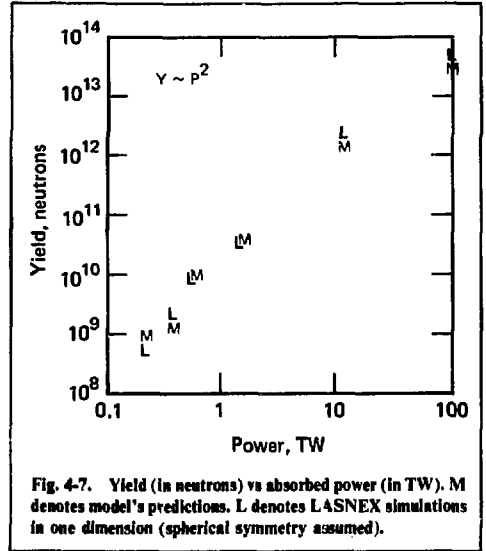


Fig. 4-7. Yield (in neutrons) vs absorbed power (in TW). M denotes model's predictions. L denotes LASNEX simulations in one dimension (spherical symmetry assumed).

between the simple model (M) and the complex LASNEX<sup>8</sup> code (L). Only the absorbed power is shown explicitly as ranging over three orders of magnitude. But the optimal targets for each power that are represented in the figure also have widely ranging parameters  $\rho_0$ ,  $R$ ,  $\Delta R$ , and  $\tau$ . Thus, we have subjected the model to a rigorous test, which it has passed. Note too that the curve follows the scaling of yield with power,  $Y \sim P^2$ , as predicted in Ref. 4.

Because our theoretical model assumes spherical symmetry, we have compared it with one-dimensional LASNEX simulations. The fact that the LASNEX code tracks the experimental yields quite accurately<sup>4,9</sup> is based on two-dimensional simulations. Imperfect spherical convergence (when the two beams are focused by  $f/2$  lenses) reduces  $\eta$ , and therefore  $\theta_1$ , and ultimately the yield  $Y$  by nearly an order of magnitude.

Note that other simple models perform just as well,<sup>4,9</sup> revealing an agreement similar to that indicated in Fig. 4-7. However, there is one test case in a region of parameter space in which the other simple models fail but this model succeeds in matching the LASNEX prediction of yields. Consider a target 200  $\mu\text{m}$  in radius, 1  $\mu\text{m}$  in thickness, 0.2  $\text{mg}/\text{cm}^3$  in DT density, 1/2 TW in absorbed power, and 750 ps FWHM. In such a case, Eq. (10) gives  $F(\tau_E) \approx 10$  and Fig. 4-6 (if it were better resolved near the origin) indicates  $f(\tau_E) = 0.075$ . Equation (15) gives  $\eta^{2/3} = 175$ . Equations (11) and (12) then produce  $\theta_1 = 7.2$  keV and thus a yield of  $5 \times 10^{10}$  neutrons. In comparison with these model values, LASNEX

predicted values are  $\eta^{2/3} = 200$ ,  $\theta_i = 7$  keV, and neutron yield =  $5 \times 10^{10}$ . The other models for the same case produce values of  $\eta^{2/3} = 54$ ,  $\theta_i = 2$  keV, and neutron yield =  $3 \times 10^8$ . The target for this test case differs from a "mainstream," exploding-pusher target as represented in Fig. 4-7: for 1/2 TW of absorbed power, its radius is twice that of a mainstream target, its DT fill is ten-fold less (DT mass is therefore the same), and its pulse is longer to match the larger radius. Despite these differences, its behavior is still that of an exploding pusher in that the center of the pusher hardly moves from its original radius. Thus, our model correctly treats this case while other models do not.

The reader is cautioned against using the formulation presented here in all parts of parameter space. If the pusher target is many hot-electron, mean free paths thick, we approach the ablative regime, because  $\lambda_{ee} \sim \theta_{eh}^2$  and for a "flux limited" hot-electron flux  $\theta_{eh} \sim I^{2/3} \sim (P/R^2)^{2/3}$ . (Plasma simulations seem to indicate a  $\theta_{eh} \sim I^{1/3}$  scaling.) Thus, in the ablative regime,  $\Delta R \gg \lambda_{ee} \sim P^{2/3} R^{-8/3}$ . If, in the other extreme, the pusher is quite thin, the suprathermal electrons decouple from the pusher, do not deposit their energy, and the pusher explodes inefficiently. In this regime  $\Delta R \ll \lambda_{ee}$ . Typical values are a  $\theta_{eh}$  of 10 keV for an intensity of  $10^{16}$  W/cm<sup>2</sup> (for 1  $\mu$ m laser light) and an approximately 1- $\mu$ m mean free path in glass for a 10-keV electron. Another regime in which the present model does not strictly hold is ion thermal quenching, in which the mean free path of a hot ion is larger than the compressed region. Thus, ion thermal conduction quenches the reaction even more quickly than hydrodynamic expansion cooling does. The criterion  $R_t < \lambda_i$  can be written  $\eta^{-1/3} R < \lambda_i \sim \theta_i^2 / \eta \rho_0$ . A 10-keV ion in DT compressed to liquid density has a mean free path of 10  $\mu$ m. Thus, when using this model, the reader should check *a posteriori* that these "forbidden" parts of parameter space have not been entered.

**Acknowledgments.** Thanks are extended to J. T. Larsen for his valuable comments and his expertise in simulating exploding-pusher targets. Thanks are also offered to E. Storm, G. E. McClellan, and D. F. Wright for their comments.

## References

1. J. H. Nuckolls, *Scaling of Exploding-Pusher Targets*, Lawrence Livermore Laboratory, Rept. UCRL-79834 (1977).
2. J. H. Nuckolls, L. Wood, A. Thiessen, and G. B. Zimmerman, "Laser Compression of Matter to Super-High Densities: Thermonuclear (CTR) Applications," *Nature* **239**, 139 (1972).
3. G. B. Zimmerman, *Non-Maxwellian Ion Distribution in Compressed Laser Targets*, Lawrence Livermore Laboratory, Rept. UCRL-76927 (1975).
4. Y. B. Zel'dovich and Y. P. Raiser, *Physics of Shock Waves and High-Temperature Hydrodynamic Phenomena* (Academic Press, New York, 1966).

5. G. B. Zimmerman, *Numerical Simulation of the High-Density Approach to Laser Fusion*, Lawrence Livermore Laboratory, Rept. UCRL-74811 (1973).
6. E. K. Storm, J. T. Larsen, J. H. Nuckolls, H. G. Ahlstrom, and K. R. Manes, *A Simple Scaling Model for Exploding-Pusher Targets*, Lawrence Livermore Laboratory, Report. UCRL-79788 (1977).

## Author

M. D. Rosen

### 4.2.3 Using Inner-Shell X Rays Produced by Collisions between Charged Particles and Atoms to Diagnose Implosion Characteristics of Inertially Confined Fusion Targets

In inertially confined fusion, the thermonuclear reaction, charged-particle deposition, and electron-ion heating rates are proportional to the fuel density  $\rho$ ; the confinement time is proportional to the fuel radius  $R$ . Therefore, the self-heating, burn efficiency, and thermonuclear burn propagation characteristics are determined by the density-radius product  $\rho R$ . An unambiguous experimental determination of the fuel  $\rho R$  is clearly necessary. Other factors that can greatly hinder the achievement of high fuel compression also need to be diagnosed. These factors are compression symmetry, pusher stability, and fuel-pusher mixing. We suggest a novel method that can diagnose all these quantities simultaneously.

The technique depends vitally on the detection of inner-shell x-rays produced by the Coulomb collision reaction,



where  $C$  represents the charged particles produced by the thermonuclear burn;  $A$ , the selected detector shell material (atom) placed between the fuel and pusher; and  $X$ , the inner-shell x ray (e.g.,  $K_\alpha$ ) characteristic of the atom  $A$ . We know the number of charged particles from an independent measurement of the thermonuclear neutron yield of the target, and we know the cross section for reaction (16). Therefore, the number of x rays produced is a direct measure of the  $\rho R$  achieved in the detector shell. Under certain assumptions, the fuel  $\rho R$  can be calculated from the measured detector shell  $\rho R$ . More significantly, if we image the x-ray line emission with sufficient resolution, the spatial distribution of the x-ray production can yield, simultaneously, compressed fuel size and symmetry, stability of the pusher, and the degree of pusher-fuel mixing.

Several important features of the technique are immediately apparent. (a) The required compression measurements are to be obtained at the burn time, which

is, in general, appreciably shorter than the implosion time. Using the thermonuclear reaction products in this technique eliminates the otherwise stringent timing requirement. (b) The x-ray energy used for the diagnosis can be varied freely to accommodate other diagnostic requirements, e.g., to minimize the effects of background and/or attenuation of the x rays in the target. Further, it is possible to mix several materials to obtain, at the same time, different x-ray line emissions. (c) The use of high-Z material in the detector shell can contribute to the shielding of the fuel against the detrimental effects of electron and/or x-ray preheat. (d) There are sufficient built-in redundancies to provide consistency checks.

For a typical exploding-pusher target consisting of a DT-filled glass microsphere, the 3.5-MeV  $\alpha$  particles and the 3-MeV protons produced, respectively, by DT and DD reactions can be used as the charged particles in reaction (16). The choice of the detector shell material is a compromise between the DT reaction yield,  $K_\alpha$  x-ray production cross section, and x-ray background.

Figure 4-8 shows that the x-ray bremsstrahlung backgrounds from the glass microsphere targets fall by about three orders of magnitude between 2 and 8 keV energy. The reduction becomes much less above 8 keV x-ray energy. Figure 4-9 shows that the variation of the  $K_\alpha$  x-ray production cross section has a weaker dependence on x-ray energy than the backgrounds between 2 and 8 keV. For maximum  $K_\alpha$  x-ray production and minimum target background, detector shell materials emitting about 8 keV  $K_\alpha$  x rays are reasonable choices.

We have studied the feasibility of using copper as the detector shell material, because copper  $K_\alpha$  x ray is about 8 keV and copper can be used for neutron-activation analysis [ $^{63}\text{Cu}(n,2n)^{62}\text{Cu}$ ] to give another independent check of the detector shell  $\rho R$  measurement.<sup>10</sup> The 8-keV x rays can be imaged with high efficiency ( $\geq 63\%$ ) by a quartz bent-crystal mirror to give the required compression quantities (more details below).<sup>11</sup> We estimate that a minimum DT thermonuclear reaction yield of about  $10^9$  is required to diagnose a detector shell  $\rho R$  of  $10^{-3}$  g/cm<sup>3</sup> using copper  $K_\alpha$  x rays and low-Z exploding-pusher targets.<sup>10</sup> A number of target experiments at the Argus laser system have had yields in excess of  $10^9$ . Therefore,  $\rho R$  determination by  $K_\alpha$  x-ray production can be achieved with low-Z exploding-pusher targets and existing laser systems.

For the ablation-driven inertially confined fusion targets that can compress fuel to high densities, the attenuation of the x rays produced in the detector shell by the target material may become large. The reduction in the x-ray flux can be offset by increasing the initial x-ray flux produced via reaction (16) (higher fusion yield from the target) while keeping the x-ray energy fixed. Alternatively, the x-ray energy can be increased by using higher Z material for the detector shell. [For

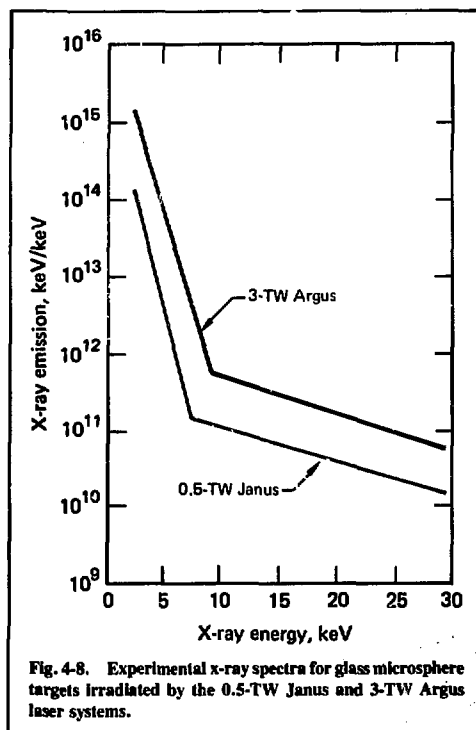


Fig. 4-8. Experimental x-ray spectra for glass microsphere targets irradiated by the 0.5-TW Janus and 3-TW Argus laser systems.

reference, 8-keV (Cu  $K_\alpha$ ) and 69-keV (Au  $K_\alpha$ ) x rays suffer about 50% attenuation on passing through, respectively, 2 and 44  $\mu\text{m}$  of gold at normal density.] Because the cross section for reaction (16) decreases rapidly with increasing Z of the detector shell material (see Fig. 4-9), higher fusion yields are again required to compensate for the lower production cross section. (The  $K_\alpha$  x-ray production cross sections by 3.5-MeV  $\alpha$  particles and 3-MeV protons on gold are, respectively, a few and tens of millibarns.) It is important to note that, because of the limited range of the charged particles emitted by DT and DD reactions, the x-ray flux produced by reaction (16) can be enhanced appreciably only by increasing the charged-particle flux instead of varying the detector shell  $\rho R$ . Too high a detector shell  $\rho R$  is ineffective in increasing the x-ray production and can contribute to the attenuation of the x rays produced elsewhere in the shell. However, this higher yield requirement for increasing Z of the detector shell material places only a moderate limitation on the range of applicability for the technique. The more restrictive constraints on the method are the consequences of the practical problems such as target fabrication and x-ray imaging. These are discussed below.

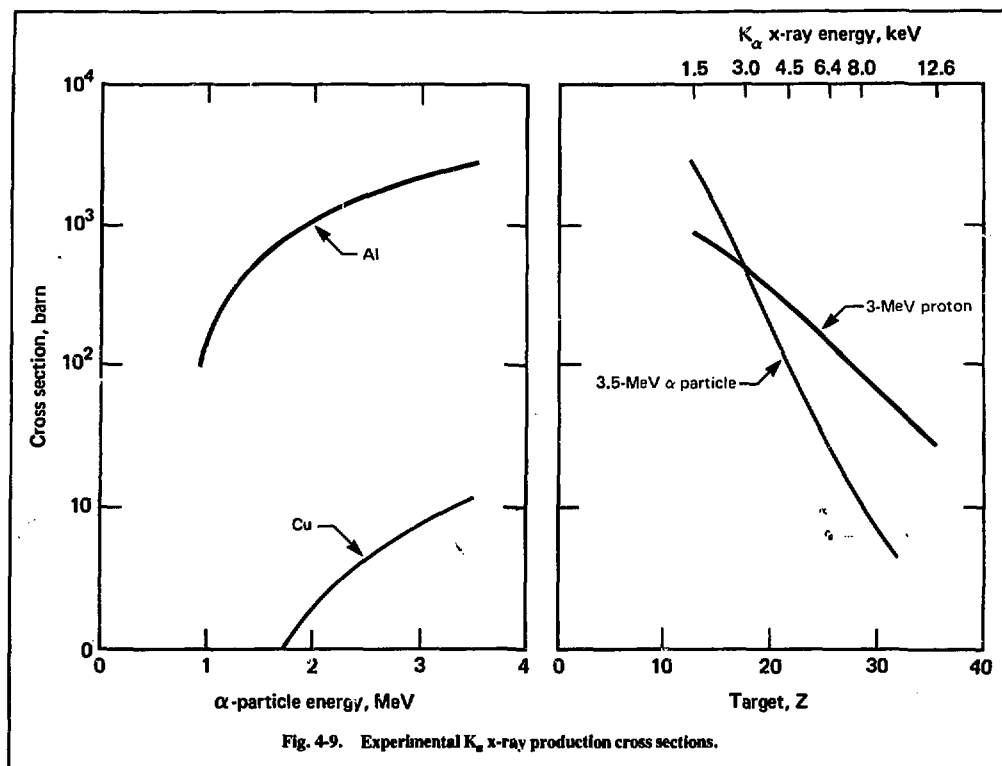


Fig. 4-9. Experimental  $K_{\alpha}$  x-ray production cross sections.

The difficulties in fabricating a target with a very thin detector shell of high-Z material on the inside surface (between the fuel and the main microsphere material) of a spherical target cannot be underestimated. It is, perhaps, possible to avoid most of the problems by using glass doped with the desired high-Z material in the target fabrication. For instance, if copper is replaced by zinc (8.6-keV  $K_{\alpha}$  x-ray energy) in the above example, then zinc borate glass (60% ZnO by weight) can be used to fabricate the glass microsphere.<sup>12</sup> The glass shell becomes both the pusher and the detector. Radiochemical analysis of neutron-activated zinc  $^{64}\text{Zn}(n,2n)^{65}\text{Zn}$  can still provide the independent check on the detector shell  $\rho R$ .

There are three options in the detection of the  $K_{\alpha}$  x rays produced in the detector shell. In decreasing order of difficulty and information content, they are: a two-dimensional image, a line (one-dimensional) image, and detecting the number of  $K_{\alpha}$  x rays produced (no spatial information).

**Two-Dimensional Image.** Two-dimensional images of the compressed detector shell from more than a single direction are necessary to give an unambiguous

determination of the fuel compression, symmetry, pusher stability, and fuel-pusher mixing. A properly contoured bent-crystal surface (two dimensions) would be required to reproduce the desired images. With the standard fabrication techniques, the distortions to the crystal structure would undoubtedly degrade the resolution obtainable and decrease the reflection efficiency. Nevertheless, high reflection efficiencies (40-50%) and a resolution of  $16\ \mu\text{m}$  have been obtained for x rays of about 2-keV energy, using spherical quartz mirrors.<sup>13</sup> Recently, wafers of quartz crystal have been made, using deposition techniques.<sup>13</sup> This development should simplify the bent-crystal fabrication difficulties, improve the resolution, and increase the reflection efficiency.

The Bragg angle and the width of the rocking curve of a crystal decrease with increasing x-ray energy. For example, the Bragg angles and the full widths of the rocking curve for  $10\bar{1}1$  plane of quartz are  $13^{\circ}19' - 8.8''$  and  $4^{\circ}48' - 3.9''$ , respectively, for 8- and 22-keV x rays.<sup>11</sup> This reduction in the Bragg angle as a function of x-ray energy forecasts increased spherical aberration effects. More importantly, the shrinking width of the rocking curve implies that more precise crystal alignment would

be required for higher x-ray energies. These constraints can be partially eased by the suitable choice of crystal material. Further, the undesirable spherical aberration effects can, in principle, be removed by the proper unfolding procedure.

**Line Image.** A one-dimensional image of the compressed detector shell can determine the fuel compression and the fuel-pusher mixing. Compression symmetry can be diagnosed by obtaining multiple one-dimensional images. These images can be obtained with cylindrical bent crystals. The constraints are similar to those discussed above for two-dimensional imaging, but the practical difficulties are much reduced.

**Detecting the Number of  $K_{\alpha}$  X Rays Produced.** The number of  $K_{\alpha}$  x rays produced in the detector shell is a measure of the compressed detector shell  $\rho R$ . An x-ray spectrometer can be used to obtain the required data. Detecting the number of x rays produced as a function of time with a spectrometer-streaking camera combination would reduce possible x-ray background and may also provide information about target implosion time.

Using the proper target, the compressed fuel  $\rho R$  can be determined by measuring the number of  $K_{\alpha}$  x rays produced in the detector shell. With moderate difficulty, multiple one-dimensional images of the compressed detector shell can be obtained to diagnose fuel compression, symmetry, and fuel-pusher mixing. Recent advances in crystal wafer fabrication may make two-dimensional x-ray imaging of the compressed target more feasible.

## References

10. Y. L. Pan and J. T. Larsen, "Problems with  $\rho R$  Measurements—Is There a Way Out?" *Bull. Am. Phys. Soc.* **22**, 1113 (1977); *Problems with  $\rho R$  Measurements—What Are the Ways Out?* Lawrence Livermore Laboratory, Rept. UCRL-79772 (1977).
11. G. Brogren, "The Reflection Properties of the  $10\bar{1}0$  Plane in Quartz," *Arkiv Fysik* **22**, 267 (1962).
12. *Handbook of Chemistry and Physics*, R. C. Weast, Ed. (CRC Press, Cleveland OH, 1974-75), 55th ed.
13. L. Knight, Lawrence Livermore Laboratory, private communication (1977).

## Author

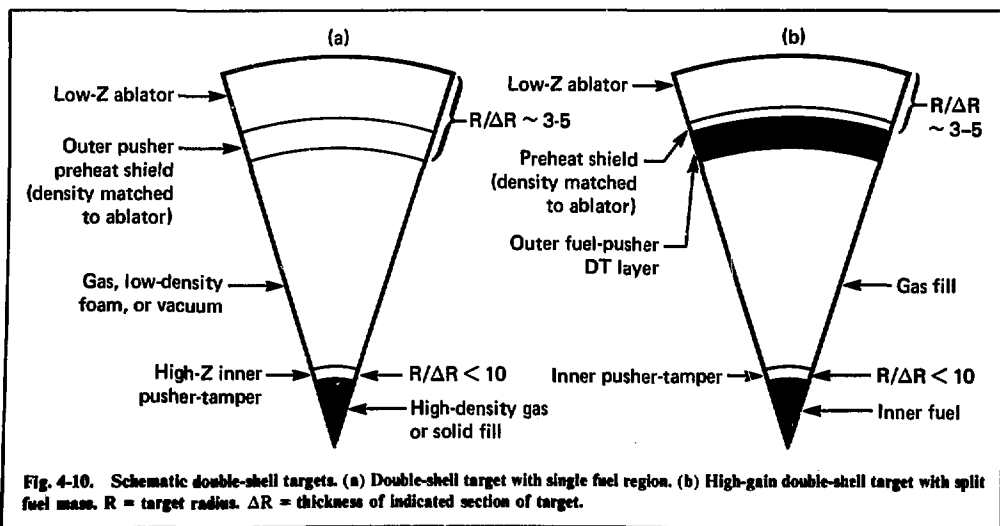
Y. L. Pan

### 4.2.4 Low-Aspect-Ratio Double Shells for High Density and High Gain

The outer shell of double-shell targets<sup>14-16</sup> discussed below is composed of a low-Z ablator and a pusher-preheat shield layer, as shown in Fig. 4-10(a), or a low-Z ablator, preheat shield, and outer fuel layer, as shown in Fig. 4-10(b). The material between shells is gas, low-density foam, or void. The inner shell is a high-Z, high-density material, and the fuel is high-density gas or solid.

By contrast with double-shell designs such as those in Ref. 15, the designs presented here have several unique features:

- Low-density outer pusher, density matched to the low-Z ablator. This feature reduces the growth of fluid instabilities at the pusher-ablator interface and



allows a larger volume, lower power, relatively stable implosion of the outer shell.

- Low-density, low-aspect-ratio outer shells that require less power and energy to implode to thermonuclear ignition velocities. This characteristic increases the target gain and reduces the required driver power.

- Low-density gas fill between shells. This feature minimizes mass between the shells and allows the large-volume, low-density outer shell to effectively implode the inner shell. In addition, when the gas is heated by compression, thermal electron conduction smoothing increases the implosion symmetry and reduces growth of fluid instabilities on the outer surface of the inner pusher. Low-level preheat also inhibits fluid instabilities at this interface by formation of favorable density gradients.

- A fuel layer, used as the outer pusher, that is ignited by the inner fuel. This feature results in very high gains.

The double-shell targets have several advantages over single-shell, high-gain targets:

- Relative insensitivity to preheat. Because of the high-density, high-Z layer surrounding the fuel at small radius, high-energy x rays and electrons are shielded from the fuel, which remains on a good adiabat. The preheat that does penetrate the inner shell does have a long time to act, however, as the outer shell runs in. To obtain this kind of preheat shielding in a single-shell target, the ablator would have to be moved into small radius to keep the mass of the preheat shield at a small enough value, and the laser power would have to be increased to accommodate the smaller volume.

- Insensitivity to laser pulse shaping. For the double-shell target with a single fuel layer, pulse shaping is not required because of the relatively massive high-density pusher surrounding the fuel. The double-fuel-layer target requires modest pulse shaping but is less sensitive to details of the pulse than a single-shell target.

- Low-intensity, low-velocity implosion. Because of velocity multiplication when the more massive outer shell collides with the inner shell, the velocities required for the outer shell are reduced. This means that light intensities on the ablator are lower, resulting in higher inverse bremsstrahlung absorption and less preheat.

Double shells have a relatively large convergence ratio, defined as the ratio of initial radius of the outer shell to final radius of the compressed fuel. Typical designs have convergence ratios of close to 100. However, the gas region provides some smoothing. Consequently, the required uniformity in implosion pressures is several percent. One way to achieve such symmetry is to use a long-wavelength laser early in the implosion. This long-wavelength light would be absorbed in a low-density corona produced by exploding a low-mass

shell outside the main target.<sup>17</sup> Many symmetrically arrayed laser beams could then be used to drive the system. For designs with a lower compression and smaller convergence, clamshell illumination would be adequate.

By controlling the amount of preheat, we can make the outer shell of the double-shell design quite insensitive to fluid instability. The inner shell is more sensitive to fluid instability and in reactor-scale high-performance designs may have to have 500-1000 Å surface finishes. This shell can be made somewhat less sensitive to instability by coating with lower density materials to produce a density gradient, and by allowing some preheat to decompress the outer portion before collision with the exterior shell.

Such designs, using 0.2- $\mu\text{m}$  light, achieve the following calculated performance levels for the listed absorbed energy:

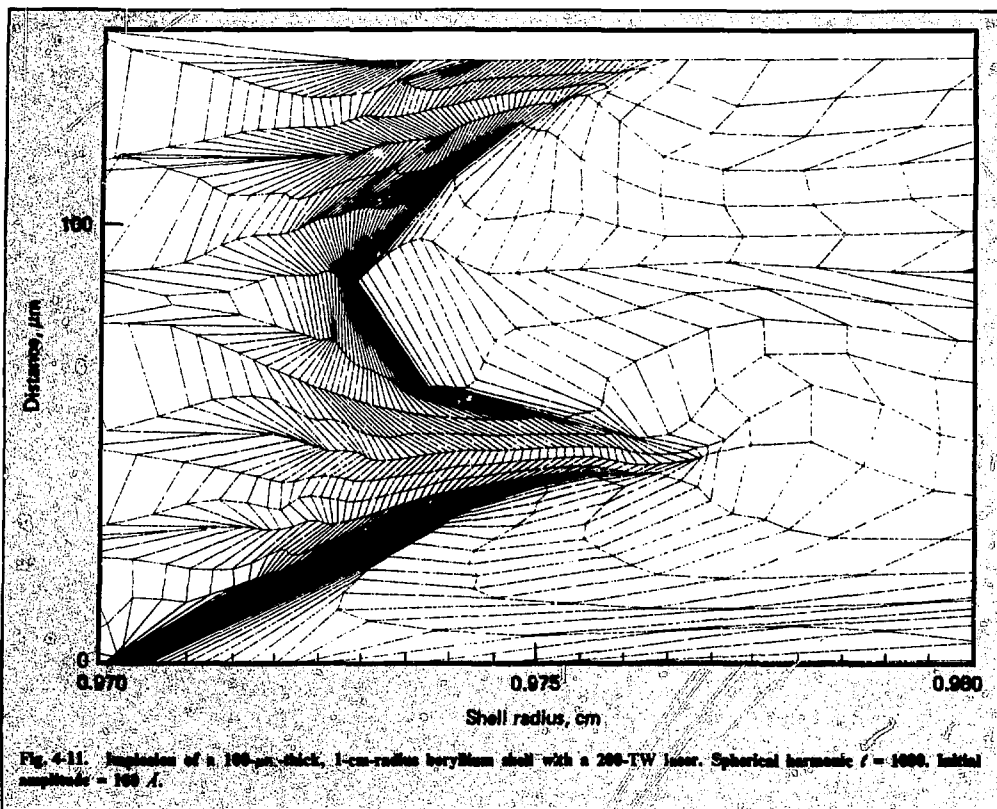
- 500-1000 $\times$  liquid density at 2 kJ,
- 10% or more of breakeven at 15 kJ,
- Gains > 10 at 200 kJ.

With 1- $\mu\text{m}$  light, the absorption efficiency is lower and preheat is more severe. These effects result in reduced performance, although designs have not yet been optimized. For example, 500-1000 $\times$  liquid density might require a Shiva-sized laser (15 kJ) instead of an Argus-sized laser (2 kJ).

Double-shell designs with all the fuel inside the inner shell have a limitation of 30-50 on the possible gain. This occurs because the massive high-Z pusher must be accelerated to velocities high enough to ignite the DT fuel, yet the pusher itself does not burn. Although required implosion velocities are typically reduced about 50% by the high-Z pusher, and although burn efficiency is increased by the tampering effect, the increase by a factor of 20-100 in imploded mass results in about an order of magnitude reduction in peak gain for targets in the 1-10 MJ size. However, it is possible to combine the velocity-multiplication effect of a double-shell target with the large fuel mass of a single shell to achieve very high gain. This is achieved by making most of the outer-shell pusher out of DT, as shown schematically in Fig. 4-10(b). By appropriate pulse shaping, the outer DT layer can act as a pusher for the inner shell.

Because of velocity multiplication between shells, such a design makes it possible to accelerate only the inner fuel to ignition velocities while accelerating most of the fuel mass to the lower velocity required for compression to the required density. The density times the radius of the outer fuel layer must be  $\geq 1$  before the inner fuel ignites, and the explosion of the inner fuel must be energetic enough to light the outer fuel. Such targets have one-dimensional calculated gains of 1000 on LASNEX with an input energy of about 4 MJ





and 150 TW. It should be possible to lower the energy and power requirements to about 1 MJ and 100 TW. Gains this high require high absorption efficiency and probably require a 0.2- $\mu$ m-wavelength laser, although work is continuing on designs that could use longer wavelengths.

Afanas'ev et al.<sup>16</sup> have proposed a very different class of targets, which they calculate to have a gain of 1000 at 1 MJ. The targets require the symmetric, stable implosion of very thin shells with ratios of target radius to shell thickness of  $\sim 100$ . Such targets have a convergence ratio three to four times greater than that of the double-shell targets presented above and are much more sensitive to preheat and fluid instabilities. Figure 4-11 shows LASNEX calculations of the condition of a 100/1 beryllium shell after moving less than 300  $\mu$ m. In this calculation, the perturbation started with a wavelength equal to the shell thickness at 1-cm radius and with an amplitude of 100  $\text{\AA}$ . These calculations indicate that the shells would not survive the implosions even with surface noise as small as a couple of angstroms.

The hydrodynamic efficiency of the targets as calculated by LASNEX is three to four times lower than the authors reported, so the gains are lower and the powers required are higher than reported. In addition, even in one-dimensional calculations, these targets require about the same energy per unit mass and only about 50% less power than the thick shells presented above. The intensity at the ablation surface is about an order of magnitude lower for the thin shells. Unless the 50% reduction in power or order-of-magnitude reduction in intensity is critical to success, the thick shells presented above represent a much lower risk approach to high-gain pellets.

## References

14. J. D. Lindl, unpublished calculations (1974).
15. R. C. Kirkpatrick, C. C. Cremer, L. C. Madsen, H. H. Rogers, and R. S. Cooper, "Structured Fusion Target Designs," *Nucl. Fusion* 15, 333 (1975).
16. J. D. Lindl and R. O. Bangerter, *Proc. Intern. Topical Conf. on Electron Beam Res. and Tech.*, Sandia Laboratories, Albuquerque, N.M. SAND-76-5122 (1975).

17. W. C. Mead and J. D. Lindl, *Symmetry and Illumination Uniformity Requirements for High-Density Laser-Driven Implosions*, Lawrence Livermore Laboratory, Rept. UCRL-78459 (1976).
18. Yu. V. Afanas'ev, N. G. Basov, P. P. Volosevich, E. G. Gamalii, O. N. Krokhin, S. P. Kurdyumov, E. I. Levanov, V. B. Rosanov, A. A. Samarskii, and A. N. Tikhonov, "Laser Initiation of Thermonuclear Reaction in Inhomogeneous Spherical Targets," *JETP Lett.* **21**, 68 (1975).

**Author**

**J. D. Lindl**

#### 4.2.5 High-Performance Inertial Confinement Fusion Targets

We consider inertial confinement fusion (ICF) target designs that may have very high gains ( $\sim 1000$ ) and low power requirements ( $< 100$  TW) for input energies of  $\sim 1$  MJ. These include targets having very low density shells, ultrathin shells, central ignitors, magnetic insulation, and nonablative acceleration.

The earliest ICF target designs were solid or hollow spheres of DT fuel.<sup>19</sup> Solid spherical targets have minimum fabrication cost. When imploded by high-performance lasers (in terms of wavelength, efficiency, power, repetition rate, and pulse shaping) these targets produce minimum-yield fusion microexplosions with high enough gains for practical applications, have near minimum laser energy requirements, and make possible minimum-size power plants ( $\sim$  a few hundred megawatts). An important disadvantage of solid targets is the very high power requirement, because the cost of ICF drivers generally increases with power.

Use of hollow rather than solid targets reduces the required driver power from more than 1000 TW to  $\sim 100$  TW. To relax the driver wavelength (or voltage) and efficiency requirements, we have increased the mass of the fuel in the canonical target. We have also introduced some intermediate and high-Z coatings for ablaters, shields, and pushers. The larger fuel mass has increased the required driver energy (to  $\sim 1$  MJ) but has relaxed the cost limitations on target fabrication (to 10-100 cents/pellet).

For some ICF driver technologies, improved target designs would be advantageous to further reduce the power and efficiency requirements. Increasing the target gain also increases the yield, which would allow further increase in the target fabrication cost. We consider several target designs that may achieve high performance levels.

**Theoretical Possibility of High Performance with Very Low Density Targets.** Consider a target (Fig. 4-12) that is made entirely of very low density materials ( $0.2$  g/cm<sup>3</sup>) and is moderately hollow ( $\Delta R/R \approx 0.1$ ,

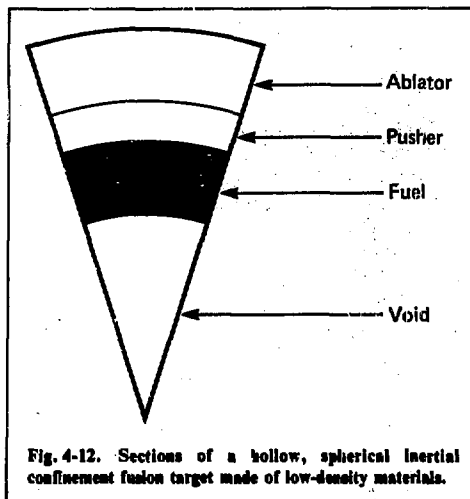


**Fig. 4-12.** Sections of a hollow, spherical inertial confinement fusion target made of low-density materials.

where  $\Delta R$  is the shell thickness and  $R$  is the shell radius). A gain of 1000 will be achieved if the following conditions are satisfied:

- Burn efficiency 40%,  $1.4 \times 10^{11}$  J/g,
- Implosion velocity  $2 \times 10^7$  cm/s,  $2 \times 10^7$  J/g,
- Implosion efficiency 14%,
- Mass of DT  $10^{-3}$  g.

The compressed spherical fuel density-radius product  $\rho r$  and the DT burn efficiency  $\phi$  are related by<sup>20</sup>

$$\frac{\phi}{1 - \phi} = \frac{r\rho}{6}.$$

Then  $r\rho \approx 4.5$  g/cm<sup>2</sup> for  $\phi = 0.4$ . For  $r\rho = 4.5$  and mass  $M = 10^{-3}$  g, the density is

$$\rho^2 = \frac{(4\pi/3)(r\rho)^3}{M}, \quad \rho = 600 \text{ g/cm}^3.$$

An implosion velocity of  $2 \times 10^7$  cm/s, corresponding to a specific energy of  $2 \times 10^7$  J/g, generates maximum density when the DT electrons are degenerate. Then

$$\text{Energy } \epsilon = \frac{3}{5} \epsilon_{\text{Fermi}} = 3 \times 10^5 \rho^{2/3} \text{ J/g},$$

$$\text{or } \rho \approx 600 \text{ g/cm}^3 \text{ when } \epsilon = 2 \times 10^7 \text{ J/g}.$$

The electron degeneracy condition is

$$\frac{5\pi^2}{12} \left( \frac{\theta}{\epsilon_{\text{Fermi}}} \right)^2 \ll 1,$$

or the electron temperature  $\theta \leq 100$  eV for  $\rho \approx 600$  g/cm<sup>2</sup>. Isentropic implosion may be achieved by pulse shaping.<sup>19</sup> To ignite an all-DT pellet, a central core having  $\rho r \approx 1/2$  g/cm<sup>2</sup> must be driven to  $\approx 10$  keV temperature.<sup>20</sup> The mass corresponding to 0.5 g/cm<sup>2</sup> is  $\sim 10^{-3}$  of the total, whereas the specific energy at 10 keV is  $\sim 10^2$  of the average, so the ignition energy is small compared to the energy of compression.

The implosion efficiency may be roughly estimated as follows. Assume the ablator weighs  $\approx 4$  mg and has a density of 0.2 g/cm<sup>3</sup>. Then, if the 5 mg of DT and ablator is initially a spherical shell with  $\Delta R/R \approx 1/10$ , the initial radius is  $\approx 3$  mm. If the average radius is 2 mm, corresponding to a volume of 1/30 cm<sup>3</sup>, an average driving pressure of  $\approx 5$  Mb is required to accelerate 1 mg to  $2 \times 10^7$  cm/s. If the peak pressure is 10 Mb, then for a 1- $\mu$ m laser the peak power is  $\approx 10$ -20 TW and the intensity is  $\approx 50$  TW/cm<sup>2</sup>.<sup>20,21</sup> Using the flux limit equation, an electron temperature of 400 eV follows, corresponding to a velocity of  $2.5 \times 10^7$  cm/s. The peak implosion efficiency is<sup>20</sup>

$$\begin{aligned} \text{Implosion efficiency} &\approx \frac{v_{\text{impl}}}{v_{\text{impl}} + K v_{\text{exh}}} \\ &\approx \frac{0.2}{0.2 + (3 \times 0.25)} \approx 0.2 \text{ peak} \end{aligned}$$

where  $v_{\text{exh}}$  is the velocity of the ablated material,  $v_{\text{impl}}$  is the velocity of the imploded material,  $K$  is a correction for the heating of the previously ablated material, and classical electron transport is assumed. At lower implosion velocities, the efficiency is smaller. LASNEX calculations with 1- $\mu$ m light show an average efficiency of somewhat less than 10%. This efficiency may be increased by use of shorter wavelength laser light.<sup>20</sup>

$$\begin{aligned} P &\sim I^{2/3} \rho_c^{1/3} \\ v_{\text{exh}} &\sim \left( \frac{1}{\rho_c} \right)^{2/3} \end{aligned}$$

At constant ablation pressure,

$$v_{\text{exh}} \sim \frac{1}{\rho_c} \sim \lambda^2,$$

where  $P$  is the ablation pressure,  $\rho_c$  is the critical density corresponding to laser wavelength  $\lambda$ , and  $I$  is the laser intensity. Hence, by reducing the wavelength, the exhaust velocity at constant ablation pressure may be reduced enough to increase the implosion efficiency to 15%.

To attain high performance levels in practical implosions, several important constraints must be observed, including (a) symmetry, (b) stability, (c) entropy, (d) absorption, and (e) fabrication.

(a) Symmetry. The implosion must be sufficiently spherically symmetric. In the example above, the central 1/2 g/cm<sup>2</sup> must be sufficiently spherical to ignite efficiently. Because the density is 600 g/cm<sup>3</sup>, the compressed radius is  $\approx 10^{-3}$  cm compared to an initial radius of 0.3 cm, a convergence ratio of 300. This implies implosion accuracies better than 1% [from  $\Delta r \sim \Delta(vt)$ ]. By use of multiple beams, electron transport in a low-density atmosphere, and shimming, it is theoretically possible to achieve such high convergence ratios.<sup>20</sup>

Shimming means correcting implosion asymmetries by introducing nonspherical variations in the shell radius and thickness during fabrication. To fully exploit shimming requires sufficiently accurate two-dimensional implosion codes, diagnostic methods capable of experimentally resolving asymmetries (e.g., radiochemical techniques), and highly reproducible drivers.

(b) Fluid instabilities. A very low density target shell may have a moderate aspect ratio ( $\sim 1/10$ ). Consequently the growth of fluid instabilities may be sufficiently controlled by density gradients in the ablation region having scale heights comparable to the wavelength of the most damaging perturbations. If necessary the scale height of the gradient may be controlled by introducing an energy spread in the electrons or ions that drive the ablation.<sup>22</sup>

(c) Entropy is controlled by pulse shaping and by avoiding excessive preheat. Experiments carried out at LLL and KMS Fusion, Inc. show that the modest pulse-shaping requirement of moderately hollow targets can be achieved. The preheat may be adequately controlled by shielding (seeding some high-Z material in the ablator material adjacent to the DT) and by enhancing inverse bremsstrahlung absorption (and reducing noncollisional absorption) by use of intermediate-Z ablators, short-wavelength lasers, and lower intensities.<sup>20</sup>

(d) Efficient absorption is obviously essential to high performance. Plasma instabilities and resonance phenomena do not absorb laser light efficiently.<sup>23</sup> Efficient absorption may be achieved by inverse bremsstrahlung at relatively low intensities ( $< 10^{14}$  W/cm<sup>2</sup>) in material with  $Z \approx 5$ -10 (higher  $Z$  materials may have excessive energy losses by x rays) with light that has a relatively favorable incidence angle and a short wavelength.

$$\begin{aligned} \text{absorption length} &\sim \rho^{-2} Z^{-1} \theta^{3/2} \lambda^{-2} \\ &\quad - \lambda^2 Z^{-1} \theta^{3/2} \end{aligned}$$

(e) Fabrication poses special problems for targets made entirely of very low density materials. Low-density foams are not sufficiently homogeneous. Otherwise, all these low-density materials are cryogenic in the liquid or solid state. In principle it is possible to make hollow shells of frozen DT and then coat these shells with mixtures of hydrogen and noble materials such as neon and argon. Alternatively, a solid sphere of liquid DT may be appropriately coated and then used to make a hollow gaseous target *in situ*.<sup>24, 25</sup> In this approach a spherically convergent laser pulse would suddenly melt or vaporize the pellet while strongly vaporizing a small region in the center. Expansion of this gaseous core would then generate the hollow sphere. Another alternative is to use either a spherical or parallel beam of laser light, ions, electrons, etc., to volume heat and vaporize an ultrathin target, which upon expansion would be transformed into a low-density target. This approach has the advantage that one or more shells in the ultrathin target need not be cryogenic during normal fabrication. An advantage of *in situ* fabrication is that, during expansion into vacuum, small fabrication imperfections would be healed. To avoid collapsing back to higher densities when the implosion pressure is applied, a preheat temperature of a few electron volts is required.

Although the above analysis indicates that gains of 1000 should be achievable with 100-kJ, 20-TW short-wavelength lasers imploding moderate-aspect-ratio low-density shells, detailed LASNEX calculations show much smaller gains. Typically, the compressional energy is severalfold higher than the theoretical minimum required to achieve efficient ignition. For hollow-shell implosions there is a conflict between the entropy and ignition conditions: It is difficult with laser energies < 1 MJ to find a pulse shape that implodes a hollow shell to high densities with small entropy changes ( $\theta \ll \epsilon_{\text{Fermi}}$ ) in the bulk of the fuel while causing the central core to reach ignition conditions ( $\theta \gg \epsilon_{\text{Fermi}}$ ). As the laser energy is increased to 1 MJ and larger, the theoretical gain of 1000 may be approached because the inertial burn time increases with DT mass, so the entropy and ignition requirements are relaxed.

**Targets with Very Thin Shells.** It has been proposed<sup>26</sup> that high performance levels may be achieved with targets having very high aspect ratio (1/100) shells of moderately high density materials (2-20 g/cm<sup>3</sup>), and that stable acceleration of such shells is feasible. Note that, if 2 g/cm<sup>3</sup> materials are used, the shell has the same mass at the same radius, but is 1/10 as thick at 10 times the density, as in the low-density approach described above. In power requirement the thinner, higher density shell has no significant advantage over the corresponding low-density shell:

$$\begin{aligned}\bar{P}R^3 &\sim \rho R^2 \Delta R v^2, \quad m \sim \rho R^2 \Delta R \\ \text{and} \\ \text{power} &\sim \bar{P}R^2 v \sim (m\rho \Delta R)^{1/2} v^3,\end{aligned}$$

where  $\bar{P}$  is the average implosion pressure,  $v$  is the implosion velocity, and  $m$  is the target mass. The key parameter is  $\rho \Delta R$ , so to a first approximation a low-density moderate-thickness shell has the same power requirement as a moderate-density ultrathin shell of the same  $\rho \Delta R$  and  $m$ . Similarly, the potential gain of the low-density shell is approximately the same as that of the higher density shell, providing some care is used in the initial stages of the pulse shape applied to the low-density shell. However, the thin shell is drastically less stable:

$$A = A_0 \exp \int \sqrt{\frac{2\pi}{\lambda}} a \, dt,$$

where  $A$  and  $A_0$  are the time-dependent and initial amplitudes of the fluid instabilities,  $\lambda$  is the wavelength, and  $a$  is the acceleration. Because the worst  $\lambda$  is  $\sim \Delta R$ , and  $at^2 \sim R$  for constant  $v$ , we have

$$A \sim A_0 \exp \sqrt{\frac{R}{\Delta R}},$$

so the thin shell has  $\sqrt{10}$  more e foldings of instability growth. Consequently, much longer wavelengths grow to disastrous amplitudes for the higher density shell than for the lower density shell. These wavelengths are so large that it is no longer possible to control their growth by density gradients, because the gradient scale height must be comparable to the wavelength and not enough material is in the shell to generate such scale heights. LASNEX calculations show disastrous failure during acceleration.<sup>27</sup>

It has been asserted that these ultrathin shells may be stabilized by other means, e.g., by faster acceleration,<sup>28</sup> by turbulence,<sup>29</sup> or by resonant acceleration.<sup>30, 31</sup> The slow acceleration conjecture is contradicted by LASNEX calculations. Turbulence stabilizes by density gradient formation, and, as noted above, not enough material is available to generate the required gradients. Resonant acceleration depends on the presence of some other damping mechanism, in this case density gradients, to control the growth of the modes whose growth rate is increased by the resonant driving. However, again density gradients are ineffective.

Overall, these ultrathin shells have no significant advantage in gain or power, a probably fatal instability, and only a minor advantage in pulse shaping.\* Some

\*LASNEX calculations show much smaller gains than claimed by Afanas'ev et al.<sup>27</sup>

noncryogenic shells (not including the DT fuel) may be fabricated, but an ultrasmooth surface finish is required. If several alternate cryogenic/noncryogenic layers are required to achieve central ignition, the fabrication problem appears to be extremely difficult.

However, one possible means of controlling the growth of fluid instabilities in ultrathin shells merits detailed calculation. Assume that the driving pressure is a few megabars or less. Then if heating by electrons, x rays, thermal waves, and shocks is kept sufficiently small, sufficient stabilization may be achieved by the shear strength of the shell, particularly when dynamic effects and the increase in shear strength and melting point with pressure are included. Calculations with two-dimensional elastic-plastic-hydrodynamic computer programs in which the stress is represented as a tensor and realistic stress-strain failure criteria are used predict substantial damping of fluid instabilities when the shear strength is of order 1% of the driving pressure.<sup>32</sup> However, if the shell is made too thin, then the growth of relatively long wavelength perturbations is not effectively controlled by material strength.

**Targets with Central Ignitors.** The performance of hollow targets may be increased somewhat by a small central ignitor.<sup>27</sup> The required implosion velocity of the outer shell may then be reduced from  $2 \times 10^7$  cm/s to  $\sim 1.4 \times 10^7$  cm/s. Twice as much fuel may then be imploded for the same energy to about one-third the density (200 g/cm<sup>3</sup>). For the low-density case considered above, the  $\rho r$  would change by  $(M\rho^2)^{1/3}$  or  $[2 \times (1/9)]^{1/3} \approx 0.6$ , from 4.5 g/cm<sup>2</sup> to 2.7 g/cm<sup>2</sup>. This would change the burn efficiency from 4.5/10.6 = 0.43 to 2.7/8.7 = 0.31. Hence the yield would increase by  $2 \times (0.31/0.43) = 1.45$ .

A cross section of a hollow shell with central ignitor is shown in Fig. 4-13. During convergence the inner part of the outer shell reaches velocities greater than  $1.4 \times 10^7$  cm/s. Upon collision with the relatively lightweight inner pusher, the velocity of the inner pusher multiplies to  $> 2 \times 10^7$  cm/s. This velocity is sufficient to compress and ignite the inner fuel. The inner fuel then produces sufficient energy to ignite the outer fuel through the intervening pusher (which, if necessary, could be fissionable by DT neutrons). A potential advantage of this approach is that the gas region is heated to several hundred electron volts, and that electron conduction in this region may improve the symmetry of the ignitor implosion. Two difficulties are mixing of the ignitor pusher material into the outer fuel, which would make ignition of the outer fuel more difficult, and fabrication. This target must be fabricated without introducing such large perturbations at the

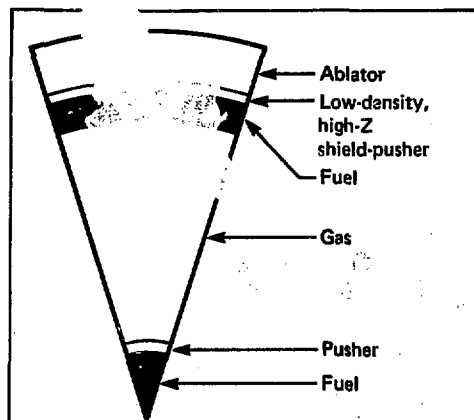


Fig. 4-13. Sector of a spherical inertial confinement fusion target having a central ignitor and an outer fuel layer. This target is capable of very high gains, and the required driving power is exceptionally low.

seams (when the ignitor is inserted through the outer shell) that the yield is seriously degraded. Finally, the outer surface of the ignitor pusher is driven purely hydrodynamically and must either be made relatively thick compared to the radius ( $\sim 1/6$ ) or have a surface finish  $< 1000$  Å, and possibly both.

Noncentral ignitors are also possible. A layer of high-Z material may be used in the fuel shell. To achieve very low density, high-Z material, a mixture of DT and Xe may be used. Then the shell may be relatively thick. There are a number of variations of the central ignitor; e.g., the central fuel may itself be moderately hollow, and/or the ignitor pusher may be light and low density, etc. These possibilities are being examined.

**Targets with Magnetic Insulation.** The implosion velocity required to reach thermonuclear temperatures may also be reduced if the ignited region contains a magnetic field to reduce cooling by electron conduction, and if the density is low enough that cooling by bremsstrahlung is not dominant.<sup>33</sup> However, with drivers capable of generating high energy densities, use of magnetic insulation does not lead to significant increases in gains or reductions in power, because reducing the implosion velocity reduces the DT density and burn efficiency (as in the ignitor example). In addition, the critical size and ignition velocity of the DT is limited by ion conduction as well as by how large an initial magnetic field it is practical to generate. Finally, for a minimum mass of low-density DT to ignite an adjacent larger mass region of high-density DT, the density mismatch must not be too large ( $\geq 10$ ). Otherwise, the

\*Conceptually this design is intermediate between solid and hollow designs.

front propagated into the dense DT is not strong enough to achieve ignition.

**Nonablative Acceleration.** The two principal inefficiencies in the ICF fusion process are in the: ablative implosion and in the driver: the former is of order 10% efficient, and the latter may be substantially less than 10% efficient. We consider the following ideal—apparently impractical—scheme in which the input energy to the target is reduced from 1 MJ to 100 kJ, the input energy to the driver reduced from more than 10 MJ to of order 100 kJ, and the driver power reduced from  $\sim 100$  TW to  $\sim 1$  GW. (With the resulting gains  $\sim 1000$ , the driver energy and pellet mass could of course be reduced by one or more orders of magnitude to make smaller reactors, or to make gigawatt-size reactors with higher driver repetition rates.) Imagine the spherical surface of a hollow DT shell divided into sectors, e.g., 12 pentagonal sectors. Each of these sectors is to be accelerated magnetically or electrostatically with high efficiency in a "gun" to a velocity of  $2 \times 10^7$  cm/s.\* If the acceleration and aiming could be precise enough, the 12 sectors could be assembled to form a sufficiently perfect spherical shell moving inward at  $2 \times 10^7$  cm/s.

A less efficient and less demanding scheme technologically is to electrostatically or magnetically accelerate  $10\text{--}10^4$  small pellets to velocities of  $2 \times 10^7$  cm/s over a distance of about 1 km. These pellets are directed spherically symmetrically onto a target, where they are vaporized by impact with a thin outer shell and jets penetrate into a region of gas. The deposition of energy in the gas heats it to temperatures of 100 eV, generating pressures of  $\approx 10$  Mb. Electron conduction strongly smooths the irregularities caused by the finite number of pellets. This pressure implodes a double-shell target with a thick low-density outer shell (Fig. 4-14).

The practicality of this approach depends on the technical details of the pellet-accelerating system, which are not yet fully analyzed. Under some conditions it may be advantageous to accelerate the multiple pellets ablatively with lasers. Calculations<sup>34</sup> show that medium-to-short-wavelength lasers operating in a relatively high efficiency ( $> 100\%$ ) mode can accelerate pellets to  $2 \times 10^7$  cm/s in distances of  $\sim 100$  m with an ablative efficiency of  $\sim 10\text{--}20\%$ . Most important, the laser power is reduced more than 1000 fold from  $\sim 100$  TW to  $\leq 10\text{--}100$  GW. Unfortunately, for  $\text{CO}_2$  lasers the ablation efficiency is only a few percent.

**Summary.** Advanced target designs seem capable of approaching gain 1000 with appropriate 1-MJ, 100-TW drivers. These targets seem well suited to im-

plosion by lasers, ions, and electron beams, and possibly also by a large number of tiny pellets.

## References

19. L. Nuckolls, L. Wood, A. Thiessen, and G. Zimmerman, "Laser Compression of Matter to Super-High Densities: Thermonuclear (CTD) Applications," *Nature* **239**, 139 (1972).
20. J. Nuckolls, *Laser Interaction and Related Phenomena* (Plenum Press, New York, 1974), Vol. 3, pp. 399 ff.
21. R. Kidder, *Physics of High Energy Density* (Academic Press, New York, 1969), p. 315.
22. J. Lindl, R. O. Bangerter, J. H. Nuckolls, W. C. Mead, and J. J. Thomson, *Effects of Density Gradient Modification on Fluid Instability in Thermonuclear Micro-Implosions*, Lawrence Livermore Laboratory, Rept. UCRL-78470 (1976).
23. K. Manes, V. C. Rupert, J. M. Auerbach, P. Lee, and J. E. Swain, "Polarization and Angular Dependence of  $1.06\text{-}\mu\text{m}$  Laser Light Absorption by Planar Plasmas," *Phys. Rev. Lett.* **39**, 281 (1977).
24. S. I. Anisimov, M. F. Ivanov, P. P. Pashinin, and A. M. Prokhorov, "Gas Shell Target for Laser Initiation of Thermonuclear Reactions," *JETP Lett.* **22**, 161 (1975).
25. J. Daiber, A. Hertzberg, and C. E. Wittliff, "Laser-Generated Implosions," *Phys. Fluids* **9**, 617 (1966).
26. Yu. Afanas'ev, N. G. Basov, P. P. Volosevich, E. G. Gamalii, O. N. Krokhin, S. P. Kurdyumov, E. I. Levanov, V. B. Rozanov, A. A. Samarskii, and A. N. Tikhonov, "Laser Initiation of Thermonuclear Reaction in Inhomogeneous Spherical Targets," *JETP Lett.* **21**, 68 (1975).
27. J. Lindl, *Low-Aspect-Ratio Double-Shell Targets for High Density and High Gain and a Comparison with Ultrathin Shells*, Lawrence Livermore Laboratory, Rept. UCRL-79735, Rev. 1 (1977).
28. Yu. Afanas'ev, N. G. Basov, E. G. Gamalii, O. N. Krokhin, and V. B. Rozanov, "Symmetry and Stability of Laser-Driven Compression of Thermonuclear Targets," *JETP Lett.* **23**, 566 (1976).
29. S. Z. Belen'sii and E. S. Fradkin, *Tr. Inst. Fiz. Akad. Nauk SSR, im P. M. Lebedeva* **29** (1965).
30. G. Wolf, "The Dynamic Stabilization of the Rayleigh Taylor Instability and the Corresponding Dynamic Equilibrium," *Z. Physik* **227**, 291 (1969).
31. J. Boris, "Dynamic Stabilization of the Imploding Shell Rayleigh Taylor Instability," *Comments on Plasma Physics and Controlled Fusion* **31**, (1977).
32. G. Maenchen, Lawrence Livermore Laboratory, private communication (1977).
33. D. J. Meeker, J. H. Nuckolls, and R. O. Bangerter, *Fusion Targets Designed to Match Present Relativistic Electron Beam Machine Parameters*, Lawrence Livermore Laboratory, Rept. UCRL-77045 (1976).
34. T. McCann and J. S. DeGroot, *Acceleration of Solid Macro-Particles by Laser-Produced Ablation*, Lawrence Livermore Laboratory, Rept. UCRL-79732 (1977).

## Authors

J. H. Nuckolls  
R. O. Bangerter  
J. D. Lindl  
W. C. Mead  
Y. L. Pan

\*The required acceleration length is  $\gg 100$  m.

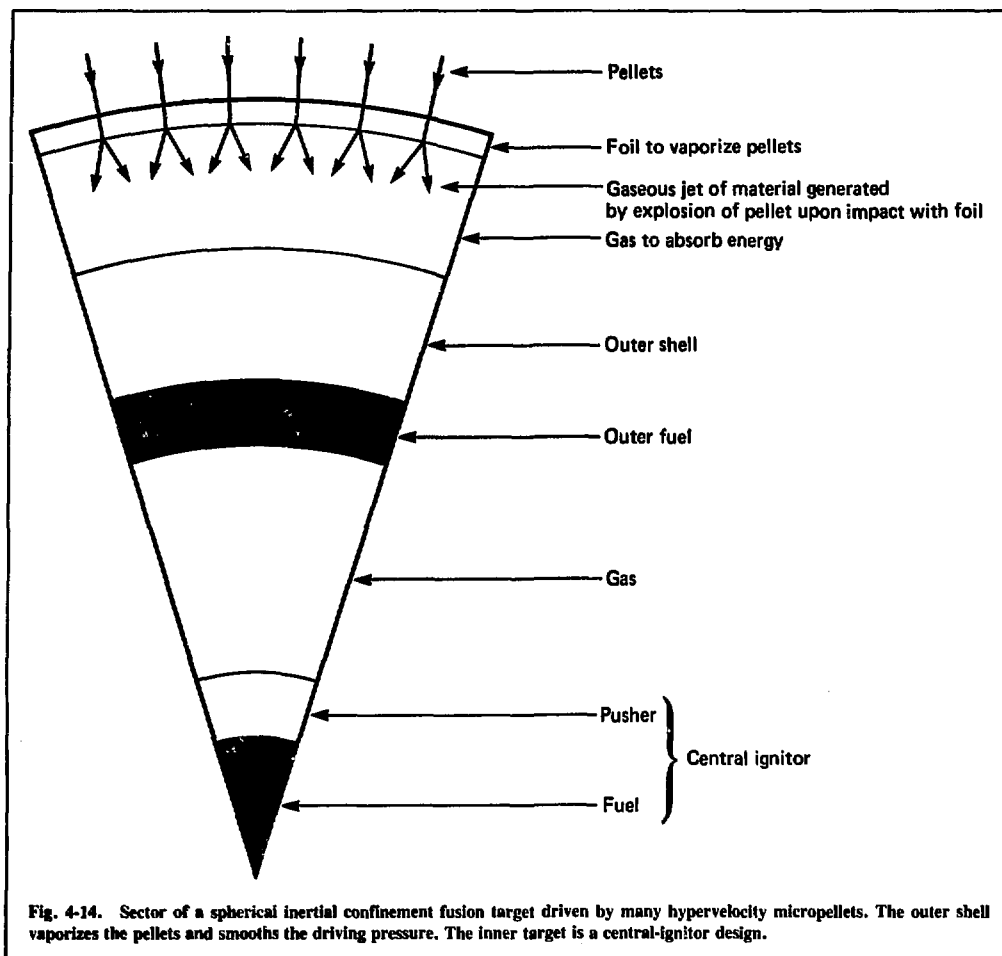


Fig. 4-14. Sector of a spherical inertial confinement fusion target driven by many hypervelocity micropellets. The outer shell vaporizes the pellets and smooths the driving pressure. The inner target is a central-ignitor design.

#### 4.2.6 Acceleration of Solid Macroparticles by Laser-Produced Ablation

The kinetic energy resulting from the acceleration of macroparticles (order 0.1 g) to velocities in excess of  $10^6$  cm/s can be used for strong shock generation, fusion studies, and fueling thermonuclear reactors. We have performed a computational study of the feasibility of accelerating a macroparticle (BB) with laser light.

Reaction to the laser-produced blowoff from one-sided laser illumination accelerates the BB. Laser-produced blowoff results when a laser beam of sufficient intensity ( $> 1 \text{ GW/cm}^2$ ) strikes a solid surface. Intensity sufficiency is established by requiring a phase change at the surface of the material. This condition

also ensures that the thermal wave, which is controlled by thermal diffusion, is closely coupled to the ablation wave. This coupling results because thermal conductivity is a strong function of temperature for heated material that produces a sharp leading edge on the thermal wave. The velocity of the heat wave is proportional to  $z/\sqrt{t}$ , where  $z$  is the spatial coordinate and  $t$  the temporal coordinate, which reduces in time.

At some point the heat diffusivity cannot provide enough heat flow out of the absorbing layer.<sup>35</sup> Thus, the temperature of the substance increases until evaporation of the surface material is responsible for heat removal. Then, thermodiffusivity stops playing a significant role and leads only to a comparatively thin

heated layer in the solid substance that is attached to the surface of the ablation wave.

Evaporation, dissociation, ionization, and creation of a laser-supported ablation wave result when this intensity minimum is exceeded. The process is depicted schematically in Fig. 4-15. The laser intensity is constrained from above by the material yield strength, producing a solid-density BB.

Understanding ablation and how to optimize laser-produced ablation comes in part from ablation modeling in the current literature. However, to gain more detailed insight into ablation than is possible from ideal models, it is necessary to perform hydrodynamic calculations that include the pertinent physics.

The threshold laser flux for ablation to be the dominant heat-removal mechanism may be estimated by comparing the specific energy in the heated zone to the energy required for phase change. The thickness of the heated zone at time  $t$  is of order of magnitude  $(at)^{1/2}$ , where  $a$  is the thermodiffusivity. The thermal energy produced at the surface up to time  $t$  is bounded by  $\phi_{abs}t$ , where  $\phi_{abs}$  is the absorbed laser flux. The specific energy of the heated zone at time  $t$  is then  $\phi_{abs}t/(\rho_0^2 at)^{1/2}$ , where  $\rho_0$  is the initial density. For vaporization to occur, the specific thermal energy should be equal to the vaporization (sublimation) specific energy  $U$  during time  $t$ , which would not exceed the laser pulse length  $\tau$ . Mathematically, this physical condition may be stated

$$\frac{\phi_{abs}t}{(\rho_0^2 at)^{1/2}} = U < \frac{\phi_{abs}\tau^{1/2}}{\rho_0 a^{1/2}} \quad (17)$$

or

$$\phi_{abs} > \frac{\rho_0 a^{1/2} U}{\tau^{1/2}} \quad (18)$$

Equation (18) specifies the threshold laser flux for surface vaporization and the minimum flux for which the vaporization of material plays the primary role in heat removal. To get an order-of-magnitude answer for the flux implied by Eq. (18), we use a handbook value for the heat of vaporization for glass ( $\text{SiO}_2$ ) of  $3.5 \times 10^{11}$  erg/g and pick  $10^{-2}$  cm<sup>2</sup>/s as the thermodiffusivity of glass, which is about an order of magnitude less than the thermodiffusivity for a good conductor. Hence, for this case the threshold flux is given by

$$\phi_{abs} = \frac{8.4 \times 10^3 \text{ W} \cdot \text{s}^{1/2}}{\tau^{1/2} \text{ cm}^2} \quad (19)$$

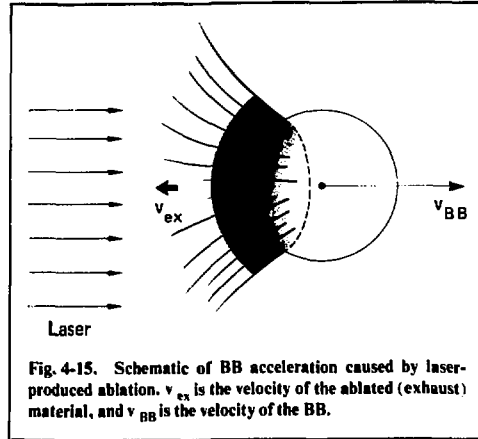


Fig. 4-15. Schematic of BB acceleration caused by laser-produced ablation.  $v_{ex}$  is the velocity of the ablated (exhaust) material, and  $v_{BB}$  is the velocity of the BB.

Suppose we want an absorbed laser flux large enough that the ablation mechanism dominates after the first 0.1 ns of the pulse. Then  $\phi_{abs} > 8.4 \times 10^8$  W/cm<sup>2</sup>.

One- and two-dimensional Lagrangian hydrodynamic calculations are performed using the LAS-NEX magnetohydrodynamic computer code. The results of these calculations are then used to infer laser intensity  $I$  and scaling laws for ablation pressure  $(\rho_a I)^{1/2}$  and mass flow rate  $(\rho_a^3 I)^{1/4}$ , where  $\rho_a$  is the density at the absorption surface. Pressure scaling is explained by energy partitioning as a function of intensity (see Table 4-2). Note that, as the intensity increases, a decreasing fraction of the energy is plasma thermal energy and an increasing fraction is reradiated. This accounts for the ablation pressure scaling with  $I^{1/2}$  rather than  $I^{2/3}$  as expected when radiation loss is neglected.<sup>36</sup> Once

Table 4-2. Energy partitioning as a function of intensity.

$I_L^a$ GW/cm <sup>2</sup>	$I_R^b / I_L$	$I_K^c / I_L$	$I_T^d / I_L$
4	0.50	0.22	0.28
7	0.54	0.22	0.24
10	0.56	0.22	0.22
15	0.58	0.22	0.20
20	0.60	0.22	0.18
40	0.64	0.21	0.15

<sup>a</sup> $I_L$  = Absorbed laser intensity.

<sup>b</sup> $I_R$  = Reradiated intensity.

<sup>c</sup> $I_K$  = Intensity that results in kinetic energy.

<sup>d</sup> $I_T$  = Intensity that results in plasma thermal energy.



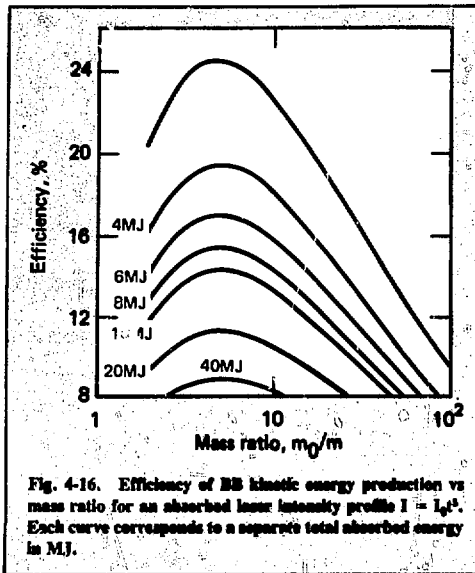


Fig. 4-16. Efficiency of BB kinetic energy production vs mass ratio for an absorbed laser intensity profile  $I = I_0 t^n$ . Each curve corresponds to a separate total absorbed energy in MJ.

ablation pressure scaling is established, mass flow scaling follows. Specifically, since  $\rho \propto (\rho_a I)^{1/2}$ , then  $T \propto (I/\rho_a)^{1/2}$  and the sound speed  $C_s \propto T^{1/2}$ , which, when coupled with mass conservation  $\dot{m} = \rho_a C_s$ , yields  $\dot{m} \propto (\rho_a I)^{1/4}$ .

To optimize the efficiency of BB kinetic energy production, the ablation parameter scalings found from the LASNEX calculations are used to calculate variations in laser intensity temporal profiles. First, a one-term power law temporal profile  $I = I_0 t^n$  is chosen, where  $t$  is the elapsed time and  $n$  is a variable parameter. The rocket equation is solved for the BB velocity. Variations in the intensity profile are made by changing  $n$  under the constraint that the total absorbed energy remains constant. Also, the energy is deposited during the time  $t_{ub}$  required to ablate all the initial mass. Second, a Gaussian temporal intensity shape  $I = I_0 e^{-t^2/t_c^2/2\sigma^2}$  is chosen, and the ratio  $t_c/\sigma$  is varied under the same constraints as the power law variation. The optimized intensity profile from both variation calculations increases the efficiency of BB kinetic energy production by less than 25% when compared to kinetic energy produced by an intensity that is constant in time.

We find from these studies that the efficiency with which BB kinetic energy can be produced from laser light varies inversely with absorbed laser energy, as depicted in Fig. 4-16. Here, the efficiency as a function of mass ratio for various total absorbed laser energies is plotted. These calculations are performed using 5- $\mu\text{m}$  laser light incident on a one-dimensional plasma slab of  $\text{SiO}_2$  initially at 0.1-eV temperature (1160K), which is

below the melting temperature of glass. The efficiency decreases from about 20% to roughly 10% by an increase in absorbed energy from 4 to 40 MJ. Allowing only efficiencies greater than 10% restricts the absorbed energy to values less than 20 MJ for 5- $\mu\text{m}$  light.

From two-dimensional LASNEX calculations we find that the density at the absorption surface  $\rho_a$ , at which most of the light is absorbed, is not a strong function of laser wavelength. In fact, the bulk of 1- $\mu\text{m}$  laser light in the  $10^{10} \text{ W/cm}^2$  intensity regime is absorbed at densities not very different from that for 10- $\mu\text{m}$  light. The density for 1- $\mu\text{m}$  light is 6 times greater than for 10- $\mu\text{m}$  light, whereas the critical density for 1- $\mu\text{m}$  light is 100 times greater than for 10- $\mu\text{m}$  light. This fact is due to the two-dimensionality of the expansion plume behind accelerating BB's coupled with the density and temperature nonlinearity of the inverse bremsstrahlung absorption coefficient.

A design of a BB accelerator can now be given. Suppose we desire a BB accelerator that produces 1 MJ of solid-density kinetic energy with final BB velocity of 20 cm/ $\mu\text{s}$ . Also suppose the laser is a large  $\text{CO}_2$  laser that produces constant-intensity laser light for  $t_{ub}$ , where  $t_{ub} = m_0/\dot{m}$ , i.e., the ratio of the initial mass to the mass flow rate. We assume, consistent with our calculations, that BB kinetic energy is produced with 10% efficiency from absorbed laser energy. Hence,  $I = 10E_k/t_{ub}$ , where  $E_k$  is the final BB kinetic energy. Letting  $m_0 = 0.5 \text{ g/cm}^2$  and  $\rho_c = 4 \times 10^{-5} \text{ g/cm}^3$  ( $Z = 10$  for  $\text{SiO}_2$ ) completes the specification of the problem. Calculated quantities are listed in Table 4-3.

Table 4-3. Typical design of a BB accelerator.

Variable	Equation	Value
Mass flow rate	$\dot{m} = B(\rho_a^3 C I)^{1/4}$	48.8 g/cm <sup>2</sup> s
Burnup time	$t_{ub} = \frac{m_0}{\dot{m}}$	0.01 s
Intensity	$I = \frac{10E_k}{t_{ub}}$	1 GW/cm <sup>2</sup>
Ablation pressure	$P_A = A(\rho_a I)^{1/2}$	0.43 kbar
Effective exhaust velocity	$v_{ex} = P_A/\dot{m}$	8.63 cm/ $\mu\text{s}$
Final mass	$m = m_0 e^{-v_{BB}/v_{ex}}$	0.05 g/cm <sup>2</sup>
Accelerator length	$s = v_{ex} t_{ub} \frac{m}{m_0} (1 - \ln m/m_0)$	0.29 km

$$A = 0.0039.$$

$$B = 0.0268.$$

$$C = 3 \times 10^{10} \text{ cm/s}.$$

This design allows for a conservative ablation pressure, hence a relatively long acceleration time and accelerator length. For acceleration times of  $10^{-2}$  s we would expect Rayleigh-Taylor instability growth to be destructive in a fluid-fluid case. However, even though the acceleration time is  $10^5$  times the minimum Rayleigh-Taylor e-fold growth time, we expect the elasticity of the solid material coupled with material strength to damp any Rayleigh-Taylor growth in BB acceleration.

Interesting engineering problems arise as to how to keep the BB within the laser beam during the entire acceleration time. Several preliminary answers that require much more detailed study are proposed:

- Use small steering lasers that are incident radially and that rely on feedback from a target-finding laser system for their direction.

- Use magnetic guide fields and metallic BB's.

- Shape the BB's for optimum stability.

These and many other engineering questions could be solved for a practical design of a laser ablation acceleration.

## References

35. O. N. Krokhin, "High-Temperature and Plasma Phenomena Induced by Laser Radiation," in *Physics of High Energy Density*, P. Caldirola and H. Knoepfel, Eds. (Academic Press, New York, 1971), 278-282.
36. R. E. Kidder, "Interaction of Intense Photon and Electron Beams on the Plasmas," in *Physics of High Energy Density*, P. Caldirola and H. Knoepfel, Eds. (Academic Press, New York, 1970), p. 318.

## Authors

T. E. McCann

J. S. DeGroot

## 4.2.7 Calculation of Actinide Burnup in ICF Pellets

To evaluate the potential of advanced inertial confinement fusion (ICF) target designs for a possibly important future application, we performed Monte Carlo calculations of neutron reactions on actinide isotopes mixed with the fuel. The application in question is ICF pellet center burnup of fission reactor waste, i.e., 14-MeV neutron fission of the very long lived actinides that pose storage problems. The pellet performance parameters calculated provide some quantitative input to systems studies of various burnup reactor concepts and fission economy plans.

Ultrahigh-gain reactor pellet designs have been discussed elsewhere. The present calculations were based on a relatively conservative, simple, one-shell design (by J. D. Lindl) with a gain of order 300. The imploded configuration of this standard pellet is reached after using about 6 MJ of laser energy, and the resulting thermonuclear yield is 1800 MJ. The same pellet configuration with its imploded density doubled served as an example of a design with improved transmutation.

A transfer matrix formed from the most recent evaluated-nuclear-data library (ENDL) neutron cross sections is used to calculate the neutron transport, reactions, and redistribution of neutrons among energy groups. Figure 4-17 shows the time-integrated neutron

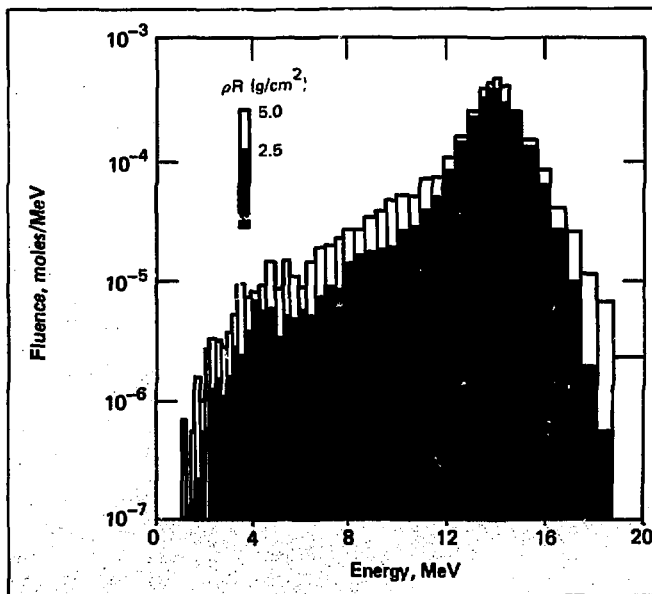
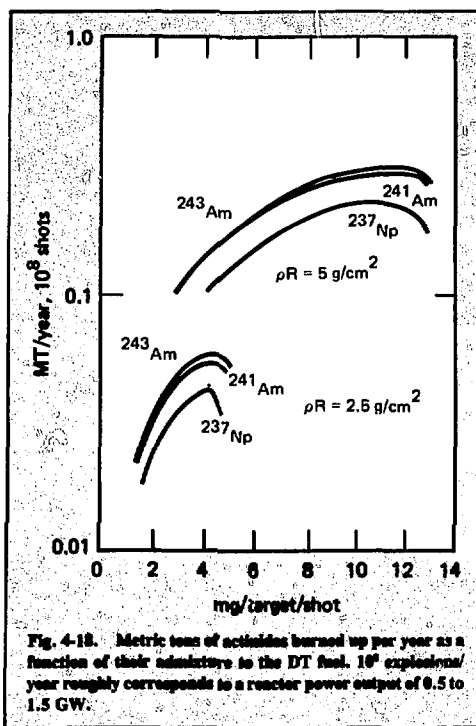


Fig. 4-17. Neutron spectra for pellets in which  $\rho R = 2.5$  and  $5 \text{ g/cm}^2$ .



spectra for the fuel region of pellets in which the fuel density  $\rho$  times the fuel radius  $R$  equals 2.5 and 5.0 g/cm<sup>2</sup>. The amount of downscattering is noticeably different from some published estimates<sup>37</sup> that did not involve the detailed explosion simulations and extensive Monte Carlo calculations performed here. The high-energy ( $> 15$  MeV) neutrons contribute noticeably to the burnup by fast fission.

Figure 4-18 depicts our burnup results. The nonelastic reactions explicitly followed for each isotope in questions are  $(n,n')$ ,  $(n,2n)$ ,  $(n,3n)$ ,  $(n,4n)$ ,  $(n,\gamma)$ , and  $(n,\text{fission})$ . The actual loss per target seed is plotted in Fig. 4-18 as metric tons burned up for  $10^8$  shots. The curves turn over because increased admixture of high-Z material to the fuel eventually squelches the thermonuclear bootstrapping by absorptive progresses. The limits in the ratio of burned to admixed actinides as depicted in Fig. 4-18 indicate that a few milligrams of active material accumulate from each shot. These are, however, similar to the amounts of tritium and activated first wall structure material produced per explosion in any ICF reactor. The complications of reprocessing unburned actinides therefore do not significantly change the operational hazard potential relative to a pure fusion plant. This advantage is in marked contrast to any hy-

brid or blanket burnup device. Safety is in fact the major advantage of pellet center burnup: only milligrams of highly toxic and active material need to be present in the fusion chamber, whereas blanket burnup requires the continued presence of tons of actinides in a small volume. The results plotted in Fig. 4-18 indicate that one ICF plant could transmute the actinide waste of up to 10 power-equivalent fission reactors. Thus, large-scale development would appear to provide a foreseeable-future technology that greatly reduces the necessity of high-integrity waste storage (burial) time from  $10^7$  to just over  $10^2$  years.

For a more detailed report, see H. W. Meldner, *Inertial Confinement Fusion and Long-Term Nuclear Waste Management*, Lawrence Livermore Laboratory, Rept. UCRL-81214 (1978), submitted to *Nucl. Sci. and Eng.*

## Reference

37. F. H. Southworth and H. D. Campbell, "Neutron Downscattering in Laser-Induced Fusing Plasmas," *Nucl. Tech.* **30**, 434 (1976).

## Author

H. W. Meldner

## 4.3 Electron- and Ion-Beam Target Design and Analysis

### 4.3.1 Magnetically Insulated Charged-Particle Targets

Electron-beam accelerators proposed for fusion applications have special target requirements. The long deposition range of the electrons, bremsstrahlung preheat, low beam power, and 20-100-ns pulse lengths are best suited to relatively large, massive targets that exhibit low output gains. However, these machines are relatively efficient and can produce very high total beam energies that, if properly utilized, might offset these inherent difficulties.

One solution to the bremsstrahlung and range problems is to use light ions instead of electrons, generated by reversing the accelerator's polarity. Light ions have been generated at powers approaching 1 TW.

A target approach that is directed to the low-power, long-pulse-length characteristics of both electron- and ion-beam accelerators uses a magnetic field in a preheated fuel region. Past reports have concentrated on providing designs to match existing machines.<sup>38, 39</sup> By adding a frozen fuel layer to the target, one can scale this approach to gain  $\sim 100$  targets. A conceptual view of this approach is shown in Fig. 4-19.<sup>40</sup> A low-

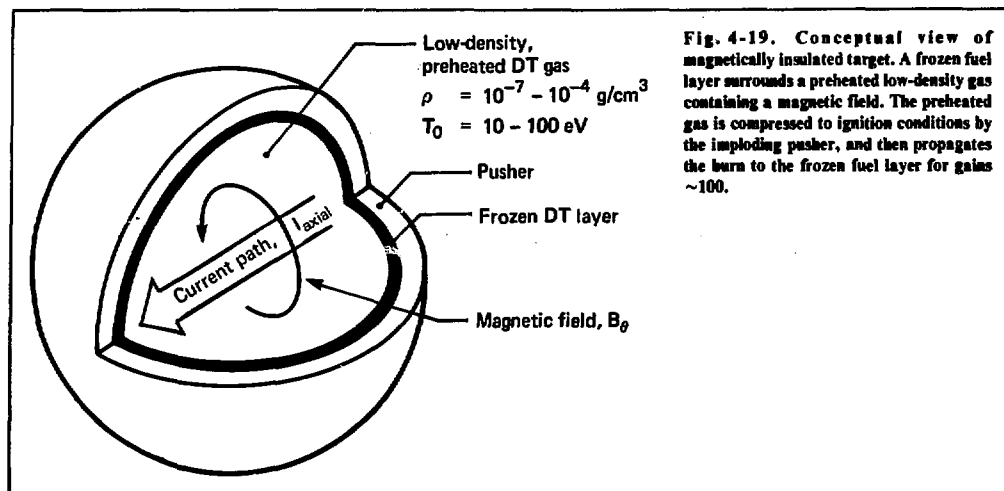


Fig. 4-19. Conceptual view of magnetically insulated target. A frozen fuel layer surrounds a preheated low-density gas containing a magnetic field. The preheated gas is compressed to ignition conditions by the imploding pusher, and then propagates the burn to the frozen fuel layer for gains ~100.

density, preheated gas is surrounded by a frozen fuel layer and a high-Z pusher/tamper. A magnetic field externally supplied is embedded in the fuel and serves two functions. If the fuel density is low enough, the magnetic field can inhibit thermal conduction from the DT to the surrounding pusher wall, allowing a nearly adiabatic compression of the preheated fuel to reach ignition conditions. A second advantage occurs at maximum compression. If the initial magnetic field is large enough, the resulting compressed field can trap the alpha particles produced by the DT fusion reactions, thereby heating the burning plasma even further.

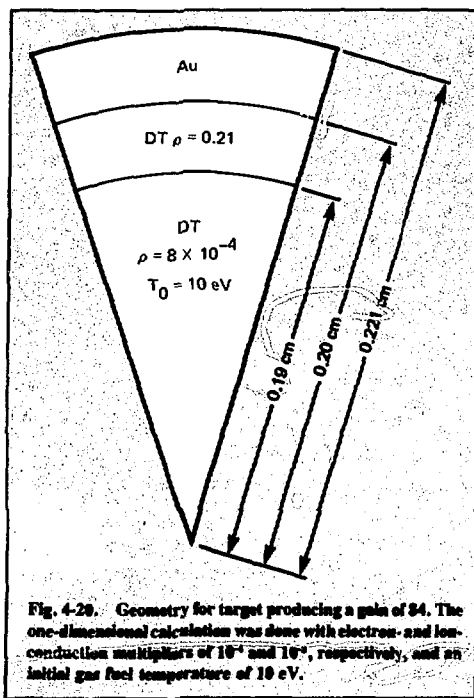
The net result is a target design that may approach minimum input requirements for the driving source.

Calculations on LASNEX show that significant yields from this target approach are possible. Table 4-4 lists typical target variables for various-sized capsules, all driven by a 10-MeV proton source. All sizes are characterized by relatively low input powers, and there are no pulse-shaping requirements for the larger shells. For a 2-MJ, 80-TW input, a gain of 84 is achieved from the target, shown in Fig. 4-20.

These minimal power and energy requirements are not attained without difficulty, however. To signifi-

Table 4-4. Summary of optimized ion-driven targets using magnetic fields.

	Fuel radius, cm			
	0.2	0.1	0.05	0.025
Input power	80TW/25ns	45TW/10ns	1TW/1.5ns 5TW/1.5-3.5ns 35TW/3.8-9.0ns	0.5TW/1.8ns 2TW/1.8-2.1ns 8TW/2.1-2.4ns 30TW/3.4-4.9ns
Input energy, MJ	2.1	0.45	0.2	0.079
Yield, MJ	180	15	0.67	0.087
Gain	84	34	3.4	1.1
Max. interface velocity, cm/ $\mu$ s	12	13	14	14
Min. fuel radius, cm	0.011	0.0045	0.0019	0.0014
Compression ratio	5900	11,000	17,000	6,000
Max. fuel temperature, keV	210	110	29	28
Max. fuel density, g/cm <sup>3</sup>	230	340	560	560
Max. fuel $\rho R$ , g/cm <sup>2</sup>	0.82	0.5	0.28	0.11



cantly reduce thermal conduction losses implies high values of magnetic field in the fuel region. Reducing the magnetic field to zero drops all the yields in Table 4-4 below breakeven. This occurs even if the field is introduced as the implosion is proceeding. Thus, initial values of magnetic field of the order of 1-10 MG are required to maintain the preheat and ensure adiabatic implosions. Larger values of magnetic field appear unnecessary, because the reduction in conductivity improves as the implosion proceeds. Conduction losses are proportional to  $1/\omega^2\tau^2$ , or  $\rho^2/B^2T^3$ , where  $\omega$  is the plasma frequency,  $\tau$  the collision time,  $\rho$  the material density,  $B$  the magnetic field, and  $T$  the fuel temperature. For a spherical adiabatic implosion, the thermal conductivity is then proportional to the radius to the fourth power, yielding smaller conduction losses later in time.

Note that the reduction in conductivity applies to both electron and ion terms. Unless the ion thermal conductivity is also inhibited 100 fold at late implosion times, ignition temperatures are not attained, and there is no significant yield. The field values specified should meet this requirement.

Several methods for producing these fields are shown in Fig. 4-21. Magnetic fields formed by injecting

long-range electron or ion beams, as shown in Figs. 4-21(a) and 4-21(b), may be neutralized and reduced by return currents. Those methods also cause perturbations in the pusher and frozen fuel surrounding the gas, which can further degrade the implosion. If these shortcomings can be removed, existing beam sources can produce the required field levels. Using the density and temperature gradients formed by localized heating [Fig. 4-21 (c)] causes smaller pusher/fuel perturbations but limits the magnitude of field produced. The most promising approach appears to be use of a fuel wire coated with minute amounts of low-Z conducting material such as beryllium, as shown in Figure 4-21 (d). This provides a current path to produce the field with minimum fuel pusher degradation. Figure 4-21 (e) depicts two additional approaches suggested for nonspherical targets.

The frozen fuel layer indicated in Fig. 4-19 is required to yield gains of order 100 or greater. The density of the gaseous fuel must be kept low, or field requirements become impractical to limit conduction losses. This forces a mass limit on the available fuel and therefore a limit on the fusion energy produced. The frozen layer removes this fuel limit but also forces one to have a minimum gaseous mass to allow the burn to propagate into this frozen outer layer. If the compressed low-density central fuel is  $\leq 0.1$  as dense as the cold outer layer, then propagation of the burn is very difficult if not impossible. At these densities, magnetic field requirements are still under 10 MG.

All the listed designs are results of one-dimensional calculations, and thus overlook some dominant nonsymmetric effects. Most methods of producing magnetic fields form a gradient in field from axis to the outer wall. This gradient drives the heated plasma to the wall, and severe turbulence can result. Not only does introducing the magnetic field produce perturbations, but the fuel becomes a very nonuniform region and should be treated with two-dimensional Eulerian codes. Considerably more promising results must come from the one-dimensional study than has been exhibited to date before such an effort can be justified.

For high-gain targets, questions of fuel cleanliness, implosion symmetry, fluid instability, and target fabrication must also be addressed.

The conclusion from the one-dimensional study is that use of magnetic fields and preheat leads to minimal power and energy requirements. However, a large number of questions remain unanswered, particularly in two-dimensional geometry. Answers to those questions could lead to increased requirements.

## References

38. D. Meeker and J. H. Nuckolls, "Fusion Targets Designed to Match Present Relativistic Electron Beam Machine Paramet-

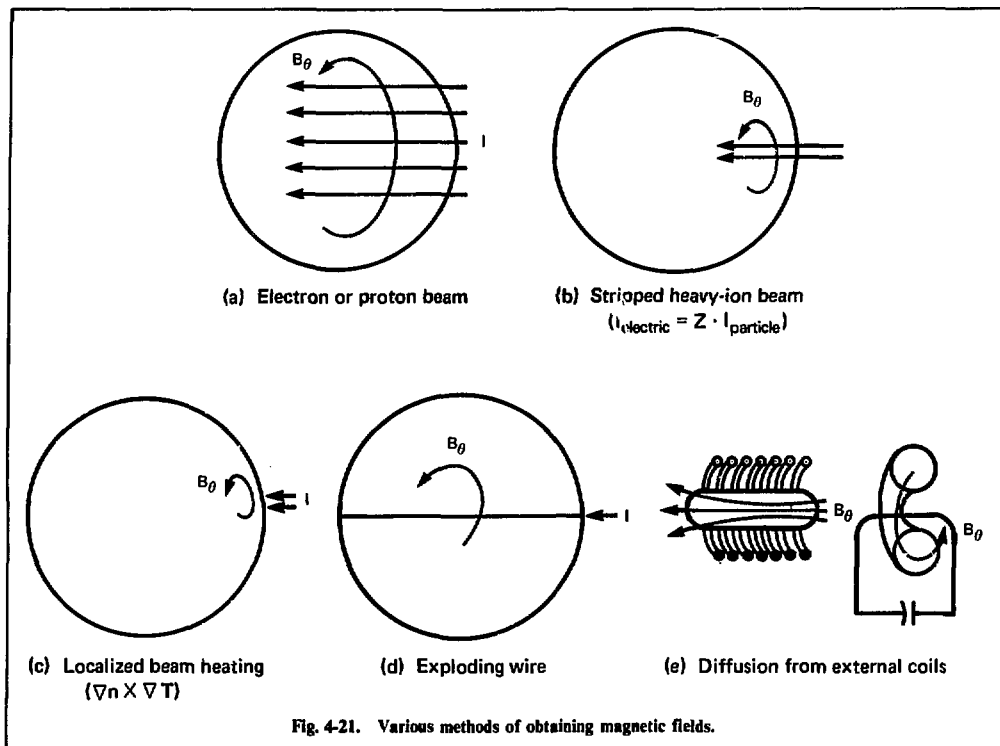


Fig. 4-21. Various methods of obtaining magnetic fields.

ers," *Laser Program Annual Report-1975*, Lawrence Livermore Laboratory, Rept. UCRL-50021-75 (1975), p. 295

39. D. J. Meeker and J. H. Nuckolls, "Electron and Ion Beam Targets," *Laser Program Annual Report-1976*, Lawrence Livermore Laboratory, Rept. UCRL-50021-76 (1977), pp. 4-46.

40. R. O. Bangerter and D. J. Meeker, "Charged Particle Fusion Targets," in *2nd Intern. Topical Conf. on High Power Electron and Ion-Beam Res. and Tech.* (Ithaca, N. Y. 1977), p. 183.

## Author

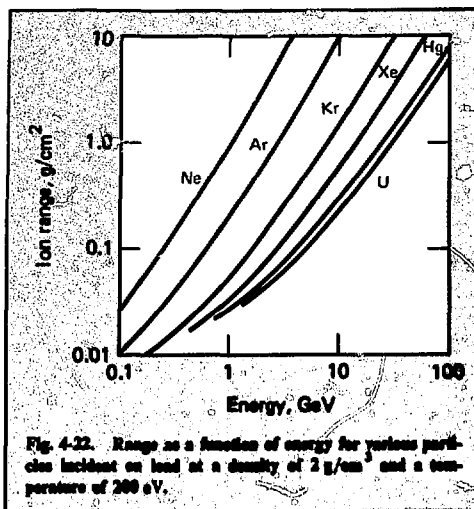
D. J. Meeker

### 4.3.2 Maximum Ion Energies for Heavy-Ion Fusion

A high-gain fusion microexplosion requires a beam power  $\geq 100$  TW. In the case of heavy-ion fusion the power is simply the product of ion energy and ion current. Because of collective effects, the production and transport of high-current, low-energy beams are far more difficult than the production and transport of

low-current, high-energy beams. In fact, the maximum ion-beam power that can be transported in a conventional alternating gradient system is proportional to (ion energy)<sup>11/6</sup>.<sup>41</sup> Therefore, for a given beam power and number of beams there is a lower limit on ion energy.

Furthermore, accelerator costs increase less rapidly than linearly with ion energy. Thus, there are significant reasons for increasing ion energy. Unfortunately, fundamental target considerations place an upper limit on ion energy. The implosion velocity required to achieve significant thermonuclear burn is determined by the rate of energy loss from the imploding fuel and the amount of energy required to compress the fuel. The velocity is only weakly dependent on fuel mass, and for a well-designed, high-gain target cannot be less than about  $2 \times 10^7$  cm/s. If one models an implosion as a simple rocket, the velocity of the payload (thermonuclear fuel)  $v$  is given by  $v = v_0 \ln (m_{tot}/m_{pay})$ , where  $v_0$  is the exhaust (ablator) velocity and  $m_{tot}$  and  $m_{pay}$  are, respectively, the total rocket mass and the mass of the payload. It can easily be shown that the efficiency of a rocket becomes poor for  $m_{tot}/m_{pay} > 10$ , so for an efficient (high-gain) target  $v$

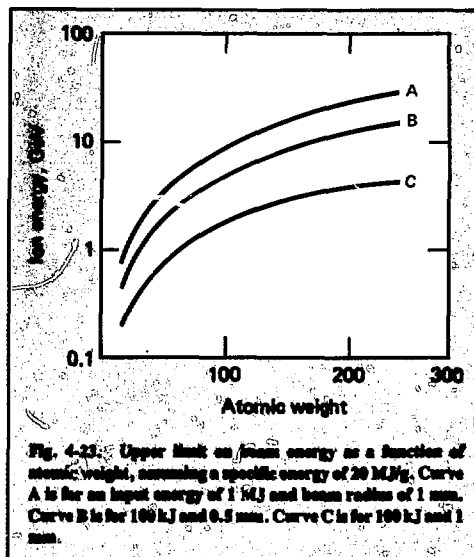


$\leq 2v_0$  so that  $v_0 \geq 10^7 \text{ cm/s}$ . The kinetic energy alone corresponding to a velocity of  $10^7 \text{ cm/s}$  is  $5 \text{ MJ/g}$ ; furthermore, the thermal energy of the heated ablator is typically larger than the kinetic energy. For practical targets the ion beam must deposit a specific energy  $> 20 \text{ MJ/g}$ .

At least two beams are required for adequate implosion symmetry, so  $2 \times 10^7 \text{ J/g} < E/m = E/2\pi r^2 R$ , where  $r$  is the focal spot radius in cm and  $R$  is the ion range in  $\text{g/cm}^2$ . For a given input energy this relation imposes an upper limit on  $R$ . Figure 4-22 shows  $R$  as a function of energy for a variety of ions. The target material is assumed to be lead at a density of  $2 \text{ g/cm}^3$  and a temperature of  $200 \text{ eV}$ . These conditions are typical of fusion targets, but in any case the range is only weakly dependent on density and temperature.<sup>41</sup>

For targets having an input energy  $\sim 1 \text{ MJ}$  the minimum reasonable focal spot radius is  $\sim 1 \text{ mm}$ . This minimum target radius is determined by the average implosion velocity and the pulse length. For a  $1\text{-MJ}$ ,  $100\text{-TW}$  target the pulse length is  $\sim 10^{-8} \text{ s}$ . The average implosion velocity is about half the peak implosion velocity of  $2 \times 10^7 \text{ cm/s}$ , so the target cannot be smaller than  $(10^7 \text{ cm/s})/10^{-8} \text{ s} = 1 \text{ mm}$ . Moreover, at  $\geq 1\text{-MJ}$  input, the small quantity of fuel that can be contained in targets smaller than  $1 \text{ mm}$  begins to limit target gain. For smaller,  $100\text{-kJ}$  targets, a focal spot size of  $0.5 \text{ mm}$  becomes reasonable.

Using the minimum target size, the minimum specific energy, and the curves in Fig. 4-22, we have calculated the maximum allowable ion energy as a



function of atomic weight for three different targets. The results are shown in Fig. 4-23.

It should be emphasized that these curves do not represent a sharp upper limit above which targets will not work at all and below which all ion energies are equally effective. In terms of specific energy we expect target gain to increase rapidly as the specific energy is increased from  $\sim 10 \text{ MJ/g}$  to  $\sim 30 \text{ MJ/g}$ . It is also true that for a given specific energy there is some advantage in going to a larger focal spot size and shorter range; or, in terms of accelerator parameters, there is some advantage in low-ion-energy, high-emittance beams. This results from the fact that larger targets allow long implosion times and therefore lower beam powers. However, fluid instabilities limit the maximum target diameter, so ranges less than  $\sim 0.03 \text{ g/cm}^2$  or focal spot sizes larger than  $\sim 1 \text{ cm}$  in radius are not useful for targets in the  $1\text{-to } 10\text{-MJ}$  input range.

## Reference

41. ERDA Summer Study of Heavy Ions for Inertial Fusion, Lawrence Berkeley Laboratory, Rept. LBL-5543 (1976).

## Author

R. O. Bangerter

## 4.4 LASNEX Overview

The LASNEX code is used to design laser, electron-beam, and ion-beam targets and to analyze experimental results. For several years LASNEX simulations of glass microsphere targets have been remarkably accurate over large variations in design parameters, laser power, and neutron yield. These targets, however, all used low-to-intermediate-Z materials, and as a result the important physics was mostly limited to absorption by resonance processes, energy transport by electrons, hydrodynamics, and thermonuclear reactions.

Simulations of recent gold disk irradiation experiments showed that the LASNEX model overestimated both laser absorption and x-ray losses. In these high-Z experiments, inverse bremsstrahlung can dominate resonance absorption of the laser light, and the plasma energy balance is determined as much by radiative emission as by electron transport. We have made several changes to improve the inverse bremsstrahlung and radiative emission models in LASNEX. Agreement with experiment has improved significantly.

The rate of absorption by inverse bremsstrahlung is proportional to  $\bar{Z}T_e^{-3/2}L$ , where  $\bar{Z}$  is the degree of ionization,  $T_e$  is the electron temperature, and  $L$  is the density gradient length. LASNEX had been overestimating  $\bar{Z}$  because it used Saha equilibrium to determine ionization. Including the effects of radiative recombinations and solving rate equations for ionization reduces  $\bar{Z}$  by about a factor of two for these experiments. LASNEX had been underestimating  $T_e$  because of various inadequacies in radiative energy balance. These are discussed below. LASNEX had been overestimating  $L$  because it neglected the hydrodynamic effects of the laser light. Use of a new ponderomotive force algorithm shows density steepening and a reduction in  $L$ . Each of these inadequacies led to an overestimation of the inverse bremsstrahlung absorption. With the improved models of ionization, radiative energy balance, and ponderomotive force, the results agree well with experiment.

The loss of energy by radiative processes becomes more important in high-Z material. Accurate simulation requires calculation of the atomic configurations, the emission and absorption properties of matter with those atomic configurations, and transport of the radiation out of the material. LASNEX had been using an inline subroutine package to generate the atomic configurations and opacities, assuming local thermodynamic equilibrium (LTE). These routines were fast but not accurate. The transport of the radiation was handled in the diffusion approximation, which did not allow for the proper variation of intensity with photon direction.

Within the LTE approximation, changes were made to use frequency-dependent opacities generated by the HOPE<sup>42,43</sup> code. This level of opacity calculation is too expensive to run inline, so tables were generated. The LTE assumption was removed by making the methods of solving the non-LTE rate equation work well for parameters of interest to laser fusion. With these improved models, LASNEX can adequately compute radiative energy loss from high-Z matter. Their use also gives us increased confidence that we are accurately calculating x-ray preheat of implosion targets.

A spectral-line postprocessing code for LASNEX has been used to design x-ray line density diagnostics for high-density, low-temperature plasmas. The method has been extended from  $10\times$  to  $100\times$  solid DT density with only slight degradations in target performance. With this scheme it is possible to diagnose densities beyond  $1000\times$  solid.

### References

42. B. F. Rozsnyai, "Spectral Lines in Hot Dense Matter," *JQSRT* **17**, 77 (1977).
43. B. F. Rozsnyai, "Relative Hartree-Fock-Slater Calculations for Arbitrary Temperature and Matter Density," *Phys. Rev. A* **5**, 1137 (1972).

### Author

G. B. Zimmerman

#### 4.4.1 New Ponderomotive Force Algorithm

The ponderomotive force in laser-produced plasmas is of current interest because the intensities available to irradiate targets are steadily increasing and because experiments to study density-profile modification have recently been performed.<sup>44</sup> The ponderomotive force of high-frequency radiation is slowly varying in time and second order in the field amplitude, thus becoming more and more significant as the intensity of the electromagnetic radiation increases. To properly model high-intensity target irradiation and to analyze and reproduce the experiments, a new ponderomotive force algorithm has been added to the LASNEX computer code.

The algorithm for the ponderomotive force in LASNEX was obtained by demanding that momentum be conserved and by using the well-known Wentzel-Kramers-Brillouin (WKB) (geometrical optics) solution for wave propagation in a plane-parallel medium.<sup>45</sup> The full analytic expression for the ponderomotive force (the gradient of the radiation stress tensor) reduces exactly to the new LASNEX prescription for cylindrical geometry (as in LASNEX), using the WKB solution for the fields.<sup>46</sup>



The algorithm for the ponderomotive force  $F_p^{\text{LASNEX}}$  in LASNEX in terms of the light intensity  $I$  and the real part of the dielectric function  $\epsilon$  may be written as follows:

$$\left( \vec{F}_p^{\text{LASNEX}} \right)_\alpha = - \frac{\partial}{\partial x_\alpha} \times \left[ (1 - \epsilon) \frac{1}{2c\epsilon^{1/2}} \right] - \frac{\partial}{\partial x_\beta} \Pi_{\alpha\beta}, \quad (20)$$

where  $\Pi_{\alpha\beta} = (I\epsilon^{1/2}/c) (\hat{I} \cdot \hat{\alpha})(\hat{I} \cdot \hat{\beta})$  and  $c$  is the speed of light.  $\hat{I}$  is a unit vector in the direction of the radiation energy flux.  $\hat{\alpha}$  and  $\hat{\beta}$  are unit vectors in a given coordinate system. If  $\hat{I}$  is in the  $r, z$  plane with

$$\hat{I} = \hat{r} \sin\theta + \hat{z} \cos\theta, \quad (21)$$

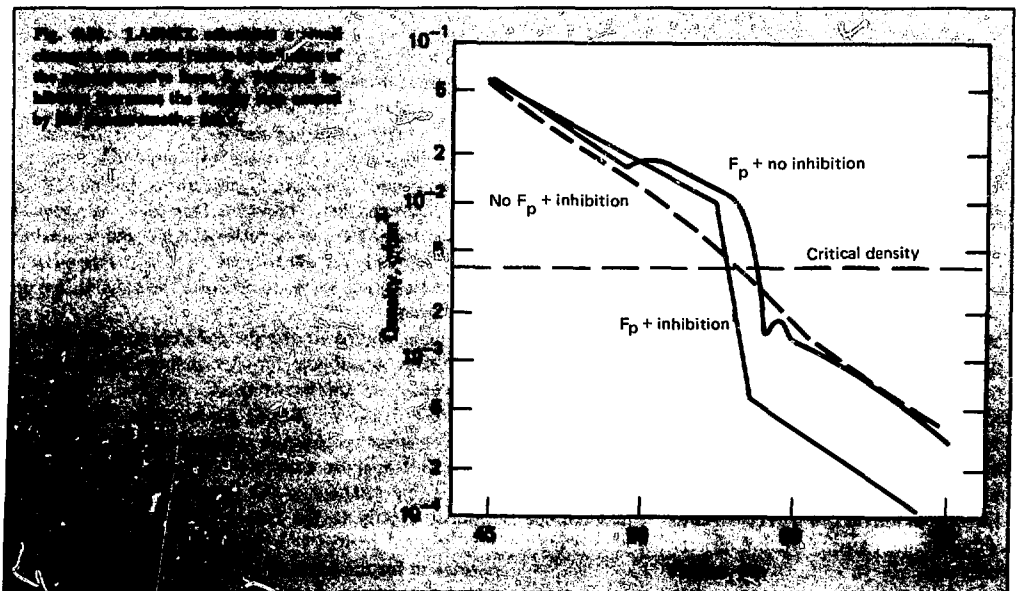
then

$$\Pi = \frac{I\epsilon^{1/2}}{c} \begin{bmatrix} \sin^2\theta & \sin\theta \cos\theta \\ \cos\theta \sin\theta & \cos^2\theta \end{bmatrix} = \begin{bmatrix} \Pi_{rr} & \Pi_{rz} \\ \Pi_{rz} & \Pi_{zz} \end{bmatrix}. \quad (22)$$

In practice the second term in Eq. (21) is handled by differencing the  $r$  and  $z$  momentum components of each light ray across a zone rather than actually forming  $\Pi_{\alpha\beta}$ . One quarter of the momentum difference is given to each zone vertex.

The algorithm described by Eq. (20) consists of two terms. The first term is the gradient of the scalar pressure, created by the plasma medium in which the light is propagating. In free space,  $\epsilon = 1$ , and the term vanishes. This pressure term does  $PdV$  work on the material. The second term is the divergence of the light momentum flux density tensor.  $\Pi_{\alpha\beta}$  is the  $\alpha$  component of the amount of light momentum flowing in a unit time through a unit area perpendicular to the  $\beta$  axis. This interpretation is seen by integrating the momentum equation over some volume and transforming into a surface integral by Green's formula. The tensor term transfers the momentum change of the light to the material and therefore ensures conservation of momentum.

Extensive calculations of one-dimensional (spherically symmetric) exploding-pusher-type targets were performed to study the effect of the ponderomotive force on target dynamics.<sup>47</sup> For the spherical glass microshells filled with DT gas and irradiated with short-duration pulses of 1.06- $\mu\text{m}$  light at normal incidence, the ponderomotive force causes a density jump to form at the critical density, although the position of the critical radius changes only slightly (see Fig. 4-24). LASNEX calculations that invoke thermal conduction inhibition (assuming the electron-ion two-stream instability as the inhibition mechanism) agree better with the experimental results of the size of the density jump than LASNEX calculations that do not invoke thermal conduction inhibition.<sup>47</sup> The lower density shelf is smaller in the calculation with inhibition, as seen in Fig. 4-24.



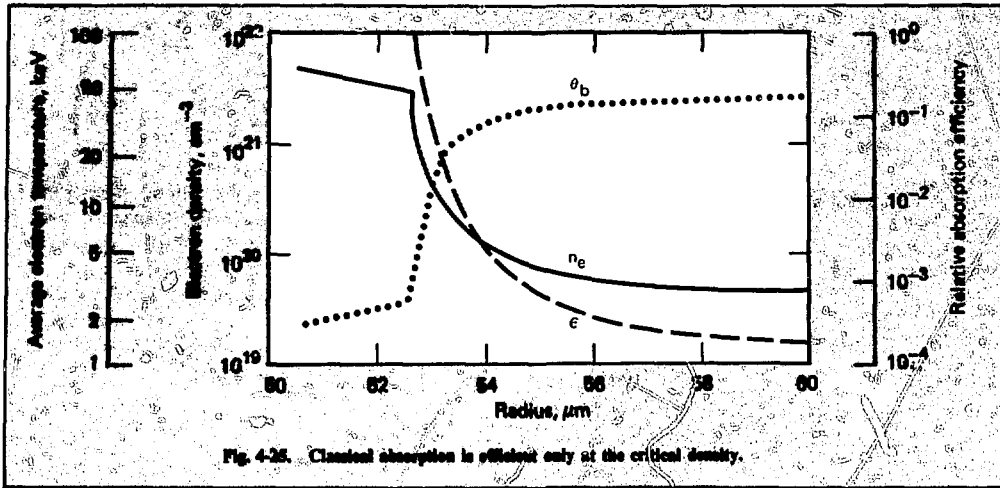


Fig. 4-25. Classical absorption is efficient only at the critical density.

The absorption process is also affected by the ponderomotive force. Collisional absorption (i.e., inverse bremsstrahlung), which has an absorption efficiency  $\epsilon$  proportional to  $n_e^2 \theta_e^{-3/2}$ , is reduced by the presence of the ponderomotive force. In the forced case, the underdense coronal region has a lower electron density gradient  $n_e$  and a steeper electron temperature gradient  $\theta_e$ . Therefore, the classical inverse bremsstrahlung absorption in the presence of the ponderomotive force is significantly smaller than in the unforced case. Figure 4-25 illustrates typical  $n_e$  and  $\theta_e$  profiles with the ponderomotive force. The classical absorption efficiency, also plotted, is efficient (i.e.,  $>0.1$ ) for only a relatively small region of  $\sim 0.3 \mu\text{m}$  just outside the critical radius. Without this steepened profile,  $\epsilon$  would not be so strongly peaked and absorption could occur over a longer path.

In summary, the classical absorption efficiency is greatly reduced by the presence of the steepened density profile caused by the ponderomotive force, and the steepened profiles obtained in LASNEX calculations with inhibited thermal transport agree better with the experimental results than those without inhibition.

## References

44. D. T. Attwood, D. W. Sweeney, J. M. Auerbach, and P. H. Y. Lee, "Interferometric Confirmation of Radiation Pressure Effects in Laser-Plasma Interactions," *Phys. Rev. Lett.* **40**, 184 (1978).
45. V. L. Ginzburg, *The Propagation of Electromagnetic Waves in Plasmas* (Pergamon Press, Oxford, 1970).
46. J. Harte and G. Zimmerman, *Ponderomotive Force in a Hydrodynamic Simulation Code*, Lawrence Livermore Laboratory, Rept. UCRL-79860 (1977).

47. J. T. Larsen and J. Harte, *Profile Modification by the Ponderomotive Force in Spherical Targets*, Lawrence Livermore Laboratory, Rept. UCRL-79757, Rev. 1 (1977).

## Author

J. Harte

## 4.4.2 Improvements to XSN Atomic Physics

XSN is the in-line subroutine package used by LASNEX to determine ionization and excitation states of atoms and to calculate their absorption and emission properties. The package is detailed in Ref. 48. Here we describe some of the basic physics, plus changes made to the XSN package to make it more appropriate and accurate for laser fusion calculations.

We can run XSN in either LTE (local thermodynamic equilibrium) or non-LTE modes. In the LTE mode, the ionic configurations are assumed to be given uniquely by the electron temperature  $\theta$ , the matter density  $\rho$ , and the atom fractions  $x_i$  of each element in the material. In the non-LTE mode, the ionic configurations are determined by solving rate equations and, in general, depend also on time and on the photon and suprathermal electron distributions. In either mode, the configurations are described by the number of electrons in each of seven levels for each element. This is the average atom approximation.

The Saha-Boltzmann equations in the LTE mode take the form

$$P_{in} = \frac{D_{in}}{1 + (317/\rho Z) A_i \theta^{3/2} \exp[-I_{in}/\theta]} \quad (23)$$

where  $P_{in}$  is the number of electrons in level  $n$  of element  $i$ ,  $A_i$  is the atomic mass of this element in amu,  $\rho$  is in  $\text{g/cm}^3$  and  $\theta$  is in keV.  $I_{in}$  is the ionization potential for this level, and  $D_{in}$  is its degeneracy (normally  $D_{in} = 2n^2$ ).  $Z$  is the number of free electrons per nucleus:

$$Z = \sum_i x_i [Z_i^{\text{nuclear}} - p_{in}] \quad (24)$$

The ionization potential is given by the derivative of the atom's potential energy with respect to population, minus a continuum-lowering correction given by Stewart and Pyatt<sup>40</sup>:

$$I_{in} = - \frac{\partial \epsilon_i^{\text{potential}}}{\partial P_{in}} - (\Delta E)_i \quad (25)$$

The atom's potential energy is the sum of level energies times population. The level energies are given by Dirac's formula in terms of the screened nuclear charge and the level number:

$$\epsilon_i^{\text{potential}} = - \sum_n \epsilon_{\text{Dirac}}(Z_{in}, n) P_{in} \quad (26)$$

In the nonrelativistic limit,  $\epsilon_{\text{Dirac}} = R_d Z_{in}^2/n^2$ . The screened nuclear charge is given by Slater screening coefficients<sup>50</sup> as

$$Z_{in} = Z_i^{\text{nuclear}} - \sum_{m < n} \sigma_{nm} P_{im} - 1/2 \sigma_{nn} P_{in} \left(1 - \frac{1}{2n^2}\right) \quad (27)$$

When continuum-lowering forces the ionization potential toward zero, the degeneracy of the level is reduced smoothly from  $2n^2$  to zero, so the populations given by Eq. (23) also vanish.

The above equations are solved by the algorithm:

- A. Guess  $P_{in}$ .
- B. Determine  $I_{in}$  [Eqs. (25)-(27)].
- C. Iterate for  $P_{in}$ ,  $Z$  [Eqs. (23), (24)].
- D. Determine new  $I_{in}$  [Eqs. (25)-(27)].
- E. Refine  $I_{in}$ .
- F. Go to C.

Step C uses Newton's method to iterate on  $Z$ . Step E uses a combined Newton's method with numerical derivatives and an underrelaxation method.

In the non-LTE mode, XSN determines level populations by solving the coupled set of rate equations:

$$\frac{dP_{in}}{dt} = (D_{in} - P_{in}) \left[ Z R_{cn}^i + \sum_m P_{im} R_{mn}^i \right] - P_{in} \left[ R_{nc}^i + \sum_m (D_{im} - P_{im}) R_{nm}^i \right] \quad (28)$$

The first term is the rate of electrons entering level  $n$  and is proportional to  $D_{in} - P_{in}$  (number of holes remaining in the level). The second term is proportional to  $P_{in}$  and represents the rate of electrons leaving level  $n$ . Each term is a sum of transitions involving the continuum and other levels. The rate coefficients ( $R_{mn}^i$ ) are the rates of transition from level  $m$  to  $n$  per electron in  $m$  per hole in  $n$ . These coefficients are, in turn, written as

$$R_{mn}^i = P_{mn}^i + T_{mn}^i Z + S_{mn}^i \quad (29)$$

where the three terms represent transitions involving a photon, a thermal electron, or a suprathermal electron. The photon- and suprathermal-induced transitions use integrals over these distributions. Photon and thermal electron rates are designed to give detailed balance where appropriate. Suprathermal rates include only upward transitions. Radiative rates assume unit Gaunt factors, while collisional rates have been fit to the results of Ref. 51.

The rate equations are solved by the algorithm:

- A. Guess  $P_{in}$  at end of time step.
- B. Determine  $I_{in}$  [Eqs. (25)-(27)].
- C. Determine all rate coefficients.
- D. Solve linearized matrix of Eqs. (24) and (28).
- E. Form new  $P_{in}$  by underrelaxation.
- F. Go to B.

In the non-LTE mode, the material pressure and energy can not be taken from standard tables, which assume LTE. Currently, the energy is calculated as the sum of contributions from free electrons and ions, potential energy of the atom, and a Coulomb correction. The free-electron energy includes partial ionization and Fermi degeneracy. Potential energy is given by Eq. (26). The Coulomb correction is taken from an ion sphere model. Material pressure includes free particles and a Coulomb correction, but it is thermodynamically inconsistent in ionization regions. We are currently working on establishing consistency.

One of the principal results of non-LTE physics in laser fusion applications is a reduction in the degree of ionization and radiation emission in high- $Z$  disks. The lowered degree of ionization and excitation is attributed to the inclusion of radiative recombination and bound-bound transitions in the rate equations. These

transitions tend to fill the lower levels with electrons, which greatly reduces radiative line emission at high frequencies. Reduced emission increases the electron temperature, which, along with the reduced degree of ionization, causes inverse bremsstrahlung laser absorption to decrease. Results from the non-LTE model show a greatly improved agreement with experimental measurements of laser absorption and radiative emission (see § 6.6).

## References

48. W. A. Lokke and W. H. Grasberger, *XSNQ-U, A Non LTE Emission and Absorption Coefficient Subroutine*, Lawrence Livermore Laboratory, Rept. UCRL-52276 (1977).
49. J. C. Stewart and K. D. Pyatt, Jr., "Lowering of Ionization Potentials in Plasma," *Astrophys. J.* **144**, 1203 (1966).
50. H. Mayer, *Methods of Opacity Calculations*, Los Alamos Scientific Laboratory, Los Alamos, N.M., Rept. AEC-D-1870 (1947).
51. D. H. Sampson and L. B. Golden, "Semiempirical Cross Sections and Rates for Excitation and for Ionization of Hydrogenic Ions by Electron Impact," *Astrophys. J.* **170**, 169 (1971).

## Author

G. B. Zimmerman

### 4.4.3 X-Ray Lines as a Density Diagnostic in DT Plasmas near 100× Solid Density

An ultimate laser fusion target that achieves several thousand times liquid densities and a few kilovolt temperatures requires near-isentropic implosions that give high densities but low temperatures. This combination makes diagnosing such targets very difficult. Because of the low temperature, not much radiation or yield is generated, and, because of the high density, what emission there is tends to be reabsorbed before it escapes. This subsection extends the line emission diagnostic first used in the LLL 10× liquid density experiments<sup>52</sup> to the 100× liquid density regime. The basis of the line calculations mentioned below is a post-processor code for LASNEX that has been described previously.<sup>53</sup>

Given an initial target design, the addition of a line diagnostic requires ensuring line visibility without perturbing the initial target designs unduly. The line intensity is most strongly affected by the temperature in the fuel region. Consequently, the attenuation in the pusher before a line photon escapes suggests using a high-Z seed and low-Z pusher. In contrast, the sensitivity of the line width to density effects decreases with increasing Z, so a balance is required. Also, the choice of pusher material affects the implosion by changing the preheat, initial density, etc., so that the implosion in general is degraded, and this loss must be minimized. These factors will now be discussed in detail.

**Line Intensity.** Assuming a simple, optically thick, homogeneous model of a fuel region surrounded by a pusher shell, the intensity ratio of line/background is given by

$$\frac{1}{c} \frac{\partial f}{\partial t} + \cos \theta \frac{\partial f}{\partial z} = \rho \kappa (f_p - f)$$

where

$I_L$ ,  $I_B$  are the line and background intensities, respectively,

$A_c$ ,  $A_p$  are the outer core and pusher radii, respectively,

$T_c$ ,  $T_p$  are the core and pusher temperatures, respectively,

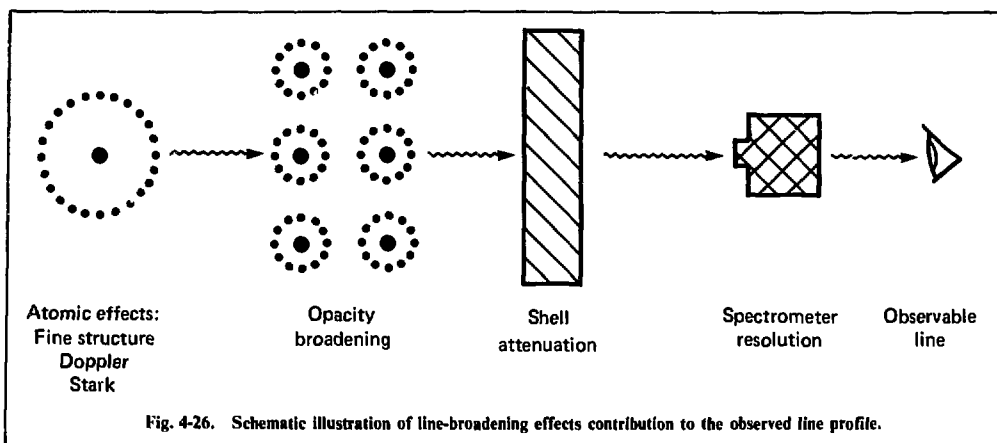
$E_L$  is the line energy,

$F_p$  is the fraction of the line that gets through the pusher.

The fundamental requirement, therefore, is to have the core hotter than the pusher. For an ablative implosion this is normally the case, because the whole idea is to maximize the efficiency of energy transfer to the fuel region. Given this requirement, one has an exponential gain factor that must make up the losses caused by shell attenuation of the line and by its lower area of emission. As an example, for  $E_L/T_c = 5$ ,  $T_c/T_p = 2$ , and  $A_c/A_p = 1/10$ , the line/background ratio is  $15 \times F_p$ . The parameters chosen in the example are similar to those taken from sample implosions. With a pusher attenuation of 2× or less (implying a low-Z material), they yield an overall line/background ratio of  $\geq 5$  for the lowest ( $n = 2$ ) helium-like resonance line, which should provide visibility of three helium-like series members. The high-density limit to this scheme occurs when the core region becomes thick in the continuum at the line position. This limit occurs at an electron density of  $10^{26} \text{ cm}^{-3}$  ( $\sim 3500 \times$  liquid density).

**Line Broadening.** Figure 4-26 shows the many components of the observed line width. We want the density component to dominate the observed width to make possible a density determination. As discussed in more detail in Ref. 54, for the hydrogen and helium-like resonance lines the intrinsic line profile is determined at the conditions of the present experiments by the Doppler and electron-impact broadening. By equating these widths, we can construct a scaling relation for the highest allowed Z of the seed as a function of electron density; Fig. 4-27 illustrates the results for electron temperatures of 250, 500, and 1000 eV.

To complete the discussion of the observed line profile, we briefly mention the effects of opacity broadening and instrument resolution. In the 3-keV region appropriate for the present experiments, crystal spectrographs can attain resolutions  $\leq 2 \text{ eV}$ , which is not significant compared to the intrinsic line width. The



opacity broadening is most important for the  $n = 2$  resonance line (the optical depth scales  $\sim 1/n^3$ , so the higher series members become thin) and is determined by the initial seed-fill pressure. The strategy we have followed is to pick an initial seed fill to obtain a calculated optical depth for the  $n = 2$  helium resonance line of  $\sim 50$  at maximum compression. This provides a large safety factor in the line intensity (i.e., the line will saturate at the black-body limit) at the cost of an extra broadening of  $\sim 3 \times$  the intrinsic line width, which of course makes the intrinsic width less certain. If the observed intensity follows the calculated one, however,

the higher series members, being optically thin, will directly indicate the intrinsic width. As one gains more confidence in his ability to see the lines, he can also lower the initial seed fill and thereby decrease the opacity effects.

**Experimental Design.** Table 4-5 shows the parameters for a  $50 \times$  implosion appropriate to the LLL Argus laser in long-pulse operation that generates an observable line diagnostic. It was necessary to modify the initial  $\sim 100 \times$  design (discussed by W. Mead<sup>55</sup>) to increase the line/background ratio in the following ways.

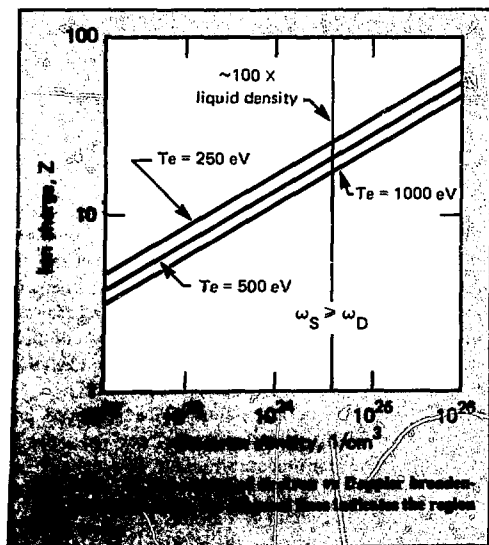
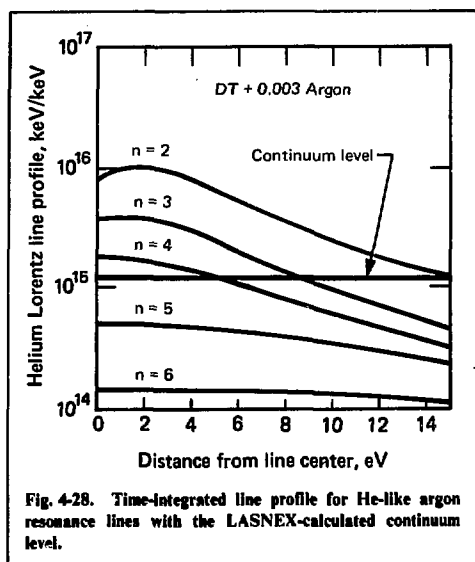


Table 4-5. Target characteristics of experiment designed to diagnose high-density compression with LASNEX results.

Goals	Density $\geq 20 \text{ g/cm}^3$ Electron temperature $\approx 550 \text{ eV}$ Line/background intensity high
Method	Slow laser pulse Large-diameter, thick-walled pellet Low-Z pusher
Experimental parameters	2500 J in 1 ns 150- $\mu\text{m}$ (inner) diameter ball, 20- $\mu\text{m}$ wall Pusher material is Be ( $Z = 4$ )
LASNEX results	$\rho_{\text{max}} = 12 \text{ g/cm}^3$ , $T_e = 0.53 \text{ keV}$ Line/background ratio = 6 for P ( $\sim 2 \text{ keV}$ line) 8 for Ar ( $\sim 3 \text{ keV}$ line)



- We lengthened the laser pulse to produce a more favorable implosion timing (and also reduced the absorbed laser power requirement).

- We enlarged the target to decrease the laser intensity, enlarge the compressed core radius, and increase the emission time at peak compression (there may be reduced laser absorption caused by more Brillouin scattering.)

The net result of these changes was to raise the line/background ratio (for both P and Ar) by an order of magnitude (mainly because of the increased core radius) with a 50% loss in final density. On the basis of the previous discussion of the scaling for line widths, phosphorus ( $Z = 15$ ), which has three resonance lines visible, is the preferred choice as a seed for a density diagnostic. As a practical matter, it is probably much easier to fill the microsphere with argon ( $Z = 18$ ). As shown in Fig. 4-28, Ar also has three resonance lines above the continuum, so it will also suffice, particularly if the higher series members are visible.

In summary, we have discussed the scaling rules for seed and pusher materials to use for diagnosing cold, dense implosions. At the  $100\times$  liquid density level, using an argon ( $Z = 18$ ) seed, this scheme incurs only modest penalties in achieved density and extra fabrication difficulty. For  $1000\times$  targets, which have high- $Z$  pushers, one would also use a high- $Z$  seed material. Depending on the expected fuel temperatures, one would use a line energy of 10-30 keV (with  $E_L \sim 5-10 T_e$ ). As shown in Fig. 4-27, the upper limit to the seed  $Z$  in this regime is 55, corresponding to a

30-keV line. The adjustments in target design to ensure line visibility are likely to be more delicate in this case than in the  $100\times$  design and need more detailed consideration.

## References

52. J. M. Auerbach, D. S. Bailey, S. S. Giaros, L. N. Koppel, Y. L. Pan, L. M. Richards, V. W. Slivinsky, and J. J. Thompson, *Neon Spectral Line Broadening as a Diagnostic for Compressed Laser Fission Targets*, Lawrence Livermore Laboratory, Rept. UCRL-79636, Rev. 1 (1977).
53. D. S. Bailey and E. J. Valco, *Calculation of Emission from Hydrogenic Ions in Super Liquid Density Plasmas*, Lawrence Livermore Laboratory, Rept. UCRL-78473 (1976).
54. D. S. Bailey, *X-Ray Lines as a Density Diagnostic in DT Plasmas near  $100\times$  Solid Density*, Lawrence Livermore Laboratory, Rept. UCRL-79861 (1977).
55. W. C. Mead, J. D. Lindl, J. J. Nuckolls, J. T. Larsen, D. S. Bailey, and Y. L. Pan, *Simulations of Intermediate-Density Laser Fusion Targets: Recent Progress in Design and Analysis*, Lawrence Livermore Laboratory, Rept. UCRL-80005 (1977).

## Author

D. S. Bailey

## 4.5 Laser Plasma Theory and Simulation

### 4.5.1 Overview

Experiments, even those with low-intensity light ( $I \sim 10^{14}$  W/cm<sup>2</sup>, Nd), continue to confirm the important role of plasma effects in laser target design. In 1977, we made significant advances in our understanding of laser plasma coupling. Our models for density-profile steepening, plasma expansion, light absorption, hot-electron temperatures, stimulated scattering, and heat-transport inhibition were tested in experiments and improved in many ways. The close interaction between calculations and experiments has been especially fruitful. A brief overview of our recent progress and its relevance to our understanding of experiments follows.

**Density-Profile Steepening.** Calculations predicted a pronounced density-profile steepening near the critical density. This steepening is very important, because the scale length near the critical density affects absorption processes, heated-electron temperatures, and heat transport. This profile steepening was recently confirmed by interferometric measurements of the density in a laser-heated plasma. Figure 4-29 shows both an early prediction of a steepened profile<sup>56</sup> and a measured profile.<sup>57</sup> In both cases, the profile is steepened to an upper density  $n_u$  that is roughly determined by pressure balance:

$$n_u \approx n_{cr} [1 + (v_L^2/v_e^2)] ,$$

where  $v_L$  is the oscillation velocity of an electron in the laser light field,  $v_e$  is the electron thermal velocity, and

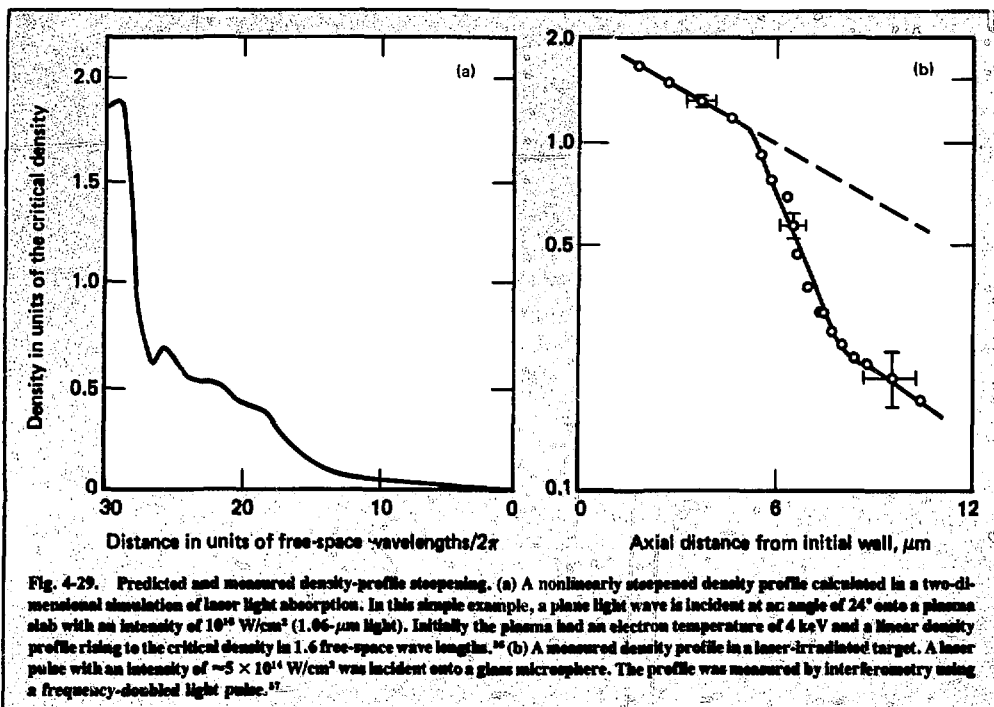


Fig. 4-29. Predicted and measured density-profile steepening. (a) A nonlinearly steepened density profile calculated in a two-dimensional simulation of laser light absorption. In this simple example, a plane light wave is incident at an angle of  $24^\circ$  onto a plasma slab with an intensity of  $10^{14}$  W/cm $^2$  (1.06- $\mu$ m light). Initially the plasma had an electron temperature of 4 keV and a linear density profile rising to the critical density in 1.6 free-space wave lengths.<sup>58</sup> (b) A measured density profile in a laser-irradiated target. A laser pulse with an intensity of  $\sim 5 \times 10^{14}$  W/cm $^2$  was incident onto a glass microsphere. The profile was measured by interferometry using a frequency-doubled light pulse.<sup>57</sup>

$n_{cr}$  is the critical density. The profile is steepened to a lower density that is determined by how the light pressure dams the plasma flow. This lower density appears to be somewhat less in the experiments than in the simulations, perhaps because of energy-transport inhibition.<sup>58</sup>

The measurements also showed a rippling or cratering of the density surfaces, which focused our attention on better incorporating surface distortions into our models. One important source of these distortions is the intensity variation in the incident light caused either by hot spots in the light beam or by the finite beam spot itself. We carried out ZOHAR simulations to model rippling by small scale-length hot spots in a light beam (§ 4.5.1) and applied a hybrid code to examine critical-surface cratering by a focused beam (§ 4.5.3). In both cases, the density surfaces are preferentially pushed in where the light intensity is greatest.

Rippling of the critical-density surface can also result from a critical-surface instability.<sup>59, 60</sup> We carried out the first three-dimensional particle simulations (§ 4.5.7) in the laser plasma field to examine the surface rippling by this instability. These simulations show that the surface principally ripples out of the plane of polarization, as had been predicted by 2.5-dimension

simulations.<sup>60</sup> We also developed a theoretical model to investigate how density-profile steepening is modified by supersonic plasma flow through the critical-density region (§ 4.6.1). A shock-like structure above the critical density was predicted and has been recently observed in microwave simulation experiments.<sup>61</sup>

**Laser Light Absorption.** In experiments with short-pulse-length, intense laser light, the absorption was predicted to be sizable over a broad range of angles, to be polarization dependent, and to range in magnitude from  $\sim 15$  to  $\sim 50\%$  as a function of polarization and angle of incidence.<sup>56</sup> As shown in Fig. 4-30, measurements of the absorption as a function of angle of incidence and polarization confirm these important features of the absorption.<sup>62</sup> Note that the measured absorption is polarization dependent, peaks at an angle of  $\approx 20^\circ$  for p-polarized light, monotonically decreases for s-polarized light, and is sizable over a broad range of angles ( $\pm 45^\circ$  roughly). The dashed line in Fig. 4-30 is the early theoretical estimate for the absorption, based on ZOHAR simulations of the absorption of plane waves. The absorption in these simulations was principally caused by resonance absorption, with a small heating caused by nonlinearly generated ion fluctuations. The solid curve is an improved theoretical estimate (§

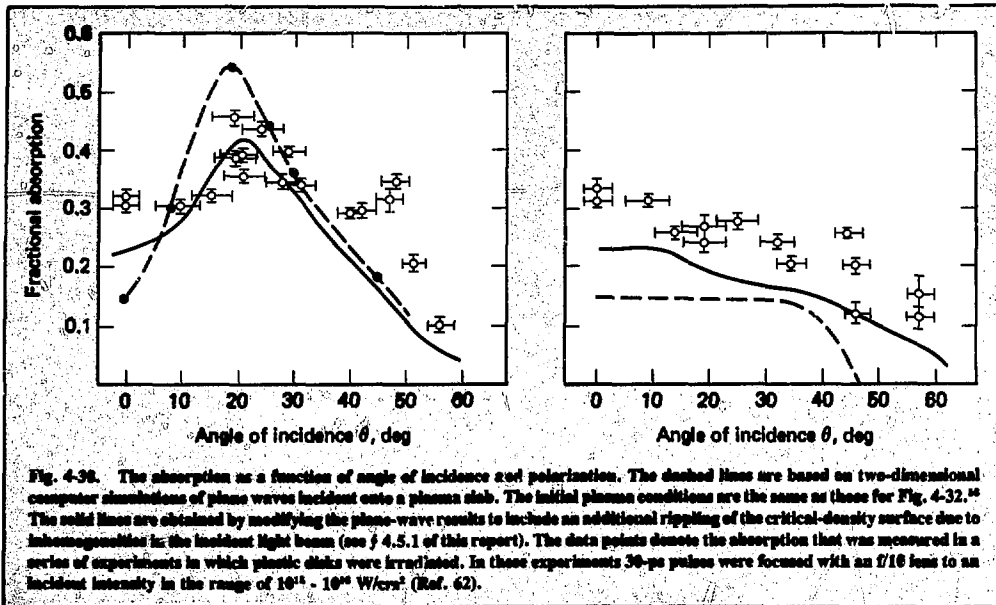


Fig. 4-30. The absorption as a function of angle of incidence and polarization. The dashed lines are based on two-dimensional computer simulations of plane waves incident onto a plasma slab. The initial plasma conditions are the same as those for Fig. 4-32.<sup>66</sup> The solid lines are obtained by modifying the plane-wave results to include an additional rippling of the critical-density surface due to inhomogeneities in the incident light beam (see § 4.5.1 of this report). The data points denote the absorption that was measured in a series of experiments in which plastic disks were irradiated. In these experiments 30-ps pulses were focused with an  $f/16$  lens to an incident intensity in the range of  $10^{14}$  -  $10^{16}$  W/cm<sup>2</sup> (Ref. 62).

4.5.1) that adds to the earlier estimate a modest surface rippling caused by hot spots in the incident light beam. As discussed in the previous subsection, such a surface rippling has been observed experimentally and calculated in computer simulations. Clearly, resonance absorption on a steepened, rippled critical-density surface is sufficient to explain important qualitative features of the absorption and even its magnitude within  $\approx 30\%$ .

However, an additional absorption of about 10 to 15% in these experiments is independent of polarization and weakly dependent on angle of incidence. As shown in earlier calculations,<sup>63-66</sup> this absorption is probably caused by a combination of inverse bremsstrahlung, ion turbulence generated by heat-flow instabilities, resonance absorption introduced by self-generated magnetic fields, and instabilities near  $1/4 n_{cr}$ . We have studied each of these effects. We extended the theory of ion turbulence driven by heat flow to include self-generated magnetic fields (§ 4.8.1). We computed the angular dependence of resonance absorption caused by self-generated magnetic fields (§ 4.5.6). We also improved the linear theory of the two-plasmon decay instability in an inhomogeneous plasma and compared the theory with simulation (§ 4.5.4). Experiments to pinpoint the role of these many effects are under consideration.

**Heated-Electron Temperatures.** Hot-electron temperatures were predicted from ZOHAR simulations of resonance absorption. We measured these tem-

peratures from the slope of the high-energy x-ray spectra observed in experiments. Figure 4-31 shows reasonable agreement between calculations<sup>67, 68</sup> and experiments<sup>69</sup> over a wide intensity range. The calculated temperature is typically somewhat larger than the temperature inferred from the x rays, but this is to be

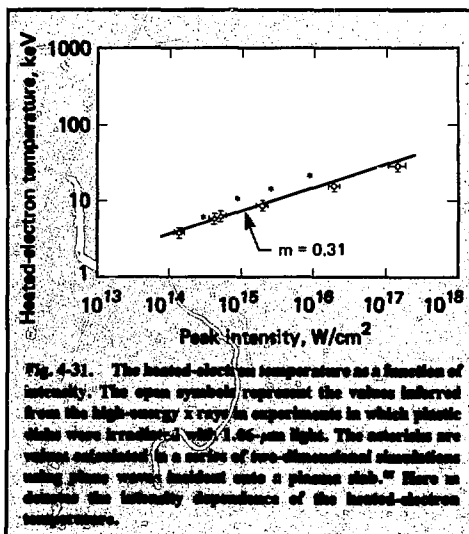


Fig. 4-31. The heated-electron temperature as a function of intensity. The open symbols represent the values inferred from the high-energy x rays in experiments in which plastic disks were irradiated with 1.06- $\mu$ m light. The asterisks are values calculated in a series of two-dimensional simulations using plane waves incident onto a plasma slab.<sup>67</sup> Here we display the intensity dependence of the heated-electron temperature.



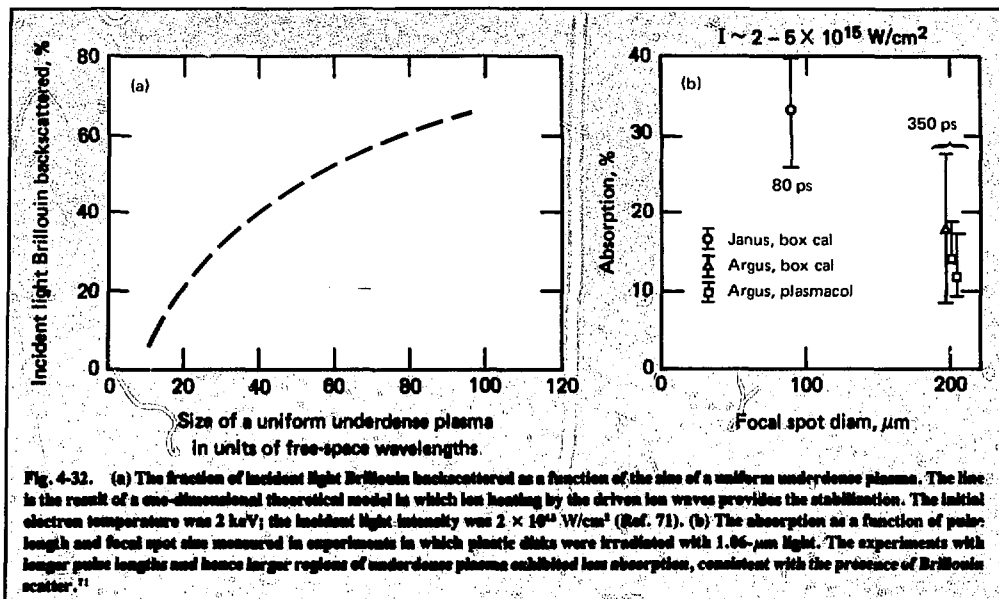


Fig. 4-32. (a) The fraction of incident light Brillouin backscattered as a function of the size of a uniform underdense plasma. The line is the result of a one-dimensional theoretical model in which ion heating by the driven ion waves provides the stabilization. The initial electron temperature was 2 keV; the incident light intensity was  $2 \times 10^{15} \text{ W/cm}^2$  (Ref. 71). (b) The absorption as a function of pulse length and focal spot size measured in experiments in which plastic disks were irradiated with 1.06-μm light. The experiments with longer pulse lengths and hence larger regions of underdense plasma exhibited less absorption, consistent with the presence of Brillouin scatter.<sup>71</sup>

expected because the latter temperature is actually a space and time average. Using simulations, we computed the dependence of the heated-electron temperature on intensity and background plasma temperature (§ 4.5.2) and incorporated an improved prescription into LASNEX. We formulated a simple theoretical model for the simulation results. The simulations also showed that the hot temperature depends on the Z of the target (first shown by experiments) and on the ion-electron temperature ratio of the plasma. Both these dependences can be quite significant for current experiments.

**Plasma Expansion.** In experiments with long-pulse-length light incident on high-Z targets, inverse bremsstrahlung begins to play an important role. The quantitative calculation of this absorption requires a detailed knowledge of the plasma expansion. We developed similar solutions for the plasma expansion that include inverse bremsstrahlung absorption, momentum deposition, and transport inhibition (§ 4.6.2). The solutions demonstrate that the profile can be strongly steepened near the critical density even by rather low intensity light. In effect, the energy deposition produces a hot, thin layer of plasma that blows off into the vacuum. The resulting ablation pressure pushes on the remaining plasma, steepening it. One important effect is to lower the amount of inverse bremsstrahlung absorption, although it can still be sizable in long-pulse-length experiments. These solutions agree with LASNEX calculations and help us to understand our recent experiments with high-Z targets (§ 5.6).

**Stimulated Scattering.** Another important effect for long-pulse-length experiments is Brillouin scatter of the laser light. As shown in Fig. 4-32(a), sizable Brillouin scatter was predicted for experiments with large regions of underdense plasma.<sup>70,71</sup> These estimates were based on both simulations and a theoretical model of Brillouin scatter incorporating the self-consistent ion heating that accompanies the scattering. These predictions were confirmed in recent experiments (§ 5.4) in which low-Z targets were irradiated by using the Argus laser (see also recent experiments at the Naval Research Laboratory (NRL)).<sup>72</sup> As shown in Fig. 4-32(b), the absorption reduced as the size of the underdense plasma increased, that is, as the pulse length and focal spot size increased. Shifts in the frequency spectra of the scattered light were consistent with the presence of strong Brillouin scatter. We also observed sizable Brillouin scatter in our subsequent experiments using high-Z targets.

We recently investigated the possibility that Raman forward scatter in the target chamber debris would prevent laser light from reaching the target in a reactor. The linear theory of this process was reexamined, and nonlinear estimates were developed (§ 4.7.2 and 4.7.3). We found that a previous linear theory of this process was incorrect and greatly overestimated the scatter.

**Energy-Transport Inhibition.** LASNEX calculations imply that an inhibition of electron energy transport is a very common feature of our experiments.

This transport inhibition has been attributed theoretically either to ion-sound turbulence generated by a heat-flow instability or to self-generated magnetic fields. To pin down the source of transport inhibition, we helped to design experiments to measure self-generated magnetic fields by Faraday rotation of a frequency-quadrupled probe beam. These designs were based on LASNEX calculations of the magnetic-field generation by the well-known  $\nabla n \times \nabla T$  source term, which is a purely classical effect.<sup>73</sup> Although we calculated magnetic fields of order 1 MG near the critical density, the corresponding experimental measurements indicate small fields ( $\leq 100$  kG).

Because the Faraday rotation measurement gives a spatial average, this result may indicate that the fields in fact are spatially fluctuating on a much finer scale length than that produced by the  $\nabla n \times \nabla T$  mechanism. This behavior had been predicted,<sup>74</sup> and recent theory and simulations lend support to this hypothesis (§ 4.8.3 and 4.8.4). The anisotropic velocity distribution generated by resonance absorption drives the Weibel instability, which leads to magnetic fields that typically fluctuate on a scale length of order  $3 \mu\text{m}$ . This result would suggest that the  $\nabla n \times \nabla T$  source term dominates only when a major part of the absorption is caused by inverse bremsstrahlung; i.e., in experiments with a large region of underdense plasma caused by a prepulse or a long pulse length. Recent measurements of the B fields at NRL also lend support to this hypothesis.<sup>75</sup>

We also further investigated transport inhibition by ion-acoustic turbulence. This mechanism is of special interest in a high-Z plasma, because the condition that ion waves are weakly Landau damped is  $Z\theta_e \gg \theta_i$  (§5.6). A very simple model of transport inhibition by ion turbulence has been used in LASNEX to successfully model many experiments. However, this model is very crude and appears to significantly overestimate the inhibition. Improved models are under investigation. For example, we recently extended the theory of this inhibition to include the possible presence of self-generated magnetic fields, which can broaden the angular distribution of the turbulence (§ 4.8.1).

**Simulation Techniques.** Several new codes were written this year. One code was developed to examine the linear theory of the two-plasmon decay instability in an inhomogeneous plasma (§ 4.5.4). The other is a one-dimensional hybrid code that combines a fluid description of a plasma (complete with a heating and heat flow) with a detailed wave-optics solution for the electromagnetic waves. Using this code, we are studying the competition between inverse bremsstrahlung and Brillouin scatter in large, underdense plasmas. The code operates on the ion time scale and can simulate very large regions of underdense

plasma. In addition, we modified one of our particle codes (OREMP) to include a model of electron-ion collisions. Finally, we analyzed both the time-step integration and the noise level in particle codes (§ 4.9.1 and 4.9.2).

**Summary.** Our understanding of laser plasma coupling has increased considerably. Our calculations have successfully predicted many important features of laser plasma experiments. In this respect, microwave-simulation experiments have also been very valuable (§ 4.10). In turn, the experimental feedback has greatly helped us to improve our models. Although we have made much progress, our understanding is weak in many crucial areas. For example, our understanding of transport inhibition is crude and still remains to be tested in detail by experiments. We also still have a great deal to learn about the competition of inverse bremsstrahlung, back and side scatter, and filamentation in long-pulse-length experiments.

## References

56. K. G. Estabrook, E. J. Valeo, and W. L. Kruer, "Two-Dimensional Relativistic Simulations of Resonance Absorption," *Phys. Fluids* **18**, 1151 (1975).
57. D. T. Attwood, D. W. Sweeney, J. M. Auerbach, and P. H. Y. Lee, "Interferometric Confirmation of Radiation-Pressure Effects in Laser-Plasma Interactions," *Phys. Rev. Lett.* **40**, 184 (1978).
58. J. T. Larsen and J. Harte, *Profile Modification by the Ponderomotive Force in Spherical Targets*, Lawrence Livermore Laboratory, Rept. UCRL-79757, Rev. 1 (1977).
59. K. G. Estabrook, "Critical-Surface Bubbles and Corrugations and Their Implications to Laser Fusion," *Phys. Fluids* **19**, 1733 (1976).
60. A. B. Langdon, B. F. Lasinski, and W. L. Kruer, *Laser Program Annual Report-1975*, Lawrence Livermore Laboratory, Rept. UCRL-50021-75 (1976), pp. 313-315.
61. R. Spielman, K. Mizuno, and J. S. DeGroot, *Measurements of Density Profiles in Presence of Supersonic Flow*, University of California at Davis, Rept. PRGR-35 (1978).
62. K. R. Manes, V. C. Rupert, J. M. Auerbach, P. Lee, and J. E. Swain, "Polarization and Angular Dependence of 1.06- $\mu\text{m}$  Laser-Light Absorption by Planar Plasmas," *Phys. Rev. Lett.* **39**, 281 (1977).
63. R. J. Fahl and W. L. Kruer, "Laser Light Absorption by Short-Wavelength Ion Turbulence," *Phys. Fluids* **20**, 55 (1977).
64. W. Manheimer, D. G. Colombant, and B. H. Ripin, "Efficient Light Absorption by Ion-Acoustic Fluctuations in Laser-Produced Plasmas," *Phys. Rev. Lett.* **38**, 1135 (1977).
65. W. L. Kruer and K. G. Estabrook, "Laser Light Absorption due to Self-Generated Magnetic Fields," *Phys. Fluids* **20**, 1688 (1977).
66. A. B. Langdon and B. F. Lasinski, "Electromagnetic and Relativistic Plasma Simulation Models," in *Methods in Computational Physics*, B. Alder, S. Fernbach, and M. Rotenberg, Eds. (Academic Press, New York, 1977), vol. 16, pp. 327-366.
67. K. G. Estabrook and W. L. Kruer, "Properties of Resonantly Heated Electron Distributions," *Phys. Rev. Lett.* **40**, 42 (1978).

68. D. W. Forslund, J. M. Kindel, and K. Lee, "Theory of Hot-Electron Spectra at High Laser Intensity," *Phys. Rev. Lett.* **39**, 284 (1977).
69. K. R. Manes, H. G. Ahlstrom, R. A. Haas, and J. F. Holzrichter, "Light-Plasma Interaction Studies with High-Power Laser Glass," *J. Opt. Soc. Am.* **67**, 717 (1977).
70. K. G. Estabrook, *Laser Program Annual Report-1976* Lawrence Livermore Laboratory, Rept. UCRL-50021-76 (1977), pp. 4-76.
71. D. W. Phillion, W. L. Kruer, and V. C. Rupert, "Brillouin Scatter in Laser-Produced Plasmas," *Phys. Rev. Lett.* **39**, 1529 (1977).
72. E. H. Ripin, F. C. Young, J. A. Stamper, C. M. Armstrong, R. Decoste, E. A. McLean, and S. E. Bodner, "Enhanced Backscatter with a Structural Laser Pulse," *Phys. Rev. Lett.* **39**, 611 (1977).
73. G. Dahlbach, W. Mead, C. Max, and J. Thomson, *Laser Program Annual Report-1975*, Lawrence Livermore Laboratory, Rept. UCRL-50021-75 (1976), pp. 271-274.
74. C. E. Max, W. H. Manheimer, and J. J. Thompson, "Enhanced Transport across Laser-Generated Magnetic Fields," *Phys. Fluids* **21**, 128 (1978).
75. J. A. Stamper, E. A. McLean, and B. H. Ripin, "Studies of Spontaneous Magnetic Fields in Laser-Produced Plasmas by Faraday Rotation," *Phys. Rev. Lett.* **40**, 1177 (1978).

#### Author

W. L. Kruer

## 4.6 Light Absorption

### 4.6.1 Laser Light Absorption on a Steepened, Rippled Critical-Density Surface

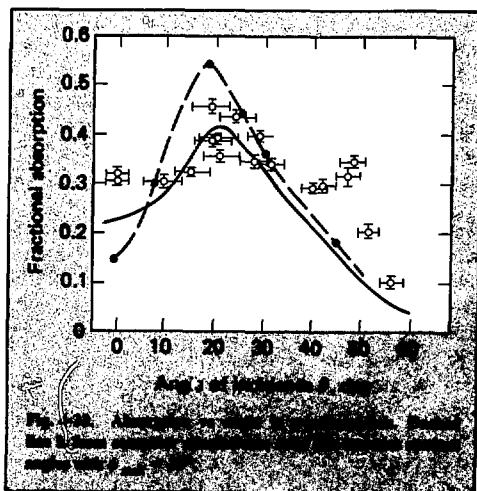
Determination of the magnitude and angular dependence of absorption of high-intensity laser light by plasma is of great importance to the laser fusion program. Recently, angle- and polarization-dependent light absorption in the intensity regime of  $10^{15}$ - $10^{16}$  W/cm<sup>2</sup> has been measured.<sup>76-78</sup> In this subsection, we discuss a simple model based on resonance absorption, absorption due to driven ion waves in a steepened density profile, and a modulated critical surface. Although not a unique interpretation of the data, this model agrees well with the shape of the experimental absorption curve, leaving about 10% angle- and polarization-independent absorption still to be accounted for.

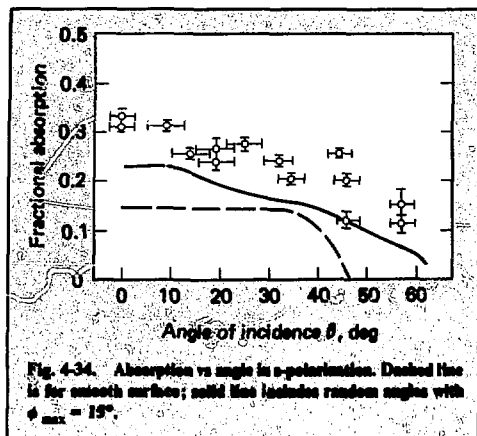
Resonance absorption has two signatures: polarization dependence and angular dependence.<sup>79</sup> The polarization dependence occurs because charge-density fluctuations are driven only if the light electric field has a component in the direction of the density gradient. This is the case if the electric field vector is in the plane of incidence (p-polarization), but not if it is normal to the plane of incidence (s-polarization). To resonantly excite charge-density fluctuations, the field must tunnel from the turning point  $n_c \cos^2 \theta$  to  $n_c$ . Here,  $n_c$  is the critical density and  $\theta$  is the angle of incidence. If  $\theta$  is

too large, the tunnelling distance is too great for effective absorption. On the other hand, if  $\theta$  is too small, the component of the field in the density-gradient direction vanishes, giving zero absorption. There is an optimum angle for absorption, given by  $\sin \theta \approx (k_0 L)^{-1/3}$ , where  $k_0$  is the free-space wave number and  $L$  is the density scale length.

Computer simulations of intense p-polarized plane light waves obliquely incident on a plasma have helped find the absorption in a self-consistent density profile.<sup>80-82</sup> Characteristically, for the intensity regime of interest, a density plateau forms at  $0.5$ - $0.7 n_c$  with a steep step through  $n_c$ . Figure 4-33 shows the experimental points for p-polarization together with the predictions from the computer simulations.<sup>81</sup> Both indicate an absorption peak at about  $20^\circ$  (corresponding to  $L \sim 1.5 \mu\text{m}$ ). However, the experimental peak is lower and broader, and it shows significantly more absorption at low and high angles than the simulations of the ideal model predict.

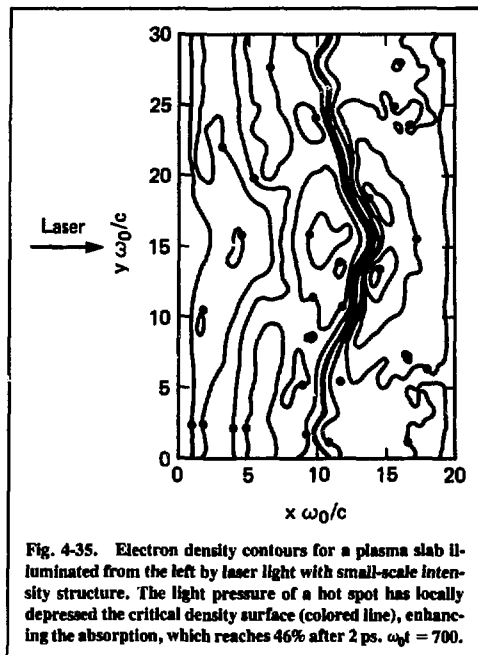
To obtain a theoretical prediction of s-polarization absorption, we assume that the 15% absorption at  $\theta = 0$  in the simulations is caused by ion-density fluctuations driven by the laser light (the analog of oscillating two-stream and parametric decay in a uniform plasma). If the density step at  $n_c$  is steep, then this absorption would be constant in s-polarization as long as the turning point of the light stays above the plateau, i.e.,  $\theta \leq 45^\circ$ . Accordingly, we take s-polarization absorption to be constant for  $\theta \leq 45^\circ$ . Comparing this model to the experimental points in Fig. 4-34, we see that the shape is roughly correct but that the experimental absorption is consistently higher.





The next element we add to the theoretical model is modulation of the critical surface. This effect is strongly suggested both experimentally and theoretically. In experiments similar to those of Ref. 76, a group at the Naval Research Laboratory observes only about 2% of the incident light backscattered into their f/14 lens, suggesting an rms scattering angle of  $\bar{\phi} \approx 5^\circ$ .<sup>83, 84</sup> In the experiments of Ref. 76, about 1% of the incident light is backscattered into the f/10 lens, suggesting an rms scattering angle of  $\sim 6^\circ$ . In both experiments the scattered light was in a cone of  $\sim 20$ - $30^\circ$  half angle, again suggesting surface inhomogeneities. Recently, Attwood et al. of LLL have interferometrically probed the plasma blowoff from plane disks in the intensity regime of interest, finding direct evidence of plasma inhomogeneities.<sup>85</sup>

A probable source for modulation of the critical surface is the intensity variation of the incident light. In the experimental intensity regime, light pressure may be equal to or greater than the plasma pressure. The laser beam used had a cloverleaf pattern, with intensity structures on the order of  $10 \mu\text{m}$  in diameter. We have performed computer simulations similar to those of Ref. 81, but with micron-scale hot spots similar to those observed on the laser beam, rather than plane waves. In a representative example, a plasma slab (with electron temperature  $T_e = 5 \text{ keV} = 3 \times \text{ion temperature } T_i$ ) was illuminated with light of average intensity  $10^{16} \text{ W/cm}^2$ , varying by a factor of four across the spot. Initially, absorption was 13% as expected for near-normal incidence. After a time corresponding to 2 ps (for ions with  $A/Z = 2$ ) the absorption reaches 46% as the critical surface dents to an optimum angle for resonance absorption on the sides of the density depression, as shown in Fig. 4-35. However, by 3 ps the depression has deepened further (Fig. 4-36) and the absorption has



dropped to 26%, which is still nearly double the absorption for normally incident plane waves. In these simulations the structure of the incident light was constant in time. If the time scales for variation of the intensity structure and for formation of optimum density depressions were matched, perhaps the absorption would remain closer to 46%. At any rate, these simulations make clear that hot spots in the incident light beam produce a significant modulation of the critical surface.

Another source for surface modulation is the instability of the critical surface, an effect which also has been seen in computer simulations.<sup>86</sup> However, the importance of such critical-surface instabilities has not yet been established, because the rippling occurs primarily outside the plane of polarization of the light.<sup>87, 88</sup>

A simple model can show the effect of these plasma inhomogeneities on the absorption of laser light. We first assume that the critical surface is randomly modulated on scale lengths longer than the freespace wavelength of the laser light. We then describe the modulation by assuming that the surface has a random tilt with respect to its initial orientation and that the tilt angle  $\theta$  is uniformly distributed from  $-\phi_{\max}$  to  $+\phi_{\max}$ , with equal probability of being in or out of the plane of incidence. If the tilt is in the

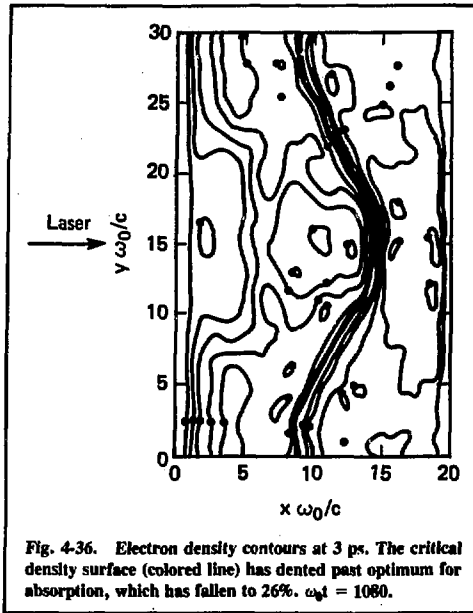


Fig. 4-36. Electron density contours at 3 ps. The critical density surface (colored line) has dented past optimum for absorption, which has fallen to 26%.  $\omega_0 t = 1060$ .

plane of incidence, the effect is to change the local incidence angle from  $\theta$  to  $\theta + \phi$ , thus averaging over the theoretical absorption curve. If the tilt is out of the plane of incidence, the effect is to change the polarization of a fraction of incident light: s-polarization becomes p, and vice versa. The power fraction changed is

$$f_{DP} = \frac{1}{2} \sin^2 \phi / (\sin^2 \theta + \cos^2 \theta \sin^2 \phi) \quad (30)$$

for both incident polarizations. The equivalent incidence angle is changed from  $\theta$  to

$$\theta' = \cos^{-1} [\cos \theta \cos \phi] \quad (31)$$

We use these relations and average over the absorption model discussed above to get absorption vs angle for a given  $\phi_{\max}$ . The solid lines on Figs. 4-33 and 4-34 show the resulting absorption curve for  $\phi_{\max} = 15^\circ$ . This choice of  $\phi_{\max}$  was suggested by the simulations modeling hot spots. Note that the agreement is much improved, although a discrepancy of about 10% angle- and polarization-independent absorption remains. Adequate agreement is seen for  $\phi_{\max}$  between 10 and  $20^\circ$ . This corresponds to an rms angle  $\bar{\phi} \sim 6\text{--}11^\circ$ , in rough agreement with the experimentally inferred values of 5–6°.

The extra 10% absorption left over may be due to one or more of several absorption processes. The two-plasmon decay instability is estimated to give  $\leq 5\%$ , primarily because of steepening of the plasma profile by plasma waves near  $\frac{1}{4} n_c$ .<sup>87,88</sup> Self-generated magnetic fields near  $n_c$  of several megagauss can give  $\sim 10\%$  absorption because of linear conversion of the extraordinary mode.<sup>89</sup> Ion-density fluctuations of magnitude  $\sim 10\%$  in the underdense plateau have been estimated to give  $\sim 10\%$  absorption in short-pulse-length experiments.<sup>90,91</sup> No data are yet available to distinguish among these absorption mechanisms.

In conclusion, we find that the experimentally observed absorption curve of Ref. 76 is reasonably well modeled by computer simulations in which the dominant absorption mechanism for p-polarization is resonance absorption with the additional assumption of a modestly rippled critical surface. In this interpretation, about 10% apparently angle- and polarization-independent absorption results from other absorption mechanisms.

## References

76. K. Manes, V. Rupert, J. Auerbach, P. Lee, J. Swain, "Polarization and Angular Dependence of 1.06- $\mu\text{m}$  Laser-Light Absorption by Planar Plasmas," *Phys. Rev. Lett.* **39**, 281 (1977).
77. J. S. Pearlman and M. K. Matzen, "Angular Dependence of Polarization-Related Laser-Plasma Absorption Processes," *Phys. Rev. Lett.* **39**, 140 (1977).
78. R. P. Godwin, P. Sachsenmaier, and R. Sigel, "Angle Dependent Reflectance of Laser-Produced Plasmas," *Phys. Rev. Lett.* **39**, 1198 (1977).
79. V. L. Ginzburg, *The Propagation of Electromagnetic Waves in Plasmas* (Pergamon Press, New York, 1964).
80. J. P. Freidberg, R. W. Mitchell, R. L. Morse, and L. I. Rudinski, "Resonant Absorption of Laser Light by Plasma Targets," *Phys. Rev. Lett.* **28**, 795 (1972).
81. K. G. Estabrook, E. L. Valeo, and W. L. Kruer, "Two-Dimensional Relativistic Simulations of Resonance Absorption," *Phys. Fluids* **18**, 1151 (1975).
82. D. W. Forslund, J. M. Kindel, K. Lee, E. L. Lindman, and R. L. Morse, "Theory and Simulation of Resonant Absorption in a Hot Plasma," *Phys. Rev. A* **11**, 679 (1975).
83. B. H. Ripin, Lawrence Livermore Laboratory, private communication (1977).
84. B. H. Ripin, "Angular Distribution of Laser Light Scattered from Laser-Product at High Irradiance," *Appl. Phys. Lett.* **30**, 134 (1977).
85. D. T. Attwood, D. W. Sweeney, J. M. Auerbach, and P. H. Y. Lee, "Interferometric Confirmation of Radiation-Pressure Effects in Laser-Plasma Interactions," *Phys. Rev. Lett.* **40**, 184 (1976).
86. K. G. Estabrook, "Critical-Surface Bubbles and Corrugations and Their Implications to Laser-Fusion," *Phys. Fields* **19**, 1733 (1976).
87. A. B. Langdon, B. F. Lasinski, and W. L. Kruer, Lawrence Livermore Laboratory, private communication (1977).

88. A. B. Langdon, and B. F. Lasinski, "Electromagnetic and Relativistic Plasma-Simulation Models," in *Methods in Computational Physics*, B. Alden, S. Fernbach, and M. Rotenberg, Eds. (Academic Press, New York, 1976), vol. 16, pp. 327-366.
89. W. L. Kruer and K. G. Estabrook, "Laser-Light Absorption and Harmonic Generation Due to Self Generated Magnetic Fields," in *Laser Interaction and Related Plasma Phenomena* (Plenum, New York, 1977), vol. 4, pp. 709-720.
90. R. J. Fachi and W. L. Kruer, "Laser-Light Absorption by Short-Wavelength Ion Turbulence," *Phys. Fluids* 20, 55 (1977).
91. W. Manheimer, D. G. Colombant, and B. H. Ripin, "Efficient Light Absorption by Ion Acoustic Fluctuations in Laser Produced Plasmas," *Phys. Rev. Lett.* 38, 1135 (1977).

## Authors

J. J. Thomson  
W. L. Kruer  
A. B. Langdon  
C. E. Max  
W. C. Mead

## 4.6.2 Properties of Resonantly Heated Electron Distributions

Recent experiments have shown that resonance absorption is an important process in the absorption of intense laser light.<sup>92-95</sup> In this subsection we present some important features of resonantly heated electrons, including their Maxwellian character and their dependences on laser light intensity and background plasma temperature. These dependences are found to result from the intensity-dependent density gradient length at the critical density  $n_{cr}$ , where the heating by plasma fields takes place. A dependence of the heated-electron energy on incident-light intensity is predicted over a wide range of intensities ( $3 \times 10^{14}$ – $10^{17}$  W/cm<sup>2</sup>, 1.06- $\mu$ m light), as indicated by recent experiments.<sup>92-95</sup> A very simple model illustrates the physics of this intensity-dependent gradient length.

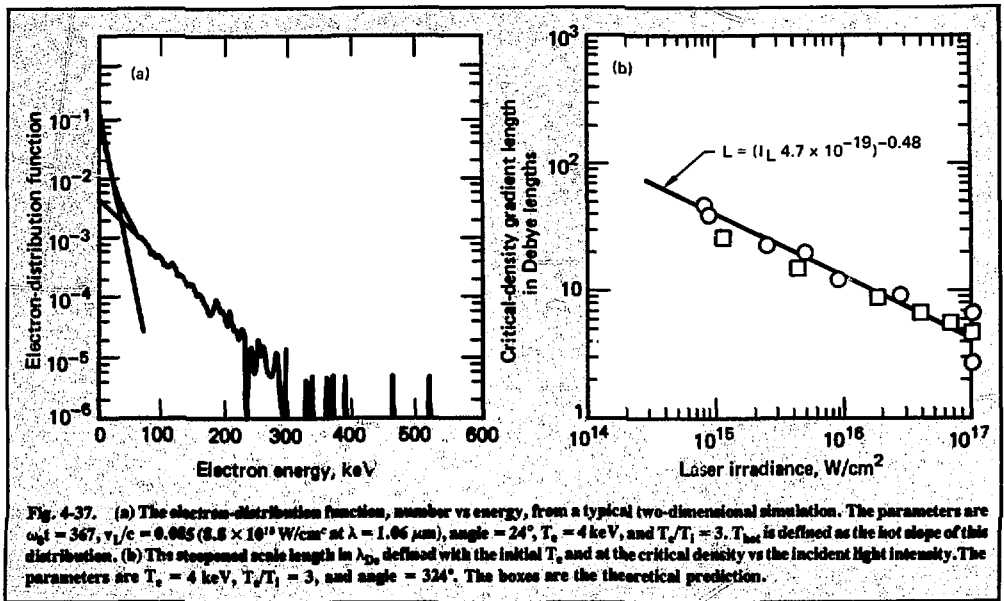
We begin with simulation results obtained with the same ideal model previously used to establish the importance of density-profile steepening and to provide estimates for the magnitude of the absorption and its polarization and angle dependence.<sup>96,97</sup> These early results predicted the qualitative features of the experimentally measured absorption (polarization dependence and broad angular dependence) and were sufficient to predict the magnitude within a factor of  $\leq 2$ . Using a two-dimensional particle simulation code with relativistic dynamics and electromagnetic fields, plane light waves are propagated from vacuum onto a plasma slab. Heated electrons reflect from the plasma sheath that forms on the vacuum side and are reemitted with their initial thermal temperature from the higher density boundary. After the density profile nonlinearly

steepens, we measured the heated-electron distribution and energy and the self-consistent scale length at the critical density.

To focus on the heated electrons caused by resonance absorption, we carried out a large number of simulations with p-polarized light incident at an angle of 24°, which is approximately the optimum angle in the steepened density profile. Figure 4-37(a) shows a typical heated-electron distribution that is well-approximated by a two-temperature Maxwellian.<sup>98-102</sup> The lower energy particles simply represent the initial thermal distribution that streams in from the higher density plasma, and the higher energy Maxwellian represents the resonantly heated electrons with "temperature"  $T_{hot}$ . This quasi-Maxwellian form of the heated-electron distribution has been suggested by laser-plasma experiments, where, typically, the high-energy x rays decrease exponentially with energy.<sup>108-102</sup> Maxwellian heated distributions have been directly observed in experiments with microwaves and have been attributed to electron heating by very localized fields.<sup>103</sup> Incidentally, we have also simulated examples of stimulated Brillouin backscatter that heat ions to a Maxwellian distribution.

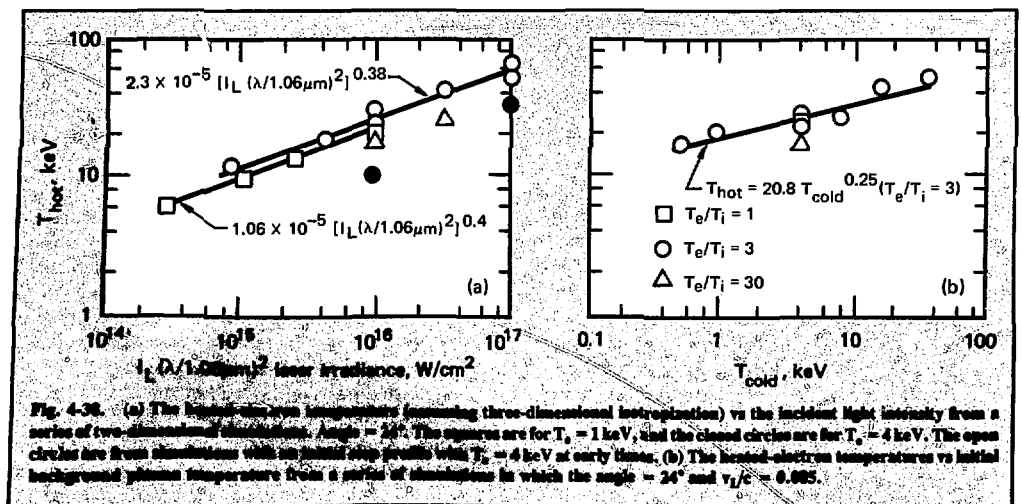
The local-density scale length near the critical density becomes quite steep. A crucial feature of the scale length  $L$  is its intensity dependence,<sup>104</sup> which is shown in Fig. 4-37(b). As the light intensity  $I_1$  (W/cm<sup>2</sup>) increases,  $L$  decreases as  $I_1^{-\beta}$ , where  $\beta \approx 0.48 \pm 0.07$  in these simulations.

This intensity dependence of the steepened scale length is important, because this scale length indirectly controls the heated-electron energies. In particular, the dependence of the heated-electron energy becomes in general weaker than the square-root dependence previously estimated.<sup>105-107</sup> This is confirmed by simulation results.<sup>108-110</sup> As shown in Fig. 4-38(a), the heated-electron energy measured in our simulations scales as  $I_1^\beta$ , where  $\beta \approx 0.39 \pm 0.07$ . The hot temperature here is defined as 2/3 of the slope of the high-energy part of the two-dimensional electron distribution, e.g., Fig. 4-37(a). Note that these are two-dimensional simulations and that the heating primarily occurs in the direction of the density gradient. If the electrons are isotropized in angle at higher density (either by collisions with highly stripped (high-Z) ions or by magnetic fields caused by the Weibel instability or other magnetic-field sources), the temperature of the isotropized distribution is 2/3 of the values from the two-dimensional simulations. Of course, the average hot-electron energy is the same in two dimensions as the hot temperature, and in three dimensions the average energy is 1.5 $\times$  the temperature. Because  $L$  also depends on the background plasma temperature  $T_c$  (keV), the heated-electron energy likewise depends on this temperature. As shown



in Fig. 4-38(b), this dependence is fairly weak<sup>109,110</sup>:  $T_{hot} \propto T_e \gamma$ , where  $\gamma \approx 0.25 \pm 0.07$ . An empirical formula that fits Fig. 4-38 reasonably well is  $T_{hot} = 1.2 \times 10^{-5} T_e^{0.25} [I_L (\lambda/1.06 \mu\text{m})^2]^{0.39}$  for  $T_e/T_i = 3$ , where  $\lambda$  is the wavelength,  $T_e$  is the electron temperature, and  $T_i$  is the ion temperature. Another formula that fits well is  $T_{hot} = T_e + 2.9 \times 10^{-8} T_e^{0.01} [I_L (\lambda/1.06 \mu\text{m})^2]^{0.125} \times [1 + (3T_i/Z T_e)^{0.25}]$ . Both formulas give about the

same answers in the parameter range of the simulations. However, they differ considerably at low  $T_e$  and/or low  $I_L$  where simulation is not yet economically feasible. For high  $T_e/T_i$ , our two data points in Fig. 4-38(b) show a shorter scale length and lower  $T_{hot}$ , presumably caused by the lower ion pressure. Of course, the significant parameter in the experiment is  $\bar{Z} T_e/T_i$ ,  $T_{hot}$  as a function of angle is shown in Fig. 4-39(a).



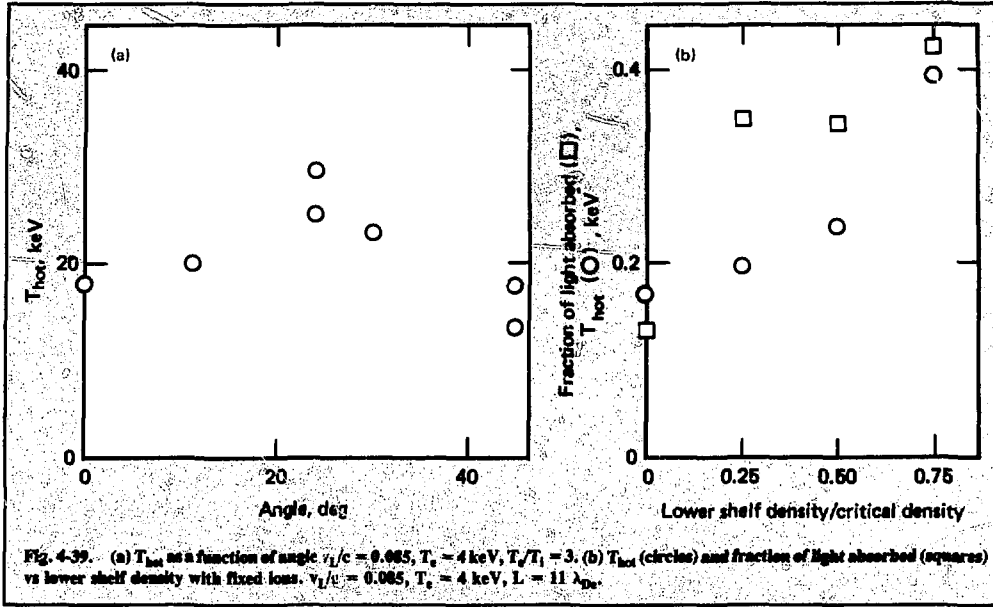


Fig. 4-39. (a)  $T_{\text{hot}}$  as a function of angle  $v_L/c = 0.085$ ,  $T_e = 4$  keV,  $T_e/T_i = 3$ . (b)  $T_{\text{hot}}$  (circles) and fraction of light absorbed (squares) vs lower shelf density with fixed ions.  $v_L/c = 0.085$ ,  $T_e = 4$  keV,  $L = 11 \lambda_{De}$ .

In the simulations, the fractional absorption  $f$  was nearly a constant at the various intensities; i.e.,  $f \approx (47 \pm 10)\%$  (less with the initial-density-step condition). Most of the runs started off with a ramp profile in which the density initially varied linearly from 0 to  $1.7 n_{cr}$  in three vacuum light wavelengths, or by a lower density shelf plus a steep gradient to a higher density shelf (see Refs. 96 and 97).

We reran the higher intensity simulations with an initial-sharp-step profile with quasipressure equilibrium, shown by the open circles in Fig. 4-38(a). Pressure equilibrium was tested by starting with maximum density too high and letting it fall down and conversely by starting too low and letting the maximum density increase with similar  $T_{\text{hot}}$ 's resulting. The temperatures with the initial-step profile were initially colder but gradually increased to approximately (but still lower than) the values obtained with the ramp profile as the lower density plateau established itself.  $T_{\text{hot}}$  increases rapidly with the shelf density because of pump swelling and longer wavelength plasma waves driven in that lower density region [Fig. 4-39(b)]. Interestingly, the absorption was higher in the case of ramp initial condition. Of course, the history of the laser pulse and hydrodynamic motion affect the density plateau.

We can gain insight into the physics by a very simple model. We adopt the capacitor model (an oscillating electric field  $E_d \cos \omega_0 t$ , where  $\omega_0$  is the laser frequency and  $t$  is time, applied to a plasma with a

linear density gradient with a scale length  $L$ ). The amplitude of the resonantly driven plasma field  $E_w$  and its spatial extent  $\ell_{\text{int}}$  can then be estimated in a warm plasma wave-breaking limit.<sup>111</sup> This gives

$$v_w = -1.5 v_e + (2.25 v_e^2 + 2 \omega_0 L v_d)^{1/2} \quad (32)$$

and  $\ell_{\text{int}} = 2(x_w + 3 \lambda_{De})$ , where  $v_e$  is the electron thermal velocity  $(T_e/m_e)^{1/2}$ ,  $\lambda_{De}$  the electron Debye length,  $v_w = eE_w/(m\omega_0)$ ,  $x_w = v_w/\omega_0$ , and  $v_d = eE_d/(m\omega_0)$ . Note that these expressions reduce to the cold plasma wave-breaking ones when the estimated thermal corrections are neglected.<sup>112</sup>

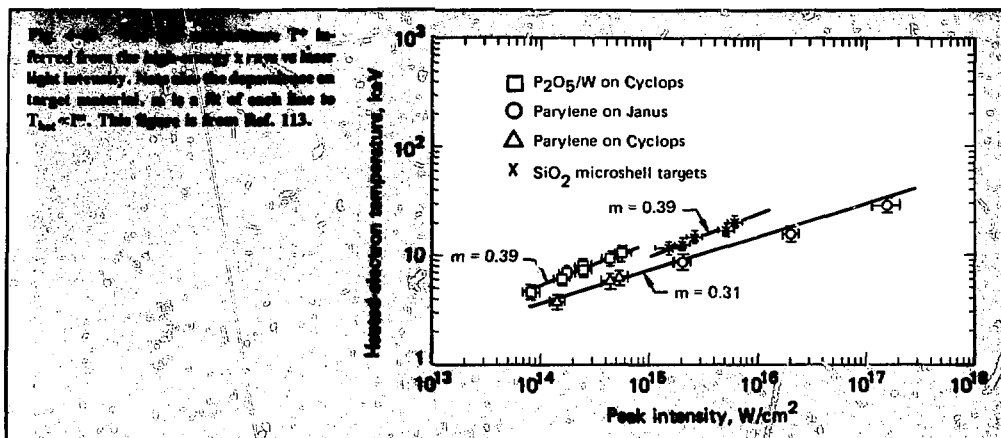
In this simplest model we next estimate the steepened scale length by simply balancing the thermal pressure with the ponderomotive pressure of the localized plasma field; i.e.,  $T_e \partial n / \partial x = ne^2/(4m\omega_0^2) \partial E_w^2 / \partial x$ . Using  $\partial E_w^2 / \partial x \approx E_w^2/(\ell_{\text{int}})$  then gives

$$L = 8(x_w + 3 \lambda_{De}) / (v_w/v_e)^2 \quad (33)$$

To relate the capacitor model to the situation of p-polarized light incident onto a plasma, we balance the energy fluxes:  $fcE_L^2/8\pi = \omega_0 LE_L^2/8$ , where  $E_L$  is the free-space value of the electric vector of the light and  $c$  is the speed of light. Hence:

$$v_d = v_L (fc/\pi\omega_0 L)^{1/2} \quad (34)$$





Equations (32)-(34) suffice to determine  $L$  and  $v_{th}$  in terms of the incident light intensity, the absorption efficiency, and the background temperature. The theoretical results for  $L$  are shown by the boxes in Fig. 4-37(b). Note that this very simple model is sufficient to capture the basic physical effect:  $L$  decreases as the intensity increases. Indeed, the predicted intensity dependence is nearly that observed in the simulations. This simple model seems to overestimate the temperature dependence of  $L$ .  $L$  is predicted to scale as  $T_e^\delta$  where  $\delta \approx 1$ , whereas the simulations show a weaker dependence of  $L$  on temperature. This discrepancy indicates that an improved model that takes into account laser light pressure, heated-electron pressure, and plasma flow is generally necessary.

We can readily understand the intensity dependence of  $T_{hot}$  in terms of the intensity dependence of  $L$ . Again appealing to the capacitor model,  $T_{hot} \propto eE_0 L$ , or, in terms of the light intensity,  $T_{hot} \propto E_0 L^{1/2}$ . Hence, we expect  $T_{hot} \propto I_L^\beta$ , where  $\beta \approx 0.26$ . This estimate is about 30% lower than the simulation results but is still in reasonable agreement.

Finally, recent experimental results indicate that the hot-electron temperature does scale less weakly than  $[I_L (\lambda/1.06\mu m)^2]^{1/2}$  over a wide intensity regime.<sup>113,114</sup> Figure 4-40, which is taken from Ref. 113, shows  $T^*$  as a function of intensity, measured in many different experiments with various target materials, where  $T^*$  is the temperature deduced from the slope of the high-energy x rays.  $T^*$  is a function of target material and, for a given material (Parylene), varies as  $I_L^{0.31}$  over a wide intensity regime from  $10^{14}$  to  $10^{17}$  W/cm<sup>2</sup> (1.06- $\mu m$  light). This dependence agrees reasonably with that suggested by these ideal simulations. More importantly, this weaker intensity dependence holds even for modest intensities like  $10^{14}$  W/cm<sup>2</sup>. This de-

pendence is consistent with our interpretation that the resonantly excited plasma waves locally steepen the density gradient, an effect that does not require a light pressure as large as the plasma pressure.

This correlation is encouraging, but a number of qualifications are in order. First,  $T^* \neq T_{hot}$ . LASNEX calculations show that  $T^*$  is often significantly lower in magnitude (factor of  $\sim 2$ ) than  $T_{hot}$  because of the space and time integrations inherent in the measurements and because of the general features of the hot-electron transport.<sup>115</sup> Second, we note that the values of  $T_{hot}$  inferred from Fig. 4-38(a) are typically 1.3 to 2 times  $T^*$  shown in Ref. 113. This discrepancy is also to be expected, because in the ideal simulations we consider the nearly optimum angle of incidence and a higher background temperature than may be obtained in the experiments. Both our simulations and simple model show that  $T_{hot}$  is smaller for other than optimum angles of incidence (see Fig. 4-39) and for smaller ion-electron temperature ratios. Although the simulations we have discussed illustrate the physics, improved models must allow for

- a distribution of angles of incidence,
- $T_e/T_i$  and ionization states,
- the admixture of other absorption processes,
- more complex particle boundary conditions than the one-pass model discussed here,
- the lower shelf density.

For example, the larger heated temperature for the higher  $Z$  targets is at least partly caused by the fact that the heated electrons are more often reflected from the high-density plasma back into the heating region. Simulations show about a 25% increase in temperature when the electrons make on the average two passes through the absorption regions.

We acknowledge conversations with A. B. Langdon and R. A. Haas.

## References

92. K. R. Manes, V. C. Rupert, J. M. Auerbach, P. H. Y. Lee, and J. E. Swain, "Polarization and Angular Dependence of 1.06- $\mu\text{m}$  Laser-Light Absorption by Planar Plasmas," *Phys. Rev. Lett.* **39**, 281 (1977).
93. J. S. Pearlman, J. J. Thomson, and C. E. Max, "Polarization-Dependent Absorption of Laser Radiation Incident on Dense-Plasma Planar Targets," *Phys. Rev. Lett.* **38**, 1397 (1977).
94. J. E. Balmer and T. P. Donaldson, "Resonance Absorption of 1.06- $\mu\text{m}$  Laser Radiation in Laser-Generated Plasmas," *Phys. Rev. Lett.* **39**, 1084 (1977).
95. R. P. Godwin, P. Sachsenmaier, and R. Sigel, "Angle-Dependent Reflectance of Laser-Produced Plasmas," *Phys. Rev. Lett.* **39**, 1198 (1977).
96. K. G. Estabrook, E. J. Valeo, and W. L. Kruer, "Two-Dimensional Relativistic Simulations of Resonance Absorption," *Phys. Fluids* **18**, 1151 (1975).
97. K. G. Estabrook, E. J. Valeo, and W. L. Kruer, "Plasma Heating and Gradient Modification by Resonant Absorption," *Phys. Lett.* **49A**, 109 (1974).
98. B. H. Ripin, P. G. Burkhalter, F. C. Young, J. M. McMahon, D. G. Colombant, S. E. Bodner, R. R. Whitlock, D. J. Nagel, D. J. Johnson, N. K. Winsor, C. M. Dozier, R. D. Bleach, J. A. Stamper, and E. A. McLean, "X-Ray Emission Spectra from High-Power-Laser-Produced Plasma," *Phys. Rev. Lett.* **34**, 1313 (1975).
99. C. Yamanaka, T. Yamanaka, T. Sasaki, and J. Mizui, "Brillouin Backscattering and Parametric Double Resonance in Laser-Produced Plasma," *Phys. Rev. Lett.* **32**, 1038 (1974).
100. J. F. Kephart, R. P. Godwin, and G. H. McCall, "Bremsstrahlung Emission from Laser-Produced Plasmas," *Appl. Phys. Lett.* **25**, 108 (1974).
101. W. C. Mead, R. A. Haas, W. L. Kruer, D. W. Phillion, H. N. Kornblum, J. D. Lindl, D. R. MacQuigg, and V. C. Rupert, "Observation and Simulation of Effects on Parylene Disks Irradiated at High Intensities with a 1.06- $\mu\text{m}$  Laser," *Phys. Rev. Lett.* **37**, 489 (1976).
102. P. Kolodner and E. Yablonovitch, "Proof of the Resonant Acceleration Mechanism for Fast Electrons in Gaseous Laser Targets," *Phys. Rev. Lett.* **37**, 1754 (1976).
103. C. P. DeNeef and J. S. DeGroot, "Electron Acceleration by a Localized Electric Field," *Phys. Fluids* **20**, 1074 (1977).
104. K. G. Estabrook, "A Density-Profile Model for Laser Pellet Interaction Codes," *Bull. Am. Phys. Soc.* **21**, 1067 (1976).
105. J. Albritton and P. Koch, "Cold Plasma Wavebreaking: Production of Energetic Electrons," *Phys. Fluids* **18**, 1136 (1975).
106. J. P. Freidenberg, R. W. Mitchel, R. L. Morse, and L. I. Rudinski, "Resonant Absorption of Laser Light by Plasma Targets," *Phys. Rev. Lett.* **28**, 795 (1972).
107. D. W. Forslund, J. W. Kindel, K. Lee, E. L. Lindman, and R. L. Morse, "Theory and Simulation of Resonant Absorption in a Hot Plasma," *Phys. Rev. A* **11**, 679 (1975).
108. E. Valeo, W. Kruer, K. Estabrook, H. Langdon, B. Lasinski, C. Max, and J. Thomson, "Collective Plasma Behaviour in Laser Plasma Experiments," in *Plasma Physics and Controlled Nuclear Fusion Research 1976* (International Atomic Energy Agency, Vienna, 1977), vol. 1, pp. 133-146.
109. D. W. Forslund, "Toward Realistic Modeling of Laser-Plasma Interaction," *Bull. Am. Phys. Soc.* **21**, 1066 (1976).
110. D. W. Forslund, J. W. Kindel, and K. Lee, "Theory of Hot-Electron Spectra at High Laser Intensity," *Phys. Rev. Lett.* **39**, 284 (1977).
111. W. L. Kruer, Lawrence Livermore Laboratory, private communication (1977).
112. P. Koch and J. Albritton, "Electron and Ion Heating through Resonant Plasma Oscillations," *Phys. Rev. Lett.* **32**, 1420 (1974).
113. K. R. Manes, H. G. Ahlstrom, R. A. Haas, and J. F. Holzrichter, "Light-Plasma Interaction Studies with High-Power Glass Laser," *J. Opt. Soc. Am.* **67**, 717 (1977).
114. R. B. Spielman, K. Mizuno, and J. S. Degroot, "Measurements of Resonant Absorption," *Bull. Am. Phys. Soc.* **22**, 1188 (1977).
115. W. C. Mead, Lawrence Livermore Laboratory, private communication (1977).

## Authors

K. G. Estabrook

W. L. Kruer

## 4.6.3 Absorption of Focused Light Beams

Recent LLL experiments on the absorption of high-intensity laser light suggest that large-scale craters are present in the underdense plasma and that these craters are a direct result of radiation pressure.<sup>116</sup> Crater formation occurs because self-steepening of the plasma density profile takes place preferentially near the center of the focal spot, indenting the critical surface where the beam is most intense. In addition, the outward flow from the ablation region is restricted by the light pressure, so the plasma is forced to expand around the laser beam.

Experiments also indicate that some mechanism is acting to smooth out the sharp angle and polarization dependence of absorption suggested by particle simulations that use planar light.<sup>117</sup> Although alternative explanations exist (notably megagauss dc magnetic fields<sup>118</sup> and ion-acoustic turbulence,<sup>119</sup> large craters seem to be important in this regard. Associated with craters are a concave critical surface and strong transverse density gradients in the underdense region that significantly refract the incoming light. Both features increase the effective angle of incidence of light and enhance resonant absorption. Even for apparent normal incidence, fractional absorption may be in the range of 30-40%.

We have developed a computational model to study craters formed by focused laser beams, their stability, and their consequences for absorption. It includes wave-optics solutions for arbitrarily focused light, a description for resonant absorption, and an isothermal hydrodynamic description of the plasma response to the ponderomotive force. For a linearly polarized focused laser beam, the ponderomotive force is inherently three-dimensional because of polarization-dependent (resonant) absorption.<sup>120</sup> However, we find a numerically tractable self-consistent approximation to the problem by assuming a circularly

polarized incident beam. In that case the ponderomotive force, and hence the plasma density profile, are azimuthally symmetric about the laser axis to first order.<sup>121</sup>

We describe the propagation of the laser light with the equation

$$\frac{\partial^2 \bar{E}}{\partial t^2} + \nu \frac{\partial \bar{E}}{\partial t} = c^2 \nabla \times \nabla \times \bar{E} - \omega_{pe}^2 \bar{E} - v_e^2 \times \{ \gamma \nabla (\nabla \cdot \bar{E}) - (\nabla \cdot \bar{E}) \nabla n_0 / n_0 \} + \nabla \sigma (\nabla \cdot \frac{\partial \bar{E}}{\partial t}), \quad (35)$$

where  $\bar{E}$  is the electric field,  $n_0$  is the background plasma density,  $\nu$  is the collisional damping rate,  $\gamma$  is the ratio of specific heats,  $\omega_{pe}^2 = 4\pi ne^2/m$ ,  $v_e$  is the electron thermal velocity,  $v_e^2 = T_e/m$ , and  $\sigma$  is a phenomenological diffusion coefficient for charge density. We give  $\sigma$  a nonlinear dependence on the electric field strength:  $\sigma = \sigma_{NL} (|\nabla \cdot \bar{E}| / 4\pi en_0)^\alpha$ , where  $\sigma_{NL}$  and  $\alpha$  are positive constants. For  $\alpha \geq 2$  the fluctuating plasma density is effectively limited to  $\delta n/n \sim 1$  because the damping grows extremely heavy for larger values. This is exactly the behavior required to model cold wavebreaking.

We solve Eq. (35) in a spherical  $(r, \theta, \phi)$  coordinate system oriented along the laser axis. For circularly polarized light and an azimuthally symmetric plasma, it is appropriate to remove the azimuthal dependence of the fields as  $\exp(i\phi)$ . Then Eq. (35) is effectively two dimensional and may be differenced on an  $r$ - $\theta$  grid. The time advancement is done explicitly, and the fields on the vacuum boundary are obtained by an adaptation of Lindman's scheme to spherical coordinates.<sup>122</sup>

The plasma dynamics are followed by solving the isothermal fluid equations:

$$\frac{\partial n}{\partial t} + \nabla \cdot (n\bar{v}) = 0 \quad (36)$$

$$M \left[ \frac{\partial}{\partial t} (n\bar{v}) + \nabla \cdot (n\bar{v}\bar{v}) \right] = -T \nabla n - \frac{nc^2}{2m\omega_0^2} \nabla \langle E^2 \rangle - \nabla \cdot \bar{Q}, \quad (37)$$

where  $n$ ,  $v$ , and  $T$  are the plasma density, velocity, and temperature, respectively,  $M$  is the ion mass, and  $\bar{Q}$  is the (nonlinear) viscosity tensor. The angular brackets  $\langle \rangle$  in the ponderomotive force driving term denote a time average over the laser period  $2\pi/\omega_0$ .

In the following example calculation we attempt to roughly model the conditions of the high-intensity, short-pulse-length disk experiments referred to

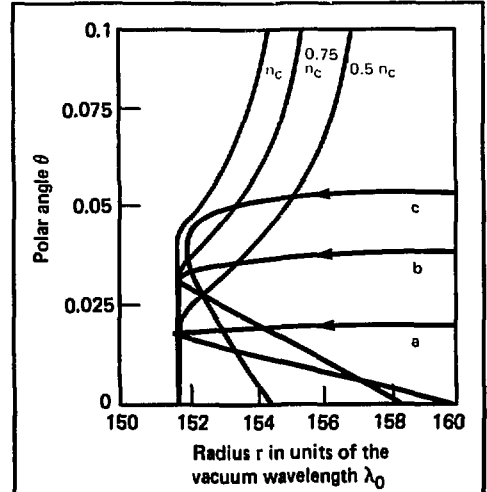
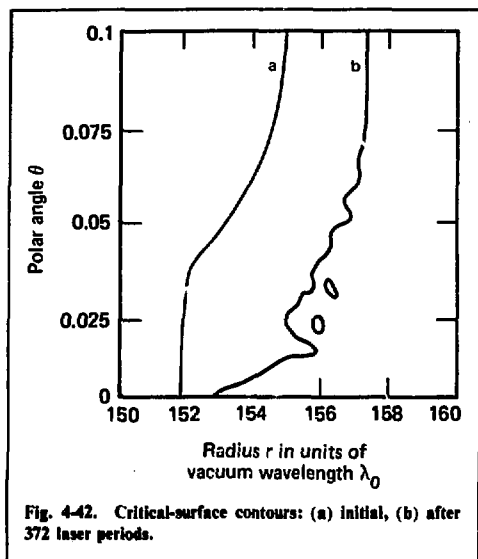


Fig. 4-41. Contour plot of the initial plasma density. Also shown are numerical solutions for trajectories of three typical rays (a, b, and c). The steepest plasma density scale length on the laser axis ( $\theta = 0$ ) is  $K_0 L = 1$ , while far off axis ( $\theta = 0.01$ ) the unsteepened scale length is  $K_0 L = 24$ . Approximately 90% of the incident power is inside ray c.

above.<sup>117</sup> We consider the situation in which a crater has been formed during the early part of the laser pulse, and begin our calculation at peak power to observe the short-term stability of the crater and its effect on absorption. The postulated initial density profile is shown in Fig. 4.41. A super-Gaussian  $[I = I_0 \exp(-(\theta/\theta_0)^4)]$  laser beam of peak intensity  $I_0 = 3 \times 10^{15} \text{ W/cm}^2$  is focused by an  $f/10$  lens onto the rear wall of the crater. The width of the crater corresponds to the diffraction-limited focal spot size of about  $20 \mu\text{m}$  (Nd light). The average electron temperature is 3.5 keV, corresponding to  $v_0/v_e = 0.6$ , where  $v_0 = eE_0/m\omega_0$  is the electron quiver velocity in the vacuum field. Inverse bremsstrahlung absorption is negligible in this example.

The critical surface at the rear of the crater is initially smooth and the density gradient very steep, so one might expect only minimal absorption of the normally incident light, perhaps a few percent. However, the calculated absorption for this initial configuration is about 17%. This enhanced absorption fraction may be understood by an examination of some typical ray trajectories, shown in Fig. 4-41. The walls of the crater guide the outermost rays (ray c) to propagate nearly parallel to the critical surface. Consequently, these rays, which can carry a substantial portion of the total power, are resonantly absorbed with great efficiency. Even rays closer to the center of the crater (rays a and



b) are refracted enough to reach the critical surface with an effective angle of incidence of  $10\text{--}20^\circ$ . Taking into account that only half the rays, on the average, have the correct polarization for this enhanced resonant absorption, and using the steepened density scale length  $k_0 L \sim 1$ , we estimate that an energy-averaged refraction of about  $25^\circ$  is sufficient to give the calculated absorption efficiency of 17%. This estimate is reasonable for the trajectories of Fig. 4-41.

Figure 4-42 shows the plasma density after 372 laser periods (about 14.5 ps scaled to  $6 m_p$ ). Plasma expansion around the laser beam has enhanced the focusing effect of the crater. As a result, the intensity on the laser axis is almost an order of magnitude larger than the nominal value of  $3 \times 10^{15} \text{ W/cm}^2$  and has severely indented the critical surface. This is apparently the asymptotic state of the plasma. The asymptotic absorption is about 40%, and the scattered light distribution reaches out to about  $45^\circ$ .

The initial density configuration in the above example was somewhat arbitrary. However, we have made calculations with no initial crater, and we find that one is formed that is quite similar to that of Fig. 4-42.

In summary, using a wave optics-hydrodynamics model, we find that the effects of a finite focal spot size can significantly increase the absorption of laser light by a plasma. In particular, a large crater forms, resulting in a convex critical surface, refraction of the incident light, and therefore enhanced resonant absorption.

## References

116. D. T. Attwood, D. W. Sweeney, J. M. Auerbach, and P. H. Y. Lee, "Interferometric Confirmation of Radiation-Pressure Effects in Laser-Plasma Interactions," *Phys. Rev. Lett.* **40**, 184 (1978).
117. K. R. Manes, V. C. Rupert, J. M. Auerbach, P. H. Y. Lee and J. E. Swain, "Polarization and Angular Dependence of  $1.06\text{-}\mu\text{m}$  Laser-Light Absorption by Planar Plasmas," *Phys. Rev. Lett.* **39**, 281 (1977).
118. W. L. Krueer and K. G. Estabrook, "Laser-Light Absorption due to Self-Generated Magnetic Fields," *Phys. Fluids* **20**, 55 (1977).
119. R. J. Faehl and W. L. Krueer, "Laser Light Absorption by Short-Wavelength Ion Turbulence," *Phys. Fluids* **20**, (1977).
120. J. H. Erkkila, *Laser Light Scattering and Absorption in Dense, Spherically Symmetric Plasmas*, Ph.D. thesis, University of California, Berkeley, CA (1975); Lawrence Livermore Laboratory, Rept. UCRL-51914 (1975).
121. J. J. Thomson, C. E. Max, and K. G. Estabrook, "Magnetic Fields due to Resonance Absorption and Laser Light," *Phys. Rev. Lett.* **35**, 663 (1975).
122. E. L. Lindman, "Free-Space" Boundary Conditions for the Time-Dependent Wave Equation," *J. Comp. Phys.* **48**, 66 (1975).

## Author

C. J. Randall

## 4.6.4 Linear Theory of the $2\omega_{pe}$ Instability in Inhomogeneous Plasmas

We have critically examined and revised the most complete theory of the  $2\omega_{pe}$  instability in a linear density gradient.<sup>123</sup> This instability, the decay of the incident electromagnetic wave into two electron plasma waves, occurs in the neighborhood of quarter-critical density. In current laser fusion experiments, this instability may be responsible for high-energy electrons. The emission of  $3\omega_0/2$  light, an important diagnostic of the underdense plasma, is a signature of this instability.

But the ZOHAR (our electromagnetic, relativistic, particle simulation code)<sup>124</sup> results for the linear phase of this instability in an inhomogeneous plasma disagree with the predictions of the unrevised theory. In general, the simulations indicate that the thresholds are higher and the wave numbers smaller than the theory predicts. The spectrum of plasma waves is a particularly essential aspect of the subsequent nonlinear evolution of this instability.

The theory contains two basic results. The condition for absolute instability puts a limit on the transverse component of the plasma wave vector:  $k_y < 0.39\omega_{pe}v_0/v_e^2$ . Here  $\omega_{pe}$  is the electron plasma frequency at quarter-critical density,  $v_0$  is the peak oscillatory electron velocity in the pump's electric field, and

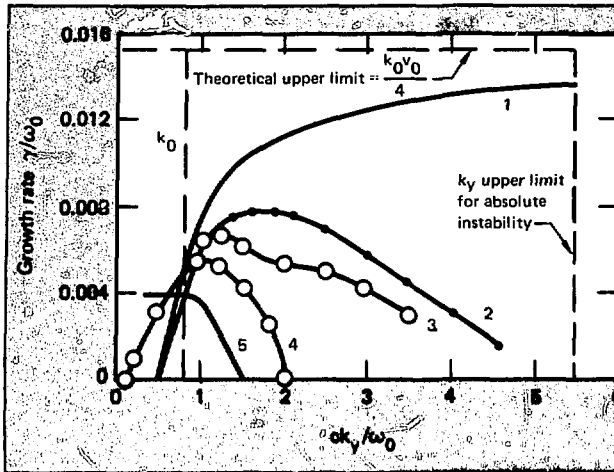


Fig. 4-43. Growth rate \$\gamma/\omega\_0\$ versus \$k\_y/k\_0\$ for \$v\_0/c = 0.07\$, \$I = 6 \times 10^{15}\$ W/cm\$^2\$, and \$T\_e = 1.3\$ keV. Curve 1 is the theoretical limit \$\gamma/\omega\_0 = k\_0 v\_0 / 4\$. Curve 2 is the fluid code results without Landau damping. Curve 3 is the fluid code results with Landau damping. Curve 4 is the ZOHAR results with Landau damping. Curve 5 is the ZOHAR results without Landau damping. The dashed line is the theoretical upper limit.

$v_e \equiv (T_e/m_e)^{1/2}$  is the electron thermal velocity. The expression for the growth rate,

$$\gamma = \frac{k_0 v_0}{4} - \frac{\omega_{pe}}{k_y L}, \quad (38)$$

where  $k_0$  is the laser wave vector and  $L \equiv \rho_{cr} (dp/dx)^{-1}$ , is combined with the  $k_y$  limit to derive a threshold expression. (The definitions of  $L$  and  $v_0$  differ in Ref. 123, and we have corrected their numerous algebraic and typographical errors.)

For typical parameters,  $v_0/c = 0.07$  or  $I = 6 \times 10^{15}$  W/cm\$^2\$ for Nd:glass lasers,  $v_e/c = 0.05$  or  $T_e = 1.3$  keV, and a gradient scale length of  $10 \mu\text{m}$ , curve 1 of Fig. 4-43 is the growth rate as a function of  $k_y$  as given by Eq. (38). This growth rate rises continually until the upper  $k_y$  limit is reached, an unsatisfying feature. The ZOHAR results, curve 5 in Fig. 4-43, have much lower growth rates and a narrower  $k_y$  spectrum.

In examining the theory, we ferreted out the fact that the approximation  $k_y \gg k_0$  was used, contrary to the claim of Ref. 123. At the plasma temperatures of interest, Landau damping limits  $k_{\text{plasma}}$  to  $\sim k_0$ . Therefore, this approximation means that the theory is questionable for our parameter region.

As an independent check, we have solved numerically the same two linearized equations that are the starting point of the elegant theoretical analysis:

$$\frac{\partial \tilde{v}}{\partial t} + \frac{\partial}{\partial x} (\tilde{v}_0 \cdot \tilde{v}) = -E - \frac{3 v_e^2}{\rho_0(x)} \frac{\partial \rho}{\partial x} \quad (39)$$

$$\frac{\partial \rho}{\partial t} + \frac{\partial}{\partial x} \cdot (\rho_0(x) \cdot \tilde{v} + \rho \cdot \tilde{v}_0) = 0. \quad (40)$$

Here,  $E(x, y, t)$  is obtained from Poisson's equation, and  $v(x, y, t)$  and  $\rho(x, y, t)$  are the first-order perturbed quantities. These equations are solved by a central-difference, leapfrog scheme. No approximation  $k_y > k_0$  is made. Additionally, a wavelength-dependent Landau damping operator is included through the Fourier transform of Eq. (40). This feature is an option in the code and allows us to isolate the effects of Landau damping.

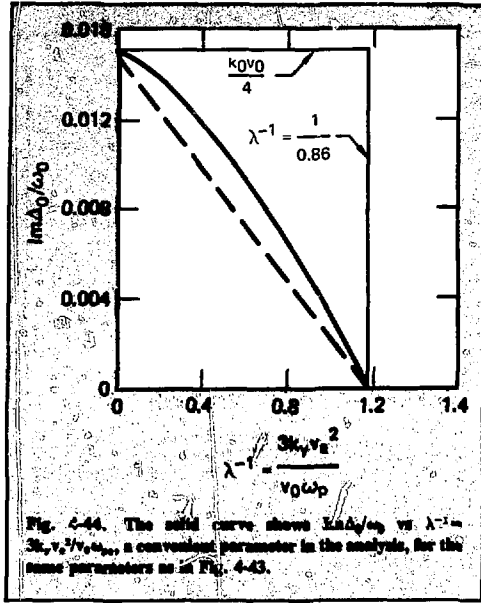
Curve 3 of Fig. 4-43 gives the fluid code results without Landau damping. Curve 4, the code results with Landau damping, is in better agreement with the ZOHAR results. The restrictions imposed by Landau damping are evident. For this parameter regime, Landau damping imposes a more stringent cutoff on  $k_y$  than the absolute instability condition.

In principle, for  $k_y > k_0$  the fluid code results without Landau damping (curve 3) should agree with the theory (curve 1). The correct expression for the growth rate, as derived in Ref. 123, is actually

$$\gamma = \text{Im} \Delta_0 - \frac{\omega_{pe}}{k_y L}. \quad (41)$$

The authors used the limiting value for  $\text{Im} \Delta_0$  rather than the actual value. If  $\text{Im} \Delta_0$  is evaluated numerically, the theoretical expression [i.e., Eq. (41)] becomes curve 2 of Fig. 4-43. This curve generally agrees with curve 3, as it should.

If, as in Fig. 4-44,  $\text{Im} \Delta_0$  is plotted as a function of  $\lambda^{-1} = 3 k_y v_e^2 / v_0 \omega_{pe}$ , a convenient parameter in the analysis, then a linear dependence for  $\text{Im} \Delta_0$  is seen as a much better choice than merely using the limiting value. Instead of Eq. (38), we get



$$\gamma = \frac{k_0 v_0}{4} \left( 1 - 12\lambda_1 \frac{k_y v_e^2}{v_0 \omega_{pe}} \right) - \frac{\omega_{pe}}{k_y L}, \quad (42)$$

where  $\lambda_1 = 0.86$ . Differentiating to get the  $k_y$  that gives the maximum growth rate, we find

$$\gamma_{\max} = \frac{k_0 v_0}{4} \left[ 1 - \left( \frac{k_0 L}{48\lambda_1} \frac{v_0^2}{v_e^2} \right)^{-1/2} \right]. \quad (43)$$

Although the threshold condition

$$k_0 L \frac{v_0^2}{v_e^2} > 48\lambda_1 \quad (44)$$

is superficially similar to the one given in Ref. 123, the assumptions underlying it are more reasonable and not based on a cancellation of errors. Furthermore, the maximum growth rate no longer occurs at maximum  $k_y$ , a pleasing correction. And the growth rates of Eq. (42) are in much better agreement with the fluid code and ZOHAR.

Since the theory and the fluid code solve a simpler problem, the remaining differences between them and ZOHAR (where  $k_y > k_0$ ) are to be expected. Only one

$k_y$  mode is allowed to grow, and no other variation transverse to the density gradient is allowed in the formulation given by Eqs. (39) and (40). Therefore, we believe that ZOHAR handles the linear problem correctly, and we have more confidence in our studies of the nonlinear evolution of the  $2\omega_{pe}$  instability.

## References

123. C. S. Liu and M. N. Rosenbluth, "Parametric Decay of Electromagnetic Waves into Two Plasmons and Its Consequences," *Phys. Fluids* **19**, 967 (1976).
124. A. B. Langdon and B. F. Lasinski, "Electromagnetic and Relativistic Plasma Simulation Models," in *Methods in Computational Physics*, B. Alder, S. Fernbach, and M. Rotenberg, Eds. (Academic Press, New York, 1976), vol. 16, pp. 327-366.

## Authors

B. F. Lasinski  
A. B. Langdon

## 4.6.5 Resonant Absorption of Laser Light by a Magnetized Plasma

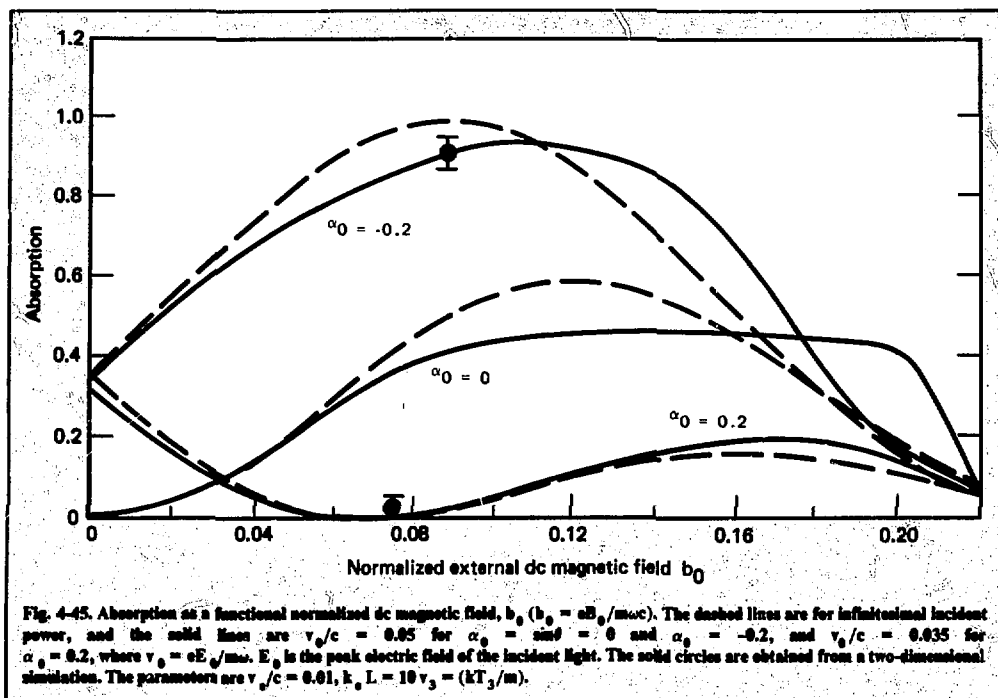
We report here a theoretical and computational investigation of resonant absorption of p-polarized light that is obliquely incident onto a plasma with an external magnetic field. The absorption must be calculated self-consistently because dc magnetic fields are generated by resonant absorption. The maximum absorption is increased to 99%. We find excellent agreement between theoretical predictions and two-dimensional particle simulation calculations.

The high-frequency electron fluid velocity  $\vec{u}_h$  is given by

$$\partial \vec{u}_h / \partial t = -(e/m) \vec{E}_h - (\gamma_e k T_e / m n_e) \nabla n_h - [(e/mc) \vec{u}_h \times \vec{B}_0] + \vec{s}_h, \quad (45)$$

where  $\vec{s}_h = -(e/mc) [(\vec{u}_h \times \vec{B}_0) + (\vec{u} \times \vec{B}_h)] - (\vec{u}_h \cdot \nabla) \vec{u}_h - (\vec{u}_h \cdot \nabla) \vec{u}_h \approx (-ie/m\omega) \nabla (\vec{u}_h \cdot \vec{E}_h)$ , to third order in the high-frequency quantities; the subscripts h and l designate high- and low-frequency quantities, respectively;  $\vec{B}_0$  and  $\vec{B}_l$  are the externally imposed and induced dc magnetic fields, respectively;  $\vec{u}_l$  is the low-frequency electron fluid velocity, e and m are the electron charge and mass, respectively;  $\gamma_e$  is the ratio of specific heats, k is Boltzmann's constant;  $T_e$  is the electron temperature; c is the speed of light; and n is the plasma density. We have used  $\partial/\partial t \rightarrow i\omega$  and<sup>125</sup>

$$\nabla \times \vec{u}_l = (e/mc) \vec{B}_l. \quad (46)$$



By combining the high-frequency Faraday's and Ampere's laws, we obtain

$$(\nabla \times \nabla \times - k_0^2) \vec{E}_h = (ik_0 4\pi e/c) (n_h \vec{u}_h + n_h \vec{u}_q) \quad (47)$$

Then we obtain  $n_h$  from  $\nabla \cdot \vec{E}_h = -4\pi e n_h$  and  $\vec{u}_h$  from Eq. (45). Equation (47) thus becomes

$$\begin{aligned} \nabla \times \nabla \times \vec{E}_h - (\gamma_e k T_e / mc^2) \nabla (\nabla \cdot \vec{E}_h) - k_0^2 \epsilon \vec{E}_h \\ = - (ie/mc) \vec{B}_0 \times (\nabla \times \nabla \times - k_0^2) \vec{E}_h \\ - (ik_0^2/\omega) [\vec{u}_q \nabla \cdot \vec{E}_h \\ + (\omega_{pe}^2/\omega^2) \nabla (\vec{u}_q \cdot \vec{E}_h)] \quad (48) \end{aligned}$$

where  $\omega_{pe}^2 = 4\pi n_e e^2/m$  and  $\epsilon = 1 - \omega_{pe}^2/\omega^2$ .

Also, we use the low-frequency Ampere's law to eliminate  $\vec{B}_q$  from Eq. (46) and obtain<sup>12a</sup>

$$\begin{aligned} \nabla \times \nabla \times \vec{u}_q = (-\omega_{pe}^2/c^2) \\ \times [\vec{u}_q + (e^2/2m^2\omega^3) \text{Im}(\vec{E}_h \nabla \cdot \vec{E}_h^*)] \quad (49) \end{aligned}$$

Equations (48) and (49) completely specify the high-frequency  $\vec{E}_h$  and the low-frequency  $\vec{u}_q$  in terms of  $\vec{B}_0$ . The induced magnetic field  $\vec{B}_q$  can be found from Eq. (46).

We now apply these equations to resonant absorption of p-polarized laser light incident obliquely onto an inhomogeneous plasma (the plane of incidence is the x-y plane,  $n_q = (x/L)n_c$ , where  $n_c$  is the critical density, and  $\vec{B}_0 = \vec{B}_0 \hat{z}$ ). The high-frequency electric field can be written as  $\vec{E}_h = [\hat{x} E_x(x) + \hat{y} E_y(x)] \exp[i(\omega t - k_0 \alpha_0 y)]$ , where  $\alpha_0 = \sin \theta$ ,  $\theta$  is the angle of incidence, and thus all the low-frequency quantities are functions of x only.

Figure 4-45 shows the resultant absorption as a function of the external dc magnetic field with the angle of incidence as a parameter. Figure 4-46 shows absorption as a function of the angle of incidence with the magnetic field as a parameter. If  $b_0 \neq 0$  and  $\alpha_0 \neq 0$ , the peak absorption occurs at a lower magnetic field or angle of incidence, and the peak absorption is higher (up to 99%). Also there is zero absorption even for substantial angles of incidence. As in previous work, we find that the absorption is almost independent of plasma temperature.

Contours of constant absorption as a function of external dc magnetic field and angle of incidence are

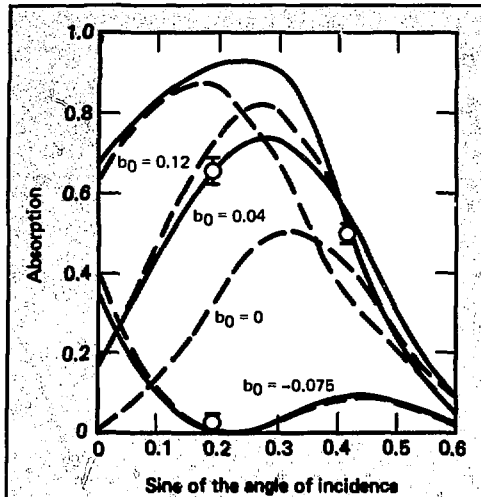


Fig. 4-46. Absorption as a function of the sine of the angle of incidence. The interpretation and parameters are the same as in Fig. 4-45, except that  $v/c = 0.835$  for the curves labeled  $b_0 = 0.04$  and  $b_0 = 0.12$ , and  $v/c = 0.65$  for the curve labeled  $b_0 = -0.075$ .

shown in Fig. 4-47 (the induced field is neglected). We see that resonant absorption increases if the external magnetic field and the angle of incidence have the same sign but decreases if they have different signs.

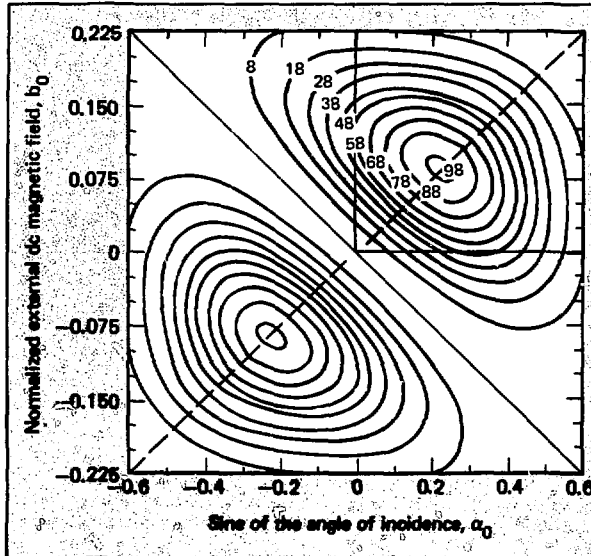


Fig. 4-47. Absorption contours as functions of  $\alpha_0$  and  $b_0$ . The drivers [see discussion following Eq. (50)] are in phase along the dashed line.

We can understand these results by considering the linearized version ( $T_e = 0$ ) of Eq. (48) (with Faraday's law) as follows:

$$(\epsilon - b_0^2)E_x = -\alpha_0(1 - b_0^2)B_h + ib_0(n_e/n_c)E_y \quad (50)$$

We see that  $E_x$  is resonant at the upper-hybrid resonant point  $\epsilon = b_0^2$  and that  $E_x$  is driven by the sum of the two terms. The first term is caused by the component of the light that is parallel with the density gradient. The second term is caused by the component of the  $\vec{u}_h \times \vec{B}_0$  force that is parallel with the density gradient. The two effects are additive or not, depending on the phase difference between  $B_h$  and  $E_y$ . We calculate this phase difference by integrating the difference between the square roots of the effective dielectric functions obtained from the linearized version of Eq. (48). We find that the drivers are in phase if  $k_0 L b_0 \approx \pi \alpha_0$  and out of phase if  $k_0 L b_0 \approx -\pi \alpha_0$  ( $3.8 \alpha_0$  is obtained from Fig. 4-47). Thus, the external magnetic field and the angle of incidence must have the same sign for maximum absorption and opposite signs for minimum absorption. The absorption is an absolute maximum if the two drivers are in phase ( $k_0 L b_0 \approx \pi \alpha_0$ ) and the drivers are maximized ( $k_0 L^{2/3} \epsilon_1 \approx 0.5$ ), where  $\epsilon_1$  is the effective dielectric function at the turning point of the electromagnetic wave,  $\epsilon_1 = 1/2 \{ \alpha_0^2 + [\alpha_0^4 + 4b_0^2(1 - \alpha_0^2)]^{1/2} \}$ , obtained from the linearized version of Eq. (48).

We have used a two-dimensional particle simulation code with fixed ions to investigate the validity of



our results. We find excellent agreement for the absorption ( $v_0/v_e = 0.35$ , the solid circles in Figs. 4-45 and 4-46).

## References

125. W. Woo and J. S. DeGroot, *Magnetic Fields Due to Laser Light Absorption*, University of California at Davis, Rept. PRG R-23 (1977); *Phys. Rev. Lett.* **40**, 1094 (1978).

## Authors

W. Woo  
K. G. Estabrook  
J. S. DeGroot

### 4.6.6 Three-Dimensional Simulations of Laser Light Absorption

The stability of the surface of an overdense plasma slab illuminated by normally incident laser light is of interest because it can affect the fraction of incident light absorbed. Rippling of the plasma boundary could lead to enhanced absorption caused by resonance absorption or trapping of radiation in bubbles. Estabrook,<sup>126</sup> Valeo and Estabrook,<sup>127</sup> and Langdon, Lasinski, and Kruer,<sup>128</sup> have shown that, with a moderate density gradient, normally incident light will cause a planar density depression behind the critical surface that traps radiation. Later, a sausage instability breaks up the planar depression into bubbles. A comparison of 2- and 2½-dimensional runs with s- and p-polarization shows that the breakup occurs preferentially in the plane of  $k_0$  and  $B_0$  (s-polarization), where  $k_0$  and  $B_0$  are the wave vector and magnetic field vector of the incident radiation.

With a steplike density gradient, rippling of the critical surface itself has been observed by Estabrook<sup>126,129</sup> and by Bezzerides et al.<sup>130</sup> With two-dimensional simulations, they again found rippling of the surface most strongly with s-polarized light.

The above-mentioned results suggest that the plasma rippling and breakup will occur predominantly in the plane of  $k_0$  and  $B_0$ . I report here results of three-dimensional simulations that support this conclusion.

The simulation code is a full three-dimensional, electromagnetic particle code, developed at Stanford University. The simulation space is covered by a  $32 \times 32 \times 32$  mesh on which field quantities are represented by quadratic spline interpolation. The boundary conditions are basically periodic, although an absorbing region can be included to simulate free-space boundaries for radiation on two walls. The laser wave is launched by a time-varying current sheet, just inside the absorbing region. This wave is normally incident on a plasma

slab, which typically occupies half the simulation volume. The particle boundary conditions are periodic, reflecting, or reemitting, as desired.

To simulate radiation trapped between two layers of plasma above critical density, the code was run with triply periodic boundaries both on fields and particles. Then, with a slab of plasma next to a vacuum region, a whole series of vacuum-slab interfaces is created (by periodicity). A wave was launched with its k-vector perpendicular to the plasma surface. After a few cycles, when the wave filled the vacuum region, its amplitude was decreased to just balance losses caused by absorption by the plasma.

Rippling of the plasma surfaces did occur, with a wavelength between one and two free-space wavelengths. As the instability grew to finite amplitude, the angled surfaces of the plasma focused the waves so that their strength was greatest where the vacuum bulged outward (into the plasma). This focusing increased the wave pressure on the plasma locally, enhancing the bulge. The same coalescence into bubbles observed by Estabrook was seen to occur here. The predominant direction of bubbling was also in the direction of the laser magnetic vector. Bubbling along the direction of the electric vector was also observed in some runs, but the amplitude in this direction was much smaller. Eventually, the trapped radiation breaks through the plasma locally, leaving islands of overdense plasma. Figure 4-48 shows particle plots for such a case. A standing plane wave is in the vacuum region with magnetic field vertical in the left view and electric field vertical in the right view.

When an absorber is placed in the vacuum region, waves reflecting off the plasma are lost. It is therefore possible to simulate incidence of a laser beam on a plasma slab. The slab initially had a density of two or three times critical. A normally incident plane wave was launched in the vacuum region and was allowed to

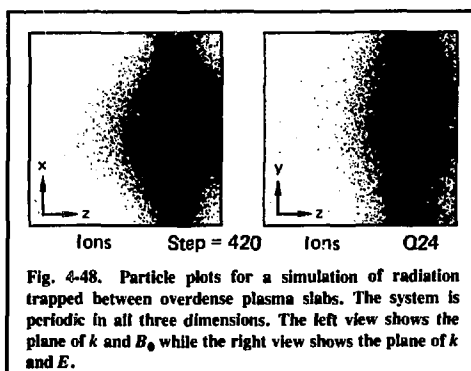


Fig. 4-48. Particle plots for a simulation of radiation trapped between overdense plasma slabs. The system is periodic in all three dimensions. The left view shows the plane of  $k$  and  $B_0$ , while the right view shows the plane of  $k$  and  $E$ .

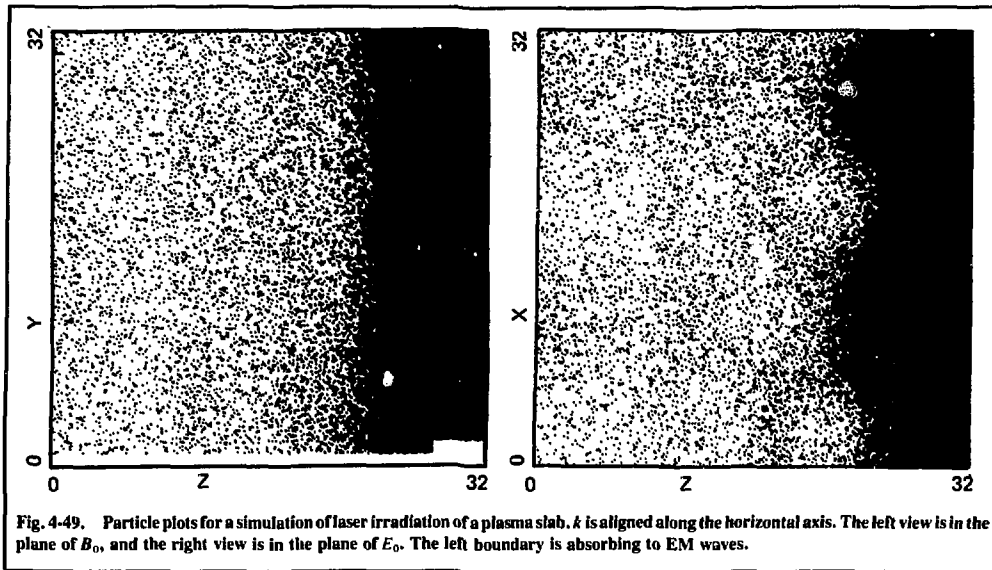


Fig. 4-49. Particle plots for a simulation of laser irradiation of a plasma slab,  $k$  is aligned along the horizontal axis. The left view is in the plane of  $B_0$ , and the right view is in the plane of  $E_0$ . The left boundary is absorbing to EM waves.

irradiate the slab. The slab density then adjusted itself to balance the radiation pressure on it. In some runs, it reached six times critical density, reducing the thickness of the slab by a factor of three. The free-space wavelength of the light was one-half to one-third the dimension of the simulation region.

Simulations to date have shown ripples appearing only in the direction of the laser magnetic field with a wavelength about 1.5 times the light wavelength. These saturate at an amplitude of about half their wavelength. Movies of the time history of field surfaces show clearly the oblique scattering of light. Figure 4-49 shows particle plots for a case with three free-space wavelengths of laser light in the system. The left view is in the plane of laser  $k_0$  and  $B_0$ , when two wavelengths of ripple are clearly visible. The right view shows the same particles at the same timestep but viewed in the plane of  $K_0$  and  $E_0$ , where  $E_0$  is the laser light electric field vector. There is no visible perturbation of the slab surface.

This result agrees with experiments reported from Osaka, Japan, in which a slab target was irradiated alternately with p- and s-polarization at a  $35^\circ$  angle with normal.<sup>131</sup> With s-polarization, a peak in reflected energy was noted at a large angle that they attribute to the presence of a rippled surface. With p-polarization, no such scattering was seen. Although our early results do not rule out perturbations along the direction of laser electric field, if they do occur, they must saturate at a much lower amplitude or occur at a much greater wavelength than those along  $B_0$ .

## References

126. K. G. Estabrook, "Critical-Surface Bubbles and Corrugations and Their Implications to Laser Fusion," *Phys. Fluids* **19**, 1733 (1976).
127. E. J. Valeo and K. G. Estabrook, "Stability of the Critical Surface in Irradiated Plasma," *Phys. Rev. Lett.* **34**, 1008 (1975).
128. A. B. Langdon, B. F. Lasinski and W. L. Kruer, *Laser Program Annual Report-1975*, Lawrence Livermore Laboratory, Rept. UCRL-50021-75 (1976), §6.3-1.
129. K. G. Estabrook, Lawrence Livermore Laboratory, private communication (1977).
130. B. Bezzerides, D. G. DuBois, D. W. Forslund, J. M. Kindel, K. Lee, and E. L. Lindman, "Recent Developments in Understanding the Physics of Laser-Produced Plasmas," *Plasma Physics and Controlled Nuclear Fusion Research 1976* (International Atomic Energy Agency, Vienna, 1977), vol. 1, pp. 133-146.
131. *Annual Report*, Osaka University, Osaka, Japan, **75** (1977).

## Author

C. Barnes

## 4.7 Profile Steepening and Plasma Expansion

### 4.7.1 Effects of Flow on Density Profiles in Laser-Irradiated Plasmas

The manner in which laser radiation pressure modifies plasma density profiles is important to laser light absorption, because the expected mix of absorption processes and transport phenomena depends sensitively on

density profiles near the critical surface. Here we show analytically that plasmas entering the critical region supersonically can exhibit compressional density profiles, in which their density depends nonmonotonically on distance from the target surface. Supersonic compressions in the critical region necessarily involve dissipation properties like those in collisionless shocks, and the plasma instabilities responsible for the dissipation can affect laser light absorption and energy transport.

In contrast, plasmas entering the critical surface subsonically exhibit the familiar density step there.<sup>132-136</sup> For some near-sonic flows, no steady profile exists. Our analysis offers new insights into recent computer hydrodynamics calculations in the sonic and supersonic regimes.

#### Jump Conditions across the Critical Surface.

Jump conditions may be obtained by integrating steady-state equations of mass and momentum conservation,  $\nabla \cdot (\rho \mathbf{v}) = 0$ ,  $\rho \mathbf{v} \cdot \nabla \mathbf{v} = -\nabla p - \nabla \cdot \mathbf{\Pi}_r$ , from a point  $\mathbf{x}_1$  on one side of the critical density to a point  $\mathbf{x}_2$  on the laser side (see Fig. 4-50). The fluid density, velocity, and thermal pressure are  $\rho$ ,  $\mathbf{v}$ , and  $p$ , respectively. For laser electric and magnetic fields  $\mathbf{E}$  and  $\mathbf{B}$ , the laser radiation pressure tensor is<sup>137-139</sup>

$$\mathbf{\Pi}_r = \frac{1}{8\pi} \langle \mathbf{E}^2 + \mathbf{B}^2 \rangle / 8\pi - \langle \epsilon_r \mathbf{E} \mathbf{E} + \mathbf{B} \mathbf{B} \rangle / 4\pi, \quad (51)$$

where  $\epsilon_r \equiv \text{Re} [1 - \omega_p^2 / \omega(\omega + i\nu)]$ , the laser frequency is  $\omega$ ,  $\omega_p^2 \equiv 4\pi n_e e^2 / m_e$ , the electron density is  $n_e$ , and the collision frequency is  $\nu$ . For light normally incident on a one-dimensional plasma, the normal component of  $\mathbf{\Pi}_r$  is  $\langle \mathbf{E}^2 + \mathbf{B}^2 \rangle / 8\pi$ . If  $\mathbf{x}_1$  and  $\mathbf{x}_2$  are close together, we need not specify the overall geometry. For spherical plasmas we require  $|\mathbf{x}_1 - \mathbf{x}_2| \ll r$ , where  $r$  is the local value of the radius.

We assume that the flow is approximately steady for the short time  $|\mathbf{x}_1 - \mathbf{x}_2|/c_1$  required to cross the critical region, where  $c_1^2 \equiv p/\rho$  evaluated at the point  $\mathbf{x}_1$ . This is well justified for current experiments that typically have  $|\mathbf{x}_1 - \mathbf{x}_2| \approx 1-2 \mu\text{m}$ ,  $c_1 \approx 3 \times 10^7 \text{ cm/s}$ , so  $|\mathbf{x}_1 - \mathbf{x}_2|/c_1$  is several picoseconds, whereas typical laser risetimes are  $> 10-20 \text{ ps}$ .

We choose  $\mathbf{x}_1$  so that  $\mathbf{\Pi}_r(\mathbf{x}_1) = 0$ , and define  $\Pi \equiv \hat{\mathbf{n}} \cdot \mathbf{\Pi}_r(\mathbf{x}_2) \cdot \hat{\mathbf{n}}$ , where  $\hat{\mathbf{n}}$  is the local normal to the critical surface. The jump conditions in a frame moving with the critical surface are then

$$\rho_1 v_1 = \rho_2 v_2, \quad (52)$$

$$p_1 + \rho_1 v_1^2 = p_2 + \rho_2 v_2^2 + \Pi. \quad (53)$$

Our procedure is to solve Eqs. (52) and (53) for the ratio of Mach numbers  $M_2/M_1$ , as a function of

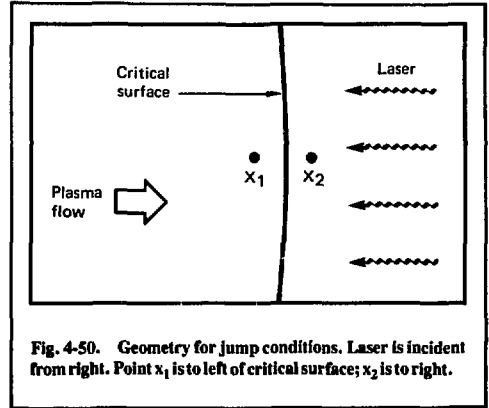


Fig. 4-50. Geometry for jump conditions. Laser is incident from right. Point  $\mathbf{x}_1$  is left of critical surface;  $\mathbf{x}_2$  is right.

$\Pi$  and  $M_1 \equiv v_1 (p_1/\rho_1)^{-1/2}$ . We replace the energy equation by the assumption that the region between  $\mathbf{x}_1$  and  $\mathbf{x}_2$  is isothermal:  $c_2 \equiv (p_2/\rho_2)^{1/2} = c_1$ . Our results are readily generalized to the case  $c_2 > c_1$ , however. Isothermality is usually well satisfied because the range of a thermal electron is typically longer than  $|\mathbf{x}_1 - \mathbf{x}_2|$ : for electron density  $n$  and temperature  $T_e$  and  $T_e$ , the electron range is  $\sim 20 \mu\text{m} \times (n_e/10^{21} \text{ cm}^{-3})^{-1} (T_e/1 \text{ keV})^2$ , whereas  $|\mathbf{x}_1 - \mathbf{x}_2|$  is at most a few times  $c/\omega_{pe} = \text{a few times } 0.17 \mu\text{m} (n_e/10^{21} \text{ cm}^{-3})^{-1/2}$ . (The critical density for  $1.06\text{-}\mu\text{m}$  light is  $10^{21} \text{ cm}^{-3}$ .) Note that Eqs. (52) and (53) remain valid in the collisionless case, provided the particle distribution functions are approximately isotropic. The solution to Eqs. (52) and (53) is

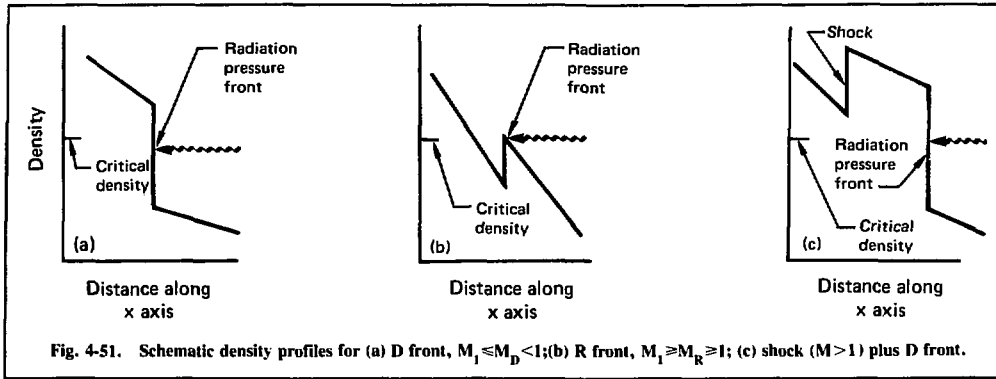
$$\begin{aligned} \frac{M_2}{M_1} &= \frac{\rho_1}{\rho_2} \\ &= \frac{1 + M_1^2 - (\Pi/\rho_1 c_1^2) \pm [(1 + M_1^2 - \Pi/\rho_1 c_1^2)^2 - 4M_1^2]^{1/2}}{2M_1^2} \end{aligned} \quad (54)$$

From the requirement that  $M_2/M_1$  be real, we obtain the region where steady-state solutions exist: either

$$M_1 \geq M_R \equiv 1 + (\Pi/\rho_1 c_1^2)^{1/2} \quad (55)$$

or

$$M_1 \leq M_D \equiv 1 - (\Pi/\rho_1 c_1^2)^{1/2}. \quad (56)$$



We call radiation pressure fronts satisfying Eq. (55) R type, and those satisfying Eq. (56) D type. (This nomenclature is borrowed from the theory of ionization fronts.<sup>140, 141</sup> R and D fronts are analogous to detonations and deflagrations, respectively, in chemical combustion.<sup>142</sup>) Note that for D fronts the requirement that the flow velocity not change sign across  $x_c$  implies  $\Pi \leq \rho_1 c_1^2$  so that  $M_D \geq 0$ . There are no steady solutions with  $M_D < M < M_R$ .

Critical fronts<sup>140, 141</sup> are those for which the equality sign holds in Eqs. (55) and (56). They have  $M_2 = 1$  and are analogous to Chapman-Jouguet deflagrations and detonations.<sup>142</sup> As in the case of ionization fronts, there is no *a priori* reason to assume that radiation pressure fronts are critical.

Straightforward algebra using Eq. (54) shows that R fronts represent compressions ( $\rho_1 < \rho_2$ ,  $M_1 > M_2$ ), whereas D fronts are rarefactions ( $\rho_1 > \rho_2$ ,  $M_1 < M_2$ ). Figure 4-51 indicates this distinction schematically. Thus, D fronts represent the density step familiar from plasma simulations.<sup>132-136</sup> Plasma flows subsonically into  $x_c$  and then accelerates. The total pressure outside the critical surface ( $p_2 + \rho_2 v_2^2 + \Pi$ ) is balanced predominantly by the thermal pressure  $p_1$ .

In contrast, R fronts have not yet received attention in the laser plasma literature. Here plasma flows supersonically into the critical region. The upstream pressure thus cannot adjust to the added inward laser momentum  $\Pi$  at  $x_c$ . When the flow reaches the critical surface, its ram pressure  $\rho_1 v_1^2$  must nearly balance the total pressure ( $p_2 + \rho_2 v_2^2 + \Pi$ ) in the underdense region. Because the upstream flow cannot adapt to the laser's radiation pressure, matter piles up in the critical density region, rising somewhat above  $\rho_c$  as shown in Fig. 4-51(b).

Table 4-6 summarizes the above results and lists some additional properties of D and R fronts that may be derived from Eq. (54). The weak and strong solutions correspond to small and large density jumps, respectively.

Fronts with  $M_1$  in the range  $M_D < M_1 < M_R$  will be fundamentally unsteady near  $\rho_c$ . In addition, we speculate that the strong R fronts described in Table 4-6 are unstable. If one imagines a perturbation that lowers the peak density slightly below critical (see Fig. 4-52), laser light will penetrate to a new critical surface well inside the original one. But at the new surface the Mach number  $M_1 > 1$  is too large to maintain the

Table 4-6. Properties of D and R radiation pressure fronts.

	D fronts	R fronts
Critical solution	$M_1 \leq M_D = 1 - (\Pi / \rho_1 c_1^2)^{1/2}$	$M_1 \geq M_R = 1 + (\Pi / \rho_1 c_1^2)^{1/2}$
Weak solution	Rarefactions ( $\rho_2 < \rho_1$ )	Compressions ( $\rho_2 > \rho_1$ )
Strong solution	$M_1 = M_D, M_2 = 1$	$M_1 = M_R, M_2 = 1$
	$1 > (\rho_2 / \rho_1) > M_D, M_2 < 1$	$M_R > (\rho_2 / \rho_1) > 1, M_2 > 1$
	$M_D > (\rho_2 / \rho_1) > 0, M_2 > 1$	$\infty > (\rho_2 / \rho_1) > M_R, M_2 < 1$

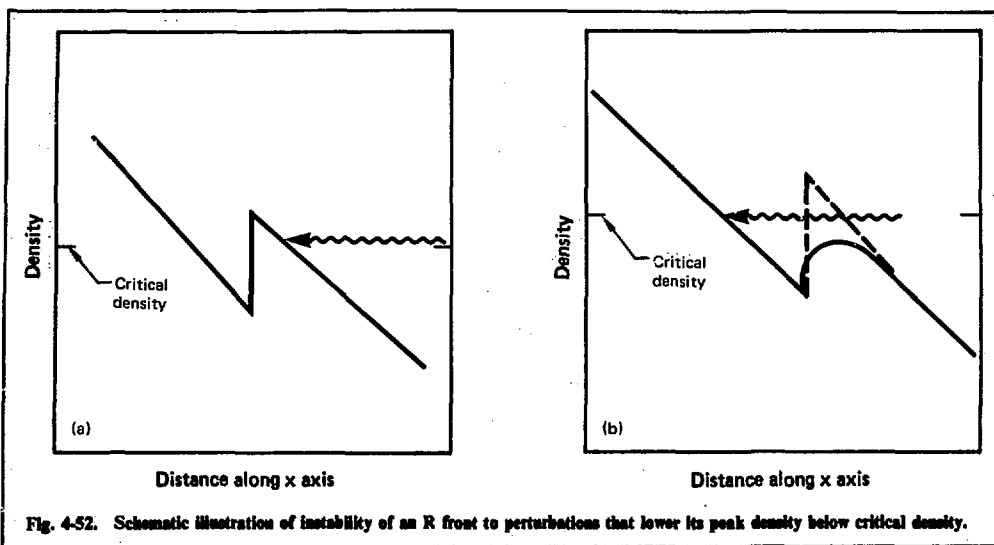


Fig. 4-52. Schematic illustration of instability of an R front to perturbations that lower its peak density below critical density.

preexisting D-type profile. Hence, the unbalanced outward force pushes the critical region back toward its original position, where the cycle can repeat.

**Shock-plus-D Fronts.** For supersonic flows we suggest an alternative configuration that seems considerably more stable than an R front. As shown in Fig. 4-51(c), a simple shock can stand upstream of the critical surface, bringing the flow speed from supersonic to subsonic. Because of the shock, the flow at  $\rho_c$  may be subsonic also, allowing an ordinary D front to exist. Because  $\rho_c$  is now permitted to lie quite far down on the D-type density step, a small perturbation to the peak density in Fig. 4-51(c) will not be likely to affect the critical surface position, and the overall configuration should be stable. Such collisionless shocks have been seen in particle-in-cell computer simulations,<sup>143</sup> for supersonic relative velocities of the plasma and critical region. Figure 4-53 shows an example of such a shock, from a simulation by A. B. Langdon. (Shock-plus-D ionization fronts are known to exist in astrophysical contexts.<sup>140,141</sup>)

For a shock-plus-D-front configuration to exist, the flow between the shock and critical surface must adjust so that the jump conditions across these two discontinuities are consistent with each other. In spherical geometry this is particularly attractive, because mass conservation ( $\rho v r^2 = \text{constant}$ ) allows flexibility in flow parameters between the shock and the critical surface. As a simple example of a shock-plus-D front, consider a case where the postshock Mach number is  $M_0 \leq 1$  and the region between the shock and  $\rho_c$  is

isothermal. Then, in spherical flow, the Mach number  $M_1$  just on the high-density side of  $x_c$  satisfies<sup>144</sup>

$$M_1^2 - \ln M_1^2 = M_0^2 - \ln M_0^2 + 4 \ln (r_c/r_s), \quad (57)$$

where  $r_c$  and  $r_s$  are the critical and shock radii, respectively. For  $M_0 < 1$ , the Mach number decreases and the density increases between  $r_s$  and  $r_c$ . To have a D front,  $M_1$  must also satisfy Eq. (56):  $M_1 \leq 1 - (\Pi/\rho_1 c_1^2)^{1/2}$ . For a given  $(\Pi/\rho_1 c_1^2)$ , a value of  $M_1$  consistent with Eq. (56) can be found simply by choosing the appropriate radius ratio ( $r_c/r_s$ ) in Eq. (57). Analogous arguments show that a shock-plus-R front structure is not allowed, if the flow is isothermal between  $r_s$  and  $r_c$ .

Thus, supersonic flows can produce two forms of compressional structures: shocks just inside the critical surface, and R fronts right at the critical surface. As with detonations,<sup>142</sup> an R front may be shown to be the limiting case of a shock-plus-D front, as the distance between the shock and the D front goes to zero. Hence, the two types of compressions are related. Both require dissipation, presumably in the form of plasma turbulence. Such dissipation may have important consequences. For example, ion-wave turbulence produced in an ion-acoustic shock can inhibit heat transport and enhance absorption processes in the critical region.

In parameter regimes where the shock is collisionless and its Mach number is sufficiently high, some outward flowing ions will be reflected by the shock front and sent back upstream<sup>145</sup>. An example of this

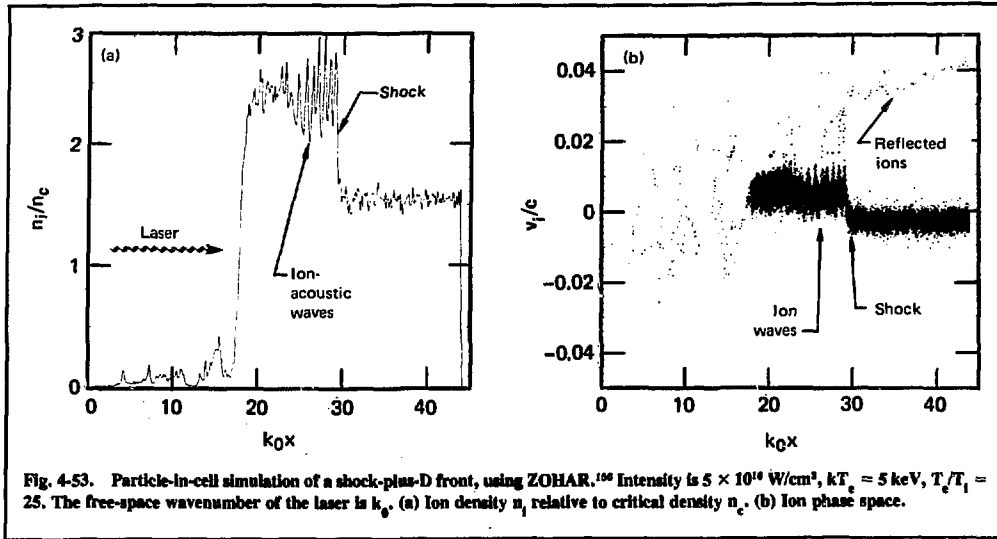


Fig. 4-53. Particle-in-cell simulation of a shock-plus-D front, using ZOHAR.<sup>150</sup> Intensity is  $5 \times 10^{16}$  W/cm<sup>2</sup>,  $kT_e = 5$  keV,  $T_e/T_i = 25$ . The free-space wavenumber of the laser is  $k_0$ . (a) Ion density  $n_i$  relative to critical density  $n_c$ . (b) Ion phase space.

phenomenon is shown in Fig. 53(b). Under some circumstances, the reflected ions may begin to affect the overall flow structure by carrying energy upstream. The expected velocity of the reflected ions is roughly given by the relative velocity of the shock and the upstream plasma, measured in the shock frame. Thus, in the lab frame, the velocity of the reflected ions is  $v_i = 2 v_{sh}$ .

The shock velocity  $v_{sh}$  is determined by pressure balance between the laser radiation pressure  $E^2/4\pi$  on the downstream side and  $\rho v_{sh}^2$  on the upstream side of the shock. This gives

$$\frac{E^2}{4\pi} \approx (\rho v_{sh}^2)_{\text{upstream}} = (\rho M^2 c_s^2)_{\text{upstream}},$$

where  $M$  is the Mach number of the shock and  $c_s = (ZT_e/M_i)^{1/2}$  is the upstream sound speed in a plasma with ions of charge  $Z$ . Solving for the Mach number, we find

$$M = \left( \frac{E^2}{4\pi n_e kT_e} \right)^{1/2} = 2 \left( \frac{I_{16}}{\theta_{\text{keV}} n_{21}} \right)^{1/2} > 1,$$

where  $I_{16} = I/(10^{16} \text{ W/cm}^2)$ ,  $\theta_{\text{keV}} = kT_e/(1 \text{ keV})$ ,  $n_{21} = n_e/(10^{21} \text{ cm}^{-3})$ , and a Nd:glass laser,  $\lambda = 1.06 \mu\text{m}$ , has been assumed.

The velocity of the reflected ions  $v_i$  and their energy per unit charge  $E_i/Z$  are then

$$v_i = 2Mc_s \approx 1.2 \times 10^8 \left[ \left( \frac{Z}{\Lambda} \right) \left( \frac{I_{16}}{n_{21}} \right) \right]^{1/2} \text{ cm/s},$$

$$E_i/Z = 4I/n_i c \approx 8(I_{16}/n_{21}) \text{ keV}.$$

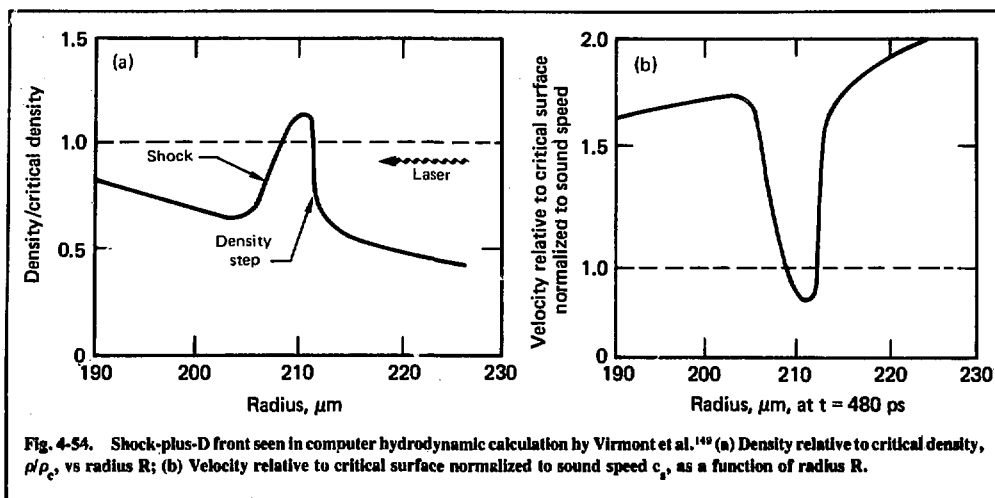
The range  $\lambda_s$  of the reflected ions is

$$\lambda_s \approx \left( \frac{60}{Z} \right) \left[ \left( \frac{I_{16}}{n_{21}} \right) \left( \frac{6.7}{\ln \Lambda} \right) \right] \mu\text{m},$$

where  $\ln \Lambda$  is the Coulomb logarithm. Hence, for typical parameters  $Z = 6$ ,  $n_{21} = 2$ ,  $I_{16} = 1$ ,  $\theta_{\text{keV}} = 1$ , the range of the reflected ions is  $\lambda_s = 5.2 \mu\text{m}$ . Thus we see that, particularly at high intensities, the reflected ions can penetrate into the upstream plasma enough to potentially affect the flow structure there.

**Conditions for Supersonic Flow Relative to the Critical Surface.** In current short-pulse implosion experiments, the critical region moves outward relative to the target surface prior to the peak of the laser pulse, and moves inward after the peak.<sup>146</sup> Hence, the second half of the laser pulse may favor supersonic flow, because the relative velocity between the plasma outflow and the inward-moving critical surface may be large.

Future experiments will emphasize use of longer laser pulses and more adiabatic, ablative implosions. If the laser risetime is long compared to the fluid's transit time from the ablation surface to the critical



surface, a global quasi-steady state will be set up. Plasma flow characteristics are then determined by the inward heat flux from the critical surface to the ablation surface. Efficient inward heat flow produces rapid ablation and thus high Mach numbers at  $\rho_c$ .

This general conclusion can be illustrated by the following idealized example. Consider a regime where the electron mean free path near  $\rho_c$  is longer than the temperature gradient scale length, so that heat is carried by free-streaming electrons. A model for the heat-flow vector  $\mathbf{q}$  in this situation that limits the heat-flow speed to a fraction of  $(kT_e/m_e)^{1/2}$  is  $\mathbf{q} = -5\phi\rho c^3 \nabla T / |\nabla T|$ , where the flux limit  $\phi \sim 1$  for normal heat flow and  $\phi < 1$  for strongly inhibited heat flow.<sup>147</sup> In a global steady state, the heat equation inside  $x_c$  is  $(\rho v/2)(v^2 + 5p/\rho) + q = \text{constant}/r^2$ . The constant may be shown to be zero by evaluating it in the unablated region where  $q = T = v = 0$ . Then the heat equation yields  $M(1 + M^2/5) = 2\phi$ , where  $M$  is the Mach number relative to the critical surface.<sup>147</sup> Thus, in this example the flow will be supersonic only if the flux limit  $\phi$  exceeds 0.6; otherwise, it will be subsonic. The first case should lead to a shock-plus-D front, and the second gives a D front alone. In terms of the more usual flux limit  $f \equiv Q/(n_e m_e v_{te}^3)$ , the condition for supersonic flow is  $f > 0.12$  for a spherical DT plasma. Here  $Q$  is the magnitude of the heat flux.

**Discussion.** Recent hydrodynamic computer studies have found behavior typical of flows for which  $M_1 > M_D$ .<sup>148,149</sup> Our work allows interpretation of these previously puzzling results. Both Brueckner<sup>148</sup> and Virmont et al.<sup>149</sup> noted compressional density profiles resembling those predicted in Fig. 4-51(c), for the case

of  $1\text{-}\mu\text{m}$  laser light. In particular, Virmont et al. found that most characteristics of the compressional profile are stationary in a frame moving with the critical surface.<sup>149</sup> In light of our analysis, we interpret this structure as a shock-plus-D front. It is illustrated in Fig. 4-54.

Mulser and van Kessel noted that density steps like that shown in Fig. 4-51(a) are seen only for subsonic flows.<sup>144</sup> This observation agrees with our prediction for D fronts. Because there was no dissipation mechanism in their model, they would not have been able to see an R front or a shock-plus-D front in the supersonic case. Instead, a density plateau near  $\rho_c$  was formed. (We have not analyzed density plateaus in the present work, but Virmont et al. have shown that such plateaus are unstable to short-wavelength perturbations.<sup>149</sup>)

Several provisos must be added to the results reported here. Our steady-state solutions may suffer from varying degrees of instability. Our jump conditions contain no suprathermal electrons. The conditions for R and D fronts have been phrased in terms of  $\Pi$ , the normal component of the radiation stress tensor just outside the critical surface. The fields  $\mathbf{E}$  and  $\mathbf{B}$  that determine  $\Pi$  must of course be found self-consistently with the density profile outside the critical surface, in a full solution to the problem.

In summary, compressions and shock-like structures in the critical region are predicted to accompany supersonic outflow relative to the critical surface. Turbulence and reflected ions associated with these structures may affect transport and laser light absorption in some regimes. Flows with near-sonic velocities have been shown to be fundamentally unsteady.

## References

132. K. Lee, D. W. Forslund, J. M. Kindel, and E. L. Lindman, "Theoretical Derivation of Laser-Induced Plasma Profiles," *Phys. Fluids* **20**, 51 (1977).
133. D. W. Forslund, J. M. Kindel, K. Lee, and E. L. Lindman, "Absorption of Laser Light on Self-Consistent Plasma Density Profiles," *Phys. Rev. Lett.* **36**, 35 (1975).
134. K. G. Estabrook, E. J. Valeo, and W. L. Krue. "Two-Dimensional Relativistic Simulations of Resonance Absorption," *Phys. Fluids* **18**, 1151 (1975).
135. R. E. Kidder, in *Proceedings of Japan-U.S. Seminar on Laser Interaction with Matter*, C. Yamanaka, Ed. (Tokyo International Book Co., Tokyo, 1975), p. 331.
136. F. S. Felfel, "Steady-State Model of a Flat Laser-Driven Target," *Phys. Rev. Lett.* **39**, 84 (1977).
137. L. P. Pitaeviskii, "Electric Forces in a Transparent Dispersive Medium," *Zh. Eksp. Teor. Fiz.* **39**, 1450 (1960) [*Sov. Phys.—JETP* **12**, 1008 (1961)].
138. J. A. Stamper and D. A. Tidman, "Magnetic Field Generation due to Radiation Pressure in a Laser-Produced Plasma," *Phys. Fluids* **16**, 2024 (1973).
139. J. J. Thomson, C. E. Max, and K. G. Estabrook, "Magnetic Fields due to Resonance Absorption of Laser Light," *Phys. Rev. Lett.* **35**, 663 (1975).
140. F. Kahn, *Bull. Astron. Inst. Neth.* **12**, 187 (1954).
141. L. Spitzer, Jr., *Diffuse Matter in Space* (Interscience, New York, 1968), pp. 184-187.
142. R. A. Strehlow, *Fundamentals of Combustion* (International Textbook Co. Scranton, 1968), Ch. 9.
143. A. B. Langdon, Lawrence Livermore Laboratory, private communication (1977).
144. P. Mulser and C. van Kessel, "Profile Modification and Plateau Formation due to Light Pressure in Laser-Irradiated Targets," *Phys. Rev. Lett.* **38**, 902 (1977).
145. D. W. Forslund and C. R. Shonk, "Formation and Structure of Electrostatic Collisionless Shocks," *Phys. Rev. Lett.* **25**, 1699 (1970).
146. S. Jackel, J. Albritton, and E. Goldman, "Critical-Density Scale-Length Measurements in Laser-Produced Plasmas," *Phys. Rev. Lett.* **35**, 514 (1975).
147. L. L. Cowie and C. F. McKee, "The Evaporation of Spherical Clouds in a Hot Gas. I. Classical and Saturated Mass Loss Rates," *Astrophys. J.* **211**, 135 (1977).
148. K. A. Brueckner, "Interpretation of Experiments in Laser-Driven Fusion," in *Plasma Physics*, H. Wilhelmsson, Ed. (Plenum Press, New York, 1977), pp. 9-27.
149. J. Virmont, R. Pellat, and A. Mora, "Density-Profile Modification by Light Pressure in Spherical Geometry," *Phys. Fluids* **21**, 567 (1978).
150. A. B. Langdon and B. F. Lasinski, "Electromagnetic and Relativistic Plasma Simulation Models," in *Methods in Computational Physics*, B. Alder, S. Fernbach, and M. Rotenberg, Eds. (Academic Press, New York, 1977), vol. 16, pp. 327-366.

## Authors

C. E. Max  
C. F. McKee

## 4.7.2 Self-Similar Solutions to Plasma Flow with Strong Collisional Heating

The purpose of this analysis is to understand the surprisingly low absorptions found in the high-Z disk experiments discussed in §6.7. Here we discuss a self-similar solution to the plasma flow that gives the qualitative features found in the LASNEX simulations of high-Z disk experiments: a sharp density drop at critical, combined with a sharp temperature rise. This combination leads to a hot, very underdense plasma with little collisional absorption.

A similarity solution corresponds to a quasi-asymptotic flow state, where the initial conditions are "forgotten." Instead of the space and time variables  $x$  and  $t$ , we have a single similarity parameter  $\xi = x/R(t)$ , where the functional form of  $R(t)$  is determined either by dimensional arguments or by the boundary conditions at  $\pm \infty$ . A familiar example is isothermal flow, where  $R' = c_s t$ , and  $c_s$  is the sound speed. The density, for example, is given by  $\rho = \rho_0 \exp(-\xi)$ .

We start with the moment equations for the fluid:

$$\frac{\partial \rho}{\partial t} + \frac{\partial}{\partial x}(\rho v) = 0, \quad (58)$$

$$\rho \left( \frac{\partial}{\partial t} + v \frac{\partial}{\partial x} \right) v + \frac{\partial P}{\partial x} = 0, \quad (59)$$

$$\left( \frac{\partial}{\partial t} + v \frac{\partial}{\partial x} \right) P + 5/3 P \frac{\partial v}{\partial x} + 2/3 \frac{\partial Q}{\partial x} = 2/3 \nu \frac{E^2}{8\pi}. \quad (60)$$

In these equations  $\rho$ ,  $v$ , and  $P$  are the plasma density, velocity, and pressure, respectively;  $Q$  is the heat flux; and  $\nu E^2/8\pi$  is the absorbed power density.

We will consider only one dimension appropriate for disk targets. The extension to higher dimensions is trivial. We neglect momentum deposition, because the light pressure is much less than plasma pressure. The heat flow vector  $Q$  is given by

$$Q = \min \begin{cases} Q_c = -K \frac{\partial T}{\partial x} \sim -\frac{\partial^2 T^{7/2}}{\partial x^2} \\ Q_{fs} = -f n m v_T^3 \left| \frac{\partial T / \partial x}{T} \right| \end{cases}, \quad (61)$$

where  $f$  is a number describing anomalous inhibition of the heat flux,  $T$  is the temperature,  $n$  is the density, and  $v_T$  is the thermal velocity. For a high-Z material, large amounts of energy are deposited at critical density. However, the free-streaming limit of  $Q$  implies the formation of a temperature shock and thus the absence of a quasi-stationary solution. The long-time behavior



of the heat flow, as suggested in LASNEX simulations, is that the magnitude of the heat flux is set by the free-steaming limit,  $Q = 1/2 Q_{fs}$ , but the sign of the heat-flux gradient is given by the classical result

$$\frac{\partial Q}{\partial x} \sim - \frac{\partial^2 T^{7/2}}{\partial x^2} \quad (62)$$

Now we go over to the similarity parameter,  $\xi = x/R(t)$ ,  $R(t) = At^\alpha$ , where  $A$  and  $\alpha$  are constants to be determined. We define the nondimensional quantities,

$$g = \rho/\rho_c, \quad \pi = P/\rho_c \dot{R}^2, \quad (63)$$

$$u = v/\dot{R},$$

where  $\dot{R} = dR/dt = A\alpha t^{\alpha-1}$ . Equations (58) - (60) become

$$\frac{du}{d\xi} + (u - \xi) \frac{d}{d\xi} \ln g = 0, \quad (64)$$

$$(u - \xi) \frac{du}{d\xi} + \frac{1}{g} \frac{d\pi}{d\xi} + \frac{(\alpha-1)}{\alpha} u = 0, \quad (65)$$

$$(u - \xi) \frac{d\pi}{d\xi} + 5/3 \pi \frac{du}{d\xi} + 2/3 \frac{f}{\epsilon} \frac{d}{d\xi} \pi^{3/2} g^{1/2} + \frac{2(\alpha-1)}{\alpha} \pi = \left[ \frac{ze^5}{6000} \left( \frac{\omega}{\omega_0} \right)^2 \omega_0 v_{os}^2 v_{TO}^3 \frac{R}{\dot{R}^6} \right] g^{7/2} \pi^{3/2}, \quad (66)$$

where  $v_{TO}/c = 4.5 \times 10^{-2}$ ,  $\omega_0 = 2 \times 10^{15}$  Hz, and  $\epsilon = (m_e/m_i)^{1/2}$ . For this system of equations to be self-similar,  $t$  must not appear explicitly. This requires

$$\frac{\dot{R}^6}{R} = A^5 t^5 \alpha^{-6} = \text{constant},$$

or  $\alpha = 6/5$ . We now define  $A$  to make the bracket on the right side of Eq. (66) unity:

$$A = \left[ \frac{ze^5}{6000\alpha^6} \left( \omega/\omega_0 \right)^2 \omega_0 v_{os}^2 v_{TO}^3 \right]^{1/5}. \quad (67)$$

Note that, because  $v_{os}^2 \sim \omega^{-2}$ ,  $A$  is independent of wavelength. A characteristic temperature can be derived:

$$T_c (\text{keV}) = \frac{500\dot{R}^2}{\epsilon^2 c^2} \sim (Zt)^{2/5}. \quad (68)$$

For a gold disk,  $I = 10^{14}$  W/cm<sup>2</sup>,  $t = 1/2$  ns,  $T_c = 11$  keV. In this analysis, we assume that  $Z$  is constant. If  $Z$

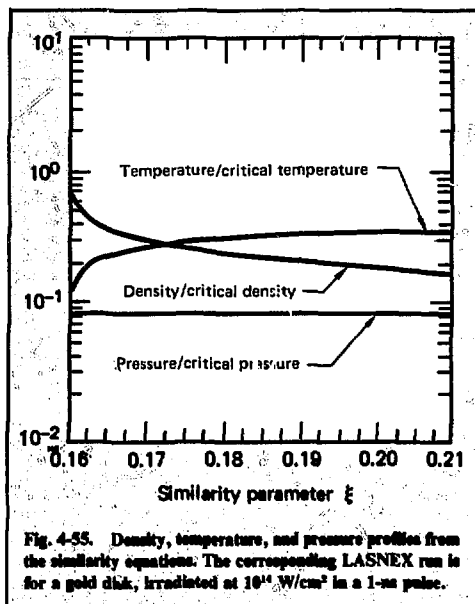


Fig. 4-55. Density, temperature, and pressure profiles from the similarity equations. The corresponding LASNEX run is for a gold disk, irradiated at  $10^{14}$  W/cm<sup>2</sup> in a 1-ns pulse.

has a temperature dependence,  $\alpha$  is changed. For example, if the plasma is in coronal equilibrium,  $Z \sim T^{1/2}$ , and  $\alpha = 5/4$ .

A numerical solution to the system of equations is shown in Fig. 4-55. Note the density drop to about 0.2 critical and the temperature rise from about 1 keV to about 5 keV.

An analysis of the equations shows that, near critical,

$$\frac{d \ln g}{d\xi} \sim - \frac{3\epsilon g}{f} / c^6, \quad (69)$$

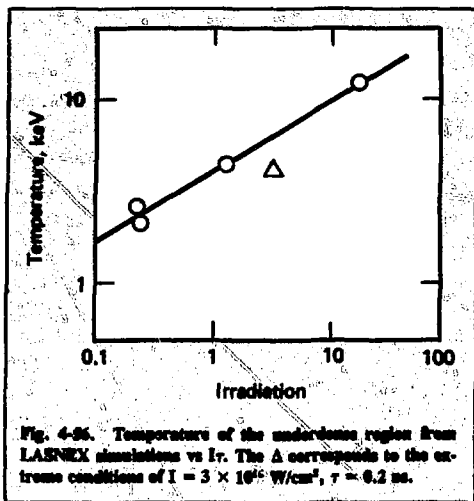
$$\frac{d \ln c^2}{d\xi} \sim \frac{3\epsilon g}{f} / c^6, \quad (70)$$

where  $c$  is the normalized sound speed  $(\pi/g)^{1/2}$ . Near critical,  $g \approx 1$  and  $c^2 \ll 1$ . Thus, there is a sharp gradient here, with scale length  $1/3 f/\epsilon c^6/g$ . Because  $\ln \pi = \ln c^2 + \ln g$ , Eqs. (69) and (70) show that the pressure is approximately constant, as can be seen in the numerical solution.

Using the near-constancy of  $\pi$ , the asymptotic steady-state limit of Eq. (66) occurs when

$$\frac{\pi_0}{3} = g^{7/2} / \pi_0^{3/2} \quad (71)$$

or,



$$g = \frac{\pi_0^{5/7}}{3^{2/7}} \quad (72)$$

and

$$c^2 = \pi_0/g = 3^{2/7} \pi_0^{2/7} \quad (73)$$

For the situation illustrated, these asymptotic values are  $g = 0.12$  and  $c^2 = 0.67$ , the latter corresponding to a temperature of 7 keV.

The fractional absorption is given by

$$f_{abs} = 1 - \exp \left[ -2 \int_{xc}^{\infty} \nu / \omega k_0 dx \right] \quad (74)$$

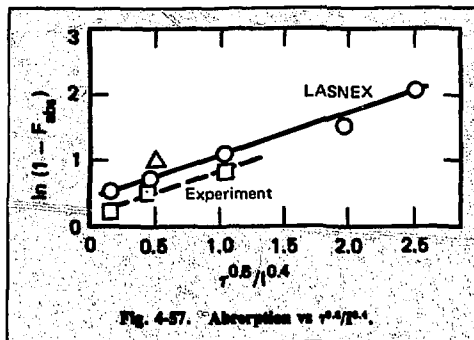
Using the scaling laws derived above, we see that

$$\ln(1 - f_{abs}) \sim \tau^{0.6} / I^{0.4} \quad (75)$$

where  $\tau$  is the laser pulse length.

Figures 4-56 and 4-57 show the agreement of these scaling laws with LASNEX simulations. Figure 4-56 shows the temperature in the underdense region vs  $(I\tau)$ . The theory predicts  $T \sim (I\tau)^{0.4}$ , whereas the slope shows  $\sim 0.35$ . Figure 4-57 shows that  $\ln(1 - f_{abs})$  is proportional to  $\tau^{0.6}/I^{0.4}$ , as predicted.

In summary, we have derived a self-similar solution to plasma flow in a high-Z plasma that exhibits the



qualitative density and temperature profiles observed in LASNEX and that also gives scaling laws for the plasma temperature and absorption.

Author

J. J. Thomson

## 4.8 Stimulated Scatter

### 4.8.1 The Competition between Inverse Bremsstrahlung and Brillouin Reflection

In experiments with long-pulse-length laser light, the size of the underdense plasma can be quite large. When the underdense plasma is large, Brillouin scatter<sup>151</sup> becomes a significant loss mechanism, as supported by recent experiments.<sup>152,153</sup> However, inverse bremsstrahlung also becomes more important in such plasmas, particularly when high-Z targets are used. It is then very important to understand the competition between Brillouin scatter and inverse bremsstrahlung (collisional absorption).

Some first estimates of this competition can be obtained by including collisional damping of the light wave in a theoretical model for Brillouin backscatter in a uniform plasma. It is shown that collisional absorption can suppress Brillouin scatter only above a characteristic density. Hence, in an inhomogeneous plasma the scatter can be decreased but not eliminated.

The analytic model treats Brillouin backscatter in a uniform underdense plasma with density  $n_p$ .<sup>154,155</sup> From Maxwell's equations and the two-fluid plasma equations, we can readily derive coupled equations for the incident and reflected light waves and the ion-density fluctuation:

$$\left[ \frac{\partial^2}{\partial t^2} + \nu \frac{\partial}{\partial t} - c^2 \frac{\partial^2}{\partial x^2} + \omega_{pe}^2 \right] A_f = - \frac{4\pi e^2}{m} A_b n_i$$

and

$$\left[ \frac{\partial^2}{\partial t^2} + \Gamma \frac{\partial}{\partial t} - v_s^2 \frac{\partial^2}{\partial x^2} \right] n_i = \frac{Z n_p e^2}{m M c^2} \frac{\partial^2}{\partial x^2} A_f A_b. \quad (76)$$

Here  $A$  is the vector potential of either the incident wave ( $A_f$ ) or the back-reflected wave ( $A_b$ ),  $\omega_{pe}$  is the electron plasma frequency, and  $v_s$  is the ion sound velocity. The energy damping rate of the ion wave is  $\Gamma$ , and the damping rate of the light waves  $\nu = (\omega_{pe}^2/\omega^2) \times \nu_{ei}$ , where  $\nu_{ei}$  is the electron-ion collision frequency. In the usual way, we remove the fast-time and spatial variations and assume that the ion wave is heavily damped; i.e., that the damping length of the ion wave is much less than the growth length of the instability. Taking the ion wave and incident light wave to have frequency  $\omega$  and  $\omega_0$ , respectively, and wave number  $k$  and  $k_0$ , respectively, we then obtain:

$$\begin{aligned} n_i &= n_p \frac{k^2 e^2 Z}{2 m M c^2} \frac{A_f A_b}{\Gamma \omega}, \\ -2k_0 c^2 \frac{\partial A_f}{\partial x} - \nu \omega_0 A_f &= \frac{\omega_{pe}^2}{2 n_p} A_b n_i, \\ 2(k_0 - k) c^2 \frac{\partial A_b}{\partial x} + \nu \omega_0 A_b &= \frac{\omega_{pe}^2}{2 n_p} A_f n_i. \end{aligned} \quad (77)$$

The solution for the reflectivity for a plasma of length  $L$  is then determined by

$$B \exp(-\beta L) = \frac{r(1-r)}{\left\{ \exp \left[ \alpha (1-r) \left( \frac{1-e^{-\beta L}}{\beta} \right) \right] - r \right\}}, \quad (78)$$

where

$$\begin{aligned} \alpha &= \frac{1}{4} \frac{n_p}{n_{cr}} \frac{v_{os}^2 k_0}{v_e^2 \left( 1 + \frac{3\theta_i}{\theta_e} \right)} (\omega/\Gamma), \\ \beta &= \frac{\nu}{C} \frac{\omega_0}{k_0 C}. \end{aligned}$$

Here  $v_{os}$  is the oscillation velocity of an electron in the incident light wave,  $\theta_i$  is the ion temperature, and  $\theta_e$  is the electron temperature ( $m v_e^2 = \theta_e$ ).  $B$  is the intensity of the back-reflected wave at  $x = L$ , normalized to the incident light intensity. Crudely this can be estimated as the noise level of the back-reflected wave, which is

enhanced, however, by scattering of the incident light wave from thermal ion density fluctuations.

This solution has a very simple physical interpretation. Defining an absorption length for the light waves ( $l_{abs} = 1/\beta$ ), we observe that the above solution reduces to that obtained by neglecting collisional damping with the substitution

$$L \rightarrow L^* = l_{abs} \left[ 1 - \exp(-L/l_{abs}) \right]. \quad (79)$$

If  $L \ll l_{abs}$ ,  $L^* = L$ . If  $L \gg l_{abs}$ ,  $L^* \simeq l_{abs}$ . The physical interpretation in this limit is straightforward: the maximum reflection is that obtained in a plasma of size  $L = l_{abs}$ .

Using Eq. (78) and assuming that  $L \gg l_{abs}$ , we can now estimate the condition in which collisional absorption (inverse bremsstrahlung) prevails over back scatter as

$$\frac{\alpha}{\beta} \lesssim 5.$$

In more physical units, this condition is

$$\frac{n_p}{n_{cr}} \gtrsim \frac{1.21}{10^{15}} \left/ \left[ \frac{\Gamma}{\omega} \frac{Z}{\theta_e^{1/2}} \left( 1 + \frac{3\theta_i}{2\theta_e} \right) \left( \frac{n_{cr}}{10^{21}} \right)^{3/2} \right] \right., \quad (80)$$

where  $I$  is the incident light intensity ( $\text{W}/\text{cm}^2$ ),  $\theta$  is the temperature (eV), and  $n_{cr}$  is the critical density for the incident light ( $\text{cm}^{-3}$ ). In other words, collisional absorption can suppress Brillouin scatter only above some characteristic density given by Eq. (80). This condition arises because the growth rate for backscatter is proportional to density, whereas the collisional damping of a light wave is proportional to the square of the density. As an example, consider 1.06- $\mu\text{m}$  light,  $I = 10^{14}$ ,  $\text{W}/\text{cm}^2$ ,  $\theta_e = 1 \text{ keV}$ , and  $Z \sim 30$ . Then, even if the ion wave is very heavily damped ( $\Gamma/\omega = 1$ ),  $n_p/n_{cr} \geq 0.15$ .

For laser light incident onto an initially solid density target, the light in fact traverses regions of different plasma density, as indicated in Fig. 4-58. As shown above, the collisional absorption can suppress the backscatter above the characteristic density; the scatter prevails below that density. It is then clear that Brillouin scatter is not eliminated by collisional absorption, although in any given density profile it is reduced by being limited to lower densities. Although the simple uniform plasma model makes clear some of the important qualitative features of the competition, quantitative calculations must of course take into account how much plasma is at the various densities, how the gradients in

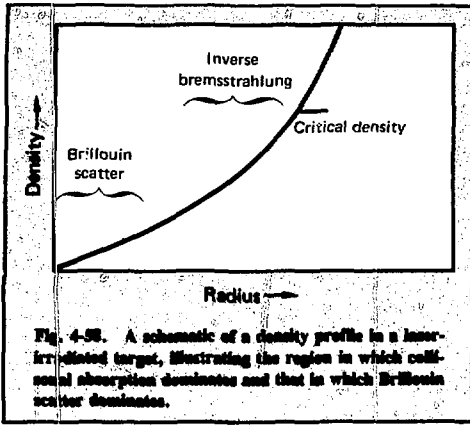


Fig. 4-56. A schematic of a density profile in a laser-irradiated target, illustrating the region in which collisional absorption dominates and that in which Brillouin scatter dominates.

density and expansion velocity reduce the scatter, and how the finite mass and heat capacity of the plasma limit the scatter.<sup>151,156</sup> These questions must be addressed in detailed computer calculations, which are now underway.

## References

151. C. S. Liu, M. N. Rosenbluth, and R. B. White, "Raman and Brillouin Scattering of Electromagnetic Waves in Inhomogeneous Plasmas," *Phys. Fluids* **17**, 1211 (1974).
152. D. W. Phillion, W. L. Kruer, and V. C. Rupert, "Brillouin Scatter in Laser-Produced Plasmas," *Phys. Rev. Lett.* **39**, 1529 (1977).
153. B. H. Ripin, F. C. Young, J. A. Stamper, C. M. Armstrong, R. Decoste, E. A. McLean, and S. E. Bodner, "Enhanced Backscatter with a Structural Laser Pulse," *Phys. Rev. Lett.* **39**, 611 (1977).
154. C. L. Tang, "Saturation and Spectral Characteristics of the Stokes Emission in the Stimulated Brillouin Process," *J. Appl. Phys.* **37**, 2945 (1966).
155. D. W. Forslund, J. M. Kindel, and E. L. Lindman, "Non-linear Behavior of Stimulated Brillouin and Raman Scattering in Laser-Irradiated Plasmas," *Phys. Rev. Lett.* **30**, 739 (1973).
156. W. L. Kruer, E. J. Valeo, and K. G. Estabrook, "Limitation of Brillouin Scattering in Plasmas," *Phys. Rev. Lett.* **35**, 1076 (1975).

## Author

W. L. Kruer

## 4.8.2 Forward Raman Scatter in Laser Fusion Reactors

Besides the usual backscattering plasma instabilities, there are stimulated scattering processes that operate in the forward direction, the scattered photon traveling in a different direction from the incident photon. In a laser fusion target chamber, there is some background gas, either from hot walls, such as in the lithium waterfall concept, or from a buffer gas designed

to protect cool walls. As the laser beams are focused, they eventually reach a high enough intensity that the background gas is ionized. The resulting plasma may then scatter the incoming laser beam. Here we consider the most efficient forward scattering process in a very underdense plasma, stimulated Raman scattering, and find limits on the background-gas density so that only a small fraction of the incoming beam is sufficiently de-collimated that it misses the target. The purpose of this analysis is to find a conservative overestimate of the scattering percentage. An important feature of this analysis is that the plasma is very underdense, i.e.,  $\omega_p < \omega_0$ , where  $\omega_p$  is the plasma frequency and  $\omega_0$  is the light frequency. The dispersion relation for Raman scatter is obtained in the usual way:<sup>157</sup>

$$\omega^2 + i\omega\nu - \omega_p^2 - 3k^2 v_T^2 = \omega_p^2 k^2 v_{os}^2 \cos\phi \left\{ \left[ 2\omega\omega_0 + \omega^2 - c^2(k^2 + 2kk_0 \cos\theta) + i(\omega + \omega_0)\nu_A \right]^{-1} + \left[ -2\omega\omega_0 + \omega^2 - c^2(k^2 - 2kk_0 \cos\theta) + i(\omega - \omega_0)\nu_A \right]^{-1} \right\}, \quad (81)$$

where  $v_{os}$  is the oscillatory velocity,  $\phi$  is the angle between the electric vectors of the incoming and scattered waves,  $\theta$  is the angle between  $k_0$ , the incoming wave vector, and  $k$ , the plasmon wave vector.  $v_T$  is the electron thermal velocity,  $\nu$  is the plasma damping rate, and  $\nu_A = \omega_p^2/\omega^2\nu$  is the electromagnetic wave damping rate. Henceforth we stay in the polarization plane and let  $\phi = 0$ .

If  $\theta = 0$ , either bracketed term in the braces may be resonant, but not both. The answer is the same for either, so we consider the second term only.

The resonance condition is

$$c^2(k^2 - 2kk_0 \cos\theta) = \omega^2 - 2\omega\omega_0. \quad (82)$$

The maximum value for  $k$  in the forward direction is

$$k_{\max} = (2\omega_p/\omega_0)^{1/2}/c \quad (83)$$

and occurs for

$$\theta = (2\omega_p/\omega_0)^{1/2}. \quad (84)$$

The corresponding scattering angle is

$$\theta_s \cong k/k_0 = (2\omega_p/\omega_0)^{1/2}. \quad (85)$$

Because the growth rate of the instability is proportional to  $k$ , the most strongly growing mode corresponds to  $k_{\max}$  and has the growth rate

$$\gamma_{\max} = 1/\sqrt{2} \omega_p v_{os}/c \quad (86)$$

with the threshold

$$\nu = \sqrt{2} \omega_0 v_{os}/c \quad (87)$$

If we put in typical numbers, Eq. (87) shows that the instability is always strongly overdriven.

Next we wish to estimate how much energy is scattered from the beam. The maximum level the plasma waves can reach is determined by particle trapping in the waves, given by

$$E_p^2/4\pi \cong n m_e \omega^2/k^2, \quad (88)$$

where  $E_p$  is the plasma wave field,  $n$  is the background gas density, and  $m_e$  is the electron mass. The plasma is locally heated by the plasma waves at a rate given by  $2\gamma_{\max} E_p^2/4\pi$ . The number of photons lost by the main beam is the same as the number of plasmons created,

$$\Delta E_0^2/4\pi\omega_0 = \Delta E_p^2/4\pi\omega_p^2 \quad (89)$$

Thus, the power lost from the main beam is

$$\nu^*(E_0^2/8\pi) = 2\gamma (\omega_0/\omega_p) (E_p^2/4\pi) \quad (90)$$

where  $\nu^*$  is a phenomenological damping rate given by this equation. The fractional energy loss over a ray path is approximately

$$f_E = \int_{\ell}^L (\nu/\omega_0) k_0 dx = (1/\sqrt{2}) (\omega_p/\omega_0)^3 \int_{\ell}^L k_0 dx / (v_{os}/c) \quad (91)$$

where we have used Eqs. (90) and (88). Distances are measured from beam focus.  $L$  is the ionization point, and  $\ell$  is the closest distance at which a scattered photon still hits the target:

$$\ell = d \left\{ f + \left[ 1/(2\sqrt{2}) \right] (\omega_0/\omega_p)^{1/2} \right\} \quad (92)$$

where  $d$  is the target diameter and  $f$  the lens f-number.

Because the beam is focused,  $v_{os}(x) \sim x^{-1}$ , thus relating  $v_{os}(x)$  to the target plane  $x = fd$ :

$$f_E \cong [1/(2\sqrt{2})] (\omega_p/\omega_0)^3 [kL^2/v_{os}/c]fd \quad (93)$$

where we have used  $\ell < L$ . Taking an ionization intensity of  $I(L) = 10^{12} \text{ W/cm}^2$ , Eq. (93) can be written

$$f_E = [10^3/(2\sqrt{2})] (n/n_c)^{3/2} \omega_0/\omega_{Nd} \times (I_0/10^{12})^{1/2} k_0 fd \quad (94)$$

Note that the frequency scaling is  $\omega_0^{-1}$ , so  $\text{CO}_2$  lasers are much more susceptible to this effect than glass lasers. For a given lens f-number, target diameter, and  $I_0$ , Eq. (94) may be used to estimate how much background gas density is allowable in order to scatter not more than 10%, say, of the incoming beam. A typical number  $n \leq 10^{15} \text{ cm}^{-3}$ .

Two effects may be used to reduce the scatter. It is well known that, if the laser has a frequency bandwidth much larger than the coherent growth rate, then the growth rate is reduced, in this case to

$$\gamma = 1/2 (\omega_p^2/\Delta\omega) (v_{os}^2/c^2) \quad (95)$$

If  $\gamma\tau \leq 1$ , where  $\tau$  is the laser pulse duration, the instability will not be able to grow. Thus bandwidth will eliminate the instability if

$$\Delta\omega/\omega_0 \cong 1/2 (\omega_p^2/\omega_0^2) (v_{os}^2/c^2) \omega_0\tau \quad (96)$$

For Nd, this typically requires bandwidths much less than a percent. The scaling here is  $\omega_0^{-3}$ , so  $\text{CO}_2$  lasers may not be able to use this method.

Another effect is that of random density fluctuations in the background gas. This tends to detune the instability by changing the local value of  $\omega_p$ . A simple calculation shows that the instability is very sensitive to this effect, and reasonable guesses for density-fluctuation parameters appear sufficient to quench the instability.

In summary, we have derived an expression for the amount of light forwardscattered from a laser beam in a target chamber. For some situations, the scattering may be appreciable. However, laser bandwidth or background density fluctuations are efficient at quenching the instability. Lower frequency lasers are more susceptible to this scattering effect.

## Reference

157. D. W. Forslund, J. M. Kindel, and E. L. Lindman, "Theory of Simulated Scattering Processed in Laser-Irradiated Plasmas," *Phys. Fluids* 18, 1002 (1975).

## Author

J. J. Thomson

## 4.9 Heat-Transport Inhibition

### 4.9.1 Cross-Field Thermal Transport Caused by Ion-Acoustic Waves in Magnetized Laser Plasmas

**Introduction.** It is now clear that large magnetic fields can be generated in laser produced plasmas. Recent measurements by Faraday rotation have indicated fields greater than 1 MG in the underdense plasma.<sup>158-160</sup> Many mechanisms can produce such magnetic fields. These include the  $\nabla n \times \nabla T$  term in the equation for  $B$ ,<sup>161,162</sup> the thermoelectric term,<sup>161-164</sup> the divergence of momentum flux of laser light,<sup>164-167</sup> currents produced by energetic electrons,<sup>168</sup> impurity seeding,<sup>169</sup> and even currents generated by turbulence in an unmagnetized plasma.<sup>170</sup> We have elsewhere summarized the scaling laws expected for these various mechanisms for generating magnetic fields<sup>171</sup>.

Although the magnetic field is large, laser-produced plasmas are so dense, so hot, and so rapidly flowing that the fields observed and predicted are not large enough to affect the dynamics. However, the magnetic field does greatly reduce cross-field electron thermal conduction, or heat flow. Reducing thermal conduction requires that  $\omega_{ce} \tau_e \gg 1$ , where  $\omega_{ce}$  is the electron cyclotron frequency and  $\tau_e$  is the electron-ion collision time. This condition is not difficult to satisfy even for magnetic fields too small to affect dynamics directly.

Thus, one expects the cross-field thermal energy flux in a magnetized plasma to be much less than the flux in an unmagnetized plasma. This inhibition of energy flux would in turn lead to much steeper electron temperature gradients than one would expect for an unmagnetized plasma. One could then ask whether the steep gradients so produced could lead to any kind of instability that would tend to raise the electron cross-field thermal flux to a value closer to that for an unmagnetized plasma.

Here we show that ion-acoustic waves that propagate perpendicular to both the magnetic field and the gradients can in fact be driven unstable. First, we derive the equilibrium. Then we calculate the linear theory for ion-acoustic waves in this equilibrium. Next we calculate the electron energy flux in a given spectrum of ion-acoustic fluctuations. Finally, we discuss how to include the effects of enhanced cross-field transport in a fluid code.

**The Equilibrium.** The basic configuration of a one-dimensional laser-produced plasma is shown in Fig. 4-59. The laser comes from the left at  $x = -\infty$ . The flow velocity and temperature gradient are in the negative  $x$  direction, and the density gradient is in the positive  $x$  direction. We assume a magnetic field  $B$  in the positive  $z$  direction (out of the plane of the paper), strong enough to affect the electron transport,  $\omega_{ce} \tau_e$

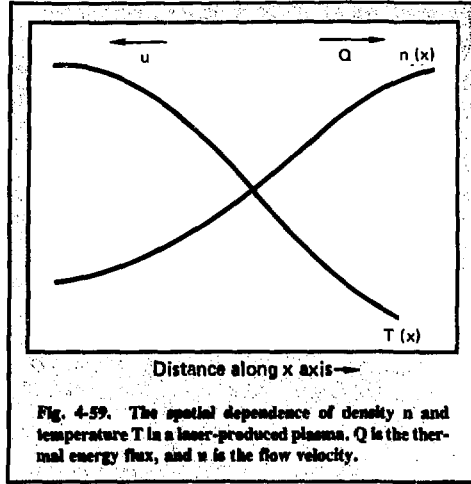


Fig. 4-59. The spatial dependence of density  $n$  and temperature  $T$  in a laser-produced plasma.  $Q$  is the thermal energy flux, and  $u$  is the flow velocity.

$\gg 1$ . We also assume that the field is too weak to affect the dynamics; i.e.,  $n\mu^2 \gg B^2/4\pi$ ,  $\omega_{pe} \gg \omega_{ce}$ , and  $\beta \gg 1$ , where  $n$ ,  $M$ ,  $u$ , and  $\omega_{pe}$  are, respectively, the number density, ion mass, flow velocity, and electron plasma frequency, and  $\beta \equiv 4\pi nT/B^2$ . The ions are assumed to be unmagnetized,  $\rho_i \gg L$ , where  $\rho_i$  is the ion larmor radius and  $L$  is a macroscopic scale length. Electrons are assumed to be strongly magnetized,  $\rho_e \ll L$ . Therefore, for the electrons to flow in the negative  $x$  direction, there must be an electric field in the negative  $y$  direction with magnitude  $B(u/c)$ . The above conditions are generally satisfied in a laser-produced plasma.

To calculate whether such a plasma is stable, it is essential to consider the effect of collisions on the equilibrium. The equilibrium is governed by a flow velocity to the left and an electron thermal conduction to the right. This thermal energy flux  $Q = -K dT/dx$ , where  $K$  is the thermal conductivity. Classical kinetic theory gives the result<sup>172</sup>

$$K = 4.66 n T_e / m \omega_{ce}^2 \tau_e \quad (97)$$

If the laser energy flux is  $I$  and the fractional absorption is  $\alpha$ , then conservation of energy flux (assuming for simplicity no change in fluid energy flux) across the region of absorption gives  $Q = \alpha I$ . Thus, thermal energy flux, and therefore a nonzero collision frequency, is inherent in the very nature of the equilibrium of a laser-produced plasma. We shall require that  $\rho_L < \lambda_{mfp} < L$ , where  $\rho_L$  and  $\lambda_{mfp}$  are the electron larmor radius and mean free path.

Cross-field thermal conduction in the  $x$  direction is always accompanied by an additional thermal flux in the  $y$  direction (along isotherms). The magnitude of the thermal flux in the  $y$  direction is independent of collisions (for  $\omega_{ce} \tau_e \gg 1$ ) and is well known in classical kinetic theory.<sup>172</sup> In the next section we show that this thermal flux in the  $y$  direction can produce an ion-acoustic instability, with wave vector in the  $y$  direction. Because the energy flux in the  $y$  direction is nearly independent of collision frequency, we use the simplest possible collision model, a Krook collision term. The steady-state Vlasov equation becomes

$$v_x \frac{\partial f}{\partial x} - \frac{e}{m} E_x \frac{\partial f}{\partial v_x} - \frac{e}{m} E_y \frac{\partial f}{\partial v_y} - \frac{e}{m} \frac{v}{c} \times \mathbf{B} \cdot \frac{\partial f}{\partial \mathbf{v}} = -\nu(f - f^0), \quad (98)$$

where  $f^0$  is a Maxwellian distribution,  $n$  the local density,  $u$  the flow velocity, and  $T_e$  the temperature, which are  $x$  dependent. The quantity  $E_x$  is determined by the  $x$  component of the electron momentum equation,

$$0 = -ne E_x - \frac{\partial}{\partial x} n T_e, \quad (99)$$

where we have taken  $u^2 \ll T_e/m$ . Assuming that the first two terms on the left of Eq. (98) are small, one can solve for the perturbed distribution function by standard means.<sup>173</sup> Using

$$f^0 = \frac{n(x)}{(2\pi T_e(x)/m)^{3/2}} \exp - \frac{m(v - u)^2}{2 T_e(x)}, \quad (100)$$

$$f \equiv f_0 + \delta f = \left\{ 1 - \left[ \frac{1}{2} \frac{m(v - u)^2}{T_e} - \frac{5}{2} \right] \times \frac{1}{T_e} \frac{dT_e}{dx} \left( \frac{\nu(v_x - u) + \omega_{ce} v_y}{\omega_c^2 + \nu^2} \right) \right\} f_0, \quad (101)$$

where  $v_x - u = v_1 \cos \theta$ ,  $v_1 = v \sin \theta$ . The first term in the parentheses of Eq. (101) causes an energy flux down the temperature gradient. The second term causes an energy flux in the positive  $y$  direction. In the limit  $\nu \ll \omega_{ce}$ , this energy flux in the  $y$  direction is independent of collisionality.<sup>172</sup> Notice that the energy flux in the positive  $y$  direction is carried by a flux of energetic electrons moving in the positive  $y$  direction and that it is balanced by a return current of slower electrons in the negative  $y$  direction. In the next section, we show that

the latter return current drives unstable ion-acoustic waves.

**Linear Theory.** Given the unperturbed distribution function in Eq. (101), we can calculate the perturbed electron distribution function with standard techniques.<sup>174</sup> The result is

$$\tilde{f}_e = n \frac{e\phi}{T_e} \left\{ 1 + \sum_l \frac{J_l^2 \left( \frac{kv_1}{\omega_{ce}} \right) \left[ \omega + \frac{kc}{eB} \frac{dT_e}{dx} \left( \frac{1}{2} \frac{m(v - u)^2}{T_e} - \frac{5}{2} \right) \right]}{-l\omega_{ce} - \omega} \right\} f^0. \quad (102)$$

Assuming that  $k$  is in the  $y$  direction, the fluctuating potential is  $\phi(y, t) = \phi \exp i(ky - \omega t) + \text{complex conjugate}$  and  $\omega_{ce} \gg \nu$ .

At this point, we use the fact that  $\omega \gg \omega_{ce}$  and  $kv_e \gg \omega_{ce}$ , where  $v_e = (T_e/m)^{1/2}$ . A great deal of analytic work and also numerical simulation has shown that in this limit the magnetic field has no effect on the microscopic dynamics of the instability. Under these circumstances, it is appropriate to average Eq. (102) over cyclotron resonances. (This procedure is discussed in more detail in Ref. 175.)

The dispersion relation for waves is obtained by setting  $\tilde{n}_i = \tilde{n}_e$ , or

$$\frac{\omega_{pi}^2}{\omega^2} = \frac{\omega_{pe}^2}{k^2 v_e^2} \left[ 1 + \int d^3 v \frac{\omega + \frac{kc}{eB} \frac{dT_e}{dx} \left( \frac{1}{2} \frac{m(v - u)^2}{T_e} - \frac{5}{2} \right)}{k v_y - \omega} f^0 \right]. \quad (103)$$

We have assumed that  $T_i = 0$  and  $k\lambda_D \ll 1$ .

As long as  $(c/eB)(dT_e/dx) \ll v_e$ , the integral term in the square brackets is much smaller than unity, so to lowest order the waves are just ion-acoustic waves that propagate with phase speed  $v_s = (T_e/M)^{1/2}$ . Making a

resonant approximation to  $(kv_y - \omega)^{-1}$ , we find that the wave frequency is given roughly by

$$\omega \approx |k|v_s \left[ 1 - i(\pi/8)^{1/2} \frac{(\omega - 3/2 \frac{kc}{eB} \frac{dT_e}{dx})}{|k|v_e} \right] \quad (104)$$

In the configuration shown in Fig. 4-59,  $dT/dx < 0$ , so, if  $k < 0$ , the ion-acoustic wave is unstable. This corresponds to a wave propagating in the negative  $y$  direction, or parallel to the return current in the  $y$  direction. For cold ions, the condition for instability is

$$3/2 \frac{c}{eBv_e} \frac{dT_e}{dx} > (m/M)^{1/2} \quad (105)$$

This condition is easily satisfied in a laser-produced plasma. For instance, if  $T_e = 5$  keV and  $B = 1$  MG, a hydrogen plasma is unstable if the temperature gradient scale length is less than about  $75 \mu\text{m}$ . If the ion temperature is not zero, one can subtract from the growth rate the ion Landau damping decrement.

The fact that condition (105) is generously satisfied in typical laser-produced plasmas allows an important simplification in the sections which follow. The wave-vector spectrum for ion-acoustic waves can be taken to be nearly isotropic in the  $x$ - $y$  plane, because the ion-acoustic instability is well above threshold. The presence of the magnetic field in the  $z$  direction also helps to isotropize the electron velocity distribution in  $x$  and  $y$ .

**Anomalous Thermal Conduction.** In this section, we calculate anomalous thermal conduction arising from ion-acoustic instabilities driven by cross-field temperature gradients. As discussed in the two preceding sections, the negative temperature gradient in the  $x$  direction causes a current of low-velocity particles in the negative  $y$  direction. This drives an ion-acoustic instability propagating in the negative  $y$  direction.

In the reference frame moving with speed  $cE_y/B$ , one can see how the instability causes an anomalous thermal flux. The instability exerts an average force on the electrons in the positive  $y$  direction that causes an average electron drift in the negative  $x$  direction. However, this force is a decreasing function of the magnitude of the particle velocity.<sup>176</sup> Thus, the lower velocity particles have a greater drift velocity in the negative  $x$  direction than do the higher velocity particles.

In a frame with no net drift in the  $x$  direction, the lower velocity particles have a drift toward negative  $x$  (up the temperature gradient), whereas the higher vel-

ocity particles have a drift toward positive  $x$  (down the temperature gradient). Because  $\langle v_x \rangle = 0$ , this distorted distribution function has an energy flux down the temperature gradient.

As long as  $u^2 \ll T_e/m$ , a condition easily satisfied in a laser-produced plasma, the electron energy flux in the frame moving with speed  $cE_y/B$  is just equal to the energy flux in a frame having no net drift minus  $5/2 \langle nu \rangle T_e$ , where  $\langle nu \rangle$  is the instability-induced particle flux. The quantity  $5/2 \langle nu \rangle T_e$  is that part of the total energy flux which is convected with the fluid motion.

We now calculate  $\langle nu \rangle$  and  $W$ , the particle and energy flux associated with the instability. If we make the transformation given below Eq. (101), the quasilinear equation for  $f(v)$  in a time-independent plasma is

$$v_1 \cos \theta \frac{\partial f}{\partial x} + \omega_{ce} \frac{\partial f}{\partial \theta} = \pi \sum_k \frac{\partial}{\partial v} \cdot k \left| \frac{e\phi(k)}{m} \right|^2 \delta(k \cdot v - \omega) k \cdot \frac{\partial f}{\partial v} \quad (106)$$

where  $\omega_{ce} = eB/mc > 0$ . On the right side of Eq. (106), the summation over  $k$  also includes a summation over  $-k$ .

By taking appropriate velocity moments of Eq. (106) and assuming  $\rho_e \ll L$ , we obtain

$$\langle nu \rangle = \sum_k \left( \frac{\pi}{2} \right)^{1/2} \left| \frac{e\phi(k)}{T_e} \right|^2 \frac{k}{|k|} \frac{v_e}{\omega_{ce}} n \times \left[ \frac{3}{2} \frac{kc}{eB} \frac{dT_e}{dx} - \omega \right] \quad (107)$$

$$W_i = \sum_k \left( \frac{\pi}{2} \right)^{1/2} \left| \frac{e\phi(k)}{T_e} \right|^2 \frac{k}{|k|} \frac{nv_e T_e}{\omega_{ce}} \times \left[ \frac{1}{2} \frac{kc}{eB} \frac{dT}{dx} - \omega \right] \quad (108)$$

The thermal energy flux corrected for fluid convection is then

$$W = W_i - \frac{5}{2} nu_i T_e = - \sum_k \left( \frac{\pi}{2} \right)^{1/2} \left| \frac{e\phi(k)}{T_e} \right|^2 \frac{k}{|k|} \frac{nv_e T_e}{\omega_{ce}} \times \left[ \frac{13}{4} \frac{kc}{eB} \frac{dT}{dx} - \frac{3}{2} \omega \right] \quad (109)$$



Thus, as long as the plasma is unstable, the energy flux is down the temperature gradient. If one assumes  $k \sim k_D/2$ , as is characteristic of ion-acoustic instabilities, Eq. (109) is an expression for the energy flux in terms of the fluctuating field strength. One can then write the anomalous thermal conduction as

$$K_{an} \approx \frac{13}{8} \left( \frac{\pi}{2} \right)^{1/2} \left| \frac{e\phi}{T_e} \right|^2 \frac{\omega_{pe}^2 v_e^2}{\omega_{ce}^2} \quad (110)$$

We close this section by noting that, if the effective collision frequency in the turbulence  $\nu_{eff}$  is greater than  $\omega_{ce}$ , energy transport is not limited by the magnetic field, but rather by ion-acoustic turbulence alone. Under such circumstances, a different expression for the thermal conduction would be appropriate. Ref. 170 discusses one such derivation of  $K_{an}$  for ion-acoustic turbulence when  $B = 0$ .

#### Application to Target-Design Computer Codes.

As shown in the numerical example at the end of the section on linear theory, magnetized laser-produced plasmas are often unstable. Because laser fusion targets are generally designed by using computer hydrodynamics codes, the presence of instability should be modeled in these codes. Eq. (110) gives an expression for the thermal conduction in the  $x$  direction in terms of fluid parameters and  $e\phi/T_e$ . To model anomalous thermal conduction, one must first determine if the plasma is unstable at a particular point. Ion Landau (and possibly collisional) damping must be figured into the growth rate. If it is stable, one simply uses classical thermal conduction. If it is unstable,  $e\phi/T_e$  must be evaluated. To do this, one can refer to the literature on the nonlinear theory of ion-acoustic instabilities.<sup>177-185</sup> The consensus of those references is that trapping or resonance broadening limits the value of  $e\phi/T_e$  to roughly  $0.1 < e\phi/T_e < 0.2$ . Assuming such a value of  $e\phi/T_e$ , Eq. (110) then gives the anomalous thermal conductivity in the unstable regions. Finally, one must check whether this value of  $e\phi/T_e$  is so large that turbulence, rather than the magnetic field, dominates the thermal conduction. If it is, then instead of Eq. (110), the appropriate thermal conductivity is the unmagnetized value, either classical<sup>172</sup> or anomalous.

In summary, we have shown that cross-field thermal conductivity in magnetized laser-produced plasmas can be increased by ion-acoustic turbulence driven by heat flow. We have discussed how this effect may be modeled in laser hydrodynamics codes.

#### References

158. J. A. Stamper, E. A. McLean, and B. H. Ripin, "Studies of Spontaneous Magnetic Fields in Laser-Produced Plasmas by Faraday Rotation," *Phys. Rev. Lett.* **40**, 1177 (1978).
159. J. A. Stamper and B. H. Ripin, "Faraday-Rotation Measurements of Megagauss Magnetic Fields in Laser-Produced Plasmas," *Phys. Rev. Lett.* **34**, 138 (1975).
160. A. Raven, O. Willi, and P. T. Rumsby, "Megagauss Magnetic Field Profiles in Laser-Produced Plasmas," *Phys. Rev. Lett.* **41**, 554 (1978).
161. J. A. Stamper, K. Papadopoulos, R. N. Sudan, S. O. Dean, E. A. McLean, and J. M. Dawson, "Spontaneous Magnetic Fields in Laser-Produced Plasmas," *Phys. Rev. Lett.* **26**, 1012 (1971).
162. J. B. Chase, J. M. LeBlanc, and J. R. Wilson, "Role of Spontaneous Magnetic Fields in a Laser-Created Deuterium Plasma," *Phys. Fluids*, **16**, 1142 (1973).
163. D. G. Colombant and N. K. Winsor, "Thermal-Force Terms and Self-Generated Magnetic Fields in Laser-Produced Plasmas," *Phys. Rev. Lett.* **38**, 697 (1977).
164. J. A. Stamper and D. A. Tidman, "Magnetic-Field Generation due to Radiation Pressure in a Laser-Produced Plasma," *Phys. Fluids* **16**, 2024 (1973).
165. J. J. Thomson, C. E. Max, and K. G. Estabrook, "Magnetic Fields due to Resonance Absorption of Laser Light," *Phys. Rev. Lett.* **35**, 663 (1975).
166. B. Bezzerides, D. G. DuBois, D. W. Forslund, and E. L. Lindman, "Magnetic-Field Generation in Resonance Absorption of Light," *Phys. Rev. Lett.* **38**, 495 (1977).
167. K. Nishihara, Y. Ohsawa, K. Mima, and T. Tange, "Magnetic-Field Generation due to Resonance Absorption," *Phys. Fluids* **19**, 1833 (1976).
168. D. G. Colombant and D. A. Tidman, submitted to *Phys. Rev. Lett.*
169. D. A. Tidman, "Seeded Megagauss Turbulence In Dense Fusion-Target Plasmas," *Phys. Rev. Lett.* **35**, 1228 (1975).
170. W. M. Manheimer, "Energy-Flux Limitation by Ion-Acoustic Turbulence in Laser-Fusion Schemes," *Phys. Fluids* **20**, 265 (1977).
171. C. E. Max, W. M. Manheimer, and J. J. Thomson, "Enhanced Transport across Laser-Generated Magnetic Fields," *Phys. Fluids* **21**, 128 (1978).
172. S. I. Braginskii, "Transport Processes in a Plasma," in *Reviews of Plasma Physics* (Consultants Bureau, New York, 1965), vol. 1, pp. 205-311.
173. K. Huang, *Statistical Physics* (John Wiley and Sons, New York, 1963), Ch. 5.
174. N. A. Krall and A. W. Trivelpiece, *Principles of Plasma Physics* (McGraw-Hill, New York, 1973), pp. 418-432.
175. W. M. Manheimer, C. E. Max, and J. J. Thomson, "Cross Field Thermal Transport Due to Ion Acoustic Waves in Magnetized Laser Plasmas," U.S. Naval Research Laboratory, Memorandum Rept. 3593 (1977), submitted to *Phys. Fluids*.
176. R. Z. Sagdeev and A. A. Galeev, *Nonlinear Plasma Theory* (W. A. Benjamin, Inc., New York, 1969), pp. 52-54.
177. M. Lampe, W. M. Manheimer, J. B. McBride, J. H. Orens, K. Papadopoulos, R. Shanny, and R. N. Sudan, "Theory and Simulation of the Beam Cyclotron Instability," *Phys. Fluids* **15**, 662 (1972).
178. W. M. Manheimer and R. Flynn, "Anomalous Resistivity and Ion-Acoustic Turbulence," *Phys. Rev. Lett.* **27**, 1175 (1971).
179. W. M. Manheimer and R. Flynn, "Formation of Nonthermal Ion Tails in the Ion-Acoustic Instability," *Phys. Fluids* **17**, 409 (1974).
180. J. H. Orens and J. M. Dawson, U.S. Naval Research Laboratory, Memorandum Rept. 2850 (1974).
181. M. Z. Caponi and R. C. Davidson, "Influence of Ion-Resonance Broadening on the Anomalous Heating and Momentum

Transfer in a Current-Carrying Plasma," *Phys. Rev. Lett.* **31**, 86 (1973).

182. J. P. Boris, J. M. Dawson, J. H. Orens, and K. V. Roberts, "Computations on Anomalous Resistance, *Phys. Rev. Lett.* **25**, 706 (1970).
183. D. Biskamp and R. Chodura, "Computer Simulation of Anomalous dc Resistivity," *Phys. Rev. Lett.* **27**, 1553 (1971).
184. D. Biskamp, K. U. Von Hagenow, and H. Welter, "Computer Studies of Current-Driven Ion-Sound Turbulence in Three Dimensions," *Phys. Lett. A* **39**, 351 (1972).
185. A. M. Sleeper, J. Weinstock, and B. Bezzerides, "Nonlinear Theory and Angular Spectrum of the Ion-Acoustic Instability," *Phys. Fluids* **16**, 1508 (1973).

## Authors

W. M. Manheimer

C. E. Max

J. J. Thomson

## 4.9.2 Qualitative Aspects of Underdense Magnetic Fields

An important absorption process for high-intensity laser light is resonant absorption, which accelerates electrons in the general direction of down the density gradient.<sup>186</sup> Consequently, the electrons are heated with an anisotropic velocity distribution. As was shown by Eric Weibel, a sufficiently anisotropic velocity distribution causes the plasma to break into filaments and surrounding magnetic fields that exponentiate because the magnetic fields compress the filaments that in turn increase the magnetic field.<sup>187</sup> A good reference for the minimum wavelength  $\lambda_{\min}$ , the fastest growing wavelength  $\lambda_f = 1.7\lambda_{\min}$ , and growth rate of that mode  $\gamma_f$  is Krall and Trivelpiece,<sup>188</sup> from which we reproduce the following:

$$\lambda_{\min}/\lambda_0 = [(n/n_e)(T_x/T_y - 1)]^{-1/2} \quad (111)$$

$$\gamma_f/\omega_{pe} = 0.31 [T_y/(m_e c^2)]^{1/2} (T_y/T_x) \times (T_x/T_y - 1)^{3/2} \quad (112)$$

These equations are in the limit of the growth rate much less than the wave vector times the electron thermal speed.  $T_x$  is the average temperature in the heated direction, and  $T_y$  is the average temperature in the cold direction.  $\lambda_0$  is the vacuum wavelength of the light,  $\omega_{pe}$  is the electron plasma frequency at the density ( $n$ ) where the Weibel occurs,  $n_e$  is the critical density,  $m_e$  is the electron mass, and  $c$  is the speed of light. The filaments occur in the direction of the hotter particles, and the consequent wavenumber is in the direction perpendicular to the hot particles. The saturation of the magnetic field  $B_{\text{sat}}$

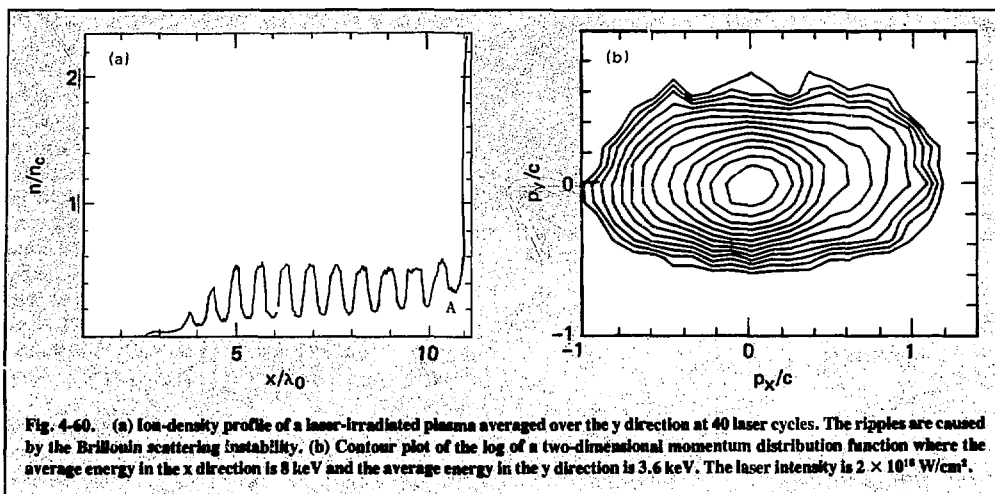
$$\omega_{\text{csat}}/\omega_0 \sim 4(\gamma/\omega_{pe})(n/n_e)(\lambda/\lambda_0)(c/v_{ex}),$$

where  $\omega_{\text{csat}} = eB_{\text{sat}}/m_e$ ,  $e$  is the electron charge,  $\gamma$  is the growth rate of the Weibel unstable wavelength  $\lambda$ , and  $v_{ex}^2 = T_x/m_e$ , was given by Davidson et al. and correlated with their one-dimensional simulations.<sup>189</sup> In one-dimensional, initial-value, periodic simulations, the magnetic field stays near the saturated value for as long as the simulations were run. However, two-dimensional, doubly periodic simulations by Morse and Neilson demonstrated that the magnetic field peaks and then rapidly drops for an initial-value problem because of wavenumbers of the magnetic field in the direction of the hot particles that, with the normal magnetic modes, rotate and isotropize the electrons.<sup>190</sup> The consequence for laser fusion is that the Weibel instability is another source for magnetic fields that can inhibit energy transport.<sup>191-193</sup>

Our problem differs from those studied in Refs. 187-190 (and references within) in that our electron distribution function is not a one-temperature Maxwellian in one direction and one-temperature Maxwellian in the other directions. Rather, down the density gradient, a heated fraction of the density ( $n_{\text{hot}}/n_{\text{cold}}$ ) of the heated-electron distribution is hot, and an unheated fraction is the same temperature as the plasma in the other directions. Krall and Trivelpiece solve this problem theoretically by simply using the average temperature in their equations for the fastest growing modes [Eqs. (111), (112)].<sup>188</sup> I ran a series of one-dimensional, electromagnetic, relativistic simulations with a  $T_{\text{cold}}$  in both directions and a fraction of the density having a  $T_{\text{hot}}$  in the nonperiodic direction to verify the fastest growing mode, its growth rate, and saturation from Ref. 188 and found that the average temperature model was indeed very good.

The growth and saturation of magnetic fields due to the Weibel instability has been examined in two-dimensional, relativistic, electromagnetic, kinetic simulations,<sup>194</sup> in the same runs used to generate the data for Ref. 185 and other runs. We found, for laser intensities of  $10^{16}$  W/cm<sup>2</sup> and cold temperatures of 4 keV, that typically several megagauss fields were generated, that the resulting heating was affected by the magnetic field with large variations in the  $E_x B_x$  at the critical surface in phase with critical-surface ripples, and that the accelerated electrons are filamented.

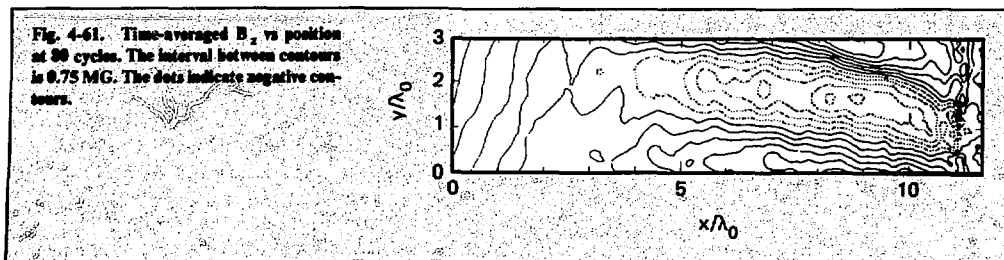
Figures 4-60 through 4-63 present a simulation example in which the laser intensity was  $2 \times 10^{16}$  W/cm<sup>2</sup> and the  $T_{\text{cold}}$  was 2.2 keV, producing a  $T_{\text{hot}}$  of 40 keV and a  $n_{\text{hot}}/n_{\text{cold}}$  of about 0.2 in the underdense region. The density profile is shown in Fig. 4-60(a). The laser is incident from the lower left at an angle of 20° to the critical surface. A plot of  $p_x$  vs  $p_y$  [Fig. 4-60(b)], where  $p_{x,y} = (v_{x,y}/c)/[1 - (v_x/c)^2 - (v_y/c)^2]^{1/2}$  over the underdense region, shows the velocity-space anisotropy at early time. At later time, the



anisotropy is much less. Figure 4-61 shows the time-averaged magnetic field  $B_z$  with direction out of the plane of the simulation. The averaging time is chosen so that the incident pump field is cancelled out. There are three sources for the magnetic fields shown here. First, at the critical density is a  $B_z$  field produced directly by resonant absorption.<sup>195-197</sup> Second, the large diagonal field is characteristic of the Weibel instability but may also result from another source discussed below. Third, a field at the very low density region [see Fig. 4-60(a)] is caused by the electrons being rotated around the ambipolar electric field. The third field is not obvious in Fig. 4-61 because it has a much lower amplitude than the others. However, it is clear from plots  $B_z$  averaged over  $y$ , because it does not change sign. Because the electrons are resonantly driven at a nonzero angle with the density gradient, away from the laser light, the Weibel occurs at a nonzero angle. Similarly, the electrons rotated around the ambipolar field have a preferred direction, driving a positive  $B_z$  field there.

As may be seen from the time-averaged two-dimensional plots of  $E_x J_z$  (Fig. 4-62) and vectors of the current density of the fast electrons (Fig. 4-63), the magnetic field has a significant effect on the heating and hot-electron transport. Note the  $E_x J_x$  is greatest where the  $J$ 's are the greatest and where the magnetic field is nearest zero (although this is not always so). The critical-density surface of the ions and electrons shows small-amplitude surface ripples with the kink of the ripple in phase with the maximum  $E_x J_x$ .<sup>198</sup> The patterns of  $B_z$ ,  $E_x J_x$ , and  $J$  do move together on the critical surface but at a speed much less than the ion-acoustic velocity at the wavelength of the periodic length.

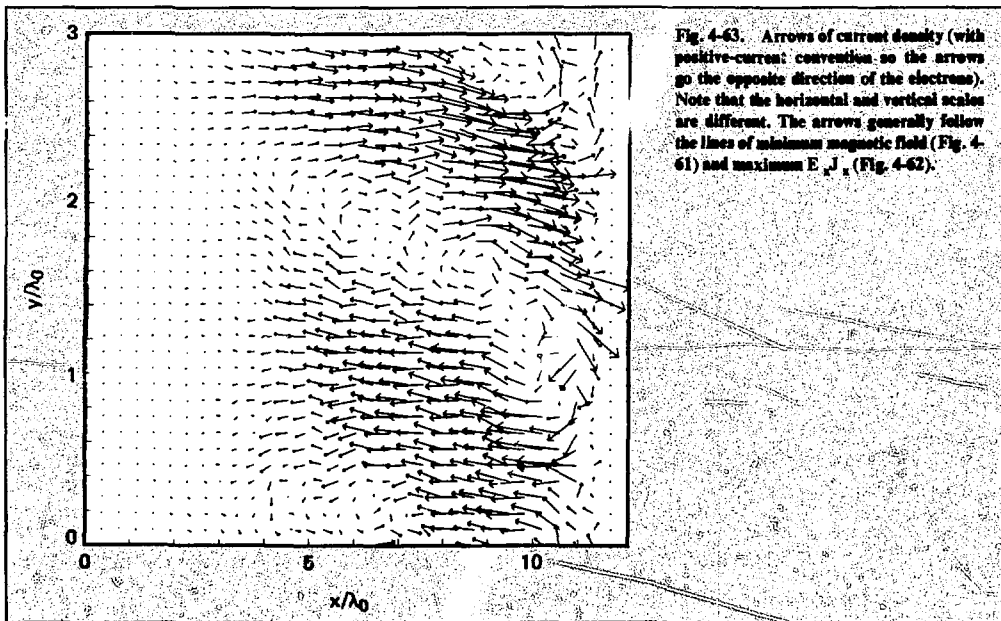
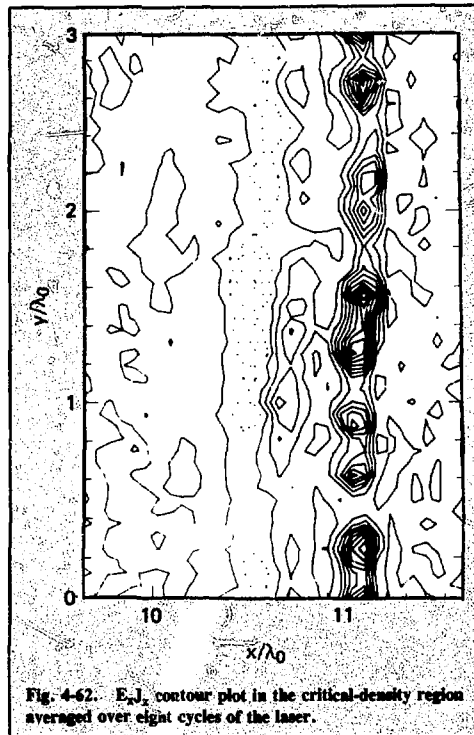
The localized heating is a feedback mechanism that probably affects the saturated magnetic field. We have tried to determine how much effect by comparing the two-dimensional saturated field with one-dimensional runs using the same distribution function as is found on the two-dimensional runs and an initial condition. The two-dimensional situation is complicated



by the finite length of the underdense plateau. One may estimate a spatial growth length by dividing the average particle velocity in the density gradient direction by the growth rate, which is in reasonable agreement with the simulations. If the underdense plasma is long enough that the magnetic instability has ample space to grow, then the saturated magnetic field is much higher than the one-dimensional simulations would predict. Two-dimensional fixed-ion runs with a smooth critical surface but similar density profile show some Weibel instability but at much less amplitude.

The dominant source of the magnetic field is unclear. The fact that we see critical-surface ripples in phase with the edge of the magnetic field, the  $J_x$ 's, and the  $E_y J_x$  indicates the possibility of a more encompassing feedback mechanism of which Weibel is only a subset. It may well be that critical-surface ripples, not Weibel, is the initiating mechanism.

The above simulations include runs in which the light was incident at a nonperpendicular angle to the critical surface. We made a run in which the light was perpendicularly incident on the critical surface, and the ripples were small enough that resonant absorption did not dominate. In this case, ion-acoustic decay and the oscillating two-stream instabilities heated electrons mainly along the critical-density surface that drove a Weibel-instability magnetic field with a wave vector along the density gradient. The magnetic field had the



beneficial effect of reducing the  $T_{\text{hot}}$  of the slowly heated electrons by deflecting them out of the heating electric fields after a short time. This was inferred by noticing that, after the time-averaged Weibel-induced B field had grown to 1 MG, the  $T_{\text{hot}}$  dropped a factor of two although other characteristics of the plasma (such as the density profile) were unchanged.

It is not clear what the  $n_{\text{hot}}/n_{\text{cold}}$  should be to match the experiment. The  $n_{\text{hot}}/n_{\text{cold}}$  and total underdense shelf density will probably depend on the time history of the laser pulse and on the target materials. The maximum wavelength of the simulated Weibel instability [Eq. (11)] is artificially limited by the width of the periodic system (the vertical direction in Fig. 4-60). Consequently, the experimental magnetic-field pattern and saturated amplitude would differ from those presented in this simulation. It is not clear what three-dimensional effects would be, particularly in view of the larger ripples expected in the direction perpendicular to the polarization (see also § 4.6.8).<sup>198</sup> In particular, in the lower density region [Figs. 4-60(a) and 4-61], the experiment might have larger amplitude magnetic fields in wavelengths lower than the system width of the simulation with similar density and  $T_x/T_y$ .

Because the sign of the magnetic field varies rapidly on a spatial scale of a few wavelengths, it is not clear how quantitatively one could observe this magnetic field with a Faraday rotation experiment. One suggestion is to look for broad-band synchrotron radiation or perhaps to focus the synchrotron light (at frequency  $B(\text{MG})/100$  of the incident light at  $1.06 \mu\text{m}$ ) onto a detector array. One could use a prism and streak camera to get a frequency spectrum vs time. However, in order for synchrotron radiation to occur,  $\omega_c$  must be greater than  $\omega_p$ .

In conclusion, we have simulated magnetic fields in the underdense region of laser-produced plasmas on one- and two-dimensional self-consistent codes. For laser intensities of  $10^{16} \text{ W/cm}^2$ , the magnetic fields have megagauss amplitudes that would inhibit heat transport and help to isotropize the electron distribution.

Valuable conversations with W. L. Kruer and C. E. Max are acknowledged.

## References

186. K. G. Estabrook and W. L. Kruer, "Properties of Resonantly Heated Electron Distribution," *Phys. Rev. Lett.* **40**, 42 (1978) and references therein.
187. E. S. Weibel, "Spontaneously Growing Transverse Waves in a Plasma due to an Anisotropic Velocity Distribution," *Phys. Rev. Lett.* **2**, 83 (1959).
188. N. A. Krall and A. W. Trivelpiece, *Principles of Plasma Physics* (McGraw-Hill, New York, 1973).
189. R. C. Davidson, D. A. Hammer, I. Haber, and C. E. Wagner, "Nonlinear Development of Electromagnetic Instabilities in Anisotropic Plasmas," *Phys. Fluids* **15**, 317 (1972).
190. R. L. Morse and C. W. Nielson, "Numerical Simulation of the Weibel Instability in One and Two Dimensions," *Phys. Fluids*, **14**, 830 (1971).
191. C. E. Max, W. H. Manheimer, and J. J. Thomson, "Enhanced Transport across Laser-Generated Magnetic Fields," *Phys. Fluids* **21**, 128 (1978).
192. E. L. Lindman, D. W. Forslund, J. M. Kinney, and W. R. Shanahan, "Magnetic Fields in Laser-Produced Plasmas," *Bull. Am. Phys. Soc.* **20**, 1378 (1975).
193. A. Ramani and G. Laval, "Heat-Flux Reduction by Electromagnetic Instabilities," *Phys. Fluids* **21**, 980 (1978).
194. A. B. Langdon and B. F. Lasinski, "Electromagnetic and Relativistic Plasma Simulation Models," in *Methods in Computational Physics*, vol. 16, edited by B. Adler, S. Fernbach, and M. Rotenberg; volume editor: J. Killeen (Academic Press, New York, 1976), 327-366.
195. J. J. Thomson, C. E. Max, and K. G. Estabrook, "Magnetic Fields Due to Resonance Absorption of Laser Light," *Phys. Rev. Lett.* **35**, 663 (1975).
196. B. Bezzerides, D. F. DuBois, D. W. Forslund, and E. L. Lindman, "Magnetic Field Generation in Resonance Absorption of Light," *Phys. Rev. Lett.* **38**, 405 (1977).
197. W. Woo and J. S. DeGroot, *Magnetic Fields Due to Laser Light Absorption*, University of California at Davis, Rept. UCD PRG R-23 (1977), submitted to *Phys. Fluids*.
198. K. G. Estabrook, "Critical-Surface Bubbles and Corrugations and Their Implications to Laser Fusion," *Phys. Fluids* **19**, 1733 (1976).

## Author

K. G. Estabrook

## 4.10 Analysis of Numerical Models for Simulation of Plasmas

Theoretical analysis has improved the understanding of the behavior and accuracy of simulation methods, for those who interpret results of such computations as well as for those who design and program the codes. This work, reported in full elsewhere,<sup>199, 200</sup> is summarized here.

First we analyze the collective behavior of hot plasma, as modified by the numerical time-integration methods used to integrate the particle equations of motion in computer simulation of plasmas.<sup>199</sup> No approximation is made in analyzing the finite-difference algorithms. We find the dispersion function that describes the response of the plasma to perturbing fields and whose zeroes give the dispersion and stability of free oscillations. This dispersion function is derived by two methods that illustrate different aspects and parameter limits. The analysis of plasma oscillations involves the same physics as in the classic Landau problem, and the results reduce to it simply and exactly in the limit  $\Delta t \rightarrow 0$ , where  $\Delta t$  is the time step. No unexpected numerical instabilities are found. The results of

this and of previous papers are combined to describe exactly the effects of both the spatial and temporal difference algorithms. We generalize the theory to a class of integration schemes, analyze some examples, and synthesize a new algorithm. We examine the possibility of developing algorithms stable at very large time steps.

Fluctuations have been of interest in computer simulation of plasmas because they interfere with modeling of collisionless phenomena. However, computer simulation has also been used as a tool to study fluctuations and other processes involving discrete-particle effects in plasma, such as transport.

Building on our previous results, we derived expressions for Debye shielding and the fluctuation spectrum.<sup>200</sup> The formulae are cast in forms that look as much as possible like the standard results of plasma kinetic theory, to facilitate comparison. We compare the results for a simulation plasma and a real plasma with a Maxwellian velocity distribution. As expected, the results agree exactly when the grid spacing and time step are small. Qualitative differences in Debye shielding and spatial spectrum arise when  $\lambda_D \lesssim \Delta x/2$ , where  $\lambda_D$  is the Debye length and  $\Delta x$  is the zone size; for example, the Debye potential oscillates as it decays. In the fluctuation spectrum, noise is found at high frequencies on the order of  $v_t/\Delta x$ , where  $v_t$  is the thermal velocity. A large time step ( $\Delta t \geq \Delta x/v_t$ ) redistributes this noise to all frequencies, producing a flatter spectrum and contributing to velocity diffusion.

Using these results, we have derived a collision operator that includes the familiar Balescu-Lenard operator in the  $\Delta x, \Delta t \rightarrow 0$  limit. We found diffusion and drag caused by density fluctuations. The other constituent is caused by the polarization of the plasma as sensed by a specified particle. We have also studied conservation properties and the H-theorem. This work was summarized in Ref. 201 and will be discussed fully in a future paper.

## References

199. A. B. Langdon, *Analysis of the Time Integration in Plasma Simulation*, Lawrence Livermore Laboratory, Rept. UCRL-80445 (1977), submitted to *J. Comp. Phys.*
200. A. B. Langdon, *Kinetic Theory for Fluctuations and Noise in Computer Simulation of Plasma*, Lawrence Livermore Laboratory, Rept. UCRL-80666 (1978), submitted to *Phys. Fluids*.
201. A. B. Langdon, "Nonphysical Modifications to Oscillations, Fluctuations, and Collisions due to Space-Time Differencing," in *Proceedings of the Fourth Conference on the Numerical Simulation of Plasmas*, J. P. Boris and R. Shanny, Eds. (U.S. Govt. Printing Office, Washington, D.C., 1971), pp. 467-495.

## Author

A. B. Langdon

## 4.11 Microwave-Simulation Experiments

### 4.11.1 Resonant Absorption, Hot-Electron Production, and Energy Transport

We have measured resonant absorption of high-power microwaves, hot-electron production, and hot-electron energy transport in the Prometheus I device.<sup>202</sup> This device models laser absorption and electron transport in a spherical segment of a laser-driven pellet. Intense microwaves are incident onto an inhomogeneous plasma with the microwave electric field parallel to the density gradient so that the microwaves are resonantly absorbed. Strong high-frequency electrostatic electric fields are excited near the critical surface (where the plasma frequency equals the microwave frequency). These fields heat the electrons, and the ponderomotive force caused by these fields strongly modifies the density profile.

The microwave-heated electrons have a bimaxwellian energy distribution up to the highest powers we have investigated ( $v_{os}/v_{e0} < 0.6$ , where oscillation velocity  $v_{os} = eE_0/m\omega$ ,  $E_0$  is the peak electric field of the incident microwaves,  $\omega$  is the microwave frequency,  $\omega/2\pi = 1.2 \times 10^9$  GHz, and the initial electron thermal velocity  $v_{e0} = (kT_{e0}/m)^{1/2}$ ). The hot-electron temperature  $T_H$  increases with microwave power  $P$ ; i.e.,  $T_H \propto P^{0.4}$  (see Fig. 4-64), as predicted by particle simulation calculations.<sup>203</sup> The hot-electron density  $n_H$  increases linearly with power, as shown in Fig. 4-65.

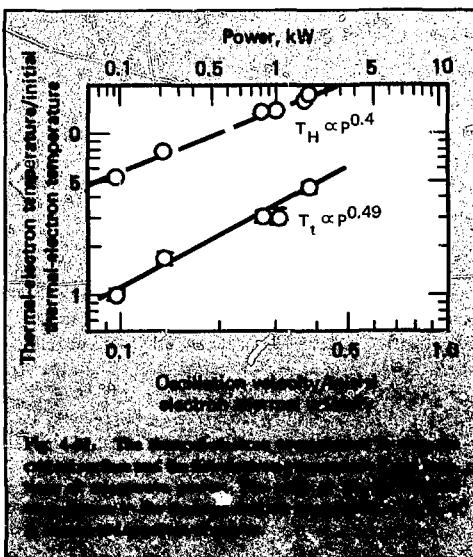


Fig. 4-64. The ratio of thermal-electron temperature to initial thermal-electron temperature versus microwave power.

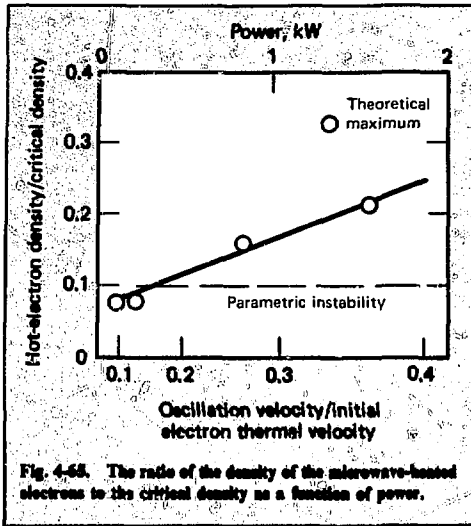


Fig. 4-65. The ratio of the density of the microwave-heated electrons to the critical density as a function of power.

Beginning at low powers ( $v_{0s}/v_{e0} > 0.1$ ), a dc electric field is excited near the critical surface and extends into the overdense region. The hot electrons are decelerated by this electric field, so the hot-electron energy flux is inhibited. The ratio  $\alpha$  of the electron energy flux  $q_e$  to the free-streaming value  $q_{fs}$  is almost independent of power in the range  $0.2 < v_{0s}/v_{e0} < 0.5$ .  $\alpha = q_e/q_{fs} = 1/2$ , where  $q_{fs} = (2/\pi)^{1/2} v_H n_H kT_H$ , and the hot-electron thermal velocity  $v_H = (kT_H/m)^{1/2}$ . The potential of the critical surface relative to the potential of the undisturbed plasma well into the overdense region is driven positive by this electric field. This potential difference increases with microwave power, as shown in Fig. 4-66. Our measurements indicate that the source of the field is the gradient in the hot-electron pressure. This gradient is caused by the decrease in the heated-electron density as the electrons spread out after leaving the critical surface. The spreading is the result of the finite diameter of the heating region. Thermal electrons are accelerated toward the critical surface by the dc electric field.

We observe large-amplitude ion waves and anomalous dc resistivity, as evidenced by the heating of the thermal electrons accelerated by the dc electric field. The thermal-electron temperature  $T_t$  in the critical region increases with power; i.e.,  $T_t \propto P^{0.49}$ , as shown in Fig. 4-64. Thus, the temperature ratio  $T_H/T_t$  is essentially independent of power.

## References

202. J. S. DeGroot, R. B. Spielman, and K. Mizuno, *Resonant Absorption and Heated Electron Thermal Conductivity*, University of California at Davis, Rept. UCD PRG R-33 (1978), submitted to *Phys. Rev. Lett.*

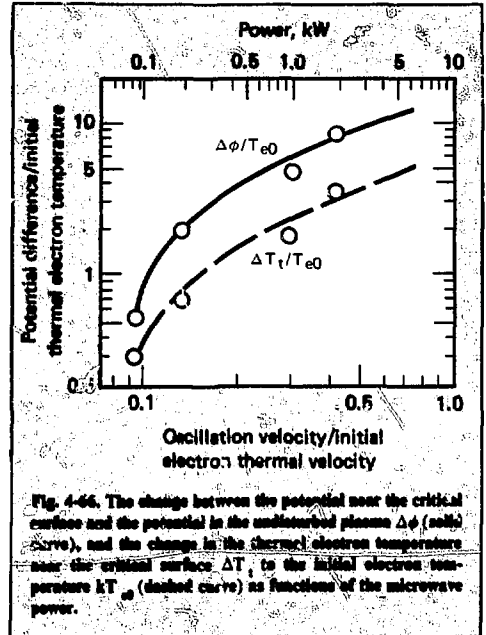


Fig. 4-66. The change between the potential near the critical surface and the potential in the undisturbed plasma  $\Delta\phi$  (solid curve), and the change in the thermal electron temperature near the critical surface  $\Delta T_t$  to the initial electron temperature  $kT_{e0}$  (dashed curve) as functions of the microwave power.

203. K. G. Estabrook and W. L. Kruer, "Properties of Resonantly Heated Electron Distributions," *Phys. Rev. Lett.* **40**, 42 (1978).

## Authors

J. S. DeGroot  
R. B. Spielman  
K. Mizuno

## 4.11.2 Electron Heating in a Plasma-Filled Capacitor

When a quasi-static radio frequency (rf) field is imposed on a plasma with a density gradient along the field, an electrostatic field is excited in the region where the electron plasma frequency is approximately equal to the frequency of the rf field. In our experiment, a 10- $\mu$ s, 1-kW, 1-GHz rf signal is applied to a plasma-filled capacitor composed of a 15-cm grid and the vacuum chamber. The temporally oscillating field resonantly drives a large, localized electric field  $> 100$  V/cm at the location where the electron plasma frequency approximately matches the microwave frequency ( $\sim 7$  cm from the rf exciter).

The resonant field accelerates electrons in both directions along the density gradient. The heated electrons are sampled by an electrostatic-energy analyzer

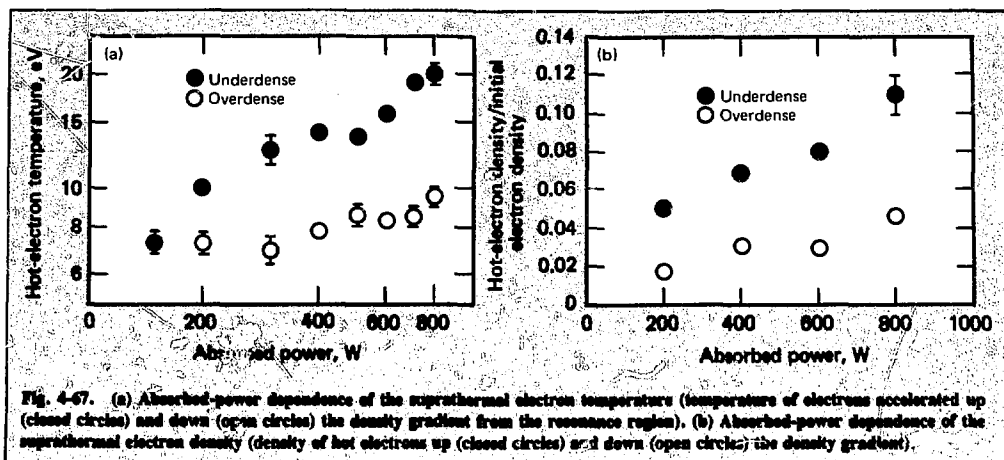


Fig. 4-67. (a) Absorbed-power dependence of the suprathermal electron temperature (temperature of electrons accelerated up (closed circles) and down (open circles) the density gradient from the resonant region). (b) Absorbed-power dependence of the suprathermal electron density (density of hot electrons up (closed circles) and down (open circles) the density gradient).

with a boxcar integrator. Figure 4-67(a) shows the absorbed-power dependence of the hot-electron temperature accelerated up and down the density gradient from the resonant region. The density of the hot electrons is determined by extrapolating the value of the hot current at the plasma potential. Figure 4-67(b) shows the absorbed-power dependence of the hot-electron density accelerated up and down the density gradient. Notice that both the temperature and the density of the heated electrons going downstream are greater than those going upstream. This can be explained by the fact that electron plasma waves propagating down the density gradient with low phase velocity can transfer energy readily to the hot electrons, whereas all electron waves are cut off beyond the critical surface.

A very interesting observation in our experiment is the generation of a return current of thermal electrons in the overdense region. This current is driven by the hot current to maintain charge neutrality at the resonant location. The measured total current of electrons traveling up the density gradient, composed mainly of the resonantly accelerated electrons, is approximately equal to a downward cold return current. Because there are no hot electrons or background electron heating measured, the increase in the electron flux going downward and the apparent shift in the plasma potential indicate that the thermal electrons are drifting toward the resonant region. The estimated drift velocity  $v_d$  is less than the electron thermal velocity  $v_e$  but many times more than the ion-acoustic speed  $c_s$ , and, in our experiment,  $T_e \sim 10 T_i$ , where  $T_e$  is the electron temperature and  $T_i$  is the ion temperature. Therefore, the electron drift velocity is well above the threshold value for the ion-acoustic instability. This is confirmed by the observation of large low-frequency fluctuations with

frequency  $\omega \approx 800$  kHz ( $\omega/\omega_i \approx 0.2$ , where  $\omega_i$  is the ion plasma frequency). These low-frequency waves propagate at approximately  $4 \times 10^5$  cm/s, are broad in angle, and saturate at about  $\delta n/n \sim 12\%$ , where  $\delta n$  is the amplitude of the density fluctuations and  $n$  is the plasma density. The instability grows for four or five periods and becomes incoherent in time. The waves propagate into the underdense region and continue to travel long after the rf is pulsed off. Ion trapping has proved to be the principal saturation mechanism for the ion-acoustic instability; i.e., the saturation level can be estimated by a simple trapping argument to be  $\delta n/n \approx \frac{1}{2} \left\{ \left[ 1/(1 + k^2 \lambda_{De}^2)^{1/2} \right] - (3T_i/T_e)^{1/2} \right\}$ , where  $\lambda_{De}$  is the Debye length and  $k$  is the wavenumber. For  $T_e \approx 10 T_i$ ,  $\delta n/n \approx 10\%$ , which agrees quite well with the observed value.

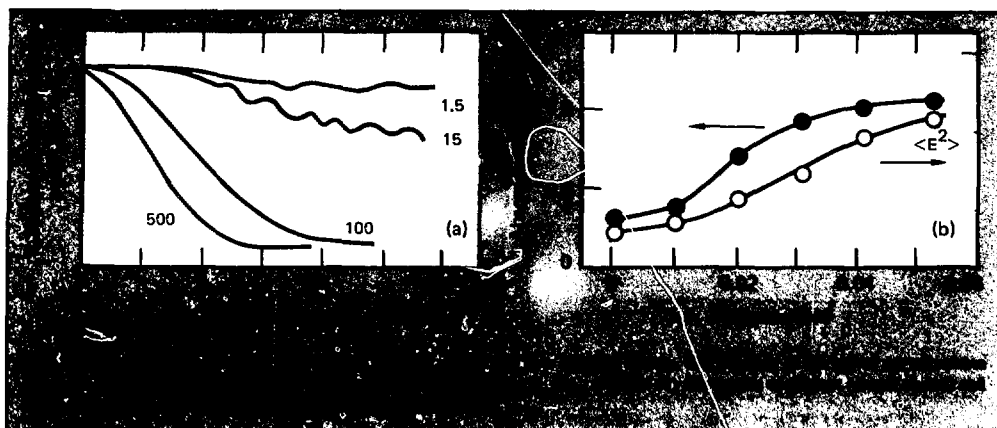
## Authors

H. M. Sze  
J. S. DeGroot

### 4.11.3 Microwave Absorption and Hot-Electron Transport in a Weak Magnetic Field

We beamed s-polarized strong microwaves ( $\omega_0/2\pi \sim 1.2$  GHz) onto an inhomogeneous plasma. The inhomogeneous scale length  $L/\lambda_0$  is about 0.8, or  $L/\lambda_{De}$  is about  $10^3$ , where  $\lambda_0$  is the wavelength of the incident microwaves and  $\lambda_{De}$  is the initial Debye wavelength. We applied a weak homogeneous dc magnetic field  $\omega_{ce}/\omega_0 \approx 0.04$  (which corresponds to a magnetic field of 4 MG in a Nd: glass laser plasma), perpendicular to both the density gradient and the microwave electric field.<sup>204</sup>

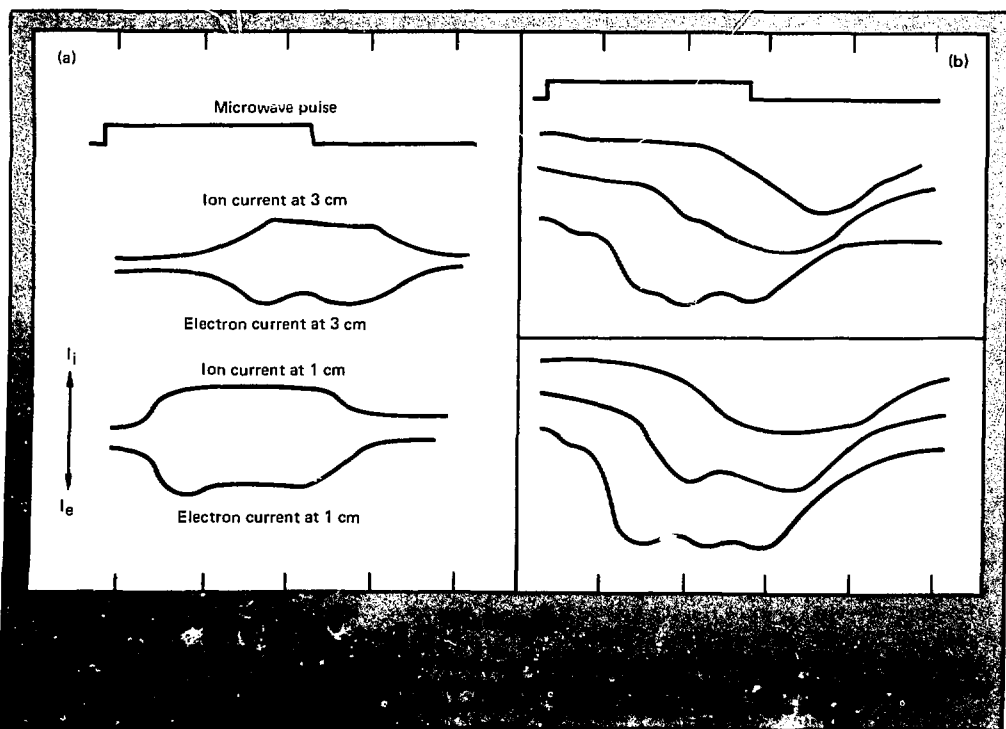




We observed that parametric instabilities are the most important absorption process of the microwaves. We detected significant absorption of the microwaves when the microwave power exceeds the well-defined threshold value of the parametric instabilities. The fraction of the absorbed microwave power increases

with the incident microwave power [Fig. 4-68(a)]. The absorption coefficient increases from 20% to 85% when the weak magnetic field is applied [Fig. 4-68(b)].

The anomalously absorbed microwaves result in electron heating by parametric instabilities. The elec-



trons heat locally to a very high temperature because the transport is substantially reduced by the magnetic field.<sup>205</sup> The electron transport along the magnetic field is reduced by an ambipolar potential. Heated electrons are transported together with the ions across the magnetic field [Fig. 4-69(a)]. The observed velocity of  $7 \times 10^5$  cm/s roughly agrees with that estimated from classical diffusion. The transport velocity decreases with decreasing collision frequency (electron-neutral collision frequency is controlled by changing the neutral gas pressure), as is expected [Fig. 4-69(b)].

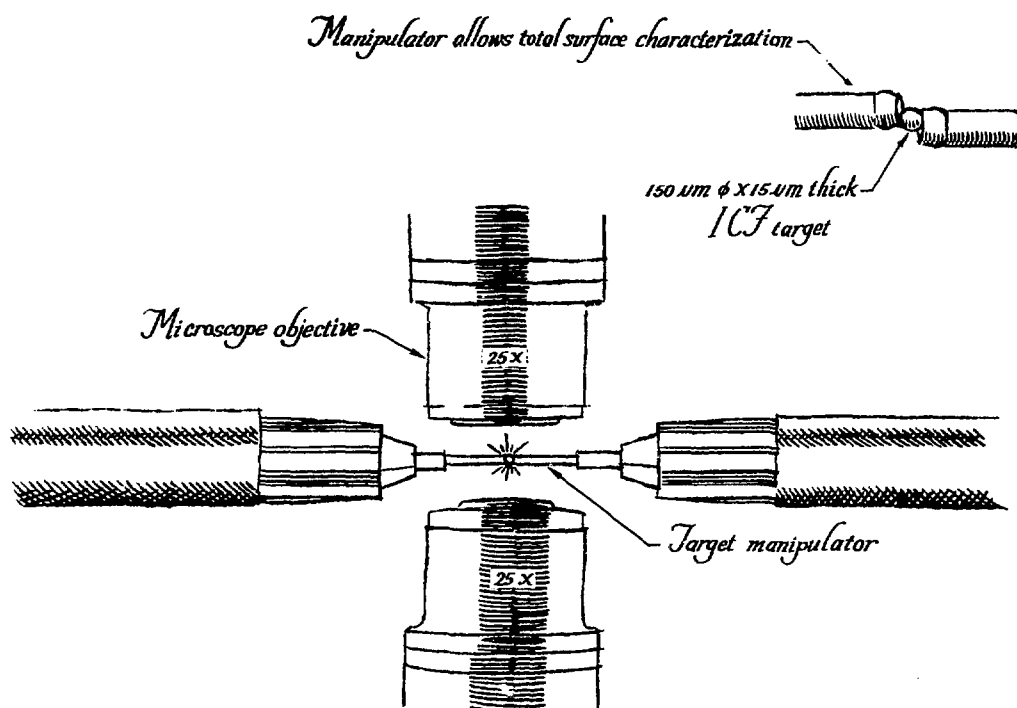
## References

204. W. L. Kruer and K. G. Estabrook, "Laser Light Absorption due to Self-Generated Magnetic Fields," *Phys. Fluids* **20**, 1688 (1977).
205. R. S. Craxton and M. G. Haines, "Hot Spots in Laser Plasmas," *Phys. Rev. Lett.* **35**, 1336 (1975).

## Authors

**K. Mizuno**  
**J. S. DeGroot**

# SECTION 5 TARGET FABRICATION



## SECTION 5

### CONTENTS

5.1	Overview	5-1
5.2	High-Quality Glass Spheres	5-5
5.2.1	Production of Hollow Glass Microspheres	5-5
	Liquid-Droplet Technique: Basic Principles	5-6
	Liquid-Droplet Generator	5-6
	Vertical-Drop Furnace	5-6
	Physical and Chemical Processes of Microsphere Production	5-6
	Concentricity	5-9
	Argon-Filled Microspheres	5-11
5.2.2	Surface Treatment of LLL Glass Microspheres	5-13
	Glass Composition	5-13
	Furnace Atmosphere	5-14
	Wash	5-15
	Long-Term Surface Passivation	5-15
	Long-Term Storage	5-16
5.3	Polymer Coating	5-16
5.3.1	Plasma Polymerization Techniques	5-16
5.3.2	Plasma Source Development	5-17
5.3.3	Process Control	5-18
5.3.4	Coating Results	5-18
5.4	Multilayer, Nonplanar Structures	5-20
5.4.1	General Fabrication Approaches	5-20
5.4.2	Coating Process	5-21
5.4.3	SiO <sub>2</sub> Coating	5-21
5.4.4	Be Coating	5-22
5.4.5	Conclusions	5-23
5.5	Developments in Characterization	5-23
5.5.1	A Microsphere Manipulator for Target Inspection	5-24
5.5.2	Total Surface Inspection Using Interferometry	5-24
5.5.3	4 $\pi$ Total Surface Inspection with the Scanning Electron Microscope	5-28
	SEM Examination System	5-28
	Sample Preparation	5-29
	Inspection Procedure	5-29
5.5.4	Microradiography	5-31
5.6	Cryogenic Targets	5-38
5.7	Production of Power-Plant Inertial Confinement Fusion Targets	5-42
5.7.1	Design Features of Power-Production Class Targets	5-45
5.7.2	Target Fabrication Development Tasks	5-46
5.7.3	Layered Shell Fabrication	5-47
5.7.4	Layered Hemishell Fabrication	5-47
5.7.5	DT Fill	5-47
5.7.6	Assembly	5-48
5.7.7	Characterization	5-48
5.7.8	Transport and Manipulation	5-48

## SECTION 5

### TARGET FABRICATION

#### 5.1 Overview

The current goal of the Laser Fusion Target Fabrication Program at LLL is the production of targets with which we can conduct meaningful, well-determined experiments to test the principles of laser-driven inertial confinement fusion. The production and characterization of adequate targets require a combination of several technical and scientific disciplines, including glass technology, polymer chemistry and physics, metrology, optics, electron microscopy, radiography, and mechanical fabrication.

A longer range goal is the development of a technology to produce future targets for research purposes, for the economic production of power.

The development of laser fusion targets began with flat disks and simple glass spheres filled with DT. As information became available on laser beam interactions with matter, changes in the target structures were inevitable. Targets such as the ball-on-plate and ball-in-plate (Saturn) evolved and were tested. More complicated structures such as the multilayer assemblies shown in Fig. 5-1 have become necessary to test and understand the laser-target interaction processes and to achieve the goals of "breakeven" and economical energy production.

Many of the most difficult problems result from the stringent design requirements for surface finish, concentricity, and target material composition. For example, the surface finish on a glass sphere required for a high-density implosion experiment may be 100 to 300 Å (peak to valley) with a few peaks (5 or 6) of 2000 to 3000 Å permitted on the entire surface of the sphere. Surfaces of such high quality are seldom found or studied in most materials research, development, or use situations. Not only must we produce extremely smooth surfaces, but we must also characterize them and measure their quality.

Section 4 of the 1976 annual report of the Laser Fusion Program<sup>1</sup> and the references listed there describe much of the previous research and development in the production of laser fusion targets. However, in 1977 several notable developments occurred that we describe in the following subsections of this report.

A laser fusion target often consists of fuel (for

example, DT gas) contained in a gas-tight hollow shell of glass, metal, or polymeric material. This shell may be bare or may be enclosed by one or more layers, or shells, of other materials, as shown in Fig. 5-1. The surrounding layers may themselves be glass, polymeric materials, metals, or cryogenic or inorganic materials. We have developed several methods of producing glass shells to be used as fuel containers. Our initial efforts to produce laser fusion targets centered on the existing glass shells that are produced commercially as fillers for plastics and other purposes. For relatively simple targets of the exploding-pusher type (in which the laser energy is rapidly delivered to the entire thickness of the shell at once, literally causing the shell to explode), the quality of the glass shell is not extremely critical. Variations in wall thickness, surface irregularities, and some bubbles or voids in the wall can be tolerated. However, even with such relaxed tolerances, only a few in  $10^6$  to  $10^9$  of the commercially produced shells are acceptable, and even then the only shells available have limited thicknesses (0.5 to 1.5  $\mu\text{m}$ ) and diameters (40 to 250  $\mu\text{m}$ ). As the requirements for higher quality became clear, it also became obvious that we needed an alternative source of spheres.

We have developed techniques for producing highly spherical glass shells with uniform walls, remarkably smooth surfaces, and ranges of diameters (50 to 500  $\mu\text{m}$ ) and wall thicknesses (0.5-20  $\mu\text{m}$ ) necessary for our purposes.

After a glass sphere is filled with DT by permeating the gas through the high-temperature glass, the sphere can be mounted on a stalk or stem to be used as a laser fusion target such as the one shown in Fig. 5-2. However, more advanced experiments leading to the compression of gaseous DT fuel to many times liquid density have required glass spheres with uniform polymeric coatings of very high quality. Because of the density and material composition specifications imposed on the layers, we chose coatings of polymerized fluorocarbon ( $\text{CF}_2$ ). Coatings of polymerized perfluorobutene up to 30  $\mu\text{m}$  thick have produced and meet the same surface quality and uniformity standards as the glass spheres. Several techniques for depositing the polymers have been studied with varying degrees of

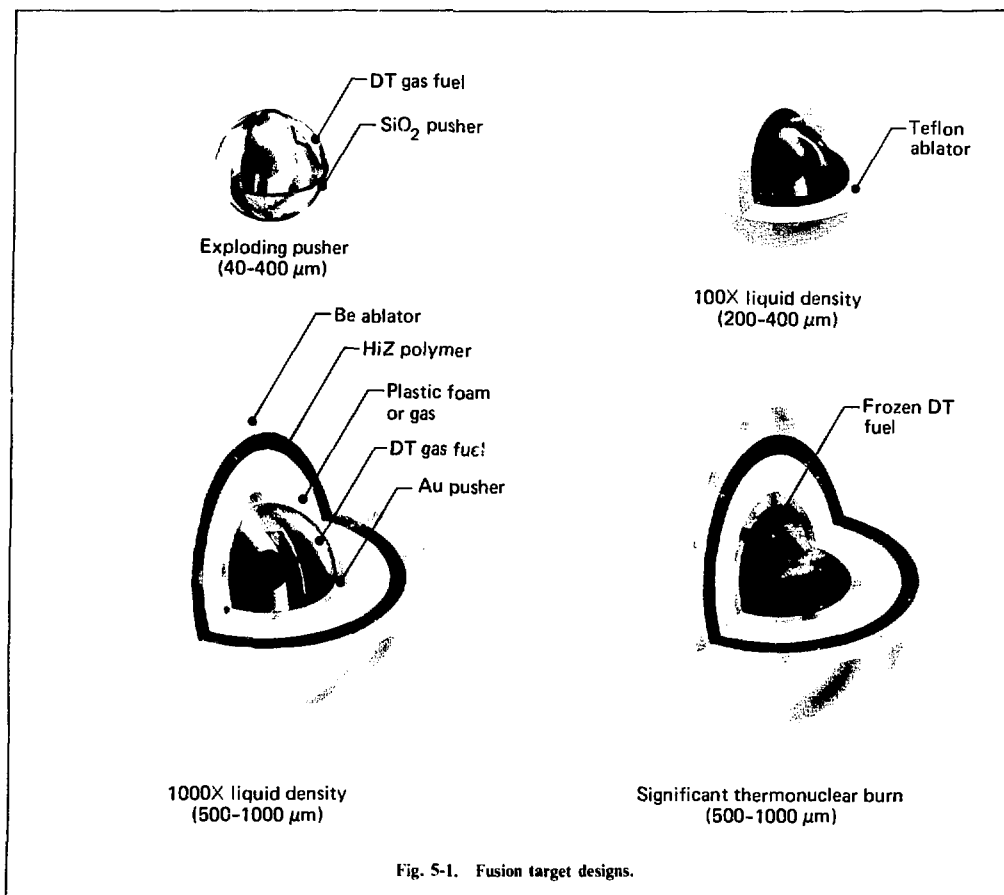


Fig. 5-1. Fusion target designs.

success. Our current production method utilizes a plasma polymerization technique and provides high-quality coatings of a fluorocarbon with a chemical composition of approximately  $\text{CF}_{1.3}$  and a density of about  $2.2 \text{ g/cm}^3$ .

Other techniques are being studied and show some promise as means of coating various polymeric materials on glass and other types of shells.

Many of the targets contemplated for future experiments, as shown in Fig. 5-1, are multilayered. We have anticipated these to some extent by developing the techniques for depositing polymeric coatings on glass shells. However, more complex structures are present in many target designs and include organo-metallic layers, beryllium, lithium and its compounds, low-density polymeric foam, glasses, various other metals, and organic and in-

organic compounds. We have chosen glass and beryllium as an initial layer pair with target possibilities. Beryllium is present in many target designs as a pusher material and, because we have used glass spheres to contain DT gas, the combination of glass and beryllium is a natural second step toward multilayer targets, following the development of the fluorocarbon-glass systems. The problems of achieving adequate surface and volume uniformity in the deposited layers of beryllium on glass are discussed in the subsection on multilayer coatings.

To provide targets for meaningful experiments, the targets must be characterized as completely as possible. It is also necessary to have detailed knowledge of the target parameters so that improvements in fabrication processes can be made and measured.

Many techniques are used to study the chemical and physical parameters of the DT fuel, the glass shells, and the various layers that compose a laser fusion target. Optical microscopy provides general surface configuration and dimensional information. However, to optically measure thickness variations of only a few hundred angstroms, we use interferometric microscopy. We study surface variations in the 100-Å range by using electron microscopy. Internal variations not observable by interference techniques for various reasons (opacity, etc.) can be studied by microradiography. Analytical information on material composition is provided by x-ray fluorescence, Auger spectrometry, ion beam probes, and other more or less standard techniques.

At each stage in the fabrication of a target, a complete characterization must be done and the production processes must be studied in detail. Adequate characterization is a continuing problem as we produce better surface finishes on glass spheres, higher quality polymeric layers, and opaque multilayer targets. As long as we were only concerned with exploding-pusher targets that could be examined with a few interferometric views, characterization was relatively simple. However, as the requirements for surface finish and concentricity became more stringent and requests mounted for full  $4\pi$  characterization, the need for an automated or semiautomated system became more obvious.

The apparently simple process of rotating a sphere in the field of view of an optical microscope or a scanning electron microscope becomes extremely difficult, when the sphere is only a few tenths or hundreds of micrometers in diameter and has walls that may be only half a micrometer thick. However, because we do fully characterize the targets to accuracies of a few hundred angstroms before and after each layer is deposited, it is necessary to be able to manipulate the targets rapidly and accurately. The methods we have developed this past year are discussed in detail in § 5.4.

Many advanced target designs call for cryogenic layers. The solutions to the problems of producing and maintaining one uniform, smooth layer of DT in the center of a target are relatively straightforward. However, if a second layer is added farther from the center of the target and if both layers must be smooth, uniform, and long-lived, the solutions are not as simple.

While cryogenic targets have not yet been experimentally used in laser fusion applications at LLL, many designs for future targets contain liquid and solid DT fuel. In anticipation of the need for

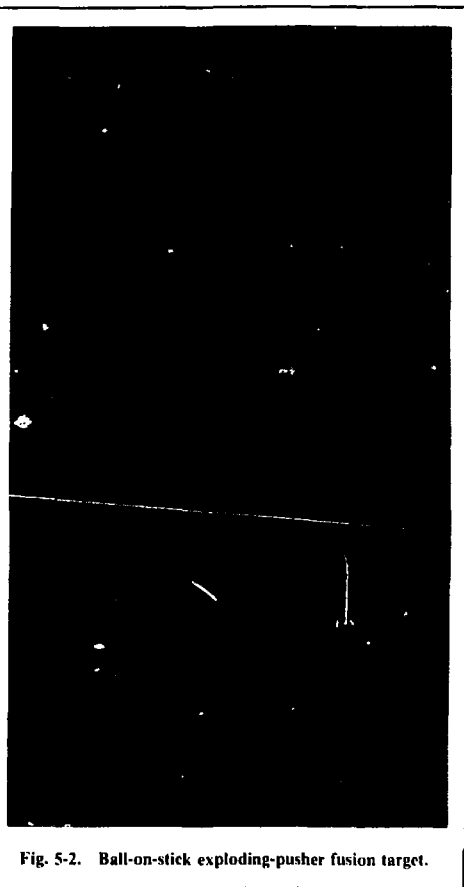


Fig. 5-2. Ball-on-stick exploding-pusher fusion target.

these targets, we have developed the capability to produce uniform layers of frozen DT fuel in glass shells particularly, but also in opaque multilayer spherical structures. In transparent targets, optical access to the DT is possible for light-beam heating and manipulation and for characterization. However, because we do not have optical access to opaque targets, we developed techniques to use light beams for material manipulation.

It would be of little benefit to produce cryogenic targets in a research laboratory environment if they could not survive a short trip to the laser target chamber. Thus, the targets could either be formed totally or partially in place in the target chamber, or they could be produced at a nearby location (the next room, for example) and transported the short distance in a carrier and "life support" system that would maintain the target at a temperature only a

few degrees above absolute zero. Both techniques offer some promise, and even a combination of the two may be worthwhile.

In any case, a cryogenic target insertion and cooling system is needed to place the target in position for laser irradiation. Together with the cryogenics group at the National Bureau of Standards in Boulder, Colorado, we have designed and are constructing a cryogenic target "pylon" to be used in connection with the Shiva laser.

The methods we have developed for producing cryogenic targets are discussed in § 5.6. In the Shiva laser system, we anticipate relatively near-term utilization of both the techniques for providing cryogenic targets and the cryogenic target inserter pylon.

The future goals of the target fabrication effort include the production of targets for power-producing reactors. As we develop techniques to produce today's targets for use in research experiments, we are simultaneously developing production techniques. Future use of inertial confinement fusion for power production will depend strongly on high-quality, low-cost target production. For example, the symmetry of the implosion process affects the maximum yield per shot, and only with a high-quality target can we approach calculated yields.

The energy produced in any economical power production system must be worth more than the input power and investment costs to produce it. In addition, to be suitable as an energy source, the cost per unit must be competitive with other production sources. Let us consider, for example, as an energy unit, a barrel of oil that costs about \$13. A barrel yields a few times  $10^9$  J of energy, which also happens to be the yield of a 1-ton nuclear burn. If a 1-ton fusion event uses a target that costs \$5, and, say, \$3 is spent per shot for other expenses such as tritium recovery, energy processing, etc., then \$5 of energy is available per shot to be usefully expended. At one shot every 10 s, available power is  $4 \times 10^8$  W. With a recirculating power of 25%, 300 MW will be the output power. With smaller yields per shot, we would fire more often and have available smaller resources per target.

Such simplistic arguments must be refined and the economics must be examined in detail. However, the inescapable target requirements remain. We must be able to produce targets at rates of 1 to 10 per second at costs of a few cents to a few dollars per target.

Critical target components are the fuel (probably gaseous, liquid, or solid DT), the immediate fuel container (glass, metal, or plastic shell), and a

series of concentric spherical layers or shells (metal, metal organics, low-density foam, glass, or other inorganic materials, around the central fuel-containing shell). The inner shell may range in inside diameter from a few hundred micrometers to a few millimeters. Successive shells may be contiguous, or there may be vacuum, gas, or rigid foam material, between some of the layers.

In some cases, the target may be entirely cryogenic, composed of layers of DT, neon, xenon, argon, methane, and other materials that are gaseous or liquid at ordinary temperatures. These types of targets can be produced in large numbers, as shown in the conceptual diagram in Fig. 5-3. We have conducted successful preliminary studies of the processes involved in the production of this "all cryogenic" target. Little doubt remains that such a cryogenic-layered target can be produced.

We have also studied other targets that can be made of glass shells and multiple layers of non-cryogenic materials.

Section 5.7 describes the tasks needed to produce reactor targets at high rates and at low cost. Some possible solutions developed for the problems involved are also presented.

We would like to acknowledge the assistance and aid of many organizations and individuals outside LLL. Several organizations assist us on a contract basis. At the University of Arizona, a group under the direction of Prof. M. Bonner Denton provides research and development in the area of plasma polymerization, levitation coatings, and organic ion beams.

In the cryogenics field, we have been ably assisted by groups at the National Bureau of Standards in Boulder, under the direction of Jess Hord, and at the University of Illinois, under the direction of Prof. Kyekyoon Kim.

Groups under the direction of W. L. Rooker and W. Ramer at the Rocky Flats plant of Rockwell International have been extremely helpful to us in areas of micromachining, model development, target assembly, and coating development.

We would be remiss if we did not point out the helpful and enjoyable discussions we have had with R. J. Fries and his group in Target Fabrication at Los Alamos Scientific Laboratory. The exchange of information and ideas between our groups is exceptionally good and very useful.

Several laboratories have been very helpful to us in the analysis of materials and their spatial distribution in samples. The Foremost-McKesson R & D Center, Dublin, California, has done chemical analysis; Applied Research Laboratories, Sunland, California, have used ion probe techniques to



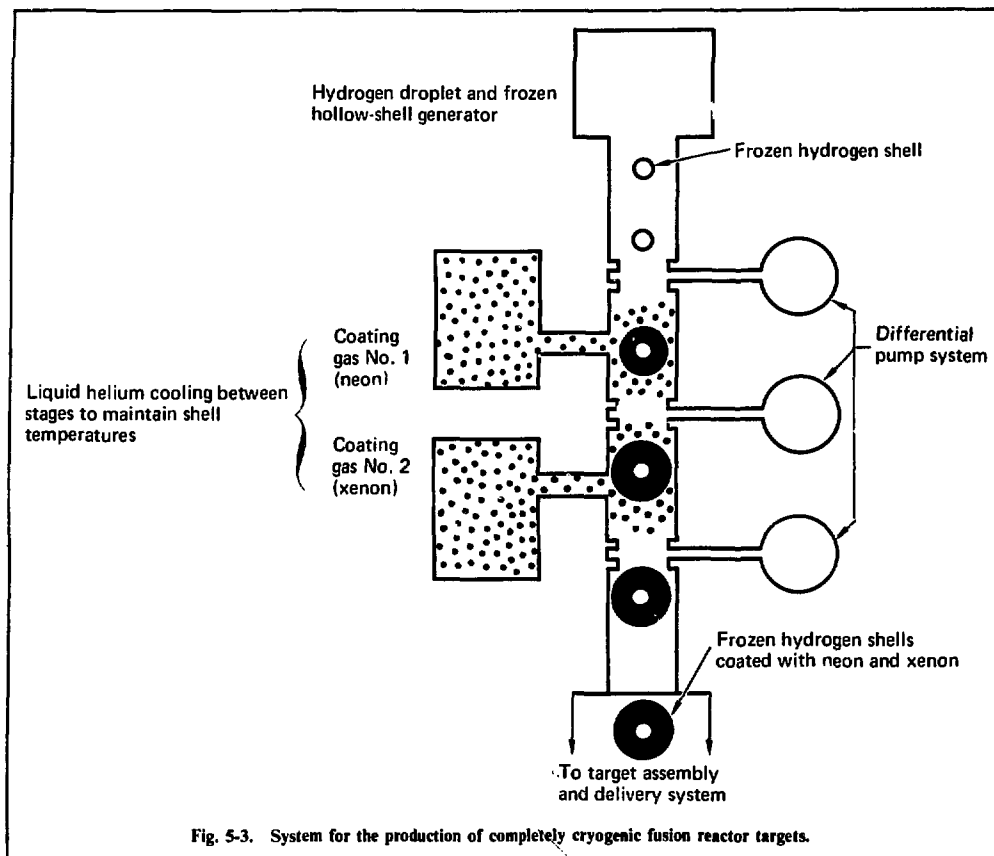


Fig. 5-3. System for the production of completely cryogenic fusion reactor targets.

analyze our samples; Physical Electronics Industries, Eden Prairie, Minnesota, have applied their Auger spectrometer methods to some of our work; and the Martin-Marietta Corporation laboratory in Denver has given excellent assistance in the analysis of gas fill of our nontritiated systems.

Several consultants have been very helpful to us this past year, but outstanding among these is Dr. Ralph Wuerker, whose experience and ideas in several areas of optics and particle control have been invaluable.

## References

1. *Laser Program Annual Report—1976*. Lawrence Livermore Laboratory, Rept. UCRL-50021-76 (1977).

## Author

C. D. Hendricks

## 5.2 High-Quality Glass Spheres

### 5.2.1 Production of Hollow Glass Microspheres

A basic target for laser fusion experiments is a hollow glass microsphere filled with 10 to 100 atm of equimolar DT. Some current targets are usually 100 to 200  $\mu\text{m}$  in diameter with wall thicknesses from 1 to 12  $\mu\text{m}$ , depending on the type of experiment being run. The criteria for target microspheres are very stringent. Sphericity, concentricity ( $P_1$  defect), and wall uniformity all must be better than 5%, or no more than a 2000- $\text{\AA}$  deviation for a 4- $\mu\text{m}$  wall. In addition, the surface finish must be better than 2000  $\text{\AA}$ , peak to valley. Finally, even the thin microspheres must hold up to 100 atm of DT over a long period of time.

Until recently, we have acquired glass target microspheres by laboriously sorting through large

quantities of commercial microspheres obtained from either Minnesota Mining & Manufacturing Co. or Emerson & Cumming Co. These microspheres are produced for use primarily as a structural filler in suitable resin composite materials. They are mass-produced, usually from glass frits or gels blown in gas flame furnaces.<sup>2</sup> The process is not well controlled because commercial microspheres need not be of particularly high quality. Thus, we find very few target-quality microspheres in the commercial batches. Furthermore, as the criteria for target microspheres become more stringent, the already low probability of finding suitable microspheres from the commercial stock rapidly approaches zero.

For that reason, and also to have control over the various compositional and geometric parameters, it has become imperative that we develop an in-house capability for producing high-quality hollow glass microspheres. We have developed several processes to meet this need; among these are the liquid-droplet technique and the dried-gel technique.

**Liquid-Droplet Technique: Basic Principles.** The liquid-droplet technique is based on the following basic principles:

- An aqueous solution can be made that contains water-soluble glass-forming compounds such as sodium silicate.
- A drop of this solution will attain a highly spherical shape in free fall as a result of surface tension.
- If the drop is subjected to a high temperature during free fall, water vapor can be entrapped within the sphere as the glass-forming compounds transform into glass.
- Under the proper conditions, the entrapped water vapor will act as an internal blowing agent, creating a hollow glass microsphere.
- The right temperatures and droplet transit times will produce hollow glass microspheres with specified diameters and wall thicknesses in a controlled fashion.

**Liquid-Droplet Generator.** To accurately control the geometric parameters of the glass microspheres, the aqueous droplets of glass-forming compounds are introduced into a long vertical drop furnace by means of a piezoelectrically driven liquid-droplet generator. By controlling the solution composition and the size of the orifice in the liquid-droplet generator, it is possible to control the diameter and wall thickness distributions of the resultant microspheres. The 1976 annual report describes the liquid-droplet generator.<sup>1</sup>

**Vertical Drop Furnace.** Figure 5-4 is a schematic of the vertical drop furnace, which consists of segments of quartz tubes, 3 in. in diameter and 1/8 in. thick, joined together to form a total length of up to 16 ft. The heating elements consist of insulated heater strips and clamshell multizone furnaces.

The vertical drop furnace is composed of four distinct sections. The top is the insertion section where the droplet-generator is situated. Below that is the drying section, 6 to 10 ft long and maintained at temperatures of 200 to 400°C. Next is the fusing section, 3 ft long, and maintained at temperatures of 1000 to 1200°C. Finally, the bottom 3 ft forms the collector section. Here, the hollow glass microspheres drop into a suitable container, and the furnace gases are drawn out in a controlled fashion through a vent.

Thermocouple-controlled power supplies drive the various heaters in the drop furnace. The furnace is well sealed and insulated throughout the heated regions. The amount of air drawn into the furnace is carefully controlled by the vacuum vent in the collector section. The lengths of the various sections have been established from an investigation of the transit times necessary during the various stages of transformation: from water droplet to hollow glass microsphere. We estimate that vertical velocities of the droplet range from about 500 cm/s near the top to as low as about 5 cm/s at the bottom of the drying region.

**Physical and Chemical Processes of Microsphere Production.** Because the creation of a hollow glass microsphere from a water droplet is a dynamic process occurring in a reasonably short time, and because the droplet travels through a long opaque furnace, we cannot directly observe the events that occur. Nevertheless, after extensive experimentation, we have been able to infer the physical and chemical processes that take place.

Microsphere production begins with the preparation of a solution containing mainly water and hydrated sodium silicate as well as lesser amounts of boric acid, potassium hydroxide, and lithium hydroxide. The solution is fed through the droplet generator and injected into the drying section of the oven.

Four separate processes occur during the transformation of the aqueous droplet into the final hollow glass microsphere: encapsulation, dehydration, transition, and refining.

During encapsulation, the drying section of the drop furnace operates as two distinct temperature zones. In the first zone, the temperature is set at 300 to 400°C. This zone is generally only about 1 to 2 ft

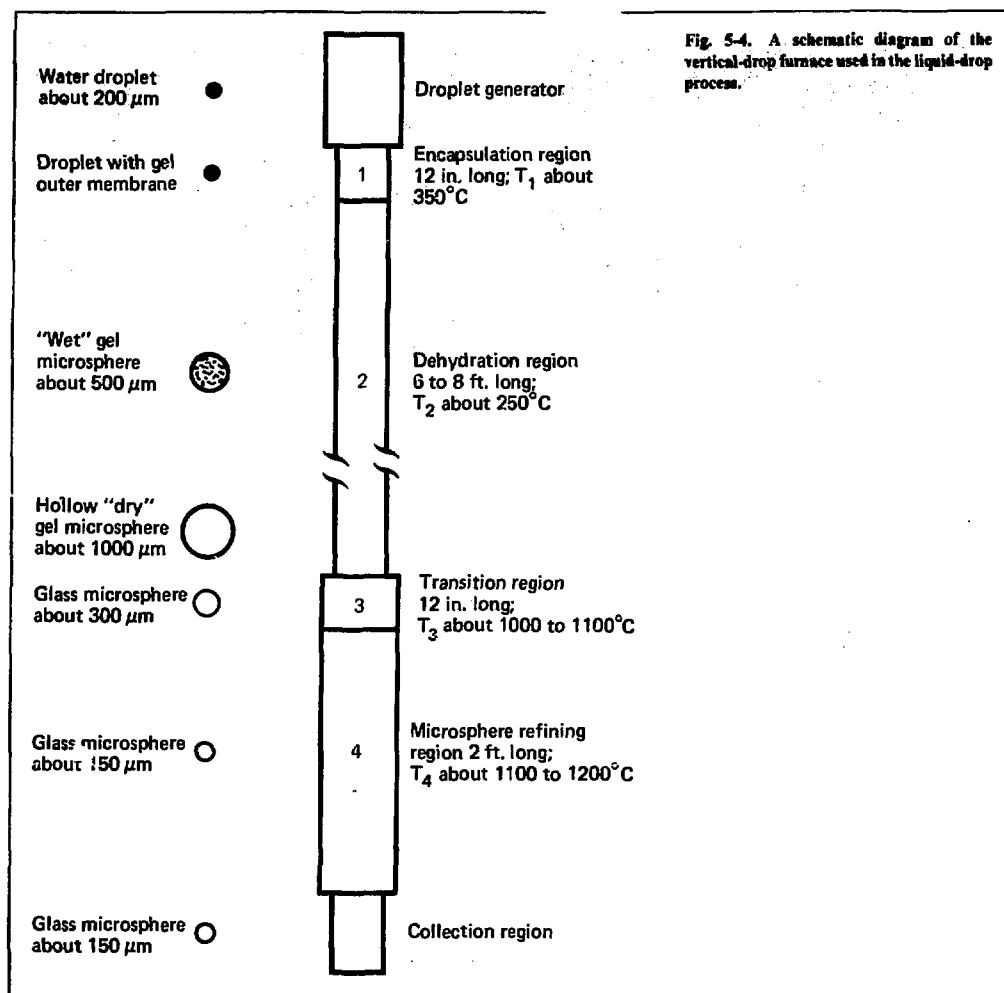


Fig. 5-4. A schematic diagram of the vertical-drop furnace used in the liquid-drop process.

long. The second zone is 4 to 8 ft long, and the temperature is about 200 to 300°C.

As the 200- $\mu\text{m}$ -diam water droplet enters the first zone, the water rapidly vaporizes from the outer surface. When the outer surface loses enough water, it forms a skin, or gel membrane. This gel membrane then encapsulates the rest of the water droplet in an elastic outer surface. As in all sections of the furnace, the temperature here must be carefully selected. It is important to achieve rapid encapsulation and, subsequently, rapid dehydration to ensure proper operation within a reasonable drop length. However, if the temperature is too high in either the first or second zones, the gel-encapsulated

droplet will explode as a result of excessive water vapor pressure, thus producing improperly sized glass microspheres. If the temperature in the first zone is too low, encapsulation will result too far down the drying section, and the gel microsphere will not be dehydrated enough for proper fusion into glass. We have found that temperatures of 300 to 400°C in the first 1 to 2 ft of the drop furnace ensure rapid encapsulation without explosion.

Once the droplet is encapsulated, the water vapor entrapped within diffuses rapidly through the thin gel membrane. The rate of water vapor production within the gel capsule is determined primarily by the temperature in the second zone of the drying



Outside diam  $\sim 1600\ \mu\text{m}$   
Wall thickness  $\sim 0.1\ \mu\text{m}$

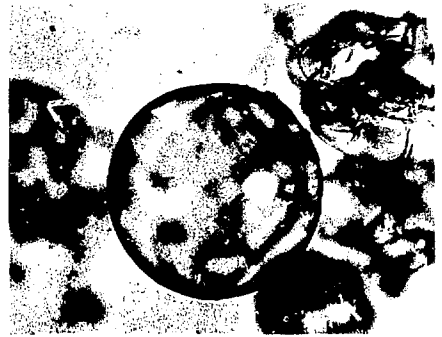
Fig. 5-5. A dehydrated hollow gel microsphere, 1.6-mm outside diameter with about a 1000-Å wall.

region. We have found that temperatures of 200 to 300°C ensure rapid dehydration of the gel capsule through the gel membrane, while preventing rupture of the membrane caused by excess water vapor pressure. Because the gel membrane is very thin (about 1000 Å) and very weak at these temperatures, the rate of diffusion of vapor through the membrane must closely equal the rate of vapor production within, so that only a few tenths of an atmosphere pressure are allowed to build up within the gel microsphere.

As the water vapor diffuses out of the gel microsphere, more of the glass-forming material—primarily sodium silicate—leaves the solution and is incorporated into the gel membrane. The water-vapor pressure within causes the surface area of the membrane to increase; thus, the gel microsphere grows in size and becomes hollow. If the transit time in the second zone of the drying region is long enough, the resulting gel microsphere will be large, spherical, and hollow, with an outer gel membrane about 1000 Å thick. These gel microspheres have been observed to be as large as 2 mm in diameter (see Fig. 5-5).

At the end of the dehydration region, the wall of the gel microsphere is quite hard, cannot easily be deformed, and will not collapse even though there is little or no excess vapor pressure within.

After leaving the dehydration region, the gel microsphere enters the transition region, which is 6



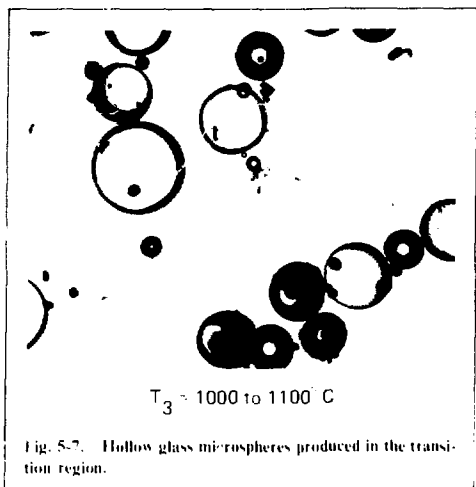
$T_3 = 800^\circ\text{C}$

Fig. 5-6. A gel microsphere beginning to deform in the transition region.

to 12 in. long and is kept at 1000 to 1100°C. The time in the transition region is the most crucial period in the liquid-droplet process, for it is here that the transformation to glass occurs. As the transformation begins, the gel wall turns to liquid, its viscosity drops, and the microsphere begins to collapse as a result of surface tension and the lack of excess internal pressure (see Fig. 5-6). The collapse is partly offset by a buildup of some internal pressure, caused by decreasing inner volume as well as by the release of new water vapor and possibly other gases during the glass formation process.

We have found that we can produce high-quality concentric glass microspheres if the gel microsphere collapse is properly controlled. In particular, we have determined that the glass-forming chemical reaction should occur fairly rapidly, thus ensuring that the gel microsphere will collapse uniformly while remaining hollow and spherical (see Fig. 5-7). On the other hand, we do not want the reaction to occur so rapidly that total collapse occurs before all parts of the gel wall turn to glass. Therefore, we must regulate the average temperature of the transition region and the transit rate through that region. With the proper regulation of these two parameters, the microspheres emerge from the transition region as hollow glass spheres, smaller and thicker than the original gel microspheres.

Below the transition region is the refining region. It is 1 to 3 ft long and is maintained at 1000 to 1200°C. In this region, the glass microspheres do not undergo any major alterations, but rather a more subtle refining process. Here, the chemical



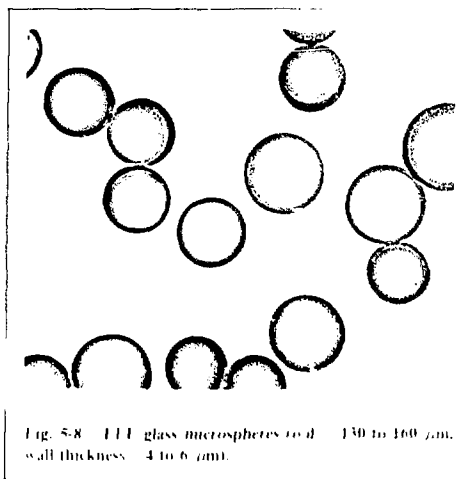
reaction is completed. Any pockets of incompletely reacted material within the wall now turn to glass, and the wall becomes homogeneous. Any small gas bubbles trapped within the walls tend to diffuse out and disappear.

Geometric parameters change somewhat as the microsphere traverses this region. The gases and vapors trapped within the microsphere diffuse out at a rate determined by the glass composition and the temperature, and the microsphere becomes slightly smaller. Simultaneously, if the viscosity of the glass is low enough, any defects in sphericity will be eliminated by the surface tension of the molten glass.

We have found that, by using these methods, we can obtain fairly high yields of glass microspheres with the desired geometric parameters, as well as excellent sphericity and concentricity. Examples of some of the microspheres produced are shown in Figs. 5-7 and 5-8.

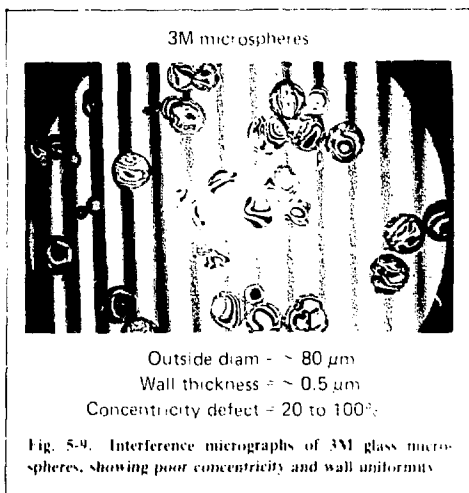
**Concentricity.** As we previously stated, hollow glass microspheres obtained from commercial sources cannot meet the concentricity specifications of high-density fusion targets (see Fig. 5-9). We have found, however, that it is possible to produce glass microspheres with the liquid-droplet technique that do meet these stringent concentricity requirements.

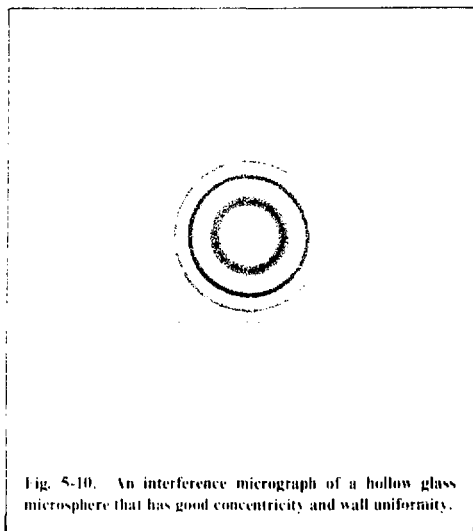
The easiest way to examine hollow glass microspheres is to use a light interference pattern from which one can readily obtain both a qualitative and quantitative measure of concentricity and wall uniformity<sup>3</sup> (as shown in Fig. 5-10).



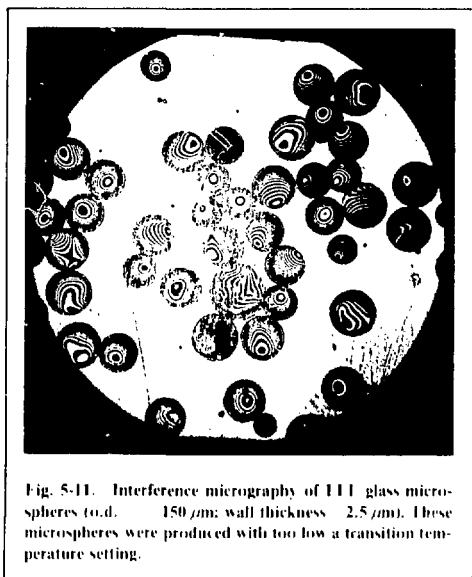
When a microsphere exhibits good wall uniformity, the interference fringes will consist of a series of highly circular concentric rings, the number of rings increasing as the wall thickness increases. If the microsphere is also concentric, then this interference pattern will be centered on the geometric center of the microsphere. The deviation of the interference pattern center from the geometric center is a measure of the concentricity defect. The deviation of the concentric rings from circular is a measure of the wall uniformity defect.

We previously stated that the transition region has the major influence on the concentricity of the

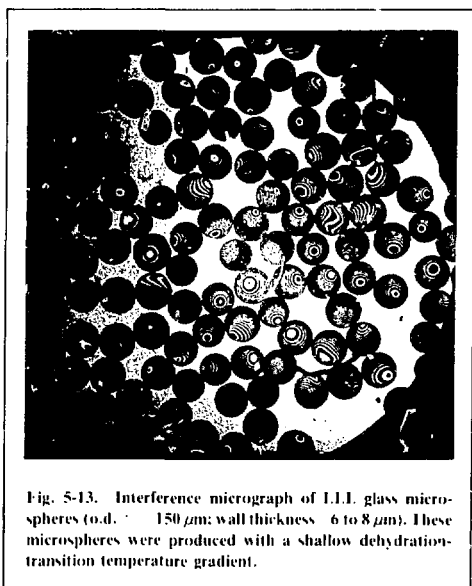
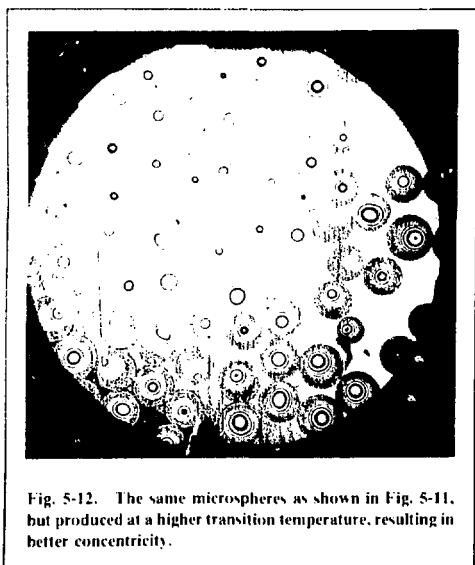




glass microspheres. The gel microspheres, in general, have a high degree of sphericity and concentricity by the time they exit the dehydration region. If the conditions in the transition region are such as to ensure a rapid and uniform collapse during the gel-to-glass transformation, then the resulting glass microspheres will also have high sphericity and concentricity.



In Fig. 5-11, we show a field of several microspheres in the interference microscope. These microspheres were produced with the transition region temperature set slightly too low. We can see that only a few of these microspheres have high concentricity or wall uniformity. In Fig. 5-12, we show



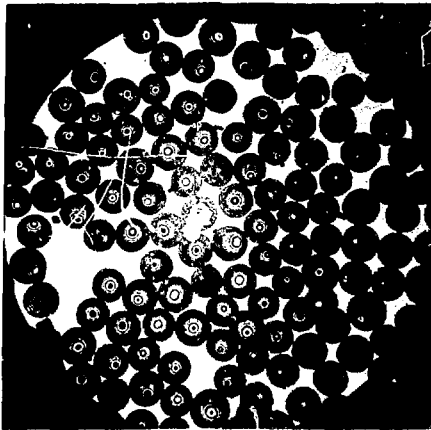
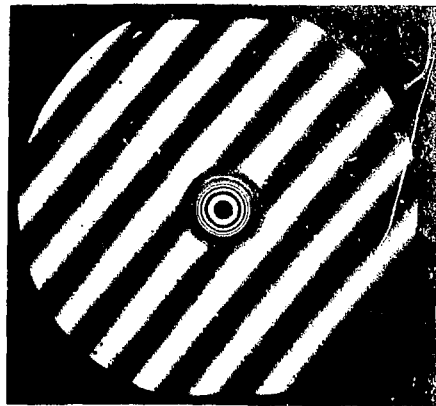


Fig. 5-14. The same microspheres as shown in Fig. 5-13, but produced at a steep dehydration-transition temperature gradient, revealing improved concentricity.



Outside diam.  $140\ \mu\text{m}$   
Wall thickness  $4\ \mu\text{m}$

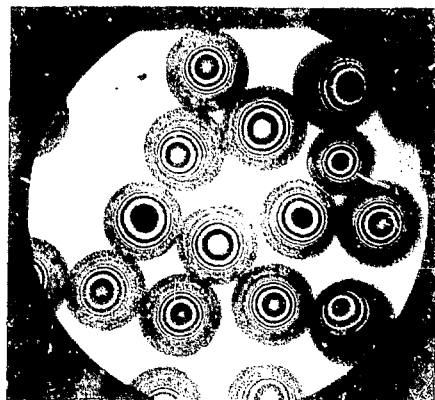
Fig. 5-15. Interference micrograph of a thin-walled glass microsphere with a measured concentricity defect of about  $3 \times 10^{-4}$ .

the output of a subsequent experiment in which the transition temperature is set at the right level. Here, the concentricity and wall uniformity have improved considerably.

Figures 5-13 and 5-14 illustrate what happens to the concentricity and wall uniformity as the temperature gradient between the dehydration region and the transition region changes. As the temperature gradient steepens, concentricity improves. This improvement is a result of the fact that the steeper gradient allows the microspheres to reach the transition temperature more rapidly, thus producing a more uniform collapse.

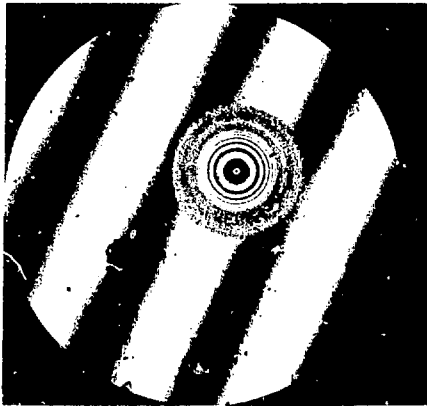
Target-quality glass spheres with inside diameters from 50 to more than  $300\ \mu\text{m}$  have been produced by the liquid-droplet technique. Wall thicknesses range from less than 1 to more than  $12\ \mu\text{m}$ . Figures 5-15 through 5-19 are examples of interference micrographs of glass spheres made by the liquid-droplet process.

**Argon-Filled Microspheres.** Our experiments clearly show that gas rapidly diffuses out of the gel microsphere in the dehydration zone of the furnace. Obviously, those gases in the furnace atmosphere that are absent in the gel microsphere must diffuse equally as rapidly into the microspheres. The inward diffusion process is driven by concentration gradients. Once the gas is inside the hollow gel microsphere, it will remain there during the transformation to glass if the partial pressures inside and outside the spheres are the same.



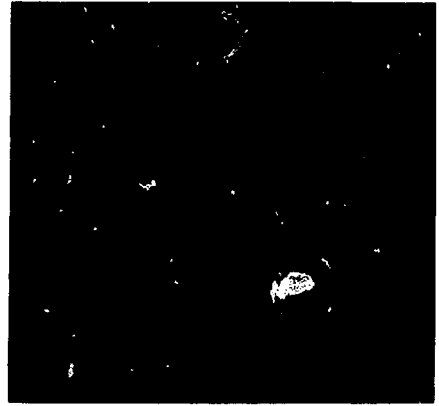
Outside diam.  $\sim 150\ \mu\text{m}$   
Wall thickness  $\sim 6\ \mu\text{m}$

Fig. 5-16. Interference micrograph of several microspheres with measured concentricity defects of only 1 to 5% (600 to 3000  $\lambda$ ).



Outside diam.  $\sim 140 \mu\text{m}$   
Wall thickness  $\sim 8 \mu\text{m}$

Fig. 5-17. Interference micrograph of a microsphere with a measured concentricity defect of about 1% (800 $\times$ ).



Outside diam.  $\sim 180 \mu\text{m}$   
Wall thickness  $\sim 12 \mu\text{m}$

Fig. 5-18. Interference micrograph of a microsphere with a concentricity defect of about 4% (4800 $\times$ ).

We have therefore found it possible to introduce gases such as argon into the glass microsphere simply by introducing the gas into the furnace. Significant amounts of argon have been introduced by this method (up to 0.5 atm). Naturally, unless the interior of the oven is pressurized, no more than 1 atm of a given gas can be introduced by this means.

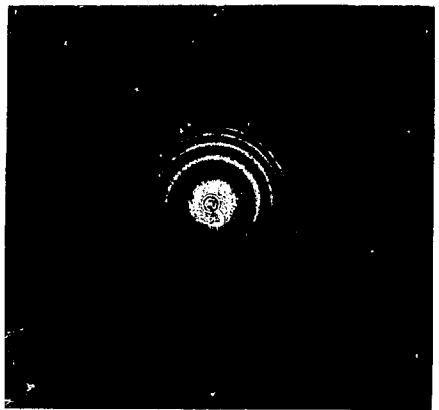
The liquid-droplet technique thus provides a very simple mechanism for introducing various gases into the glass microspheres.

## References

1. W. B. Beck and D. E. O'Brien, *Glass Bubbles Prepared by Rotating Solid Glass Particles*, U.S. Patent 3,365,315 (Oct. 23, 1968).
2. B. W. Weinstein and C. D. Hendricks, *Interferometric Measurement of Laser Fusion Targets*, Lawrence Livermore Laboratory, Rept. UCRL-7847, Rev. 1 (1977).

## Authors

A. Rosenzweig  
C. D. Hendricks



Outside diam.  $\sim 300 \mu\text{m}$   
Wall thickness  $\sim 3 \mu\text{m}$

Fig. 5-19. Interference micrograph of a microsphere with a concentricity defect of about 2% (600 $\times$ ).



## 5.2.2 Surface Treatment of LLL Glass Microspheres

As we have seen, it is extremely difficult to find any commercial microspheres that can meet the stringent surface smoothness of 2000 Å or better that is required for high-density laser fusion targets (see Fig. 5-20). The two main problems with these surfaces are devitrification and weathering.

- The basic glass composition of commercial microspheres permits devitrification or phase separation.<sup>4</sup> This phase separation, generally into high-SiO<sub>2</sub> and low-SiO<sub>2</sub> phases, occurs slowly at room temperature but much more rapidly in the hydrogen atmosphere and 400°C conditions of the DTI fill process.

- Commercial glass microspheres are alkali silicates, and thus the surfaces tend to weather or deteriorate with time. Weathering occurs when the alkalis react with water vapor in the atmosphere to form alkali-hydroxides.<sup>7</sup> These hydroxides, in turn, form etch pits on the microsphere surfaces.

**Glass Composition.** We have developed the compositions of the LLL glass microspheres to satisfy the following conditions:

- The liquid-droplet technique requires the use of an aqueous solution of glass-forming oxides.

- The melting point of the glass must be several hundred degrees lower than the operating temperatures of the ovens to ensure rapid and complete gel-to-glass fusion.

- The viscosity of the glass must be low at the operating temperature of the furnace to ensure high sphericity and concentricity.

- The composition should be such as to inhibit both devitrification and weathering.

Among the various glass-forming oxides, only alkali oxides are water soluble to any significant degree. Of these, the Na<sub>2</sub>O-SiO<sub>2</sub> binary system most easily forms a glass at relatively low temperatures. Thus, the basic composition used in the liquid-droplet system is Na<sub>2</sub>O-SiO<sub>2</sub> in the weight percent ratio of approximately 71% SiO<sub>2</sub> and 22% Na<sub>2</sub>O. This particular composition has been chosen because it is close to the eutectic in the Na<sub>2</sub>O-SiO<sub>2</sub> phase diagram, thus resulting in a low melting temperature.<sup>6</sup> In addition, a eutectic composition reduces the possibility of devitrification. Another reason to choose the Na<sub>2</sub>O-SiO<sub>2</sub> system is that this particular alkali glass has a lower viscosity at temperatures below the 1200°C operating temperature of our furnaces than do the other alkali glasses. A low viscosity is essential to ensure high sphericity and concentricity of the microspheres.

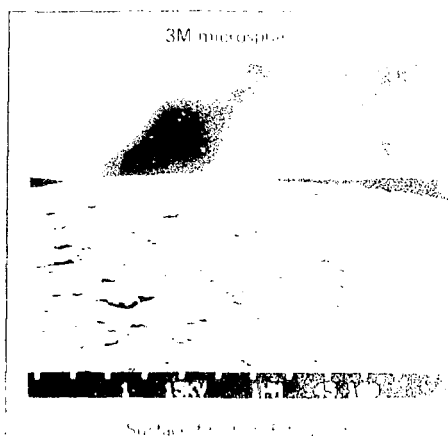


Fig. 5-20 SEM photograph of the surface of a glass microsphere obtained from 3M.

We cannot use a pure Na<sub>2</sub>O-SiO<sub>2</sub> glass, because this alkali glass is highly susceptible to weathering or deterioration as a result of exposure in the atmosphere. We believe the primary mechanism for this deterioration is the reaction of NaOH (the glass is attacked by water) with subsequent etching of the surface by gaseous NaOH. This deterioration is minimized by the relatively high molar fraction of SiO<sub>2</sub> in the structure.

The binary Na<sub>2</sub>O-SiO<sub>2</sub> glass is somewhat expensive, so we have added some modifiers such as K<sub>2</sub>O and Li<sub>2</sub>O to the network formers such as B<sub>2</sub>O<sub>3</sub>. The glass modifiers Na<sub>2</sub>O, K<sub>2</sub>O, and Li<sub>2</sub>O break up the continuity of the SiO<sub>2</sub> network, the glass softening and melting point markedly drops as a result. K<sub>2</sub>O in pure SiO<sub>2</sub> network formers such as B<sub>2</sub>O<sub>3</sub> breaks up the network structure of the pure SiO<sub>2</sub> glass, thus lowering the viscosity but not significantly affecting the softening point.

B<sub>2</sub>O<sub>3</sub> is introduced to reduce the viscosity of the glass without adverse changes in the composition and durability. K<sub>2</sub>O and Li<sub>2</sub>O change the Na<sup>+</sup> ion mobility as a result of the interpositions created by the large K<sup>+</sup> ions and the smaller Li<sup>+</sup> ions. Thus, the addition of Na<sub>2</sub>O, K<sub>2</sub>O, and Li<sub>2</sub>O has little adverse effect on the low-melting temperature and viscosity of the basic Na<sub>2</sub>O-SiO<sub>2</sub> system, but it does increase the durability of the glass considerably.

Table 5-1. Glass forming oxides.

Component	Solution, wt%	Final glass, wt%
$\text{SiO}_2$	66.3	70.6
$\text{Na}_2\text{O}$	22.7	21.9
$\text{B}_2\text{O}_3$	2.9	2.0
$\text{K}_2\text{O}$	8.0	5.4
$\text{Li}_2\text{O}$	0.10	0.1

To date we have obtained the best results with the liquid-droplet system, using aqueous solutions of sodium silicate, boric acid, potassium hydroxide, and lithium hydroxide. The relative composition of the glass-forming oxides in the solution and in the final glass is shown in Table 5-1.

The composition of the resulting microspheres differs slightly from that of the solution. This difference primarily results from the loss of some of the alkali by vaporization in the hot fusing region of the oven.

We performed various experiments in which we altered the composition of the aqueous solution. We found that any significant alteration of the basic  $\text{SiO}_2\text{:Na}_2\text{O}$  ratio in either direction increases the softening point, an expected result because we are close to a eutectic. The melting point cannot increase by more than  $100^\circ\text{C}$  without encountering several difficulties. These difficulties are similar to those observed when the temperature of the transition region is not high enough. That is, instead of high-quality microspheres, we obtain multicellular spheroids, or hollow microspheres with bubbles in the wall or with large concentricity defects.

Similarly, we found that keeping the  $\text{SiO}_2\text{:Na}_2\text{O}$  ratio at the required value, but changing the amounts of the minor constituents, also decreases the quality of the resulting microspheres. Increasing the amount of  $\text{B}_2\text{O}_3$  significantly above 3% increases the melting point and gives us the same problems we encounter when we alter the  $\text{SiO}_2\text{:Na}_2\text{O}$  ratio.

Significantly increasing the amounts of  $\text{K}_2\text{O}$  and  $\text{Li}_2\text{O}$  in the liquid-droplet composition also has harmful results, promoting the occurrence of devitrification and fracturing of the glass during subsequent heat treatments such as the DT fill. These problems result from the severe lattice distortions caused by the large mismatch in ionic radius between  $\text{Na}^+$ ,  $\text{K}^+$ , and  $\text{Li}^+$  ions. On the other hand,

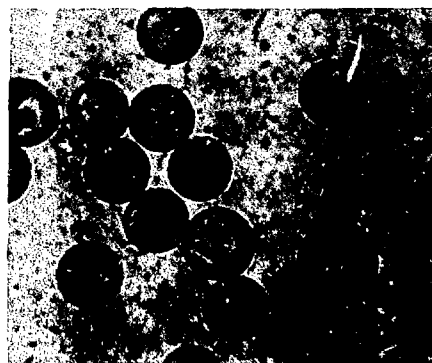


Fig. 5-21. Glass microsphere showing the presence of etch pits caused by the action of reactive alkali condensate from the oven.

decreasing the amounts of  $\text{B}_2\text{O}_3$ ,  $\text{K}_2\text{O}$ , or  $\text{Li}_2\text{O}$  tends to decrease the durability of the glass.

**Furnace Atmosphere.** We have found it necessary to supply a mild downdraft in the liquid droplet furnace. This downdraft helps guide the very light gel microspheres from the drying section into the fusion section. Without this downdraft, these extremely buoyant microspheres tend to be caught up in the convective currents present in the furnace. In addition, the downdraft sweeps the alkali vapors released from the fusing microspheres out of the furnace. If this is not done, these highly reactive alkali vapors tend to recondense on the cold microspheres in the collector and cause rapid deterioration of the surfaces (Fig. 5-21).

The applied downdraft must be kept as low as possible. If it is too great, the constant inflow of cold air creates a significant thermal load on the furnace, thus preventing it from reaching the correct processing temperatures.

We have also found that introducing  $\text{AlCl}_3$  vapor into the furnace improves the durability of the microsphere surfaces. We believe that this improvement is caused by the removal of free alkali vapor in the oven through reactions that form the alkali chloride. These reactions reduce the amount of alkali vapor that can recondense onto the glass microspheres. In addition, there may be some ion exchange at the microsphere surface whereby some of the alkali (Na or K) ions are replaced by Al ions. The presence of Al ions reduces the mobility of Na ions within the glass network, thereby reducing the rate of weathering.

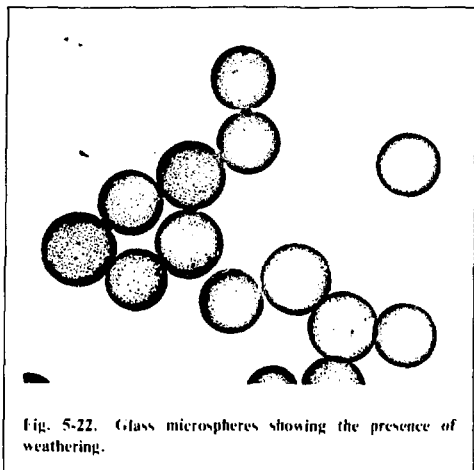


Fig. 5-22. Glass microspheres showing the presence of weathering.

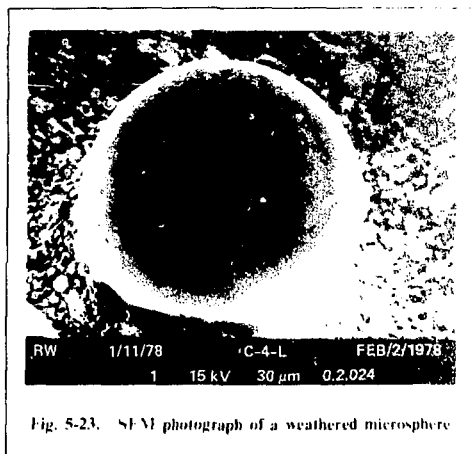


Fig. 5-23. SEM photograph of a weathered microsphere

**Wash.** Once the glass microspheres are produced, it is imperative that they be carefully washed in a suitable acid wash to remove all the reactive alkali from the surface, leaving good, clean surfaces. However, a conventional acid wash, such as an HCl or HF wash, does not prevent weathering or deterioration within a matter of days. In Fig. 5-22 we show a batch of washed microspheres that exhibit the water-spotting marks indicative of etch-pit weathering. Figure 5-23 is an SEM micrograph of the surface of a weathered microsphere, clearly showing the NaOH etch pits.

After extensive experimentation, we have developed an acid wash procedure that not only cleans the reactive alkali from the surface, but also significantly inhibits weathering. This procedure involves several cycles of washes with a 0.5N  $\text{HNO}_3$  + 0.1N  $\text{NH}_4\text{F}$  solution heated to  $90^\circ\text{C}$ , followed by washes with hot distilled water, acetone, and finally ethanol.<sup>7</sup> Initial microprobe analysis indicates that this wash procedure etches out a significant amount of the alkali (primarily Na) from the first micron of the microsphere wall. This alkali depletion significantly inhibits the weathering process at the surface.

Figure 5-24 shows microspheres that were washed with this procedure and left out in humid air for several weeks. There is no sign of weathering. Figure 5-25 consists of SEM photographs of washed LLL microspheres. Surface smoothness is better than 1000 Å, thus meeting the requirements of high-density targets.

**Long-Term Surface Passivation.** We have conducted long-term passivation studies. In these studies, we coat the microspheres with a silane or

other passivating agent. The coating need only be a few monolayers deep to protect the surface from weathering. We have found that coatings with a Dow Corning silane Z-6070 in cyclohexene + 0.1% diethylamine gives the best long-term protection from weathering.

There are, however, questions about the desirability of such a coating during the DT fill process. Preliminary experiments indicate that, unless this coating is washed off prior to DT fill, the  $400^\circ\text{C}$  hydrogen atmosphere reacts with the coating, leaving small particles of debris on the surface. It is thus necessary to remove the silane coating before the DT fill.

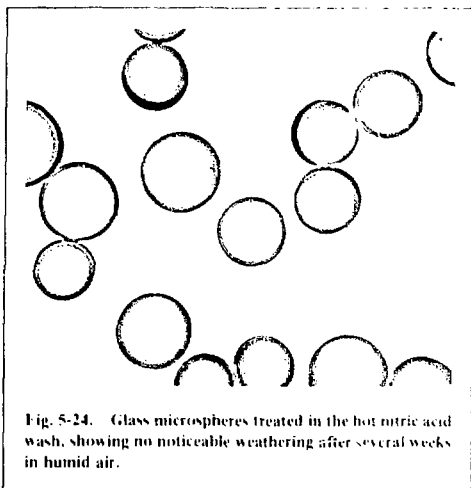


Fig. 5-24. Glass microspheres treated in the hot nitric acid wash, showing no noticeable weathering after several weeks in humid air.

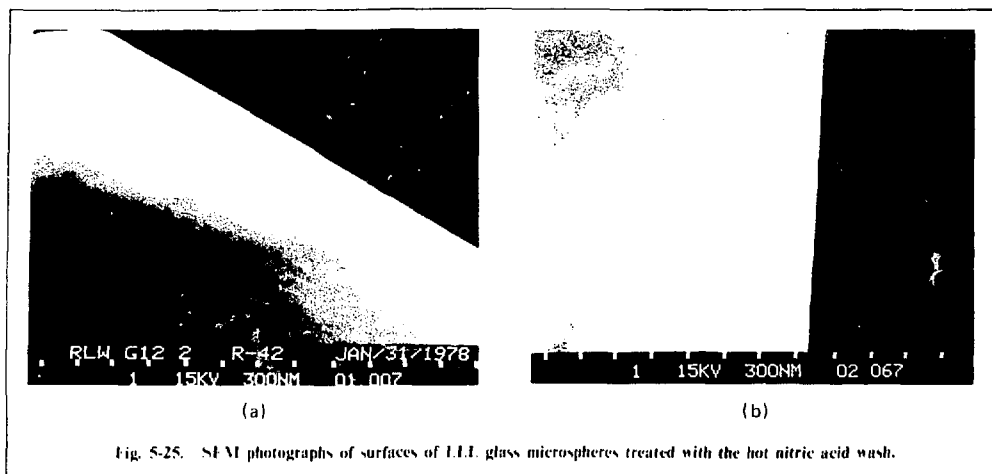


Fig. 5-25. SEM photographs of surfaces of LLL glass microspheres treated with the hot nitric acid wash.

**Long-Term Storage.** Because the long-term passivation method is not without problems, we have relied on long-term storage of washed microspheres in evacuated desiccators. We found, however, that evacuated desiccators cannot prevent eventual surface weathering. We have, therefore, developed a much more effective long-term storage procedure. In this procedure, freshly-washed microspheres are placed in plastic vials filled with ethanol. These vials are then sealed. The ethanol liquid and vapor coat the microspheres completely and prevent weathering. We have found that microspheres stored up to two months in these vials are still completely clean and show no signs of weathering. Thus, they can be held indefinitely and filled with DT at any time, with no additional washes needed before filling.

## References

1. R. H. Doremus, *Glass Science* (John Wiley & Sons, New York, 1973).
2. D. G. Holloway, *The Physical Properties of Glass* (Wykeham Publications, London, 1973).
3. F. M. Leorn, C. R. Robbins, and H. F. McMurdie, *Phase Diagrams for Ceramists*, (American Ceramic Society, Columbus, Ohio, 1964), pp. 94 and 184.
4. A. Rosencwaig, Lawrence Livermore Laboratory Internal Document CDH 77-606 (1977). Readers outside the Laboratory who desire further information on LLL internal documents should address their inquiries to the Technical Information Department, Lawrence Livermore Laboratory, Livermore, California 94550.

## Authors

A. Rosencwaig  
C. D. Hendricks

## 5.3 Polymer Coating

Ablatively driven laser fusion targets require a thick shell surrounding the DT fuel. A practical shell design is a composite of an inner glass ball, to contain and subsequently drive the gas inward, and an outer plastic ablator. This ablator must satisfy several special conditions. It must be density-matched to the glass shell, have a low atomic number, and be smooth and uniform to prevent Rayleigh-Taylor instabilities from disrupting the spherical symmetry of the fuel compression. Many technologies exist for the deposition of thin films. The semiconductor industry has refined several techniques (such as evaporative and chemical-vapor deposition) for depositing multiple thin layers of controlled composition onto integrated circuit wafers. However, exposure of DT-filled glass microspheres to environments of these coating processes would cause excessive heating of the glass shell, allowing the DT fuel to escape.

### 5.3.1 Plasma Polymerization Techniques

A study of the literature indicated that plasma polymerization of organic monomers appeared to satisfy some of the design constraints of fusion target coatings. Plasma coatings had been found by previous investigations<sup>8,9</sup> to be homogeneous, pinhole-free, and of the required density. A wide range of monomers, including hydrocarbons,<sup>10</sup> fluorocarbons,<sup>11</sup> and silanes,<sup>12</sup> have been plasma-polymerized. This technique also offered the flexibility to adapt to future coating requirements. The plasma polymerization technique, in addition, does

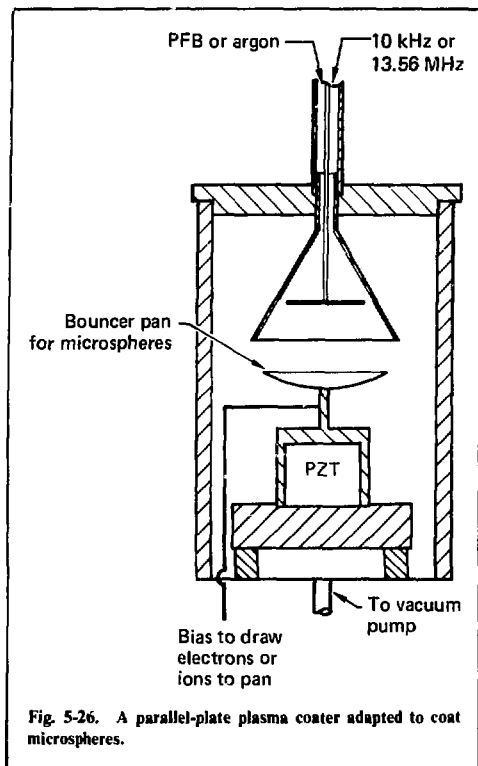


Fig. 5-26. A parallel-plate plasma coater adapted to coat microspheres.

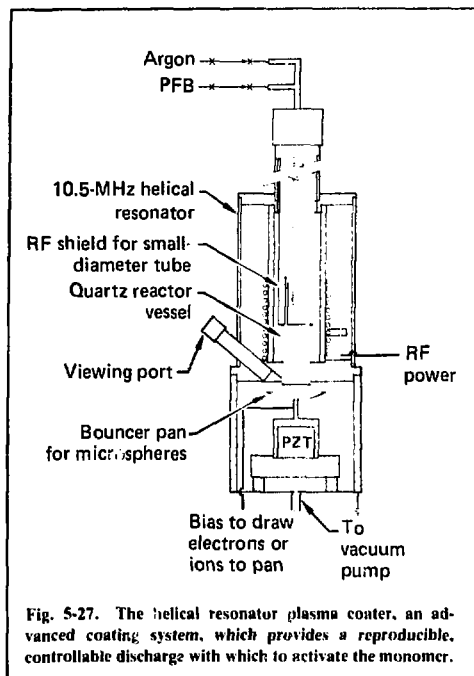


Fig. 5-27. The helical resonator plasma coater, an advanced coating system, which provides a reproducible, controllable discharge with which to activate the monomer.

### 5.3.2. Plasma Source Development

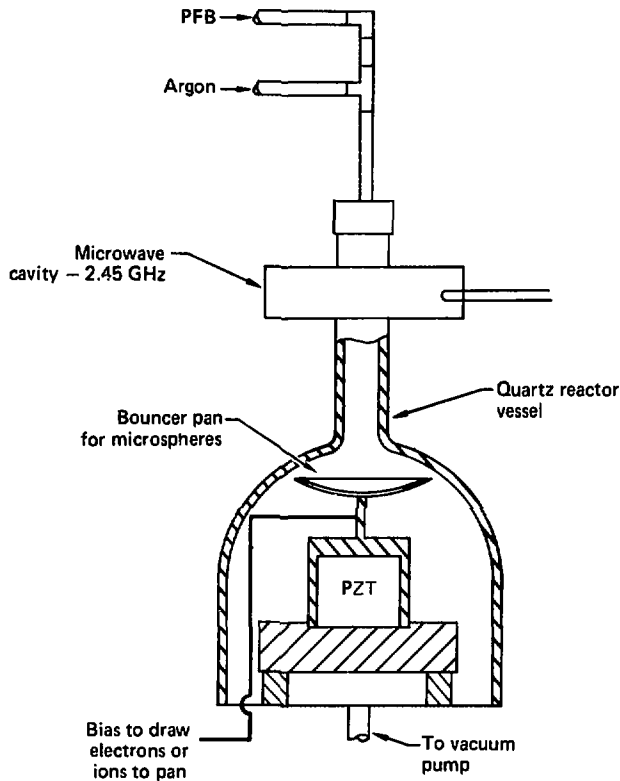
The disadvantages of the parallel-plate apparatus were overcome by developing the helical resonator (Fig. 5-27) as a plasma source. The helical resonator inductively couples energy to the plasma, eliminating electrodes and the problems associated with them. The helical resonator is unusual in its ability to produce low-pressure discharges in electronegative gases because the magnetic field lines inhibit the flow of charged species to the walls. The plasma is ignited within an interchangeable quartz reaction tube. Changing the reactor tube size provides a means for altering the electron temperature (which affects plasma composition). An rf shield that varies the length of the discharge region controls the amount of time the flowing monomer is subjected to the plasma environment. These improvements increase the coating rate to  $2\mu\text{m/h}$  at optimum surface-finish conditions and provide a controllable, reproducible discharge with which to activate the monomer.

A third system for producing a plasma consists of a resonant 2.45-GHz microwave cavity surrounding a 10-mm-diam quartz tube (Fig. 5-28). The monomer in the tube is activated by this electrodeless microwave discharge and then flows down

not heat the glass microspheres above  $190^\circ\text{C}$ , thus preserving the DT fill. However, surface finishes that are possible with known processes did not meet the target design criteria. Therefore, we developed plasma polymerization into a routine production procedure for coating laser targets.

To adapt plasma polymerization to coat glass shells, we developed a piezoelectrically driven bouncer pan. This vibrating pan, which circulated the microspheres to allow uniform coating, was the lower electrode in the early parallel-plate-discharge coater (Fig. 5-26). The parallel plate design, described extensively in the literature, had several problems as a plasma coater for shells. First, the electrodes became coated; arcing on the electrodes then dislodged polymer particles that stuck to the glass shells. Second, the power per unit volume is almost a constant in a parallel-plate discharge regardless of power input; increased power simply resulted in increased plasma volume. This restriction limited coating rate to  $0.5\mu\text{m/h}$  at a pressure of 70 mTorr, the optimum condition for coating smoothness. An improved plasma source was developed to alleviate these problems.

Fig. 5-28. The microwave plasma coater, which produces an electrodeless discharge in a flowing gas stream. The plasma does not contact the coated microspheres.



ambient roughness on the order of 100 to 300 Å when observed over the entire  $4\pi$  steradians of the surface. These surfaces meet the current requirements for ablatively driven laser fusion targets.

**References**

8. I. G. Linder and A. P. Davis, *J. Phys. Chem.* **35**, 3649 (1931).
9. M. Nanomi, H. Kobayashi, A. I. Bell, and M. Shen, *J. Appl. Phys.* **44**, 4317 (1973).
10. K. Jesch, J. E. Bloor, and P. I. Kronick, *J. Polym. Sci. A-1* **4**, 1487 (1977).
11. H. Yasuda and I. S. Hsu, *J. Polym. Sci.* **15**, 2411 (1977).
12. M. Giazicki, A. M. Wrobel, and M. Kryszewski, *J. Appl. Polym. Sci.* **21**, 2013 (1977).

**Authors**

W. L. Johnson  
C. W. Hatcher

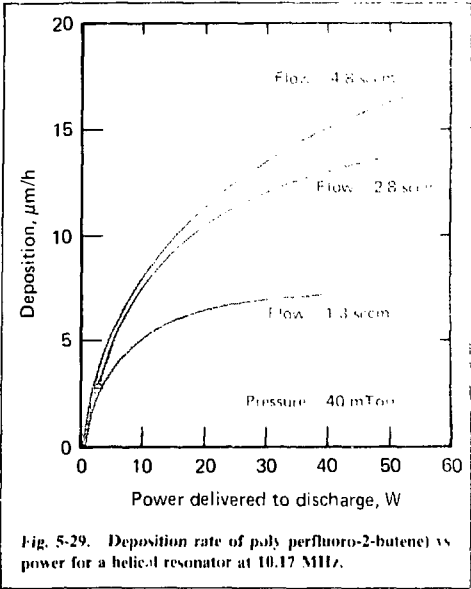


Fig. 5-29. Deposition rate of poly(perfluoro-2-butene) vs power for a helical resonator at 10.17 MHz.

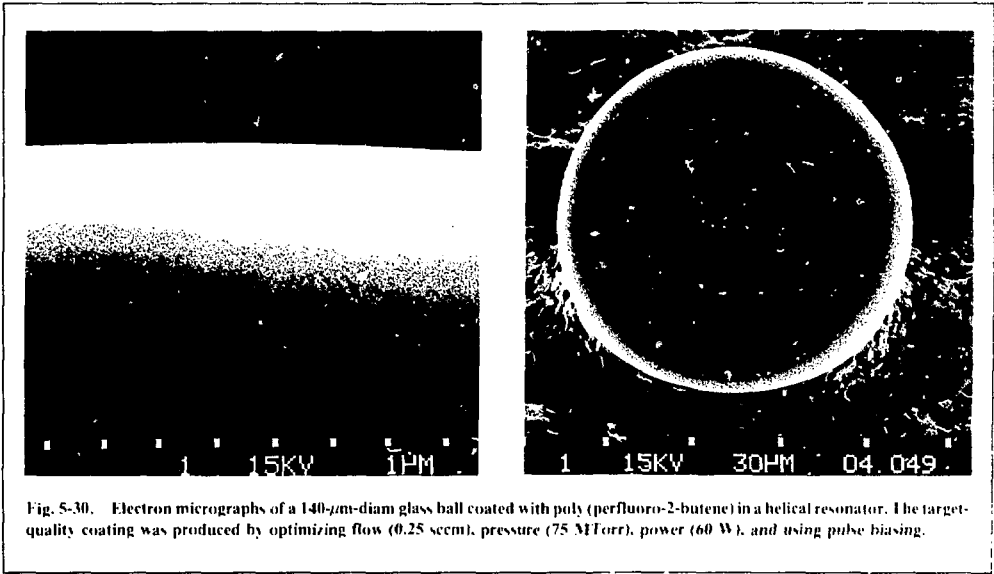


Fig. 5-30. Electron micrographs of a 140- $\mu\text{m}$ -diam glass ball coated with poly(perfluoro-2-butene) in a helical resonator. The target-quality coating was produced by optimizing flow (0.25 sccm), pressure (75 MTorr), power (60 W), and using pulse biasing.

## 5.4 Multilayer, Nonplanar Structures

The advanced target designs for high-density, ablatively driven implosions require complex, multilayer structures. Considerations of hydrodynamic instability, preheat, and maximized compression necessitate exacting specifications on layer density, uniformity, and surface finish. Achieving the high degree of perfection required is a difficult task; each coating step must be designed to preserve the integrity of the preceding layers. The entire structure must also withstand thermal contraction stresses from the cryogenic temperatures necessary for a solid DT layer inside the structure.

Multilayer structures under development include low-density plastic and metal foams, substituted hydrocarbons forming CCI-CF-CH progressions, and various metal, plastic, and glass combinations. To this end, we have coated glass spheres with CF, CH, AlN, SiO<sub>2</sub>, and Al in thicknesses from 10 to 20  $\mu\text{m}$ . We have explored the properties of other materials coated on glass substrates, including gold, carbon, boron, copper, beryllium, and low-density fluorocarbon foam. For applications involving shells within shells, we have thoroughly developed the method of coating a precision-machined mandrel, then etching the mandrel away, leaving a freestanding film. We have used this method to form hemispheres of gold, uranium alloys, SiO<sub>2</sub>, and Be/SiO<sub>2</sub> double layers. The mandrel technique can be extended to almost any combination of materials and layers needed for advanced target designs.

In 1977, we developed the multilayer called for in the advanced target design shown in Fig. 5-31. The following discussion of the specific design in Fig. 5-31 details many additional general considerations involved in constructing multilayer structures.

Note that, while a large body of literature exists on coatings, we found no reports about thick nonplanar coatings with specifications of appropriate bulk density, and peak-to-valley surface finish and uniformity of  $\pm 1\%$ . The principal difficulty in obtaining such desirable layer properties by vapor deposition is the tendency for all defects to grow proportionally faster than the surrounding unperturbed layer. Thin films less than a few micrometers thick always look impressive. Considerable effort is necessary, however, to obtain thick films with the same structure and surface finish. Section 5.3 describes the production of fluorocarbon-coated glass spheres, and § 5.6 discusses solid DT layers inside such spheres.

### 5.4.1 General Fabrication Approaches

The direct approach to the design in Fig. 5-31 would be to start with a glass microsphere of the appropriate wall thickness and diameter, fill it with DT fuel, and then deposit each successive layer. Each layer in turn would serve as the substrate for the succeeding coating. Unfortunately, a low-density plastic foam with a cell size less than 1  $\mu\text{m}$  is currently unavailable. A second problem is that the high deposition temperatures currently used for glass and Be would destroy any plastic. The present approach involves joining two finished hemispheres around a DT-filled, CF-coated glass microsphere held in place with Parylene films. The resulting joint may introduce a defect in the shell, limiting the design appeal.

Our process uses a diamond-turned hemispherical mandrel on the end of a Kovar rod. The rod is a convenient handle for position, temperature, and electrical control during the coating. Kovar mandrels appear to be the best choice for the Be/SiO<sub>2</sub>-layer study for three reasons: the linear

Fig. 5-31. An example of a multilayer, multishell target design for high-density, ablatively driven implosion.

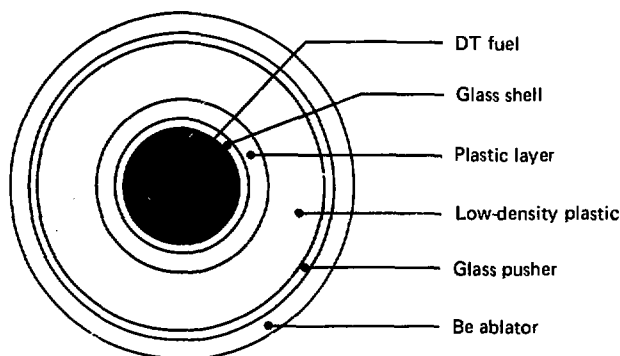
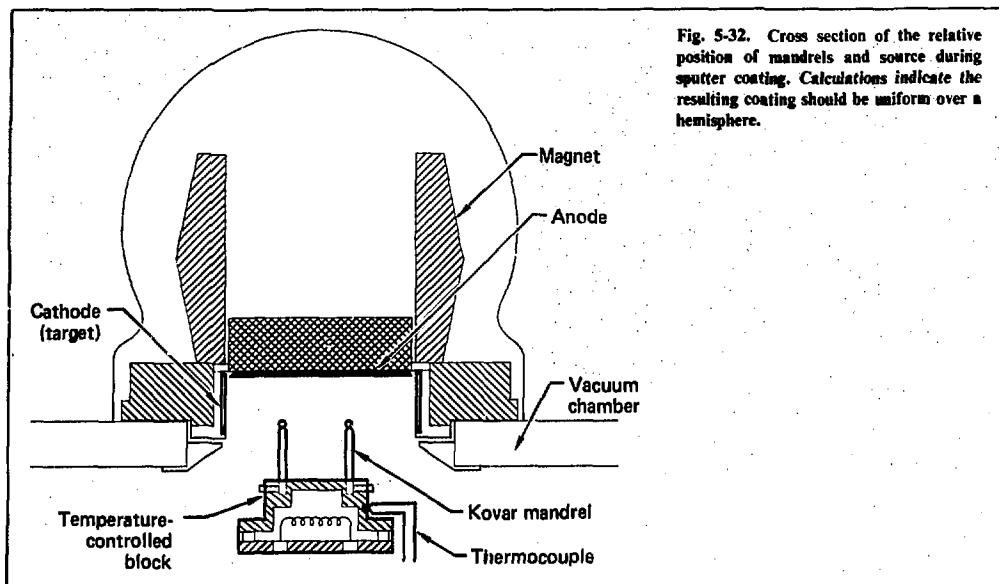




Fig. 5-32. Cross section of the relative position of mandrels and source during sputter coating. Calculations indicate the resulting coating should be uniform over a hemisphere.



thermal expansion coefficient of Kovar is midway between that of  $\text{SiO}_2$  and Be; glass adheres well to Kovar; and nitric acid dissolves Kovar but not Be.

#### 5.4.2 Coating Process

The specifications of the Be/ $\text{SiO}_2$  shell call for a 7- $\mu\text{m}$   $\text{SiO}_2$  layer and a 20- $\mu\text{m}$  Be layer. The tolerance is 0.5  $\mu\text{m}$ , including long-wavelength thickness variations (uniformity) and short-wavelength surface roughness. Density variations, cracks, and bubbles are equivalent to thickness variations that are limited by the integral of density along a radial line. Of course, the smallest variations are the most desirable to minimize potential hydrodynamic instabilities during the implosion.

We routinely coat glass microspheres uniformly with plastic by maintaining them in constant, random motion during deposition. In contrast, the uniformity on mandrels is chiefly a function of deposition geometry. Uniformity may be achieved by either a complicated mechanical movement, similar to a single crystal x-ray goniometer designed to convert a directional vapor flux into a uniform coating, or by achieving an isotropic vapor flux. We chose a cylindrically symmetric source with axial rotation for simplicity and adaptability to multiple mandrel coating. The disadvantage of our approach is an increase in the oblique flux component, which makes achieving the required surface finish more difficult.

The source used for the initial study of both Be and  $\text{SiO}_2$  coatings is a Sloan Model S-300 sputtergun with a 3-in.-diam by 0.93-in.-long target, as shown in Fig. 5-32. Calculations indicate that a mandrel on the gun axis would receive a uniform coating with the hemisphere 0.7 in. below the mid-plane of the intense plasma region and rotated around the target axis. For higher production, a ring of mandrels on a 1-in. circle, 0.5 in. below, should receive a uniform coating, provided they are rotated around both the mandrel axis and the target axis. A diamond-turned Kovar mandrel coated with both Be and  $\text{SiO}_2$  by this method but without any rotation is shown in the microradiograph in Fig. 5-33. The pole-to-equator variation in thickness is about 15%, indicating that the vertical position in the sputtergun was too low. Note that both the glass and Be layers can be independently measured for both thickness and uniformity by the microradiographic technique.

#### 5.4.3 $\text{SiO}_2$ Coating

Figure 5-34 shows an SEM photomicrograph of the surface of an 8- $\mu\text{m}$  layer of  $\text{SiO}_2$  sputtered onto a Kovar mandrel. This coating was rf-sputtered at a temperature of 400°C and pressure of 5 Pa. The coating shows several large conical growth defects and, at higher magnification, a surface composed of small, closely packed bumps. The layer has good mechanical properties and adhesion.

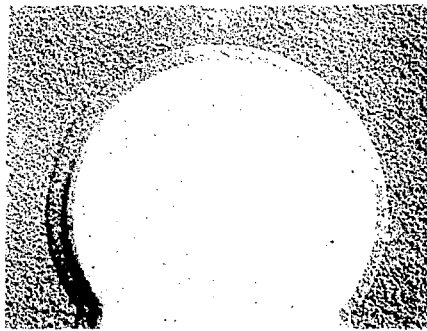


Fig. 5-33. Computer-enhanced microradiograph of Be and  $\text{SiO}_2$  layers on a Kovar mandrel. Note both layers are visible. The pole-to-equator thickness variation is about 15%, indicating the mandrel was too low during coating.

and is transparent and colorless. Because vapor deposition usually tends to amplify substrate defects, the glass surface shown in Fig. 5-34 is not desirable for subsequent Be coating even without the cone growths.

Much research has been published on the growth structure of both evaporated<sup>13,14</sup> and sputtered<sup>15,16</sup> coatings. The consensus is that both the cone growth and the granular surface common to coatings of most materials are caused by low surface mobility and geometric shadowing processes. A surface bump receives more coating flux and shadows the adjacent areas; hence, bumps grow

larger. The large cones are probably caused by large isolated substrate defects such as flakes, dirt, or tooling marks and defects on the mandrel surface. Small-scale granularity results from smaller scale roughness on the machined surface, or ultimately from statistical fluctuations in the vapor flux. Typically, higher temperatures increase the surface adatom mobility, allowing the transport of material from bumps to valleys. However, large cone defects will persist to very high temperatures because of the large transport lengths required.

#### 5.4.4 Be Coating

The SEM photomicrograph in Fig. 5-35 shows a preliminary result of the Be/ $\text{SiO}_2$  shell study. The mandrel pictured is coated with 20  $\mu\text{m}$  of Be over 7  $\mu\text{m}$  of  $\text{SiO}_2$ . The Be was sputtered at 250°C and 3 Pa of argon. A 100-V negative bias drew an argon ion current from the plasma to bombard the mandrel. Ion bombardment effectively suppressed the shaggy growth caused by the oblique vapor flux. The open granular surface suggests that the Be is highly crystalline and has a density somewhat less than bulk Be. Be is well known for its tendency to crystalize, and is difficult to prepare in the amorphous state.

The bumps evident in the Be/ $\text{SiO}_2$  coating may be caused by several factors. Thermodynamically, Be should be able to reduce  $\text{SiO}_2$  to form BeO and Si. A local reaction might cause a bump to form in the coating, or it might erratically affect the entire interface. Arcs in the glow discharge during initial target clean-up are known to cause spits of cathode material that may initiate cone growth. Dc sputter-

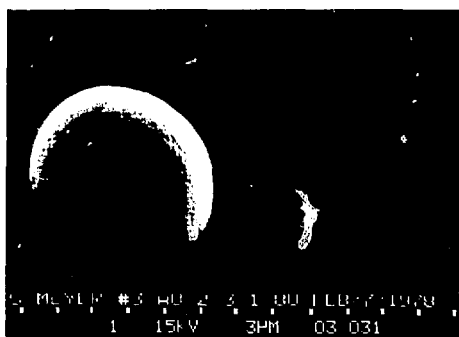


Fig. 5-34. SEM photomicrographs of 8- $\mu\text{m}$ -thick  $\text{SiO}_2$  coating on a Kovar mandrel, showing both the granular surface and large cone growth.

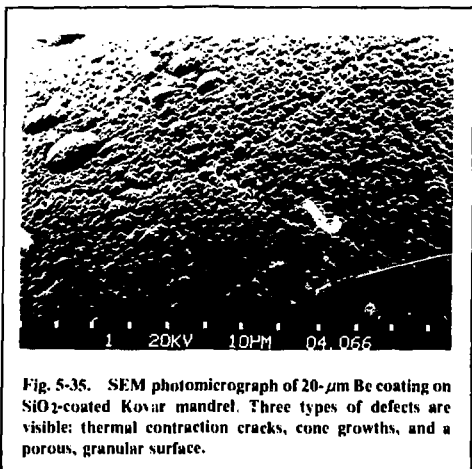


Fig. 5-35. SEM photomicrograph of 20- $\mu$ m Be coating on  $\text{SiO}_2$ -coated Kovar mandrel. Three types of defects are visible: thermal contraction cracks, cone growths, and a porous, granular surface.

ing is particularly prone to these spits when the target is oxidized after cycling the deposition system. Cone growths in the Be layer may be mere continuations of bumps already present in the  $\text{SiO}_2$  layer, or may nucleate on shards of glass deposited on the surface during cool-down and removal from the glass coating system.

The cracks in the Be layer are thermal contraction fractures from the cooling down after Be deposition; this is always a problem with any brittle material. The brittle Be is unable to withstand the tensile stress caused by the large expansion coefficient mismatch between Be and Kovar. Substituting Ni mandrels and soft glass for the  $\text{SiO}_2$  is one way to avoid cracking.

### 5.4.5 Conclusions

This year's developments demonstrate the basic soundness of our approaches to multilayer structures. Perfecting both the sphere and mandrel coating processes will enable construction of a wide variety of advanced targets. The remaining challenges are to refine and extend processes to additional materials, to extend the techniques to a much larger number of layers, and to develop methods suitable for high rate production.

### References

13. B. A. Movchan and A. V. Demchishin, "Study of the Structure and Properties of Thick Vacuum Condensates of Nickel, Titanium, Tungsten, Aluminum, Oxide, and Zirconium Dioxide," *Fiz. Metal. Metalloved.* **28** (83), part 2 (1969).
14. R. F. Bunshah and R. S. Juntz, "The Influence of Ion Bombardment on the Microstructure of Thick Deposits

Produced by High Rate Physical Vapor Deposition Processes," *J. Vac. Sci. Technol.* **9**, 239 (1977).

15. J. A. Thornton, "High-Rate Thick Film Growth," *Ann. Rev. Mater. Sci.* **7**, 239 (1977).
16. R. D. Bland, G. J. Kominiak, and D. M. Mattox, "Effect of Ion Bombardment During Deposition on Thick Metal and Ceramic Deposits," *J. Vac. Sci. Technol.* **11**, 671 (1974).

Author

S. F. Meyer

## 5.5 Developments in Characterization

Precise measurement of the targets used in laser fusion experiments remains a vital part of the target fabrication process, both to ensure the quality of the final targets and to aid in developing fabrication techniques. Most of the techniques used to characterize targets are described in detail in previous reports.<sup>17-22</sup> In this subsection, we review briefly the techniques currently used and describe the advances achieved during 1977.

The dimensions of target parts are currently measured with an image-splitting microscope that has a precision of about 1  $\mu$ m. The mass of target parts is measured with a quartz torsion microbalance to an accuracy of a few nanograms. The amount of DT gas in a target ball is determined by counting the x rays that result from the tritium decay—a measurement that is accurate to 10 to 20%, depending on the type of microsphere. The wall thickness and uniformity of the targets are measured by several techniques, including optical interferometry, contact microradiography, and scanning electron microscopy. Interferometry is accurate to about 0.05  $\mu$ m for measuring the wall thickness and the height of defects more than a few micrometers wide. The SEM is used to measure the height of defects with small lateral dimensions.

The major advances in target measurement during 1977 were associated with the target fabrication for high-density experiments. Exploding-pusher targets used in early fusion experiments were relatively insensitive to nonuniformities in microsphere walls. We only needed to examine the targets in one or two orientations to ensure that no gross defects had been overlooked. High-density, ablative implosions, on the other hand, are much more sensitive to nonuniformities in target wall thickness. The entire surface of these targets must be examined for defects. To do this, we developed a manipulator

that enables us to scan the entire surface of a microsphere easily and rapidly.<sup>23</sup> This manipulator has been coupled with both an interference microscope<sup>24</sup> and an SEM.<sup>25</sup>

Many of the targets used in high-density experiments have multilayered walls. Such targets require techniques for independently measuring the thickness and uniformity of the different layers. To this end, and for the inspection of opaque targets, we have developed new techniques for contact microradiography of targets.<sup>26</sup> The most notable developments are a manipulator for rotating the microspheres during inspection without contaminating them, and least-squares fitting routines for analyzing the radiographs.

## References

17. R. R. Stone, D. W. Gregg, and P. C. Souers, "Nondestructive Inspection of Transparent Microtargets for Laser Fusion," *J. Appl. Phys.* **46**, 682 (1975).
18. C. D. Hendricks, R. D. Behymer, J. A. Brown, G. W. Heaton, E. R. McCunn, and B. W. Weinstein, *Fabrication and Characterization of Laser Fusion Targets*, Lawrence Livermore Laboratory, Rept. UCRL-76679 (1975).
19. B. W. Weinstein, "White Light Interferometric Measurement of the Wall Thickness of Hollow Glass Microspheres," *J. Appl. Phys.* **46**, 5305 (1975).
20. B. W. Weinstein and C. D. Hendricks, "Interferometric Measurements of Laser Fusion Targets," *Applied Optics* (to be published).
21. R. Jay Fries and Eugene H. Farnum, "Nondestructive Fuel Assay of Laser Targets," *Nuc. Instrum. and Meth.* **126**, 285 (1975).
22. I. M. Moen, C. D. Hendricks, and B. W. Weinstein, "Improvements in the X-Ray Counting Measurement of the Tritium Content of Glass Microsphere Laser Fusion Targets," *Bull. Am. Phys. Soc.* **21**, 1137 (1976).
23. B. W. Weinstein, C. D. Hendricks, C. M. Ward, and D. L. Willenborg, "A Simple Manipulator for Rotating Small Sphere," *Rev. Sci. Instrum.* (to be published).
24. B. W. Weinstein, D. L. Willenborg, J. T. Weir, and C. D. Hendricks, *4 $\pi$  Interferometric Measurements of Laser Fusion Targets*, Lawrence Livermore Laboratory, Rept. UCRL-80142 (1977).
25. C. M. Ward, C. D. Hendricks, and B. W. Weinstein, *A Technique for Full Surface Examination of Small Spheres in the Scanning Electron Microscope*, Lawrence Livermore Laboratory, Rept. UCRL-80269, Rev. 1 (1978).
26. R. M. Singleton, C. D. Hendricks, and B. W. Weinstein, *Microradiographic Measurement of Laser Fusion Targets*, Lawrence Livermore Laboratory, Rept. UCRL-80148 (1977).

Author

B. W. Weinstein

### 5.5.1 A Microsphere Manipulator for Target Inspection

The conventional techniques for manipulating a target microsphere during inspection have been to

roll it with a fine probe, or to hold the sphere on a vacuum chuck and rotate it. Both methods have serious drawbacks. Rolling a sphere with a probe cannot be done precisely. It is often impossible to know the relative orientation as the microsphere is moved. Vacuum chuck manipulators are cumbersome, slow, difficult to align, and impossible to use in a vacuum chamber.

We have developed a manipulator that overcomes these problems. The principle of operation is illustrated in Fig. 5-36. The microsphere is held between two flat, pliable surfaces at the ends of small capillary tubes. As the tips are translated parallel to the surfaces, the microsphere rolls between them. If the two tips are moved simultaneously in opposite directions, the ball does not translate, but simply rolls about its center. Because the tips can be moved in either of two perpendicular directions, the microsphere can be rolled about either of two orthogonal axes.

We tried several methods of fabricating the rolling surface. The most satisfactory tips were formed by extruding silicone rubber from the end of a small capillary tube (see Fig. 5-36). To form the flat surface on the tip, the extruded silicone rubber was pressed against a glass slide coated with collo-  
dion (as a release agent).

This new manipulation scheme has proven simple and versatile. It can be used in any orientation, can be made quite compact, requires no precise alignment, and can be used in a vacuum chamber or other special environment with no modifications. The accuracy of positioning is limited only by the accuracy of the manipulators used to move the tips. The manipulator is very gentle. We have never unintentionally broken a ball with it. Two versions of the manipulator are described in § 5.4.2. One is used with an interference microscope and the other with an SEM.

Author

B. W. Weinstein

### 5.5.2 Total Surface Inspection Using Interferometry

We use a double-pass, Twyman-Green interference microscope for the bulk of our sorting and inspection of transparent laser fusion targets (hollow glass and polymer-coated microspheres). This instrument is well suited to measure transparent fusion targets. It is very sensitive to the defects that are important in high-density implosion

100  $\mu\text{m}$

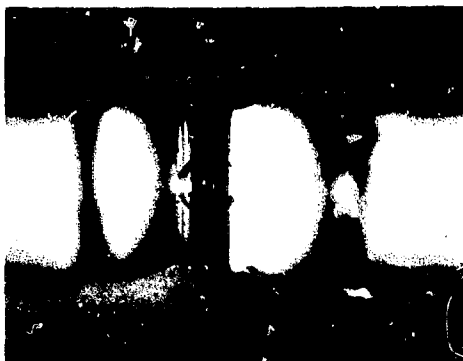
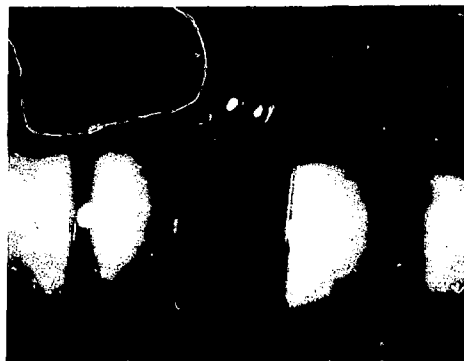


Fig. 5-36. Operation of the microsphere manipulator. (a) The ball is inserted between two flat, pliable tips. (b) The tips are moved together to hold the ball. (c) Differential motion of the tips causes the ball to rotate about its center without translating.

experiments (bumps or depressions a few micrometers in diameter and a few tenths of a micrometer high). Also, large numbers of microspheres can be scanned in the interferometer with relative ease.

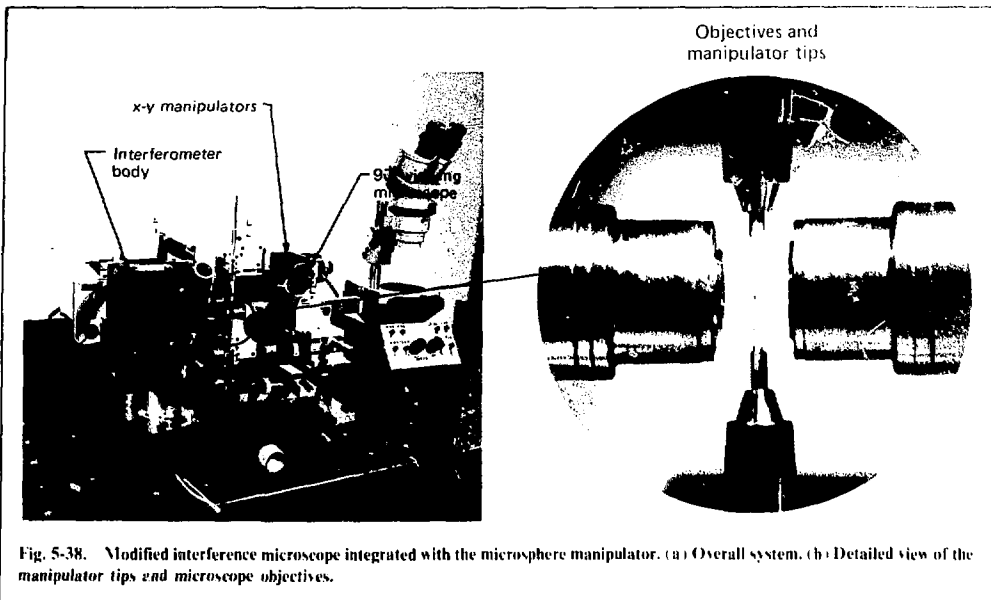
We have developed a modified version of the Twyman-Green interference microscope that is compatible with our manipulator. Figure 5-37 shows a diagram of the modified microscope. Ordinarily, a mirror surface is placed in the object plane of the interferometer, and the sample is placed on this mirror. In our modified design, a new objective lens in each arm transfers an image of a mirror into the object plane of each of the microscope objectives. To preserve high-quality white light interference, the two new objectives must be a matched set, and the distance between these objectives and their associated mirrors must be equal within the coherence length of white light (about  $1\ \mu\text{m}$ ). With

this modification, the manipulator tips can be inserted in the focal plane of the interference microscope. Figure 5-38 shows the integrated system and Fig. 5-39 shows an interference photograph of a microsphere between the manipulator tips. We use a vacuum chuck mounted on an x-y-z manipulator to insert a ball between the tips (as shown in Fig. 5-40).

As shown in Fig. 5-38, each manipulator tip is attached to a pair of stepper motors. The stepper motors are interfaced to an LSI-11 minicomputer that can be programmed to drive the tips.

The controlling program that we use has a "manual" mode in which the operator specifies individual rotations, and a "scanning" mode in which the microsphere is continuously rotated so that the observer systematically sees its entire surface. During these rotations, the minicomputer keeps track of the orientation of the microsphere and continuously

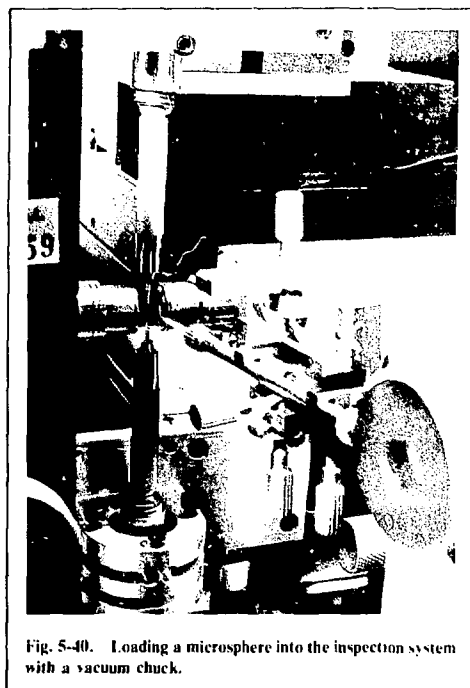
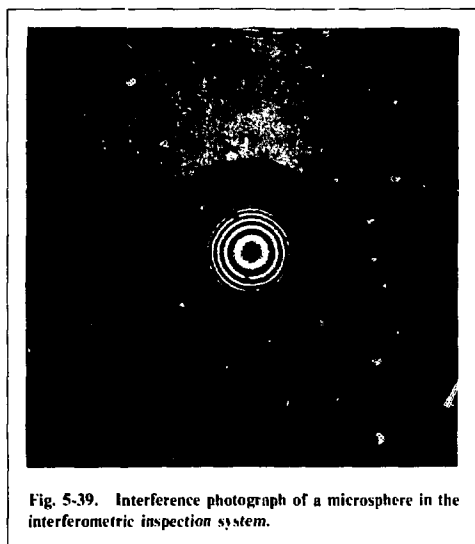




target. If necessary, special measurements such as radiography or SEM examination can be performed as final measurements of the structure of the sphere.

**Author**

**B. W. Weinstein**



### 5.5.3 $4\pi$ Total Surface Inspection with the Scanning Electron Microscope

Scanning electron microscopy provides the best means of observing target defects. Those defects with lateral dimensions less than a few micrometers are difficult or impossible to measure with an interference microscope. Thus, SEM provides a method of examining these smaller defects and is applicable to actual target characterization when coupled with the  $4\pi$  manipulator.

**SEM Examination System.** In 1977, a manually operated version of the  $4\pi$  manipulator that would fit within the chamber of a Cambridge S-180 SEM was fabricated. Because of chamber size limitations, this stage must be smaller than the interferometer versions and must have controls that operate the stage through the vacuum-vessel wall. In addition, because the insulating target and manipulator tips may cause charging problems, it is necessary to conductively coat both.

Figure 5-41 shows the SEM  $4\pi$  manipulator stage being loaded with a microsphere held by a vacuum chuck. The tips are gold-coated and are attached to their holders with conductive epoxy. In the present SEM, only one tip is moved and other remains stationary. The pillar on the right holds the fixed tip that is attached to a simple actuator to adjust tip spacing. On the left, a cross slide provides y motion to the moving tip and causes a rotation

about the electron beam axis ( $Oz$ ). The assembly is in turn raised and lowered by a stage z-motion platform, thus providing the  $Oy$  motion. A combination of these two motions can be used to rotate a sphere through  $4\pi$  steradians. Both motions feed through the stage to micrometer actuators with mechanical position readouts. Position adjustments can be made to about  $2\text{ }\mu\text{m}$ . This is marginally adequate for  $4\pi$  mapping. The difficulties in stage operation currently account for a large part of the time expended in making a  $4\pi$  examination. An additional difficulty is that, with one fixed tip, every rotation requires either a focus or a position change.

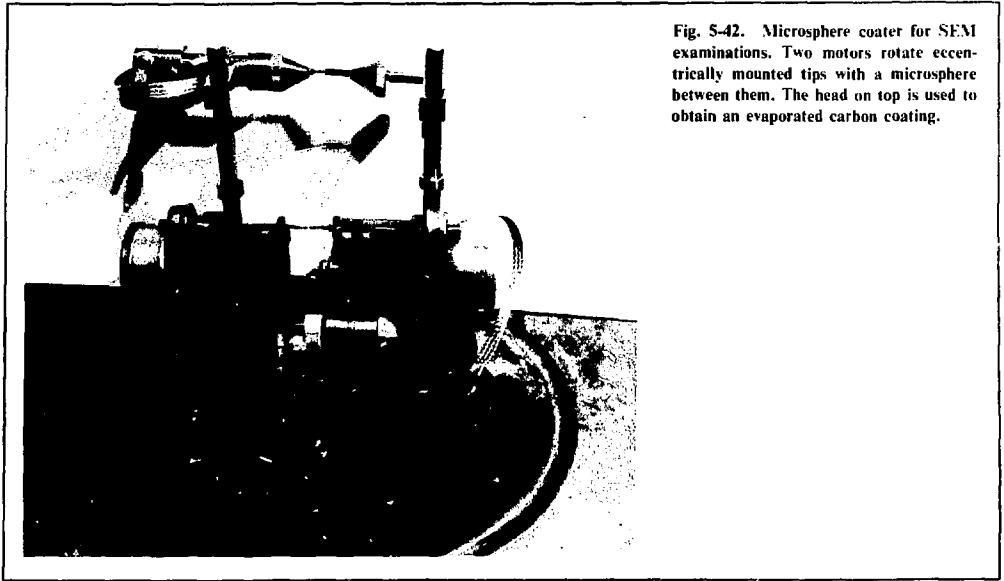
Manipulation of the microsphere is only part of the system required for full surface examination. The mapping of a typical  $140\text{-}\mu\text{m}$ -diam sphere at  $3,000\times$  magnification requires over 140 different photographs. These photographs can be assembled into a photomontage, but this is time consuming and geometrical map distortions can make the result difficult to interpret. As an alternative image storage device, a raster-scan video disk is incorporated into the system. An SEM can be used to examine samples at television sweep rates; however, there is a large amount of noise in the recorded image and many distortions in the picture as a result of problems in the electron beam scanning system. A standard video tape or video disk will not work effectively because the inherent image contrast is low

Fig. 5-41. The  $4\pi$  SEM manipulator stage. The left tip is moved by the cross slide and the z-stage platform to provide microsphere rotation against the fixed tip on the right.





Fig. 5-42. Microsphere coater for SEM examinations. Two motors rotate eccentrically mounted tips with a microsphere between them. The head on top is used to obtain an evaporated carbon coating.



and most small details would be hidden in the noise. Thus, for this application we have incorporated a new version of a video disk that raster-scans at normal electron microscope recording rates, resulting in a 1000-times increase in electrons per pixel and a corresponding improvement in signal-to-noise ratio.

The disk can store 300 images that can be displayed on a TV monitor and played back at a variety of speeds to give the operator a total view of rotating microsphere in the SEM. Permanent storage is made by recording the disk onto videotape.

As an additional feature, the video disk can play back two images superimposed on each other. This feature can be used to display stereo images of the sample or to overlay elemental maps.

**Sample Preparation.** In contrast to the interferometer, sample preparation is very important for  $4\pi$  examinations in the SEM. A conducting film must be applied uniformly to the microsphere to reduce charging. Approximately 100 Å of vapor-deposited carbon is applied, using a coating process adapted from the  $4\pi$  manipulation technique. This coater is shown in Fig. 5-42 and is composed of two eccentrically driven tips that orbit at differing rates. A microsphere between the tips will rotate through  $4\pi$  and expose the entire surface to the evaporator head. Deposition monitors measure the amount of carbon evaporated. An aperture is located between

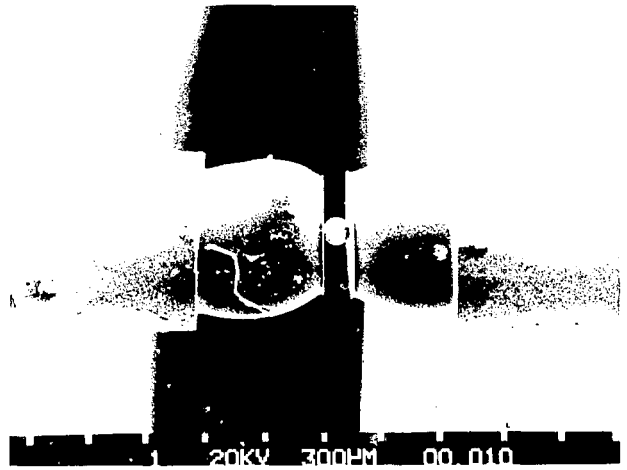
the sphere and the evaporation head to reduce sample contamination from carbon flakes generated in the deposition system by the coating process.

**Inspection Procedure.** Contamination of the microspheres is an ever-present possibility, so candidate samples are handled in a laminar-flow clean bench. The handling components are cleaned prior to all operations. This is especially critical with the tips because they contaminate very easily and then transfer particles onto the sphere. To clean the tips, solvent-softened electron-microscope replicating tape is clamped between the tips and allowed to dry. This removes both large debris and microdust, leaving very clean surfaces.

The coater is loaded by using a vacuum chuck to bring the microsphere between the tips, which are then brought together until contact on both surfaces is obtained. Two orthogonal microscopes are used to ensure that the sphere is centered. The loaded coater is placed in a vacuum system and the 100-Å carbon coating applied. The sphere is removed with a vacuum chuck (again under the flow bench) and transferred to the manipulator stage for SEM inspection (see Fig. 5-43).

For SEM examination, we use 15-keV electrons and a beam current of 10 pA. Because the carbon coating is kept as thin as possible, sample-charging remains somewhat of a problem. We use an analog homomorphic signal processor to reduce the image effects of charging. A distinctive feature

Fig. 5-43. SEM micrograph of a sphere placed between the ball manipulator tips. Contamination such as is visible here builds up quickly outside the flow bench and requires that tips always be cleaned prior to inserting a microsphere.



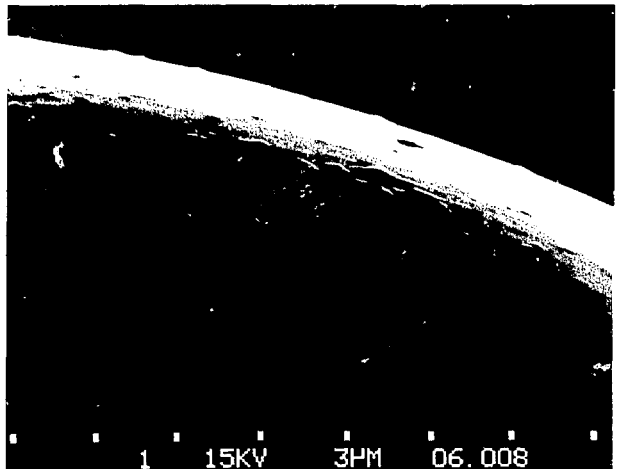
that can serve as a reference pole is identified, and a scan pattern is executed that provides full surface coverage. Each step is about  $60\text{ }\mu\text{m}$ , depending on magnification, and up to 156 photographs are recorded on the video disk. If a montage is desired, *Polaroid* photos are made simultaneously.

The completed scan is played back on the video disk to allow the operator to determine which defects require additional analysis. The  $4\pi$  examinations are performed with viewing normal to the sur-

face, so defect height is difficult to measure. Areas requiring additional measurements are repositioned to the electron collector side of the sphere and examined in profile (Fig. 5-44). In this location, a specially designed energy-dispersive x-ray detector that looks sideways between the tips can be used to obtain additional elemental information.

Figure 5-45 is a portion of a  $1000 \times 4\pi$  map of a microsphere that is almost target quality. In the lower center, we can see a group of defects that are a

Fig. 5-44. Defects on the surface of a  $15\text{-}\mu\text{m}$ -thick glass ball. The defects have been rolled to the edge for measurement in profile. At this location the defects can also be examined by EDS for their elemental composition.



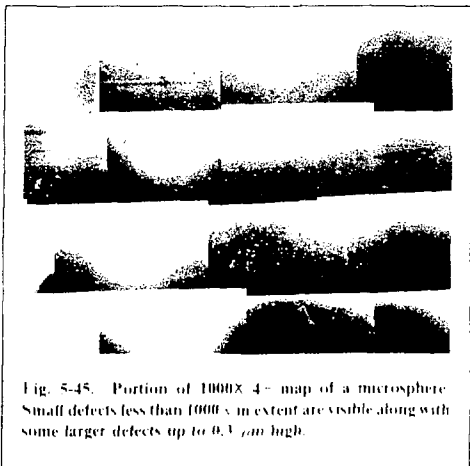


Fig. 5-45. Portion of 1000X 4+ map of a microsphere. Small defects less than 1000 Å in extent are visible along with some larger defects up to 0.3  $\mu$ m high.

few micrometers wide and less than 0.3  $\mu$ m high. These are visible in the interferometer but difficult to measure. The small white dots are less than 1000 Å high or wide and are completely undetectable by interferometry. A full map such as this requires up to 24 h to prepare.

To resolve difficulties with this system and to speed up examination time, we are building a computerized stage so that a completely automated system will be possible.

#### Author

C. M. Ward

### 5.5.4 Microradiography

Contact microradiography is a technique we have developed to further characterize targets with either opaque or transparent coatings. It has several advantages over other measurement techniques. Microradiography can distinguish defects in transparent coatings from those in the glass shell, and it can measure the internal structure in targets with opaque coatings.

Contact microradiography is a straightforward procedure. The microspheres are placed directly on a high-resolution glass film plate, typically Kodak HRP film, and the film plate is exposed to x rays in a vacuum chamber as shown in Fig. 5-46. The bremsstrahlung x rays used for exposure are emitted from a tungsten anode that is excited by electrons with an accelerating voltage from 3 to 10 kV. We choose the electron voltage to match microsphere

thickness and diameter. Because the thicknesses are on the order of 1 to 10  $\mu$ m, voltages are required to minimize attenuation of the x rays. The film plate is located about 50 cm from the x-ray source, which itself has a diameter of about 1 mm. The x-ray images are recorded with 100X magnification and have a geometric resolution about 0.2  $\mu$ m for a 200- $\mu$ m-diam. microsphere. Film-density mottling limits this resolution in practice to about 0.5  $\mu$ m. Examples of magnified microradiographs are shown in Fig. 5-47 for a single-walled glass microsphere, a Cf-coated glass microsphere, and a Kovar mandrel-coated with SiO<sub>2</sub> and Be. Measurements of coating and shell wall thicknesses and nonuniformities can be made with about 1- $\mu$ m accuracy by examining the image under a microscope at high magnification. Short- and small-scale defects can be detected, and it is possible to distinguish multiple layers of coatings as shown in Fig. 5-47(c).

We have encountered three problems in using microradiography for routine characterization: how

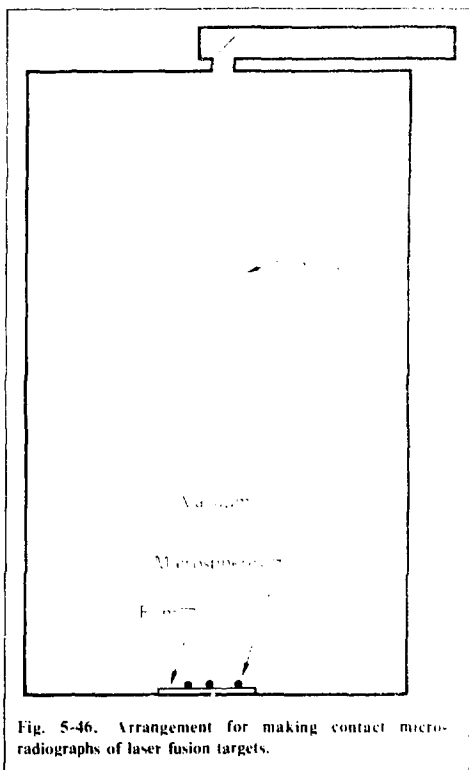


Fig. 5-46. Arrangement for making contact microradiographs of laser fusion targets.

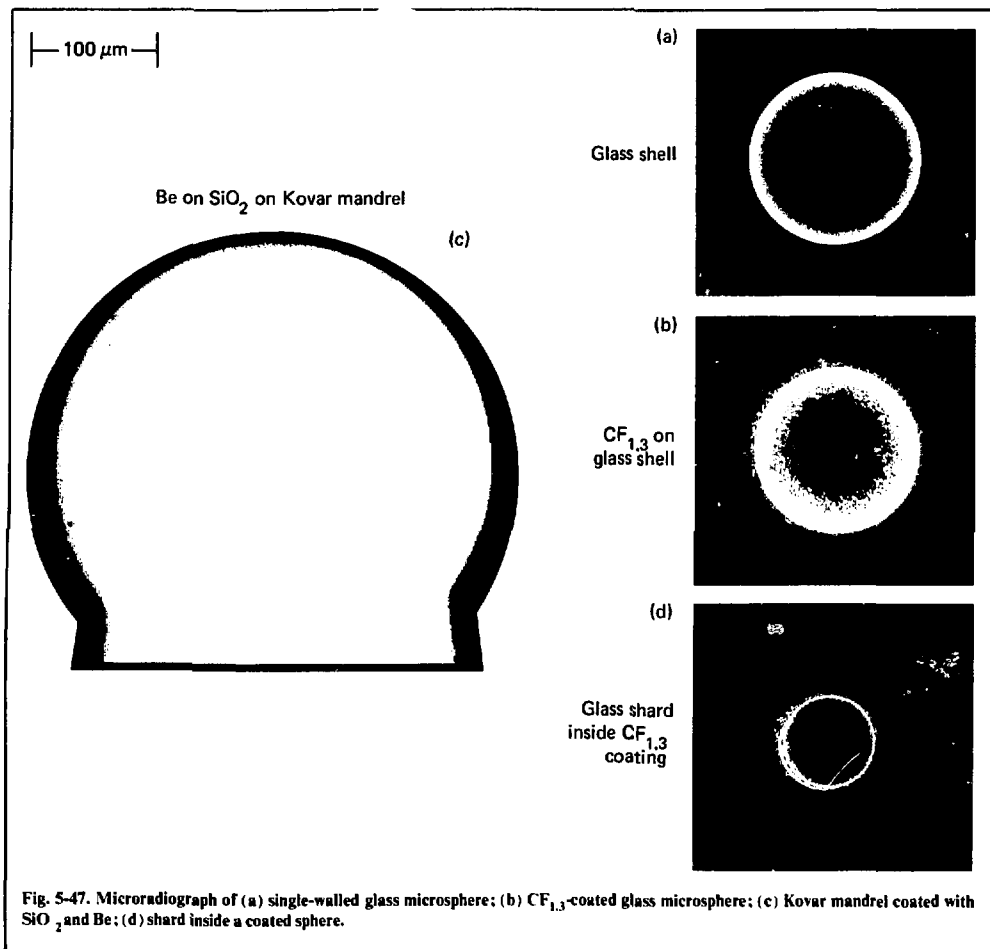


Fig. 5-47. Microradiograph of (a) single-walled glass microsphere; (b) CF<sub>1.3</sub>-coated glass microsphere; (c) Kovar mandrel coated with SiO<sub>2</sub> and Be; (d) shard inside a coated sphere.

to hold the microspheres in position for measurement without damage, how to make x-ray images of several views of the target, and how to get high-precision measurements of defects from the microradiographs. To meet these problems, we have developed a batch microsphere manipulator/holder and computer analysis techniques.<sup>27</sup> These approaches are different from work done at other laboratories.<sup>28,29</sup>

The microspheres must be held in place during exposure. If glue or oil is used as a holding agent, the microspheres are contaminated and are not useful for high-density implosion experiments. Our novel solution to this difficulty is to hold the balls between two plastic films, one of which is directly

against the photographic emulsion. A batch of microspheres can be rotated in an arbitrary direction by keeping the plastic film fixed against the plate, and by translating the second film [as shown in Fig. 5-48(a)]. Optimum resolution is achieved because the microspheres are at most only a few micrometers from the photographic plate. These microspheres can be routinely recovered for future use as targets. The microsphere holder is shown disassembled in Fig. 5-48(b). The plastic films are made of 2- $\mu\text{m}$ -thick Formvar. The ring on the right is inserted face down in the fixed part of the stage. The microspheres can be loaded onto either film, using a vacuum chuck. The ring on the left is then inserted onto the movable part of the translation

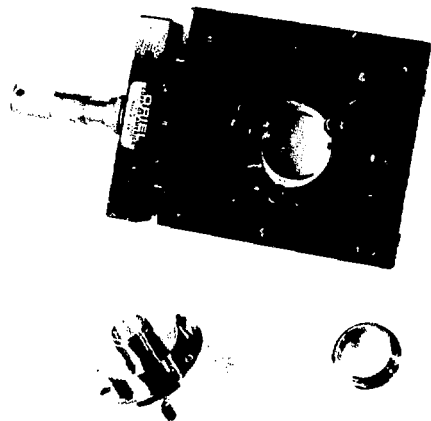
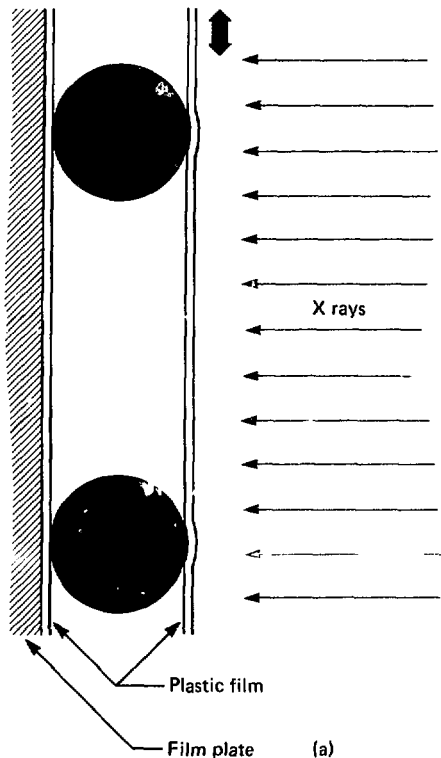
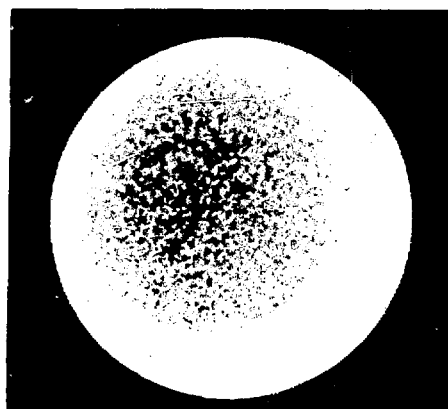


Fig. 5-48. Batch manipulator/holder for microradiography. (a) Principle of operation. (b) Disassembled manipulator.



100  $\mu\text{m}$

Mean x-ray energy: 5 keV

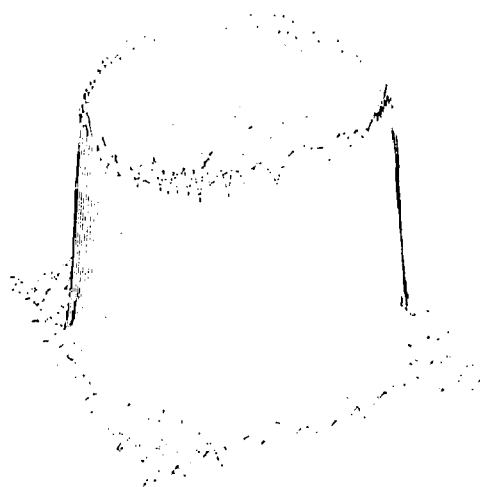


Fig. 5-49. Microradiograph of a glass microsphere and its computer representation.

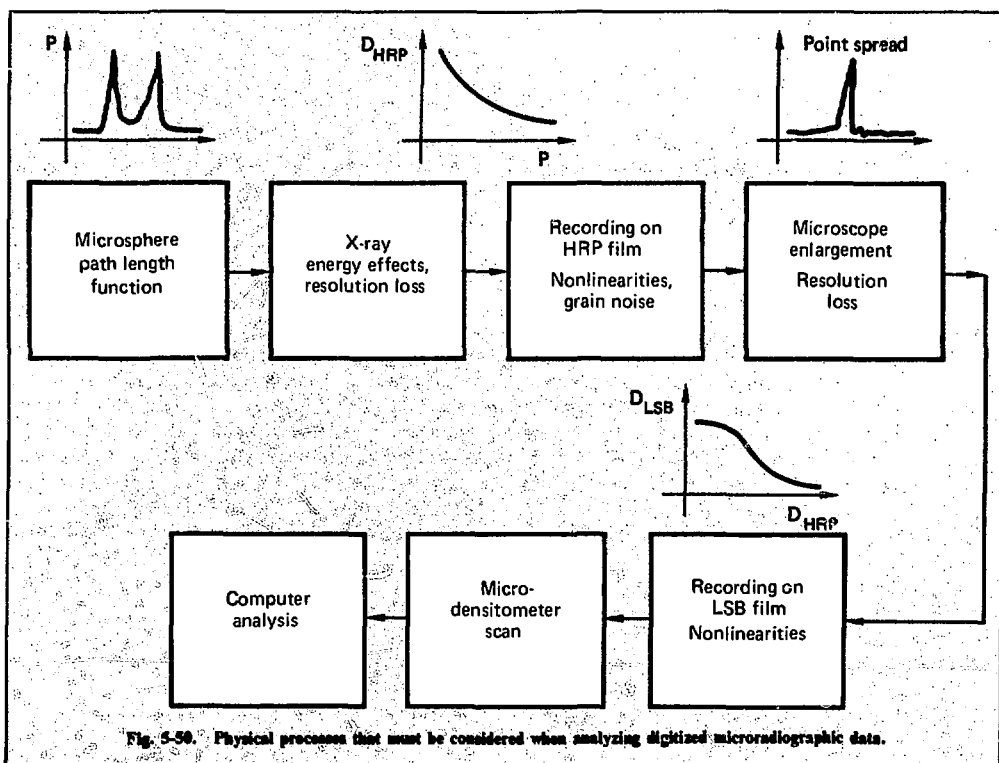


Fig. 5-50. Physical processes that must be considered when analyzing digitized microradiographic data.

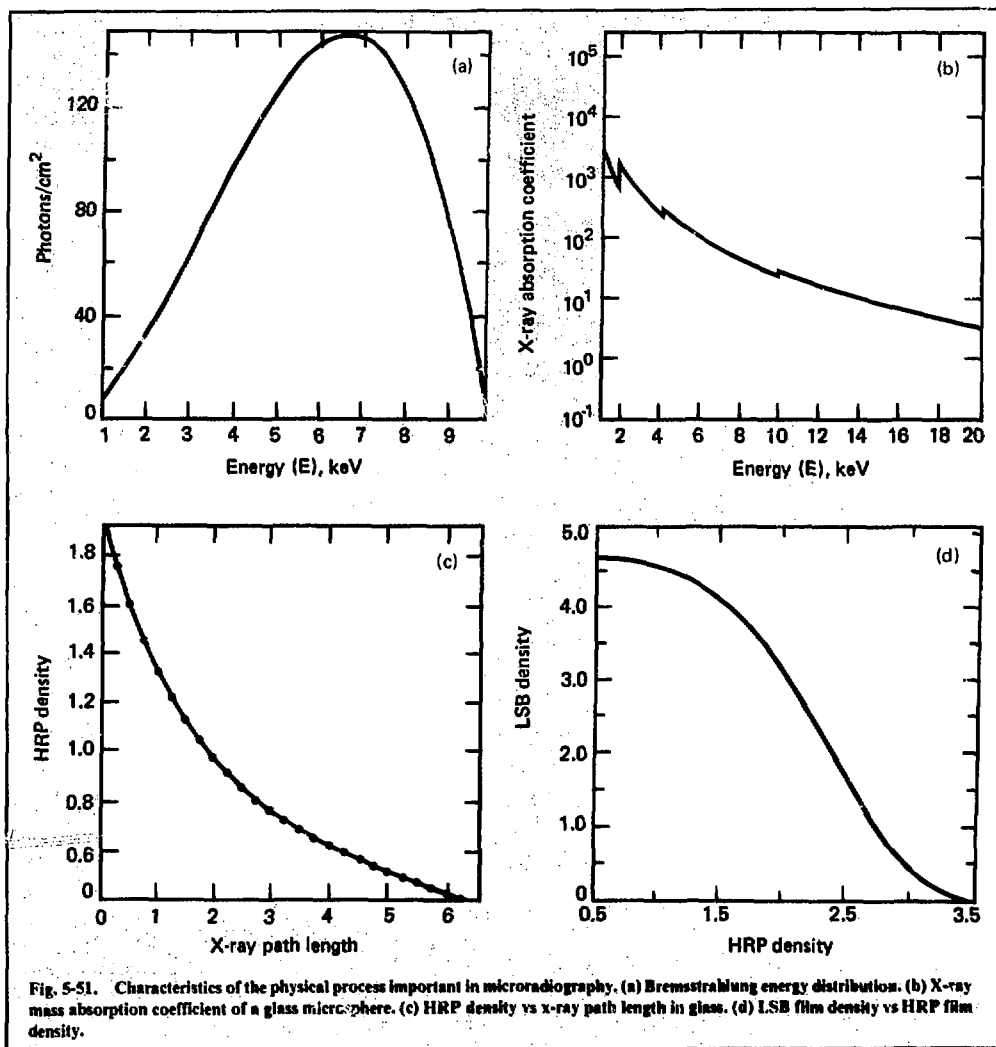


Fig. 5-51. Characteristics of the physical process important in microradiography. (a) Bremsstrahlung energy distribution. (b) X-ray mass absorption coefficient of a glass microsphere. (c) HRP density vs x-ray path length in glass. (d) LSB film density vs HRP film density.

this wedge and compute a calibration curve, using this image and the known exposure parameters [see Fig. 5-51(c)]. A nonlinear relation also exists between the HRP film density and the LSB film density. It is determined by exposing a photographic density edge onto the LSB film before it is developed. From the digitization of this wedge image, we can determine the correspondence of LSB film density to HRP density, as shown in Fig. 5-51(d). The relation between x-ray path length and LSB film density is now established by combining the data shown in Fig. 5-51.

One of the most prevalent types of defects that occur in hollow microspheres is a nonconcentricity (see Fig. 5-52). For a single-walled sphere, a nonconcentricity defect is the offset between the inner and outer centers. This type of defect is also the easiest to model and cross-check with interferometric measurements. We developed a computer model to characterize nonconcentricity with high precision and accuracy. This model relates the outer diameter, wall thickness, and nonconcentricity of the microsphere to the x-ray path length through it. The x-ray path length as a function of

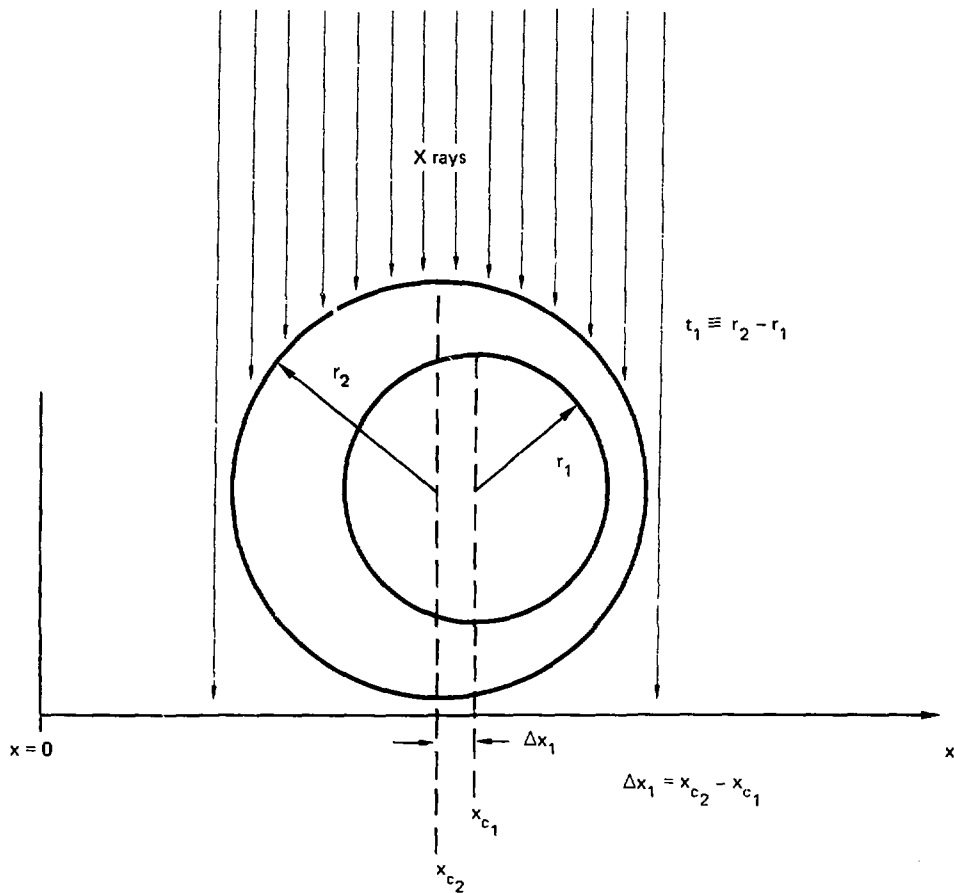


Fig. 5-52. Concentricity defect in a single-walled microsphere.



Microsphere No. 2332  
 Batch No. 9-019  
 Mean x-ray energy — 5 keV  
 Outer diameter — 132.4  $\mu\text{m}$   
 Thickness — 4.2  $\mu\text{m}$   
 Nonconcentricity — 0.6  $\mu\text{m}$

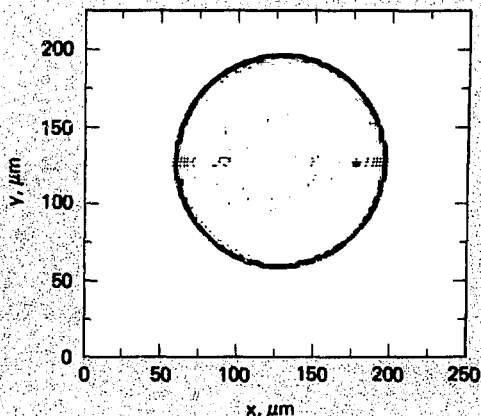
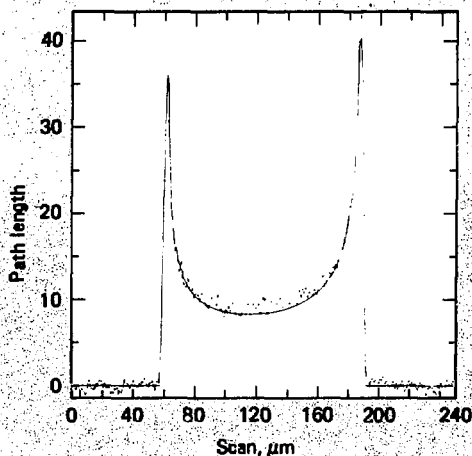
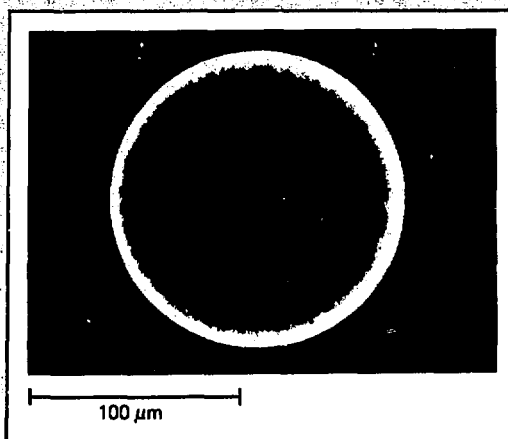


Fig. 5-53. Computer-analyzed microradiograph of a single-walled glass microsphere.

We have developed a microradiographic procedure that enables us to measure microsphere targets coated with single and multiple layers. We use the batch manipulator/holder to make microradiographs of several views of the microspheres so they can be recovered for use as laser fusion targets. We have also developed computer analysis techniques to quantitatively characterize single-walled targets and are extending these techniques for application to coated microspheres.

## References

27. R. M. Singleton, C. D. Hendricks, and B. W. Weinstein, *Microradiographic Measurement of Laser Fusion Targets*.

Lawrence Livermore Laboratory, Rept. UCRL-80148 (1977).

28. T. H. Henderson, D. E. Cielaszyk, and R. J. Simms, *Microradiographic Characterization of Laser Fusion Pellets*, KMS Fusion, Ann Arbor, Michigan, Rept. KMSF-U543 (1976).
29. R. H. Day, T. L. Elsberry, R. P. Kruger, D. M. Stupin, and R. L. Whitman, *X-Ray Microradiography of Laser Fusion Targets*, Los Alamos National Laboratory, Los Alamos, New Mexico, Rept. LA-UR-77-1651 (1977).

## Author

R. M. Singleton

## 5.6 Cryogenic Targets

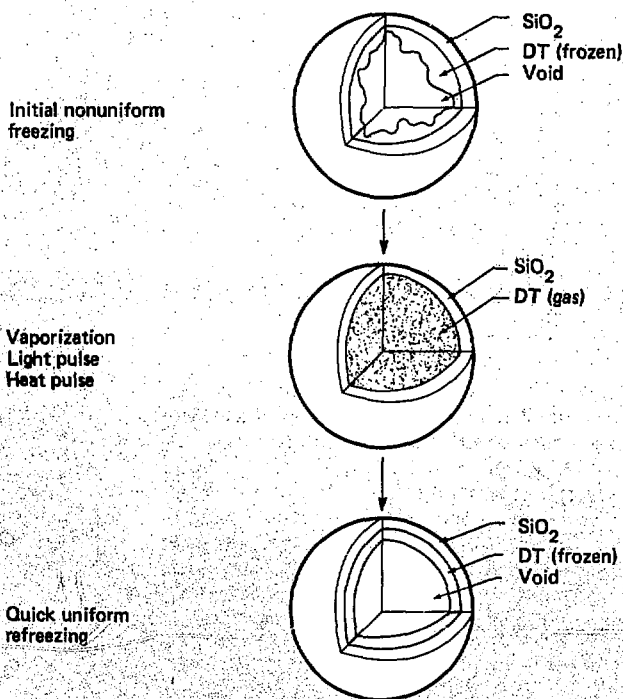
In advanced designs for high-performance laser targets, the DT fuel is at cryogenic temperatures, thus adding a completely new dimension to target fabrication. Not only must we prepare the DT fuel in the proper form and symmetry, but we must also ensure the integrity of the entire target at low temperatures. In addition, because the cryogenic targets can survive for only a very short time when surrounded by room-temperature radiation, special equipment for transporting and maintaining the targets in the laser target chamber is also needed. One example, as illustrated by the significant-thermonuclear-burn target shown in Fig. 5-54, is a hollow, multilayered sphere with an inner shell of uniformly frozen DT. As discussed in previous subsections, the individual layers must be properly interfaced and uniform because imperfections can seriously degrade target performance. The target design for scientific breakeven, which incorporates a liquid DT center, displays another possibility that may necessitate special low-temperature assembly techniques. In general, successful cryogenic laser fu-

sion experiments will require methods and apparatus for fabricating and handling a variety of low-temperature targets.

As a first step, we have developed techniques at LLL for freezing and characterizing a uniform layer of DT on the inside surface of hollow glass microspheres.<sup>30</sup> The gas-filled microsphere is placed inside a freezing cell and cooled to about 5 K. The cell volume surrounding the microsphere is filled with low-pressure (0.5 Torr) helium that acts as a heat-exchange gas. Upon initial cooling, the DT freezes in a nonuniform manner because gravity and surface tension act on the DT layer as it passes relatively slowly through the liquid state. However, by subsequently vaporizing and then rapidly refreezing the DT, we produce a uniform layer as illustrated in Fig. 5-54.

We use two methods of vaporizing the DT. In the first method, a light pulse focused on the microsphere vaporizes the DT without significantly affecting the freezing cell. The cold He gas in the freezing cell cools the microsphere, and the DT quickly refreezes. This method was first demonstrated by J. Miller<sup>31</sup> of LASL. We have ad-

Fig. 5-54. Technique for forming a uniformly frozen DT layer.



vanced this technique by using a much simpler and smaller freezing cell and Dewar, thus showing that a completely isothermal environment for the target is not required. The freezing cell temperature is not controlled, and there is no need to measure the temperature to better than about  $\pm 1$  K. Because the freezing cell surrounding the target must be removed before firing the laser, it is advantageous for the system to be small. This permits rapid removal of the cell with a minimum of disturbance. In addition, we are able to bring microscope objectives close to the target to obtain a high spatial resolution and adequately characterize the frozen DT layer.

The light-pulse method of vaporization requires optical access to the target and depends on the optical properties of the target. To overcome these limitations, we have developed a more general technique. A heat pulse from an electrical heater momentarily warms the freezing cell to about 40 K, thus vaporizing the DT. The small freezing cell has a fast thermal response and returns to 5 K within 5 s. This is quick enough for the DT to refreeze uniformly because it passes through the liquid state to the solid state in a few tens of milliseconds. The heat-pulse technique should work for the more complicated, multilayered transparent or opaque targets to be used in the future. Also, because optical access to the internal structure of the target is not necessary, interfacing with the laser target chamber is easier.

The heart of the apparatus is the copper freezing cell (shown in Fig. 5-55) that is attached to the cold tip of a Helitran Model LT-3-110 refrigerator. The glass microsphere is suspended between two 500-Å-thick Parylene films sandwiched between two copper washers as shown in Fig. 5-56. This suspension minimizes the discontinuity at the contact points because the films are tangent to the surface. The assembly is mounted in the center of the cell. The cell volume surrounding the microsphere is filled with He gas to a pressure of about 0.5 Torr. Quartz windows cemented to stainless steel insets in the cell provide optical access. The windows in the room-temperature vacuum jacket protrude through the liquid  $N_2$  radiation shield. The distance from the center of the cell to the outside surface of the exterior windows is only 7 mm.

To characterize the quality of the DT layer, we use the optical arrangement illustrated in Fig. 5-57. Parallel light from an argon laser illuminates the microsphere. The light is collected by a microscope objective, passed through an optical wedge, and then imaged on the face of a silicon vidicon TV

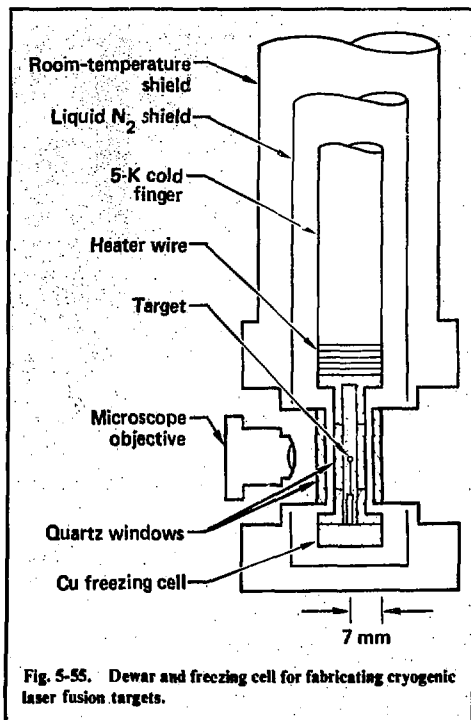


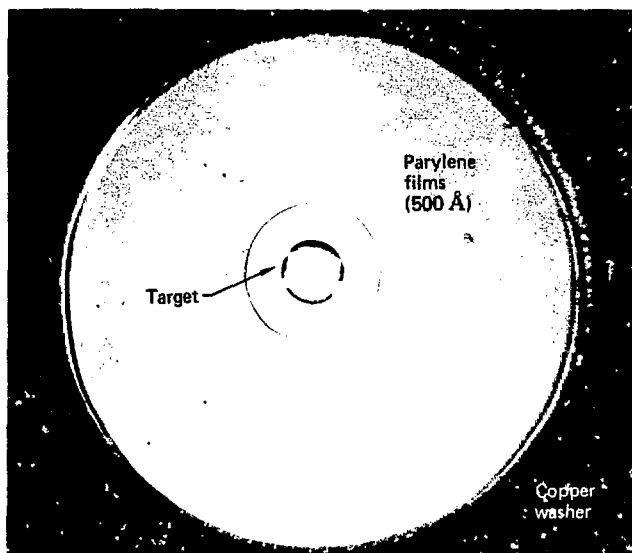
Fig. 5-55. Dewar and freezing cell for fabricating cryogenic laser fusion targets.

camera. The interference pictures of the freezing process are recorded on a video disk and video tape.

Because both surfaces of the wedge are 70% reflective, the wedge produces multiple images of the microsphere. Light that passes through the microsphere and DT layer overlaps and, therefore, interferes with light that passes next to the microsphere. The symmetry of the interference pattern on the microsphere image indicates the uniformity of the DT layer and the glass shell.

We have specially designed the wedge interferometer, illustrated in Fig. 5-58, to be compatible with a high-spatial-resolution microscope objective. The important parameters are the separation of the multiple sphere images and the phase uniformity of the background illumination. For a given focal length objective and image magnification, the wedge angle determines the separation. The image separation should be at least two to three times the diameter of the magnified sphere image, so that the interference patterns associated with each image do not overlap. Superimposed on the microsphere images is a background bull's-eye pattern, consisting of the Newton rings produced by the illumination

Fig. 5-56. Glass sphere suspension for isotropic targets.



o.d. 94  $\mu$ m  
 t 3.8  $\mu$ m  
 DT film 21.5 mg/cc

light as it diverges through the center of the wedge. The wedge thickness must be made small enough so that the center of the bull's-eye pattern is large compared to the sphere image, and to ensure phase uni-

formity of illumination over the sphere. For a 13-mm focal length microscope objective (10 $\times$  magnification) and 100- $\mu$ m-diam microsphere, the wedge should have about a 6-deg angle and be

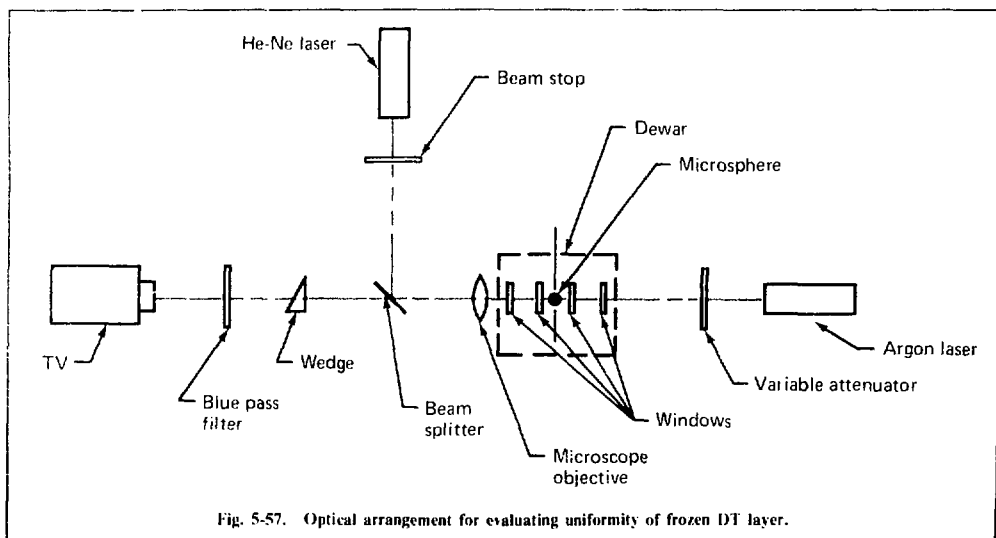


Fig. 5-57. Optical arrangement for evaluating uniformity of frozen DT layer.

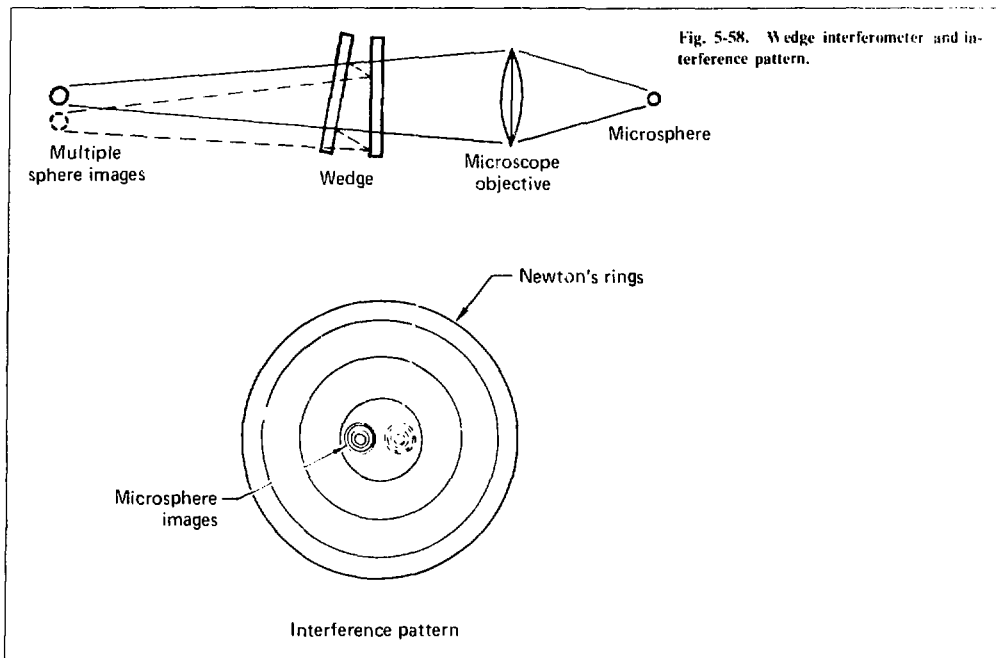


Fig. 5-58. Wedge interferometer and interference pattern.

about 200  $\mu\text{m}$  thick. Rather than trying to fabricate such a tapered piece of glass, we use two mirrors in a modified Burleigh VS-25 variable-spaced etalon to replace the wedge. The variable etalon has the further advantage that image separation and background phase uniformity can be optimized for each viewing lens and microsphere. Translating the wedge parallel to the bisector of the wedge angle adjusts the overall phase of the pattern.

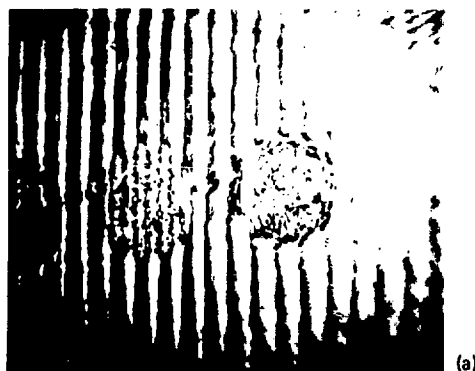
Typical interference patterns of the microsphere with both vaporized and frozen DI are shown in Fig. 5-59. The microsphere has an outside diameter of 94  $\mu\text{m}$ , a 3.8- $\mu\text{m}$  wall thickness, and the DI layer is 1.1  $\mu\text{m}$  thick when frozen. These photos were taken during a heat-pulse sequence. It is evident that the DI has retrofrozen quite uniformly. We obtained similar data for a light pulse.

To quantify the quality of the frozen DI layer, it is convenient to expand the defects in terms of spherical harmonics. A first-order defect occurs when the inner surface of the DI layer is not concentric with the outer surface. This causes the expected circular interference pattern not to be centered on the sphere image. By adding a quantified linear phase gradient to the interference pattern until the pattern is centered on the sphere image, the

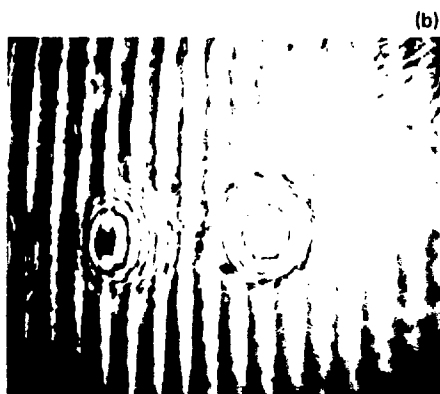
amount of nonconcentricity can be quantitatively measured quite simply and accurately.<sup>10</sup> By eye, we find that the DI layer in Fig. 5-59 is concentric to better than 20%. More sensitive image analysis techniques should also extend to sensitivities of 5% or less.

Higher order defects show up as deviations in the interference pattern from the sphere image from a perfect set of concentric circles. The microsphere that we used for these experiments has some defects. We have not yet evaluated whether the magnitude of the higher order defects is any in the DI layer. Our optics can easily resolve thickness variations in the DI on the order of 0.6  $\mu\text{m}$ . Detecting variations at least as small as 0.1  $\mu\text{m}$  should be possible.

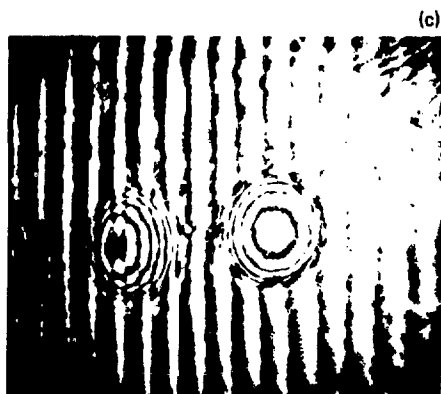
We have shown, using a relatively simple cryogenic apparatus, that it is possible to produce a uniform layer of DI on the inside surface of a hollow sphere. However, interfacing this target with the Shiva laser facility imposes several constraints on the cryogenic equipment. We have written the specifications for a cryogenic pylon and target support that meet both the target fabrication and Shiva laser system requirements. The cryogenic pylon is being designed and constructed by the National Bureau of Standards laboratory in Boulder.



(a)



(b)



(c)

Fig. 5-59. Interference photos of glass microsphere during frozen DT layer formation. The images on the left are an artifact of the interference process. (a) Initial nonuniform freezing of DT, temperature about 5K. Note mosaic pattern caused by DT distribution. (b) Vaporization of DT by fast heat pulse, temperature  $>30$  K. Residual pattern of glass microsphere. (c) Quick uniform refreezing, temperature about 5K. Circular fringes similar to those in (b) indicate that the DT has frozen uniformly.

## References

30. R. L. Woerner and C. D. Hendricks, "Fabrication of Cryogenic Laser Fusion Targets," in the *Technical Digest of the Proc. of the Topical Meeting on Inertial Confinement Fusion*, San Diego, Calif. February 7-9, 1978.
31. J. F. Miller, "A New Method for Producing Cryogenic Laser Fusion Targets," *Adv. in Cryog. Eng.* 23, K. D. Timmerhaus, Ed. (to be published).
32. B. W. Weinstein and C. D. Hendricks, *Interferometric Measurement of Laser Fusion Targets*, Lawrence Livermore Laboratory, Rept. UCRL-78477, Rev. 1 (1977).

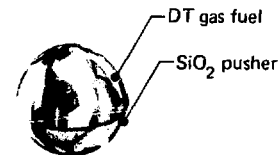
## Author

R. L. Woerner

## 5.7 Production of Power-Plant Inertial Confinement Fusion Targets

For the inertial confinement approach to fusion energy production to be economically feasible, some means must be provided to produce the targets in a completely automated system at rates of about 10/s. This system must reliably produce a high-quality, well-controlled product.

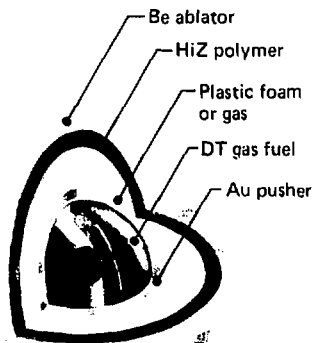
The general concept of the targets to be considered is shown in Fig. 5-60. Although these targets are specific, the generalized concepts for automating the fabrication of these targets will be useful for other targets and will display one approach to the problem of a target factory.



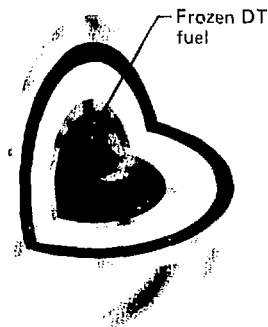
Exploding pusher  
(40-400  $\mu\text{m}$ )



100X liquid density  
(200-400  $\mu\text{m}$ )



1000X liquid density  
(500-1000  $\mu\text{m}$ )



Significant thermonuclear burn  
(500-1000  $\mu\text{m}$ )

Fig. 5-60. Generalized target designs shown in increasing sophistication and yield.

Table 5-2. Ball-on-stalk target specifications.

Ball diameter	Selected to $\pm 5 \mu\text{m}$ Measured to better than $1 \mu\text{m}$
Wall thickness	Selected to $\pm 0.2 \text{ mm}$ Measured to better than $\pm 0.05 \mu\text{m}$
Sphericity	Selected to better than 1% Measured to better than 1%
Surface finish	Selected to better than 1000 A Measured to better than 100 A (contour mapped over entire surface if necessary)
Fuel fill	Filled to $\pm 20\%$ Selected and measured to $\pm 10\%$ (5% if necessary)
Stalk	Pulled from glass tube or rod or selected from $\text{Al}_2\text{O}_3$ or C fibers
Cement	Epoxy or other suitable bonding agent
Assembly	Under microscope by hand or with use of micromanipulators

than one man-day of effort. However, when the research mode of inertial confinement fusion is joined by the power production mode, the targets must be produced at high rates, must be of high quality, and may need to be produced at costs of less than about 50 cents if ICF power production is to be economical.

To approach the problems of production of inexpensive targets, several aspects of the fabrication processes must be reconsidered:

- Fuel container production (glass, plastic, or metal shells, or the fuel itself as its own container).

- Layer coating.
- Surface and interface characteristics.
- Fuel state.
- Required production rate.

Let us examine first the unlikely situation in which the target is a solid, cryogenic sphere of DT. Solid spheres of cryogenic materials including hydrogen have been produced at high rates. For example, Hendricks and his colleagues at the University of Illinois have generated hydrogen spheres at rates of up to  $10^5/\text{s}$  and diameters greater than  $100 \mu\text{m}$ . The unused spheres can be recirculated and the fuel reused.

Because simple solid spheres are unlikely targets, modifications must be considered. A target

that is again somewhat unlikely in its simplest form is the simple hollow spherical shell of frozen hydrogen (DT). Such hollow shells have been experimentally produced by Hendricks' group at Illinois.<sup>33</sup> The shells have been generated at high rates and very low cost per target.

Such unlikely targets are only stepping stones to more realistic, more complicated ones. Consider a possible multishell target composed of a frozen core of fuel (DT) surrounded by several concentric shells of various materials, possibly including neon, argon, and hydrogen. Studies leading to production of such multilayer cryogenic shells have been underway for some time with experimental success. Experimental and analytical research is being carried out on similar layered structures with a central hollow shell of DT. Such targets can be formed in a sequence of steps in a column or columns containing the coating materials. Each of the coatings is in an isolated chamber at a temperature suitable for condensation on the previous layer.

However, we must consider the possibility that the layered structures may not be totally cryogenic—only the innermost layer of DT fuel may be at a low temperature. For such a target type, can we still consider depositing coatings and layers on the target in a production-line mode? It should be obvious that we can do so. Consider a spherical multilayer target in which the fuel is contained inside a thin hollow shell of glass as with current targets. By perfecting and optimizing current techniques of glass shell production, such as those used by LLL, KMSF, 3M, etc., we expect that a high yield of target-quality shells can be produced at high rates (about  $10^3/\text{s}$  at LLL; similar rates are assumed for the KMSF processes). In a production system, the glass shells must be characterized as they come from whatever unit generates them. Computer-sensed, -analyzed, and -controlled techniques must be used to measure the appropriate parameters and either accept or reject the shells—all at a rate of perhaps  $10^3/\text{s}$ . Current technology in computerized image dissection and analysis as well as optical matrix sensor methods are capable of performing such tasks. For example, a hologram of an ideal spherical shell can be stored in digital form in the computer memory. As a real shell passes through a suitable optical system, a holographic image of the real shell can be produced and projected onto a matrix of sensors. The output of the sensors can then be compared with the stored image elements of the ideal shell. If the two sets agree well enough, the shell is accepted and passed to the next stage of the system. If the sets do not agree, the shell is rejected. Throughout the target production process, similar



techniques will be used for characterization after every step. At no point in the process can we afford to manually pick up and examine or manipulate one target. At \$25 per hour, one second of manpower costs 0.69 cents. One minute of effort to "look at" or "pick up" a target costs about 42 cents.

Assume the characterization is accomplished and we have  $10^3$  high-quality, empty, hollow shells arriving each second at some point in our production line. If they accumulate for just over one day, there will be enough microspheres for a one-shot-per-second power plant for one year, if every process in the production line were perfect. Because the various steps are not perfect, enough shells must be made so that the unsatisfactory targets may be thrown away, with still enough targets remaining for power plant operation. The shell generation system must run almost continuously to allow for rejection of some targets at each coating step. After perhaps  $10^6$  satisfactory shells have accumulated, a batch DT fill process may be done. The time constant for DT filling is a few hours; to ensure uniform results, a 24-h period should be satisfactory. Following the batch DT fill process, the shells would again enter the production line individually to be coated with various required layers of material. There are coating processes under development that should enable us to deposit many micrometers of polymers on glass shells in a short time. Coating processes used by the chemical industry may be adaptable to our needs. Coating materials, their properties, and the methods by which they can be deposited will require creative research and development before the targets can be produced for a few cents, but it can be done.

The successful development of inertial confinement fusion for power production depends critically on the feasibility of high-rate, high-yield target production. The production rates and allowable cost-per-target scale with the output power yield of the target. Target yields of 0.01, 0.1, and 1.0 tons (1-ton yield is approximately  $4 \times 10^9$  J) require production rates of 10, 1, and 0.1/s, respectively, and allow economic power production in projected power plant designs with per-target cost of 0.01, 0.10, and 1.00 dollars, respectively. These estimates are based on the current assumptions of driver and target performance scales to a power-producing target.

With these rate and allowable cost requirements, and considering the delicate nature of the product, this process system in all probability must be totally automated.

Each process will occur in a controlled environment. The overall production yield of the process

must exceed 95%, or much of the output power will be used to drive defective targets.

Another constraint on the process is that the inventory of tritium be low. The largest part of the inventory exists in the form of targets, and the total inventory scales with process time for a target. The absolute value of the inventory also depends critically on the target concept and at which step in the processing the fill occurs.

### 5.7.1 Design Features of Power-Production Class Targets

Production-class targets as shown in Fig. 5-60 consist of multilayered concentric shells. The outside surfaces of these shells and the interfaces between the layers must be smooth enough to satisfy Rayleigh-Taylor stability requirements. At the outside surface of the target, which ranges from 1 to 10 mm in diam, the most unstable Rayleigh-Taylor spatial wavelength is approximately 50  $\mu$ m with an allowable defect height of 100  $\text{\AA}$ . (Other wavelength defects have allowable heights similar to those described in Fig. 5-61.) These successive layers on the target must be concentric with tolerances of 1 to 3  $\mu$ m. In the multishell targets, one or more of the layers can be voids, thus creating the need to levitate the shells. The concentricity of levitated shells is the same as for the layers (1 to 3  $\mu$ m).

The outermost layer is composed of low-Z, low-density materials that perform efficiently as ablaters. Some examples are Be, LiH, or frozen  $\text{H}_2$ . Intermediate pusher layers are mostly low-atomic-number materials seeded with a small atomic fraction of high-Z material. The inner pusher, ex-

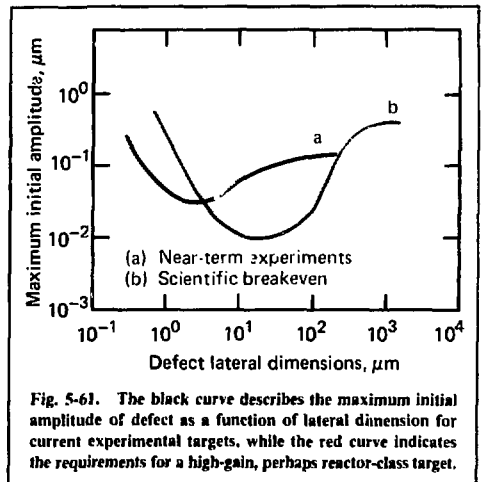


Fig. 5-61. The black curve describes the maximum initial amplitude of defect as a function of lateral dimension for current experimental targets, while the red curve indicates the requirements for a high-gain, perhaps reactor-class target.

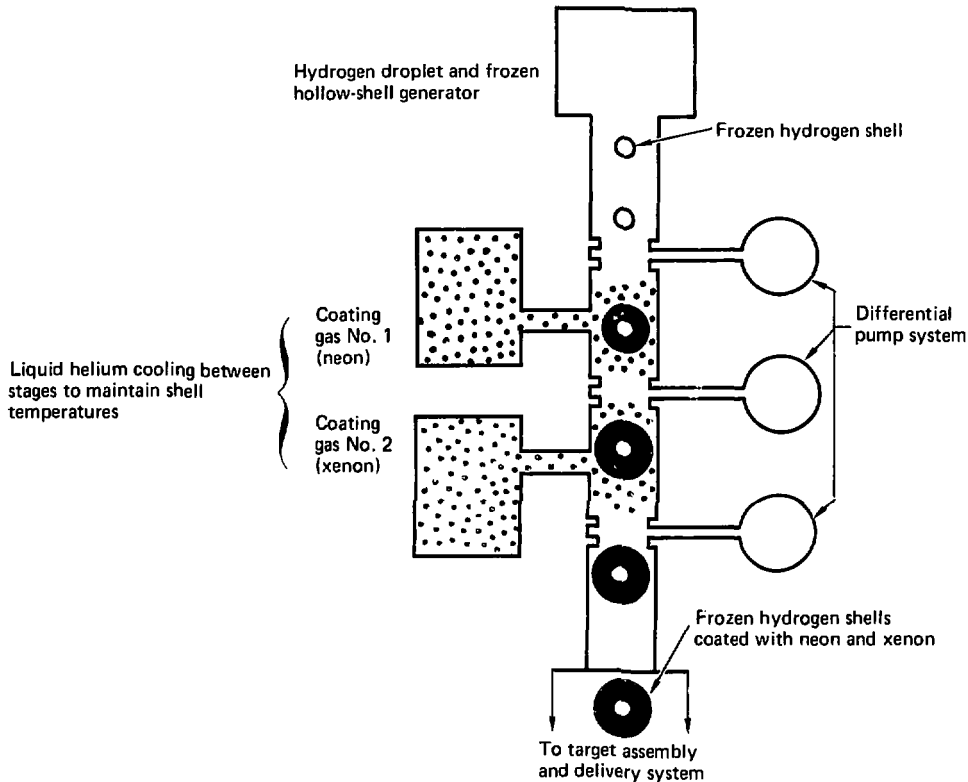
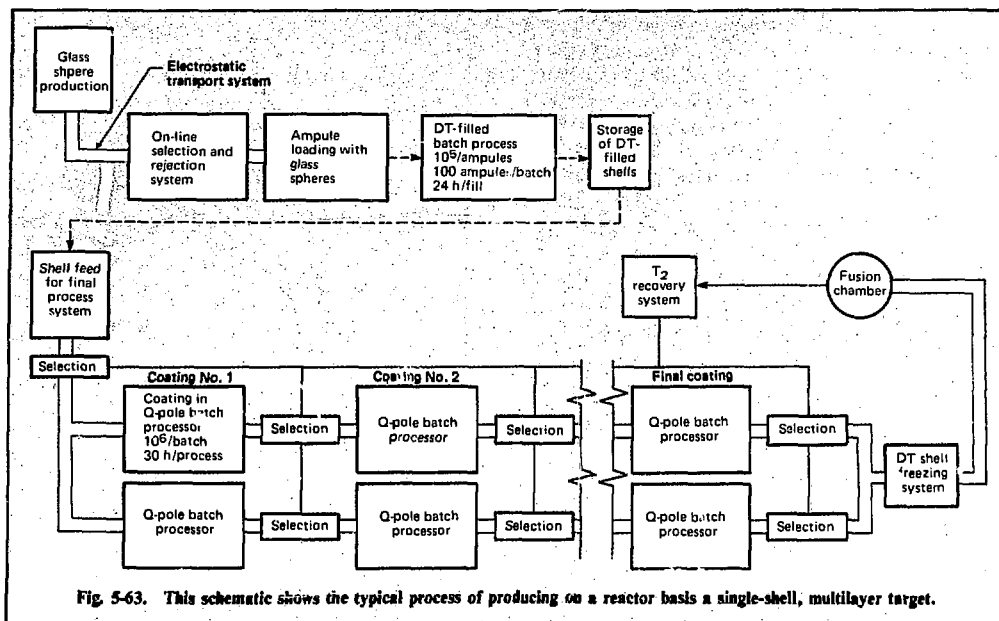


Fig. 5-62. Multilayer cryogenic target production, accomplished by sequentially condensing layers on the fuel core.



### 5.7.3 Layered Shell Fabrication

In a double-shell target, the inner shell has a diameter up to several hundred micrometers with a diameter-to-wall ratio of about 10:1. This shell is the inner pusher and can be made of higher-atomic-number materials. It may consist of a thin mandrel coated to produce the proper shell material. Processes currently used to generate glass shells and subsequently coat them with polymerized fluorocarbon must be greatly refined, until only a few easily detectable defects can be expected to limit the yield of that process.

In the single-shell target, the shell must be about 1 to 10 mm in diam. Shells of this size have been made of glass and plastics, but techniques must be extended to materials of low atomic number, perhaps seeded with high-atomic-number elements. Techniques must be developed to construct the shells with a fuel fill tube attached, or to attach a fill tube on a production basis without degrading surface finish.

The coating of the shells, while preserving the surface finish, requires much development. We must study grain boundary growths, stoichiometry of materials, and coating conditions to ensure amorphous material deposition. We must develop methods to adapt the coating-material-atmosphere production processes to the target transport and

manipulation system. If we have to coat fuel-filled shells, we must then further develop systems by which surfaces can be coated at cryogenic temperatures.

If we condense layers on a cryogenic mandrel for target production, we must determine the nature of materials coated below the freezing point of DT (20 K).

Therefore, to produce an inner or single shell, we must develop processes to fabricate shells of various materials within design specifications. Techniques also must be generated to coat shells and to make these processes compatible with the transport and manipulation systems.

### 5.7.4 Layered Hemishell Fabrication

In double-shell targets, the outer shell may be constructed from hemishells. Micromachined mandrels coated in layers may have the hemishell mating edge machined before the mandrel is etched away. As with the shell coating, we must also develop coating techniques and etching methods.

### 5.7.5 DT Fill

In reactor targets, the fuel must be at high density in the single shell. The filled shell must be coated to form a layered structure that meets the design constraints to avoid Rayleigh-Taylor instability during the implosion process.

There is considerable advantage to filling a target with fuel after much of the processing is complete. In the double-shell target, most of the tritium is contained in the outer shells. Thus, the hemishells can be made with reasonably standard non-cryogenic techniques, allowing the frozen fuel to be added just before the hemishell sealing process. The amount of tritium in inventory depends primarily on the time the tritium spends in targets being processed. The procedure to fill targets after they are assembled could reduce, by as much as a factor of five, the tritium inventory needed if the fill remains with the target throughout processing.

### 5.7.6 Assembly

To produce reactor targets, we need to assemble hemishells with internal concentric shells to the required high accuracy and at production rates. If a fill tube is not feasible, assembly and bonding must be accomplished at  $<20$  K to avoid excessively high pressures and to retain the fuel. Methods that support concentric shells with minimal material are required. Polymeric films as thin as  $100 \text{ \AA}$  are used to support spherical shells in a concentric configuration. Other techniques of support, using gas jets or electric or magnetic fields for example, represent the next level of development. Because small-scale defects are allowed on production targets (1 to  $5\text{-}\mu\text{m}$  wavelengths with 1 to  $5\text{-}\mu\text{m}$  height), the seam and some minor surface damage can be tolerated if relatively long-wavelength tolerances (approximately  $50 \mu\text{m}$ ) are met.

### 5.7.7 Characterization

The defect in production targets that concerns us most has an extremely low aspect ratio: defect height/spatial wavelength  $\sim 10^{-4}$ . Many of the materials suggested for these layered shells or hemishells are opaque to visible light, precluding the use of highly developed optical techniques. The lack of intense coherent radiation sources at short wavelengths makes it very difficult to attain resolutions as low as  $100 \text{ \AA}$ .

Assembled targets or subassemblies are difficult to characterize quickly and efficiently. The  $\rho R$ -type defects in seams of hemishells as well as pieces damaged during assembly are particularly difficult to measure. Production processes need to be developed to the point where it is necessary to monitor, at most, one or two easily detected defect types per process step to be assured of quality control. Occasional (say, one out of a thousand) targets can be withdrawn and completely characterized for statistical monitoring of the processes.

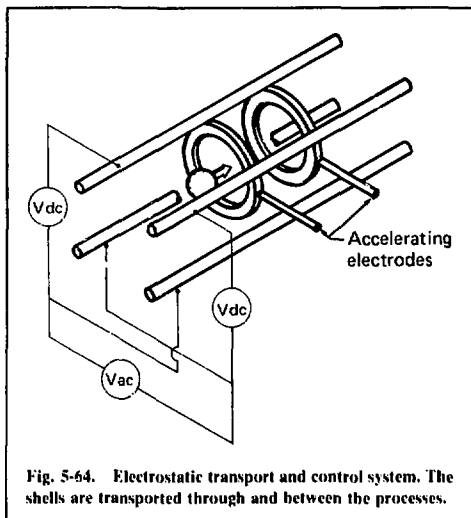


Fig. 5-64. Electrostatic transport and control system. The shells are transported through and between the processes.

### 5.7.8 Transport and Manipulation

The surface finish requirement makes it difficult to transport and manipulate the shells, hemishells, and partially or totally assembled targets. Support and transport methods include electrostatic, electrodynamic, gas jet, acoustic, magnetic, and focused laser-light-beam levitation. Of these, the electrostatic or electrodynamic techniques currently appear to offer the most useful methods. Other methods, including reliable containment and manipulation of small parts without damage, must be developed.

A schematic of a target factory is shown in Fig. 5-63. The glass shells are produced by means of a droplet generator that delivers droplets of glass solution into vertical furnaces. Axial airflow centers the glass solution droplets and particles in the drying and blowing sections of the heating cycle. Vertical airflow and gravity move the particles through the furnaces. These furnaces can be sectional to obtain any length required. An electrostatic transport system can transport particles between furnace sections and into and through subsequent portions of the system. The electrostatic transport and control system consists of quadruple rails, as shown in Fig. 5-64. Electrodes, located in the rail, sense the particle charge and velocity, while other stations adjust the charge and velocity to the required values. Masuda et al.<sup>34,35</sup> have given much attention to these systems of particle transport.

The transport system receives the particles from the furnace section and delivers them to a

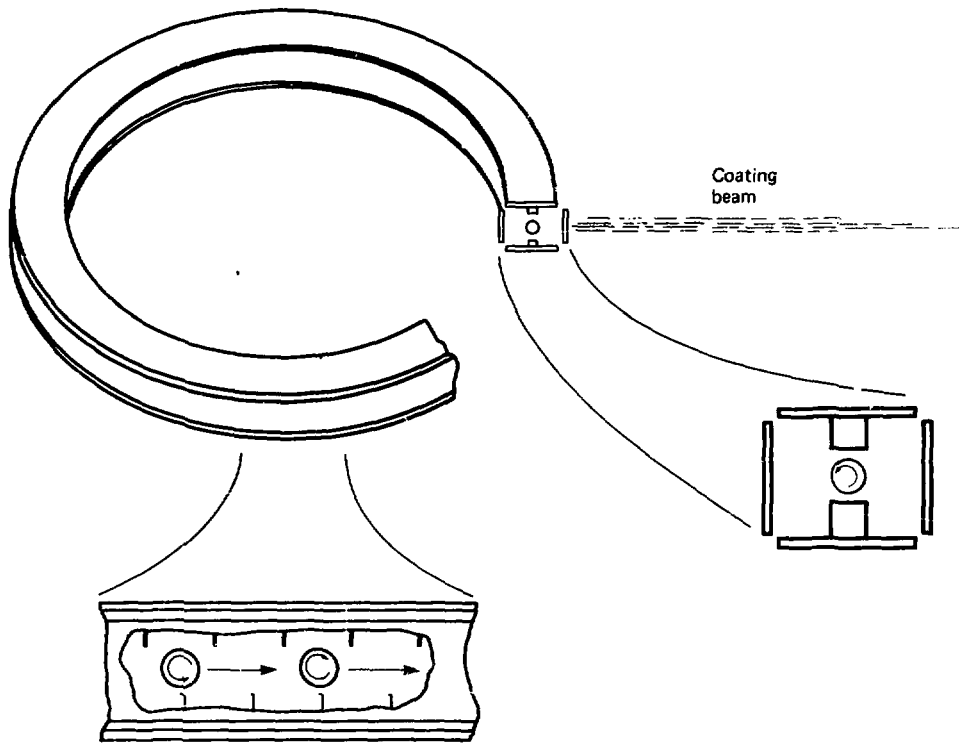


Fig. 5-65. Coating batch processor. This system allows a batch of shells to be sequentially processed to achieve uniform surface.

## References

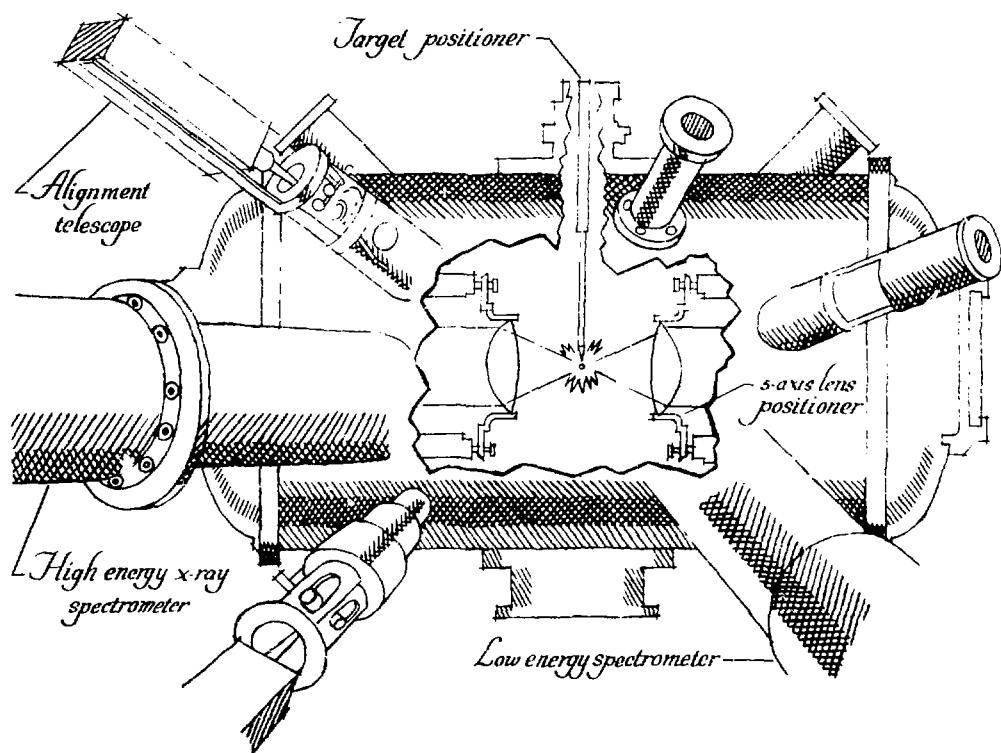
33. C. D. Hendricks, I. Foster, and R. J. Turnbull, "Hollow Hydrogen Spheres for Laser Fusion Targets," *Applied Physics Letter* **26**, 580 (1975).
34. S. Masuda and K. Fujibayashi, "Advances in Static Electricity," in *Proc. of the 1st International Conference on Static Electricity* (Vienna, Austria, 1970), Vol. 1, pp. 384-397.
35. S. Masuda, K. Fujibayashi, and K. Ishida, "Advances in Static Electricity," in *Proc. of the 1st International Conference on Static Electricity* (Vienna, Austria, 1970), Vol. 1, pp. 398-414.
36. R. E. Wuerker, H. Shelton, and R. V. Langmuir, *J. Appl. Phys.* **30**, 342 (1959).
37. R. L. Woerner, "Cryogenic Laser Fusion Target Fabrication at LLL," unpublished post-deadline talk at the Cryogenic Engineering Conference (Boulder, Colorado, Aug. 2-5, 1977).
38. J. R. Miller, "A New Method for Producing Cryogenic Laser Fusion Targets," in *Proc. of APS Plasma Physics Meeting* (San Francisco, California, Nov. 15-19, 1976).
39. J. R. Miller, "A New Method for Producing Cryogenic Laser Fusion Targets," in *Proc. of 1977 Cryogenic Engineering Conference* (Boulder, Colorado, Aug. 2-5, 1977), to be published in *Advances in Cryogenic Engineering*, **23**.

## Authors

**C. D. Hendricks**  
**W. L. Johnson**

# SECTION 6

## LASER FUSION EXPERIMENTS AND ANALYSIS



## SECTION 6

### CONTENTS

6.1	Overview . . . . .	6-1
6.2	Determination of the Scale Height and Density Jump at Critical Density from Measurements of the Polarization Ellipse of the Scattered Light . . . . .	6-1
6.3	Interferometry for Absorption Physics Studies . . . . .	6-5
6.4	Polarization and Angular Dependence of 1.06- $\mu\text{m}$ Laser Light Absorption by Planar Plasmas . . . . .	6-7
6.5	Brillouin Scattering in Laser-Produced Plasmas . . . . .	6-12
6.6	Time-Resolved High-Energy X-Ray Spectra Measurements . . . . .	6-17
6.7	Experimental and Theoretical Investigation of High-Z Disks Irradiated with 1.06- $\mu\text{m}$ Laser Light . . . . .	6-21
6.8	Exploding-Pusher Target Experiments on Argus . . . . .	6-28
6.9	Images of High-Energy X-Ray and Thermonuclear Alpha Particle Emissions from Exploding-Pusher Targets on Argus . . . . .	6-31
6.9.1	High-Energy X-Ray Images . . . . .	6-31
6.9.2	Thermonuclear Alpha Particle Images . . . . .	6-34
6.10	A Simple Model for Exploding-Pusher Targets . . . . .	6-38
6.10.1	Derivation of the Simple Model . . . . .	6-38
6.10.2	Compression Phase . . . . .	6-38
6.10.3	Explosion Phase . . . . .	6-38
6.10.4	Acceleration or Useful Energy Phase . . . . .	6-39
6.10.5	Neutron Production . . . . .	6-41
6.10.6	Comparison of Simple Model with Experimental Results . . . . .	6-41
6.10.7	Conclusions . . . . .	6-46



## SECTION 6

# LASER FUSION EXPERIMENTS AND ANALYSIS

### 6.1 Overview

Experiments performed in 1977 determined critical parameters in the interaction of intense laser light with plasma. Using plastic disks and the Janus laser, we measured the variation of the absorption fraction with the angle of incidence and polarization, the spatial and temporal density profiles in the critical density region, and the x-ray spectral emission history. The results of these experiments generally agreed well with theory and computer calculations. We also conducted experiments with high-Z disks on the Argus laser in which we varied the laser intensity, spot size, and pulse length, and measured the absorption fraction and x-ray emission. The results of these experiments — and the results of experiments with other targets — emphasized important theoretical uncertainties in the mix of collisionless and collisional absorption, in inhibited transport of thermal and superthermal electrons, in fast-ion losses, in stimulated scatter, and in multi-frequency non-LTE opacities. More sophisticated experiments are planned to improve our understanding of these complex physical processes.

#### Authors

H. G. Ahlstrom  
J. H. Nuckolls

### 6.2 Determination of the Scale Height and Density Jump at Critical Density from Measurements of the Polarization Ellipse of the Scattered Light

In §5-7.2 of the 1976 annual report, we discussed a method of estimating the scale height and density jump from ellipsometric measurements of the scattered 1.06- $\mu\text{m}$  light. An instrument to measure the Stokes parameters of the scattered light was also described in §3-3.3. In 1977, we measured the polarization ellipse of the light specularly reflected from tilted Parylene disks irradiated by 30-ps, 1.06- $\mu\text{m}$  light pulses focused by an  $f/10$  lens. We present those measurements here.

The s- and p-polarized components of the light

incident upon the tilted disk obey different wave equations and have different complex-amplitude reflectivities. In particular, the difference in phase shifts between the s- and p-polarized components increases approximately monotonically from 0 to 180° as the scale length for an assumed ramp density profile decreases from infinity to zero. If the density ramp is truncated at some finite plateau density at the higher density end, the phase difference approaches some limit 180°- $\epsilon$  short of 180° as the scale length becomes very short. However, the phase difference is independent of this upper plateau density for scale lengths long enough to prevent the evanescent field from seeing this plateau. Knowledge of the phase difference does not uniquely specify either the scale length or the density jump, because an infinity of combinations of scale lengths and upper and lower plateau densities gives the same phase difference. However, there is a definite upper limit to the possible scale length and a lower definite limit to the possible density jump.

The ellipsometer (Fig. 6-1) measures the amounts of light  $I(\theta)$  polarized in four different linear polarization states (electric field at angles  $\theta = 0, 45, 90$ , or  $135^\circ$ ), and in the left and right circular polarizations ( $I_{LH}$  and  $I_{RH}$ , respectively). Only four of any such set of measurements can be independent. Because the amounts of light polarized in orthogonal states must sum to the total light energy, we have the two linear relationships:

$$I(0^\circ) + I(90^\circ) = I(45^\circ) + I(135^\circ) = I_{RH} + I_{LH}.$$

This redundancy will reveal an incorrect measurement.

The ellipsometer looked at the light reflected back at an angle of 45° to the beam axis (Fig. 6-2). The target was tilted by 22.5°, so we observed the peak of the specularly reflected light. The laser beam had its electric vector at approximately 45° to the plane of incidence, ensuring that the s- and p-polarized components had nearly equal amplitudes. The short pulse length of 30 ps and small spot size of 80- $\mu\text{m}$  diam minimized the importance of stimulated Brillouin scattering. At the high intensities of about  $4 \times 10^{15} \text{ W/cm}^2$ , particle code simulations predict substantial profile modification. The light was collimated by a concave gold mirror. Because the light was normally incident upon this mirror, the only effect on the polarization state was to reverse the handedness of the ellipse.

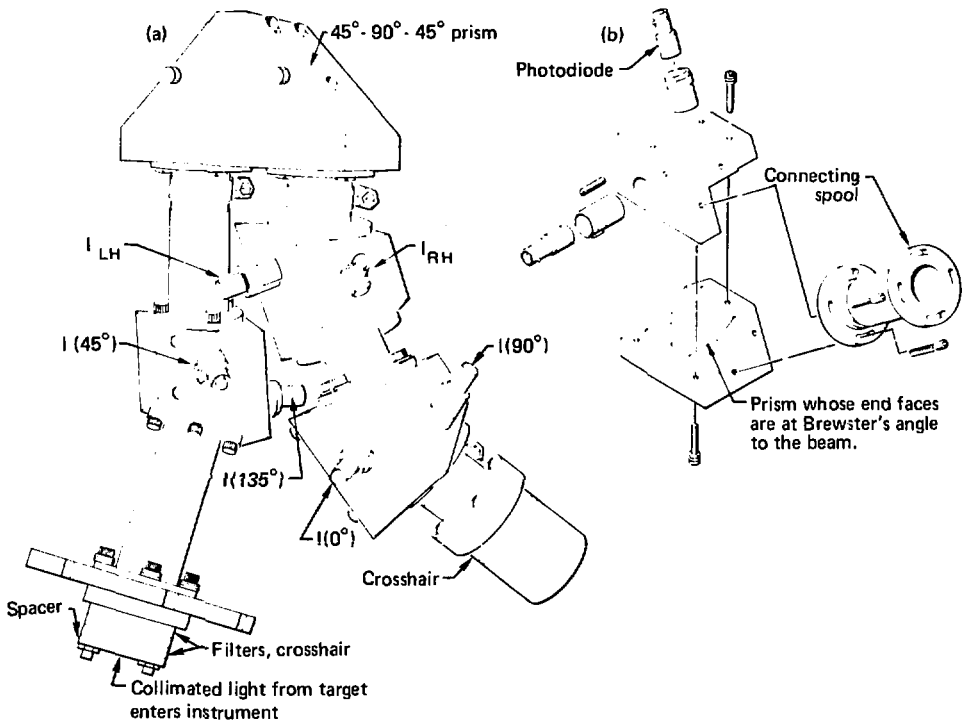
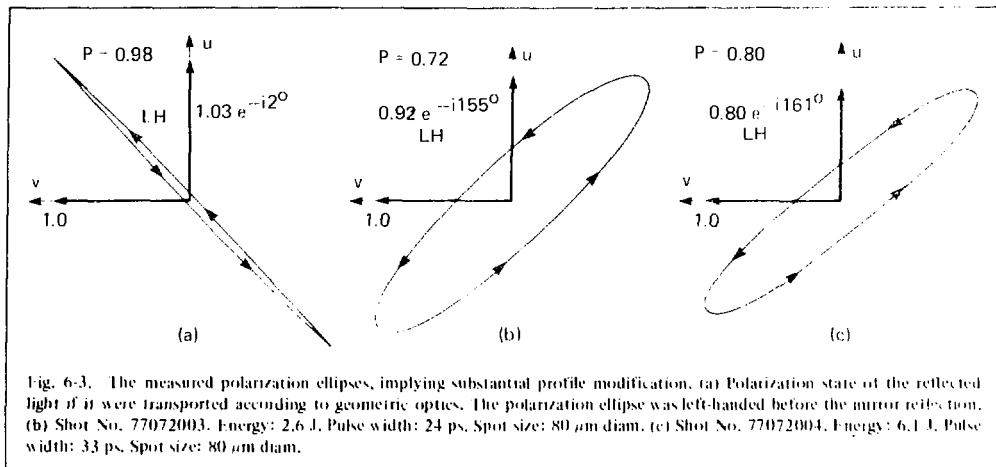


Fig. 6-1. (a) Ellipsometer for determining the polarization ellipse of the scattered light, (b) Polarization analyzer block.



the electric vector to rotate clockwise when viewed along the  $\mathbf{k}$  vector. This labelling is to remind one that the mirror reflection has reversed the handedness of the polarization ellipse.

The difference in the phase shifts for the  $u$  and  $v$  components is  $153^\circ$  for shot No. 77072003 and  $159^\circ$  for shot No. 77072004. This difference in-

dicates a scale length substantially less than  $1\mu\text{m}$ , as can be seen from Fig. 6-4. The density jump must also be at least on the order of the critical density magnitude (Fig. 6-5). The curves in Figs. 6-5 and 6-6 for  $22.5^\circ$  and  $20^\circ$  incidence angles, respectively, are included to show the effect of the angular width of the beam.

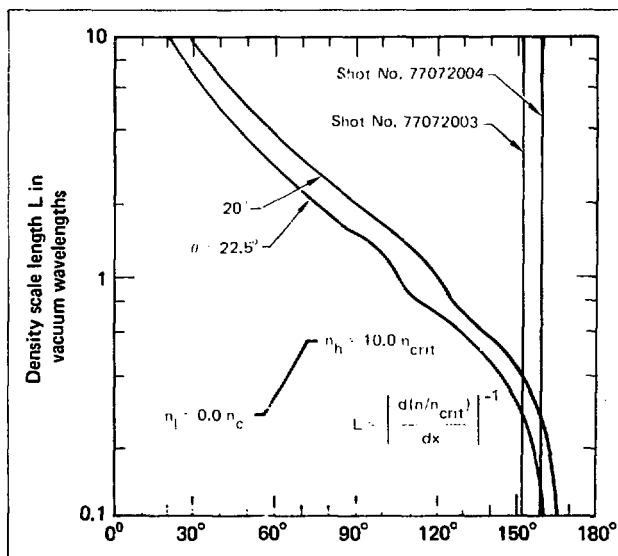


Fig. 6-4. Measured phase difference, which also sets an upper limit for the density scale length around critical density.

Fig. 6-5. Observed phase difference, which establishes a lower limit to the magnitude of the density jump. The shaded area is the measurement. The angle of incidence is  $22.5^\circ$ .

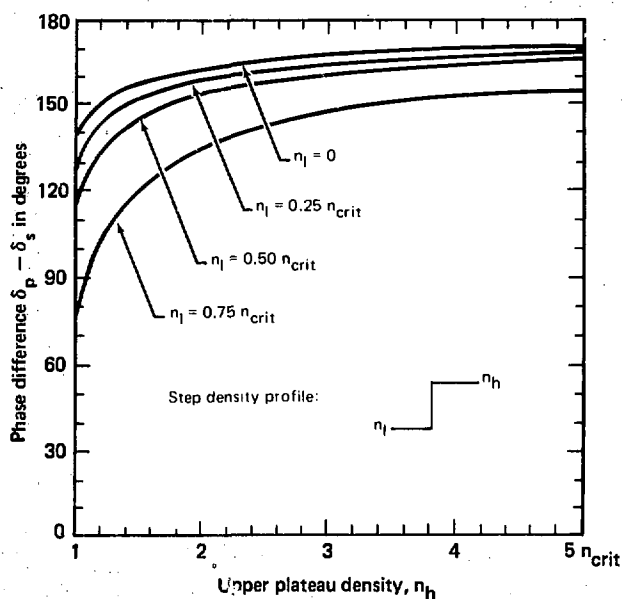
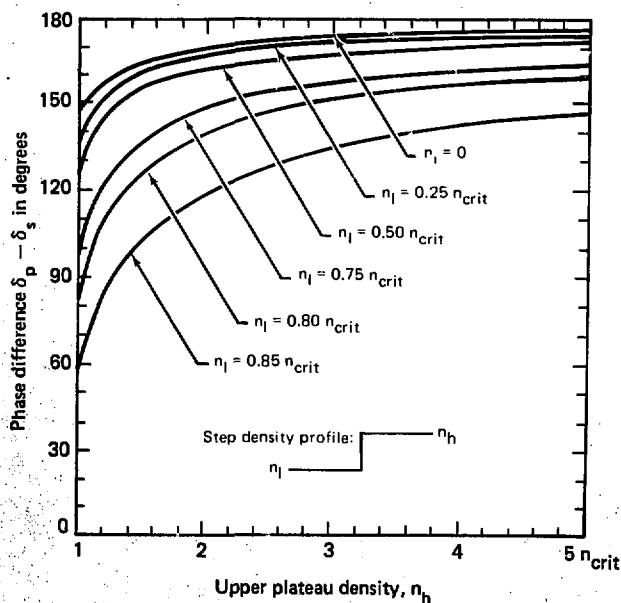


Fig. 6-6. Observed phase difference, which establishes a lower limit to the magnitude of the density jump. The shaded area is the measurement. The angle of incidence is  $20^\circ$ .

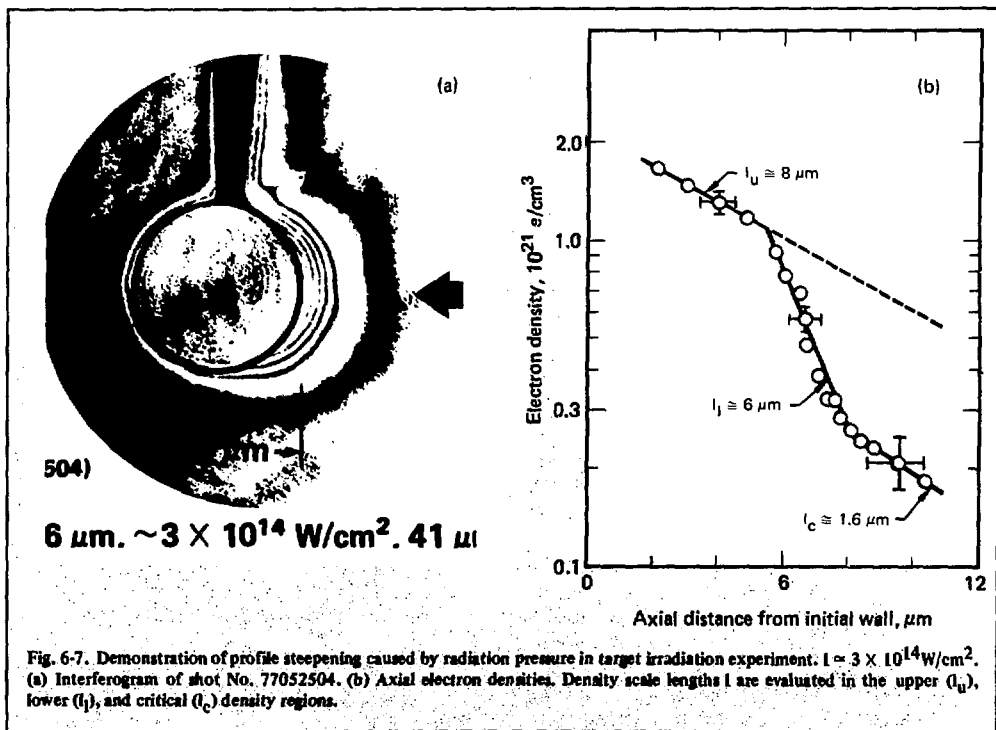


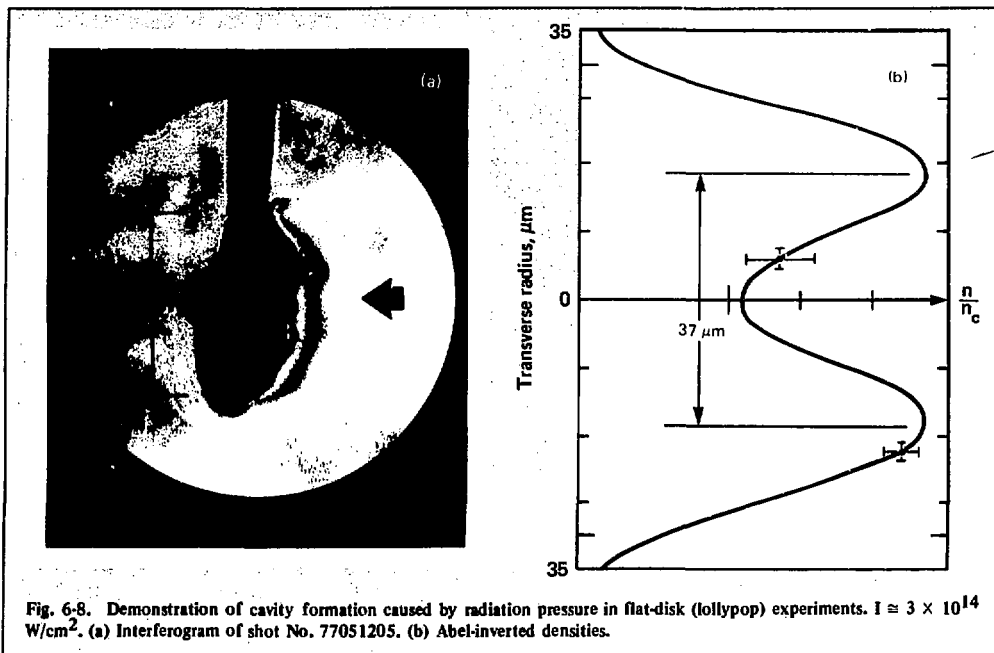
### 6.3 Interferometry for Absorption Physics Studies

The ultraviolet probing/holographic interferometry technique has been improved during 1977, to the point where it now plays a significant role in contributing to our understanding of absorption physics.<sup>1-3</sup> The system uses a 15-ps, 2660-Å probe pulse and provides a spatial resolution somewhat better than 1  $\mu\text{m}$ . New experiments, performed with ball and disk targets at the Janus laser facility, show that for short (30 ps) irradiation pulses the density scale lengths are  $\sim 10 \mu\text{m}$  everywhere, and that in the critical-density region they are  $\sim 1 \mu\text{m}$ . Further, these results show that radiation pressure affects the transverse nature of isodensity contours, producing both large- and small-scale electron-density depressions.

An example of a well-focused interferogram, along with its analysis, is shown in Fig. 6-7. In this target experiment, a 41- $\mu\text{m}$ -diam glass microsphere was irradiated with a 30-ps, 1.06- $\mu\text{m}$  laser pulse at an intensity of  $3 \times 10^{14} \text{ W/cm}^2$ . The resulting interferogram [Fig. 6-7(a)] has been Abel-inverted, with axial electron densities plotted in Fig. 6-7(b).

These results demonstrate that radial density profiles are indeed steepened by radiation-pressure effects. A simple but instructive model for this effect is to consider a static balance of partial pressures at the critical surface, where the high-density side has only particle pressure, while the lower density laser side has both a thermal (particle) component and a portion caused by momentum transferred by photon reflections, viz.  $n_u kT = n_l kT + 2I_0/c$ , where  $n_u$  and  $n_l$  are the upper and lower shelf densities,  $kT$  is the thermal temperature,  $I_0$  is the laser intensity, and  $c$  is the speed of light. The model must then be modified for flow field dynamics, temperature differences across the interface, and fractional absorption on a realistic density profile. Typical numerical results from the model indicate an equivalence of thermal and radiation pressures at  $10^{21} \text{ e/cm}^3$ , 1 keV temperature, and a laser intensity of  $3 \times 10^{15} \text{ W/cm}^2$ . The density step in Fig. 6-7, where the intensity is only  $3 \times 10^{14} \text{ W/cm}^2$ , is thus larger than expected, probably because of temperature differences localized by inhibited energy transport in the critical region. This is discussed in §4.4.1, where radial profiles are calculated with and without transport inhibition.



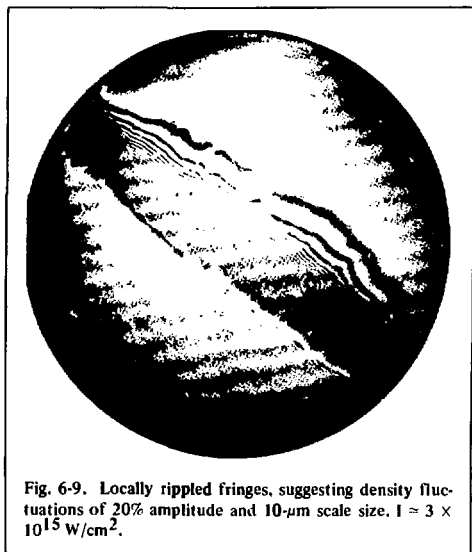


As a practical matter, these results show that for 30-ps experiments the scale lengths are less than  $10 \mu\text{m}$  everywhere, and approximately  $1 \mu\text{m}$  near the critical surface. The measured profile in Fig. 6-7 suggests that resonance absorption plays the major role in absorbing laser light. The shallow profile of  $100\text{-}\mu\text{m}$  scale length or larger, required for efficient absorption by classical inverse bremsstrahlung or parametric decay, does not exist. Further confirmation of density-contour deformation is observed in our experiments with flat disk targets, often referred to as "lollypops." An example is shown in Fig. 6-8(a), with the Abel-inverted densities shown in Fig. 6-8(b) for a plane transverse to the incident light. The density cavity or well formation shown in Fig. 6-8(b) has a transverse scale approximately equal to that of the incident light. Large-scale, two-dimensional density depressions such as this have recently been calculated by Randall and DeGroot, as discussed in §4.6.3.

In addition to large-scale density cavities, we have also observed small-scale rippling of the critical surface in our higher intensity experiments with Parylene lollypop targets. An example is shown in Fig. 6-9.

Localized fringe variations are primarily caused by density changes because optical path

lengths are essentially equal within small areas of the target. These density variations are most likely produced by hot spots in the incident light beam.



The hot spots push electrons out of their way with the increased radiation pressure. This process is unstable because the low-density region is of higher refractive index, thus tending to focus the incident light farther. This process of "filamentation" causes a localized mixing of angle and polarization of the incident wave, leading to a smoothing of measured absorption characteristics expected for the dominant resonance-absorption process.<sup>4</sup> In addition, these localized ripples very likely have strong surface currents because of the partial absorption of light (transverse momentum of the partially reflected waves is not conserved, a portion having been transferred to the electrons). These randomly oriented surface currents would then lead to randomly oriented magnetic fields, estimated by particle-in-cell computer simulations to be in the megagauss range. These predictions have appeared in previous annual reports, are updated in §4.6.4 of this report, and are discussed in the literature.<sup>5</sup>

In summary, using holographic interferometry with a 2660-Å probe wavelength, we have studied the plasma surrounding laser-irradiated targets with a resolution of 1  $\mu\text{m}$  and 15 ps. Results indicate that for short-pulse experiments gradient lengths are sufficiently short, and density depressions sufficiently large, that only resonant absorption plays a significant role, and that density fluctuations provide mixing of s- and p-polarization at the absorption surface. We anticipate different results in future experiments with nanosecond irradiation pulses.

## References

1. *Laser Program Annual Report — 1976*, Lawrence Livermore Laboratory, Rept. 50021-76 (1977), p. 3-34.
2. D. T. Attwood, D. W. Sweeney, J. M. Auerbach, and P. H. Y. Lee, "Interferometric Confirmation of Radiation-Pressure Effects in Laser-Plasma Interactions," *Phys. Rev. Lett.* **40**, 184 (1978).
3. *Laser Program Annual Report — 1975*, Lawrence Livermore Laboratory, Rept. 50021-75 (1976), p. 428.
4. K. R. Manes, V. C. Rupert, J. M. Auerbach, P. H. Y. Lee, and J. E. Swain, "Polarization and Angular Dependence of 1.06- $\mu\text{m}$  Laser-Light Absorption by Planar Plasmas," *Phys. Rev. Lett.* **39**, 281 (1977).
5. K. G. Estabrook, "Critical-Surface Bubbles and Corrugations and Their Implications to Laser Fusion," *Phys. Fluids* **19**, 1733 (1976).

## Authors

**D. T. Attwood**  
**J. M. Auerbach**  
**E. L. Pierce**  
**J. T. Larsen**  
**K. G. Estabrook**  
**C. J. Randall**

## 6.4 Polarization and Angular Dependence of 1.06- $\mu\text{m}$ Laser Light Absorption by Planar Plasmas

The production of laser-heated inertially confined thermonuclear plasmas involves several stages. Foremost among these is the coupling of laser energy into the target plasma; therefore, the nature of this laser-light-absorption process has been the subject of much theoretical and experimental research.<sup>6-20</sup> Estabrook, Valeo, and Kruer have carried out two-dimensional relativistic simulations of plasma absorption.<sup>6</sup> Their calculations show a maximum absorption efficiency of approximately 50%, generation of suprathermal particles, and strong steepening of the density profile in the vicinity of the critical density. The dominant mechanism in these calculations is resonance absorption, which, in this context, refers to a collisionless plasma-heating mechanism arising for obliquely incident radiation. If the radiation's electric-field vector has a component along the density-gradient direction, electron plasma waves may be excited, leading to plasma heating.

Recent experimental evidence supports the proposition that an important process governing the absorption of laser pulses less than  $\sim 100$  ps in duration with intensities between  $\sim 10^{14}$  and  $\sim 10^{16}$  W/cm<sup>2</sup> is resonance absorption.<sup>13-20</sup> Here, we report the results of an experimental attempt to observe the polarization and angular dependence of the absorption of 1.06- $\mu\text{m}$  optical plane waves incident on flat slabs, i.e., conditions similar to those used in Estabrook, Valeo, and Kruer's simulations. Using the Janus laser facility, we have produced direct experimental evidence of resonance absorption.

The experimental design used for these measurements is indicated schematically in Fig. 6-10. The  $\sim 100$ -GW 1.06- $\mu\text{m}$  laser pulses ( $30 \pm 6$  ps in duration) were provided by one beam of the Janus laser/target interaction facility.<sup>21</sup> The Janus oscillator-amplifier laser system is capable of routinely delivering  $\sim 400$  GW in two beams to laser fusion targets; however, for this study Janus was limited to  $\lesssim 100$ -GW single-beam irradiations to avoid the complications that nonlinear intensity-dependent phase distortions might have introduced.<sup>22</sup> The laser pulses were focused onto the  $\sim 300$ - $\mu\text{m}$ -diam,  $\sim 20$ - $\mu\text{m}$ -thick Parylene (C<sub>8</sub>H<sub>8</sub>) disk targets by an aspheric f/10 lens. The input-beam profile at the f/10 lens was approximately rectangular ("top hat" beam); thus, the diffraction-limited focal-spot diameter should have been  $\sim 26$   $\mu\text{m}$ . In practice, the full aperture of the lens was not

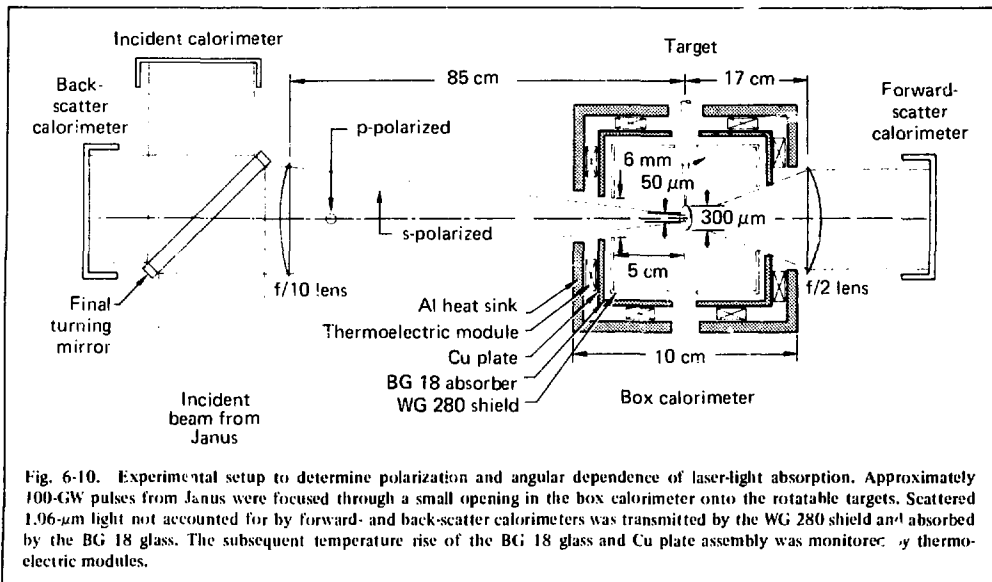


Fig. 6-10. Experimental setup to determine polarization and angular dependence of laser-light absorption. Approximately 100-GW pulses from Janus were focused through a small opening in the box calorimeter onto the rotatable targets. Scattered 1.06- $\mu\text{m}$  light not accounted for by forward- and back-scatter calorimeters was transmitted by the WG 280 shield and absorbed by the BG 18 glass. The subsequent temperature rise of the BG 18 glass and Cu plate assembly was monitored by thermoelectric modules.

used and astigmatism  $\leq 1$  wave was observed in the beam. A typical target and target-plane intensity distribution are shown in Fig. 6-11. The intensity distribution, Fig. 6-11(c) and (d), was recorded on every target shot and varied slowly because of laser-disk heating and minor misalignment; however, the focal-spot diameter at the target was always within the range  $40 \pm 17 \mu\text{m}$ .<sup>13</sup> Using a microscope, we prealigned each target so that we knew the orientation of its normal with respect to the target manipulator. After insertion into the target chamber, the target was illuminated by diffused 1.06- $\mu\text{m}$  light through the  $f/10$  lens and moved into focus by using the  $f/2$  lens. The target manipulator was then rotated through the desired angle  $\theta$ . Because the laser spot in the target plane was observed through the same  $f/2$  lens, it could be located to within  $\pm 5 \mu\text{m}$  of the center of each transparent target. The Rayleigh range calculated for this  $f/10$  focusing geometry is between 200 and 500  $\mu\text{m}$ . As expected, the laser-spot area changed only slightly for a several-hundred-micron axial translation of the  $f/10$  lens.

Laser-pulse duration was determined on every target shot by an optical streak camera located at the laser output. A typical temporal pulse shape is displayed in Fig. 6-11(b). Because the plasma expansion velocity has been measured to be  $(3 \pm 1) \times 10^7 \text{ cm/s}$ , the plasma front moves only 12  $\mu\text{m}$  during the laser pulse. In summary, the target

was presented with an almost planar wavefront, and the pulse duration was short enough to preserve the angle between the laser beam and the target normal to reasonable accuracy. We chose the intensity range attained in this experiment,  $10^{15}$  to  $10^{16} \text{ W/cm}^2$ , because it was within the range of Estabrook, Valeo, and Krueer's simulations, relevant to spherical target work, and high enough to minimize classical collisional (inverse bremsstrahlung) absorption.

After striking the target, the scattered laser light was collected by an enclosing box calorimeter indicated in Fig. 6-10.<sup>13,18,23</sup> The 1.06- $\mu\text{m}$  radiation was transmitted by the WG 280 glass shield and absorbed by the BG 18 glass. Because the shield stopped ions, electrons, and all but the most energetic x rays ( $\geq 15 \text{ keV}$ ), this calorimeter provided an accurate measure of scattered light. A backscatter calorimeter measured light reflected back into the focusing lens cone and, similarly, forward-scattered radiation was directed into another calorimeter. Each of these calorimeters was calibrated in situ and corrected for extraneous effects such as stray flashlamp light, because the experiment required better than 1% accuracy from each detector. We recalibrated the laser calorimeters after each configuration change, i.e., prior to p-polarization shots, upon changing to s-polarization, and when returning to p-polarization to check several points at the end of the experiment. In addition, the



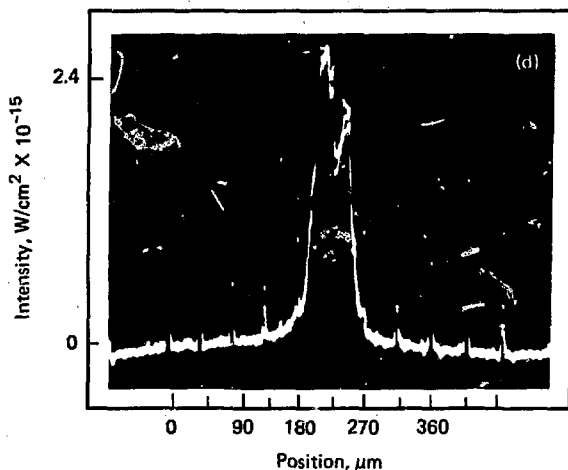
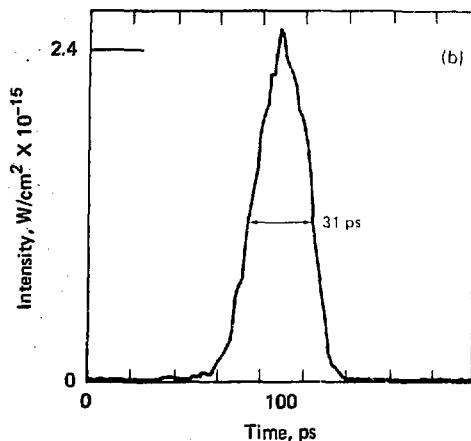
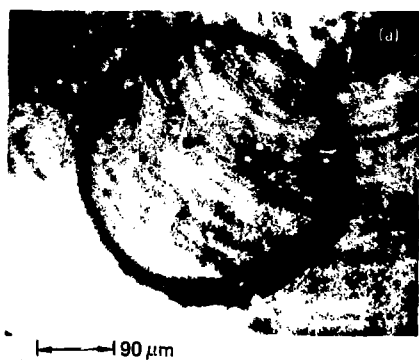
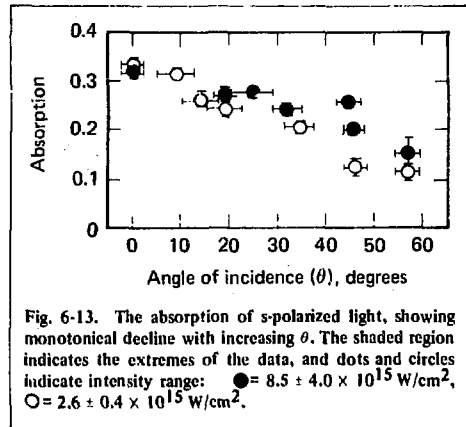
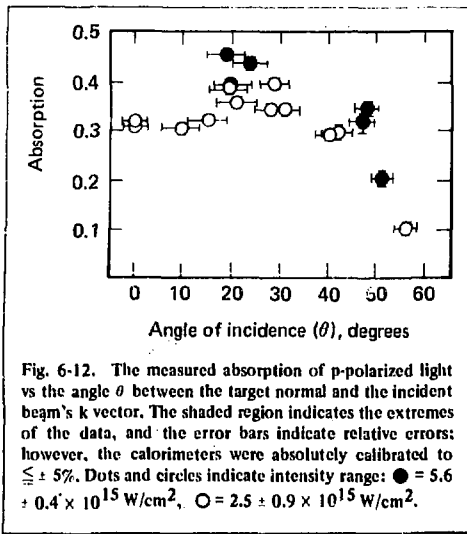


**Fig. 6-11. Typical target and target-plane intensity distribution: (a) target, (b) target-plane intensity distribution and temporal pulse, (c) beam image, and (d) beam profile provided by a scan through the beam image. A streak camera located at the laser system output measured the temporal shape of the pulse reaching the target on every shot.**

transmissions and reflections of all optical elements were measured in place for each polarization. Finally, the polarization of the incident laser light was measured by polarimetry of the pulsed beam and was adjusted to within  $1^\circ$  of the desired state.

Figures 6-12 and 6-13 show the measured absorptions for p- and s-polarized light, respectively. The absorption measured at normal incidence should be the same for both polarizations, and indeed it is the same, within measurement accuracy. For s-polarized radiation, the absorption decreases monotonically with angle of incidence, as expected

from the simulations. For p-polarized light, a maximum of  $\approx 35\text{--}45\%$  occurs between  $\theta = 20$  and  $25^\circ$ . For comparison, the calculated absorption of p-polarized light reached a maximum value of  $\approx 50\%$  at an angle of  $\approx 24^\circ$ . The data points fell into two target-surface intensity groups, as indicated in Figs. 6-12 and 6-13. The shaded regions indicate the approximate extremes of our measurements, and the higher values of absorption at each angular setting correspond to higher intensity at the target surface. This intensity effect is particularly evident in the s-polarized light-absorption measurements and



probably accounts for the elevated p-polarized light absorptions observed at 20 and 50°. Even with the range of intensities and absorptions encountered on different trials, the resonance for p-polarized light is clearly evident while no similar maximum was observed in the s-polarized light measurements.

The angle corresponding to the absorption maximum for p-polarization, coupled with Ginzburg's resonance-absorption function,<sup>24</sup> implies a scale length of

$$L = \left( \frac{0.8}{\sin \theta} \right)^3 c / \omega \approx 1 \text{ to } 2 \mu\text{m},$$

in agreement with previous results obtained by polarimetry.<sup>19</sup> Here,  $c$  is the velocity of light and  $\omega$  is the laser light frequency.

A seven-channel x-ray spectrometer was used to measure the continuum thermal x-ray temperature on several shots.<sup>25</sup> Typical temperatures obtained were of the order of 600 eV. By assuming a linear-ramp electron-density profile with a scale height of 1 to 2  $\mu\text{m}$ , we may estimate the classical collisional absorption:

$$A \approx \left[ 1 - \exp\left(\frac{32}{15} \frac{\nu L}{c} \cos^5 \theta\right) \right] \leq 0.08$$

where  $\nu$  is the electron-ion collision frequency. Hence, at  $\theta = 0^\circ$ , a substantial (>20%) absorption caused by anomalous or nonlinear effects was observed, which is more than the  $\approx 15\%$  value predicted by the simulations.

Quantitative differences between the calculated and measured p-polarized light absorption may be caused partly by the departure of the experiment from the ideal illumination configuration assumed in the calculations, which treated plane waves incident onto a planar target. Indeed, the incident radiation was not perfectly collimated, and the targets were not identical or perfectly flat. A three-dimensional rippling of the critical-density surface either by instabilities or by inhomogeneities in the intensity profile of the light beam may also account for some of the discrepancies.<sup>26,27</sup> These surface distortions can broaden the angular dependence of the absorption and reduce its dependence on polarization.<sup>28</sup> In addition, other mechanisms may be playing some role in the absorption. These mechanisms include short-wavelength ion turbulence,<sup>29,30</sup> resonance absorption due to self-generated magnetic fields,<sup>31</sup> and the  $2\omega_{pe}$  instability.<sup>32</sup>

The fraction of the incident energy back-scattered into the f/10 focusing lens reached a maximum of 2% for  $\theta = 0^\circ$ , but was 1% or less for all other angles investigated. This small percentage of directly back-scattered radiation suggests a diffuse scattering surface and may present indirect experimental evidence of cratering; however, the initial roughness of the target face could have the same effect. In any case, this low backscatter suggests that stimulated back-reflection was not significant in this measurement.

In summary, we observed a clear maximum in the p-polarized laser light absorption by Parylene targets at angles of incidence between 20 and 25° in qualitative agreement with theory.<sup>6</sup> The s-polarized light measurements exhibit a monotonic decrease of

the absorption with the angle of incidence. This clear signature of the resonance-absorption phenomenon, observed at intensities and pulse durations typical of exploding-pusher laser-fusion studies, identifies resonance absorption as a significant absorption mechanism for this class of experiments.

## References

- K. G. Estabrook, E. J. Valeo, and W. I. Kruer, "Two-Dimensional Relativistic Simulations of Resonance Absorption," *Phys. Fluids* **18**, 1151 (1975).
- J. P. Freidberg, R. W. Mitchell, R. L. Morse, and I. L. Rudzinski, "Resonant Absorption of Laser Light by Plasma Targets," *Phys. Rev. Lett.* **28**, 795 (1972).
- D. W. Forslund, J. M. Knidel, K. Lee, I. L. Lindman, and R. L. Morse, "Theory and Simulation of Resonant Absorption in a Hot Plasma," *Phys. Rev. A*, **11**, 679 (1975).
- B. Ripin, P. G. Burkhalter, F. C. Young, J. M. McMahon, D. G. Colombant, S. F. Bodner, R. R. Whitlock, D. J. Nagel, D. J. Johnson, S. K. Winsor, C. M. Dozier, R. D. Bleach, J. A. Stamper, and F. A. McLean, "X-Ray Emission Spectra from High-Power-Laser-Produced Plasmas," *Phys. Rev. Lett.* **34**, 1313 (1975).
- E. Fabre and C. Stenz, "CO<sub>2</sub> Laser-Beam Absorption by a Dense Plasma," *Phys. Rev. Lett.* **32**, 823 (1974).
- C. Yamanaka, I. Yamanaka, I. Sasaki, J. Mizui, and H. B. Kang, "Brillouin Backscattering and Parametric Double Resonance in Laser-Produced Plasma," *Phys. Rev. Lett.* **32**, 1038 (1974).
- B. Ripin, "Angular Distribution of Laser Light Scattered from Laser-Produced Plasma at High Irradiance," *Applied Phys. Lett.* **30**, 134 (1977).
- K. R. Manes, H. G. Ahlstrom, R. A. Haas, and J. F. Holzrichter, "Light-Plasma Interaction Studies with High-Power Glass Lasers," *J. Opt. Soc. Am.* **67**, 717 (1977).
- J. S. Pearlman, J. J. Thomson, and C. E. Max, "Polarization-Dependent Absorption of Laser Radiation Incident on Dense-Plasma Planar Targets," *Phys. Rev. Lett.* **38**, 1397 (1977).
- I. Kolodner and E. Yablonovitch, "Proof of the Resonant Acceleration Mechanism for Fast Electrons in Gaseous Laser Targets," *Phys. Rev. Lett.* **37**, 1754 (1976).
- W. C. Mead, R. A. Haas, W. I. Kruer, D. W. Phillion, H. N. Kornblum, J. D. Lindl, D. R. MacQuigg, V. C. Rupert, "Observation and Simulation of Effects on Parylene Disks Irradiated at High Intensities with a 1.06- $\mu$ m Laser," *Phys. Rev. Lett.* **37**, 489 (1976).
- W. I. Kruer, R. A. Haas, W. C. Mead, D. W. Phillion, and V. C. Rupert, "Collective Behavior in Recent Laser-Plasma Experiments," in *Plasma Physics: Nonlinear Theory and Experiments*, H. Wilhelmsson, Ed. (Plenum Press, New York, 1977) pp. 64-81.
- R. A. Haas, W. C. Mead, W. I. Kruer, D. W. Phillion, H. N. Kornblum, J. D. Lindl, D. R. MacQuigg, V. C. Rupert, and K. G. Tinsell, "Irradiation of Parylene Disks with a 1.06- $\mu$ m Laser," *Phys. Fluids* **20**, 322 (1977).
- D. W. Phillion, R. A. Terche, V. C. Rupert, R. A. Haas, and M. J. Boyle, "Evidence for Profile Steepening in Laser-Irradiated Plasmas," *Phys. Fluids* **20**, 1892 (1977).
- E. K. Storm, J. E. Swain, H. G. Ahlstrom, M. J. Boyle, V. C. Rupert, and D. W. Phillion, "Laser-Fusion Experiments Utilizing a 4m Illumination System," *J. Appl. Phys.* **49**, 959 (1978).
- Laser Program Annual Report -- 1974*, Lawrence Livermore Laboratory, Rept. UCRL-50021-74 (1974), p. 35.
- J. A. Gilaze, "High-Energy Glass Lasers," *Optical Engineering* **15**, 136 (1976).
- S. R. Gunn, *Calorimeters for Diagnosis of Laser Fusion Experiments*, Lawrence Livermore Laboratory, Rept. UCID-17308 (1976).
- V. I. Ginzburg, Ed. *The Propagation of Electromagnetic Waves in Plasmas*, 2nd ed. (Pergamon Press, Oxford, 1970).
- V. W. Shvinsky, H. N. Kornblum, and H. D. Shav, "Determination of Suprathermal-Electron Distributions in Laser-Produced Plasmas," *J. Appl. Phys.* **46**, 1973 (1975).
- K. G. Estabrook and E. J. Valeo, *Bubbles and Their Implications for Laser Fusion*, Lawrence Livermore Laboratory, Rept. UCRL-77146 (1975).
- J. J. Thomson and C. Randall, Lawrence Livermore Laboratory, private communication (1977).
- J. J. Thomson, W. I. Kruer, A. B. Langdon, C. E. Max, and W. C. Mead, "Theoretical Interpretation of Angle- and Polarization-Dependent Laser Light-Absorption Measurements," *Phys. Fluids* **21**, 707 (1978).
- R. J. Faehl and W. I. Kruer, "Laser Light Absorption by Short-Wavelength Ion Turbulence," *Phys. Fluids* **20**, 55 (1977).
- W. Manheimer, "Energy-Flux Limitation by Ion Acoustic Turbulence in Laser-Fusion Schemes," *Phys. Fluids* **20**, 265 (1977).
- W. I. Kruer and K. G. Estabrook, "Laser Light Absorption and Harmonic Generation Due to Self-Generated Magnetic Fields," in *Laser Interaction and Related Plasma Phenomena*, H. Schwatz and H. Hora, Eds. (Plenum Press, New York, 1978), vol. 4B, pp. 709-720.
- A. B. Langdon and B. F. Lasinski, "Electromagnetic and Relativistic Plasma Simulation Models," in *Methods in Computational Physics*, J. Killeen, Ed. (Academic Press, New York, 1976), vol. 16, pp. 327-366.

## Authors

**K. R. Manes**  
**V. C. Rupert**  
**J. M. Auerbach**  
**P. H. Y. Lee**  
**J. E. Swain**  
**W. I. Kruer**

## 6.5 Brillouin Scattering in Laser-Produced Plasmas

Laser fusion experiments<sup>33-41</sup> concerning the absorption of 1.06- $\mu\text{m}$  laser light with intensity  $\gtrsim 10^{15} \text{ W/cm}^2$  generally found that Brillouin scatter<sup>42-45</sup> is limited at a low level, an effect that has been attributed theoretically to the small mass and heat capacity of the small, underdense plasma.<sup>43-45</sup> With the advent of more powerful lasers, it is becoming common to investigate the absorption of intense light in experiments with long pulses and large focal spots. These experiments, characterized by a much larger region of underdense plasma, more closely approximate future experiments with shaped pulses. For example, a simple estimate shows that the size of the underdense plasma  $L \approx R$ , where  $R$  is the radius of the focal spot, provided the pulse length is long enough for plasma to expand that far.

With large regions of underdense plasma, stimulated scattering of the incident laser light becomes a concern. First, we briefly present a simple estimate for Brillouin scattering that takes into account the finite heat capacity of the underdense plasma. Although crude, this model suffices to estimate magnitudes and to emphasize the strong ion heating concomitant with the scatter. Then, we present results of experiments in which Parylene disks are irradiated with intense 1.06- $\mu\text{m}$  light by using long pulse lengths and large focal spots. The absorption is found to be significantly degraded, as predicted. From the suprathermal x-ray spectrum, we estimate the energy spent in generating fast electrons. That energy, when normalized to the laser energy, is also very much reduced. Because much theoretical and experimental evidence indicates that these fast electrons originate near critical density, this finding also indicates scattering.

At intensities so high that the light pressure is much greater than the plasma pressure, the induced reflectivity can self-limit by simply pushing the underdense plasma aside.<sup>45</sup> However, in general, we must consider the complementary regime in which the light pressure is less than the plasma pressure. For example, this regime is obtained when the laser intensity  $I_L \sim 3 \times 10^{15} \text{ W/cm}^2$  and the plasma with density  $\lesssim 1/3-1/2$ , critical density  $n_{cr}$  is rather hot (electron temperature  $\theta_e \sim 3-5 \text{ keV}$ , as indicated by the high-energy x rays). The induced reflectivity can then be estimated by postulating that long-term ion heating controls the level of the scatter. In the scattering, a small fraction of the incident light energy is transferred to an ion wave and then damped into the ions. Because the massive ions transport energy slowly, even a small energy deposi-

tion drives them to a high temperature, i.e., ion temperature  $\theta_i \sim O(\theta_e)$ . This heating, in turn, reduces the reflectivity by making the ion waves heavily damped.

A simple description illustrates the numbers. Assuming that the intensity is well above the threshold set by gradients, we model the underdense plasma as uniform with size  $L$ . We consider only backscatter and anticipate that strong ion heating will lead the ion waves to be heavily damped in the final stage. Then, an analytic solution of the coupled wave equations gives for the induced reflectivity  $r$ :<sup>43,44,46</sup>

$$\frac{B}{r} = \frac{1-r}{\exp[x(1-r)] - r},$$

where

$$x = (1/4) \left( \frac{n_p}{n_{cr}} \right) k_0 L \left( \frac{v_L}{v_e} \right)^2 \frac{v_i}{\omega_i} \left( 1 + \frac{3\theta_i}{2\theta_e} \right).$$

Here,  $B$  is the noise level of the back-scattered wave, relative to the incident intensity,  $n_p$  is the plasma density,  $L$  is the plasma size,  $v_L$  is the oscillation velocity of electrons in the incident light wave with free-space wavenumber  $k_0$ , and  $v_e$  is the electron thermal velocity;  $\theta_e$  is the electron temperature,  $\theta_i$  is the ion temperature,  $v_i$  is the ion wave damping,  $\bar{Z}$  is the mean ionization state, and  $\omega_i$  is the ion wave frequency;  $v_i$  is assumed to be given by ion Landau damping and so is a function of  $\bar{Z}\theta_e/\theta_i$ .

To close this description, we need to estimate the ion temperature. The simplest assumption is that all the ions are heated and that they carry away energy as rapidly as possible, i.e., in a free-streaming limit. We balance this energy flux with that deposited into ion waves, giving

$$r I_L \frac{\Delta\omega}{\omega_0} = n_p \theta_i v_i,$$

where  $\Delta\omega/\omega_0 = 2k_0 v_s/\omega_0$  is the fraction of the reflected energy given to the ion waves, and  $v_s$  is the ion sound velocity.

The solid lines in Fig. 6-14 show  $\theta_i$  and  $r$  as functions of plasma size from this simple model. In this example,  $(v_L/v_e)^2 = 0.4$ , which corresponds to  $I_L = 3 \times 10^{15} \text{ W/cm}^2$  and  $\theta_e = 3 \text{ keV}$ . Note from Fig. 6-14(a) the strong ion heating as anticipated. Even a modest reflectivity deposits sufficient energy into the ions to drive them to a mean temperature comparable to the electron temperature. Fig. 6-14(b)

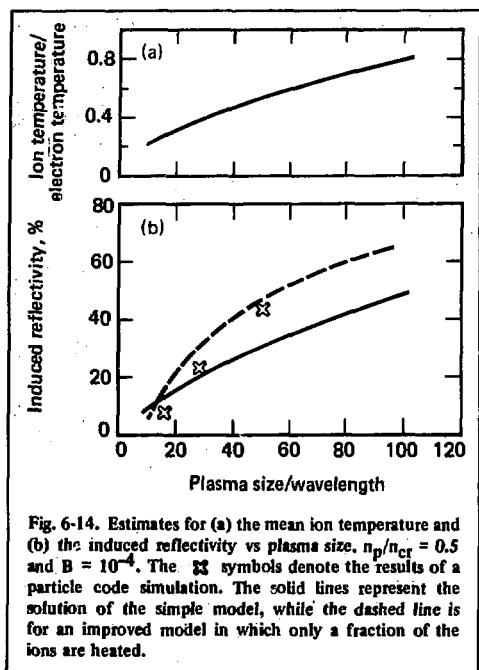


Fig. 6-14. Estimates for (a) the mean ion temperature and (b) the induced reflectivity vs plasma size,  $n_p/n_{cr} = 0.5$  and  $B = 10^{-4}$ . The 'x' symbols denote the results of a particle code simulation. The solid lines represent the solution of the simple model, while the dashed line is for an improved model in which only a fraction of the ions are heated.

provides an estimate for the magnitude of the induced reflectivity. For  $L \approx 10 \times \text{wavelength } \lambda_0$ ,  $r \approx 10\%$ . For  $L \approx 50-100 \lambda_0$ ,  $r \approx 50\%$ . Note that  $r$  does not increase very rapidly with  $L$  in this model. As  $r$  increases, the ion heating increases, which acts to reduce the increase in  $r$ .

Improved models for the ion heating give similar results. Simulations<sup>43-45</sup> have shown that in general only a fraction of the ions are heated (by trapping in the ion waves). To model this effect, we balance the energy deposition into ion waves with that carried off by a fraction of the ions ( $n_h/n_p$ ) heated to an effective temperature  $\theta_h \approx Mv_s^2$ , where  $M$  is the ion mass. The dashed line in Fig. 6-14(b) shows the reflectivity thus obtained. Note that the magnitudes are similar. Finally, using a code with particle ions and fluid electrons, we carried out some simulations of this model. These simulations account for the microscopic nature of the heating as well as its spatial dependence. The calculated reflectivities in the heated state (with  $n_p = 1/3$  the critical density) are denoted by the crosses in Fig. 6-14(b).

These one-dimensional estimates are probably conservative because several effects are overlooked. First, both back- and side-scatter occur. Well above threshold, the scattered light is expected to come back in a broad range of angles as the side-scattered

light refracts out of the plasma. This side-scatter occurs primarily out of the plane of polarization, which is another signature for Brillouin scatter. Secondly, it takes some time for the ions in the underdense plasma to heat to a steady state. During this time, the reflectivity is larger than that shown in Fig. 6-14(b). Finally, we have assumed a rather modest noise level ( $B \approx 10^{-4}$ ); but the estimated reflection length is only logarithmically sensitive to this value.

Experiments were carried out at the Argus laser facility with  $1.06\text{-}\mu\text{m}$  light focused by  $f/1$  lenses.<sup>47</sup> The pulses were Gaussian with a duration of  $150\text{--}400$  ps measured between half-intensity points and had little substructure. The laser beam was only a few times diffraction-limited, and little aberration was visible at the spot sizes used in these experiments. The minimum detectable energy in any prepulse is 70 to 73 dB lower than the main pulse energy. No prepulse was detected on any shot for which data are presented here, although for a couple of the shots in Fig. 6-15, no prepulse photo was obtained. The spot diameters ( $100\text{--}250 \mu\text{m}$ ) are measured between half-intensity points, which in the near field corresponds to the ray cone having  $18^\circ$  half-angle. Ninety percent of the energy is within the ray cone of  $24^\circ$  half-angle, while the average intensity near the axis is correctly given if one assumes a uniform beam of  $20^\circ$  half-angle. The targets were Parylene disks ( $\text{C}_8\text{H}_8$ ,  $22 \mu\text{m}$  thick,  $300 \mu\text{m}$  diam), which were oriented normal to the beam.

The light absorption was measured in two independent ways. One technique was to measure the nonabsorbed light, using a box calorimeter.<sup>48</sup> An innermost glass box that was thermally isolated from the rest of the calorimeter transmitted only the scattered light, not x rays or particles. Calorimeters measured both the incident light and the light collected by the focusing lenses. Even though the box calorimeter was rotated by  $15^\circ$  from perfect alignment with the laser electric field, the two side panels out of the plane of polarization saw almost twice as much energy as the other two side panels. On similar shots with the box calorimeter not in place, an array of photodiodes confirmed this strong polarization dependence, which is expected of Brillouin scattering.

The second technique was to measure the energy in the plasma blowoff and x rays by using an array of plasma calorimeters.<sup>48</sup> These calorimeters were positioned both in and out of the plane of incidence; however, no polarization dependence in the ion blowoff was observed. No plasma calorimeter could be placed closer than  $52.5^\circ$  to the incident beam direction because of mechanical in-

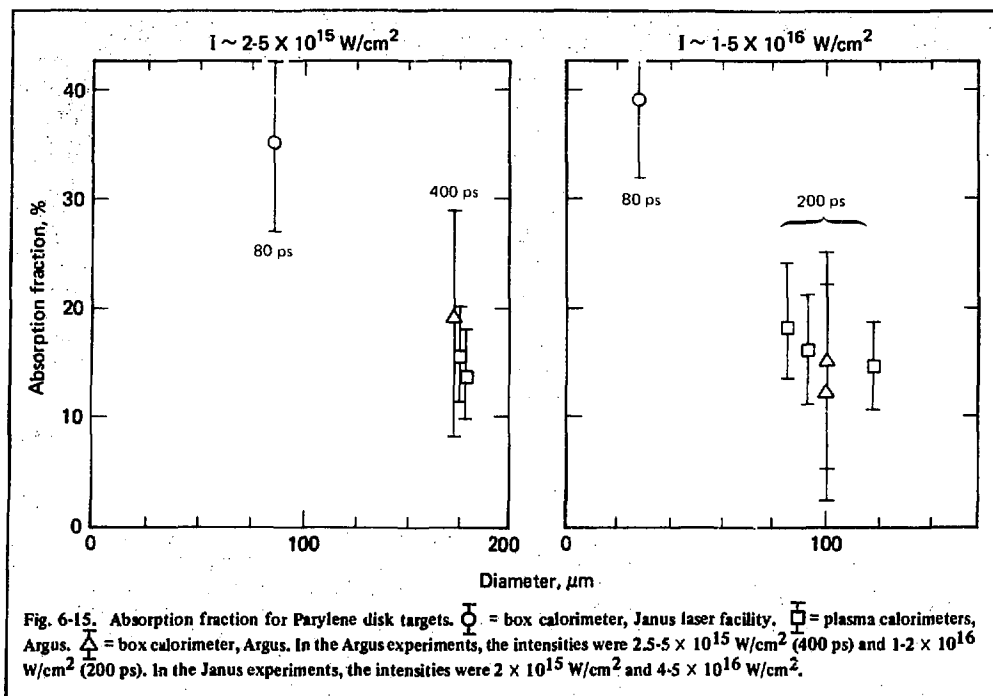


Fig. 6-15. Absorption fraction for Parylene disk targets.  $\bigcirc$  = box calorimeter, Janus laser facility,  $\square$  = plasma calorimeters, Argus.  $\triangle$  = box calorimeter, Argus. In the Argus experiments, the intensities were  $2.5\text{--}5 \times 10^{15} \text{ W/cm}^2$  (400 ps) and  $1\text{--}2 \times 10^{16} \text{ W/cm}^2$  (200 ps). In the Janus experiments, the intensities were  $2 \times 10^{15} \text{ W/cm}^2$  and  $4\text{--}5 \times 10^{16} \text{ W/cm}^2$ .

interference with the focusing lens assembly. Therefore, we needed to know the general shape of the plasma blowoff energy distribution. To obtain this information, on one shot the Parylene disk was tilted  $26^\circ$  from the normal and the distribution was mapped by a ring of calorimeters in the plane of incidence. Assuming the plasma blowoff to have remained symmetric about the normal, we found the form  $A + B \cos^3 \theta$  to fit the data for the blowoff to the front. The angle of incidence  $\theta$  is measured away from the target normal. To obtain the energy in the blowoff to the back, the calorimeter measurements there were averaged and multiplied by  $2\pi$  solid angle.

In Fig. 6-15, we compare the measured absorption efficiencies with those observed in previous experiments with shorter pulse lengths and smaller focal spots (and hence smaller regions of underdense plasma). The results are grouped into two intensity regimes, one in the  $2\text{--}5 \times 10^{15} \text{ W/cm}^2$  intensity range and the other in the  $1\text{--}5 \times 10^{16} \text{ W/cm}^2$  range. In each case, the circles are previous results<sup>36,37</sup> obtained with the Janus laser by using 80-ps pulses of  $1.06\text{-}\mu\text{m}$  light. The data at the large spot sizes are those obtained with the Argus laser.

Note that, in each intensity regime, the absorption is degraded by a factor of  $\approx 2$  in the experiments with longer pulses and larger spots (and hence larger regions of underdense plasmas). The reduction in absorption is not just a function of focusing. The data in Fig. 6-15 indicate that, at a fixed spot size ( $\sim 90 \mu\text{m}$  diam), the absorption degrades with increasing pulse length.

In the Argus experiments, a large fraction of the incident light ( $\sim 30\text{--}50\%$ ) is reflected back into the  $f/1$  focusing lens. The frequency spectrum of this light provides additional evidence for the role of stimulated scattering. Fig. 6-16(a) shows the spectrum obtained for a  $140\text{-}\mu\text{m}$ -diam glass ball irradiated by two opposing beams (north beam: 220 ps FWHM, 220 J, and south beam: 150 ps FWHM, 198 J). The light collected by the north focusing lens was imaged onto the  $25\text{-}\mu\text{m}$  slit of a  $5/4\text{-meter}$  Czerny-Turner-type spectrograph. The spectrum was recorded by an optical multichannel analyzer with a resolution of about  $1 \text{ \AA}$ . At least 85% of the back-reflected light was shifted to the red side of the laser line. If the critical-density surface moved outward during most of the laser pulse, this result implies that almost all this light was Brillouin-scattered. As additional support for this conclu-

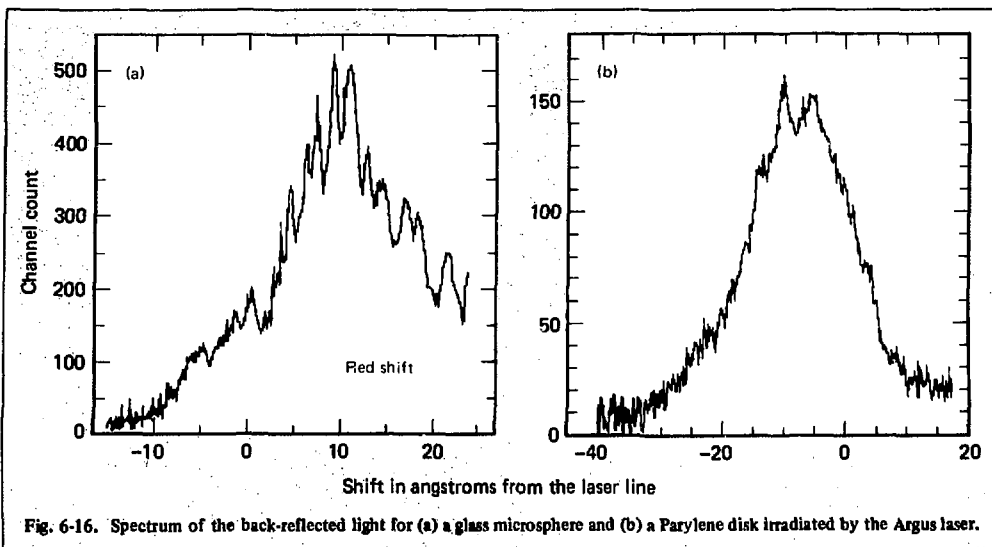


Fig. 6-16. Spectrum of the back-reflected light for (a) a glass microsphere and (b) a Parylene disk irradiated by the Argus laser.

sion, the light absorption was measured to be only  $12 \pm 5\%$  by an array of plasma calorimeters.

In general, the Doppler shift caused by plasma expansion can overcome that caused by the ion waves. This is the case with the disk experiments. In Fig. 6-16(b) the spectrum for a Parylene-disk shot (100- $\mu\text{m}$ -diam spot, 148 J, 198 ps FWHM) is shown. Note that the reflected line is rather broad and extends only partially to the red (longer wavelengths). The line has a width of  $\sim 2 k_0 v_s$ , as expected, because the ion waves are heavily damped. In contrast, in a disk experiment in which little Brillouin scatter was expected (28-ps pulse length,  $\sim 50\text{-}\mu\text{m}$ -diam focal spot), the back-reflected line was narrower (11 Å wide) and had its center shifted farther (23 Å) to the blue (shorter wavelengths). We therefore regard the broad spectrum in Fig. 6-16(b), which is in part red-shifted, as evidence for Brillouin scatter.

Collisionless absorption processes, such as resonance absorption or the parametric decay and oscillating two-stream instabilities that all occur near critical density, can efficiently transfer light energy into fast electrons by wave breaking. From the suprathermal x-ray spectrum, we can easily estimate the total energy spent creating these fast electrons if we make several simplifying approximations: namely, that these fast electrons lose most of their energy collisionally, that the concomitant bremsstrahlung radiation is fairly isotropic, and that the opacity is not important. Because Parylene

is low Z, we know the last approximation at least to be good for photons having energies on the order of the observed creation temperatures. We assume isotropy because the x-ray measurements were made with the seven-shooter and four-shooter x-ray diagnostics in a single location, and we have no idea of the angular variation of the high-energy x rays. For the experiments on Argus, the seven-shooter looked at the target edge-on (disks were 500  $\mu\text{m}$  in diameter), while in the Janus experiments to which we compare these results, the seven-shooter looked at the irradiated side of the disk at an angle of  $30^\circ$  to the face.

For simplicity, the creation spectrum of fast electrons is assumed to be Maxwellian, and each electron is assumed to be collisionally slowed at the mean rate. The nonrelativistic bremsstrahlung cross section derived by Bethe and Heitler in the Born approximation is used. The total x-ray spectral intensity in the dimensionless units  $\text{keV}/\text{keV}$  at energy  $\hbar\omega$  is then

$$E_{\text{rad}}(\hbar\omega) = \int_0^\infty \underbrace{\frac{N_h}{kT_h} e^{-E_0/kT_h}}_{\text{Maxwellian distribution of electrons}} \left\{ \int_0^{x_{\text{max}}(E_0, \hbar\omega)} N_{\text{ion}} \right. \\ \times \underbrace{\left[ \frac{16 \alpha r_0^2 Z^2}{3 \beta^2} \ln \left( \frac{(\sqrt{E} + \sqrt{E - \hbar\omega})^2}{\hbar\omega} \right) \right]}_{\text{bremsstrahlung cross section}} dx \Bigg\} dE_0,$$

where the outermost integral sums over the possible creation energies  $E_0$ , and the innermost integral integrates over the distance each electron travels before it is slowed down to a kinetic energy equaling the photon energy  $\hbar\omega$  at distance  $x_{\max}(E_0, \hbar\omega)$ . Also,  $Z$  is the atomic number,  $r_0$  is the classical electron radius ( $2.818 \times 10^{-13}$  cm),  $\alpha$  is the fine-structure constant ( $1/137$ ),  $\beta$  is the fraction of light speed at which the electron is currently moving, and  $E(E_0, x)$  is the energy of an electron created with energy  $E_0$  after traveling a distance  $x$ .

The integrals can be evaluated if, to get the range, we use the mean loss rate for a nonrelativistic electron moving in fully ionized plasma:

$$\frac{dE/\mu}{dx} = \frac{-2\pi Z N_{\text{ion}}}{E/\mu} r_0^2 \ln \Lambda,$$

where  $E/\mu$  is the ratio of the kinetic energy to rest energy and  $\Lambda$  is the ratio of the maximum to minimum impact parameter. The bremsstrahlung spectrum thus obtained is

$$E_{\text{rad}}(\hbar\omega) = \frac{4}{3\pi} N_h \alpha \left( \frac{\theta_h}{\mu} \right) \frac{\langle Z^2 \rangle}{\langle Z \rangle \ln \Lambda} e^{-\mu/2} K_0(\mu/2),$$

where  $K_0$  is a modified Bessel's function and  $\mu$  is the ratio of the photon energy  $\hbar\omega$  to the creation temperature  $\theta_h$ , expressed as an energy.

Figure 6-17 shows the x-ray spectra for two high-intensity Parylene-disk shots. We observe that the suprathermal tail is drastically reduced when the region of underdense plasma is made large. The x-ray spectral intensity in keV/keV has been normalized to the incident laser energy in joules. The open symbols show the experimental points obtained by unfolding the seven-shooter and four-shooter data, while the solid symbols show the fit to a Maxwellian suprathermal-electron-creation spectrum of temperature  $\theta_h$ . Half-filled-in symbols designate the experimental points used for fitting. The order-of-magnitude difference in relative levels between the tails argues strongly for reduced absorption at critical density in the long-pulse, large-spot Argus experiments. Another surprise in this data is that the suprathermal temperatures are nearly the same although both intensities are near  $10^{16}$  W/cm<sup>2</sup>. The suprathermal temperature  $\theta_h$  increases with  $\lambda^2$  and with the cold background-electron temperature  $\theta_c$ . Thus, we would have expected  $\theta_h$  for the Argus experiment to be lower, because the actual intensity at critical density should be less.

The only approximation made that can substantially alter this conclusion, namely, that in the

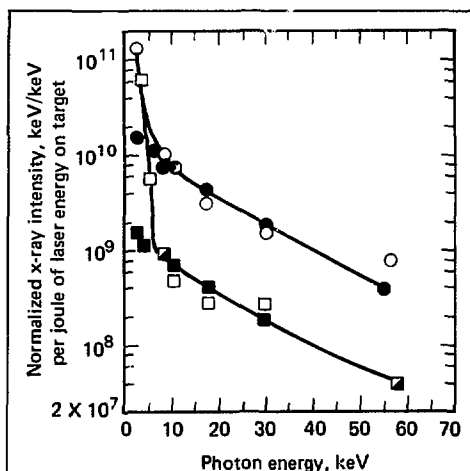


Fig. 6-17. The x-ray spectra for two high-intensity Parylene disk shots, showing that the suprathermal tail is drastically reduced when the region of underdense plasma is large. Circles represent short-pulse, small-spot shots (7.28 J, 51 ps, 30- $\mu$ m-diam spot,  $I = 2 \times 10^{16}$  W/cm<sup>2</sup>,  $\theta_h$  (fit) = 21 keV, 1.9 J (26%) absorbed at critical density). Squares represent long-pulse, large-spot shots (237 J, 307 ps, 104- $\mu$ m-diam spot,  $I = 0.9 \times 10^{16}$  W/cm<sup>2</sup>,  $\theta_h$  (fit) = 22 keV, 4.9 J (2%) absorbed at critical density).

Argus experiments only a small fraction is absorbed near critical density, is the assumption that most of the suprathermal electron energy is lost collisionally, not to the ambipolar electric field.

We are grateful for the encouragement and support of J. Emmett, J. Nuckolls, H. Ahlstrom, and C. Hendricks. We thank F. Rainer, C. Swift, and the others who helped with these experiments. We acknowledge useful discussions with W. Mead, K. Estabrook, and J. Larsen.

## References

33. B. H. Ripin, J. M. McMahon, E. A. McLean, W. M. Manheimer, and J. A. Stamper, "Time-Resolved Laser-Plasma Backscatter Studies," *Phys. Rev. Lett.* **33**, 634 (1974).
34. M. Lubin, in *Plasma Physics and Controlled Nuclear Fusion* (International Atomic Energy Agency, Vienna, 1974), vol. II, p. 459.
35. P. Lee, D. V. Giovanielli, R. P. Godwin, and G. H. McCall, "Harmonic Generation and Frequency Mixing in Laser-Produced Plasmas," *Appl. Phys. Lett.* **24**, 406 (1974).
36. R. Haas, W. C. Mead, W. L. Kruer, D. W. Phillion, H. N. Kornblum, J. D. Lindl, D. MacQuigg, V. C. Rupert, and K. G. Tirsell, "Irradiation of Parylene Disks with a 1.06- $\mu$ m Laser," *Phys. Fluids* **20**, 322 (1977).



37. R. Haas, H. D. Shay, W. L. Kruer, M. J. Boyle, D. W. Phillion, F. Rainer, V. C. Rupert, and H. N. Kornblum, "Interaction of 1.06- $\mu\text{m}$  Laser Radiation with Planar Targets," *Phys. Rev. Lett.* **39**, 1533 (1977).
38. C. Yamanaka, T. Yamanaka, T. Sasaki, J. Mizui, and H. B. Kang, "Brillouin Backscattering and Parametric Double Resonance in Laser-Produced Plasma," *Phys. Rev. Lett.* **32**, 1038 (1974).
39. A. A. Offenberger, M. R. Cervenak, A. M. Yam, and A. W. Pasternak, "Stimulated Brillouin Scattering of  $\text{CO}_2$  Laser Radiation from Underdense Plasma," *J. Appl. Phys.* **47**, 1451 (1976).
40. B. H. Ripin, F. C. Young, J. A. Stamper, C. M. Armstrong, R. Decoste, E. A. McLean, and S. E. Bodner, "Enhanced Backscatter with a Structured Laser Pulse," *Phys. Rev. Lett.* **39**, 611 (1977).
41. A. Offenberger, Anomalous Absorption Conference, Ann Arbor, Mich., 1977.
42. C. S. Liu, M. N. Rosenbluth, and R. B. White, "Raman and Brillouin Scattering of Electromagnetic Waves in Inhomogeneous Plasmas," *Phys. Fluids* **17**, 1211 (1974), and many references therein.
43. D. W. Forslund, J. M. Kindel, and E. Lindman, "Theory of Simulated Scattering Processes in Laser-Irradiated Plasmas," *Phys. Fluids* **18**, 1002 (1975).
44. D. W. Forslund, J. M. Kindel, and E. Lindman, "Plasma Simulation Studies of Stimulated Scattering Processes in Laser-Irradiated Plasmas," *Phys. Fluids* **18**, 1017 (1975).
45. W. L. Kruer, E. J. Valeo, and K. G. Estabrook, "Limitation of Brillouin Scattering in Plasmas," *Phys. Rev. Lett.* **35**, 1076 (1975).
46. C. L. Tang, *J. Appl. Phys.* **37**, 3945 (1959).
47. D. R. Speck and W. W. Simmons, "Argus Laser Fusion Facility," *Bull. Am. Phys. Soc.* **21**, 1173 (1976).
48. S. R. Gunn, *Calorimeters for Diagnosis of Laser-Fusion Experiments*, Lawrence Livermore Laboratory, Rept. UCID-17308 (1976).

## 6.6 Time-Resolved High-Energy X-Ray Spectra Measurements

In laser-produced plasmas, most of the electromagnetic radiation the plasma emits lies in the soft x-ray regime. The x rays generated from bremsstrahlung and recombination radiation yield direct information about the electron temperature. On the other hand, suprathermal or "hot" electrons are generated by the resonance-absorption mechanism as well as by other collective instabilities such as parametric decay, oscillating two-stream, and ion-turbulence heating. The hot x-ray emissions arise from the nonthermal high-energy tail on the electron energy distribution. For ablatively driven laser fusion targets, calculations show that suprathermal electrons generated by plasma instabilities tend to preheat the fuel and thus have a detrimental effect on target performance.<sup>49</sup> It is, therefore, important to study the temporal behavior of x-ray emission spectra of laser-produced plasmas for a better understanding of laser-plasma interactions and fusion target performance.

We have obtained temporally resolved x-ray emission spectra from laser-irradiated high-Z disk targets that show the evolution of hot x rays in time. The disk targets were gold or gold alloy, and the laser pulses were 200–400 ps FWHM with intensities  $\sim 10^{15} \text{ W/cm}^2$ .

The instrument used for the measurements is the X-1 x-ray streak camera described in detail in earlier laser program annual reports.<sup>50,51</sup> For the present purpose, we used filter packs with a number of separate K-edge filters to produce a temporal variation of the x-ray spectrum transmitted through the various K-edge filters. A typical 11-channel filter pack used with the streak camera is shown in Fig. 6-18. Filter elements from chlorine to silver provide the energy range ( $\sim 1$ –20 keV), and channels with the same element but different thicknesses

### Authors

D. W. Phillion  
W. L. Kruer  
V. C. Rupert

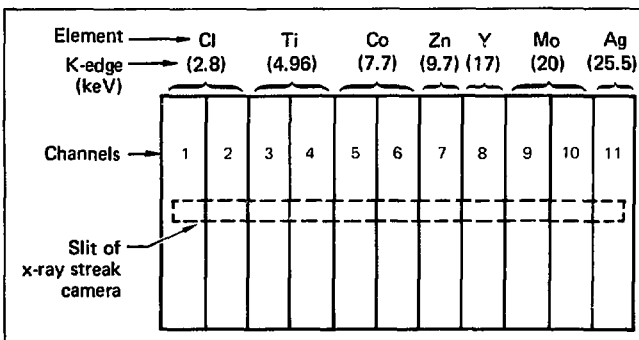


Fig. 6-18. A typical filter pack used with the x-ray streak camera to give temporally and spectrally resolved x-ray spectra.

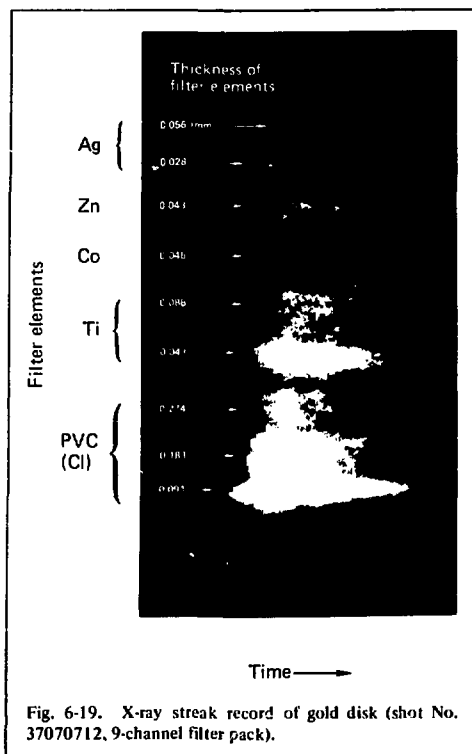


Fig. 6-19. X-ray streak record of gold disk (shot No. 37070712, 9-channel filter pack).

provide a large dynamic range in emission intensities and error-bar estimates.

A typical streak record is shown in Fig. 6-19. This is a record for a gold-disk target irradiated by a 240-ps FWHM laser pulse with an intensity of  $\sim 3 \times 10^{15} \text{ W/cm}^2$ . The result was obtained by using a 9-channel filter pack. From streak records like these, one can obtain the temporal response of each filter channel, i.e., the x-ray intensity vs time for each channel.

The hot x rays, i.e., emissions at the higher energy channels, have a temporal behavior that qualitatively follows the laser pulse. This can be seen from Fig. 6-20. These results were obtained from gold-disk targets irradiated by  $\sim 200$ -ps FWHM pulses with intensities of  $\sim 3 \times 10^{15} \text{ W/cm}^2$ . The fact that the temporal x-ray emissions from the higher energy channels behave like the laser pulse for short laser pulses ( $\sim 200$  ps) can be explained qualitatively by arguing that the hot electrons, and therefore the hot x rays, are generated by the resonance-absorption mechanism.<sup>52</sup> Because the ratio of the electron quiver velocity to the thermal velocity is maximum at the peak of the laser pulse,

the highest-energy electrons are generated at the peak; also, generation of electrons is most copious at the peak. For laser pulses longer than  $\sim 200$  ps FWHM, it is not necessarily true that the time behavior of the hot x-ray emissions follows the laser pulse; we do not have enough data to be certain.

From the time-resolved emissions obtained from each filter, the time-resolved x-ray spectra can be constructed. Figure 6-21 shows an example for a gold-disk target irradiated by a 416-ps FWHM Gaussian pulse. The laser intensity was  $1.69 \times 10^{15} \text{ W/cm}^2$  (Shot No. 37102612) and an 11-channel filter pack was used. This figure illustrates how the suprathermal tail evolves in time. The high-energy tail is being detected at about 180 ps before peak x-ray emission, increasing to a maximum value of 9 keV at the peak, and then decreasing with decreasing laser power. It is interesting to note in this case that, although the laser pulse is Gaussian in time, the high-energy x-ray spectra are not symmetric in time with respect to peak emission, having somewhat higher values before the peak than after the peak. On the other hand, the cold x-ray temperature  $\theta_c$  appears to be decoupled from the hot x-ray temperature  $\theta_h$ , having a value of approximately 0.7 keV throughout the laser pulse. It should be noted that the presence of prominent gold spectral lines at about 2.5 keV makes the determination of  $\theta_c$  somewhat uncertain.

The experimental results are compared with LASNEX code predictions in Figs. 6-22(a) and (b) for the hot and cold x-ray temperatures, respectively. The code predictions of  $\theta_h$  and  $\theta_c$  were obtained operationally by taking slopes of the x-ray power spectrum as computed by LASNEX. The error bars on the LASNEX curves represent the differing values of  $\theta$  one obtains when choosing different sets of points for slope measurements. The LASNEX computation is made under the assumption that inverse bremsstrahlung is the principal absorption mechanism and that about 20% of the light that reaches the critical surface is absorbed resonantly, creating a suprathermal tail. The electrons are put into a distribution such that

$$T_H = T_B + 49.4(I\lambda)^{0.425} T_B^{0.04} \left(1 + \frac{3T_i}{ZT_B}\right)^{0.25}, \quad (1)$$

where  $T_B$  is the average electron temperature,  $T_i$  is the ion temperature,  $I$  is the laser intensity in units of  $10^{17} \text{ W/cm}^2$ ,  $\lambda$  is the incident laser wavelength in microns, and  $Z$  is the charge state of the target material. Note that  $T_H$  is the hot-electron temperature and is not the same as the operationally defined  $\theta_h$ . Equation (1) is based on particle simula-

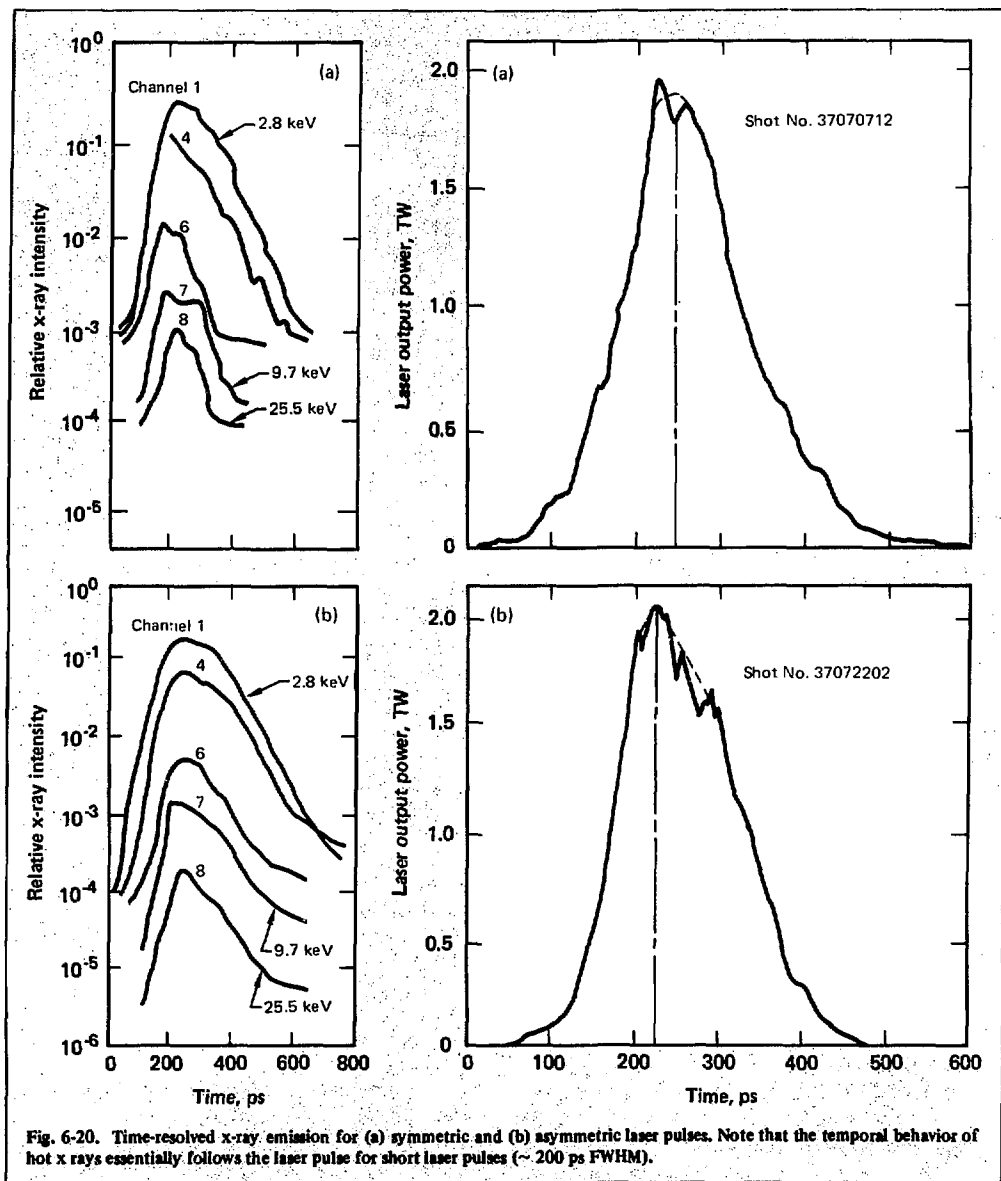


Fig. 6-20. Time-resolved x-ray emission for (a) symmetric and (b) asymmetric laser pulses. Note that the temporal behavior of hot x rays essentially follows the laser pulse for short laser pulses ( $\sim 200$  ps FWHM).

tions done by Kent Estabrook. For the case where the heat flux is inhibited by ion-acoustic turbulence, thought to occur readily in high-Z plasmas,<sup>53</sup> there is qualitative agreement between code predictions and experiment, the code predicting somewhat higher values than the measurements [see Fig. 6-22(a), inhibited-transport curve]. On the other

hand, if the heat flux is not inhibited, the plasma corona is cooled, thereby increasing the inverse bremsstrahlung, and only 10% of the light ends up being resonantly absorbed. Figure 6-22(a) clearly shows how such a mix of absorptions [see noninhibited-transport curve in Fig. 6-22(a)] does not match the observed data. The code predictions

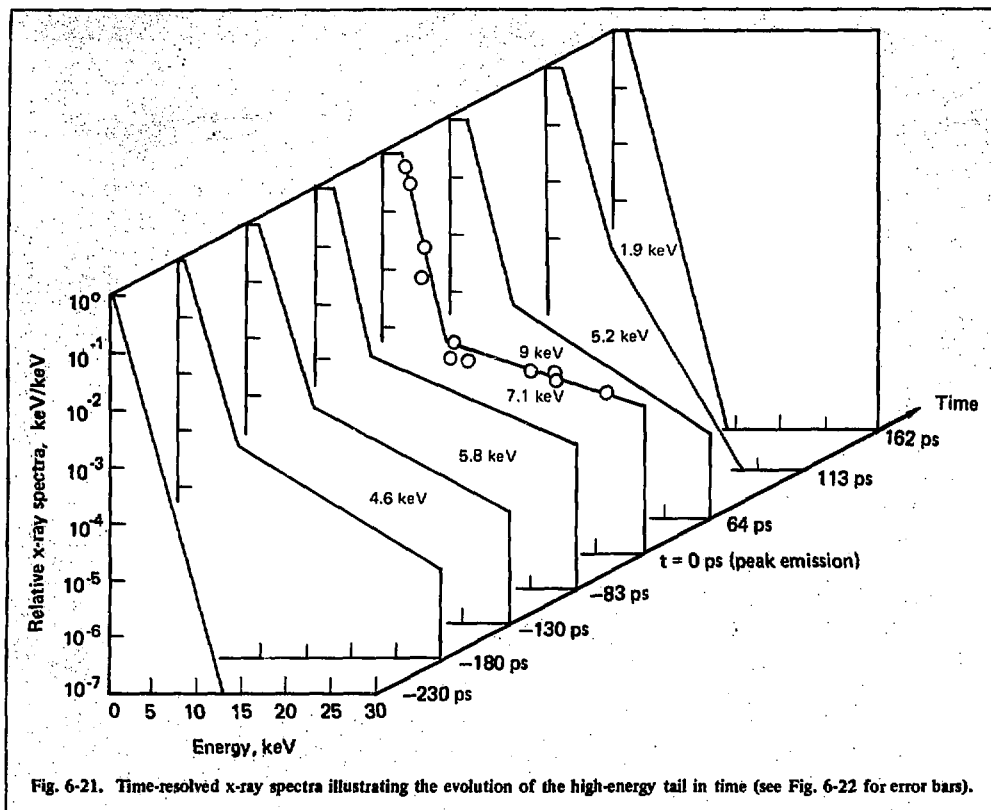


Fig. 6-21. Time-resolved x-ray spectra illustrating the evolution of the high-energy tail in time (see Fig. 6-22 for error bars).

for the cold x-ray temperatures yield values that are slightly lower than the measured values [see Fig. 6-22(b)], but, again, the major feature is in good agreement with the experiment; namely,  $\theta_c$  is fairly constant throughout the laser pulse.

Independent measurement on the same experiment with the seven-shooter<sup>54</sup> yields time-integrated data of  $\theta_c = 0.7 \pm 0.15$  keV and  $\theta_h = 14.1 \pm 3$  keV, which are in reasonable agreement with the x-ray streak-camera data as well as the code predictions.

The spectra for the  $\sim 200$ -ps high-intensity shots are not presented because, for short pulses with high intensity ( $> 3 \times 10^{15}$  W/cm<sup>2</sup>), the x-ray spectra become quite hard; i.e., the spectrum is not decreasing rapidly enough with increasing energy. This creates a difficulty with the K-edge filter technique because the filters become very "leaky" and the energy channels become unacceptably broad. The result is that the high-energy tail slope on the unfolded x-ray spectra becomes horizontal

or even has positive slope. Both the x-ray streak camera and the seven-shooter<sup>54</sup> have experienced such difficulties. This problem has been resolved for time-integrated measurements by using the filter-fluorescer technique,<sup>55</sup> and the same approach is being implemented by using the x-ray streak camera.

In conclusion, we have succeeded in obtaining time-resolved high-energy x-ray spectra measurements by using the x-ray streak camera with multi-channel filter packs. The results enable us to observe the hot x-ray temperature evolve in time and to qualitatively predict the experimentally observed values by LASNEX computations when the inhibited-transport model is used.

## References

49. J. Nuckolls, L. Wood, A. Thiessen, and G. Zimmerman, "Laser Compression of Matter to Super-High Densities: Thermonuclear (CTR) Applications," *Nature* **239**, 139 (1972).

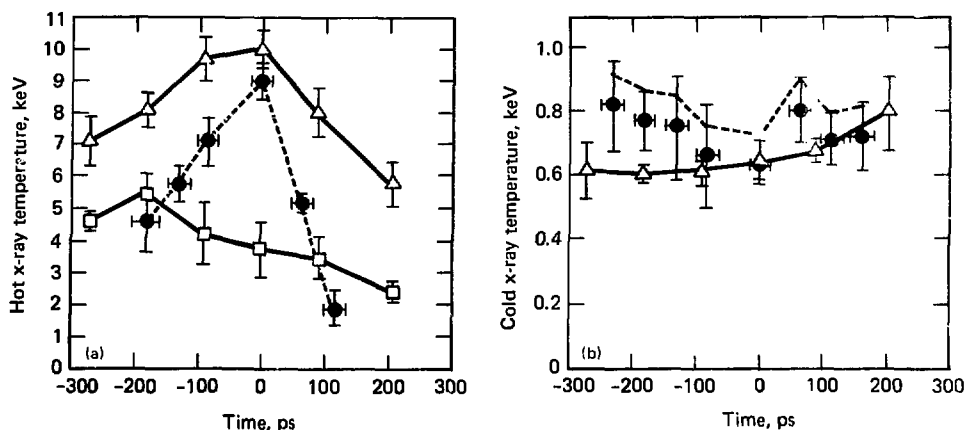


Fig. 6-22. Comparison of measured and LASNEX-predicted (a) hot and (b) cold x-ray temperatures as functions of time. Circles are experiment points. Triangles are LASNEX points for inhibited transport. Squares are LASNEX points for noninhibited transport. Zero time refers to peak of the laser pulse. Note that the inhibited transport model yields a qualitative agreement between code predictions and experiment.

50. L. Coleman and D. Attwood, "Ultrafast X-Ray Streak Camera," *Laser Program Annual Report — 1974*, Lawrence Livermore Laboratory, Rept. UCRL-50021-74 (1975), p. 315.
51. D. T. Attwood, L. W. Coleman, and I. W. Houghton, "Time-Resolved X-Ray Emission," *Laser Program Annual Report — 1975*, Lawrence Livermore Laboratory, Rept. UCRL-50021-75 (1976), p. 418.
52. G. Estabrook, E. J. Valeo, and W. L. Kruer, "Two-Dimensional Relativistic Simulations of Resonance Absorption," *Phys. Fluids*, **18**, 1151 (1975).
53. See §6.7 of this report.
54. H. Kornblum, Lawrence Livermore Laboratory, private communications (1977).
55. K. G. Tirsell, "Multichannel Filter-Fluorescer Experiment for X-Ray Measurements above 2 keV," §3.4.5 of this report.

## Authors

P. Lee  
M. Rosen

## 6.7 Experimental and Theoretical Investigation of High-Z Disks Irradiated with 1.06- $\mu\text{m}$ Laser Light

High-Z disks have been irradiated at 1.06  $\mu\text{m}$  using one beam of the Argus laser system. The light intensity has been varied from  $7 \times 10^{13}$  to  $3 \times 10^{15}$  W/cm<sup>2</sup> by changing laser energies from 100 to 500 J, laser pulse widths from 200 to 1000 ps, and

irradiated spot diameters from 150 to 500  $\mu\text{m}$ . Because of the high Z of the material (typically gold), inverse bremsstrahlung, the classical light-absorption mechanism, become an important effect and competes strongly with resonance absorption and stimulated scattering. The details of the competition among these processes are quite subtle, and the present experiments represent an extension of previously reported work<sup>56,57</sup> into longer pulse, higher intensity parameter regimes.

Plasma and x-ray energy is directly measured<sup>58</sup> by using calorimeters that detect ions and x rays but subtract out the scattered 1- $\mu\text{m}$  light. The distribution of the target energy is integrated, which gives the absorbed energy. The scattered light is measured with Si PIN diodes (100-Å bandwidth filter) and 1.06- $\mu\text{m}$  calorimeters, giving a measurement of the light not absorbed by the target and thus the absorption. Finally, an enclosing 1.06- $\mu\text{m}$  calorimeter performs the same task as the PIN diodes, but covers the solid angle around the disk continuously. The absorptions for the various intensity shots are listed in Table 6-1. (The error bars to be placed on the data are roughly 10%. Thus, a 50% absorption could be 45 to 55%.) Sub-keV five-channel L- or K-edge filtered x-ray detectors, with 300- to 500-ps time resolution, measure the low-energy x-ray distribution wherein most of the x-ray energy lies, as do flat-response sub-keV calorimeters.<sup>59</sup> Because of the limited number of these

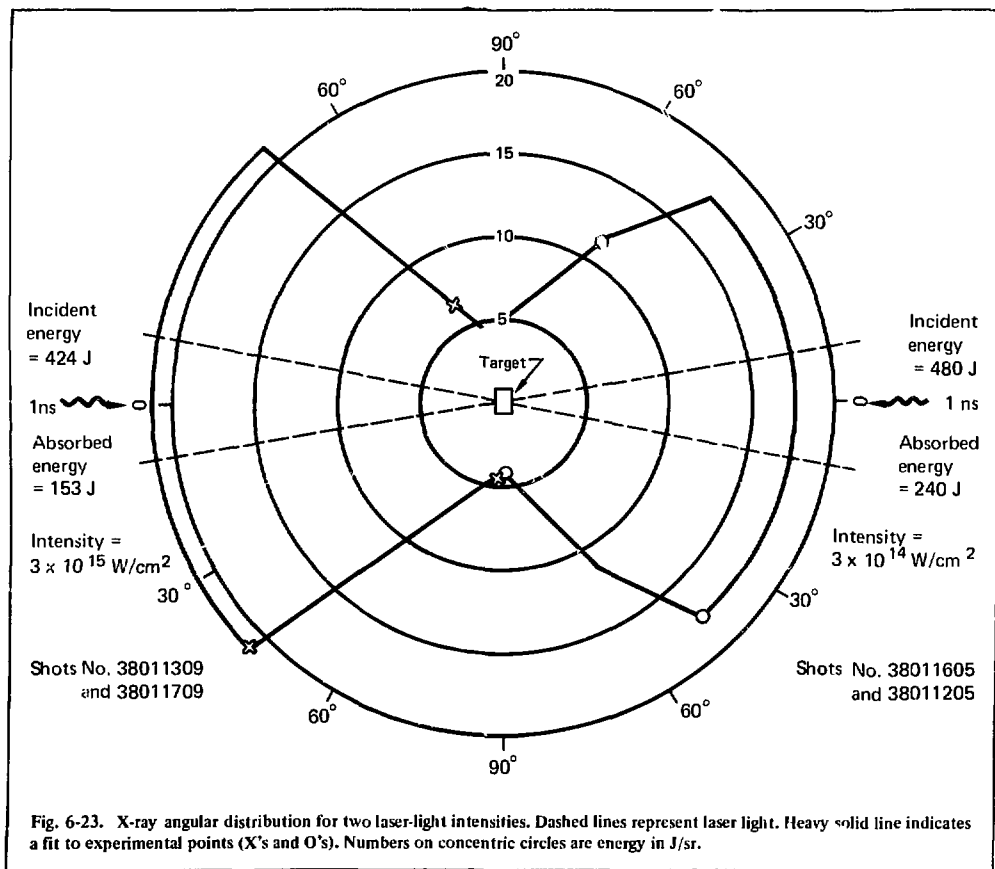
**Table 6-1. Experimentally measured absorptions.**

Intensity (W/cm <sup>2</sup> )	$3 \times 10^{15}$	$3 \times 10^{14}$	$3 \times 10^{14}$
Energy (J)	450	450	45
Absorption (%) at angle of incidence			
$\theta = 0^\circ$	36	50	54
$45^\circ$	33	42	

detectors and their limited access to a target enclosed in a box calorimeter, the targets are shot in two configurations: first at  $0^\circ$  to the incident laser pulse, and second at  $45^\circ$ . In this way, we determine the angular distribution of the x rays, integrated over  $4\pi$ , which contributes to our understanding of the energy balance in these experiments. Angular distributions for two intensities are shown in Fig. 6-23. Crystal spectrometers above 1 keV give infor-

mation on characteristic line emission and on the continuum between 2 and 5 keV. Suprathermal electrons produce hot x-ray tails in the spectra, which are measured by using K-edge filtered Si PIN diodes. Thus, we can obtain a rather complete spectrum, an example of which is discussed later in this subsection. An x-ray microscope gives spatially resolved emission regions, also discussed later in this subsection, while an x-ray streak camera gives time-resolved information discussed in §6.6 of this report.

We use the LASNEX<sup>60</sup> code to model the relevant physics of these experiments. The absorption model we use allows for inverse bremsstrahlung as a light ray refracts through the underdense plasma. In addition, 30% of whatever light that reaches the critical surface (some of which has been absorbed on the way in by inverse bremsstrahlung) is absorbed by collective effects such as resonance absorption. This 30% number is based on plasma



simulations<sup>61</sup> and on absorption experiments on Parylene disks.<sup>62</sup> The important physical effect of stimulated scattering is not included in the LASNEX modeling, although we estimate its effect on the absorption later in this subsection.

The general energy balance of these experiments can be described as follows. The absorbed laser light heats electrons at the critical surface and below. Electron thermal conduction then heats the overdense region, where the electron-ion coupling is strong. Energy is lost in ionizing the high-Z atoms and in heating the electrons and ions. Further losses are caused by radiation and convective energy of ion blowoff into the vacuum. LASNEX simulations without inhibited electron thermal transport, stimulated scattering, and non-LTE ionization physics predict 99% absorption for the nanosecond-pulse experiments. The high-Z material cooled the electrons radiatively, increasing the collision frequency ( $\nu_{ei} \sim ZT_e^{-3/2}$ , where  $T_e$  is the electron temperature) and thus increasing the inverse bremsstrahlung absorption. In addition, the long pulse created a long scale length in which the absorption could occur. However, the experimental results showed absorptions of 50% or less (recall Table 6-1). We have found that inhibited electron thermal conduction, non-LTE ionization physics, and stimulated scattering are important effects to be included in the modeling. The inhibition reduces transport into the overdense region. Thus, only a small amount of material is heated to several keV temperatures and forms a hot, low-density corona. This results in a sharp transition from cool, overdense material, which has not been reached by the inhibited thermal front, to the hot corona. This sharp transition reduces the absorption scale length. At critical density, an electron-electron collision can take tens of picoseconds. An ion moving at the sound speed across this thin transition layer (a few microns

thick) takes only a few picoseconds. This is shorter than characteristic relaxation times, so a steady-state treatment is inaccurate. In addition, radiatively induced transitions dominate over collisional three-body recombination in the hot, low-density corona. Thus, non-LTE ionization physics must be used instead of the usual Saha equilibrium model. The non-LTE physics tends to lower the Z and thus further reduces the absorption towards experimental levels.

Figure 6-24 illustrates the mechanics of a leading candidate for inhibited conduction: the ion-acoustic instability.<sup>63-65</sup> The cold return current neutralizing the hot-electron current causes a shifted Maxwellian distribution centered around a drift velocity  $v_d$ . Once  $v_d$  becomes greater than the sound speed  $c_s$ , the positive slope at  $c_s$  causes electron Landau growth, leading to ion turbulence and the enhanced collisionality and transport inhibition associated with it. This result assumes that  $c_s \gg$  ion velocity  $v_i$  so that there is no ion Landau damping to counter the instability. The simplest nonlinear model is to assume that the resulting ion turbulence causes  $v_d$  to hover near the point of onset of significant growth, i.e.,  $v_d \approx c_s$ . Thus, the inhibition is roughly  $c_s$ /electron velocity  $v_e \approx 0.01$ . The condition  $c_s \gg v_i$  is equivalent to  $ZT_e \gg$  ion temperature  $T_i$ , which is achieved in much of parameter space in high-Z plasmas. However, theoretical uncertainties in growth rate and saturation level lead to some questions about the actual level of transport inhibition produced. Other possible mechanisms are macroscopic and microscopic magnetic fields.

Figure 6-25 contrasts electron density and temperature profiles for an inhibited-vs-non-inhibited LASNEX calculation. Note the steepened profile and hot corona of the inhibited modeling. The position of the critical surface  $x_c$  moves further out in the noninhibited case than in the inhibited

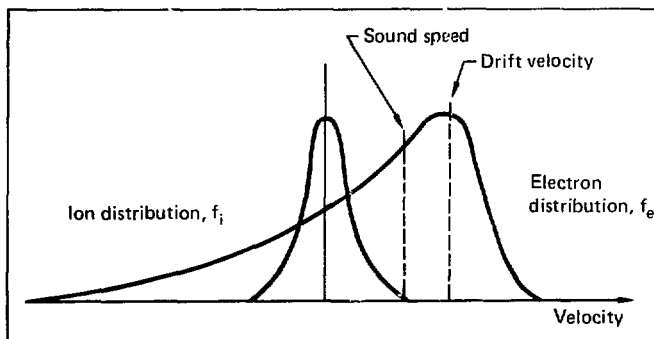
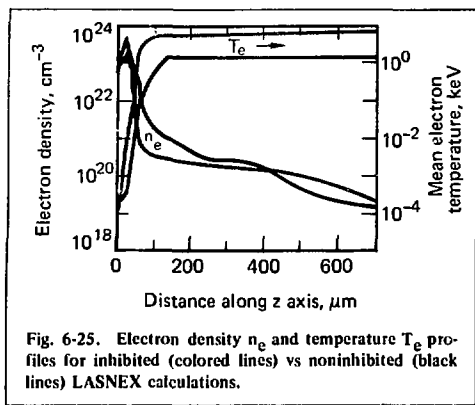


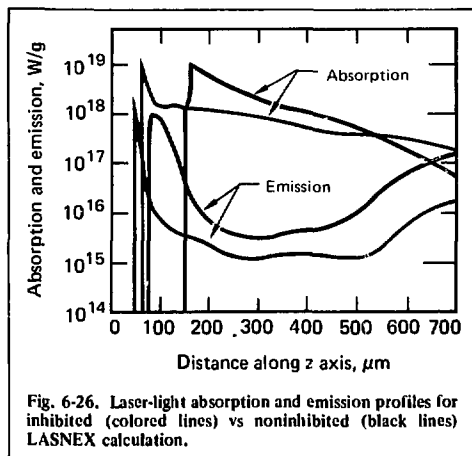
Fig. 6-24. Ion-acoustic instability, which inhibits heat flux. Electron distribution with suprathermal tail and cold return current satisfies current  $J \sim \int f_e v dv = 0$ , but heat flux  $Q \sim \int f_e v^3 dv \neq 0$ . As pictured here, drift velocity  $v_d >$  ion sound speed  $c_s \gg$  ion thermal velocity  $v_i$ , and ion turbulence will grow.



one, because enhanced thermal transport inward blows more bulk plasma outward. Figure 6-26 shows how the absorption and emission profiles differ in the two cases. Note the much wider emission region for the noninhibited case. This large width implies too much energy lost through radiation (70% of the absorbed energy), whereas the experimental levels of 35% ( $\pm 10\%$ ) are much closer to the 40% implied by the thinner emission region of the inhibited case.

Table 6-2 compares the LASNEX absorption results (both inhibited and noninhibited modeling) vs experiments at normal incidence, and clearly shows the importance of including the inhibition. Nonetheless, there are still discrepancies even in the inhibited case. Theoretical estimates of stimulated Brillouin scattering can be obtained by interfacing the models<sup>66</sup> and simulations<sup>67</sup> with the density and temperature profiles from LASNEX runs. The estimates for the  $3 \times 10^{15}$  W/cm<sup>2</sup> shots predict that  $\approx 50\%$  of the laser energy can be lost because of backscattering, never to reach the critical surface.

In support of the estimates is the strong experimental evidence that such processes are indeed occurring. Light that is back-scattered through the lens shows clear red (longer wavelength) shifts, a signature of Brillouin backscatter. Figure 6-27

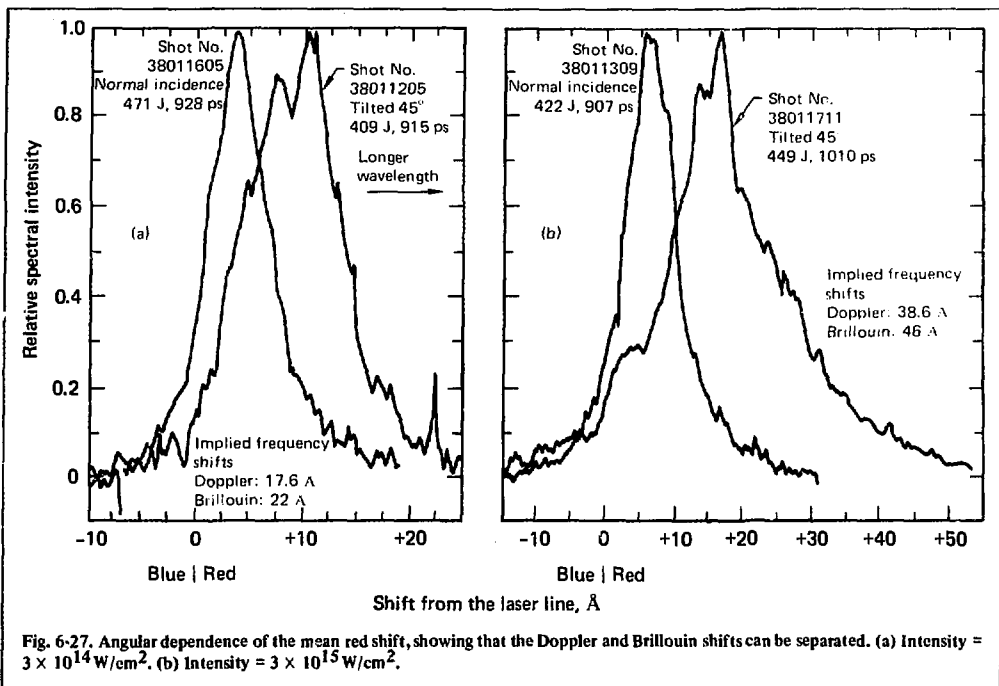


shows these red shifts for the high-intensity shots, for both 0 and 45° disk tilts. Because backscatter red shifts are reduced by Doppler blue (shorter wavelength) shifts of the outwardly moving matter, the 45° tilted disk has its blue shift component reduced by  $\cos 45^\circ$ , and thus the 45° case shows a larger red shift. From the different shifts at 0 and 45°, we have two equations in two unknowns (red shift and blue shift), and  $T_e$  can be determined to within a factor of two or three. That factor is caused by uncertainties about where (in  $n/n_c$ , where  $n$  is plasma density and  $n_c$  is critical density) the backscatter occurs. The  $T_e$  values of a few keV for  $3 \times 10^{14}$  W/cm<sup>2</sup> and 20 keV for  $3 \times 10^{15}$  are supported by the simulations to within the uncertainties of these measurements. The 50% loss figures are approximately what is needed to bring the LASNEX absorption numbers into agreement with the experiments for the high-intensity cases (40% becomes 20%, and 60% becomes 30%). For lower intensities ( $3 \times 10^{14}$  W/cm<sup>2</sup>), 15% loss caused by stimulated scattering is predicted, reducing the 70% absorption figure to 60%, in close agreement with the 50% experimental number. These corrections are summarized in Table 6-3.

Table 6-2. LASNEX absorption results vs experiment at normal incidence.

Energy, J	Time, ps	Intensity, W/cm <sup>2</sup>	Absorption of laser light, %		
			Noninhibited LASNEX	Inhibited LASNEX	Experiment
300	200	$3 \times 10^{15}$	60	40	20
450	1000	$3 \times 10^{15}$	90	60	36
450	1000	$3 \times 10^{14}$	99	70	50





Asymmetries detected in the light scattered in and out of the plane of polarization are another indication that Brillouin side-scatter is occurring. In fact, it was the polarization dependence of the scattered light that provided the first experimental evidence of the importance of Brillouin scattering. The LASNEX simulations do not yet model stimulated scattering. Another effect not included in the simulations (this time in the direction of raising the absorption) is an enhanced collision frequency (and hence enhanced absorption) caused by the ion-acoustic turbulence that has created the flux inhibition. Without quantitatively treating these two effects, we cannot be certain that our model is completely accurate.

There is additional evidence that the model is correctly simulating the experiment. Figure 6-28 shows an x-ray microscope picture of a 2-keV emission region for low-intensity runs compared with LASNEX simulations, with the obvious conclusion that only the inhibited model can match the experiment. Figure 6-29 shows the time behavior of the 400-eV x rays (which are near the peak of the emission spectrum) for the two models. Once again, the experiment agrees more closely with the inhibited model. Figure 6-30 shows the close agreement of the predicted spectra with the experimentally observed one as long as the inhibited non-LTE model is used. In contrast, LTE's overestimation of the ionization (its neglect of photorecombinative processes) results

Table 6-3. LASNEX absorption results (corrected for stimulated scattering) vs experiment.

Energy, J	Time, ps	Intensity, $\text{W/cm}^2$	Stimulated-scattering factor	Absorption of laser light, $\sigma_0$				
				Inhibited LASNEX		Corrected LASNEX	Experiment	
300	200	$3 \times 10^{15}$	0.5	x	40	=	20	20
450	1000	$3 \times 10^{15}$	0.5	x	60	=	25	36
450	1000	$3 \times 10^{14}$	0.85	x	70	=	40	50

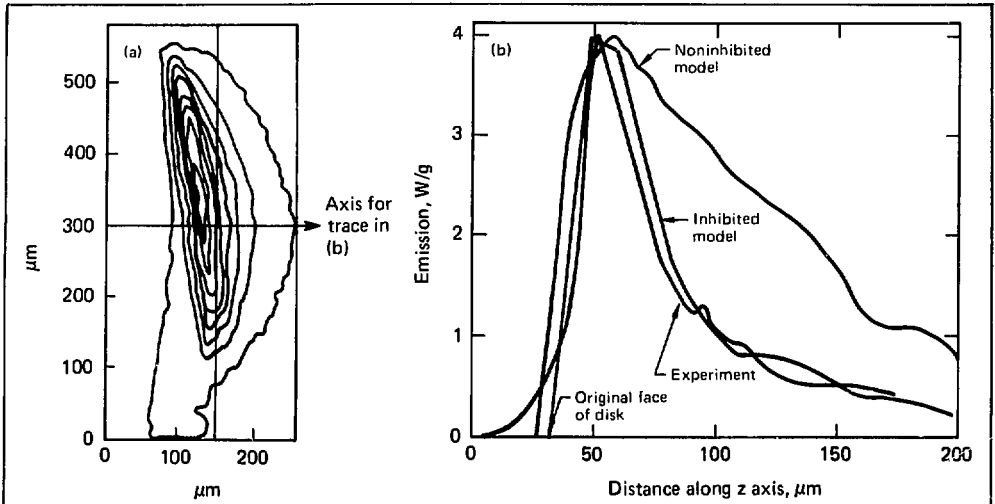


Fig. 6-28. 2-keV x-ray microscope image of the edge of the target disk (a) and LASNEX simulations (b) compared with densitometer trace through the image in (a), implying that transport inhibition exists.

in the superenhancement of high-energy spectral lines and thus fails to match the experimentally observed spectrum. In addition, we note that even the inhibited non-LTE model has a hot x-ray tail that is too high in absolute level. We interpret this

discrepancy as another indication of Brillouin scattering that denies the incident light access to the critical surface. This restriction cuts down the resonance-absorption fraction and thus the level of the hot x-ray tail.

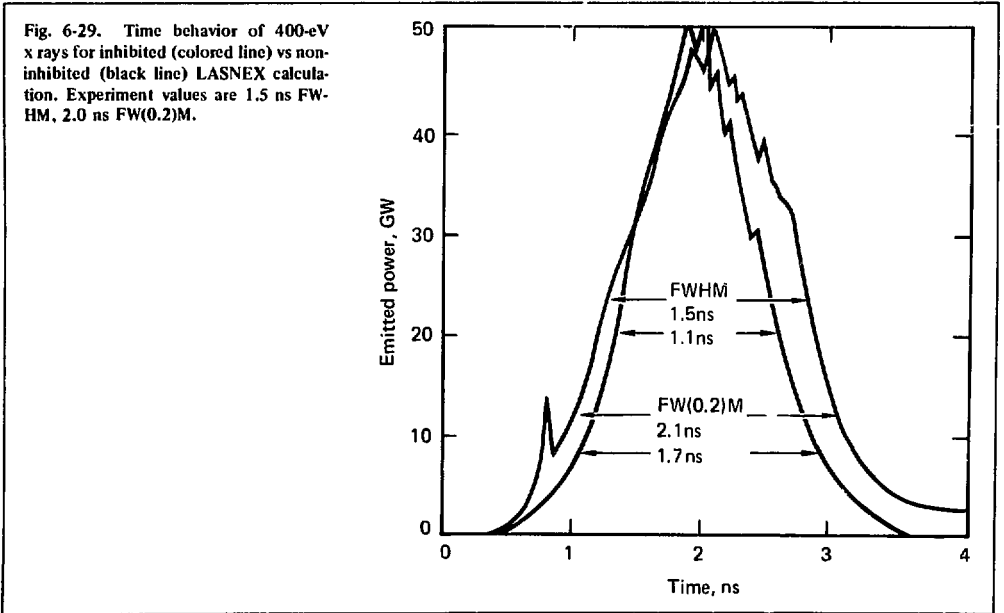


Fig. 6-29. Time behavior of 400-eV x rays for inhibited (colored line) vs non-inhibited (black line) LASNEX calculation. Experiment values are 1.5 ns FWHM, 2.0 ns FW(0.2)M.

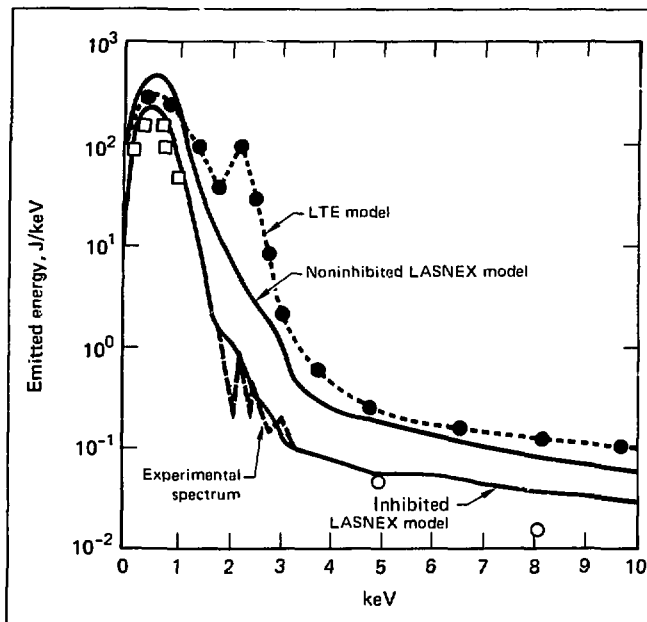


Fig. 6-30. Inhibited LASNEX model matching experimental spectrum. Non-inhibited and LTE models do not match. Open circles and squares are experimental points.

Although the model described here gives results that generally agree with the experimental data, we have not determined that this model uniquely fits the data. Both two-dimensional effects and zoning affect the simulations. The assumed degree of transport inhibition seems uncomfortably high theoretically and has not been determined experimentally. Nor are the amounts of stimulated scattering or absorption by collective processes reliably known theoretically or experimentally. Further, the laser pulse duration has been varied over a factor of only five.

In conclusion, inhibited electron thermal conduction, non-LTE ionization physics, and stimulated scattering are important effects to consider when modeling the interaction of 1.06- $\mu\text{m}$  laser light with high-Z materials. Our model correctly predicts many aspects of these experiments. Further work is needed in several areas, particularly on quantitatively simulating Brillouin scattering and self-consistently treating the ion-acoustic turbulence, which not only inhibits thermal transport but also enhances absorption. The effects of two-dimensional plasma expansion and zoning are uncertain as well and are under study at this time. More experimental work is needed to develop a way to look at the spectral shifts of the side-scattered light (not just the back-scattered light, as is presently done) to quantify the total amount of stim-

ulated scattering. In addition, we need to develop methods of measuring the transport inhibition and the collective and collisional absorptions.

## References

56. R. A. Haas, H. D. Shay, W. L. Kruer, M. J. Boyle, D. W. Phillion, F. Rainer, V. C. Rupert, and H. N. Kornblum, "Interaction of 1.06- $\mu\text{m}$  Laser Radiation with Planar Targets," *Phys. Rev. Lett.* **39**, 1533 (1977).
57. P. J. Mallozzi, H. M. Epstein, R. G. Jung, D. C. Applebaum, B. P. Fairand, and W. G. Gallagher, "X-Ray Emission from Laser-Generated Plasmas," in *Fundamental and Applied Laser Physics*, M. S. Field, A. Javan, and N. A. Kurnit, Eds. (John Wiley and Sons, New York, 1973), pp. 165-200.
58. H. G. Ahlstrom, *Laser Fusion Implosion and Plasma-Interaction Experiments*, Lawrence Livermore Laboratory, Rept. UCRL-79819 (1977). This paper reviews much of the instrumentation involved in diagnosing experiments on Argus.
59. H. N. Kornblum and V. W. Slivinsky, "Fast-Response, Subkiloelectronvolt X-Ray Detector with a Subnanosecond Time Response," *Rev. Sci. Instrum.* **49**, 1204 (1978).
60. G. B. Zimmerman, *Numerical Simulations of the High-Density Approach to Laser Fusion*, Lawrence Livermore Laboratory, Rept. UCRL-74811 (1973).
61. K. G. Estabrook, E. G. Valeo, and W. L. Kruer, "Two-Dimensional Relativistic Simulations of Resonance Absorption," *Phys. Fluids* **18**, 1151 (1975).
62. K. R. Manes, V. C. Rupert, J. M. Auerbach, P. Lee, and J. E. Swain, "Polarization and Angular Dependence of 1.06- $\mu\text{m}$  Laser-Light Absorption by Planar Plasmas," *Phys. Rev. Lett.* **39**, 281 (1977).

63. B. D. Fried and R. W. Gould, "Longitudinal Ion Oscillations in a Hot Plasma," *Phys. Fluids* **4**, 139 (1961).
64. R. C. Malone, R. L. McCrory, and R. L. Morse, "Indications of Strongly Flux-Limited Electron Thermal Conduction in Laser-Target Experiments," *Phys. Rev. Lett.* **34**, 721 (1975).
65. D. W. Forslund, "Instabilities Associated with Heat Conduction in the Solar Wind and Their Consequences," *J. Geophys. Res.* **75**, 17 (1970).
66. D. W. Phillion, W. L. Kruer, and V. C. Rupert, "Brillouin Scatter in Laser-Produced Plasmas," *Phys. Rev. Lett.* **39**, 1529 (1977).
67. K. G. Estabrook, Lawrence Livermore Laboratory, private communication (1977).

## Authors

**M. D. Rosen**  
**V. C. Rupert**  
**W. C. Mead**  
**J. J. Thomson**  
**D. W. Phillion**  
**V. W. Slivinsky**  
**M. J. Boyle**  
**W. L. Kruer**

## 6.8 Exploding-Pusher Target Experiments on Argus

A series of thin-walled, large-diameter, spherical targets were irradiated at the Argus laser fusion facility during 1977. Two f/1 aspheric lenses focused approximately 3 TW of 1.06- $\mu\text{m}$  light tangentially down on 100- to 150- $\mu\text{m}$ -diam microsphere targets. Gaussian pulse widths (FWHM) between 150 and 200 ps were used. Departing significantly from previous high-power, short-pulse exploding-pusher experiments at LLL in which the incident power was delivered in times between 30 and 80 ps, these experiments extended the pulse duration of exploding-pusher parameter space investigated to

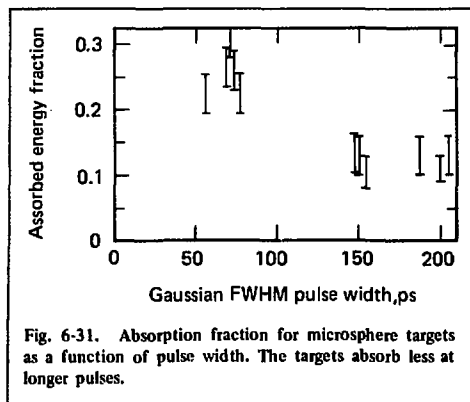


Fig. 6-31. Absorption fraction for microsphere targets as a function of pulse width. The targets absorb less at longer pulses.

date at LLL. In particular, a nonoptimized exploding-pusher target regime was examined. Here, we report the results of these long-pulse, large-diameter experiments, comparing them with the previous short-pulse, small-diameter experiments. We compare the absorption characteristics, the neutron yields, and the energy loss (or gain) of the thermonuclear alpha particles generated within the compressed core of the imploded microspheres. Table 6-4 summarizes and compares the parameters and pertinent results.

Figure 6-31 shows the absorption fraction for microsphere targets as a function of pulse width. These absorption data result from a variety of techniques, including energy balance from discrete Si-PIN-diode scattered-light detectors, plasma calorimeters, and near- $4\pi$  scattered 1.06- $\mu\text{m}$  light calorimetry (box calorimeter). Similar f/1 focusing optics and tangential marginal-ray focusing strategies were used for all these experiments. At the longer pulse widths, the target absorbs only about 10% of the light; the short-pulse absorption fractions are approximately twice that amount.

**Table 6-4. Parameters and results of previous and present microsphere implosion experiments.**

	Previous experiments (short pulse, small diameter)	Present experiments (long pulse, large diameter)
Target parameters	85- $\mu\text{m}$ -diam, 0.8- $\mu\text{m}$ wall, 2 mg/cm <sup>3</sup>	150- $\mu\text{m}$ -diam, 1.0- $\mu\text{m}$ wall, 2 mg/cm <sup>3</sup>
Laser parameters	120 J, 40 ps, 3 TW	550 J, 150 ps, 3.8 TW
Absorption fraction	22%	10%
Yield ratio	$2 \times 10^{-5}$	$6 \times 10^{-8}$
Alpha and proton energy shifts	- 250 keV (He <sup>4</sup> ) - 100 keV (D-D)	+ 300 keV (He <sup>4</sup> ) + 200 keV (D-D)
Back-scattered spectrum	—	~80% red shifted
Ion temperature	5-6 keV	3-3.5 keV

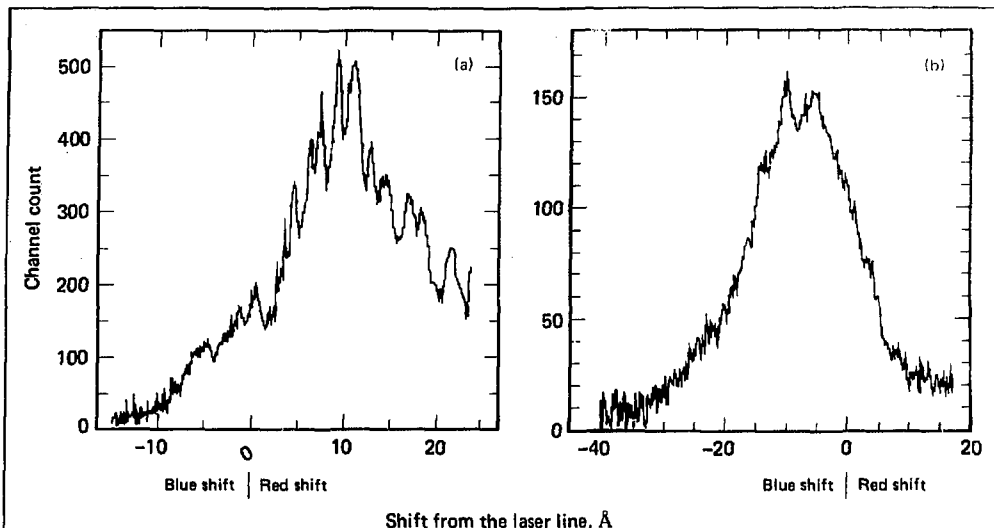


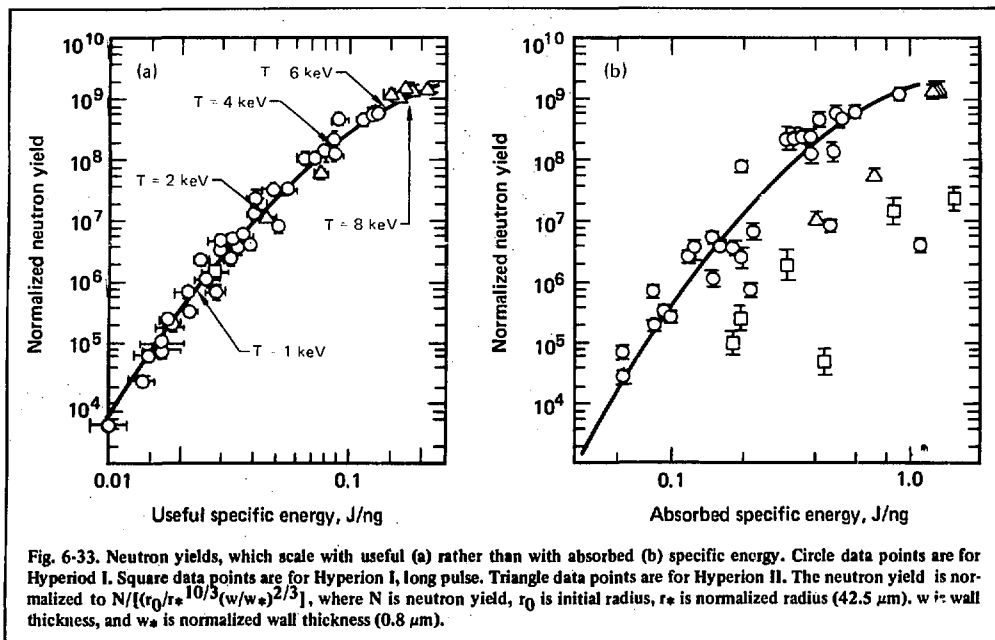
Fig. 6-32. Spectrum of the back-reflected light, which broadens and shifts to the red in large-spot, long-pulse, high-intensity experiments. (a) Spherical glass microshell,  $f/1$  lenses,  $140\text{-}\mu\text{m}$  spot diam,  $150\text{ ps}$ ,  $420\text{ J}$ ,  $5 \times 10^{15}\text{ W/cm}^2$ , 12% absorbed. (b) Parylene disk,  $f/1$  lens,  $100\text{-}\mu\text{m}$  spot diam,  $198\text{ ps}$ ,  $148\text{ J}$ ,  $10^{16}\text{ W/cm}^2$ , 12% absorbed.

This trend for long-pulse results is accompanied by an increased red shifting of the  $1.06\text{-}\mu\text{m}$  light back-reflected into the focusing lens. While the back-reflected spectrum has not yet been directly measured for short-pulse, spherical-target conditions, planar targets irradiated at similar intensities and with short pulses exhibit primarily blue-shifted spectra. In contrast, the typical long-pulse back-reflected spectra from spherical targets, illustrated in Fig. 6-32, appear to be nearly 80% red shifted. The long-pulse conditions are favorable for formation of long density gradients in the underdense plasma, which in turn produce favorable conditions for stimulated Brillouin scattering (SBS). The lower observed absorptions and the red-shifted reflectivity spectra are consistent with SBS, playing a significant role in these long-pulse experiments.

In Fig. 6-33 we plot the long-pulse, large-ball neutron yields against the absorbed specific energy and compare them with other short-pulse results. Variations in target geometry (i.e., microsphere diameter and wall thickness) have been accounted for by the normalizations indicated. The solid line reflects the neutron dependence on the Maxwellian-averaged DT thermonuclear cross section, assuming that the ion temperature is proportional to the absorbed specific energy. Clearly, the normalized long-pulse yields do not fall along the curve. Simple

scaling models better correlate the apparent variations in neutron yield for exploding-pusher microsphere targets. One such model postulates a simple relationship between the laser-energy absorption times and the hydrodynamic implosion times (see §5.6.3). Obviously, laser absorption after the implosion of the microsphere target can no longer contribute to the increase in thermonuclear events. The more exact specification of this laser-absorption cutoff time results in the definition of useful rather than absorbed specific energy. Upon replotting the data with useful energy as the independent variable [Fig. 36(b)], all the neutron data appear consistent with the anticipated temperature dependence of the Maxwellian-averaged thermonuclear cross section  $\langle\sigma v\rangle$ . The reduced ion temperatures implied by these degraded yields were indeed directly measured, as presented in Table 6-4. Hence, the significantly reduced thermonuclear gains correspond to the nonoptimum matching between the incident pulse and the target geometry parameters as anticipated.

Finally, we obtained interesting results concerning the net energy change experienced by the  $3.52\text{-MeV}$  alpha particles born within the core of the compressed target as a result of the thermonuclear events. The energy spectra of the alpha particles were determined by time-of-flight tech-

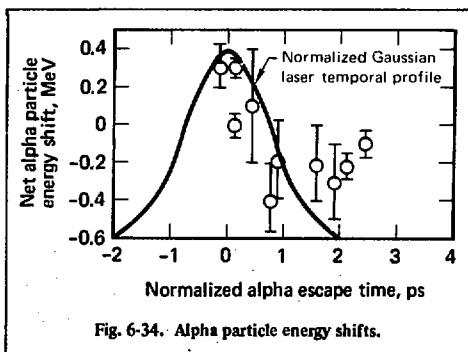


niques, using magnetic spectrometers for both the short- and long-pulse experiments. As indicated in Table 6-4, the net change in the alphas' energy appears to vary with incident laser pulse width. In short-pulse experiments, the peak of the alpha-particle distribution is downshifted approximately 250 keV in traversing the fuel and pusher. In several long-pulse experiments, on the other hand, net energy gains are observed.

Upon closer examination, the amount of alpha energy upshift depends on the time relative to the peak of the incident laser pulse, where the thermonuclear reaction products traverse the coronal region of the microsphere target. One may estimate this time by using the exploding-pusher scaling model discussed earlier with respect to neutron yields. Inputting the target geometry (diameter, wall thickness, DT fill) and laser conditions (power, pulse width, absorption fraction), one may calculate thermonuclear burn times with respect to the peak of the pulse. Assuming that the alpha particles exit the TN burn region with a constant velocity characteristic of their 3.5-MeV creation energy, one may estimate alpha transit times from the core to the outer absorbing coronal region, assumed to be at the initial radius of the microsphere. The time of TN burn and the alpha transit time combine to define an alpha escape time with respect to the peak

of the incident laser pulse. The alpha energy data from all the experiments may then be examined by plotting net energy shifts against these relative escape times, which have been normalized to their respective laser pulse's FWHM, as is done in Fig. 6-34. To help show the correlation, a representative, normalized Gaussian laser temporal profile has been superimposed on the data in Fig. 6-34.

Only where the alphas exit the pellet at times near the peak of the laser pulse is the alpha energy distribution upshifted (i.e., long-pulse, nonoptimized, exploding-pusher experiments). Conversely,



where the alphas are calculated to exit the outer regions of the pellet at times after the incident pulse, a nearly constant energy loss is observed. This energy loss is associated primarily with the nominal energy loss encountered through the pellet's fuel and pusher. On the other hand, we postulate that the observed energy upshifts are related to electrostatic accelerations that occur as the alpha particles traverse the regions near critical density, where the ongoing absorption processes have generated incident-intensity-dependent (hence, time-dependent) electric fields.

**Author**

**M. J. Boyle**

## 6.9 Images of High-Energy X-Ray and Thermonuclear Alpha Particle Emissions from Exploding-Pusher Targets on Argus

Using the zone-plate coded-imaging (ZPCI) technique, we have obtained high-resolution images of thermonuclear alpha particle emissions and high-energy x-ray emissions ( $\sim 10$ -20 keV) from exploding-pusher targets. Introductory concepts of the ZPCI technique and its suitability for imaging low-level emissions from laser fusion targets have been discussed previously.<sup>68</sup> Our emphasis here is on recent advances that extend the technique to higher energy x-ray emissions ( $\gtrsim 10$  keV) and significantly improve resolution in images of alpha particle emissions. In particular, the discussion highlights, first, our improved understanding of the ZPCI spectral response for high-energy x rays and advances in zone-plate fabrication that allow ZPCI of high-energy x rays, and, second, work on coded-image reconstruction in higher order for improved resolution of alpha particle emission.

### 6.9.1 High-Energy X-Ray Images

The motivation for high-energy x-ray imaging of laser fusion targets is to obtain information about the generation and distribution of suprathermal electrons that may in turn provide important details concerning laser light absorption processes and fuel preheat. The signature of the suprathermal electron distribution appears as a high-energy tail on the measured x-ray spectrum (Fig. 6-35). We have developed a capability—which is being continually improved—for imaging the time-integrated

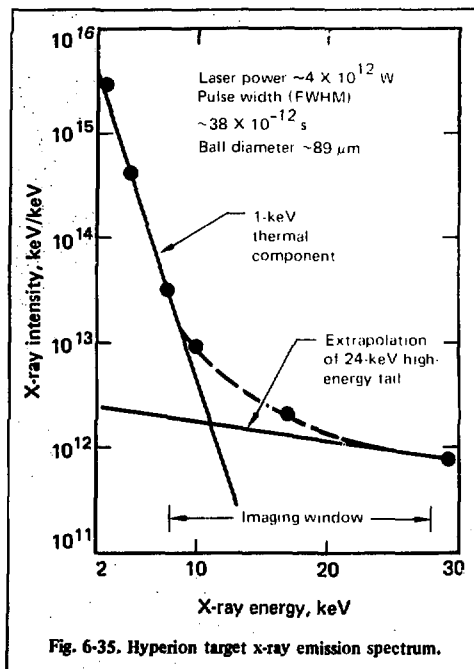


**Fig. 6-35. Hyperion target x-ray emission spectrum.**

spatial distribution of the suprathermal x-ray emission from exploding-pusher targets.

Imaging suprathermal x-ray emission presents three primary challenges: the relatively low intensity of suprathermal x-ray emission requires efficient radiation collection; the fractional high-energy x-ray transmission through the opaque zones of a coded aperture requires a more detailed spectral unfold of the final reconstructed image; and accurate interpretation of the spectral components in the reconstructed image requires an unambiguous determination of the suprathermal component in the measured x-ray spectrum.

Use of a coded-imaging technique allows high-resolution imaging while maintaining a large solid angle for radiation collection, thereby obviating the first of the above problems. On the other hand, coded-imaging techniques suffer from their own special class of problems in broadband x-ray imaging applications. These problems are particularly troublesome when attempting to image high-energy x rays that are fractionally transmitted through the "opaque" regions of the coded aperture.<sup>69</sup> Figure 6-36 provides a simple illustration of this problem. A pair of x-ray point sources of equal power (photons/s) are imaged, using a Fresnel zone-plate

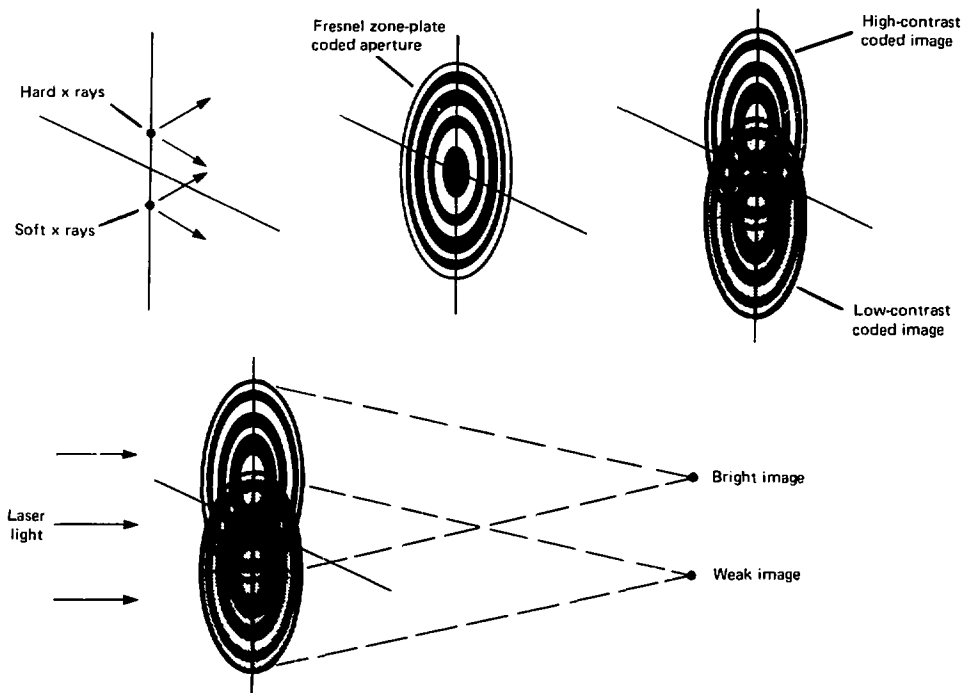
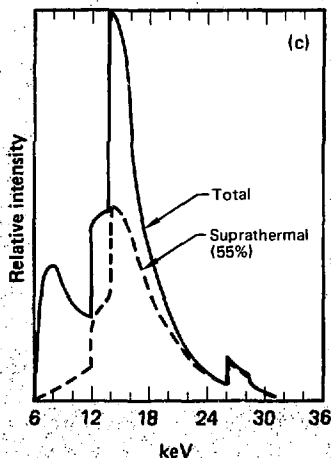
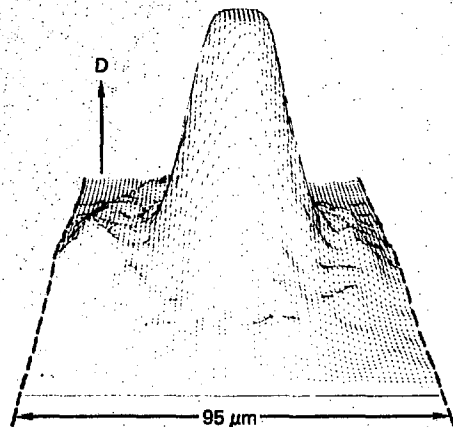


**Fig. 6-36.** The two-step ZPCI technique. First, hard x rays cast a low-contrast zone-plate image and soft x rays cast a high-contrast zone-plate image. Second, reconstruction of the coded image produces two source images of unequal intensity.





(a)



**Shot parameters:**

Target ball diameter:  $89 \mu\text{m}$

Power on target:  $4 \times 10^{12} \text{ W}$

Pulse width (FWHM):  $38 \times 10^{-12} \text{ s}$

Neutron yield:  $(1.4 \pm 0.3) \times 10^9$

Shot No. 36120906; RX1291-1C

**Fig. 6-37. Zone-plate coded-image suprathermal x-ray data (preliminary results). (a) Reconstructed x-ray image. (b) Three-dimensional film density contour representation. (c) X-ray spectral distribution in image.**

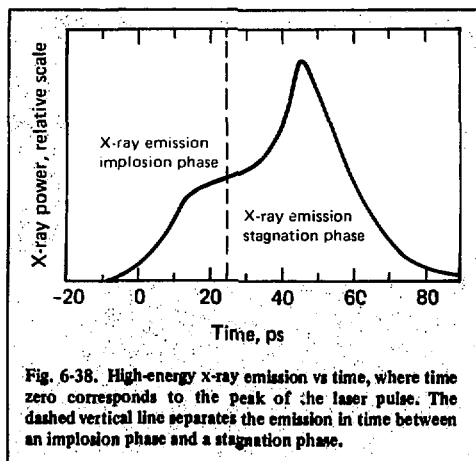


Fig. 6-38. High-energy x-ray emission vs time, where time zero corresponds to the peak of the laser pulse. The dashed vertical line separates the emission in time between an implosion phase and a stagnation phase.

pressed region, and a portion of the target stalk at the top.

LASNEX computer simulations of this target-irradiation experiment show that the high-energy x-ray emission within the spectral window of the zone-plate camera can be separated into two distinct phases in time and space. Details of these emission phases are presented in Figs. 6-38 and 6-39. Figure 6-38 is a plot of the high-energy x-ray emission under discussion vs time, where time zero corresponds to the peak of the laser pulse. A dashed vertical line separates the emission in time between an implosion phase (produced by suprathermal-electron bremsstrahlung emitted during the early implosion stages of the glass shell, when it has moved only slightly from its original position) and a stagnation phase (bremsstrahlung produced by electrons heated in the stagnating pusher as peak compression is approached). Figure 6-39 shows the numerical simulations of two-dimensional x-ray images and associated spectra for the two separate phases of emission. During the implosion phase, the dominant high-energy x-ray emission occurs in the glass shell in its nearly original position. This suprathermal emission has a temperature of  $\approx 24$  keV, in agreement with the measured value. During the stagnation phase, the integrated high-energy x-ray emission is roughly 10 times greater than that during the implosion phase. The dominant high-energy emission occurs in the compressed pusher region closest to the hot fuel and has a temperature  $\approx 4.5$  keV. Comparing this analysis of the high-energy x-ray emission processes with the ZPCI data, we can surmise that a volume compression greater than  $60\times$  was achieved in this experiment.

## 6.9.2 Thermonuclear Alpha Particle Images

Zone-plate coded imaging has been used to image the alpha particle emissions from exploding-pusher targets.<sup>70</sup> Using coded-image reconstruction in higher order — an idea first proposed by researchers at the University of Rochester<sup>71</sup> — we have significantly improved the resolution of alpha particle images.

Figure 6-40 illustrates the concepts underlying this innovative procedure for image-resolution improvement. In simple terms, when a coded image is recorded with sufficiently short wavelength radiations, the high-spatial-frequency information is accurately recorded. If one can appropriately extract the recorded high-spatial-frequency information, a high-resolution image can be produced. The use of a Fresnel zone plate as the coded aperture in ZPCI allows a very convenient optical means for reconstructing the high-spatial-frequency information that has been recorded. The reconstruction of the high-spatial-frequency information is achieved by merely recording the higher order images during normal image reconstruction.

Figure 6-41 shows the results of an application of the higher order reconstruction technique to laser fusion diagnostics. Reconstructed images of the alpha emission from laser-compressed microsphere targets are shown in first and third order. The three-fold improvement in resolution in the third-order image is evident by the high degree of spatial structure within the thermonuclear burn region. Such structure does not exist in the first-order image (resolution  $\approx 10\ \mu\text{m}$ ) and is highly suggestive of a moderate scale breakup of the glass shell at stagnation. Imperfections in the glass shell, or nonuniformity of the laser irradiation pattern, or both, can result in a nonspherically symmetric compression. Even though the implosion/explosion phase of the shell is stable against fluid instabilities, the stagnation phase (during which the DT reactions take place) may not be stable. In addition, the alpha images show that the majority of the DT reactions occur in the central region of the core, not in its periphery. This is consistent with calculations showing that the glass pusher wall moderates the DT ion temperature at the periphery to a value roughly  $1/4$  that at core center.

Figure 6-42 shows experimental results that directly illustrate the resolution improvement that can be achieved by image reconstruction in higher order. A coded image corresponding to a point-source pair separated by approximately  $6\ \mu\text{m}$  is reconstructed in first, third, and fifth order. In first order (resolution  $\approx 9\ \mu\text{m}$ ), the point pair is not resolved. In third order (resolution  $\approx 3\ \mu\text{m}$ ), the

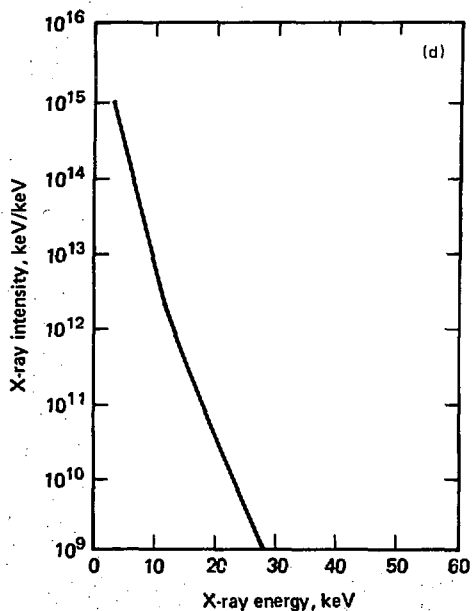
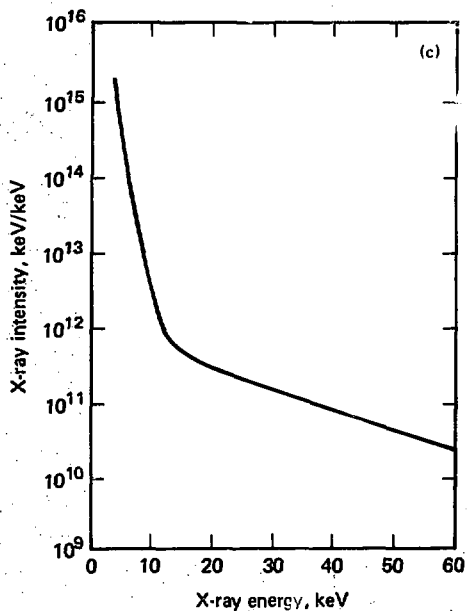
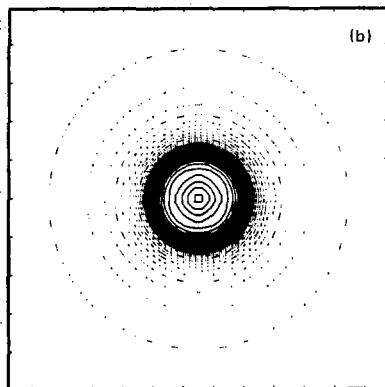
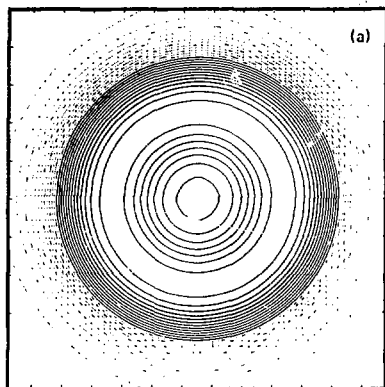


Fig. 6-39. Two-dimensional image for implosion (a) and stagnation (b) phases. X-ray intensity for implosion (c) and stagnation (d) phases.

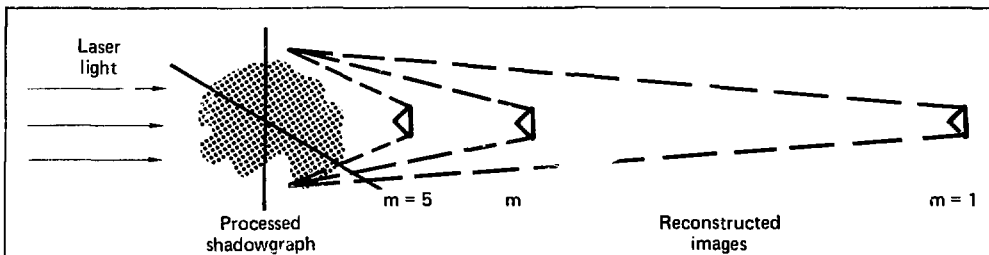


Fig. 6-40. Image reconstruction in higher order for improved resolution. The coded image, when illuminated, will project real images at all odd orders:  $m = 1, 3, 5, \dots$ . The planar resolution  $\delta$  and tomographic resolution  $\Delta$  of the ZPCI technique improve linearly with the reconstruction order: i.e.,  $\delta_m = \delta_1/m$  (planar resolution),  $\Delta_m = \Delta_1/m$  (tomographic resolution). Limitations: 1. The coded image (shadowgraph) must have been recorded with sufficiently short wavelength radiations to cast crisp zone-plate shadows. The higher order reconstructed images are particularly sensitive to edge definition in the shadowgraph. 2. The image (S/N) suffers in the higher order reconstructions because image intensity varies inversely as the square of the order number.

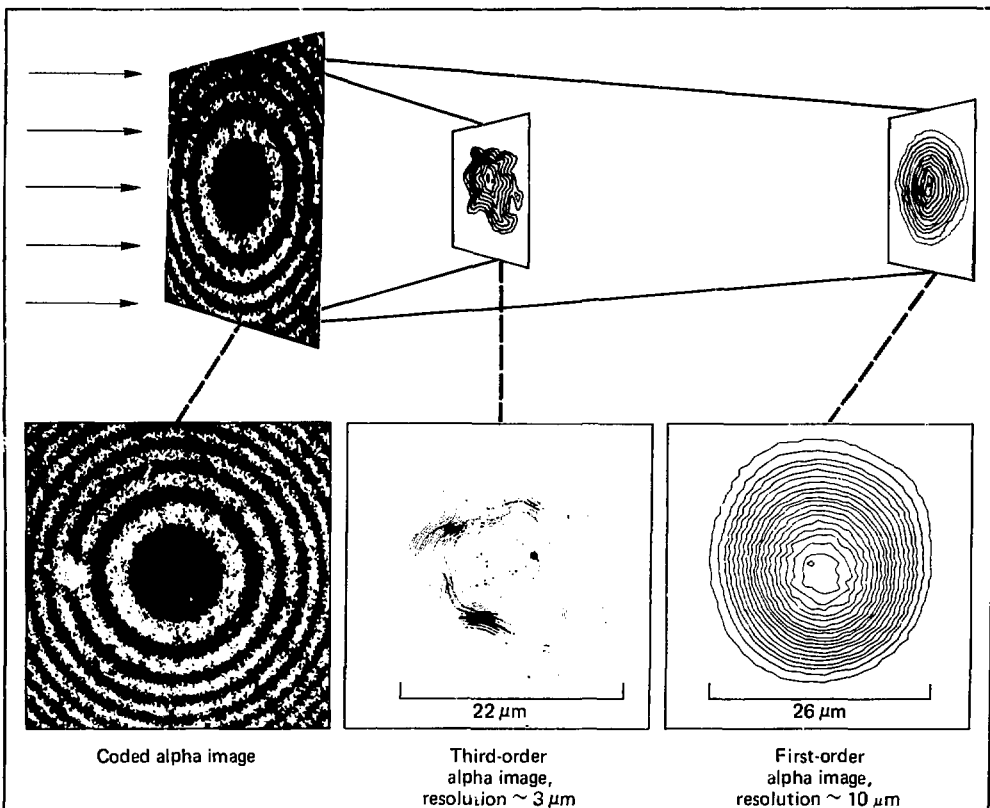


Fig. 6-41. Image of the thermonuclear burn in a laser fusion target, reconstructed in first and third order. A zone-plate coded image acts as a generalized diffraction grating, focusing incident laser light into multiple, well-separated, reconstructed images – each image a complete, three-dimensional representation of the source. Each separate reconstructed image is designated by an order number  $M$ . Higher order (shorter reconstruction distance) images are reduced in intensity by  $1/M^2$  – therefore, reduced signal-to-noise ratio – but their resolution is improved  $M$ -fold. A third-order image, having a threefold resolution improvement, allows us to see spatial detail not apparent in a first-order image.

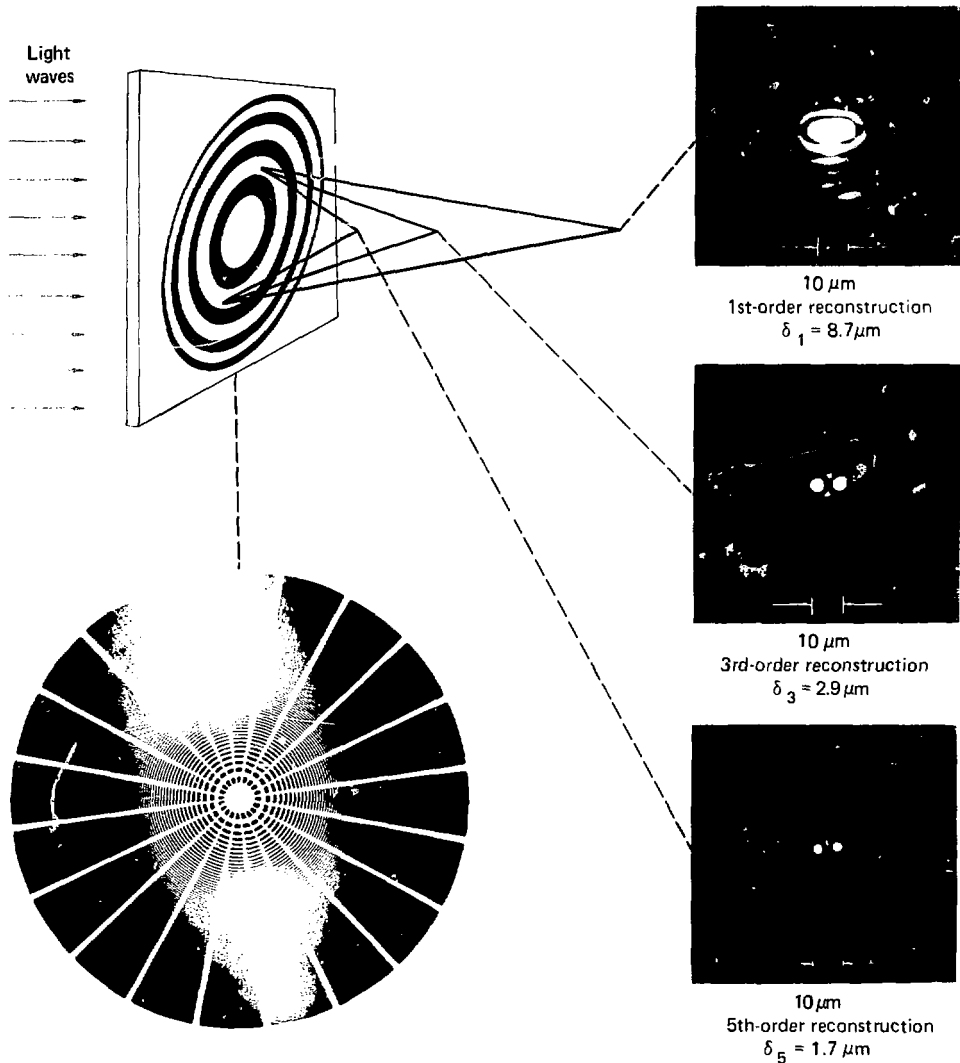


Fig. 6-42. Higher order reconstruction of zone-plate coded images, giving improved resolution.

point pair is well resolved. In fifth order (resolution  $\approx 2 \mu\text{m}$ ), the points are even more effectively resolved.

## References

68. *Laser Program Annual Report — 1976*, Lawrence Livermore Laboratory, Rept. UCRL-50021-76 (1977), §3-4.8, 3-5.9, and 5-33.
69. N. M. Ceglio and H. I. Smith, "Micro-Fresnel Zone Plates for Coded Imaging Applications," *Rev. Sci. Instr.* **49**, 15 (1978).
70. N. M. Ceglio and L. W. Coleman, "Spatially Resolved  $\alpha$  Emission from Laser Fusion Targets," *Phys. Rev. Lett.* **39**, 20 (1977).
71. J. Gur and J. M. Forsyth, "Optical Simulation of a Technique for Obtaining Submicron Resolution X-Ray Images in Laser Pellet Compression Experiments," *App. Opt.* **17**, 1 (1978).

## Authors

N. M. Ceglio  
J. T. Larsen

## 6.10 A Simple Model for Exploding-Pusher Targets

In the 1976 annual report, we presented a simple scaling law for exploding-pusher targets.<sup>72</sup> At that time, the scaling law was limited to targets with a fixed initial DT fill, and we made no attempt to derive the individual scaling parameters from first principles. In this report, we describe our progress in understanding the basic physical behavior of exploding-pusher targets and our resulting improved modeling capability. Relying on both LASNEX simulations and empirical fits to experimental results, we have upgraded the scaling law to the point where we derive the scaling parameters introduced without justification in last year's report and develop the simple scaling law into a simple model.

### 6.10.1 Derivation of the Simple Model

We will approximate the behavior of an exploding pusher by assuming that it consists of three distinct phases. In order of temporal sequence, these are:

- The pusher heating phase during which the pusher/fuel interface accelerates to a significant velocity.

- The acceleration or useful energy phase.
- The compression phase.

For pedagogical reasons, let us consider these processes in a slightly different order from that listed.

### 6.10.2 Compression Phase

Detailed LASNEX simulations indicate that, once the pusher has exploded and the initial shock and electron thermal waves have propagated through the fuel, the final compression phase of an exploding-pusher target is nearly adiabatic with an effective  $\gamma \approx 1.5$ . To use this fact to determine the compression and the fuel conditions at peak stagnation, however, we must know the initial postshock conditions. Rather than try to solve this complex problem, we use the fact that LASNEX one-dimensional simulations show that the average compressed fuel density can be approximated by that produced by filling the initial target volume by the imploding fraction ( $1/2$ ) of the pusher mass  $M_p$ . In other words, the compression can be written as

$$C = \beta \frac{M_p}{4/3\pi(r_0 - w/2)^3 \rho_0}, \quad (2)$$

where  $\rho_0$  is the initial DT fuel density,  $w$  and  $r_0$  are the shell wall thickness and radius, respectively, and  $\beta$  is a parameter that is determined by experiments. For targets of interest,  $w/r_0 \ll 1$  and Eq. (2) simplifies to

$$C = \beta(3/2) (\rho_p/\rho_0) (w/r_0), \quad (3)$$

with  $\rho_p$  the pusher density. We thus assume that the compression is independent of the pusher dynamics. Comparing this expression with  $\alpha$  imaging experiments suggests that  $\beta = 3.5$ . This result appears to be independent of the incident laser power and final neutron yield as long as we are in the exploding-pusher regime. An interesting consequence is that the final DT ion fuel temperature can be determined independently of the compression. This consequence will be explored further during the discussion of the acceleration phase.

### 6.10.3 Explosion Phase

This phase is characterized by rapid heat addition to the glass pusher caused by energy disposition both by suprathermal electrons and by a thermal wave (propagating at near supersonic speeds) driven by laser absorption at the critical-density region. The explosion phase is assumed to be complete when the shockwave or supersonic thermal wave

has propagated through the pusher and thus initiated the large-scale, rapidly accelerating motion of the pusher/fuel interface. This time we define as  $t_c$ .

Using the same arguments as presented in the 1976 annual report, we use this assumption to write the explosion condition as

$$\int_{-\infty}^{t_c} \left( \frac{\eta P(t)}{4\pi r_0} \right)^{1/3} dt = 0.49w, \quad (4)$$

where  $\eta$  is the laser absorption fraction, and  $P(t)$  is input laser power. The numerical constant differs from that in the 1976 annual report. Here, we assume that during the explosion phase the shell expands to four times its initial thickness. We used the value 10 in the 1976 annual report. Equation (4) agrees well with detailed LASNEX one-dimensional simulations.

The simple model prescription for determining the point on the Gaussian input pulse when the pusher explodes is, thus, given by Eq. (4) and the assumption that the pusher/fuel interface has moved in twice the original pusher wall thickness at that time.

#### 6.10.4 Acceleration or Useful Energy Phase

During this phase, the pusher/fuel interface is assumed to reach its peak velocity, at which time the implosion process is assumed to be effectively uncoupled from further absorption of the laser light. This condition was reached when the pusher/fuel interface had moved in 32% of the initial radius in the specific one-dimensional simulation mentioned in the 1976 annual report. Truncating the laser pulse at this time in the LASNEX calculation produced 2/3 of the maximum neutron yield with no significant change in the pusher/fuel interface trajectory. The final compression for that calculation was 75; i.e., the pusher/fuel interface traversed 76% of the initial radius before stagnating. For the simple model, we assume that these two ratios of 32% to 76% (0.42) are canonical values determining the fraction of the absorbed energy that is useful for determining the neutron yield. Using the expression for the compression given by Eq. (2) and the results from the discussion of the explosion phase, we can then find the cutoff condition by solving

$$\int_{t_c}^{t_c} v_p(t) dt = 0.42r_0(1 - C^{-1/3}) - 2w \quad (5)$$

for the cutoff time  $t_c$ , where  $v_p(t)$  is the instantaneous pusher/fuel interface velocity and  $w/r_0 \ll 1$  is assumed. The useful absorbed energy  $E_c$  is thus defined as

$$E_c = f\eta \int_{-\infty}^{t_c} P(t) dt, \quad (6)$$

where  $f$  is that fraction of the absorbed energy that goes into the imploding portion of the pusher mass. The pertinent questions now are:

(1) Given  $E_c$ , how do we determine the fuel-averaged DT ion temperature?

(2) How do we find  $v_p(t)$ ?

(3) What is  $f$ ?

(1) Assuming that a cutoff condition has merit (i.e., that the laser pulse may be truncated at  $t = t_c$  without significantly affecting the target performance) and ignoring conduction losses during the compression phase for  $t > t_c$ , the simplest approach is to set

$$E_c = \alpha(KE)_p + \frac{3}{2}N_p kT_p + \frac{3}{2}N_e kT_e + \frac{3}{2}N_i kT_i. \quad (7)$$

Here,  $N_p$ ,  $N_i$ , and  $N_e$  are the total number of pusher particles, fuel ions, and fuel electrons, respectively;  $T_p$ ,  $T_i$ , and  $T_e$  are the pusher temperature, the fuel ion temperature, and the fuel electron temperature, respectively; and  $\alpha(KE)_p$  represents that fraction of the pusher kinetic energy that has not been converted to thermal electric energy at stagnation. This statement is also consistent with the earlier derivation of the average compression. LASNEX calculations suggest that  $T_e = 1/5 T_i$  at stagnation. A simple estimate of electron-ion equilibration times shows that the pusher electrons and ions are in thermal equilibrium with each other and that  $T_p = T_e$ . Assuming that the average charge state of the pusher is 9, we can easily evaluate Eq. (7) to give

$$T_i = 69.6 \frac{\frac{E_c}{M_p} - \alpha \frac{1}{2} v_c^2}{1 + 1.28 \times 10^{-3} \frac{r_0 \rho_0}{W}}, \quad (8)$$

with  $E_c$  in joules,  $M_p = 1/2$  of the pusher mass in nanograms,  $v_c$  = the pusher velocity at  $t = t_c$  in J/ng,  $\rho$  in mg/cm<sup>3</sup>,  $r_0$  and  $w$  in  $\mu$ m, and  $w/r_0 \ll 1$  assumed.

(2) Experimental measurements of the space- and time-resolved x-ray emission from exploding-pusher targets suggest the relationship

$$\frac{1}{2} M_p V_p^2(t) = 0.15 \int_{-\infty}^t \eta P(t) dt. \quad (9)$$

Substituting Eq. (9) in Eq. (5) produces peak implosion velocities in excellent agreement with those reported in §3-4.2 of the 1976 annual report. Good agreement is also obtained with the average implosion velocity measurements discussed in §8.5.5 of the 1975 annual report.

(3) Measurements of the asymptotic ion expansion energy indicate that approximately 20-30% of the absorbed energy escapes in the form of fast ions that do not contribute to the implosion process. Simply dividing the remaining absorbed energy equally between the inward- and outward-moving portions of the pusher mass results in  $f \sim 0.35$ . Using this value in Eqs. (6) and (8), however, produces fuel-averaged ion temperatures greater than those observed experimentally and suggests a value for  $f$  of approximately 0.25. Rather

than making an attempt to derive an expression for  $f$  and  $\alpha$ , we simply normalized Eq. (8) to experimentally determined fuel temperatures, with the result

$$T_i = 7 \frac{\left[ \int_{-\infty}^{t_c} \eta P(t) dt \right] / M_p}{1 + (1.28 \times 10^{-3})(r_0 \rho_0 / W)} \quad (10)$$

A graphical representation of this three-phase modeling of the exploding-pusher behavior, and thus the prescription for finding  $E_c$ , is shown in Fig. 6-43, where we compare the pusher/fuel interface velocity and trajectory history as determined from solving Eqs. (2)-(11) with a LASNEX one-dimensional simulation. The solid curve is the one-dimensional result when the Gaussian input pulse is

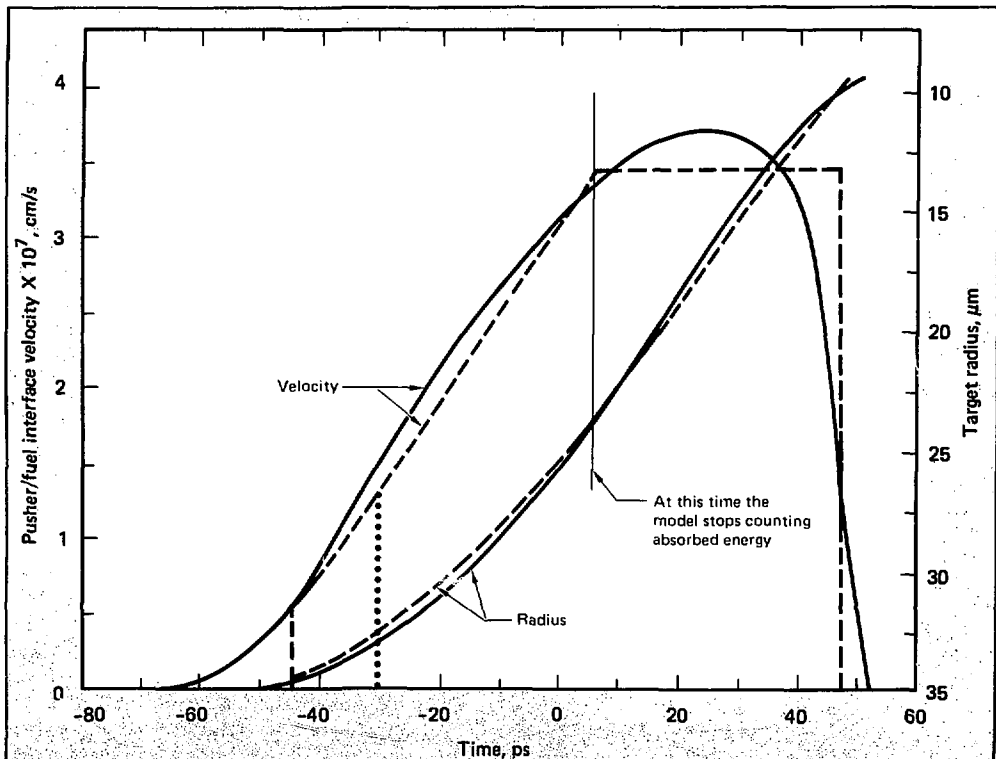


Fig. 6-43. A graphic representation of three-phase modeling of the exploding-pusher behavior, and thus the prescription for finding useful absorbed energy  $E_c$ . We compare the pusher/fuel interface velocity and trajectory history (dashed lines) as determined by solving Eqs. (2)-(11) with a LASNEX one-dimensional simulation (solid lines) when the input pulse is truncated to give a neutron yield  $\sim 2/3$  of maximum. The dotted line is from Ref. 72.



truncated at the time when the shell has moved 32% of the initial radius. The dashed lines show the result of applying the prescription outlined above. The difference between the present model and the assumptions made in the 1976 annual report is also shown. This model is thus equivalent to assuming that the shell integrates the absorbed energy until the shock wave has propagated through the pusher and completed the explosion phase at time  $t = t_c$ , as found from Eq. (4). At this point, the pusher/fuel interface is assumed to have moved in a distance of 2 w and acquired an initial velocity proportional to the square root of the absorbed energy until that time. It then continues with velocity proportional to the square root of the absorbed energy at any given time, until  $t = t_c$ . We then assume that at this time the inward-moving pusher and fuel are uncoupled from further absorption of laser energy and continue with constant velocity until the final radius, as determined from Eq. (2). Comparison of Eqs. (8)–(10) shows that, for fixed target parameters,  $T_i \sim E_c/M_p \sim v_c^2$ ; i.e., the final fuel-averaged DT ion temperature is proportional to the square of the peak pusher velocity obtained. This result agrees with LASNEX one-dimensional simulations.

### 6.10.5 Neutron Production

LASNEX simulations suggest that the neutron production has a Gaussian temporal behavior. Thus, in the nomenclature of Ref. 72,  $N = n_D n_T \langle \sigma_v \rangle V \tau_g$  at the maximum ion temperature, where  $n_D$  and  $n_T$  are the final D and T number densities,  $\langle \sigma_v \rangle$  is the DT Maxwell-averaged cross section, V is the final compressed volume, and  $\tau_g$  is the temporal FWHM of the neutron production curve. Detailed LASNEX simulations suggest that  $\tau_g = 1/2\Delta\tau$ , where  $\Delta\tau$  is the estimate for the burn time derived in Ref. 72.

The simple model estimate for the neutron yield of an exploding pusher target is thus

$$N = 4.5 \times 10^5 \rho_0^2 C^{2/3} (r_0 - w)^4 T^{-7/6} \times \exp(-19/T^{1/3}), \quad (11)$$

with  $\rho_0$  in  $\text{mg}/\text{cm}^3$ ,  $r_0$  and  $w$  in  $\mu\text{m}$ , C found from Eq. (2), and T found from Eq. (10). For  $w/r_0 \ll 1$ , Eq. (11) can be written

$$N = 2.5 \times 10^8 \rho_0^{4/3} w^{2/3} r_0^{10/3} T^{-7/6} \times \exp(-19/T^{1/3}). \quad (12)$$

### 6.10.6 Comparison of Simple Model with Experimental Results

The neutron yield is one of the more sensitive indications of the success of any implosion fusion experiment. Plotted against an improper parameter, however, trends and proper scaling relations are not apparent. This is shown in Fig. 6-44, where the neutron yield from a variety of experimental conditions is plotted as a function of peak input power. The open data points are from LLL Janus, Cyclops, and Argus 1.06- $\mu\text{m}$  Nd:glass laser facilities using f/1, f/2.5, and lens/elliptical-mirror focusing optics with Gaussian temporal pulses. The solid points are results from LASL, using their 10.6- $\mu\text{m}$  CO<sub>2</sub> laser having a triangular temporal pulse with a 10–90% rise time of  $\sim 160$  ps and a fall time of  $\sim 2.2$  ns.<sup>73</sup> The absence of any relevant trend or scaling parameter is obvious. Taking the optimum results, the peak neutron yield appears to be increasing approximately as the peak power squared. This correlation, however, would clearly not tell an experimenter in which direction to change his target and laser parameters from a nonoptimal result. In comparison, Fig. 6-45 shows the same data normalized by  $\rho_0^{4/3} w^{2/3} r_0^{10/3}$ , as suggested by Eq. (12), and plotted as a function of the model-inferred fuel-averaged DT ion temperature from Eq. (10). The correlation has clearly improved, collapsing nearly all the data to the model-predicted curve. The vertical error bars indicate experimental uncertainty in the neutron yield, while the horizontal error bars indicate the uncertainty in the absorbed energy, which ranged from  $(13 \pm 4)\%$  for the f/2.5 Cyclops results up to a maximum of  $(40 \pm 5)\%$  for the Hyperion results on Argus that yielded  $1.6 \times 10^9$  neutrons. Considering that the experimental parameters ranged from P  $\sim (0.2\text{--}4.4)$  TW,  $w \sim (0.4\text{--}1.2)$   $\mu\text{m}$ ,  $r_0 \sim (20\text{--}100)$   $\mu\text{m}$ , and  $\rho_0 \sim (0.53\text{--}9)$   $\text{mg}/\text{cm}^3$ , the agreement is indeed satisfactory. The model-inferred DT ion temperatures also agree reasonably with those inferred from alpha and neutron time-of-flight measurements, as indicated in Table 6-5.

Figure 6-46(a) shows the model-predicted variation of neutron yield with initial DT fill for a range of laser and target parameters. The curves show that both the optimum fill and the rate of change of N with  $\rho_0$  are strong functions of laser and target

Fig. 6-44. Neutron yield as a function of peak input power for experiments using a 1.06- $\mu\text{m}$  Nd:glass laser with  $f/0.07$ ,  $f/1$ , and  $f/2.5$  optics (open symbols) and a 10.6- $\mu\text{m}$   $\text{CO}_2$  laser using  $f/2$  optics (closed triangles). Uncertainty in power  $\sim \pm 10\%$ . Uncertainty in neutron yield  $\sim \pm 20\%$ . Target diameter = 40-150  $\mu\text{m}$ . Target wall thickness = 0.4-1.2  $\mu\text{m}$ . Pulse length = 25-200 ps.

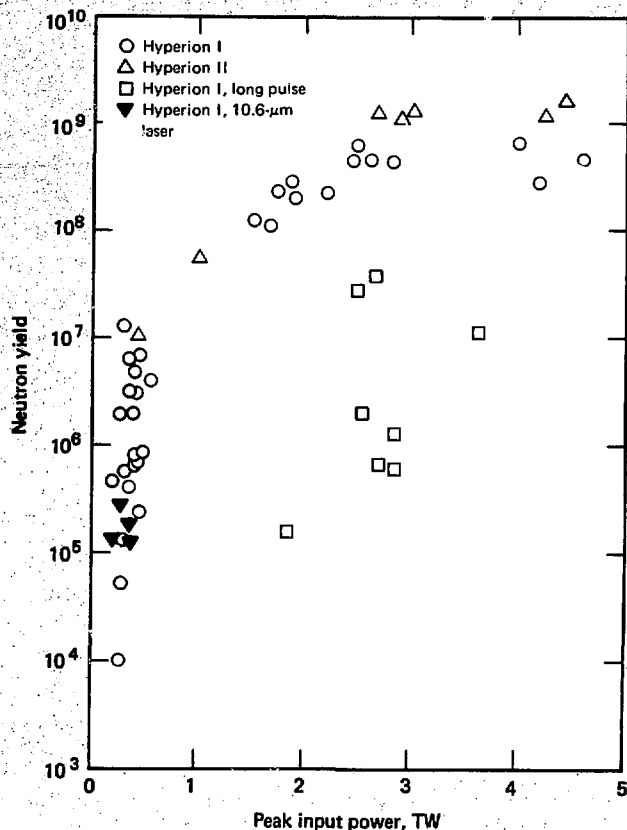
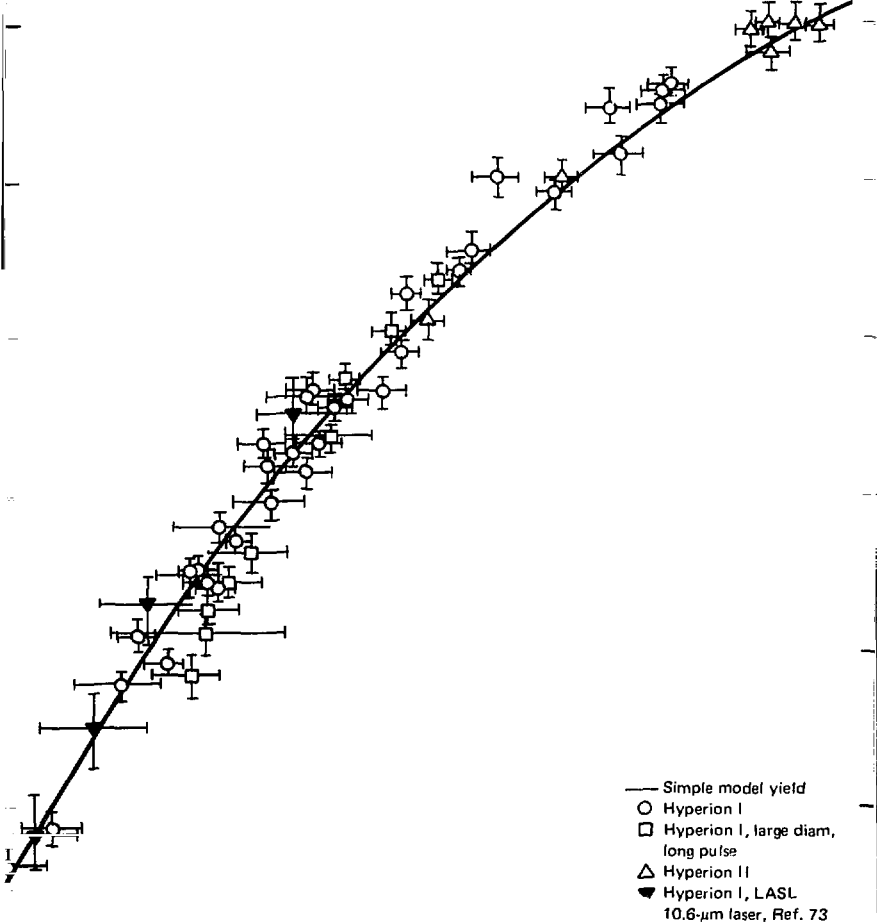


Table 6-5. Comparison of model-derived fuel-averaged DT ion temperatures with neutron and alpha time-of-flight data.

Shot No.	Fuel-averaged ion temperature	
	From neutron and alpha time of flight	From model
36100115	7.9	7.6
36100116	7.5	7.3
36120702	5.5	5.1
36120906	7.5	7.1
36120910	5.8	5.6
36120911	7.2	9.1

parameters. Because the laser and target parameters varied during the experiment sequence, the experimental points cannot be plotted in Fig. 6-46(a). Because  $\rho_0$  also strongly influences the peak DT ion temperature [see Eq. (10)], there is no simple way to normalize the data. A direct comparison between the model prediction and experiments is shown in Fig. 6-46(b), where we plot the ratio of predicted vs measured yield as a function of  $\rho_0$ . All experiments with  $\rho_0 > 3 \text{ mg/cm}^3$  and  $\rho_0 < 1.6 \text{ mg/cm}^3$  have been plotted, while only a small subset representative of the experiments with  $1.6 \text{ mg/cm}^3 < \rho_0 < 3 \text{ mg/cm}^3$  are shown. The data plotted cover the same laser and target parameter range indicated in Fig. 6-45.



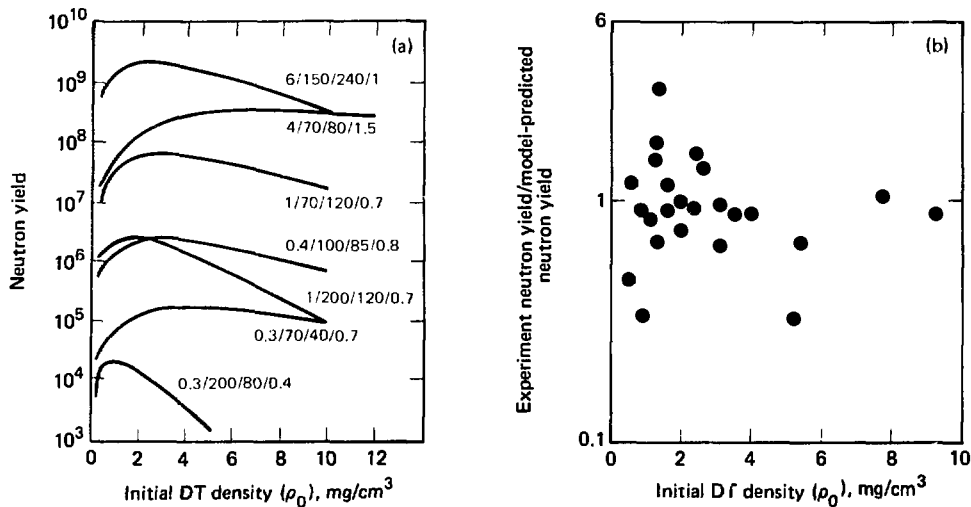


Fig. 6-46. (a) Model-predicted neutron yield as a function of initial DT fill for a range of laser and target parameters indicated by the sequence power (TW)/FWHM (ps)/diam ( $\mu\text{m}$ )/wall thickness ( $\mu\text{m}$ ) next to each curve. Absorption is 22% in each case. (b) Ratio of experimental to model-predicted neutron yield as a function of initial DT fill. Uncertainty in experimental results of neutron yield  $\leq \pm 20\%$ . Variation in model-predicted neutron yield  $\leq \pm 50\%$  because of uncertainty in absorbed energy. Uncertainty in initial DT density  $\leq \pm 20\%$ .

Figure 6-47 shows the variation of neutron yield with initial target diameter. Here, the neutron yield is normalized as indicated to remove the density, wall thickness, and laser condition variations, as the data again span more than a decade in incident peak power and nearly a factor of seven in

laser pulse FWHM. The least-squares fit through the data, giving a slope of 3.28, agrees with the expected slope of  $10/3$ . Finally, Fig. 6-48 shows an example of specific experimental results compared with the model predictions. The experimental parameters are listed in the caption and were chosen to

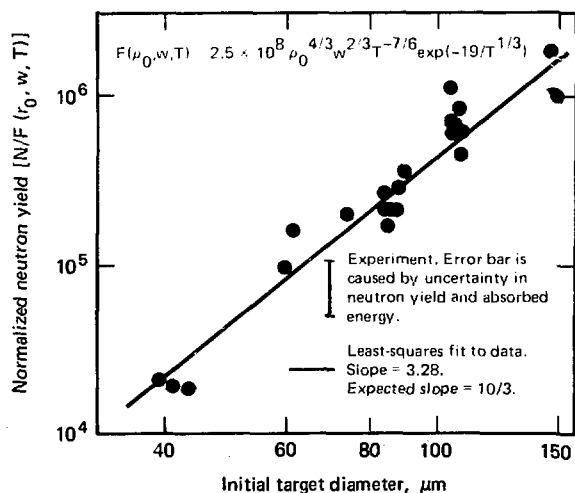
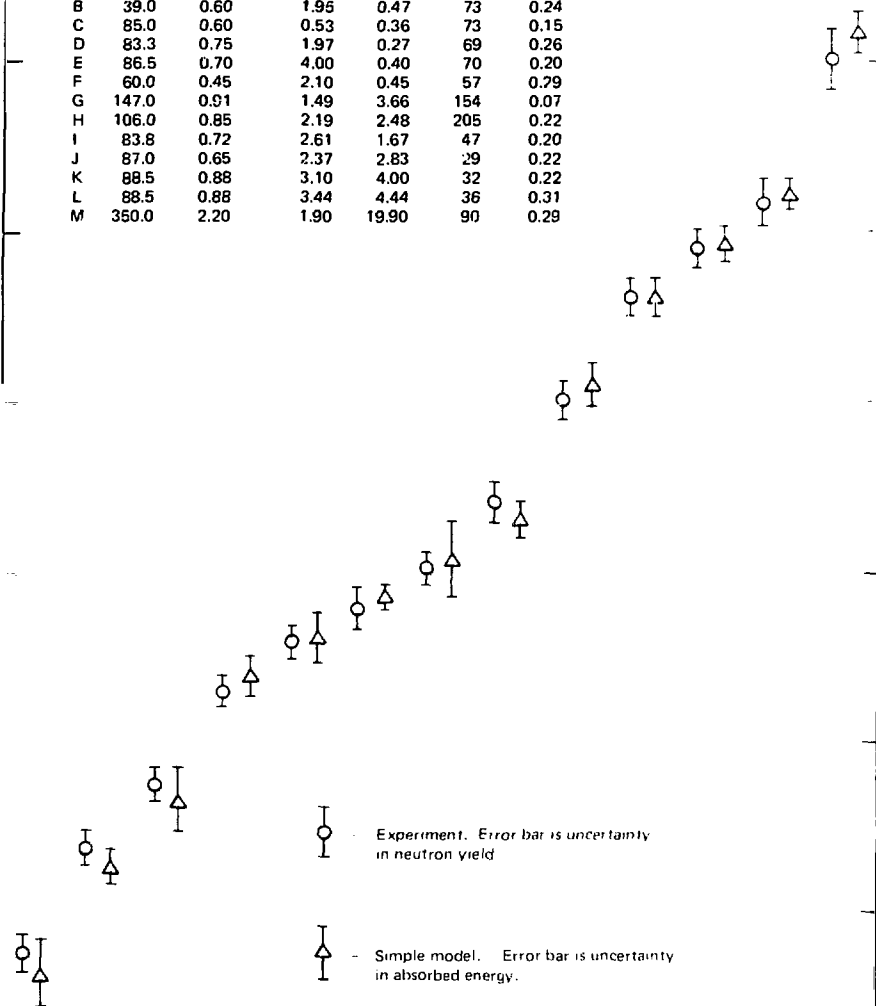


Fig. 6-47. Normalized neutron yield plotted as a function of initial target diameter. The least-squares fit gives a slope of 3.28, in reasonable agreement with the model-predicted value of  $10/3$  ( $r_0/w \gg 1$ ).  $T$  is the model-derived, fuel-averaged ion temperature.

	D ( $\mu\text{m}$ )	w ( $\mu\text{m}$ )	$\rho_0$ ( $\text{mg}/\text{cm}^3$ )	P (TW)	$\tau$ (ps)	$\eta$ (abs)
A	87.8	0.63	9.20	0.18	100	0.20
B	39.0	0.60	1.95	0.47	73	0.24
C	85.0	0.60	0.53	0.36	73	0.15
D	83.3	0.75	1.97	0.27	69	0.26
E	86.5	0.70	4.00	0.40	70	0.20
F	60.0	0.45	2.10	0.45	57	0.29
G	147.0	0.91	1.49	3.66	154	0.07
H	106.0	0.85	2.19	2.48	205	0.22
I	83.8	0.72	2.61	1.67	47	0.20
J	87.0	0.65	2.37	2.83	29	0.22
K	88.5	0.88	3.10	4.00	32	0.22
L	88.5	0.88	3.44	4.44	36	0.31
M	350.0	2.20	1.90	19.90	90	0.29



represent a cross section of the experimental parameter space with neutron yields from  $10^3$  to  $10^{10}$ . The agreement is reasonable, and, together with Figs. 6-44 through 6-48, lend considerable after-the-fact credence to the simplifying assumptions that were made during the development of the model. It suggests not only that much of the physics was not "swept under the rug," but that the picture of an exploding pusher that is defined within the limitations of the assumptions is reasonable.

#### 6.10.7 Conclusions

We have developed a simple model that can be used to predict neutron yields for variations in initial DT fill, wall thickness, target radius, and laser input conditions. The model also elucidates the more important processes occurring in exploding-pusher experiments. We have obtained agreement

with experimental results to within a factor of two over six orders of magnitude in neutron yield for a large portion of the target and laser input-parameter space.

#### References

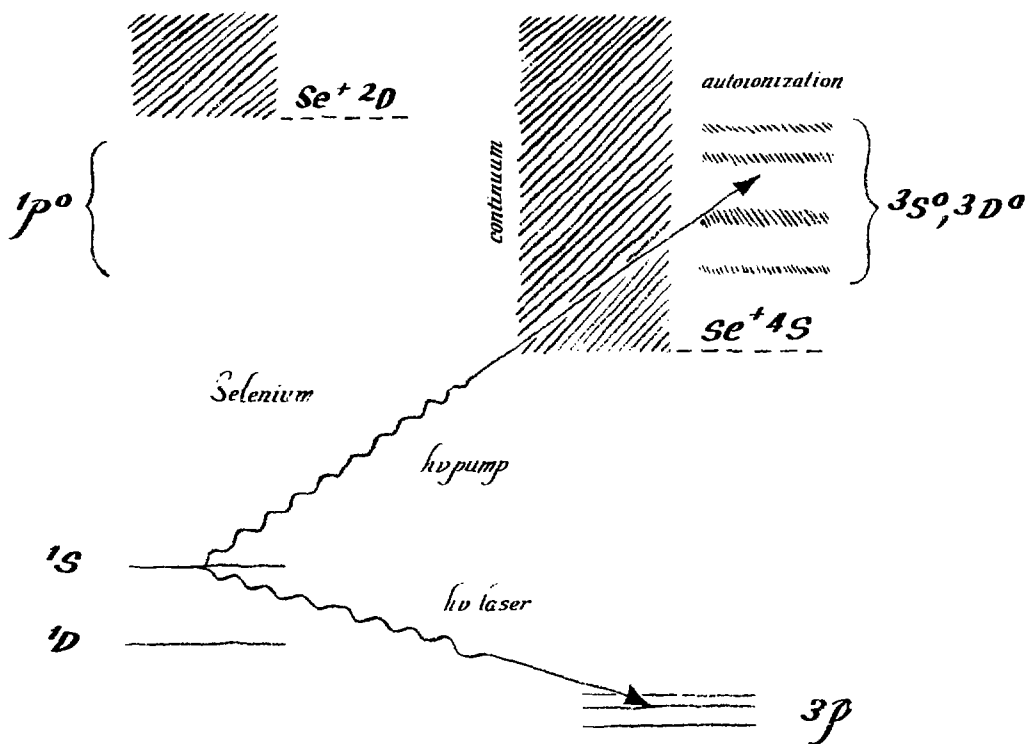
72. *Laser Program Annual Report — 1976*, Lawrence Livermore Laboratory, Rept. UCRL-50021-76 (1977), §5-5.3.
73. D. Giovanelli, Los Alamos Scientific Laboratory, private communication (1977).

#### Author

E. K. Storm

# SECTION 7

## ADVANCED LASERS



# SECTION 7

## CONTENTS

7.1	Introduction and Summary	7-1
7.2	System Considerations	7-7
7.2.1	Computational Objectives and Capabilities	7-7
7.2.2	Total Laser System Efficiency	7-9
7.2.3	Laser System Architectures—Energy Extraction	7-13
	Multipass Amplifier Scaling—Storage Laser Media	7-13
	Multipass Amplifier Energy Extraction—Storage Laser Media	7-14
7.2.4	Propagation of Laser Energy	7-16
	Phase and Amplitude Distortion Processes	7-16
	Focusing Aberrated Laser Beams and Laser Media Optical Quality Constraints	7-17
7.3	Group VI Lasers	7-20
7.3.1	Introduction	7-20
7.3.2	Rare-Gas Excimer Pumps	7-23
	Xe <sub>2</sub> <sup>+</sup> and Kr <sub>2</sub> <sup>+</sup> Superfluorescent Light Source	7-23
	Xe <sub>2</sub> <sup>+</sup> Absorption/Gain Measurements	7-25
	Rare-Gas Excimer Potential Curves and Lifetimes	7-27
	Photoionization of Rare-Gas Excited States	7-28
7.3.3	Photolytic Production of <sup>1</sup> S Metastable Atoms	7-30
	Photolytic Experiments	7-30
	Electronic Structure of OCS	7-35
	<sup>1</sup> S— <sup>1</sup> S Quenching Processes	7-37
	Photoionization of <sup>1</sup> S Metastable Atoms	7-37
7.3.4	Group VI Laser System Analysis	7-40
	Photolytic Drivers—Lasers	7-41
	Pump Radiation Transport	7-44
	Group VI Amplifier Excitation Characteristics	7-47
	Group VI Amplifier Extraction Characteristics	7-47
	Group VI Amplifier Average Power Considerations	7-48
	Group VI Laser Amplifier Efficiency	7-48
7.3.5	Scaling Group VI Lasers to Large Apertures	7-50
7.4	Laser Systems Using Rare-Earth Molecular Vapor	7-53
7.4.1	Physics Issues	7-54
	Experimental Studies	7-54
	NdAlCl Complexes	7-54
	Nd(thd) <sub>3</sub> Chelates	7-56
	TbAlCl Complexes	7-56
	Tb(thd) <sub>3</sub> Chelate	7-61
	Theoretical Studies	7-63
7.4.2	Design and Scaling of Multikilojoule Laser Systems	7-64
7.5	Rare-Earth:Solid-State Hybrid Laser Systems	7-69
7.5.1	Physics Issues	7-69
7.5.2	Design and Scaling of a Multikilojoule Hybrid Laser System	7-73
7.6	Raman Laser Systems	7-76
7.6.1	Introduction	7-76



7.6.2	Theory and Modeling of KrF Laser Systems . . . . .	7-78
	KrF Band Homogeneity . . . . .	7-78
	Optical Absorbers . . . . .	7-79
	Amplifier Modeling Predictions . . . . .	7-80
7.6.3	Raman Compression Theory . . . . .	7-83
	Principal Physical Limitations . . . . .	7-83
	Raman Modeling . . . . .	7-87
	Nonparametric Losses . . . . .	7-90
	Beam Quality Limitations . . . . .	7-91
	Scaling and Optimization . . . . .	7-93
7.6.4	Compression Experiments in Methane . . . . .	7-93
	Narrow Linewidth Operation and Spatial Beam Quality of a KrF Discharge Laser . . . . .	7-94
	Gain and Saturation in a KrF-Pumped Methane Raman Amplifier . . . . .	7-98
	Effects of Pump Beam Divergence on Backward Raman Amplification . . . . .	7-102
	Gas Breakdown and Self-Focusing . . . . .	7-102
7.6.5	Pulse Compressor Systems . . . . .	7-104

## SECTION 7

### ADVANCED LASERS

#### 7.1 Introduction and Summary

We anticipate using single-pulse laser systems and facilities that are currently operating (Shiva), under construction (Antares), and in design (Nova) to achieve the *scientific* milestones of the DOE Inertial Confinement Fusion (ICF) Program. Achieving the major ICF *applications* milestones, however, will require more average power than these single-pulse laser facilities can attain. Accordingly, the ICF program includes as a necessary element the development of advanced drivers capable of delivering both high peak and average powers to fusion targets and meeting other stringent technical and cost performance objectives. We can project a nominal set of laser system performance requirements for power plant service (Table 7-1). We combine the results of current implosion experiments with LASNEX computer code simulations of high-density implosions and with preliminary analyses of fusion reactor concepts. Determining a precise set of parameters for an optimized laser system from the ranges given in Table 7-1 will require detailed tradeoffs among all reactor subsystems that lie well beyond the precision of current technical knowledge. However, we believe that operation at longer wavelengths will require the laser system to deliver higher energies at higher system efficiency for constant reactor performance. We expect the laser performance requirements given in Table 7-1 to evolve with improved understanding of pellet physics and reactor design, particularly with respect to operating wavelength and efficiency. However, for now they serve as a useful guide for the identification and exploratory development of advanced laser systems for fusion applications.

**Table 7-1. Laser system performance requirements for fusion power plants.**

Property	Value range
Laser wavelength	250-2000 nm
Pulse energy	1-3 MJ
Pulse duration	5-10 ns
Peak power	200 TW
Pulse-repetition rate	A few hertz
Average power	10 MW
Overall efficiency	$\geq 1\%$

The first major milestone of the ICF program toward the development of a fusion reactor driver system calls for the demonstration by the end of FY 81 of a single-pulse kilojoule laser system capable of further scaling to the performance levels given in Table 7-1. This requirement dictates that laser system scaling models, each validated at a reasonably high energy level — say about 100 J — are needed before selection of a candidate medium can be made for this development scenario. Moreover, the most significant figure of merit for differentiating between energetically scalable systems is the overall laser system efficiency. The effort reported in this section is directed toward achieving the applications milestones of ICF. Our emphasis in the past year has centered necessarily on the kilojoule milestone; however, we have kept in mind throughout the average power character of the longer term goals.

We have viewed laser media and systems concepts capable of the performance specified in Table 7-1 in terms of two basic types:

- Energy-storing media in which the population inversion is radiatively and nonradiatively stable for times  $>1 \mu\text{s}$ .
- Highly radiating laser media in which the population inversion decays radiatively on the timescale of a few nanoseconds.

By early 1977, we had identified and begun exploratory work on four new laser media concepts (see Table 7-2) with the potential for meeting ICF applications requirements. The photolytic and rare earth systems use energy-storage laser media, two in the gas phase and one in the solid-state phase. The Raman system uses a highly radiating medium (rare gas-monohalide excimer-KrF) whose long-pulse, coherent output is compressed in time via a nonlinear Raman-scattering process.

The time available is relatively short to proceed from concept identification and scientific validation, through technical demonstration, to milestone demonstration, for both the kilojoule and succeeding average power laser systems. Accordingly, in 1977 we conducted preliminary systems assessments of these four laser approaches to provide a quantitative basis for system comparison, to identify high-leverage physics and technical areas of risk, and to set priorities for future technical effort. To conduct this assessment, we developed preliminary device and system models for each laser

**Table 7-2. Potential laser systems for fusion applications.**

Generic species concept	Active species	Pump source	Medium type
Photolytic group VI atoms	Sulfur (S), selenium (Se)	E-beam-driven rare gas excimers ( $Kr_2^*$ , $Xe_2^*$ )	Storage
Rare-earth molecular vapors	Tb-Al-C1, TbThd <sub>3</sub>	E-beam-driven rare gas monohalide excimer (KrF)	Storage
Rare-earth solid-state hybrids	Tm <sup>3+</sup> : glass, crystal	E-beam-driven rare gas monohalide excimer (XeF)	Storage
Raman stacker/compressors	Methane (CH <sub>4</sub> )	E-beam-driven rare gas monohalide excimer (KrF)	Nonstorage

candidate. We then iteratively exercised these models for a number of alternative device geometries to arrive at preliminary technical designs for kilojoule/terawatt laser systems. (While we were conducting these studies, the ICF Advanced Laser Milestone was characterized as a nominal kilojoule/terawatt system. The Office of Laser Fusion has recently modified the milestone definition; it is now characterized as a nominal kilojoule/10 ns system.) Throughout these analyses, we integrated into the comparative assessment new experimental and theoretical data generated for these media by ongoing parallel efforts. We also examined each system for any major physics or technological breakpoints in scaling to energies >100 kJ/beamline. In particular, we emphasized the projection of overall systems efficiency at the kilojoule/terawatt level on the basis of "comparable technical risk." Such analyses necessarily entail considerable technical judgment in projecting efficiencies of individual laser subsystems and processes (power conditioning, deposition, medium conversion, extraction, beam transport, etc.). We have made a major effort to be equitable in these judgments and have used an advocacy process; we believe that the projected systems efficiencies are quantitatively significant in relation to one other and, as a set, they are the likely achievable efficiencies to within a factor of two. Achievement of the projected system efficiencies is predicated on the demonstration of assumed values for a few important physics parameters identified in the various models that have not yet been directly measured.

In our comparison, we analyzed seven kilojoule-level laser designs. For the photolytic Group VIa atomic laser media, we analyzed three multipass power amplifier designs that are differentiated by the methods of photolytic pumping. In one design, coherent 172-nm radiation produced in a xenon excimer pump laser photolyzes the OCS<sub>e</sub> fuel. In the other two designs, incoherent fluorescence radiation from xenon excimer molecules

photolyzes the OCS<sub>e</sub> fuel. In the "solid window" version, the fluorescing xenon gas is physically separated from, but closely coupled to, the photolytic laser medium through a solid window capable of transmitting hard (172-nm) ultraviolet radiation. In the "windowless" version, the fluorescing xenon gas medium flows in streams parallel and adjacent to the flowing laser medium. Matched pressures and velocities lead to the elimination of potentially troublesome solid ultraviolet transmitting windows. In studying photolytic Group VI laser media, we have strongly emphasized the use of selenium as the active species and system operation on the visible-wavelength transauroral transition. This selection stems from the observation that operation on the infrared auroral transitions of either sulfur or selenium will lower attainable efficiencies inversely with the transition wavelength, other factors being equal. For sulfur, evidence suggests that the stimulated emission cross section of the transauroral transition is about an order of magnitude lower than that of the auroral transition. This precludes the ready development of large energy-storing amplifiers for operation at the shorter wavelength. For selenium, the two transition cross sections are essentially equal; we anticipate operation on the transauroral transition in large, energetic amplifiers. In view of these considerations, we must base the utility of the  $Kr_2^*/OCS$  system on compensating efficiency factors associated with the  $Kr_2^*$  pump medium or other dynamical process, or both. To date we have been unable to identify such compensating factors.

We examined three specific designs of kilojoule-class lasers that use trivalent rare earth ions as the active species. The first was an XeF excimer laser-pumped Tm<sup>3+</sup>:glass laser system characterized by a relatively low specific thermal loading of the glass medium. This system can be directly compared with rare earth molecular vapor laser systems in which the average power-thermal loading problem is solved by flow cooling of the laser medium.

We explored designs based on two different molecular carriers of the optically active terbium ( $Tb^{3+}$ ) ion to illustrate the issues associated with the distinct chemical, physical, and kinetic properties of these vapors. For the final system, we analyzed the performance of a backward-wave pulsed Raman stacker-compressor laser that uses the KrF excimer medium as a pump and methane gas ( $CH_4$ ) as the Raman medium.

Because "system efficiency" is a singularly important parameter in comparing the potential of various systems, we must make a few general comments to define the term. As developed below in §7.2.1, total laser system efficiency ( $\epsilon_L$ ) is defined as 100 times the ratio of the optical power *delivered to the target* ( $P_L$ ) to the total power consumed ( $P_{IN}$ ) in generating the delivered power

$$\epsilon_L = \frac{P_L}{P_{IN}} = \frac{P_L}{P_{EC} + P_{FC}}$$

where  $P_{EC}$  = total electrical power input to the laser pump medium, and  $P_{FC}$  = power consumed in flowing and reconditioning the spent laser and pump media. The  $P_{FC}$  must be made large enough to achieve beam quality at the laser exit adequate for further transport to the target, as well as to recycle the laser media for reuse on a closed-cycle basis. The transport efficiency  $\epsilon_T$  of the laser output power ( $P_O$ ) to the target will in general be a function of the optical quality of the beam and therefore a function of  $P_{FC}$ .

$$\epsilon_T = \frac{P_L}{P_O} \quad (1)$$

and

$$\epsilon_L = \left( \frac{P_O}{P_{EC} + P_{FC}} \right) \epsilon_T = \epsilon_O \epsilon_T, \quad (2)$$

where  $\epsilon_T$  depends implicitly on  $P_{FC}$ . The quantity  $\epsilon_O = P_O / (P_{EC} + P_{FC})$  is the efficiency of the laser system up to the exit aperture and may be rewritten as

$$\epsilon_O = \frac{1}{\left( \frac{P_{EC}}{P_O} \right) + \left( \frac{P_{FC}}{P_O} \right)} = \frac{1}{\frac{1}{\epsilon_{EC}} + \frac{1}{\epsilon_{FC}}},$$

where  $\epsilon_{EC}$  is the laser electrical efficiency and  $\epsilon_{FC}$  is the laser flow factor of merit (because  $\epsilon_{FC}$  may exceed unity, it is improper to refer to the quantity as an efficiency). In the analysis below, we do not explicitly evaluate the beam transport efficiency  $\epsilon_T$ . However we have incorporated the issue of transport by estimating the ratio of  $\epsilon_{FC} = P_L / P_{FC}$  required to produce optical beams such that  $\epsilon_T$  will be high enough to prevent significant degradation of total laser system efficiency  $\epsilon_L$ .

The data in Table 7-3 summarize the major conclusions of our analyses of the seven laser systems. In this table, we have divided laser efficiency  $\epsilon_O$  into two parts: pump source and laser medium that converts pump radiation into a format useful for target irradiation. These two subsystem blocks are further partitioned into constituent efficiencies or factors to display the processes or subsystems that dominate the reduction of overall system efficiency and thereby command our future attention. For each system we have identified an approach to significantly improve efficiency of the most limiting process or subsystem; these items are identified by the use of a square containing a higher projected efficiency in order to flag it as a higher risk situation.

The first conclusion we draw from these data is that, based on information available to date, all analyzed systems potentially can meet or exceed the Table 7-1 minimum efficiency requirement of 1%. All systems also appear technologically scalable in energy to reactor-class systems, although the technological issues differ among systems.

The second major conclusion is that, on an "equal risk" basis, the KrF/ $CH_4$  Raman stacker/compressor laser system concept offers a system efficiency significantly higher than the others, possibly reaching 4-6%. Because this laser system also operates at the shortest wavelength (0.27  $\mu m$ ), and enjoys a large range of system architectures and technological options for implementation, we conclude that it has the highest potential of those studied to meet anticipated fusion application needs.

Our third major conclusion is that projected system efficiencies are relatively low (1-6%) primarily because of basic inefficiencies of the pumping sources when they are coherent. The laser medium that converts this coherent radiation into a format useful for fusion applications is, by comparison, relatively efficient. We, therefore, must seek and identify intrinsically more efficient coherent pump sources. Otherwise, we must find more efficient processes for utilizing efficiently produced radiation from incoherent pump sources

**Table 7-3. Projected system efficiencies (%) of several potential fusion lasers.**

		Potential fusion lasers						
Symbol	Efficiency component	Xe <sub>2</sub> <sup>+</sup> pumped OCSs			Rare-earth ions			Raman
		Laser pumped	Fluorescence (windowless)	Fluorescence (window)	ExF pumped Tm <sup>3+</sup> :glass	KrF pumped Tb:Thd <sub>3</sub>	KrF pumped Tb-Al-Cl	KrF/CH <sub>4</sub> compressor
Pump source	$\epsilon_1$ E-beam generation, transport, and deposition	65	65	65	65	65	65	65
	$\epsilon_2$ Pump medium, electron-to-light conversion	5-10 [20] <sup>a</sup>	45	45	5-7.5 [15]	10-15 [25]	10-15 [25]	10-15 [25]
		3.2-6.5 13 <sup>b</sup>			3.3-4.9	6.6-9.8	6.6-9.8	6.6-9.8
	$\epsilon_3$ Pump electrical efficiency		29	29		16	16	16
		3.2-6.2			3.0-4.4	6-8	6-8	6-8
	$\epsilon_4$ Total pump efficiency	12	23 <sup>c</sup>	27	8	12	12	12
Laser	$\epsilon_5$ Transport/coupling	90	20-40 [60]	20-40 [60]	90	90	90	80
	$\epsilon_6$ Fill factor	80	80	80	80	80	80	80
	$\epsilon_7$ Extraction $\times$ quantum	22	22	22	35	28 <sup>d</sup>	28	55-75 <sup>e</sup>
		0.5-1.0	0.8-1.6	0.9-1.8	0.8-1.0	1.2-1.6	1.2-1.6	2.1-4
	$\epsilon_{8f}$ Laser system electrical	1.9	2.4	2.6	2.0	2.4	2.4	6
		0.5-1.0	0.8-1.5	0.9-1.7	0.8-1.0	1.1-1.5	1.1-1.5	2.0-4
	$\epsilon_9$ Total system after flow	1.9	2.3	2.5	2.0	2.3	2.3	6

<sup>a</sup>Percent efficiency with possible breakthrough.

<sup>b</sup>Totals with breakthrough increment.

<sup>c</sup>Requires cleaner pump medium - more flow.

<sup>d</sup>Assumes unit quantum efficiency.

<sup>e</sup>Second Stokes gain suppression.

(e.g., xenon excimer fluorescence — Table 7-3) or develop laser media that operate in a fusion pulse format using conditioned electrical energy directly.

Of course, efficiency projections such as those given in Table 7-3 do not present a complete picture. Each system offers its own, generally distinct technological advantages and challenges; and each carries with it a currently incomplete description of all important physical processes. We develop this aspect of system assessment below, however. Table

7-4 briefly summarizes the principal physical and technological issues for these systems.

For photolytic Group VI lasers, the most influential items are associated with the pump source. The efficiency of a xenon rare-gas excimer laser pump is strongly dependent on three factors:

- Photoionization cross section of the Xe<sub>2</sub><sup>+</sup> excimer.
- Mixing rate of the two populated excimer excited states (1 $\Sigma$  and 3 $\Sigma$ ).

**Table 7-4. Key physics and technology issues for several potential fusion lasers.**

Potential fusion lasers				
Issue	Group VI	Solid-state hybrid	Rare-earth molecular vapor	Raman stacker/compressor
Efficiency after flow, %	0.5-1.9(2.5)	0.8-1.0(2.0)	1.1 = 1.5(2.3)	2.4(6)
Leverage items	Pump laser efficiency; fluorescence; coupling efficiency.	Pump laser efficiency; low $\lambda_2$ material; high thermal conditions.	Pump laser efficiency; single-component vapors	Pump laser efficiency; second Stokes suppression.
Physics risks	Storage time at high inversion density; minority quenchers.	Nonradiative decay channels	Unit quantum yield; spectral homogeneity.	High-order nonlinearities.
Technology risks	vuv optics; gas reconstitution.	Transverse temperature gradients; cyclical stress.	High-temperature optomechanical design; fuel integrity.	uv optics; gain control of pump medium.

● Nonsaturable losses present in the electrically excited medium.

The cross sections (rates) characterizing these processes are not yet sufficiently known to definitively project the ultimate efficiency of an optimized xenon excimer laser pump. Accordingly, we are currently focusing significant experimental, theoretical, and computational effort in this area. By contrast, the fluorescence dynamics of the e-beam-excited xenon excimer medium are fairly well understood and characterized; the major gain would lie in developing concepts for more efficient coupling of the fluorescence radiation to the Group VI fuel. We are pursuing novel optical design and "sandwich" geometries in this area.

In our efficiency projections for Group VI selenium lasers, we have assumed long storage times ( $>1\mu\text{s}$ ). This assumption appears technically warranted, although deleterious quenching of excited Group VI atoms by photo-generated electrons and heavy-particle minority species requires additional study to optimize energetic amplifiers with microsecond-long storage times. The major technological risks associated with Group VI lasers center on the development of vacuum ultraviolet (vuv) optics able to withstand the intense pump fluxes at 170 nm. For coherent pumping, we need to develop high-reflectivity, large-aperture mirrors and windows. For fluorescence pumping with a solid window geometry, the vuv-transmitting windows must withstand large cumulative doses of both vuv radiation and relativistic electrons. In the "windowless" geometry, the vuv optics problem is largely nonexistent; but the added problem of mixed pump and fuel gases arises, and systems efficiency may be decreased because of increased flow power requirements. We have not considered efficiency reduction due to pump and fuel medium reconstitution in our analyses to date. While we do not expect this factor to dominate the overall system efficiency, we must treat it quantitatively if this design concept is to be pursued further.

We consider next the  $\text{Tm}^{3+}$ :glass hybrid system (excimer laser-pumped solid-state laser). High-leverage areas include using a pump laser with substantially higher efficiency than projected for the XeF excimer laser (5-7%), and identifying and using host materials with lower nonlinear refractive index and higher thermal conductivity than glasses. As a class, crystalline materials offer considerably higher thermal conductivities and, in some cases, very low nonlinear refractive indices. We are currently searching for host materials that are compatible with useful active ions and that can be scaled to large sizes with acceptable optical quality. In

terms of physics issues, we have estimated non-radiative decay rates due to multiphonon and ion-ion interactions for the  $\text{Tm}$ :glass system. Experimental documentation of the important non-radiative (thermal) rates would be needed before the selection and development of such a hybrid laser system. Preliminary analysis suggests that axial-gradient cooling techniques can achieve usefully high average power from a solid-state laser. The optical quality of radiation extracted from such a system will depend largely on the extent to which we can control transverse temperature gradients. We judge that adequate temperature control can be achieved in principle; however, design solutions depend on the specific details of the pump deposition and laser medium dynamics. In view of the projected performance of the  $\text{Tm}^{3+}$ :glass system — in comparison with alternative systems — we feel this particular hybrid laser system does not warrant such detailed analysis. Rather, further effort in this system area will center on identifying intrinsically better pump and medium combinations.

We consider next the rare-earth molecular-vapor laser systems. Again we are forced to recognize the importance of identifying more efficient pump sources. Although we considered laser pump sources for the Tb-based systems analyzed to date, the long population inversion lifetimes possible in selected rare-earth molecular vapors appear amenable to incoherent pump sources, such as flashlamps, provided efficient spectral coupling can be achieved. This is particularly true for the aluminum halide complexes, although laser amplifiers based on aluminum halide complex vapor media must operate at a relatively high total pressure (2-4 atm  $\text{Al}_2\text{Cl}_6$ ) because of their two-component chemical nature. For this reason, we anticipate significant design issues with respect to maintaining adequate beam quality in the extracted radiation. Accordingly, we put a premium on using single-component rare-earth ion carriers, such as the thd-chelates suitably buffered with a rare gas, as amplifier media.

In our efficiency analyses of the rare-earth molecular-vapor systems, and in the absence of direct experimental measurements, we have assumed unity quantum yields (one molecule in the upper laser level for each photon absorbed) for the two Tb-vapor media. The relative simplicity of the electronic structure of the Tb-Al-Cl molecule provides a technical rationalization for this assumption. However, this is not true for the more complex thd-metallo-organic molecule; the true quantum yield is a more open issue. This situation represents a major remaining physics uncertainty for these

vapor systems. Quantum yields that are much lower than unity will reduce projected efficiencies for these systems below the minimum level of interest. In this respect, we are currently conducting laser oscillator experiments with these vapor species to place a lower bound on the quantum yield. A secondary physics issue concerns the spectral homogeneity of the gain-medium transition for pulse extraction times  $\approx 10$  ns. To date, there has been no quantitative characterization of the transition lineshape at the temperatures and pressures of interest for fusion amplifiers. While we can assume a nominally homogeneous gain line due to collisional coupling of Stark and rotational states within the fluorescence envelope, this issue must be addressed experimentally before development of large-scale devices.

Technologically, the principal issues associated with rare-earth molecular-vapor laser systems center on successful optical-mechanical designs of amplifier structures for the relatively high operating temperatures anticipated (300-500°C). The design must also accommodate the flow of working material consistent with optical pumping requirements and maintenance of fuel purity. Devising successful design solutions for lasers using the two-chemical-component aluminum halide vapor medium appears to be a particularly great challenge.

Finally, we consider the KrF/CH<sub>4</sub> Raman stacker/compressor laser system. Although it uses the most efficient and energetically scalable excimer laser pump yet demonstrated, developing techniques to increase the efficiency of KrF or other narrow-band excimer laser pumps is clearly desirable. Considerable current effort at LLL and elsewhere to understand the full kinetics of the KrF and other excimer lasers should lead to significant improvement in laser efficiency under narrow-band conditions. From the viewpoint of systems scaling, developing techniques to suppress gain at the second Stokes frequency will be singularly advantageous. Such techniques will allow a high compression ratio per Raman stage and will greatly reduce system complexity. Several techniques to suppress second Stokes gain have been proposed; they will receive considerable attention in the near future.

As discussed more fully below, we have already conducted an array of key experiments to demonstrate the scientific feasibility of the Raman compressor concept. These include the following:

- Measurement of the Raman gain coefficient in the backward direction and its dependence on pressure and pump linewidth.
- Demonstration of pump saturation and

measurement of the backward wave saturation influence.

- Demonstration of stable spatial growth of the backward Stokes wave when pumped with a spatially scrambled pump beam.

The favorable experimental results and their agreement with theoretical models increase our confidence in our performance projections of large-scale systems for fusion applications. However, much remains to be done to refine our physics models, particularly with respect to the dynamics of second Stokes generation and its coupling to higher order nonlinearities. Suppression of the second Stokes wave will reduce uncertainty concerning higher order nonlinearities and will provide the system-scaling benefits cited above.

The major technological issues for the Raman systems are fairly obvious. First, transmitting and reflecting optics at 0.27  $\mu\text{m}$  must be substantially improved over those now available. Current conceptual designs of large systems call for optics capable of handling beam fluences up to 4 J/cm<sup>2</sup> (i.e., a factor of about five over currently available optics). No significant effort has yet been expended to develop high-damage-threshold optics at 0.27  $\mu\text{m}$ . Although fewer optical materials are suitable for service at 0.27  $\mu\text{m}$  than are suitable at 1  $\mu\text{m}$ , we feel that adequate optics can be developed by using the methodology that successfully developed 1- $\mu\text{m}$  optics for Nd:glass systems. The second significant technological issue is the mode control of the intrinsically high-gain KrF pump amplifier medium. We have been successful in presaturating KrF power amplifiers pumped by electrical discharges. These relatively small ( $< 1$ -J) amplifiers have been demonstrated to be spectrally and energetically controllable with modest levels of injected radiation. Using this information, together with a preliminary analysis of the stabilization of KrF power amplifier of large transverse dimensions ( $\sim 40$  cm), we judge that adequate gain control can be achieved. However, we must still demonstrate this experimentally.

To summarize, we conclude that the KrF/CH<sub>4</sub> Raman pulse stacker/compressor concept offers the highest programmatic potential of all systems studied. We expect to develop this concept through continuing experimental, analytical, and theoretical efforts on the problems and issues identified in our preliminary studies. These activities will include the following:

- Refined determination of limiting physical processes.
- Characterization and improvement of optical components for system use.

- Demonstration of combined stacking and compression.

- Technical demonstration of an e-beam KrF power amplifier capable of operating in a controlled manner at the 100-J level.

We will technically coordinate these activities through continued development of Raman stacker/compressor laser system models.

Parallel efforts will recognize the tremendous value of laser-driver systems with efficiencies >10%. We will continue searching for more efficient pump sources to significantly improve the potential of systems already identified and to use in entirely new laser media and systems concepts.

In the sections that follow, we discuss the theoretical, analytical, computational, and experimental research on advanced lasers systems conducted during 1977. Section 7.2 addresses several laser systems issues common to all the laser system candidate media studied: definition of laser subsystem efficiency factors, laser system architecture options, and laser medium homogeneity and laser beam focusing requirements. Sections 7.3-7.6 discuss in succession, photolytic Group VI atomic lasers, rare-earth molecular vapor lasers, rare-earth solid-state hybrid lasers, and Raman stacker/compressor lasers. We develop an assessment of each laser systems in terms of the following:

- Concept definition and microscopic laser parameters.
  - Laser experiments.
  - Laser system model.
  - Laser scaling and efficiency projection.

## Authors

W. Krupke  
E. V. George  
C. Bender

## 7.2 System Considerations

### 7.2.1 Computational Objectives and Capabilities

Analysis of laser system performance requirements for fusion power plants enables us to identify the physical and technological constraints that a candidate laser medium must satisfy. In general, the candidate laser must operate in a wavelength regime where high optical power and energy transport can be achieved with low loss. Laser media excitation and extraction techniques must be both efficient

and scalable, and efficient average-power operation must be possible. Finally, the overall laser system must be reliable and economical.

The above constraints limit the technical parameter space of candidate fusion lasers. Accordingly, we put a premium on high-level, sophisticated laser system modeling for critical evaluation of candidate laser media before undertaking even preliminary scaling. We are using an extensive set of computer codes to analyze all advanced laser concepts being pursued at LLL. These codes are of two types: *simulation codes* that evaluate and verify the basic physics of a laser element and *rapid lumped-element codes* that approximate each element for integration into a total system design and optimization code. Table 7-5 summarizes the specific major computational tools developed and used in our analytical assessment, which includes Raman pulse compression, Group VI, and rare-earth systems.

For example, Fig. 7-1 is a detailed block diagram of the computational method used to analyze the dynamics of electrically excited media. This code calculates self-consistent electron energy distribution functions and excited-state populations for electrically excited laser media. The code treats electron beam and discharge electric field energy depositions self-consistently by developing a source function for the secondary electrons produced by slowing down a high-energy primary. It then uses this source function in the electron Boltzmann equation that governs the dynamics of secondary electrons in the presence of the electron beam and applied electric field. Next, the code employs the electron distribution that results to compute rate constants for electron collisional processes. It uses these rate constants in a kinetic rate equation analysis of the charged-particle and excited-state populations present in the medium. At prescribed time intervals, the code employs these populations to recompute the electron distribution function by resolving the appropriate Boltzmann equation until the population and electron distribution function reach a steady state. If a laser radiation field is present, spontaneous and stimulated emission, and photoabsorption processes are included in the kinetic model. The estimated run time for this code on a standard CDC 6600 is greater than one hour. However, we have exploited the vectorization and overlay software features of the LLL CDC 7600 computer system for a greatly reduced run time. For the full calculation presented in our discussion of rare-gas excimer and rare-gas halide laser modeling, typical run times were 0.5 to 1.5 min. (This includes media kinetics and amplifier performance analysis.)



**Table 7-5. Synopsis of computer codes used to assess advanced laser concepts.**

Computer code application	Features
<b>Electrically excited media:</b> <ul style="list-style-type: none"> <li>• Electron beam</li> <li>• Discharge</li> <li>• Electron beam/sustainer discharge</li> </ul>	<ul style="list-style-type: none"> <li>• Electron beam deposition</li> <li>• Non-Maxwellian electron kinetics</li> <li>• Generalized heavy particle kinetics</li> <li>• Generalized photon kinetics</li> <li>• Oscillator</li> <li>• Amplifier</li> </ul>
<b>Optically pumped media:</b> <ul style="list-style-type: none"> <li>• Bleaching or photodissociation wave</li> </ul>	<ul style="list-style-type: none"> <li>• 1D bleaching wave with generalized kinetics</li> <li>• Fluorescence-driven 2D bleaching wave</li> <li>• Pump coupling efficiency</li> </ul>
<b>Raman compressor dynamics:</b> <ul style="list-style-type: none"> <li>• Extraction</li> <li>• Parasitics</li> </ul>	<ul style="list-style-type: none"> <li>• 4-wave Raman interaction (pump laser, forward 1st Stokes, backward 1st and 2nd Stokes)</li> </ul>
<b>Short-pulse laser system energy extraction:</b> <ul style="list-style-type: none"> <li>• Electrically excited media</li> <li>• Optically excited media</li> <li>• Raman compressors</li> </ul>	<ul style="list-style-type: none"> <li>• Generalized Frantz-Nodvik multipass</li> <li>• Finite pump, transit, and lower level relaxation times.</li> <li>• Nonuniform gain and pump depletion</li> <li>• Pulse focusing and stacking</li> <li>• Laser system staging and optimization</li> </ul>

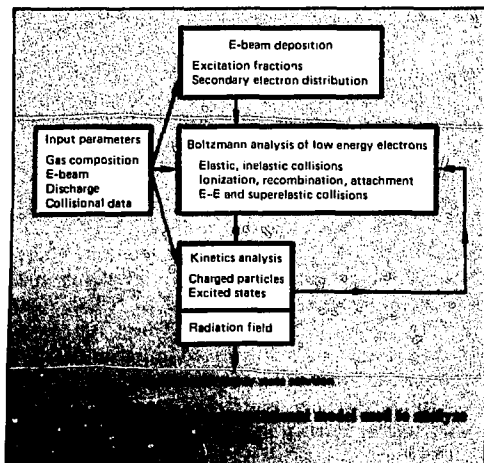
The major Raman amplifier code simulates compressor physics. It includes the four major waves coupled in the transient semiclassical theory. Some spinoff codes used for approximate analyses include a rapid two-wave code that simulates the two major waves in varying geometries and configurations, estimating parasitic growths and phase

distortion integrals. We have also used a rapid two-wave code to study statistical aspects of beam inhomogeneities, verifying much analytic work on this problem. Finally, we have developed a rapid lumped-element code for total system design optimization; it uses the Frantz-Nodvik equations.

We have approximated the KrF\* pump elements using the Schultz-Dubois theory, and have constructed several codes of varying sophistication. We have incorporated one of these, together with the compressor code, into a design code that can rapidly evaluate the performance of various system concepts. It gives details of pulse shapes and parasitics and estimates the beam quality of the output. The average running time of this optimization code is about 10 s on the LLL CDC 7600.

In general, the computational capability summarized in Table 7-5 has provided a rapid quantitative assessment of both basic physics and technological feasibility of several laser concepts. We view it as a mechanism for identifying key technical issues and scaling limitations for advanced laser concepts.

In the remainder of §7.2 we consider several average-power fusion laser systems issues addressed during the past year: in §7.2.2, the effect of flow conditioning on total laser system efficiency; in §7.2.3, laser system architecture configurations and



multipass amplifier extraction analyses; and in §7.2.4, the relationship between laser beam focusability and laser medium homogeneity requirements.

#### Author

R. A. Haas

#### Major Contributors

D. Eimerl  
R. D. Franklin  
W. L. Morgan  
C. W. Werner

### 7.2.2 Total Laser System Efficiency

Efficiency and scalability are two very important and separate aspects of a large laser system. A power plant laser system of high efficiency will have lower recirculating power needs and lower capital equipment costs. Efficiency depends on several factors:

- Losses due to power conditioning.
- Electron beam generation.
- Optical pump photon production.
- Coupling to the laser molecule.
- Optical extraction.
- Pumping, cooling, and chemical regeneration of the flowing gases.

By "scalability" we mean the ability to reach the high pulse energy requirements of a laser fusion reactor by creating power amplifier modules of significant size. A laser with large single aperture and high energy per pulse lowers costs by reducing complexity in the number of beams and components. In any given laser system, a tradeoff between efficiency and scalability to achieve an optimal system is usually possible. It now appears that achieving high efficiency — rather than high energy per pulse or high average power — will be our most difficult problem in visible gas fusion laser systems.

A number of considerations in the determination of overall laser system efficiency are often overlooked. We can view a high-average-power gas laser system as three separate conditioning subsystems: optical, electrical, and gas (see Fig. 7-2). We then define the total system efficiency  $\epsilon_L$  of a fusion reactor as the laser power  $P_L$  delivered to the target divided by the total power, electrical  $P_{EC}$ , and flow conditioning  $P_{FC}$ , required to operate the laser:

$$\epsilon_L = \frac{P_L}{P_{EC} + P_{FC}} = \frac{P_L/P_0}{\frac{P_{EC}}{P_0} + \frac{P_{FC}}{P_0}} = \frac{\epsilon_T}{\frac{1}{\epsilon_{EC}} + \frac{1}{\epsilon_{FC}}} \quad (3)$$

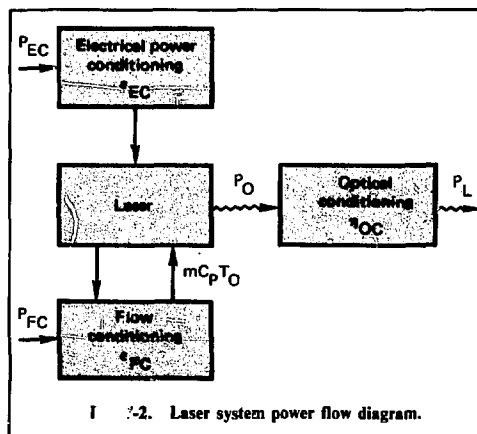
where  $P_0$  is the laser output power;  $\epsilon_T = P_L/P_0$  the laser energy transport efficiency;  $\epsilon_{EC} = P_0/P_{EC}$ , the electrical efficiency; and  $\epsilon_{FC} = P_L/P_{FC}$ , the flow conditioning factor. The laser energy transport efficiency  $\epsilon_T$  takes account of laser beam power losses incurred by the beam as it travels from the output of the final amplifier to the pellet. In a well-designed optical transport system  $\epsilon_T$  might be in the 90-95% range. The electrical conditioning efficiency is the ratio of laser output power to electrical power input to operate the laser. For an e-beam-pumped laser, it is the product of the component efficiencies for the e-beam electrical pulse forming network (80-90%), e-beam formation and deposition (70-80%), laser medium excitation, and laser power extraction efficiencies:

$$\epsilon_{EC} = \epsilon_{PF} \epsilon_{EB} \epsilon_{LM} \epsilon_{EXT}$$

The flow conditioning efficiency accounts for the power required to circulate the gas, adequately damp acoustic disturbances, remove waste heat, and chemically regenerate the laser gas.

From Eq. (3), we can see that total laser system efficiency  $\epsilon_L$  is effectively the product of the optical efficiency and the smaller of the electrical or flow subsystem efficiencies. Usually, most of the power invested in the system will operate a large final amplifier, where most of the laser energy will be generated. Consequently, the performance characteristics of this amplifier will largely determine overall laser efficiency. The average output power of this amplifier can be written

$$P_0 = \epsilon_0 L_F A_L \nu_L \quad (4)$$



where  $\mathcal{E}_O = E_L/\epsilon_T V$ , the laser output energy per pulse per unit volume. The volume of the final amplifier is

$$V = L_F A_L,$$

where  $L_F$  is the amplifier's length in the gas flow direction, and  $A_L$  is its corresponding cross sectional area. The laser system produces pulses at a repetition frequency  $\nu_L$ .

If we disregard chemical regeneration, the flow conditioning power for this final amplifier is:

$$P_{FC} = \xi p_L U_L A_L \left( \frac{T_O}{T_L} \right), \quad (5)$$

where  $U_L$  is the speed of the flowing laser gas,  $p_L$  is the pressure of the laser medium,  $T_L$  is the temperature of the laser medium and  $T_O$  is the stagnation temperature of the gas. If we treat the laser flow system as an ideal wind tunnel<sup>1</sup> and disregard the energy added to the laser medium from excitation, then

$$\xi = \left( \frac{\gamma}{\gamma - 1} \right) \left[ \left( 1 - \frac{\Delta p}{p_0} \right)^{\frac{1-\gamma}{\gamma}} - 1 \right], \quad (6)$$

where  $\gamma$  is the gas specific heat ratio,  $\Delta p$  is the pressure drop required to maintain the gas flow against losses from acoustic damping devices, etc., and  $p_0$  is the reservoir or stagnation pressure. Subsonic flows are needed to minimize the generation of entropy (thermal) or acoustic disturbances. Furthermore, if we use low-pressure-drop acoustic damping schemes, the expression for  $\xi$  in Eq. (6) simplifies considerably because the reservoir and laser sections are at nearly the same temperature and pressure, and  $\xi \cong \Delta p/p_L$ . The flow-conditioning power is then simply  $P_{FC} \cong \Delta p U_L A_L$ .

We can obtain the flow-conditioning factor by combining Eqs. (4) and (5):

$$\epsilon_{FC} \cong \frac{\mathcal{E}_O/p_L}{f(\Delta p/p_L)}, \quad (7)$$

where  $f = U_L/L_F \nu_L$  is the laser medium exchange factor — the ratio of the distance the gas flows between pulses to the optical cavity size in the flow

direction. (Laser medium exchange factors of approximately one to two are typical of subsonic gas lasers.) From Eq. (7), we can see that three dimensionless parameters determine the flow efficiency:  $(\mathcal{E}_O/p_L)$ ,  $f$ , and  $\Delta p/p_L$ . To achieve high flow-system efficiency, we must keep the medium exchange factor and pressure drop as low as possible. In addition, the laser output energy per unit volume must be as large as possible in comparison with the laser medium pressure, which is equal to two-thirds of the gas thermal energy density. In energy density units,  $p_L = 10^2$  J/litre-atm. (The ratio  $\mathcal{E}_O/p_L$  is sometimes called the volumetric efficiency or the specific laser output energy of the laser amplifier.) For most applications, the flow pressure drop is due to the acoustic damping devices<sup>2-4</sup> that must be positioned both upstream and downstream from the laser excitation region. We can write the cumulative pressure drop across a given section for subsonic flow systems as

$$\Delta p_i \cong \kappa_i \frac{1}{2} \rho_i U_i^2, \quad (8)$$

where, for the  $i$ th section,  $\kappa_i$  is the loss coefficient,  $\rho_i$  is the density at the section entrance, and  $U_i$  is the gas velocity at the section entrance. The loss coefficient  $\kappa_i$  is related to the dimensionless coefficient of resistance  $\lambda_i$  by<sup>5</sup>

$$\kappa_i = \frac{L_{Fi} \lambda_i}{d_{hi}}, \quad (9)$$

where  $L_{Fi}$  is the length and  $d_{hi}$  is the hydraulic diameter of the  $i$ th section. We can approximate the cumulative pressure drop for subsonic flow systems as

$$\Delta p = \sum_i \kappa_i \frac{1}{2} \rho_i U_i^2 \sim \left( \sum_i \kappa_i \right) \frac{1}{2} \rho U^2 = \kappa \frac{1}{2} \rho U^2. \quad (10)$$

Experience suggests that values of  $\kappa$  in the 5-30 range are achievable.<sup>2-4</sup> If  $a_0$  is the gas sound speed, we can relate the relative pressure drop to the flow Mach number  $M = U/a_0$ :

$$\frac{\Delta p}{p} = \left( \frac{\gamma}{2} \right) \kappa M^2. \quad (11)$$

The flow system factor is then

$$\epsilon_{FS} \approx \frac{2\epsilon_0/p_L}{f\kappa\gamma M^2} \quad (12)$$

We can maximize the flow system factor by minimizing the flow Mach number, medium exchange factor, and loss coefficient. We can write this result in terms of more fundamental quantities by noting that, if  $\tau_s = L_F/a_0$  is the acoustic transit time in the flow direction, then

$$M = \frac{U}{a_0} = \frac{fL_F\nu_L}{a_0} = f(\tau_s\nu_L) \quad (13)$$

Substituting Eq. (13) into Eq. (12) gives the flow conditioning factor as

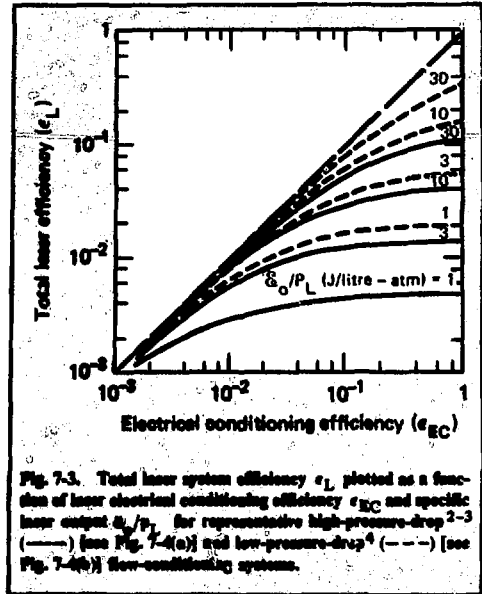
$$\epsilon_{FS} \approx \frac{2\epsilon_0/P_L}{\gamma\kappa(\tau_s\nu_L)^{2f^3}} \quad (14)$$

or

$$\epsilon_{FS} \approx \frac{2 \times 10^{-2} \epsilon_0 (\text{J/litre}) p_L (\text{atm})}{\gamma\kappa \tau_s^2 \nu_L^2 f^3} \quad (15)$$

The flow system efficiency is a sensitive function of the medium exchange factor  $f$ , the product of acoustic transit time and laser repetition frequency  $\tau_s\nu_L$ , the total acoustic damping system flow loss coefficient  $\kappa$ , and the specific laser output energy  $\epsilon_0/p_L$ . Clearly, from Eq. (15) the flow system factor is maximized by minimizing the medium exchange factor, the acoustic transit time, the laser repetition frequency, and the loss coefficient and by increasing the specific laser output. The acoustic transit time depends directly on the laser amplifier aperture size, atomic weight of the laser gas, and gas temperature (i.e.,  $\tau_s^2 \propto L_F^2 M/T$ ).

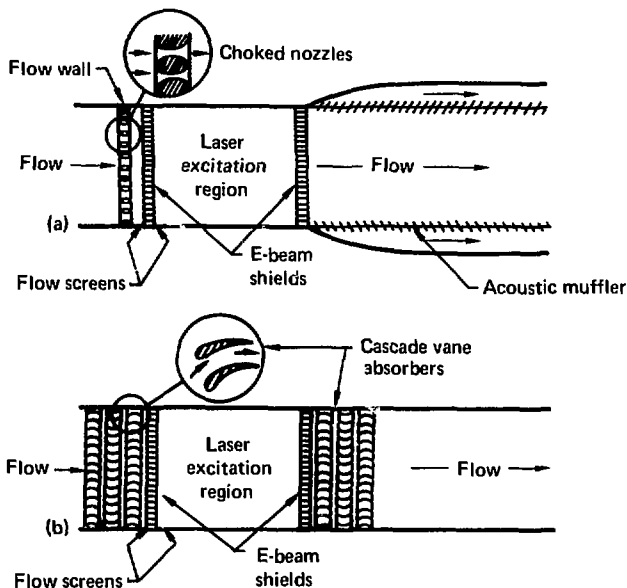
Figure 7-3 illustrates the significance of the volumetric efficiency of a laser amplifier. We have plotted total laser system efficiency as a function of laser electrical conditioning efficiency for representative high-pressure-drop<sup>2-3</sup> [Fig. 7-4(a)] and low-pressure-drop<sup>4</sup> [Fig. 7-4(b)] flow-conditioning systems. (We took the energy transport efficiency  $\epsilon_0$



to be 95% and the volumetric efficiency as a parameter.) In the high-pressure-drop system, the laser medium and flow screen arrangements require a significant pressure drop. For a total pressure drop around the flow-conditioning circuit we assume a pressure ratio of three for the pumps. We also assumed that a medium exchange factor of 1.5 was required. Figure 7-3 clearly shows the importance of achieving a high volumetric efficiency in the laser medium for this case. For example, if the laser system electrical efficiency is 4% and the laser medium can only operate at a volumetric efficiency of 1 J/litre-atm, then total system efficiency is 0.4%, an order of magnitude lower than the electrical efficiency. To achieve its full electrical efficiency, this laser would have to operate at >50 J/litre-atm.

Figure 7-3 further illustrates the potential advantage of a low-pressure-drop system. Let us assume a low-pressure-drop system — as illustrated in Fig. 7-4b — with a 5-psi pressure drop (comparable to an ordinary wind tunnel) and a medium exchange factor of 1.5. Again, if the laser system electrical efficiency is 4% and the laser medium operates with a volumetric efficiency of 1 J/litre-atm, the total laser system efficiency is 1%. The flow penalty diminishes as the volumetric efficiency increases. At 30 J/litre-atm, total system efficiency is nearly equal to the electrical efficiency of 4%. Figure 7-3

Fig. 7-4. Representative (a) high-pressure-drop<sup>2-3</sup> and (b) low-pressure-drop<sup>4</sup> flow-conditioning systems used to control acoustic disturbances generated after laser excitation for high-average-power laser systems.



clearly shows the profound implications that flow-conditioning penalties can have for a laser system.

Figure 7-3 suggests that a laser medium must operate at as high a volumetric efficiency as possible — preferably 10 J/litre-atm — to achieve its full electrical efficiency with a low-pressure-drop acoustic damping system. In some laser media we can anticipate that high electrical efficiencies are achievable only at low volumetric efficiencies. For instance, excited-excited-state kinetic losses involving the laser species may preclude operation at high volumetric efficiencies. Also, operation at high volumetric efficiency or specific laser output may produce large specific thermal loadings and pressure pulses that must then be dissipated. For example, take the case of the 4%-efficient laser operating at a specific output of 10 J/litre-atm: if 40% of the electric energy appears as specific thermal energy — 100 J/litre-atm — very strong acoustic disturbances will be generated. In this case, a high-pressure-drop system may be needed to achieve the required acoustic damping and optical medium quality. On the other hand, if the laser medium is highly radiative so that only 4% (or 10 J/litre-atm) of the electrical energy appears as thermal energy, then a low-pressure-drop system may be sufficient to achieve high medium optical quality. This example illustrates the potentially strong interplay between

the total laser system efficiency requirement, optical transport, and laser kinetics. In general, gaseous laser media that are radiatively efficient and that operate at volumetric efficiencies in the 10-to-30-J/litre-atm range have the greatest promise of achieving the highest average-power total laser system efficiencies.

## References

1. H. W. Liepmann and A. Roshko, *Elements of Gas Dynamics* (John Wiley and Sons, New York, 1957).
2. D. R. Ausherman, I. E. Alker, and E. Baum, "Acoustic Suppression in a Pulsed Chemical Laser," AIAA Paper No. 78-237 (presented at the AIAA 16th Aerospace Sciences Meeting, Huntsville, Alabama, January 1978).
3. J. Schwartz, R. J. Golik, C. L. Merkle, D. R. Aushermann, and E. Fishman, *Fluid Mechanics of Fusion Lasers*, TRW, Rept. 31775-6002-RU-00 (1978).
4. R. M. Feinberg, R. S. Lowder, and O. L. Zappa, *Low Pressure Loss Cavity for Repetitively Pulsed Electric Discharge Lasers*, AFWL, Rept. TR-75-99, February 1975.
5. H. Schlichting, *Boundary Layer Theory* (McGraw-Hill Book Co., New York, 1968).

Author

R. A. Haas

Major Contributor

M. J. Monsler

### 7.2.3 Laser System Architectures — Energy Extraction

As noted in §7.1, a fusion reactor laser system must deliver a multi-100-TW pulse of short-wavelength radiation to each fusion pellet. Design of such a laser system requires careful consideration of the energy and power extraction characteristics of each of its amplifier elements and the staging or systems architecture within which these elements must function. In addition to the physics and technology issues associated with the development of large-scale amplifier elements, economic and reliability constraints will require the development of innovative systems architectures. In current Nd:glass laser designs, the systems architecture consists of a cascaded chain of amplifiers [Fig. 7-5(a)] driven by a master oscillator. The final amplifier stores most of the energy in these amplifiers; however, it accounts for perhaps 20-30% of the total cost of the laser system. This suggests that architectures based on large-scale regenerative [Fig. 7-5(b)] or multipass [Fig. 7-5(c)] amplifier configurations may be employed to achieve significant economic and reliability benefits. In these systems, a large amplifier is used to build up a low fluence or intensity input pulse to the level at which efficient extraction occurs. The "front end" on such a system can be simple and reliable and would account for only a small fraction of overall system cost. Currently, the technology of large-aperture, fast ( $\leq 1 \mu\text{s}$ ) electro-optical switches permits only 5-to-10-cm apertures to be practical without segmentation; thus, large-scale regenerative systems appear compelling only if the switch aperture scaling can be developed. On the other hand, for many media it is possible to build large-aperture, high-energy, and power-gain amplifiers suitable for multipass operation. In these systems after only a few passes, say five, a small signal can be efficiently amplified to high intensity. These systems are particularly promising because they are simple, potentially more reliable, relatively inexpensive, and potentially more efficient. All this is because the effective relaxation time may be extended to allow lower level extraction and gain recovery. In the most general case, we consider a large-scale amplifier that is pumped one or more times and through which an extraction pulse repetitively passes to remove the available energy. The optimum pump-extraction scenario will depend on the character of the laser medium. In the following we analyze the scaling and multipass energy extraction characteristics of large-scale storage laser amplifiers.

**Multipass Amplifier Scaling — Storage Laser Media.** Efficiently pumping and extracting energy

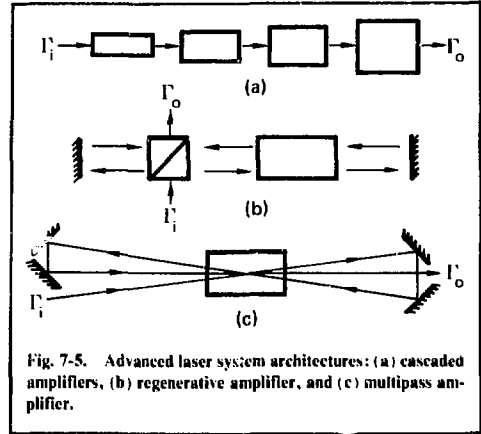


Fig. 7-5. Advanced laser system architectures: (a) cascaded amplifiers, (b) regenerative amplifier, and (c) multipass amplifier.

from a storage laser amplifier requires that the collisional and radiative lifetime  $\tau_L$  of the upper laser level must exceed the pump time  $\tau_P$ . The output fluence must be less than the optical damage fluence  $\Gamma_{\text{damage}}$  and the initial small signal gain-amplifier length product  $\alpha_o L$  must be as large as possible. At high energy densities, the maximum  $\alpha_o L$  is determined by fluorescence depumping and parasitic oscillation limitations. For storage lasers with large radiative lifetimes ( $\geq 10 \mu\text{s}$ ), parasitic oscillation sets the more severe limitation.

Along the propagation axis of a laser amplifier, optical damage and parasitic oscillation limitations require that the upper laser level line density  $N_{uo}L$  must be less than the smaller of  $\Gamma_{\text{damage}}/h\nu_L$  and  $(\alpha_o L)_{\text{max}}/\sigma$ , where  $\sigma$  is the stimulated emission cross section. Therefore, the amplifier is damage-fluence-limited if  $\sigma > \sigma_o = (\alpha_o L)_{\text{max}} h\nu_L / \Gamma_{\text{damage}}$ . For a damage fluence of  $10 \text{ J/cm}^2$  and  $(\alpha_o L)_{\text{max}} \sim 4$ , the optimal cross section is  $\sigma_o(\text{cm}^2) \sim 8 \times 10^{-20} / \lambda(\mu\text{m})$ , or  $3 \times 10^{-19} \text{ cm}^2$  at  $0.25 \mu\text{m}$  and  $8 \times 10^{-20} \text{ cm}^2$  at  $1 \mu\text{m}$ .

Of course, for larger damage fluences, smaller cross sections are optimal. The maximum energy that can be extracted from such an amplifier module is

$$E_L < E_{L_{\text{max}}} = \Gamma_{\text{damage}} \frac{(\alpha_o L)^2}{(\sigma N_{uo})^2} \max. \quad (16)$$

This result shows the advantage of operating at high damage fluences, low small signal gains, and large gain-length products or large amplifier lengths. For the previous example, if  $\alpha_o \sim 10^{-2} \text{ cm}^{-1}$  (corre-

sponding to an amplifier length of 4m), the maximum amplifier energy capacity is about 1 MJ. In practice, it is generally not technically feasible to excite the volume or build optical components for a 4-by-4-m aperture; hence, smaller apertures will likely be used.

**Multipass Amplifier Energy Extraction — Storage Laser Media.** In energy storage laser media, both the characteristic pump time and the upper level lifetimes are long in comparison with the extraction time. In addition, for many circumstances of interest, the lower laser level is either rapidly relaxed or remains unrelaxed (bottlenecked) during extraction. Under these circumstances, the laser pulse output energy fluence  $\Gamma_n^0$  at the end of the  $n$ th extraction pass is determined by integrating

$$\frac{d\Gamma_n}{dz}(x_{\perp}, z) = \alpha_{0n}(x_{\perp}, z)\Gamma_s \left[ 1 - e^{-\Gamma_n(x_{\perp}, z)/\Gamma_s} \right] - \gamma\Gamma_n(x_{\perp}, z), \quad (17)$$

from the input fluence  $\Gamma_n^i(x_{\perp}, z)$ . The quantity  $x_{\perp}$  accounts for the possible variance in the small signal gain  $\alpha_0$  and pulse energy fluence  $\Gamma_n$  across the amplifier aperture in the directions normal to the  $z$ -propagation axis. The small signal gain prior to the  $n$ th pass is

$$\alpha_{0n} = \sigma \left[ N_{u_n} - \left( \frac{g_u}{g_L} \right) N_{L_n} \right] \quad (18)$$

where  $N_u$  and  $N_L$  are the upper and lower total population densities and  $g_u$  and  $g_L$  are the corresponding upper and lower degeneracies, respectively. The quantity  $\gamma$  accounts for nonsaturable photoabsorption losses that may be present. The saturation fluence for a bottlenecked system is

$$\Gamma_s = \frac{h\nu_L}{1 + \left( \frac{g_u}{g_L} \right) \sigma} \quad (19)$$

If the lower level is rapidly relaxed during extraction, we can use the current formulation, provided we impose the limit  $g_u/g_L \rightarrow 0$ . We have studied Eq. (17) in some detail; it admits an analytic solution only when the nonsaturable loss vanishes.

If the optical transmission per pass of the multipass pulse optical relay system is  $T$  and non-

saturable loss is absent, the solution of Eq. (17) becomes

$$\Gamma_n^0 = \Gamma_s \ln \left\{ \exp \left( \int_0^L \alpha_{0n} dz \right) \left[ \exp \left( \frac{\Gamma_{n-1}^0}{\Gamma_s} \right) - 1 \right] + 1 \right\}. \quad (20)$$

The laser pulse energy fluence depends on the input fluence  $\Gamma_{n-1}^0$ , the saturation fluence and the small signal gain integrated from the input. The extraction efficiency after the  $n$ th pass is

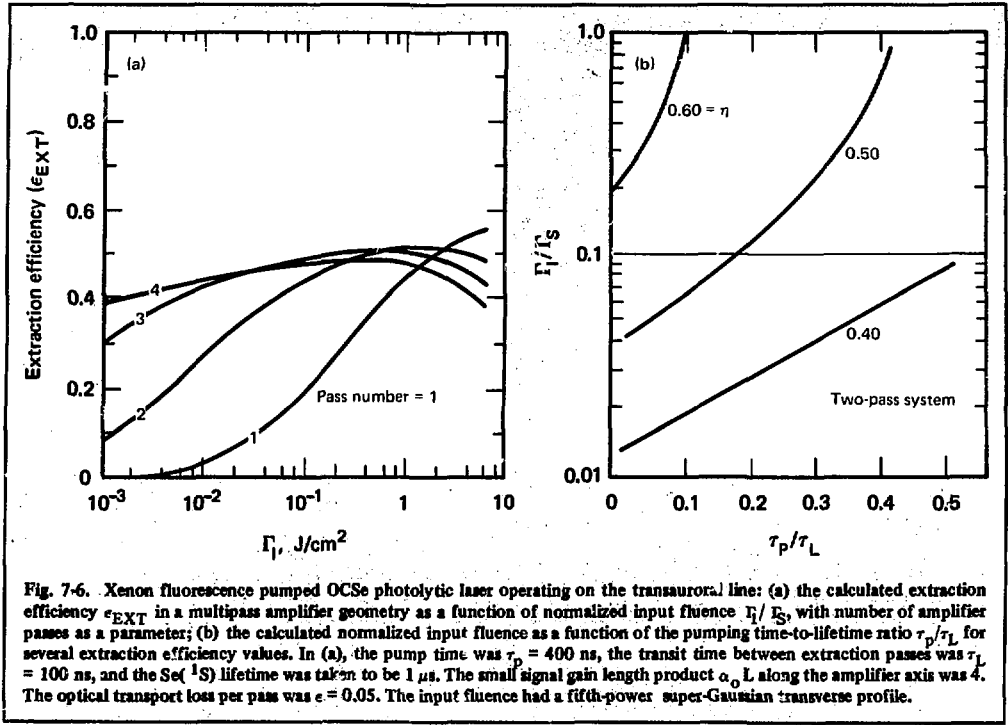
$$\epsilon_{\text{ext}} = \frac{\Gamma_n^0 - \Gamma_i^0}{N_{u_0} h\nu_L L} = \frac{\Gamma_n^0 - \Gamma_i^0}{\left( 1 + \frac{g_u}{g_L} \right) (\alpha_0 L \Gamma_s)}, \quad (21)$$

where  $\alpha_0 L$  is the initial small signal gain that would be achieved in the absence of any upper or lower laser level relaxation during excitation. In general, the amplifier gain distribution immediately before the first extraction pass depends on the pumping mechanism. For example, if the upper laser level lifetime is  $\tau_L$  and the laser medium is pumped uniformly for a time  $\tau_p$ , then

$$\int_0^L \alpha_{01} dz = (\alpha_0 L) \left( \frac{\tau_L}{\tau_p} \right) \left\{ 1 - \exp \left[ -\frac{\tau_p}{\tau_L} \right] \right\}, \quad (22)$$

If the amplifier is pumped transversely from two sides along the  $x$ -axis by a bleaching wave, then excited-state quenching produces a nonuniform transverse initial gain profile after the bleaching wave has excited the medium. When the two bleaching waves meet at the center of the amplifier, the gain distribution is

$$\int_0^L \alpha_{01} dz = (\alpha_0 L) \exp \left[ -\left( \frac{2|x|}{L_1} \right) \left( \frac{\tau_p}{\tau_L} \right) \right] \frac{-L_1}{2} \leq x \leq \frac{L_1}{2}, \quad (23)$$



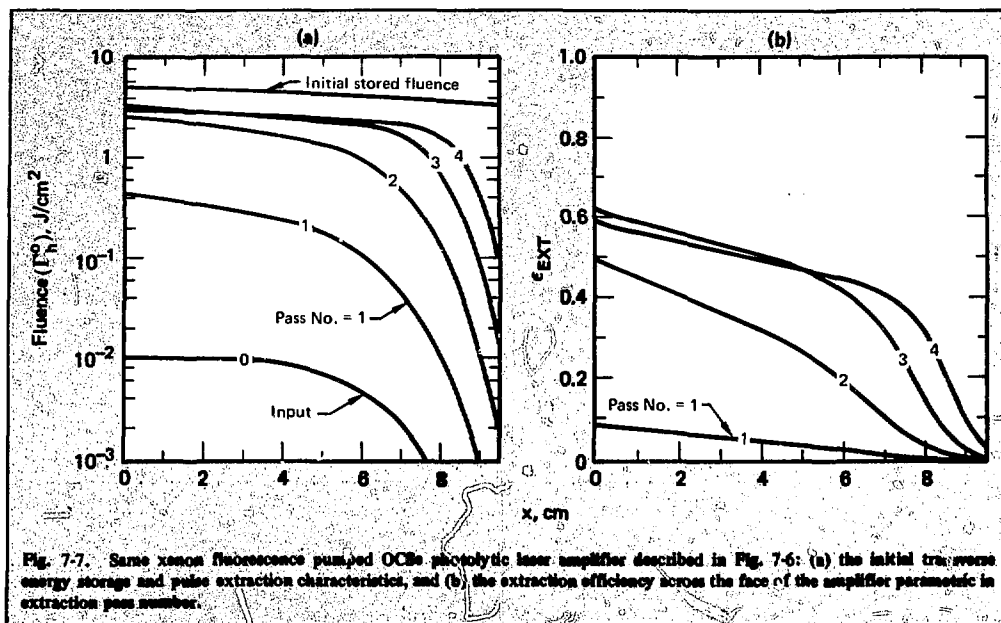
where the transverse amplifier width is  $L_\perp$ . In deriving Eq. (23), we have assumed that the excited-state density decay is exponential and does not lead to population of the lower laser level. By using conservation of energy, we obtain the small signal gain integral for the  $n$ th pass ( $n > 1$ ) given by

$$\int_0^L \alpha_{0n} dz = \sigma e^{(-\tau_T/\tau_L)} \int_0^L N_{u_{n-1}} dz - \sigma \left( \frac{g_u}{g_L} \right) \int_0^L N_{L_{n-1}} dz - \left( \frac{\sigma}{h\nu_L} \right) \left( \Gamma_{n-1}^0 - T \Gamma_{n-2}^0 \right) \left\{ \frac{g_u}{g_L} + e^{(-\tau_T/\tau_L)} \right\}, \quad (24)$$

where  $\tau_T$  is the time between extraction passes. The simultaneous solution of Eqs. (20)-(24) constitutes the model of the multipass amplifier. For initial gain and input fluence distributions that are non-

uniform across the amplifier, we solve these equations by partitioning the transverse aperture into 40 elements and solving Eqs. (20)-(24) for each element. We have used this multipass amplifier analysis method to study Group VI, Rare Earth Hybrid and RGH/Raman Pulse Compressor systems. We discuss the results of these calculations later in §7. Figures 7-6 and 7-7 show results of a multipass extraction analysis for a Group VI laser amplifier. Figure 7-6(a) shows extraction efficiency as a function of centerline input fluence, parametric in extraction pass number. (The input pulse was a fifth-power supergaussian and  $\alpha_0 L = 4$ .) Figure 7-6(b) shows the effect of a finite  $\tau_p/\tau_L$  ratio on the extraction efficiency of a two-pass amplifier. Figures 7-7 (a) and (b) give the initial gain distribution and transverse extraction characteristics for this Group VI amplifier as a function of extraction pass number for  $\alpha_0 L = 4$  and for a centerline input fluence of  $10^{-2} \text{ J/cm}^2$ . [Because of quenching during bleaching, the initial gain at the amplifier's edge is  $0.67 (\alpha_0 L)$ .] The nonuniform initial gain distribution leads to a significantly nonuniform transverse output pulse shape and extraction efficiency char-





acteristic. As Fig. 7-7(b) shows, optical transit losses begin to reduce the centerline extraction efficiency before the energy at the edge of the amplifier can be efficiently extracted. We present a more extensive discussion of these results in §7.3.4.

Author	Major Contributor
R. A. Haas	C. V. Duncan

#### 7.2.4 Propagation of Laser Energy

Focusing requirements for target irradiation place constraints on the optical quality of media in which the laser light is generated and through which the laser light must pass on its way to the target. Early Nd:glass laser development experiments revealed that nonlinear phase and amplitude distortion produced by small-scale self-focusing could cause serious defocusing at high peak power. Since then the development of laser glasses with much lower nonlinear indices and the development of spatial filtering and optical relay beam-transport techniques have greatly reduced this problem. In

this section, we identify sources of phase and amplitude distortion in gaseous media and compare them to establish their relative importance. We then consider focusing of beams and the constraints imposed by beam aberrations.

#### Phase and Amplitude Distortion Processes.

Phase and amplitude distortions due to several mechanisms degrade the propagation of high-intensity laser light through gaseous media in a laser system. The more important mechanisms are likely to include the following:

- Gas flow turbulence in amplifiers and beam transport tubes.
- Density disturbances generated by volumetric energy deposition.
- Saturation.
- Shock-wave generation by hot electrodes or electron-beam foil energy loading.

The index of refraction for a gas is close to unity and can be written  $n = 1 + \beta(\rho/\rho_s)$ , where  $\rho_s$  is the gas density at standard conditions (1 atm, 273 K) and  $\beta$  is the Gladstone-Dale constant, which depends only weakly on wavelength in the visible for most gases of interest. Table 7-6 lists representative values of  $\beta$  at 589.3 nm reduced to 1 atm and 20°C. Note that  $\rho$  is approximately an order of magnitude smaller for helium and neon than for other common gases.

**Table 7-6. Gladstone-Dale refractive index coefficients<sup>a</sup> for 589.3-nm light reduced to 1 atm and 20°C.**

Gas	$\beta \times 10^4$	Gas	$\beta \times 10^4$
Air	2.92	Hydrogen	1.32
Ammonia	3.76	Krypton	4.27
Argon	2.81	Mercury	9.33
Benzene	17.62	Methane	4.44
Bromine	1.32	Neon	0.67
Carbon dioxide	4.51	Nitric oxide	2.97
Carbon monoxide	3.38	Nitrogen	2.97
Carbon tetrachloride	17.68	Nitrous oxide	5.16
Chlorine	7.73	Oxygen	2.72
Fluorine	1.95	Water vapor	2.54
Helium	0.36	Xenon	7.02

<sup>a</sup>G. W. C. Kaye and T. H. Laby, *Tables of Physical and Chemical Constants* (Longman, New York, 1973).

For geometric optics, nonuniformities in the refractive index across the beam  $\Delta n_{\perp} = \beta \Delta \rho_{\perp} / \rho_s$  can produce average phase variations:

$$\Delta \phi_{\perp} = \frac{k \beta \rho_0}{\rho_s} \int_0^L \frac{(\Delta \rho)_{\perp} dz}{\rho_0} = \frac{k \beta \rho_0}{\rho_s} \left\langle \left( \frac{\Delta \rho_{\perp}}{\rho_0} \right) \right\rangle L, \quad (25)$$

and average angular deflections

$$\Delta \theta_{\perp} = \beta \frac{\rho_0}{\rho_s} \int_0^L \frac{|\nabla_{\perp} \rho| dz}{\rho_0} = \beta \frac{\rho_0}{\rho_s} \left( \left\langle \frac{|\nabla_{\perp} \rho|}{\rho_0} \right\rangle \right) L \quad (26)$$

where  $\rho_0$  is the density of the medium;  $\perp$  denotes displacement normal to the axis of propagation,  $k$  is the laser light wave number, and  $L$  is the propagation distance in the medium. The mean quantities  $\Delta \phi_{\perp}$  and  $\Delta \theta_{\perp}$  depend on the character of the density fluctuations and are nonzero only if the density fluctuations are not random or are not fully turbulent. This is often the case in high-average-power lasers because acoustic disturbances set up characteristic density variations that depend on specific boundary conditions and are, therefore, not fully random. If the medium is turbulent, the average phase and angular deflection of a ray vanishes, but its mean-square value does not. As an example, if we can characterize the density (refractive index) of the turbulence by a Gaussian correlation function with scale length  $l$ , then the square roots of the mean-square phase and angular deflection quantities are approximately<sup>6-7</sup>

$$\left[ \left\langle (\Delta \phi_{\perp})^2 \right\rangle \right]^{1/2} = \frac{1}{2^{1/2}} \pi^{1/4} (kL)^{1/2} k \beta \left( \frac{\rho_0}{\rho_s} \right) \left[ \left\langle \left( \frac{\Delta \rho_{\perp}}{\rho_0} \right)^2 \right\rangle \right]^{1/2}, \quad (27)$$

and

$$\left[ \left\langle (\Delta \theta_{\perp})^2 \right\rangle \right]^{1/2} = 2\pi^{1/4} \left( \frac{L}{l} \right)^{1/2} \beta \frac{\rho_0}{\rho_s} \left[ \left\langle \left( \frac{\Delta \rho_{\perp}}{\rho_0} \right)^2 \right\rangle \right]^{1/2}. \quad (28)$$

These results, when compared with Eqs. (25) and (26), indicate that random fluctuations produce less distortion than nonrandom correlated or ordered inhomogeneities of comparable scale length. In general, the density fluctuations generated in an average-power gas laser amplifier are neither fully ordered nor random; they have properties specific to the scale size of the device and the acoustic damping devices. Therefore, Eqs. (25)-(28) are useful only in estimating the bounds that distortions can have and the approximate conditions that must be achieved for adequate beam quality. For example, for density fluctuations of the same magnitude, small-scale-length turbulence ( $l \ll L$ ) produces larger deflections than large-scale ( $L \sim l$ ) or ordered disturbances. Phase fluctuations are larger for smaller wavelength, whereas average deflections are virtually independent of wavelength. (We clarify significance of these results below.) Laser operation at a density  $\rho_0$  less than or equal to standard density with a gas mixture composed primarily of helium or neon is highly desirable. For example, density fluctuations of the same character and magnitude in xenon at 10 atm produce distortions 200 times those produced in helium at 1 atm. For a 500-nm laser amplifier of length 4 m containing helium (argon) at 1 atm, and for  $(\Delta \rho_{\perp} / \rho_0) \sim 10^{-3}$ , the relative phase variations are  $(\Delta \phi_{\perp} / 2\pi) \sim 0.28(2.3)$ , respectively. Recent experimental and theoretical studies<sup>2-4</sup> of average-power lasers indicate that we can achieve  $(\Delta \rho_{\perp} / \rho_0)$  values in the  $10^{-4}$  to  $10^{-3}$  range.

**Focusing Aberrated Laser Beams and Laser Media Optical Quality Constraints.** The output beam of a fusion laser system must satisfy focusability constraints that are governed by the requirements of target irradiation. Several criteria and formulations relating focusability requirements

to laser medium homogeneity have been proposed. However, as we show here, some of these criteria are inadequate; in some cases they are misleading.

The simplest criterion is to require the laser spot size to be equal to or somewhat smaller than the pellet cross section (on the order of a few millimeters). For a near-diffraction-limited system, the Strahl focal plane intensity ratio has been used to estimate the ratio of the diffraction-limited spot size to the aberrated spot size. For a Gaussian beam, this gives the radius constraint

$$r_t \geq 1.22 \frac{\lambda f_L}{D} \left[ 1 - \sum_j (\Delta\phi_j)^2 \right]^{-1/2}. \quad (29)$$

The quantity  $1 - \sum_j (\Delta\phi_j)^2$  is the Strahl ratio (the ratio of the intensity on-axis in the focal plane to the intensity for a diffraction-limited spot size). Because this expression is not rigorous and only approximately valid for  $\sum_j (\Delta\phi_j)^2 \ll 1$ , it is of relatively little value here because fusion lasers operating in the visible and ultraviolet will likely have  $\sum_j (\Delta\phi_j)^2 > 1$ . Also note that misapplication of Eq. (29) can lead to erroneous conclusions, particularly for media and laser wavelength dependence of the focusability constraint.

A more accurate approach than Eq. (29) to the requirement that beam spot size be less than target diameter is to use the results of Talanov's completely rigorous and very powerful moment theory<sup>8</sup> for the propagation of aberrated laser beams. According to this theory, several integral invariants or spatial moments of the intensity distribution of a propagating laser beam remain invariant throughout beam propagation.

Application of this theory indicates that, after passage through a focusing lens of focal length  $f_L$ , the minimum mean-square radius of an aberrated laser beam is

$$\langle r^2 \rangle_{\min} \approx f_L^2 \left\langle \left( \frac{\nabla_{\perp} \phi_0}{k} \right)^2 - \frac{r_{\perp} \nabla_{\perp} \phi_0}{f_L k} + \left( \frac{\nabla_{\perp} E_0}{k E_0} \right)^2 \right\rangle \quad (30)$$

where  $\phi_0(r_{\perp})$  and  $E_0(r_{\perp})$  are the phase and amplitude distributions, respectively, of the beam across the input to the lens. The quantity  $\langle f \rangle$

denotes the intensity-weighted average of the function  $f$  across the beam profile at the input to the lens. We can also derive expressions similar to Eq. (30) for the focal length and depth of focus of the aberrated laser beam. If the input phase distribution  $\phi_0$  is due primarily to linear sources, then the geometrical optics term  $\nabla_{\perp} \phi_0 / k$  is essentially independent of laser wavelength and only the diffraction term  $(\nabla_{\perp} E_0 / k E_0)^2$  contributes a wavelength dependence. (We discuss the implications of this below.) With Eq. (30), the focusability condition becomes  $r_t^2 \geq \langle r^2 \rangle_{\min}$ . To estimate the constraint imposed by this condition, suppose  $L_{\perp}$  is the averaged density fluctuation producing the phase distortion  $\phi_0$ . The focusability condition is approximately

$$r_t^2 \geq f_L^2 \left\{ \beta^2 \left( \frac{\rho_0}{\rho_s} \right)^2 \left\langle \left( \frac{\Delta \rho_{\perp}}{\rho_0} \right) \right\rangle^2 \left( \frac{L}{L_{\perp}} \right)^2 + \left( \frac{\lambda}{D} \right)^2 \right\}. \quad (31)$$

If the density fluctuations are sufficiently large that the diffraction contribution is small, then the condition of Eq. (31) becomes a constraint on the relative density fluctuations in the laser medium:

$$\left\langle \left( \frac{\Delta \rho_{\perp}}{\rho_0} \right) \right\rangle \lesssim \left( \frac{r_t}{f_L} \right) \frac{1}{\beta} \left( \frac{\rho_s}{\rho_0} \right) \frac{L_{\perp}}{L}. \quad (32)$$

From this simple criterion, the medium quality constraint is reduced by minimizing the focal length of the focusing lens, the Gladstone-Dale constant  $\beta$  of the working medium, and the operating density  $\rho_0$  relative to standard density  $\rho_s$  and by maximizing the transverse scale length of the characteristic density fluctuations of the medium. As an example, suppose the working medium is helium at 1 atm, that mirror damage requires a standoff distance of  $f_L = 50$  m, and that the target specification is  $r_t = 1$  mm (5 mm). If the density disturbance in the amplifier is such that  $L/L_{\perp} = 10$ , then Eq. (31) requires that the average density fluctuations in the medium satisfy  $\langle \Delta \rho_{\perp} / \rho_0 \rangle \lesssim 5.7 \times 10^{-4}$  ( $2.8 \times 10^{-3}$ ). These constraints are not trivial; however, in high-average-power CO<sub>2</sub> lasers, values of  $\langle \Delta \rho_{\perp} / \rho_0 \rangle$  in the range of  $10^{-4}$  to  $10^{-3}$  have been achieved. Clearly, if the working gas were xenon at 1 atm, these constraints would approach the boundaries of the current state of the art in optical quality control for average power laser media.

The condition  $r_t^2 \geq \langle r^2 \rangle_{\min}$  is useful because it uses a rigorous result from Talanov's moment

theorems. However, it is still not precise enough for our use since it does not specify the fraction of incident laser energy contained within the specified radius  $r_t$ . It is easy, for example, to construct intensity distributions in which a significant fraction of the energy in the beam lies outside the mean-square radius  $\langle r^2 \rangle_{\min}$ . A more accurate and useful criterion, therefore, is that the fraction of total laser power incident on the target that lies outside the radius  $r_t$ ,  $\Delta P_{r_t}/P_0$ , be less than a certain value, say 0.01:

$$(\Delta P_{r_t}/P_0) \leq 0.01.$$

Although we have not made this calculation for the general case of arbitrary phase and amplitude distortion, a simple example gives insight into the possible character of the general result. If the refractive index fluctuations of the medium are statistically random with a Gaussian correlation function whose scale length is  $l$ , and if diffraction effects are not important, then<sup>6,7</sup>

$$\frac{\Delta P_{r_t}}{P_0} = e^{-\langle r^2 \rangle_{\text{eff}}/l^2}, \quad (33)$$

where

$$\begin{aligned} r_{\text{eff}}^2 &= \left[ \langle r^2 \rangle \right]^{1/2} = 2\pi^{1/4} f_L \left( \frac{L}{l} \right)^{1/2} \\ &\quad \beta \left( \frac{\rho_0}{\rho_s} \right) \left[ \left( \frac{\Delta \rho}{\rho_0} \right)^2 \right]^{1/2} \end{aligned} \quad (34)$$

Here, we assume that gas density fluctuations make the principal contribution to the root-mean-square refractive index fluctuation. Note that we can derive this Eq. (34) expression for the mean-square radius from the Talanov theory by using  $\langle r^2 \rangle_{\min} = f_L^2 \langle (\nabla_{\perp} \phi_0/k)^2 \rangle$  and the approximations of Tatarski and Chernov.<sup>6,7</sup> From Eqs. (33)-(34) the radius outside which 0.01 of the total beam power resides is

$$\begin{aligned} r_t &= 2.15 r_{\text{eff}} = 5.7 f_L \left( \frac{L}{l} \right)^{1/2} \beta \left( \frac{\rho_0}{\rho_s} \right) \\ &\quad \left[ \left\langle \left( \frac{\Delta \rho}{\rho_0} \right)^2 \right\rangle \right]^{1/2} \end{aligned} \quad (35)$$

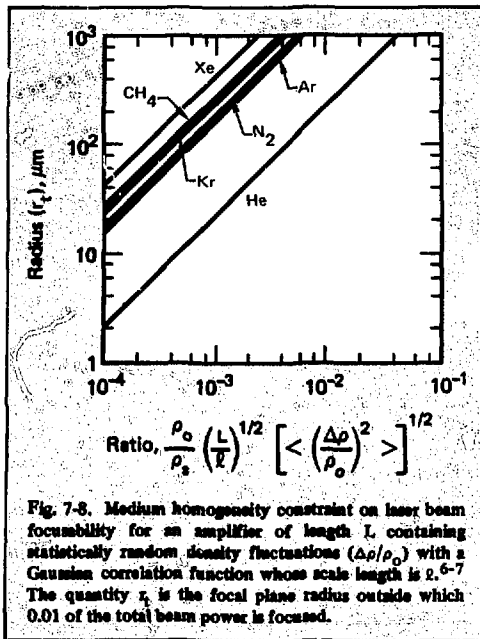


Fig. 7-8. Medium homogeneity constraint on laser beam focussability for an amplifier of length  $L$  containing statistically random density fluctuations  $(\Delta \rho/\rho_0)$  with a Gaussian correlation function whose scale length is  $l$ .<sup>6-7</sup> The quantity  $r_t$  is the focal plane radius outside which 0.01 of the total beam power is focused.

Again, because of the large aberration geometrical optics limit, the criterion is essentially independent of wavelength. We note that the primary difference between the current criterion and the one developed approximately from the Talanov theory applied to ordered density fluctuations [i.e., Eq. (31)] is the ratio of the medium length to the characteristic inhomogeneity scale length entered as the square root for the random and linearly for ordered-density fluctuations. Random scattering tends to reduce the refractive spreading. From Eq. (35), the medium quality condition becomes

$$\left[ \left\langle \left( \frac{\Delta \rho}{\rho_0} \right)^2 \right\rangle \right]^{1/2} \lesssim \frac{1}{5.7} \left( \frac{r_t}{f_L} \right) \frac{1}{\beta} \left( \frac{\rho_s}{\rho_0} \right) \left( \frac{l}{L} \right)^{1/2} \quad (36)$$

Figure 7-8 plots the constraints imposed by Eq. (36) for several gases. The results indicate the potentially significant advantages associated with the use of such low  $\beta$  gases as helium or neon, operation at low pressure, and elimination of small-scale turbulence or density inhomogeneities.

Although these results are somewhat qualitative, they indicate the type of analysis that must be performed to relate visible and ultraviolet laser

media optical-quality requirements to fusion reactor target irradiation constraints. The Fig. 7-8 estimates show that, for gaseous media, control of density fluctuations in large-scale average-power fusion laser amplifiers will be an important — but apparently tractable — technological problem.

## References

6. L. A. Chernov, *Wave Propagation in a Random Medium* (McGraw-Hill Book Co., New York, 1960).
7. V. I. Tatarski, *Wave Propagation in a Turbulent Medium* (McGraw-Hill Book Co., New York, 1961)
8. S. N. Vlasov, V. A. Petrishev, and V. I. Talanov, *Izv. VUZ Radiofiz.*, **14**, 1353 (1971).

## Author

R. A. Haas

## Major Contributor

A. J. Glass

## 7.3 Group VI Lasers

### 7.3.1 Introduction

We and others have discussed the possibility of energy storage lasers based on the  $^1S$  metastable state of Group VI atoms, oxygen, sulfur, or selenium (see annual report for 1974, 1975, and 1976, and Refs. 9-10). If we can produce excited-atom densities on the order of  $10^{16} \text{ cm}^{-3}$  in a buffer and maintain them for times of order  $10^{-6} \text{ s}$ , the  $^1S_0$ - $^1D_2$ , electric quadrupole transition and in some cases the  $^1S_0$ - $^3P_1$ , magnetic dipole transition of these atoms should produce usable gain coefficients. Figure 7-9 shows the energy levels and transitions of interest for selenium as an example. The selenium laser transitions of possible interest are the "auroral" line at 776.9 nm and the "transauroral" line at 488.7 nm. The terminology arises from the analogous forbidden lines of oxygen, which are well known in atmospheric spectroscopy.

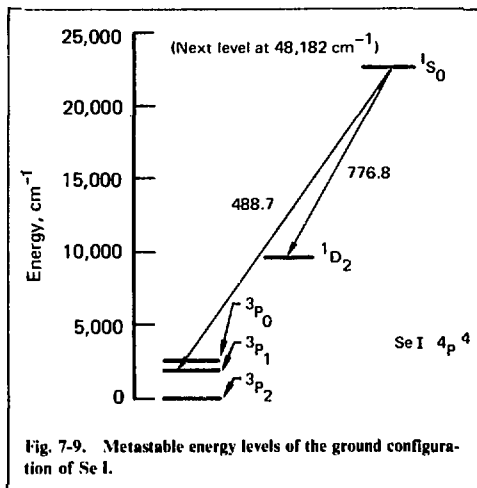


Fig. 7-9. Metastable energy levels of the ground configuration of Se I.

As we noted earlier, the laser pumping mechanism for  $^1S$  metastables need not directly produce an inversion because collisional deactivation of the lower laser state —  $^1D_2$  or  $^3P_2$  — is typically much faster than collisional deactivation of the  $^1S$  state. Note, for the case of selenium, the  $^3P_1$  lower laser level at  $1989 \text{ cm}^{-1}$  is sufficiently high to prevent its thermal population from the  $^3P_2$  ground state at room temperature. Inversion of the  $^1S_0$ - $^3P_1$  transition for sulfur and oxygen is more restricted, since their  $^3P_1$  levels are at  $397 \text{ cm}^{-1}$  and  $159 \text{ cm}^{-1}$ , respectively.

We calculated stimulated emission cross sections for these electric-dipole-forbidden transitions assuming Doppler-broadened linewidths and theoretically calculated radiative lifetimes.<sup>11</sup> Table 7-7 gives the resulting values at line center, together with the optical pulse fluence ( $h\nu/\sigma$ ) required to deplete the inversion density to  $e^{-1}$  of its initial value. The two cross sections for selenium represent the possible range, which depends on the spectral

Table 7-7. Laser properties of group VI metastable atoms.

$^1S_0 - ^1D_2$	O	S	Se
Wavelength	557.7 nm	772.5	776.8
Gain cross section	8.7(-20) $\text{cm}^2$	4.5(-19)	4.8—9.6(-19)
Saturation fluence	4.0 J/ $\text{cm}^2$	0.57	0.53—0.27
$^1S_0 - ^3P_1$	O	S	Se
Wavelength	297.2 nm	488.9	488.7
Gain cross section	5(-22) $\text{cm}^2$	3(-20)	4—8(-19)
Saturation fluence	1300 J/ $\text{cm}^2$	14	1—0.5

overlap of the lines produced by different selenium isotopes in natural abundance. The larger value assumes precise spectral overlap. The smaller value assumes no overlap (i.e., an isotope shift much larger than the Doppler linewidth, approximately 800 MHz). Hyperfine splitting is of no significance because of the lack of nuclear spin for these atoms.

For buffer pressures greater than a few hundred torr, collisional broadening of the atomic lines reduces the cross sections below the values shown in Table 7-7. Buffer gases also give rise to the collision-induced molecular emission near the  $^1S_0$ - $^1D_2$  atomic line. This phenomenon is well known for O( $^1S$ )<sup>12-14</sup> and S( $^1S$ ).<sup>15</sup> In the past year we have shown that it also occurs for selenium and can be a convenient monitor of Se( $^1S$ ) decay. Collision-induced emission results when the  $^1S$  atom and its collision partner are in close proximity because of the transition-dipole moment induced by the collisional perturbation.<sup>16,17</sup> Because the atomic levels are shifted during collision, the molecular emission occurs in a broad band whose width is typically greater than kT,  $6 \times 10^6$  MHz. Because the molecular emission is broad, the gain cross section for collision-induced emission rivals that of the atomic line only for buffer pressures of many atm. Nevertheless, the total collision-induced fluorescence integrated over its spectrum dominates the the atomic fluorescence even for buffer pressures as low as 100 Torr.

During 1977, we directed our experiments toward low-pressure Group VI lasers, where photolysis of simple triatomic molecules using an external light source produces  $^1S$  excited atoms. Several factors led to our concentration on low-pressure photolytic devices in preference to e-beam excited, high-pressure, collision-induced lasers which we previously studied:

- Minimizing the index of refraction of the laser medium to reduce flow costs and improve medium homogeneity for possible repetitive operation.

- Improving laser medium efficiency by using photolytic radiation at a wavelength with a high quantum yield for  $^1S$  atom production.

- Investigating laser possibilities on S( $^1S$ ) and Se( $^1S$ ) atoms, which are not significantly produced by direct e-beam excitation.

Fluorescence and laser emission from rare-gas excimers conveniently match the spectral bands needed for production of  $^1S$  metastable atoms. Figure 7-10 shows the fluorescence spectrum of Xe $_2^*$  at 172 nm produced by e-beam excitation of high-pressure xenon, along with the spectrum transmitted through 1.1 torr-cm OCSe. The strong ab-

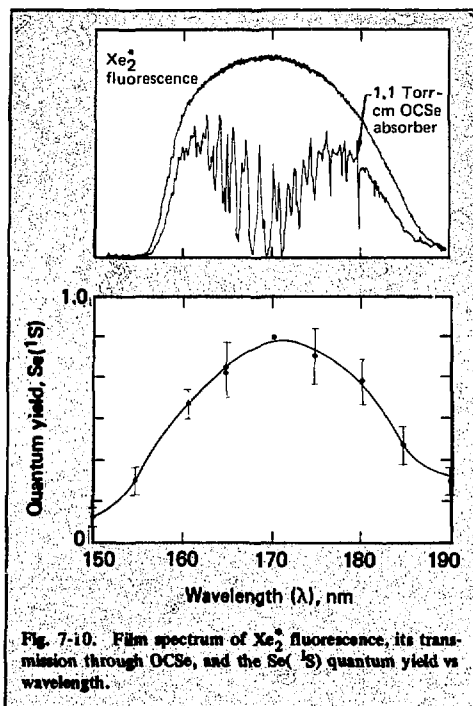


Fig. 7-10: Film spectrum of Xe $_2^*$  fluorescence, its transmission through OCSe, and the Se( $^1S$ ) quantum yield vs wavelength.

sorption band of OCSe corresponds to the region of high quantum yield of Se( $^1S$ ) shown below.<sup>18</sup> The quantum yield, as weighted over the Xe $_2^*$  spectrum is approximately 0.8. Similarly, Fig. 7-11 shows that the Kr $_2^*$  fluorescence at 146 nm overlaps the region of high quantum yield of S( $^1S$ ) by photodissociation of OCS.<sup>19</sup> Finally O( $^1S$ ) is produced by Ar $_2^*$  photodissociation of N $_2$ O near 126 nm.<sup>20</sup> (Black and coworkers measured the quantum yield curves under LLL contract support.)

The use of rare-gas excimer radiation as a pump source for Group VI metastable atoms is attractive not only for its spectrum but also for its high fluorescence efficiency. Careful measurements that were described in the 1975 annual report determined that the Ar $_2^*$ , Kr $_2^*$ , and Xe $_2^*$  fluorescence efficiency is about 50% at 1 atm when excited with an e-beam depositing about 10 mJ/cm<sup>2</sup>. As discussed in the 1976 annual report, these high values give rise to the possibility of high-efficiency rare-gas excimer lasers operating in the vuv. Analysis of these lasers,<sup>21</sup> however, has indicated that efficiency is limited by optical absorption by excited species in the laser media, specifically photoionization of the excimers themselves. This difficulty is not apparent in fluorescence efficiency measure-

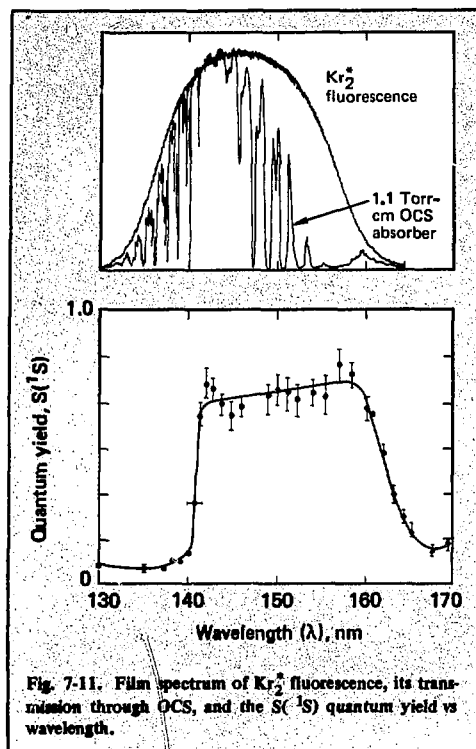


Fig. 7-11. Film spectrum of  $\text{Kr}_2^+$  fluorescence, its transmission through OCS, and the  $\text{S}(^1\text{S})$  quantum yield vs wavelength.

ments, where the volume studied is optically thin to the emitted radiation.

In §7.3.2 we describe both the experimental and theoretical 1977 work that was directed toward understanding rare-gas excimers as drivers for Group VI photolytic lasers. We discuss the performance of a superfluorescent device operating at high pressure ( $\sim 10$  atm) and high e-beam current-density ( $\sim 100$  A/cm<sup>2</sup>). While this excimer laser does not operate with either high efficiency or good beam quality, its output is sufficient to perform both  $\text{Se}(^1\text{S})$  and  $\text{S}(^1\text{S})$  laser experiments. We also describe a separate experiment designed to measure both the  $\text{Xe}_2^+$  gain at 175 nm and the medium absorption at a slightly longer wavelength. The measured gain-to-loss ratio at the  $\text{Xe}_2^+$  laser wavelength can be used to compare to laser performance predicted by modeling calculations.

Theoretical work on the rare gas excimers has included completely ab initio calculations of the  $\text{Xe}_2^+$  and  $\text{Xe}_2^+$  potential curves. We compare calculated emission wavelengths and radiative lifetimes with experimental measurements. Also we have used the Stieltjes imaging method described in the

1976 annual report to calculate photoionization cross sections for  $\text{Ne}^+$  and  $\text{Ar}_2^+$ . These calculations provide input data for modeling rare-gas excimer laser performance.

In §7.3.3, we describe experiments and theoretical calculations of the production and quenching of  $^1\text{S}$  metastable atoms. Photolytic experiments have concentrated on determining the time decay of  $\text{S}(^1\text{S})$  and  $\text{Se}(^1\text{S})$  atoms produced at concentrations greater than  $10^{16}$  cm<sup>-3</sup>. We discuss the important role that photo-produced electrons can play in  $^1\text{S}$  decay. In late 1977 and early 1978, we demonstrated laser oscillation for the  $\text{Se}(^1\text{S}_0-^3\text{P}_1)$ ,  $\text{Se}(^1\text{S}_0-^1\text{D}_2)$ , and  $\text{S}(^1\text{S}_0-^1\text{D}_2)$  atomic transitions. We include a preliminary description of their laser performance.

Theoretical work on  $^1\text{S}$  photolytic production treats the potential surfaces relevant to OCS dissociation and the origin of the structure in the dissociative bands. We discuss possible mechanisms for  $\text{S}(^1\text{S})$  deactivation by collisions with other  $^1\text{S}$  atoms, self-deactivation, and associative ionization. Finally, we present a semiempirical method for determining  $^1\text{S}$  photoionization. This work provides a basis for predicting electron densities in the photolytic media.

In §7.3.4, we synthesize our results to obtain a systems model of a Group VI photolytic laser. We discuss critical issues concerning the performance of a rare-gas excimer driver, as well as general schemes for using efficient rare-gas excimer fluorescence. We discuss the optical coupling efficiency and deposition profiles of a fluorescence driven system and novel geometries designed to produce high coupling efficiency. Our estimates of the efficiency of various components of a hypothetical Group VI laser are consolidated to predict overall laser system efficiency.

Finally, in §7.3.5 we describe the possible scaling of Group VI lasers to the very large sizes required for laser fusion. Because they are optically thick to the pump radiation, the Group VI parent molecules must be totally bleached to excite a large aperture amplifier (Fig. 7-12). We discuss the prac-

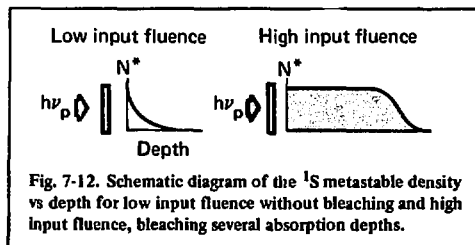


Fig. 7-12. Schematic diagram of the  $^1\text{S}$  metastable density vs depth for low input fluence without bleaching and high input fluence, bleaching several absorption depths.

tical relationship between the amplifier aperture and length. We show how scalability depends on excited-state density, storage time, and pump intensity. We summarize this information in a conceptual design of a 1-kJ Group VI photolytic laser.

## References

9. J. R. Murray and C. K. Rhodes, *The Possibility of a High-Energy-Storage Visible Laser on the Auroral Line of Oxygen*, Lawrence Livermore Laboratory, Rept. UCRL-51455 (1973).
10. J. R. Murray and C. K. Rhodes, *J. Appl. Phys.* **47**, 5041 (1976).
11. R. H. Garstang, *J. Res. Natl. Bur. Std.* **68A**, 61 (1974).
12. D. L. Cunningham and K. C. Clark, *J. Chem. Phys.* **61**, 1118 (1974).
13. G. Black, R. L. Sharpless, and T. G. Slinger, *J. Chem. Phys.* **63**, 4546 (1975).
14. R. Atkinson and K. H. Welge, *J. Chem. Phys.* **64**, 531 (1976).
15. G. Black, R. L. Sharpless, and T. G. Slinger, *J. Chem. Phys.* **63**, 4551 (1975).
16. P. S. Julienne, M. Krauss, and W. Stevens, *Chem. Phys. Lett.* **38**, 374 (1975).
17. T. H. Dunning and P. J. Hay, *J. Chem. Phys.* **66**, 3767 (1977).
18. G. Black, R. L. Sharpless, and T. G. Slinger, *J. Chem. Phys.* **64**, 3985 (1976).
19. G. Black, R. L. Sharpless, T. G. Slinger, and D. C. Lorents, *J. Chem. Phys.* **62**, 4274 (1975).
20. G. Black, R. L. Sharpless, T. G. Slinger, and D. C. Lorents, *J. Chem. Phys.* **62**, 4266 (1975).
21. C. W. Werner, E. V. George, P. W. Hoff, and C. K. Rhodes, *IEEE J. Quantum Electron.* **QE-13**, 769 (1977).

## Author

H. T. Powell

## 7.3.2 Rare-Gas Excimer Pumps

### Xe<sub>2</sub><sup>+</sup> and Kr<sub>2</sub><sup>+</sup> Superfluorescent Light Source.

We have used the MEG II e-beam facility as a high-intensity, rare-gas excimer light source to perform Group VI photolytic experiments. The high-pressure "10-pass amplifier" described in the 1976 annual report, together with pure rare gases, produces Xe<sub>2</sub><sup>+</sup> radiation at 172 nm and Kr<sub>2</sub><sup>+</sup> radiation at 146 nm. The MEG II machine produces a 1-MeV 50-ns e-beam with an average current density of 100 A/cm<sup>2</sup> over an area of 10 by 50 cm. The e-beam energy of 2500 J is coupled through a 5-mil-thick titanium foil into a high-pressure gas cell with an e-beam absorption depth of 3 cm.

At high Kr and Xe pressures, the rare-gas amplifier operates in a superfluorescent mode, requiring no mirrors and producing a high-intensity output in the long direction of the cell. Identical photolytic cells are mounted symmetrically at each end. One is used for photolytic experiments; the other houses a simple carbon sheet calorimeter to monitor the vuv energy on each shot. The output beam passes through a 1-cm-thick MgF<sub>2</sub> window with an open aperture of 0.8 × 8 cm. Because of the geometry of the vuv source, the long axis of the photolytic cell is aligned vertically (see Fig. 7-13). At low operating pressure, the vuv output is proportional to pressure. Above 75 psi Xe or 200 psi Kr, the output energy exhibits a rapid increase with pressure, indicating the onset of superfluorescence. The increase in the vuv output is accompanied by spectral narrowing, as shown in Figs. 7-14 and 7-15. (We recorded these spectra on film with a 0.5-m spectrometer operating in second order.) The Xe<sub>2</sub><sup>+</sup> superfluorescent linewidth is about 3 nm and is clearly red-shifted from the peak of the 20-nm-wide Xe<sub>2</sub><sup>+</sup> fluorescence. The Kr<sub>2</sub><sup>+</sup> spectrum in Fig. 7-15 shows various absorption lines. These absorptions become more prominent in the superfluorescent regime as small differences in the amplification coefficient are exponentiated. The strongest absorption lines are the Xe impurity line at 147 nm and various CO absorption bands.

The maximum output energies into the photolytic cell that we obtained are 2.1 J at 172 nm from exciting xenon at 200 psi and 1.3 J at 146 nm from krypton at 400 psi. We estimate the Xe<sub>2</sub><sup>+</sup> output from both ends to represent about 1% of the deposited energy in the available optical aperture. Figure 7-16 shows the time dependences of the superfluorescence to be similar. At the leading edge of the excitation pulse both the Xe<sub>2</sub><sup>+</sup> and Kr<sub>2</sub><sup>+</sup> superfluorescence exhibit a sharp spike whose source is unknown. However, it may indicate a more favorable ratio of medium gain to medium loss in the transient regime compared with steady-state excitation.

We obtained the maximum energy performance with extremely pure rare gas. We purified the rare gas with a titanium getter system and passed it through a molecular sieve cooled to dry ice temperature for a total impurity level of ~1 ppm. The output on the second shot typically declines by 30-50%. We attribute this decline to impurities liberated into the gas that either absorb the excimer radiation or collisionally intercept the excimer production chain. Obviously we are careful in preventing Xe impurities in the case of Kr. After several tens of shots, the output fluence degrades to



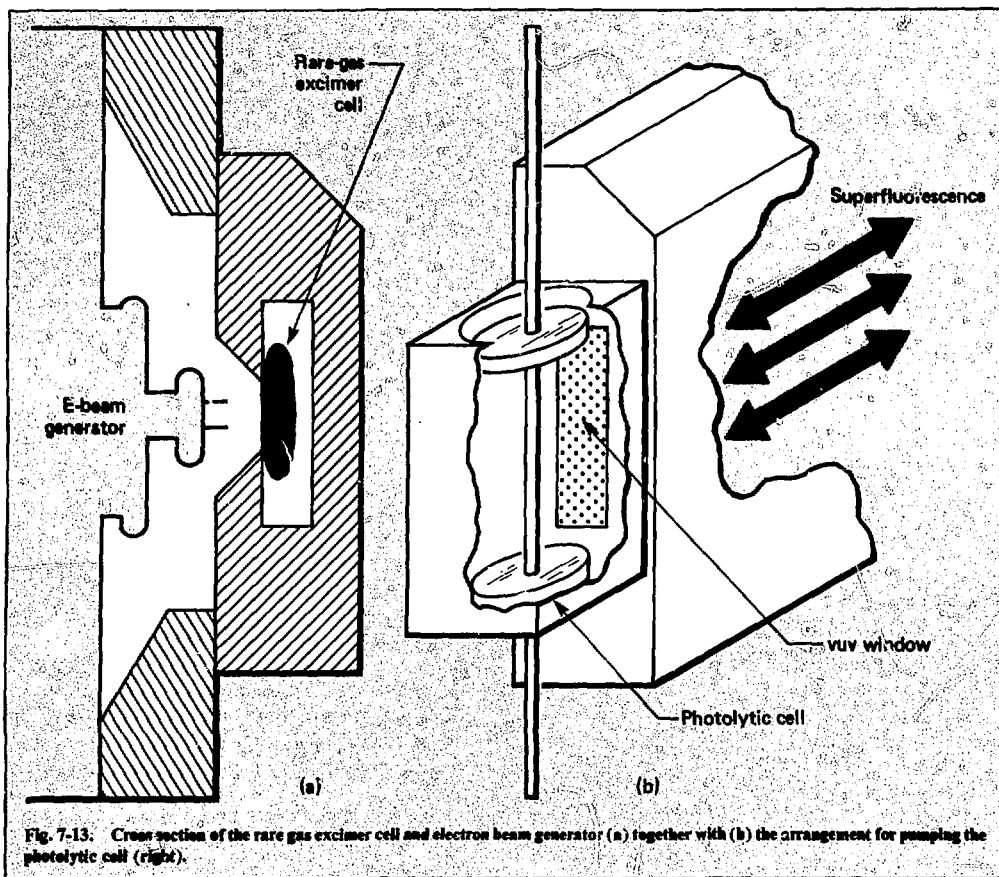


Fig. 7-13. Cross section of the rare gas excimer cell and electron beam generator (a) together with (b) the arrangement for pumping the photolytic cell (right).

one-tenth the initial value, approximately the level we expected from simple fluorescent operation.

Two different results suggest the importance of absorption by excited states. A single reflecting mirror, having either a  $\text{MgF}_2$ -overcoated Al coating or a commercial dielectric coating, has little effect on the output energy, even when carefully aligned with the photolytic cell window to form an optical cavity. (The reflecting mirrors are extensively damaged during each shot.) A second pass produced by a mirror apparently does not cause further light amplification. Note that the maximum observed output powers are about  $6 \text{ MW/cm}^2$  for  $\text{Xe}_2^*$  and  $4 \text{ MW/cm}^2$  for  $\text{Kr}_2^*$ . These values are considerably less than the calculated saturation fluences, and imply substantial nonsaturating loss in the rare-gas excimer media.

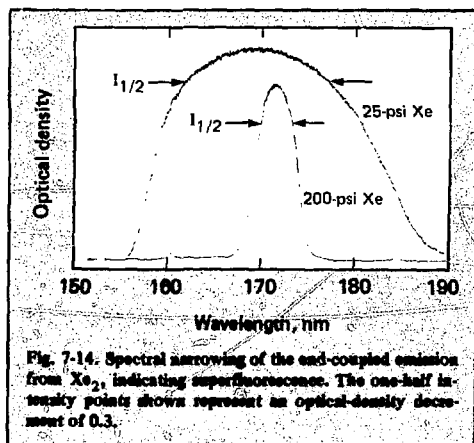
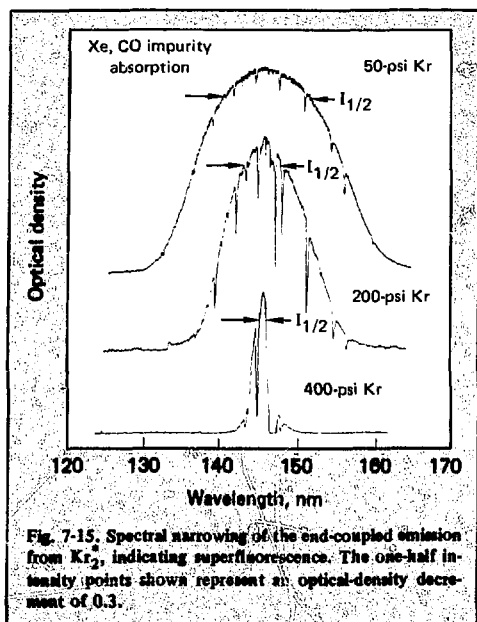


Fig. 7-14. Spectral narrowing of the end-coupled emission from  $\text{Xe}_2$ , indicating superfluorescence. The one-half intensity points shown represent an optical-density decrement of 0.3.



In a second experiment, we inserted a small, evacuated calorimeter mounted behind a reentrant  $\text{MgF}_2$  window into the excited gas volume from the back of the rare gas cell. We compared the  $\text{Xe}_2^*$  sidelight fluorescence (approximately  $50 \text{ mJ/cm}^2$ ) both with and without high-intensity superfluorescence in the axial direction. To prevent superfluorescence, we inserted beam blocks into the rare gas cell to limit the gain length. We saw no effect,

however, on the sidelight emission as a function of axial intensity. This result also suggests that non-saturable medium absorption limits the vuv superfluorescence power to a value less than the fluence required for saturating the rare-gas excimer population.

**$\text{Xe}_2^*$  Absorption/Gain Measurements.** We have measured the  $\text{Xe}_2^*$  gain at  $175 \text{ nm}$  in e-beam-excited xenon and the absorption at  $219 \text{ nm}$  for the same experimental conditions. From these measurements we can infer the medium-gain-to-loss ratio of  $172 \text{ nm}$  and predict the efficiency of a  $\text{Xe}_2^*$  amplifier. Our results indicate that, under certain conditions, photoionization from the excimer states is not the only important absorption process.

Figure 7-17 is a schematic of the experiment. The probe laser is a z-pinch, pulsed-discharge device operating at  $10 \text{ mTorr Kr}$  pressure that emits  $50\text{-}100\text{-ns}$  laser pulses from  $\text{Kr}^{++}$ . (See Refs. 22, 23.) The probe laser operates at either  $219 \text{ nm}$  or  $175 \text{ nm}$ , depending on mirror selection. The laser radiation is directed through a beam splitter that allows most of the laser beam to enter a  $10\text{-cm}$ -long experimental cell. The remaining portion of the beam,  $I_m$ , is directed through an appropriate  $10\text{-nm}$ -wide bandpass filter onto a photodiode. This serves as a signal that allows us to monitor shot-to-shot variations of the probe laser. The radiation passing through the cell,  $I_r$ , traverses a  $7\text{-m}$  vacuum beam pipe to a  $0.3\text{-m}$  monochromator and finally to a second photodiode. The long propagation path and spectral selectivity reduce the background  $\text{Xe}_2^*$  fluorescence in relation to the probe signal. A third filter-photodiode combination monitors the fluorescence from the xenon cell.

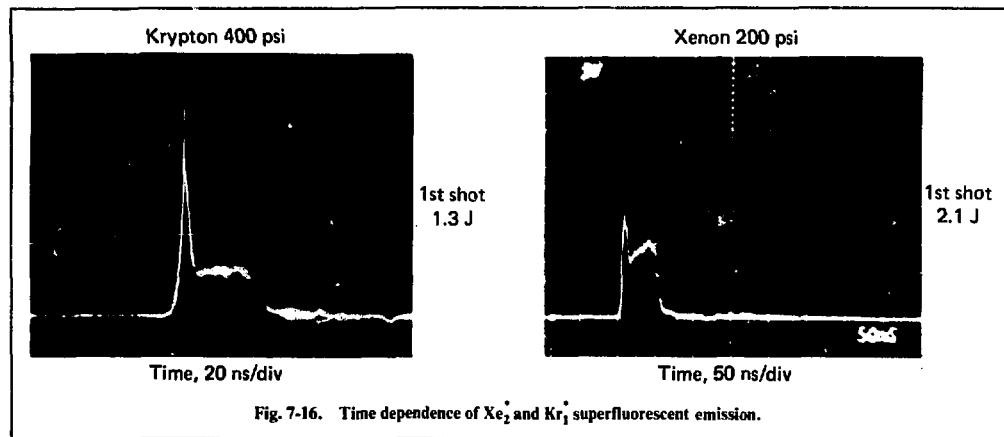


Fig. 7-16. Time dependence of  $\text{Xe}_2^*$  and  $\text{Kr}_2^*$  superfluorescent emission.

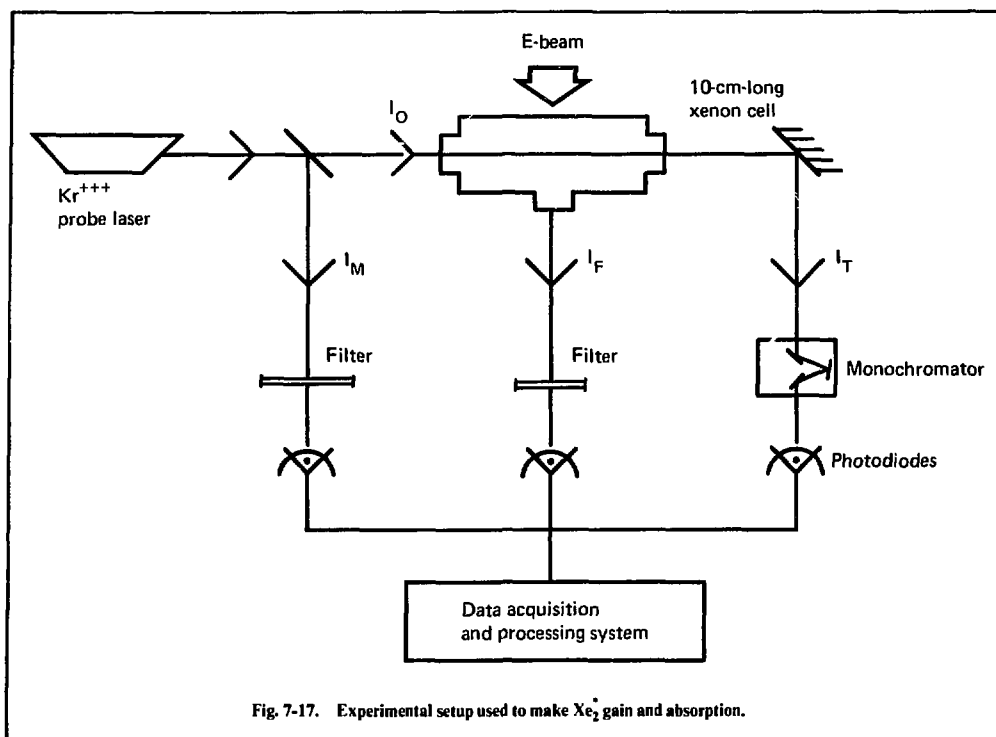


Fig. 7-17. Experimental setup used to make  $\text{Xe}_2^+$  gain and absorption.

Transient digitizers acquire all signals which are then stored on floppy disks for subsequent analysis. A minicomputer processes the data and corrects for shot-to-shot probe laser variations. We measure both the transmitted and monitor signals,  $I_T^0$  and  $I_M^0$ , before each run. The measured absorption or gain is  $RI_T(t)/I_T^0(t)$ , where the normalization constant

$$R = \int I_M^0(t) dt / \int I_M(t) dt$$

accounts for changes in probe laser energy. The temporal jitter in the laser pulse makes a time-dependent normalization factor unreliable. We account for jitter by varying the time center of the reference signal  $I_T^0(t)$  as indicated by the relative jitter of the monitor signal between the reference and data shots.

We select xenon cell pressures and electron beam current levels that permit us to observe both gain and loss over a 10-cm path length and to make comparisons with other available data. Figure 7-18a illustrates the results of an absorption measurement at 100 psi Xe, 850 A/cm<sup>2</sup> excitation current, and a

219-nm probe laser wavelength.  $I_O$  is the computer-normalized input intensity ( $I_O = RI_T^0$ ) and  $I_T$  is the transmitted beam. The peak absorption is about 0.12 cm<sup>-1</sup>; it is approximately constant during the 50-ns e-beam excitation. If we assume a quantum defect scaling of the photoionization cross section,<sup>24</sup> we can extrapolate the 0.12 cm<sup>-1</sup> absorption coefficient at 219 nm to yield an absorption coefficient of 0.06 cm<sup>-1</sup> at 172 nm. Figure 7-18b illustrates a net gain of 0.09 cm<sup>-1</sup> at 175 nm under identical conditions. Combining this result with the absorption data, we calculate a total gain of 0.15 cm<sup>-1</sup>. This result agrees well with the gain values computed from calibrated  $\text{Xe}_2^+$  fluorescence intensity measurements made earlier with this device.<sup>25</sup>

We measured the absorption coefficient at several pressures at constant e-beam current. Fig. 7-19 shows the results. If the absorption were only from the  $\text{Xe}_2^+(^1\Sigma)$  and  $\text{Xe}_2^+(^3\Sigma)$  states, we would expect an approximately linear dependence between pressure and absorption coefficient. The observed dependence is weaker than linear, indicating that absorption from states other than excimer laser states may be significant at low pressure. One such

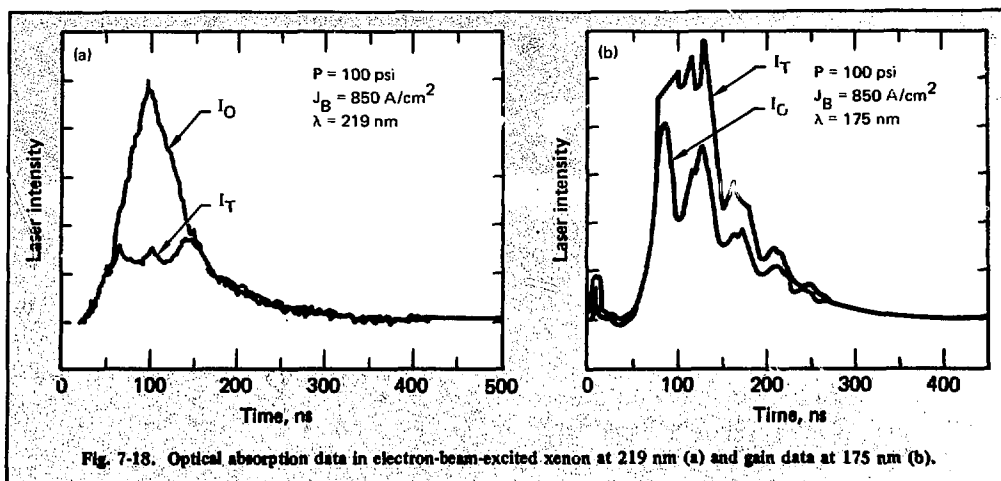


Fig. 7-18. Optical absorption data in electron-beam-excited xenon at 219 nm (a) and gain data at 175 nm (b).

process could be photoionization from the  $\text{Xe}^*(6p)$  state.

We conclude that photoionization as a significant loss process is not limited to  $\text{Xe}_2^+$ . The uncertainties in the current experiment, specifically the proper wavelength-scaling of the photoionization cross section, prevent us from accurately determining the absorption coefficient at 172 nm. However, the pressure scaling of the photoabsorption at 219 nm indicates that several states are responsible. The estimated gain-to-loss ratio at 172 nm is 2.5 (0.15/0.06). This suggests that the extractable stimulated emission power may be limited to 1.5 times the  $\text{Xe}_2^+$  saturation fluence.

**Rare-Gas Excimer Potential Curves and Lifetimes.** Designing kinetic and radiative models to describe the fluorescence and coherent emission of rare-gas excimers requires knowledge of radiative lifetimes, cross sections for photoionization, optical absorption, and stimulated emission. Previous theoretical studies on the states of  $\text{Xe}_2^+$  are limited to the empirical potential energy curves estimated by Mulliken.<sup>26,27</sup> We have computed potential energy curves for the ground  $1\Sigma_g^+$  state of  $\text{Xe}_2$ , the first four states of the  $\text{Xe}_2^+$  ions, and the eight  $\text{Xe}_2^+$  excimer states corresponding to the addition of a  $6s_{\sigma_g}$  Rydberg electron to these ion cores. We used averaged relativistic effective core potentials to approximate the inner shell electrons and the self-consistent field approximation for the valence electrons. The calculations used the LS-coupling scheme with the effects of spin-orbit coupling empirically included in the resulting potential energy curves.<sup>28</sup>

A comparison of results using nonrelativistic and averaged relativistic core potentials indicates that relativistic effects are not important for many properties of  $\text{Xe}_2$  molecules. The calculated spectroscopic constants for  $\text{Xe}_2^+$  are in good agreement with all-electron, configuration-interaction calculations, suggesting that the computed values for  $\text{Xe}_2$  excimers should also be reliable.

Table 7-8 gives a summary of the calculated spectroscopic and radiative properties for the three lowest excited states of  $\text{Xe}_2$ . Potential energy curves for  $\text{Xe}_2$ ,  $\text{Xe}_2^+$ , and  $\text{Xe}_2^+$  are given in Fig. 7-20. The curves for  $\text{Xe}_2$  do not include interactions with the attractive potential curves arising from the  $6p$  states

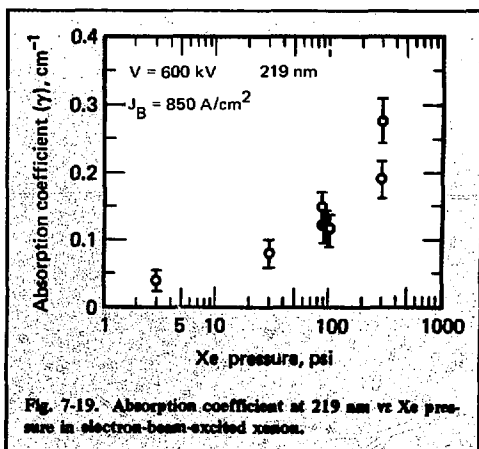


Fig. 7-19. Absorption coefficient at 219 nm vs. Xe pressure in electron-beam-excited xenon.

Table 7-8. Calculated spectroscopic constants and radiative lifetimes for  $\text{Xe}_2^+$ .

Property	Electronic state		
	1	0	0
$R_e(a_0)$	5.73	5.73	5.72
$D_e(\text{eV})$	0.79	0.78	0.77
$W_e(\text{cm}^{-1})$	118.0	117.3	118.5
$E(\text{eV})^a$	6.89	6.90	6.99
(ns)	172	—	5.55

<sup>a</sup>A vertical energy at the bottom of the excited-state potential well to the repulsive ground state of  $\text{Xe}_2$ .

of  $\text{Xe}^*$ . The calculated vertical excitation energies for these states are generally too low by about 0.4 eV when compared with experimental results. This

error is consistent with errors found in previous Hartree-Fock calculations on Rydberg excited states.

Our computed lifetime for the  $0_u^+$  laser state is 5.6 ns. The estimated uncertainty is 0.6 ns from comparison of experiments with similar calculations on the Xe atom. Experimental values for the  $0_u^+$  excimer lifetime lie in the range 5.5-6.5 ns.<sup>29</sup> Because of the lack of configuration-interaction with the excited 6p states, the calculated lifetime of 172 ns for the  $1_u$  state is less accurate. The best experimental values give radiative lifetime for this state of 100 ns.<sup>29</sup>

#### Photoionization of Rare-Gas Excited States.

Excited-state photoionization has been identified as a key loss mechanism that determines the ultimate efficiency obtainable from rare-gas excimer lasers.

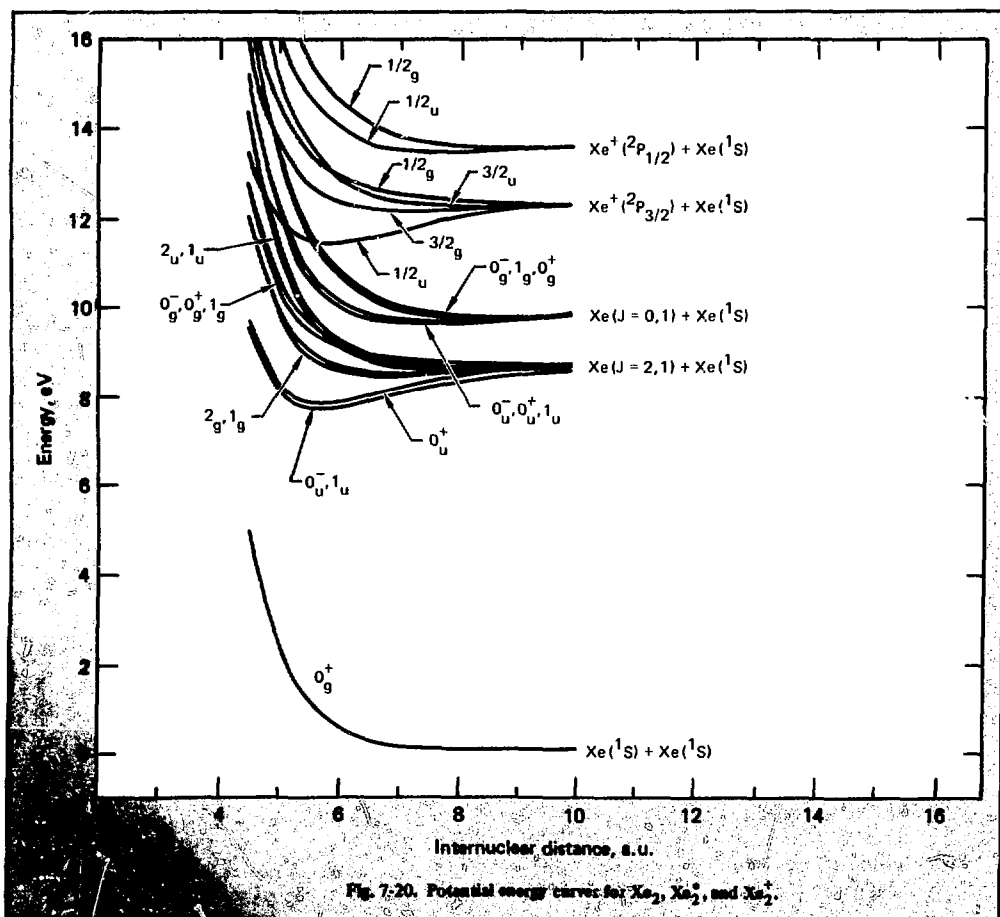


Fig. 7-20. Potential energy curves for  $\text{Xe}_2$ ,  $\text{Xe}_2^+$ , and  $\text{Xe}_2^{2+}$ .

Although direct excimer photoionization is probably the dominant absorption process at high pressures, experiments suggest that photoionization of both transient and metastable excited atomic species, which are important precursors in the excimer formation cycle, may be important at lower pressures.

Theoretical studies at LLL have concentrated on obtaining accurate photoionization cross sections for the  $1^3\Sigma_u^+$  excimer states of both  $\text{Ne}_2^+$  and  $\text{Ar}_2^+$ ,<sup>30</sup> as well as the  $3P^0$  metastable states of  $\text{Ne}^*$  and  $\text{Ar}^*$ .<sup>31</sup> In obtaining these cross sections, we have used fully ab initio all-electron wavefunctions and have paid careful attention to the importance of many-electron effects, such as electron correlation and core polarization. Our computational method (see the 1976 annual report) is based on the construction of a large set of excitation energies and oscillator strengths in a discrete set of normalizable Gaussian basis functions. The resulting "pseudo-spectrum" is then input to a moment analysis that provides an approximation to the photoionization continuum. We have demonstrated the applicability and usefulness of this technique in studies on a number of other atomic and molecular systems.<sup>32</sup>

In Fig. 7-21 we show for the  $3P^0$  state of neon the total photoionization cross section as a function of photon energy that was obtained from our most extensive calculations. The results use both the dipole-length (dashed curve) and velocity (solid curve) form of the transition moment; these would coincide for an exact calculation and their closeness is a measure of the accuracy of our results. For comparison, we show the cross section dependence obtained by others<sup>33</sup> using a model potential (dotted curve). Both our results and the model calculations show that the cross section passes through a "Cooper minimum" near threshold, although the minimum we find is not as deep. The minimum calculated by the model potential is incorrect because it fails to account for the three ways in which the photo-ejected electron can be coupled to the  $2p^5$  ion core to produce an allowed transition; each such channel produces a minimum at a different energy. At higher energies, however, there is generally good agreement between the two studies.

The valence shells of the lowest excited manifold of the rare-gas excimers are isoelectronic and described by a single configuration:

$$\left[ n\pi_g^4 n\pi_u^4 m\sigma_g^2 m\sigma_u(m+1)\sigma_g \right]^{1,3} \sum_u^+ \quad (37)$$

For  $\text{Ne}_2^+$ ,  $n=1$  and  $m=3$ ; for  $\text{Ar}_2^+$ ,  $n=2$  and  $m=5$ . Photoionization can lead only to production

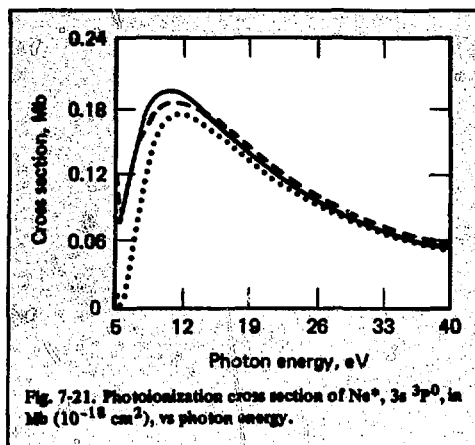


Fig. 7-21. Photoionization cross section of  $\text{Ne}^*$ ,  $3s\ 3P^0$ , in Mb ( $10^{-18}\text{ cm}^2$ ), vs photon energy.

of the lowest, weakly bound  $2\Sigma_u^+$  state of the residual molecular molecular ion in a simple frozen-core model where core-relaxation and channel-coupling are ignored. We have found, however, that the frozen-core model may seriously underestimate the cross section for an open shell configuration, where the photoionization profile may be dominated in certain energy regions by electronically excited autoionizing states. Specifically, we have found that it is essential to consider an intravalence excitation described by the configuration

$$\left[ n\pi_g^4 n\pi_u^4 m\sigma_g^2 m\sigma_u(m+1)\sigma_g \right]^{1,3} \sum_g^+ \quad (38)$$

This state, which must be regarded as autoionizing, may be thought of as the lowest member of a Rydberg series converging to the fourth state ( $2\Sigma_g^+$ ) of the molecular ion, corresponding to the highest state in Fig. 7-20. This state has a very large oscillator strength to the initial  $1\Sigma_u^+$  excimer state, since the transition corresponds to the excitation  $m\sigma_g \rightarrow m\sigma_u$ . The transition moment is large because the wave functions overlap strongly. Furthermore, this autoionizing Rydberg state does not appear in the spectrum as a narrow transition, but rather as a broad band that couples strongly to the background continuum in the low-energy portion of the spectrum. Others have calculated the analogous absorption band for the diatomic rare gas ions,  $\frac{1}{2}u - \frac{1}{2}g$ .<sup>34,35</sup> Figure 7-22 shows the total photoabsorption profile of  $\text{Ar}_2^+$  calculated for an internuclear spacing of 4.8 Bohr. There are two important features to note: the large peak centered at

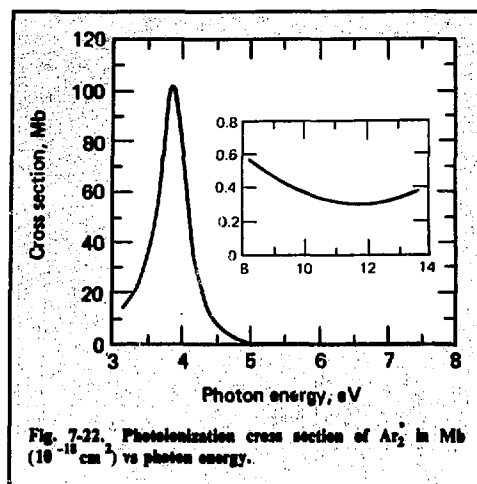


Fig. 7-22. Photoionization cross section of  $\text{Ar}_2^+$  in Mb ( $10^{-18} \text{ cm}^2$ ) vs photon energy.

3.9 eV, due to the  $^1\Sigma_g^+$  autoionizing state, and the small value of the cross section at the  $\text{Ar}_2^+$  fluorescence energy, 9.8 eV. Note that, at photon energies above 12 eV, the photoionization cross section begins to increase again, due to the opening of channels associated with higher states.

We have also studied the dependence of the  $^1\Sigma_u^+ \rightarrow ^1\Sigma_g^+$  profile on internuclear spacing. The peak value of the cross section does not vary significantly, but its position shifts as expected for a repulsive final state. The cross sections for the  $^3\Sigma_u^+$  state of  $\text{Ar}_2^+$  are very similar to the  $^1\Sigma_u^+$  values.

On the basis of these calculations, we conclude that the vertical photoabsorption of  $\text{Ar}_2^+$  at the excimer wavelength, 126 nm, is not a sensitive function of the internuclear distance and is given with good accuracy by  $4 \times 10^{-19} \text{ cm}^2$ . However, to obtain an accurate value for the cross section in the low-energy region (0-5 eV) dominated by autoionization, it will be necessary to properly account for the vibrational motion of the nuclei.

## References

22. J. B. Marling, *IEEE J. Quantum Electron.* QE-11, 822 (1975).
23. J. B. Marling, *Appl. Phys. Lett.* 31, 181 (1977).
24. D. C. Lorents, P. J. Eckstrom, and D. Huestis, *Excimer Formation and Decay Process in Rare Gas*, (Stanford Research Institute, Menlo Park, CA, 1973).
25. H. T. Powell and J. R. Murray, Lawrence Livermore Laboratory, Livermore, CA, private communication (1977).
26. R. S. Mulliken, *J. Chem. Phys.* 52, 5170 (1970).
27. R. S. Mulliken, *Radiation Res.* 59, 357 (1974).
28. W. R. Wadt, *J. Chem. Phys.* 68, 402 (1978).

29. J. W. Keto, R. E. Gleason, Jr., T. D. Bonifield, G. K. Walters, and F. K. Soley, *Chem. Phys. Lett.* 42, 125 (1976).
30. T. N. Rescigno, A. U. Hazi, and A. E. Orel, *J. Chem. Phys.* 68, (1978).
31. A. U. Hazi and T. N. Rescigno, *Phys. Rev. A* 16, 2376 (1977).
32. T. N. Rescigno, C. F. Bender, V. McKoy, and P. W. Langhoff, *J. Chem. Phys.* 68, 970 (1978); T. N. Rescigno, C. F. Bender, and V. McKoy, *Phys. Rev. A* 17, 645 (1978); T. N. Rescigno and P. W. Langhoff, *Chem. Phys. Lett.* 51, 65 (1977).
33. K. J. McCann and M. R. Flannery, *Appl. Phys. Lett.* 31, 599 (1977).
34. W. J. Stevens, M. Gardner, A. Karo, and P. Julienne, *J. Chem. Phys.* 67, 2860 (1977).
35. W. R. Wadt, *J. Chem. Phys.* 68, 402 (1978).

## Authors

H. T. Powell  
D. Prosnitz  
N. W. Winter  
T. N. Rescigno

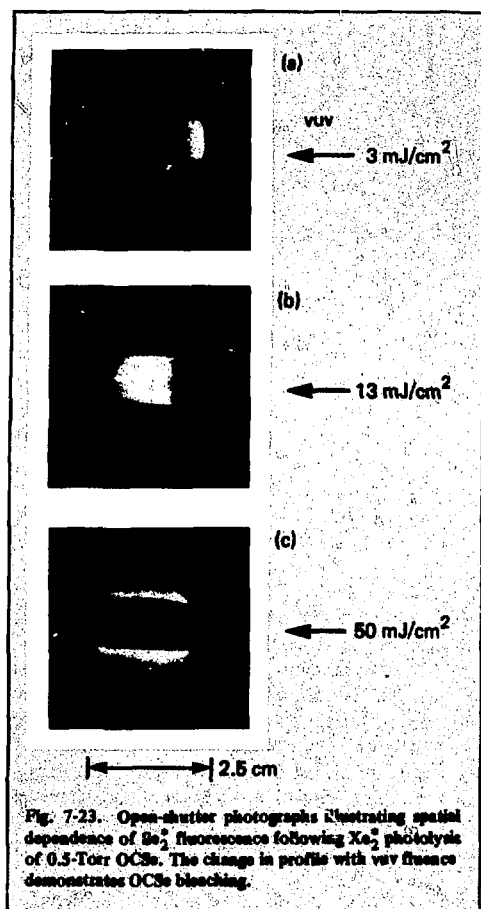
## Major Contributors

J. J. Ewing  
C. W. Werner  
A. U. Hazi  
A. Orel

## 7.3.3 Photolytic Production of $^1\text{S}$ Metastable Atoms

**Photolytic Experiments.** Using the MEG II vacuum ultraviolet (vuv) source described in §7.3.2, we performed experiments to study production of  $\text{Se}(^1\text{S})$  and  $\text{S}(^1\text{S})$  atom concentrations greater than  $10^{16} \text{ cm}^{-3}$ . Figure 7-23 shows the experimental setup. A GaAs photomultiplier tube (PMT) with a 10-ns response time measured the time dependence of fluorescence emitted from the photolyzed gas. A 10-nm-wide band pass filter isolated the spectral region of interest. In some cases, the photomultiplier was coupled by fiber optics to a translatable, lens-pinhole spatial filter to obtain spatially resolved kinetic signals. Subsequently, we installed an intensified-silicon, intensified-target optical multi-channel analyzer (OMA) to view the photolyzed gas from the other direction. The OMA was attached to a 0.3-m spectrometer; it provided the time-integrated fluorescence spectrum. Both the PMT and OMA require extensive rf and lead shielding to prevent interference from electrical noise and x rays produced by the e-beam source.

The stainless steel photolytic cell has a vacuum and fill system that is separate from the superfluorescent rare-gas cell. The bore of the photolytic cell is 2.5 cm; it is excited over a length of 8.5 cm and width of 0.8 cm by the vuv light source. Internal mirrors with feedthrough micrometer adjustments and separation of 12 cm could be mounted internal to the photolytic cell for laser experiments.



The carbonyl sulfide (OCS) generally used was of commercial purity. We found that careful distillation of the OCS caused no apparent change in the observed kinetic signals. Carbonyl selenide was prepared and purified for us by standard procedures,<sup>36</sup> and stored in glass containers at dry ice temperature (see also Ref. 18, §7.3.1). Carbonyl selenide is not readily available commercially, presumably because of its instability to chemical decomposition.<sup>37</sup> Typically OCSe was filled from the cooled, glass storage-vessel immediately before use. However, in separate experiments with a mass spectrometer, significant OCSe decomposition was not found, even after 24 hours' exposure to the photolytic cell.

Exciting a photolytic laser aperture of significant width requires bleaching the parent molecules. Calculated values of the saturation fluence  $h\nu/\phi$  for

photo-dissociating the parent to  $e^{-1}$  of its initial concentration are 12 mJ/cm<sup>2</sup> for OCSe at 172 nm and 100 mJ/cm<sup>2</sup> for OCS at 146 nm. These values are only approximate for Xe<sub>2</sub><sup>+</sup> and Kr<sub>2</sub><sup>+</sup> radiation because the absorption coefficient varies considerably over the emission band width. If the quantum yield results of Black are maintained at high pump power, bleaching a given density of parent molecules by excimer radiation should produce very nearly that density of <sup>1</sup>S-excited atoms.

The fluorescence from Se<sub>2</sub>,  $B^3\Sigma_u^- \rightarrow X^3\Sigma_g^-$ , provides a convenient method for observing the OCSe bleaching. The chemiluminescent quenching reaction<sup>38</sup>  $Se(^1S) + OCSe \rightarrow Se_2 + CO$  produces strong fluorescence that extends for 400 to 700 nm. This emission requires the presence of both Se(<sup>1</sup>S) and OCSe. Thus regions of the photolytic cell that are unexcited or where the OCSe is completely removed by photolysis appear to be dark. Open-shutter photographs (Fig. 7-23) through the bore of the photolytic cell illustrate this effect. For small vuv fluence, the Se<sub>2</sub> fluorescence is concentrated near the input window, as expected from an absorption depth of about 0.6 cm at 0.5 Torr OCSe. As the Xe<sub>2</sub><sup>+</sup> fluence increases, the region of brightest emission occurs farther across the photolytic cell, corresponding to deeper penetration of the higher fluence pump beam. Figure 7-23(c) shows complete bleaching across the cell aperture and Se<sub>2</sub> fluorescence appears only from the edge of the vuv beam. These photographs are qualitatively consistent with an expected OCSe saturation fluence of about 10 mJ/cm<sup>2</sup>.

The temporal and spectral dependence of the fluorescence signals are a strong function of spatial position under bleaching conditions. We eliminated end effects by using reentrant windows in contact with the photolyzed gas. We further defined the observed volume by using pinholes or — in some cases — by limiting the photolyzed volume by placing a solid metal insert in the photolytic cell.

We generally employed collision-induced emission to increase the <sup>1</sup>S fluorescence signal. This emission occurs from either weakly bound or collisional rare gas-<sup>1</sup>S molecules that have a much greater emission rate than the unperturbed atom. Such induced emission is linearly proportional to the perturber density, and it responds rapidly to changes in the <sup>1</sup>S atom density by collisional equilibration. Figure 7-24 shows examples of the spectra of Se(<sup>1</sup>S<sub>0</sub>-<sup>1</sup>D<sub>2</sub>) caused by collisions with rare gases. We obtained these spectra with the OMA; they are somewhat distorted because of reduced response near the edges. Emissions peak at the position of the Se atomic line, 776.8 nm; they



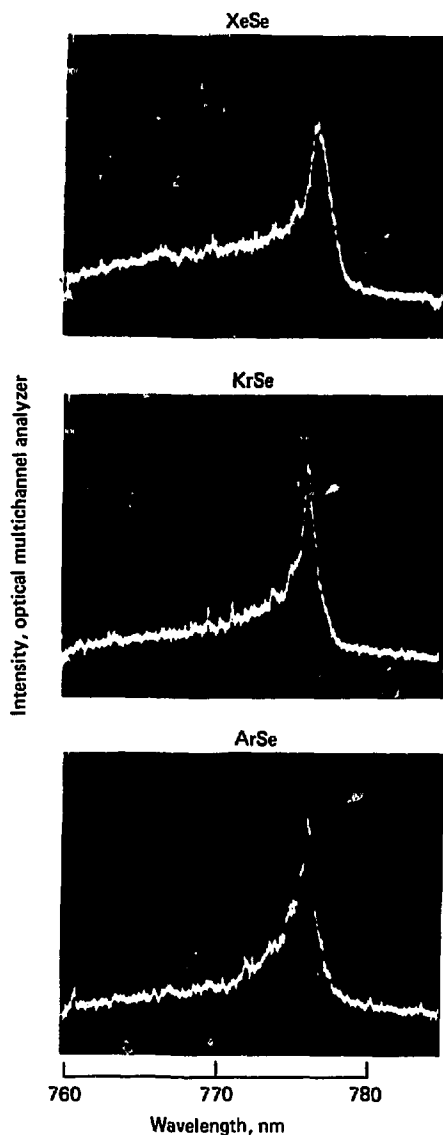


Fig. 7-24.  $\text{Se}(^1\text{S}_0 - ^1\text{S}_2)$  spectra collision induced by rare gases above 1 atm. The zero level is at the first major vertical division.

exhibit a blue wing that is more extensive for the heavier rare gases. These spectra are analogous to those reported in the 1974 annual report for collision-induced emission of  $\text{O}(^1\text{S}_0 - ^1\text{D}_2)$ . Unlike  $\text{XeO}$ , but similar to  $\text{KrO}$  and  $\text{ArO}$ , the rare-gas

selenide bands show no apparent vibrational structure. The sharp feature near the atomic line probably represents emission to a shallow  $^1\Pi$  lower state, which correlates with  $\text{Se}(^1\text{D})$ , the blue wing emission to a deeper bound  $^1\Sigma$  state. Similar collision-induced emission also occurs for the  $\text{S}(^1\text{S}_0 - ^1\text{D}_2)$  transition.

We studied the decay kinetics of  $\text{S}(^1\text{S})$  produced by photolysis as a function of  $\text{Kr}_2^+$  fluence. Typically we added several hundred torr krypton to the photolytic mixture to increase the  $\text{S}(^1\text{S})$  fluorescence. The OMA was not available during  $\text{S}(^1\text{S})$  experiments; however, we confirmed  $\text{S}(^1\text{S})$  emission around 770 nm by its proportionality to Kr pressure. We assumed, as we found previously at low densities of  $\text{O}(^1\text{S})$ , that the presence of a rare gas does not significantly affect the collisional decay of  $^1\text{S}$  atoms.

The  $\text{S}(^1\text{S})$  quenching time is a strong function of absorbed photolytic energy. At very low input fluence, the  $\text{S}(^1\text{S})$  decay observed for 2 Torr OCS and 1000 Torr Kr is exponential with a time constant of about 20  $\mu\text{s}$ , as expected for quenching by OCS, as well as possible impurities. As Fig. 7-25(a) shows, the  $\text{S}(^1\text{S})$  dependence becomes nonexponential at 25  $\text{mJ}/\text{cm}^2$  input and the decay time reduces to  $\sim 1 \mu\text{s}$ . The dependence of decay rate on energy deposition is demonstrated by its change with distance from the photolytic window. Although the peak signal is highest near the window, it displays a rapid initial decay. Careful comparison shows a crossover at about 1  $\mu\text{s}$  (i.e., more deposition gives less signal). This conclusion is strongly evident at 85  $\text{mJ}/\text{cm}^2$  fluence. The fluorescence shows a large spike with a 100-ns decay to a low level. Longer lasting fluorescence is clearly observed farther from the window and at lower deposited energy.

The very great change in decay kinetics with input fluence — virtually a threshold effect — made careful variation of parameters quite difficult. The short storage times are incompatible with a proposed energy-storage medium, and laser attempts at 772 nm using a Kr buffer were unsuccessful. We did not know the source of rapid  $\text{S}(^1\text{S})$  quenching during these experiments, although we considered self-quenching a prime candidate.

The OMA became available for  $\text{Se}(^1\text{S})$  kinetics experiments using  $\text{Xe}_2^+$  photolysis of  $\text{OCSe}$ . The quenching of  $\text{Se}(^1\text{S})$  by its parent,  $\text{OCSe}$ , is quite rapid, having a measured rate constant of  $1.6 \times 10^{-10} \text{ cm}^3 \text{ s}^{-1}$  (Ref. 38). We might expect the  $\text{Se}(^1\text{S})$  storage time to actually lengthen at high fluence, where the  $\text{OCSe}$  is bleached, because  $\text{Se}(^1\text{S})$  quenching by the product CO has been measured to be small.<sup>39</sup> To observe  $\text{Se}(^1\text{S})$  fluorescence signals,

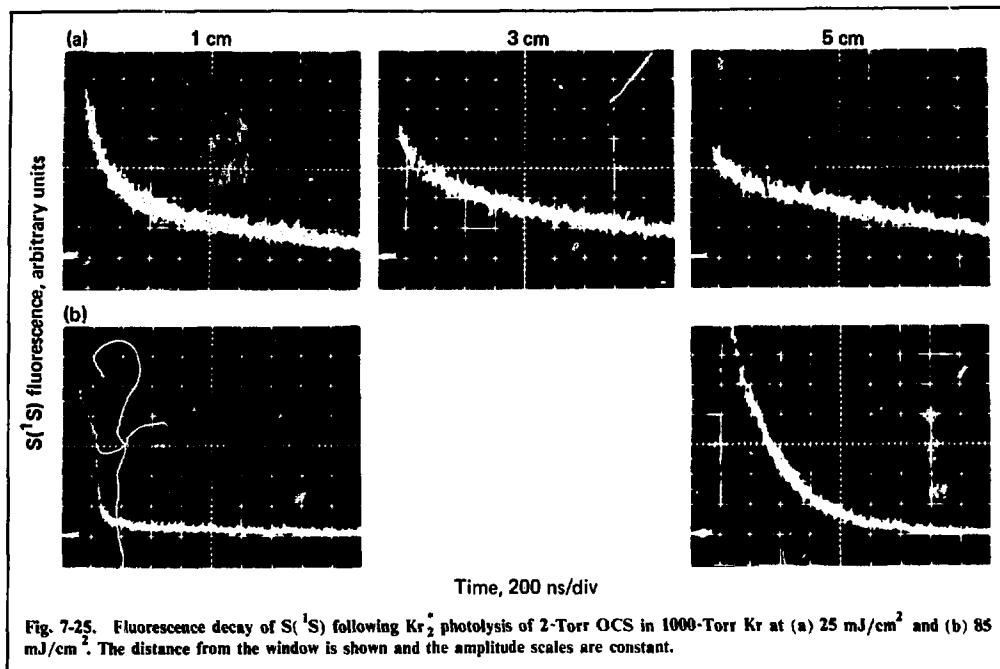


Fig. 7-25. Fluorescence decay of  $S(^1S)$  following  $Kr_2$  photolysis of 2-Torr OCS in 1000-Torr Kr at (a)  $25 \text{ mJ/cm}^2$  and (b)  $85 \text{ mJ/cm}^2$ . The distance from the window is shown and the amplitude scales are constant.

we used xenon both to collision-induce the  $Se(^1S_0-^1D_2)$  transition and to quench  $Se_2^*$  background emission at 780 nm.

Figures 7-26(a) and (b) show the variation in the  $Se(^1S)$  decay caused by changing the input fluence used to photolyze OCS. In Fig. 7-26(a), a 0.8-Torr OCS, 250-Torr Xe mixture is excited by a vuv fluence of  $6 \text{ mJ/cm}^2$ , somewhat less than the OCS saturation value. The  $Se(^1S)$  decay is exponential and depends on OCS density with a rate constant of about  $3 \times 10^{-11} \text{ cm}^3 \text{ s}^{-1}$ . It is not clear why, but this value is about a factor of five smaller than the previously measured value. The observed spectrum is the broad, blue-degraded XeSe ( $^1S_0-^1D_2$ ) emission. The top of the spectrum is "wrapped around" and appears near the baseline because the peak signal exceeds the digital counter scale of the OMA.

Figure 7-26(b) shows a similar mixture excited by  $15 \text{ mJ/cm}^2$ . The  $Se(^1S)$  atoms are rapidly quenched; the phenomenon is reminiscent of high-intensity,  $S(^1S)$  experiments. However, the OMA reveals a number of Xe lines from states above 12 eV at this input intensity. Further, use of an Ar buffer produces highly excited Ar lines. The disappearance of the  $^1S$  atoms appears to be correlated with these unexpected buffer emissions.

These observations suggest the presence of hot electrons that can excite various states of the rare-gas buffer. Some electrons are expected from  $Se(^1S)$  photoionization by the pump radiation. These electrons are heated in superelastic collisions with the excited  $^1S$  atoms. These hot electrons can both excite the atomic buffer and produce additional electrons by impact ionization. Thus, the  $^1S$  density effectively drives an electron avalanche until the excited states are depleted. This mechanism explains the rapid, threshold-like behavior observed for both  $S(^1S)$  and  $Se(^1S)$  quenching. This same electron-avalanche mechanism has been proposed to explain the rapid and complete ionization that follows high-intensity excitation of alkali atoms.<sup>40,41</sup>

Molecular buffer gases can counter this electron-heating instability by providing a reservoir for electron cooling through vibrational excitation. This is demonstrated in Fig. 7-26(c), which reflects the same conditions as Fig. 7-26(b), except for the addition of 250 Torr  $CO_2$  to the photolytic mixture. The electron problem is apparently suppressed: the Xe lines are absent and the  $Se(^1S)$  atoms become long-lived.

The use of molecular buffers was a major element in demonstrating laser oscillation of Group VI

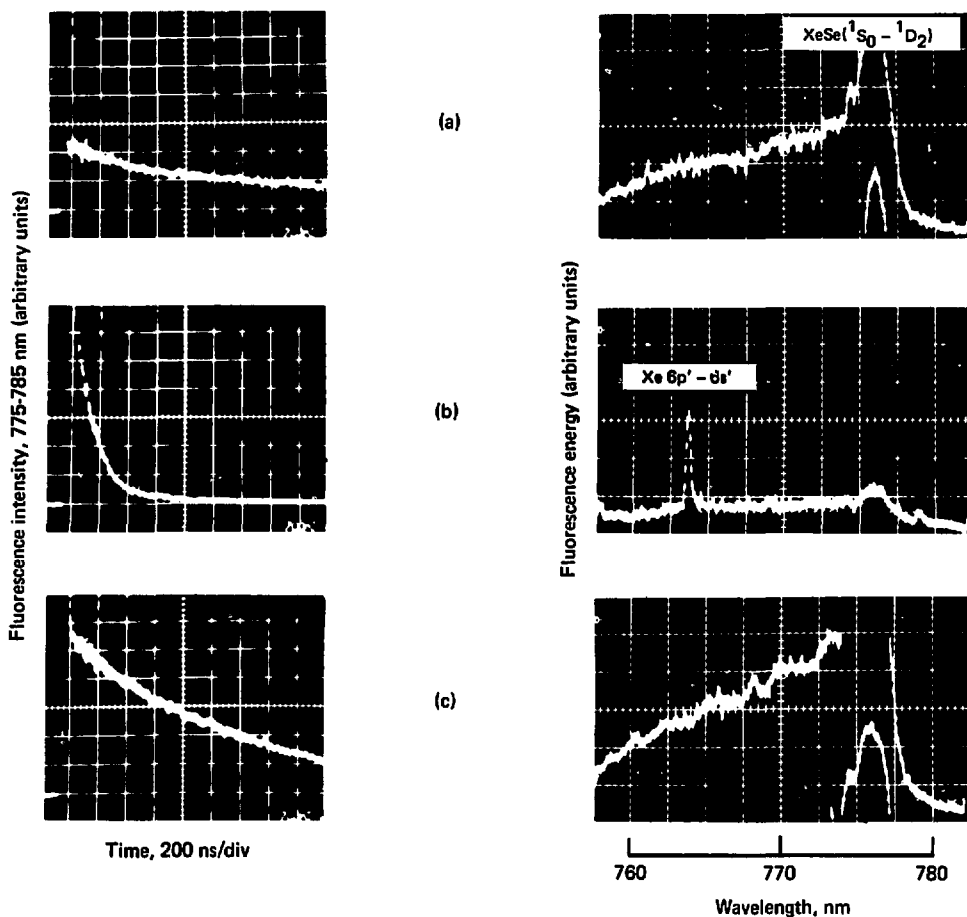


Fig. 7-26. Fluorescence intensity in a 10-nm-wide bandpass about 780 nm vs time, along with the integrated fluorescence spectrum. A mixture of 0.8-Torr OCSe and 250-Torr Xe was photolyzed at 172 nm by (a) 6 mJ/cm<sup>2</sup>; (b) and (c) 15 mJ/cm<sup>2</sup>. The photolyzed mixture additionally contains 250-Torr CO<sub>2</sub> in case (c).

atoms. In the Se laser experiments, we photolyzed approximately 1 Torr OCSe in 50 Torr CO. We used a CO buffer to quench any population in either the Se(<sup>3</sup>P<sub>1</sub>) or Se(<sup>1</sup>D<sub>2</sub>) lower laser level<sup>42</sup> (produced either directly or by quenching), while causing only negligible quenching of the Se(<sup>1</sup>S<sub>0</sub>). Figure 7-27 shows a comparison of fluorescence and laser signals obtained with and without cavity mirrors for the <sup>1</sup>S<sub>0</sub>-<sup>3</sup>P<sub>1</sub> case. Separate experiments with mirrors optimized for the two different Se lines produced comparable performance, as we expected from their similar gain cross sections and common upper state.

We collected the fluorescence signal from the entire cell aperture; the signal includes contributions from both Se(<sup>1</sup>S) (the sharp line) and Se<sub>2</sub><sup>+</sup> (the undulatory background).

After mirrors were installed, we observed laser oscillation, identified by its distinct time-dependence and relatively high cavity intensity, as monitored through a 0.1% transmission mirror. The peak laser signal outside the cavity was comparable to the peak fluorescence signal without mirrors. The observed emission spectrum in the laser case is reduced to the Se(<sup>1</sup>S<sub>0</sub>-<sup>3</sup>P<sub>1</sub>) line alone. Using

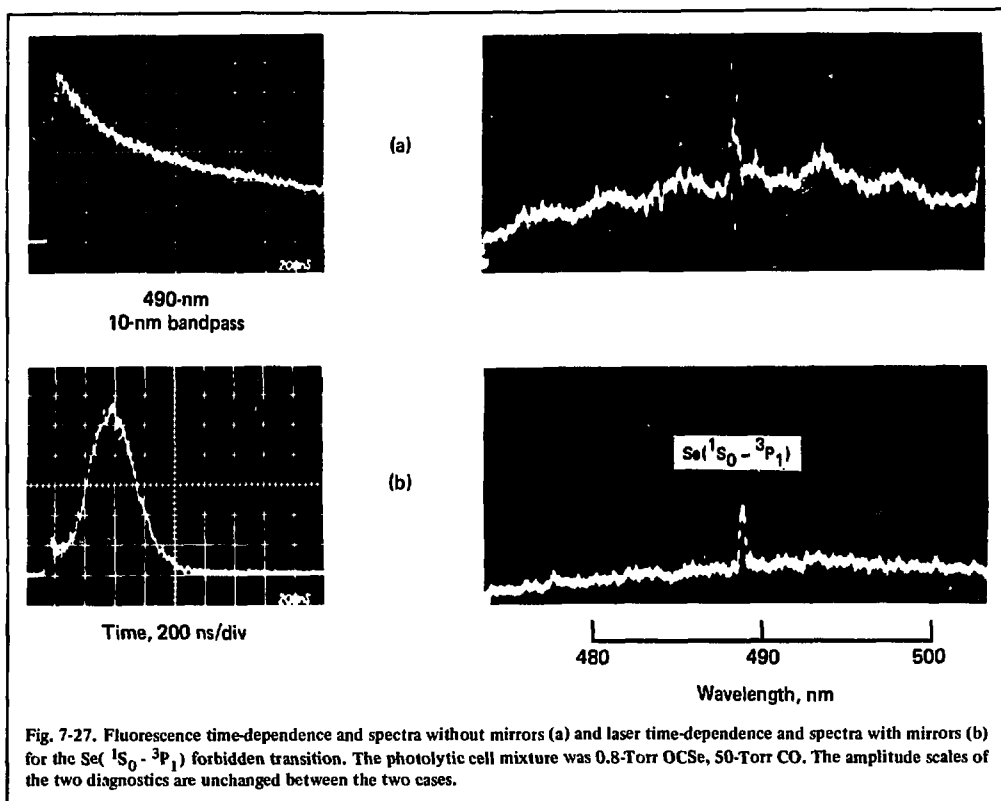


Fig. 7-27. Fluorescence time-dependence and spectra without mirrors (a) and laser time-dependence and spectra with mirrors (b) for the  $\text{Se}(^1\text{S}_0 - ^3\text{P}_1)$  forbidden transition. The photolytic cell mixture was 0.8-Torr OCS, 50-Torr CO. The amplitude scales of the two diagnostics are unchanged between the two cases.

Ar reference lines, we measured the laser line positions to be within 0.1 nm of the 488.8- and 777.0-nm forbidden Se transitions. For subsequent laser shots, we were required to clean deposited selenium from the lower laser mirror.

Early in 1978, we also obtained laser oscillation for the  $\text{S}(^1\text{S} - ^1\text{D}_2)$  line, using  $\text{Kr}_2$  photolysis of 1.5-Torr OCS in 50-Torr  $\text{SF}_6$  (see Fig. 7-28). We selected an  $\text{SF}_6$  buffer to both cool and attach photoelectrons. The peak laser output intensity in this case is 25 W, approximately  $10^6$  times the fluorescence output. The spectrum confirms the 772.5-nm,  $\text{S}(^1\text{S}_0 - ^1\text{D}_2)$  line.

The output intensity of the Se and S lasers is limited by small gains and relatively short storage times. The laser builds up from a small fluorescence level until the gain decays to the cavity threshold level due to collisions. The higher output from sulfur corresponds to a longer buildup period because of slower  $\text{S}(^1\text{S})$  quenching. The demonstration of lasing confirms the presence of  $^1\text{S}$  concen-

trations of order  $10^{16} \text{ cm}^{-3}$ , which are needed to exceed an estimated loss of 1% per pass. Experiments are continuing to determine the optimum photolytic mixture and to verify the energy content of the photolyzed medium.

**Electronic Structure of OCS.** The electronic spectrum of OCS consists of three distinct continuum transitions at 5.54 eV, 7.44 eV, and 8.12 eV, with Rydberg structure at shorter wavelengths.<sup>43</sup> Absorption into the 8.12 eV band produces  $\text{CO}(^1\Sigma^+)$  and  $\text{S}(^1\text{S})$  with a high quantum yield (see Ref. 19, §7.3.1). However, the spectrum in this region has considerable structure and suggests a bound-to-bound transition (see Fig. 7-11, §7.3.1). Structured absorption bands such as this can be produced by bound-to-free transitions, as Pack has shown.<sup>44</sup> However, this requires the excited-state potential curve to have a maximum or a flattening along the dissociation coordinate in the Franck-Condon region of the ground state, so that the bound-free Frank-Condon factors have a narrow

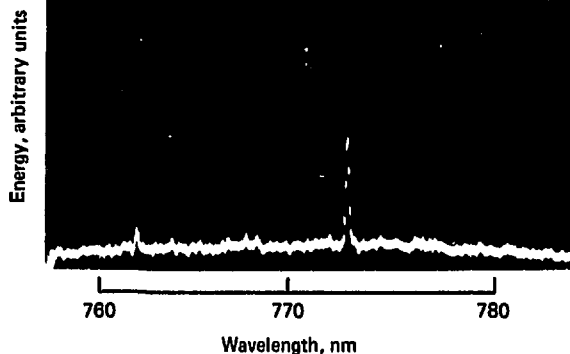
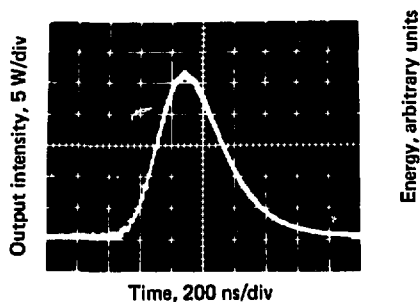


Fig. 7-28.  $S(^1S_0 - ^1D_2)$  laser intensity and spectrum obtained at 1.5-Torr OCS, 50-Torr  $SF_6$  with a  $Kr_2^+$  photolysis fluence of 50  $mJ/cm^2$ .

energy dependence. Such a maximum is apparent for symmetric triatomic molecules such as  $CO_2$ , but not necessarily for OCS.

Simple considerations of bonding in the excited states of OCS suggest that the  $^1\Sigma^+$  states arising from the  $CO(^1\Sigma^+) + S(^1S)$  and  $CO(^3\Pi) + S(^3P)$  asymptotes should interact, leading to an avoided crossing. We performed configuration interaction calculations to quantify the nature of the excited  $^1\Sigma^+$  states of OCS for linear geometries and several OCS distances. Figure 7-29 shows the calculated potential curves. The important features are the avoided crossing at about  $3.75 a_0$  and the deep minimum in the  $2^1\Sigma^+$  curve at  $3.0 a_0$ . The small splitting of the two upper  $^1\Sigma^+$  indicates that absorption into the  $3^1\Sigma^+$  state at 12.8 eV will likely also produce  $S(^1S)$  by dissociating along the diabatic potential curve. The well in the  $2^1\Sigma^+$  state shows that the structure observed for the 8.12-eV absorption band is probably due to bound-to-bound transitions. The calculated transition energy for this state has considerable error, which is characteristic of mixed valence and Rydberg states. Further work now in progress should refine and improve the potential energy curves.

We have performed calculations on several other low-lying excited states of OCS to calibrate the potential surface calculations on the  $^1\Sigma^+$  states. Table 7-9 compares the vertical excitation energies with the results of configuration interaction calculations and experiment. The agreement with experiment for the  $^1\Sigma$  and  $^1\Delta$  states is good, as we found with earlier calculations on  $N_2O$  (Ref. 45) and  $CO_2$  (Ref. 46). The Hartree-Fock calculations did not in-

clude 3d polarization functions, while the configuration interaction calculations did. The 1.4-eV disagreement for the  $^1\Delta$  excitation energy predicted by the two calculations arises primarily from the difference in basis sets. Understanding why the more extensive calculations for this state disagree more with experiment than the simple ones is, in our view, quite important. Test calculations on  $N_2O$  and  $CO_2$  indicate that the simple calculations benefit from cancellation of errors caused by electron correlation and limitations in the basis set.

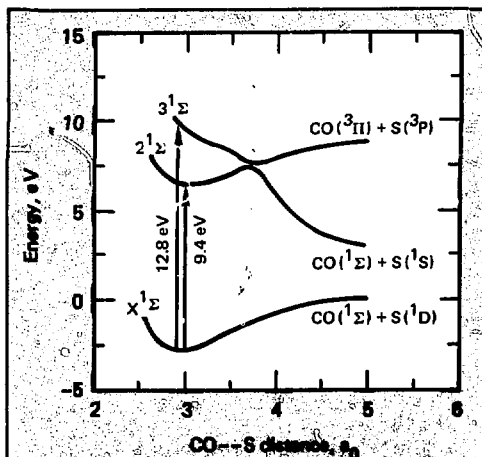


Fig. 7-29. Theoretical potential energy curves for OCS.

**Table 7-9. Calculated and experimental excitation energies for OCS.**

State	Hartree-Fock	Configuration interaction	Experiment
$X^1\Sigma^+$	0.0 eV	0.0 eV	0.0 eV
$3\Sigma^+$	4.5		
$3\Delta$	4.8		
$1,3\Sigma^-$	5.1		
$1\Delta$	5.2	6.6	5.5
$^3\Pi$	7.0		
$1\Pi$	7.2		7.4
$2^1\Sigma^-$		9.4	8.1
$3^1\Sigma^-$		12.8	
$OCS^+ \ ^2\Sigma^-$	10.7		11.2

The last important point for this theoretical study to clarify is the actual mechanism for the dissociation of the  $2^1\Sigma^+$  state to yield  $S(^1S)$ . We are currently undertaking calculations for bent geometries to answer this question.

**$^1S$ - $^1S$  Quenching Processes.** We have carried out semiquantitative ab initio molecular structure calculations to assess collisional processes that may limit the lifetime of the upper laser level. The processes of main concern are self-quenching:

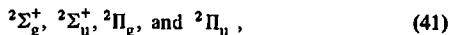


and associative ionization:



The latter process is energetically possible because the minimum in the diatomic ion lies below two separated  $^1S$  atoms. The calculations we describe below show that neither process makes a significant contribution to  $^1S$  quenching.

We used a double-zeta quality contracted-Gaussian basis set<sup>47</sup> augmented with a full set of d-polarization functions ( $\alpha = 0.8$ ) to determine the ground state,  $^3\Sigma_g^-$  and the lowest seven  $^1\Sigma_g^+$  states of the  $S_2$  molecule. We also determined the doublet states



which asymptotically approach  $S(^3P) + S(^4S)$ . We used valence orbital full configuration interaction

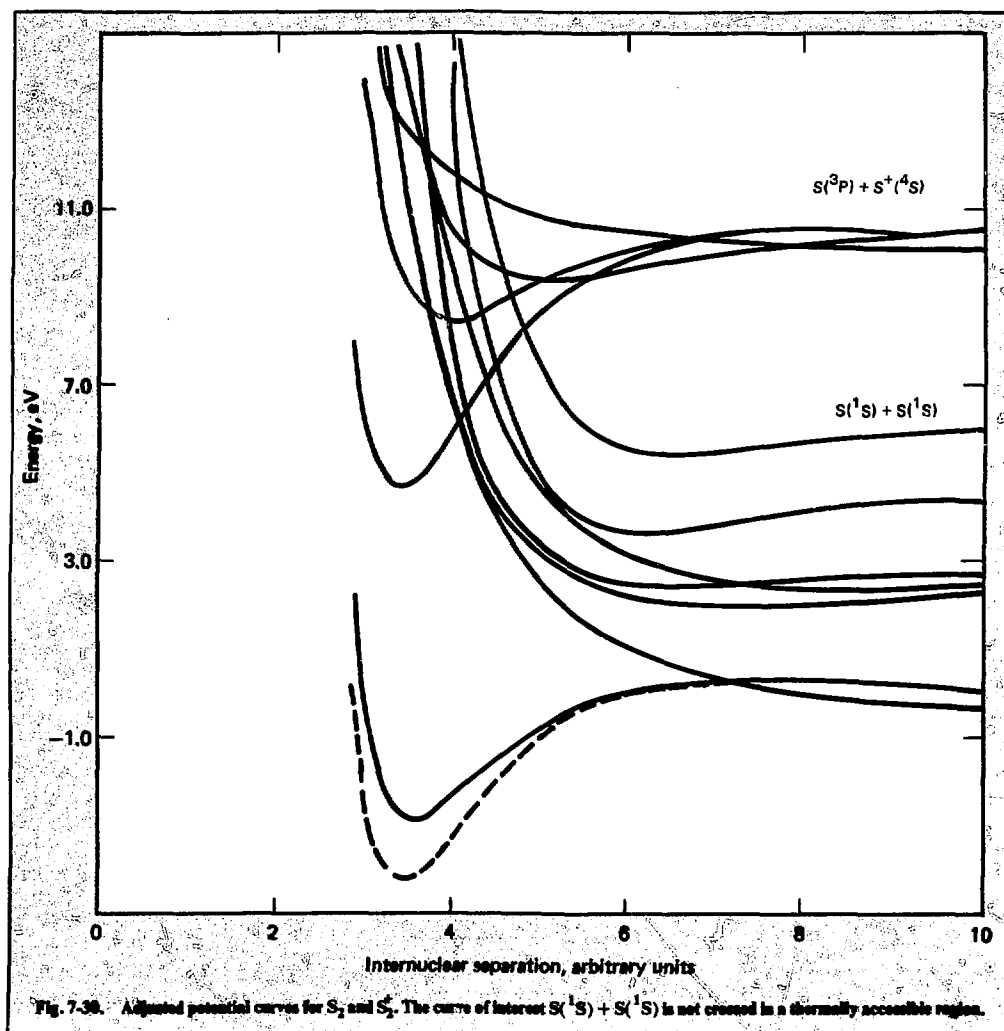
(CI) wavefunctions to describe these states. The number of spin eigenfunctions used for most states was about 130; about 50 were used for  $^3\Sigma_g^-$  and  $^1\Sigma_g^+$ . A calculation for a fixed internuclear distance proceeds as follows: after computing all necessary one- and two-electron integrals, the self-consistent field equations were solved for the ground state of  $^3\Sigma_g^-$ . Then the CI wavefunctions and eigenvalues (energies) were determined for the neutral and ion molecules. The internuclear separation was varied between 2 and 10 a.u.

The asymptotic energy separations of the excited states are in reasonable agreement with experiment. The  $S(^1D)$ - $S(^3P)$  separation is approximately 0.3 eV in error and the  $S(^1S)$ - $S(^3P)$  approximately 0.1 eV in error. The computed positions of the equilibrium internuclear separation for the ground state of the neutral molecule and the ion are within 10% of the experimental values. However, the binding energy of both the neutral and ion are nearly 1 eV in error. We can reduce this error by including more configurations.<sup>48</sup>

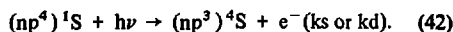
Using standard techniques,<sup>49</sup> we have constructed semiquantitative potentials that yield experimental asymptotic properties and internuclear separations. (Figure 7-30 shows these curves.) The curves indicate that direct self-quenching to lower states via curve-crossings will not be a problem. The barrier for associative ionization appears to be at least  $>2$  eV; hence, the process will have a very small rate at room temperature. By depressing the ion curves to correspond to excited Rydberg states of  $S_2$ , we have also shown that self-quenching caused by curve-crossing with excited Rydberg states will have a barrier no lower than 0.25 eV, which is still sizable. These calculations indicate that neither self-quenching nor associative ionization will lead to significant losses in the upper laser level. We have drawn similar conclusions from scaling the  $S_2/S_2^+$  curves to the  $Se_2/Se_2^+$  system.

**Photoionization of  $^1S$  Metastable Atoms.** In both the  $Kr_2^+/OCS$  and  $Xe_2^+/OCSe$  systems, the energy of the excimer pump photons is sufficient to photoionize the  $^1S$  state producing the ground,  $^4S$  state of the ions (see Ref. 50). As a result, we must consider the photoionization of  $O(^1S)$ ,  $S(^1S)$ , and  $Se(^1S)$  a potentially serious loss mechanism. If the appropriate cross sections were large, photoionization would be detrimental in two ways: by directly depopulating the  $^1S$  state and by producing low-energy electrons that can rapidly deactivate the excited states via superelastic collisions.

Figure 7-31 is a schematic of the energetically possible photoabsorption processes from the  $^1S$  state. Ionization of a p-electron from the  $(np^4)^1S$



state can lead to the  $(np^3)^4S$  state of the positive ion:



The parity selection rule requires that the ejected electrons be either  $s$  or  $d$ . Thus, the continua associated with the  $^4S$  state of the ion are  $^3,^5S$  and  $^3,^5D$ , and electric dipole transitions from the  $^1S$  state to the  $^4S$  state of the ion are spin-forbidden in L-S coupling because of the  $\Delta S=0$  selection rule. In principle, there are two mechanisms by which the photoionization of the  $^1S$  state can gain intensity:

spin-orbit coupling of the LS states and transitions occurring via magnetic quadrupole radiation.<sup>51</sup> However, in the current case, magnetic quadrupole transitions are forbidden because of the  $\Delta L=0, \pm 1$  ( $L=0 \not\leftrightarrow L=0$ ) selection rule. We have assumed that the most important effect is the spin-orbit coupling between the  $^1S_0$  and  $^3P_0$  states of the initial  $(np^4)$  configuration. (The spin-orbit coupling in the final states has been neglected.) With these assumptions, the  $^1S$  absorption cross section, at frequency  $\omega$ , is given by

$$\sigma(^1S, \omega) = \frac{\omega}{\omega + \Delta E} \lambda^2 \sigma(^3P, \omega + \Delta E), \quad (43)$$

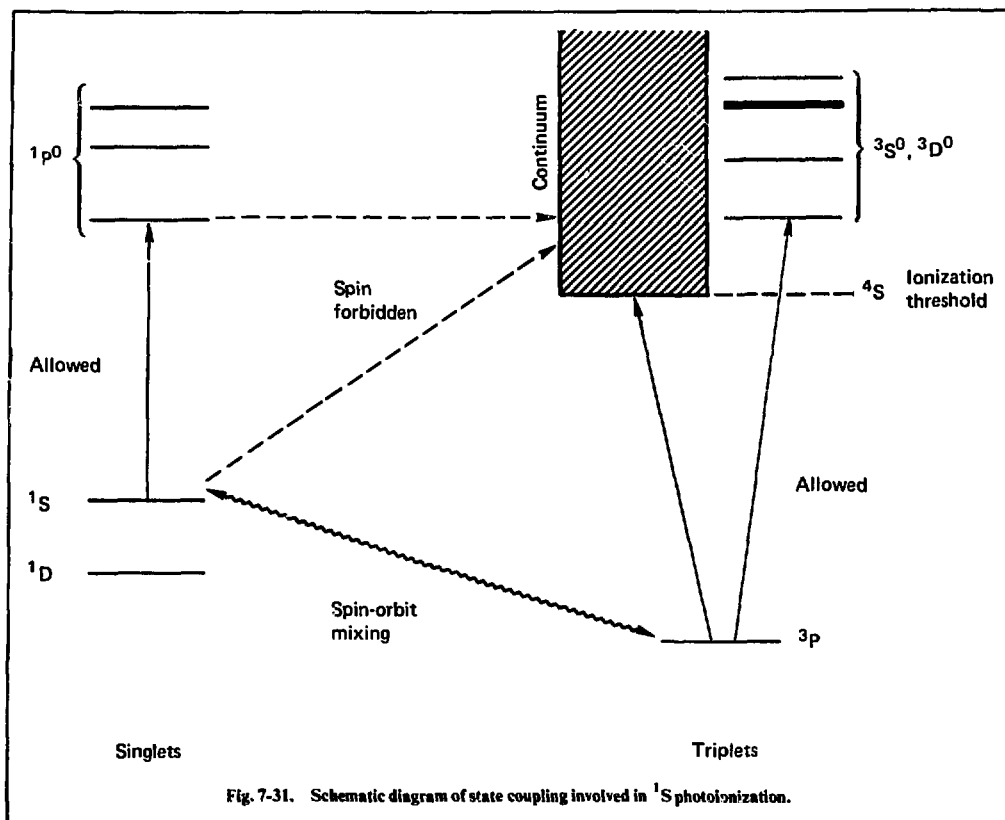


Fig. 7-31. Schematic diagram of state coupling involved in  $1S$  photoionization.

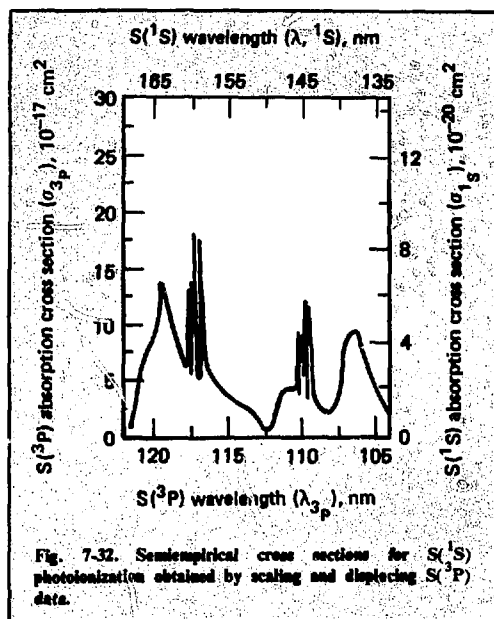
where  $\sigma(^3P)$  is the corresponding  $^3P$  cross section,  $\lambda$  is the spin orbit mixing coefficient between  $1S$  and  $^3P$ , and  $\Delta E$  is the energy difference between  $1S$  and  $^3P$ .

Figure 7-32 illustrates the results obtained for sulfur where  $\sigma(^3P)$  has been measured.<sup>52</sup> At the  $Kr_2^f$  wavelength of 146 nm, the predicted  $S(^1S)$  cross section is about  $2 \times 10^{-20} \text{ cm}^2$ . Unfortunately, no experimental cross section is available for  $Se(^3P)$ . We have calculated  $\sigma(^3P)$  for selenium using a technique applied previously to rare-gas excited states,<sup>53</sup> obtaining a  $1S$  cross section of  $2.5 \times 10^{-19} \text{ cm}^2$  at the  $Xe_2^f$  wavelength of 172 nm. Table 7-10 summarizes the calculated photoionization cross sections for  $O(^1S)$ ,  $S(^1S)$ , and  $Se(^1S)$  at the appropriate excimer pump wavelengths.

In studying the photoionization of open-shell atoms or molecules that have several low-lying states of the positive ion, we must consider the potential contribution of autoionization to the total photoionization cross section. In the current case,

several series of Rydberg states converge to the  $(np^3)^2D$  and  $^2P$  states of the positive ions and lie above the first ionization threshold. In particular, we have studied the  $(np^3n's)^1P$  and  $(np^3n'd)^1P$  states, which are connected to the  $(np)^4 1S$  state by allowed electric dipole transitions. The calculations predict that the  $(3p^4)^1S \rightarrow (3p^34d)^1P$  transition in sulfur occurs near 146 nm with an  $f$ -number of 0.026. A similar,  $(4p^4)^1S \rightarrow (4p^34d)^1P$  transition in selenium, lies near 173.5 nm with  $f=0.09$ . However, we expect these transitions to contribute negligibly to the total photoionization cross section because of their small widths. The widths of these  $1P$  levels, lying above the  $4S$  threshold, are determined by the rates of autoionization. In LS-coupling, the decay of the  $(np^3n'd)^1P$  levels into the  $^3,5S$  and  $^3,5D$  continua of the  $4S$  state of the ion is forbidden by the  $\Delta S=0$  selection rule. Furthermore, the matrix element  $\langle ^2D | H_{\text{spin-orbit}} | ^4S \rangle$  vanishes for the  $np^3$  configuration;<sup>54</sup> thus, autoionization of the  $1P$  states below the  $^2D$  threshold can occur only





through second-order effects. A similar effect has been observed in oxygen.<sup>55</sup>

We also must consider the contribution of ( $np^3n's$ ) and ( $np^3n'd$ )  $^3S$  and  $^3D$  autoionizing states to the photoionization cross section of the ( $np^4$ )  $^3P$  state. As Fig. 7-32 shows, these states dominate the  $^3P$  absorption spectrum in certain energy regions and can seriously affect the  $^1S$  cross section via spin-orbit coupling. We have included this effect in our calculation for sulfur, but not for selenium.

From our calculations, we conclude that spin-forbidden photoionization cross section of  $Se(^1S)$  [and possibly of  $S(^1S)$ ] is sufficiently large to produce a significant concentration of electrons at high photolytic fluences.

Table 7-10. Spin-forbidden photoionization cross sections.

	Wavelength, Å	Cross section, cm <sup>2</sup>	Cross section, cm <sup>2</sup> (includes AI)
O( $^1S$ )	1265	$1.2 \times 10^{-22}$	$1.5 \times 10^{-22}$
S( $^1S$ )	1460	$8.6 \times 10^{-21}$	$1.9 \times 10^{-20}$
Se( $^1S$ )	1720	$2.5 \times 10^{-19}$	—

## References

- OCSe was prepared by R. L. Sharpless at the Stanford Research Institute, Menlo Park, CA.
- R. H. Purcell and F. D. Zaborbux, *J. Chem. Soc. (London)* **1937**, 1029.
- G. Black, R. L. Sharpless, and T. G. Slanger, *J. Chem. Phys.* **64**, 3993 (1976).
- O. J. Dunn, S. V. Filseth, and R. A. Young, *J. Chem. Phys.* **59**, 2892 (1973).
- T. B. Lucatorto and T. J. McIlrath, *Phys. Rev. Lett.* **37**, 428 (1976).
- T. J. McIlrath and T. B. Lucatorto, *Phys. Rev. Lett.* **38**, 1390 (1977).
- W. J. R. Tyerman and A. B. Callear, *Trans. Faraday Soc.* **62**, 2312 (1966).
- G. W. Rabalais, J. M. McDonald, V. Scherr, and S. P. McGlynn, *Chem. Rev.* **71**, 73 (1971).
- R. T. Pack, *J. Chem. Phys.* **65**, 4765 (1976).
- N. W. Winter, *Chem. Phys. Lett.* **33**, 300 (1975).
- N. W. Winter, C. F. Bender, and W. A. Goddard, *Chem. Phys. Lett.* **20**, 489 (1973).
- S. Huzinaga and C. Arnau, *J. Chem. Phys.* **53**, 451 (1970).
- B. Liu and R. Saxon, IBM, San Jose, private communications (1977).
- R. Parr, Univ. of North Carolina, private communication (1977).
- C. E. Moore, *Atomic Energy Levels NBS-457* (US GPO Washington, DC, 1949).
- M. Mizushima, *Phys. Rev.* **134**, A883 (1964).
- G. Tondello, *Astroph. J.* **172**, 771 (1972).
- A. U. Hazi and T. N. Rescigno, *Phys. Rev. A* **16**, 2376 (1977).
- E. U. Condon and G. H. Shortley, *The Theory of Atomic Spectra* (Cambridge Univ. Press, London, 1963).
- P. M. Dehmer, W. L. Luken, and W. A. Chupka, *J. Chem. Phys.* **67**, 195 (1977).

## Authors

H. T. Powell  
N. W. Winter  
C. F. Bender  
A. U. Hazi

## Major Contributor

J. J. Ewing

## 7.3.4 Group VI Laser System Analysis

The laser driver for a fusion power reactor must be efficient (>1%) and scalable to large energies (>1 MJ). In this section, we discuss the major components of photolytic Group VI lasers and relate them to efficiency and aperture scalability. Our discussion is partitioned according to pump kinetics, vuv radiation coupling, Group IV media excitation, energy storage, optical extraction, and average power considerations. We consider the Xe<sub>2</sub>

excimer radiation-pumped OCSe system in detail because it appears to offer the highest potential laser system efficiency.

**Photolytic Drivers — Lasers.** Several figures of merit for pump system evaluation are radiation production efficiency, coupling efficiency, and technological risks associated with untested transport designs. In this article we consider the radiation production and coupling efficiencies for rare-gas excimer laser and fluorescence pumps. Previous experimental investigations indicate the fluorescence efficiency of rare-gas excimers can be 40-50%.<sup>56</sup> By contrast, laser medium efficiencies measured for high-pressure systems have been low<sup>57</sup> (see §7.3.2). We have modeled laser performance in other regimes to determine if high efficiency is attainable and have also calculated coupling efficiencies for practical fluorescence pump geometries.

We described the kinetics model<sup>58</sup> used for high-pressure, rare-gas excimer lasers in the 1976 annual report (see also Ref. 21, §7.3.1). We have extensively revised this model to improve the treatment of electrically excited low-pressure ( $\approx 1$  atm) xenon (for details of the computational method see §7.2.1 and Fig. 7-1). We have dealt with the effects of a non-Maxwellian electron distribution by solving the Boltzmann equation with appropriate cross section data. Table 7-11 summarizes the new electron collisional processes incorporated in the current model. We have carefully treated electron coupling processes between the various excited Xe states and to  $\text{Xe}^+$  because of their greater importance at low pressures. We isolated the effects of particular kinetic data and determined the sensitivity of laser performance to various kinetic assumptions. We also determined the dependence of laser performance on electron beam power deposition and the addition of a sustainer field.

Figure 7-33 shows the dependence of electron fractional power transfer into various energy loss channels on  $E/N$  (electric field to total gas density ratio) for 2.0 atm xenon excited by an electron beam with a power deposition of  $50 \text{ kW/cm}^3$ . The fractional electron power transfer for a given electron energy loss process is defined as the electron power flowing into this process divided by the total electrical power deposited in the electron gas. The total power  $P_T$  deposited in the electron gas is the sum of the e-beam and discharge-Joule-heating depositions. The quantity  $P_{SE}$  is the power flow into the secondary electrons that is predominantly due to the Joule heating by the applied electric field. The ratio  $P_{SE}/P_T$  is, therefore, a direct measure of the fraction of the total electrical power deposited in the medium due to the applied electric field.

**Table 7-11. Electron kinetic processes included in electrically excited xenon model.**

Process	Notes
$\text{Xe} \rightleftharpoons \text{Xe}^*(6s)$	a
$\text{Xe} \rightleftharpoons \text{Xe}^{**}(6p,5d,6s')$	a
$\text{Xe} \rightarrow \text{Xe}^+$	b
$\text{Xe}^* \rightleftharpoons \text{Xe}^{**}$	c
$\text{Xe}^* \rightarrow \text{Xe}^+$	d
$\text{Xe}^{**} \rightarrow \text{Xe}^+$	e
$\text{Xe}_2^* (^1\Sigma_g^+ \Sigma) \rightarrow \text{Xe}_2^{**} \rightarrow \text{Xe}^* + \text{Xe}$	f
$\text{Xe}_2^* \rightarrow \text{Xe}_2^+$	g
$\text{Xe}_2^* (^3\Sigma) \rightleftharpoons \text{Xe}_2^* (^1\Sigma)$	h

<sup>a</sup>These cross sections were obtained from the total excitation cross section measured by Schaper and Scheibner<sup>59</sup> by using the electron energy loss spectra of Delage and Carrette<sup>60</sup> as a guide to partition this cross section into  $\text{Xe}^*(6s)$  and  $\text{Xe}^{**}(6p,5d,6s')$  components. This results in most of the excitation going into the  $\text{Xe}^{**}$  energy loss process. This is consistent with the results of Refs. 61-63 on the  $\text{Xe}(6p)$  excitation analogy and with the results obtained for Ar by Peterson and Allen and Eggarter.<sup>64,65</sup>

<sup>b</sup>Ref. 66.

<sup>c</sup>Analogy with Cs( $6s \rightarrow 6p$ ).<sup>67</sup>

<sup>d</sup>Ref. 68.

<sup>e</sup>Classical scaling of cross section for  $\text{Xe}^* \rightarrow \text{Xe}^+$ . Ref. 68, using the procedure discussed by Rudge.<sup>69</sup>

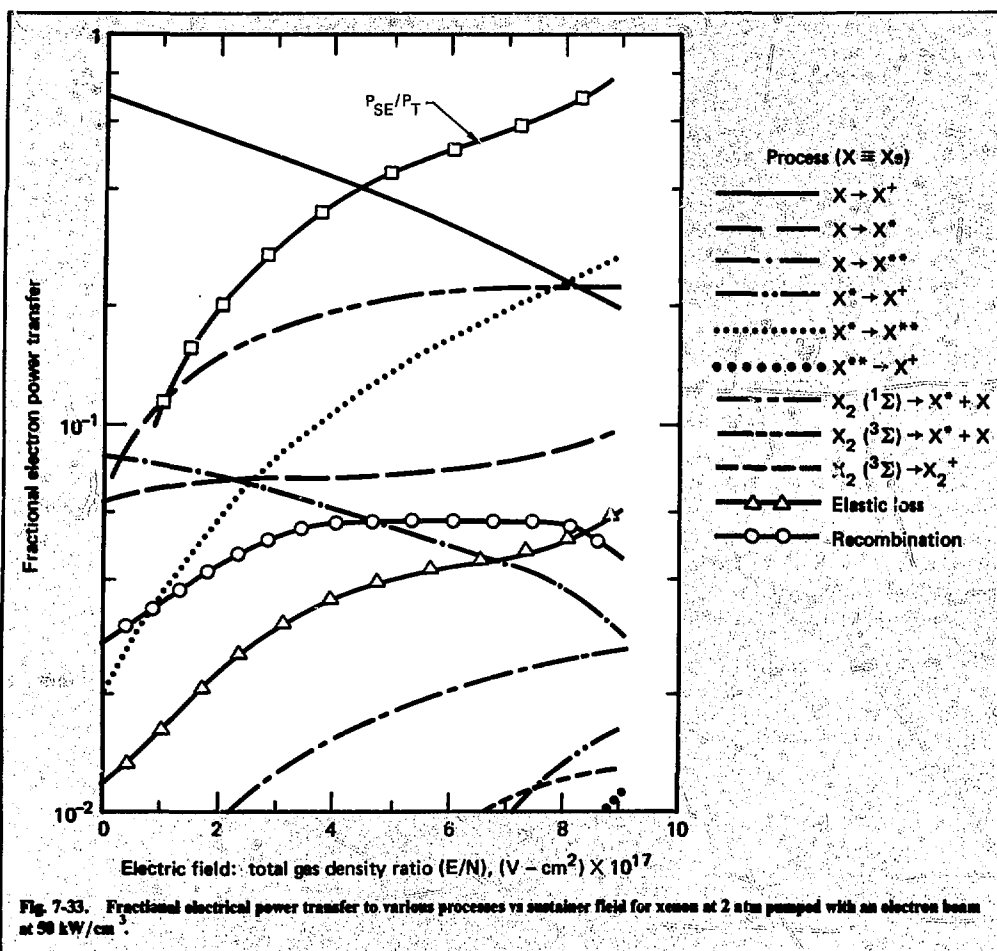
<sup>f</sup>Employed the cross section for  $\text{Xe}^* \rightarrow \text{Xe}^{**}$  and assumed instantaneous predissociation of  $\text{Xe}_2^{**}$  to form  $\text{Xe}^* + \text{Xe}$ .

<sup>g</sup>Employed the cross section for  $\text{Xe}^* \rightarrow \text{Xe}^+$  as an approximation.

<sup>h</sup>Shape derived by classical scaling of  $\text{O}_2 (^X^3\Sigma_g^-) \rightarrow \text{O}_2 (b^1\Sigma_g^+)$  (Ref. 70) cross section. Peak value of cross section for  $\text{Xe}_2(^3\Sigma) \text{Xe}_2(^1\Sigma)$  was varied around the nominal value of  $10^{-13} \text{ cm}^2$ .

In general, the results presented in Fig. 7-33 are model dependent. However, several qualitative features of the fractional power transfer diagram have general significance. In the absence of an applied electric field, 70% of the e-beam energy goes directly into ionization, 8.2% into production of the  $\text{Xe}^{**}$  manifold ( $6s', 6p, 5d$ ), 6.4% into  $\text{Xe}^*(6s)$  states, and the remainder into other excitation processes. Because the upper laser level in a  $\text{Xe}_2^*$  laser is formed by three-body recombination of  $\text{Xe}^*$  atoms, it is clear that pure e-beam excitation does not directly produce this state. Most of its energy flows into the larger energy loss process of ionization. Ultimately the ion production can give excimer radiation through the recombination channel, although at greater energy expense compared to direct  $\text{Xe}^*$  production.

Figure 7-33 permits determination of the effect of using an electric field to enhance direct  $\text{Xe}^*$  production. When an electric field is applied, the fractional power transfer into ionization and produc-



tion of  $\text{Xe}^{**}$  states decreases and the fractional power transfer into  $\text{Xe}^*$  states increases. These are favorable effects. However, the relative increase in the fractional transfer into  $\text{Xe}^*$  is relatively small and most of the power begins to flow into low-energy loss processes (e.g., dissociation of excimers, excitation of  $\text{Xe}^*$  to  $\text{Xe}^{**}$ , elastic losses, etc.). This is because the electric field efficiently heats the low-energy electrons, which then give up their energy to low-energy loss processes involving excited states and transitions among excited states. The application of an electric field actually leads to a reduction in laser and fluorescence efficiency compared to pure e-beam pumping.

The electron distribution functions computed for Fig. 7-33 were generally non-Maxwellian. In the

absence of an applied electric field the electron kinetic temperature (defined as two-thirds the mean energy) was approximately 0.8 eV. For an  $E/N$  of  $8 \times 10^{-17} \text{ Vcm}^2$ , the electron kinetic temperature was approximately 1.7 eV. In both cases, the assumption of a Maxwellian distribution gave rate constants for low-energy loss process within a factor of two of the non-Maxwellian values. However, for such large energy loss processes as ionization, errors of several orders of magnitude were possible. In addition, we found that the fractional ionization due to excited states such as  $\text{Xe}^*$  and  $\text{Xe}^{**}$  increased rapidly as the discharge  $E/N$  was increased, and ultimately it destabilizes the discharge. Indeed, at high values of  $E/N$ , we observed an instability characteristic of the multistep ionization instability.<sup>71</sup>

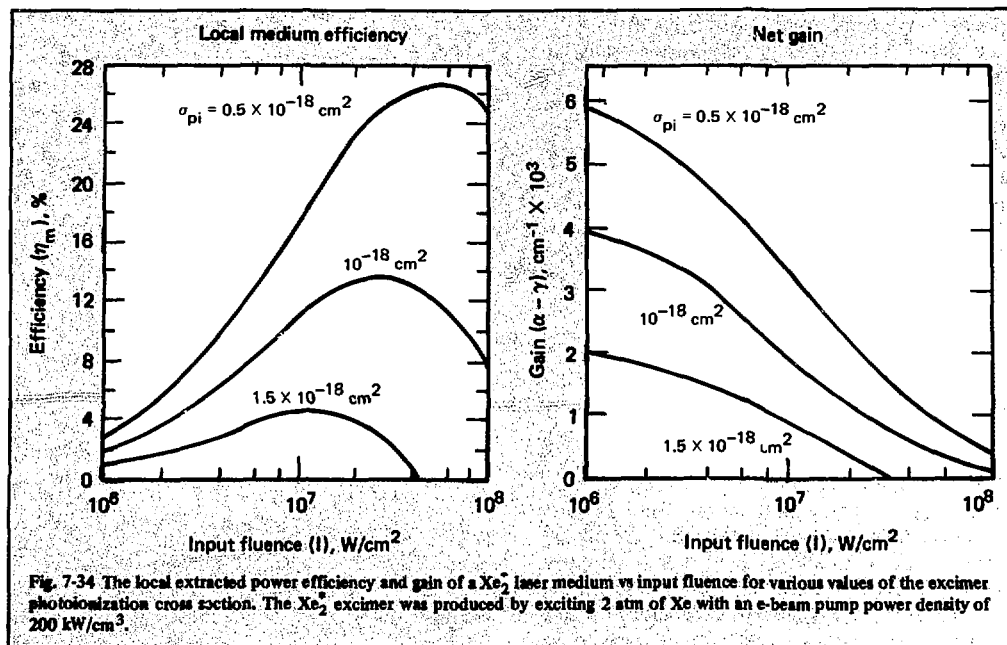


Fig. 7-34 The local extracted power efficiency and gain of a  $\text{Xe}_2^+$  laser medium vs input fluence for various values of the excimer photoionization cross section. The  $\text{Xe}_2^+$  excimer was produced by exciting 2 atm of Xe with an e-beam pump power density of  $200 \text{ kW/cm}^2$ .

The local medium efficiency for optical extraction by stimulated emission is given by

$$\eta_m = \frac{\Delta I}{P_T \Delta X} = \frac{(\alpha - \gamma) I}{P_T}, \quad (44)$$

where  $\alpha$  is the gain,  $\gamma$  the loss coefficient,  $I$  the local total laser radiation intensity, and  $P_T$  the total electrical power density deposited in the medium. Both  $\alpha$  and  $\gamma$  generally depend on field intensity; their small signal values are defined as  $\alpha_0$  and  $\gamma_0$ . In the  $\text{Xe}_2^+$  model, we determined the stimulated emission cross sections of the  $^1\Sigma$  and  $^3\Sigma$  excimer states from the radiative lifetime measurements of Keto<sup>72</sup> and the  $\text{Xe}_2^+$  emission bandwidth. The absorption coefficient  $\gamma$  was caused by photoionization of the excimers and  $\text{Xe}^*$  and  $\text{Xe}^{**}$  atoms. The photoionization cross section of  $\text{Xe}^*$  was  $3 \times 10^{-20} \text{ cm}^2$  (Ref. 73), and of  $\text{Xe}^{**}$ ,  $10^{-18} \text{ cm}^2$  (Ref. 73). We left as a free parameter the value of the excimer photoionization cross section.

We found predictions of laser medium efficiency and net small signal gain were most sensitive to magnitudes of the rate constants for neutral and electron collisional mixing of the singlet and triplet excimer states and to the excimer photoionization cross section. The singlet-to-triplet conversion rate

by xenon atoms was  $2.5 \times 10^{-13} \text{ cm}^3 \text{ s}^{-1}$ , between the value previously used (Ref. 21, §7.3.1) and a measurement of Keto.<sup>74</sup> Singlet and triplet electron mixing occurred with a rate constant of  $1.2 \times 10^{-7} \text{ cm}^3 \text{ s}^{-1}$  at an electron temperature of 0.6 eV.<sup>71,74</sup> Figure 7-34 shows the variation in laser medium performance as a function of the excimer photoionization cross section at 2 atm Xe and an input power of  $200 \text{ kW/cm}^2$ . We found the absorption to be dominated by excimer photoionization. The ratio of the  $^3\Sigma$  to  $^1\Sigma$  populations was about 10. The  $\text{Xe}_2^+$  gain/absorption experiments of §7.2 suggest  $\text{Xe}^*$  and  $\text{Xe}^{**}$  contribute strongly to the absorption; their contribution may be more important at the much higher power depositions used in those experiments.

Since the medium gain is approximately balanced by absorption, there is a strong dependence on the assumed value of excimer photoionization cross section. Quantum defect calculations on  $\text{Xe}_2^+$  give a value of  $2 \times 10^{-18} \text{ cm}^2$  (Ref. 24, §7.3.2). However, the calculations for  $\text{Ar}_2^+$  in §7.3.2 suggest that the quantum defect results should be reduced by about a factor of 2 at the excimer wavelength for better agreement with the ab initio values. If  $\sigma_{pi} = 10^{-18} \text{ cm}^2$ , the maximum local medium efficiency is 13% and the net small signal gain is  $0.4\% \text{ cm}^{-1}$ . Note that the electrical efficiency for energy

extraction via stimulated emission increases with laser power until medium saturation occurs at about  $10 \text{ MW/cm}^2$ .

Although the predicted medium efficiency is reasonably attractive and may be quite good if  $\sigma_{pi}$  turns out to be less than  $10^{-18} \text{ cm}^2$ , the low gain and high saturation flux place difficult constraints on amplifier design. For an assumed input power of  $1 \text{ MW/cm}^2$ , a  $\text{Xe}_2^+$  amplifier would be 28 m long to achieve 11% overall efficiency and 62 MW output power. The high output power required by the high saturation flux exceeds current damage thresholds for vuv optics.

Figure 7-35 shows that the xenon laser performance improves as e-beam pump power increases. This increase results from a more favorable ratio of the  $^1\Sigma$  to  $^3\Sigma$  populations caused by electron mixing. At a constant input energy of  $0.25 \text{ J/cm}^2$ , a power deposition of  $200 \text{ kW/cm}^2$  corresponds to an e-beam current of about  $10 \text{ A/cm}^2$  for  $1 \mu\text{s}$ . Previous experiments suggest that the  $\text{Xe}_2^+$  production efficiency degrades above about  $100 \text{ A/cm}^2$  (see Ref. 25, §7.3.2).

The results of the laser pump analysis roughly bracket anticipated laser performance levels based on uncertainties in kinetic data. Our current best estimate for critical kinetic data lead us to conclude that xenon excimer pump laser efficiency will probably lie in the 5-10% region. As expected, the  $\text{Xe}_2^+$  laser performance deteriorates when a sustainer field is added. For an e-beam power deposition of  $50 \text{ kW/cm}^2$ , the optimum efficiency for energy extraction by stimulated emission was reduced from about 11% to 5% by adding an electric field of  $8 \times 10^{-17} \text{ V cm}^2$ .

**Pump Radiation Transport.** For the Group VI systems of interest, the effective absorption cross sections  $\sigma_A$  for photolyzing the parent molecules into the desired final states lie in the range of  $10^{-17}$  to  $10^{-16} \text{ cm}^2$ . Desired  $^1\text{S}$  excited-state densities are in the range of  $10^{16}$  to  $10^{17} \text{ cm}^{-3}$ , requiring a parent molecule pressure of 0.3-3 Torr, assuming unit quantum yield and complete dissociation. Accordingly, the characteristic absorption length for the photolytic pump radiation (defined as  $\lambda_A = N_A^{-1} \times \sigma_A^{-1}$ ) will lie in the range of 0.1-1 cm. The pump fluence required to photodissociate one absorption depth of parent molecules is the pump saturation fluence,  $\Gamma_{ps} = h\nu_p / \sigma_A$ . Photodissociation of a medium several optical depths thick requires the pump fluence to be several times  $\Gamma_{ps}$ . The input pump radiation propagates through the media, fully dissociating the parent molecules, until it reaches a point where the pump fluence at that position lies below the bleaching fluence. The spatial

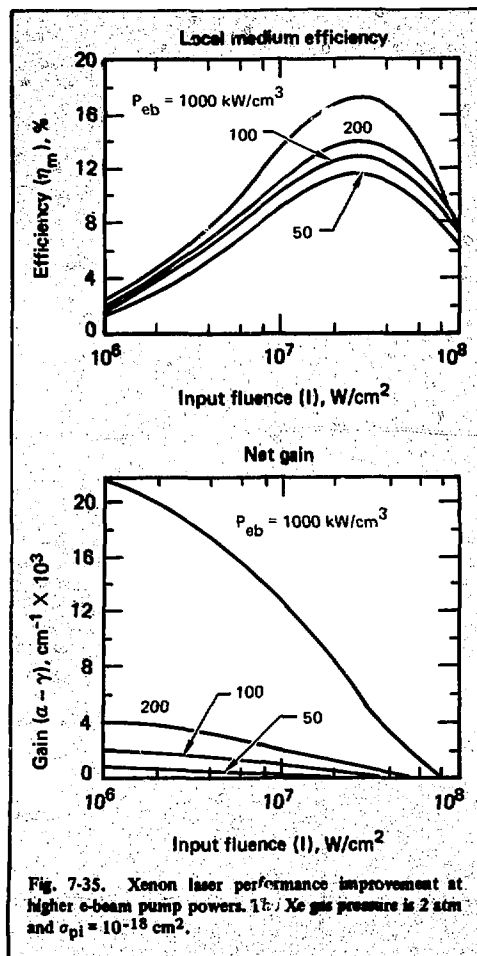


Fig. 7-35. Xenon laser performance improvement at higher e-beam pump powers. 1b:  $\text{Xe}$  gas pressure is 2 atm and  $\sigma_{pi} = 10^{-18} \text{ cm}^2$ .

position where bleaching takes place propagates as a wave through the photolytic medium (hence the term "bleaching-wave excitation"). The velocity of propagation of the bleaching-wave front, whose thickness is of order  $\lambda_A$ , is given by

$$V = \frac{I_p}{N_A h\nu_p} \quad (45)$$

where  $I_p$  is the pump intensity and  $\nu_p$  is the pump frequency. For parent-molecule pressures in the Torr range and pump intensities of 1 to  $10 \text{ MW/cm}^2$ , the bleaching-wave velocities are much less than the speed of light, typically  $10^6$  to  $10^7 \text{ cm/s}$ .

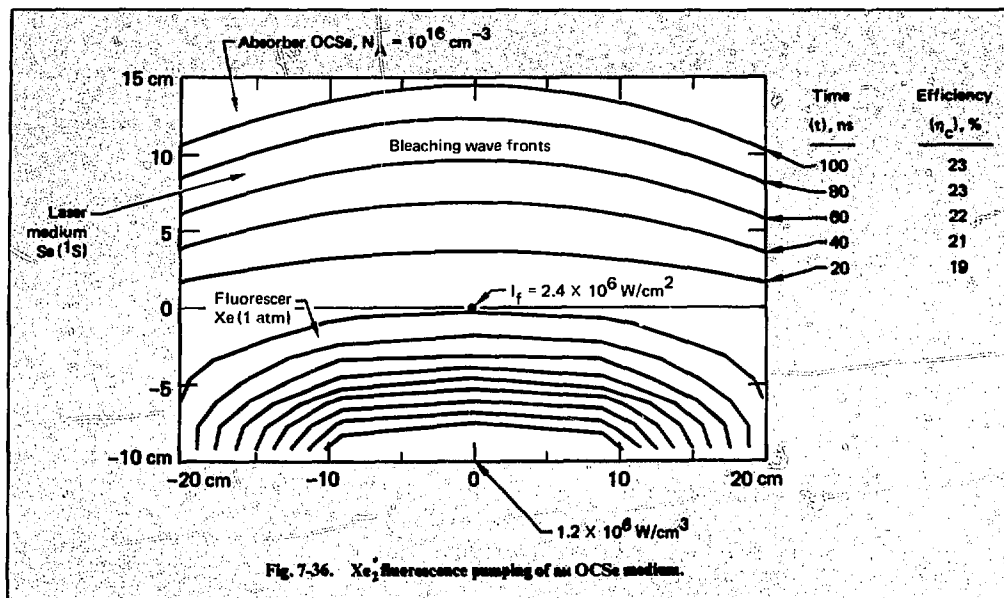


Fig. 7-36.  $\text{Xe}_2^+$  fluorescence pumping of an OCS medium.

Such slow velocities limit the maximum aperture of an amplifier when kinetic quenching processes are considered. (We address this scaling limit in §7.3.5.)

Pump radiation coupling to the photolytic medium is greatest with laser pumping because laser radiation is highly collimated. The only inefficiencies are losses by mirrors or windows in the beam path. In this case, the major design issue is the efficiency of the driver laser. On the other hand, the rare-gas excimer fluorescence efficiency is quite high using electron beam pumping. Hence, the major design issue for fluorescence-pumped devices is radiation transport into the photolytic medium.

It is useful to define a fluorescence-coupling efficiency as the fluorescence energy absorbed in the photolytic amplifier divided by the total emitted fluorescence energy:

$$\eta_c(t_B) = \frac{N_A h \nu_p V_A(t_B)}{\int_0^{t_B} \int_{V_F} \frac{dE_p}{dt}(\underline{x}', t') dV', dt'} \quad (46)$$

where  $dE_p/dt$  is the fluorescence power per unit volume,  $V_A$  is the volume of photolyzed medium at time  $t_B$  after initiation of the pumping process, and  $V_F$  is the fluorescer volume. The coupling efficiency

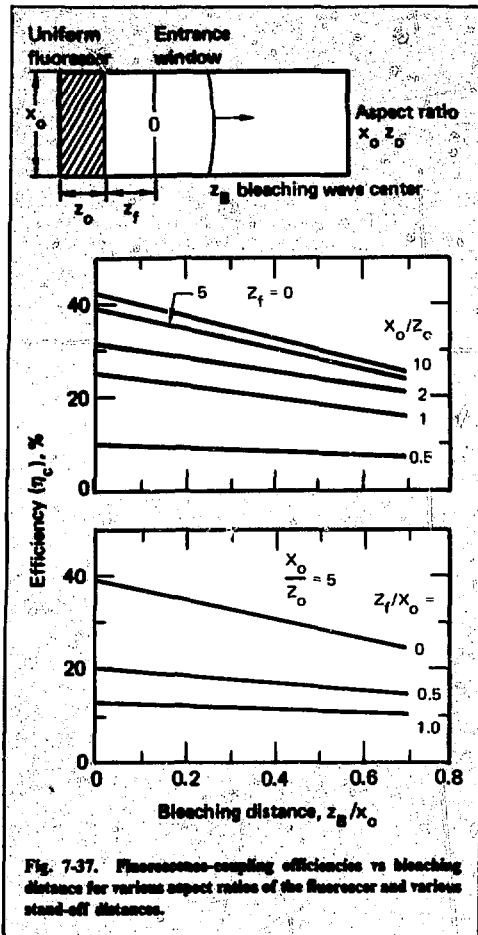
$\eta_c$  therefore depends on the geometry and the propagation of the bleaching wave. The bleaching-wave front position  $\underline{x}_B$  is determined by

$$\frac{d\underline{x}_B}{dt_B} = \frac{I_p(\underline{x}_B, t_B)}{N_A h \nu_p} \quad (47)$$

$$I_p(\underline{x}, t) = \int_{V_F} \frac{(\underline{x} - \underline{x}')}{4\pi|\underline{x} - \underline{x}'|^3} \frac{dE_p}{dt}(\underline{x}', t) dV',$$

where we integrate over the volume of the fluorescer  $V_F$  and the radiation propagation time from  $\underline{x}'$  to  $\underline{x}$  is taken as instantaneous on the timescale over which the pump fluorescence changes. Although surface reflections are neglected in the derivation of Eq. (47), this result could be used with the method of images to construct the intensity distributions where reflections are important.

Figure 7-36 shows the results of a computer calculation for one-sided fluorescence photolysis of OCS by  $\text{Xe}_2^+$  radiation. The fluorescence cell in the lower part contains Xe at 1 atm and is irradiated for 100 ns by a 300-kV, 100-A/cm<sup>2</sup> e-beam. Isointensity contours for e-beam deposition were calculated by the three-dimensional Monte Carlo deposition code SANDYL.<sup>75</sup> The peak e-beam deposition is 1.2 MW/cm<sup>3</sup>, and the peak fluorescence intensity in



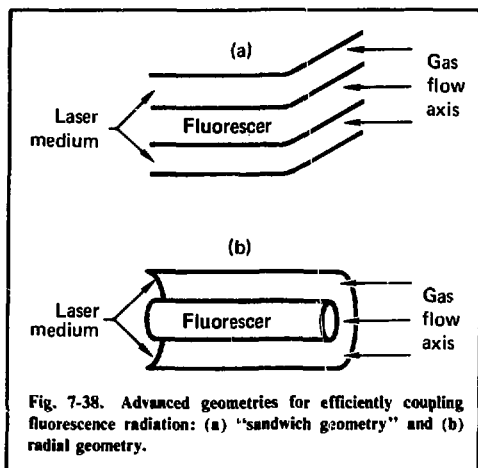
the laser medium cell is  $2.4 \text{ MW/cm}^2$ . We assume the radiated xenon power density equals 0.4 times the electron beam deposition; however, the excimer kinetics code could be used to calculate the local fluorescence intensity.

The upper portion of Figure 7-36 shows the progressive photolysis of OCSe by the fluorescence-driven bleaching wave. The values in the column labeled  $\eta_c$  represent the efficiency for converting the fluorescence radiation into  $\text{Se}^{(1)\text{S}}$  atoms in the volume bounded by the bleaching-wave front and the input window. By 100 ns, 23% of the photons emitted from the fluorescer region have produced  $\text{Se}^{(1)\text{S}}$  atoms in the absorber region.

The general characteristics of fluorescence coupling are exhibited by analytic solution of Eqs. (46)-(47) for the case of a strip fluorescer of width

$x_0$  and depth  $z_0$  (see Fig. 7-37). Close to the fluorescer,  $z \ll x_0$ , the coupling efficiency is approximately 0.5; far from the fluorescer, where  $z_B$  is the position of the bleaching wave front, the bleaching wave is cylindrical and the coupling efficiency is approximately  $x_0/\pi z_B$ . Figure 7-37 shows the results of a parametric study of the effects of fluorescer aspect ratio  $x_0/z_0$  and standoff distance  $z_f$  on radiation coupling efficiency for a uniform fluorescer. Incorporating a standoff distance between the fluorescer and the entrance window to the absorber might be necessary to reduce e-beam damage to the solid window or to reduce the flux of electrons into the laser cavity in a windowless device. The results plotted in Fig. 7-37 indicate that coupling efficiencies approaching 40% can be achieved with fluorescers having aspect ratios of between 5 and 10. Clearly, the standoff distance between the fluorescer and absorber must be minimized to achieve high coupling efficiencies.

The preceding calculations enable us to bracket anticipated fluorescence coupling efficiencies. For simple planar geometries, coupling efficiencies of 15-40% may be achieved. Figure 7-38 presents hypothetical advanced fluorescence geometries that could produce higher coupling efficiency. In the "sandwich geometry" [Fig. 7-38(a)], two-sided coupling is achieved by containing the fluorescer volume between two absorbing regions. We envision windowless operation using coflowing gas streams at the same pressure for both fluorescer and laser media. Electron-beam pumping is possible either from the edge of the fluorescing medium or directly through the photolysis region, provided a low-Z buffer, like helium, is used. Cylindrical



geometries [e.g., Fig. 7-38(b)] obviously have high coupling efficiency. Bringing the electron beam to the fluorrescer again presents problems. Injecting the beam either from the end or radially outward from a central-core diode are possible solutions. Radial geometries are ideally suited to a fluorrescer pumped by a longitudinal discharge, provided we identify an efficient discharge-pumped medium.

Although the advanced geometries potentially offer a coupling efficiency greater than 40%, each presents unresolved technical problems that we term technical risks in our system analysis. For example, in windowless geometries, secondary electrons injected into the laser medium must be controlled by recombination to prevent excited-state quenching. Conversely, for windowed systems, window damage will play an important role in the pump configuration and coupling efficiency.

**Group VI Amplifier Excitation Characteristics.** The previous analysis indicates that photolytic Group VI amplifiers may be excited to relatively high energy-storage densities (<10 J/litre) by excimer fluorescence on laser radiation. However, achievable bleaching-wave velocities are finite ( $10^6$  to  $10^7$  cm/s). Under these circumstances,  $^1\text{S}$  quenching losses in the bleaching-wave front and after bleaching can affect amplifier efficiency and the uniformity of gain across the aperture. In some cases, the quenching rate of an  $^1\text{S}$  atom by its parent molecule can be quite significant. For example, the  $\text{Se}(^1\text{S})$  quenching time by 1 Torr OCSe is 300 ns (see Ref. 38, §7.3.3). If the bleaching time of parent molecules is much less than their quenching time, i.e.,

$$\frac{\sigma}{h\nu_p} I_p \gtrsim 5 N_A k_q, \quad (48)$$

then the effect of parent quenching is eliminated. At 1 Torr OCSe, the above condition is met for pump fluxes greater than  $3 \times 10^5 \text{ W/cm}^2$ .

The recent experimental results we discuss in §7.3.3 indicate that several kinetic processes can lead to quenching of the  $^1\text{S}$  state after photolysis has taken place. The most serious quencher appears to be photoelectrons generated by photoionization after  $^1\text{S}$  states by pump radiation. These electrons and their attendant  $^1\text{S}$  quenching can rapidly multiply, if cooling mechanisms or electron loss processes at low electron energy are not provided to counteract superelastic heating by  $^1\text{S}$  atoms. We have used molecular additives, such as CO, to extend  $\text{Se}(^1\text{S})$  lifetimes at  $10^{16} \text{ cm}^3$  concentrations to greater than 1  $\mu\text{s}$ .

We are now incorporating the effect of electron generation and heating into our bleaching kinetics code. These calculations indicate that photoelectron heating by superelastic collisions and multiplication by collisional ionization produces electron densities sufficient to quench the  $\text{Se}(^1\text{S})$  population in 100 ns at  $^1\text{S}$  densities of  $10^{16} \text{ cm}^3$ . These calculations also confirm that additives may lengthen the  $^1\text{S}$  lifetime by one or more of the following: electron cooling, recombination, and attachment. We are addressing the limitations on pump duration, pump intensity, and aperture size in a spatially dependent model.

**Group VI Amplifier Extraction Characteristics.** Issues that must be addressed in assessing energy extraction from short-pulse fusion-laser amplifiers include efficiency, power amplification, parasitics control, beam distortion in average-power systems, and amplifier staging. Multipass architectures are attractive for Group VI laser systems because the required input energies are low, while extraction efficiencies are high. Analysis of superfluorescence and parasitic depumping suggests that the single amplifier gain  $\alpha_0 L$  is limited to four or five, primarily by parasitics. Analysis of extraction from a multipass Group VI amplifier must include — in a self-consistent manner — the spatial dependences of the gain media and short-pulse input beam. Figure 7-39 illustrates such a calculation for the transverse fluorescence pumping of an amplifier module containing OCSe by xenon excimer radiation. Figure 7-39(a) shows the extraction efficiencies  $\eta_x$  and input fluence  $\Gamma_i$  characteristics for a multipass amplifier configuration (see §7.2). The laser transition chosen is the selenium transauroral line at 488.7 nm, and we assume that the lower level is fully bottlenecked. Under these conditions, the maximum value of  $\eta_x$  is 75%. The short-pulse input fluence is taken to be a fifth-power exponential  $\exp[-(R/R_0)^5]$ , where  $R_0$  is on the order of the amplifier radius  $R_A$ . The other relevant parameters are (1) transverse pumping time, 400 ns, (2) kinetic lifetime, 1  $\mu\text{s}$ , (3) optical transit time between extraction passes, 100 ns, (4) optical loss per pass, 5%, and (5) maximum small-signal gain  $\alpha_0 L = 4$ . Under these conditions, the maximum extraction efficiency approaches 50%. This lower value (compared with 75%) is a direct consequence of the finite pump time, the optical fill factor and transport losses, and the short lifetime (1  $\mu\text{s}$ ) associated with the excited-state population.

Figure 7-39(b) shows the effect of varying the kinetic lifetime on the input fluence requirement for a two-pass amplifier configuration for several desired extraction efficiencies. As anticipated, the



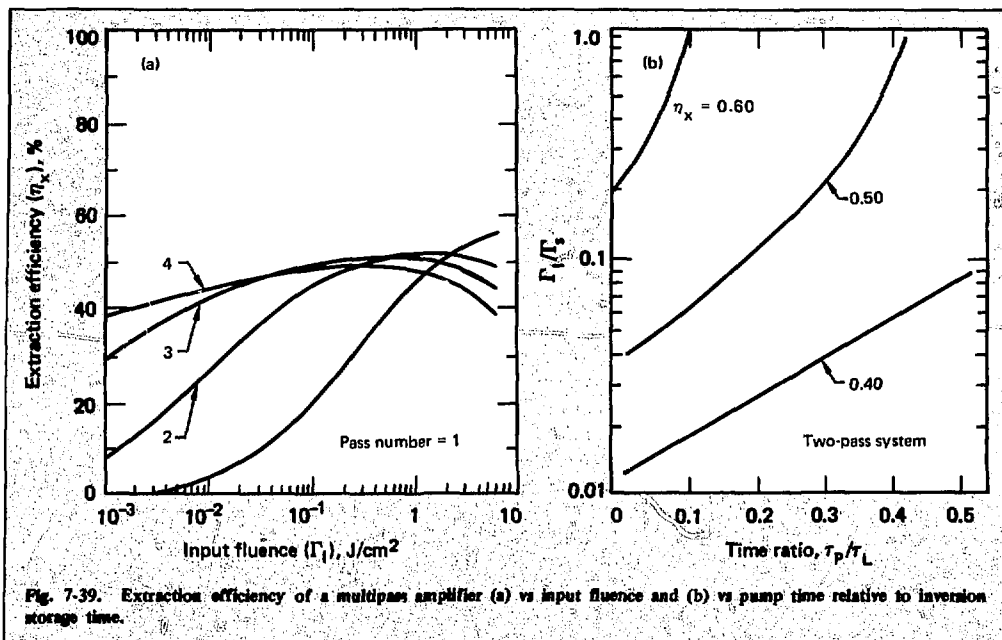


Fig. 7-39. Extraction efficiency of a multipass amplifier (a) vs input fluence and (b) vs pump time relative to inversion storage time.

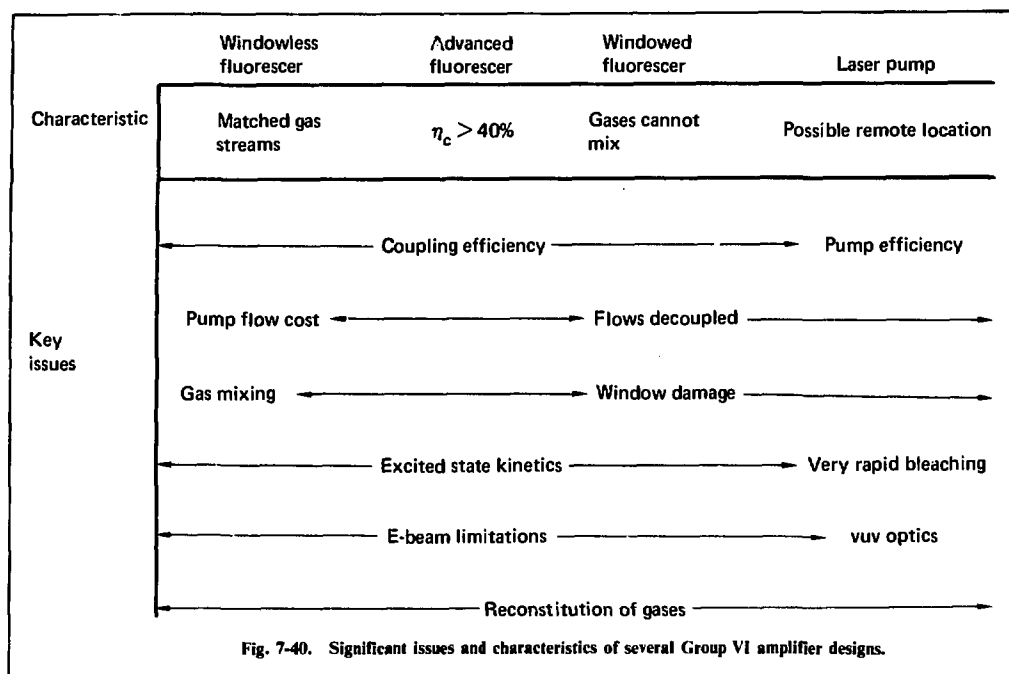
longer is the kinetic lifetime compared to the pumping time, the lower is the required input fluence for a given extraction efficiency. In addition, for a given fluence, the device extraction efficiency decreases as the kinetic lifetime decreases, if the pump time is constant.

**Group VI Amplifier Average Power Considerations.** After laser excitation, as much as 40% of the pump energy absorbed in the photodissociation of OCSe appears as thermal energy in the medium. For the Group VI systems of interest, this leads to thermal depositions of approximately 10 J/litre-atm and, hence, initial relative pressure and temperature disturbances of order 0.1. As we discuss in §7.2, residual density disturbances produce laser beam amplitude and phase modulation that reduce the focused power of the beam on the target. The results discussed in §7.2 indicate that acoustic damping systems must achieve relative density fluctuation levels of 10<sup>-4</sup> to 10<sup>-3</sup> for efficient fusion reactor target irradiation. These values are within the current state of the art for low-pressure-drop, acoustic-damping systems. It now appears possible to achieve specific energy densities in the photoalytic medium in excess of 10 J/litre-atm. Thus, according to Fig. 7-3 (§7.2.2), flow conditioning should not seriously affect the overall system efficiency. However, if a catalytic bed is re-

quired to reconstitute the laser medium, flow costs may rise significantly. Chemical and flow costs are strongly coupled; however, we have not yet carefully examined chemical regeneration of OCSe.

**Group VI Laser Amplifier Efficiency.** The total system efficiency and scalability of photolytic Group VI laser amplifiers are sensitive to the architecture of the device and the technology risks of the design. Figure 7-40 gives key technical issues and characteristics for four different system configurations. Because many issues remain unresolved, the efficiency estimates for each configuration represent optimistic assumptions about the solution of particular technical problems. For example, damage to vuv optics and windows, laser gas reconstitution, impurity control of rare-gas medium, and excited-state kinetic lifetime are significant technical issues common to most device configurations. The advanced fluorescer configuration in Fig. 7-40 covers all proposed fluorescence pumping schemes that may achieve coupling efficiencies greater than 40%.

Table 7-12 summarizes the component and overall efficiencies for both coherently and incoherently pumped photolytic lasers that are based on the selenium transauroral line. The first row describes the conversion of raw electrical power into deposited e-beam energy in the pump. This



value represents our best guess of the optimized efficiency; it includes the diode voltage source, foil and support structure loss, and medium backscatter of electrons. The second row gives the intrinsic pump efficiency for either an  $\text{Xe}_2^+$  laser or fluorescer pump. The italicized value is conceivable if a breakthrough in laser efficiency occurs (e.g., medium absorption by photoionization might be circumvented

or it could be found much less important than currently thought). The third row summarizes total pump efficiency after flow costs. The flow penalty is higher for the windowless fluorescer in comparison with the window case because of the need for greater acoustic damping. The transport/coupling row describes the optical coupling efficiency of pump radiation to the photolytic medium. The

Table 7-12. Laser system efficiencies (%) for several selenium laser configurations.

Efficiency component	Laser system			
	Xe <sub>2</sub> <sup>+</sup> laser OCSe	Windowless fluorescer OSCe	Window fluorescer OSCe	
Pulse-forming, deposition, and fill factors (e-beam)	←————— 65 —————→			
Pump medium	5-10 20	45	45	
Pump after flow costs	3.2-6.2 12	23	29	
Transport/coupling	90	20-40 60	20-40 60	
Optical fill factors	←————— 80 —————→			
Extraction × quantum	←————— 22 —————→			
Laser electrical	0.5-1.0 1.9	0.8-1.6 2.4	1.0-2.0 3.0	
Total laser after flow in laser	0.5-1.0 1.9	0.8-1.5 2.3	1.0-1.9 2.8	

fluorescence-coupling values assume simple planar geometries; the italicized value is a hypothetical, advanced coupling scheme. The fill factor presumes an incomplete overlap of multipassed beams in the photolytic amplifier. The extraction times quantum value is obtained from the energy ratios of the 489-nm output photon to the 172-nm input photon multiplied by an assumed extraction efficiency of 60%. The final two rows summarize the projected amplifier efficiency and include a relatively small flow cost. Again, the italicized values require a breakthrough.

In conclusion, we believe that Group VI laser systems that are photolytically driven by rare-gas excimers can potentially meet the minimum efficiency requirement (1%) of a laser fusion driver. Their operation at greater than 2% efficiency may be possible but will require a significant breakthrough in photolytic driver technology. In any case, implementation of these devices will require solving several difficult technical problems.

## References

56. C. E. Turner, Jr., P. W. Hoff, and J. Taska, *Proc. Int. Topical Conf. on Electron Beam Research and Technology*, Albuquerque, N.M., 1975, Sandia Laboratories, Rept. SAND-76-5122, and *Laser Program Annual Report—1975*, Lawrence Livermore Laboratory, Rept. UCRL-50021-75 (1976), §9.
57. Xe<sub>2</sub> laser experiments have been reviewed by C. K. Rhodes, *IEEE J. Quantum. Electron.* **QE-10**, 153 (1974).
58. D. C. Lorents, *Physica* **82c**, 19 (1976).
59. M. Schafer and H. Scheibner, *Beit. Plasma Phys.* **9**, 45 (1969).
60. A. Delage and J. D. Carette, *Phys. Rev.* **A14**, 1345 (1976).
61. I. P. Zapesochnyi and P. V. Feltsan, *Optics and Spect.* **20**, 291 (1966).
62. P. V. Feltsan and I. P. Zapesochnyi, *Ukr. Fig. Zh.* **13**, 205 (1968).
63. P. S. Ganas and A. E. S. Green, *Phys. Rev.* **A4**, 182 (1971).
64. L. R. Peterson and J. E. Allen, Jr., *J. Chem. Phys.* **56**, 6068 (1972).
65. E. Eggarter, *J. Chem. Phys.* **62**, 833 (1975).
66. D. Rapp and P. Englander-Golden, *J. Chem. Phys.* **43**, 1464 (1965).
67. I. P. Zapesochnyi, E. N. Postor, and I. S. Aleksaklen, *Sov. Phys. JETP* **41**, 865 (1976).
68. D. Ton-That and M. R. Flannery, *Phys. Rev.* **A15**, 517 (1977).
69. M. R. A. Rudge, *Rev. Mod. Phys.* **40**, 564 (1968).
70. S. Trajmar, D. C. Cartwright, and W. Williams, *Phys. Rev.* **A4**, 1482 (1971); D. C. Cartwright, S. Trajmar, W. Williams, and D. L. Hvestis, *Phys. Rev. Lett.* **27**, 704 (1971).
71. D. D. Daugherty, J. A. Mangano, and J. H. Jacob, *Appl. Phys. Lett.* **28**, 581 (1976).
72. J. W. Keto, R. E. Gleason, Jr., and G. K. Walters, *Phys. Rev. Lett.* **33**, 1865 (1974).

73. K. J. McGann and M. R. Flannery, *Appl. Phys. Lett.* **31**, 599 (1977), for Xe<sup>+</sup>; H. A. Hyman, *Appl. Phys. Lett.* **31**, 14 (1977), for Xe<sup>++</sup>.
74. J. W. Keto, unpublished paper presented at the U.S.-Japan Joint Seminar on The Glow Discharge and Its Fundamental Properties, Boulder, CO, 1977.
75. H. M. Colbert, Sandia Laboratories, Rept. SCL-DR-720109 (1973).

## Author

R. A. Haas

## Major Contributors

R. D. Franklin  
J. J. Ewing  
M. J. Monsler  
C. D. Duncan

## 7.3.5 Scaling Group VI Lasers to Large Apertures

In this article, we discuss the potential scaling of photolytic Group VI lasers to power-plant size, along with the nominal sizing of a kilojoule prototype device. Two principal characteristics limit the ultimate aperture size and extractable energy content of a Group VI laser: the time the medium can store energy before quenching and the single-pass gain-lengths that can be tolerated without parasitic oscillations. Other features linked to the pump and pump coupling approach also have a secondary impact on scaling. Storage time is an important parameter because it sets an upper limit on the pump time before quenching lowers the extraction efficiency. Hence, we can obtain limits on the total number of molecules bleached. From our modeling of extraction of Group VI lasers with spatially varying gain (Section 7.3.4), we found that 50% extraction efficiency  $\eta_x$  can be achieved if  $\tau_p \leq 1.4 \tau_u$ , where  $\tau_u$  is the <sup>135</sup>I lifetime and  $\tau_p$  the pumping-pulse duration, and extraction begins only after the amplifier has been bleached. Alternatively, extraction can be time-sequenced to occur in a smaller region near the front of the bleaching wave as the medium is being photolyzed. Such a scheme will have extraction efficiencies higher than 50% and scalability somewhat improved over what we describe below, at the cost of markedly increased system complexity. If a sequenced extraction scheme is not used, then limiting the pump time — and, correspondingly, the depth to which a Group VI medium may be bleached for a given pump intensity — limits one dimension of the laser. Suppression of parasitic laser oscillation suggests that one transverse dimension is limited such that  $g_0 L \leq 4$ . A similar longitudinal constraint is assumed, although saturable absorbers or spatial separation

may be used to isolate amplifier modules along the propagation length.

Consider a Group VI amplifier photolyzed from two sides. During the pump pulse, a bleaching wave propagates into the gas a distance  $l$  from each side. Thus the transverse aperture dimension is given by  $2l$ , where  $l$  is the depth a bleaching wave can propagate in a time  $\tau_p$  at a photolyzing intensity  $I_p$ :

$$\ell = \frac{\tau_p I_p}{N^* h \nu_p} \quad (49)$$

For cases of interest, this transverse dimension is limited by kinetics to distances shorter than the transverse gain standoff limit. Assuming that one transverse dimension and the longitudinal dimension are constrained by gain standoff,

$$L_{1,2} = G_{1,2} / \sigma_L N^*,$$

where  $\sigma_L$  is the largest stimulated emission coefficient for the upper laser level. The total volume of this amplifier is given at these limits as

$$V = L_1 L_2 \cdot 2\ell = \frac{2 G_1 G_2 \tau_p I_p}{(\sigma_L)^2 (N^*)^3 h \nu_p} \quad (50)$$

The extractable laser energy for the photolytic amplifier is

$$E_x = N^* h \nu_L V \eta_x = \frac{2 G_1 G_2}{(\sigma N_A)^2} \eta_x \left( \frac{h \nu_L}{h \nu_p} \right) \tau_p I_p, \quad (51)$$

where we take  $N^*$  equal to  $N_A$ , the ground-state density assuming a yield of unity for photolytic production of excited states from precursor molecules. Note that high stored and extractable energies per aperture are obtained by decreasing  $N_A$ . This results in larger apertures, larger laser volumes, and greater total energy stored before the onset of parasitic depumping. However, the practicalities of possible laser mirror dimensions and the decrease in laser efficiency from increase in flow costs for low-specific-energy density dictates that the excited-state number density be greater than about  $2 \times 10^{16}$  per  $\text{cm}^3$ , corresponding to a volumetric extracted energy density of order 4 J/litre at 50% extraction efficiency for the transauroral line in selenium. For the photolytic S and Se lasers,  $\sigma_L = 5 \times 10^{-19} \text{ cm}^2$ ,

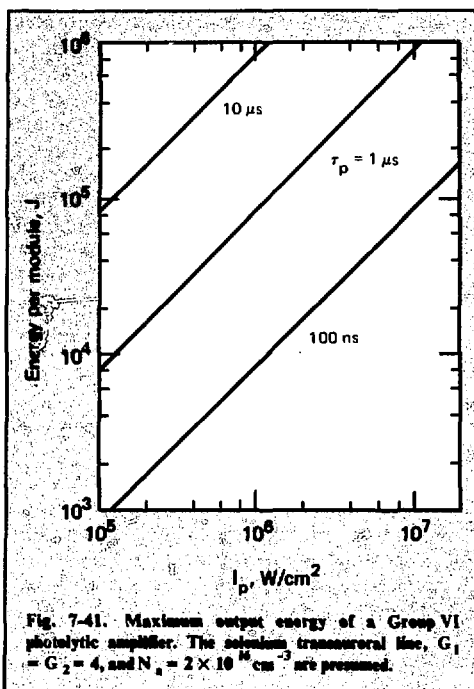


Fig. 7-41. Maximum output energy of a Group VI photolytic amplifier. The selenium transauroral line,  $G_1 = G_2 = 4$ , and  $N_A = 2 \times 10^{16} \text{ cm}^{-3}$  are presumed.

this excited-state number density corresponds to a gain of 1/m and longest gain dimensions of order 4m.

Figure 7-41 is a scaling map that shows the module energy that may be possible for a  $\text{Se}(\text{S}_{0-3}\text{P}_1)$  amplifier. (We assume two-sided irradiation from a fluorescent or laser pump.) For this case  $h\nu_L/h\nu_p = 0.35$ ,  $\sigma = 5 \times 10^{-19} \text{ cm}^2$ . The extracted energy is degraded from the total number of excited states bleached by  $\eta_x$ . We assume  $\tau_p = 0.4 \tau_L$  and  $\eta_x = 0.5$ . If  $G_1 = G_2 = 4$  and  $N^* = 2 \times 10^{16}$  per  $\text{cm}^3$ , we find that the energy stored per module is  $E_s = 5.6 \times 10^4 \tau_p I_p$ . The scaling map shows the extractable energy variation with  $I_p$ , where  $\tau_p$  is a parameter. Experiments suggest that, at  $N^* = 2 \times 10^{16} \text{ cm}^{-3}$ , the storage time may be as long as 1  $\mu\text{s}$ , giving  $\tau_p \approx 400 \text{ ns}$ . If we use excimer fluorescence pumping to bleach the medium, the pump intensity available will probably be limited to values  $\sim 2 \text{ MW/cm}^2$  (see Fig. 7-36, §7.3.4). Hence, we could achieve fluorescence-pumped amplifiers of 45-kJ energy. The amplifier dimensions would be of order 40 cm  $\times$  4 m  $\times$  4 m. The use of saturable absorbers along the laser path could yield beam-line energies of order 200 kJ, consistent with propagation of a focusable beam through the medium. For

the case of the Se laser, the bleaching intensity must be  $\sim 10^5$  W/cm<sup>2</sup> to avoid OCSe quenching in the head of the bleaching wave of the Se(<sup>1</sup>S) before the OCSe is photolysed. This can be readily obtained with a fluorescer. If longer energy storage times and pump pulse durations could be obtained, fluorescence pumping could yield a larger stored energy per aperture. However, e-beam fluence and diode closure limitations would then become important, limiting such amplifiers to roughly  $10^5$  J.

Because of their higher intensities, coherent pump sources could (in principle) allow larger Group VI apertures to be built. If we can attain intensities incident on the sides of the photolytic cell of  $10^7$  W/cm<sup>2</sup>, single apertures of order 200 kJ are possible with a  $\tau_p = 400$  ns. The efficiency of the overall system would, of course, be degraded by the projected lower efficiency of the pump lasers. Note that, even at a pump intensity of  $10$  MW/cm<sup>2</sup> for 400 ns, the bleaching wave can only propagate 1 m into the gas from each side; furthermore, transverse-gain standoff in the direction of bleaching wave propagation is not difficult, because  $\sigma_L N \tau_L \sim 2$ .

In building very large photolytic Group VI laser amplifiers, we must find satisfactory solutions for several technological problems. For the case of fluorescence pumping, high system efficiency is achieved by closely coupling the pump to the medium, preferably with a large aspect ratio of illuminated height to bleaching depth. This appears to be a very natural result in the 50-kJ fluorescence-pumped module because the bleaching depth is limited by quenching. Coupling efficiencies of order 40% should be achievable in such geometries. For large-area fluorescers, superfluorescence in the pump must be controlled to avoid depleting intensity of pump fluorescence. Broad-area e-beams must have magnetically isolated modules to prevent beam pinching in the diode; e-beam modules of order 20 per side would be required for a 50-kJ Se laser. Problems with fluorescer and laser gas mixing must be solved, if a windowless fluorescence pumped geometry is used. If a window separates the Group VI medium from the fluorescer, we must solve problems with optical damage from vuv photons, scattered electrons, and x rays from the e-beam, and mechanical fracture due to shock waves. Laser pumping is, in principle, more attractive, if we assume an efficient vuv laser source can be found. However, once found, we must still have vuv window and mirror materials to withstand the high vuv fluences of the photolytic pump.

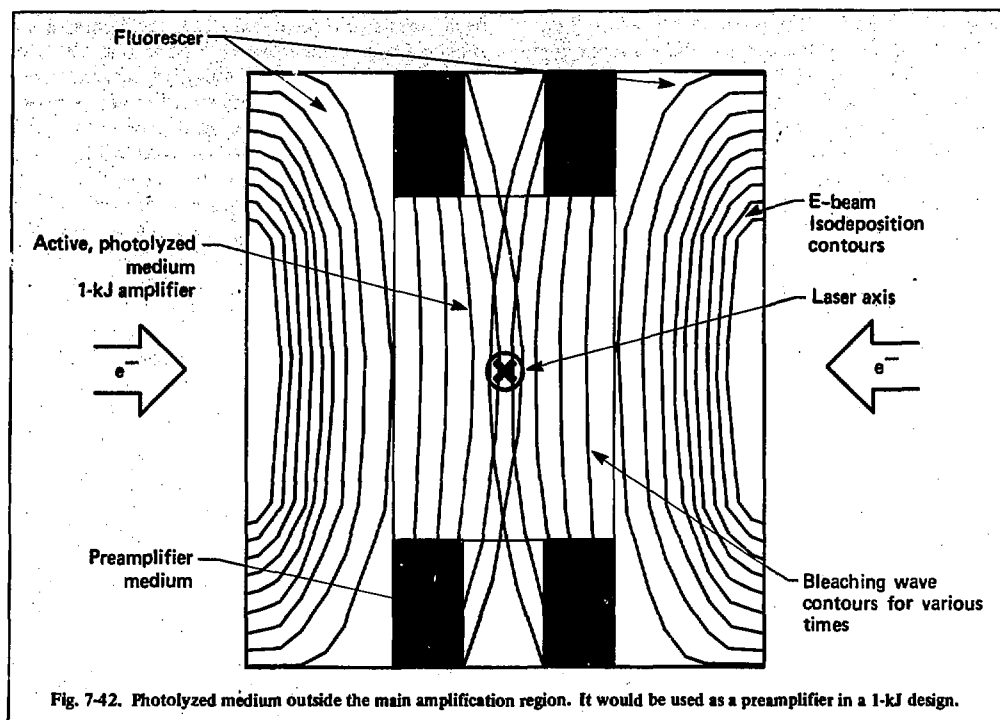
A large system naturally will contain more than the final storage amplifier. The preamplifier re-

quirements are dictated by the number of passes used to saturate the amplifier. Modeling calculations suggest that a three-pass extraction scheme will lead to reasonable efficiencies and fluence gains. For a 50-kJ amplifier with  $\sigma_0 L = 4$ , a fluence gain of order 25 could be achieved at  $\eta_x \approx 50\%$ . Accordingly, the driver for the first 50-kJ amplifier in each chain should be of order 2 kJ. An output fluence of order  $2$  J/cm<sup>2</sup> would be achieved. If we assume saturable absorbers for interstage isolation, the output from the 50-kJ amplifier could be further amplified. The extraction efficiency for these final amplifiers could be slightly higher than 50%.

A key step on the road to a large-scale photolytic Group VI system is a 1-kJ prototype. Table 7-13 gives approximate parameters for a 489-nm Se laser. The gain length, 4.2 m, and the corresponding longitudinal gain,  $\sigma_0 L = 4$ , are similar to the projected lengths for a larger amplifier. Excited-state densities of order  $3 \times 10^{16}$  cm<sup>-3</sup> are also close to what would be used in a larger scale system. This device would operate with a slightly pressure-broadened line, with a saturation fluence of  $1.3$  J/cm<sup>2</sup>. Hence, an aperture of  $375$  cm<sup>2</sup> is required to produce 1 kJ. The preamplifier must produce of order 50-100 J, to yield 50% extraction efficiencies in a three-pass system. For simplicity and low risk, we assume fluorescence pumping. We presume an amplifier of 25-cm height and 15-cm width with a fluorescence coupling efficiency of 20%. The electron current density and pump pulse duration, and the resulting photolyzing intensity would be chosen at levels such that the bleaching wave would propagate slightly more than 7.5 cm in a time such that  $\tau_p/\tau_u \approx 0.4$ . Until a greater knowledge of Se(<sup>1</sup>S) quenching kinetics is available, this remains a variable. For a case of extremely rapid quenching ( $\tau_u = 250$  ns) an e-beam current density of  $100$  A/cm<sup>2</sup> applied for 100 ns

Table 7-13. Specifications of fluorescence-pumped, 1-kJ, Se 489-nm laser.

Length	4.2 m
Height	25 cm
Depth	15 cm
On-axis gain	e <sup>4</sup>
OCSe density	$3 \times 10^{16}$ /cm <sup>3</sup>
Buffer pressure	1000 Torr
Preamplifier	50 to 100 J
Electron-beam height	30 cm (two-sided pumping)
Pump duration	$100 \text{ ns} \times \tau_u/400 \text{ ns}$
Beam current	$100 \text{ A/cm}^2 \times 400 \text{ ns}/\tau_u$



results in a bleaching depth of greater than 10 cm. For such large beam currents, diode modularization must be achieved. Longer storage times would allow the use of lower beam current densities for longer times. We can achieve scaling to larger amplifier energies by increasing the amplifier height to the transverse gain standoff limit and by bleaching the medium to a depth limited by decay kinetics and e-beam characteristics.

The preamplifier for the 1-kJ laser must also have a long gain-length because the medium has low gain. A straightforward approach uses photolyzed molecules otherwise wasted in the 1-kJ amplifier. Regions of such gas exist outside the 15-by-25 cm aperture. Calculations of the number of molecules bleached in the outer regions of a 1-kJ amplifier (see Fig. 7-42) show that ~800 J may be available. Input energies of under 1 J would be needed to extract sufficient energy from these outer edges to drive the final amplifier. Sufficiently long storage time, optical isolation, and beam cleanup from the several passes through the preamplifier would all be required.

The overall efficiency of the KJ device would be about 1%. The major steps in this efficiency

chain are the following:

- Conversion of electrical stored energy into deposited energy in the gas, 65% efficiency.
- Fluorescence efficiency, 45%.
- Coupling efficiency, 20%.

The area of maximum leverage is the coupling efficiency; factors of two improvements are likely, possibly more with advanced geometries.

#### Author

J. J. Ewing

#### Major Contributors

R. A. Haas  
M. J. Monsler  
R. D. Franklin  
C. D. Duncan

### 7.4 Laser Systems Using Rare-Earth Molecular Vapor

In the 1976 annual report, we described our continuing studies on trivalent rare-earth ( $\text{RE}^{3+}$ ) vapors and their potential as gain media for advanced fusion lasers. Two significant properties

possessed by  $\text{RE}^{3+}$  vapors vs  $\text{RE}^{3+}$  solids (i.e.,  $\text{Nd}^{3+}$ :glass) are (1) that the gas phase species can have markedly reduced self-focusing properties (because the nonlinear index  $n_2$  is expected to be smaller), thereby permitting damage-free operation and large energy extractions from amplifiers, and (2) that system operation at high average power is possible through gas recycling and cooling.

With the  $\text{RE}^{3+}$  vapors, high excited-state densities ( $>10^{17} \text{ cm}^{-3}$ ) can be maintained for usefully long times ( $>1 \mu\text{s}$ ) with projected overall wall-plug efficiencies of a few percent. This relatively high efficiency appears to be possible with recently discovered classes of efficient, though nonenergy-storing, gas lasers that are used to optically excite selected  $\text{RE}^{3+}$  vapor media. The rare-gas halide lasers are good examples of such optical pumps, e.g., KrF at 248 nm and XeF at 352 nm. Last year, we discussed the kinetics and preliminary gain studies at 1.06  $\mu\text{m}$  for NdAlCl complexes and Nd(thd)<sub>3</sub> chelate vapors as well as initial studies on TbAlCl and Tb(thd)<sub>3</sub> vapors that have potential laser transitions at 435 and 545 nm.

The following discussion on  $\text{RE}^{3+}$  vapor gain media is divided into two sections. The first section describes the updated experimental and computational work on the  $\text{Nd}^{3+}$  and  $\text{Tb}^{3+}$  vapors. The second section discusses the results of a preliminary study of systems modeling and scaling for the TbAlCl and Tb(thd)<sub>3</sub> media.

## Author

R. Jacobs

### 7.4.1 Physics Issues

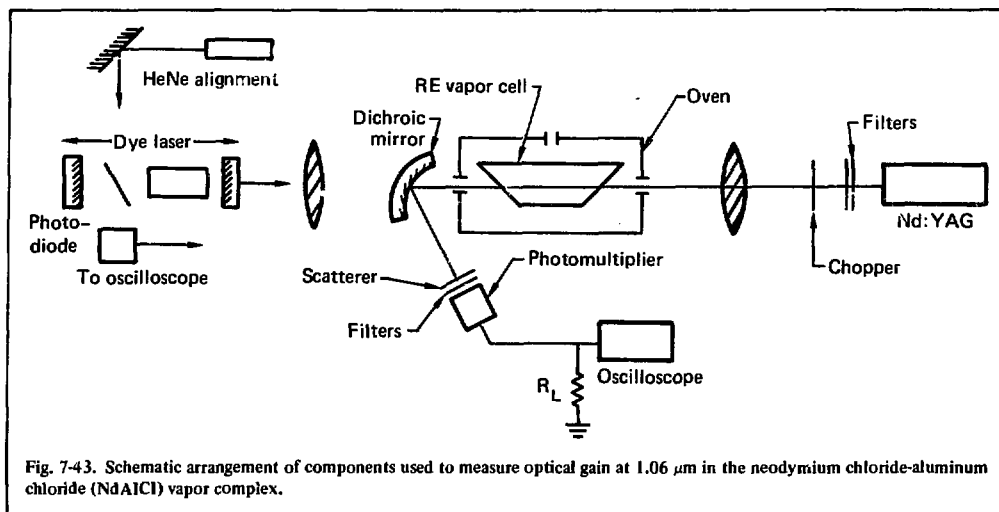
**Experimental Studies.** Of the three potential  $\text{RE}^{3+}$  vapor carriers identified last year [ $\text{RE}^{3+}$  trihalides,  $\text{RE}^{3+}$  AlCl complexes, and  $\text{RE}^{3+}$  (thd)<sub>3</sub> chelates], we continued our experimental studies on the  $\text{Nd}^{3+}$  and  $\text{Tb}^{3+}$  complexes and chelates. The  $\text{RE}^{3+}$  trihalides are considered to be less attractive because of their low vapor pressures, i.e.,  $\approx 1$  Torr at  $>1000^\circ\text{C}$ ; such elevated temperatures would have a strong negative impact on overall laser system efficiencies and complicate the problems of materials compatibility.

**NdAlCl Complexes.** We studied the kinetics behavior of the  $\text{Nd}^{3+}$ : $^4\text{F}_{3/2}$  level at 1.06  $\mu\text{m}$  ( $^4\text{F}_{3/2} \rightarrow ^4\text{I}_{11/2}$  transition) for the NdAlCl complexes under conditions of weak<sup>76</sup> and strong<sup>77,78</sup> excitation, i.e., low and high excited-state densities. The main conclusion from these studies was that

excited-state densities of  $\approx 2 \times 10^{17} \text{ cm}^{-3}$ , corresponding to a stored energy density of  $\approx 35 \text{ J/litre}$  at 1.06  $\mu\text{m}$ , could be sustained for usefully long times ( $>10 \mu\text{s}$ ). During the past year, such conditions were exploited<sup>79</sup> to demonstrate optical gain for the experimental arrangement diagrammed in Fig. 7-43. A 33-cm-long, temperature-regulated oven surrounds a double Brewster-angle quartz cell (1.6 cm i.d., 18 cm long) containing NdCl<sub>3</sub> and AlCl<sub>3</sub> as the starting materials. For the cell temperature range used in the gain measurements (300 to 450  $^\circ\text{C}$ ), the NdAlCl vapor varies in pressure from 15 to 60 Torr while the pressure of the Al<sub>2</sub>Cl<sub>6</sub> complexing agent varies from 6 to 7 atm. An etalon-tuned, flashlamp-pumped dye laser (Candella ED 6254) with a flat-flat resonator structure optically excites the  $\text{Nd}^{3+}$  ions at 5872 Å and thus produces a population inversion between the  $\text{Nd}^{3+}$ : $^4\text{F}_{3/2}$  and  $^4\text{I}_{11/2}$  states. The dye laser medium consists of a  $3 \times 10^{-5} \text{ M}$  solution of rhodamine 6G in methanol.

We obtained maximum dye laser energies at 5872 Å ( $\pm 3$  Å) of 1 to 2 J with pulse lengths of 1 to 1.5  $\mu\text{s}$ . The multimode output of the dye laser decreases about 50% in energy after a few days operation and remains fairly stable thereafter. The pump energy is focused by a 115-cm focal length lens through a curved (60-cm radius), dielectric-coated quartz substrate and into the rare-earth vapor cell. The dichroic mirror transmits 95% at 5872 Å and reflects 99% at the 1.064- $\mu\text{m}$  wavelength of the counterpropagating Nd:YAG probe laser (General Photonics YAG2,  $\approx 70\text{-mW}$  output power). Measurements with the NdAlCl cell removed indicate that  $\geq 25$  to 50 mJ is directed along the 1-cm length of the cell position within a 0.64-mm diameter (determined using stainless steel pinholes). This pump energy density, considered in conjunction with vapor pressure data and absorption cross sections,<sup>80</sup> is sufficient to excite one-half of the available NdAlCl molecules in the irradiated volume to the  $\text{Nd}^{3+}$ : $^4\text{F}_{3/2}$  state.

The Nd:YAG probe laser depicted in Fig. 7-43 has its TEM<sub>00</sub> mode output amplitude modulated with the indicated chopper wheel into 1-ms-long pulses, during which interval the dye laser pulse is generated. The probe laser is focused by a 100-cm focal length lens that spatially and temporally overlaps the optically pumped rare-earth vapor volume (focused probe beam diameter  $\leq 0.6 \text{ mm}$ ). The probe laser beam is then directed by the angled mirror onto an S-1 sensitive photomultiplier tube (RCA 7102, 1.25-in.-diam photocathode); output from the photomultiplier tube is displayed on an oscilloscope with differential amplifiers (Tektronix 555) to monitor the voltage generated



across a  $50\text{-}\Omega$  load resistor. The chopper wheel, with its light-emitting diode and detector, controls the triggering of both the dye laser and oscilloscope. A coarsened, fused silica substrate diffuses the probe laser beam before it passes through a  $200\text{-}\text{\AA}$  (FWHM) bandpass filter at  $1.064\ \mu\text{m}$  for detection by the photomultiplier.

Optically induced thermal inhomogeneities (schlieren effects) in the vapor medium are manifested as the probe laser intensity decreases via displacement of the  $1.06\text{-}\mu\text{m}$  beam in tests with the scattering plate removed and with small (1- to 2-mm diameter) apertures placed in front of the bandpass filter. Depending on the dye laser energy and the rare earth cell pressures, the time scale for such disturbances is observed as soon as  $10\ \mu\text{s}$  after the excitation pulse. In separate tests using the  $4416\text{-}\text{\AA}$  output of a HeCd laser as a probe beam, the schlieren effects are observed to occur on a comparable time scale. Accordingly, for the gain measurements, the diffuser, filter, and photomultiplier face are placed fairly close ( $\approx 15\ \text{cm}$ ) to the dichroic mirror to provide as large a solid angle for detection as possible (see Fig. 7-43). This technique eliminates the schlieren effects on the detected probe laser intensity. However, with this arrangement, some vapor fluorescence in the  $1.06\text{-}\mu\text{m}$  spectral region is inevitably detected. Thus, two traces are required to obtain the temporal evolution of the net optical gain: first, the probe and fluorescence signals are recorded together,  $I_p + I_f$ , and then, the fluorescence intensity  $I_f$  from a second excitation of the neodymium vapor, with the pulse laser blocked,

is subtracted from the  $I_p + I_f$  signal (see Fig. 7-44). For these two-part-gain data, the pulsed dye laser amplitude is recorded with a photodiode on a second channel of the dual-trace oscilloscope (Fig. 7-43) to ensure that the excitation intensity is constant. The zero intensity value for the chopped probe beam is offset from view in Fig. 7-44 so that the  $I_p + I_f$  and  $I_f$  signals are recorded on the same sensitivity range. The indicated 10% gain flag is referenced to this offset baseline. The unamplified

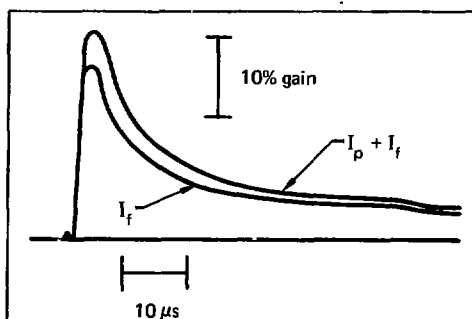


Fig. 7-44. Representative reduced gain data at  $1.06\ \mu\text{m}$  in the neodymium chloride-aluminum chloride ( $\text{NdAlCl}$ ) vapor complex at  $350^\circ\text{C}$ . The oscilloscope trace labeled  $I_p + I_f$  is a sum of the probe laser (with baseline offset) and rare earth vapor fluorescence signals. The scope trace designated  $I_f$  is a temporal record of the fluorescence with the probe laser blocked. Thus, the time-dependent optical gain in the medium is the difference between the two traces.



peak probe beam amplitude in Fig. 7-44 is represented by the horizontal straight line.

As seen in Fig. 7-44, the peak single-pass optical gain for the excited NdAlCl vapor is  $\approx 4$  to 5%, corresponding to a gain coefficient of  $\geq 0.25\%/cm$ . A simple comparison can be made with the expected peak gain by evaluating  $\exp(\Delta N \sigma_L L)$ , where  $\Delta N$  is the inversion density,  $\sigma_L$  is the stimulated emission cross section at  $1.06\ \mu m$ , and  $L$  is the vapor gain length. The inversion density  $\Delta N$  for the cell conditions represented by Fig. 7-44 is one-half the available number density of NdAlCl molecules, or  $\Delta N \approx 2 \times 10^{17}\ cm^{-3}$ . Taking  $\sigma_L$  to be  $\approx 2 \times 10^{-20}\ cm^2$  from the Judd-Ofelt analysis,<sup>77</sup> the estimated single-pass gain at  $1.06\ \mu m$  for the 18-cm-long cell ( $L$ ) therefore is  $\approx 8\%$ , for a gain coefficient of  $\approx 0.4\%/cm$ . Considering the relatively coarse determinations of  $\Delta N$  and  $\sigma_L$ , the agreement between the predicted and observed gains is satisfactory. We obtained similar results for  $\sigma_L$  in gain measurements over the temperature range from 300 to 450°C. The gain signal amplitudes are observed to be appropriately dependent on the optical excitation intensity, the degree of overlap between the pump and probe laser beams, and the NdAlCl vapor density.

Despite the existence of optical gain for the NdAlCl vapor medium, three sources of cumulatively larger intracavity loss prohibit the demonstration of laser oscillation, i.e., window etching, impurities, and schlieren effects. Further details on this aspect are given in Ref. 79.

The NdAlCl vapor gain medium can be scaled to larger dimensions in an efficient manner by using the relatively efficient XeF discharge laser at 351 nm as the optical excitation source after resonant Raman laser conversion in barium vapor to the 585-nm spectral region. A photoconversion efficiency  $> 80\%$  has been demonstrated for this case.<sup>81</sup>

**Nd(thd)<sub>3</sub> Chelates.** The volatile (10 Torr at 235°C) and thermally stable<sup>82</sup> RE(thd)<sub>3</sub> chelates (2,2,6,6-tetramethyl-3,5-heptanedione) are potential laser media, in part because of their relatively large Judd-Ofelt intensity parameters.<sup>83</sup> In contrast to the two-component transition metal trihalides discussed above, the gaseous RE<sup>3+</sup>(thd)<sub>3</sub> chelates offer the practical advantage of being a low-total-pressure, single-component vapor.

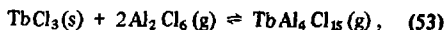
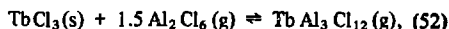
With this motivation, we monitored the  $1.06\text{-}\mu m$  fluorescence decay from vapor phase Nd(thd)<sub>3</sub> as a function of local number density and temperature, using the previously described flash-lamp-pumped dye laser for direct excitation into the Nd<sup>3+</sup> 587-nm absorption band.<sup>78</sup> The  $1.06\text{-}\mu m$  fluorescence decay rate for the Nd<sup>3+</sup>:<sup>4</sup>F<sub>3/2</sub> level is seen to be essentially independent of (1) local

temperature for a fixed number density and (2) Nd-chelate molecular number density for a fixed ambient temperature. The first behavior contrasts markedly with observed Tb(thd)<sub>3</sub> chelate vapor kinetics, whereas the second feature is similar to previous work.<sup>84</sup> The peak fluorescence intensity at  $1.06\ \mu m$  for the Nd(thd)<sub>3</sub> chelate is observed to scale essentially linearly with pump intensity up to flux values of  $\approx 10\ MW/cm^2$ , indicating that no significant multiphoton absorption or molecular dissociation processes occur on the pumping time scale. The fluorescence lifetime of about  $0.5\ \mu s$  is found to be independent of excited state density for excited-state densities  $\geq 10^{17}\ cm^{-3}$  ( $\geq 25\ J/litre$ ). Such kinetic behavior is consistent with a deactivation mechanism that is dominated by the excitation of a few high-energy molecular vibrations. Accordingly, deuterated and fluorinated RE(thd)<sub>3</sub> chelates (which have lower energy fundamental vibrations) may exhibit longer fluorescence lifetimes.

We also made gain measurements for the Nd(thd)<sub>3</sub> chelate vapor subsequent to the NdAlCl studies.<sup>79</sup> This lower gain Nd<sup>3+</sup> vapor species required a significantly more stable  $1.06\text{-}\mu m$  probe laser to generate reproducible results. However, as noted, the kinetics studies do reveal that  $\geq 25\ J/litre$  can be stored in the Nd-chelate vapor for times of  $\approx 1\ \mu s$ , suitably long for laser fusion purposes.

**TbAlCl Complexes.** There are at least three reasons for preferring Tb<sup>3+</sup> over Nd<sup>3+</sup> vapor for a fusion laser gain medium: (1) the terbium vapor uses the output of the efficient KrF laser at 248 nm directly, whereas the neodymium vapor requires Raman shifting of the 351-nm XeF laser wavelength, (2) the laser cross section for Tb<sup>3+</sup> is estimated<sup>85</sup> to be about 2.5 times larger than that for Nd<sup>3+</sup>,  $5 \times 10^{-20}\ cm^2$  vs  $2 \times 10^{-20}\ cm^2$ , respectively, and (3) the terbium transition wavelengths are in the visible spectral region, not in the near infrared, and thus may be better suited for laser fusion target coupling, i.e., 435 and 545 nm for Tb<sup>3+</sup> vs  $1.06\ \mu m$  for Nd<sup>3+</sup>.

Analogous to the work by Øye and Gruen<sup>80</sup> on NdAlCl complexes, the following reactions are considered operative in forming the TbAlCl molecular vapor from the TbCl<sub>3</sub> and AlCl<sub>3</sub> starting materials:



where s and g refer, respectively, to the solid and gaseous phases. The vapor pressure properties of

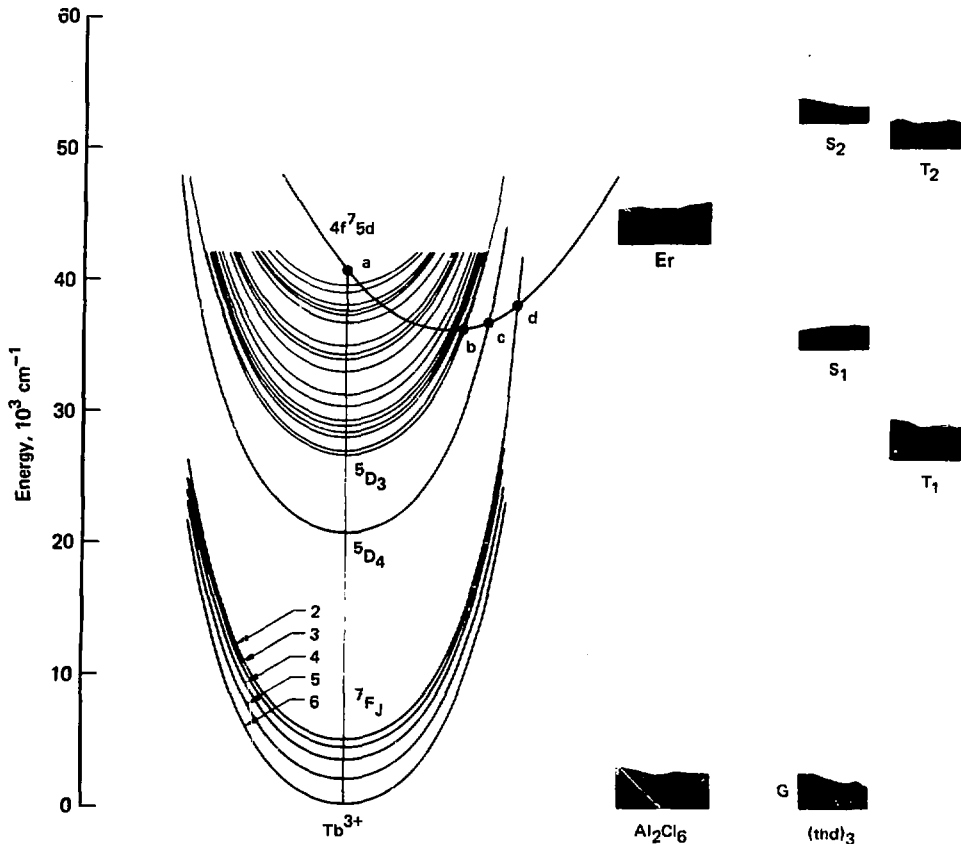


Fig. 7-45. The  $\text{Tb}^{3+}$  configuration coordinate diagram for the  $\text{TbAlCl}_6$  complex and  $\text{Tb}(\text{thd})_3$  chelate molecular vapors. Also shown are the electronic states of  $\text{Al}_2\text{Cl}_6$  and the singlet and triplet manifolds of the chelate.

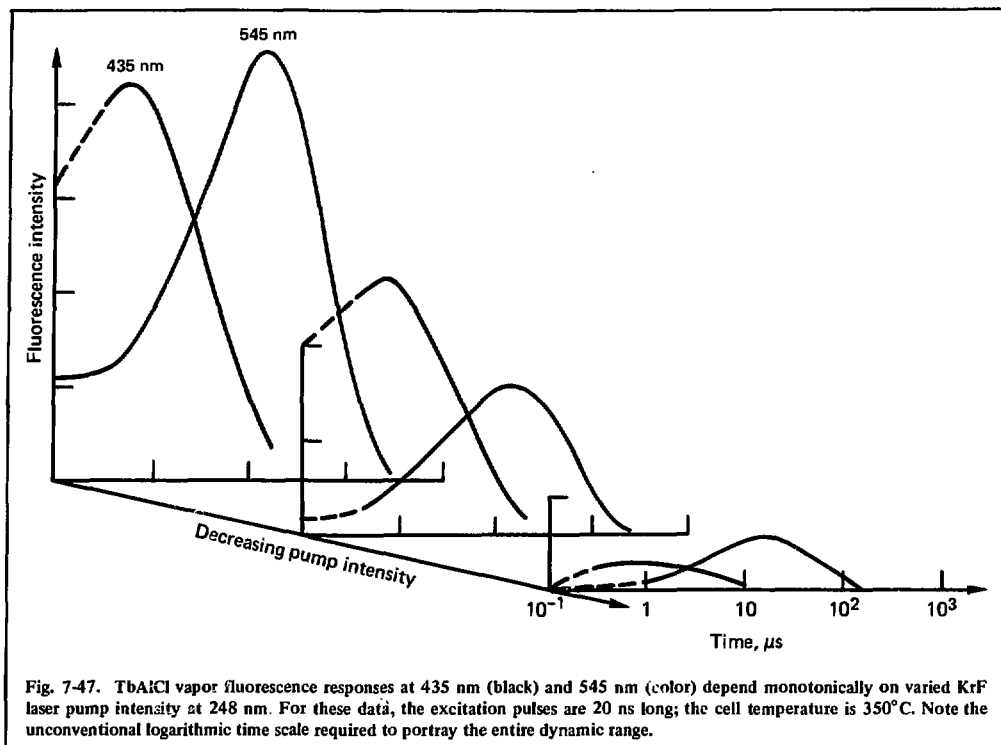
Fig. 7-46. Fluorescence from the TbAlCl complex vapor at 435 and 545 nm, excited by 20-ns-long focused KrF radiation (248 nm) entering at the left of the oven-heated cell. The quartz cell diameter is  $\approx 1$  in. The edge of the Brewster-angle window can be discerned.



Pumping of large-scale TbAlCl systems is contemplated with long-pulse ( $\approx 1 \mu\text{s}$ ) KrF lasers via excitation of the  $4f^75d$  electronic state. This energy is expected to convert to the multitude of closely spaced  $4f^8$  electronic levels followed by rapid ( $<100$  ns) nonradiative relaxation to the  $^5D_3$  metastable level. Further transfer of energy from  $^5D_3$  to  $^5D_4$  can proceed more slowly through a near-resonant bimolecular collision of the type  $\text{Tb}(^5D_3) + \text{Tb}(^7F_6) \rightarrow \text{Tb}(^5D_4) + \text{Tb}(^7F_0)$ . The quenching rate for this process is estimated to be  $5 \times 10^{-13} \text{ cm}^3/\text{s}$  on the basis of related  $4f$ - $4f$  collisional interaction probabilities observed for the NdAlCl vapor.<sup>76</sup> Direct  $4f^75d \rightarrow ^5D_3$  and  $4f^75d \rightarrow ^5D_4$  energy transfers are also possible (points b and c, Fig. 7-45); the efficiency of these processes depends on the precise shape, location, and interaction strength between the  $4f^8$  and  $4f^75d$  potential surfaces. The possibility of  $4f^75d$  level relaxation directly to the  $4f^8$  ground electronic state (point d, Fig. 7-45) is judged to be unlikely for this molecule based on semiempirical molecular orbital calculations<sup>87</sup> and high values for excited-state quantum yields in preliminary experiments.<sup>88</sup>

Figure 7-46 shows the fluorescence from TbAlCl vapor at 435 and 545 nm excited by focused 248-nm KrF laser pulses of 20-ns duration.<sup>89</sup> The photograph is taken through a purposely enlarged section of the temperature-regulated oven. The KrF laser pump intensity was varied up to values of  $10 \text{ MW}/\text{cm}^2$ . In Fig. 7-46, the right-angle geometry with respect to the pump beam axis is used to monitor the  $\text{Tb}^{3+}$  vapor fluorescence responses with suitable optical filters and photomultipliers. The same geometry is used with a pair of calibrated pinholes and a photomultiplier to observe a well-defined viewing region in the emitting volume to help determine the time-dependent quantum yields of the excited state.

Figure 7-47 illustrates the temporal behaviors for the TbAlCl complex fluorescence intensities at 435 and 545 nm for parametrically reduced KrF laser pump flux at the fixed cell temperature of  $350^\circ\text{C}$ . The 20-ns-long, 248-nm pump intensity is reduced by a factor of about three for the middle traces and by another factor of three for the traces at the right side of Fig. 7-47. We note that the fluorescence intensities properly decrease with



diminishing excitation flux. However, detailed differences do exist between relative peak heights in a nonmonotonic fashion; these are currently being interrogated with computer modeling. As expected, the 545-nm fluorescence response consists of a prompt component (see point c, Fig. 7-45) followed by an augmented component that is well correlated with collisional transfer from the  $^5D_3$  metastable level of  $Tb^{3+}$  as evidenced by the telltale decay of the 435-nm fluorescence.

The decay time constant for the 545-nm intensity is  $\approx 100 \mu s$ , significantly less than the few milliseconds predicted for the radiative lifetime.<sup>86</sup> This difference is attributed to a combination of excited-state-excited-state bimolecular collisional deactivation and nonradiative decay. The responsible mechanisms and characteristic rates are being evaluated with computer codes that use data as a function of pump flux for a fixed cell temperature and, as represented by Fig. 7-48, where the roles of these fixed and variable parameters are interchanged. For the 300°C cell temperature case, the radiative lifetime for the  $^5D_4$  state, as represented by the 545-nm decay, approaches the predicted

value of a few milliseconds. The traces for the higher temperature case at 450°C, taken at the same excitation flux, show markedly reduced fluorescence lifetimes for the  $Tb^{3+}:^5D_3$  and  $^5D_4$  metastable states. Again, the reduction in the  $^5D_4$  lifetime is attributed both to excited-state-excited-state collisional quenching and to nonradiative deactivation.

We can estimate the  $^5D_4$  excited-state density for 450°C at  $\approx 10 \mu s$  with a knowledge of the ground-state molecular density ( $\approx 2 \times 10^{18} \text{ cm}^{-3}$ ), the measured<sup>88</sup> absorption cross section at 248 nm ( $\approx 1.3 \times 10^{-19} \text{ cm}^2$ ), and the focused pump flux, along with an assumed unit value for the excited-state quantum yield (i.e., one excited state generated per absorbed pump photon). The estimate gives a  $^5D_4$  excited-state density of about  $7 \times 10^{-16} \text{ cm}^{-3}$  at 450°C, corresponding to a stored energy density of 25 J/litre. As seen in Fig. 7-48, this inversion is sustained for the relatively long time, for laser fusion purposes, of 10  $\mu s$ . This inversion density, when combined with the estimated<sup>85</sup> laser cross section for the  $Tb^{3+}:^5D_4 \rightarrow ^7F_5$  transition at 545 nm of  $5 \times 10^{-20} \text{ cm}^2$ , yields a gain coefficient of

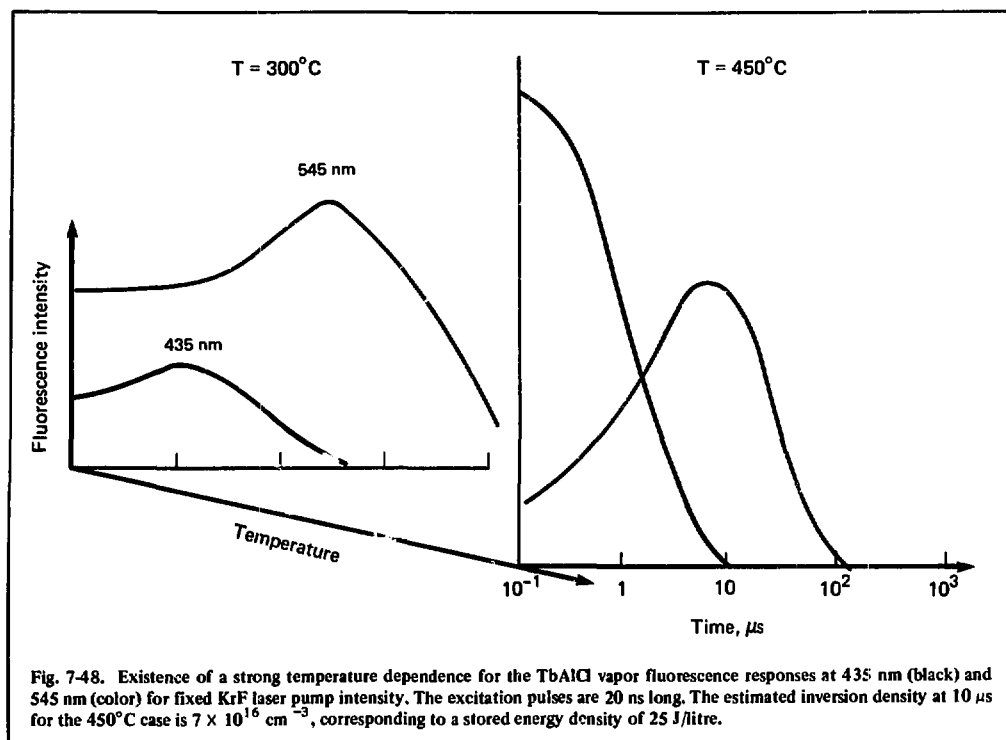


Fig. 7-48. Existence of a strong temperature dependence for the  $\text{TbAlCl}$  vapor fluorescence responses at 435 nm (black) and 545 nm (color) for fixed KrF laser pump intensity. The excitation pulses are 20 ns long. The estimated inversion density at 10  $\mu\text{s}$  for the 450°C case is  $7 \times 10^{16} \text{ cm}^{-3}$ , corresponding to a stored energy density of 25 J/litre.

0.3%/cm. Such performance properties make the  $\text{TbAlCl}$  vapor complexes attractive gain media for advanced fusion laser systems.

The kinetics data, as exemplified by Figs. 7-47 and 7-48 for the  $\text{TbAlCl}$  vapor complexes, are computer-fitted, using the simple rate equation model depicted in Fig. 7-49. The objective of the modeling is to elicit the various rate constants indicated in the figure and thereby characterize the energy flow for the excited  $\text{TbAlCl}$  vapor medium. The  $\text{Tb}^{3+} : ^5\text{D}_3 \rightarrow ^5\text{D}_4$  collisional transfer is described by  $k_T$ , whereas the bimolecular encounters of interacting pairs of  $^5\text{D}_3$  or  $^5\text{D}_4$  excited molecules are represented by the rate constants  $k_{33}$  and  $k_{44}$ , respectively. Typical results from such a computer fitting procedure<sup>90</sup> are displayed in Fig. 7-50. For this case, the agreement between experiment and the simple rate equation formalism is quite good. Although this work is still in progress,<sup>90</sup> the preliminary value for  $k_T$  is  $\approx 7 \times 10^{-13} \text{ cm}^3/\text{s}$ . Best fitted values for the other rates in Fig. 7-50 are the subject of a future publication.

We attempted a laser demonstration for the  $\text{TbAlCl}$  molecular complexes to exploit the

favorable conditions implied by the kinetics studies.<sup>91</sup> The experimental approach is similar to that shown in Fig. 7-43 for  $\text{NdAlCl}$ , except that for the  $\text{Tb}^{3+}$  vapor a focused 1-J KrF laser is used to excite a 50-cm-long complex cell at 350°C. The relevant input dichroic mirror transmits >85% at 248 nm and reflects >98% at 435 and 545 nm. The output mirror coupling is a few tenths of a percent at these wavelengths. No laser oscillation was observed in the initial tests, for which the single-pass gains are evaluated to be only 8 to 10% per pass. This evaluation assumes no excited-state absorption ESA, the published value for the laser cross section<sup>85</sup>  $\sigma_L$ , and unit quantum yield QY for generating the  $\text{Tb}^{3+}$  metastable states. Because the laser attempts were effectively an integration of these uncertainties, additional work is needed to pinpoint the precise single pass gains; i.e., optical gain measurements are needed to address the issues of ESA and  $\sigma_L$  value, along with refined determinations for QY. Obviously, a slight reduction in either  $\sigma_L$  or QY could produce single-pass gains too low to overcome the fixed intracavity losses and therefore prevent laser action.

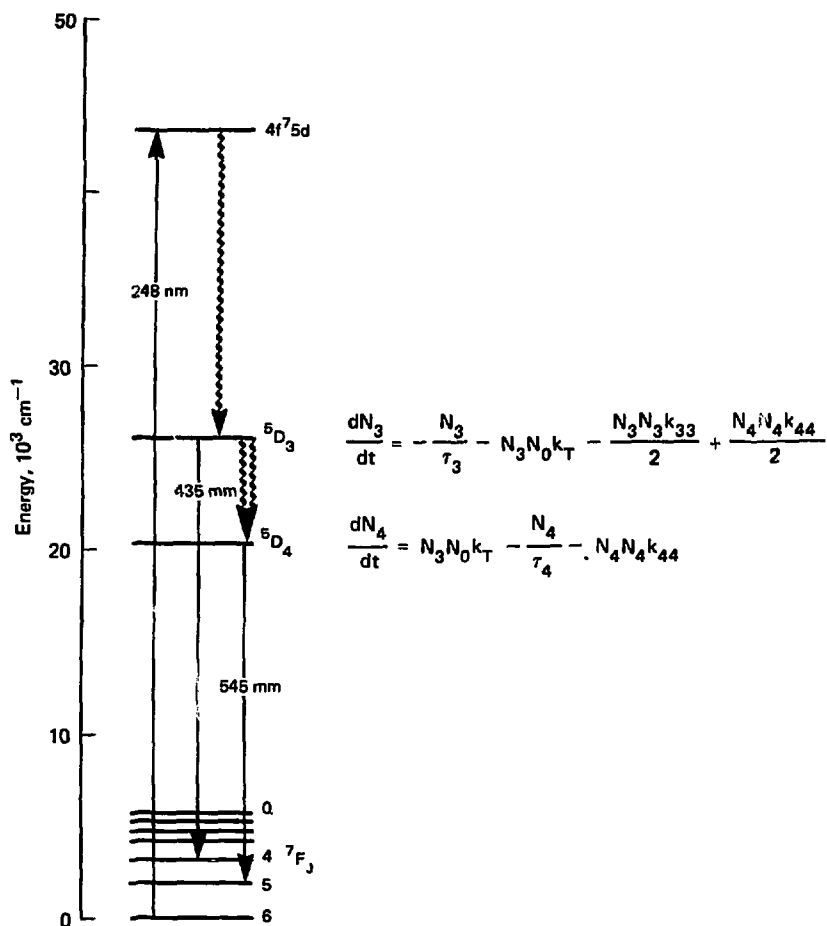


Fig. 7-49. Simple rate-equation model for characterizing the  $\text{TbAlCl}_3$  vapor fluorescence responses as represented in Figs. 7-47 and 7-48. The  $\text{Tb}^{3+}$ :  $^5D_3 \rightarrow ^5D_4$  collisional transfer rate is  $k_T$ ; excited-state deactivation rates are designated as  $k_{33}$  and  $k_{44}$ .

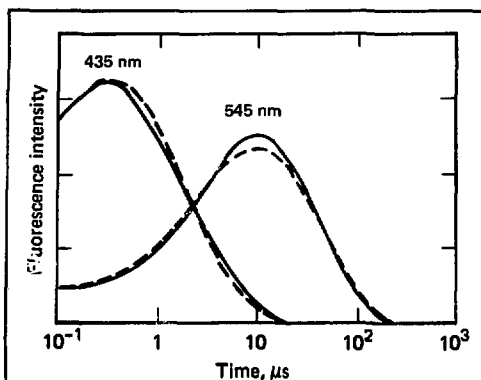


Fig. 7-50. Re-presentative results at 400°C, comparing observed fluorescence responses for TbAlCl<sub>3</sub> vapor complexes, as in Figs. 7-47 and 7-48, against the rate-equation model shown in Fig. 7-49. The relative amplitudes at 0.1 μs were varied parameters along with the parameters shown in Fig. 7-49. Solid curves denote actual data; dashed curves denote computer fitting.

fluorescence from the  $^5D_3$  state is not detected, implying either rapid deactivation of this level ( $< 20$ -ns pump pulse length) or the absence of any chelate excitation transfer to this state.

Results for  $^5D_4$  relaxation have been obtained for a fixed molecular number density ( $7 \times 10^{16} \text{ cm}^{-3}$

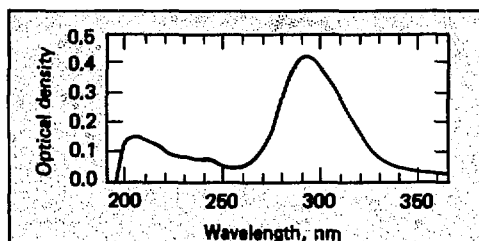
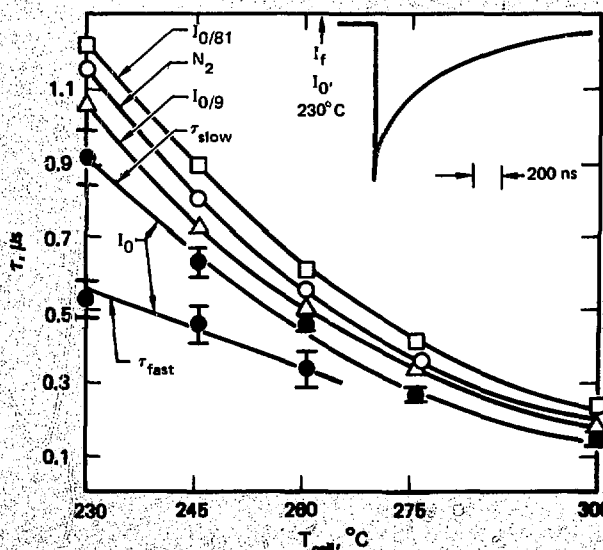


Fig. 7-51. Absorption spectrum for Tb(thd)<sub>3</sub> chelate vapor taken with a temperature-regulated spectrophotometer. For these data, a 1-cm-long sample was used and maintained at 160°C.

at 200°C) as a function of ambient temperature and 248-nm-pump intensity by using a two-temperature cell.<sup>84</sup> As seen in Fig. 7-52, lifetimes for weak pump fluxes monotonically decrease from 1.2 to 0.2 μs for increases in local temperature from 230 to 300°C. These findings are in agreement with the earlier study<sup>84</sup> that used relatively low intensity nitrogen laser excitation at 337 nm (designated as the N<sub>2</sub> trace in Fig. 7-52). As seen in Fig. 7-52 and its insert, the highest pump flux  $I_0$  produces decay traces that are clearly resolved into two decay times,  $\tau_{\text{fast}}$  and  $\tau_{\text{slow}}$ . The fast decay times are ascribed to excited state-excited state nonradiative processes involving bimolecular encounters of Tb<sup>3+</sup>: $^5D_4$  species. In all cases, the  $^5D_4$  level is strongly

Fig. 7-52. Dependence of the  $^5D_4$  fluorescence lifetime in Tb(thd)<sub>3</sub> chelate vapor on the ambient temperature  $T_{\text{cell}}$  for a fixed number density  $\tau_{\text{slow}}$  (and adjacent curves) and on the intensity of the uv pump laser  $\tau_{\text{fast}}$ . The various curves for  $\tau_{\text{slow}}$  are attributed to varying local heating conditions as a function of varied pump flux. For all cases, the fluorescence lifetimes are significantly reduced from the radiative value of  $\approx 1$  ms. The responsible quenching mechanisms are discussed in the text.



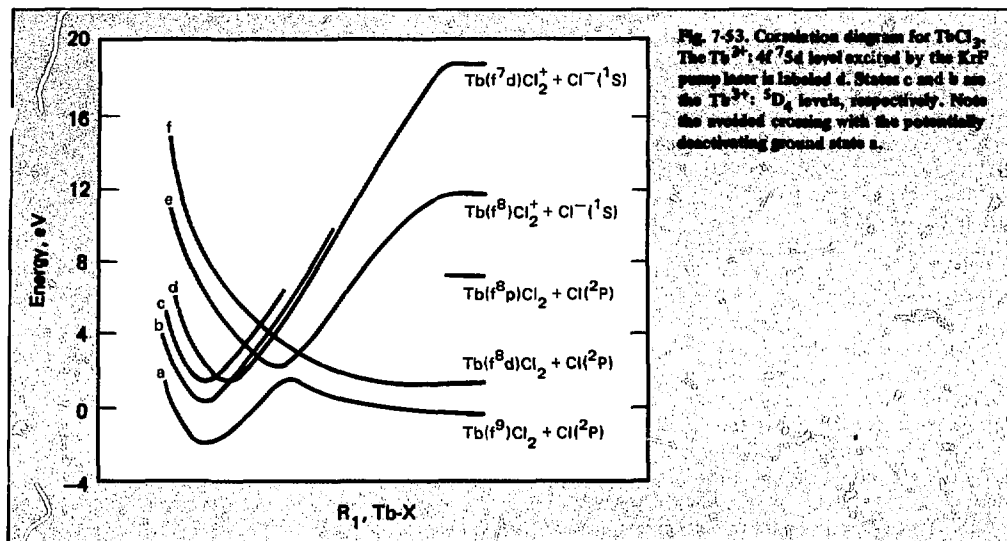


Fig. 7-53. Correlation diagram for  $\text{TbCl}_3$ . The  $\text{Tb}^{3+} 4f^7 5d$  level excited by the KrF pump laser is labeled d. States c and b are the  $\text{Tb}^{3+} {}^5D_4$  levels, respectively. Note the avoided crossing with the potentially deactivating ground state a.

quenched from its radiative lifetime of  $\approx 1$  ms through intramolecular deactivation by the carrier chelate.<sup>84</sup> The slight offsets among the various decay curves in Fig. 7-52 are attributed to the effects of local gas heating subsequent to excitation by the uv lasers.

For  $\text{Tb}(\text{thd})_3$  laser amplifiers at  $200^\circ\text{C}$  (Fig. 7-52), and again assuming unit quantum efficiency for excited-state generation per absorbed pump photon, inversion densities of  $\approx 7 \times 10^{16} \text{ cm}^{-3}$  (25 J/litre) are sustained for times of  $\approx 0.33 \mu\text{s}$ . Preliminary quantum yield measurements have been made, but we require more accurate spectroscopic input parameters to ascertain final values. Because of the tortuous pathways the excitation energy must traverse before reaching the  $\text{Tb}^{3+} {}^5D_4$  level, it is quite possible that the excited-state generation efficiency could be appreciably less than unity. Thus, the ultimate utility of this advanced fusion laser candidate depends critically on this efficiency.

**Theoretical Studies.** Theoretical studies on candidate rare-earth vapor lasers have consisted of approximate molecular orbital calculations to determine the electronic structures of candidate compounds and possible decomposition products. We have constructed a qualitative picture of the potential curves for the dissociation of the rare earth trihalides. Calculations have been completed on  $\text{Tb}(\text{AlCl}_4)_3$  and the electronic structure is found to be very similar to  $\text{TbCl}_3$ . We carried out similar calculations on  $\text{AlCl}_3$  and  $\text{Al}_2\text{Cl}_6$  to identify possible absorptions in an  $\text{RE}(\text{AlCl}_4)_3$  laser medium.

Results of calculations conducted previously,<sup>92,93</sup> were used in conjunction with spectroscopic data and chemical intuition to estimate the shapes of the potential curves describing the dissociation process  $\text{TbCl}_3 \rightarrow \text{TbCl}_2 + \text{Cl}$ . The curves, which describe the ground state and a few low lying excited states, are shown in Fig. 7-53. The relative positions of the excited states of  $\text{TbCl}_3$  were estimated, using semiempirical molecular orbital methods (a,d-f); experimental f-f transitions were used to position excited states with different f electron coupling (b,c). Experimental data were used to position the asymptotic states. The topology of the lowest f $\rightarrow$ d excited curve (d) was inferred from experimental data that indicate that the vertical transition from the ground state (a) strikes the repulsive wall of the excited state. The only curve-crossing expected in this system is crossing of the charge transfer configuration that gives rise to the binding of the molecules.

We have completed calculations on two geometries of  $\text{TbAl}_3\text{Cl}_{12}$ . The purpose of these calculations was to test our hypothesis that the rare earth trihalides could be used as a model for larger and more complicated trivalent rare earth compounds that are being considered as fusion laser vapor gain media. Semiempirical molecular orbital methods were used to study this system, which included 108 electrons. Two molecular geometries were used: one with  $D_{3h}$  symmetry, the other with  $D_3$  symmetry. Both correspond to reasonable molecular structures. The calculated charges on the various atoms indicate that there is little difference



between the two geometries, particularly for the charge on the terbium. The effect of the complex ligand on the electronic structure is to provide for additional excited states. However, because the unoccupied orbitals available for excitation are all centered on the rare earth, the transition probabilities are expected to be very small. The positions of these excited states are very close to those calculated for  $TbCl_3$ . The only difference is the larger energy separation between the lowest and highest unoccupied d orbitals for terbium. This is a characteristic ligand effect and very difficult to predict a priori.

Semiempirical calculations also have been carried out on  $AlCl_3$  and  $Al_2Cl_6$ . The positions of the excited states were determined: the first excited state in  $AlCl_3$  is 5 eV above the ground state, and the first excited state in  $Al_2Cl_6$  is greater than 10 eV above the ground level. These results rule out absorption as a possible loss mechanism in the laser media. However, the short wavelength transition for  $Al_2Cl_6$  may affect the nonlinear index of refraction that depends inversely on wavelength.

## References

76. R. R. Jacobs, W. F. Krupke, J. P. Hessler, and W. T. Carnall, *Opt. Commun.* **21**, 395 (1977).
77. R. R. Jacobs and W. F. Krupke, *Electronic Transition Lasers II*, L. E. Wilson, S. N. Suchard, and J. I. Steinfeld, Eds. (MIT Press, Cambridge, MA, 1977).
78. W. F. Krupke and R. R. Jacobs, in *The Rare Earth In Modern Science and Technology*, G. J. McCarthy and J. J. Rhyne, Eds. (Plenum Press, New York, 1978), p. 519.
79. R. R. Jacobs and W. F. Krupke, *Appl. Phys. Lett.* **32**, 31 (1978).
80. H. A. Øye and D. M. Gruen, *J. Amer. Chem. Soc.* **91**, 2229 (1969).
81. N. Djeu and R. Burnham, *Appl. Phys. Lett.* **30**, 473 (1977).
82. J. E. Sicre, J. T. Dubois, K. J. Eisentraut, and R. E. Sievers, *J. Amer. Chem. Soc.* **91**, 3476 (1969).
83. D. M. Gruen, in *Progress in Inorganic Chemistry*, S. J. Lippard, Ed. (Wiley-Interscience, NY, 1971), Vol. 14, p. 119.
84. R. R. Jacobs, M. J. Weber, and R. K. Pearson, *Chem. Phys. Lett.* **34**, 80 (1975).
85. J. P. Hessler, F. Wagner, Jr., C. W. Williams, and W. T. Carnall, *J. Appl. Phys.* **48**, 3260 (1977).
86. W. F. Krupke, *Electronic Transition Lasers I*, J. I. Steinfeld, Ed. (MIT Press, Cambridge, MA, 1976).
87. C. Bender, Lawrence Livermore Laboratory, private communication (1977).
88. R. R. Jacobs, Lawrence Livermore Laboratory, private communication (1977).
89. R. R. Jacobs and W. F. Krupke, *Technical Digest, Topical Meeting on Inertial Confinement Fusion*, San Diego, CA, February 1978, p. ThB6-1.
90. R. Franklin, Lawrence Livermore Laboratory, private communication (1977).
91. R. R. Jacobs and W. F. Krupke, *Technical Digest, 10th Intl. Quantum Electronics Conf.* Atlanta, GA, May 1978, p. 712.
92. *Laser Program Annual Report — 1976*, Lawrence Livermore Laboratory, Rept. UCRL-50021-76 (1977), p. 6-24.
93. C. Bender and E. Davidson, "Systematics of the Electronic States of the Rare Earth Trihalides," submitted to *J. Inorganic Chem.* (1978).

## Authors

R. Jacobs  
W. Krupke  
C. Bender

## Major Contributor

R. Franklin

## 7.4.2 Design and Scaling of Multikilojoule Laser Systems

Multikilojoule system architectures are being considered for the  $Tb(thd)_3$  chelate and  $TbAlCl$  complex vapors. For the  $Tb(thd)_3$  chelate vapor case, the laser medium would typically be used at a number density of  $2 \times 10^{17} \text{ cm}^{-3}$  at 225°C, buffered with helium gas at, say, 1 atm. For a device with  $\approx 50 \text{ kJ}$  of energy available at 545 nm, the medium is envisioned to flow through a volume measuring 400 cm long, 100 cm high, and 30 cm wide. This volume would be pumped optically with KrF lasers through large-area, opposing, quartz side windows. The optical extraction pulse would propagate through the medium several times, nominally along the 400-cm length and perpendicular to the mutually orthogonal pump and medium flow directions. The characteristics of a KrF-pumped  $TbAlCl$  vapor system are very similar to those of the  $Tb(thd)_3$  chelate system.

The microscopic parameters of the  $Tb(thd)_3$  and  $TbAlCl$  laser media are summarized in Table 7-14 and a set of nominal values for large scale power amplifiers is given in Table 7-15. We note that the  $Tb(thd)_3$  chelate laser medium is optically thick at the KrF pump wavelength and exhibits a bleaching fluence of only  $0.08 \text{ J/cm}^2$ . The  $TbAlCl$  amplifier medium also is optically thick when pumped along the 100-cm direction. Under the pump conditions chosen for the  $Tb(thd)_3$  chelate, the medium will be fully bleached but not dissociated in  $\approx 0.2 \mu\text{s}$ , a time less than the population inversion storage time  $\approx 0.4 \mu\text{s}$ . For  $TbAlCl$ , the medium will be fully bleached in  $\approx 0.5 \mu\text{s}$ , considerably less than the 10- $\mu\text{s}$  population inversion storage time. Thus, for a  $Tb(thd)_3$  chelate vapor

**Table 7-14. Microscopic parameters for Tb(thd)<sub>3</sub> chelate and TbAlCl vapor laser amplifiers.**

Parameter	Tb(thd) <sub>3</sub> chelate	TbAlCl
Pump wavelength, nm	248, KrF	248, KrF
Pump cross section, cm <sup>2</sup>	10 <sup>-17</sup>	1.3 × 10 <sup>-19</sup>
Pump bleaching fluence, J/cm <sup>2</sup>	0.08	6.2
Laser wavelength, nm	545, <sup>5</sup> D <sub>4</sub> → <sup>7</sup> F <sub>5</sub>	545, <sup>5</sup> D <sub>4</sub> → <sup>7</sup> F <sub>5</sub>
Laser cross section, cm <sup>2</sup>	(5 × 10 <sup>-20</sup> ) <sup>a</sup>	(5 × 10 <sup>-20</sup> )
Laser saturation fluence, J/cm <sup>2</sup>	7.3	7.3
Quantum defect	0.46	0.46
Internal conversion efficiency	(1)	(1)

<sup>a</sup>Values in parentheses are estimated and thus subject to confirmation by direct measurement.

maximum gain length product of  $\alpha_0 L = 4$ , 83 kJ of energy can be stored in the <sup>5</sup>D<sub>4</sub> level for times of approximately 0.4  $\mu$ s (10  $\mu$ s for TbAlCl), and that consistent with level degeneracies (and assuming lower level bottlenecking during the time of extraction) a little more than half this energy (50 kJ) can be extracted. For the Tb(thd)<sub>3</sub> chelate, moderation of the medium temperature rise after excitation can be

achieved with an increased helium buffer pressure, although this will cause some degradation of the output beam quality. Such attractive device performance is predicated on the assumption of a near unity quantum conversion of pump photons to terbium molecules in the <sup>5</sup>D<sub>4</sub> metastable level. This particular aspect is under evaluation in small-scale experiments.

**Table 7-15. Device parameters for 50-kJ Tb(thd)<sub>3</sub> chelate and TbAlCl vapor laser amplifiers.**

Parameter	Tb(thd) <sub>3</sub> chelate	TbAlCl
Tb(thd) <sub>3</sub> density, cm <sup>-3</sup>	2 × 10 <sup>17</sup>	2 × 10 <sup>17</sup>
Medium temperature, °C	225	300
Inversion density, cm <sup>-3</sup>	2 × 10 <sup>17</sup>	2 × 10 <sup>17</sup>
Inversion lifetime, $\mu$ s	≤ 0.4	≥ 10
Stored energy density, J/litre	73	73
Available energy density, J/litre	40	40
Small signal gain coefficient, m <sup>-1</sup>	1	1
Maximum gain length product	≤ 4	≤ 4
Maximum dimension, cm	400	400
Buffer pressure, atm	≈ 1 (He)	2.2 (Al <sub>2</sub> Cl <sub>6</sub> )
Available energy, J/litre-atm	40	18
Total stored energy, kJ	91	91
Total available energy, kJ	50	50
Pump pulse width, $\mu$ s	0.1	0.5
Pump fluence, J/cm <sup>2</sup>	2.5	8.3
Pump flux, MW/cm <sup>2</sup>	25	17
Bleaching velocity, cm/s	1.5 × 10 <sup>6</sup>	9.2 × 10 <sup>7</sup>
Bleaching time, $\mu$ s	0.1	0.5
Height, cm	100	100
Width, cm	30	30

In general, the overall efficiency of a large scale Tb(thd)<sub>3</sub> chelate or TbAlCl vapor laser system will depend on the pump laser efficiency and on the extraction efficiency of the rare-earth vapor laser medium. On the basis of an assumed KrF pump laser efficiency of 6 to 12%, we estimate an overall rare-earth vapor laser system efficiency of 1 to 2% (see Table 7-16). As seen in Table 7-16, an electron-beam pumped KrF laser (§7.6.2) can be expected to have a medium efficiency (electrical deposition to

extracted laser energy) of 10 to 15%. This value is limited primarily by the presence of nonsaturable photoabsorption losses in the KrF laser medium (§7.6.2). Thus, this pump medium efficiency leads to an estimated overall pump laser efficiency of 6 to 8% because flow-conditioning penalties (§7.2.2) are small. If discharge excitation is employed, the KrF laser medium efficiency may be as high as 25%, leading to an overall KrF pump laser efficiency of 12%.

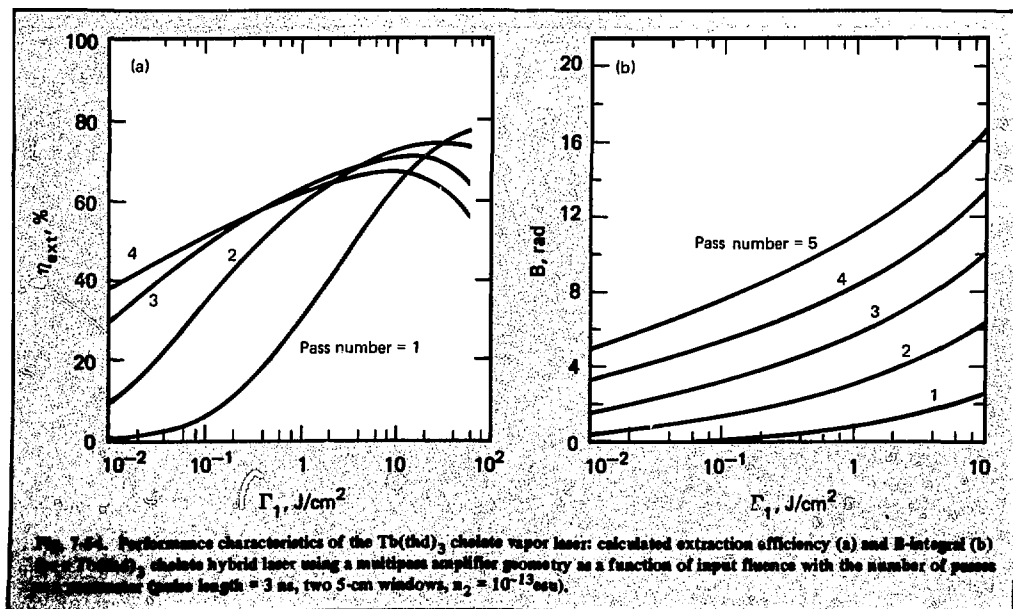
Table 7-16. Component efficiencies (%) for KrF pumped Tb(thd)<sub>3</sub> chelate and TbAlCl rare earth vapor lasers.

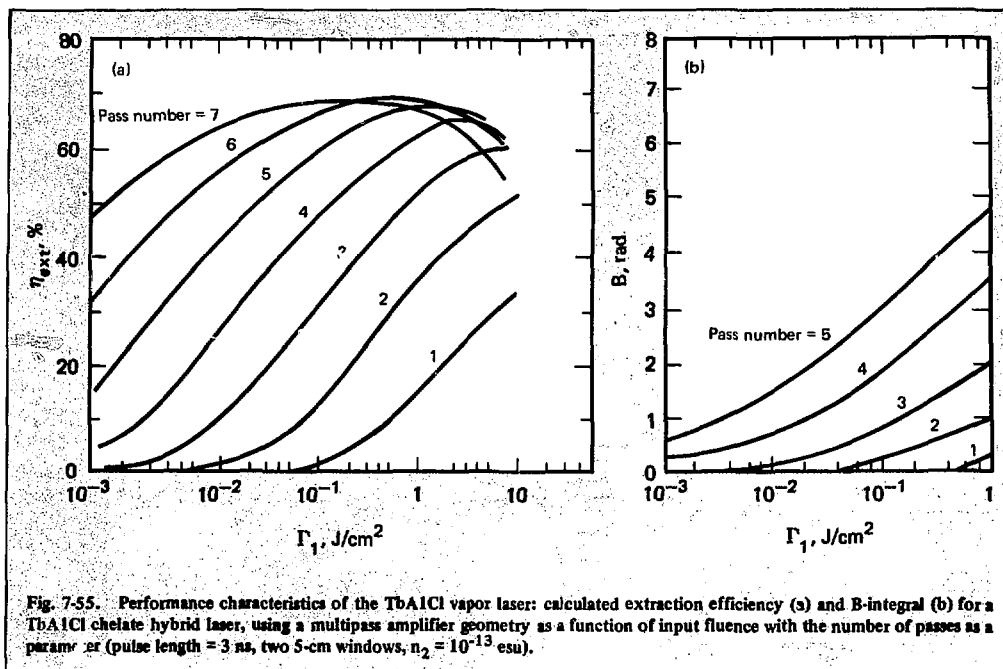
Efficiency component	Tb(thd) <sub>3</sub> chelate and TbAlCl
<b>Pump</b>	
Pulse forming, deposition, and fill factors (electron beam)	65
Pump medium	10 to 15 (25) <sup>a</sup>
Pump after flow costs	6 to 8 (12) <sup>b</sup>
Transport/coupling	90
<b>TB medium</b>	
Optical fill factors	80
Extraction × quantum yield	28 <sup>c</sup>
Laser electrical	1.1 to 2.0 (2.6) <sup>b</sup>
Total laser after flow in laser	1.0 to 1.9 (2.5) <sup>b</sup>

<sup>a</sup>Percentage efficiency with possible breakthroughs.

<sup>b</sup>Total efficiency with breakthrough increment in footnote a.

<sup>c</sup>Assumes unit quantum yield.





The extraction characteristics of multipass Tb(thd)<sub>3</sub> chelate and TbAlCl vapor amplifiers are shown in Figs. 7-54 and 7-55, respectively. The extraction properties for the Tb(thd)<sub>3</sub> chelate and TbAlCl devices have been calculated assuming (1) pump pulse times of 0.1  $\mu$ s and 0.5  $\mu$ s, respectively, (2) upper laser level lifetimes of 0.4  $\mu$ s and 10  $\mu$ s, respectively, (3) a single-pass loss of 5%, (4) a single-pass transit time of 0.1  $\mu$ s, and (5) a fifth-power exponential spatial pulse shape. The initial small signal, gain amplifier length product  $\alpha_0 L$  is 4.0 and 2.0 for the Tb(thd)<sub>3</sub> chelate and TbAlCl amplifiers, respectively. Because of its short upper laser level lifetime ( $\approx 0.4$   $\mu$ s), the Tb(thd)<sub>3</sub> system must be pumped very quickly,  $\lesssim 0.1$   $\mu$ s. However, a reasonable multipass architecture requires an approximate 0.1- $\mu$ s optical delay between passes. Energy extraction from Tb(thd)<sub>3</sub> is further complicated by the medium's high saturation fluence of 7.3 J/cm<sup>2</sup>.

Under these circumstances, efficient multipass extraction from a Tb(thd)<sub>3</sub> chelate laser system requires high input fluences [see Fig. 7-54(a)]. Optimum performance can be achieved by using a two-pass or a cascaded amplifier [Fig. 7-54(a)] extraction scheme. However, the accumulated B-integral [Fig. 7-54(b)] may become large enough to require laser beam spatial filtering or thinner window struc-

tures. Thus, for the Tb(thd)<sub>3</sub> chelate vapor laser, the total system architecture will be complicated primarily because the laser must have a large "front end" to drive the final large-scale amplifier(s).

As shown in Fig. 7-55, the TbAlCl medium with its long lifetime performs well in a multipass system architecture. Relatively small input fluences are required to extract large energy fluences efficiently from the TbAlCl medium. Therefore, the total laser system architecture for the TbAlCl laser can be much simpler than that for the Tb(thd)<sub>3</sub> chelate. However, laser beam spatial filtering probably will be required for the TbAlCl laser to control phase aberrations that accumulate on the beam due to its passage through the high density Al<sub>2</sub>Cl<sub>6</sub> medium (see §7.2.4).

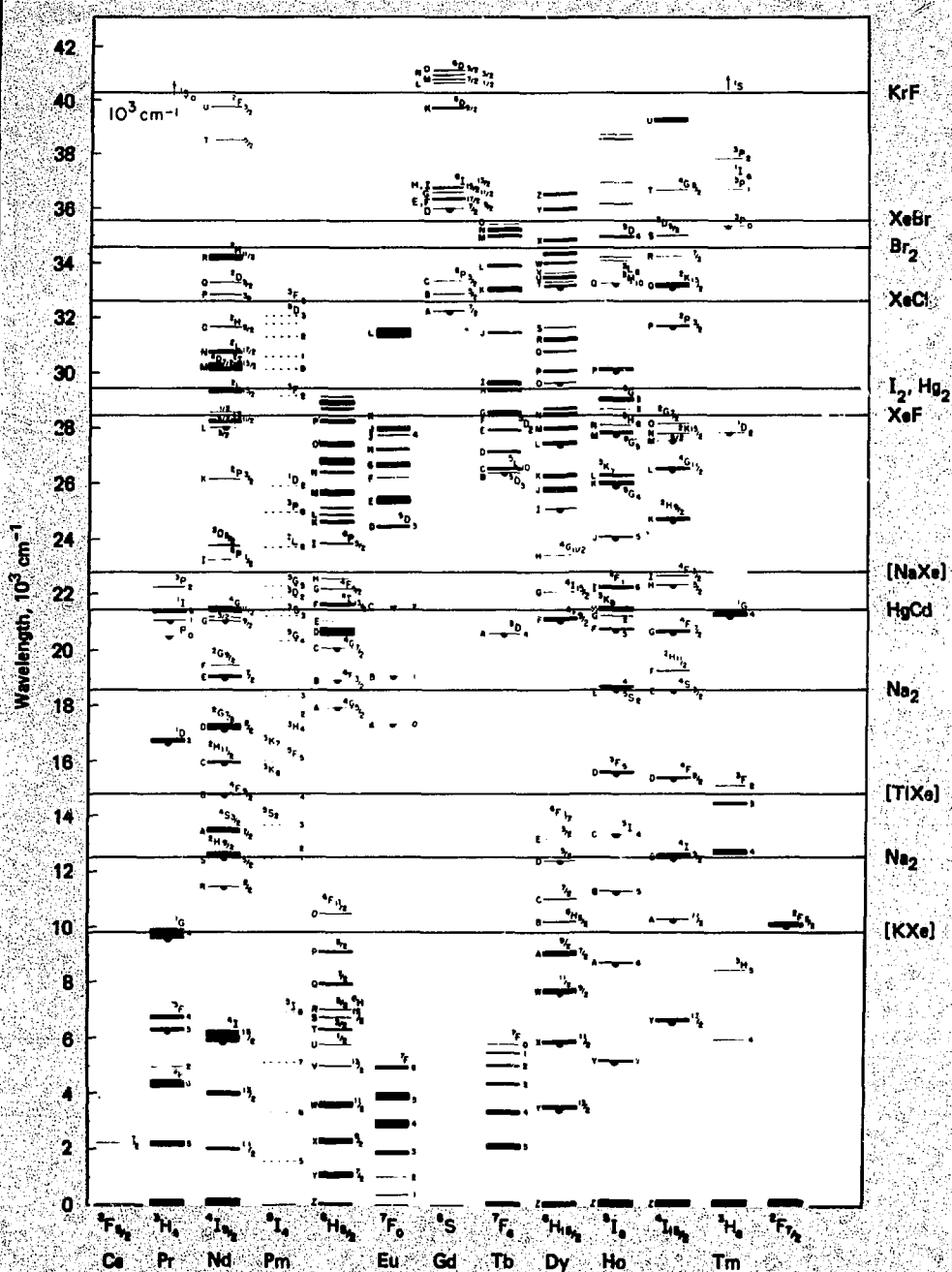
These system architectures and extraction considerations are accounted for in Table 7-16, where we see that overall rare-earth vapor laser system efficiencies of 1 to 2% may be achievable with these media. Furthermore, it is clear that the area offering most significant improvement in total laser system efficiency of the rare-earth vapor hybrid systems is pump efficiency.

Author

R. A. Haas

Major Contributor

W. F. Krupke



## 7.5 Rare-Earth:Solid-State Hybrid Laser Systems

The rapid development of efficient, though nonenergy-storing, uv and visible gas lasers has rekindled the search for energy conversion media that can serve as fusion laser amplifiers. Representative of such optical drivers are the KrF laser at 248 nm and the XeF laser at 351 and 353 nm. Numerous metastable levels among the trivalent rare earths ( $\text{RE}^{3+}$ ) in solid hosts are being evaluated as the corresponding storage systems. The vapor phase trivalent rare earths are discussed in §7.4.

In Fig. 7-56, an overlay of wavelengths is presented for a variety of efficient gas laser excimer sources against the backdrop of energy levels for the  $\text{RE}^{3+} 4f$  ground electronic configurations. With this listing of excitation lasers, we have begun to examine the various possible  $\text{RE}^{3+}$ :host combinations that can serve as the solid state gain media for high-average-power fusion lasers.<sup>94</sup> Attractive features of these hybrids include the facts that: (1) for selected cases, a small and acceptable thermal loading of the host can occur, (2) any deposited thermal energy can be distributed in a controlled manner, and therefore beam propagation can be optimized via adaptive optics and a pumping arrangement, and (3) large energy density storage is possible in the absence of strong quenching by excited-state-excited-state processes, e.g., about 500 J/litre at  $1.06 \mu\text{m}$  is stored for  $\approx 0.33 \text{ ms}$  in the Shiva amplifiers.

In the following subsections, these properties are shown to be satisfied by the representative case of  $\text{Tm}^{3+}$  excited by the XeF laser at 351 and 353 nm in several host media. The detailed physics issues are first presented for this  $\text{RE}^{3+}$  system in §7.5.1, followed in §7.5.2 by the results of a preliminary multikilojoule scaling study for a high-average-power  $\text{Tm}^{3+}$ :silicate glass fusion driver.

### References

94. W. F. Krupke, *Solid State Lasers and Average Power Applications*, Lawrence Livermore Laboratory, Memorandum No. WFK-76-307 (August 19, 1976).

### Author

R. Jacobs

### 7.5.1 Physics Issues

In Fig. 7-57, the level structure for the  $\text{Tm}^{3+} 4f^{12}$  ground electronic configuration is shown.

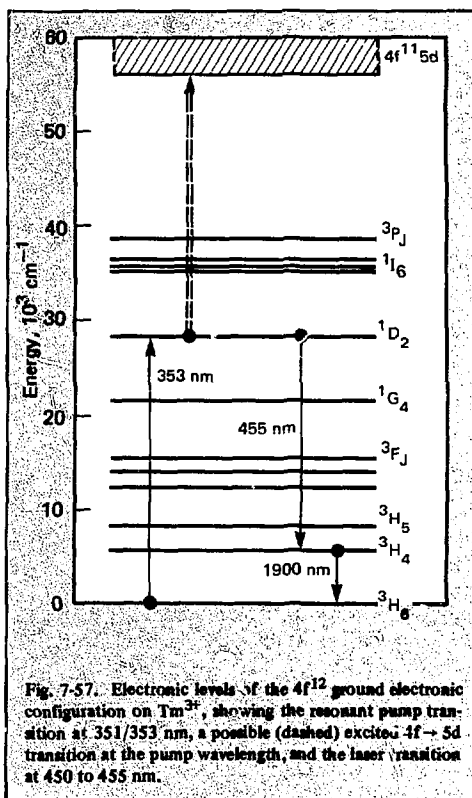


Fig. 7-57. Electronic levels of the  $4f^{12}$  ground electronic configuration on  $\text{Tm}^{3+}$ , showing the resonant pump transition at 351/353 nm, a possible (dashed) excited  $4f \rightarrow 5d$  transition at the pump wavelength, and the laser transition at 450 to 455 nm.

Three-level laser action is envisioned whereby the 351/353-nm pump light of the XeF laser populates the  $^1\text{D}_2$  level via the  $^3\text{H}_6 \rightarrow ^1\text{D}_2$  absorption with subsequent lasing taking place on the  $^1\text{D}_2 \rightarrow ^3\text{H}_4$  transition at  $\approx 450$  to 455 nm. A prime attraction of this candidate fusion laser is that the ratio for nonradiative  $W_{\text{NR}}$  to radiative  $W_{\text{R}}$  decay of both the upper ( $^1\text{D}_2$ ) and lower ( $^3\text{H}_4$ ) laser levels is significantly less than unity, i.e.,  $W_{\text{NR}}/W_{\text{R}} \ll 1$ , thereby minimizing host heating. Using representative decay rates for typical host media, we estimate the deposited heat as a fraction of the absorbed XeF laser energy to be only several percent. Ion-ion deactivations are not considered to be significant enough to alter this conclusion. For what heating does take place, a host with high thermal conductivity is desired. Generally, this requirement dictates the use of crystalline rather than glass hosts; the thermal conductivity ratios are about 10 times greater for crystals ( $\approx 0.1$  vs  $0.01 \text{ W/cm}^\circ\text{C}$ ). Unfortunately, because the laser system must be size scalable, the possible crystal candidates are limited to only a handful. A prime contender is

CaF<sub>2</sub>, which has been fabricated commercially to about 30-cm-size single crystals. A severe problem exists for this host, however, in that the divalent Ca<sup>2+</sup> ion sites cannot properly accommodate RE<sup>3+</sup> dopant ions. This leads to a clustering phenomenon for which the single ion absorption and emission properties become unacceptably altered. Studies of Er<sup>3+</sup>/CaF<sub>2</sub> have been made to detail this behavior.<sup>95</sup> Kinetics experiments also have been conducted for Tm<sup>3+</sup>:CaF<sub>2</sub> where such anticipated clustering was manifested as a decreasing peak fluorescence intensity as a function of increasing Tm<sup>3+</sup> concentration for a fixed optical pump flux at 351/353 nm.<sup>96</sup>

Two other attractive crystal hosts that may be size-scalable are KY<sub>3</sub>F<sub>10</sub> and yttrium lithium fluoride (YLF). Recent investigations of Re<sup>3+</sup>:KY<sub>3</sub>F<sub>10</sub> indicate that single crystals several inches in dimension are readily fabricated.<sup>97</sup> Commercially, YLF is routinely grown to 3-cm sizes with good optical quality. Furthermore, each of these crystals has a nonlinear index of refraction about  $0.6 \times 10^{-13}$  esu, half that for silicate laser glass. In spite of their lower thermal conductivities, glass hosts do have acceptably low  $n_2$  values and are scalable to fusion amplifier dimensions. As will be seen in §7.5.2, a system evaluation for a terawatt-class Tm<sup>3+</sup>:glass fusion laser indicates that total efficiencies  $\gtrsim 2\%$  are possible at a repetition rate  $> 1$  Hz, using turbulent helium gas cooling of the amplifier disks.<sup>98</sup>

Thus, the attractions of high-average-power RE<sup>3+</sup>:solid-state laser systems dictate the following requirements for the constituents: (1) the host must be a low  $n_2$  material, have high thermal conductivity, be scalable in size with good optical quality, and provide the RE<sup>3+</sup> ions with sites that lack inversion symmetry to induce the otherwise parity-forbidden transitions between pairs of 4f levels; (2) the RE<sup>3+</sup> emitter must possess a level structure emitting in the near uv to the visible spectral range with small level coupling to lattice phonons, thereby resulting in minimal matrix heating; and (3) the excitation source must be efficient and size-scalable. As noted previously, existing experimental and computational evidence indicate that selected Tm<sup>3+</sup>:solids, optically pumped by the efficient XeF discharge laser, can satisfy these criteria.

Estimates for the Tm<sup>3+</sup>:<sup>1</sup>D<sub>2</sub> radiative lifetime were obtained using the Judd-Ofelt model for ligand field-induced electric dipole transitions within the shielded RE<sup>3+</sup> 4f ground electronic configuration. The usefulness of this method is well established for RE<sup>3+</sup>-doped crystals<sup>99</sup> and glasses.<sup>100,101</sup> Additional information on the effec-

tive fluorescence linewidth enables us to predict the induced emission cross section. The Judd-Ofelt theory was utilized<sup>96</sup> for Tm<sup>3+</sup>:silicate and phosphate glasses and for Tm<sup>3+</sup>:CaF<sub>2</sub>. The predictions for the <sup>1</sup>D<sub>2</sub> radiative lifetime ranged from 30 to 100  $\mu$ s with the corresponding <sup>1</sup>D<sub>2</sub>  $\rightarrow$  <sup>3</sup>H<sub>4</sub> induced emission cross section varying from  $\approx 1$  to  $5 \times 10^{-20}$  cm<sup>2</sup> (which, in the absence of excited-state absorption, is equal to the laser cross section  $\sigma_l$ ).<sup>96</sup> These estimated radiative lifetimes are all suitably long for fusion laser application when considered in conjunction with the relatively efficient XeF pump laser operating at pulselengths of  $\approx 1$   $\mu$ s. The predicted laser cross sections are largest for the Tm<sup>3+</sup>:phosphate glasses.

To verify the <sup>1</sup>D<sub>2</sub> radiative lifetime estimates, we obtained fluorescence decay data using standard techniques.<sup>96</sup> These data reveal a distinctive double exponential relaxation for both the Tm<sup>3+</sup>:silicate glass and the Tm<sup>3+</sup>:CaF<sub>2</sub> samples. The resultant time constants are independent of excitation flux or, equivalently, of excited-state density. The ratios between the slow and fast decay times are  $\approx 6$  to 7. In Fig. 7-58, preliminary results for the short-time fluorescence decay constant  $\tau_1$  is plotted as a function of Tm<sup>3+</sup> density for a pump flux  $\gtrsim 20$  MW/cm<sup>2</sup>. As seen in Fig. 7-58, the fast decays in CaF<sub>2</sub> are about 10 times faster than the decays for the glass hosts. In all cases, these decays are less than the predicted radiative lifetimes. However, for

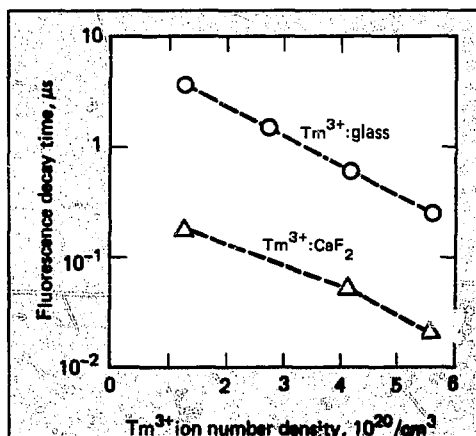


Fig. 7-58. Measured prompt decay component for the Tm<sup>3+</sup>:<sup>1</sup>D<sub>2</sub> level at 451 nm as a function of Tm<sup>3+</sup> concentration. For these preliminary data, the fluorescence was excited by a 20-nsec-long XeF laser pulse focused to a flux level  $> 20$  MW/cm<sup>2</sup>;  $\tau_1$  is independent of  $I_p$ .

a fusion amplifier at an ion density of about  $1 \times 10^{20} \text{ cm}^{-3}$ , the  $^1\text{D}_2$  level lifetimes in silicate glass are a few microseconds, suitably long for efficient operation of the XeF laser pump.

The mechanisms responsible for the fast and slow decays are not yet positively identified.<sup>96</sup> Quite possibly, however, the prompt decay component is the result of a near-resonant multipolar deactivation described by  $^1\text{D}_2 + ^3\text{H}_6 \rightarrow ^1\text{G}_4 + ^3\text{H}_4 + \text{Q}$  ( $600 \text{ cm}^{-1}$ ): alternate quenching mechanisms can be identified with the aid of Fig. 7-57. Such processes, of course, can contribute to host heating, depending on the specific values of radiative  $W_R$  vs multiphonon-induced nonradiative  $W_{NR}$  decay rates for the product energy levels. Estimates for the resulting matrix heating yield values similar to those given earlier; i.e., because  $W_{NR}/W_R \ll 1$  for these newly excited states, only several percent of the absorbed XeF laser energy can lead to host heating.

To examine the possibility of two-pump-photon absorption (see Fig. 7-57, dotted arrow), the results of Fig. 7-59 were obtained. Here, peak fluorescence amplitude  $I_f$  is converted to excited state density and plotted as a function of pump flux  $I_p$  for the  $\text{Tm}^{3+}$ :silicate glass sample. Use of the peak fluorescence intensity in this manner is legitimate because the 20-ns pump time is appreciably faster than the observed decay times. The resulting linear response of output vs input implies that two-pump-photon absorption plays a minor role. Otherwise, a saturation behavior would be indicated in these data. This is an especially welcome result because the precise locations of the high-lying 5d states are not known. The attendant excited-state absorption

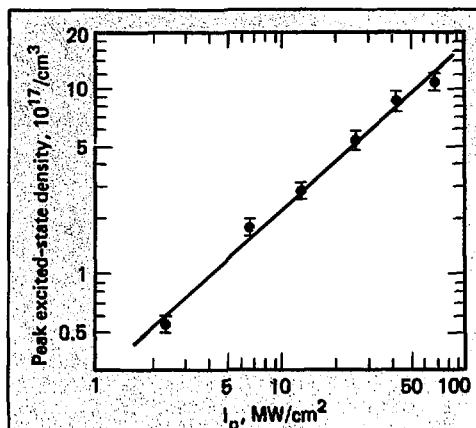


Fig. 7-59. Peak fluorescence intensity for the  $\text{Tm}^{3+}$ :  $^1\text{D}_2 \rightarrow ^3\text{H}_4$  transition at 451 nm, expressed as the peak  $^1\text{D}_2$  number density vs XeF laser pump intensity. The  $\text{Tm}^{3+}$  dopant concentration is  $5.6 \times 10^{20} \text{ cm}^{-3}$  for the silicate glass host.

cross section could be large because it describes a parity-allowed transition from the  $^1\text{D}_2$  level to the  $4f^{11}5d$  configuration.

In Fig. 7-60, the peak fluorescence intensity  $I_f$  is plotted as a function of  $\text{Tm}^{3+}$  ion concentration for parametrically varied pump flux  $I_p$ . To within the experimental uncertainty,  $I_f$  scales linearly with  $\text{Tm}^{3+}$  concentration; for fixed  $\text{Tm}^{3+}$  concentration,  $I_f$  scales linearly with  $I_p$ . Corresponding results (not shown) for  $\text{Tm}^{3+}$ : $\text{CaF}_2$  show *negative* slopes with increasing  $\text{Tm}^{3+}$  concentration although, for a

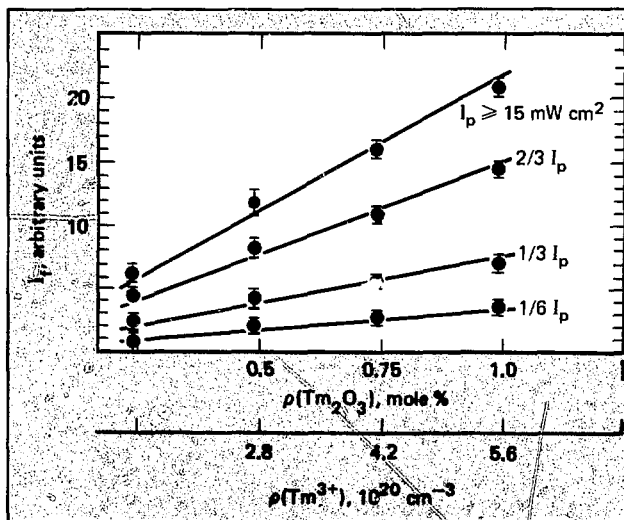


Fig. 7-60. Peak fluorescence intensity  $I_f$  at 451 nm for  $\text{Tm}^{3+}$ :silicate glass vs  $\text{Tm}^{3+}$  concentration as a function of parametrically varied 20-ns-long XeF laser pump intensity  $I_p$ .

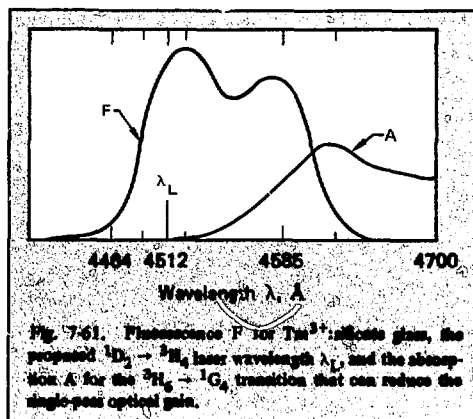


given  $\text{Tm}^{3+}$  doping level in  $\text{CaF}_2$ , the peak fluorescence intensity is linearly dependent on  $I_p$ . The lack of linear scaling with increasing concentration in  $\text{CaF}_2$  is attributed to the clustering phenomenon. The trivalent dopant ion ( $\text{Tm}^{3+}$ ) is not accommodated substitutionally at the divalent  $\text{Ca}^{2+}$  lattice site; rather, the  $\text{Tm}^{3+}$  ion is accommodated interstitially with unknown charge compensation characteristics.<sup>95</sup> As noted previously, such pairings of  $\text{Tm}^{3+}$  ions result in altered "free ion" absorption and fluorescence properties that render them unsuitable for fusion laser amplifier use.

The main conclusion from these kinetics experiments is that the  $\text{Tm}^{3+}$ :glass media can store large excited-state densities ( $\gtrsim 10^{18} \text{ cm}^{-3}$ , i.e.,  $>400 \text{ J/litre}$ ) for the attractively long times ( $\gtrsim 0.2 \mu\text{s}$ ) that are suitable for fusion laser systems.

We evaluated single-pass gains for the  $\text{Tm}^{3+}$ :solid-state candidates, in part, by use of the Judd-Ofelt-determined laser cross section  $\sigma_L$ . Additionally, an accounting was made for a slight amount of  $\text{Tm}^{3+}$  ground-state absorption ( $^3\text{H}_6 \rightarrow ^1\text{G}_4$ ) at the proposed laser wavelength of 451 nm. Figure 7-61 illustrates this situation for  $\text{Tm}^{3+}$ :silicate glass, showing the  $^1\text{D}_2 \rightarrow ^3\text{H}_4$  fluorescence spectrum together with the culprit  $^3\text{H}_6 \rightarrow ^1\text{G}_4$  absorption. The cross section for absorption from the  $^3\text{H}_6$  level at the proposed 4512-Å laser wavelength is  $<2.3 \times 10^{-22} \text{ cm}^2$ . For available XeF laser sources and  $\text{Tm}^{3+}$ :silicate host materials, single-pass gains of  $\approx 7\%$  per pass can be obtained.<sup>96</sup> We attempted to demonstrate laser action but our ability to generate reproducible and therefore convincing results was plagued by two-pump-photon-induced damage at those intensities necessary to achieve the desired gains. However, this situation can be circumvented for a practical and scalable fusion system by use of less intense pump fluxes.<sup>98</sup>

In addition to silicate and phosphate glass hosts, we can use materials with bandgaps exceeding the two-photon energy at the XeF laser wavelength, i.e.,  $>7.5 \text{ eV}$ . Hosts such as the  $\text{KY}_3\text{F}_{10}$  and YLF crystals, as well as  $\text{BeF}_2$ , can be damaged only by a higher order three-photon absorption mechanism, not by the two-photon process that damages oxide-based glasses. Theoretical estimates<sup>102</sup> for the larger bandgap hosts reveal that damage-free pumping with XeF lasers may be possible with intensities  $\gtrsim 1 \text{ GW/cm}^2$ . As desired, these alternate  $\text{RE}^{3+}$  hosts have additional system attractions including: (1) low  $n_2$  values, i.e.,  $<0.6 \times 10^{-13} \text{ esu}$ , (2) adequate thermal conductivities, and (3) potential for size-scalability with the preservation of good optical quality. Such  $\text{Tm}^{3+}$ -doped



materials, along with other  $\text{RE}^{3+}$ :solid-state host combinations, will be the subjects of continued fusion laser system evaluation. However, the full impact of these new gain media as advanced fusion lasers, when considered against competitive approaches, hinges on increasing the pump laser efficiencies.

## References

95. D. R. Tallant, M. P. Miller, and J. C. Wright, *J. Chem. Phys.* **65**, 510 (1976); D. R. Tallant and J. C. Wright, *J. Chem. Phys.* **63**, 2074 (1975).
96. R. R. Jacobs, *Prospects for High Average Power  $\text{Tm}^{3+}$ :Solid State Fusion Laser Amplifiers*, Lawrence Livermore Laboratory, Memorandum No. AL-78-535 (May 26, 1978).
97. P. Porcher and P. Caro, *J. Chem. Phys.* **65**, 89 (1976); P. Porcher and P. Caro, Lawrence Livermore Laboratory, private communication (1977).
98. W. F. Krupke and E. V. George, *Opt. Eng.* **17**, 238 (1978); W. F. Krupke, E. V. George, and R. A. Haas, *Laser Handbook III* (North-Holland, Amsterdam, 1978).
99. L. A. Riseberg and M. J. Weber, *Progress in Optics XIV*, E. Wolf, Ed. (North-Holland, Amsterdam, 1975).
100. W. F. Krupke, *IEEE J. Quantum Electron.* **QE-10**, 450 (1974).
101. R. R. Jacobs and M. J. Weber, *IEEE J. Quantum Electron.* **QE-12**, 102 (1976).
102. L. Smith, Lawrence Livermore Laboratory, private communication (1978).

## Authors

R. R. Jacobs  
W. F. Krupke

## Major Contributor

R. B. Lopert

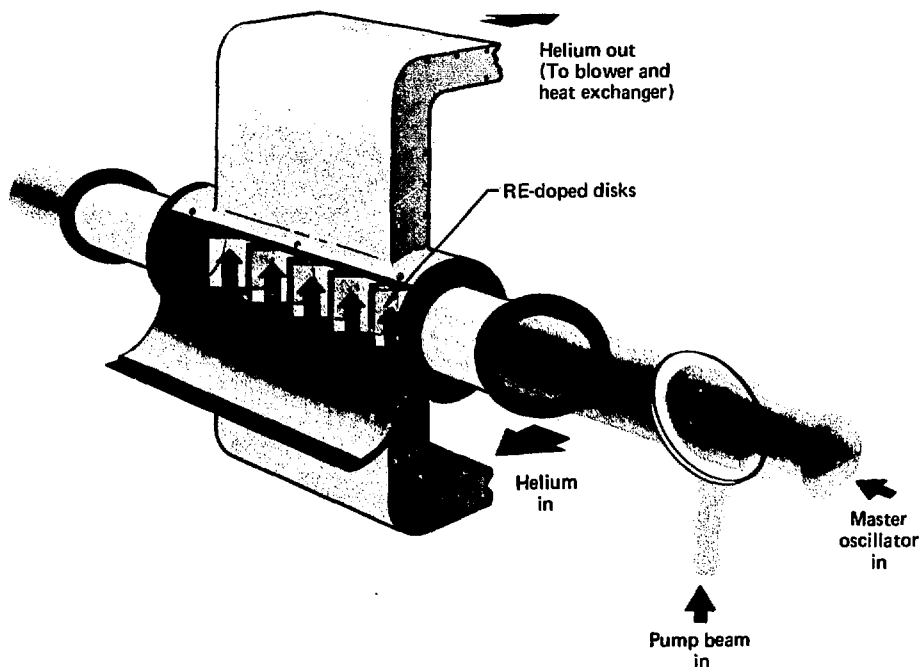


Fig. 7-62. Conceptual design of a rare earth hybrid fusion laser amplifier.

### 7.5.2 Design and Scaling of a Multikilojoule Hybrid Laser System

Here, we consider some of the principal issues and the characteristic parameters for a  $\text{Tm}^{3+}$  hybrid laser of, say, 10 kJ. A diagram of such an amplifier is shown in Fig. 7-62. A number of square  $\text{Tm}^{3+}$ :glass slabs of thickness  $t$  and transverse dimension  $W$  are held in a parallel arrangement with a channel width  $s$  between adjacent slabs. Helium gas at a nominal pressure of 1 atm is flowed through the channels under turbulent flow conditions at a Mach number  $M$ , Reynolds number  $Re$ , and Nusselt number  $Nu$ . In this schematic design, XeF pump radiation is propagated through the slabs at Brewster's angle and coaxially with an input extraction pulse at 451 nm, corresponding to the  $^1\text{D}_2 \rightarrow ^3\text{H}_4$  transition. In more practical designs, we might expect to pass the extraction beam through the amplifier several times at small angles to the axial symmetry axis. Pump beams tailored in intensity in the transverse plane would be propagated in the amplifier along the axial symmetry axis.

An optimum hybrid laser design must take into account the interdependence of many physical parameters including:  $\text{Tm}^{3+}$  ion concentration, upper laser level lifetime, time interval between passes through the amplifier, single-pass gain, pump and output fluences compared to optical damage fluence, and B-integral value. Procedures to optimize all these factors have not yet been fully developed, but some feeling for characteristic values can be derived in the following example.

Table 7-17 lists a nominal set of values for  $\text{Tm}^{3+}$ :glass. We assume a total optical thickness for the slabs of  $L = 20$  cm. For the selected  $\text{Tm}^{3+}$  ion density (0.12 mol-%), the fluorescence lifetime of the  $^1\text{D}_2$  upper laser level is  $\approx 4 \mu\text{s}$  (see Fig. 7-58) and the absorption coefficient is  $\alpha_p = 0.1 \text{ cm}^{-1}$ . If we assume an excited state density of  $2 \times 10^{18} \text{ cm}^{-3}$  ( $\approx 800 \text{ J/litre}$ ), the small signal gain coefficient is  $0.1 \text{ cm}^{-1}$  and the effective saturation fluence is  $5 \text{ J/cm}^2$ ; this fluence value takes into account level degeneracies and the fact that the system will bottleneck in the terminal laser level (this level is radiative with a multimillisecond lifetime).

Table 7-17. Characteristic parameters for a Tm:glass laser host medium.

Property	Value
Pump cross section $\sigma_p$ , cm <sup>2</sup>	$1.5 \times 10^{-21}$
Laser cross section $\sigma$ , cm <sup>2</sup>	$5 \times 10^{-20}$
Saturation fluence $I_s$ , J/cm <sup>2</sup>	5
Tm <sup>3+</sup> ion concentration N ions/cm <sup>3</sup>	$7 \times 10^{19}$
<sup>3</sup> D <sub>2</sub> level lifetime $\tau_{l, \mu s}$	<4
Pump absorption coefficient $\alpha_p$ , cm <sup>-1</sup>	0.1

The extraction properties of such a device have been calculated, assuming a pump pulse time of 0.5  $\mu$ s, a single pass loss of 5%, a single-pass transit time of 100 ns, a fifth-power exponential spatial pulse shape, and a nonlinear refractive index of  $0.7 \times 10^{-13}$  esu. Figure 7-63(a) plots the calculated extraction efficiency as a function of input fluence, with the number of passes as a parameter. Figure 7-63(b) shows the corresponding accumulation of B-integral parametrically with the number of passes (3-ns-long extraction pulse). These figures indicate that, for an input fluence of a few hundred millijoules per square centimeter, an extraction efficiency of 40% can be achieved with a B-value of five and with five passes. The B-value could, in principle, be lowered with spatial filtering and optical relaying between transits, but with some addi-

tional loss per pass. Alternatively, at an input fluence of 1 J/cm<sup>2</sup>, the extraction efficiency is again near 40% in four passes, but with a B-value of only three. The energy stored in such an amplifier depends on the maximum transverse aperture at which the gain can be stably stored. For a maximum gain length product of five, the maximum transverse dimension (without segmenting of the slabs) is  $W = 40$  cm. Thus the output energy of such a device can be approximately 10 kJ.

The pump and output beam fluences, summarized in Table 7-18, are tractable values in terms of optical damage limits and the nominal output fluence from an XeF pump laser. Assuming an XeF pump laser efficiency of 5 to 10%, we estimate an overall hybrid laser system efficiency of 0.7 to 2.0%, including flow cooling as shown in Table 7-19. According to Table 7-19, an electron-beam-pumped XeF laser can be expected to have a medium efficiency (i.e., electrical deposition to extract laser radiation) of 5 to 7.5%. This value results primarily from lower laser level bottlenecking and pump quantum efficiency considerations. This 5-to-7.5% pump medium efficiency leads to an overall pump laser efficiency of 3 to 5% because flow-conditioning penalties are small (§7.2.2). When pump radiation coupling and multipass extraction losses are included, together with the fact the Tm<sup>3+</sup> lower laser level is bottlenecked, the estimated total laser system efficiency is 0.7 to 1.1%. If discharge excitation is employed, the XeF

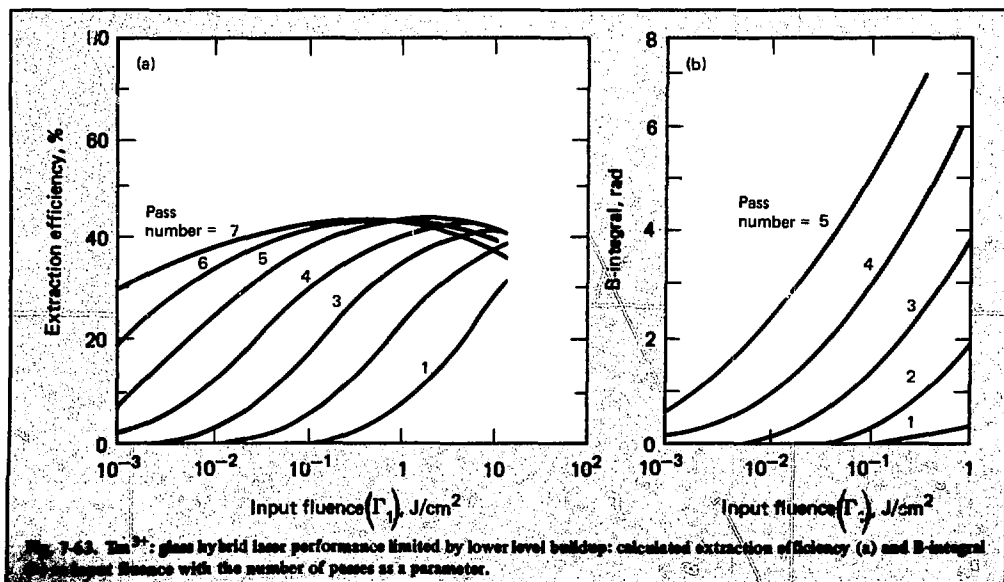


**Table 7-18. Characteristic parameters for a 10-kJ Tm:glass amplifier.**

Property	Value
Slab width, cm	40
Slab thickness, cm	2
Number of slabs	10
Gain length $L$ , cm	20
Pump pulse width, $\mu$ s	0.5
Pump fluence $I_p$ , J/cm <sup>2</sup>	6
Pump intensity $I_p$ , MW/cm <sup>2</sup>	12
Excited-state density $N^*$ , cm <sup>-3</sup>	$2 \times 10^{16}$
Stored energy density, J/litre	800
Gain coefficient $\alpha_0$ , cm	0.1
Extraction efficiency $\epsilon_{\text{ext}}$ , %	40
Laser output fluence $I_0$ , J/cm <sup>2</sup>	10
B-integral	5
Laser pulse width $t_L$ , ns	3
Output energy $E_0$ , kJ	8
Total beam power $P_0$ , TW	3

**Table 7-19. Component efficiencies (%) for a XeF-pumped Tm<sup>3+</sup>:glass laser.**

Efficiency component	Value
Pulse forming, deposition, and fill factors (electron) beam	65
Pump medium	5 to 7.5 (15) <sup>a</sup>
Pump after flow costs	3 to 5 (8) <sup>b</sup>
Transport/coupling	90
Optical fill factors	80
Extraction $\times$ quantum yield	35 <sup>c</sup>
Laser electrical	0.7 to 1.1 (2.0) <sup>b</sup>
Total laser after flow in laser	0.7 to 1.1 (2.0) <sup>b</sup>

<sup>a</sup>Percentage with possible breakthroughs.

<sup>b</sup>Total with breakthrough increment.

<sup>c</sup>Bottlenecked lower laser level.

medium efficiency may be as high as the indicated 15%, leading to an overall laser system efficiency of 2%. On the basis of this analysis, it is clear that the two items that would lead to significantly larger total efficiencies for the rare-earth solid-state hybrid system are improved pump efficiency and eliminated Tm<sup>3+</sup> lower laser level bottlenecking.

For reasons of simplicity, mechanical stability, and minimum optical losses, it is desirable to divide the gain medium into the fewest number of slabs. However, for given specific thermal deposition and cooling rates, a thicker slab will suffer greater temperature rise and surface stress than a thin slab. Some simple estimates can be made for the mechanical power consumption required to cool the laser for a typical slab thickness  $t$ . In the first approximation, we assume that the slab is thermally loaded uniformly with a specific thermal power  $\epsilon_L \nu_L$  (W/cm<sup>3</sup>), where  $\epsilon_L$  is the specific thermal energy deposited in the glass and  $\nu_L$  is the pulse repetition rate. The combination of uniform thermal loading and surface cooling will set up a parabolic thermal gradient normal to the slab surface with temperature  $T_C$  at the midplane of the slab and temperature  $T_f$  at the slab surface.<sup>103</sup>

We assume that cooling is achieved by flowing helium at about 1 atm through the cooling channels of width  $s$  at velocity  $u$ . If the Reynolds number of the flow is greater than  $10^4$ , the gas flow is turbulent, and generally the boundary layer will be a fraction of the channel thickness. The Reynolds number  $Re$  is related to the gas density  $\rho$  and viscosity  $\mu$  by  $Re = \rho us / \mu$ . If the slab is cooled symmetrically from two sides, the midplane temperature  $T_C$  is related to the face temperature  $T_f$  and the cooling gas temperature  $T_g$  by the expressions

$$\Delta T_c = T_c - T_f = (\epsilon_L \nu_L t^{2/8} K), \quad (54)$$

$$T_c = T_g + \left( \frac{\epsilon_L \nu_L t^2}{8K} \right) \left( 1 + \frac{4K}{ht} \right), \quad (55)$$

where  $K$  is the thermal conductivity<sup>104</sup> of the laser medium ( $\approx 0.01$  W/cm<sup>2</sup>·°C for glass) and  $h$  is the heat transfer coefficient.<sup>105</sup> The heat transfer parameter is related to the thermal conductivity of the helium cooling gas  $K$  (He)  $\approx 1.44 \times 10^{-3}$  W/cm·°C, the Nusselt number  $Nu$ , and the channel thickness  $s$  by the expression

$$h = K(\text{He}) Nu / s. \quad (56)$$

In the temperature range of interest to us, it can be shown<sup>105</sup> that  $Nu \approx 1.5 \times 10^{-2} (Re)^{0.8}$ , so that Eq. (53) becomes

$$T_c = T_g + 14.5 \epsilon_L \nu_L t^2 \left( 1 + \frac{0.168(s)^{0.2}}{t(M)^{0.8}} \right), \quad (57)$$

where  $M$  is the cooling gas Mach number.

For the Tm:glass amplifier considered above, and for a 1-Hz pulse repetition rate, we obtain from Eq. (54),  $\Delta T_c = 1.9 t^2$ , for  $t$  in centimeters and  $T_c$  in degrees Celsius. For  $t = 2$  cm (e.g., 10 slabs),  $\Delta T_c = 7.5^\circ\text{C}$ . This temperature difference will give rise to a surface stress (tension) of about 600 psi.<sup>103</sup> We note that this stress is isoplanar in the central portion of the slab and will cause no depolarization of a linearly polarized extraction pulse properly incident to the slab at Brewster's angle. Of course, edge effects, not considered here, will appear within a distance  $2t$  from the edge of the slab. However, because of spatial rolloff of the extraction beam profile in this region, the edge effects will be of greatly reduced importance.

For the slab dimensions assumed in this example, and assuming a flow velocity of 100 m/s (0.1 M) and a channel width of  $s = 1$  cm, Eq. (57) shows that  $T_c = T_g + 13.3^\circ\text{C}$ . Thus, it is easy to calculate that the temperature rise of the cooling gas is only a few degrees in this case. The selection of channel thickness and flow velocity will largely be determined by balancing the rise in  $T_c$  against the rise in the power to drive the flow. Preliminary estimates based on reasonable assumptions of ducting losses, heat exchanger losses, and pump efficiency indicate that mechanical cooling power will be a few tenths of a watt per square centimeter of slab surface for a flow velocity of  $\approx 100$  m/s. These values are small compared to the electrical power per unit area of glass required of the XeF pump laser. Thus it appears that flow cooling will not dominate the overall systems efficiency.

However, it is clear from this simple analysis that materials with higher thermal conductivity and lower specific thermal loading would be advantageous. Such materials would allow for a fewer number of slabs, thicker slabs, and reduced flow cooling power. We are continuing our efforts to identify materials with suitable active ions and matching pumps. In any event, it will be necessary to extend the simple analysis outlined here to include nonuniform thermal loading as well as a detailed treatment of the optical stress field.

## References

103. B. A. Boley and J. H. Werner, *Theory of Thermal Stresses* (John Wiley & Sons, Inc., New York, 1960), Ch. 9.
104. J. R. Thornton, W. D. Fountain, G. W. Flint, and T. G. Crow, *Appl. Opt.* **8**, 1087 (1969).
105. R. B. Bird, W. E. Stewart, and E. N. Lightfoot, *Transport Phenomena*, (John Wiley & Sons, Inc., New York, 1960), pp. 396-407.

## Author

R. A. Haas

## Major Contributor

W. F. Krupke

## 7.6 Raman Laser Systems

### 7.6.1 Introduction

The backward wave Raman pulse compression scheme has been regarded for several years as a possible technique for generating short pulses for fusion applications.<sup>106</sup> The LLL experimental and analytical program to evaluate this concept has been spurred by the development of high-efficiency, short-wavelength lasers such as KrF at 248 nm and XeF at 353 nm. A preliminary discussion of this concept was given in the 1976 laser program annual report.<sup>107</sup>

Over the past year, considerable progress has been made with the Raman pulse compression approach. An experimental measurement of small signal backward wave gain at the Stokes frequency for scattering of line-narrowed KrF pump radiation in methane has been performed.<sup>108</sup> Measurements of saturation effects in this Raman media also have been made.<sup>109</sup> An analytical assessment of the limitations on the efficiency of both backward wave Raman amplifiers and KrF laser amplifiers has been developed. From this analysis and from a technological assessment of scalability to high energies, we have identified several systems approaches that can yield large temporal pulse compressions ( $>30$ ) at high conversion efficiencies ( $\approx 50\%$ ). The analysis also reveals that overall efficiencies of greater than 3% are possible in systems that are scalable to power and energy levels suitable for power plant drivers. The development of the pulse compression scheme to higher efficiencies ( $>5\%$ ) is possible with improved subsystem efficiencies in either the Raman medium or the pump laser.

The detailed analysis described here is based on backward wave Raman pulse compression in gaseous methane of the radiation from the most efficient short-wavelength laser source known, the 248-nm KrF laser. The results quoted are for this

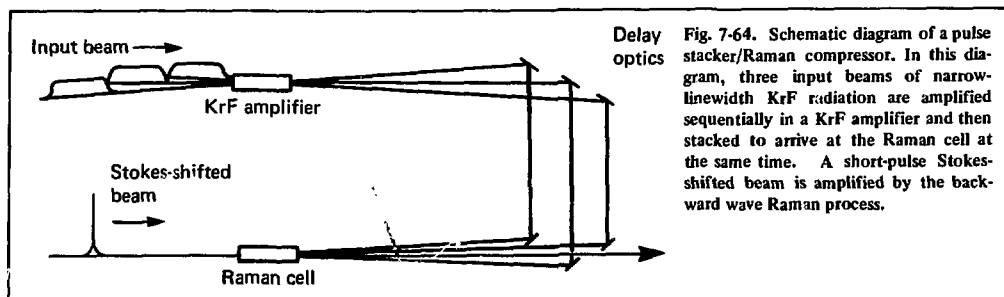


Fig. 7-64. Schematic diagram of a pulse stacker/Raman compressor. In this diagram, three input beams of narrow-linewidth KrF radiation are amplified sequentially in a KrF amplifier and then stacked to arrive at the Raman cell at the same time. A short-pulse Stokes-shifted beam is amplified by the backward wave Raman process.

particular system, but several more general conclusions are drawn. Pulse compression factors of about 10 to 20 at conversion efficiencies of  $\approx 60\%$  appear possible with molecular scatterers, yielding a net intensification of  $\approx 6$  to 12. When Raman pulse compression is combined with geometric pulse compression schemes, often termed "pulse stacking" or "angle multiplexing," in either the KrF pump medium, the Raman medium, or both, total system pulse compression factors greater than 50 can be achieved at comparable high overall efficiencies.

Several important benefits are derived from this combination of compression scenarios. A high-compression hybrid scheme allows for a longer pump laser pulse duration for a given short-pulse-length requirement. Use of a longer pump pulse relaxes the pulsed power requirements for the electrical power conditioning of the pump system. Ultimately, the use of the potentially higher efficiency electron-beam sustained discharge lasers may be compatible with a pulse compression scenario in the power plant context. The hybrid stacker-compressor schemes also allow shorter propagation lengths through the Raman active medium, resulting in superior beam quality. Combination of multiple pump beams in the Raman medium yields a system with markedly reduced optical complexity compared to a pure pulse stacking scheme in a high gain medium such as KrF.

Figure 7-64 shows a schematic diagram of a hybrid stacker-compressor laser system. In this scheme, a KrF amplifier of pulse length  $\tau_p$  is sequentially extracted by  $n$  input beams, each of pulse length  $\tau_p/n$ . For simplicity, we show the case for  $n=3$  in Fig. 7-64. The input beams are angle-coded and can be separated and recombined with appropriate delays on each beam to yield one pulse of duration  $\tau_p/n$  and power  $n\eta_m P_o$ , where  $\eta_m$  is the mirror and optical transport efficiency and  $P_o$  is the characteristic output power achievable for that amplifier. The beams are recombined in a Raman active medium where a counterpropagating pulse at

the Stokes frequency extracts the pump radiation. The resulting short pulse has a duration of  $\tau_p/n\kappa$ , where  $\kappa$  is the Raman compression ratio. The resultant power in the short pulse is given by

$$P_{sp} = \kappa \eta_R n \eta_m P_o \quad (58)$$

where  $\eta_R$  is the Raman conversion efficiency.

Our principal reason for initiating a program to study and develop backward Raman converters for a KrF laser is to obtain the increase in intensity by pulse compression. In addition, the spatial quality of the Raman beam can be far superior to the spatial quality of the laser pump beam, and thus constraints on medium homogeneity and beam quality in the KrF laser pump can be far less restrictive than in a laser that produces a beam of adequate quality and focusability for target illumination. Maintaining the required high medium quality may be a much less severe problem in the Raman converter cell than in the KrF amplifiers. The high quantum efficiency of Raman conversion gives an energy deposition per litre-atmosphere of working medium for a typical compressor design that is two orders of magnitude lower than the energy deposition in the KrF pump. Thus density variations may be easier to control with the Raman laser system.

Several experiments have confirmed the improvement of spatial coherence obtained with a Raman or Brillouin amplifier. These include studies using diffuse illumination and propagation of a divergent pump beam by grazing incidence reflection in a pipe. Beams from separate lasers or optical delay trains also can be used to pump a single Raman cell, as proposed in the stacker-compressor concepts. The pump beam in any of these cases serves as an energy storage reservoir for the Stokes beam. The important criterion for using a pump beam of low focusability is that the gain for the Stokes pulse, integrated along any axis down the

length of the compressor cell, be reasonably constant. Obviously, there will be severe local variations in intensity and therefore in gain caused by interference between beams and by intensity fluctuations in the pump, but these variations are not important so long as they average out over the length of the cell.

In the following section, we describe the basic media physics of the KrF laser and the modeling of KrF amplifiers, emphasizing achievable  $P_0$  and medium efficiency. A discussion of the fundamentals and modeling of Raman compressors details the achievable values of  $\eta_R$  and  $\kappa$ . A summary of recent pulse compression experiments also is given, and finally we discuss the technology issues of large compressor systems.

## References

106. A. J. Glass, *IEEE J. Quant. Elect.* 3, 516 (1967).
107. J. R. Murray and A. Szoke, *Laser Fusion Annual Report — 1976*, Lawrence Livermore Laboratory, Rept. UCRL-50021-76 (1977), p. 6-40.
108. J. R. Murray, J. Goldhar, and A. Szoke, *Appl. Phys. Lett.* 32, 551 (1978).
109. J. R. Murray, J. Goldhar, D. Eimerl, and A. Szoke, *Appl. Phys. Lett.* 33 (1978), in press.

## Author

J. J. Ewing

## 7.6.2 Theory and Modeling of KrF Laser Systems

To be viable in a pulse stacker/Raman compressor system, the KrF laser must exhibit three critical properties: (1) it must operate with a narrow linewidth ( $\approx 0.3 \text{ cm}^{-1}$  for high backward-wave Raman gain), (2) it must operate with high overall efficiency ( $>5\%$ ), and (3) it must provide the highest possible flux ( $>10^7 \text{ W/cm}^2$ ) to minimize the required pulse stacking and Raman compression. Narrow linewidth and high efficiency can only occur together if the upper laser level is homogeneous. Theoretical calculations of emission spectra from each vibrational state as well as line-narrowing experiments suggest that this is indeed the case. High efficiency and highest possible flux are intimately linked to the efficiency with which excitation can be extracted in the presence of the several absorbers present in these electrically excited systems.

**KrF Band Homogeneity.** Consider the question of the line widths and spectra produced by a high power KrF laser. The potential curves for KrF as

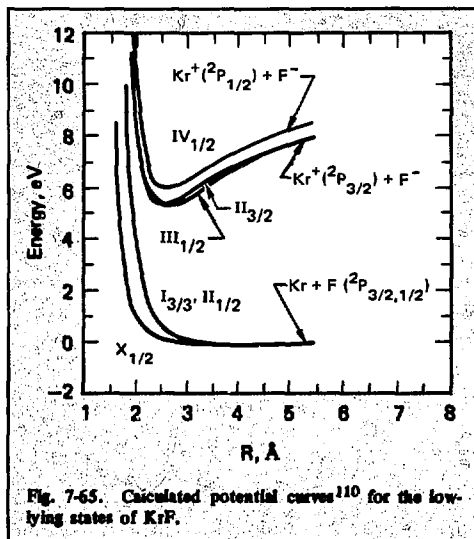


Fig. 7-65. Calculated potential curves<sup>110</sup> for the low-lying states of KrF.

calculated by Dunning and Hay<sup>110</sup> are shown in Fig. 7-65. The KrF\* molecule can be regarded as a  $\text{Kr}^+ \text{F}^-$  ion pair complex that emits to the repulsive covalent KrF ground state by transferring an electron from the  $\text{F}^-$  to the  $\text{Kr}^+$ .<sup>111</sup> Gain at 248 nm is provided by the strong  $\text{B}_{1/2} \rightarrow \text{X}_{1/2}$  transition, sometimes also referred to as the  $\text{III}(1/2) \rightarrow \text{I}(1/2)$  transition or the  $\text{B}^2\Sigma(1/2) \rightarrow \text{X}^2\Sigma(1/2)$  transition. A comparison of the frequently used KrF state designations is given in Table 7-20 along with the approximate experimental energies of the states at the minimum of the excited-state energy curves. Using the calculated potential energy curves and transition moments for KrF,<sup>110,114</sup> the bound-free emission spectra have been theoretically determined. Using the state designations of Dunning and Hay,<sup>110</sup> the five strongest transitions are predicted to be  $\text{III}(1/2) \rightarrow \text{I}(1/2)$ ,  $\text{IV}(1/2) \rightarrow \text{I}(1/2)$ ,  $\text{II}(3/2) \rightarrow \text{I}(3/2)$ ,  $\text{III}(1/2) \rightarrow \text{II}(1/2)$ , and  $\text{IV}(1/2) \rightarrow \text{II}(1/2)$ .

The spontaneous emission probability for the bound-free transition from an individual upper state vibrational level  $|v\rangle$  to a continuous state  $|\epsilon\rangle$  is given by

$$A_v(\nu) = \frac{64 \pi^4 \nu^3}{3h} |\langle v | \mu_{nm} | \epsilon_m \rangle|^2, \quad (59)$$

where  $n$  and  $m$  denote the upper and lower electronic states and  $\mu_{nm}$  is the transition moment connecting them.<sup>115,116</sup> The frequency-dependent A-coefficients given by the above expression have

Table 7-20. Labels of rare-gas halide electronic states.

Parenthood	Approximate energy, eV	Common designations		
		Ref. 112	Ref. 110	Ref. 113
Kr + F	0.1	X $^2\Sigma(1/2)$	I(1/2)	X $_{1/2}$
	1	A $^2\Pi(1/2, 3/2)$	II(1/2), II(3/2)	A $_{1/2, 3/2}$
Kr <sup>+</sup> + F <sup>-</sup>	5	B $^2\Sigma(1/2)$	III(1/2)	B $_{1/2}$
	5	C $^2\Pi(3/2)$	II(3/2)	C $_{3/2}$
	5.7	D $^2\Pi(1/2)$	IV(1/2)	D $_{1/2}$

been calculated for the first four vibrational levels of the upper laser level III(1/2) and are plotted in Fig. 7-66. The A-coefficient for each level has been multiplied by a Boltzmann weighting for  $T = 450$  K. The total probability obtained by summing over the vibrational levels also is shown. The frequencies for the calculated transitions are too large by  $1540\text{ cm}^{-1}$  when compared with experimental data. Most of this error can be attributed to the upper state well depth; however, the shape of the well and, consequently, the vibrational wavefunctions used in the calculations are expected to be accurate. From Fig. 7-66, it is clear that the maxima for the four levels overlap closely (the peak probabilities for  $v = 1, 2$ , and 3 are within  $60\text{ cm}^{-1}$  of  $v = 0$ ). This leads us to predict that the upper laser level is homogeneous.

Similar calculations have been performed on each of the strong transitions in KrF. A composite of the five bands is given in Fig. 7-67. Each band

has been plotted relative to the III(1/2)  $\rightarrow$  I(1/2) laser transition. There is a reasonable amount of overlap, including the weak IV(1/2)  $\rightarrow$  II(1/2) transition that extends under the III(1/2)  $\rightarrow$  I(1/2) band. Because spontaneous emission spectra are calculated completely ab initio, the only remaining unknowns are the relative populations of each of the excited states. Our calculations are useful for extracting this information from the experimental spectra.

**Optical Absorbers.** Most of the optical absorbers that compete with the KrF\* gain at 248 nm have been characterized either experimentally or theoretically (see Table 7-21). Recent theoretical studies on the heteronuclear ion ArKr<sup>+</sup> and the photoionization of Ar<sub>2</sub><sup>+</sup> suggest that these species should also absorb strongly near 248 nm; thus, this ion needs to be included in laser modeling.

To determine the optical absorption of ArKr<sup>+</sup>, accurate potential energy curves have been calculated for this ion.<sup>117</sup> The curves, including spin-orbit coupling, are shown in Fig. 7-68. The two

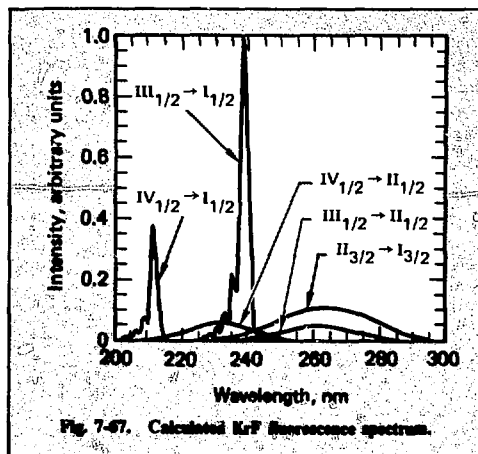
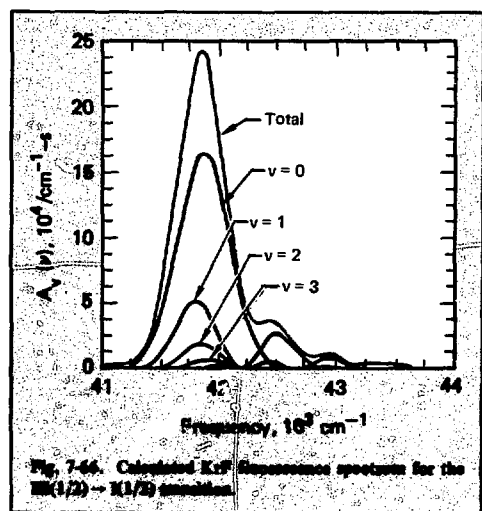




Table 7-21. Absorption processes at 249 nm.

Process	Cross section $\sigma$ , cm <sup>2</sup>
$\text{Ar}^* + h\nu \rightarrow \text{Ar}^+ + e$	$5.1 \times 10^{-21}$
$\text{Kr}^* + h\nu \rightarrow \text{Kr}^+ + e$	$1.7 \times 10^{-20}$
$\text{F} + h\nu \rightarrow \text{F}^+ + e$	$5.6 \times 10^{-18}$
$\text{Ar}_2^+ + h\nu \rightarrow \text{Ar}^+ + \text{Ar}$	$1.3 \times 10^{-17}$
$\text{F}_2 + h\nu \rightarrow 2\text{F}$	$1.5 \times 10^{-20}$
$\text{Kr}_2^+ + h\nu \rightarrow \text{Kr}^+ + \text{Kr}$	$1.6 \times 10^{-18}$
$\text{Kr}_2\text{F}^* + h\nu \rightarrow 2\text{Kr} + \text{F}$	$1.6 \times 10^{-18}$
$\text{Ar}^{**} + h\nu \rightarrow \text{Ar}^+ + e$	$4.2 \times 10^{-18}$
$\text{Kr}^{**} + h\nu \rightarrow \text{Kr}^+ + e$	$4.3 \times 10^{-18}$

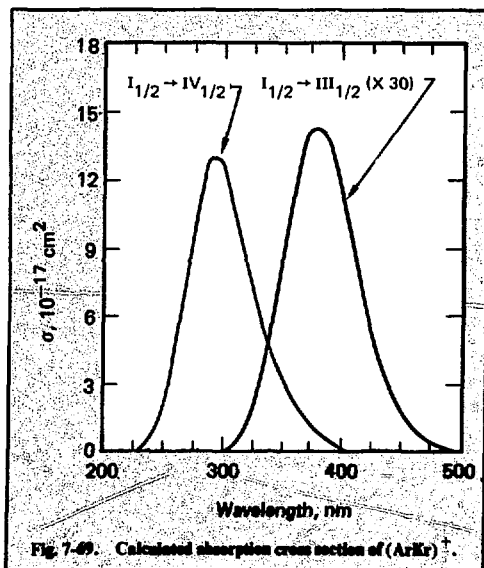
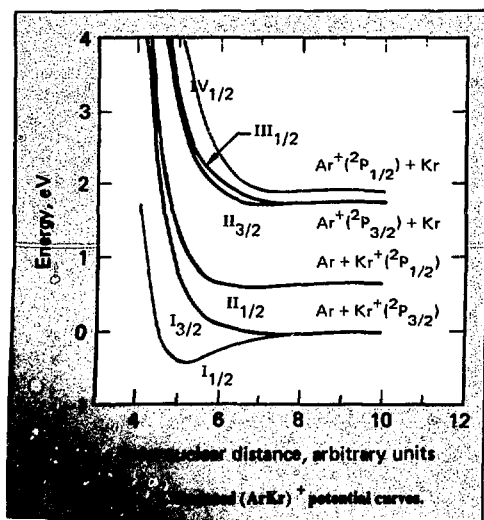
strongest absorptions were found to be from the ground I(1/2) state to either the III(1/2) state or the IV(1/2) state. Only the latter transition I(1/2)  $\rightarrow$  IV(1/2) is significant at the KrF wavelength. The calculated absorption cross sections are plotted in Fig. 7-69. At 248 nm, the I(1/2)  $\rightarrow$  IV(1/2) absorption cross section is  $1.5 \times 10^{-17}$  cm<sup>2</sup>. This is comparable to the cross section for Ar<sub>2</sub><sup>+</sup>, the other positive ion absorber.

The question of relative concentrations of these ions is being studied. It is important to note that the ArKr<sup>+</sup> diatomic ion absorption probably is also carried over in general shape and cross section to the ArKrF<sup>+</sup> excited state, one of the species that can be formed in the thermolecular quenching of KrF\*. A similar argument has previously been made

to estimate the absorption of the Ar<sub>2</sub>F<sup>+</sup> and Kr<sub>2</sub>F<sup>+</sup> excited species.

Calculation of the photoionization cross section of Ar<sub>2</sub><sup>+</sup> is discussed in §7.3.2 and the cross section is plotted in Fig. 7-22. Although the photoionization cross section is small near the 9.8-eV fluorescence energy of Ar<sub>2</sub><sup>+</sup> ( $4 \times 10^{-19}$  cm<sup>2</sup>), it is considerably larger near the 5-eV transition energy of KrF\*, due to the 3.9-eV autoionizing peak ( $\sim 2 \times 10^{-18}$  cm<sup>2</sup> at 248 nm). More accurate calculations are needed, including the internuclear distance dependence, and hence the vibrational temperature dependence, of the autoionization contribution. It appears, however, that photoionization of Ar<sub>2</sub><sup>+</sup> may need to be included in the modeling of the KrF laser in the high-pressure regimes where Ar<sub>2</sub><sup>+</sup> forms rapidly.

**Amplifier Modeling Predictions.** High medium efficiency and reasonably high intensity operation (10 MW/cm<sup>2</sup>) have been demonstrated separately for the KrF laser. Electrical excitation by the volumetrically scalable techniques of electron-beam and electron-beam-controlled discharges has been demonstrated as well. However, the regions of parameter space used in the stacker-compressor fusion laser context have not yet been fully characterized. The combinations of pulse durations, energy deposition rates, gain and loss lengths, and pressure of operation need to be charted for this pump. As a result, we have developed a comprehensive KrF kinetic model with which we are



able to calculate the optical extraction efficiency of the amplifier medium subsystem in the presence of optical absorbers that can limit the efficiency and scalability of uv lasers.

The extraction efficiency of KrF amplifiers is influenced by the facts that energy is contained in three different KrF\* electronic states, that collisional quenching by two- and three-body processes lowers the gain by competing with excited-state fluorescence or stimulated emission, and that non-saturating losses decrease the efficiency of an amplifier as the gain length is increased. Cross relaxation between electronic states remains a subject for future research, but previous measurements of emission from the excited states of these species suggest that the bulk of the excitation flows through the upper laser level. Therefore, our model neglects cross-relaxation.

The saturation intensity of a KrF amplifier is governed by the collisional and spontaneous decay rates of KrF\*. The dominant decay rates are typically F<sub>2</sub> quenching and three-body formation of the ionic-triatomic species ArKrF\* and Kr<sub>2</sub>F\*.<sup>118</sup> Electron superelastic quenching of KrF\* also may be important under conditions of high electron density. The optical saturation power is given by

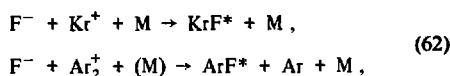
$$I_s = \frac{h\nu_L}{\sigma} \sum_i \frac{1}{\tau_i}, \quad (60)$$

where  $1/\tau_i$  gives the rates for KrF\* decay by the various processes. The stimulated emission cross section is given by  $\sigma$ . Table 7-22 summarizes the typical quenching rate constants of KrF\*, obtained from various sources, that are used in this model.

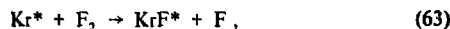
Intrinsic optical absorptions that compete with the KrF\* gain at 248 nm can have a substantial effect on the efficiency and output power of KrF amplifiers. Table 7-21 lists several species and their cross sections at 248 nm that are believed to be present in electrically excited Ar/Kr/F<sub>2</sub> mixtures. Many of these species are unavoidable in either electron-beam or electric-discharge excitation of KrF\* because they are integral links in the kinetic chain. The F<sub>2</sub>-based lasers, which to date have provided the best performance on KrF, have an unavoidable non-saturating loss of about 0.2%/cm for typical laser mixtures. The ion recombination channel for production of excited states, viz



followed by



produces non-saturating losses as a result of both negative ions and positive dimer ions that are present at pressures above  $\approx 1$  atm. The production of excited states by neutral chemistry by reactions such as



leads to absorption by atoms in metastable (and higher) excited states.

Because most of the absorption cross sections are small and because the decay rates of the species are large, it usually is a good approximation to consider these absorptions as non-saturable at the power levels of interest. Except ions to this generalization are Kr<sub>2</sub>F\* and ArKrF\* which may be formed by three-body quenching of KrF\*. Because KrF\* presumably is saturated in a high-power amplifier, these species also are depleted; this has been demonstrated experimentally.<sup>119</sup>

The effect of non-saturable loss on KrF amplifier performance is illustrated by a simple model. The saturated gain is given by

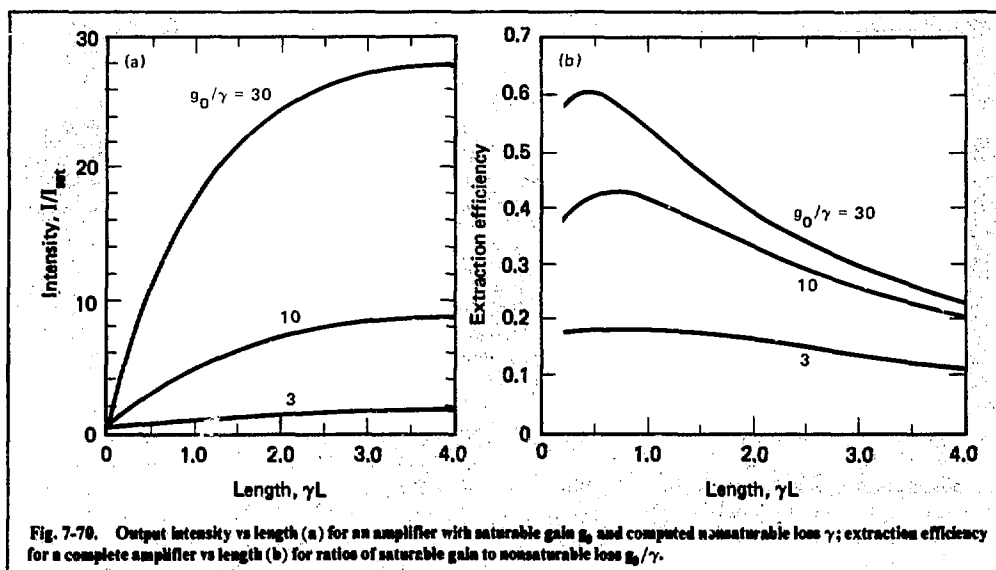
$$\frac{1}{I} \frac{dI}{dz} \approx \frac{\alpha_0 - \gamma_0^s}{1 + I/I_s} - \gamma, \quad (64)$$

where  $\alpha_0$  is the excited-state gain coefficient,  $\gamma_0^s$  is the saturating absorption due to the excited state itself or to species that form subsequently in the kinetic chain, and  $\gamma$  is the presumed non-saturable absorption coefficient. Numerical solutions of Eq. (64) are shown conveniently in terms of the non-dimensional variables  $I/I_s$ ,  $\gamma L$ , and  $g_0/\gamma$ , where  $L$  is the amplifier length, and  $g_0 = \alpha_0 - \gamma_0^s$ .

The output power and efficiency of an amplifier of length  $L$  are shown in Fig. 7-70 for different assumed values of the ratio of intensity dependent

Table 7-22. KrF\* ( $B_{1/2}$ ) quenching processes.

Reaction	Rate Constant
KrF* $\rightarrow$ KrF + F	$1.5 \times 10^6 \text{ s}^{-1}$
KrF* + Ar + Ar $\rightarrow$ ArKrF* + Ar	$8 \times 10^{-32} \text{ cm}^6/\text{s}$
KrF* + Kr + Ar $\rightarrow$ Kr <sub>2</sub> F* + Ar	$6.5 \times 10^{-31} \text{ cm}^6/\text{s}$
KrF* + Kr + Kr $\rightarrow$ Kr <sub>2</sub> F* + Kr	$5 \times 10^{-31} \text{ cm}^6/\text{s}$
KrF* + F <sub>2</sub> $\rightarrow$ products	$7.7 \times 10^{-10} \text{ cm}^2/\text{s}$



gain to nonsaturable loss  $g_0/\gamma$ . An input intensity of  $I_s/2$  is assumed for this figure. The asymptotic intensity at infinite length is  $I_s[(g_0/\gamma)-1]$ . However, it is obvious from Fig. 7-70(b) that this power is approached only with a high penalty in extraction efficiency. Trading off output power and efficiency, it seems reasonable to build power amplifiers such that  $\gamma L \approx 1$  to 2. It also is clear that the ratio  $g_0/\gamma$  should be carefully optimized for a practical amplifier.

Experimental measurement of the net gain at the line center and the background absorption off the KrF band have been reported by Hawryluk et al.<sup>120</sup> The ratio of gain to total loss as measured in these experiments is about three for a current density of  $1.5 \text{ A/cm}^2$  and a 3-atm mixture of Ar/Kr/F<sub>2</sub> in the ratio 0.937/0.06/0.003. We calculate the saturation parameter for these conditions to be  $\approx 3 \text{ MW/cm}^2$ . Figure 7-70 predicts a rather dismal output power and efficiency for this gain-to-loss ratio if indeed the absorption is completely nonsaturable. However, much better performance is predicted and has been achieved at higher pump current densities. Experimental characterization of gains and losses and their saturation characteristics under conditions relevant to pulse compressors is still needed.

According to very simple considerations, high values for the ratio  $g_0/\gamma$  in KrF amplifiers are favored by low pressure mixtures excited by high currents. Concentrations of molecular absorbers

such as Ar<sub>2</sub><sup>+</sup> and Kr<sub>2</sub>F\* are reduced at low pressures. Also, the gain in these amplifiers is proportional to current whereas the absorption due to ionic species scales roughly as the square root of the current.

Therefore, the ratio of gain to absorption is improved at high current. However, practical requirements of useful gain and of foil survival at high current limit the minimum pressure and the maximum current. For a 50-ns electron beam, current densities of 50 to 200 A/cm<sup>2</sup> and an operating pressure in the range of 1 to 3 atm seem reasonable.

Detailed calculations of the performance of an electron-beam-pumped KrF amplifier have been conducted using a comprehensive computer code. Our kinetic modeling (see Fig. 7-1) treats three major aspects of this problem: (1) generalized kinetics of electrons, heavy particles, and photons; (2) electron beam energy deposition in arbitrary mixtures, including proper partitioning among excited states; and (3) non-Maxwellian electron kinetics by solution of the Boltzmann equation. The power of this computer code stems from its calculation of excited-state densities and electron densities that are consistent with electron scattering rates from the Boltzmann solution. The kinetics also can be coupled to energy extraction calculations for homogeneous amplifiers or oscillators.

We have studied pure electron-beam pumping for several mixtures of Ar/Kr/F<sub>2</sub> and for several current densities. Typical results for amplifier performance at 1 atm are shown in Fig. 7-71. These

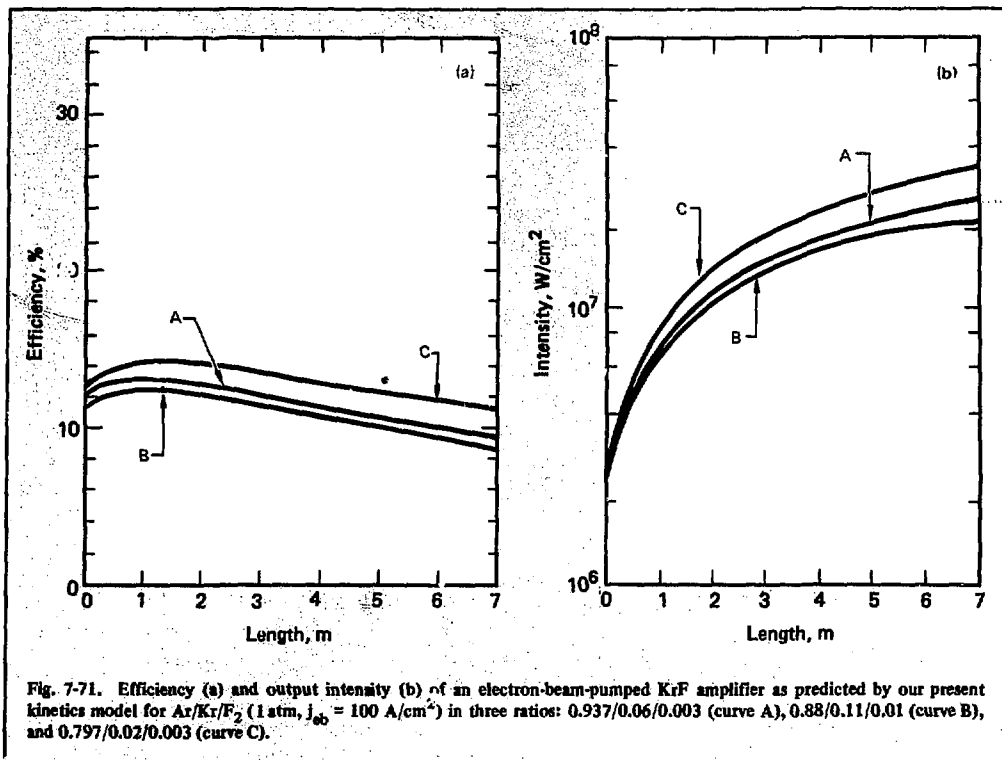


Fig. 7-71. Efficiency (a) and output intensity (b) of an electron-beam-pumped KrF amplifier as predicted by our present kinetics model for Ar/Kr/F<sub>2</sub> (1 atm,  $j_{\text{eb}} = 100 \text{ A/cm}^2$ ) in three ratios: 0.937/0.06/0.003 (curve A), 0.88/0.11/0.01 (curve B), and 0.797/0.02/0.003 (curve C).

results show good medium efficiency and power gain. The rollover of output power is caused by nonsaturable losses. It is clear from these calculations that significant contributions in KrF amplifier power and efficiency can be made by the proper choice of the mixture ratio. The calculations predict efficiencies in the 10 to 14% range; output fluxes  $>10 \text{ MW/cm}^2$  may be achieved. At higher pump power depositions, comparable efficiencies and higher output fluxes are predicted with the present model. Because high pump power depositions create high gains, control of parasitic waves is an important issue that will determine amplifier scalability.

## References

110. T. H. Dunning and P. J. Hay, *Appl. Phys. Lett.* **28**, 649 (1976).
111. J. J. Ewing and C. A. Brau, *Phys. Rev.* **A12**, 129 (1975).
112. J. J. Ewing and C. A. Brau, *Appl. Phys. Lett.* **27**, 350 (1975).
113. J. Tellinghuisen, A. K. Hays, J. M. Hoffman, and G. C. Tisone, *J. Chem. Phys.* **65**, 4473 (1976).

114. P. J. Hay and T. H. Dunning, *J. Chem. Phys.* **66**, 1306 (1977).
115. G. Herzberg, *Spectra of Diatomic Molecules* (Van Nostrand, Princeton, NJ, 1950).
116. F. H. Mies, *Mol. Phys.* **26**, 1233 (1973).
117. C. F. Bender and N. W. Winter, *Appl. Phys. Lett.* (1978), in press.
118. D. C. Lorents, R. M. Hill, D. L. Huestis, M. V. McCusker, and H. H. Nakano, *Electronic Transition Lasers II* (MIT Press, Cambridge, MA, 1977), p. 30.
119. J. A. Mangano, J. H. Jacob, M. Rokni, and A. M. Hawryluk, *Appl. Phys. Lett.* **31**, 26 (1977).
120. A. M. Hawryluk, J. A. Mangano, and J. H. Jacob, *Appl. Phys. Lett.* **31**, 164 (1977).

## Authors

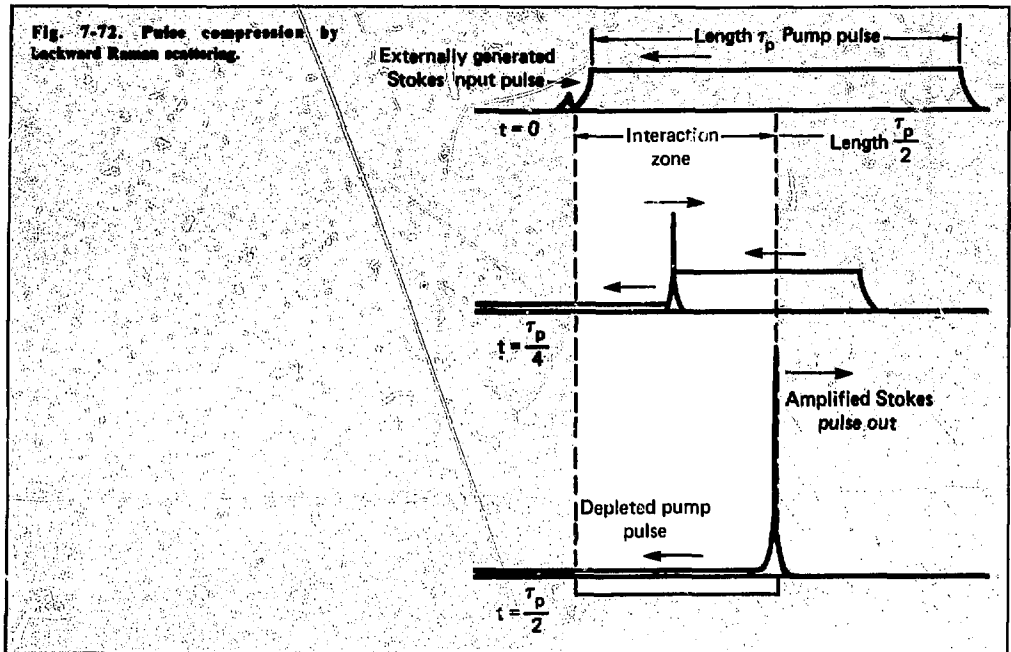
N. Winter  
R. Haas

## Major Contributor

J. J. Ewing

## 7.6.3 Raman Compression Theory

**Principal Physical Limitations.** The principle of operation of a Raman compressor is illustrated



in Fig. 7-72. A short Stokes pulse is amplified by depleting a longer counterpropagating pump pulse in a Raman active medium. This produces a higher intensity in the Stokes pulse than was present originally in the pump. Thus the compressor can be viewed as an energy storage laser in which energy is stored in a collimated beam of pump photons rather than in excited states. The stored energy is extracted exactly as in the usual energy storage amplifier by the counterpropagating Stokes pulse. Raman cross sections are high at uv wavelengths so that a KrF-pumped vibrational backward Raman compressor will operate at near atmospheric pressure.

Physical processes exist which limit the intensity gain that can be produced in a Raman compressor stage of this sort, and which therefore determine certain features of system design and scaling of these compressors. These processes also influence the choice of a particular Raman scatterer for the active medium.

To be applicable to a fusion power plant, the output of a Raman compressor amplifier chain must be focusable, and the chain as a whole must achieve some minimum efficiency. Compression efficiency in the Raman medium is limited by the growth of other nonlinear optical parasitic waves and by absorptions. The most important sources of

inefficiency are (1) the production of forward and transversely propagating pulses at the Stokes frequency, (2) the Raman conversion of the backward traveling pulse to another, possibly nonfocusable wave at the second Stokes frequency, and (3) two-photon absorption in the Raman medium. The beam quality of the output is limited primarily by density fluctuations in the Raman medium. Although there are many other phenomena that have been considered in the regime of operation of the Raman compressors, these effects dominate the basic design of a compressor system.

Another key requirement for fusion applications is reproducibility of compressor performance. It is well known that the stimulated Raman effect may vary greatly with small changes in experimental conditions, especially in the small signal regime. Therefore, an analysis of the reproducibility of compressor performance is required, especially under inhomogeneous pumping conditions. Although this analysis is still in progress, it appears that satisfactory reproducibility can be achieved by operating the backward wave amplifiers in a saturating regime with high-quality Stokes waves, and only narrow-band pumps. For a variety of reasons, the gain for forward scattering (co-propagating pump and Stokes waves) is always higher than the gain for waves intersecting at other

angles, including the backward scattering angle employed in a compressor. This higher forward gain can lead to Raman superfluorescence in the forward direction that can withdraw energy from the pump and reduce the efficiency of the compressor. One important parameter in describing this phenomenon is the ratio of forward to backward Raman gain coefficients, denoted as  $R$ . A second important parameter is the maximum forward gain that can be tolerated before the onset of saturating forward superfluorescence.

Our model calculations reveal that for a typical cell, the permissible small signal gain for a forward Stokes pulse growing from fluorescence noise is  $e^{20}$  to  $e^{25}$ . Therefore, for a typical power amplifier with  $e^5$  gain in the backward direction, a forward-to-backward gain ratio of  $R=4$  to 5 can be tolerated. However, because the forward-to-backward gain ratio  $R$  affects the gain for the production of second Stokes parasites, it is desirable to have a lower value of  $R$ . Effects leading to a large forward-to-backward asymmetry must therefore be analyzed carefully to determine their impact on the choice of Raman scatterer and operating pressure and to define the requirements levied on the pump laser.

The most subtle cause of forward-to-backward asymmetry is parametric coupling that occurs for Raman scattering in the exact forward direction. Stimulated Raman scattering may be treated as a parametric process in which the pump wave and Stokes wave are coupled by a phased array of Raman scatterers.<sup>122</sup> This phased array or "material excitation" also can couple other waves in the medium, an effect exploited in four-wave mixing devices such as CARS, coherent anti-Stokes Raman spectrometers.

In a medium with very very low dispersion (such as the near-atmospheric-pressure gases of interest in a compressor) and in the exact forward direction, a consequence of this parametric coupling process is that the forward Raman gain becomes independent of the linewidth of the pump laser, remaining proportional only to the line profile of the scatterer. However, this condition holds only when the Stokes wave being amplified is exactly matched to the pump wave in phase and frequency distribution.<sup>123</sup> This matching condition is produced, for example, by superfluorescence in the forward direction. We note that parasitic superfluorescent conversion of the backward traveling Stokes wave to the second Stokes wave is a forward scattering process with respect to the short pulse. In all other directions, the gain is proportional to the convolution of the scatterer and laser line profiles. For quasi-Lorentzian lines, this gives a gain propor-

tional to  $(\Delta\nu_s + \Delta\nu_p)^{-1}$ , where  $\Delta\nu_s$  and  $\Delta\nu_p$  are the respective linewidths of the scatterer and the pump laser. For forward superfluorescence, the effective  $\Delta\nu_p$  is zero.

For application to Raman compressors, the practical effect of the parametric coupling in the forward direction is to require that the pump laser have a linewidth small enough so that useful backward gain can be achieved without depletion of the pump laser by forward superfluorescence. Thus, a pump laser linewidth comparable to or less than the linewidth of the Raman scatterer is required. This is the criterion that sparks the interest in narrow-linewidth KrF laser extraction as previously discussed.

A second contribution to forward-to-backward gain asymmetry arises from the asymmetry of the Doppler width in Raman scattering at low gas pressures. The Doppler shift in a scattering process may be shown to be proportional to the change in wave vector in the scattering.<sup>124</sup> This gives a Doppler shift which, after integrating over velocity distributions, yields a Doppler width that is proportional to  $k_p - k_s$  in the forward direction and to  $k_p + k_s$  in the backward direction. The ratio of the Doppler width in the backward direction to the Doppler width in the forward direction for KrF scattered by methane, for example, is 26. This clearly leads to a violent forward bias in the gain for a scatterer that has a linewidth dominated by the Doppler width. Thus, the scatterers most appropriate for a compressor should have large, homogeneous linewidths that are much greater than the Doppler width and that are composed of many collision-broadened and overlapping lines of a closely spaced Q-branch transition. Widely separated, narrow, Doppler-dominated lines, such as the completely resolved Raman Q-branch lines of molecular hydrogen, should be of less utility. A large Raman linewidth for the scatterer also permits the use of a pump laser with a linewidth that is relatively straightforward to achieve.

In practical cases, the effect of Doppler broadening is mitigated because Doppler broadening is decreased by collisions in a gas. At near zero pressure, the velocity appearing in the Doppler shift is the thermal velocity. When the pressure is increased to the point that a scatterer suffers several collisions in less than a wavelength, the thermal velocity is replaced by the much smaller diffusion velocity, which is itself inversely proportional to pressure. Figure 7-73 shows the calculated Doppler contribution to the backward Raman linewidth for several Raman scatterers of possible interest for use in a Raman compressor. We note that for methane

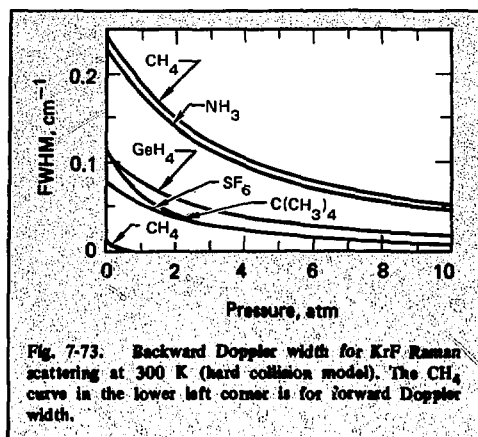


Fig. 7-73. Backward Doppler width for KrF Raman scattering at 300 K (hard collision model). The  $\text{CH}_4$  curve in the lower left corner is for forward Doppler width.

with a Q-branch linewidth of  $0.3 \text{ cm}^{-1}$ , the Doppler contribution to the backward linewidth is always less than a factor of two; for  $\text{SF}_6$ , which is thought to have a Q-branch linewidth of 1 to  $1.5 \text{ cm}^{-1}$ , the Doppler contribution is negligible. In the past, stimulated Raman experiments have typically been conducted at pressures above 10 atm where Doppler contributions are always negligible except for materials such as  $\text{H}_2$  and  $\text{D}_2$ . The forward Doppler width also is always negligible for any of the scatterers, as shown for methane in Fig. 7-73.

A third cause of forward-to-backward asymmetry influences the design of the pump laser. In the case of forward scattering, the Stokes pulse propagates along with the pump pulse and, at each point, always sees the same part of the pulse and the same intensity. If there is a large peak intensity at some point in the pump pulse, the gain for forward superfluorescence will be high at that point. In the backward direction, however, the Stokes pulse sweeps through the entire pump pulse and experiences a gain determined by the average intensity rather than by the peak intensity. The practical effect of this process is that intensity spikes in the pump pulse can be converted to forward Stokes superfluorescence and thus be useless in the backward compression. Therefore, the pump laser must have a reasonably smooth intensity profile in space and time with only a small fraction of its energy in intense spikes.

When stimulated Raman scattering experiments are conducted at very high intensities, the Raman output is not confined to the first Stokes wave corresponding to a single Raman shift from the pump, but in fact comes out in a wide variety of higher order Stokes and anti-Stokes waves. Some of

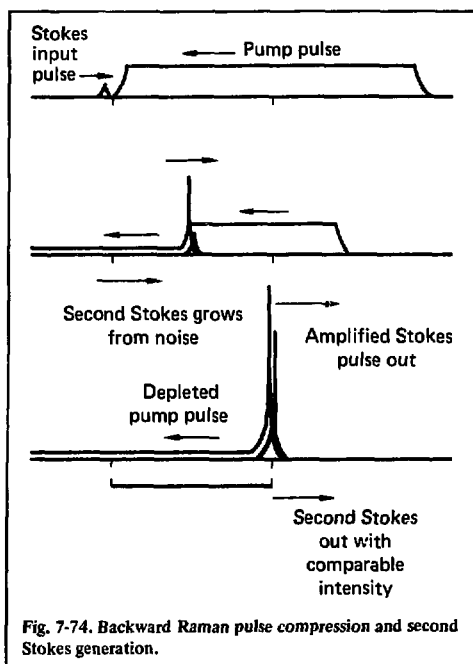


Fig. 7-74. Backward Raman pulse compression and second Stokes generation.

these waves are produced in a conventional gain process. Some waves are produced by parametric coupling through a material excitation that has been established by other waves in the medium in a manner similar to that discussed for the forward-to-backward asymmetry. The higher order process, occurring first and setting up the material excitation required for more complex processes, is a conversion of the backward first Stokes pulse (the desired output from the compressor) to a copropagating backward second Stokes pulse.

The conversion of the backward first Stokes pulse to the backward second Stokes pulse is illustrated in Fig. 7-74. The backward first Stokes output of the compressor grows in intensity as it depletes the pump wave. This intense first Stokes wave may then serve as a pump to produce gain and fluorescence for a backward second Stokes pulse propagating along with the backward first Stokes pulse. Because this conversion is a forward scattering process, the enhanced forward gain process discussed above can play a very important role. In addition, because this conversion is a superfluorescent process that grows from noise rather than from a carefully controlled input pulse, the focusability of the second Stokes radiation will, in most cases, be inadequate for transport to a target. A spatially

coherent second Stokes pulse might be injected to overcome this particular limitation, but our analysis of this possibility indicates that such an injection would lead to considerable complexity and to the excitation of undesirable parametric processes without providing sufficient compensating benefits.

The second Stokes gain depends primarily on two parameters, the extraction efficiency  $\eta_R$  (defined as the Stokes photons out minus the Stokes photons in divided by the pump photons), and the product of the forward-to-backward gain ratio times the compression ratio  $R_k$ . The second Stokes pulse displays a fairly weak dependence on the backward gain, no discernible dependence on the pump pulse shape, but some dependence on the backward first Stokes pulse shape.

The production of the second Stokes pulse leads to a design tradeoff for the backward first Stokes intensity that is produced in a compressor stage. Efficient depletion of the pump wave requires a high backward Stokes intensity in the compressor, but suppression of a backward second Stokes pulse conflicts with this and requires that the backward first Stokes intensity be kept low. To address this trade-off, we have developed a general four-wave code that treats arbitrary pump and backward first Stokes input pulses and then calculates the behavior of these pulses as well as the growth of the forward first Stokes and the backward second Stokes, using the general theory of Raman scattering. The code includes the effects of gain saturation and has been used to define the required operational parameters of potential large scale Raman amplifiers.

**Raman Modeling.** The power gain and saturation characteristics of the compressor are treated most simply with a plane wave model. If the pump and Stokes waves always overlap inside the cell, these equations can be transformed into the Frantz-Nodvik<sup>125</sup> equations for a saturating storage amplifier together with the appropriate boundary conditions.<sup>126,127</sup> In the fusion application, this approximation is expected to be quite good. In the Frantz-Nodvik theory, the extraction efficiency for an amplifier  $\eta$  is given by

$$G\eta = \ln \left[ \frac{1 + \Phi_0 e^G}{1 + \Phi_0} \right], \quad (65)$$

where  $G$  is the gain length product. Also,

$$\Phi_0 = -1 + \exp J/S. \quad (66)$$

is a function of the ratio of input fluence  $J$  (in  $J/cm^2$ ) to the saturation fluence  $S$ ,

$$S = 2\omega_s/\omega_L \gamma c. \quad (67)$$

Here,  $\gamma$  is the gain coefficient for backward Raman scattering (in  $cm/W$ ). The input fluence  $J$  is given by

$$J = \int dt I_s(t). \quad (68)$$

Figure 7-75 plots in the input fluence required to achieve a given extraction efficiency parametrically for different gains.

Of course, an arbitrarily high extraction efficiency cannot be achieved in a Raman amplifier because of the onset of parasitic waves. The most strongly driven parasitic waves are the forward and transversely propagating pulses at the Stokes frequency and the backward second Stokes pulse.<sup>107,128,129</sup> Anti-Stokes waves are not included because, if they are important, the losses are already too large. Similarly, other Raman processes are not important if the compressor operates on the strongest transition. The transverse parasitic wave experiences a gain that varies with both its longitudinal and radial position in the cell. In an optimally designed system, the pump fills the cell aperture uniformly, eliminating the radial dependence. Then,

$$G_T = (\gamma_T/\gamma_F) G_F - n \ln R, \quad (69)$$

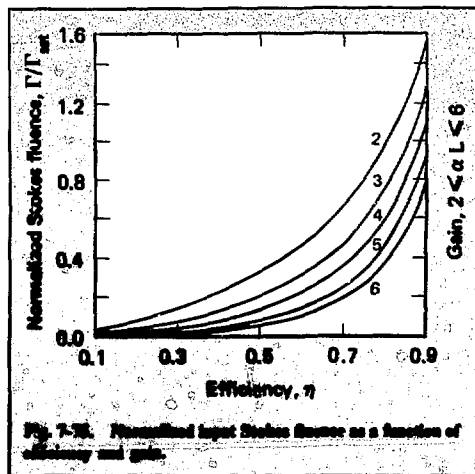


Fig. 7-75. Normalized input Stokes fluence as a function of efficiency and gain.



where  $R$  is the reflection coefficient and  $G_F$  is the forward gain in the absence of a backward wave. The  $\gamma_T/\gamma_F$  term is the ratio of the transverse to forward small signal gain, and  $n$  is the number of reflections that the parasitic wave may make while the pump is present in the cell. The gain required for the transverse wave to deplete the pump is generally less than that for the forward wave. Consequently, it is possible for the device to superfluoresce transversely but not in the forward direction. For a suitable choice of  $R$ , the transverse wave may be suppressed. With reflectivities of 1% per surface, transverse gain suppression requires that the Raman amplifier aperture be less than approximately one-half the amplifier gain length. This is not a severe limitation on amplifier scaling.

Assuming that the transverse waves have been suppressed, the basic equations describing the four waves are as follows.<sup>130</sup> If

$$D_a^{f,b} = \frac{\partial}{\partial z} \pm n_a \frac{\partial}{\partial ct} \mp \frac{\nabla_{\perp}^2}{2ika}, \quad (70)$$

and the Manley-Rowe factors are the frequency ratios,

$$M_{a,b} = (\nu_p/\nu_s, \nu_s/\nu_{2s}), \quad (71)$$

then

$$\begin{aligned} D_p^f E_p^f &= -\frac{1}{2} \left( \gamma^f M_a Q_1 E_s^f + \gamma^b M_a Q_3 E_s^b \right), \\ D_s^f E_s^f &= \frac{1}{2} \left( \gamma^f Q_1^* E_p^f - \gamma^b M_b Q_4 E_{2s}^b \right), \\ D_s^b E_s^b &= -\frac{1}{2} \left( \gamma^b Q_3^* E_p^f - \gamma^f M_b Q_2 E_{2s}^b \right), \\ D_{2s}^b E_{2s}^b &= -\frac{1}{2} \left( \gamma^b Q_4^* E_s^f + \gamma^f Q_2^* E_s^b \right). \end{aligned} \quad (72)$$

Here,  $E$  is the electric field,  $\gamma^b$  and  $\gamma^f$  are the backward and forward gain coefficients, respectively. The  $Q_i$  terms are the molecular quadrupole waves,

$$\begin{aligned} (Q_1, Q_2, Q_3, Q_4) &= \Gamma \int_{-\infty}^t dt' e^{-\Gamma(t-t')} \\ &\times E_p^* E_s^f, E_s^b E_{2s}^b, E_p^* E_s^b, E_s^f E_{2s}^b, \end{aligned} \quad (73)$$

where  $\Gamma$  is the HWHM for the Raman line (in rad/s).

Contrary to the generation of higher order Stokes pulses in the forward direction, there is no parametric process involving all four waves in the backward process. In the steady-state plane-wave regime, these equations (72) reduce to the Frantz-Nodvik equations. In general, the solutions are not simple, but may be obtained accurately in the region where the parasitic waves are weak and do not distort the pulses that feed them. The coupling between the two parasitic waves may be ignored in this region because it is small and of the same order as the weaker processes already neglected.

From the point of view of the gain experienced by the backward wave, the effect of the growth of a forward Stokes wave is to shorten the compressor cell to the length at which the forward parasitic wave grows to the pump intensity. If that length is  $l_g$  and if the cell has length  $l$ , then the pump has converted to the forward Stokes wave over a length  $l-l_g$ . In this case, the efficiency of extraction is reduced by a little more than  $l_g/l$  as a result of the mismatch between the pump pulse length and the effective cell length  $l_g$ . Thus, the forward superfluorescence limit is a soft limit in that, as  $l_g$  decreases below  $l$ , the compressor performance deteriorates slowly. The design criterion for the suppression of the forward Stokes wave is

$$\frac{\gamma^f}{\gamma^b} \equiv R < \frac{g_f}{G}, \quad (74)$$

where  $g_f$  is the maximum tolerable gain above which forward superfluorescence occurs and  $G$  is the gain in the backward direction.

The gain experienced by the second Stokes wave may be obtained analytically in the Frantz-Nodvik plane-wave limit of Eqs. (72) and (73). If  $t$  is a position coordinate in the backward Stokes pulse, then integration of the Frantz-Nodvik result for the Stokes wave gives

$$I_{2s}(t) = I_0 \exp g_{2s}(t), \quad (75)$$

where

$$g_{2s}(t) = 2RL/Gc(\Phi'/\Phi) \ln \left[ 1 + \frac{e^{G-1}}{1 + \Phi^{-1}} \right], \quad (76)$$

and

$$\Phi(t) = -1 + \exp S^{-1} \int_{-\infty}^t I^{in}(t') dt' . \quad (77)$$

Namely, the gain experienced by the parasitic wave depends on its location in the driving wave. For the parasitic wave to be suppressed,  $g(t)$  must be less than the limit

$$g_{2s}(t) < \ln I_s^m / i_0 , \quad (78)$$

where  $I_s^m$  is the peak intensity in the Stokes wave. The gain  $g$  depends on the pulse shape through  $\Phi$ . For example, if the Stokes pulse is steeply rising, a spike develops that strongly pumps the parasitic wave. Thus, Eq. (78) depends on both the magnitude and the shape of the pulse. In general, the gain at the second Stokes frequency may be written in terms of the efficiency and the backward gain by eliminating  $I^{in}$  from Eq. (77). One obtains

$$g_{2s}^m / R\kappa = F_s(G, \eta) \quad (79)$$

where  $R$  is the forward-to-backward gain ratio, and  $\kappa$  is the pulse compression,

$$\kappa = 2L/c\tau \quad (80)$$

where  $\tau$  is the full width at half maximum (FWHM) of the injected Stokes pulse. The function  $F_s$  depends only on the backward gain, the efficiency, and the input Stokes pulse shape: it is independent of the Stokes fluence. To avoid second Stokes production, we must have

$$g_f < g_{2s}^m , \quad (81)$$

where  $g_f$  is the maximum tolerable gain for a forward process. Therefore, the performance of the device is limited by the inequality,

$$Z \equiv \frac{g_f}{R\kappa} < F_s(G, \eta) . \quad (82)$$

The parameter  $Z$  is a critical design parameter. Because  $F_s$  is only weakly dependent on  $G$ , Eq. (82) shows that second Stokes production is primarily a limit on the efficiency. The inequality may be used either to evaluate the maximum efficiency or to limit  $Z$  if  $\eta$  is chosen. For example, for Gaussian in-

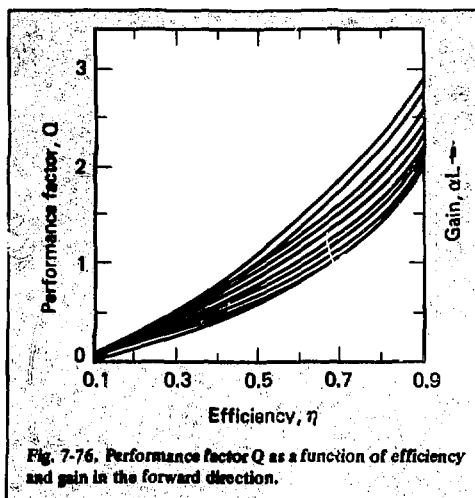


Fig. 7-76. Performance factor  $Q$  as a function of efficiency and gain in the forward direction.

put pulses,  $F_s$  is given by Fig. 7-76, for which a good fit is

$$F_s = a_1 (1 + a_2 g) (1 + a_3 \eta + a_4 \eta^2) , \quad (83)$$

where

$$\begin{aligned} a_1 &= 0.1036 , \\ a_2 &= 0.1032 , \\ a_3 &= -1.6171 , \\ a_4 &= 20.941 . \end{aligned} \quad (84)$$

In the region of interest,  $F_s \approx 2$ , and using  $g_f \approx 20$  gives

$$R\kappa \leq 10 . \quad (85)$$

If the second Stokes wave is not small, it burns a hole in the backward Stokes pulse. This happens quasi-discontinuously as the limit [Eq. (72)] is violated. Thus, the second Stokes limit is a hard limit, for which the efficiency drops rapidly to unacceptable low values (<10%) as it is exceeded. Efficient compressions greater than 10 will require suppression of the second Stokes wave or artificial reduction of the ratio  $R$  below unity. Figure 7-77 illustrates the hole-burning effect for  $Z=1.5$  and  $F_s=2$ . We clearly see the potentially debilitating effect of the backward parasitic wave.

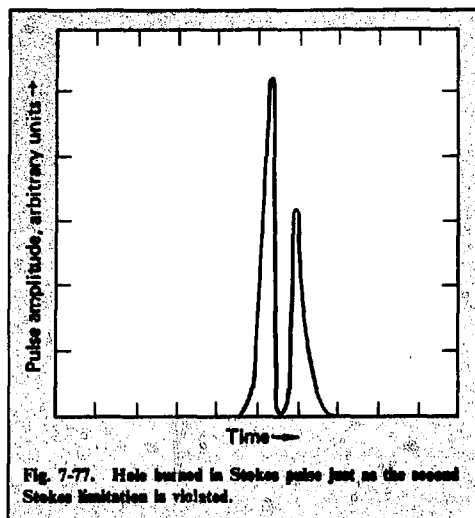


Fig. 7-77. Hole burned in Stokes pulse just as the second Stokes limitation is violated.

The predictions of the Frantz-Nodvik plane-wave limit have been tested using a numerical simulation of the system [Eqs. (72) and (73)] in the limit where diffraction may be neglected. The results verify all the above conclusions, including the softness of the forward wave limit and the sharpness of the backward wave limit. The estimate  $g_r \approx 20$  is probably conservative. For pathological pulse shapes (e.g., "top hat" pulses), the rise time is so short that the transient theory must be used. However, such pulses are not of interest because they are incompatible with laser target requirements.

Diffraction effects, very important in focused geometries, are less important in collimated systems. Hard apertures, mode beating, and other effects cause spatial nonuniformities in the pump and Stokes waves. A small diffractive effect is expected in the forward process as a result of nonuniform gain. In the backward process, the pump is temporally (i.e., longitudinally) integrated, and only whole beam diffraction caused by a transverse intensity profile on the pump is observed. This effect is very small in a large aperture saturating compressor. In general, diffraction is a weaker effect than refraction by density fluctuations. The gain-induced diffraction angle is  $\lambda/d = 1$  to  $10 \mu\text{rad}$ .

Figure 7-78 details the efficiency limitation, as a function of  $Z$  and gain, for Gaussian input Stokes pulses and a flat pump pulse. The weak dependence on the gain is evident and the importance of  $R$  is emphasized. It is clear from Fig. 7-78 that good ef-

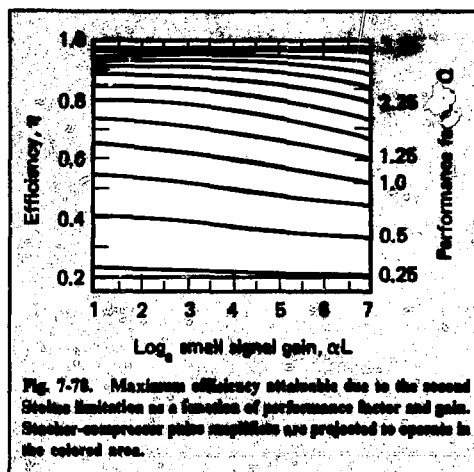


Fig. 7-78. Maximum efficiency obtainable due to the second Stokes limitation as a function of performance factor and gain. Stocher-compressor pulse magnitudes are projected to operate in the colored area.

iciency can be maintained in a Raman compressor so long as  $R$  is kept as small as possible and the compression ratio is not too large. However, it is also obvious that suppression of the second Stokes gain, and thus operation at higher  $Z$ , is an area of high leverage for improving the performance of a Raman compressor and should be carefully researched. Atomic vapor scatterers, or selective absorbers for the second Stokes frequency, are techniques for relaxing second Stokes limitations. Practical compressors can be built without second Stokes suppression, but systems will be much less complex if suppression can be achieved.

In designing practical Raman amplifiers, it is also important to know what values of net fluence amplification can be achieved for a given value of  $Z$ . Figure 7-79 plots the fluence multiplication that can be achieved with given Stokes fluence input in units of the saturation fluence. Upper limits on input fluence for various values of  $Z$  are shown by the shaded areas. It is clear that fluence gains of approximately 30 can be achieved for a reasonable value of  $Z=1$ , corresponding to  $R=2$ ,  $\kappa=10$  or  $R=4$ ,  $\kappa=5$ . The Raman preamplifier should provide a Stokes beam with a fluence of about one-tenth of a saturation fluence.

**Nonparametric Losses.** The dominant absorption process in a sensibly designed compressor is at least two quantum; if two-photon absorption is allowed, it may represent a design limitation.<sup>130</sup> The absorption may involve two pump photons, two Stokes photons, or one of each. Because of pulse compression, two-photon absorption at the Stokes frequency probably will dominate. Two-photon absorption may occur either in the medium

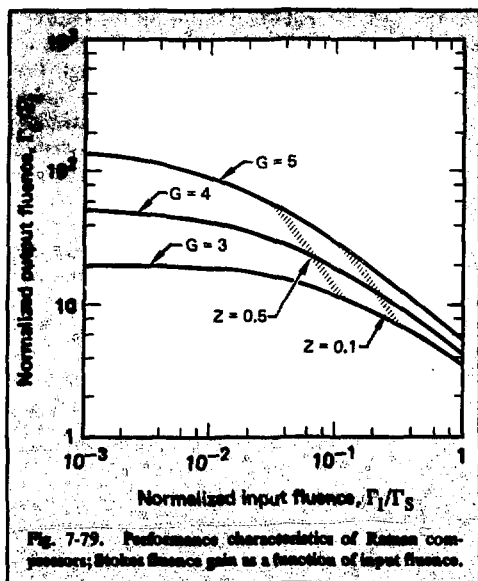


Fig. 7-79. Performance characteristics of Raman compressors; Stokes fluence gain as a function of input fluence.

or in the optical windows. The loss in extraction efficiency due to two-photon absorption is

$$\frac{\delta\eta}{\eta} = \frac{3}{2} \alpha^p I_p L + \frac{\alpha^p}{\gamma^R} \bar{g}_2 \left( 1 + \frac{\alpha^{ps}}{\alpha^p} \right) \quad (86)$$

Here,  $\alpha^j$  is a two-photon absorption coefficient and  $\bar{g}_2$  is the intensity-weighted mean of the second Stokes gain. This result is an underestimation of the loss because optimal pulse shapes have been assumed. Also, catastrophic losses due to breakdown may appear, but at 1-ns pulse lengths the thresholds are typically an order of magnitude larger than those allowed by damage considerations.

The two-photon absorption may be estimated reliably by relating the two-photon absorption rate to the Raman gain  $\gamma^R$ . This ratio can be expressed in terms of molecular parameters alone:

$$\frac{\alpha}{\gamma^R} = \sum_r 2 \left( \frac{M^r}{M_R} \right)^2 \frac{\Gamma_R}{\Gamma_r} f^r \quad (87)$$

The index  $r$  denotes a particular final state and  $f^r$  is the absorption line strength normalized to unity at its peak. Consideration of the various dipole matrix elements involved yields, approximately,

$$\xi \equiv \frac{\alpha}{\gamma^R} \approx 2 \times 10^{-3} \bar{f} \quad (88)$$

where  $\bar{f}$  represents the total contribution from all final states. This is a rapidly varying function of the distance above the band edge at which the optical frequencies lie. From Eq. (84),

$$\frac{\delta\eta}{\eta} \leq 0.04 \bar{f} \quad (89)$$

and it is clear that, for some molecules, two-photon absorption may represent a more severe limit than second Stokes production, depending on  $\xi$ .

The absolute value of the two-photon absorption has been estimated in methane<sup>130</sup> to be

$$\alpha = 7 \times 10^{-14} \text{ cm/W-atm} \quad (90)$$

**Beam Quality Limitations.** Under conditions where the bandwidths of the pump and the input Stokes wave are narrow compared to the Raman linewidth, both spatial and temporal inhomogeneities aggravate the production of parasitic waves. The forward gain under temporally inhomogeneous pumping has been calculated recently,<sup>131</sup> showing that

$$G_f = \bar{G}_f \left( 1 + \frac{I_r}{I_m} v \left( 1 + v^2 \right) - \frac{1}{2} \right) \quad (91)$$

where  $I_r$  is the intensity ripple,  $I_m$  is the mean intensity, and

$$v = \frac{2\pi^{1/2} \Gamma_r}{\bar{G}_f} \quad (92)$$

The forward Stokes field may have a variety of amplitude and phase variations. The one most strongly driven by a temporally stochastic pump has a phase that is strongly correlated with that of the pump. The phase diffusion of the pump is significant only in determining the source of the forward Stokes wave; it does not determine the gain because gain depends only on the intensity of the pump [see Eq. (91)]. This applies to both parasitic waves driven by a forward process.

In the backward process, hole-burning and phase diffusion do not occur because of the averag-

ing effect of the relative velocity of the waves. The gain in the backward process is unaffected by noise on either wave if

$$B_b \left[ (\Gamma \tau_p)^{-1} + (\Gamma \tau_s)^{-1} \right] < 1, \quad (93)$$

where the  $\Gamma$  is the HWHM of the Raman line and  $\tau_p$  and  $\tau_s$  are the noise correlation time for the pump and Stokes waves, respectively. Consequently, the extra contribution to the forward processes appears in the performance factor as an increase in  $R$  above its value under monochromatic conditions. Because only the pump is expected to be noisy, only the soft forward limits are affected. Evidently, the condition (93) is not a stringent one.

In nearly dispersionless media such as methane, the presence of spatial inhomogeneity reduces the gain by a factor  $n$ , which is, loosely speaking, the number of spatially incoherent molecular waves generated in the Raman process. This number is  $R$  times as large for backward processes as for forward processes, because the backward gain is smaller by  $R$  and because a higher degree of collinearity is required to maintain coherence. Also, under conditions where both the pump and Stokes waves are broad in frequency compared to  $\Gamma$ , a parametric four-wave process appears when the Fourier spectrum of the pump field is broad compared to the intensity spectrum. This further aggravates the production of parasitic waves. Thus, to achieve a compression of five or more, the pump and Stokes must be of high mode quality and narrow band; i.e.,

$$G \Delta \nu_p \leq 2 \Gamma, \quad (94)$$

corresponding to pump linewidths of approximately  $0.1 \text{ cm}^{-1}$ , and

$$\delta \theta \leq \left( \frac{8G\lambda}{L} \right)^{1/2}, \quad (95)$$

corresponding to a beam divergence of  $\approx 1 \text{ mrad}$ .

A number of computer codes have been developed to study laser wave noise. In particular, temporal pump modulation of a plane wave pump has been investigated in both the forward and backward processes. The method involves directly solving the integral equations for the Stokes wave under pumping by an arbitrary wave. A statistical treatment of noise becomes possible if many cases

are examined. An important feature of the noise effects is that the output becomes irreproducible from experiment to experiment. That is, although the mean output may depend only weakly on the noise component of the pump (being an ensemble average), an individual member of the ensemble may have an output that differs greatly from the mean. In the forward direction, this irreproducibility is quite strong even for moderate noise components. However, in the backward direction, the mean square deviation of the output in the ensemble is small and thus the backward process is reproducible from shot to shot.

The Stokes pulse aberrations are caused by refraction resulting from gas density variations, and by self-focusing. The phase aberration may be estimated from the formulas,<sup>132</sup>

$$\delta \phi_T \approx k \delta n (aL)^{1/2}, \text{ turbulent}, \quad (96)$$

$$\delta \phi_A \approx k \delta n L, \text{ acoustic}, \quad (97)$$

where  $a$  is the scale length of the turbulence and  $\sigma_n$  is the index change. The acoustic modes are generated by energy deposition in the last pulse. The turbulence is driven by random fluctuations in temperature and pressure, viscous drag, ground vibrations, etc. Use of  $\delta \rho / \rho = 10^{-4}$ , an optimistic value, results in several waves of phase distortion that must be removed with spatial filters and other special techniques (e.g., phase conjugators).

The optical nonlinearity of the gas leads to self-focusing, which has been measured in methane at optical frequencies. Using a simple dispersion model to extrapolate to 250 nm gives

$$\gamma = 3.5 \times 10^{-8} \text{ cm/W} \cdot \text{atm}. \quad (98)$$

the associated B-integral is approximately unity.<sup>133</sup> Thus, self-focusing effects would be less than refractive effects.

The effect of anomalous dispersion also has been considered.<sup>134</sup> The gain at the Stokes frequency causes a variation in the real part of the refractive index over the Stokes bandwidth. This variation is

$$\delta \phi \approx \frac{G}{4} \frac{\Delta \nu_S}{\Delta \nu_R}, \text{ or } \delta \phi \approx 0.5 \text{ rad}, \quad (99)$$

and is an order of magnitude smaller than the variation due to density variations.

**Scaling and Optimization.** The major design consideration for a fusion driver is the phase aberration that may be tolerated at the output. From this, the amplifier length is determined and then the maximum pump pulse length. The tolerable phase aberration is given by the required focal spot size at the target. Thus, the mean scatter satisfies

$$\theta < r_s/F. \quad (100)$$

If  $d$  is the transverse scale of the phase aberration and  $D$  is the aperture, then

$$\theta^2 = \left( \frac{1.2\lambda}{D} \right)^2 + \frac{\lambda^2}{4\pi^2} \left( \frac{\delta\phi_T^2}{d_T^2} + \frac{\delta\phi_A^2}{d_A^2} \right) \quad (101)$$

Assuming that the acoustic contribution dominates, and choosing

$$\begin{aligned} r_s &= 1 \text{ mm}, \\ f &= 100 \text{ m}, \\ d &= D/3 = 30 \text{ cm}, \\ (\delta\rho/\rho) &= 10^{-4}, \end{aligned} \quad (102)$$

a density limit can be obtained from Eq. (97), such that

$$\rho\tau_p \leq 500 \text{ ns/atm}. \quad (103)$$

The limit may be relaxed by increasing the aperture to lengthen the acoustic wavelength. However, this limit (103) is too high because other defocusing effects have been neglected. The design pulse length is limited by the density for which the Raman line becomes inhomogeneous or for which  $S(\rho)$  increases beyond a damage fluence.

The density limitation (103) implies a minimum pump intensity required to achieve gain

$$I_p = GS_0\rho\tau_p \geq 20 \text{ MW/cm}^2, \quad (104)$$

where  $S_0$ , the saturation fluence at 1 atm, is  $\approx 2 \text{ J/cm}^2$  and the gain  $G$  is  $\approx 5$ . However, achieving this pump intensity with a KrF laser may require special components (e.g., pulse stackers, telescopes) or special geometries.

In conclusion, the Raman cell itself is constrained in length by random refraction and in aper-

ture by transverse gain. Most serious is the conflict between focusability and damage, suggesting that flow systems and optical components will be high priority items in future studies. The second Stokes limit implies a compression of 10 or less. The search for resonant systems or selective absorbers will determine the ultimate achievable compression.

## References

122. N. Bloembergen, *Nonlinear Optics* (Benjamin Press, New York, 1966).
123. S. A. Akhmanov, Yu E. D'yakov, and L. I. Pavlov, *Sov. Phys. JETP* **39**, 249 (1978).
124. S. C. Rautian and I. I. Sobel'mann, *Sov. Phys. Uspekhi* **9**, 701 (1967).
125. L. M. Frantz and J. S. Nodvik, *J. Appl. Phys.* **34**, 2346 (1963).
126. A. J. Glass, Lawrence Livermore Laboratory, Internal memorandum TDA-77-047 (1977).
127. D. Eimerl, Lawrence Livermore Laboratory, Internal memorandum TDA-77-103 (1977).
128. D. Eimerl, Lawrence Livermore Laboratory, Internal memorandum TDA-77-140 (1977).
129. D. Eimerl, Lawrence Livermore Laboratory, Internal memorandum TDA-77-254 (1977).
130. D. Eimerl, *Design Considerations for Raman Compressors in Inertial Confinement Fusion*, Lawrence Livermore Laboratory, Rept. (1978), to be published.
131. D. Eimerl, *Theory of Temporal Stochasticity in Raman Scattering in Dispersionless Media*, Lawrence Livermore Laboratory, Rept. UCRL-80957 (1978).
132. L. A. Chernov, *Wave Propagation in a Random Medium*, (Dover Press, New York, 1967).
133. D. Eimerl, Lawrence Livermore Laboratory, Internal memorandum TDA-78-005 (1978).
134. D. Eimerl, Lawrence Livermore Laboratory, Internal memorandum TDA-77-232 (1977).

## Authors

D. Eimerl  
R. Haas  
J. Murray

### 7.6.4 Compression Experiments in Methane

There are many Raman (and perhaps Brillouin) scattering schemes that might be applied to the design of a pulse compressor for fusion applications. We are concentrating our efforts on one of these candidates that has been extensively studied in both stimulated and spontaneous Raman scattering, and which exhibits the best properties for a compressor of the various candidates for which extensive information is available. The candidate chosen is the Q-branch of the  $2916\text{-cm}^{-1}$   $\nu_1$  sym-

metric stretch vibration of methane. This transition has a very high Raman cross section<sup>135</sup> and consists of a large number of overlapping Q-branch lines, resulting in an homogeneous transition of width 0.3  $\text{cm}^{-1}$  which, at moderate pressures,<sup>136</sup> appears to be pressure independent, although some features of the spectrum have not been explained.

The Raman gain cross section for KrF radiation scattered by methane can be predicted from the known scattering cross section at 488 nm, using Placzek's Raman dispersion model. In terms of pump intensity  $I_p$  (in  $\text{W}/\text{cm}^2$ ) at 248 nm, the small signal backward gain is calculated to be

$$1.9 \times 10^{-11} \frac{\rho}{\Delta\nu_s + \Delta\nu_p} I_p L \quad (105)$$

Here,  $\rho$  is the methane density in Amagat units ( $2.68 \times 10^{19} \text{ cm}^{-3}$ , or 1.1 atm at 300 K),  $L$  is the cell length in centimeters, and  $\Delta\nu$  is in wavenumbers. This representation of gain as  $\gamma I L$  can be recast as  $\sigma \Delta n L$ , where  $\sigma$  is a conventionally defined gain cross section and  $\Delta n$  is the photon density in the pump beam.<sup>137</sup> A saturation energy fluence  $h\nu/\sigma$  can then be defined as the energy required in the first Stokes pulse to reduce the pump intensity to  $e^{-1}$  of its initial value. Because the backward first Stokes pulse sweeps through the pump pulse and sees twice as many photons per unit volume as a stationary observer, it may be shown<sup>138</sup> that  $e_{sb}$  is  $2h\nu/\sigma$  for this case.

The predicted backward saturation fluence for methane as a function of pressure is shown in Fig. 7-80, assuming a pump linewidth of  $0.1 \text{ cm}^{-1}$  and the Lorentzian line behavior of Fig. 7-73. The predicted value of  $R$  also is shown, assuming that the methane Q-branch is a quasi-Lorentzian line above about 1 atm as indicated by recent CARS spectra.<sup>136</sup> At low pressure where individual lines are resolved,  $R$  will rise as shown. The model used here assumes that all linewidth effects add independently.

These predictions must be tested on a small scale so we can gain confidence in their validity before we make a serious commitment to this technology. During 1977, we began these experimental verifications, using small KrF TEA discharge lasers and methane amplifiers at high pressure (10 to 25 atm), where saturation phenomena can be studied at the low pulse energies available from the discharge lasers. Further study at higher energies will follow in 1978 to verify these predictions in more detail and with higher KrF and Raman pulse energies.

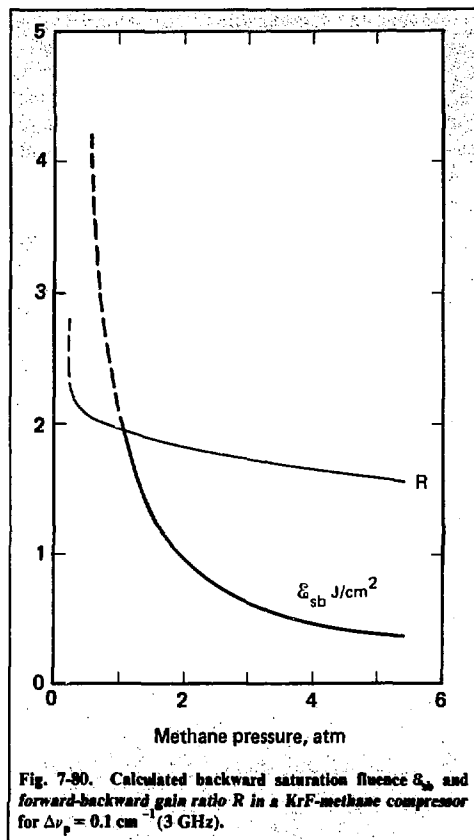


Fig. 7-80. Calculated backward saturation fluence  $e_{sb}$  and forward-backward gain ratio  $R$  in a KrF-methane compressor for  $\Delta\nu_p = 0.1 \text{ cm}^{-1}$  (3 GHz).

**Narrow Linewidth Operation and Spatial Beam Quality of a KrF Discharge Laser.** A characteristic feature of the KrF spectrum is its broad gain or fluorescence profile (Fig. 7-81). A free running KrF laser has its linewidth reduced to  $50 \text{ cm}^{-1}$  (Fig. 7-81). However, this linewidth is still much too wide for many potential applications, particularly for backward Raman pulse amplification.

The laser spectral linewidth can be reduced in a straightforward manner by inserting frequency-selecting elements such as prisms and etalons into the laser cavity. The reduction of linewidth is, unfortunately, accompanied by a dramatic drop in the laser output power. This drop is partially due to the additional intracavity losses. Also, because of the short duration of the gain, there is not enough time for the flux to build up to the saturating levels needed for efficient extraction of the available energy.

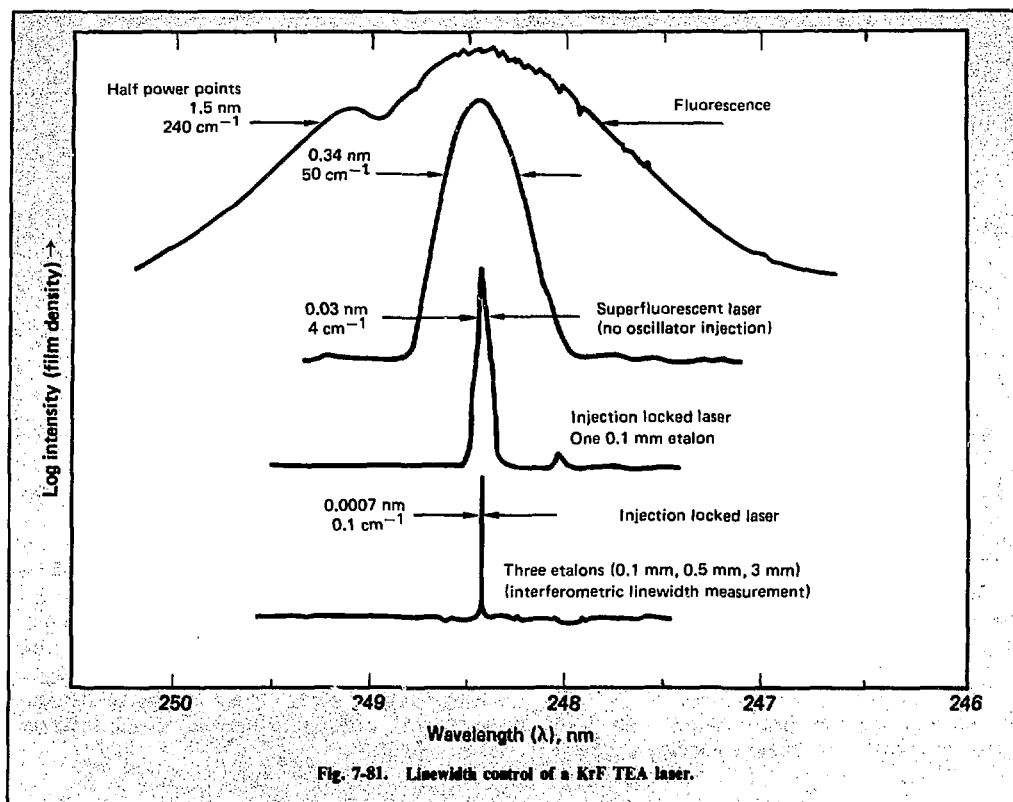


Fig. 7-81. Linewidth control of a KrF TEA laser.

To extract the available laser energy efficiently in the narrow linewidth output, it is necessary to use an oscillator-amplifier system. Our experiments with a separate line-narrowed oscillator and an injection-locked regenerative amplifier<sup>138</sup> revealed that all the available laser energy of the regenerative amplifier can be extracted in a narrow line controlled by the weak oscillator. A similar approach has been used successfully with other laser systems such as dye lasers.<sup>139</sup>

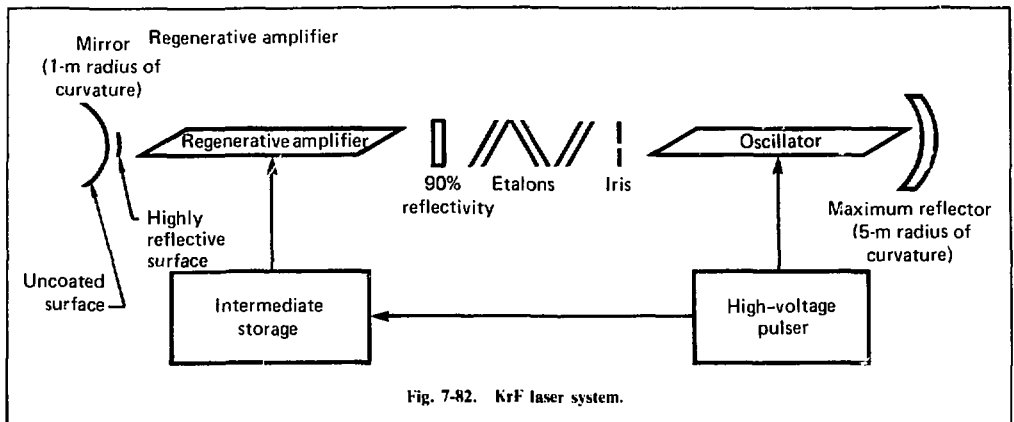
A reliable oscillator-regenerative amplifier system based on this principle was constructed and used for a number of experiments (see Fig. 7-82). The gain medium for the oscillator and the amplifier is provided by a fast transverse discharge through a uv preionized mixture of  $F_2/Kr/He$  in the ratio of 4/100/900. Typical operating pressures are 1 to 1.5 atm. The cross section of the gain medium is approximately 2 by 0.5 cm, and the length of each discharge is 100 cm. Each laser body is machined from Teflon to ensure fluorine compatibility and has  $CaF_2$  windows set at Brewster's angle. Elec-

trode profiles are similar to those used for  $CO_2$  TEA lasers (Fig. 7-83).

Each discharge laser has 32 nominally 0.5-nf barium titanate peaking capacitors that are pulse charged in less than 100 ns to the typical voltages of 30 to 45 kV needed for discharge breakdown. A current pulse from discharging these peaking capacitors has a characteristic full width of 20 ns and provides the excitation for the laser. The amplifier is fired 50 ns after the oscillator, allowing sufficient time for the oscillator output to reach maximum. The uv preionization is pulsed 100 ns before the main discharge.

A flat dielectric mirror with 90% reflectivity and a maximum reflector with a concave 5-m radius of curvature form the resonator cavity for the oscillator. An aperture  $\approx 1$  mm in diameter is used to improve the spatial beam quality. The spectral linewidth is determined by the etalons inserted into the laser cavity. One 0.1-mm gap etalon reduces the linewidth from 50 to 5  $cm^{-1}$ . Addition of the 0.5-mm etalon reduces the linewidth to 1  $cm^{-1}$ , and

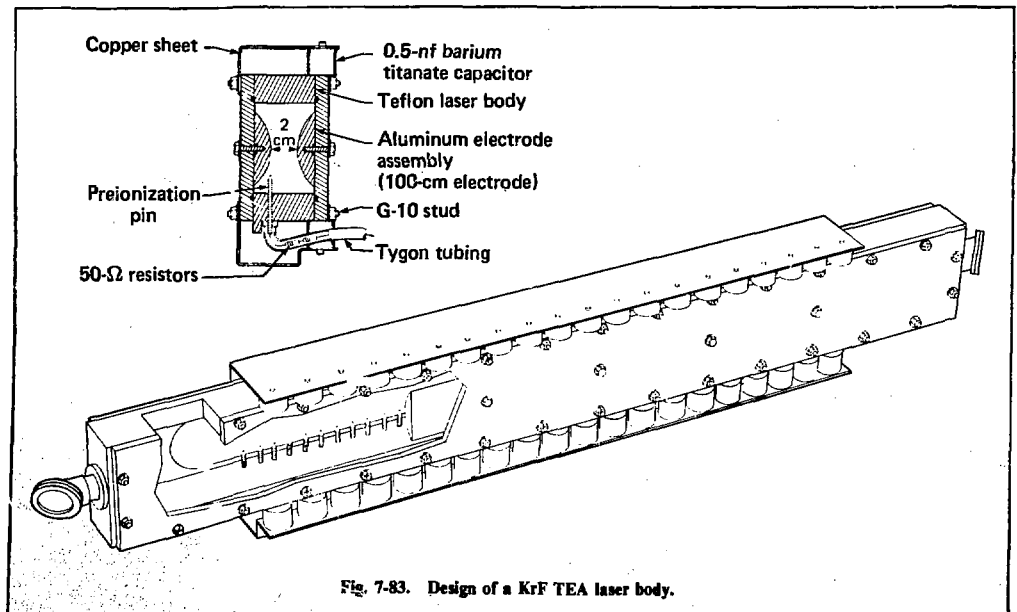




a 3-mm etalon reduces the width even further to  $0.1 \text{ cm}^{-1}$ . The 0.1-mm etalon is an air gap resonator, whereas the other two are solid etalons made of uv grade fused silica. All reflecting surfaces of the etalons are coated for 75% reflectivity at 250 nm; the outside surfaces of the air gap etalon are coated for antireflection.

The output coupling mirror of the oscillator also serves as the back mirror for the cavity of the regenerative amplifier. In this configuration, all the

output power of the oscillator is injected into the amplifier. The regenerative amplifier cavity is a half-symmetric unstable resonator with a magnification of eight. The output mirror is convex with a 1-m radius of curvature. The mirror is uncoated except for the central region where, in a 1- by 4-mm area, high-reflectivity coating is deposited. The injected beam from the oscillator passes through the amplifier, hits the high-reflectivity spot on the convex mirror on the return trip, and expands to fill the gain volume.



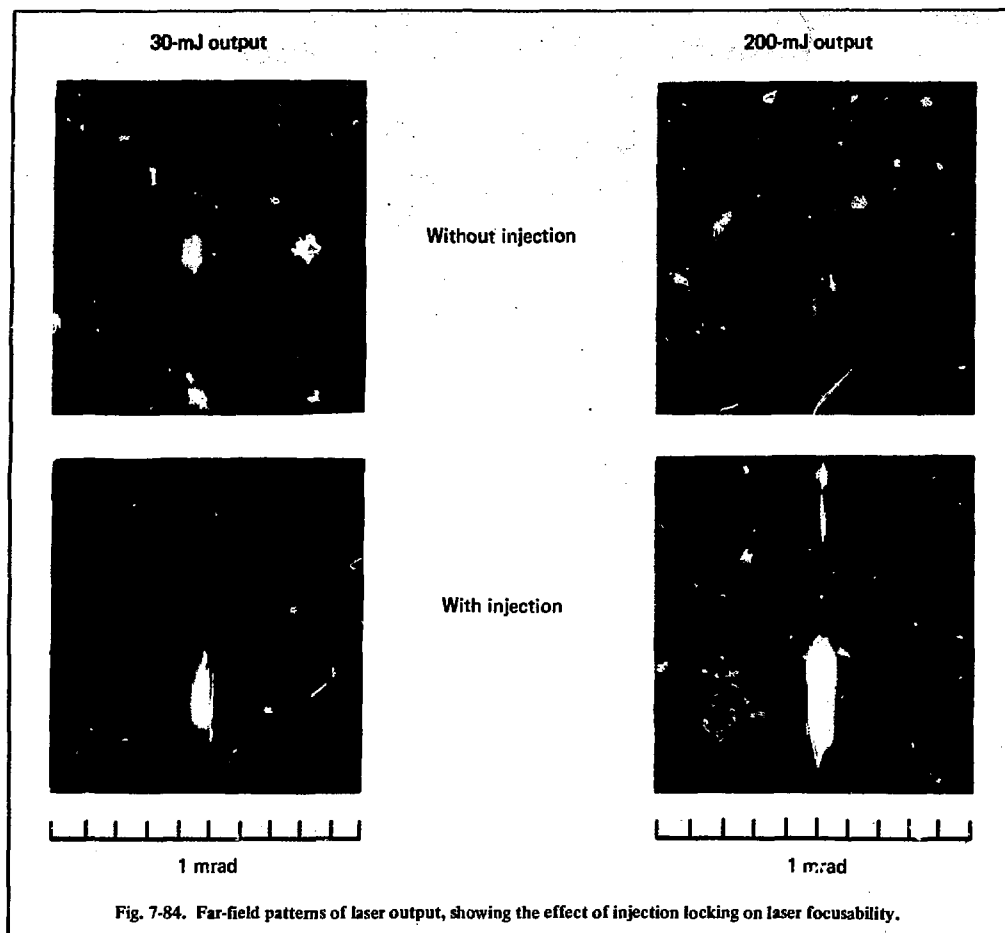


Fig. 7-84. Far-field patterns of laser output, showing the effect of injection locking on laser focusability.

The system generates laser pulses with a characteristic duration of 20 ns and with an energy  $>150$  mJ per pulse. The output energy from the system is independent of the oscillator output power. However, the far field beam profile and the spectrum of the output vary drastically with the oscillator input.

For oscillator powers  $\gtrsim 200$  W, the output spectrum of the system collapses down to that of the oscillator, greatly increasing the spectral brightness. The linewidth of laser output is monitored with a 1-m spectrometer and a high-finesse Fabry-Perot interferometer. With all three etalons in the oscillator cavity, a linewidth of  $0.1 \text{ cm}^{-1}$  is obtained. The fact that all the laser power can be extracted in a narrow linewidth demonstrates that the laser transition is broadened homogeneously,

as expected from the theoretical model for the KrF molecule.

In addition to increasing the spectral brightness, the injection locking of the unstable resonator dramatically improves the focusability of the output beam. Without any injection, the field inside the unstable resonator builds up from very divergent fluorescence. It takes two to three round trips through the cavity for the resonator mode to be established. Because the time for these round trips is comparable to the entire laser pulse, the divergence of the output will begin very large but will be decreasing in time. With injection locking, the laser builds up from the field of the oscillator, and therefore has less divergence from the start. Figure 7-84 illustrates the far field patterns for the

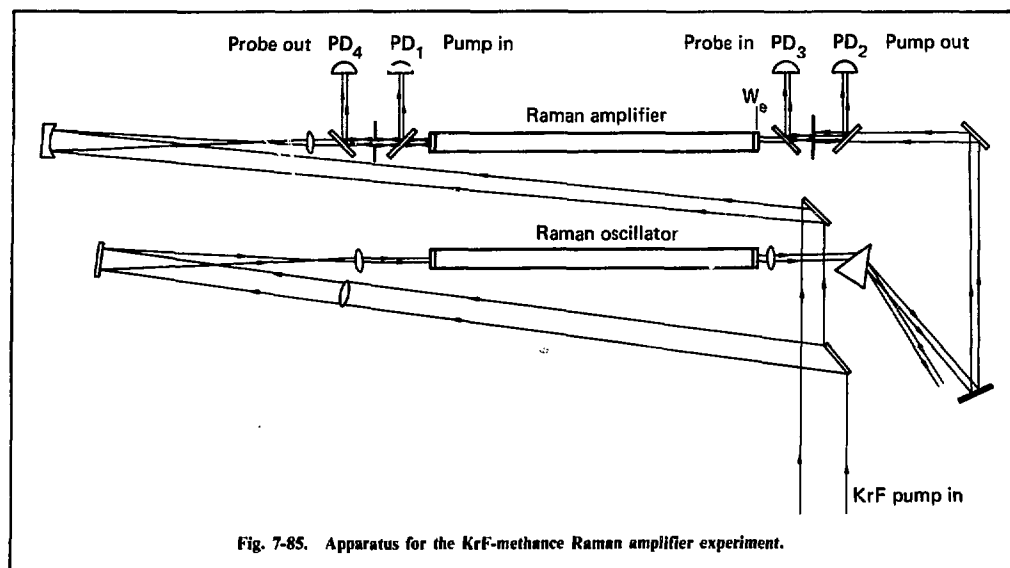


Fig. 7-85. Apparatus for the KrF-methane Raman amplifier experiment.

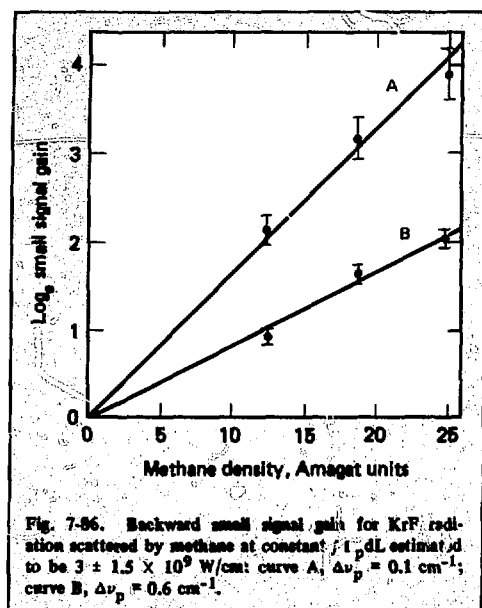
output with and without the injection locking. The beam quality with injection locking is limited only by the laser medium homogeneity. We see that the output is diffraction limited in the dimension parallel to the discharge, and is several times the diffraction limit in the perpendicular direction. Very high current densities in the laser medium cause this divergence, and the medium acts as a negative cylindrical lens. Most of this aberration should be correctable by appropriate external optics.

**Gain and Saturation in a KrF-Pumped Methane Raman Amplifier.** We have studied a methane Raman amplifier, using the KrF oscillator-amplifier system described above. These measurements were made with 30 to 50 mJ of KrF output energy to minimize the spatial variations that occur at high output energies. The output pulse is split into two equal parts, one of which is focused softly by a beam-contracting telescope through a 2-m-long Raman oscillator containing methane gas at 10 to 30 atm (see Fig. 7-85). The pump at 249 nm induces superfluorescent output at the first Stokes wavelength of 268 nm, which then passes through a prism monochromator and enters a 2-m-long Raman amplifier cell at the same pressure as the oscillator cell. The other half of the KrF pump pulse passes through a beam-contracting telescope and is directed through the same collimating apertures as the probe pulse but in the opposite direction. The transit time through the optics is arranged so that

the leading edges of the probe pulse and the KrF pump pulse meet at the exit window of the amplifier cell  $W_e$ : the transit time (length) of the Raman oscillator cell is selected to be 6.5 ns so that the leading edge of the probe pulse sweeps through the peak 13 ns of gain produced by the pump pulse. The counterpropagating beams are nominally 3 mm in diameter (the measurements discussed here are for the central 1.5-mm region of the beams). Beamsplitters and biplanar photodiodes, with appropriate neutral density and bandpass filters, are used to record the pump and probe pulses before and after they pass through the amplifier. The intensity calibration of the diodes is derived from comparisons with a calorimeter.

Figure 7-86 presents a plot of backward gain data obtained with this apparatus vs methane pressure at two pump laser linewidths. The data were obtained by varying the etalons in the KrF injection oscillator.<sup>111</sup> Gain is seen to be proportional to pressure for each linewidth (as predicted above), implying that any change in the linewidth of the methane Raman transition over this pressure range is small compared to the laser linewidth used in the experiment. The gain also shows the predicted  $(\Delta\nu_s + \Delta\nu_p)^{-1}$  dependence to within the precision of the experiment.

An absolute determination of the methane Raman gain coefficient requires an accurate knowledge of the pump intensity in the amplifier cell as well as precise lineshape information; it can-



not yet be stated with high precision. We estimate from the data shown in Fig. 7-86 that the backward Raman gain is given by

$$\exp \left[ (2 \pm 1) \times 10^{-11} (\Delta\nu + 0.3)^{-1} \int I_p dL \right], \quad (106)$$

where the units are as defined above and, for this condition,

$$\int I_p dL = 3 \pm 1.5 \times 10^9 \text{ W/m}. \quad (107)$$

The measured backward gain agrees with the theoretical prediction given above to within the accuracy of the experiment.

Forward gain for superfluorescence produced from the collimated pump beam in the amplifier cell is inferred by observation of the intensity of forward superfluorescence in the amplifier at higher pump intensities. The intensity of this superfluorescence is independent of laser linewidth over the range studied, even at linewidths as high as 30 to 50  $\text{cm}^{-1}$  (produced by removing all etalons from the injection oscillator). This also agrees with the theory presented above.

Large signal gain effects have been investigated with this apparatus<sup>140</sup> by raising the pump and probe intensities in the amplifier until saturation effects become apparent. Figure 7-87 shows typical pulse shapes for the Stokes input and output pulses under saturating conditions in the amplifier. The modulation on the Stokes input pulse is produced by mode-beating in the KrF oscillator. Later portions of the Stokes pulse see lower gain than the leading edge of the pulse because they enter the amplifier cell after a large part of the pump pulse has already exited, and because they see a pump pulse that has been depleted by the leading edge of the Stokes pulse. Figure 7-87 also illustrates the pulse shapes predicted by a computer model of the experiment, which integrates the equations that describe Raman scattering, assuming uniform plane waves and a saturation fluence of 50  $\text{mJ/cm}^2$ . This saturation fluence is near the theoretical prediction of  $\Phi_s = (2/\gamma_c) = 56 \text{ mJ/cm}^2$  for methane in the backward direction pumped by a laser with a 0.1- $\text{cm}^{-1}$  linewidth.

Similar data for the pump pulse with and without the presence of a counterpropagating Stokes pulse are shown in Fig. 7-88. Each of these photographs is an overlay of three pulses that averages out some of the underlying noise on the pulses and reveals the underlying shape more clearly. Figure 7-88 illustrates pump depletion by amplification of the Stokes pulse, showing a maximum intensity depletion of about 60% in this central region of the pump beam. Electronic integration of the pulses shown in Fig. 7-88 indicates a depletion of 30% of the total pulse energy in the central 1.5-mm area of the beam and about a 20% depletion in the entire beam for these conditions.

The energy fluence of the Stokes and pump beams was measured using a calorimeter. The pump beam in the absence of a counterpropagating Stokes pulses has an energy of 4.2 mJ in the central 1.5-mm region; the pulse diverges to about 1.5 by 4 mm at the exit of the cell. The fluence of the pump beam as it enters the cell thus is about 240  $\text{mJ/cm}^2$ . The pump suffers a whole-beam depletion of 20% in the presence of the Stokes pulse, i.e., an energy loss of 0.8 mJ.

The Stokes beam in the absence of a pump beam has an energy of 0.54 mJ in a nominal 1.5-mm diameter. In the presence of the pump, the energy gain is 2.2, adding 0.65 mJ to the Stokes beam in the central 1.5-mm region. This is in reasonable agreement with the energy lost by the pump, assuming that some Stokes energy is outside the central 1.5-mm region sampled and that the measurements must be taken on different shots in

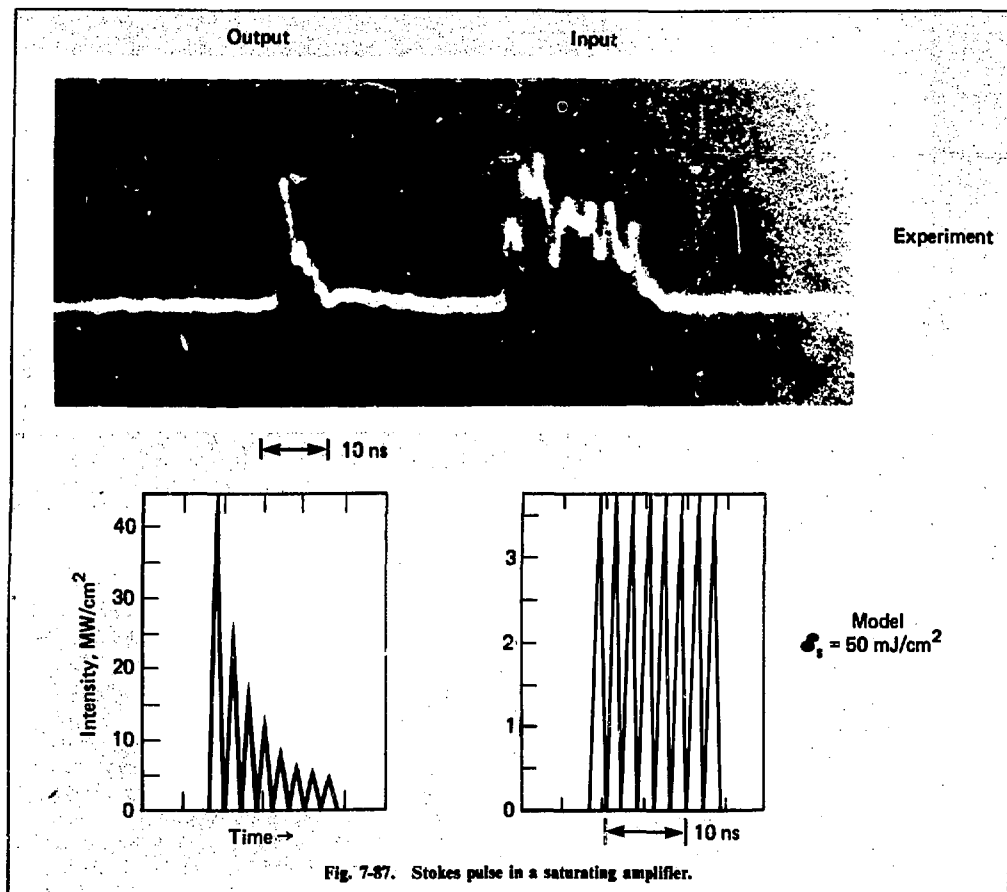


Fig. 7-87. Stokes pulse in a saturating amplifier.

the presence of some fluctuation in pump and Stokes pulse energies. The Stokes input fluence is  $\approx 30 \text{ mJ/cm}^2$  and is amplified to  $66 \text{ mJ/cm}^2$ , of which 40% is in the first 1-ns spike. This is an intensity of  $26 \text{ MW/cm}^2$ , about twice the  $12\text{-MW/cm}^2$  intensity of the KrF pump beam, demonstrating intensity enhancement in a saturating backward Raman amplifier.

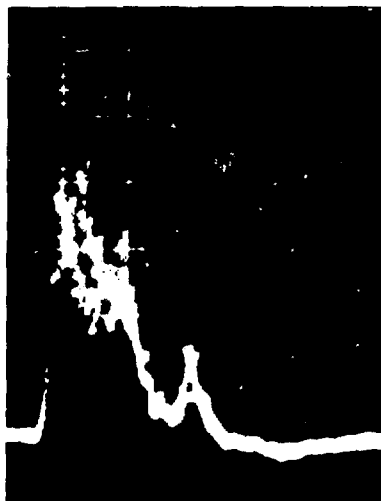
Analysis of the experimental results is complicated by the variable overlap of the Stokes and pump pulses in the amplifier and by the divergence of the pump as it propagates down the cell. Neglecting the small correction resulting from energy added to the tail of the Stokes pulse by gain produced by the tail of the pump pulse, the intensity of the pump at the position of maximum depletion should be given by  $I = I_0 e^{\mathcal{E}/\mathcal{E}_s}$ , where  $\mathcal{E}$  is the Stokes output fluence and  $\mathcal{E}_s$  is the saturation fluence, or

$56 \text{ mJ/cm}^2$ . This predicts  $I/I_0 = 0.31$  for the experiment, a value which is in good qualitative agreement with the measured value of 0.4.

Table 7-23 compares model results for energy gain and extraction for several assumed values of  $\mathcal{E}_s$  with the gain and extraction observed in the experiment. The model cannot be expected to give a precise duplication of the experiment, however, because the pump and Stokes beams do not have perfectly uniform and regular intensity profiles in space and time, and because plane-wave behavior is assumed in the model. We note, for example, that the pump beam diverges in one dimension as it propagates through the cell. This phenomenon is associated with the discharge effects in the KrF pump laser discussed previously. The integrated fluence  $\int I_p dL$  down the cell is thus only about two-thirds the value in a plane-wave case, reducing the

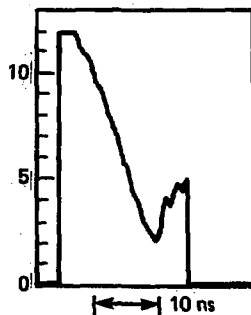
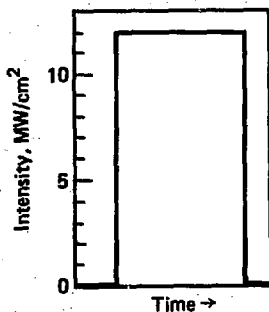
No  
Stokes

Saturating  
Stokes input =  
 $30 \text{ mJ/cm}^2$



Experiment

10 ns



Model  
 $\mathcal{E}_s = 50 \text{ mJ/cm}^2$

Fig. 7-88. Effect of Raman saturation on KrF pump transmission (pump input =  $240 \text{ mJ/cm}^2$ ).

**Table 7-23. Comparison of computer model values with experimental data for a backward Raman amplifier: pump input = 240 mJ/cm<sup>2</sup>, Stokes input = 30 mJ/cm<sup>2</sup>.**

Assumed saturation fluence, mJ/cm <sup>2</sup>	Stokes energy gain	Pump peak intensity depletion, %	Pump energy depletion, %
<b>Computer model</b>			
37.5	4.7	97	54
50	4.1	89	44
70	3.3	62	32
90	2.8	46	24
110	2.4	37	19
<b>Experiment</b>			
—	2.3	60	30

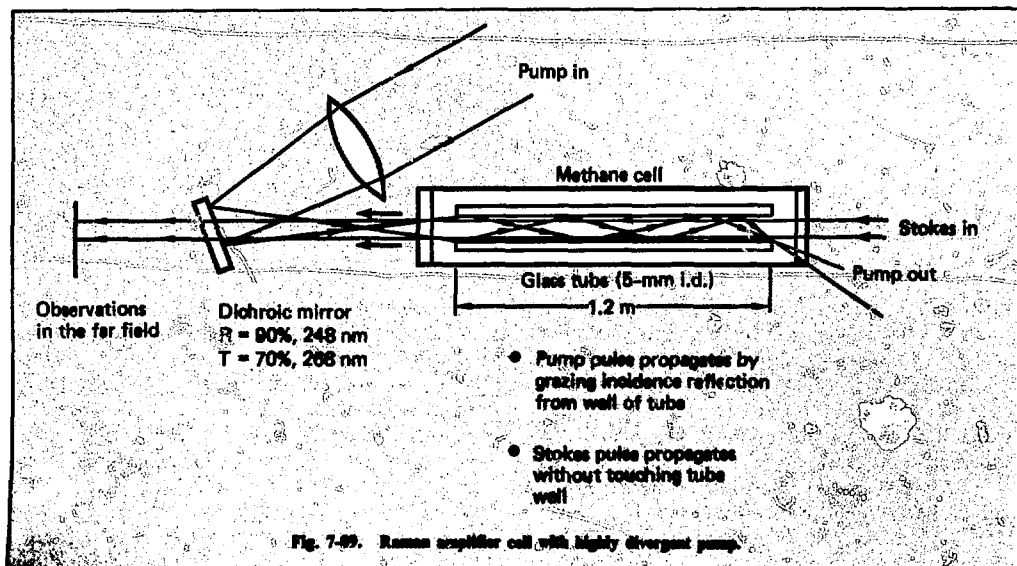
of about two. Further experiments will be required to improve the precision of these measurements and to verify the results at the lower methane pressures where a large compressor system would operate.

**Effects of Pump Beam Divergence on Backward Raman Amplification.** We performed a preliminary qualitative experiment to verify the absence of beam distortion in the backward Stokes pulse when it is amplified with a pump beam that contains severe, small-scale intensity variations and a large divergence angle. The experiment was per-

formed using the apparatus shown in Fig. 7-85 but with the amplifier replaced by a grazing incidence reflection cell as shown in Fig. 7-89. The 200-mJ pump beam is brought to a focus in front of the cell and allowed to diverge into the cell so that it propagates through the 5-mm glass tube by successive reflections at grazing incidence from the inside wall. This produces severe interference fringes in the pump beam with a small scale length in the transverse and longitudinal directions. This also imposes an angular spread on the beam given by the angle of the cone that enters the cell, in this case about  $\approx 4$  deg. A near-diffraction-limited Stokes pulse is propagated through the cell in the backward direction, and the beam quality is observed in the near and far field for the amplified and unamplified pulses. No change in beam profile is observed on amplification, in agreement with similar experiments performed elsewhere.<sup>141,142</sup> More quantitative measurements will be performed in the future.

**Gas Breakdown and Self-Focusing.** Gas breakdown by multiphoton ionization is a potential problem for a Raman compressor that reaches very high peak intensities. Little data are available in the uv region of the spectrum. We have studied the transmission of 248-nm radiation in several gases to determine the practical limits on transmission of short pulses with high fluence at this wavelength.

At 248 nm, unlike breakdown at infrared wavelengths, the electron density never becomes large enough to cause transmission through the



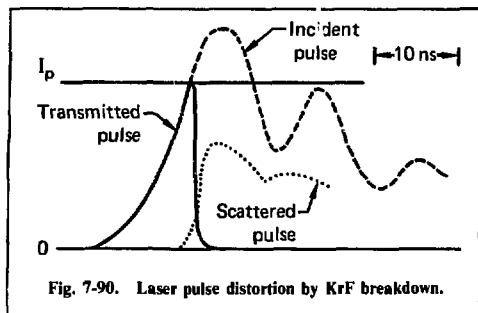


Fig. 7-90. Laser pulse distortion by KrF breakdown.

breakdown plasma to fall to zero. There is, however, strong scattering of a collimated beam from the breakdown plasma. Self-focusing to very small filament diameters could give similar scattering and may be a part of the breakdown mechanism. We have determined the intensity at which a KrF laser pulse, rising in  $\approx 8$  ns, begins to be strongly scattered from the plasma. Typical traces of the incident, transmitted, and scattered pulses are shown in Fig. 7-90.

For these experiments, the KrF pulse is focused into a gas cell with a 25-cm lens and the intensity at the focal spot is estimated from other data on the beam divergence. The relative value of  $I_p$  for different gases and pressures is thought to be reasonably accurate. The absolute vertical scale on the graph is less accurate and is the subject of continuing studies.

Values of  $I_p$  determined for several gases are given in Fig. 7-91. Determined by the present definition,  $I_p$  is larger by a factor of three to five than the typical breakdown threshold intensities taken previously<sup>143,144</sup> in the uv. We note, therefore, that this is a somewhat different diagnostic technique than the observation of a visual flash and probably requires a more fully developed breakdown plasma than the production of the flash. In addition, there are uncertainties in the focal volume intensity in this and other experiments. There are also the usual uncertainties in risetime effects and intensity-vs-energy considerations in the development of the breakdown plasma.

These  $I_p$  measurements are important because they predict the intensity below which a 3-to-5-ns pulse may be propagated without serious distortion and scattering. We note that  $5 \times 10^{10}$  W/cm<sup>2</sup> for a 5-ns pulse corresponds to an energy fluence of 250 J/cm<sup>2</sup>, so that pulses propagating in the tens of joules per square centimeter are safe in any of these gases. Because damage to optical windows probably will hold pulse fluences even lower than 10 J/cm<sup>2</sup> at

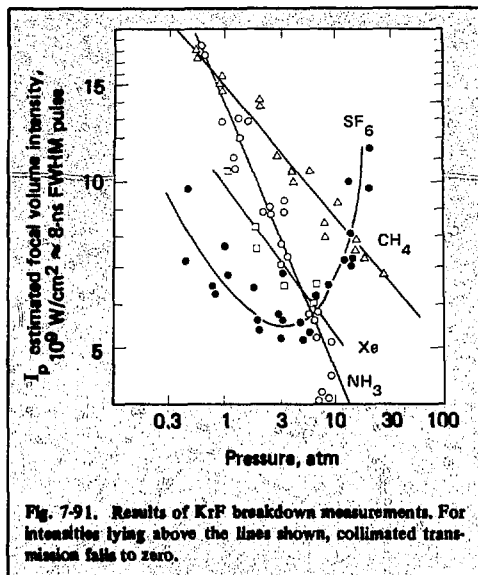


Fig. 7-91. Results of KrF breakdown measurements. For intensities lying above the lines shown, collimated transmission fails to zero.

this wavelength, optical breakdown in a Raman amplifier probably will not be a serious limit in gases such as methane and SF<sub>6</sub>. (This is not true for the usual focused superfluorescent Raman oscillator where fluences exceeding several hundred joules per square centimeter are reached very easily.) The design of oscillators for a Raman compressor is, therefore, seriously affected by optical breakdown, as observed in our gain experiments. However, other design options are available to replace the simple focused beam oscillator, and these will be examined in the future.

## References

135. W. R. Fenner, H. A. Hyatt, J. M. Kellam, and S. P. S. Porto, *J. Opt. Soc. Amer.* **63**, 73 (1973).
136. A. D. May, M. A. Henesian, and R. L. Byer, *Can. J. Phys.* **56**, 248 (1978).
137. M. Maier, W. Kaiser, and J. A. Giordmaine, *Phys. Rev.* **177**, 580 (1969).
138. J. Goldhar and J. R. Murray, *Opt. Lett.* **1**, 199 (1977).
139. I. Bigio, "Injection Locked Unstable Resonator Dye Laser," in *High Power Lasers and Applications*, K. Kompa and H. Wolfe, Eds. (Springer-Verlag, New York, 1978).
140. J. R. Murray, J. Goldhar, and A. Szoke, *Appl. Phys. Lett.* (1978), to be published.
141. D. P. Bortfeld and W. R. Sooy, *Appl. Phys. Lett.* **7**, 283 (1965).
142. A. A. Betin and G. A. Pasmanik, *JETP Lett.* **23**, 528 (1976).
143. C. DeMichelis, *IEEE J. Quant. Elect.* **5**, 183 (1969).



## Authors

J. Murray  
J. Goldhar  
A. Szoke

### 7.6.5 Pulse Compressor Systems

A number of pulse compressor systems have been identified and analyzed; the discussion here is based on the use of KrF laser pumping of a methane backward wave Raman compressor. However, these compression scenarios can be used equally well for the other pump lasers or for Raman scatterers. The generality of these schemes is important because the short wavelengths and high intensities of both a KrF pump laser and the methane-scattered short pulse place a large premium on improving our knowledge and control of the damage of uv optical components.

The KrF laser analysis reveals that the intensity achievable from a KrF amplifier is limited by non-saturable losses. Building a long amplifier chain to increase intensity can be done only at the cost of

lowered medium extraction efficiency. Generally speaking, we wish to build a KrF amplifier with a high gain-to-nonsaturating-loss ratio and build the laser to a length  $L$  such that the loss length  $\gamma L$  is in the range of one to two. Under such circumstances, narrow linewidth intensities of  $\approx 20 \text{ MW/cm}^2$  and medium efficiencies of  $\approx 15\%$  may be possible with suitably designed KrF amplifiers. High gain-to-loss ratios, high extracted intensities, and high efficiencies are produced with high excitation rates. If we presume electron beam pumping, these conditions are met for pump current densities of  $\approx 100 \text{ A/cm}^2$ , exciting Ar/Kr/F<sub>2</sub> mixtures in the range of 1 to 3 atm. Foil damage and F<sub>2</sub> depletion constraints limit the pulse length beam current products to  $\approx 2 \times 10^4 \text{ ns} \cdot \text{A/cm}^2$ . Hence, for the  $100\text{-A/cm}^2$  case, pulse lengths are limited to  $\approx 200 \text{ ns}$ .

Electron beam controlled discharges have the potential for higher system efficiency. Most likely, these controlled discharge systems will operate at somewhat longer pulse lengths and lower output intensities because of the greater inductance of the circuitry characterizing these systems and because of the discharge instabilities that occur when attempts are made to increase the gain per unit length.

Efficiency estimates for a Raman compression system using a KrF pump are given in Table 7-24.

Table 7-24. KrF/Raman compressor system efficiencies (%).

Subsystem	Efficiency component	Pure electron beam	Discharge <sup>a</sup>	Pure Raman	Raman/stackers
KrF	Electrical pulse forming	90	90		
	Transport into medium	75	90		
	Useful medium fill factor	80	90		
	Extracted medium	10 to 15	15 to 20		
	Laser electrical	5 to 8	10 to 13		
	KrF laser after flow <sup>b</sup>	4 to 7	8 to 11		
Compressor	Optical transport			90	80 <sup>c</sup>
	Raman fill factor			90	90
	Raman medium extraction			50 to 75 <sup>d</sup>	50 to 75 <sup>d</sup>
	Compression conversion			40 to 60	35 to 55
		Electron beam/ pure Raman	Electron beam/ beam/stacker	Discharge <sup>e</sup> / pure Raman	Discharge <sup>e</sup> / stacker
Total system	After flow	1.6 to 4.2	1.4 to 3.8	3.2 to 6.7	2.8 to 5.9

<sup>a</sup>Assumes electron-beam-controlled discharge with an enhancement of 3. These efficiencies have not yet been demonstrated.

<sup>b</sup>Assumes low-pressure-drop flow conditioning.

<sup>c</sup>Assumes only one stage of stacking.

<sup>d</sup>Control of second Stokes parasitic waves for high value.

<sup>e</sup>May require multiple compressions or stackings.

Two classes of KrF laser are shown: pure electron beam pumping, which is more highly developed, and electron beam controlled discharge pumping with a discharge enhancement of three. The KrF subsystem efficiency before flow costs is projected to range from 4 to 7% for electron pumping and from 8 to 14% for discharge pumping. For use in fusion applications, efficient discharge pumping may require larger pulse compressions.

The compressor system can operate at  $\approx 60\%$  conversion efficiency or possibly a bit less if optical pulse stacking is used together with backward wave Raman compression. The energy costs for gas conditioning in both media are calculated to be small. This is not unreasonable because the beam quality of the pump does not need to be extremely high and because the energy deposition in the Raman medium is negligible. The total system efficiency, of course, depends on the combination of pump and compressor performance, which is intimately linked to the desired fusion laser pulse duration. However, system efficiencies of  $\approx 2$  to  $4\%$  appear to be achievable; advances in both pump technology and Raman medium parasitic control could yield efficiencies  $>5\%$ .

Scaling of the pump and Raman apertures is limited in different ways because the KrF medium is a high-gain electrical laser, whereas the Raman medium is a low-gain optically excited medium. The power or energy output per aperture that can be obtained in the KrF system is considerably less than that achieved from the Raman medium. Ultimately, either system is limited in the transverse dimension by gain suppression considerations and by feasible mirror dimensions. For electron-beam-pumped KrF lasers, small signal gains of  $\approx 10\%/cm$  or more will be encountered. Thus, laser apertures larger than  $\approx 2$  m in the longest transverse dimension will suffer from fluorescence or parasitic depumping, even with strong presaturating fields.

If we assume a circular 2-m-radius mirror, a KrF aperture with some transverse gain suppressing baffles, and an output intensity of  $20 \text{ MW/cm}^2$ , each electron-beam-pumped KrF aperture could yield a power output of 0.6 TW. This corresponds to 60 kJ in a nominal 100-ns pulse. To achieve such a gain-limited KrF amplifier, we must assume some modularization of the electron beams driving the laser medium, because any one individual electron beam driver is constrained by magnetic pinching to occupy an area  $\lesssim 2000 \text{ cm}^2$  for the beam contents anticipated. This is considerably smaller than the approximate  $10^5 \text{ cm}^2$  outer area needed to excite the above-mentioned 60-kJ amplifier. Systems without

electron beam modularization will have considerably smaller single-aperture energies.

For an electron-beam-controlled discharge in KrF, apertures smaller than the gain limit will be encountered because the discharge current in the laser will pinch the electron beam used to stabilize the discharge. The individual medium apertures, as defined by the current return leads in the discharge circuit, will be limited to  $\lesssim 0.2 \text{ m}^2$ . At the  $g_0/\gamma$  ratios calculated for such electron discharges, intensities of  $\approx 10 \text{ MW/cm}^2$  appear possible with good extraction efficiency; powers of 20 GW per individual discharge aperture would be obtained. For pulse lengths of  $\approx 500 \text{ ns}$ , energies per discharge aperture of 10 kJ are then achievable. The individual discharge apertures are smaller than the 2-m-radius mirror postulated above for a 0.6-TW electron beam excited system. We can easily imagine arraying on an annulus with several discharge apertures; an increase in the power per beam line to about 0.25 TW could be anticipated.

The Raman medium has low gain and thus the transverse dimensions can be relatively large. Raman apertures of several square meters are possible, corresponding to several hundred kilojoules per aperture. It is presumed that several pump lasers can be combined in one Raman aperture.

There are a variety of ways in which the KrF and Raman lasers can be combined to yield a high-intensity short pulse suitable for fusion applications. Table 7-25 lists some of these arrangements. The compressor architectures are arranged in the approximate order of complexity, starting with two pure KrF schemes, followed by Raman compression schemes that do not use angle-coded sequential extraction of either the pump or Raman medium, and then two classes of compressors that use combinations of one or two stages of pulse stacking or Raman compression. The important figures for each scenario are the achievable net compression and the compression efficiency. Compressions of up to 200 may be possible with compression efficiencies of  $>50\%$ . Thus, the potential high-efficiency, long-pulse discharge lasers may be compressed from pulse durations of  $\approx 500 \text{ ns}$  to high-intensity pulses of  $\approx 5 \text{ ns}$ .

The laser systems using pure KrF are conceptually the simplest. In principle, a pure electron-beam-driven KrF amplifier chain could be used to produce pulses of  $\approx 10 \text{ ns}$  for power plant applications. At a  $20\text{-MW/cm}^2$  output intensity, 320 0.6-TW apertures, 2 m in diameter, are required to produce the 200-TW power levels thought to be required. Although this yields a laser of high efficiency (4 to 7% electrical), this option is tremen-

**Table 7-25. Some pulse compressor system architectures.**

General class	Name	Feature	Net compression regime for 50% conversion
Pure KrF	Direct KrF	320 apertures for 200-TW	1
	Pulse stacked KrF	Angle-coded KrF: trade laser apertures for N mirrors per aperture	5
Raman compressors	Single compression	Raman compression only	10
	Double compression	Two stages, requires Raman oscillator at second Stokes frequency	36
Stacker-compressors	Stacker-compressor	Angle-coded pump, single-stage Raman	40
	Compressor-stackers	Angle-coded Raman medium, single-stage Raman	40
Higher hybrids	Stacker-compressor-compressor	Angle-coded pump, two-stage Raman	200
	Stacker-compressor-stacker	Angle-coded pump and Raman medium, single-stage Raman	200
	Compressor-stacker-compressor	One angle-coded Raman medium, two-stage Raman	200

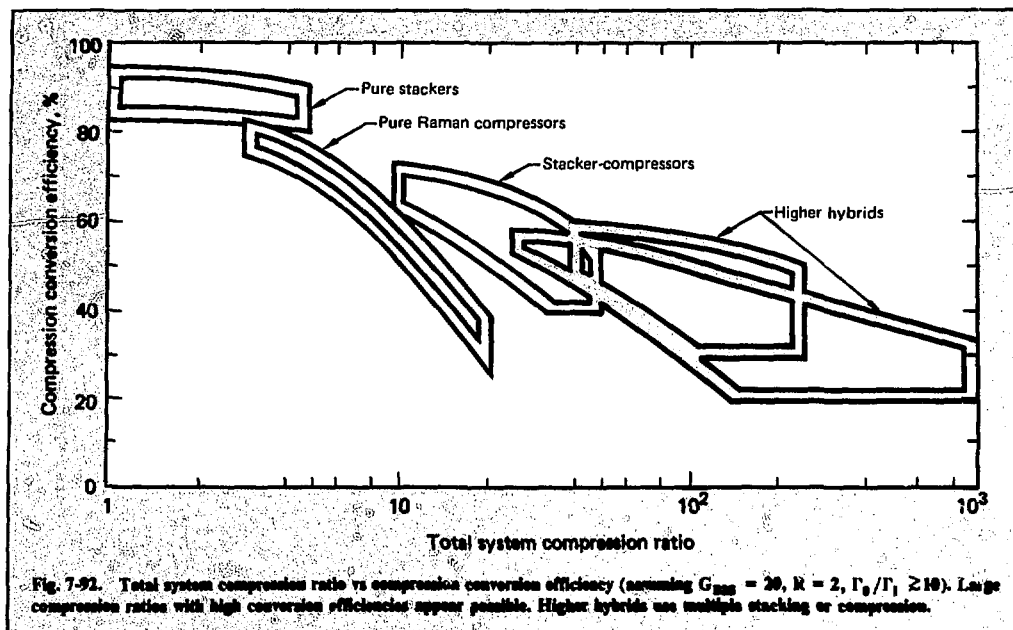
dously complicated because all the KrF laser media and the turning mirrors associated with each aperture must be suitable for focusing on the fusion target. The total mirror aperture facing the target is large,  $\approx 10^3 \text{ m}^2$ .

The use of angle-coded sequential extraction followed by pulse stacking can simplify a pure KrF scheme somewhat. This approach decreases the number of laser apertures because each aperture is used for  $n$  pulse durations for  $n$  beams extracting the medium. Thus, for a pulse stacking of  $n=4$ , 80 apertures are needed to obtain the 200-TW power level. However, the KrF medium homogeneity requirements are just as high as with a pure KrF system. In addition, the total mirror area facing the target is as high as with direct KrF. It can be argued that more than four pulse stackings could be used, or that intensities greater than  $20 \text{ MW/cm}^2$  could be drawn from an amplifier. However, the general result remains the same: a pure KrF system is extremely complex in optical layout. A most important point in favor of pulse stacking is the high efficiency that can be achieved. A pulse compression of  $\approx 5$  can be achieved with an efficiency of  $\approx 90\%$ .

Pure Raman compressors can compress a pump pulse with 50% efficiency for compressions of  $\approx 10$ . Thus, power intensifications of  $\approx 5$  can be achieved. A 200-TW system can be driven by a 40-TW pump, implying only 64 of the large KrF apertures. Assuming four backward wave Raman amplifiers of 50 TW each, each amplifier is then pumped by sixteen 0.6-TW pump lasers that are combined in the larger area Raman cell. The pump

lasers need not have a high beam quality because they only irradiate a large Raman amplifier, not a small fusion target. If we use two stages of Raman compression, larger compressions of  $\approx 36$  can be obtained for a net conversion efficiency of 50%. It is interesting to note that two compression stages can be more efficient than one stage of large compression. However, two-stage Raman compression does suffer from the fact that it is a three-color system, i.e. pump, first Stokes, and second Stokes.

By combining angle-coded sequential extraction in either the pump (stacker-compressor) or the Raman medium (compressor-stacker), large compressions at high efficiency can be achieved. The general distinctions and detailed tradeoffs between these two similar approaches remain to be quantified. However, because of the high efficiency (though limited compression range) that is available by stacking, stacker-compressor systems can be more efficient in certain compression ranges than a pure Raman compressor alone. To achieve a compression of 30, for example, it is more efficient to pulse stack with  $n=4$  and Raman compress by  $\kappa=7.5$  than it is to directly Raman compress by  $\kappa=30$ . This is illustrated in Fig. 7-92, where the compression efficiency is plotted as a function of total compression ratio for some of these compression systems. Optical transport efficiencies of 85 to 95% and a maximum stacking in any medium of five are assumed. The efficiency domain of Raman compressors is taken from computer calculations of the conversion efficiency, assuming a parasitic second Stokes gain limit of 20, a forward-to-backward gain

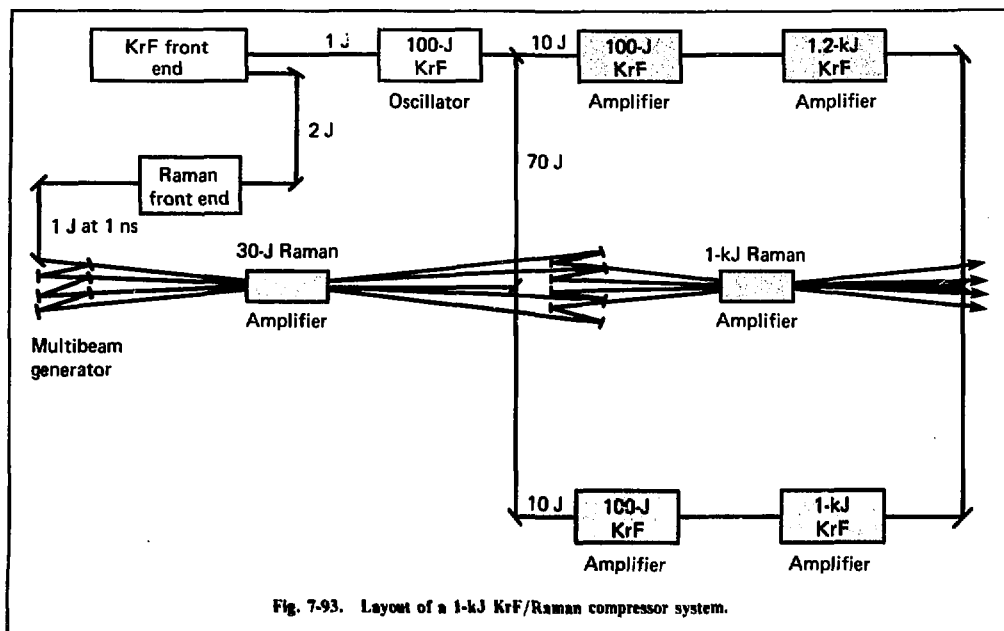


ratio of two, and a fluence gain of 10 or more in the Raman amplifier.

Taking the 200-TW example again, a compressor stacker with one Raman amplifier and angle-multiplexed by four beams could yield a net pulse compression of 40 at 50% efficiency, i.e., a power gain of 20. Thus, the 200-TW laser system requires 10 TW of pump radiation. This could be provided by sixteen 0.6-TW pump lasers. Operation of these lasers for 200 ns would correspond to 2 MJ of pump energy with 1 MJ in the 5-ns short pulse. The Raman laser radiation is divided into four beams that are separated in time by 50 ns. Each beam is amplified in the backward wave Raman amplifier and the beams can be combined on the target by appropriate delays.

If desired, even larger compressions can be obtained by stacking or compressing more than once. These large compression systems may be of use for compressing long-pulse discharges, for cleaning up a Raman beam, or for obtaining pulses close to 1 ns from long pump pulses. As an example of such a system, Fig. 7-93 shows a conceptual 1-kJ/1-TW/1-ns system layout. The final Raman power amplifier is pumped by two 1200-J KrF amplifier chains whose outputs are combined in the Raman amplifier. The pump lasers, driven by electron beams,

operate for 50 ns. The desired short pulse that is focused on target is 1 ns long. Thus, a net compression of 50 at an efficiency of 40% is desired. This can be achieved with  $\kappa = 12$  and  $n = 4$ . The system shown in Fig. 7-93 is a compressor-stacker; the angle-coded sequential extraction occurs in the Raman medium. Assuming KrF amplifier intensities of 20 MW/cm<sup>2</sup> and fluences of 1 J/cm<sup>2</sup> in the 50-ns pulse, each KrF amplifier needs to have an aperture of 1250 cm<sup>2</sup>. This can be achieved with a 40-cm-diam circular aperture, or with a rectangular aperture measuring 20 by 60 cm. Cylindrical or rectangular geometries are favored for a KrF electron-beam-pumped medium to achieve a fill factor >50%. With the cylindrical geometry, an electron-beam voltage of  $\approx 500$  keV is required for operating pressures near 2 atm. The KrF medium gain length is 2 m. The current flowing in the diodes surrounding the KrF laser is  $\approx 50$  A/cm<sup>2</sup>. Diode modularization is presumed. The final KrF amplifiers require 100 J of KrF narrow-linewidth preamplifiers to lock the final amplifiers onto the narrow linewidth needed for the Raman process. These preamplifiers have an aperture area roughly one-tenth that of the final amplifier, i.e., 15-cm diameter for a cylindrical device. The preamplifiers require  $\approx 10$  J to be frequency-locked. A parallel Raman amplifier chain



also will be used. Because the fluence gains can be higher,  $\approx 30$  per stage, the final amplifier requires about a 30-J input pulse. Assuming that four beams, separated by 12.5 ns, will extract the Raman medium, the input for each beam needs to be 7.5 J. The Raman preamplifier to produce this power requires about 60 J of KrF pump radiation and four input Stokes beams of 250 mJ each.

## Authors

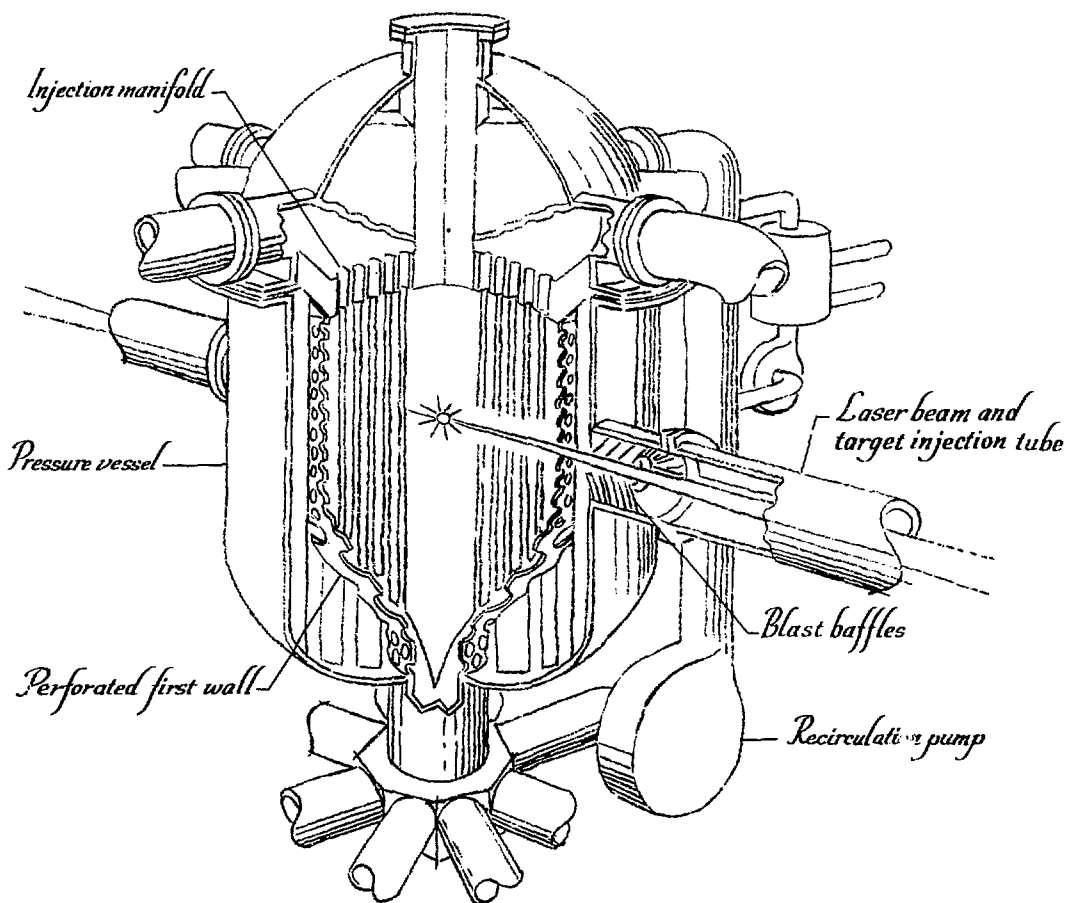
**J. J. Ewing**  
**R. A. Haas**

## Major Contributors

**D. Eimerl**  
**J. Murray**  
**L. Schlitt**  
**J. C. Swingle**

# SECTION 8

## SYSTEMS AND APPLICATIONS STUDIES



## SECTION 8

### CONTENTS

8.1	Overview . . . . .	8-1
8.2	Conceptual Design Study . . . . .	8-2
8.2.1	Performance Parameters . . . . .	8-2
8.2.2	Reactor, Optical, and Laser Systems . . . . .	8-5
	Reactor Design . . . . .	8-5
	Final Focusing System . . . . .	8-7
	Laser System . . . . .	8-7
8.2.3	Liquid Metal Circulation System . . . . .	8-10
	Introduction . . . . .	8-10
	Model and Constraints . . . . .	8-10
	Pumping Power . . . . .	8-11
	Pump Selection . . . . .	8-12
	Pump Configuration . . . . .	8-13
	Summary . . . . .	8-13
8.2.4	Liquid Lithium Corrosion . . . . .	8-14
	Introduction . . . . .	8-14
	Dissolution Attack . . . . .	8-14
	Intergranular Attack . . . . .	8-16
	Material Selection . . . . .	8-17
	Summary . . . . .	8-18
	Corrosion Studies . . . . .	8-18
8.2.5	Cost Considerations . . . . .	8-18
8.2.6	Summary . . . . .	8-20
8.3	Neutronic Studies for Fluid Reactors . . . . .	8-21
8.3.1	Energy Deposition, Tritium Breeding, and Radiation Damage . . . . .	8-21
	Introduction . . . . .	8-21
	System Model . . . . .	8-21
	Energy Deposition . . . . .	8-21
	Tritium Breeding . . . . .	8-22
	Radiation Damage . . . . .	8-22
	Helium Production . . . . .	8-22
	Displacement Damage . . . . .	8-23
	Damage Limits and Wall Life . . . . .	8-24
	Conclusions . . . . .	8-25
8.3.2	Target-Dependent Effects . . . . .	8-25
8.4	First-Wall Response and Fluid-Response Studies . . . . .	8-29
8.4.1	Interaction of Debris with First Wall . . . . .	8-30
8.4.2	Liquid Sheets and Jets . . . . .	8-36
	Jet Stability—Lithium Fall Reactors . . . . .	8-36
	Lithium Fall Response—ICF Microexplosion . . . . .	8-37
	Qualitative Response of the Fall . . . . .	8-38
	Fall Response to Neutron Energy Deposition . . . . .	8-40
	Fall Response to X Rays . . . . .	8-40
	Vaporization Effects . . . . .	8-42
	Wall Response to Liquid Impact . . . . .	8-42
	Quantitative Results . . . . .	8-43
	Discussion of Results . . . . .	8-43
8.4.3	Ion-Beam Fusion Reactor Studies . . . . .	8-45

8.5	Optical Design Considerations for Laser Fusion Power Plants . . . . .	8-50
8.5.1	Final Focusing System . . . . .	8-50
	Protection of the Final Optics . . . . .	8-52
	Transparent Optics . . . . .	8-53
	Insulating Substrates . . . . .	8-54
	Dielectric Coatings . . . . .	8-54
	Metal Mirrors . . . . .	8-55
	Testing Requirements . . . . .	8-56
	Gas Refraction Lens . . . . .	8-56
	Conclusions . . . . .	8-56
8.5.2	Propagation in the Target Chamber . . . . .	8-58
8.6	Status of Laser Driven Fusion-Fission Energy Systems . . . . .	8-59
8.6.1	Fuel Cycles and Blanket Selection . . . . .	8-60
8.6.2	LLL/Bechtel Hybrid Design Study . . . . .	8-60
	Fission Blanket . . . . .	8-61
	Tritium-Breeding Blankets . . . . .	8-62
	First-Wall Design . . . . .	8-62
	Reactor Performance . . . . .	8-63
	Cost Analysis of the LLL/Bechtel Design . . . . .	8-68
8.6.3	LLL/Westinghouse Hybrid Design Study . . . . .	8-64
8.6.4	Conclusions . . . . .	8-71
8.7	Other Civilian Applications . . . . .	8-74
8.7.1	Synthetic Fuel Production . . . . .	8-74
8.7.2	Propulsion Systems . . . . .	8-78
	Engineering Considerations for Fusion Propulsion . . . . .	8-79
	Terrestrial Laser Fusion Propulsion . . . . .	8-80
	Marine Laser Fusion Propulsion . . . . .	8-80
	Aircraft Propulsion . . . . .	8-83
	Extraterrestrial Laser Fusion Propulsion . . . . .	8-84
	Conclusions . . . . .	8-85
8.7.3	Actinide Burning . . . . .	8-87
	Introduction . . . . .	8-87
	WFPS Study . . . . .	8-87
	Laser Fusion-Driven Actinide Burner Study . . . . .	8-89
	Comparison of the Two Studies . . . . .	8-90
	Actinide Burning in Laser Fusion Pellets . . . . .	8-91
	Discussion . . . . .	8-91
	Conclusions . . . . .	8-92
8.8	Environmental and Safety Features . . . . .	8-93
8.9	Long-Range Planning . . . . .	8-95



## SECTION 8

### SYSTEMS AND APPLICATIONS STUDIES

#### 8.1 Overview

Our program of target physics experiments and laser development should enable us to demonstrate the scientific feasibility of inertial confinement fusion (ICF) in the early to mid-1980's. It is imperative that we have a clear vision of the eventual applications, along with a perspective on the time scales required and technology to be developed before we can obtain a balanced view of the expected payoffs and problems. We are directing our systems studies toward providing management information on the opportunities and problems expected in bringing future applications to fruition. Our objective is to better plan a program that will yield maximum benefits in the shortest time and at acceptable cost.

We use the following tools in our systems studies:

- Energy supply studies.
- Parametric analyses of components and systems.
- Conceptual power plant designs and test facilities.
- Assessments of emerging technologies.
- Long-range planning of technology development.

With these techniques, we attempt to identify the high-leverage applications and the combinations of technologies best suited to realize these applications with acceptable risk. We are also problem-finders, in the sense of attempting to foresee potential problem areas with sufficient advance warning to prevent their becoming actual program-pacing items. In this regard, we have an early opportunity and responsibility to innovate, to find a way around problems before they consume enormous amounts of program resources.

Applications fall naturally into two categories, commercial and military. By far, the biggest payoff to the country of a successful inertial fusion program is in power production: using fusion energy to produce electric power (and perhaps fissile fuel and synthetic gas) in an environmentally sound and economically competitive manner. The time required to begin realizing this payoff is substantial, perhaps three decades, but the goal of a

power source that uses an inexhaustible fuel is extremely attractive and important. On a shorter time scale, we can pursue concurrently a complementary program in military applications that can yield very significant information. Research into the fundamental physics of matter is useful in nuclear weapons design. Studying the interaction of radiation with matter is useful in assessing the vulnerability of military components and systems.

In the sections that follow, we present the results of a continuing systems studies effort to examine the commercial and military applications of ICF. We also present an assessment of some important considerations in technology development. We begin with the results of conceptual design study of a small (380-MW<sub>e</sub>) electric power plant that uses a lithium "waterfall" reactor concept in conjunction with a photolytic selenium laser system. The laser operates at 1 MJ/1.4 Hz with an overall efficiency of 2%; it takes advantage of parallel redundant modules for high reliability. The reactor has a thermal power of 1160 MW<sub>t</sub> and a total system efficiency of 31%; it is designed to last 30 years without first-wall replacement.

Subsequently, we detail considerations of neutronics (including effects dependent on target design, tritium breeding, and structural damage), the establishment and breakup of fluid blankets, liquid metals pumping, and corrosion questions. We analyze the interactions of x rays and debris with the first wall for both pure fusion and fusion-fission dry wall reactors. Finally, because the survivability of the final focusing scheme is important for any laser fusion power plant, we describe optical elements whose lifetimes are sufficiently long ( $\geq 1$  year) to avoid compromising power plant availability. A fusion source is rich in neutrons; therefore, breeding fissile fuel for lightwater reactors (LWR's) is an attractive commercial application. In addition, the fission process is rich in energy. A fusion-fission hybrid reactor designed to combine these features can meet a broad spectrum of fissile-fuel-producing and energy-multiplying requirements. In two hybrid reactor studies, we demonstrate the ability to produce more than 10 times more fissile fuel per unit of thermal energy output than a fission breeder, while requiring far

lower laser and target performance than pure fusion. We have assessed other potential applications, including synthetic gas production, propulsion, and actinide burning. We also present initial results of environmental and safety studies of laser fusion reactors, concentrating on the two most crucial aspects: tritium containment and large liquid metal system safety.

In previous years, we have made significant contributions to the planning of pure fusion reactor development programs. In 1977, we concentrated on the commercialization phase, investigating several scenarios for the introduction of both pure fusion and fusion-fission hybrids into the U.S. energy economy. Results are given as a function of first introduction date, unit size and construction time, and mix between pure fusion and hybrid reactors.

Fusion offers to contribute significantly to the world's energy needs. We must make an enormous commitment of human and financial resources to carry out the scientific explorations and technological developments required. However much the effort, the problems and the efforts expended are dwarfed by the immensity of the payoff—an inexhaustible and affordable source of energy that is compatible with our environment.

Author

M. J. Monsler

## 8.2 Conceptual Design Study

### 8.2.1 Performance Parameters

Recent developments in target design at LLL have greatly enhanced the prospects for commercial fusion power. The conceptual laser fusion power plant we briefly review here represents the first step in a self-consistent study to exploit the recent advances in target design.<sup>1</sup> We describe this conceptual design and evaluate it on its ability to cope with the major problems affecting the technical feasibility of a laser fusion power plant. Our conclusion is that the development of the following four items will allow the efficient generation of electricity with high plant capacity factors:

- A high-average-power driver with the required efficiency (>1%) and reliability (>70%).
- A first wall able to withstand the effects of x rays, debris, and neutrons from microexplosions.
- Structural materials that can withstand the cumulative damage effects of high-energy neutrons and cyclical stresses.

● Final-focusing elements that can be protected or placed sufficiently far from microexplosions to prevent compromising the availability of the power plant.

Advanced high-gain target designs make it possible to reduce projected laser system requirements to the following parameters<sup>1</sup>:

- Pulse energy 300-3000 kJ
- Peak power  $\geq 200$  TW
- Pulse rate 1-10 Hz

Table 8-1. Laser fusion power plant parameters.<sup>a</sup>

<u>Overall performance</u>	
Thermal power	1160 MW <sub>t</sub>
Thermonuclear power	1000 MW <sub>t</sub>
Gross electrical power	460 MW <sub>e</sub>
Net electrical power	380 MW <sub>e</sub>
Thermal cycle efficiency	38%
Recirculating power fraction	17%
System efficiency	33%
<u>Laser and pellet parameters</u>	
Laser energy	1 MJ
Pulse repetition rate	1.43 Hz
Laser power	1.43 MW
Pellet gain (Q)	700
Pellet yield	700 MJ
Laser system efficiency ( $\eta_L$ )	2%
Number of modules	10
Number of beams	4
<u>Reactor parameters</u>	
Geometry	Cylindrical
Inner radius	4 m
Height	8 m
Lithium fall thickness	0.6 m
Equivalent first-structural-wall fusion neutron flux	4 MW/m <sup>2</sup>
Tritium breeding ratio	1.7
Blanket energy multiplication	1.24
Reactor materials	
Structure	Stainless steel
Coolant	Lithium

<sup>a</sup>These parameters do not actually characterize a specific laser system; rather, they are representative of several laser systems currently under investigation at LLL.

- Wavelength 250-2000 nm
- Overall efficiency  $\geq 1.0$

Even with these relaxed requirements, however, no current high-power laser can satisfy all criteria. However, we are encouraged to note that several laser media now in the research stage seem potentially able to meet these requirements; they apparently can also be scaled to both high peak and high average power.

In addition to relaxing laser system requirements, high-gain targets have features that significantly influence reactor design:

- High energy yield per pellet.
- Relaxed requirements for uniform target illumination.
- Relaxed requirements for target surface-finish tolerances.

Because the high energy yield for each pulse might lead to increased first wall damage by x rays and debris from the fusion microexplosion, we selected a fluid wall reactor concept for our design.<sup>2,3</sup> In this approach, the first structural wall is shielded from x rays and debris by a thick, falling region of liquid lithium. Also, the fall design calls for sufficient

moderating material to reduce neutron damage levels in structural materials by more than an order of magnitude. We can therefore anticipate smaller blanket structures that are survivable for the useful lifetimes of power plants. Relaxing uniform illumination requirements permits us to plan for fewer-sided target irradiation (two to four beams) with longer focal-length optics ( $f/10$  to  $f/100$ ). At focal lengths of 10 m, the final optics would survive the microexplosion but might have to be replaced at relatively short intervals. At focal lengths of 100 m, the damaging effects are reduced by two orders of magnitude. This assures the survival of the final focusing elements for sufficiently long periods to avoid compromising the plant capacity factor. Finally, the relaxation in target surface-finish requirements is expected to translate into a reduction in target fabrication costs per unit of output energy.

Table 8-1 lists the characteristics of our laser fusion power plant,<sup>4,5</sup> and Fig. 8-1 shows the power flow. We begin with the input of electrical power from the switchyard to the laser system. The laser system converts electrical energy to coherent light energy with an overall efficiency of 2%, requiring

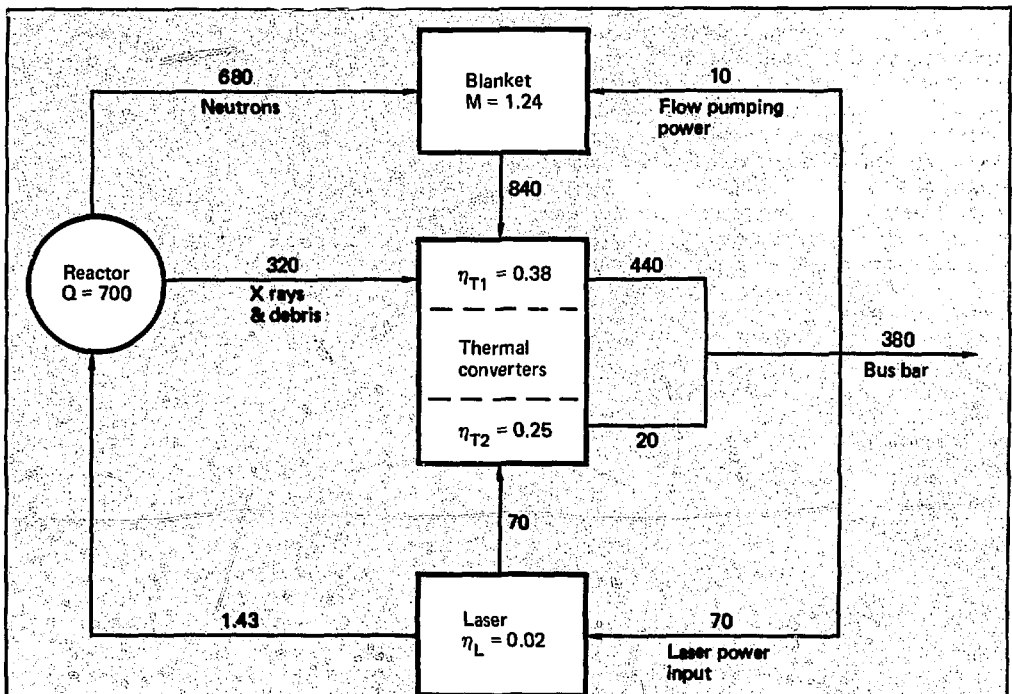


Fig. 8-1. Power flow diagram for laser fusion power plant (all powers are given in MW).

Laser fusion  
power plant with  
lithium waterfall reactor

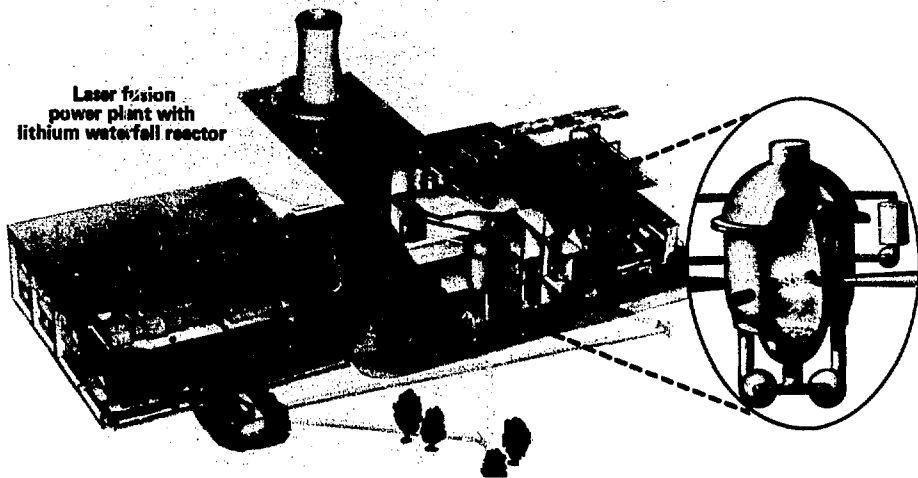


Fig. 8-2. The LLL laser fusion electric power plant concept.

70 MW of input electrical power. The light energy implodes the pellet, compressing deuterium-tritium fuel in the reactor to produce thermal energy with a gain of  $Q = 700$ . Specifically, fusion targets producing 700 MJ of thermonuclear energy are ignited by a 1-MJ laser at the rate of 1.43 pulses per second. The fusion neutron energy, accounting for approximately 68% of the total yield, is multiplied by 1.24 in the lithium blanket for a resulting thermal power of 1160 MW. The thermal energy is converted to electrical energy at 38% efficiency. The laser waste heat is discharged at an average temperature of 350°C. This waste heat can be converted to electrical energy with an overall efficiency of approximately 25%. Of the total 460 MW<sub>e</sub> produced, 80 MW<sub>e</sub> of electrical power is recirculated for plant operation (laser and lithium flow). This leads to a power plant with a net electrical production of 380 MW<sub>e</sub> with an overall system efficiency of 33%.

Figure 8-2 is an artist's concept of the plant layout. An important feature of this design is that the laser system is housed separately from the reactor containment building. Several advantages result from this isolation:

- Building costs and construction time are substantially reduced.
- Access to the laser system for maintenance and operation is increased.
- It becomes easier to isolate the final optics from vibrational disturbances.

- Safety is increased.

In the sections that follow, we discuss features of the reactor, laser final focusing, and liquid metal circulation systems, as well as the important considerations of materials and corrosion.

## References

1. J. Nuckolls, *Laser Fusion Overview*, Lawrence Livermore Laboratory, Livermore, Calif., UCRL-77725 (1976).
2. J. A. Maniscalco and W. R. Meier, "Liquid Lithium Waterfall Inertial Confinement Fusion Reactor Concept," *Trans. ANS Summer Meeting* (1977).
3. W. R. Meier and J. A. Maniscalco, *Reactor Concepts for Laser Fusion*, Lawrence Livermore Laboratory, Livermore, Calif., UCRL-79654 (1977).
4. J. A. Maniscalco, W. R. Meier, and M. J. Monsler, "Conceptual Design of a Laser Fusion Power Plant," presented at the 70th Annual Meeting of the American Institute of Chemical Engineers, New York, N.Y., November 1977. [Also UCRL-79652, Lawrence Livermore Laboratory, Livermore, Calif. (1977).]
5. J. A. Maniscalco, W. R. Meier, and M. J. Monsler, "Design Studies of a Laser Fusion Power Plant," *Proceedings of the IAEA Workshop on Fusion Reactor Design*, Oct. 1977, Madison, Wisconsin. [Also UCRL-80081, Lawrence Livermore Laboratory, Livermore, Calif. (1977).]

## Author

M. J. Monsler

## 8.2.2 Reactor, Optical, and Laser Systems

**Reactor Design.** Our desire to circumvent the ten years (or more) required for advanced material development and testing strongly influenced the design of the reactor. Our aim was to develop a simple concept that could be constructed with existing materials using current state-of-the-art technology.<sup>6</sup> The liquid lithium waterfall concept meets these criteria.<sup>7,8</sup>

The concept (Fig. 8-3) features a thick, continuously recyclable first wall of liquid lithium that protects the first structural wall from direct exposure to microexplosions. Each shot disassembles the waterfall, which is reestablished between each shot. The lithium is continuously pumped to the top of the vacuum chamber through a reservoir region separating the first structural wall from the pressure vessel. A small fraction of the lithium flow circulates as the primary coolant to the heat exchanger. The return flow from the heat exchangers is injected through a vortex generator to protect the top of the chamber.

The principal purpose of the fall is to reduce neutron radiation damage in blanket structural materials, allowing them to survive for the useful life of the plant. Besides moderating neutrons, the fall also absorbs photons (x rays and reflected laser light) and pellet debris (alpha particles, unburned fuel, and other pellet material). Because the fall is separated from the chamber wall, any shock wave produced in the fall will not be directly transmitted to the structural wall.

Although spherical geometry in reactor design makes the best use of a point-source of energy, we selected the cylindrical geometry shown in Fig. 8-3 for several reasons. The sheet of lithium protecting the top of the reactor is thinner than the primary fall; hence, it provides less protection from neutron damage. Consequently, it is advantageous to locate the top of the chamber farther from the microexplosion than the side walls. At the bottom of the vacuum chamber, the lithium is in direct contact with the walls; shock waves can be directly transmitted to the chamber walls at this point. We can reduce the intensity of the directly transmitted shock wave by moving the bottom region farther away and decreasing the surface area of the lithium pool at the bottom.

The falling liquid region contains enough lithium to significantly reduce neutron damage to the reactor structural materials from atomic displacements and gas production. The damage limits for 316-SS stainless steel at an operating temperature of 500°C are estimated to be 150 displacements per atom (dpa) and 500 atom-parts-per-

million (appm) of helium production.<sup>9</sup> For an unprotected stainless steel wall operating at a neutronic wall loading of 1 MW/m<sup>2</sup> (generally considered to be the lower flux limit for an economically attractive fusion reactor), the damage limit for helium production would be reached in only 2.3 full-power years. This would present a severe maintenance problem and would generate large amounts of radioactive waste. At this wall loading, a fusion reactor would operate with power densities an order of magnitude lower than those of a light water reactor.

Multiplying neutron wall loading (in MW/m<sup>2</sup>) by wall lifetime (in years) gives a figure of merit for any fusion reactor design. This product, the allowable first-wall fluence,<sup>10</sup> increases exponentially with the protective thickness of the lithium fall (see Fig. 8-4). We have evaluated the requirements of a system that maintains a minimum protective lithium thickness of 60 cm. A characteristic unique to inertial confinement fusion is that the emitted 14-meV neutrons are attenuated by the compressed DT fuel. Our computer calculations, using the TARTNP Monte Carlo neutronics code,<sup>11</sup> indicate that a fusion target with a compressed density-radius product  $\rho R$  of  $\sim 3$  g/cm<sup>2</sup>\* is roughly equal to 13 cm Li in terms of reducing helium production; hence, the compressed target increases the effective blanket thickness to 73 cm. Because helium production dominates, the allowable fluence is 90 MW-yr/m<sup>2</sup>. By implication, the system could be operated at  $\sim 4$  MW/m<sup>2</sup> for the 30-year plant life at a 70% capacity factor. Thus, for a given power, the reactor can be made smaller with structures that never require replacement.

The liquid lithium waterfall concept has excellent energy-conversion, energy-removal, and tritium-breeding characteristics. Nearly 99% of the total energy is deposited directly in the primary lithium coolant. This essentially eliminates cyclical thermal stresses in the structural walls. Thermal conversion efficiencies approaching 40% can be obtained by operating at corrosion-limited temperatures of 500°C. Tritium is bred at a rate that is more than adequate. With no structural material between the fusion neutrons and the lithium fall, the design takes full advantage of the tritium-producing reaction with <sup>6</sup>Li that occurs only with high-energy neutrons. A tritium-breeding ratio of 1.7 can be obtained, and the excess tritium produced in such a

\*This is a nonoptimized target; other  $\rho R$  values are being evaluated.

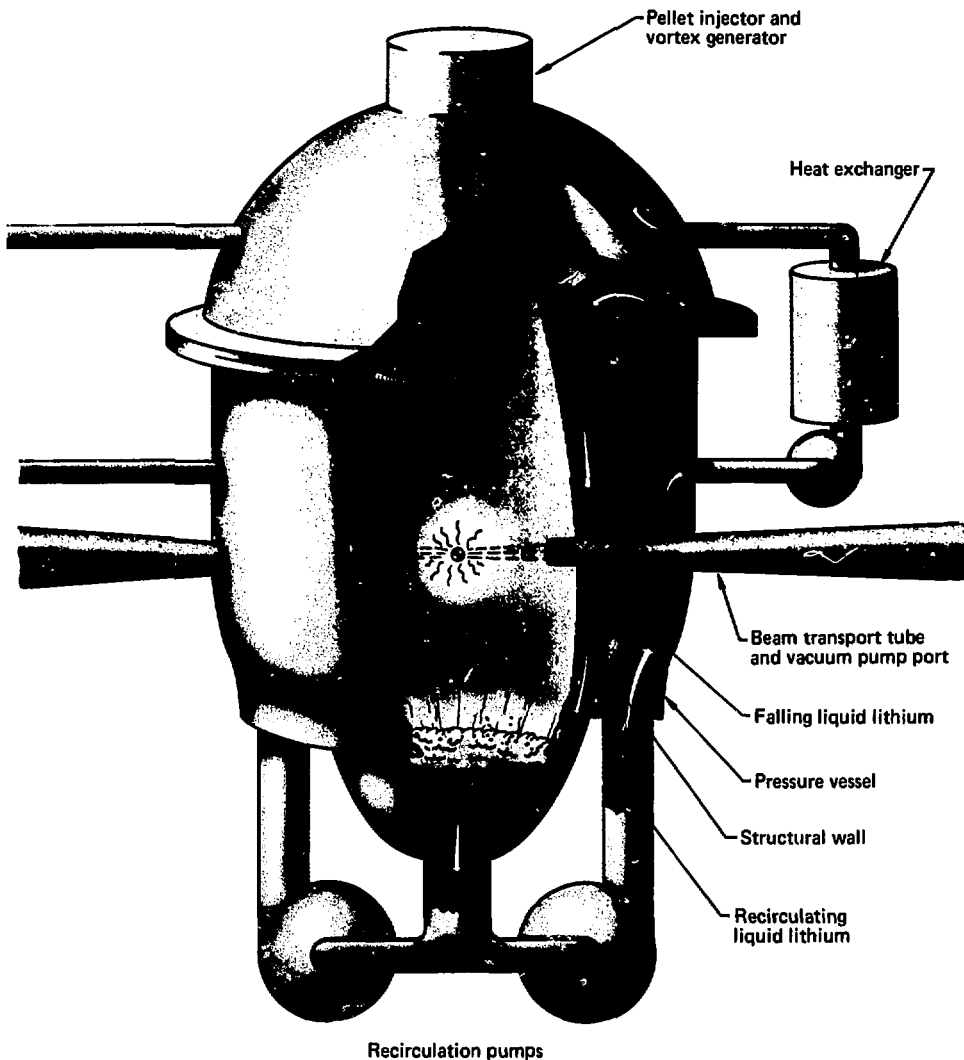
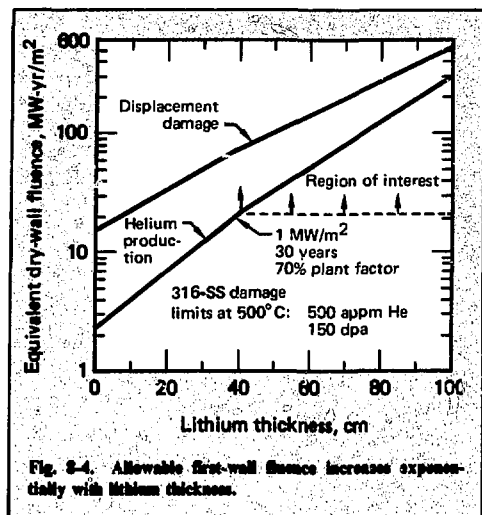


Fig. 8-3. Liquid lithium waterfall concept.



pressure above the required 0.1-Torr vacuum condition. However, so much liquid lithium is present in the chamber during the microexplosion that the temperature rise at each pulse is quite small; furthermore, the liquid lithium waterfall acts as a condensing vacuum pump for the chamber.

The pumping power required to recirculate the lithium fall has been estimated on the basis of the kinetic and static head requirements, with the fall inlet conditions determined by two constraints:

- The fall must have sufficient velocity to reestablish itself between microexplosions.
- A minimum attenuating thickness of 60 cm must be maintained.

The required pumping power increases with chamber size and with pulse repetition rate. For 1-2 Hz, the power required is less than 2% of the gross electric power production of the reactor. Because the laser system operates more economically at higher repetition rates, multiple reactor chambers may be coupled with a single laser.

**Final Focusing System.** The laser light travels to the reactor through underground evacuated pipes. The beam enters the containment vessel through a window and converges to a line focus in the center of a narrow slot that serves as a fast-acting valve. The valve provides secondary containment protection in case of window failure. A fixed off-axis parabolic focusing mirror directs the beam onto a mirror flat that is exposed to the neutron flux. The mirror flat may be mounted on a carousel of several mirrors to provide redundancy in case of catastrophic failure. Separate vacuum pumps are

located on each side of the fast-acting containment valve to prevent gas breakdown.

The final focusing mirrors are located at the turning point of the beam tubes in a direct pathway to the thermonuclear microexplosion. As a result, these mirrors are exposed to the x rays, debris, and neutrons from the fusion reaction. The most effective technique for preventing x rays and debris from striking the final optic assembly involves a simple region of gas with a relatively high atomic number.<sup>9</sup> Photoelectric interactions in this gas stop the x rays, and collisions thermalize the debris. Some protection for the final optic assembly is also afforded by the target (if it has a thick pusher tamper region) and by the lithium vapor already in the chamber. Accordingly, the density-length product of additional gas required to stop the remaining x rays is very design-dependent; but we can estimate the requirement from mean-free-path arguments. We envision a region several meters long near the optical surface in which gas flows toward the target. The gas is injected at the optical surface to provide some face cooling and protection from particulates. It is then pumped out of the tube at an intermediate station, filtered, and reinjected. (The amount of gas used is critical; too much could result in interaction with the laser beam. The gas must also be replaced between shots.) Our calculations indicate that a few cm-atm of high-Z gas, such as xenon, would attenuate x rays with energies less than 3 keV by more than two orders of magnitude<sup>9</sup>; hence, a 10-m section of the beam tube containing a few Torr of high-Z gas should be sufficient. All ions and debris would be stopped in this absorbing region.

Because we have methods for preventing the x rays, ions, and debris from damaging the final optics, the minimum separation distance can be based on expected neutron damage. Calculations show that metal mirrors at 100 m can survive both types of damage for several years.<sup>9</sup> If these results are too conservative, the mirrors can be closer (20-50 m).

**Laser System.** A preliminary conceptual design of a short-wavelength, high-energy, high-average-power gas laser system is included in this power plant. A previous study<sup>12</sup> also used a photolytic (oxygen) laser system as a basis for a commercial power plant; however, in the current study, we consider a different range of operating parameters and offer improved estimates of efficiencies and sizes.

We begin the problem-finding process involved in conceptualizing full-scale systems, by using a promising class of optically pumped gas lasers that appear to satisfy the target requirements. We cannot say that the photolytic lasers considered in this study will in fact be the type that will be developed

to very large size—too much laser physics research remains to be done. However, as a class, photolytic lasers adequately represent the pulsed power, e-beam, gas flow, chemical regeneration, optical quality, and component damage problems characteristic of a high-average-power fusion laser.

Figure 8-5 shows one possible configuration of a photolytic laser system that appears very scalable to large volumes and high energy per pulse. The fluorescer gas and laser gas regions are kept apart by the stability of coflowing streams of different gases. The pressure and velocity of the two gases are matched; the density, temperature, and Mach number generally are different. This offers the singular advantage of eliminating transmitting windows, which probably would be unable to withstand damage from both the high-fluence levels of photons and 1-MeV electrons and the steady and shock-pressure loads over large spans (greater than 30 cm).

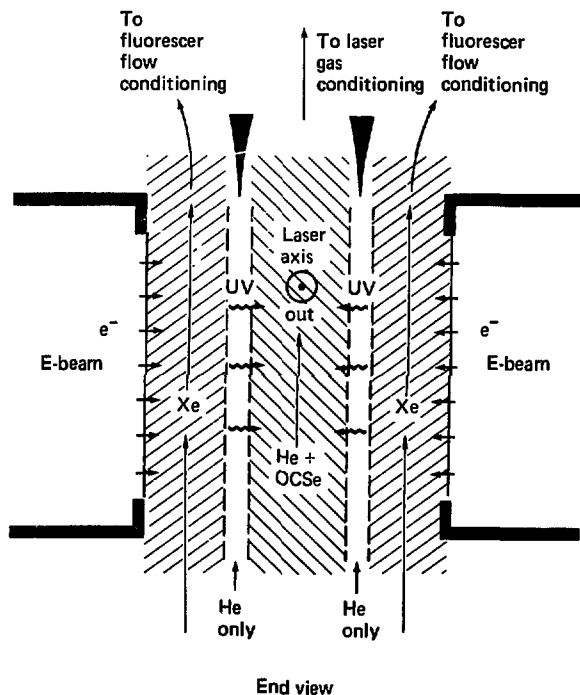
The lasing sequence is begun by firing two opposed  $\sim 1$ -MeV e-beams for approximately 1  $\mu$ s. In the selenium laser sketched in Fig. 8-5, electrons radiolyze the xenon and result in copious xenon ex-

cimer ( $\text{Xe}_2^*$ ) fluorescence radiation. The lasing medium consists of approximately  $3 \times 10^{16} \text{ cm}^{-3}$  COSe in 1 atm helium buffer gas, which matches the fluorescer gas pressure and provides sufficient heat capacity to minimize the increase in gas temperature. The fluorescence radiation dissociates the parent molecules, resulting in  $\text{Se}^*$  atoms that form a laser medium suitable for a high-energy storage amplifier.

The molecular absorber is optically thick vis-à-vis the fluorescence radiation. Photolysis occurs when a bleaching wave, driven into the medium, dissociates the molecule and causes the mixture to become transparent. The sequence ends with injection of a 1-ns laser pulse that depopulates the medium during amplification.

Efficiency and scalability are two very important and separate aspects of a large laser system. A laser system of high efficiency has lower recirculating power needs and lower capital equipment costs. Efficiency depends on losses caused by power conditioning, fluorescence production, coupling to the laser molecule, optical extraction, and also pumping, cooling, and chemical regeneration of the

Fig. 8-5. Flowing windowless geometry.





flowing gases. On the other hand, a laser with a large single aperture size and energy per pulse lowers costs by reducing complexity in the number of beams and components. Scalability depends on optical and e-beam foil-damage limits, pump constraints, flow and gas uniformity constraints, parasitic suppression, thermal distortion of optical elements, and a configuration that simultaneously confronts all important technological barriers.

We have considered both these important aspects in this conceptual design of a selenium laser. The primary purpose of the study is to obtain a model of all required power flows, mass flows, efficiencies, and sizes that remain within the known physics constraints. We have not attempted to design a laser system to be built tomorrow.

Table 8-2 gives a summary of the design parameters of this photodissociation selenium laser that is pumped by flowing xenon "flashlamps" in a windowless geometry. The principal features of this system are as follows. Ten 100-kJ modules operate at 1.4 pulses per second, producing 1.4-MW average optical power (1-ns pulses of 1000-TW peak power) at 489-nm wavelength (in the blue green). The optical power is produced at 2% overall efficiency. Each of the ten output beams has a 0.6-m by 2.32-m cross section. The beams are divided and combined into the four beam clusters that enter the reactor. The conceptual design is conservative from the standpoint of materials and technology; we have used reasonable optical and materials damage limits. Of course, many laser physics uncertainties are not yet resolved, because this laser is still in the research phase.

An accurate impression of such a full-scale power plant driver is given in the artist's conception of Fig. 8-2. The middle floor contains the laser cavities, electron beams, and pulse transmission lines. These large, cylindrical, energy storage devices extend horizontally from each side. The flow systems (one for the He + OCS flow and another for the xenon flow) are on the top floor. The bottom floor contains all the rectifiers, power supplies, and electrical isolators. A key feature of the design is an optical tunnel that runs the length of the building; it is vibrationally isolated from the laser building. All mirror mounts are attached to the tunnel structure, in isolation from the compressors and e-beam pulsing loads. The laser beams from the ten modules are generated vertically and then turned and carried in beam tubes to the reactor.

Two system advantages to this design are immediately apparent. First, modularity of the laser system allows the use of spare modules to greatly

Table 8-2. Parameters of the 125-kJ, 1.4-pps amplifier module.

Energy on target	125 kJ
Energy out of laser module	139 kJ
Pulse repetition frequency	1.4 Hz
Pulse duration	1 ns
Optical cavity volume	4.63 m <sup>3</sup>
Length in beam direction	2.55 m
Width in flow direction	2.4 m
Width in e-beam direction	0.75 m
Width of each fluorescer region	0.35 m
COSe molecule density	10 <sup>17</sup> cm <sup>-3</sup>
Pressure	2 atm
Mirror fluence	7.72 J/cm <sup>2</sup>
Optical efficiency	95%
Electrical efficiency	3.5%
Flow efficiency	5.3%
Overall system efficiency	2%
Volumetric efficiency	15 J/litre-atm
Flow velocity	5.5 m/s

enhance system reliability and availability (e.g., one module could be ready in the event of an unscheduled breakdown of an operating module, while another was being reconditioned). Second, the laser system is separate from the reactor building, housed in an ordinary—and less expensive—industrial building.

## References

- G. J. Nuckolls, *Laser Fusion Overview*, Lawrence Livermore Laboratory, Livermore, Calif., UCRL-77725 (1976).
- J. A. Maniscalco and W. R. Meier, "Liquid Lithium Waterfall Inertial Confinement Fusion Reactor Concept," *Trans. ANS Summer Meeting* (1977).
- W. R. Meier and J. A. Maniscalco, *Reactor Concepts for Laser Fusion*, Lawrence Livermore Laboratory, Livermore, Calif., UCRL-79654 (1977).
- M. J. Monsler and J. A. Maniscalco, "Optical Design Considerations for Laser Fusion Reactors," *Optics in Adverse Environments*, Vol. 121, *Proceedings of SPIE 21st Annual Technical Symposium*, Bellingham, Washington, Aug. 22-26, 1977 [Also UCRL-79990, Lawrence Livermore Laboratory, Livermore, Calif. (1977).]
- H. I. Avci, G. L. Kulcinski, *The Effects of a Liquid ISSEC on Radiation Damage Parameters in Laser Fusion Reactor First Walls*, University of Wisconsin, Rept. UWFD-205 (April, 1977).
- E. F. Plechaty and J. R. Kimlinger, *TARTNP: A Coupled Neutron-Photon Monte Carlo Transport Code*, Lawrence Livermore Laboratory, Livermore, Calif., UCRL-50400, Vol. 14 (1976).

12. R. R. Buntzen and C. K. Rhodes, *Laser Systems for Laser Fusion*, Lawrence Livermore Laboratory, Livermore, Calif., UCRL-75367 (1974).

Author

M. J. Monsler

### 8.2.3 Liquid Metal Circulation System

**Introduction.** Protecting the reactor structures from radiation damage in the fluid wall concept depends on establishing a thick curtain of liquid lithium between the microexplosion and the first structural wall. During this year, we investigated the variation of the lithium flow rate and pumping power required to circulate the fall as a function of such reactor parameters as pulse repetition rate, chamber size, and fall thickness. The results of these studies, coupled with radiation damage correlations (§ 8.3.1), indicate low-repetition-rate systems with fall thicknesses on the order of 1 m and reduced chamber dimensions.

**Model and Constraints.** Figure 8-6 shows the model used for the calculations. The flow inlet forms an annulus of thickness  $x_0$ . The inner edge of the annulus is at a radius  $(1-\alpha)R_w$ ; thus the maximum inlet thickness is  $\alpha R_w$ , where  $R_w$  is the chamber radius at the horizontal midplane.  $\alpha$  is a geometric factor from 0 to 1.0 relating the maximum inlet thickness to the wall radius. The vertical distance from the inlet to the midplane is related to the wall radius by  $H_m = \beta R_w$ , where  $\beta$  is a geometric factor relating fall height to wall radius.

The fall is injected vertically downward with an inlet velocity  $v_0$ . As the fluid is accelerated by gravity, continuity requires the thickness of the annulus to decrease; the thickness at a distance  $H$  from the inlet is given by

$$x = \frac{x_0 v_0}{\sqrt{v_0^2 + 2gH}},$$

where  $g$  is the acceleration due to gravity. The effective attenuating thickness of the fall is  $x/\cos \theta$ , where  $\theta$  is the angle of incidence of the source neutrons. The minimum effective thickness occurs slightly below the horizontal midplane; the exact position depends on the injection velocity. The midplane is also where the wall of a cylindrical chamber is closest to the microexplosion; it is thus most affected by the neutron flux. For these reasons, con-

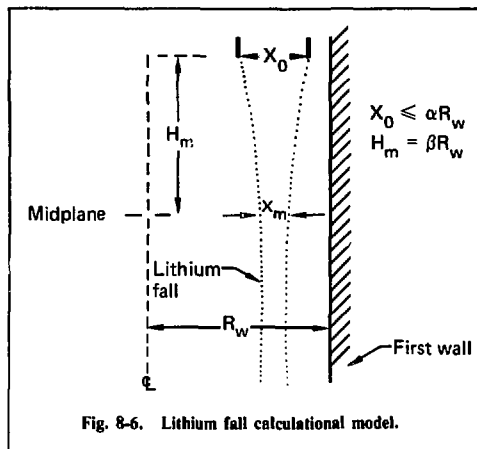


Fig. 8-6. Lithium fall calculational model.

straints on the thickness of the fall are determined by midplane conditions.

One constraint on the inlet velocity is that it must be great enough that some minimum thickness  $x_m$  is maintained at the midplane, while the inlet thickness is limited to  $x_0$ . In terms of our calculational model,

$$v_0 \geq x_m \left( \frac{2g \beta R_w}{\alpha^2 R_w^2 - x_m^2} \right)^{1/2}.$$

Our studies of the interaction of the microexplosion and the lithium fall indicate that the flow pattern is completely disrupted by the energy deposition. Accordingly, the inlet velocity must also be sufficient to reestablish the fall prior to the next microexplosion. Assuming a clearing ratio of unity, the fall must clear a distance of  $2H_m$  within a time  $t$  equal to the inverse of the pulse-repetition frequency:

$$v_0 \geq 2\beta R_w / \tau - g\tau/2.$$

In general, the change from the clearing constraint to the thickness constraint occurs as the fall thickness is increased and the wall radius, or repetition rate, or both, are decreased.

Figure 8-7 shows the flow rate for 0.5- and 1.0-m-thick falls (midplane thickness) at 1 and 2 Hz as a function of the chamber radius. For this example, the inlet thickness is set at  $x_0 \leq 0.5 R_w$  and the height  $H_m = 0.866 R_w$  ( $\alpha = 0.5$ ,  $\beta = \sqrt{2\alpha - \alpha^2}$ ).

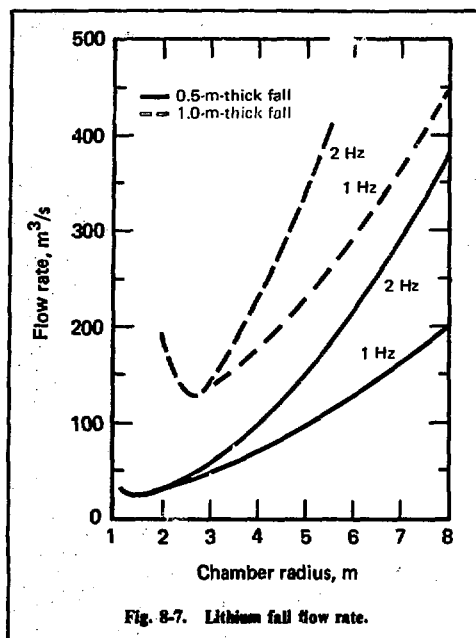


Fig. 8-7. Lithium fall flow rate.

The value of  $\beta$  is the result of setting the inner edge of the inlet at a distance  $R_w$  from the center of the chamber.

Several trends are noted in Fig. 8-7. The flow rate increases with increasing chamber radius, repetition rate, and fall thickness. The difference in flow rate for systems with different repetition rates decreases with decreasing chamber radius and becomes zero when the flow is thickness-constraint-limited for both. Thickness-constraint-limited flow reaches a minimum value, indicating a tradeoff between the reduced flow area and increased flow velocity. For a given thickness requirement  $x_m$ , the minimum flow rate occurs at

$$R_w = \frac{1.29 x_m}{\alpha}$$

If the chamber radius is governed by considerations of radiation damage, we can specify the radius as a function of protective lithium thickness and thermonuclear power. From the results reported in the neutronics section of this report, the minimum wall radius is given by

$$R_w = \sqrt{P_{TN}/6.3} e^{-1.85x_m} \text{ meters,}$$

where

$P_{TN}$  = thermonuclear power, MW,

and

$x_m$  = minimum fall thickness, m.

This expression holds only for type-316 stainless steel with damage limits of 500 appm-He and 165 dpa over a 21-full-power-year lifetime.

We use the specific flow rate (i.e., the flow rate per unit of thermonuclear power) as a figure of merit for the fall circulation system. It is an important value because the pumping power, total lithium inventory, and number of pumps required are all proportional to the flow rate. Figure 8-8 shows the specific flow rate as a function of  $x_m$  for a system with a thermonuclear power of 3600 MW<sub>th</sub> at both 1 and 2 Hz. Again, we set  $\alpha = 0.5$  and  $\beta = 3.866$ . The specific flow rate decreases with increasing lithium thickness and is at a minimum in the range 1.0-1.15 m for this case. The difference between the 1- and 2-Hz systems approaches zero as the flow becomes thickness-constraint-limited for the 2-Hz case at 1.15 m. The exact point of the minimum is a function of the system power and selected geometry ( $\alpha$ ,  $\beta$ ), but the trends are similar.

**Pumping Power.** Another important parameter for the system is the pumping power required to circulate the lithium fall. We base the pumping power estimates on the kinetic and static head requirements that dominate frictional and fitting losses. The pumping power is

$$P_p = (1/2 v_0^2 + gH) \rho v_0 A_0,$$

where

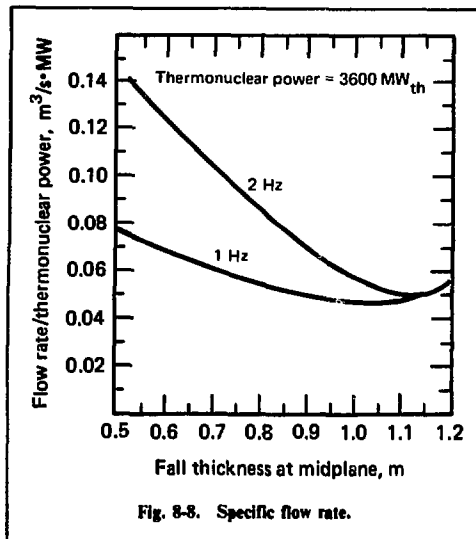
$v_0$  = inlet flow velocity,

$H$  = total fall height =  $2H_m$

$A_0$  = inlet flow area.

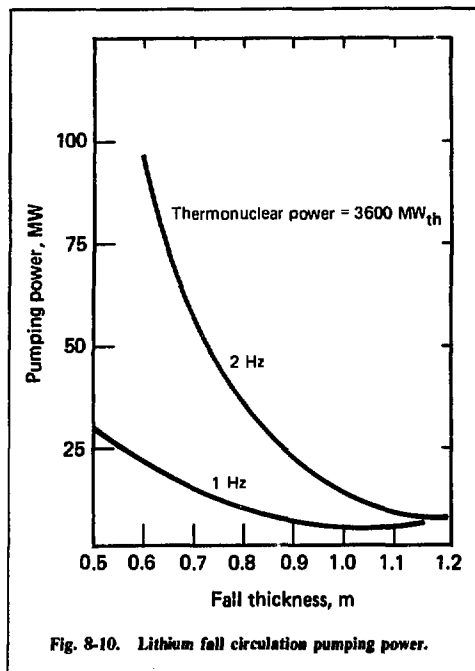
Figure 8-9 shows the circulation pumping power as a function of chamber radius for 0.5- and 1.0-m-thick falls at 1 and 2 Hz. Similar to the flow rates, pumping power increases with increasing chamber size, repetition rate, and fall thickness. The difference between the 1- and 2-Hz cases approaches zero as the chamber radius decreases.

The fraction of the total system power required to circulate the fall is of even greater interest. As before, we must take into account the fact that a chamber with a larger fall thickness will be smaller for any given thermonuclear power level. Figure 8-10 shows the pumping power as a function of fall



thickness for a constant 3600-MW<sub>th</sub> system. The same trends are apparent here as with the specific flow rate. The sensitivity to repetition rate, however, is even greater, reflecting the  $v_0^2$  term in the pumping power equation. Limiting the required circulation power to 1% of the gross electrical power would require fall thicknesses greater than 0.75 and 1.0 m for the 1- and 2-Hz cases shown here.

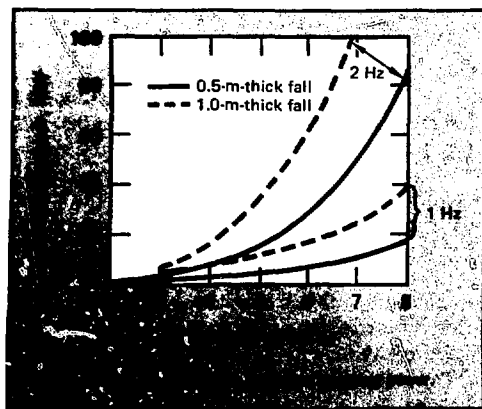
**Pump Selection.** The total plant tritium inventory is directly proportional to the lithium inventory, because the tritium concentration in liquid lithium is fixed for any given recovery scheme. Accordingly, the desired system configuration is one with minimal lithium volume. Most of the lithium is



found in the circulation pipes leading to and from the pumps, not in the reactor chamber.

The net positive suction head (NPSH) requirement of the pump is an important parameter for determining system volume. Because a vacuum exists in the reaction vessel, the required NPSH must be provided by a static head of lithium above the pump corrected for friction losses between the vessel discharge and pump inlet. The higher the NPSH required, the farther below the reaction vessel the pump must be, thus increasing the lithium volume of the system. For centrifugal or axial mechanical pumps (or both), pump characteristics are determined by the pump-specific speed ( $N_s = N\sqrt{Q}/H^{3/4}$ , where  $N$  = pump speed in rpm,  $Q$  = flow in gpm, and  $H$  = pump-developed head in feet) and pump-suction-specific speed ( $S_s = N\sqrt{Q}/\text{NPSH}^{3/4}$ ).

In addition to the thermal conversion system, the Liquid Metal Engineering Center is responsible for the conceptual design of the circulation pumps and piping loop. Two mechanical pumps will be compared, a conventional centrifugal pump ( $N_s = 2500$ ,  $S_s = 8000$ ) and an advanced technology, combined axial centrifugal pump ( $N_s = 2500$ ,  $S_s = 20,000$ ). The high-specific-speed pump has a much lower NPSH requirement and



should result in a substantial reduction in lithium inventory.

Mechanical pumps are capable of high efficiencies—in the 80-90% range—and will result in the lowest circulation pumping power. The pumping powers for configurations with large fall thicknesses ( $\sim 1$  m) are so low, however, that we will be investigating less efficient pumps whose lower NPSH demands could further reduce the fall circulation system lithium inventory. An attractive candidate is the helical rotor electromagnetic (EM) pump. This pump appears capable of efficiencies in the 30-40% range, with flow rates of  $\sim 25$  m<sup>3</sup>/s. The NPSH requirements of this pump are essentially zero.

Additional advantages of EM pumps for the lithium circulation system are that they do not require seals, they have no liquid-free surfaces, and they do not penetrate the lithium system boundary—except for instrumentation. The pump internal volume need not be greater than an equivalent length of pipe, further reducing lithium inventory. The obvious disadvantage of EM pumps is their inefficiency. Other potential disadvantages are a higher initial cost and a larger pump envelope containing the magnets and auxiliary cooling equipment.

**Pump Configuration.** Lithium fall pumps are critical components within the laser fusion power plant. The design of the pumps and the configuration of the fall circulation system will affect the plant availability.

Repairing a lithium fall pump is likely to be very difficult. No valves are planned for the fall circulation system design because none are needed during normal operation; furthermore, large liquid metal valves for reactor systems are extremely expensive. Thus, if a pump fails, no means of isolating the pump from the fall circulation loop would be available. Repair work requiring removal of a pump shaft, for example, would require total system shutdown for a lengthy period.

Several strategies for minimizing plant downtime from fall recirculation pump failures are possible:

- A plant with multiple reaction chambers would allow only one unit to be down because of a single pump failure. The disadvantage of this approach is that as the plant becomes more complex—containing a larger number of components and systems—the probability of failure increases.

- A fall circulation system with many pumps could be designed to operate with one or more pumps down at any time; however, the more pumps

in the system, the more likely the occurrence of pump failure. But, with a large number of pumps, the effect of a single pump failure is less severe. If fixed-speed pumps are used to minimize problems with speed control, the remaining working pumps would be unable to increase flow to compensate for a failed pump. With many pumps, the change in fall flow caused by a single pump failure would be only a small fraction of total flow rate. If mechanical pumps are used, removing a pump shaft would require shutting down the system. This down time could be minimized by using special equipment to block the flow through the failed pump line while that pump is removed from the system for repair.

- A fall circulation system with very few pumps is less likely to suffer from pump failure than one with more pumps. But the consequences of failure would be more severe. In a system with variable-speed pump drives, two or three pumps could accommodate the fall recirculation load of a three- or four-pump system. Special equipment could again be used to block flow through the line associated with a failed pump, so that system shutdown would occur only during pump removal and reinstallation. A drawback of this system is that the pumps must be designed to operate at higher flow rates and higher speeds. These pumps must be able to operate at a higher suction-specific speed than their normal operating level. This means the pumps would be larger and more expensive than would otherwise be required.

We have not yet studied expected pump failure rates. Considerations of system simplicity favor the third strategy. Cost is more difficult to determine, though it seems probable that a smaller number of larger pumps will result in a more cost-efficient system.

**Summary.** The lithium circulation system is an integral part of the lithium fall reactor concept. Analysis of various configurations indicates that reduced flow rates and pumping power are possible with designs featuring fall thicknesses on the order of 1 m; these designs allow smaller chamber sizes and increased power densities. In selecting a suitable pump, we want high efficiency and low NPSH to minimize lithium inventory. In this respect, we will compare (high-efficiency) mechanical pumps with EM pumps that have lower efficiency but reduced NPSH requirements.

**Author**

W. R. Meier

## 8.2.4 Liquid Lithium Corrosion

**Introduction.** The use of liquid lithium is an essential feature of the fluid wall reactor concept for laser fusion. The flowing lithium provides protection from radiation damage, efficiently absorbs and removes the fusion energy, and breeds tritium to refuel the fusion reaction. Along with the advantages of using liquid lithium in our system come the detrimental effects resulting from its corrosive nature. Resistance to corrosion is, therefore, an important consideration in selecting a material for the fusion chamber and associated piping. On the basis of economy, availability, and fabricability, the selection of a suitable engineering material for use with liquid lithium should focus on the ferrous (iron-based) alloys. Proper selection of a material that must serve for 30 years of subjection to high temperatures, thermal gradients, cyclical stress, radiation damage, and flowing liquid lithium, requires a clear understanding of the many ways lithium can degrade the material. It is also necessary to identify the rate-controlling mechanism so that we can apply techniques to reduce corrosion.

Although corrosion from liquid lithium is similar to that from liquid sodium, lithium is generally considered more corrosive. The principal types of liquid-metal corrosion include the following:

- Simple dissolution.
- Temperature-gradient mass transfer.
- Concentration-gradient or dissimilar metal mass transfer.
- Intergranular penetration.
- Impurity reactions.

Because several of these processes in fact occur simultaneously, we propose a more generic outline with two forms of corrosion in this discussion. The first is dissolution attack, which includes the first three items, and the second is intergranular attack. Impurities play an important role in both categories, but they appear to be more significant in the mechanisms of intergranular attack.

The variables that can influence the type and severity of liquid-metal corrosion on a given type of material include the following:

- Temperature.
- Temperature gradient.
- Cyclic temperature fluctuation.
- Flow characteristics.
- Impurity levels in the liquid metal and the container material.
- Ratio of metal surface area to liquid volume.
- Surface condition of the container material.

- Number of materials in contact with the same liquid metal.

- Physical and mechanical condition of the container material (i.e., stress and stress gradients).

**Dissolution Attack.** In a system with temperature gradients, dissolution occurs in the high-temperature region, where the solubility is higher; deposition from the supersaturated lithium occurs as it passes through the low-temperature region. Figure 8-11 illustrates this dissolution-mass transport-deposition process. The actual mass transport processes are more complex, because they are influenced by both the chemical and thermal gradients. The chemical activity gradient is a function of the ratio of the concentration of the dissolved species in the liquid metal to the saturation concentration. The rate of this corrosion is also a function of temperature, impurity level in the liquid lithium, fluid flow rate, and alloy content.

The rate of dissolution attack is very sensitive to ferrous alloy composition. Alloying elements that have large differences in solubility over the temperature range of the system are most subject to mass transport. Nickel is an example of an element that performs poorly in liquid lithium. As nickel is leached from austenitic (face-centered-cubic) stainless steel, the surface is transformed to ferrite, a body-centered-cubic structure. The conversion of the surface to a nickel-free ferrite would probably slow the corrosion rate of the stainless steel after extended periods in lithium. In general, the susceptibility to dissolution attack increases with increasing nickel content in ferrous alloys. Other elements, even those with lower solubilities, can exhibit high rates of dissolution attack in liquid lithium. When such elements enter the lithium to maintain the equilibrium solubility, they react with impurities and produce compounds. This compound formation reduces the apparent concentration in the liquid lithium for these elements and thus promotes accelerated dissolution of such elements from the container material. Chromium from ferrous alloys is susceptible to compound formation with nitrogen and carbon. This enhances dissolution attack when sufficient quantities of impurities are present in the liquid lithium.

The nature of dissolution attack suggests that using alloys with limited nickel and—possibly—chromium content is more desirable. In fact, pure iron has demonstrated excellent resistance to corrosion in liquid lithium. Pure iron, however, does not have the mechanical properties suitable for pressure vessel and coolant loop design. It is, therefore, essential to search for an optimal alloy content. Figure 8-12 illustrates the Fe-Cr-Ni alloy

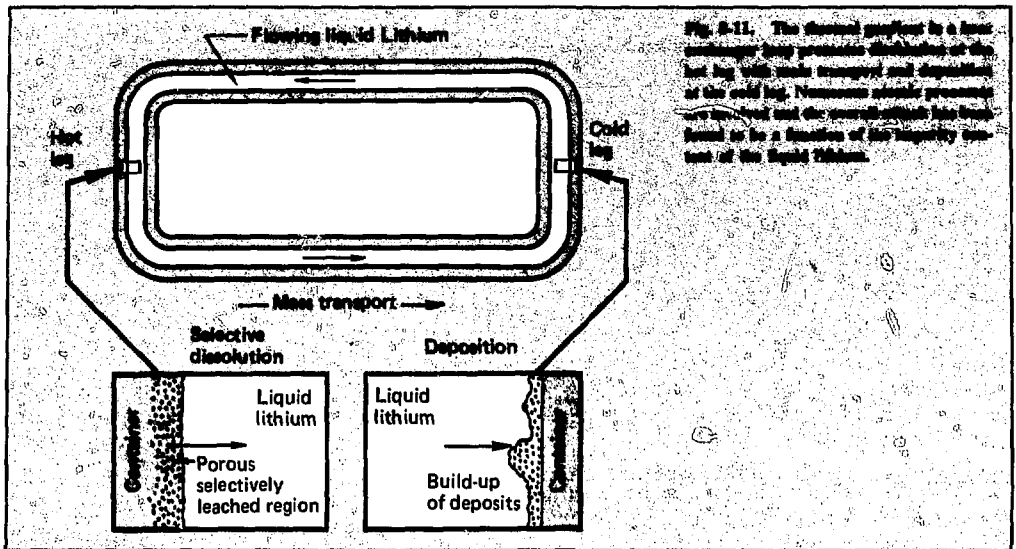


Fig. 8-11. The chemical gradient in a heat exchanger loop promotes dissolution on the hot leg with mass transport and deposition at the cold leg. Numerous similar processes are involved and the overall attack has been found to be a function of the impurity content of the liquid lithium.

system and indicates that the selection of a corrosion-resistant alloy will most likely be centered on the iron-rich region of this diagram. Proper impurity control in both the ferrous container alloy and the liquid lithium will increase the compatibility of engineering alloys with liquid lithium.

In designing a system for containing liquid lithium, we want to avoid using dissimilar alloys. The chemical-potential gradients of certain alloying components may become extremely large across

joints of dissimilar alloys. These gradients would promote mass transport of such alloying components through the liquid lithium, causing dissolution attack on one alloy and possible deposition of the alloying component on the other, as Fig. 8-13 shows. Interstitial elements, such as carbon, are especially susceptible to this type of mass transport. This susceptibility is caused by their large diffusion coefficients in both the solid container material and the liquid lithium.

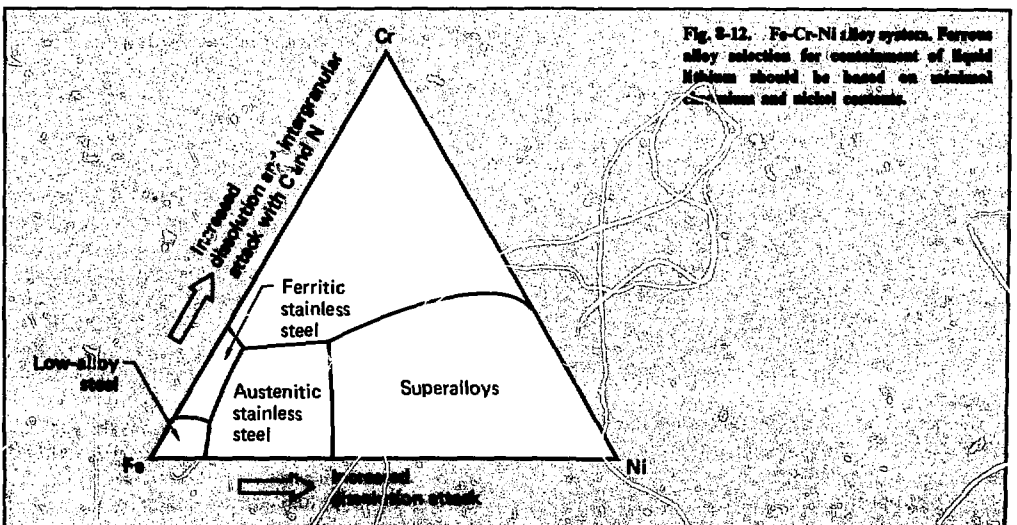
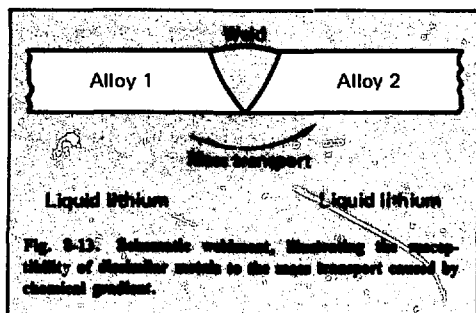


Fig. 8-12. Fe-Cr-Ni alloy system. Ferrous alloy selection for containment of liquid lithium should be based on minimal chromium and nickel contents.

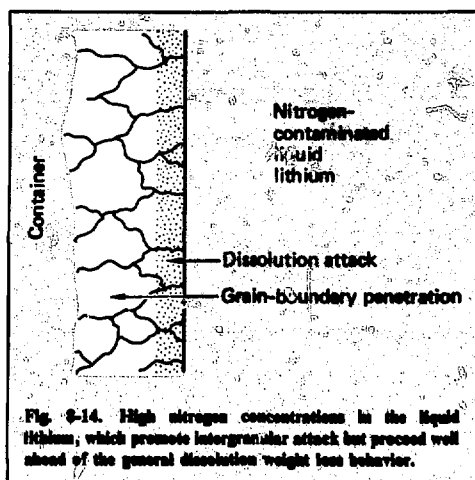


Another factor that influences dissolution-deposition corrosion is the flow rate. Study of the corroded surfaces of test materials shows that the mechanisms in static and flowing liquid lithium are different. The rate of corrosion increases with increasing flow velocity until a limiting velocity is reached. Finally, it has been determined that the nitrogen impurity level accelerates the corrosion rate.

**Intergranular Attack.** Grain-boundary penetration by lithium is another form of corrosion that becomes a serious concern when the liquid contains over 500 ppm nitrogen. Here, the lithium actually forces its way into the metal along the planes where separate metal crystals meet and their atomic lattices do not align. The grain-boundary penetration at higher nitrogen concentrations proceeds well ahead of the dissolution attack into the materials, as Fig. 8-14 illustrates. Tests show a complete loss of mechanical integrity along the penetrated grain boundaries.

Grain-boundary penetration and subsequent corrosion along the boundary are also a function of the temperature history of the steel. In the temperature range from 450 to 750°C, the chromium ions tend to form chromium carbides at the grain boundaries. The region adjacent to the grain boundary is then deficient in chromium; it is said to be sensitized to grain-boundary or intergranular corrosion. One theory suggests that the dissolution process selectively leaches the nickel in this region, leaving a semiporous, corroded structure with little mechanical integrity, as suggested in Fig. 8-15.

The chromium that diffuses to form carbides may also react with nitrogen impurities that accumulate at the grain boundaries. The carbon and nitrogen may either originate in the steel or enter the material by diffusion from the liquid lithium. Another model for intergranular corrosion is based on the concept that lithium reacts with these grain-boundary carbides and nitrides to form corrosion



products that are susceptible to cracking (see Fig. 8-16).

One approach to inhibiting intergranular corrosion is to stabilize the steel with minor additions of titanium or niobium. The additives capture most of the carbon and nitrogen, preventing the formation of chromium carbides and nitrides. It is also possible to thermally stabilize the material: the steel is heat-treated to replenish the chromium-depleted regions along the grain boundaries by transport of Cr from the interior portions of the grains.

We must develop a better understanding of the role of carbon in intergranular corrosion. If liquid lithium corrosion attack takes the form of a chromium-depletion and nickel-leaching process (Fig. 8-15), thermal stabilization would help. But if corrosion occurs from lithium attack of the chromium carbides (Fig. 8-16), we must consider a more expensive steel alloy containing stabilizing additives and less carbon.

Applying stress to ferrous alloys exposed to liquid lithium can increase the rate of corrosion dramatically. Figure 8-17 shows how grain-boundary penetration of pure iron is promoted by either tensile or compressive loading. Experiments have shown that the coefficient of the grain-boundary penetration rate is proportional to the strain rate in the material. The major concern is that the stress level at which this stress-induced corrosion process occurs in pure iron lies in the same range as normal residual stress levels for the material when it is not in a stress-relieved state. This raises serious questions about the usefulness of current, liquid lithium corrosion data for unstressed specimens in predicting the service life of container



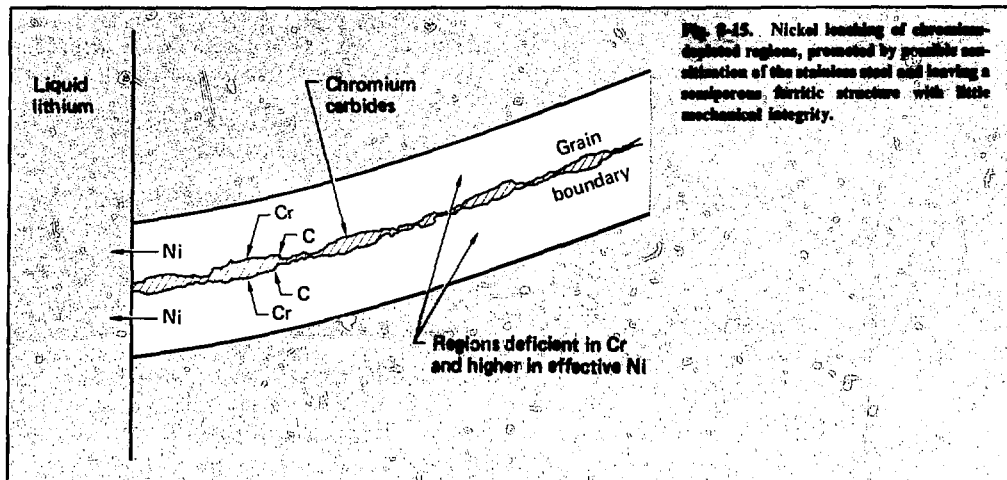


Fig. 8-15. Nickel loading of chromium-depleted regions, promoted by possible dissolution of the stainless steel and leaving a spongy, fibric structure with little mechanical integrity.

materials. In particular, we need better data concerning the corrosion behavior associated with weldments subject to constraints.

**Material Selection.** The resistance of stainless steels to severely corroding environments is usually the result of a dense protective oxide layer covering the surface. However, because liquid lithium reduces these protective oxides, corrosion resistance must have some other basis. Many other materials with excellent corrosion resistance (e.g., pure iron and refractory metals) have very poor mechanical properties, or poor fabricability, or high cost. It is therefore necessary to study many other available

commercial alloys, including the stainless steels. Although the selection process also should examine alloys that are presently included in the pressure vessel codes.

Most compatibility studies have been with the 300-series (chromium-nickel) austenitic stainless steels. Although the nonferromagnetic characteristic of austenitic steel may be an essential feature for magnetic confinement fusion, it is not required in laser fusion applications. In general, these alloys have shown less corrosion resistance than pure iron, but they have acceptable resistance at moderate temperatures ( $<600^{\circ}\text{C}$ ). The high-strength characteristics of these steels is also an important feature.

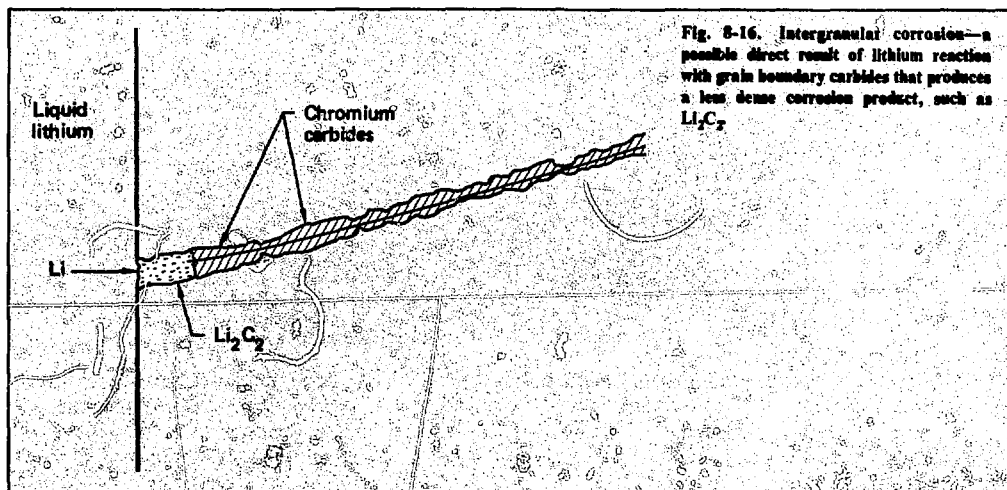
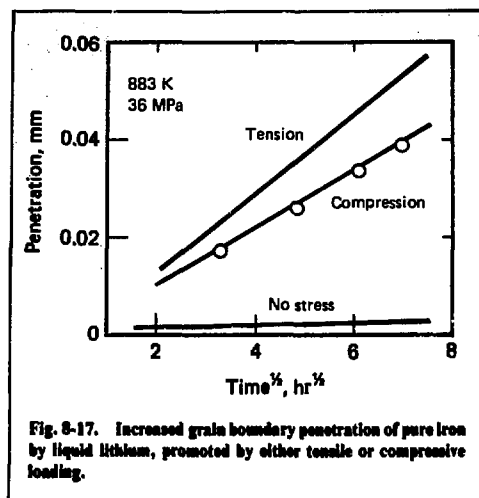


Fig. 8-16. Intergranular corrosion—a possible direct result of lithium reaction with grain boundary carbides that produces a less dense corrosion product, such as  $\text{Li}_2\text{Cr}$ .



The ferritic (chromium) stainless steels show similar behavior, with the lower chromium alloys offering better resistance. In both cases, higher carbon contents and nitrogen impurities result in increased corrosion rates.

For laser fusion applications, the low-alloy ferritic steels appear very attractive. These alloys contain no nickel and have much lower chromium concentrations than austenitic stainless steels. Chromium may be difficult to obtain in quantity in the United States by the turn of the century. Further, any nickel dissolved in lithium and flowing through a high neutron flux can form such undesirable radioactive products as  $^{58}\text{Co}$  and  $^{60}\text{Co}$ . These low-alloy steels offer excellent economy as well as excellent properties for pressure vessel construction. It will be advantageous, as with the austenitic stainless steels, to use low-carbon alloys (to prevent carbide formation) with microalloying additions of niobium or titanium to stabilize the material against grain-boundary attack.

**Summary.** The general effects of lithium on iron-base alloys are summarized as follows:

- High temperature, temperature gradients, and chemical-activity gradients promote dissolution and mass transport.
- Corrosion rates increase with the nickel content of stainless steel alloys.
- Carbon and nitrogen impurities in lithium accelerate corrosion.
- Stresses and flow increase corrosion rates.
- Lithium may react with carbides and promote cracking along grain boundaries.

- Chromium depletion in stainless steels results in nickel dissolution from the chromium-depleted (nickel-rich) regions adjacent to grain boundaries.

- The use of extra-low-carbon steels and stabilized grades effectively decreases corrosion by lithium.

**Corrosion Studies.** In 1977, the Systems Studies and Applications group began to support the Colorado School of Mines (CSM) in lithium-corrosion experiments that are of interest to the laser fusion program. In these screening tests, CSM exposes spot-welded and bent specimens of both Type-304 stainless steel and 2.25 Cr-1.0 Mo (a low-alloy ferritic steel) to 500°C static lithium. The metal strips are bent to give some indication of the effects of tension and compression on the corrosion mechanism. Attack in the weld zones is also being investigated as a critical concern. CSM is also conducting these preliminary experiments at high nitrogen concentrations in the lithium and has designed them to highlight any catastrophic effects.

In later experiments, CSM will investigate the effects of various heat treatments (to thermally stabilize the metal), stabilized grades of 2.25 Cr-1.0 Mo (niobium additives), and controlled low-nitrogen conditions. These experiments are only the beginning of the work needed to establish material requirements for laser fusion applications. Verification of a low-alloy ferritic steel as an acceptable engineering material for containing liquid lithium will be a significant economic advantage for laser fusion. Fortunately, the wealth of liquid metal experience gained with liquid sodium will speed the design of systems for containing, pumping, controlling, and monitoring liquid lithium. (See Ref. 13 for more detail.)

## References

13. D. L. Olson and D. K. Matlock, "The Essential Chemical and Physical Properties of Ferrous Alloys Needed for Containment and Liquid Lithium," presented at *Lithium-77, Symposium on Lithium Needs and Resources*, Corning, N.Y., October 1977. (To be published in the journal *Energy*.)

## Author

W. R. Meier

## 8.2.5 Cost Considerations

We have performed an initial cost sensitivity analysis to guide future design efforts for the reactor, laser, and total power plant. We begin with some general considerations of power plant efficiency.

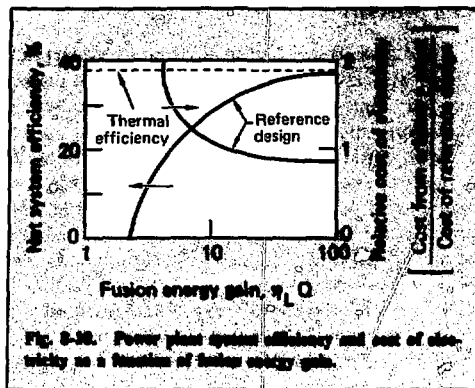


Fig. 8-18. Power plant system efficiency and cost of electricity as a function of fusion energy gain.

One of the most important parameters of a laser fusion power plant is the fusion energy gain. It is defined as the product of the laser system efficiency  $\eta_L$  and the thermonuclear pellet gain  $Q$ . The fraction of the system electrical power production required to operate the laser decreases as the value of  $\eta_L Q$  increases.

The net system efficiency of the power plant, defined as the ratio of net power to reactor thermal power, is plotted as a function of fusion energy gain in Fig. 8-18. At very large values of  $\eta_L Q$ , the recirculating power fraction is small and the net system efficiency approaches the thermal efficiency. The Fig. 8-18 curve is based on a thermal cycle efficiency of 38%, which is consistent with the selected maximum operating temperature of 500°C. Our reference design, with a value of  $\eta_L Q = 14$ , has a net system efficiency of 33%.

Figure 8-18 also shows the cost of electricity as a function of  $\eta_L Q$ . The cost of electricity from an arbitrary design, compared to our reference design point, is inversely proportional to the net system efficiency. This is because plant capital costs generally scale with the gross electrical power (which is fixed for a given thermal power and thermal efficiency), while revenues scale with the net electrical power. At the reference design point, the cost of electricity is much more sensitive to a decrease in  $\eta_L Q$  than to an increase. Decreasing  $\eta_L Q$  by a factor of 2 results in a 30% increase in electricity cost, while increasing  $\eta_L Q$  by an order of magnitude results in only a 20% decrease in cost.

Figure 8-19 compares the cost of an arbitrary reactor chamber with the reference design chamber as a function of chamber radius. The curve is based on the assumption that chamber costs are proportional to the square of the chamber radius. It is thus

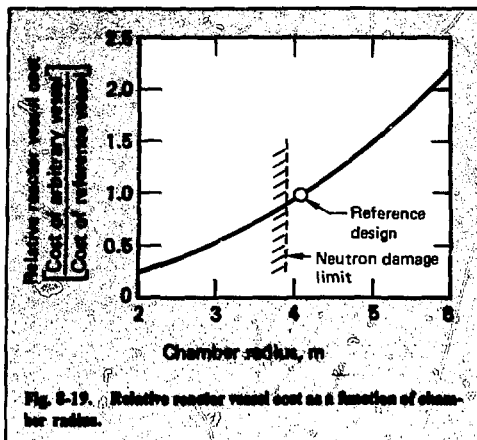


Fig. 8-19. Relative reactor vessel cost as a function of chamber radius.

advantageous to use the smallest chamber possible, consistent with neutron-damage limitations. As we noted above, the minimum radius for a structure that could survive for the life of the plant at the selected thermonuclear power is 3.9 m, leading us to select a first-wall radius of 4 m.

We cannot yet determine the cost of a high-average-power, short-wavelength laser fusion system, but we can estimate the sensitivity of cost to pulse-repetition frequency and efficiency. We consider a power plant of fixed thermal power and fixed average laser power. The direct capital cost is comprised of electrical conditioning equipment (energy storage, e-beam, etc.), flow-conditioning equipment, optics, building, and instrumentation and controls. The electrical and flow systems account for the majority of costs in most gas laser concepts. In laser systems with <10% electrical efficiency, the cost of energy storage is a significant fraction of the total cost. The costs of electrical power conditioning are proportional to the amount of energy storage required and are, therefore, inversely proportional to the electrical efficiency. However, the additional cost of increasing the pulse-repetition frequency by a factor of 2 is very slight. We would, therefore, expect the cost for electrical power conditioning in a laser system of fixed average power to decrease as pulse-repetition frequency increases.

The flow system is the other major cost component. Its cost is generally proportional to the rate of waste power removal; essentially, the cost is proportional to the laser average power divided by the efficiency. Varying the pulse-repetition rate at a constant power level, therefore, does not affect the cost of flow conditioning (at least in terms of first-order effects).

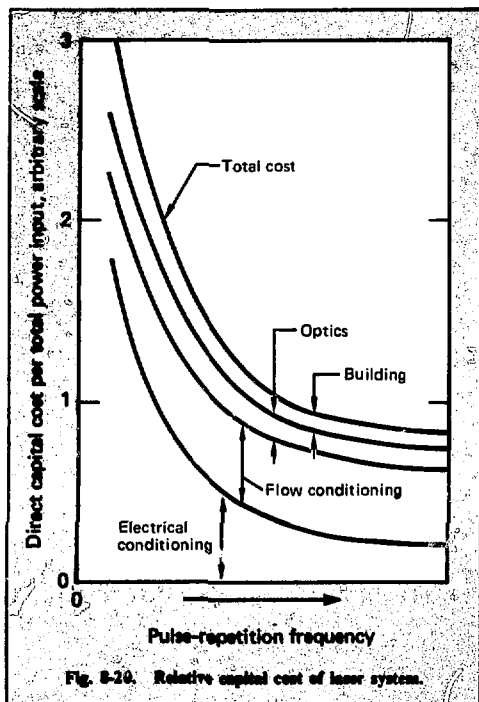


Fig. 8-20. Relative capital cost of laser system.

These considerations lead us to expect the cost per megawatt of laser systems to decrease as pulse-repetition rate increases. The volume and cost of energy-storage and pulse-conditioning equipment decreases with decreasing energy per pulse, without an offsetting increase in flow costs. Figure 8-20 plots the relative contributions of each category of a photolytic gas laser system to the total direct capital cost as a function of pulse-repetition frequency. The relative costs are normalized to the total input electrical power recirculated to the laser system from the generating system. We cannot fix absolute costs until we have defined a laser system much more completely than we have to date.

From the standpoint of laser capital cost, it appears most cost-effective to operate the laser at higher pulse-repetition rates. We estimate that increasing the pulse-repetition rate from 1 to 5 Hz might decrease the laser system cost by a factor of 2 to 3. Finally, the total direct cost of the laser system will vary inversely with its overall efficiency.

#### Authors

W. R. Meier  
M. J. Monster

## 8.2.6 Summary

We have completed a preliminary conceptual design of a laser fusion power plant based on advanced high-gain targets. We conducted a parametric analysis of this system to choose attractive design points and to show the sensitivity of the design to uncertainties in both the physics and technology. Although still highly conceptual, this power plant design has provided an understanding of both integrated engineering requirements and potential problem areas.

The lithium waterfall reactor has emerged as a promising concept. It appears to offer solutions for all the potential problems previously associated with inertial confinement fusion systems. It eliminates first-wall problems that result from x rays and pellet debris and minimizes cyclical thermal stresses. Also, the thick falling region of lithium attenuates neutrons to the point where the blanket structure could survive for the lifetime of the power plant at high power densities.

On the basis of the encouraging results of this study, we will conduct a more definitive conceptual design study next year. We will couple the lithium waterfall reactor to one of the more promising laboratory-stage lasers and will perform a detailed analysis of the major power plant components (reactor, laser, lithium system, and optical transport system). We will also examine the plant layout and costing of the design. The follow-on design will be influenced by several results of this year's (1977) study:

- Several advantages result from separating the large volume laser system from the reactor containment building.
- We need fusion energy gains ( $\eta_L Q$ ) of 10 or more.
- Laser system cost per unit of input power decreases as pulse-repetition frequency increases.
- The pumping power required to recirculate the lithium fall increases rapidly as pulse-repetition frequency increases (it becomes excessive when the frequency is greater than 3 Hz).
- These last two items suggest that it may be advantageous to have one laser system service several lithium waterfall reactors. Several smaller reactor modules may lead to shorter construction times and may increase the availability of the power plant.
- The laser system is composed of 10 modules in parallel but only 8 are used at any time. Modularity and redundancy of the laser system will lead to a highly reliable laser system.

The principal remaining uncertainties in the physics and engineering of the lithium waterfall

reactor are: the time history of the vapor in the chamber, after the microexplosion, as the vapor condenses on the (relatively cold) lithium liquid, and the transient stress in the first wall caused by fluid impact as the fall disassembles. Both phenomena are quite difficult to calculate, but we expect to model the fall disassembly and reestablishment with considerably improved accuracy in 1978. This will allow us to begin preliminary engineering design of the reactor with greater confidence.

Author

M. J. Monsler

### 8.3 Neutronic Studies for Fluid Reactors

In this section we deal with the important neutronic aspects of the lithium fall reactor concept. We first investigate how major system parameters vary as a function of fall thickness. (Throughout these studies we used a single compressed-target configuration. Subsequently, we analyze effects of different compressed-target configurations on these parameters.)

#### 8.3.1 Energy Deposition, Tritium Breeding, and Radiation Damage

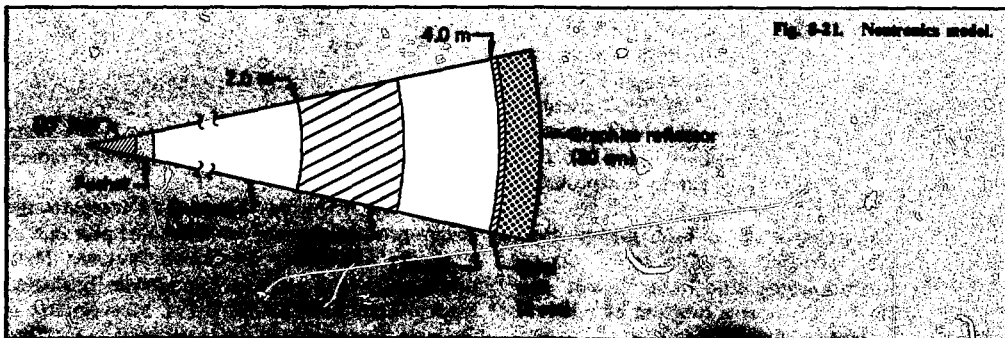
**Introduction.** We have conducted neutronic studies to determine how system nuclear performance varies as a function of the fall thickness. We used the TARTNP Monte Carlo neutronics code<sup>14</sup> to establish several reactor system parameters. These include the tritium-breeding ratio, spatial energy deposition profile, total energy deposition per DT fusion event, and helium production and atomic displacement rates in the first structural wall.

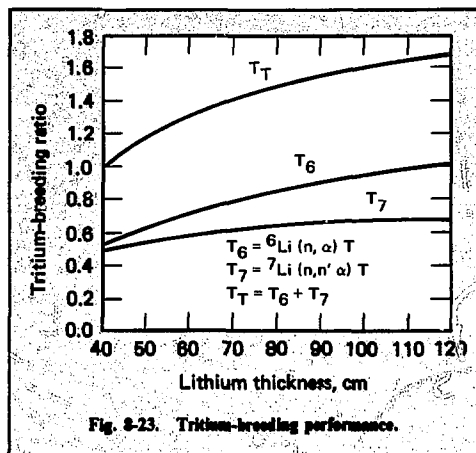
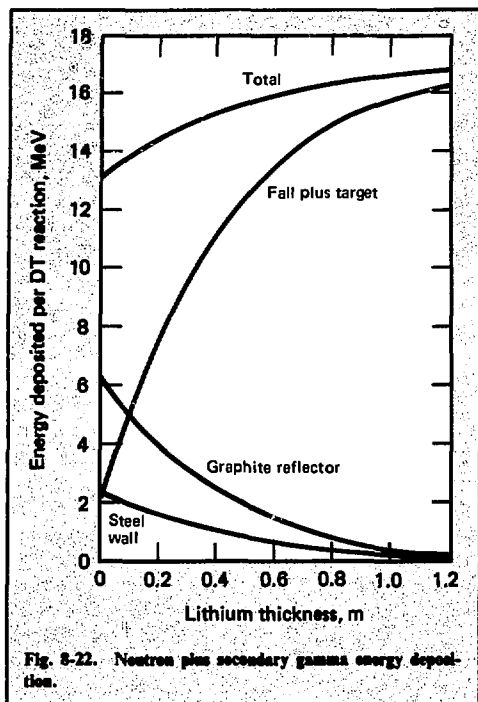
An important design change in the lithium fall concept that we reported in the 1976 Annual Report is the elimination of the recirculating reservoir region. As presently envisioned, the lithium recirculates to the top of the chamber through upcomers outside the pressure vessel. We made the change to eliminate induced stress on the pressure vessel that would result from neutron energy deposition in the lithium within the confined recirculating reservoir region. In the current configuration, it is necessary to deposit nearly all the fusion energy and to obtain an adequate tritium-breeding ratio in the fall alone. To meet the first constraint requires ~100-cm thickness of lithium. With this much protection, radiation damage to the first structural wall substantially decreases. The system can operate at neutron wall loadings an order of magnitude greater than early fusion chamber designs, yet the structural materials will never require replacement.

**System Model.** Figure 8-21 shows the one-dimensional, spherical geometry model used in this study. A 14.1-MeV fusion neutron source is uniformly distributed throughout a DT-fuel region that has a compressed density-radius product  $\rho R = 3.0$  g/cm<sup>2</sup>. The fuel region is surrounded by a pusher region that is compressed to  $\rho R = 0.8$  g/cm<sup>2</sup>. We discuss the neutron spectrum of this target with several different compressed configurations, at the end of this section.

Surrounding the target is a 2-m region of lithium vapor, a variable thickness of liquid lithium representing the fall, another lithium vapor region between the fall and the first structural wall, and a graphite reflector outside the first wall.

**Energy Deposition.** Figure 8-22 graphs the neutron-induced energy deposition in MeV per DT reaction. The curves show how the energy deposition in the different zones varies with the fall thickness, and they enable us to construct a spatial energy deposition profile for a selected fall





thickness. The curve labeled "total" is the sum of the lower three curves and the energy leakage.

Note that, on the average, neutrons deposit 2.1 MeV or 15% of their original 14.1 MeV in the fuel target. This energy, together with the 3.5-MeV alpha-particle energy, accounts for 32% of the target energy and reaches the inner surface of the fall in the form of x rays and debris. Exoergic neutron reactions with blanket materials (primarily  ${}^6\text{Li}$ ) result in a net energy gain for the system. We define the system energy multiplication  $M_s$  as the total energy deposited in the system divided by 17.6 MeV, the thermonuclear energy per DT event. As we noted above, it is necessary to deposit as much of the system energy as possible in the lithium fall. For a 100-cm-thick lithium region, the total energy deposited per DT reaction is 20.5 MeV, which represents a system energy multiplication of 1.16. In this case, more than 96% of the energy is deposited directly in the lithium.

**Tritium Breeding.** Figure 8-23 graphs the tritium-breeding performance. The three curves show the tritium-breeding ratio from  ${}^6\text{Li}$  and  ${}^7\text{Li}$  and the total of the two as a function of lithium thickness. While a thickness of only 40 cm is re-

quired to obtain an adequate breeding ratio ( $T_T > 1$ ), energy deposition considerations require  $\sim 100$  cm. For a 100-cm lithium fall, the tritium-breeding ratio is 1.6. Potentially, this excess tritium could be useful for fueling other DT fusion applications where tritium breeding is more difficult. If no market develops for the tritium, a neutron poison could be added to the lithium stream to compete with the lithium for neutrons.

**Radiation Damage.** We are evaluating radiation damage to the first structural wall in terms of two parameters: the helium production and atomic displacement rates. Both rates are time-integrated and do not represent the instantaneous rate at the time of the fusion event.

Both rates are expressed for one unit of equivalent neutron wall loading to permit comparison with other fusion concepts. The equivalent neutron wall loading is defined as

$$\phi_n = \frac{0.8 P_{TN}}{4\pi R_w^2},$$

where  $P_{TN}$  = thermonuclear power (yield times repetition rate), MW; and  $R_w$  = first-wall radius, m.

**Helium Production.** Figure 8-24 compares the helium production cross sections ( $n, \alpha$ ) plus ( $n, n' \alpha$ ) from the Livermore Evaluated Nuclear Data Library (ENDL) and the Brookhaven Evaluated Nuclear Data File (ENDF/B-IV). Most notable is the large discrepancy in the cross sections for iron.

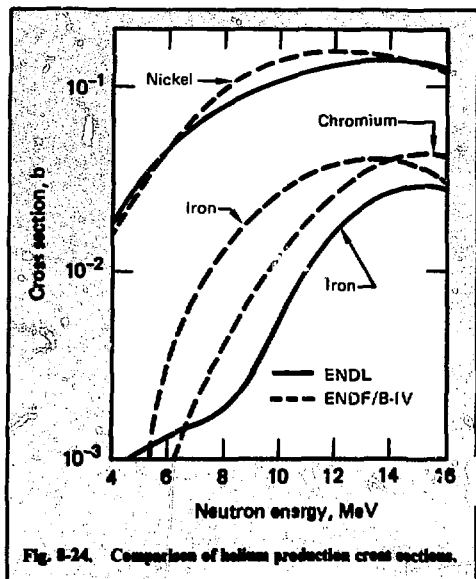


Fig. 8-24. Comparison of helium production cross sections.

The ENDF value is higher than the ENDL value; at 15 MeV it is only 25% greater, but the difference increases with decreasing neutron energy to a factor of 7 times higher at 9 MeV. This discrepancy arises from a lack of experimental measurements and poorly developed systematics for calculating cross sections. Because the products of  $(n, \alpha)$  and  $(n, n' \alpha)$  reactions with  $^{56}\text{Fe}$  (92% of natural Fe) are the stable isotopes  $^{53}\text{Cr}$  and  $^{52}\text{Cr}$ , we cannot measure these cross sections with conventional activation techniques. No measurements of helium production cross sections have been made on natural iron, and only one measurement has been made for  $^{56}\text{Fe}$  (see Ref. 15). This one-point measurement was at 14.6 MeV (see Ref. 16).

To determine what effect this cross section discrepancy would have on the helium production rate, we modeled the case of a 100-cm-thick fall and 2-cm iron wall with the two libraries. The result was that the ENDF/B-IV library gave a helium production rate 2.6 times greater than the ENDL library.

The cross sections for nickel agree quite well, reflecting the fact that the  $(n, \alpha)$  cross section for  $^{58}\text{Ni}$  (68% of natural Ni) can be evaluated from activation data. The ENDL library does not contain a cross section for chromium because of the lack of experimental data. The ENDF cross section for chromium is included in Fig. 8-24; it falls between the two libraries' cross sections for iron.

In this study we have replaced the Cr content of

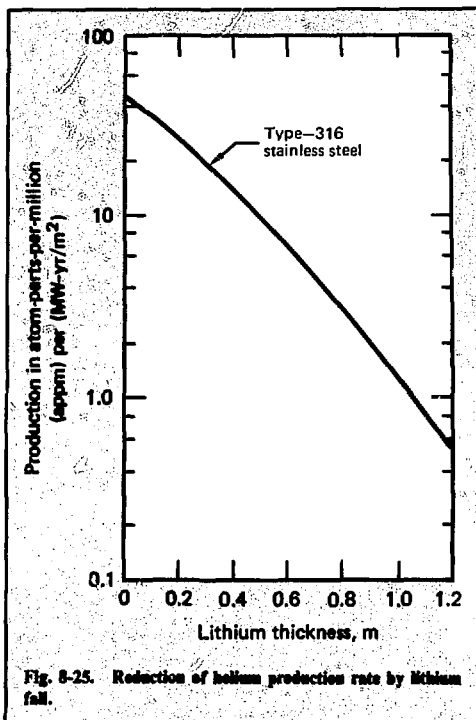
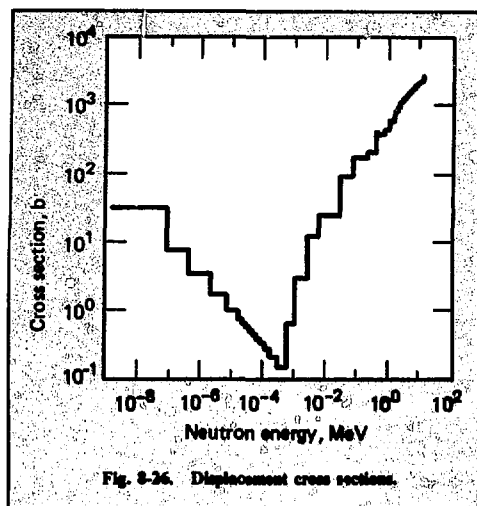


Fig. 8-25. Reduction of helium production rate by lithium fall.

the first structural wall with Fe because ENDL does not include a helium production cross section for Cr. The implicit assumption is that Cr has alpha-producing cross sections similar to those for Fe. The resulting helium production cross section for 316-SS at 15 MeV is 42 mbarn. A recent measurement of 316-SS at the LLL RTNS produced a value of  $48 \pm 7$  mbarn at 15 MeV (see Ref. 17). Thus, the value used in these neutronics calculations is within the uncertainty range, but it falls near the low end of the measured experimental value.

Figure 8-25 illustrates the reduction in the helium production rate realized by protecting the first wall with a region of lithium. The production rate is shown in appm-He per  $(\text{MW}\cdot\text{yr}/\text{m}^2)$  of equivalent neutron wall loading. The production rate in a wall protected by 100 cm of lithium is 1.3 appm per  $(\text{MW}\cdot\text{yr}/\text{m}^2)$ , a reduction by a factor 35 over an unprotected wall.

**Displacement Damage.** We calculated displacement damage rates and used the modified cross sections calculated by Doran and Graves.<sup>18</sup> These cross sections are somewhat higher than an earlier set<sup>19,20</sup> used in similar studies.<sup>21,22</sup> Figure 8-26 shows the cross section for 18-10 stainless steel



(similar to Type 316) collapsed to the 50 energy-group structure of TARTNP.

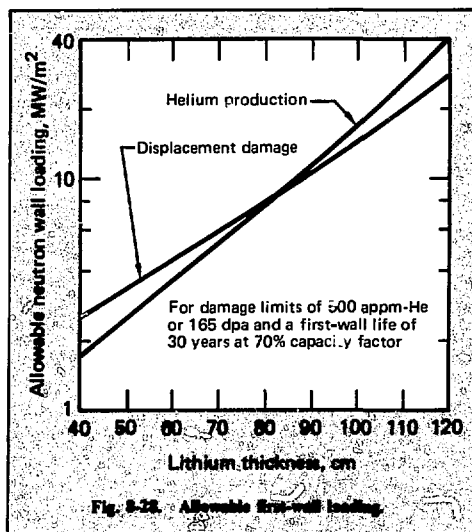
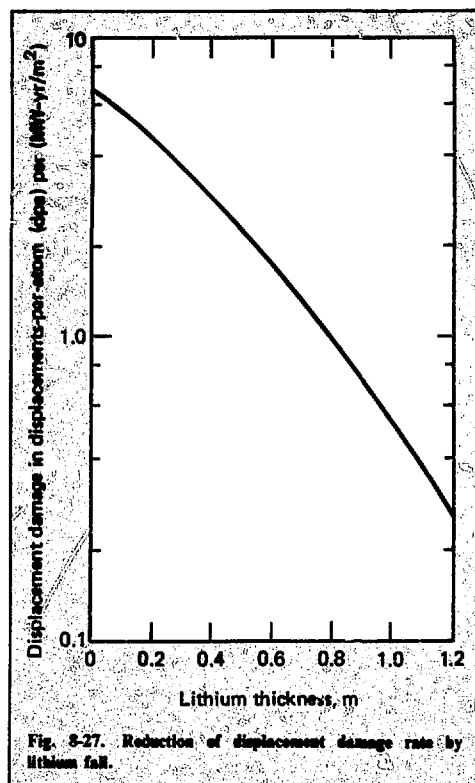
The recommended value of 40 eV was used for the effective displacement energy. For neutron energies  $< 10^{-4}$  MeV, the displacement cross section varies as  $E^{-1/2}$  from a value of 20b at 0.025 eV.<sup>19</sup>

The effectiveness of the lithium fall in reducing the displacement damage rate in SS is shown in Fig. 8-27. The damage rate in a wall protected by 100 cm of lithium is 0.53 dpa per (MW-yr/m<sup>2</sup>), which is lower than for an unprotected wall by a factor of 13.

**Damage Limits and Wall Life.** We can estimate the radiation-damage-limited life of the first wall from these damage rates if we select an appropriate ultimate damage limit (total dpa, or total appm-He, or both). Kulcinski<sup>21</sup> suggests a limit of 500 appm for 316-SS operated at 500°C. He also suggests a limit for dpa-induced void swelling of 10% for fusion reactors. Using the correlation for 20% cold-worked 316-SS from Ref. 14, we find that 10% swelling would be reached after 165 dpa.

Combining the production rates with these damage limits (500 dpa-He and 165 dpa) allows us to determine the life of the first wall, expressed in MW-yr/m<sup>2</sup>, as a function of lithium thickness. Then, if we assume that the first wall must remain below the ultimate damage limits for the life of the power plant (30 years at 70% capacity factor), we can determine the allowable neutron wall loading.

Figure 8-28 shows how the allowable wall loading increases with increasing lithium thickness. Below ~80 cm, helium production is the limiting factor, and above 80 cm, displacement damage





limits the system. With 100 cm of lithium protection, the allowable wall loading approaches 15 MW/m<sup>2</sup>. This wall loading is an order of magnitude higher than early fusion reactor designs and corresponds to power density greater by a factor of 40.

**Conclusions.** In terms of nuclear performance, the distinctive feature of the fluid wall design is that the energy-absorbing "blanket" region (lithium fall) is actually inside the first structure wall. By requiring that 95% of the system energy be deposited in the lithium within the vacuum chamber, we can reduce radiation damage enough to allow high power-density chamber designs to be built with no replaceable components. We have also found that such designs result in high blanket-energy multiplication and high tritium-breeding ratios.

## References

14. J. Kimlinger and E. Plechatz, *TARTNP: A Coupled Neutron-Photon Monte Carlo Transport Code*, Lawrence Livermore Laboratory, Livermore, Calif., UCRL-50400, Vol. 14 (1976).
15. M. H. MacGregor et al., *Neutron-Induced Interactions: Index of Experimental Data*, Lawrence Livermore Laboratory, Livermore, Calif., UCRL-50400, Vol. 3, Rev. 2 (1976).
16. C. Spera and J. M. Robson, *Nucl. Phys.* **127**, 81 (1969).
17. R. C. Haig, S. M. Grimes, and J. D. Anderson, "Hydrogen and Helium Production Cross Sections for 15 MeV Neutrons on Type 316 and 304 Stainless Steel," *Nuc. Sci. and Eng.* **63**, 2 (1977).
18. D. G. Doran and N. J. Graves, "Neutron Displacement Damage Cross Sections for Structural Metals," in *Irradiation Effects on the Microstructure and Properties of Metals*, ASTM STP 611 (1976), pp. 463-482.
19. D. G. Doran, *Nucl. Sci. Eng.* **49**, 130, 1972.
20. D. G. Doran, *Nucl. Sci. Eng.* **52**, 398, 1973.
21. G. L. Kulcinski et al., *Protection of CTR Metallic First Walls by Neutron Spectral Shifting*, Univ. of Wisconsin Report UWFD-127 (1975).
22. H. I. Avci and G. L. Kulcinski, *The Effect of a Liquid ISSEC on Radiation Damage Parameters in Laser Fusion Reactor First Walls*, Univ. of Wisconsin Report UWFD-205 (1977).

## Author

W. R. Meier

## 8.3.2 Target-Dependent Effects<sup>23</sup>

Until recently, most studies of inertial confinement fusion reactors incorporated a monoenergetic 14.1-MeV neutron source. However, problems

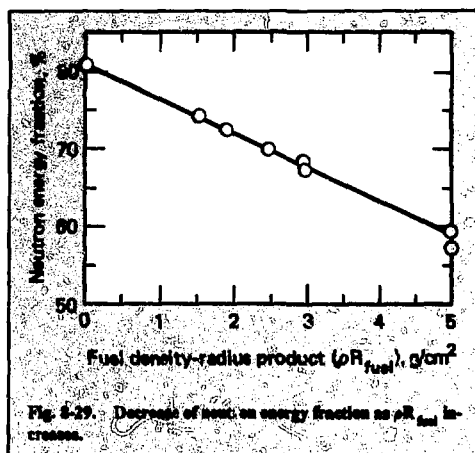


Fig. 8-29. Decrease of neutron energy fraction as  $\rho R_{\text{fuel}}$  increases.

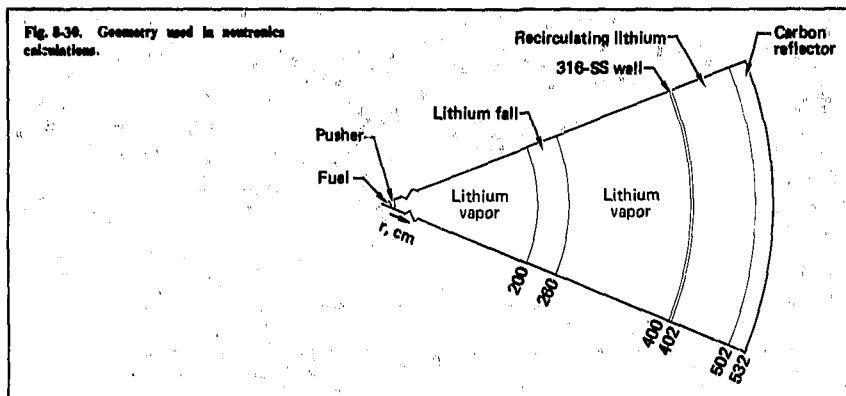
arose because of the need for neutrons to transit the compressed fuel and pusher regions before leaving the target. At the compression levels proposed, the target represents as much as one mean free path to 14-MeV neutrons; accordingly, we anticipated significant interactions. This article summarizes the effects of the fuel compression, pusher composition, and pusher compression on three reactor parameters:

- Tritium breeding ratio (TBR) = Tritium atoms bred/DT event.
- System multiplication factor ( $M_s$ ) = Thermal energy/thermonuclear energy.
- Helium production in the first wall = He atoms produced/DT event.

As the compression of the fuel region increases, more neutrons interact and deposit energy within the target. Thus, the fraction of the thermonuclear energy that escapes the target in the form of neutrons decreases (Fig. 8-29). (The LLL Monte Carlo neutronics-photonics code TARTNP<sup>24</sup> was used for these calculations.) We assumed the neutrons were born at a monoenergetic 14.1 MeV and that they were distributed uniformly throughout the fuel region with an isotropic angular distribution. The multiple points at  $\rho R = 3$  and 5 represent targets with different pushers. A Monte-Carlo-neutronics thermonuclear-burn code used to check the results gave good agreement.

We must specify reactor geometry to determine the effect of the target on reactor parameters. We based the one-dimensional calculations on an early version of the LLL liquid lithium waterfall reactor (Fig. 8-30). Figure 8-31 shows the effect of the fuel density-radius product  $\rho R$  on the three reactor

Fig. 8-30. Geometry used in neutronics calculations.



parameters. To focus on the importance of including the target in reactor calculations, we plotted the ratio between the value obtained by using a 14.1-MeV point source and the value obtained when the target is considered. We found helium production in the first wall to be the most sensitive reactor parameter. When we ignored the target, He production and TBR were overpredicted and  $M_s$  was underpredicted.

In Fig. 8-32, the pusher composition and compression are also varied. The fuel  $\rho R$  is clearly the dominant variable. The figure also shows the results

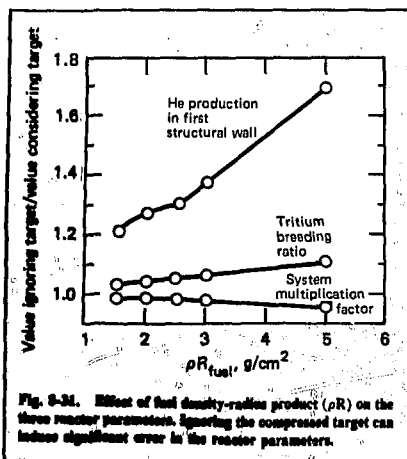
of two burn-code runs we used to verify the TARTNP runs. The disagreement at  $\rho R = 2.5$  is a result of early termination of the burn code.

Completely ignoring the pusher does not introduce large errors (Fig. 8-33). We tested a wide variety of pusher compositions and compressions; the largest effect was a 16% error in He production for the  $\rho\Delta R = 1.9$ , LiD pusher. By comparison, if the entire target is ignored, the error increases to  $\sim 70\%$ .

The results presented above reflect a uniformly distributed source in the fuel region. Table 8-3 considers the other simple option, a point source in the target center. We used the burn-code results as the "standard" to evaluate the two sources. The distributed source is clearly more realistic.

Because He production in the first wall could be a limiting factor in a reactor design, the effect of the compressed target and the lithium wall in reducing that production are important. Figure 8-34 plots the reduction in He production as a function of lithium fall thickness. The compressed target reduces He production by 20%. The combined effect of the target and 60-cm fall is a 90% reduction in first-wall He production.

Since we assumed all neutrons were born at the same energy level, the energy width of the high-energy spike in the TARTNP result is quite narrow. However, because the fusing ions have a distribution of energies and directions, the neutrons are actually born with an energy distribution centered on 14 MeV, and the spike is broader. Although the spike width has little effect on TBR,  $M_s$ , or Helium production, it is of some significance in the first-wall damage because of atom displacements. This



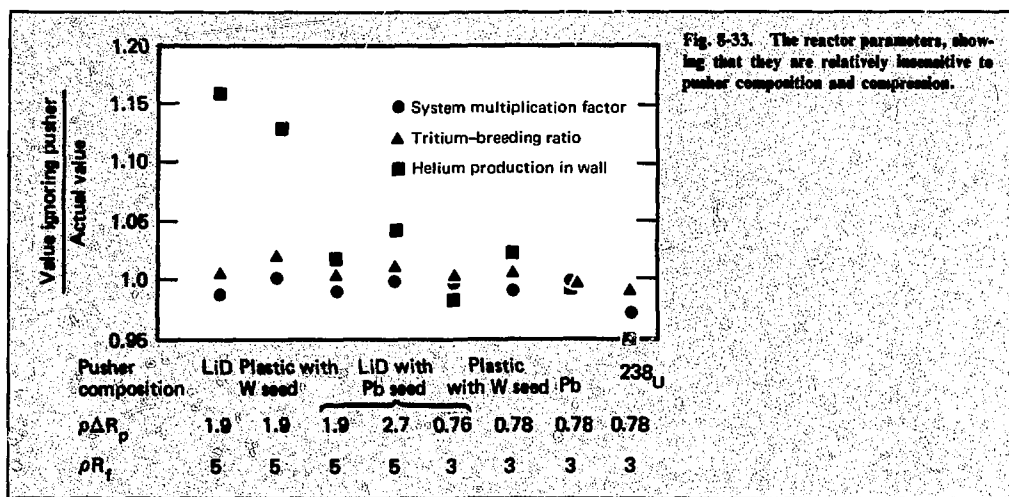
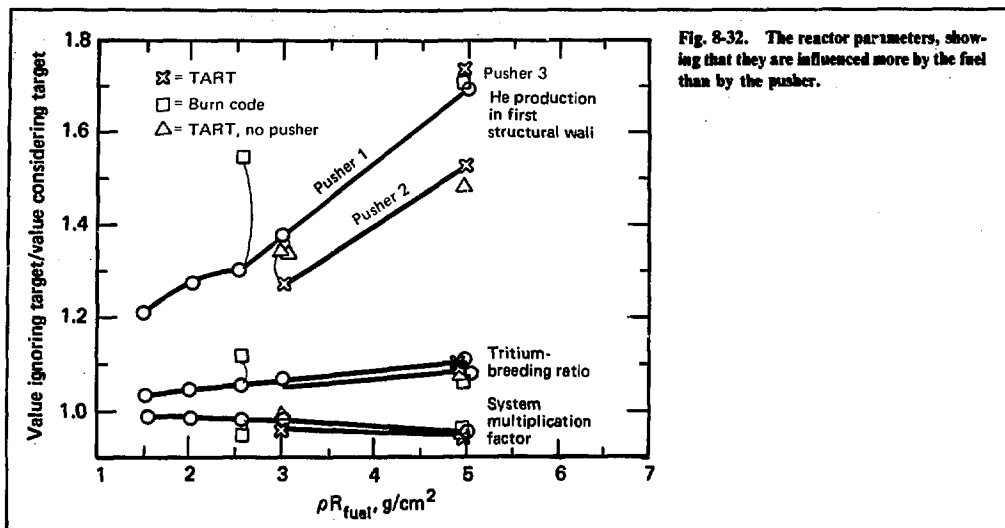
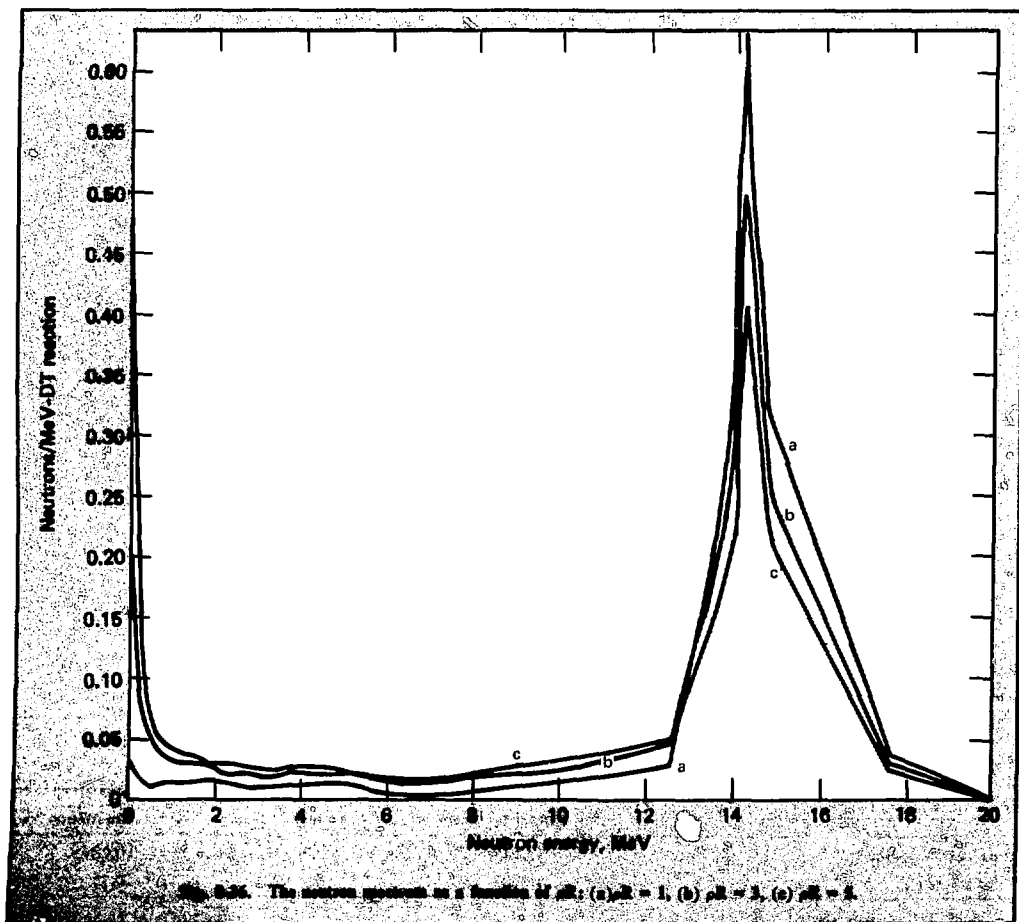
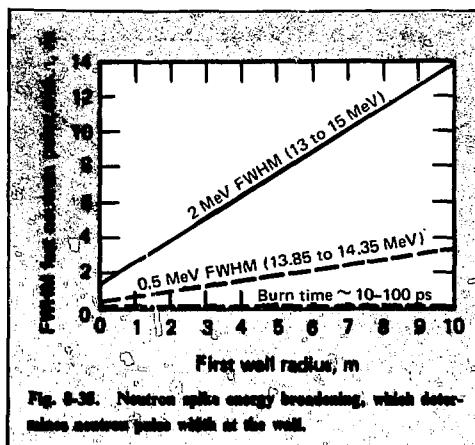
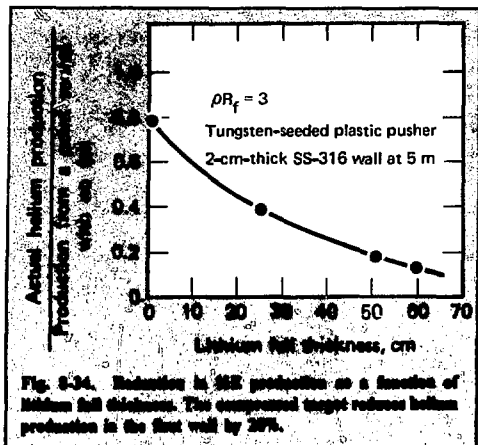


Table 8-3. Consideration of point source in the target center. An isotropic distributed source in the compressed fuel region is more realistic than a point source.

	$\left( \frac{\text{TART value}}{\text{Burn-code value}} \right)$		
	System multiplication factor	Tritium breeding ratio	Helium production rate
Distribution source	1.0185	0.9893	0.9878
Point source	1.0287	0.9587	0.8417

$\rho R_f = 5$ , LiD pusher seeded with Pb,  $\rho \Delta R_p = 1.92$ .



damage depends on the neutron dose rate as well as on the total dose, and the width of the energy spike results in a spread of the arrival times at a given distance (Fig. 8-35).

If we use a nonburn code such as TARTNP, we can make the energy spike more realistic by specifying

Table 8-4. Neutron spectrum from a  $\rho R$  3 target. Because the target temperature  $>1$  keV, neutrons below that energy level were considered to be thermal.

Energy of neutron tally groups	Neutrons/group DT reaction
1 1.307E-09	0.
2 8.322E-08	0.
3 4.234E-07	0.
4 2.091E-06	0.
5 6.737E-06	0.
6 1.468E-05	0.
7 2.277E-05	0.
8 2.940E-05	0.
9 4.048E-05	0.
10 4.918E-05	0.
11 6.097E-05	0.
12 7.155E-05	0.
13 8.431E-05	0.
14 9.811E-05	0.
15 1.338E-04	0.
16 1.789E-04	0.
17 3.267E-04	0.
18 6.042E-04	0.
19 1.058E-03	5.000E-05
20 2.561E-03	4.000E-04
21 5.763E-03	1.585E-02
22 2.646E-02	9.150E-03
23 7.002E-02	1.920E-02
24 2.075E-01	1.265E-02
25 3.777E-01	6.900E-03
26 5.123E-01	1.025E-02
27 7.527E-01	9.050E-03
28 1.025E+00	8.550E-03
29 1.338E+00	1.050E-02
30 1.694E+00	1.125E-02
31 2.091E+00	9.900E-03
32 2.530E+00	1.030E-02
33 3.011E+00	9.350E-03
34 3.533E+00	1.180E-02
35 4.069E+00	1.460E-02
36 4.704E+00	1.220E-02
37 5.353E+00	1.015E-02
38 6.042E+00	9.400E-03
39 6.737E+00	1.230E-02
40 7.548E+00	1.410E-02
41 8.322E+00	1.600E-02
42 9.177E+00	2.160E-02
43 1.012E+01	2.445E-02
44 1.101E+01	3.335E-02
45 1.199E+01	4.880E-02
46 1.307E+01	1.323E-01
47 1.386E+01	7.540E-02
48 1.413E+01	1.397E-01
49 1.441E+01	1.961E-01
50 1.519E+01	1.430E-01
2.000E+01	

ing the energy distribution of source neutrons. The resulting neutron spectrum for three values of fuel  $\rho R$  is shown in Fig. 8-36.

Reactor calculations should include the effects of the compressed target. Two options are available: we may include the target in the neutronics calculation (we have used this option at LLL for both pure fusion and hybrid reactor calculations since November 1977), or we may use the neutron spectrum from a target calculation as a source for reactor calculations. Table 8-4 tabulates one such source spectrum.

## References

23. J. Blink, P. Walker, and H. Meldner, "Energy Partition and Neutron Spectra From Laser Fusion Reactor Targets," *Trans. ANS*, 27, 70, San Francisco, Calif. (1977).
24. J. Kimlinger and E. Plechatz, *TARTNP: A Coupled Neutron-Photon Monte Carlo Transport Code*, Lawrence Livermore Laboratory, Livermore, Calif., UCRL-50400, Vol. 14 (1976).

## Authors

J. A. Blink  
P. E. Walker  
H. W. Meldner

## 8.4 First-Wall Response and Fluid-Response Studies

The first-wall response to an inertially confined fusion (ICF) microexplosion determines the design and cost of the reactor in a number of ways. Capital costs increase as a function of first-wall radius. A portion of the operating costs decrease as the lifetime of the first wall increases. Because the lifetime of the first wall increases as a function of the radius, tradeoffs are possible between designs for low operating cost (large radius) and designs for low capital cost (small radius).

Much of our effort is devoted to first-wall design, which has a major effect on the economics of the reactor cavity. In addition to conceiving wall designs, we are developing analytic modeling techniques to estimate the response of the first wall to the various forms of microexplosion energy release. This year, we improved our model for the microexplosion charged-particle energy deposition in the first wall and continued our investigation of

the dry wall sacrificial liner for ion-beam-initiated ICF reactors. In addition, we investigated the flow stability of high Reynolds number sheets and jets. We also studied the response of a thick liquid lithium falling curtain to the microexplosion in an attempt to determine and resolve the critical issues for the lithium fall reactor concept.

We developed a methodology for estimating the microexplosion charged-particle energy deposition in the first wall. The methodology is based on a Maxwellian energy distribution of the particles and various stopping-power and particle-energy relationships.<sup>25</sup> We can determine the spatial distribution of the deposited energy for the various stopping-power regimes of a material bombarded by various species of Maxwellian energy-distributed particles. This energy deposition allows the estimation of an energy-attenuation coefficient that may be used in simplified energy transport calculations.

Five critical issues for the lithium fall reactor concept<sup>26</sup> follow:

- Stability of the fall.
- Response of the fall to the microexplosion.
- Response of the first structural wall to the microexplosion.
- Restart of the fall between microexplosions.

- Ability of the fall to pump down the chamber between shots.

We have investigated fall stability<sup>27</sup> and the response of the fall to the microexplosion.<sup>28</sup>

Extrapolation of data from the literature, as well as preliminary results of experiments conducted at U.C.-Davis, indicate that the fall appears stable over its length in the reactor cavity. The fall disassembles from the microexplosion energy deposition and subjects the first structural wall to high pressures and stresses. We feel that these stresses can be reduced by reconfiguring the fall.

We conducted a parametric investigation of the dry first-wall liner concept for ion-beam-initiated ICF reactors, setting pellet yields between 400 and 4000 MJ.<sup>29</sup> The least expensive first-wall liner for a 4000-MW reactor was graphite over stainless steel. For a first-wall neutron flux of 5 MW/m<sup>2</sup> and a lifetime of one year, the minimum cost occurred with microexplosion yields of less than 530 MJ. General Atomics Corporation (GAC) examined both graphite and silicon carbide, first-wall liners for a 4000-MJ microexplosion.<sup>30-32</sup> They found that a graphite liner for this microexplosion was limited to a minimum wall radius of 17 m because of stress. In addition, they determined that a SiC liner was limited to a minimum wall radius of 20 m because of the surface evaporation rate.

## References

25. J. Hovingh and S. L. Thomson, "Energy Deposition from Microexplosion Particle Debris in the First Wall of an Inertially-Confined Fusion Reactor," *Proc. 7th Symp. on Eng. Problems of Fusion Research*, Vol. I, 162, Knoxville, Tenn. (1977).
26. J. A. Maniscalco and W. R. Meier, "Liquid Lithium 'Waterfall' Inertial Confinement Reactor Concept," *Trans. ANS 1977 Summer Mtg.*, 62, New York (1977).
27. S. W. Kang, "Jet Stability in the Lithium Fall Reactor," *Proc. 3rd Topical Mtg. on Tech. of Controlled Nucl. Fusion*, Santa Fe, N. Mex. (1978).
28. J. Hovingh, J. Rink and L. Glenn, "Response of a Lithium Fall to an Inertially Confined Fusion Microexplosion," *Proc. 3rd Topical Mtg. on Tech. of Controlled Nucl. Fusion*, Santa Fe, N. Mex. (1978).
29. J. Hovingh, *First Wall Costs of an Ion-Beam Fusion Reactor*, Lawrence Livermore Laboratory, Livermore, Calif., UCID-17555 (1977).
30. G. R. Hopkins, R. J. Price, R. E. Bullock, J. A. Dalessandro, and J. Hovingh, "An Assessment of Carbon and Silicon Carbide as First Wall Materials in Inertial Confinement Fusion Reactors," *Proc. 3rd Topical Mtg. on Tech. of Controlled Nucl. Fusion*, Santa Fe, N. Mex. (1978).
31. J. A. Dalessandro, "First Wall Thermal Stress Analysis for Suddenly Applied Heat Fluxes," *Proc. 3rd Topical Mtg. on Tech. of Controlled Nucl. Fusion*, Santa Fe, N. Mex. (1978).
32. G. R. Hopkins, R. J. Price, R. E. Bullock, J. A. Dalessandro, and N. B. Elsner, *Carbon and Silicon Carbide as First Wall Materials in Inertial Confinement Fusion Reactors*, Lawrence Livermore Laboratory, Livermore, Calif., UCRL-13854 (GA-A14894) (1978).

## Author

J. Hovingh

## 8.4.1 Interaction of Debris with First Wall

The fuel pellet of an ICF reactor consists of a core of deuterium and tritium that is compressed and heated to thermonuclear conditions, and of a surrounding layer of material that is ablated during the source-energy deposition. Some fusion-produced alpha particles interact with the core and the ablated layer. The pellet debris reaches thermal equilibrium as it expands. In a typical fusion reactor, the chamber is evacuated to allow the transport of source energy; therefore, the debris expands into a vacuum. If there is no interaction between the

debris and the background gas, a complete expansion occurs and the Maxwellian distribution of the debris velocity in the direction of the expansion is maintained.

In previous work,<sup>33</sup> we assumed that the debris particles deposit their energy uniformly over their range in the first wall. Here, we use the actual distribution of the particle energy loss into the wall as a function of distance, to determine the average debris energy deposition in the wall.

Figures 8-37 and -38 show the stopping power for deuterons, tritons, and alpha particles in five materials. Haggmark of Sandia-Livermore used the Johnson-Gibbons formulation.<sup>34</sup> The stopping-power points are based on the actual range of the particles in the material. At low energies, where nuclear stopping dominates the particle energy loss, the projected range is much less than the actual range. At high energies, where electronic stopping power dominates, the projected range is essentially equal to the actual range.

The curves in Figs. 8-37 and -38 plot the stopping power based on the projected range of the particle in the material. For the lowest energy<sup>35</sup> region, the stopping power is based on Schiøtt's<sup>35</sup> formulation. For the second lowest energy region, the stopping power is based on the electronic stopping

power formulation given in Ref. 36. Finally, for the highest energy regions, the stopping power is a logarithmic fit to Haggmark's stopping-power points.

The projected range of the particles in various materials is shown in Figs. 8-39 and -40. The points are from Haggmark, and the curves are the result of integration of the stopping power curves from Figs. 8-37 and -38. The curves adequately fit Haggmark's points.

Because niobium and molybdenum have approximately the same stopping power and range, we treat them here as one material.

The energy lost by a particle as a function of energy is given by

$$-\frac{dE}{dx} = S(E), \quad (1)$$

where  $S(E)$  is the stopping power in the material. The distance into the wall at which a particle of incident energy  $E_0$  has reached energy  $E$  is, therefore,

$$x = \int_E^{E_0} \frac{dE}{S(E)}. \quad (2)$$

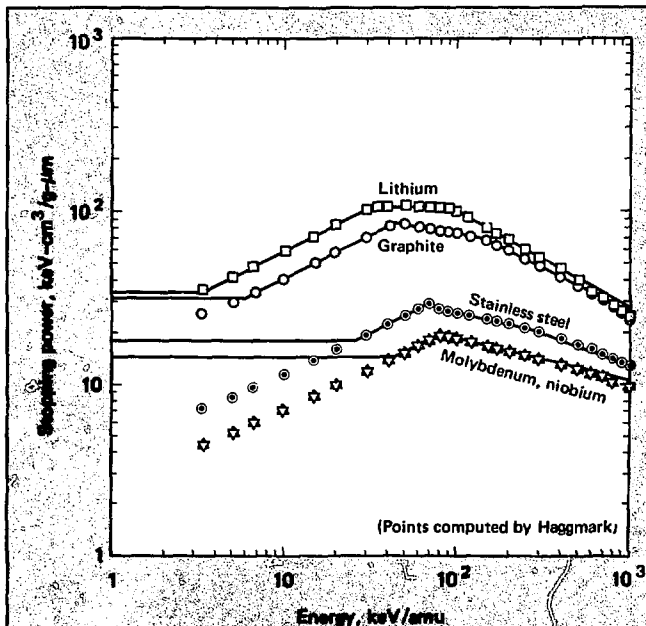


Fig. 8-37. Stopping power for  $Z = 1$  particles in various materials.

Fig. 8-38. Stopping power for  $Z = 2$  particles in various materials.

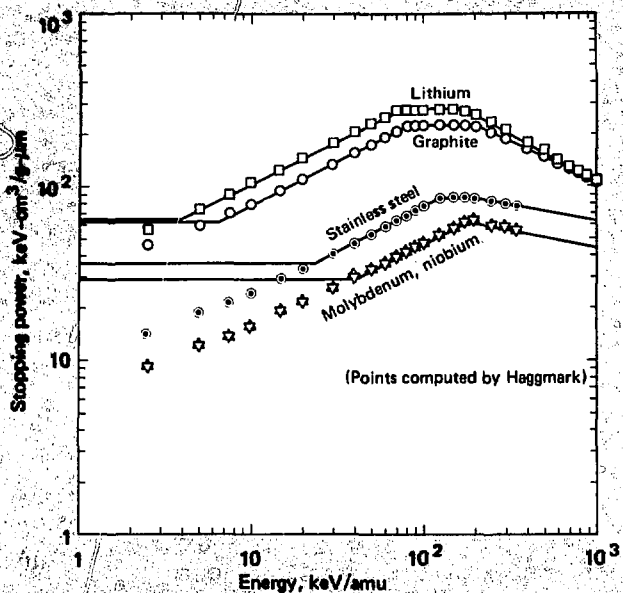
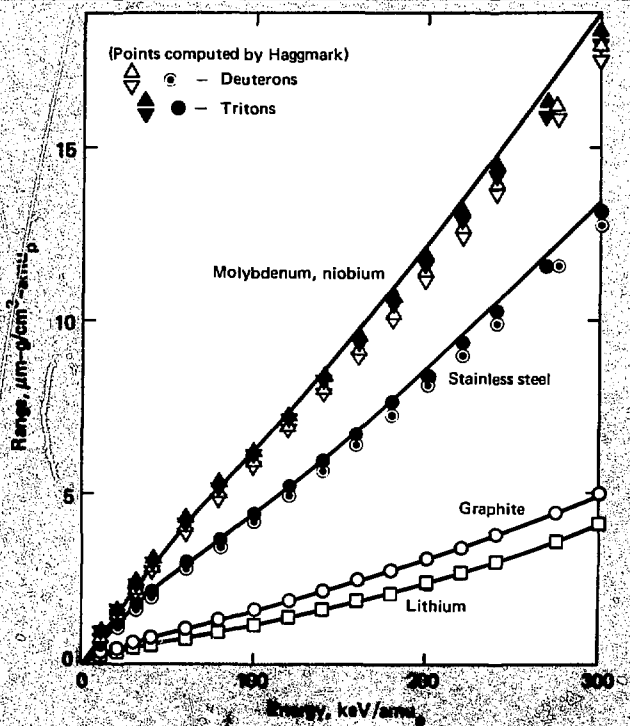


Fig. 8-39. Projected range-energy curves of  $Z = 1$  particles in various materials.





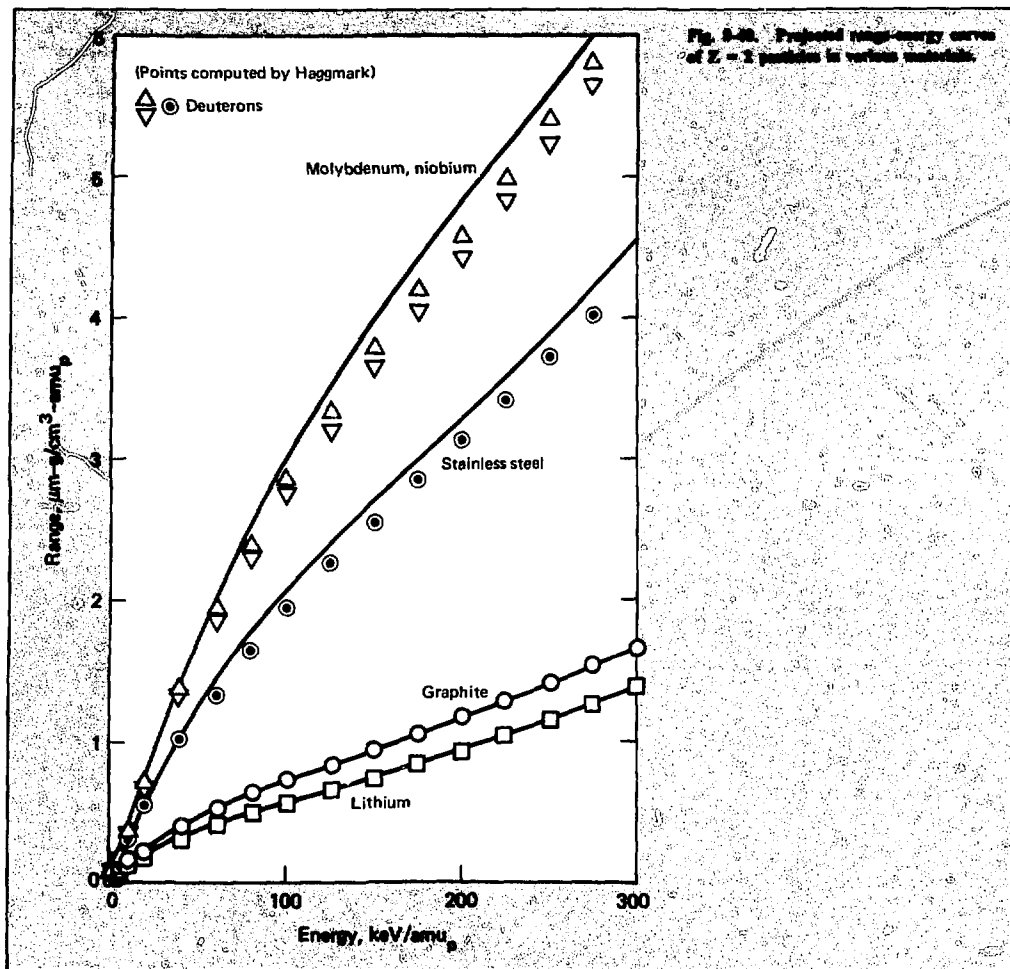


Fig. 8-38. Projected range-energy curves of  $Z = 2$  particles in various materials.

The energy deposited by a group of particles at  $x$ , when those particles have a Maxwellian distribution at the surface, is

$$\langle S \rangle = \frac{2}{\sqrt{\pi}} \int_{y_1}^{\infty} S(x, y) y^{1/2} e^{-y} dy, \quad (3)$$

where  $y = E_0/kT$ . The lower limit represents particles that penetrate at least the distance  $x_1$ ,

$$x_1 = \int_0^{E_0} \frac{dE}{S(E)}. \quad (4)$$

We obtain the temporal distribution of energy deposition at the surface from Eq. (3) by integrating over the incident energies corresponding to the arrival time of the debris at the wall:

$$E_0 = \frac{1}{2} m (R/t)^2. \quad (5)$$

If we assume that the particle energy is deposited uniformly such that  $S(E) = \alpha$ , a constant, Eq. (4) gives  $x_1 = E_0 \alpha$ , and

$$\langle S \rangle = \frac{2\alpha}{\sqrt{\pi}} \int_{\frac{\alpha x}{kT}}^{\infty} y^{1/2} e^{-y} dy. \quad (6)$$

This result was used in Ref. 33.

In the general case,  $S(E)$  cannot be represented by one continuous function to good accuracy; the integration must be broken into regions of validity for separate functions.

We used Eq. (3) and the limits from Eq. (2) to integrate the stopping power curves of Figs. 8-37 and -38. The energy deposition normalized to the energy fluence at the first wall in various candidate first-wall materials is shown in Fig. 8-41 for a deuterium-tritium pellet with an average debris particle energy of 50 keV/amu. Figure 8-42 shows the deposition in graphite for various average debris particle energies.

The energy attenuation coefficient of the wall material  $\sigma$  is defined

$$q'''(x) = q_0''' e^{-\sigma x}, \quad (7)$$

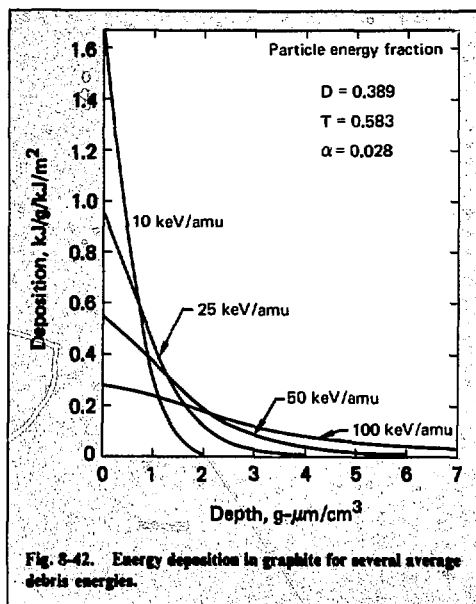


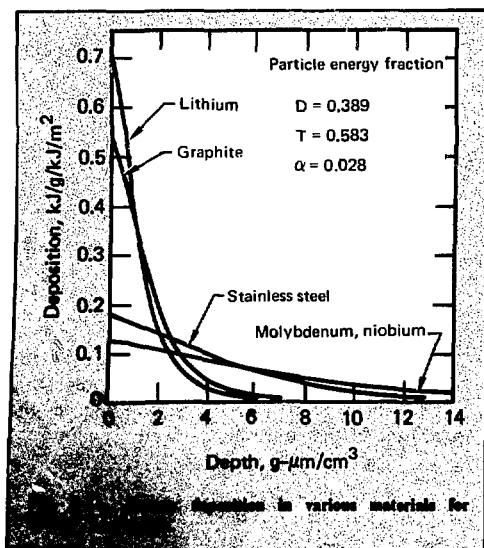
Fig. 8-42. Energy deposition in graphite for several average debris energies.

where  $q'''(x)$  is the energy generation in the wall at a position  $x$ , and  $q_0'''$  is the energy generation at the surface. The values of  $\sigma$  that fit the results shown in Figs. 8-41 and -42 at the  $1/e$  point are shown in Table 8-5.

The energy deposition at the surface, calculated by the above method, results in a larger surface deposition and a larger energy attenuation coefficient than do the methods used in previous calculations,<sup>34,37</sup> as shown in Fig. 8-43. However, if the average energy is less than 0.27 times the energy at the lowest energy-inflection point in Figs. 8-37

Table 8-5. Specific energy attenuation coefficient for a typical DT microexplosion.

Material	Average particle energy, keV/amu	Attenuation coefficient, cm <sup>2</sup> /g·μm
Graphite	10	1.4
	25	0.83
	50	0.51
	100	0.29
Lithium	50	0.69
Stainless steel	50	0.19
Molybdenum, niobium	50	0.14



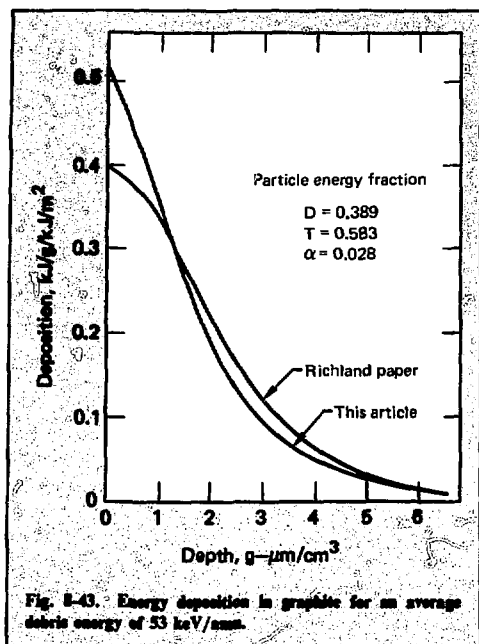


Fig. 8-43. Energy deposition in graphite for an average debris energy of 53 keV/amu.

and -38, the constant-deposition model using stopping power based on Schiøtt's work is the easiest available model; it accounts for 95% of the debris energy.

The temporal pulse width of the energy at the first wall is given by

$$\Delta\tau = 1.38 \times 10^{-6} \left( \frac{R^2}{E} \right)^{1/2} \text{ s}, \quad (8)$$

where  $R$  is the reactor first-wall radius in metres and  $E$  is the average energy of the particle in keV/amu. Using this time, we can determine the temperature rise in the solid wall for a given energy attenuation coefficient. The surface temperature rise determined by this method is within 5% of the value that would be determined by treating the debris energy as a surface flux, if

$$\sigma \sqrt{\alpha \Delta\tau} > 20, \quad (9)$$

where  $\alpha$  is the thermal diffusivity of the first-wall material. Table 8-6 gives the maximum average

Table 8-6. Maximum average energy consideration for calculational models.

Model material	Constant stopping power max $\bar{E}$ , keV/amu	Surface flux	
		$\bar{E}$ R 0.4	$\left\{ \begin{array}{l} \bar{E} \text{ in keV/amu} \\ R \text{ in meters} \end{array} \right.$
Lithium	0.94		1.0
Graphite	1.6		2.0
Stainless	7.0		3.0
Niobium	12.0		6.0
Molybdenum	12.0		5.0

energies for which the stopping power can be treated as a constant and for which the surface temperature rise can be estimated, using a surface heat flux.

It is apparent from Table 8-6 that, for reactors of reasonable size, the debris energy deposition can be treated as a surface flux when nuclear stopping dominates the particle energy loss.

Our methodology allows an accurate calculation of the energy deposition of the pellet debris in the first wall of reactors. This energy deposition allows estimation of an energy attenuation coefficient to use in simplified energy transport calculations.

## References

33. J. Hovingh, "First Wall Response to Energy Deposition in Conceptual Laser-Fusion Reactors," *J. Nucl. Mat.* 63, 158 (1976).
34. W. S. Johnson and J. F. Gibbons, *Projected Range Statistics in Semiconductors*, Stanford University (1969).
35. H. E. Schiøtt, "Approximations and Implantation Rules for Ranges and Range Straggling," in *Ion Implantation*, Eisen and Chadderton, Eds. (London, Gordon and Breach, 1970), p. 197.
36. J. Lindhard, M. Scharff, and H. E. Schiøtt, "Range Concepts and Heavy Ion Ranges," *Kgl. Danske Vid. Selsk. Mat-Fys. Medd.* 33, No. 14 (1963).
37. J. Hovingh, "First Wall Studies of a Laser-Fusion Hybrid Reactor Design," *Proc. 2nd Topical Mtg. on the Tech. of Controlled Nucl. Fusion*, II, 765 (1976).

## Authors

J. Hovingh  
S. Thomson (Bechtel National, Inc.)

## 8.4.2 Liquid Sheets and Jets

In the lithium fall reactor concept, lithium serves as a protective liner, preventing microexplosion debris from impinging directly on the reactor structure. Prior to each microexplosion, the fall must be stable to allow laser beam energy to traverse the cavity without interference and to ensure that microexplosion products do not impinge directly on the structure. Preliminary analysis indicates that jets with an inlet velocity of 4 m/s and inlet diameter of 0.1 m would have an intact length of 10 m, which is the height of the fall in the reactor chamber. An increase in either the diameter or the velocity of the jets would also increase their intact length.

U.C.-Davis is studying the stability of sheets and jets. Their experiments use water as the fluid medium. Preliminary results show that convergence of hollow cylindrical jets, caused by the effects of surface tension, will not be an issue for equivalent lengths of a lithium fall envisioned for a reactor. In addition, sheet falls seem to be stable in turbulence and high-amplitude forced vibrations. Flow separation around protrusions through the flow sheet is, however, a problem.

Additional considerations in developing the lithium fall reactor concept are the response of the fall to the energy of the microexplosion product energy, and the interaction of the fall with the structure. The fall disassembles from the energy deposition within it, and reassembles as a slug prior to impact with the structure. For a 2700-MJ microexplosion, a loop stress of 100 MPa (1 kbar) results in a 1-m-thick structure located 4 m from the fall. Reconfiguring the fall into, say, multiple jets reduces the stresses in the structure and permits a decrease in structural thickness.

**Jet Stability—Lithium Fall Reactor.** A previous analysis of the hydrodynamic aspects of liquid lithium jet stability identifies a variety of physical factors that might affect jet breakup and attempts to approximate their relative influences.<sup>38</sup> That analysis also treats areas of uncertainty and presents plans for experimental verification and further theoretical analysis.

The current reactor design calls for a chamber pressure of  $10^{-1}$  Torr, temperature of 800 K, chamber radius of 5 m, jet/sheet half-thickness of 30 cm, and exit jet velocity of 10 m/s. The combination yields the Reynolds number of  $3 \times 10^6$  and the jet Weber number of  $4 \times 10^4$ . The physical factors that may cause breakup of turbulent jets are ambient conditions, fluid properties, nozzle configurations, and possible vibrations of the reactor after pellet microexplosion.

Applying the stability criterion for the ambient effects (Ref. 39) yields the result that the jet is insensitive to present ambient conditions, i.e., the Weber number based on the chamber density is  $10^{-3}$ , which is much lower than the critical value (5.3). However, it is not clear in the current design whether the low-density effects on jet breakup behavior are negligible. We are currently conducting experiments to reduce the degree of this uncertainty.

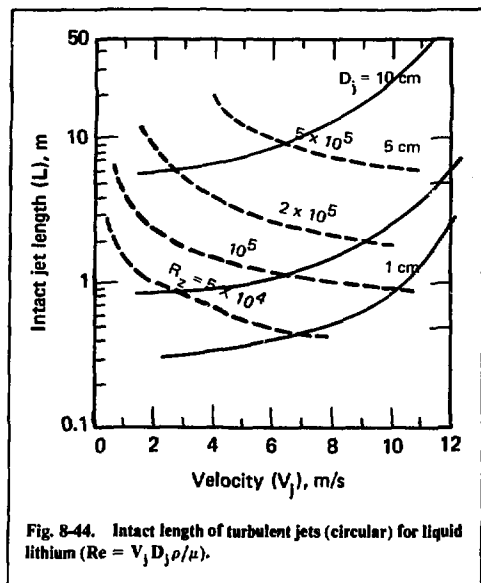
We considered fluid-property effects on jet disintegration in terms of the Ohnesorge number, which is a measure of the relative importance of viscosity and surface tension in controlling stability. This number is  $\sim 10^{-4}$ , signifying a dominant surface-tension effect. It is known that surface tension tends to inhibit the growth of irregular disturbances at the turbulent surface.<sup>40,41</sup> However, the paucity of test data at very high Reynolds numbers, say  $10^6$ , prompts us to perform experiments in this range.

Study of the effect of nozzle configuration on jet breakup shows liquid sheets to be more stable than circular jets from orifices of equal area.<sup>42</sup> In both situations, various profile patterns of the jet velocity depend upon nozzle-exit geometry. Moreover, the jet must undergo "relaxation" from a no-slip condition to a more uniform profile downstream. Additionally, viscosity would affect this transitional behavior at the interface. We are currently conducting an analysis to determine the extent of the influence of viscosity on jet-breakup behavior.

Tentative estimates of the turbulent jet-breakup length, based partly on empirical correlations, indicate a plateau value at high Reynolds numbers, a phenomenon similar to the laminar-jet cases.<sup>43,44</sup> These estimates of breakup length for various jet inlet velocities and diameter are plotted in Fig. 8-44. Intact jet lengths well in excess of the current 10 m for reasonable inlet velocities and diameters imply a stable turbulent jet flow for the laser fusion reactor. However, other physical factors may affect the jet breakup, as we note above. Until further investigation and experimentation have given us better data, we consider these estimates to be preliminary.

Experimental investigation of the hydrodynamic behavior of the lithium waterfall blanket between fusion microexplosions has focused on three key issues:

- Length for convergence or pinch-in of a hollow cylindrical waterfall, caused by surface tension forces.
- Hydrodynamic instabilities stemming from either natural or external disturbances.



● Behavior of the waterfall in passing around a simulated laser beam transport tube.

Experiments to simulate the lithium "waterfall" have used water in two flow geometries: hollow annulus and sheet jet. Both falls are relatively thick, with Weber numbers ( $We \equiv \rho V^2 h / \sigma$ ) much larger than unity to simulate the lithium waterfall. Experimental results indicate that surface tension forces should cause negligible pinch-in of either flow geometry in the laser fusion application.

Experiments have revealed no hydrodynamic instabilities induced by natural disturbances from flow turbulence or laboratory conditions. This is true for either the hollow cylindrical or sheet geometries for fall lengths much greater than the equivalent length of the lithium waterfall. We attribute this to the fact that natural disturbance levels are small for these high-momentum flows.

We mounted an electromechanical shaker on the sheet waterfall apparatus, to simulate the much larger amplitude disturbances possible in a reactor that are caused by ringing of the entire structure between microexplosions. Experiments to date indicate that these relatively thick sheet flows do not break up even when excited by very high amplitude forced vibrations. The sheet jet has grown to saturated amplitudes almost an order of magnitude larger than its thickness, and almost two orders of magnitude larger than the initial excitation amplitude, without any sign of breakup for fall dis-

tances over 100 times the initial sheet thickness. The initial experiments took place in air. We will conduct future experiments at reduced ambient pressures to determine the influence of ambient pressure on waterfall stability.

The third series of experiments simulated the penetration of a laser beam transport tube through a hollow cylindrical waterfall. The results show that these high momentum flows split and form a roughly inverted V-shaped opening below the penetration, as expected. We tried various wedge-shaped penetrations to simulate streamlining of the top of the laser light tubes. The split angle decreases as the wedge angle decreases, again roughly as predicted by potential flow theory. Multiple or staged lithium waterfalls will evidently be needed to fill openings created by the laser light tubes.

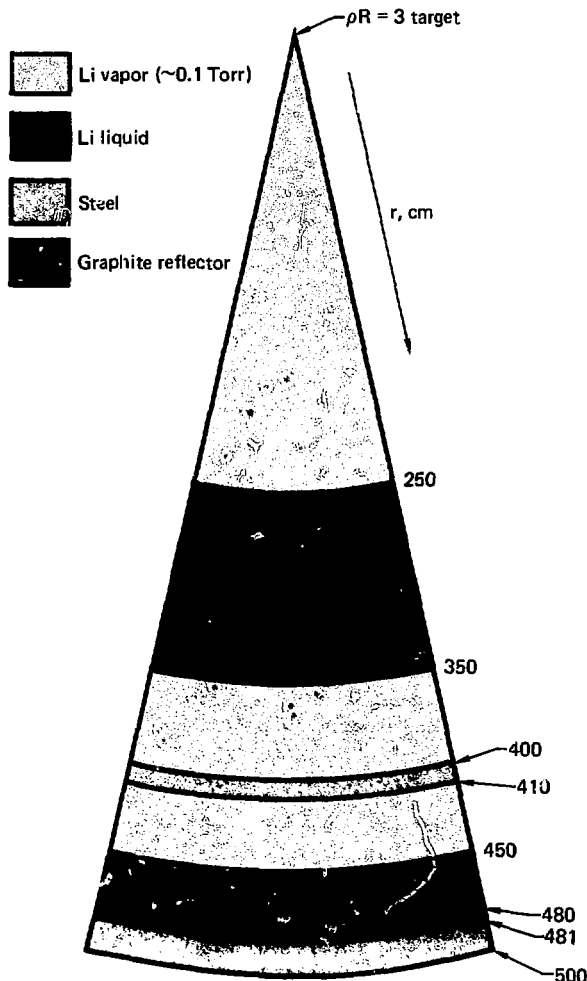
**Lithium Fall Response—ICF Microexplosion.** Survival of the first wall from repeated stresses caused by microexplosion products is one of the most difficult technical problems encountered in designing an ICF reactor. Limited range products, such as soft x rays and charged particle debris, are deposited in such short times that pressure pulses produced in the first wall cause it to have a much shorter lifetime than the remainder of the power plant.<sup>45,46</sup> In addition, damage from high-energy neutrons can shorten structure lifetime.<sup>47</sup>

A thick lithium fall circulated in front of the structure can mitigate microexplosion product damage. This fall would absorb limited range products and would moderate and attenuate neutrons. Thus, in principle, the structure could have a lifetime approaching that of the power plant.

In this article, we describe the output from a 2700-MJ microexplosion, the interaction of the microexplosion products with the fall, the response of the fall, and the resulting loading and stresses in the reactor structure. We based our calculations on a 1-m-thick fall in a 4-m-radius chamber with spherical geometry for initial fall inner radii ranging between 0.5 m and 2.5 m.

The DT fusion reactions in the compressed target ( $\rho R_{\text{fuel}} \approx 3$ ) release about 80% of their energy as 14.1-MeV neutrons and 20% as 3.5-MeV alpha particles. However, the compressed target attenuates and absorbs the alpha particles and some neutrons. The DT reactions produce 2700 MJ, of which 35 MJ are lost to endoergic neutron reactions in the target, 1800 MJ escape the target as neutrons, and the remaining 865 MJ escape as x rays and energetic target debris. The x rays include a hard component generated from the hot, burning pellet and cold components radiated from the cooling debris as it expands.

Fig. 8-45. Geometry used in early response calculations. Later calculations used the fall location as a parameter.



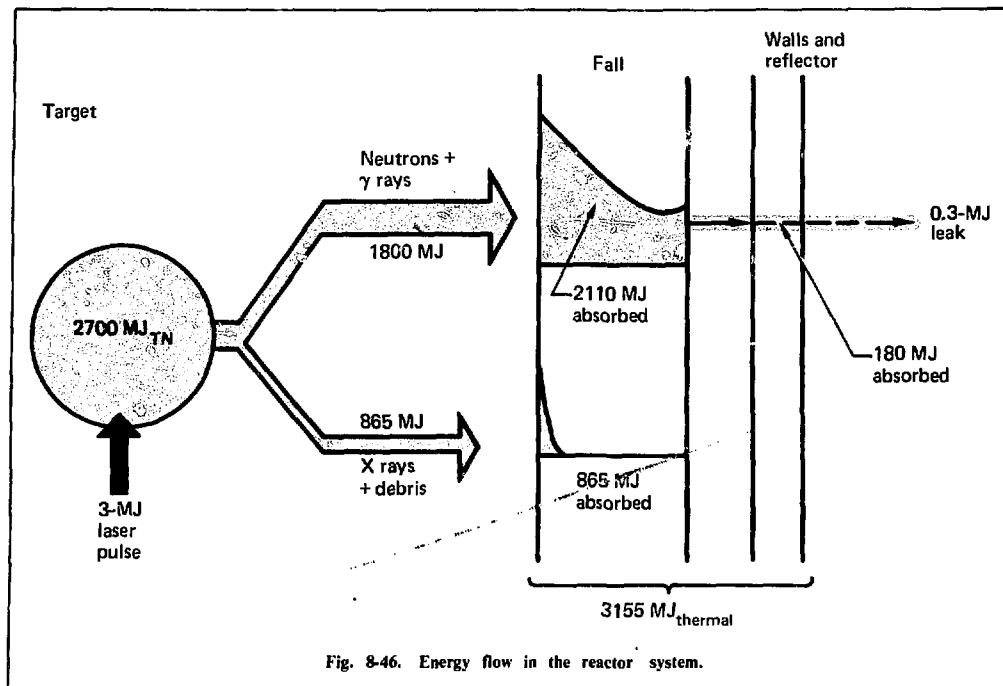


Fig. 8-46. Energy flow in the reactor system.

The liquid strikes the structural wall and causes both erosive and inertial loading. Our initial calculations used spherical geometry with a point source and cylindrical geometry with a line source. These geometries produce the worst loading on the structural wall. Later in this article, we suggest several alternate geometries that could mitigate the loads.

Figure 8-47 shows a "snapshot" of the reactor at 50 ns. The x-ray pulse arrives at 8 ns and the soft portion is absorbed near the inner edge of the fall. The resulting high energy density in the thin region vaporizes a portion of the liquid. This very hot gas moves inward toward the chamber center, while a pressure wave moves outward through the liquid at  $\sim 0.5$  cm/ $\mu$ s.

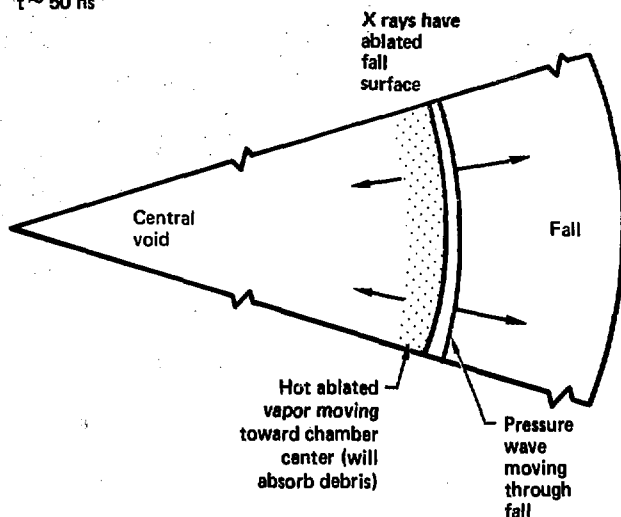
Figure 8-48 is a snapshot of the reactor at 50  $\mu$ s. Hot gas has filled the chamber center and is beginning to exert outward pressure on the fall. The pressure wave induced by the soft x rays is now about 25 cm into the fall. Hot gas has already absorbed the target debris. Neutron and hard x-ray energy deposited throughout the fall (primarily in the 55-ns-to-1- $\mu$ s time frame) has resulted in a sudden temperature rise in the fall. Thermal expansion:

waves are already moving on both surfaces of the fall.

Figure 8-49 shows the velocity distribution of the fall at 200  $\mu$ s, when both the x-ray-induced and neutron-induced pressure waves have traversed the fall thickness. The narrow x-ray pulse has spalled the outer few cm of the fall, and thermal expansion from neutron deposition has produced a velocity profile in the fall. Although thermal stress has been relieved, the fall will continue to expand because of its inertia. Finally, hot vapor in the reactor center is pushing outwards on the fall.

As time progresses, the leading edge of the fall (x-ray spall region) breaks into drops because of its velocity profile and the diverging geometry. Meanwhile, the majority of the fall is being compacted into an accelerating liquid slug. Figure 8-50 shows the two possible fall profiles at the time when the leading edge of the fall strikes the wall. If the spall velocity is high and the fall is initially much closer to the wall than the microexplosion, the fall will impact as shown in Fig. 8-50a. If the spall velocity is low and the fall is initially far from the wall, the slug will overtake the drops before they reach the wall (Fig. 8-50b).

Fig. 8-47. Lithium fall response-I. At  $t \sim 50$  ns, the x-ray energy has been absorbed, but the neutrons are still in flight.



#### Fall Response to Neutron Energy Deposition.

For energy deposited in a time so short that pressure cannot be relieved,<sup>51</sup> the pressure rise at any position  $x$  is

$$\Delta P(x) = \rho \Gamma [q'''(x)/\rho], \quad (10)$$

where  $\rho$  and  $\Gamma$  are the density and the Grüneisen constant of the material, respectively, and  $[q'''(x)/\rho]$  is the energy deposition per unit of mass at position  $x$ . A relief wave moves into the material and spalls the surface, if it exceeds the tensile strength.

For a liquid with essentially no tensile strength, the velocity of the spalled material at any position  $x$  is given by

$$V(x) = \lim_{\delta \rightarrow 0} \left( \frac{1}{2\rho c \delta} \int_{2x}^{2(x+\delta)} \Delta P(y) dy \right), \quad (11)$$

where  $c$  is the acoustic velocity of the material, and  $\Delta P(y)$  is the pressure rise at position  $y$ .

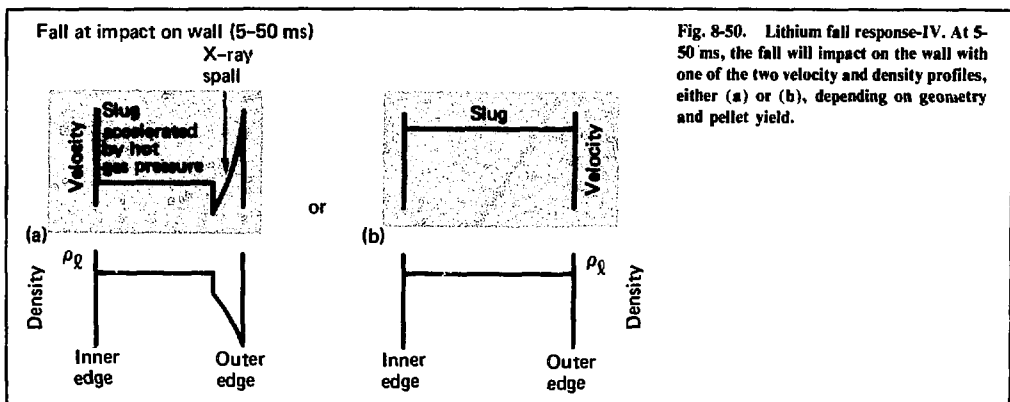
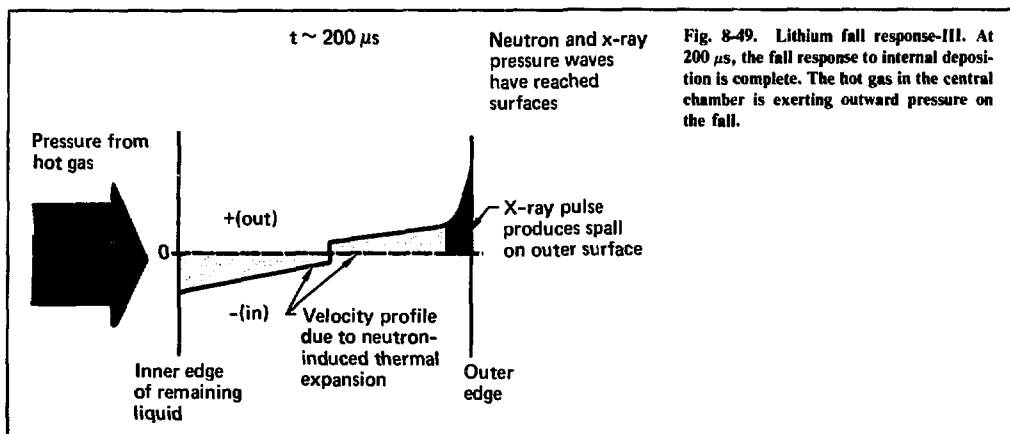
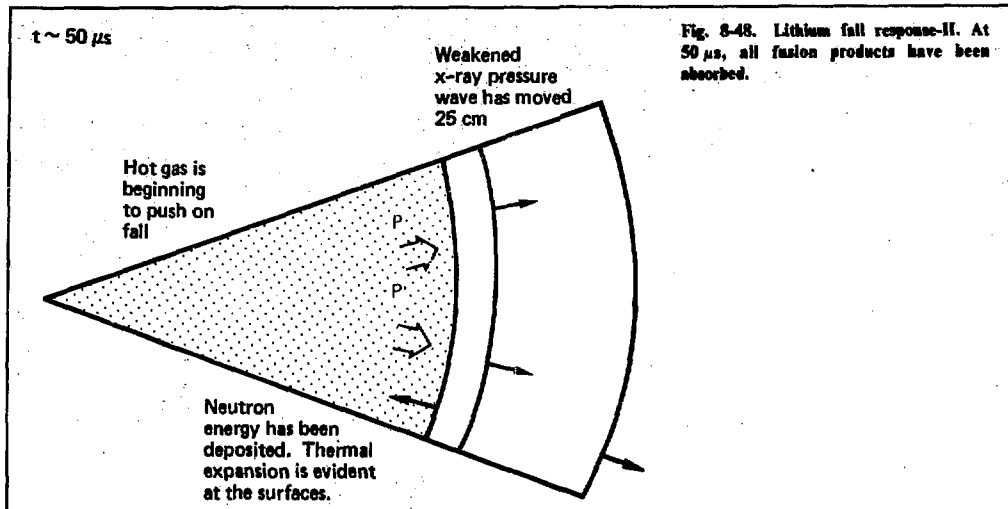
Neutron energy is deposited throughout the thickness of the fall, because the 14-MeV neutron mean free path in lithium is long. Pressure rise in the lithium is therefore small because the specific energy is small. The fall disassembles into the cavity from

the front surface with a relief wave moving into the fall at about the acoustic velocity of the material. The velocity of the spalled material into the chamber is essentially that given by Eq. (11). The momentum from the spalled lithium causes the back surface of the fall to move toward the structure with a velocity profile that is the mirror image of the lithium moving into the cavity. Lithium striking the structure is a mixture of vapor and droplets because of the velocity profile and the geometrical divergence.

We used CHART-D, a coupled radiation-hydrodynamic code, to evaluate the analytic results.<sup>52,53</sup> The analytic model describes the response of the fall to the neutrons very well.

**Fall Response to X Rays.** Hard x rays have little effect on the motion of the fall because their specific energy is low. The range of soft x rays in the lithium fall is short compared with the range of the neutrons. This range difference results in high specific energies and associated high pressures at the inner surface of the fall. The analytic model used for spall produced by neutron deposition does not apply here, because the material properties vary over the large pressure gradient in the thin deposition region. Large pressure gradients cause the pressure wave to form a shock wave that moves through the fall. However, the relief wave from the front surface travels faster than the shock wave, thus the pressure wave moving through the fall is highly attenuated by the time it reaches the back surface of the fall.





Because of large pressure gradients, we calculated the response of the fall to x rays, using codes such as CHART-D<sup>53</sup> or AFTON.<sup>54,55</sup> The fine zoning required to adequately represent the x-ray energy deposition in the fall requires excessively long computational times with CHART-D. However, we have solved the zoning problem, using the variable zoning option of AFTON. In this option, the problem initially has fine zones in the deposition region and coarse zones elsewhere. As time progresses, AFTON resizes the zones so that zoning is always fine in the region of the moving pressure pulse.

Because the ultimate target design is still unknown, we must consider a wide range of x-ray yield fractions and spectra. We are unable to consider actual target parameters here. However, for a  $\rho R = 3$  target, about 32% of the output is in the form of x rays and debris. If we postulate the worst case, when all this energy is soft x rays, the spall velocity may be as much as 100 times the neutron spall velocity. On the other hand, if all the energy were hard x rays, the spall velocity might be on the same order as the neutron spall velocity. Of course, both views are unrealistic, but they do bound the parameter space. Because the equation of state used for these calculations needs improvement, our results have large error bars.

At first glance, the above results are discouraging; however, because of the diverging geometry and the velocity profile in the spall, the leading edge of the fall strikes the wall as a series of drops. Although the pressure under each drop is very large, the pressure duration is small, resulting in low hoop stress. Further, the relatively long time between pressure pulses permits relief of the hoop stress between impacts. Therefore, the inertial loading of the wall by the x-ray spall is not significant. Because of the insensitivity of the hoop stress to the x-ray spall velocity, we use a value of 10 times the neutron spall velocity in the remainder of this article. However, the erosive loading of the wall is very dependent on the x-ray spall velocity. (The erosive loading of the wall will be addressed in 1978.)

**Vaporization Effects.** Lithium ablated from the fall by x-ray deposition converges toward the reactor center and absorbs target debris energy. Within tens of microseconds, this hot lithium vapor fills the central chamber and exerts pressure on its container, the fall. Detailed calculations of the pressure require an accurate equation of state; however, we have made crude estimates, using two simple models:

- X-ray energy is input as a surface heat flux. An energy balance between heating, thermal con-

duction in the fall, and evaporation, is performed. (Recondensation of vapor is not included.)

- X-ray energy is deposited instantaneously. Lithium that receives more than the latent heat of vaporization (21 kJ/g) vaporizes. (Recondensation or heat conduction before vaporization is not included.) Results from the two models are in remarkable agreement.

We determine the fall response to cavity pressure by solving the equation of motion of a spherical shell with internal pressure and no stress. We treat the cavity gas as an isentropic expansion of a monatomic gas. The velocity of the fall at radius  $r$  is

$$v(r) = \sqrt{\frac{PAr_0}{m} \left[ 1 - \left( \frac{r}{r_0} \right)^{-2} \right]},$$

where  $P$ ,  $A$ ,  $r_0$ , and  $m$  are the initial cavity pressure, inner surface area, radius, and mass of the fall, respectively. The time of arrival of the fall at a radius  $r$  is

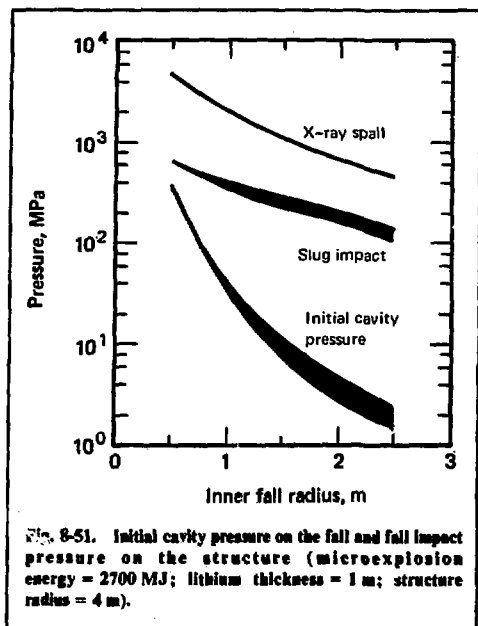
$$t(r) = \sqrt{\frac{mr_0}{PA} \left[ \left( \frac{r}{r_0} \right)^2 - 1 \right]}.$$

**Wall Response to Liquid Impact.** The pressure of liquid colliding with the wall is  $P = \rho c v$ , where  $\rho$ ,  $c$ , and  $v$  are the density, acoustic velocity, and velocity of the condensed lithium, respectively. The pressure pulse width is  $\Delta\tau = 2w/c$ , where  $w$  is the thickness of the condensed lithium region impacting on the wall. The hoop stress in a thin wall, caused by the impact of condensed-phase lithium, is at the end of the pulse approximately

$$\sigma = \rho c v \left( \frac{R}{\delta} \right) \left[ 1 - \cos \left[ \sqrt{8(1 + \nu)} \left( \frac{w}{R} \right) \left( \frac{c_w}{c} \right) \right] \right],$$

where  $c_w$ ,  $R$ ,  $\delta$ , and  $\nu$  are the acoustic velocity, radius, thickness, and Poisson's ratio of the wall, respectively. For small  $(w/R)$ , the same equation becomes

$$\sigma \approx \rho c_w v \left( \frac{c_w}{c} \right) \left( \frac{w}{R} \right) \left( \frac{w}{R} \right) 4(1 + \nu).$$



The peak stress in a thin wall occurs after the condensed phase lithium has disassembled from the wall, and the wall has reached its maximum expansion. This stress is

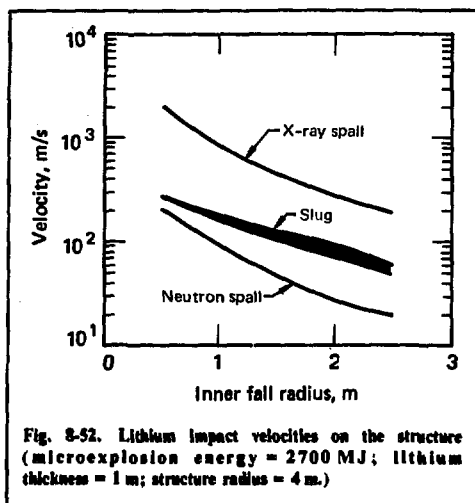
$$\sigma_{\max} = \rho c_v \left( \frac{R}{\delta} \right) \sqrt{2 [1 - \cos] \sqrt{8(1 + \nu)} \left( \frac{w}{R} \right) \left( \frac{c_w}{c} \right)}$$

For small ( $w/R$ ), the peak stress is

$$\sigma_{\max} \approx c_w v \left( \frac{w}{\delta} \right) \sqrt{8(1 + \nu)}.$$

The stress at the end of the pressure pulse decreases as the structure radius or thickness increases. The maximum stress also decreases with increasing structure radius or thickness, but here the thickness is the dominant variable.

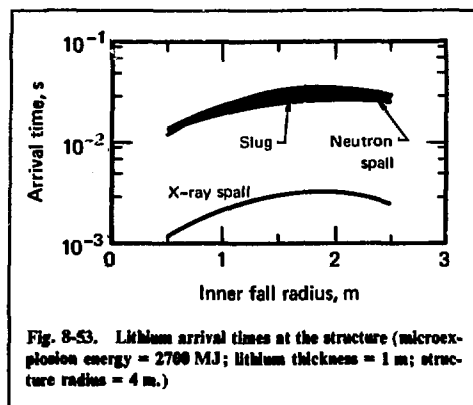
For *droplets* moving at a reasonable velocity, the hoop stress, even in a relatively thin wall, is small. However, localized pressures under the drops are still proportional to ( $\rho c v$ ). These pressures, while not producing a high hoop stress in the structure, cause localized spall on the surface of an unprotected structure, gradually eroding it.



**Quantitative Results.** We used the methodology described above to analyze the response of the fall and to estimate the stress in the wall from the fall impact. The 2700-MJ microexplosion was contained in a 4-m-radius chamber protected by a 1-m-thick fall placed in various initial positions. Figure 8-51 shows the cavity pressure from the two thermodynamic models used for estimating the vaporization from the inner fall surface. The velocities of the slug, neutron spall, and x-ray spall appear in Fig. 8-52. We assumed the x-ray spall velocity was 10 times the neutron spall velocity. Arrival times at the structure for the x-ray spall, the neutron spall, and the liquid slug are shown in Fig. 8-53. Note that the slug has a higher terminal velocity than the neutron spall. Nevertheless, the slug arrives at the structural wall at the same time as the neutron spall and at a later time than the x-ray spall. Pressure levels on the wall resulting from slug impact and x-ray spall impact are graphed in Fig. 8-51.

Figure 8-54 graphs the product of the wall thickness and hoop stresses in the wall from slug impact for both 4-m and 5-m chamber radii. These stresses increase with the initial inner fall radius in spite of the decreasing slug velocity and pressure. The reason for this apparent anomaly is that, for a given fall thickness, slug thickness at the wall is much smaller for a small, initial inner fall radius. Therefore, because the pressure duration is less, stress levels are lower.

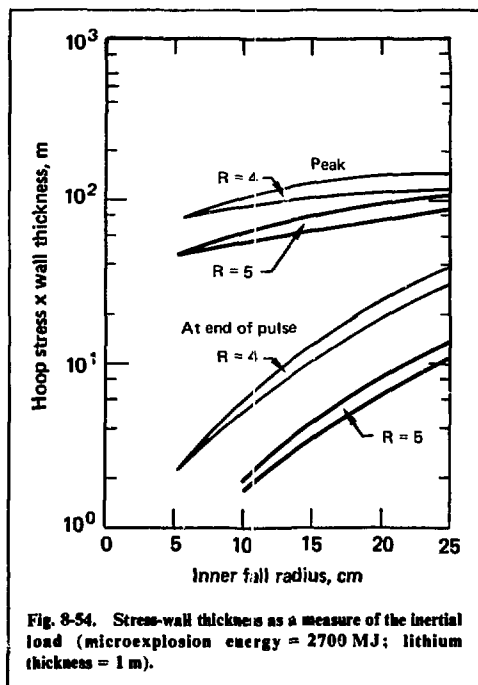
**Discussion of Results.** The results for the 2700-MJ microexplosion are not promising for a 1.0-m-thick fall in this geometry. Allowable wall hoop



stresses are about 100 MPa (1 kbar). To survive for 30 years at reasonable temperatures of about 700 K, the wall should have a thickness of about 1.0 m (which is unrealistic and violates the thin-shell approximation used to calculate the stresses). The effects of lithium corrosion and neutron damage on the wall strength must not be excessive. It appears that a fall near the reactor center results in smaller wall loads in this geometry; this trend is also desirable from the standpoint of pumping power and tritium inventory.

Because the loads in this "worst case" geometry are within a factor of 10 of the 30-year limit for a 0.1-m-thick wall at a reasonable radius, it is likely that better fall configurations will result in acceptable loads. Multiple cylindrical falls or a series of small circular jets would reduce the wall loading (due to thermal dissipation and motion in the  $z$  and  $\theta$  directions, i.e., increased entropy), as well as distributing it in time. The series of small circular jets also vents much of the pressure in the reactor center, which greatly reduces "slug-type" loading on the wall. Alternatively, a thin inner fall near the microexplosion could absorb the soft x rays and debris, while a thick outer fall near the wall absorbs the harder x ray and neutrons. We could initially configure the inner fall to optimize its venting via the Rayleigh-Taylor instability.

We have not analyzed the effect of the x-ray spall erosive pressures on the wall lifetime. The hoop stress from this pressure is very low, but the rate of removal of structural material is currently unknown. In addition, this erosive pressure from x-ray spall is only an estimate based on 10 times the pressure of the neutron spall. For better quantitative results, additional work must be done to determine the equation of state of expanded lithium and the opacities of lithium for low-energy photons.



We could cover the microexplosion side of the structure with a thin layer of liquid lithium to reduce the effect of droplet erosion on the structure. Unfortunately, a sufficient amount of hard x-ray energy might pass through the lithium fall and be deposited in the structure to produce a small pressure rise within the structure. The particle velocity of the structural material could couple to the thin lithium layer, causing the lithium to spall off the surface of the structure before the droplets arrive. However, a screen placed over the inner surface of the wall could rely on surface tension to ensure the wall and screen are always covered with liquid lithium.

## References

38. J. A. Maniscalco and W. R. Meier, *Conceptual Design of a Laser Fusion Power Plant*, Lawrence Livermore Laboratory, Livermore, Calif., UCRL-79652 (1977).
39. R. W. Fenn and S. Middleman, "Newtonian Jet Stability: the Role of Air Resistance," *A.I.C.H.E. Journal* 15, 379 (1969).
40. J. T. Davies, *Turbulence Phenomena* (New York, Academic Press, 1972).

41. A. A. Townsend, "The Mechanism of Entrainment in Free Turbulent Flows," *J. Fl. Mech.* **26**, 689 (1966).
42. R. P. Fraser and P. Eisenklam, "Drop Formation From Rapidly Moving Liquid Sheets," *A.I.C.H.E. Journal* **8**, 672 (1962).
43. R. E. Phennay, "The Breakup of a Turbulent Liquid Jet in a Gaseous Atmosphere," *J. Fl. Mech.* **60**, 689 (1973).
44. T. Kusui, "Liquid Jet Flow into Still Gas," *Bull. JSME* **11**, 1084 (1968).
45. J. Hovingh, "First Wall Response to Energy Deposition in Conceptual Laser Fusion Reactors," in *Surface Effects In Controlled Fusion Devices*, Bauer, Finfgeld, and Kaminsky, Eds. (Amsterdam, North-Holland Publishing Co., 1976), p. 158.
46. J. Hovingh, "First Wall Studies of a Laser-Fusion Hybrid Reactor Design," *Proc. 2nd Topical Mtg. on Tech. of Controlled Nucl. Fusion*, G. Kulcinski, Ed., Vol. II, 765, USERDA Report CONF-760935-P2 (1976).
47. G. L. Kulcinski, "Radiation Damage: The Second Most Serious Obstacle to Commercialization of Fusion Power," in *Radiation Effects and Tritium Technology for Fusion Reactors*, Watson and Wiffen, Eds., Vol. I, 17, USERDA Report CONF-750989 (1976).
48. E. Plechaty and J. Kimlinger, TARTNP: A Coupled Neutron-Photon Monte Carlo Transport Code, Lawrence Livermore Laboratory, Livermore, Calif., UCRL-50400, Vol. 14 (1976).
49. R. K. Cole, Jr., BUCKLE: A Program for Rapid Calculations of X-ray Deposition, Sandia Laboratories, Albuquerque, N. Mex., Report SC-RR-69-855 (1970).
50. J. Hovingh and S. L. Thomson, "Energy Deposition from Microexplosion Particle Debris in the First Wall of an Inertially-Confined Fusion Reactor," *Proc. 7th Symp. on Eng. Problems of Fusion Research*, Vol. I, 162, Knoxville, Tenn. (1977).
51. J. Hovingh, "Design Considerations in Inertially-Confined Fusion Reactors," in *Proc. of the Institute, Curriculum Development in Fusion-First Wall Design Consideration*, G. H. Miley and W. H. Sawyer, Eds., Argonne National Laboratory, Argonne, Ill. (1976).
52. S. L. Thompson, Improvements in the CHART D Energy Flow Hydrodynamic Code V: 1972/73 Modifications, Sandia Laboratories Report SLA-73-0477 (1973).
53. S. L. Thompson and H. S. Lauson, Improvements in the CHART D Radiation Hydrodynamic Code II: A Revised Program, Sandia Laboratories, Albuquerque, N. Mex., Report SC-RR-71-0713 (1972).
54. J. Trulio and K. Trigger, Numerical Solution of the One-Dimensional Hydrodynamic Equations in an Arbitrary Time-Dependent Coordinate System, Lawrence Livermore Laboratory, Livermore, Calif., UCRL-6522 (1961).
55. L. A. Glenn, "AFTON Revisited—An Improved Algorithm for Numerical Solution of Initial Value Problems in Continuum Mechanics" (to be published as a USDOE report in the UCRL series).

## Authors

J. Hovingh  
S. W. Kang  
J. A. Blink  
M. A. Hoffman

## 8.4.3 Ion-Beam Fusion Reactor Studies

This article expands a first-wall design study for a 4000-MW<sub>t</sub> fusion reactor rated at  $4 \times 10^9$  J per microexplosion that was performed for the ERDA Summer Study of Heavy Ions for Inertial Fusion.<sup>56</sup> Here, we broaden the parameter space considered in the earlier work and present results of a restudy that is based on more complete graphite properties.

To investigate possible reactor first-wall designs and a gross electrical output of 1320 MW<sub>e</sub>, we assumed a reactor power of 4000 MW<sub>t</sub>. We varied the thermonuclear yield between 400 and 4000 MJ per microexplosion, while fixing total yield in x-ray and debris energy at 32% of the thermonuclear yield (2% in x-ray energy and 30% in debris energy).

We assumed two first-wall lifetime criteria. The first is a surface-recession-rate criterion based on losing 10 mm of first-wall material per year. The second is a neutron-damage criterion based on a neutron fluence of about  $10^{26}$  n/m<sup>2</sup>, which is a 1-year exposure to a first-wall neutron flux of 5 MW/m<sup>2</sup>.

Materials considered for the first wall included niobium, stainless steel, and two types of graphite. We assumed the first type of graphite to be isotropic and the second type to be highly anisotropic, with the direction of maximum thermal conductivity in the radial direction of the reactor.

For a given blanket design (including structure), several first-wall designs are apparent. Basically, they consist of using a liner, mounted independently of the blanket, that can be replaced without removing the entire blanket. Because the impulse load from the pellet can be accommodated for millions of shots (without giving consideration to neutron damage) by a 20-to-30-mm-thick cylindrical shell of either niobium or stainless steel at 800 K, the following designs are possible:

- Stainless steel or niobium liner, 40 mm thick.
- Niobium inner liner, 20 mm thick, in a 30-mm-thick stainless steel shell.
- Graphite inner liner, 20 mm thick, in a 30-mm-thick stainless steel shell

Gas or liquid metal can cool the backside of these liners. Note that the inner liner is not a load-carrying member. Its only uses are to reduce the vacuum pumping loads, increase lifetime, and decrease the cost of the liner. It reduces costs by using cheaper stainless steel as structural material to support more expensive niobium, or to support graphite, a material that is weak in tension.

Table 8-7 gives fabricated costs of first-wall materials. These costs are only best guesses and should not be regarded as especially accurate. For comparison, Fleischer et al.<sup>57</sup> give a fabricated cost of 316 stainless steel as \$13.20/kg and Nb-1 Zr as \$176/kg. Hopkins et al. give a cost of H-451 graphite of \$5/kg before machining.<sup>58</sup>

Figures 8-55 and -56 graph the effects of microexplosion energy on costs for a first-wall lifetime of one year with various materials, along

Table 8-7. Fabricated costs per kilogram of various first-wall materials.

Stainless steel	\$30
Niobium	\$120
Graphite (isotropic)	\$22
Pyrolytic graphite	\$3000

with neutron flux at the first wall. Figure 8-55 bases first-wall costs on the factors given in Table 8-8. Figure 8-56 shows the first-wall cost, per-unit-of-time integrated gross electric power output of a 4000-MW<sub>e</sub> reactor operating with a thermal conversion efficiency of 0.33.

The graphite and stainless steel first walls are the least expensive, while pyrolytic graphite and

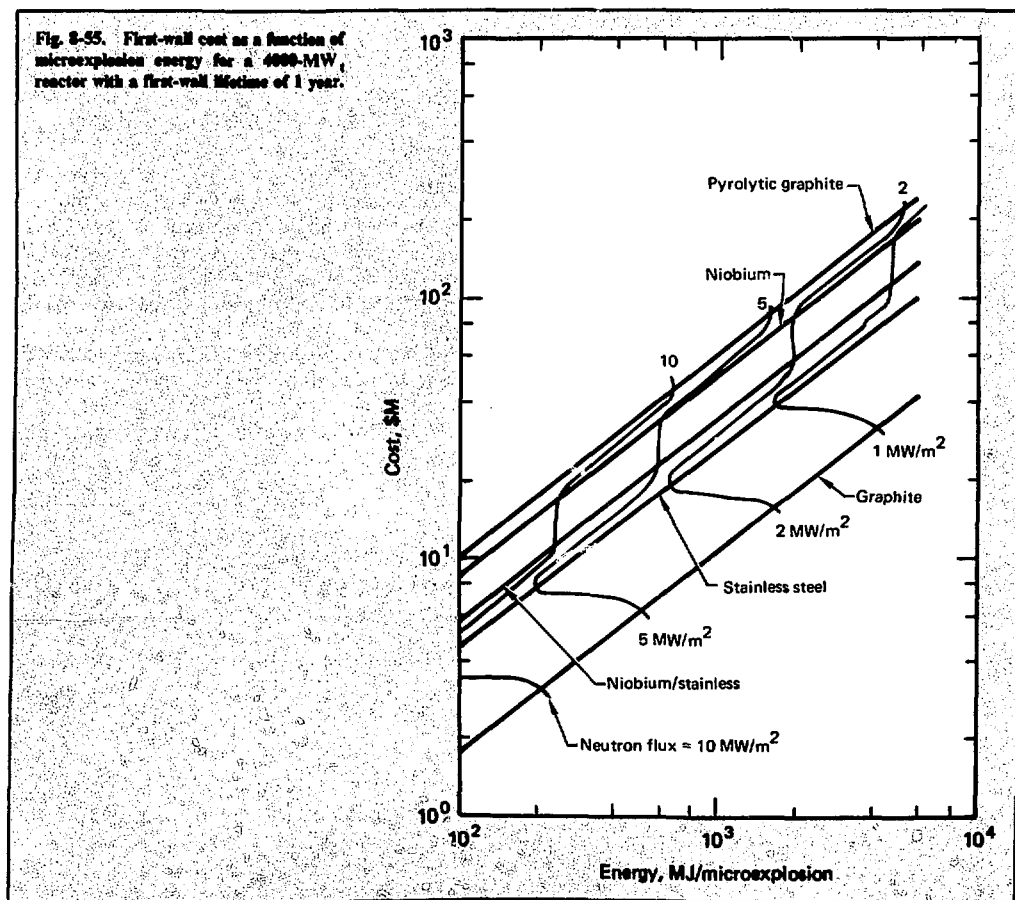


Table 8-8. Cost of first walls in a 4000-MW<sub>e</sub> reactor based on a first-wall neutron flux of 5 MW/m<sup>2</sup> and a lifetime of 1 year. (First-wall radius is 6.6 m.)

Cost units	\$M	Mills/kWh <sub>e</sub>
Material combination		
Stainless	7.6	0.66
Niobium	34	2.9
Niobium/stainless	23	2.0
Graphite/stainless	6.3	0.55
Pyrolytic graphite/stainless	87	7.5

solid niobium first walls are the most expensive. For a given first-wall neutron flux, the solid niobium wall costs about five times more than composite niobium over stainless steel. As expected, the first-wall cost for a 1-year lifetime decreases as the neutron flux increases and as the microexplosion energy decreases.

Figures 8-57 and -58 show first-wall costs and cost-per-unit-of-time integrated gross electrical power for several materials as a function of microexplosion energy for a 1-year lifetime, with a flux of 5 MW/m<sup>2</sup>. Because the damage threshold of stainless steel from high-energy neutrons is a fluence of about 10<sup>26</sup> n/m<sup>2</sup>, the maximum first-wall neutron flux of a 1-year lifetime due to neutron damage is 5 MW/m<sup>2</sup>. The minimum first-wall cost occurs when the lifetime limit associated with neutron damage is the same as that for surface recession.

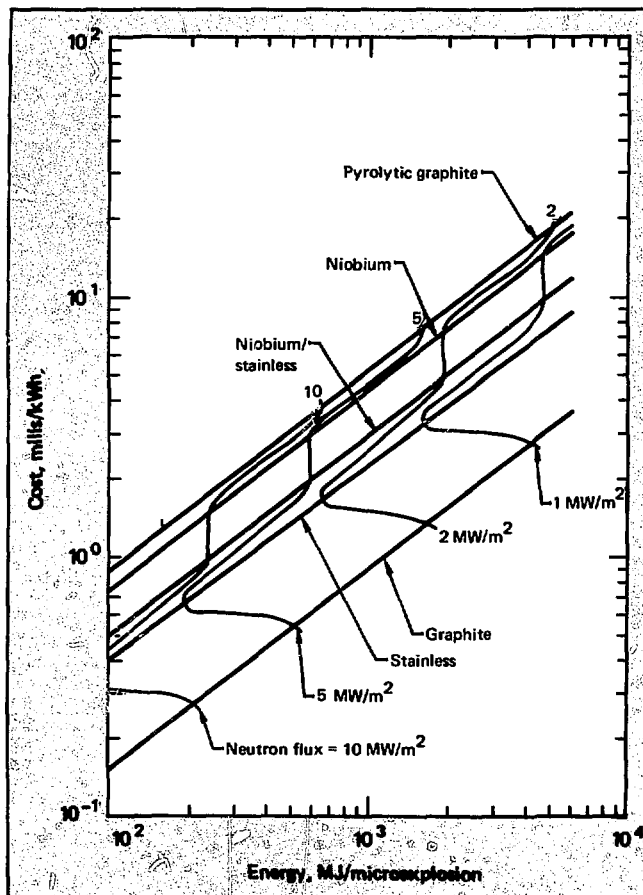
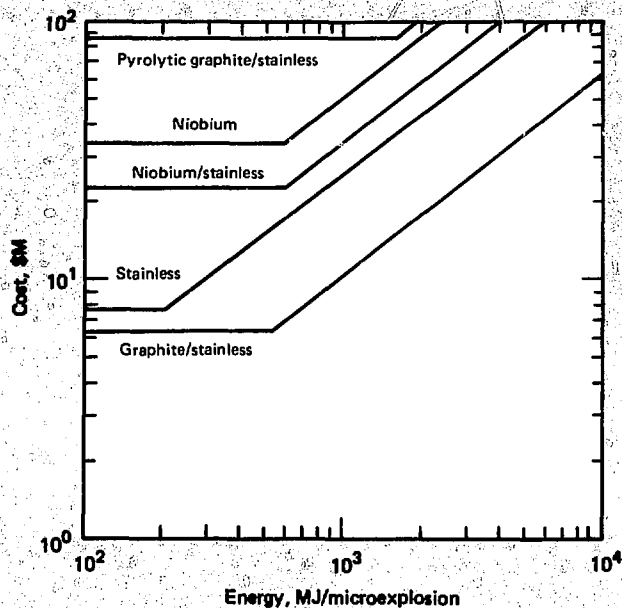


Fig. 8-56. First-wall cost in mills/kWh<sub>e</sub> as a function of microexplosion energy for a 4000-MW<sub>e</sub> reactor with a first-wall lifetime of 1 year.

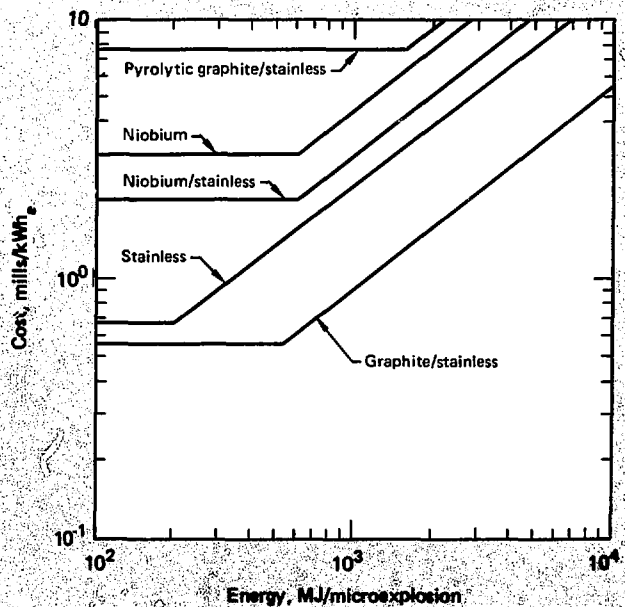
Fig. 8-57. First-wall cost as a function of microexplosion energy for a 4000-MW reactor with a first-wall maximum neutron flux of  $5 \text{ MW/m}^2$  and a lifetime of 1 year.



Note that operating at a fixed neutron flux, but with smaller microexplosions, does not affect first-wall cost. Operating at higher microexplosion energies

results in increased first-wall costs for a given wall lifetime. Table 8-8 gives costs of various first-wall material combinations for a 1-year lifetime and

Fig. 8-58. First-wall cost in mills/kWh, as a function of microexplosion energy for a 4000-MW reactor with a first-wall maximum neutron flux of  $5 \text{ MW/m}^2$  and a lifetime of 1 year.





first-wall flux of  $5 \text{ MW/m}^2$  for a 4000-MW<sub>t</sub> reactor.

Table 8-9 presents maximum pellet performance, which is defined as the pellet yield for which first-wall lifetime constrained by surface recession matches that constrained by neutron damage. The table lists various first-wall materials in a 4000-MW<sub>t</sub> reactor based on a first-wall neutron flux of  $5 \text{ MW/m}^2$  and a lifetime of 1 year. Table 8-9 also gives earlier estimates of maximum pellet performance,<sup>59</sup> with a comparison of recession rates at a first-wall neutron flux of  $5 \text{ MW/m}^2$  for the current and earlier work. If the recession rate exceeds the estimate based on vapor-pressure considerations due to, say, sputtering, then maximum pellet performance can be reduced. For example, let us assume the surface recession rate from sputtering is 45 times that caused by vaporization, and that the first wall is graphite. A reduction of maximum pellet yield from 530 to 450 MJ still allows a lifetime of 1 year in a 4000-MW<sub>t</sub> reactor with a neutron flux of  $5 \text{ MW/m}^2$  at the first wall.

If the first wall is neutron-flux-limited for a given lifetime, pyrolytic graphite can cost no more than isotropic graphite. For a given first-wall neutron flux, the allowable microexplosion energy for pyrolytic graphite is about three times the energy for isotropic graphite. Pyrolytic graphite has poor dimensional stability under irradiation.

We consider solid niobium an uneconomical choice for the first wall: it costs about 50% more than the composite niobium over stainless steel. This composite makes the desirable qualities of niobium as a first-wall material available at lower cost than solid niobium.

For a reactor with given power and given maximum pellet yield, smaller microexplosions than the maximum result in a constant first-wall flux. This is because the given lifetime of the first wall is determined by neutron damage. At a given fuel cycle cost, the use of smaller-than-maximum microexplosions necessitates a reduction in the allowable cost of each pellet because of the higher pulse repetition frequency. This reduction in cost per pellet may not be possible. Microexplosions larger than the maximum result in a decrease in first-wall flux, because the lifetime of the first wall is now limited by the surface-recession rate. This also results in higher first-wall and blanket costs for a given first-wall lifetime; for a given system cost in mills/kWh<sub>e</sub>, it requires lower fuel cycle costs (also in mills/kWh<sub>e</sub>). For these reasons, we conclude that the design condition for minimum first-wall costs may not result in minimum power plant costs.

The least expensive first wall for a 4000-MW<sub>t</sub> ion-beam-initiated reactor requiring a low preshot

Table 8-9. Maximum pellet performance for first-wall materials in a 4000-MW<sub>t</sub> reactor based on a first-wall neutron flux of  $5 \text{ MW/m}^2$  and a lifetime of 1 year. (First-wall radius is 6.6 m.)

Material	Energy, MJ		Recession rate ratio <sup>a</sup>
	Maximum	Other <sup>b</sup>	
Stainless	210	170	16
Niobium	600	510	29
Graphite	530	450	46
Pyrolytic graphite	1600	1300	130

<sup>a</sup>Early work by author.

<sup>b</sup>Current work to early work at flux of  $5 \text{ MW/m}^2$ .

cavity pressure calls for a design involving either isotropic graphite over stainless steel or solid stainless steel. These walls can be built for less than \$10 million or about 0.6 mills/kWh<sub>e</sub> (gross electric) with a neutron flux of  $5 \text{ MW/m}^2$ . Microexplosion energies as large as 200 MJ can be used in the solid stainless steel. Lower fluxes increase the allowable microexplosion energy, with a concurrent increase in first-wall cost.

Because graphite is such a promising material for a first-wall liner, we have contracted with General Atomic Corporation to further investigate the properties of graphite and silicon carbide and to study methods of attaching these materials to stainless backing plate.<sup>58</sup>

Table 8-10 gives a self-consistent set of materials property data for nuclear-grade H-451 graphite. These data—along with other physical properties, including surface evaporation rates—result in a 4000-MW<sub>t</sub> reactor that uses 4000-MJ microexplosions with 32% of its energy in x rays and debris. The reactor would be limited to a minimum radius of 17 m, based on peak compressive-stress limits. The peak compressive-stress limit is more restrictive than the surface-recession-rate limit for a convectively cooled liner (minimum radius of 15 m) and less restrictive than for a radiatively cooled liner (20 m). A silicon carbide liner is limited by surface recession rate with a minimum radius of greater than 20 m for a convectively cooled liner.

Because of the decreased first-wall radius made possible by convective cooling, we considered a number of methods for bonding the ceramic materials to stainless steel coolant tubes. These include concepts in which plates are mechanically attached over small areas with soft material between

Table 8-10. H-451 graphite: thermal and mechanical properties.

Property	Direction in log	Unirradiated value at:					Value after irradiation to $10^{26}$ n/m <sup>2</sup> at:				
		300 K	800 K	1300 K	1800 K	2300 K	300 K	800 K	1300 K	1800 K	2300 K
Thermal conductivity (W/m-K)	Axial	141	82	58	48	42	—	25	34	41	42
	Radial	134	79	55	46	40	—	23	31	39	40
Thermal expansivity ( $10^{-6}$ K <sup>-1</sup> )	Axial	4.0	4.0	4.6	5.0	5.4	—	4.6	2.6	2.5	—
	Radial	4.5	4.5	5.1	5.5	5.9	—	5.2	2.9	2.8	—
Specific heat, $C_p$ (J/kg-K)	—	710	1620	1890	1990	2050	710	1620	1890	1990	2050
Tensile strength <sup>a</sup> (MPa)	Axial	13.7	15.4	17.1	18.9	20.6	—	23.1	28.4	26.7	—
	Radial	10.8	12.2	13.5	14.9	16.2	—	18.3	22.4	21.1	—
Flexural strength <sup>a</sup> (MPa)	Axial	20.3	22.9	25.4	28.0	30.5	—	34.4	42.1	39.6	—
	Radial	17.4	19.6	21.8	24.0	26.1	—	29.4	36.2	33.9	—
Compressive strength <sup>a</sup> (MPa)	Axial	51.9	58.4	64.9	71.4	77.9	—	87.6	107.6	101.0	—
	Radial	49.6	55.8	62.0	68.4	74.9	—	83.7	102.8	96.7	—
Young's modulus <sup>a</sup> (GPa)	Axial	7.9	8.5	9.1	9.7	10.3	—	19.1	25.0	19.4	—
	Radial	6.9	7.4	8.0	8.5	9.0	—	16.7	22.0	17.0	—
Poisson's ratio <sup>a</sup>	All	0.11	0.11	0.11	0.11	0.11	—	0.11	0.11	0.11	—
Tensile fatigue limit <sup>a,b</sup> (99% survival to $10^5$ cycles, MPa)	Axial	6.0	6.8	7.5	8.3	9.0	—	11.8	14.5	13.6	—
	Radial	5.4	6.1	6.8	7.4	8.1	—	9.9	12.1	11.4	—

<sup>a</sup>Data at high temperatures extrapolated.<sup>b</sup>Tension-compression stress cycle.

the plates and cooled metal to enhance heat conduction. Other methods call for rigidly attaching plates over most of their areas. Any of these methods would require considerable development; cost effectiveness studies to evaluate their ultimate potential are needed.

## References

56. J. Hovingh, "Ion-Beam Reactor First Wall Design," Appendix 1.3, *ERDA Summer Study of Heavy Ions for Inertial Fusion*, USERDA Report LBL-5543 (December, 1976).
57. L. R. Fleischer, R. R. Hoiman, and H. B. Kellogg, "Trade-Offs in Laser-Fusion Power Systems: Module Size," *Trans. ANS 1975 Winter Mtg.*, San Francisco (November, 1975).
58. G. R. Hopkins, R. J. Price, R. E. Bulloch, J. A. Dalessandro, and N. B. Elsner, *Carbon and Silicon Carbide as First Wall Material in Inertial Confinement Fusion Reactors*, US DOE Report UCRL-13854 (GA-A14894), (March, 1978).
59. J. Hovingh, "First Wall Costs of an Ion-Beam Fusion Reactor", *Trans. ANS 1977 Summer Meeting*, New York (June 1977).

## Author

J. Hovingh

## 8.5 Optical Design Considerations for Laser Fusion Power Plants

In our design studies of laser fusion power plants, we have begun to examine the long-term survivability, performance, and maintainability required of the optical elements that must withstand  $10^7$ - $10^8$  shots per year in a hostile nuclear environment. We discuss the realistically available options for protecting the final optics in a future power plant, including any dependency on specific features of the target and reactor concept chosen.

### 8.5.1 Final Focusing System

Our conceptual laser system is housed separately from the reactor containment building both to minimize building costs and construction time and to increase laser access and maintainability. The laser light travels to the reactor through underground evacuated pipes that link the two buildings. The beam enters the containment vessel through a window and is focused through a small slot in a fast-acting valve. Considerations of gas breakdown compel us to use two tactics to avoid breakdown in the small opening of the safety valve: a line focus to avoid the extreme power densities of a focal point and pump down to reduce the density as necessary. The valve provides secondary containment protection in case of window failure. A fixed,

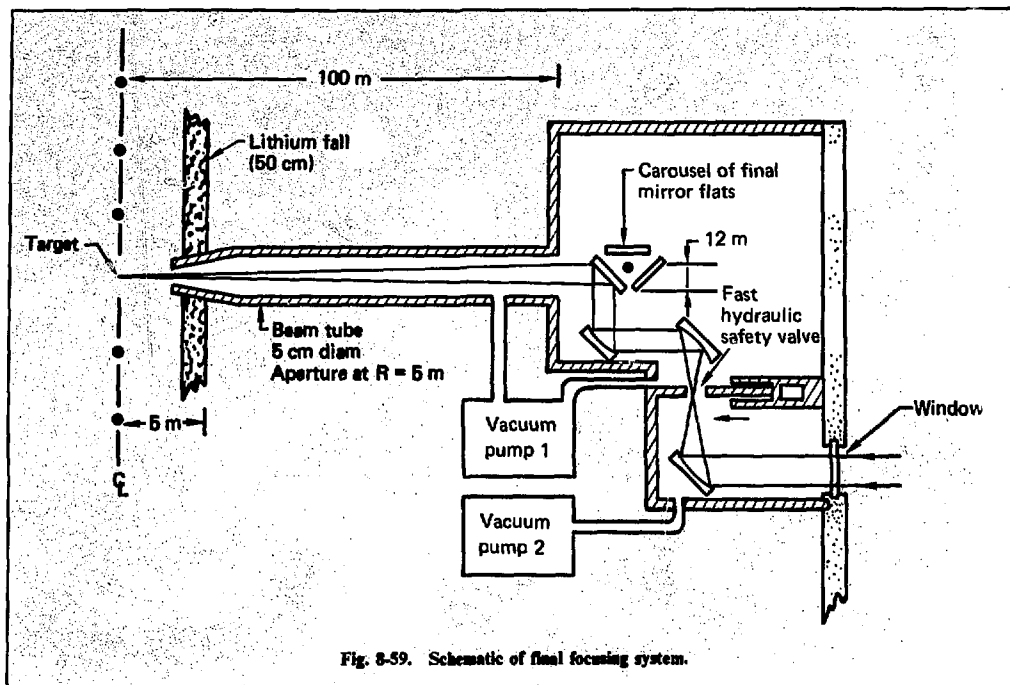


Fig. 8-59. Schematic of final focusing system.

off-axis, parabolic focusing mirror directs the beam onto a mirror flat that is exposed to the neutron flux. The mirror flat may be mounted on a carousel of several mirrors, if more than one are needed. Because of their location—at the turning point of the beam tubes in a direct pathway to the thermonuclear microexplosion (see Fig. 8-59)—the final focusing mirrors are exposed to x rays, debris, and neutrons from the fusion reaction. Figure 8-59 also shows separate vacuum pumps on each side of the fast-acting containment valve.

We must postulate the operating conditions of

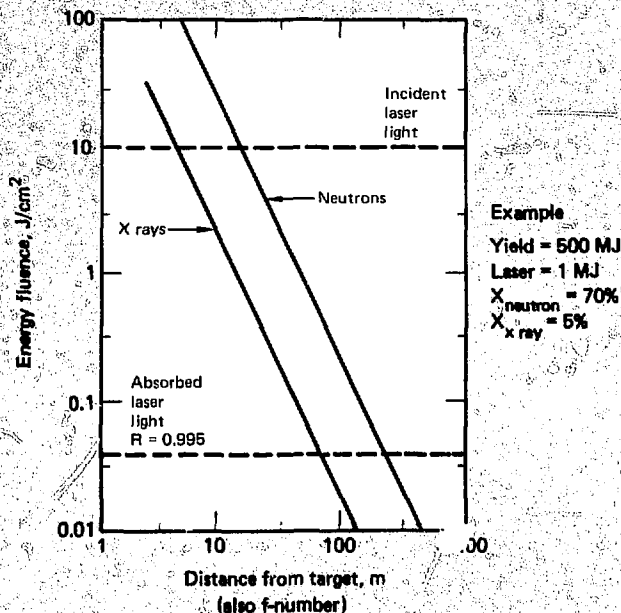
laser fusion power plants to assess the exposure levels of the final optics. Our present estimates of these conditions are listed in Table 8-11. For our calculations, we used the LASNEX computer code, which takes advantage of extensive experience at LLL in laser fusion target interactions and fusion physics. In Table 8-11, we have also listed some parameters for a specific system, notable only in that it allows us to use a concrete example.

In addition to the high projected target gains that significantly relax the laser efficiency required to obtain an attractive recirculating power fraction,

Table 8-11. Requirements for a laser fusion power plant and an example chosen for present calculations.

	Laser system requirements for laser fusion	An example for this article
Average power, MW	1-10	1
Pulse energy, kJ	300-3000	1000
Pulse width, ns	1-10	1
Pulse power, TW	>200	500
Pulse rate, Hz	1-10	2
Wavelength, $\mu\text{m}$	0.25-2	1
Efficiency, %	>1	—

Fig. 8-60. X-ray and neutron fluence as a function of distance. High f-number optics significantly reduce incident energy fluences.



we have a second important finding.<sup>60</sup> Laser-target interaction calculations lead to relaxed illumination requirements that allow high f-number optics. We envision many beams combined into a few clusters for target illumination. This has an important impact on designing the final optics for survival; we can greatly increase the mirror distance from the microexplosion to minimize the damaging neutron fluence.

The optical damage threshold for a laser is relatively fixed, say at  $10 \text{ J/cm}^2$  (the actual threshold depends on pulse length and laser wavelength). For a 1-MJ laser energy pulse, we must therefore have at least  $10 \text{ m}^2$  of mirror area facing the microexplosion. Clearly it is an important advantage to place the mirrors as far as possible from the target to reduce the intercepted solid angle. For example, the solid angle subtended by mirrors located at a distance of 100 m is  $8 \times 10^{-5}$ , an impressive reduction in exposure. This is a dramatic departure from previous thought. In a 1974 paper on this subject, Teitel places the final optic 4-8 m from the target, presenting a truly challenging problem.<sup>61</sup>

To better visualize the impact of high f-number optics on optical survivability, we have graphed in Fig. 8-60 the x-ray and neutron fluence as a function of distance for the example given in Table 8-11.

Although the actual fractions of x rays and neutrons are dependent on target design, we chose 70% neutrons, 5% x rays, and 25% debris for this illustration. Note that, in moving 100 m away, the x-ray fluence falls below the level of the absorbed laser light, and the neutron fluence per shot is at the  $0.2 \text{ J/cm}^2$  level. We examine the long-term consequences of this neutron dose below, after discussing protection options other than high f-number optics.

**Protection of the Final Optics.** We can identify several techniques for protecting the final optics against various types of incident radiation. We list some of these in the protection matrix of Fig. 8-61. Only the solid-angle reduction allowed by high f-number optics reduces fluences of neutrons, ions, x rays neutral particles, and blast effects. Some techniques are specifically tailored to one effect, such as the use of a magnetic field to deflect ions. Against x rays and ions, we could perhaps use a continuously replaced transparent film similar to sandwich wrap.

A rotating shutter might effectively stop charged and neutral debris, accelerated lithium, chunks of a misfired target, energetic deuterium ions, traveling at  $v = 10^7 \text{ m/s}$  for example, the time of flight from target to shutter 15 m away would be 1.5 ms. Assume a six-bladed shutter, for which each blade would need to

Protection technique	Neutrons	Ions	X rays	Neutral particles, shock waves
Solid-angle reduction	X	X	X	X
Magnetic field		X		
Transparent film		X	X	
Gas streaming		X	X	X
Rotating shutter		X		X
Gas refractor	X	X	X	X
Liquid metal mirrors		X	X	X

Fig. 8-61. Matrix of protection techniques and types of radiation.

rotate only  $\Delta\phi = \pi/6$  rad to close the aperture. The angular velocity required is 350 rad/s = 3333 rpm. Rotating 60-cm-diam blades at this rate would not be a problem.

The disadvantages of the rotating shutter concept are threefold:

- It will not stop x rays or neutrons.
- It will become highly activated.
- The rotating blades must endure loads parallel to the spin axis, a very unfavorable situation for long-lifetime rotating components. Although a shutter might be feasible, other non-mechanical options now seem more attractive.

Suggestions of liquid metal mirrors, as components that could restore themselves after each shot in the same manner as lithium first walls, have led us to investigate mercury, gallium, and sodium. Unfortunately, they have a common disadvantage: their optical absorptivity is so high in the visible to near-infrared ( $0.1 < a < 0.25$ ) that vaporization of surface materials occurs during a 1-ns pulse. Thus, we must reject liquid metal mirrors because of their unacceptably low damage thresholds.

The most effective technique for preventing x rays and debris from striking the final optic assembly involves the use of a simple region of gas with a relatively high atomic number. Photoelectric interactions in this gas stop the x rays, and collisions thermalize the massive debris. The x-ray and debris-energy spectra depend on interactions in the pusher-tamper region of the target, as well as in the lithium vapor. Therefore, the density-length product of additional gas that might be required to stop the remaining x rays is very design-dependent; however, we can estimate the requirements from mean free-path arguments. Envision a region several meters long near the optical surface, in which gas flows toward the target. The gas is injected at the optical surface to provide some face cooling and protection

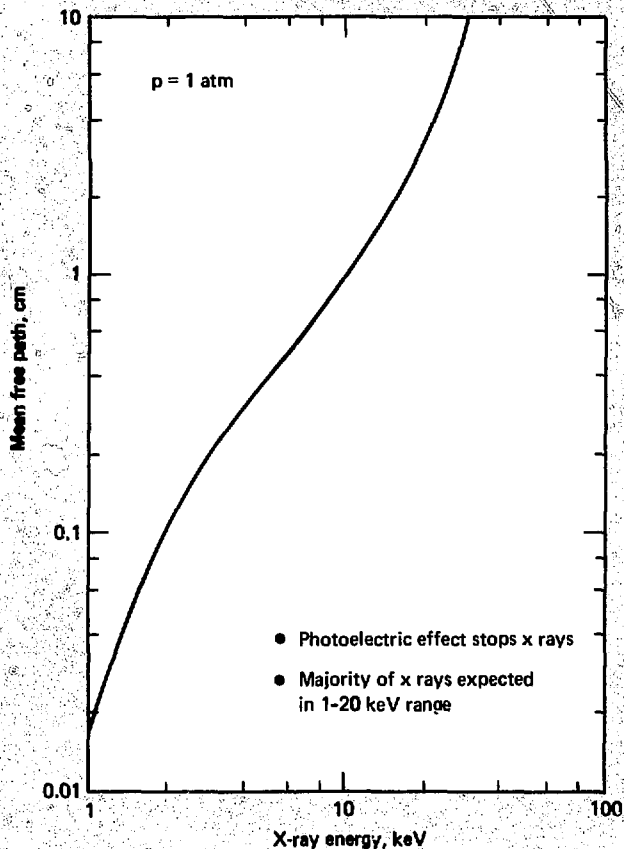
from particulates. An intermediate station pumps the gas out of the tube and reinjects it. (Too much gas should be avoided to prevent optical degradation of the laser beam. The gas must also be replaced between shots.)

Xenon is an effective high-Z absorber, although we could use almost any gas that is otherwise compatible. In Fig. 8-62, we graph the mean free path of x rays as a function of their energy in one atmosphere of xenon gas, using data from the LLL photon cross-section library.<sup>62</sup> We expect x rays throughout the 100-eV-to-20-keV region of the spectrum. The softer x rays have extremely short mean free paths in both the gas and mirror. Fortunately, these soft x rays are readily absorbed in the lithium vapor. From Fig. 8-62, we see that 0.21 cm-atm xenon will provide one attenuation mean free path for 3-keV x rays. To obtain a factor-of-100 reduction in x-ray intensity, we must provide approximately 4.6 mean free paths of gas, equivalent to 0.97 cm-atm xenon.

A 10-m section of beam tube containing 1 Torr xenon should be able to absorb the radiation over a distance sufficiently long to prevent generation and effective transmission of shock waves. Pressure disturbances created in this low-density gas are unlikely to have sufficient amplitude to affect the mirror. An additional benefit of this scheme is that the counter-flowing gas isolates the cooled optical surface from the hot lithium vapor, which might otherwise tend to condense on the optical surface.

**Transparent Optics.** The optical damage limit and the energy per pulse required on target combine to dictate the area of the final mirror or lens. We anticipate  $\sim 10 \text{ m}^2$  area in a few arrays of final optical elements each 1-2 m in diameter. For these elements, we expect to use mirrors rather than lenses. It currently appears substantially more cost-effective to diamond-turn large mirror blanks on an

Fig. 8-62. X-ray stopping power of xmas gas.



interferometer-controlled lathe than to cast and polish glass blanks of similar size, for equal degrees of surface accuracy. (This statement is less true for short wavelengths and may change as technology evolves.) Additionally, bulk neutron damage thresholds are generally lower in glasses than in metals. In all cases, we are concerned more with loss of optical performance from radiation-induced physical or optical changes than with changes in strength, embrittlement, etc.

**Insulating Substrates.** Let us assume the mirror substrate is a glass, such as ULE or fused silica, with either a dielectric coating or a metallic film coating. The thresholds are likely to be determined by non-uniform change of shape due to structural deformation of the lattice, which occurs at lower thresholds than such catastrophic damage as cracking. Disorder phases can also appear. Volumetric expansion in insulators is not likely to arise from helium

production, since the diffusivity of helium in such glasses as  $\text{SiO}_2$  is high.<sup>63</sup> For example, density variations of  $\pm 2\%$  are characteristic of neutron doses of  $2 \times 10^{19} \text{ cm}^{-2}$  (crystalline quartz decreases by this amount and vitreous silica increases by about the same fraction).<sup>64</sup> This dose corresponds to a 2.6-year lifetime at a distance of 100 m in our example. The quartz continues to decrease in density, saturating at  $\sim 15\%$  for  $2 \times 10^{20} \text{ n/cm}^2$ .

**Dielectric Coatings.** The performance of dielectric coatings in a 14-MeV neutron environment is largely unknown. Data on radiation damage to thin dielectric films are available solely for electron and uv irradiation and not for neutrons. We have identified the following damage mechanisms:

- Decrease in damage threshold from increased absorptance of induced color centers.
- Delamination caused by uneven stresses from swelling damage.<sup>65</sup>

- Degraded optical performance stemming from layer thickness, index-of-refraction changes, or both. Increased bulk absorption should not by itself be harmful, because the layer is so thin and the marginal heat load is so small.

Color center formation in glasses such as BK-7 can be severe in the visible range at quite moderate doses, but the impact on performance is highly dependent on laser wavelength. At  $1.06\text{ }\mu\text{m}$ , for example, color center absorption is far less than in the visible range. In recent LLL experiments, multicomponent glasses such as BK-7, when subjected to  $\gamma$  and neutron irradiation, discolored at three orders of magnitude lower dosage than a high purity fused silica.<sup>66</sup> Furthermore, at the highest dosage ( $3 \times 10^9$  rad), the BK-7 disintegrated, while the fused silica had only slightly discolored. Because significant annealing of color centers can occur at elevated temperatures, coated mirrors could perhaps be allowed to run hot, if other factors permit. A large selection of available coating materials and extremely high control of impurities should enable us to minimize this effect.

Effective multilayer coatings for high reflectivity require strict limits on variations in the index of refraction and layer thickness. Both are compromised by radiation damage, because the index of refraction also changes as density changes. The reflectivity of a coating is a relatively easy parameter to measure, and the neutron doses of interest are within current experimental reach. As a result, we are optimistic that coating performance in a neutron environment is an approachable and solvable problem. Of course, since the resistance to surface damage by x rays and debris is small, these types of radiation must be avoided.

**Metal Mirrors.** The final optic could be a metal mirror, with or without coatings. If the metal acts only as a substrate for a dielectric coating, absorptivity is irrelevant. However, in both coated and uncoated modes, high dimensional stability is required to maintaining surface accuracy. The mirror is heated by an average-power input of neutrons and absorbed laser radiation and we can readily calculate laser radiative heat load. Taking an optical absorptivity of 1%, an incident fluence per pulse of  $10\text{ J/cm}^2$ , and a pulse repetition frequency of 2 Hz, we obtain a power input density of  $0.2\text{ W/cm}^2$ . This level poses no serious problem, because conduction cooling can prevent distortion of the mirror surface at this heat load. The neutron heating contribution is comparable, perhaps slightly higher.

We have identified two potential mechanisms that could lead to shortened lifetimes for metal mirrors:

- Increase in optical absorption by reduction of electron conductivity in a damaged lattice (uncoated mirror).

- Increase in optical distortion caused by swelling from  $(n, \alpha)$  helium production reactions (both uncoated and coated).

The first effect occurs throughout the metal, but is only important within a few skin depths of the mirror surface. The dislocations and other lattice damage impede the freedom of the electrons (compared with that in an undamaged solid). The restricted electron mean free path is effectively a loss mechanism; the electrons absorb more energy from the optical field and are poorer reradiators. Sparks estimates that the effect saturates with an increase in absorptance of about a factor of 2 at a neutron dose of  $10^{19} - 10^{20}\text{ n/cm}^2$  (see Ref. 67).

If this increase in absorption occurs, two immediate consequences are possible: the waste heat removal requirement doubles (this should be no essential limitation), and the damage threshold may decrease if the damage is from a thermal source. (If the intrinsic damage threshold is dependent on electric field strength, however, there may be no consequence.) Alternatively, we can simply increase the mirror area as compensation.

The second possible important effect is surface distortion from the nonuniform swelling of the metal. The helium produced in  $(n, \alpha)$  reactions migrates to form microscopic bubbles. These bubbles can cause surface distortion on the order of a wavelength of light, which degrades optical performance. No experimental data are available to demonstrate this postulated optical effect, but we can predict its onset based on well-known volumetric swelling rates of neutron-irradiated materials. The University of Wisconsin has tabulated some swelling rates as a function of temperature for 316 stainless steel for two swelling rate conditions, nominal and maximum possible.<sup>68</sup> Higher temperature favors swelling, with an increase in temperature from 250 to  $350^\circ\text{C}$ , bringing more than an order-of-magnitude increase in volumetric swelling rate. For a first-wall neutron flux of  $7.65\text{ MW/m}^2$ , and a first-wall temperature of  $300^\circ\text{C}$ , the Wisconsin study calculates a swelling rate of  $0.323\%$ /year nominal,  $1.04\%$ /year maximum.

We want to determine the time required for volumetric swelling to cause a nonuniform  $\lambda/8$ -surface change at  $1.06\text{ }\mu\text{m}$  in a 1-cm-thick mirror

Table 8-12. Mirror lifetime based on helium production in metal substrate material and subsequent surface distortion.

Mirror distance, m	Neutron flux, MW/m <sup>2</sup>	Years to distort $\lambda/8$	
		Nominal swelling	Maximum swelling
50	$2.2 \times 10^{-2}$	4.3	1.3
100	$5.5 \times 10^{-3}$	17.1	5.3
200	$1.4 \times 10^{-3}$	68.5	21.3

blank. Unfortunately, we have no swelling information on copper or other substrate materials at 14 MeV and will use stainless steel data to bound the effect. For an equivalent 14-MeV dry wall neutron flux at the 5-m inner radius of the structural wall of 2.2 MW/m<sup>2</sup>, we can calculate the mirror lifetime based on the time required to distort a distance of one-eighth wave. (See Table 8-12 for results.) In this example, we estimate the linear deformation by  $\Delta x/x = (\Delta V/V)^{1/3}$ , where  $(\Delta V/V)$  is the volumetric swelling, and we scale the linear deformation proportionally with neutron flux.

Note that a lifetime of 5 to 16 years is obtainable for a mirror distance of 100 m, a relatively favorable outcome. The 300°C temperature is an extremely conservative assumption. Moreover, two circumstances may alleviate this swelling problem and lead to mirrors that could essentially last the life of the plant. First, some metal alloys, such as nickel-rich inconel, contract with radiation damage. Perhaps a similar alloy with exceptional dimensional stability can be found, because neither strength nor ductility is really a dominant issue. Second, simple adaptive optical components for wavefront correction may be able to largely remove the effect of moderate distortions introduced by the final optical element.

With a lifetime limitation of several years at 100 m, the technological risk of assuming a 1-year time between routine change-outs of the final metal mirror seems acceptable. It would occur at the time of the normal yearly plant shutdown for preventative maintenance. If we have been too conservative, we would simply bring the mirrors in closer, perhaps to 75 or 50 m, or would consider lifetimes in the 10-year range. Because the possibility of rather catastrophic, unexpected optical damage always exists, we may provide some desirable "insurance" by including a remotely operated carousel of a few mirrors.

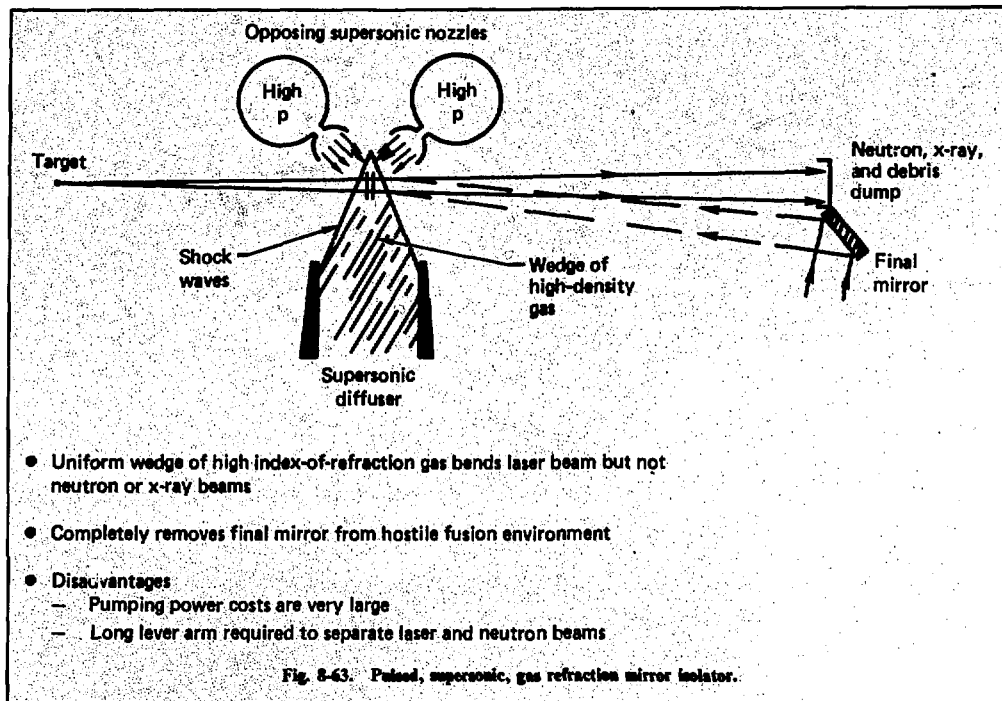
**Testing Requirements.** The solid-angle reduction allowed by the use of high f-number optics is of

fundamental importance in eliminating the need for new and expensive test facilities. This is because the neutron flux the mirrors experience is 100 times less than those on a reactor first wall and is therefore experimentally accessible much earlier. For example, the Rotating Target Neutron Source (RTNS-II) at LLL<sup>69</sup> is scheduled to produce a continuous flow of 13- to 15-MeV neutrons at the rate of  $4 \times 10^{13}$  n/s in the summer of 1978. If the RTNS were used to irradiate a 1-in.-diam sample of our final optic, we could obtain a neutron flux of 0.18 MW/m<sup>2</sup>, about the right level to obtain significant data within a few weeks. In the very near future, it will be possible to obtain superb data on radiation damage to optics without waiting for fusion test reactors. Only the question of pulsed vs continuous irradiation will remain.

**Gas Refraction Lens.** We briefly mention the only known scheme for preventing any radiation from the fusion microexplosion from impinging on the mirror. The device is related to an aerodynamic window (i.e., it uses a pulsed supersonic stream of gas to create a density distribution that acts exactly like a prism). It forms a wedge of higher index-of-refraction material that bends light, but not neutrons or debris. X rays are practically unaffected. Shown in Fig. 8-63, the concept follows our philosophy of substituting a self-renewing medium for a supermaterial. Because there is a great deal of experience with this technology in the high-energy laser field, we are confident it is feasible and has acceptably low optical distortion. Obviously, passive techniques are preferable, but the existence of an active alternative solution is reassuring.

**Conclusions.** Our conceptual design studies of commercial power reactors promise 30-year lifetimes and high availability through the use of innovative designs such as the liquid lithium fall reactor. In seeking optical system designs that are successful in solving difficult problems with near-term technology, we have identified some promising approaches. The most interesting approach is the use





of high f-number optics in long-beam tubes, a concept that minimizes the solid angle subtended by the final optics and significantly reduces neutron fluences (see Fig. 8-64). Blast effects and lithium vapor are removed in a baffled section near the opening of the beam tube to the reactor. This section acts as both silencer and condenser. At the mirror end, a region of heavy gas such as xenon flows from the mirror toward the chamber and is recirculated back to the mirror. This region effectively absorbs debris and x rays; only neutrons survive. At a distance of 100 m, only  $8 \times 10^{-5}$  of the neutrons created actually reach the mirror. Therefore, we need consider only neutron damage mechanisms.

Coated metal mirrors would be most desirable. The three most significant limitations on mirror lifetime identified are:

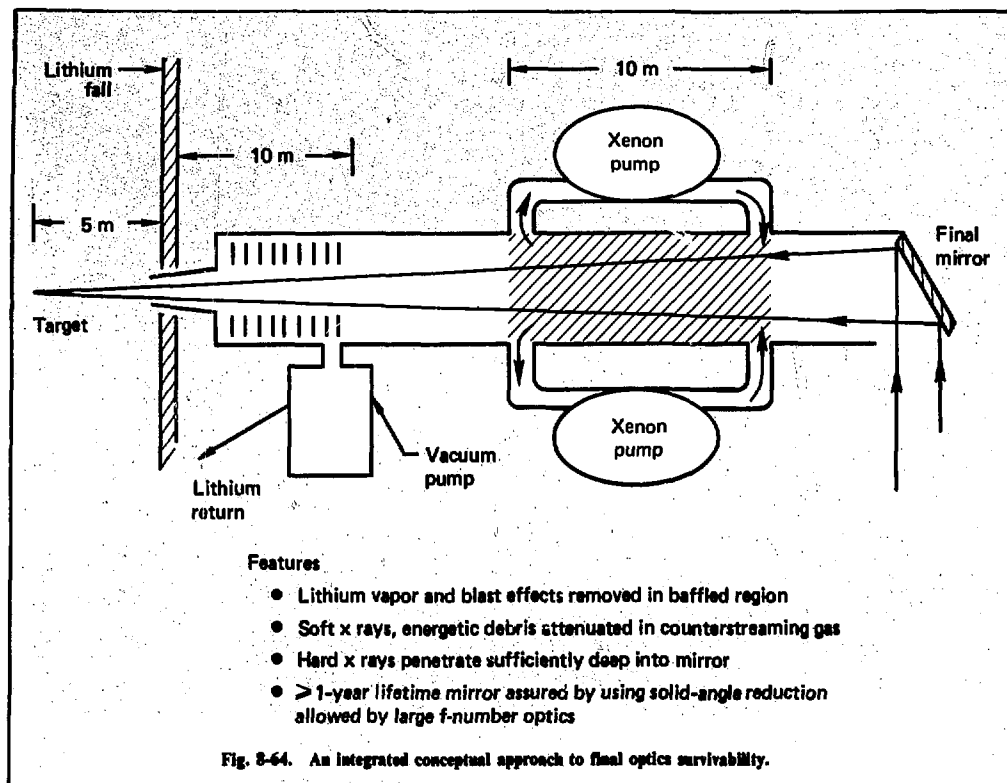
- A swelling-induced increase in surface distortion.
- Changes in dimension, index of refraction, and state of stress in dielectric multilayer coatings.
- Increase in absorption of the metal mirror if coatings are not used.

It appears that we can anticipate mirror lifetimes greater than a year, with a good chance for

10-year lifetimes. Most importantly, significant experimental research and development can be performed in the very near future without new and expensive dedicated test facilities. Therefore, we can be reasonably confident that the use of high f-number optics will lead to designs for final optical systems that do not adversely affect plant availability factors.

## References

60. J. Nuckolls, "Laser Fusion Overview," presented at the *Ninth International Quantum Electronics Conference*, June 14-18, 1976, Amsterdam, the Netherlands. [Also Lawrence Livermore Laboratory, Livermore, Calif., Rept. UCRL-77725 (1976)].
61. R. J. Teitel, "Anticipated Radiation Damage Problems to Laser Optics," *J. Nucl. Materials* **53**, 349-353 (1974).
62. E. F. Plechaty, D. E. Cullen, and R. J. Howerton, *Tables and Graphs of Photon Interaction Cross-sections from 1.0 keV to 100 MeV Desired from the LLL Evaluated Nuclear Data Library*, Lawrence Livermore Laboratory, Livermore, Calif., UCRL-50400, Vol. 6, Rev. 1 (1975).
63. Report to the American Physical Society by the study group on physics problems relating to energy technologies; Radiation Effects on Materials, *Reviews of Modern Physics* **47**, Suppl. No. 3 (Winter 1975).



64. J. Wong and C. A. Angell, *Glass Structure by Spectroscopy* (New York, Marcel Dekker, Inc., 1976).
65. N. J. Broadway, *Radiation Effects Design Handbook*, Section 2, "Thermal-Control Coatings," NASA CR-1786, June 1971.
66. M. Moran, Lawrence Livermore Laboratory, Livermore, Calif., unpublished results.
67. M. Sparks and M. Guinan, "Radiation Damage and Heating of the First Mirror in Proposed Commercial Laser Fusion Systems" (to be published as a UCRL).
68. H. I. Avci and G. L. Kulcinski, *The Effects of a Liquid ISSEC on Radiation Damage Parameters in Laser Fusion Reactor First Walls*, University of Wisconsin Report UWFD-205, April 1977.
69. J. C. Davis et al., "Rotating Target Neutron Source II: Progress Report," *Proc. 2nd Topical Mtg. on Tech. of Controlled Nucl. Fusion*, Vol. IV (Richland, Wash., CONF-760935-P4, Sept. 21-23, 1970).

#### Author

M. J. Monsler

#### 8.5.2 Propagation in the Target Chamber

Beam decollimation is perhaps the most important issue in our consideration of beam interaction with residual gas in the target chamber. As the beam approaches the target, its intensity increases far beyond the ionization threshold, creating a plasma several centimeters long. The decollimation may be caused by refractive effects in the nonuniform plasma, Brillouin and Raman scattering, or by many other inelastic phenomena. In a nonuniform plasma, stimulated processes are suppressed, and the low density ( $\sim 10^{15}/\text{cm}^3$ ) probably precludes decollimation by other effects. However, stimulated scattering may occur in uniform plasma; in particular, stimulated Raman scattering (SRS) may have a significant effect. Plasma uniformity is certainly a central issue, but it is extremely complex to analyze. In the worst case of a static, uniform plasma, we can easily calculate the SRS. This provides an upper bound on the allowed plasma density, which is certainly more severe than would be measured in a reactor chamber.

In the SRS process, a light wave at frequency  $\omega_L$  and a plasma wave at  $\omega_p$  generate an oscillating dipole moment that radiates at  $\omega_L \pm \omega_p$ . Because the radiated or Stokes wave does not copropagate with the driving wave, the energy in the Stokes wave is decollimated, and it may miss the target. The precise loss depends on the target size, the final focusing geometry, and the angular divergence of the laser beam. For a diffraction-limited beam, a lens at  $f/3$ , a target size of 0.5 mm, and a plasma density of  $10^{15}/\text{cm}^{-3}$  at temperature  $T \sim 1\text{-}10$  eV, Thomson calculates that about 10% of the beam would be defocused.<sup>70</sup> Thus, the instability may be significant. Thomson also shows that increasing the laser bandwidth suppresses the instability, and that the fractional energy loss scales as the inverse of the frequency.  $\text{CO}_2$  lasers are thus much more susceptible to the instability than Nd or ultraviolet lasers. We reemphasize that this is a conservative overestimate and that effects from plasma non-uniformity and radiation pressure can lower the energy loss dramatically.

The question became the subject of a lively and vigorous debate when Sparks and Sen claimed that the classical analysis was incorrect.<sup>71</sup> Substituting their own controversial analysis, they obtained total decollimation of the beam, and thereby challenged the viability of laser fusion. Their analysis is incorrect, however; it is appropriate for a turbulent medium driven below threshold for stimulated scattering. Thus, it applies solely to very weak lasers in turbulent plasmas. The phase coherence of SRS and the high laser intensity run counter to their analysis.<sup>72</sup> Their analysis can, in fact, produce many interesting and unusual phenomena that we have not yet observed.<sup>72,73</sup>

Our conclusion is that decollimation from stimulated scattering may be significant in laser fusion target chambers. It limits the density to about 0.1 Torr in the least favorable case of a uniform plasma for the given parameters. The actual limit is larger by an undetermined amount; it depends on the focussing geometry, target size, beam quality, and plasma uniformity. Because we expect the atmosphere in a lithium curtain chamber to be a turbulent gas with vapor pressure between 0.1 and  $5 \times 10^{-3}$  Torr, we do not anticipate any problems.

## References

70. J. J. Thomson, *Stimulated Raman Scatter in Laser Fusion Target Chambers*, Lawrence Livermore Laboratory, Livermore, Calif., UCRL-80233.
71. M. Sparks and P. N. Sen, *Phys. Rev. Lett.* 39, 751 (1977).
72. D. Eimerl, Lawrence Livermore Laboratory, Livermore, Calif., Internal Memo, TDA, 77-257.

73. D. Eimerl, *Phys. Rev. Lett.* 40, 934 (1978).

**Author**

**D. Eimerl**

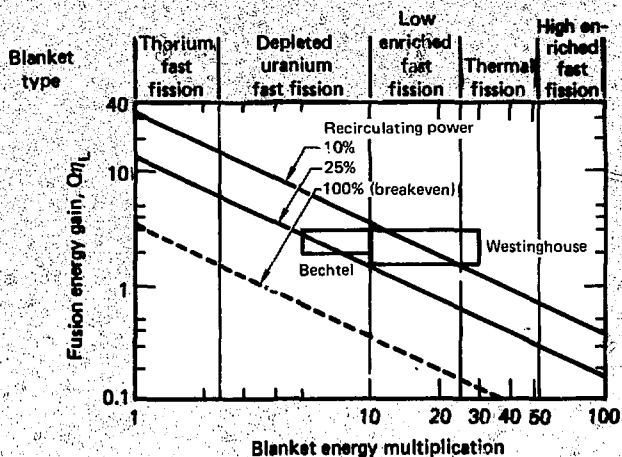
## 8.6 Current Status of Laser Driven Fusion-Fission Energy Systems

Since the early 1950's, interest in fusion-fission hybrid systems has been motivated by their combination of the attractive features of two technologies.<sup>74,75</sup> The fission system is power-rich (200 MeV per fission reaction), and the fusion system is rich in fast neutrons. The 14.1-MeV fusion neutrons produce fission in fertile materials such as  $^{232}\text{Th}$  or  $^{238}\text{U}$ , generating large amounts of energy and fissile materials.

For several years, we have been investigating the potential for producing fissile fuel and electricity with the laser fusion-fission hybrid reactor.<sup>76-78</sup> Our earlier studies primarily used neutronic methods of analysis to identify attractive hybrid concepts and to estimate the upper bound of performance. These neutronic studies demonstrated that laser fusion hybrids could be designed to meet a broad spectrum of fissile-fuel-producing and energy-multiplying requirements. The studies also demonstrated that hybrids produce 10 times more fissile fuel (per unit of thermal energy generated) than fission breeder reactors. Finally, they showed that laser fusion hybrids produce electricity with laser and target performance requirements much lower than for pure fusion.

The neutronic results were encouraging, but it was apparent that a more accurate assessment of the hybrid's potential and a definitive ranking of more promising concepts would require studies dealing with the engineering, safety, and economic issues as well. With this in mind, we engaged Bechtel and Westinghouse to assist in a more realistic assessment of the laser fusion hybrid's potential in a fission-power-generation economy. With Bechtel, we have been engaged in a joint effort to conceptually design a laser fusion hybrid that emphasizes fissile fuel production.<sup>79,80</sup> The primary objective of our joint effort with Westinghouse has been to conceptually design a laser fusion hybrid that emphasizes power production, while also producing fissile fuel.<sup>81</sup> In this article, we briefly describe and analyze the hybrid designs from these two engineering studies. Our evaluation of the performance of both hybrid designs is based on operational

Fig. 8-65. Fusion energy-gain requirements for hybrid systems.



parameters such as system efficiency, recirculating power fraction, blanket energy multiplication, fissile fuel production, power density, and fuel burnup. Finally, we present the results of a detailed cost analysis of the LLL/Bechtel design that was performed by Bechtel.

### 8.6.1 Fuel Cycles and Blanket Selection

The fissionable material selected for the blanket and the type of blanket configuration together determine the energy multiplication and the amount of fissile fuel bred by the hybrid reactor. For example, natural uranium gives an energy multiplication of about 10 in a fast-fission blanket design, while the multiplication is 2 to 3 times larger with a thermal fission blanket configuration. However, the fissile fuel bred (per unit of thermal energy) with the fast blanket would be a factor of 3 to 4 larger than the quantity obtained from the thermal blanket. For a given recirculating power fraction, the blanket energy multiplication determines the fusion energy-gain requirements of the fusion power plant. (Fusion energy gain is defined as the product of laser efficiency and pellet gain.) Figure 8-65 plots the summary results of our earlier neutronic studies.<sup>77-79,81</sup> We have plotted the required fusion energy gain as a function of blanket energy multiplication and recirculating power fraction for several blanket types. (We assumed thermal efficiency of 35% in calculating the curves.) The shaded areas depict the regimes (energy multiplication, blanket type, fusion energy gain, and recirculating power fraction) that we have emphasized in our design studies with Bechtel<sup>79,80</sup> and Westinghouse.<sup>81</sup>

Table 8-13 lists the salient features of the Bechtel and Westinghouse designs and the main differences between them. As we noted above, the main product of the LLL/Bechtel design is fissile fuel and, in the LLL/Westinghouse design, the major product is electricity. We achieved the emphasis on electricity production in the Westinghouse design by designing a fission blanket with high first-wall flux, energy multiplication, and power density. The resulting smaller power plant has less recirculating power and higher system efficiency for the same fusion energy gain.

The capital cost of the LLL/Bechtel hybrid has been estimated by Bechtel to be three times more expensive than a light water reactor (LWR) of equivalent power. We have not made a detailed cost estimate of the LLL/Westinghouse design. However, because of its reduced fissile fuel performance, it would have to cost less than the LLL/Bechtel design (approximately two times more than an LWR) to be as attractive.

### 8.6.2 LLL/Bechtel Hybrid Design Study

For the last two years, we have joined with Bechtel Corporation to conceptually design a laser fusion hybrid reactor.<sup>79,80</sup> LLL has provided the overall direction, the neutronic data, and the fusion portions of the design. Bechtel has provided the fission section of the hybrid, the design of the thermal energy transport and conversion system, the tritium recovery system, and the layout of the complete power plant. Bechtel has also estimated operating and capital costs. The hybrid concept chosen for this design study is a depleted uranium fueled, fast-fission blanket that produces fissile fuel and elec-

Table 8-13. Comparison of design parameters for two studies.

	LLL/Bechtel	LLL/Westinghouse
Fuel	Depleted uranium	Enriched fuel
Blanket energy multiplication	$M < 10$	$M > 10$
Required fusion energy gain	$> 2$	$> 1$
Principal product	Fissile fuel	Electricity
Fuel production	6-7 LWR's <sup>a</sup>	3-4 LWR's
First wall	Graphite cylindrical liner	Spherical wet wall
Wall loading	$\sim 1 \text{ MW/m}^2$	$\sim 10 \text{ MW/m}^2$
Power density	$\sim 40 \text{ W/cm}^3$	$\sim 250 \text{ W/cm}^3$
Reactor configuration	Single cylindrical cavity	Multiple spherical cavities
Capital cost	$3 \times \text{LWR}$	$\sim 2 \times \text{LWR}$

<sup>a</sup>LWR = Light water reactor.

tricity. The design maximizes fuel production at the expense of energy multiplication. The selection of depleted uranium limits blanket energy multiplication to a factor of less than 10; therefore, fusion energy gains greater than 1 are required to produce electricity with recirculating power fractions less than 25%. This fusion energy-gain requirement is an order of magnitude lower than the requirement for pure laser fusion. Another objective of our design study was to use state-of-the-art fission technology in the design of the hybrid blanket. Accordingly, we chose stainless steel for the structure and cladding material and sodium for the fission blanket coolant.

We completed the first iteration of the conceptual design last year and reported it in the literature.<sup>79,80</sup> A second iteration improved the performance and reduced the cost of the reactor.<sup>82</sup> This more recent design is summarized in this article. The functional shape of the reactor is shown in Fig. 8-66; it is basically a 10-m diameter cylindrical structure with a height-to-diameter ratio of 1.0. The reactor consists of a cylindrical shell with a removable top cover. The fusion targets are injected from the top, the laser beams enter from the side, and all coolant piping enters and exits at the top. A depleted uranium-fueled fission blanket is positioned radially around the fusion chamber. The energy in the fission blanket (amounting to 80% of the total energy) is removed with a sodium coolant system that enters and exits from the upper plenum. This radial blanket is divided into eight segments that can be individually removed. Liquid lithium-cooled graphite-moderated blankets are positioned in the top and bottom of the reactor and behind the fission zone. These lithium blankets moderate and capture neutrons and breed tritium.

**Fission Blanket.** In selecting depleted uranium over natural uranium, we noted that the energy multiplication and net Pu production of natural uranium were 14% and 3% higher, respectively. However, this increased performance was not large enough to outweigh the cost and availability advantages of utilizing the enormous U.S. stockpile of depleted uranium. Fission blankets were not positioned in the top and bottom of the reactor. In this way, we avoided the difficulties of maintaining coolant flow when the top is removed to gain access to the fusion chamber. This decision resulted in a 30% decrease in both fissile fuel production and energy multiplication for the design. However, it was consistent with our desire to use state-of-the-art-fission technology. In the initial design, the fission blanket was 25 cm thick with two sets of fuel elements in front and back. The revised design for this reactor has a thicker fission blanket (41 cm) with three rows of fuel elements; it is divided into eight segments. Figure 8-67 shows a detailed view of one of the eight radial blanket segments, and Table 8-14 presents the fission blanket data. Each segment has 81 hexagonal process tubes, each containing one depleted uranium fuel element. (Half of the outer row process tubes are initially empty to satisfy the tritium-breeding requirements.) Each fuel element is a 19-rod cluster of wire-wrapped stainless-steel-clad fuel pins similar to those used in early sodium-graphite reactors (SGR's). The configuration of the fuel pins in the hexagonal process tube and the details of the cladding are shown in Fig. 8-68. The uranium in these fuel pins could be used interchangeably in low-alloy metal form, metal alloy (7% Mo), or as a compound, such as UC or UO<sub>2</sub>. The low multiplication (approximately 6) of the

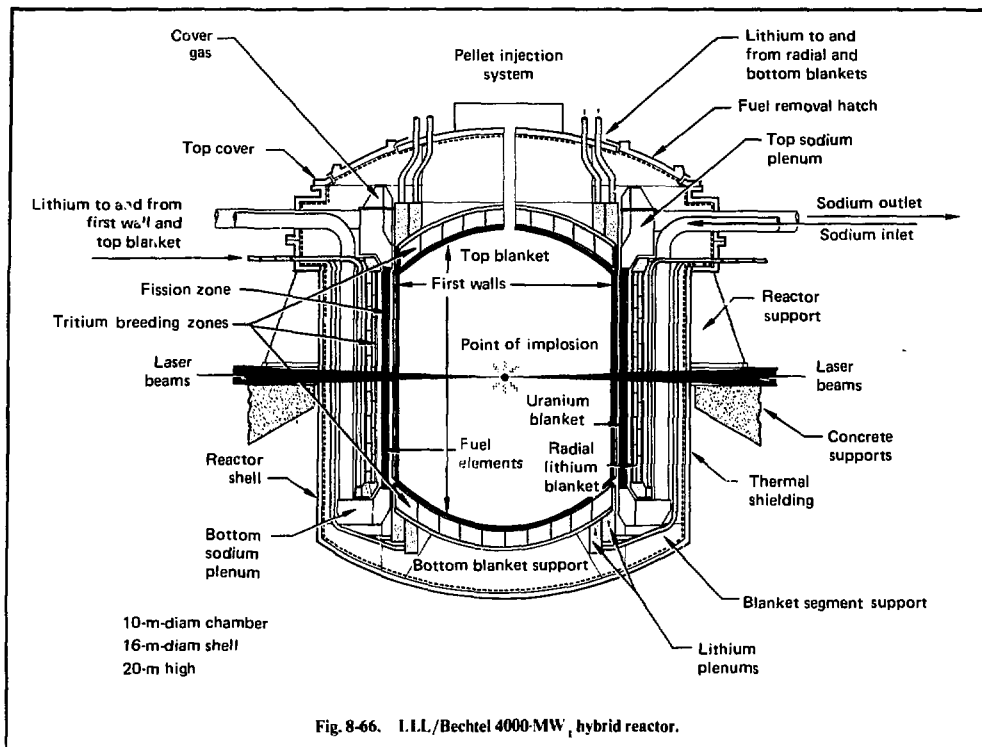


Fig. 8-66. ILL/Bechtel 4000-MW<sub>t</sub> hybrid reactor.

uranium compounds prohibits their use despite their attractive burnup and high-temperature properties (approximately 100,000 MWD/MTU at a maximum temperature of 100°C). The U-7% Mo alloy has a multiplication<sup>6</sup> of approximately 8 and its <sup>239</sup>Pu production is about 25% lower than the production obtained from low-alloy metal.

We selected low-alloy metal for several reasons. It provides the highest energy multiplication (approximately 10) and fissile fuel production performance; its maximum temperature limit of 600°C is not overly restrictive with a liquid metal coolant; and, finally, the disadvantages of its low burnup limit of 6500 MWD/MTU were offset by cheaper fabrication costs and our desire to keep the fissile inventory low.

**Tritium-Breeding Blankets.** The reactor contains three tritium-breeding zones (TBZ's): a lithium-cooled radial blanket surrounds the fission blanket (Fig. 8-66), and the two others are positioned at the top and bottom of the reactor. The sections of the TBZ contained in each radial blanket segment (Fig. 8-67) have a 2-cm-thick stainless steel (SS) inner wall immediately behind the fission

blanket, followed by 6 cm lithium, 50 cm graphite, 2 cm lithium, and a 2-cm thick SS outer wall. The lithium flows from an inlet header at the top to a bottom plenum and then upward through the two sections surrounding the graphite. The top and bottom blankets, identical in composition, are positioned 500 cm from the center of the reactor; they are shaped like cylindrical curved pancakes. The first 2 cm are SS, followed by 10 cm of a beryllium region (76% Be, 20% Li, 4% SS by volume), 70 cm of a graphite region (86% C, 10% Li, 4% SS), 10 cm of a lithium region (96% Li, 4% SS), and a 2-cm SS outer wall. The neutron multiplication resulting from beryllium's large (n, 2n) cross section enhances the production of tritium. The TBR for the top and bottom blankets is approximately 1.7, which allows a TBR less than 1 in the side blanket while maintaining an overall TBR of 1.1. The reduced TBR requirement in the side blanket permits a thicker fission blanket that produces more fissile fuel.

**First-Wall Design.** The first wall has the difficult task of protecting the blanket structure from the effects of x rays and debris produced by the ther-

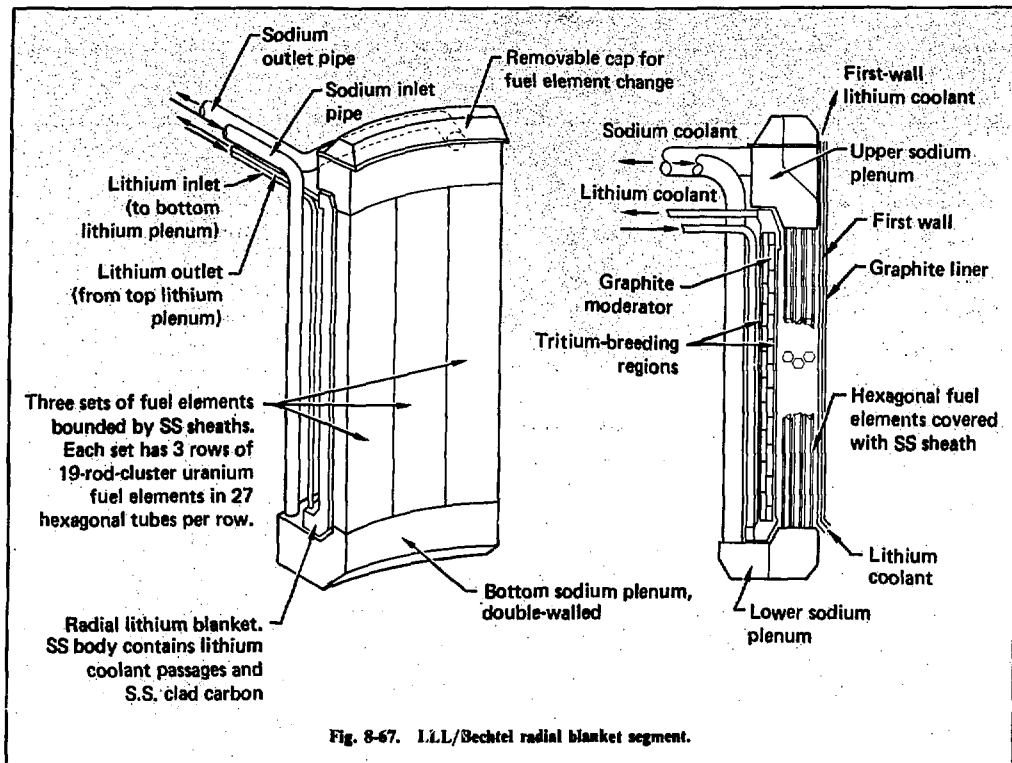


Fig. 8-67. LLL/Bechtel radial blanket segment.

monuclear microexplosion. In the LLL/Bechtel design, we selected a sacrificial liner of graphite to perform this task. The sacrificial liner is designed like a birdcage; it is attached to the top fusion blanket and reactor cover and it can be removed after the top cover is lifted. The design and performance of the first wall are of critical importance, because the wall's lifetime and replacement time will significantly affect plant availability. The protective first wall also moderates and captures neutrons; therefore, its thickness and composition will influence the performance of the fission blanket. With this in mind, we have tried to design a thin liner that could last at least 1 year. In the first design, the wall consisted of a lithium-cooled, 2-cm-thick graphite liner with a density of  $0.82 \text{ g/cm}^3$ , supported by a light stainless steel structure (66.6% C, 9.7% SS, 23.7% void).<sup>83</sup> The effect of this wall on the overall performance of the reactor was to reduce the energy multiplication and tritium breeding by 6 and 12% respectively, with the graphite and SS accounting, more or less, for the same absorption fraction of the neutron flux. In the revised design, the first wall

consists of lithium-cooled, 1-cm-thick graphite blocks brazed onto a 1-mm molybdenum backing (Fig. 8-69a).<sup>78</sup> The coolant flows through a corrugated structure welded to the first-wall backing. The brazed connection between the metal structure and the graphite blocks is needed to enhance conduction of heat from the graphite to the coolant. If the graphite is radiatively cooled, the high surface temperature will accelerate ablation, and it will be difficult to design a thin sacrificial wall that could last a year. On the top of the reactor, the first wall is cooled directly by the lithium in the top fusion blanket (Fig. 8-69b). A separate lithium circuit cools the first wall that protects the sides and bottom of the reactor (250-MW energy deposited). The first wall and cooling structure together form an integral cage that can be removed intact from the reactor vessel.

**Reactor Performance.** Optimization of the reactor performance over the life of the blanket requires a tradeoff between power production, fuel management, tritium breeding, and plutonium production. From the beginning of the cycle, the energy genera-

Table 8-14. Depleted-uranium fission blanket data.

Item	Inner row	Middle row	Outer row
Number of fuel elements	216	216	108
Element height — total	9.8 m	9.8 m	9.8 m
— active	8.8 m	8.8 m	8.8 m
Mass of uranium	244 Mg	296 Mg	150 Mg
Number of fuel rods	19	19	19
Fuel rod diameter	26 mm	27 mm	27 mm
Fuel rod pitch	1.15	1.107	1.107
Uranium slug o.d./i.d.	24/11 mm	24/0 mm	24/0 mm
Uranium volume fraction	41	53	31
Sodium volume fraction	47	35	57
Stainless steel volume fraction	12	12	12
Process tube o.d. — corners	15.94 cm	15.94 cm	15.94 cm
— flats	14.34 cm	14.34 cm	14.34 cm
Process tube wall thickness	3 mm	3 mm	3 mm
Fuel cladding wall thickness	0.4 mm	0.4 mm	0.4 mm
Maximum uranium temperature	600°C		
Maximum sodium velocity	10 m/s		

tion and tritium breeding increase, while the net plutonium production decreases until fresh fuel is added. To maintain a constant output power of 4000 MW, the laser pulse repetition rate is decreased from the initial value to compensate for increasing energy multiplication as plutonium accumulates in the fission blanket. Reactor performance for this mode of operation is summarized in Table 8-15. The operational parameters presented in Table 8-15 were calculated for a fission blanket lifetime of 3 full-power years (4.28 calendar years). During this period, the front row fuel elements are alternately rotated and replaced at intervals of 0.75 full-power years. All fuel elements are replaced at 3 full-power years. Blanket energy multiplication increases from 6.0 to 8.3 during the cycle and the first wall neutron flux decreases from 2.0 to 1.3 MW/m<sup>2</sup> as the fusion power is decreased to keep the reactor output power constant. The maximum power density reached during the cycle is 220 W/cm<sup>3</sup>, and it occurs in the first centimetre of the fission blanket.

The fuel burnup limit of 0.6% occurs in the front-row fuel at 1.5 years and in the second-row fuel at 3 years. The total plutonium production by the end of the 3-year cycle is 10,500 kg, sufficient to fuel six (4000 MW) LWR's with a conversion ratio of 0.6

**Cost Analysis of the LLL/Bechtel Design.** Bechtel's estimate of the capital cost of the laser fusion hybrid reactor plant is based on conceptual design information. A large portion of the total plant, including the thermal energy transfer and conversion, cooling, and auxiliary systems, represents conventional technology. Accordingly, the cost estimating is based largely on background experience. The reactor, the laser, and tritium systems are conceptual, and their cost is estimated by unit and component cost methods. The total plant is based upon commercial operation; therefore, we assume costs apply to fifth-of-a-kind facilities.

A capital and operating cost summary of the 1200-MW<sub>e</sub> laser fusion-fission power plant is presented in Table 8-16. For comparison, the cost of



Fig. 8-68. Fuel element and process tube configuration.

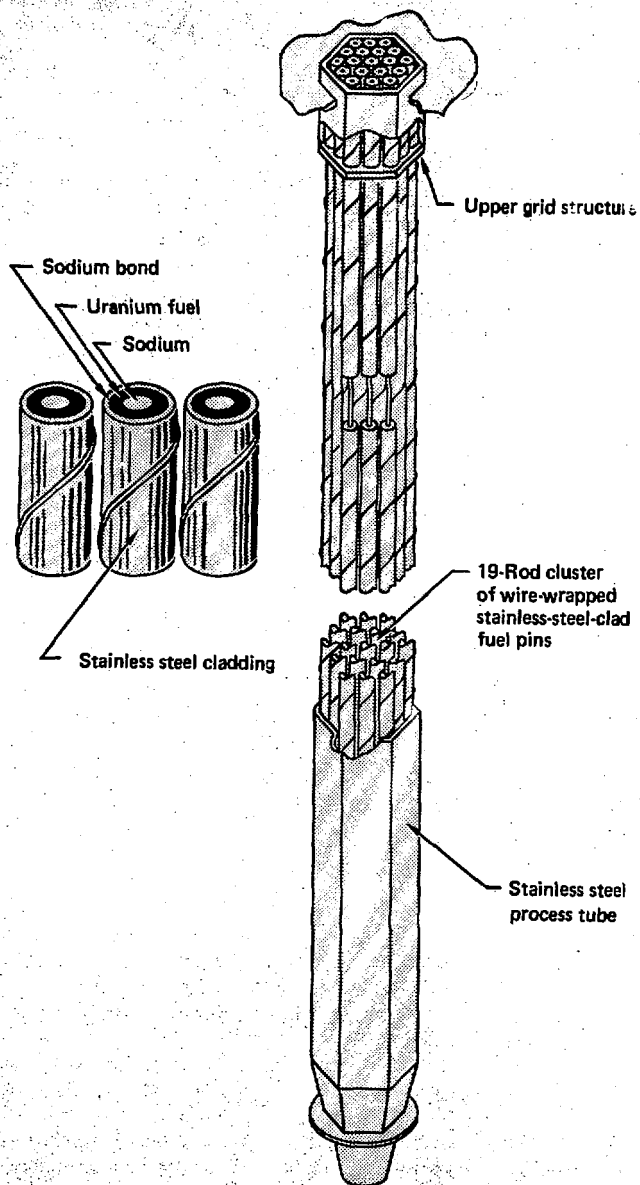
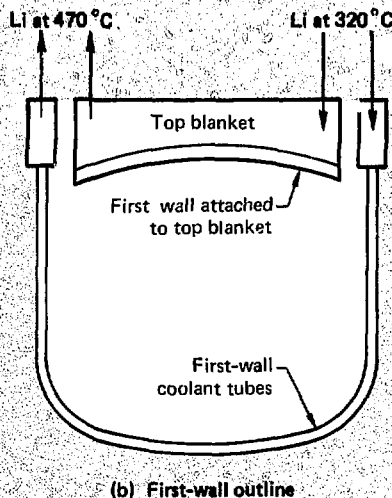
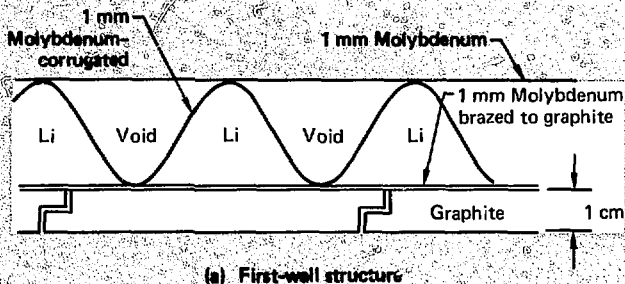


Fig. 8-69. LLL/Bedford first-wall structure.



the hybrid is contrasted with cost estimates for a typical LWR. The LWR cost estimates reflect 1976 price and wage levels, while the hybrid estimates use 1977 levels. Neither estimate provides for future escalation.

The indirect costs in Table 8-16 reflect an estimate of 9 years to construct the LWR and 10 years for the more complex laser fusion hybrid. As a result, the indirect costs of the hybrid account for a larger fraction of its total capital cost of \$2.239 billion. If we consider cost-per-kilowatt installed, the hybrid is 2.8 times more expensive than the LWR.

The cost of electricity from the hybrid is 56 mills/kWh, approximately twice the cost of LWR electricity. The capital portion of the operating cost

is by far the dominant factor in the estimated cost of electricity; for both reactors it is based on a 15% rate of return on the capital invested. The fuel cycle cost for the laser fusion hybrid is negative because of revenues obtained from the sale of its plutonium at \$30/g.

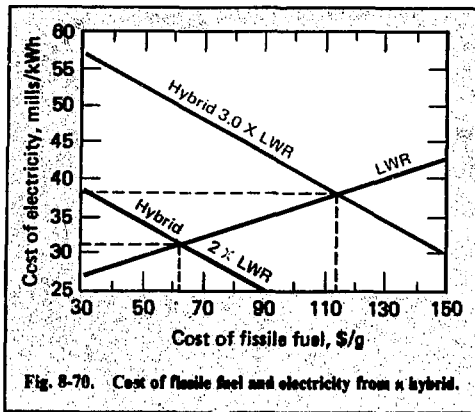
The major issue concerning a laser fusion hybrid is not how much it will cost nor the price at which it can generate electricity. Rather, it is the cost of electricity in a scenario that features hybrids providing fissile fuel for existing burner reactors. In Fig. 8-70 we plot the cost of electricity as a function of the cost of fissile fuel for hybrids with varying capital costs. The intersection points of the curves determine the cost of electricity and fissile fuel in the hybrid-LWR scenario. These results indicate that

Table 8-15. Operation performance summary of the LLL/Bechtel hybrid reactor.

	Start of life	End of life	Cycle avg.
System performance			
Thermal power, MW <sub>t</sub>	4000	4000	4000
Fusion thermal power, MW <sub>t</sub>	850	550	700
Gross electrical power, MW <sub>e</sub>	1520	1520	1520
Net electrical power, ME <sub>e</sub>	1195	1232	1210
Recirculating power fraction	0.22	0.19	0.20
System efficiency, %	30.0	30.8	30.4
Blanket performance			
Blanket energy multiplication	6.0	8.3	7.15
Tritium breeding ratio	0.99	1.07	1.03
Net fissile production, kg/MW <sub>t</sub> -yr	1.0	0.84	0.88
Maximum power density in fuel, W/cm <sup>3</sup>	189	220	204
Average power density in fuel, W/cm <sup>3</sup>	78.4	91.3	84.9
First-wall flux, MW/m <sup>2</sup>	2.0	1.3	1.65

Table 8-16. Capital and operating cost analysis of the LLL/Bechtel hybrid.

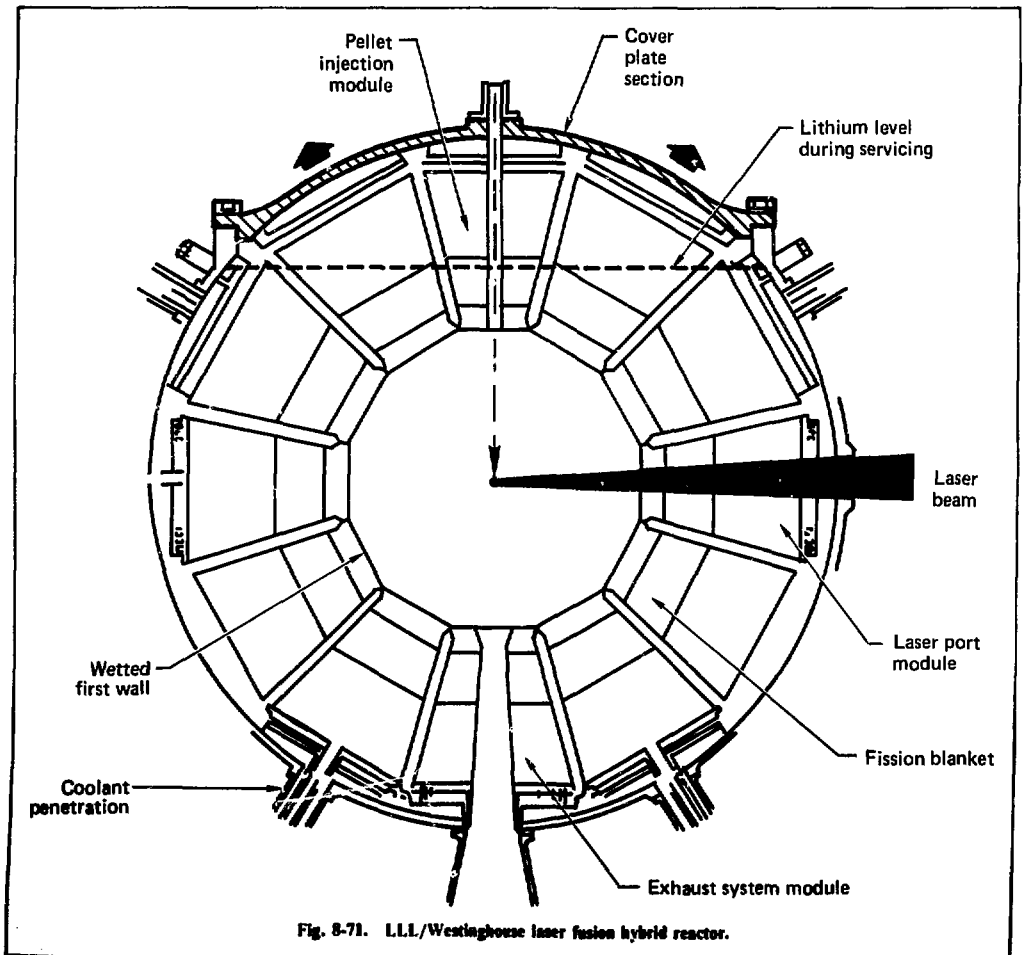
Capital cost item \$10 <sup>6</sup>	LWR 1200 MW(e)	Laser fusion hybrid 1200 MW(e)
Laser system	NA	149
Nuclear steam supply system (NSSS)	78	344
Other mechanical	101	230
Civil and structural	142	165
Piping	77	120
Instrumentation	9	32
Electrical	43	90
Total direct	450	1130
Field costs	79	215
Engineering services	80	215
Contingency	91	390
Owners cost at 8%	56	156
Interest during construction at 8%	197	615
	(9 yr)	(10 yr)
Total indirect	503	1591
Total cost	953	2721
Cost per kW installed (\$)	794	2239
Operating cost item (mills/kWh)		
Capital	19.42	55.0
Fuel	6.3	-1.0
Operating and maintenance	5	2.0
Total operating	32	56.0



the cost of electricity is quite insensitive to the capital cost of the laser fusion hybrid. Specifically, the cost of electricity is quite insensitive to the capital cost of the laser fusion hybrid. Specifically, the cost of electricity increases by only 20 to 40% when the capital cost of the hybrid changes from 2 to 3 times more than the LWR.

### 8.6.3 LLL/Westinghouse Hybrid Design Study

The main differences between the Bechtel and Westinghouse designs are listed in Table 8-13. In the Westinghouse design, electricity production was emphasized by designing a fission blanket with higher energy multiplication ( $M \geq 10$ ) and a higher power density than the Bechtel design. The resulting smaller power plant has less recirculating power and

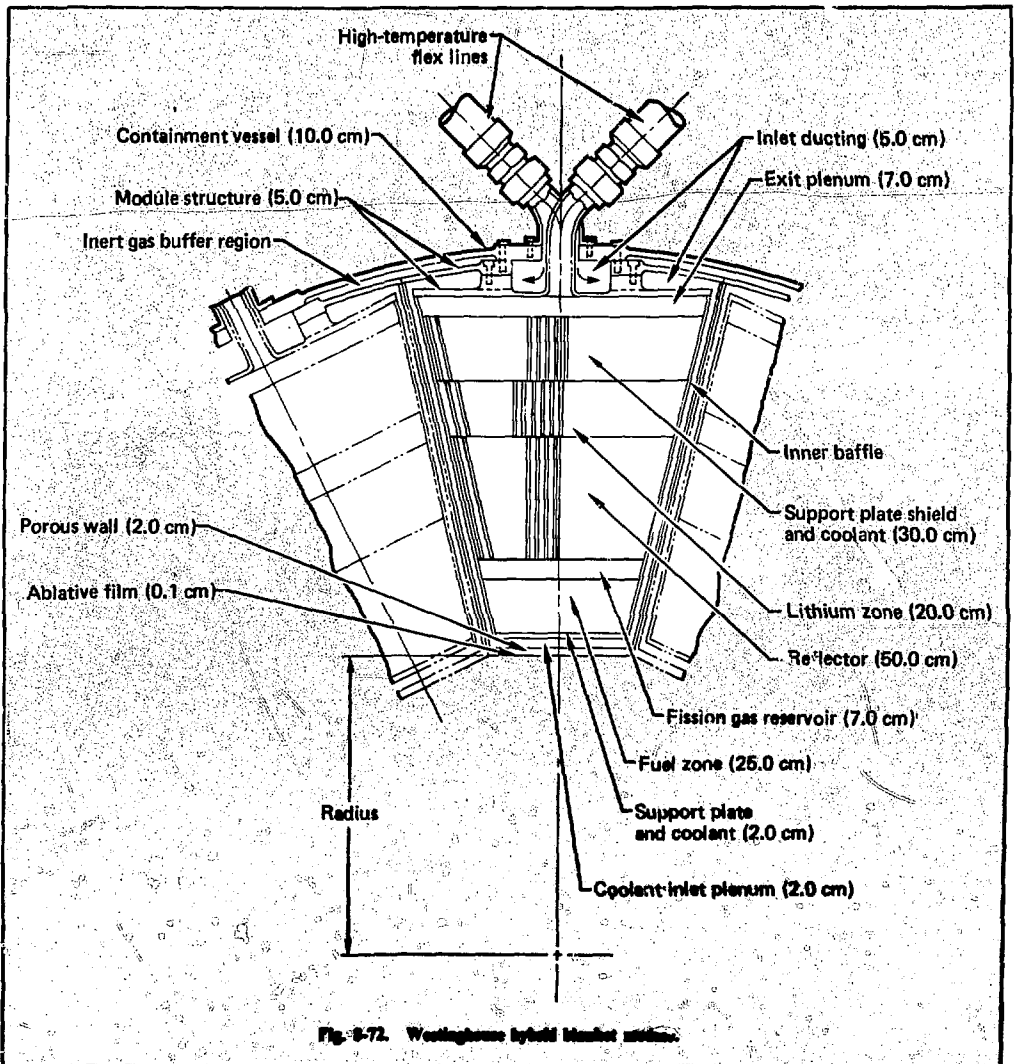


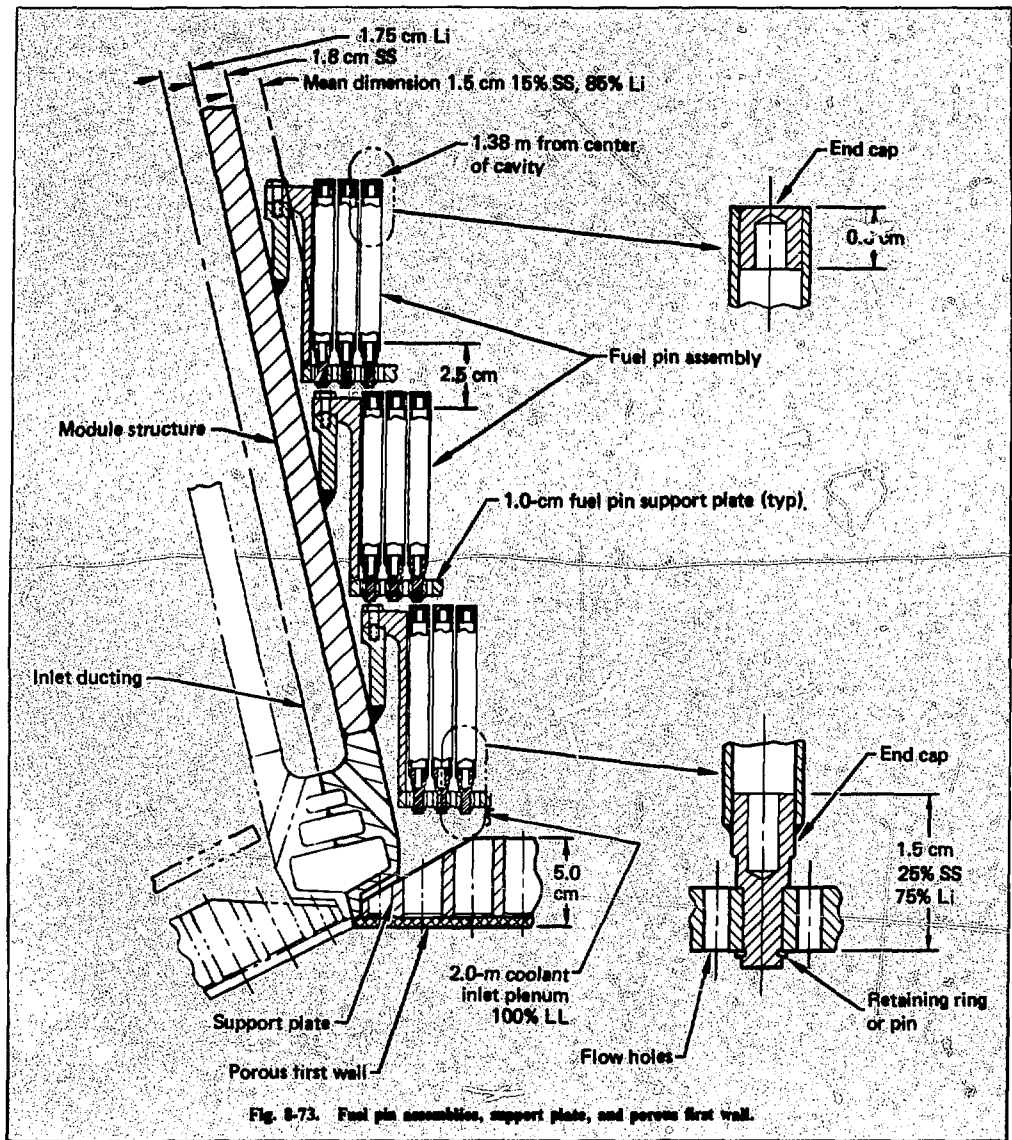
a higher system efficiency for an equal fusion energy gain.

Westinghouse<sup>81</sup> has chosen a very compact structure with a high first-wall loading ( $10 \text{ MW/m}^2$  vs  $1.65 \text{ MW/m}^2$  for the Bechtel design). The reactor consists of a spherical cavity, of 1-m radius, surrounded by a modular blanket to facilitate fuel handling and maintenance procedures. Figure 8-71 is a schematic representation of the reactor. Four of these units are located within the reactor building; three run simultaneously, while one undergoes maintenance. We selected a lithium wetted wall con-

cept to accommodate the high first-wall loading. In this approach, a thin film of liquid lithium protects the first structural wall from x rays and debris produced by the fusion microexplosion.

Figure 8-72 shows the structure of each module; Fig. 8-73 presents a detailed view of the fuel pin assemblies in a module. The compositions of the module zone, are given in Table 8-17. Different fuels were considered: uranium metal alloys, uranium carbide (UC), uranium nitride (UN), spent LWR fuel  $(\text{U,Pu})_{\text{LWR}}$  in metal alloy and carbide form, and metal and uranium carbide fuel with





higher enrichments of plutonium (3 and 5%). The most attractive fuel appears to be spent fuel from LWR's in carbide form. Spent LWR fuel is attractive because it is cheap and readily available, and the carbide form is preferable because it allows high fuel burnup at the high fuel temperatures resulting from high power-density operation. Table 8-18 lists the composition of the LWR fuel. From an initial

$^{235}\text{U}$  enrichment of 3.1%, the fissile concentration drops to approximately 1.6%. It consists of unburnt  $^{235}\text{U}$  plus two fissile isotopes of plutonium ( $^{239}\text{Pu}$  and  $^{241}\text{Pu}$ ) that are generated from neutron captures in  $^{238}\text{U}$  and  $^{240}\text{Pu}$ .

Table 8-19 gives the operational parameters calculated for all of the fuels listed above. Note that a fast-blanket design using carbide fuel requires a

Table 8-17. Zone compositions for Westinghouse hybrid designs.

Zone	Zone thickness	Zone description	Composition, vol%			
			Design 1	Design 2	Design 3	Design 4
1		Cavity				
2	0.1 cm	Ablative film	100 - Li			
3	2.0	Porous wall	50 - 316 SS; 50 - Li			
4	2.0	Coolant plenum	10 - 316 SS; 90 - Li			
5	2.0	Support plate and coolant	50 - 316 SS; 50 - Li			
6	25.0	"Fuel zone"	15 - Li 23.1 - 316 SS 9.3 - void 52.6 - U-7Mo	15 - Li 23.1 - 316 SS 9.3 - void 52.6 - UC	15 - Li 23.1 - 316 SS 9.3 - void 52.6 - UN	15 - Li 23.1 - 316 SS 9.3 - void 52.6-(U,Pu)C <sup>a</sup>
7	7.0	Fission gas reservoir	75.14 - void; 9.86 - 316 SS; 15 - Li			
8	50.0	Reflector	80 - C; 10 - 316 SS; 10 - Li			
9	20.0	Lithium zone	16 - 316 SS; 84 - Li			
10	30.0	Support plate and coolant	50 - 316 SS; 50 - Li			
11	7.0	Exit plenum	10 - 316 SS; 90 - Li			
12	5.0	Module struct	100 - 316 SS			
13	5.0	Inlet ducting	10 - 316 SS; 90 - Li			
14	10.0	Containment vessel	100 - 316 SS			

<sup>a</sup>U, Pu has composition of spent LWR fuel or higher <sup>239</sup>Pu enrichments (see text).

Pu enrichment of 5% or larger to achieve an energy multiplication greater than 15. The energy multiplication in the LLL/Westinghouse Design is not as high as in other reported blankets because of the high volume fraction of structure (approximately 25%) in the blanket region and the use of natural lithium as the blanket coolant. Additional blanket structure is required because of the high wall loadings (10 MW/m<sup>2</sup>) and power densities selected for the design.

We studied the time-dependent performance of the reactor over a 2-1/2-year operating period for the spent fuel in carbide form. Figure 8-74a shows the increase in energy multiplication and tritium breeding, along with the decrease in the plutonium production rate during burnup. The change of fuel burnup and power density (at maximum and average locations) as a function of time are shown in Fig. 8-74b. The time-averaged values for the energy multiplication, power density, and tritium breeding ratio during the 2.5 years are summarized in Table 8-20, together with the total amount of Pu produced and the total burnup by the end of this period. We must emphasize power density and fuel burnup are parameters that vary in space as well as in time. The values in Table 8-20 are spatially averaged over the dimensions of the fission blanket. Power density and fuel burnup are maximum at the

inner edge of the blanket because of the large fission cross sections for high-energy source neutrons.

The initial tritium-breeding ratio of 0.73 reaches a value of 1.2 at the end of the 2-1/2-year period. The initial tritium-breeding ratio could be increased by enriching the lithium in <sup>6</sup>Li or by reducing the amount of structural and shielding material used behind the fission blanket.

#### 8.6.4 Conclusions

The hybrid reactor design that we completed in collaboration with Bechtel features a cylindrical fast-fission blanket fueled with depleted uranium. The inner radius of the blanket is 5 m with a height

Table 8-18. Typical composition of spent LWR fuel.

Initial U-235 = 3.1% Burnup 32,000 MWD/MTU		
Element	kg/initial MTU	%
U-234	0.14	0.014
U-235	8.6	0.889
U-236	4.0	0.414
U-238	945.0	97.72
Pu-239	5.4	0.558
Pu-240	2.1	0.217
Pu-241	1.3	0.134
Pu-242	0.5	0.052

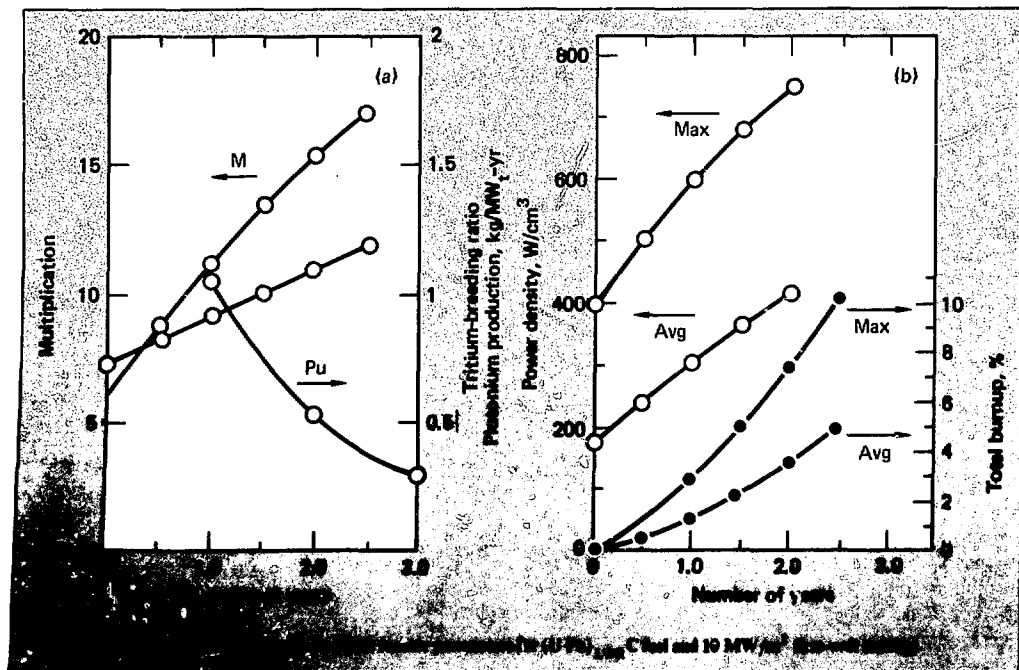
Table 8-19. Operational parameters for several hybrid blanket designs.

Initial operational characteristics <sup>a</sup>	U-7% Mo	UC	UN	(U,Pu) <sub>LWR</sub> -7% Mo	(U,Pu) <sub>LWR</sub> <sup>C</sup>	(U,Pu) <sub>3%C</sub>	(U,Pu) <sub>5%C</sub>
Blanket energy multiplication, M	6.7	5.5	6.3	8.5	6.6	10.4	15.4
Average power density in the fuel, W/cm <sup>3</sup>	173	142	153	223	170	275	414
Net <sup>239</sup> Pu production in kg/MW <sub>th</sub> per year	1.35	1.44	1.15	1.05	1.15	0.73	0.46
Number of fissile atoms per source neutron	1.48	1.31	1.13	1.49	0.25	1.27	1.21
Average burnup, %	0.85	0.90	0.95	1.15	1.10	1.80	2.75
Tritium breeding ratio	0.75	0.78	0.79	0.84	0.80	0.90	1.14

<sup>a</sup>All values normalized to a first-wall fusion neutron fluence of 10 MW/m<sup>2</sup> per year.

of 10 m. The average energy multiplication of the fast-fission blanket for a three-year period is 7.15, and the fissile production is 0.88 kg/MW<sub>f</sub>-yr. This is enough fissile material to fuel approximately six LWR's of equivalent thermal power. By contrast, the hybrid design that we completed with

Westinghouse is a spherical fission blanket fueled with spent LWR fuel. The four reactor chamber vessels employed each have an inner radius of 100 cm. The average blanket energy multiplication for a 2.5-year period is 11 and the fissile production is 0.63 kg/MW<sub>f</sub>-yr. This is enough fissile material to





fuel four LWRs of equivalent thermal power. The results presented here show that the Westinghouse design provides 50% more energy multiplication than the Bechtel design; however, this enhanced energy multiplication is gained at the expense of a 30% reduction in fissile fuel production.

Our earlier neutronic scoping studies identified several attractive features of laser-driven fusion hybrids:

- Hybrids can be designed to meet a broad spectrum of energy-multiplying and fissile fuel-producing requirements.

- Hybrids can operate in a regime that requires an order of magnitude less laser/pellet performance than pure laser fusion.

- Hybrids produce ten times more fissile fuel than breeder reactors.

It is encouraging to note that, in general, these attractive features have remained in this comparative analysis, which has been conducted at a higher level of engineering design detail than the earlier studies. During these more detailed engineering design studies with Bechtel and Westinghouse, we came to several conclusions:

- Laser fusion hybrids should not be designed purely as power producers, because they will cost two to three times more than LWR's and be more expensive than fast breeder reactors. Therefore, hybrids that are plausible must produce fissile fuel for existing burner reactors. (In Fig. 8-70, we show that the cost of electricity in an LWR-hybrid scenario is insensitive to the capital cost of the hybrid. It will increase over present prices by only 20-40% when the hybrid cost is two to three times more than an LWR.)

- Hybrids that produce fissile fuel for existing LWR's can extend the energy available from those economically proven reactors by two orders of magnitude.

- Laser-driven hybrids can accommodate a fission blanket in a more straightforward manner than magnetic confinement systems.

**Table 8-20. Time-averaged values of the operational parameters for the LLL/Westinghouse hybrid.**

	(U,Pu) <sub>LWR<sup>C</sup></sub>
Average energy multiplication	11.0
Average tritium breeding ratio	0.98
Maximum power density in fuel, W/cm <sup>3</sup>	640.0
Average power density in fuel, W/cm <sup>3</sup>	330.0
Total burnup in percent	5.8
Net <sup>239</sup> Pu production in kg/MW <sub>e</sub> -year	0.63

The results presented here have led us to conclude that hybrid studies should remain a continuing and integral part of the laser fusion technology effort. Future studies should seek to establish a closer link between evolving laser fusion performance and the fissile fuel requirements of fission burner reactors. If this is done, it will be possible to maximize the ratio of energy from hybrid-fueled LWR's to hybrid energy, thereby making the cost of electricity in the combined scenario less sensitive to hybrid capital cost.

## References

74. F. Powell, "Proposal for a Driven Thermonuclear Reaction Cover," LWS-24920, U.S. Atomic Energy Commission (1953).
75. D. H. Imhoff et al., "A Driven Thermonuclear Power Breeder," CR-6, California Research Corporation (1954).
76. J. A. Maniscalco and L. Wood, *Advanced Concepts in Fusion-Fission Hybrid Reactors*, Lawrence Livermore Laboratory, Livermore, Calif., UCRL-75835 (1973).
77. J. A. Maniscalco, "Fusion-Fission Hybrid Concepts for Laser-Induced Fusion," *Nuc. Tech.* **28**, 98 (1975).
78. A. G. Cook and J. A. Maniscalco, <sup>235</sup>U Breeding and Neutron Multiplying Blankets for Fusion Reactors, *Nuclear Technology*, **30**, (July 1976).
79. J. A. Maniscalco, *A Conceptual Design Study for a Laser Fusion Hybrid*. [See also L. F. Hansen and J. A. Maniscalco, "Neutronic Study of a Laser Fusion Hybrid Reactor Design," *Proc. 2nd Topical Mtg. on Tech. of Controlled Nucl. Fusion*, Conf-760935-P2, Vol. II, 657(a), 677(b) (1976), Richland, Washington, September 21-23, 1976.]
80. W. O. Allen et al., Laser Fusion-Fission Reactor System Study, Job 12013 Bechtel Corporation Research and Engineering Project Report, June 1976 [also Lawrence Livermore Laboratory Report, UCRL-13720 (1976)].
81. L. F. Hansen, R. R. Holman, and J. A. Maniscalco, "Scoping Studies of Blanket Designs for a Power-generating Laser Fusion Hybrid Reactor," *Transactions ANS* **26** (New York, June 12-16, 1977).
82. "Laser Fusion-Fission Reactor Systems Study," Job 12013, Bechtel Corporation Research and Engineering Project Report (July 1977).
83. J. Hovingh, "First Wall Studies of a Laser Fusion Hybrid Reactor Design," *Proc. 2nd Topical Meeting on Tech. of Controlled Nucl. Fusion*, Conf-760935-P2, Vol. II, p. 675, (Richland, Washington, September 21-23, 1976).

## Authors

**J. A. Maniscalco**  
**J. A. Blink**

## 8.7 Other Civilian Applications

Inertially confined fusion (ICF) has many other civilian applications beyond electric power and fissile fuel production. During 1977, we briefly examined other ICF applications to find those with an earlier economic impact potential than electric power production. In addition, we examined ICF applications that may complement a fusion electric power economy by extending our rapidly depleting natural fuel supplies. The ICF applications we examined include synthetic fuel production, actinide burning, and propulsion.<sup>84</sup>

Synthetic fuel production using ICF cannot have an economic impact prior to fusion power production because it cannot compete with the projected cost of gas from coal gasification. However, the cost of ICF should decrease in a maturing fusion economy, and the cost of our diminishing supplies of fissile fuel will increase. ICF synthetic fuel production can extend our coal reserves when methane is its end product or it can provide an inexhaustible supply of hydrogen to substitute for natural gas.

Burning long-lived actinide waste products from fission reactors by using ICF neutrons does not appear to have a potential short-term economic impact because of severe technology problems. These technology problems are more severe than in a fuel-producing fusion-fission hybrid reactor. If, however, we operate on a fission economy and if society judges the long-term radiological hazards from fission reactor actinides high enough to merit constructing actinide burners, then ICF could best perform the role.

Propulsion systems powered by ICF reactors could be used to drive large aircraft, ships, and extraterrestrial craft. These systems will not have an early economic impact since they must be very reliable, and will be fueled from the excess tritium produced by commercial fusion electric power producers. These propulsion systems will stretch out our natural portable fuel supplies. Aircraft propulsion systems powered by ICF reactors do not appear to be an attractive alternative to chemical-fueled systems because ICF reactors have a lower power density than the current chemically fueled propulsion plants. ICF plants could provide propulsion for intrasolar or interstellar missions in the distant future. Marine propulsion appears to be the least demanding system, with the earliest payoff. Since ICF reactors for marine propulsion also appear to be attractive as small stationary power plants for isolated military and civilian location, conceptual design studies should go forward.

While these other applications of ICF will not have an earlier economic impact than fusion electric power production, they are of interest because they can complement a fusion electric power economy. We present additional details of work on these alternative applications below.

### References

84. J. Maniscalco, J. Blink, R. Buntzen, J. Hovingh, W. Meier, M. Monsler, and P. Walker, *Civilian Applications of Laser Fusion*, Lawrence Livermore Laboratory, Livermore, Calif., UCRL-52349 (1977).

### Author

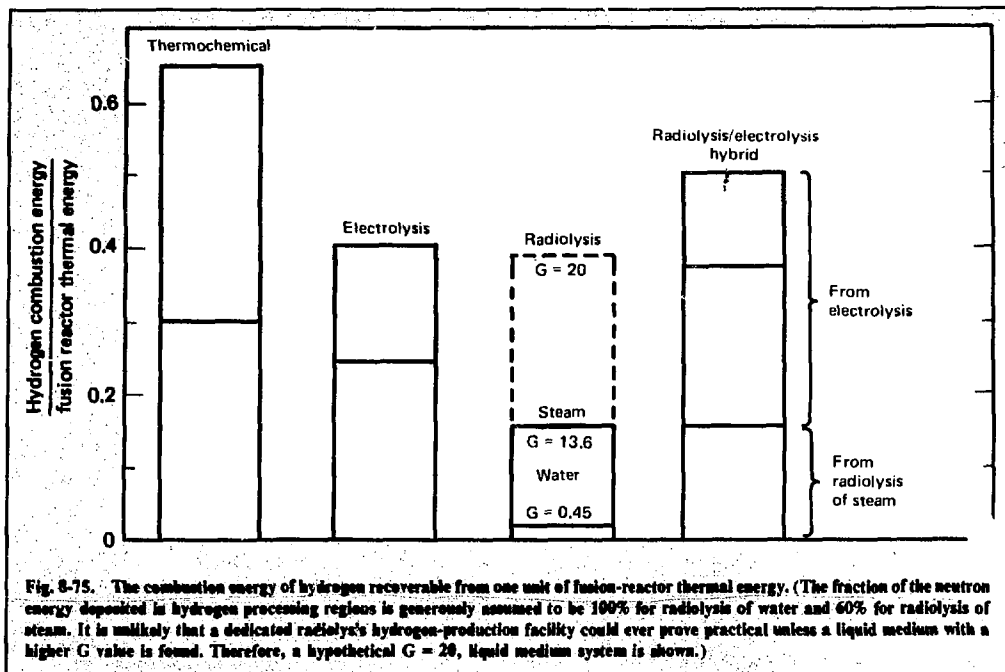
W. Meier

### 8.7.1 Synthetic Fuel Production

Our oil and natural gas supplies are declining rapidly. Hence, the ability to produce large quantities of portable chemical fuels for our homes, industries, and vehicles will be a necessity within the next 100 years. Natural gas has been the preferred fuel for residential heating and industrial-process heat; it is environmentally acceptable, convenient to use, and, until recently, low in cost and in ample supply as a natural resource. Depletion of natural reserves has added emphasis to the search for alternative fuels. The role of hydrogen, both as a fuel and as an intermediate product used in the production of synthetic fuels, is being considered. An example of synthetic fuel production is the reduction of both carbon and carbon monoxide by hydrogen at high temperatures to form methane ( $\text{CH}_4$ ). Methane is the principal constituent (typically about 85%) of natural gas.

Any large-scale, long-range scheme for the production of synthetic fuels should not require further depletion of fossil-fuel reserves. It is inconsistent, for example, to use natural gas when producing hydrogen for use as a substitute fuel. However, the abundance and general availability of water make water an ideal feedstock for hydrogen production processes. A laser fusion reactor could supply the energy necessary to decompose the water, and such a system would represent a virtually inexhaustible source of hydrogen.

Depending on how energy from the fusion reaction is used, water-cracking processes can be classified as thermochemical, electrolytic, or radiolytic. Figure 8-75 compares the various conversion processes on the basis of recoverable hydrogen-combustion energy per unit of thermal energy available.



The thermal energy from the reactor could support a sequence of high-temperature chemical reactions in various hydrogen-producing thermochemical processes. While these thermochemical processes generally do not consume the chemical reactants, they often use large quantities of hazardous and corrosive chemicals. Practical energy-conversion efficiencies for typical thermochemical processes range from about 30 to 65%.<sup>85,86</sup> In other words, up to 65% of the fusion energy is recoverable as thermal energy by burning the hydrogen produced.

Laser fusion reactors could also generate electricity for subsequent electrolysis of water to produce hydrogen. The electricity simply supplies the energy required to decompose water, a reaction that absorbs 68 kcal per mole of hydrogen produced. For existing electrolysis plants, the combustion energy of the hydrogen produced is 60 to 100% of the electrical energy input.<sup>85,87</sup> Assuming a 40% thermal-to-electric conversion efficiency for the laser fusion power plant, the electrolysis process produces hydrogen with an overall energy-conversion efficiency of 24 to 40%.

Hydrogen production by radiolysis can be achieved in several ways, but all require an intense source of radiation. The penetrating neutron radi-

ation of a laser fusion reactor could be utilized for radiolysis by incorporating sufficient quantities of  $H_2O$  in the blanket regions surrounding the fusion vacuum chamber.<sup>86,88</sup>

A concept often used in the discussion of radiation-induced chemical processes is the  $G$  value. The  $G$  value for the formation of a chemical species is defined as the number of molecules produced per 100 eV of energy deposited in the production regions by incoming radiation. The generally accepted  $G$  value for  $H_2$  from water is 0.45, while  $G$  values as high as 13.6 have been measured in experiments using pure steam exposed to high-energy neutrons.<sup>88</sup> Radiolytic hydrogen production is clearly more efficient in steam than in liquid water.

Figure 8-76 is a power-flow diagram for a laser fusion hydrogen-production plant that also generates electricity. Note that more than 25% of the energy released by the fusion microexplosion is carried by the pellet debris, alpha particles, and x rays. This energy is deposited in the vacuum chamber wall and thus is not available for radiolytic decomposition.

Figure 8-76 also shows that  $P_n$  is the total energy deposited in the reactor as a result of neutron interactions with blanket materials. It is important to note that only a fraction  $\alpha$  of the

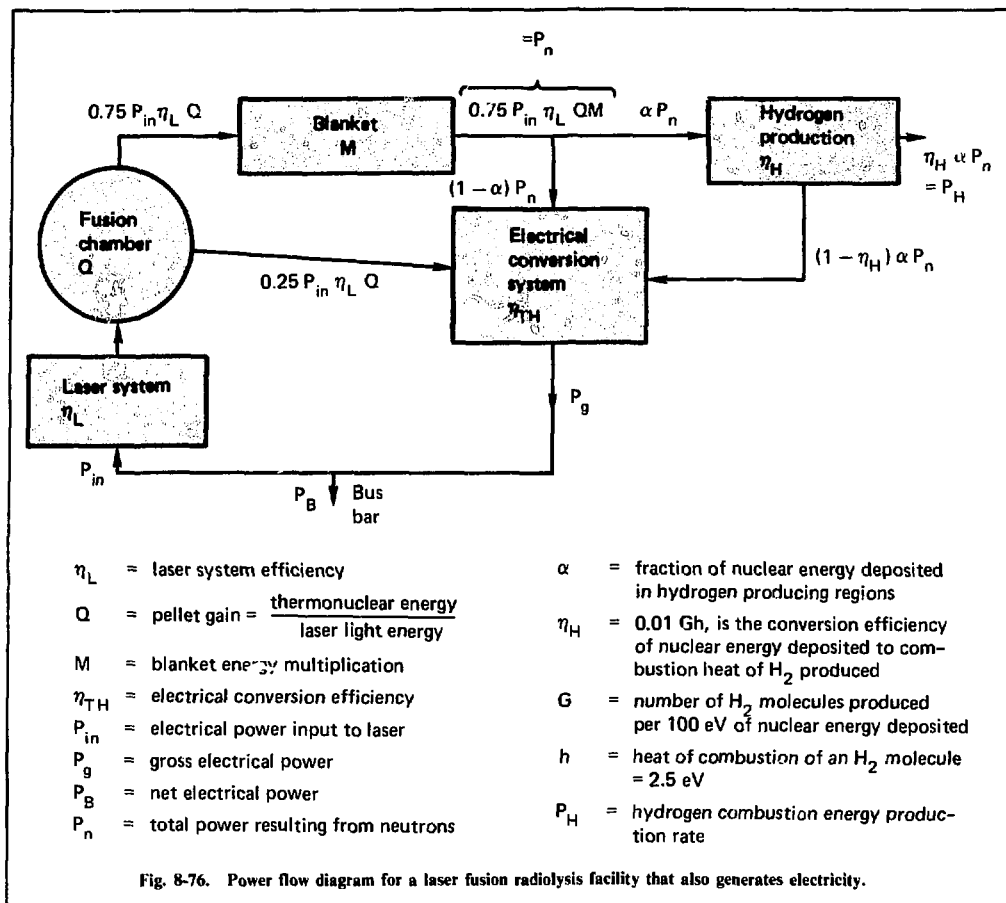


Fig. 8-76. Power flow diagram for a laser fusion radiolysis facility that also generates electricity.

available neutron energy is actually deposited in the steam blankets; the remainder is deposited in reactor structural materials and thus is unavailable for radiolysis of  $H_2O$ . For example, less than 40% of the fusion neutron energy could be deposited in a 3-m-thick region of pressurized steam at 1000 psia. Not all of the nuclear energy deposited in the steam is used in subsequent radiolysis and  $H_2$  production. The term  $\eta_H$  is the conversion efficiency of nuclear energy deposited in the steam to potential combustion energy of the hydrogen produced. It is related to the  $G$  value for the formation of  $H_2$  by

$$\eta_H = 0.01 Gh.$$

where  $h$  = heat of combustion of an  $H_2$  molecule = 2.5 eV.

The maximum experimental  $G$  value of 13.6 results in a value of  $\eta_H = 0.34$ . In other words, 34% of the energy deposited in the steam is converted to potential hydrogen combustion energy, while 66% appears as thermal energy in the system. The total fraction of  $P_n$  that is converted into thermal energy is

$$(1 - \alpha) + (1 - \eta_H) \alpha = 1 - \eta_H \alpha.$$

The product  $\eta_H \alpha$  is an indication of the system efficiency for hydrogen power production, reflecting not only the efficiency in converting deposited nuclear energy to hydrogen but also the efficiency at which this energy is deposited in the hydrogen-producing regions. The overall energy-conversion efficiency is the ratio of the potential

combustion energy of produced hydrogen to the total nuclear energy deposited in all regions of the reactor. As shown in Fig. 8-76, the combustion energy of hydrogen produced is

$$P_H = \eta_H \alpha P_n$$

while the total energy deposited is

$$P_T = P_n + 0.25 P_{in} \eta_L Q = P_n + \frac{P_n}{3M}$$

The overall energy-conversion efficiency is then

$$\eta = \frac{P_H}{P_T} = \eta_H \alpha \left( \frac{3M}{3M + 1} \right)$$

The blanket energy multiplication  $M$  can be increased above 1.0 by adding boron to the steam blankets. Thermal neutrons absorbed by  $^{10}\text{B}$  release 2.35 MeV of high LET radiation according to the reaction



Thus, values of  $M$  as high as 1.2 might be possible.

Using the values of  $\eta_H = 0.34$  (corresponding to  $G = 13.6$  in steam),  $M = 1.2$ , and generously assuming  $\alpha = 0.6$  for a steam blanket, the overall energy-conversion efficiency is only 16%. Liquid water blankets have much lower efficiencies (even though  $\alpha$  may be nearly unity) as a result of the very low  $G$  value of 0.45. This gives a value of  $\eta_H = 0.01$ , and for  $\alpha = 1$  results in an overall energy-conversion efficiency of less than 0.8%.

If tritium-breeding zones are required, they would reduce the fraction  $\alpha$  of neutron energy available for hydrogen production. Because lithium is vigorously reactive with water, special precautions would be required to reduce the potential hazard. Also, because boron absorbs the neutrons required to breed tritium, it could not be used as an energy multiplier. A net reduction in the overall energy conversion efficiency for radiolysis results when tritium-breeding requirements are considered.

Therefore, while radiolytic hydrogen production by a laser fusion reactor may be technically

feasible, it is unlikely that a radiolysis facility using  $\text{H}_2\text{O}$  could prove practical. Near-term R&D efforts in neutron radiolysis should concentrate on chemical schemes that could yield much higher  $G$  values, preferably in liquid media. Chemicals with hydrogen bond energies less than those in  $\text{H}_2\text{O}$  would be likely candidates, and the use of a liquid would offer more efficient energy absorption than a gaseous medium. For example, with a  $G$  value of 20 in a liquid medium, laser fusion radiolysis would have an overall energy-conversion efficiency of 37.5%, which is competitive with the alternative processes for producing hydrogen in a laser fusion reactor (see Fig. 8-75).

An option for the water-based radiolysis system would be the use of the remaining thermal energy ( $\approx 85\%$  of the total) for the production of electricity. The electricity could be sold on the electric power grid or used to generate more hydrogen by electrolysis. The overall energy-conversion efficiency of a radiolysis/electrolysis hybrid system is given by the sum of the overall radiolysis efficiency and the overall electrolysis efficiency applied to the remaining thermal energy; i.e.,

$$\eta = \alpha \eta_H \left( \frac{3M}{3M + 1} \right) + \eta_E \eta_{Th} \left[ 1 - \alpha \eta_H \left( \frac{3M}{3M + 1} \right) \right],$$

where  $\alpha$ ,  $\eta_H$ , and  $M$  are defined as before, and

$\eta_E$  = electric-to-hydrogen conversion efficiency,  
 $\eta_{Th}$  = thermal-to-electric conversion efficiency.

Thus, when the overall radiolysis conversion efficiency is 16%,

$$\eta = 0.16 + 0.84 \eta_E \eta_{Th}$$

As before, if we assume  $\eta_{Th} = 0.4$  and  $\eta_E = 0.6$ –1.0, the overall energy-conversion efficiency for the radiolysis/electrolysis hybrid system is 36–50%.

Current natural gas costs are about \$1 per million Btu but may climb to \$3 per million Btu before the end of the century.<sup>89</sup> The present estimated cost of synthetic gas from coal gasification plants is about \$4.5 per million Btu for the current process to as low as \$3.5 per million Btu for future plants.<sup>90</sup> In situ coal gasification may be able to produce gas at a cost of about \$2 per million Btu.<sup>91</sup>

Table 8-21. Energy source components of the cost of hydrogen.

	Cost of source energy, \$/million Btu	Energy conversion efficiency	Energy source component of hydrogen cost, \$/million Btu <sup>a</sup>
Thermochemical	2.46	0.30-0.65	3.80-8.20
Electrolysis	2.93	0.24-0.40	7.30-12.20
Radiolysis	2.46	0.16-0.38 <sup>b</sup>	6.50-15.40
Radiolysis/electrolysis	2.93	0.36-0.50	5.90-8.10

<sup>a</sup>Does not include cost of chemical processing plant, electrolysis units, or radiolysis components required.

<sup>b</sup>0.16 and 0.38 correspond to G values of 13.6 and 20, respectively.

The cost of hydrogen produced by the various laser fusion-driven processes is at least equal to the cost of energy from the fusion reactor divided by the overall energy-conversion efficiency. For comparison, assume a laser fusion power plant produces electricity at a cost of 25 mills/kWh. (This is comparable to the estimated cost of electricity from LWR and coal stations ordered in 1976 and online in 1985, quoted in 1976 dollars.) Also, assume that the capital component of the electricity cost is 80% of the total and that the electrical power generation equipment comprises 20% of this capital cost. (The turbine generators and building comprise about 20% of a typical LWR capital cost.)<sup>92</sup> At a thermal-to-electrical conversion efficiency  $\eta_{TE}$  equal to 0.4, the cost of energy is \$2.93 per million Btu for processes requiring only thermal energy.

Table 8-21 gives the source-energy components of the cost of hydrogen produced by the various processes. These values reflect only the cost of using a laser fusion reactor as the source of energy for the various processes. Additional costs will vary for the different processes, depending on the cost of the components required. Large electrolysis units, for example, will add approximately \$1 per million Btu to the cost of hydrogen.<sup>90</sup>

It is clear there is no economic incentive for the production of synthetic fuels with laser fusion, at the current price of natural gas nor at the projected cost of gas from coal gasification. Even so, such a system may eventually be required. Oil and natural gas currently account for about 75% of this nation's energy consumption. As these fuels are depleted, the ability to produce large quantities of portable fuel will become a necessity. Laser fusion-driven hydrogen-production processes represent a virtually inexhaustible supply of portable fuel.

## References

85. S. S. Penner and L. Icerman, *Energy: Non-Nuclear Energy Technologies* (Addison-Wesley Publishing Co., Inc., Reading, Mass., 1975).
86. V. C. Rogers, G. M. Sandquist, and R. Baird. "Radiolytic Hydrogen Production from a Laser Fusion System." *Proceedings, Eleventh Inter-society Energy Conversion Engineering Conference*, Nevada, 1976 (American Institute of Chemical Engineers, New York, 1976).
87. *Hydrogen Energy*, R. N. Verziroglu, Ed. (Plenum Press, New York, 1975).
88. N. Vegelatos et al., *Radiolytic Production of Hydrogen Using Laser Fusion*, IRT Corporation, IRT 7020-001 (1976).
89. *The Energy Daily* (Washington, D.C., April 15, 1977), 5, 74.
90. *Nuclear Power Issues & Choices*, S. M. Kenny, Jr., Chairman (Ballinger Publishing Co., Cambridge, Mass., 1977).
91. *An In-Depth Evaluation of LLL's R&D Program for the In Situ Gasification of Deep Coal Seam*, Lawrence Livermore Laboratory, Livermore, Calif., TID-27008 (1976).
92. W. Allen, Bechtel Corporation, San Francisco, Calif., private communication (May 1977).

Author

W. Meier

## 8.7.2 Propulsion Systems

As the cost of the fossil fuels generally used for transportation continues to increase, the demand for nuclear fuels will also increase. To date, fission power has been the only nuclear fuel. Fusion will have no decisive economic advantage (in cost or power density) over fission for marine propulsion, which is the only near-term propulsion application.

Furthermore, fission propulsion technology will be well entrenched when fusion becomes available. Therefore, we don't expect deployment of fusion powered ships unless fission power is eliminated as an alternative due to social or environmental concerns. The established fission propulsion technology could be fueled from laser fusion hybrid reactors to insure a long-term fuel supply if fission propulsion continues to be socially acceptable.

Fusion-powered aircraft do not appear to be feasible from both engineering and environmental viewpoints. Fusion-powered extraterrestrial propulsion systems could be a long-term application of laser fusion.

Nuclear systems of any kind present a potential environmental hazard. In this respect, however, fusion systems have an advantage over fission systems because they use and produce smaller amounts of radioactive elements. The radiation hazards in fusion systems are primarily the tritium supply and radionuclides in the blanket material. A 0.1-kg mass of tritium in the fusion fuel supply amounts to  $10^6$  Ci of uniquely low level biological hazard activity, but that level represents around 1.5 million kWh of usable fusion energy. The blanket material only has  $10^7$  Ci of radionuclides and represents a nonvolatile, localized hazard. A fission reactor, on the other hand, has  $10^{10}$  Ci of very volatile fission products for a power rating of  $10^9$  W<sub>e</sub> ( $3 \times 10^5$  mechanical hp).<sup>93</sup>

Nuclear-power propulsion systems will become more and more attractive as the price of oil rises, and less environmentally sensitive countries might pursue such alternatives vigorously. Ultimately, fusion, fission, and fossil-powered systems will have to compete on a system-by-system basis. Tradeoffs of performance, cost, and environmental effects will be used to select a system for a given role.

A propulsion plant must be capable of operating at a range of power levels. Laser fusion

will have power level flexibility through the ability to quickly vary either the pulse rate or the pellet yield.

Much of the considerable experience gained in marine nuclear-fission propulsion is applicable to the fusion system concept. Both fission and fusion systems have high technology costs, high fixed costs, and low fuel costs relative to fossil systems. Fusion fuel costs for material consumed will be negligible, but production costs might be quite high. Nuclear power (and fusion in particular) is essentially clean power, reducing pollution caused by fossil fuel combustion. Moreover, the prime candidates for marine nuclear propulsion are ships of high horsepower—larger, faster ships. This implies a reduction in the absolute number of ships needed to carry any given cargo tonnage, a situation that has safety and environmental advantages.

**Engineering Considerations for Fusion Propulsion.** In general, a fusion reactor power plant for a propulsion system must be designed for minimum specific volume and mass. Thus, the reactor will operate with a high first-wall loading. Details on the specific volumes and masses for several types of propulsion applications are shown in Table 8-22.

Fusion gain  $\eta_L Q$  (the ratio of the thermonuclear yield to the electric power driving the laser system) must be large for a reasonable system efficiency and a small specific volume and mass. For anticipated laser system efficiencies, the volume and mass of the laser system per unit of power input to the laser (power stored) is roughly constant. Therefore, the larger the fusion energy gain, the smaller the *laser system* specific mass and volume.

Reactor-chamber optical and first-wall materials, in which the short-ranged microexplosion energy is deposited, must have long lifetimes to increase the vehicle availability and decrease the operating costs. Shielding must be provided to protect cargo, as well as passengers, from the high-

Table 8-22. Summary of propulsion system characteristics.

Application	Technical risk	Power	Constraints <sup>a</sup>	
			Maximum specific mass	Maximum specific volume
Marine				
Navy	Moderate	90 MW <sub>s</sub>	30 kg/kW <sub>s</sub>	80 m <sup>3</sup> /MW <sub>s</sub>
Commercial	Low	90 MW <sub>s</sub>	90 kg/kW <sub>s</sub>	200 m <sup>3</sup> /MW <sub>s</sub>
Airborne	High	130 MW <sub>s</sub>	0.4 kg/kW <sub>s</sub>	1.5 m <sup>3</sup> /MW <sub>s</sub>
Space	Highest	130 GW <sub>t</sub>	0.05 kg/kW <sub>t</sub>	Not critical

<sup>a</sup>Maximum permitted for competition with other options. Conversion factors: 1 kg/kW = 1.6 lb/hp; 1 m<sup>3</sup>/MW = 26 ft<sup>3</sup>/khp.

energy neutrons. In addition, the reactor system and other vehicle components that are subject to neutron activation or that collect activated material must be easily accessible and designed for remote maintenance. Although these considerations are not discussed in detail in this report, they must be considered in designs of fusion propulsion applications.

**Terrestrial Laser Fusion Propulsion.** Terrestrial propulsion systems, including marine and aircraft propulsion, will probably operate on a parasitic, DT fuel cycle using tritium produced in larger stationary fusion reactors. The first wall of the reactor will be a dry wall and will either be magnetically protected or covered with a sacrificial liner. The use of a wet wall or fluid wall will be possible only if the reactor is mounted on a stable platform.

The reactors will operate on a Brayton cycle with helium, rather than a liquid metal as a cooling medium to minimize the hazard in the event of an accident.

The blanket for thermalizing the 14-MeV neutrons will consist of graphite with cooling passages for the helium. The porosity of the 2-m-thick blanket will be about 50%, and it will be divided into two zones of equal thickness. The inner half of the blanket will be graphite to thermalize the neutrons. The outer half of the blanket will be  $B_4C$  which will thermalize and capture the remaining neutrons.

To minimize the specific volume and mass, the reactor must operate with a high first wall flux. To achieve a long lifetime with a given power and flux, it is desirable to operate with small microexplosions and a high PRF. The size of the microexplosions and reactor gain decrease with a decrease in the laser output energy. Thus, a required reactor performance can be determined explicitly for a specific mass, volume, and lifetime. This required performance must be checked with laser energy—pellet gain relationships to determine that the reactor performance will satisfy the total-system power requirements.

Approximately two-thirds of the tritium used in the pellets will not be burned. The unburned tritium from the microexplosions must be collected by a vacuum system and stored aboard the vehicle while it is in transit. This requirement is based on economics, as well as on the radiological hazards associated with the tritium.

Advanced systems may directly convert the charged-debris energy to drive the lasers and the vehicle auxiliaries. The neutron energy will be used to drive the turbines using a Brayton cycle.

**Marine Laser Fusion Propulsion.** Fission-powered ships are already in wide use, and laser fu-

sion reactors will have environmental advantages over their fission counterparts. Furthermore, the cost and performance of laser fusion reactors are estimated to be comparable to fission reactors. With the continuing rise in fossil fuel prices, both fission and fusion propulsion systems promise to be economically competitive. They have the additional advantage that refueling at sea or in foreign ports is not required.

The technology involved in marine laser fusion applications closely follows the development of fission marine propulsion systems. Design requirements for fusion-propelled ships are based on what has been learned from the widespread fission marine technology.

Requirements, however, differ according to the needs of the ship owners. Ships intended for military use have different requirements than those intended for commercial use (see Table 8-22). Military ships need to be fast and maneuverable, with low specific-weight and specific-volume propulsion systems. Commercial uses tend to emphasize the economic aspects of the laser fusion-driven propulsion units.

Superconductivity will strongly influence Navy power in the future because, above about 20,000 hp, it provides the minimum weight, space, and component systems to convert mechanical to electrical energy and vice-versa. This will provide more flexibility and more operational freedom.

A number of new ship concepts will be tested by the Navy in the next decade. Successful designs will be placed in service near the end of this century and potentially could be propelled by fusion power plants. Table 8-23 lists these ship concepts and their planned displacement and speed ranges.

The shaft horsepower (shp) requirement for each ship concept varies considerably and depends on internal design features, such as weapons/sensor suite and auxiliary power loads. Figure 8-77 shows the specific power requirements of the ships from which shp requirements can be identified. The shp is related to the cube of the speed for conventional displacement vessels so that very sophisticated propulsion systems will be needed to meet such a range of requirements. By the year 2000, Navy vessels will require higher speed capabilities to retain certain attack options, and surface-effects ships (SES) or hydrofoils may be utilized.<sup>94</sup> If the SES and hydrofoils are powered by nuclear reactors having low specific weight and volume ratios, they could exhibit essentially unlimited range, rapid response speed, and no need of fuel supply ships and foreign ports.

Figure 8-77 includes the fuel weight for conven-



Table 8-23. Ship types under consideration by the Navy.

	Displacement, tons	Speed, knots	shp, 10 <sup>3</sup> hp
Conventional displacement	>20,000 (carrier)	< 35	250
	>10,000 (escort)	≤ 35	100
	>3,000 (patrol)	≤ 35	40
Small waterplane area twin hull (SWATH)	>10,000 (carrier)	< 35	200
	>3,000 (escort)	≤ 50	120
Hydrofoil	<3,000 (patrol)	≤ 65	300
Surface-effects ship (SES)	2,000 (patrol)	≤100	140
	8,000 (escort)	≤100	800
Submarine	<10,000 (FBM)	≤ 30	60
	<4,000 (attack)	≤ 50	120

tional ships. Depending on endurance, a considerable amount of fuel is consumed on conventional ships that could be part of a fusion propulsion plant of increased payload fraction.

The trend in naval propulsion is to greater shp and lower specific weights and volumes. Fusion systems, on this basis alone, must have performance goals that equal the minimum requirements for the larger combatants of the future. These ships will probably fall in the 10,000-ton displacement range and require 100,000 to 500,000 shp at specific weights and volumes of less than 30 kt/kW<sub>s</sub> (50 lb/shp) and 80 m<sup>3</sup>/MW<sub>s</sub> (2 ft<sup>3</sup>/shp). Presently, for instance, a 4000-ton nuclear submarine has a power-plant specific volume of 160 m<sup>3</sup>/MW<sub>s</sub> (4 ft<sup>3</sup>/shp).

An SES weighing 8000 tons and powered by four low-specific-weight fission units of 200,000 hp each has been studied. It would have a payload capability of 1900 tons. For comparison, a fossil-fueled ship, carrying the same payload 3500 nautical miles with the same speed capability, would have a gross weight of about 17,600 tons and require at least 1.5 million hp. The lower ship cost and reduced fuel costs of the nuclear propelled ships are substantial economic advantages and are well worth development effort by the Navy.<sup>95</sup>

Fusion propulsion systems for commercial marine applications, unlike those for military applications, are not built to the lowest specific weight or volume specifications. Economics are a much more important consideration. As before, the dis-

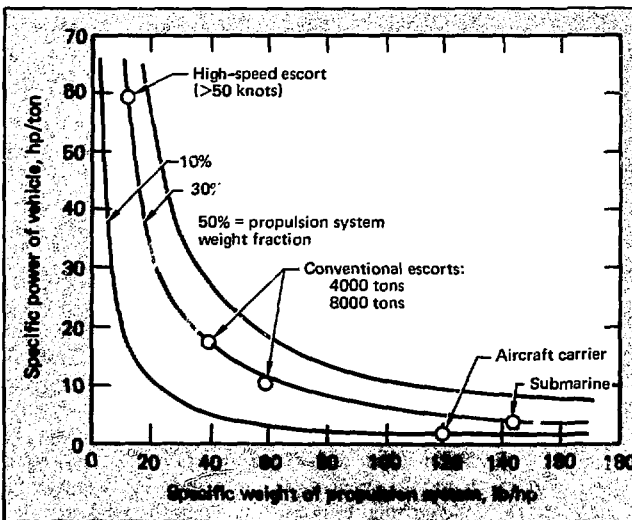


Fig. 8-77. Propulsion-system specific weights for Navy vessels.

cussions about the potential for fusion-powered commercial ships are based on analyses and experience with nuclear fission propulsion.

The commercial maritime industry has been unable to sustain major research and development efforts; consequently, most important advances have been adapted from other industrial or military technology. Naval propulsion-machinery research and development programs have been particularly significant. Therefore, fusion propulsion systems will probably not be installed in commercial ships unless they are first developed for military use.

The selection of ship size and speed are the most important design decisions confronting a prospective owner. Conventionally, with fossil fuel systems, the speed has been kept lower than is commercially desirable because of the high costs required to increase them only slightly. There has been, however, a steady increase in the size of ships because larger sizes take only a little more power. Typical relationships between size, speed, and power for conventional bulk carriers are illustrated in Fig. 8-78.<sup>96</sup> The dramatic increase in the power required for increased speed is clearly shown. Fusion-powered container ships and tankers will probably be in the 250,000 to 450,000 dwt class with propulsion power of about 120,000 hp.

Fusion propulsion in the sea-going submersible cargo/tanker ship would be feasible in the 25- to 30-knot range. Below that, the speed-power ratio is too low to benefit from the addition of fusion propulsion.

Another future concept applies to tankers operating in icing conditions. It is projected that a single 400,000-ton displacement, semisubmerged tanker<sup>97</sup> could transport more than twice as much as two conventional tankers. The propulsion requirement for this ship is, again, in the 125,000 shp range.

It appears that, if nuclear (fission) propulsion becomes competitive with fossil fuel propulsion for merchant ships, the breakeven point will occur first for ships with the following characteristics.<sup>98</sup>

- High power requirements: 100,000 to 120,000 shp or more.
- High ship utilization: short turn-around time in port, small numbers of loading and discharge ports per voyage, and high load factors, i.e., a high ratio of cargo carried to available ship space.
- Large (relative) size: for container ships or other quick-turn-around liner vessels, 15,000 dwt or more; and for tankers, from 150,000 dwt to 300,000 dwt and up.
- Longer trade routes.
- Subsidies: reduce the shipowner's risk and

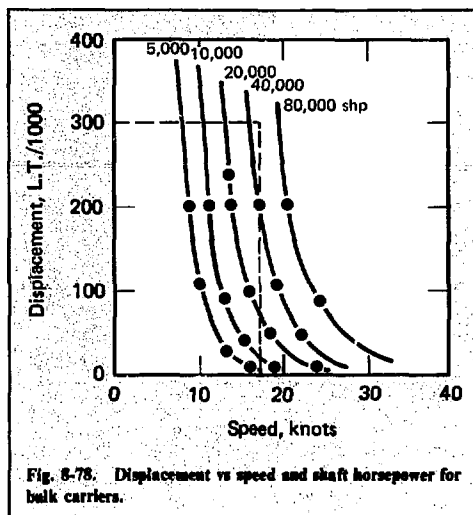


Fig. 8-78. Displacement vs speed and shaft horsepower for bulk carriers.

reduce the break-even point at which the higher capital costs of the nuclear-powered ship are offset by fuel cost savings.

These requirements will most likely hold for commercial fusion propulsion applications as well. Specific weight and volume requirements will be relaxed over those given for Navy ships by a factor of two or more.

A marine fusion reactor propulsion system will operate on a closed Brayton cycle. For a thermal converter efficiency of 35% and propulsion power of 120,000 shp, the reactor thermal power required will be 260 MW<sub>t</sub>. In addition, assuming a power to the laser of 100 MW and to the auxiliary equipment of 50 MW, the total thermal power required from the fusion reactor will be 700 MW<sub>t</sub>. The electric power for the laser and auxiliaries will be produced from a turboalternator.

The thermal power cycle can consist of either a primary coolant cycle only, where the reactor coolant is circulated directly through the turbine-compressor system, or a cycle where the primary coolant heats a secondary coolant, which is circulated through the turbine-compressor system. The tradeoff between the alternative power cycles is a smaller system specific volume and specific mass because of the elimination of a heat exchanger versus the requirement of remote maintenance for the turbine-compressor system.

The laser-system specific volume and mass are about 10 m<sup>3</sup>/MW and 0.3 kg/kW, respectively, based on the power input to the laser. The specific mass of the reactor system controls the design (for

the nonoptimum system selected). With a first-wall flux of  $1 \text{ MW/m}^2$ , the specific volume and mass of the combined laser and reactor system are  $50 \text{ m}^3/\text{MW}$  and  $30 \text{ kg/kW}_s$  respectively. The anticipated lifetime of the first wall is about 25 years for a pulse-repetition frequency of 10 Hz.

Based on these simple calculations for a nonoptimized, highly conceptual fusion reactor system, it appears that small inertially confined fusion reactors with fusion energy gains of about seven could compete with advanced fission propulsion systems.

The reactor proposed for marine propulsion also appears to be attractive as a small stationary power plant for isolated military and civilian applications. Therefore, the development of small stationary power plants can be a spinoff from, or result in the spinoff of, fusion-powered propulsion plants.

**Aircraft Propulsion.** As with marine propulsion, some experience gained in the development of fission reactors for aircraft propulsion can be applied to the development of fusion reactors. This experience is embodied in what remains from the Aircraft Nuclear Propulsion (ANP) project, which was terminated in the early 1960's. This program was plagued with unpredictable technical problems associated with the helium and liquid-metal-cooled reactors of that era and with components, such as air-heat exchangers, bearings, pumps, seals, and the reactor-shield assembly. These problems, as well as uncertain cost benefits and, finally, public concern about the risk involved, led to the demise of the program. The latter problem is still of concern with aircraft nuclear propulsion.

Because of increased public environmental awareness, it is unlikely that any nuclear-powered aircraft (fission or fusion) will be built even if it is technically feasible. If these concerns disappear, the following potential applications for long-range nuclear-powered aircraft can be visualized for both land-based and sea planes:

- Logistic aircraft employed for carrying commercial cargo and for rapid military-force deployment.
- Patrol aircraft for forward defense against submarine-launched ballistic missiles, terminal defense against ballistic missiles, command and control, warning and command, and ICBM launch surveillance.
- A strategic-missile carrier.

In this article, we discuss only the commercial cargo application. The allowable fusion reactor mass is based on the chemical fuel load it displaces. Reactor masses and powers are converted to maximum allowable specific mass for several large

**Table 8-24. Maximum fusion reactor specific mass for several aircraft gross weights.**

Aircraft gross weight, $10^6 \text{ lb}$	0.8	1	2	10
Total aircraft cruiser power, $\text{MW}_t$	170	200	360	1600
Maximum reactor specific mass <sup>a</sup> , $\text{kg/kW}_s$	0.9	0.5	0.4	0.25

<sup>a</sup>Additional  $\Delta V$  can be used during the mission, to reduce the transit time.

proposed aircraft in Table 8-24. The table shows that as aircraft size (hence, reactor size) increases, the allowable reactor specific mass decreases. However, since larger systems will use their mass more efficiently, this relationship is not immediately prohibitive. Small reactor systems probably cannot compete economically with chemically fueled aircraft because of their high capital cost per unit of power. The increase in fossil fuel prices over the last decade could change that evaluation; however, the higher cost estimated for fusion reactors compared to fission systems\* will offset the chemical fuel price increase to some degree. Therefore, we consider the design of an ICF reactor for a two-million-pound aircraft. This design must have a specific mass of less than about  $0.4 \text{ kg/kW}_t$  to avoid displacing payload. A maximum specific volume constraint of about  $0.5 \text{ m}^3/\text{MW}_t$  must also be satisfied, but it is more speculative because the reactor mass distribution will not match the chemical-fuel load distribution it replaces.

A fusion-reactor for an aircraft propulsion system will operate on an open Brayton cycle. Assuming a thermal-converter efficiency of 35% for a cruise power of  $125 \text{ MW}_s$ , the reactor thermal power will be  $360 \text{ MW}_t$ . For a laser input power of  $95 \text{ MW}$  and auxiliary equipment input of  $10 \text{ MW}$ , the total thermal power required from the reactor is  $650 \text{ MW}_t$ . The electric power for the lasers and auxiliaries will be produced from a turboalternator.

The energy transfer from the reactor to the air passing through the compressor-turbine combination can consist of a primary cycle to the combustion chamber, or of a closed primary cycle driving

\*Based on cost estimates of a laser fusion hybrid electrical plant.

<sup>†</sup>The specific mass based on power supplied to the engines during cruising. Power recirculated to the fusion reactor and temporary power surges during takeoffs are not considered.

an open secondary cycle to the combustion chambers. The one-loop cycle is desirable because of its lower specific volume and mass.

For the reference reactor, the first-wall flux must be greater than  $10 \text{ MW/m}^2$  even if only the reactor (without the laser system) is to satisfy the maximum specific volume and mass constraints. If the effective density of the blanket material were somehow reduced by a factor of 5 without degrading performance, the product of thermal-converter efficiency and fusion gain must be 3.3 for the reactor alone to satisfy the maximum specific mass constraint with a first-wall flux of  $10 \text{ MW/m}^2$ . However, the specific volume of the reactor alone would still be higher than the maximum permitted specific volume.

Thus, based on these kinds of calculations, it appears that a laser fusion power plant for aircraft propulsion is not technically feasible because it will not be able to compete with chemical or fission systems on a specific mass or volume basis.\*

**Extraterrestrial Laser Fusion Propulsion.** Two primary applications of fusion propulsion in space are presently visualized: an earth-moon shuttle or ferry and a interplanetary spacecraft for manned missions. The applications can take advantage of the enormous gain in specific impulses<sup>†</sup> relative to chemical rockets. Nucleons are accelerated in fusion reactions to velocities on the order of  $10^7 \text{ m/s}$ , theoretically making impulses on the order of  $10^6 \text{ s}$  obtainable.<sup>93</sup> Chemical rockets have specific impulses limited to less than 450 s. Fission systems are limited to specific impulses of less than 2000 s.<sup>99</sup>

Spacecraft capability is normally measured in terms of  $\Delta V$ .\*\* This index is the sum of all propulsive energy required for translations between stable orbits throughout the entire mission in units of feet per second. The  $\Delta V$  is a function of the specific impulse of the propulsion system and the payload and spacecraft structure fractions. Approximate  $\Delta V$ 's for various missions are given in Table 8-25.

Chemical systems, because of their low specific impulses, have  $\Delta V$  values most suitable for near-earth operations. For example, if a chemical system was designed to make a manned Venus reconnaissance, the payload fraction would be negligible.

**Table 8-25. Spacecraft capability required for various missions.**

Mission	$\Delta V, \text{ f/s}^a$
Escape from Earth's gravity	$40 \times 10^3$
Round trip from an Earth orbit to the Moon's surface	$40 \times 10^3$
Manned Venus reconnaissance	$150 \times 10^3$

<sup>a</sup>Additional  $\Delta V$  can be used during the mission to reduce the transit time.

Even with an advanced fission/chemical staged rocket (nuclear stage specific impulse of approximately 1200 s) the payload would only be about 2% of the total vehicle weight.

Reasonable translunar shuttle times should be on the order of 24 hours. A fission system with a  $\Delta V$  of 43,000 f/s, i.e., 3,000 f/s more than required, could make the trip in the 24 hours specified. Fusion systems with abundant  $\Delta V$  could make the trip much faster so that local maneuvers would consume a large part of the transit time. Such a high-performance vehicle has been postulated, using a laser fusion propulsion system. Figure 8-79 gives the calculated performance for a  $0.55 \times 10^6$  specific-impulse system which produces 130 GW<sub>t</sub> and weighs approximately 300 tons.

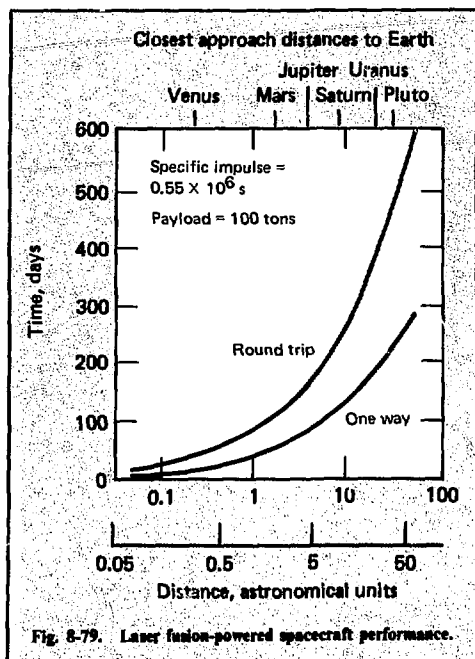
A laser-fusion extraterrestrial propulsion system will consist of a sustained series of fusion microexplosions within an axially asymmetric magnetic mirror (Fig. 8-80). The thrust of the vehicle is produced by the redirection of the charged plasma debris from the microexplosion through the larger of the mirror-loss cones and out the rear of the spacecraft.

The power plant of a specific-impulse-maximizing spacecraft bears very little resemblance to that used in terrestrial propulsion systems. Thrust is no longer produced as a by-product of a thermal cycle, but directly in the form of plasma debris from the fuel pellet. Neutrons and x rays produced in the fireball are worse than useless; if intercepted, their energy must be rejected to space. The target design must maximize the ratio of ion energy to neutron and x-ray energy, while at the same time minimizing required laser energy. Vehicle mass is dominated by the need for heat rejection to space—which must be done radiatively. Waste heat is developed in two ways: component inefficiencies and neutron and x-ray interception. The above factors dictate an unenclosed thrust chamber so that

\*This assumes that the same fraction of the aircraft is devoted to payload.

<sup>†</sup>Specific impulse = impulse per unit weight, i.e.,  $(ma)\Delta t/(mg) = (\Delta v/\Delta t)\Delta t/g = \Delta v/g$  (unit is time).

\*\*This is the spacecraft  $\Delta V$ . In the definition of specific impulse,  $\Delta v$  refers to the velocity of the driving particles.



less than 2% of the solid angle seen by the microexplosion is occupied. Thus, while charged particles are redirected by the magnetic mirror providing thrust, most of the unwanted neutrons and x rays escape to space harmlessly. Only 2% of the neutrons hit the superconducting-magnet radiation shields, payload shadow shields, and laser beam mirrors. Even this 2% represents a large heat-rejection load, but it has some value because it permits tritium breeding in the lithium shields.

The optimal pellet is an intermediate  $\rho R$  design, mostly deuterium with just enough tritium to facilitate ignition. Such a pellet burns far more efficiently than low  $\rho R$  pellets that require a smaller specific laser size. Furthermore, it allows laser reexcitation energy to be produced by direct conversion from the interaction of the charged plasma debris with an induction coil. Between 50 and 70% of the fusion energy is in charged debris from the microexplosion.

Hyde, Wood, and Nuckolls did two slides on rocket propulsion with laser-fusion microexplosions.<sup>93,100</sup> Their design utilizes heat-pipe radiation to dump the neutron and photon heat from the structure, radiation shields, and lasers into space. The lithium for tritium breeding is circulated using MHD pumps utilizing the existing mirror magnetic field.

Three major propulsion-system components are vulnerable to meteoroid damage. The laser and coil shield must be made almost invulnerable to meteoroid damage; therefore, they are protected by a double-wall bumper shield. The heat pipes are protected by only a single wall, and the loss of a portion of them has been anticipated in the design.

Hyde et al. estimate the total propulsion-system mass to be 300 tons, distributed as shown in Table 8-26. About 112 tons of laser system mass and 14 tons of the thrust chamber mass are from their heat-rejection systems. Thus, the mass of the heat-rejection system constitutes 40% of the total mass of the propulsion system. The neutron shield mass in the thrust chamber is 20 tons while the mass of the coils in the thrust chamber is about 15 tons.

The specific-impulse-maximizing spacecraft study includes a pellet design that requires 1 MJ of laser light from a 33% efficient electron-beam-excited system. The total yield from the microexplosion is 260 MJ, with 120 MJ producing thrust. The power needs of the propulsion system are almost exclusively those of the laser because refrigeration and  $\text{Li}^6$ -pumping power are negligible. For a PRF of 500, the system develops 2.2 tons of thrust at a specific impulse of  $5.5 \times 10^5$  s, or an exhaust velocity of  $6 \times 10^6$  m/s. For a spacecraft with a 300-ton propulsion system and a 200-ton deuterium fuel load, a payload of 100 tons can make a round trip to any point in the solar system in one year. Interstellar missions of a few decades in transit time are also feasible with a laser fusion propulsion system.

**Conclusions.** Laser fusion reactors for propulsion (as they are now viewed) would operate in a low-yield, high-PRF mode with high first-wall fluxes. From inertial considerations, the first wall should be a dry wall rather than a wet or fluid wall. These reactors could operate on a parasitic fuel cycle from larger stationary fusion-power reactors.

Table 8-26. Mass of spacecraft fusion propulsion system.

Component	Mass, tons
Propulsion system (total)	300
Laser system	151
Thrust chamber	54
Energy distributor	17
Refrigeration	9
Tanks	25
Miscellaneous parts	44



Fig. 8-80. Laser fusion-powered extraterrestrial spacecraft.

Although there is an apparent need for advanced, low-fuel-cost propulsion systems, it is too early to determine if laser fusion will be an economical alternative to future chemical or fusion plants for marine propulsion. Aircraft applications appear even more uncertain because of the stringent specific volume and mass technical constraints. Laser fusion propulsion plants for extraterrestrial propulsion are possible, provided there is a demand for interplanetary or interstellar missions.

## References

93. R. Hyde, L. Wood and J. Nickolls, "Propulsion Applications of Laser-Induced Fusion Microexplosions," *Proc. First Topical Meeting on the Technology of Controlled Nuclear Fusion*, 1, 159 (San Diego, Calif., 1974).
94. R. J. Creagon, *Power and Energy—Navy—2000 A.D.*, Marine Board of National Research Council (August 6, 1975).
95. F. R. Riddell, *Effect of Specific Weight and Volume Changes in Power Machinery on the Size and Speed of Submarines—A Preliminary Analysis*, IDA Paper P-1233 (December 1976).
96. *Oceanborne Shipping: Demand and Technology Forecast—Part I*, Litton Systems (June 1968).
97. "Semi-Submerged Tanker for Arctic Waters," *The Naval Architect* (May 1975).
98. *Nuclear Merchant Ships*, National Academy of Sciences, Maritime Transportation Research Board (1974).
99. H. F. Crouch, *Nuclear Space Propulsion*, (Astronuclear Press, Granada Hills, Calif., 1965).
100. R. Hyde, L. Wood, and J. Nickolls, "Prospects for Rocket Propulsion With Laser-Induced Fusion Microexplosions," *AIAA/SAE 8th Joint Propulsion Specialist Conference Paper 71-1063*, New Orleans, Louisiana, November 1972.

## Authors

J. Hovingh

R. Buntz

J. Blink

### 8.7.3 Actinide Burning

**Introduction.** The neutrons from DT-fusion systems can convert long-lived fission waste products (primarily actinides) to short-lived or stable isotopes. This method could serve as a mechanism to relax requirements for long-term geological storage of high-level radioactive wastes. Actinide half-lives are quite long, even in comparison to such geological phenomena as ice ages and earthquake fault movements. Storage of long-lived wastes is difficult because these events can render a disposal area unacceptable.

If the fission products in disposed high-level waste generated from spent commercial power reactor fuels are allowed to decay naturally, the long-lived actinides in the waste will dominate the hazard after only 400 years. Although it is not possible to eliminate the long-term hazard, it can be substantially reduced (more than two orders of magnitude) via a two-step waste recycling process consisting of waste partitioning (or separation) followed by actinide transmutation (primarily burning by fission). In the partitioning step, the bulk of actinides are separated from the disposed waste. They are then shipped to an actinide transmutation reactor to be destroyed. To achieve the desired reduction in the disposed waste hazard, separation factors of 99.99% plutonium; 99.9% uranium, americium, curium, and iodine (a fission product); and 95% neptunium are required.<sup>101</sup> Because this represents a considerable advancement beyond the 99.5% separations currently achieved for uranium and plutonium, it is expected that partitioning technology will require significant development.

Ideally, to achieve the maximum possible disposed waste hazard reductions, the separated actinides should be entirely destroyed in the actinide burner. However, the actinides cannot be entirely fissioned during a single fuel cycle period that is limited by the fuel element damage rate and fission product buildup. Thus, the remainder of the actinides (unburned) are discharged from the actinide burner. These will be reprocessed again, supplemented with fresh actinides from fission reactors, and charged as fresh fuel to the actinide burner. Some actinides initially charged to the actinide burner will constitute an additional feed to the disposed waste stream because of the reprocessing inefficiency.

A consequence of the above is that a principal figure of merit for an actinide burner will be the average, or mean, life of an actinide atom in the actinide burner, divided by the actinide burner fuel cycle period.<sup>102</sup> This ratio determines the actinide

burnup, which in turn determines the additional number of recycles that an average actinide atom in the system experiences before it is burned. In this sense, the total long-lived hazard of a unit of disposed fission fuel is a function of the separation factor and the number of recycles required.

To minimize the total disposed hazard, three goals for an actinide partitioning transmutation scheme are apparent:

- High separation factors.
- Short in-reactor actinide mean life.
- Long fuel cycle period (high burnup).

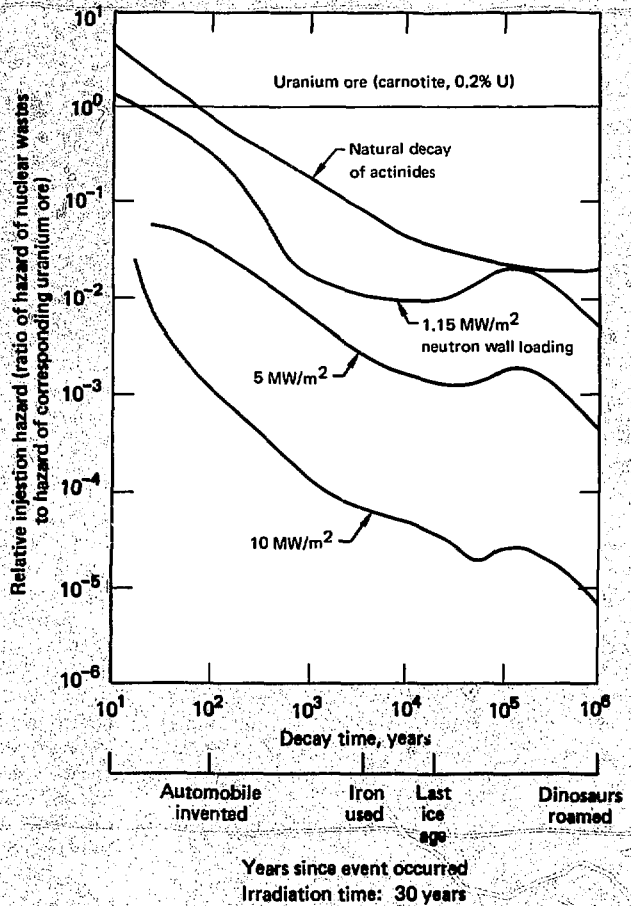
In addition, a fourth goal would be to maximize the actinide throughput to service as many fission reactors as possible. Finally, a fifth goal, relevant to the case in which a final charge of actinides is to be burned in situ, is that the long-term hazard of irradiated actinides should be several orders of magnitude less than the hazard associated with a full charge of unirradiated actinides. Of course, these goals neglect the significant, and perhaps prohibitive, short-term hazards associated with the increased circulation of actinide wastes during the partitioning and transmutation process.

Several studies have investigated the possibility of recycling actinide wastes in thermal fission reactors<sup>103</sup> and fast breeder reactors.<sup>104</sup> These studies have shown that it is possible to burn actinides in fission reactors and that the process is more efficient in the harder neutron spectra of fast breeder reactors. Logically, fast-neutron-rich fusion systems could even more effectively serve the same role. Two studies of actinide burning in fast spectrum fusion reactor blankets have been completed.

**WFPS Study.**<sup>105</sup> An EPRI-sponsored Westinghouse study was based on a beam-driven Tokamak fusion-fission hybrid reactor used for actinide depletion. Intended for mid-to-late 1980's technology, this reactor provides a fusion neutron wall loading of approximately 1 MW/m<sup>2</sup>, corresponding to approximately 10<sup>14</sup> n/cm<sup>2</sup>·s in the 14-MeV energy range. The fission blanket is fueled with actinides contained in the high-level waste from the LWR-U cycle. The Mo-TZM clad actinide oxide fuel is primarily comprised of <sup>237</sup>Np, <sup>241</sup>Am, and <sup>243</sup>Am, which represent almost 90% of the partitioned actinides and the principal contributors to the very long-term radioactive hazards in LWR waste. These actinides are the only fissionable material contained in the helium-cooled blanket, but they provide sufficient neutron multiplication for neutron fluxes in the range of 10<sup>5</sup> n/cm<sup>2</sup>·s.

The WFPS report analyzed the reduction of the long-term hazard of actinides charged to the reactor

Fig. 8-81. Comparison of relative ingestion hazards from actinides as functions of decay time.



rather than the reduction of the overall long-term hazard of the disposed waste (including the actinides added to the disposed waste after each recycle of the fuel). In this sense, the long-term hazard of actinide waste irradiated for 30 years at 1.15, 5, and 10 MW/m<sup>2</sup> was investigated. For all three cases, the same average thermal blanket power (13,000 MW) was achieved by lowering the actinide "enrichment" (and thus blanket criticality) with increasing wall loadings. The relative ingestion hazard vs decay time is shown for the three wall loadings in Fig. 8-81. The relative ingestion hazard is an index that consists of the ratio of the ingestion hazard of a given amount of high-level nuclear waste to the ingestion hazard of the amount of naturally-occurring parent uranium ore from which the wastes were

produced. Formulation of a relative hazard index on this basis is considered to be a realistic measure of the effects of high-level wastes, because it compares the hazard potential of wastes with that of naturally occurring radioactive substances which would exist if the uranium was not used in the LWR. However, concentration effects which make the waste hazard per unit volume much greater for the irradiated waste than the parent ore are not indicated through the use of this index.

For a neutron wall loading of 1.15 MW/m<sup>2</sup>, the hazard index of the irradiated actinides initially decreased relative to the natural decay curve. At 10<sup>5</sup> years, however, it increased back to the natural decay level. These results were similar to those generated in a BNWL study of actinide irradiation



in a moderated neutron spectrum, beryllium blanket.<sup>106</sup>

Although the initial depletion rates of actinide species loaded into the Westinghouse actinide burner are several orders of magnitude higher than the natural-decay rates, it was found that neutron absorption dominates over fission. Because of this effect, considerable quantities of  $^{238}\text{Pu}$ ,  $^{244}\text{Cm}$ , and  $^{242}\text{Cm}$  are produced before ultimately fissioning. The net effect of producing these nuclides is a *significant increase in the hazard index in the first few years of irradiation*, because of the relatively shorter half-lives of  $^{242}\text{Cm}$ ,  $^{244}\text{Cm}$ , and  $^{238}\text{Pu}$  when compared to the other actinides. Additionally, the  $^{242}\text{Cm}/^{238}\text{Pu}$  decay chain gives rise to very radiotoxic long-term daughter products. In fact, all the actinides associated with fission reactor waste will create a dozen or so radioactive daughter products before decaying to stable Pb or Bi isotopes. Thus, in a meaningful evaluation of the long-term radiotoxicity, one must follow the decay chains for approximately  $10^6$  years to see the effects of radioactive daughter products on the potential ingestion hazard.

In the case of a  $10\text{-MW/m}^2$  wall loading, the Tokamak actinide burner benefits from two effects related to lower actinide concentrations (for constant power) in the blanket. Because lower concentrations (by about a factor of four) lead to lower criticality, the neutron spectrum will harden because of an increase in the ratio of 14-MeV fusion neutrons to about 1-MeV fission neutrons. In the harder spectrum, the capture-to-fission ratio decreases while neutron multiplication from the (n,2n) reaction increases. Also, lower actinide concentrations at constant power imply that the actinide mean life decreases. This has the effect of depleting the actinides, including nuclides produced in the actinide burner itself, more quickly. For example, the destruction (i.e., capture and fission) half life for  $^{238}\text{Pu}$  decreases from almost 7 to 2 years when the wall loading is increased from  $1.15$  to  $10\text{ MW/m}^2$ .

The Westinghouse group reports that the post-irradiation decay hazard index of actinides irradiated for 30 years at  $10\text{ MW/m}^2$  can be reduced by three orders of magnitude relative to natural decay (Figs. 8-81 and 8-82). They conclude that low wall loadings or short irradiation periods are only marginally attractive, and that a total first-wall fluence approaching  $300\text{ MW}\cdot\text{yr/m}^2$  is required for effective reduction of the hazard associated with actinide waste charged to the actinide burner.

The WFPS study has shown that, from the

standpoint of economics, the actinide burner can produce a very large amount of useful energy (approximately  $13,000\text{ MW}_e$ ). Moreover, this energy can be supplied at conditions of fluid temperature and pressure suitable for useful power generation. The plant WFPS used with the actinide burner provides  $1050\text{ MW}_e$  for its required circulating power, as well as a surplus of approximately  $10,000\text{ MW}_e$  for useful export. In view of the extremely large power of the plant, it was not considered reasonable to supply this export power in the form of electricity. Instead, a hydrogen production plant was coupled to the reactor to create a marketable product from its power. The total capital cost for the reactor and plant (excluding escalation an interest during construction) was estimated to be approximately \$4.7 billion in 1975 dollars. On the basis of capital cost per unit of thermal output, this figure is approximately three times that of an LWR. Assuming a 10-year design and construction period, with operation in the mid-1980's (which is extremely optimistic), provision for escalation would require \$4.6 billion and the interest during construction another \$3.9 billion. This represents a total plant cost of \$13.2 billion. If one examines operating costs, including amortization of the \$13.2-billion investment over a 30-year plant life and credits the hydrogen production at the same price per Btu content as that for oil, there is a net operating deficit of \$1.9 billion per year, which can be assigned as the incremental cost for disposing of the actinide inventory.

To put this cost in perspective, the actinide burner has the capability to fission 4 metric tons of actinide per year, based on a power generation of  $13,000\text{ MW}_e$  with an availability of 80%. Since depletion of these actinides by fission corresponds to disposal of fission-reactor actinide waste produced in the generation of  $1.5 \cdot 10^{12}\text{ kWh}$ ,\* a 1.3-mills/kWh incremental cost can be assigned to the fission-reactor power plant for actinide burning. This is about a 4% increase in the total generation cost for a nuclear plant scheduled for 1985 startup. However, the actinide burner concept has not been optimized, and significant cost improvements may be feasible.

**Laser Fusion-Driven Actinide Burner Study.** At present, laser fusion appears to be capable of attaining a  $5\text{-to-}10\text{-MW/m}^2$  fusion neutron wall loading. In addition, the ability to utilize simple geometry

\*Two hundred twenty-two plants ( $1\text{ GW}_e$  each), operating at 75% capacity, produce  $1.5 \cdot 10^{12}\text{ kWh/yr}$ . Each produces about  $0.018\text{ MT/yr}$  of actinides in the LWR-U fuel cycle.

makes the laser fusion reactor an attractive candidate for actinide burning. Recognizing these attributes, Berwald and Duderstadt (University of Michigan) have performed scoping studies<sup>107</sup> for an actinide burner adapted from a University of Wisconsin pure laser fusion reactor design. The goal was to identify a fusion-driven actinide burner system that could be expected to perform efficiently within the framework of anticipated fusion technology. Reasonable extrapolations in technologies that could be expected to develop during the same time frame as the fusion driver itself were utilized.

The laser fusion-driven actinide waste burner (LDAB) system investigated uses partitioned fission reactor generated actinide wastes dissolved in a molten tin alloy as fuel. A novel fuel processing concept based upon work by Anderson and Parlee<sup>108</sup> concerning the high-temperature precipitation of "actinide-nitrides" from a liquid tin solution is proposed. This concept will allow for fission product removal to be performed at high burnup within the device. Thus, the LDAB actinide transmutation process may represent less short-term hazards than solid fuel systems with a fixed fuel cycle period, because the need to refabricate and transport actinide wastes once charged to the system is eliminated.

The LDAB is a power producing hybrid reactor. With an equilibrium blanket energy multiplication of 30 in actinide fission regions about the axial midplane of a cylindrical cavity, a total system blanket energy multiplication of 12 is attained. This corresponds to a reduction in the laser system recirculating power fraction from 24% (pure fusion reactor) to 2.7%. The equilibrium neutron wall loading of  $5.7 \text{ MW/m}^2$  represents an average flux of  $6.4 \times 10^{15} \text{ n/cm}^2\text{-s}$  in the fission regions. The overall system power is approximately  $22,000 \text{ MW}_{\text{th}}$  with an average fission power density of  $287 \text{ W/cm}^3$  in the actinide fuel regions.

No attempt has been made to optimize this system, but potential performance seems impressive. In one possible fuel management scenario, the LDAB attains an effective equilibrium composition in 15 years. The equilibrium LDAB consumes  $7.60 \text{ MT/yr}$  of actinide waste corresponding to the waste output from 134 LWR's operating with full plutonium recycle ( $1000 \text{ MW}_e$ ,  $33,000 \text{ MW}\cdot\text{d/t}$ , 33% thermal efficiency, 75% capacity factor). With an actinide loading of 34 t, the mean life of an actinide atom in the system is only 4.5 yr.

If the 134 LWR's and one LDAB are evaluated as one system, the LDAB will produce 5.5% of the system power. If the cost of LDAB power genera-

tion is three times that of LWR power generation, then the system power generation costs will be 11% above the LWR power generation costs. If the LDAB burns LWR-uranium recycle waste instead of LWR-plutonium recycle waste, it might serve 420 reactors with only a 3.7% increment in power generation costs. As in the WFPS design study, the blanket thermal power could also be utilized for synthetic fuel production.

Although the LDAB has the potential to efficiently burn actinide wastes, process the wastes generated in a large system of commercial reactors, and reduce the short-term hazard caused by transporting and fabricating actinide fuels, its performance represents an optimistic goal. Its realization will require significant development in the fields of high-level waste partitioning, laser fusion and hybrid systems, fusion environment materials, and pyroprocessing. However, these results suggest that high-burnup solid-fuel hybrid blanket designs with considerably less technological risk might attain adequate performance as actinide burners. In particular, HTGR fuel pellets appear to have burn-up capabilities in excess of 25%.<sup>109</sup>

**Comparison of the Two Studies.** The LDAB's efficiency as an actinide burner is compared with the efficiencies of the WFPS Tokamak and other actinide burner systems in Table 8-27, which is taken from Ref. 102. The fully loaded Tokamak actinide burner designs evaluated by Westinghouse relate to initial rather than equilibrium blanket compositions. However, the quality of actinide fuel improves dramatically during the evolution to equilibrium. For example, the LDAB is able to reduce its actinide and neutron wall loadings by 60 and 43%, respectively, while still achieving its initial power density (or equivalently its initial actinide throughput) during its evolution to equilibrium. Since the actinide mean life is the actinide loading divided by the throughput, it follows that the mean life in an equilibrium actinide burner is quite improved over that of a design based on initial conditions only. Also, the reactor can be designed for a relaxed equilibrium wall loading with only a slightly longer evolution to equilibrium.

Thus, for consistency in comparison, data for equilibrium composition Tokamak actinide burners is required. To satisfy this requirement, calculated performances for the two Tokamak designs shown in Table 8-27 were deduced from Ref. 105 and the LDAB evolutionary performance. The  $5.7\text{-MW/m}^2$  Tokamak has the same wall loading as the LDAB. This wall loading is optimistic for a beam-driven Tokamak design, but the results indicate that the neutronic performance of actinide oxide fueled

Table 8-27. Equilibrium actinide burner performance.

	LWR <sup>a</sup>	LMFBR <sup>a</sup>	Tokamak, <sup>b</sup> 5.7 MW/m <sup>2</sup>	LDAB, 5.7 MW/m <sup>2</sup>
Actinide inventory (MT)	1.8	0.48	24	34
Power density (W/cm <sup>3</sup> )	—	—	230	285
Actinide throughput (MT/yr)	0.057	0.056	4.7	7.6
One GW <sub>e</sub> LWR's served	1 <sup>c</sup>	4.8 <sup>c</sup>	261 <sup>d</sup>	134 <sup>d</sup>
Actinide mean life (yr)	31	8.6	5.1	4.5
Fractional fuel burnup (%)	9.6	13 <sup>e</sup>	11	25 <sup>f</sup>
Fuel irradiation period (yr)	3	1.1	0.55	1.5
Additional reprocessing cycles	9.4	6.8	8.3	3

<sup>a</sup>LWR and LMFBR analysis discussed in Refs. 102 and 107.

<sup>b</sup>Tokamak performance deduced from nonequilibrium results presented in Ref. 105 and adjusted for equilibrium cycle using Ref. 102 results. Wall loading equivalent to LDAB.

<sup>c</sup>LWR-Pu burns self-generated waste. LMFBR (1200 MW<sub>e</sub>) burns self-generated waste plus waste from three 1200-MW<sub>e</sub> LWR-U's.

<sup>d</sup>Tokamak burns LWR-U cycle waste (0.18 MT/GW<sub>e</sub> yr). LDAB burns LWR-Pu cycle waste (0.057 MT/GW<sub>e</sub> yr).

<sup>e</sup>Burnup applies to waste actinides only. LWR and LMFBR regular fuel burnup (33,000 and 100,000 MWD/MT, respectively) determines fuel irradiation period.

<sup>f</sup>Nominal 25% burnup assumption requires further investigation.

blankets may be similar to the molten tin-actinide alloy blanket. The major difference in the LDAB and the Tokamak relates to the possibility for higher fractional burnup in the molten tin LDAB fuel (25%) as opposed to the oxide Tokamak fuel (10%). Of course, the Tokamak results are only indicative of equilibrium performance. Better estimates will require detailed neutronics studies.

As shown in the table, fusion reactors can burn two orders of magnitude more actinide waste than can fission reactors because they are fueled entirely with actinides. Thus, fusion-driven actinide burner schemes would employ only a few reactors devoted solely to this task. Note that although the LDAB has a larger actinide throughput, it serves fewer LWR's than the Tokamaks. This is because of the larger actinide production in plutonium vs uranium burning reactors.

**Actinide Burning in Laser Fusion Pellets.** An additional technique for burning actinide wastes in an ICF reactor is to burn the actinides in a fusion fuel pellet. This technique increases the neutron fluence per shot in the actinides by a factor greater than 10<sup>9</sup>. Calculations have shown that much of the actinide materials seeded into the pellet can be burned. The disadvantage of burning the actinide in pellet form is that pellet fabrication and processing of fission product waste become more complicated. This process is important because a given mass of actinides will need to be reprocessed several times before it is completely fissioned. In addition, the rate of actinide mass burned in pellets will be much

less than that in a blanket, because there is a limit to the pellet mass that can be compressed by a given ignitor-beam energy.

**Discussion.** The preceding discussion of actinide depletion is based on the premise that all actinide isotopes that contribute to the hazard index are undesirable nuclides. On the other hand, <sup>238</sup>Pu, <sup>244</sup>Cm, and <sup>242</sup>Cm have identifiable commercial applications as beneficial radioisotopes. For example, <sup>238</sup>Pu is useful for portable and remote power sources that include pacemakers, artificial hearts, and space and terrestrial power stations. The principal deterrent to the use of these nuclides has been their unavailability and high cost. The actinide burner may be a prolific source of these radioisotopes, which are produced by actinide transmutation. The <sup>238</sup>Pu isotope is the principal contributor to the increase in the hazard index during irradiation, and its daughter product <sup>226</sup>Ra is largely responsible for a secondary peak in the hazard index at approximately 10<sup>5</sup> years (Fig. 8-82).

Thus, a value judgment is needed to weigh the beneficial and potentially detrimental attributes of nuclear materials. In fact, Fig. 8-81 suggests that, in terms of the relative hazard index defined earlier, even unirradiated actinides represent a comparatively small, long-term radiotoxic hazard. In view of these considerations and recent studies of waste transport into the ecosystem, the issue of long-term hazard potential from actinides should be reexamined.

The environmental and safety considerations

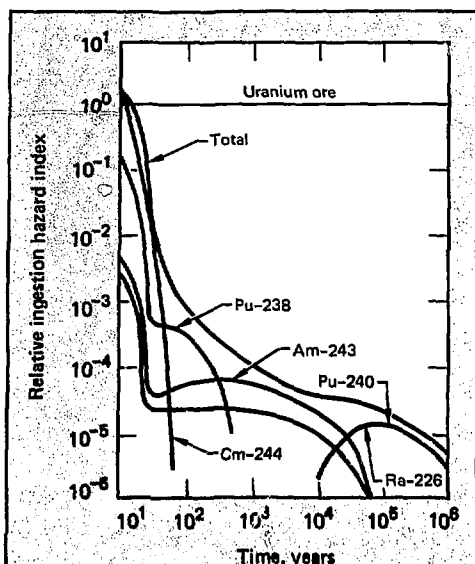


Fig. 8-52. Effect of irradiation with a  $10\text{-MW/m}^2$  fusion neutron wall loading on the long-term ingestion hazard potential of LWR actinides following 30 years of irradiation in the actinide burner.

associated with the actinide burners pose a variety of new problems, although there are parallels with present fission reactor plants. The most significant environmental constraint will be the need to contain large inventories of fission products and tritium. These inventories will be one and several orders of magnitude higher than the corresponding inventories for a current fission reactor power plant. Therefore, features such as multiple containment and cleanup systems must be carefully designed. With regard to safety considerations, the actinide burner power will be several times the 3800 MW, currently imposed as an upper limit for LWR's. Furthermore, the actinide-fuel inventory represents a very large collection of those components of high-level radioactive wastes having the most adverse long-term toxicity characteristics. Thus, we anticipate that a serious program to design, develop, and construct such a plant would have to include provision for an extensive review of the regulatory implications. The principal consideration in the 3800-MW limit is the desire to obtain operating experience with reactors up to that size in a comparatively mature LWR technology. The possibility of constructing actinide burner blanket segments on a smaller modular scale and at lower power density

should be considered. On the other hand, a single actinide burner of the type described in this study could service a large number of LWR's and would not be restricted by siting constraints that tend to favor location near electrical load centers.

**Conclusions.** The most effective means of reducing the long-term radiotoxicity from the actinides is depletion by fissioning the actinides. To effectively burn actinides in a fusion reactor, the product of irradiation time and first-wall fusion neutron flux must be on the order of  $300\text{ MW yr/m}^2$  ( $10^{10}\text{ MJ/m}^2$ ). The fusion reactors that burn actinides will be very large with power levels from 10 to 50 GW. Because of their size, they will generate too much power to be tied to a grid. The excess energy can be used for hydrogen production by electrolysis or for desalinization of water to help reduce the incremental cost assigned to LWR power plants for waste disposal.

It appears that the ICF reactor will be more attractive for actinide-burning applications than alternative systems (LWR, LMFB, and magnetically confined fusion). However, the actinide-burning process is of questionable desirability for the following reasons:

- Compared to immediate encapsulation and storage of actinides, increased handling of high-level wastes is required.
- The short-term hazards increase during early irradiation because of the production of additional actinides from neutron capture.
- Some actinides isotopes are quite useful and should not be burned.
- Reduction of effective half-life from the natural half-life for actinides is of questionable value. Even without irradiation, the actinides present the same ingestion hazard as the parent ore after a relatively short storage period (100 years).

If society decides that the long-term radiological hazards from fission-reactor actinide wastes are high enough to merit construction of actinide burners, then initially confined fusion technology can best perform the required irradiation.

## References

101. H. C. Claiborne, *Effect of Actinide Removal on the Long Term Hazard of High Level Waste*, Oak Ridge National Laboratory, Oak Ridge, Tennessee, Rept. ORNL-TM-4724 (1975).
102. D. H. Berwald and J. J. DuJerstadt, "Preliminary Design and Neutronic Analysis of a Laser-Fusion Driven Actinide Waste Burning Hybrid Reactor," *Nuclear Technology* (awaiting publication).

103. A. G. Croff, Parametric Studies Concerning Actinide Transmutation in Power Reactors," *Trans. Amer. Nucl. Soc.* **22**, 345 (1975).
104. S. L. Beaman and E. A. Aitken, "Feasibility Studies of Actinide Recycle in LMFBR's as a Waste Management Alternative," American Nuclear Society Summer Annual Meeting, Toronto, Canada (1976).
105. R. P. Rose et al., *Fusion-Driven Actinide Burner Design Study*, Vol. 1, Westinghouse Fusion Power System Department, Westinghouse Electric Corporation, Rept. WFPS-TME-033 (1976).
106. U. P. Jenquin and B. R. Leonard, "Actinide Transmutation in Fusion Reactor Blankets," American Nuclear Society Summer Annual Meeting, Toronto, Canada (1976).
107. D. H. Berwald and J. J. Duderstadt, "Preliminary Design and Neutronic Analysis of a Laser-Fusion Driven Actinide Waste Burning Hybrid Reactor," Department of Nuclear Engineering, The University of Michigan, Ann Arbor, Michigan (October, 1977).
108. R. N. Anderson and N. A. D. Parlee, "Continuous Removal of Fission Products in a Nitride-Fueled Reactor," *Nuclear Technology* **13**, 300 (1972).
109. K. R. Schultz et al., "A U-233 Fusion Fission Power System Without Reprocessing," General Atomic Co. Rept. GA-A14636 (1977).

## Authors

J. Hovingh  
J. Blink

## 8.8 Environmental and Safety Features

As the conceptual design of the liquid lithium waterfall fusion reactor evolves at LLL, our interest in considerations of safety and the environment is increasing.<sup>110</sup> In fact, even though we have not yet proposed a set of definitive conditions, we have already incorporated several environmental and safety-related features in the reactor design. Major design choices that are now pending, such as the inclusion of an intermediate heat-transfer loop, will certainly be influenced fundamentally by both concerns.

Battelle Pacific Northwest Laboratories, LASL, and UCLA have each examined the general environmental effects and safety of laser fusion generating stations.<sup>111-113</sup> Where these reports considered features of a specific design, the concept chosen is characterized by multiple spherical cavities operated in the range of 100 MW<sub>th</sub> per chamber, dry or lithium-wetted first structural walls, and 8 or more short-focal-length laser beams entering each cavity through glass ports. Each of

these characteristics leads to specific safety and environmental effects. The liquid lithium waterfall concept under study at LLL includes the following features (see Fig. 8-2):

- A single chamber producing 1000 MW<sub>th</sub> of power.
- Liquid lithium fall protection of the first structural wall.
- 100-m-long windowless laser tunnels for target illumination.
- Four-beam irradiation in the horizontal plane.

In this article, we explore some safety and environmental consequences of these design features and identify areas for research.

We selected the 60-cm thickness of the liquid lithium fall in the LLL concept to achieve an order-of-magnitude decrease in the flux of 14.1-MeV neutrons at the reactor wall. This decrease results in a relatively small cylindrical chamber of 4-m radius for the 1000-MW<sub>th</sub> design. Lessening the flux of high-energy neutrons reaching the first structural wall of SS-316 also reduces neutron-produced helium deposition to 14.6% of the amount that would occur if the liquid fall were not present. This reduction, combined with similar reductions in displacements per atom (dpa) damage, should allow use of the cylindrical portion of the reactor vessel for the entire 30-year life of the plant. Figure 8-83 compares the mass and activity of wastes produced in two reactors, one with lithium fall protection and the other without. An additional advantage is reduction of 14.1-MeV neutrons that reach high-Z materials in the first structural wall, which leads to a lower activation product inventory in the wall surface. The head of the reactor vessel constitutes approximately 10% of the cavity surface area. Because it is protected by a lithium fall thinner than the cylindrical portion of the vessel, the head will require periodic replacement during the life of the plant. The lengthened life expectancy and reduced activation of structural materials will result in the following advantages with respect to other inertial or magnetic containment designs:

- Lower utilization of resources.
- Decreased occupational hazards from handling activated materials during wall or liner replacement.
- Less radioactive and nonradioactive waste accumulation.

Figure 8-84 represents a comparison between the LLL design and UWMAL-1, a typical tokamak reactor, for several specific isotopes.

Corrosion of wall materials and their subsequent deposition in the lithium coolant must be

Fig. 8-83. Comparison of mass and activity of wastes produced in two reactors. The liquid lithium fall greatly reduces wastes of activated steel.

(Unprotected lithium fall based on head and liner replacement each 2 years for a 30-year plant life)

(Protected lithium fall based on head replacement each 4 years and no wall replacement for 30-year plant life)

Quantity of steel wastes discharged  
Unprotected

=====  $5.98 \times 10^5$  kg

Protected

=====  $9.56 \times 10^4$  kg

Activity of steel wastes discharged  
Unprotected

=====  $5.95 \times 10^6$  Ci

Protected

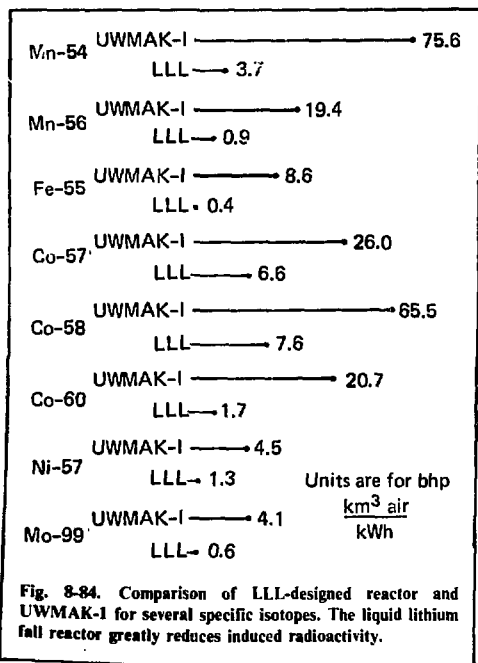
=====  $2.385 \times 10^5$  Ci

minimized to reduce transport of activation products to other parts of the heat transfer system. One possible solution is to use low-corrosion materials such as ferritic steel or 2-1/4% chrome-1% molybdenum steel as the first structural wall. The lithium waterfall concept allows flexibility in the choice of materials, because of the absence of magnetic field requirements, decreased thermal and mechanical cyclical stresses, and a relatively

moderate operating temperature (500°C). Because chromium and nickel are likely to be in short supply and are not domestically available, the selection of high ferritic materials is also favorable from the standpoint of environmental impact.

The lithium fall and chamber contain approximately 100 metric tons of liquid lithium. Another 500 to 800 metric tons circulate in the heat transfer, pumping, and tritium-recovery systems, depending on pump optimization. Consequently, efficient tritium-recovery schemes are needed to maintain a low tritium inventory in the circulating lithium. In the LLL concept, the reactor, heat transfer system, and tritium recovery facility are all located within a single containment building. We believe an appropriate design-basis accident for such a power plant would be a rupture of the lithium outlet line from the reactor vessel, followed by a liquid metal spill and possible fire. The use of catch pans and liners such as those designed by Hanford Engineering Development Laboratories (HEDL) for the Fast Flux Test Facility (FFTF) should greatly reduce the consequences of such an accident, especially because lithium is much less reactive than the liquid sodium used as a coolant in the FFTF.

The liquid lithium fall reactor chamber is penetrated by four windowless laser beam tubes that run underground for 100 meters. The use of large f-number optics results in reduced activation and radiation damage of the final optical flat mirrors.<sup>114</sup> Research is required to develop designs to maintain Class I containment along the beam tubes and at the turning optics that effectively couple the laser containment to the reactor system. Possible solutions to this requirement, such as the use of fast-acting valves and a spatial-filter penetration scheme, are being investigated.<sup>115</sup>



Lawrence Livermore Laboratory, in concert with architectural engineering firms and reactor vendors, is proceeding toward a definitive reactor design. We are investigating questions of containment structure design, activation and transport of wall materials, corrosion, and efficient tritium extraction. In this way, these environmental and safety issues will achieve equal footing with engineering considerations in the tradeoffs that precede selection of final design parameters.

## References

110. J. Maniscalco et al., "A Laser Fusion Reactor Design Study," paper presented at the Optical Meeting on Inertial Confinement Fusion, sponsored by IEEE and OSA at San Diego, Calif. (February 1978).
111. J. R. Young and B. F. Gore, "Potential Environmental Effects of Fusion Power Plants," *Proc. 2nd Topical Mtg. on Tech. of Controlled Nucl. Fusion*, Richland, Washington (Sept. 1976).
112. L. Booth et al., "A Preliminary Assessment of Environmental Effects of Laser Fusion Generating Stations," paper prepared for the Director, Division of Laser Fusion, U.S. Energy Research and Development Administration (January 1977).
113. W. E. Kastenburger et al., "Some Safety Consideration in Laser Controlled Thermonuclear Reactors," prepared for the Electric Power Research Institute, UCLA, July 1975-June 1976 (to be published).
114. T. E. Botts, C. K. Chan and A. Z. Ullman, "Safety Considerations of Laser Related Penetration in LCTR Central Power Stations," *Proc. 2nd Topical Mtg. on Tech. of Controlled Nucl. Fusion*, Richland, Washington (Sept. 1976).
115. M. J. Monsler, "Final Optics for Laser Fusion Reactors," paper presented at the Topical Meeting on Inertial Confinement Fusion, sponsored by IEEE and OSA at San Diego, Calif. (Feb. 1978).

Author

P. E. Walker

## 8.9 Long-Range Planning

LLL's input to the OLF long-range plan is described in the 1976 Annual Report.<sup>116</sup> This year, we have provided input to the Inexhaustible Energy Resources Study (DOE HQ) and to the Battelle Pacific Northwest Laboratory effort supporting the OLF long-range plan.

We also examined the sensitivity of fusion deployment rates<sup>117</sup> to several variables. Our model uses US electric grid history up to the present and a DOE projection<sup>118</sup> of the grid size and mix through

the year 2000 (1390 GWe total and 380 GWe fission in 2000). All plants are retired after 30 years. In a given year, we force the constructed total capacity to equal the sum of the retired capacity plus the new demand. We have five types of plants: large (>1 GWe) pure fusion, small (sub-GWe) pure fusion, hybrid, fission, and fossil. The variables include:

- Pure fusion and hybrid introduction date (1995, 2005, 2105).
- Number of fission plants fueled by one hybrid of equivalent size. (Hybrid fuel production capacity in excess of US fission fuel demand was not allowed.)
- Total grid growth rate after 2000:

Rate, %	2050 grid, GWe
0	1390
1	2286
2	3741
2.5	4778
3	6094

We assume industrial capability to produce new plants (fusion, hybrid, or fission) grows at a given rate until a certain capacity is reached and then grows at a different, lower rate. Priority of construction is fusion, hybrid, fission, and fossil. (In scenarios without hybrids, the fission and fossil capacities are aggregated.) The specific growth rates used are shown in Table 8-28.

Table 8-28. Growth rates.

Rate	Early Rate, %/yr	Switch point (% of 2050 potential)	Late rate, %/yr
High	50	15	20
Medium	40	10	15
Low	30	5	10

In addition to the exponential introduction scheme described above, we tested a more conservative scheme. It allows six GWe of new orders when the demonstration plant comes on-line, two GWe ordered per year until the first six GWe are on-line, and exponential growth thereafter. We used a five-year construction period for sub-GWe units and eight years for multi-GWe units, including hybrids.

The dependent variable in the study was the percentage of the grid served by advanced

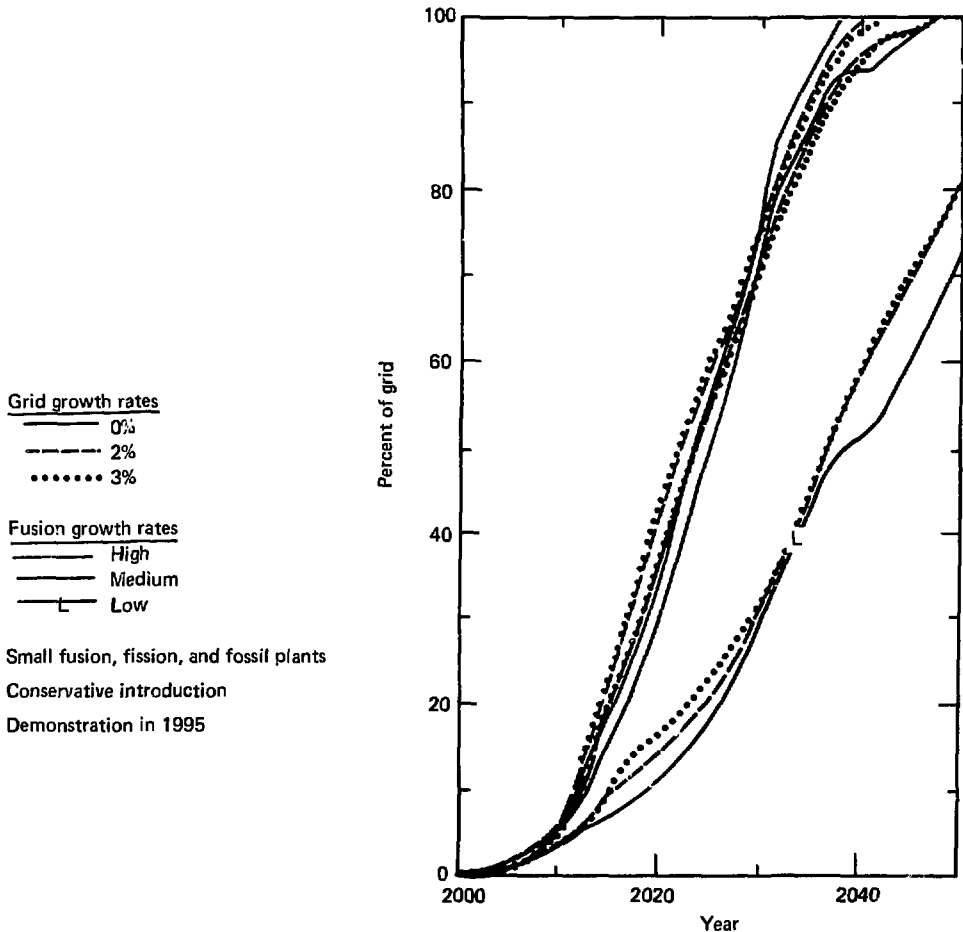


Fig. 8-85. Comparison of grid growth rates and fusion growth rates. Deployment is more sensitive to the fusion construction capability growth rate than to the overall grid growth rate.

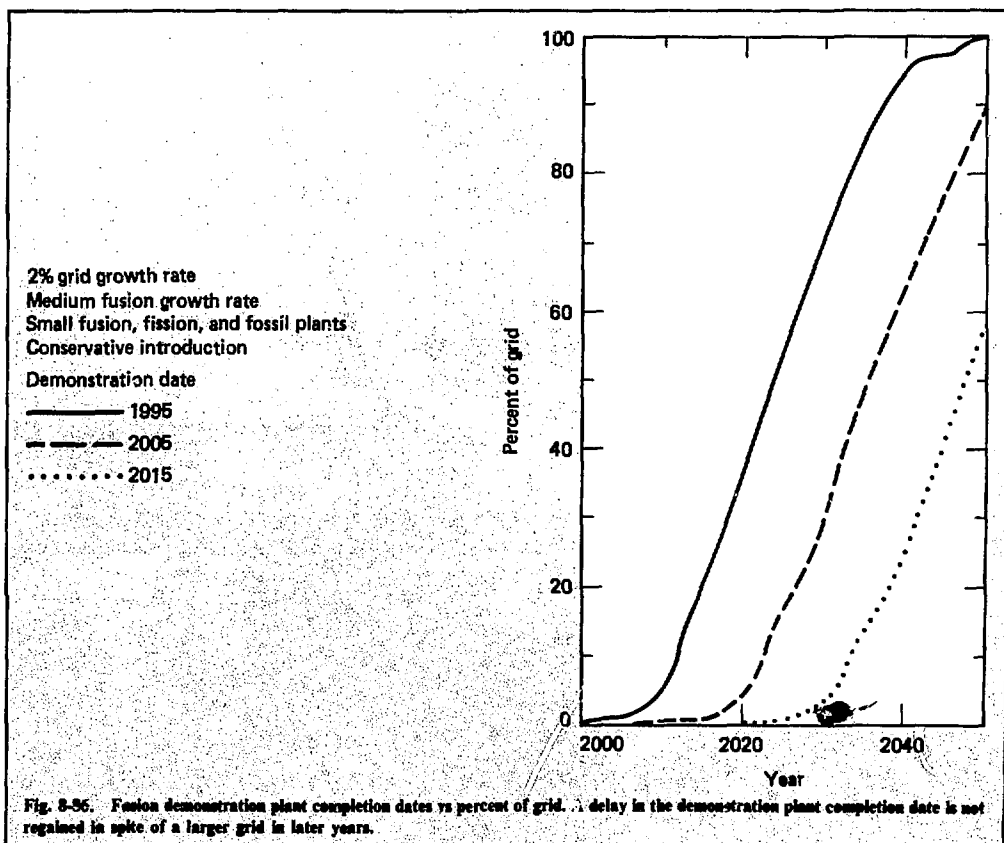


fission plants (Fig. 8-89). The number of fission plants fueled by one hybrid is a significant parameter. Of course, if hybrids are deployed at all, they will be an interim measure designed to solve short-term demands until the more environmentally acceptable pure fusion reactors are deployed. Figure 8-90 shows that the combined hybrid-fusion scenario deploys much faster than scenarios for either technology considered alone. Twenty years after the demonstration plants come on-line, fusion, hybrid, and hybrid-fueled plants could account for almost 50% of the grid. If the fusion demonstration is delayed by 10 years, the fusion-hybrid-fueled plants and hybrid-fueled plants account for 50% of the grid five years later than for simultaneous demonstration (Fig. 8-91). The 10-year delay in the fusion demonstration also results in a peak hybrid-plus-hybrid-fueled capacity of 70% vs a 27% peak

for simultaneous demonstration (Fig. 8-92). Low industrial growth capability also results in higher peak hybrid penetration (Fig. 8-93).

Although the model used in this sensitivity analysis is crude, several interesting results emerge:

- Pure fusion will take considerable time to have an impact on the grid (~10% in 20 years, ~25% in 25 years).
- Hybrid-plus-hybrid-fueled fission plants deploy faster (~10% in 10 years, ~25% in 20 years).
- Small units deploy faster than large units.
- Deployment is sensitive to the early introduction rate and the industrial capability growth rate, and it is relatively insensitive to the overall demand growth rate.
- Delay in completing a demonstration plant is not regained later.
- In a combination hybrid-fusion scenario,



2% grid growth rate  
Medium fusion growth rate  
Small fusion, fission, fossil plants  
Demonstration in 1995

Introduction scheme

— Exponential (IERS)  
— Conservative

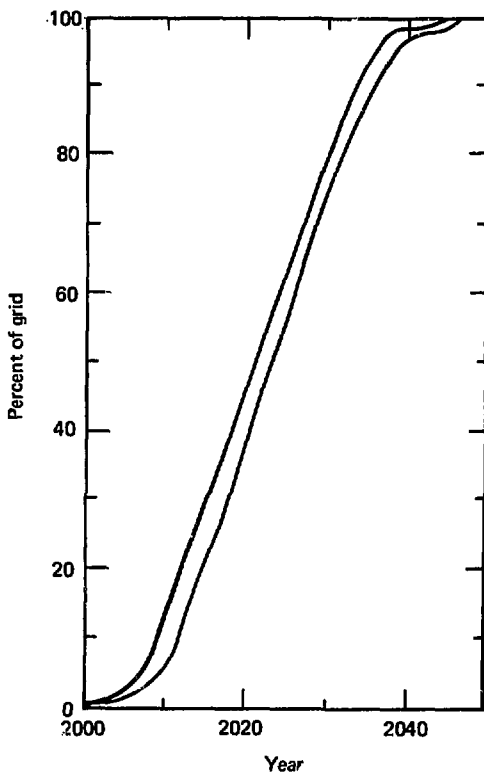


Fig. 8-87. Exponential and conservative introduction schemes for fusion demonstration plant. Deployment is sensitive to the early introduction scheme.

2% grid growth rates  
 Demonstration in 1994  
 Conservative introduction

Unit size

— Small fusion units  
 — Large fusion units

Fusion growth rates

- - - High  
 — Medium  
 ..... Low

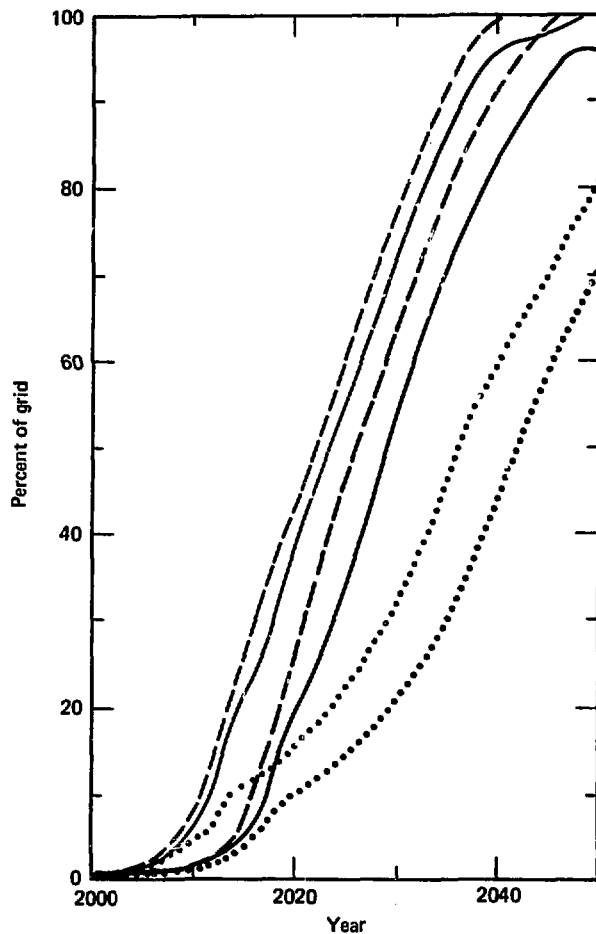


Fig. 8-88. Fusion growth rates for small and large fusion units. Small units deploy faster than large units.

Hybrid, fusion, and fission growth rates

—— Medium

—— Low

Plant type

—— Small fusion (no hybrids in grid)

Hybrid + hybrid fueled (no fusion in grid)

----- 4 fission/hybrid

..... 6 fission/hybrid

- · - · - 10 fission/hybrid

Conservative introduction

2% grid growth rate

Demonstration in 1995

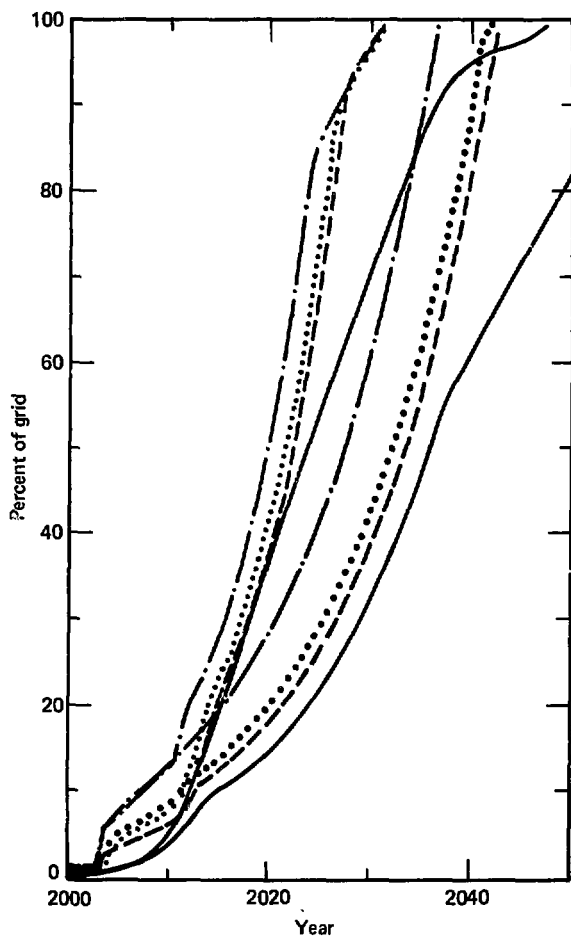


Fig. 8-89. Hybrid, fusion, and fission grow in rates for various plant types. Hybrids can impact the grid much faster than pure fusion.

2% grid growth rate  
 Medium-small fusion, hybrid,  
 and fission growth rates  
 Conservative introduction  
 Demonstration in 1995  
 6 fission plants fueled by each hybrid

— Fusion alone  
 - - - Hybrid alone  
 ..... Fusion-hybrid combination  
 (fusion + hybrid fueled %)

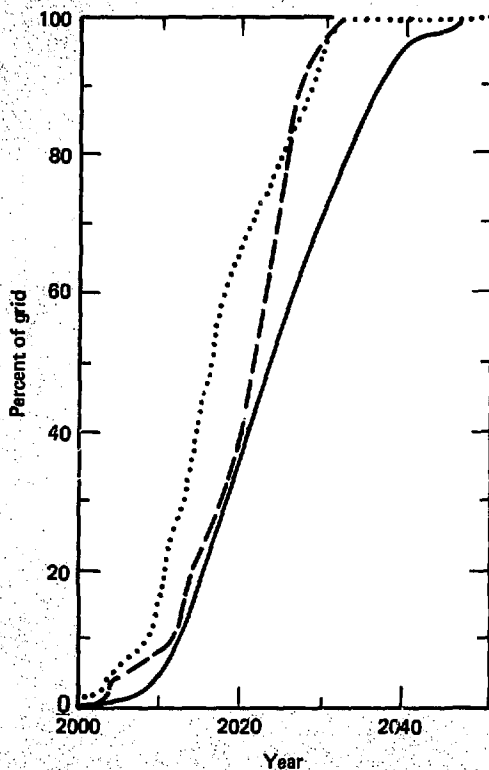


Fig. 8-90. Combined hybrid-fusion scenario, which deploys faster than either type of plant could alone.

2% grid growth rate

Medium hybrid, small fusion, and  
fission growth rates

6 fission plants fueled by one  
hybrid

Conservative introduction

Hybrid demonstration in 1995

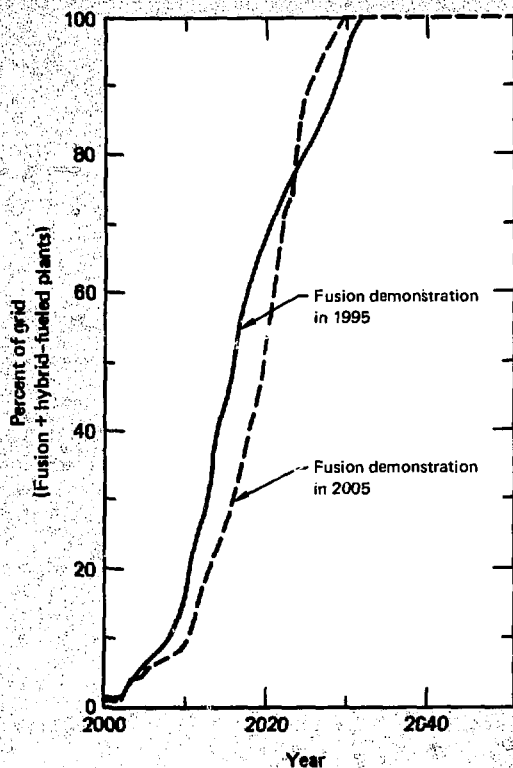


Fig. 8-91. Effect of a 10-yr delay in pure fusion demonstration on the combined hybrid-fusion scenario. The result is a 5-yr delay in reaching 50% of the grid for the combined hybrid-fusion scenario.

2% grid growth rate  
 Medium-small fusion, hybrid, and  
 fission growth rates  
 Conservative introduction  
 Hybrid demonstration on-line in 1995  
 6 fission plants fueled by each hybrid

Plant type

- Hybrid + hybrid-fueled
- - - Small fusion

Fusion demonstration date

- Fusion demonstration in 2005
- - - Fusion demonstration in 1995

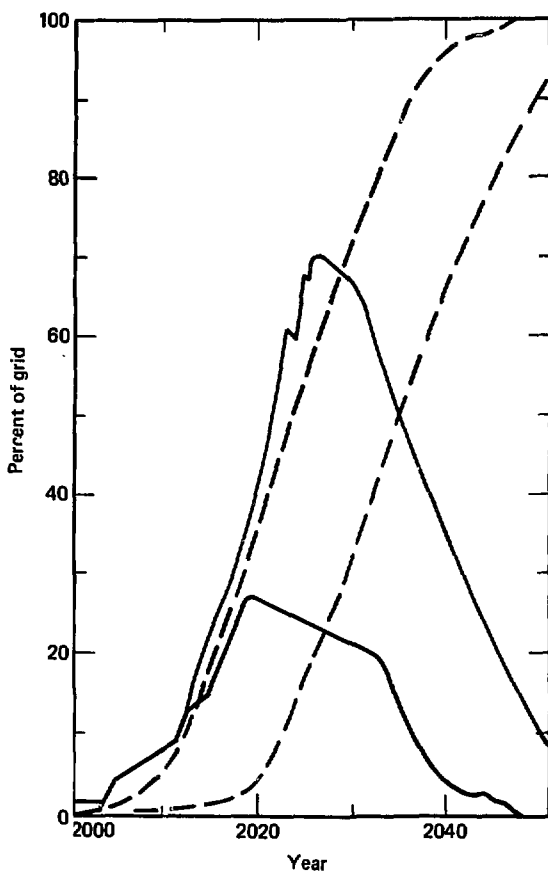


Fig. 8-92. Effect of a 10-yr delay in pure fusion demonstration on peak hybrid penetration.

2% grid growth rate  
 Conservative introduction  
 Hybrid and fusion demonstrations on-line in 1995  
 Hybrid, small fusion, fission, and fossil  
 plants  
 6 fission plants fueled by each hybrid

#### Plant type

— Hybrid + hybrid-fueled

- - - Fusion

#### Deployment rate

— High deployment rate

— Medium deployment rate

—L— Low deployment rate

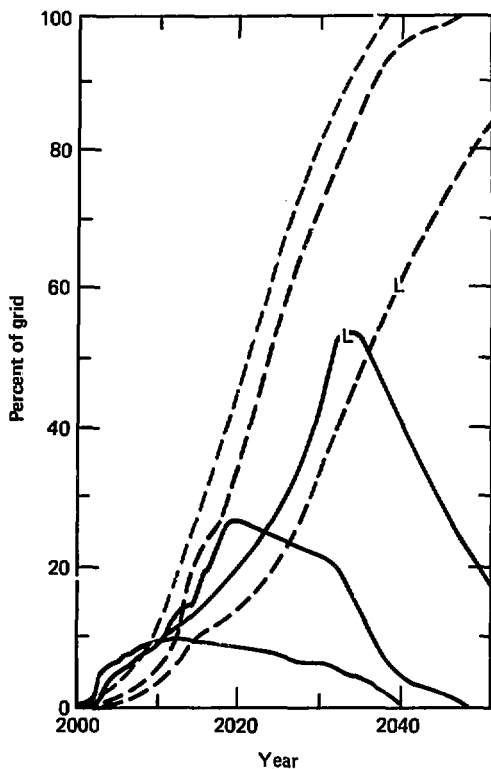


Fig. 8-93. Sensitivity of peak hybrid penetration to the construction capability growth rate.

peak hybrid penetration is minimized for early fusion demonstration and high industrial growth capacity.

#### References

116. *Laser Program Annual Report—1976*, Lawrence Livermore Laboratory, Livermore, Calif., UCR-L-50021-76 (1976).
117. J. Blink and J. Chin, "Laser Fusion Deployment

Scenario," *Trans. A.N.S.*, **27**, 16, San Francisco, Calif., (1977).

118. E. Hanrahan et al., "The Changing Nuclear Picture: Uranium and Separative Work Requirements," presented at the Atomic Industrial Forum Fuel Cycle Conference '77, Kansas City, Mo. (April 1977).

#### Authors

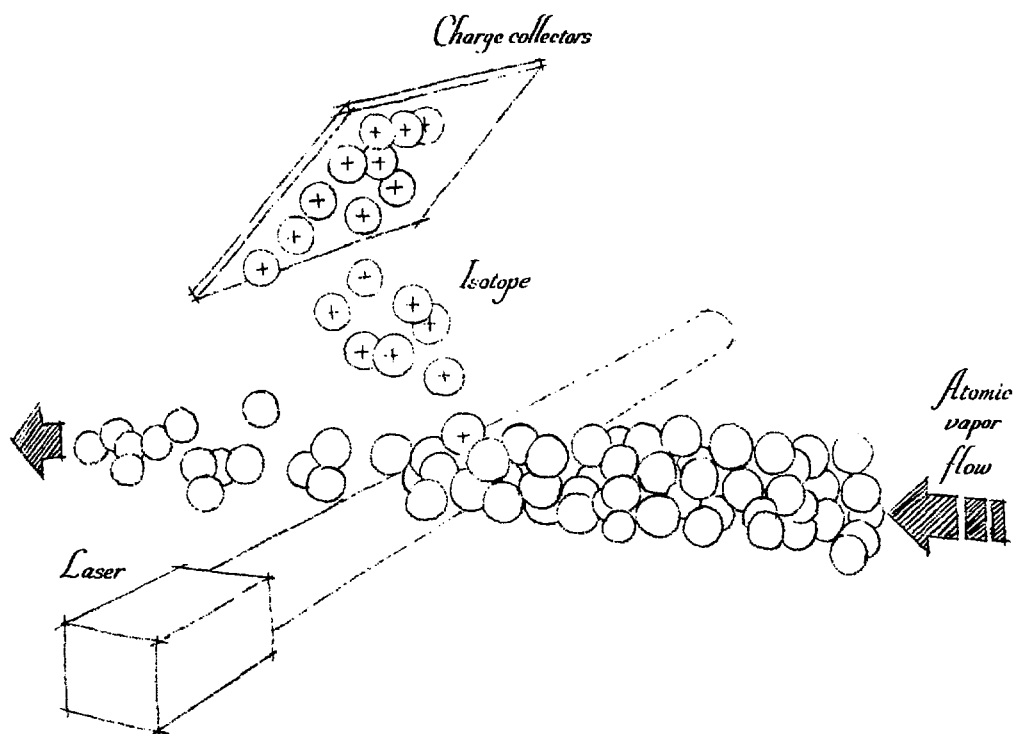
J. A. Blink

J. A. Maniscalco



# SECTION 9

## LASER ISOTOPE SEPARATION PROGRAM



## SECTION 9

### CONTENTS

9.1	LIS Overview . . . . .	9-1
9.2	Atomic Vapor Lanthanide Spectroscopy with Lasers . . . . .	9-2
9.2.1	Lanthanide First Ionization Potentials . . . . .	9-2
	Results . . . . .	9-3
	Discussion . . . . .	9-5
9.2.2	Ionization Potentials of Singly, Doubly, and Triply Ionized Lanthanides . . . . .	9-8
9.2.3	Actinide First Ionization Potentials . . . . .	9-8
9.3	Measuring Absolute Elastic Scattering Cross Sections in the Uranium-Krypton System . . . . .	9-9
9.4	Laser Photochemistry . . . . .	9-10
9.4.1	Reactions of Excited State Alkaline Earth Elements . . . . .	9-10
9.4.2	Associative Ionization Reactions of Strontium . . . . .	9-15
9.4.3	Facility for Laser-Molecular Beam Photochemistry . . . . .	9-21
9.5	Multiphoton Dynamics . . . . .	9-24
9.5.1	Excitation Equations . . . . .	9-24
9.5.2	Multiphoton Resonances . . . . .	9-27
9.5.3	Additional Studies Related to Multiphoton Dynamics . . . . .	9-28
9.5.4	Numerical Modeling . . . . .	9-30
9.6	Relaxation Kinetics of Metastable Excited States . . . . .	9-32

## SECTION 9

# LASER ISOTOPE SEPARATION PROGRAM

### 9.1 LIS Overview

Since the completion of Project Morehouse in early 1975—an experiment designed to demonstrate scientific feasibility of laser isotope separation (LIS) of uranium—our primary task has been to evaluate the technology and the physics scaling laws for LIS processes utilizing atomic vapor as the working medium. Our evaluations indicate that different atomic vapor LIS processes can be used for either primary enrichment or tails stripping (i.e., the uranium ore supply can be increased by economically processing tails from the present gaseous diffusion and from the planned gas centrifuge enrichment plants).

Key components of the LIS processes advocated in our program already exist—no new inventions are required. These available components can be utilized for LIS through emphasized research engineering, scale-up, and engineering hardening. Although many scientific, technical, and engineering problems must be addressed before atomic vapor LIS can be used in commercial operations, we are confident that they can be solved if adequate resources are applied at the proper time.

Many LIS process options appear to be both feasible and economically attractive; several options offer a potentially high payoff. Furthermore, the subsystem options can be utilized interchangeably. Therefore, we prefer to keep these options open, not exclusively singling out one combination of component concepts at this time. We feel that, by adopting this matrix of options, we can greatly reduce residual risk and offer the potential for continuing cost reductions.

Two of the major objectives of our program are (1) to demonstrate a reference LIS process as quickly as possible so that we can establish the economics of LIS and aid in an expeditious implementation, and (2) to continue a concerted LIS process development program to assure that the economic goal for the reference LIS process is met and to provide the basis for realizing even greater economic potential.

The LIS program is structured in four principal overlapping phases. Some uncertainty in the timing of these phases results from the unpredictability of funding and national requirements for nuclear power:

- Technology Evaluation (1978-1980). The basic LIS process parameters will be determined and components options established

- Component and System Demonstration (1980-1984). The LIS components will be scaled to size and integrated into an operating system.

- Engineering Demonstration (1984-1987). Operability, maintainability, and economics will be established sufficiently to permit commitment to a full-scale production facility.

- Production Demonstration (1987-1992). Full-scale production facility for tails depletion will be brought into operation.

The necessary technology for atomic vapor LIS is nearly complete: many crucial experiments are being conducted currently and components in all critical areas are being developed. In addition, most of the required physics and technology are now well defined, curtailing the risks involved in the planned approach to LIS uranium enrichment. Thus, an LIS plant can be developed in time to meet the uranium enrichment needs of this country.

A thorough review of the research and development of previous years directly relevant to the atomic uranium vapor LIS processes is documented elsewhere. Here, we do not detail the entire uranium LIS effort; rather, we present only a few selected topics concerning alternate applications of LIS to related sciences and technologies.

Although the major goal of the LIS program is to develop an economic method using lasers for the large-scale enrichment of uranium, the same technology can be used, to a large degree, for enriching many other elements. For example, the techniques developed for the laser enrichment of uranium have, in the past year, been applied to the study of many fundamental problems encountered in photochemistry and atomic physics.

Whereas some of the studies reported here deal with the evaluation of the atomic uranium LIS

program, others concern the physics and chemistry of new laser-driven processes. Measurements on the scattering of uranium atoms and on the kinetics of metastable excited atomic states, as well as modeling of the physics of atomic multiphoton ionization, are reported here as examples of research closely aligned with the existing atomic uranium LIS program. Studies of new laser-driven processes have led to several experiments on the chemistry of laser-excited atoms, as described here. We also discuss the systematic study of the photoionization of the lanthanide series elements, to demonstrate the ability of the photoionization methods developed at LLL to reveal unifying features in the behavior of highly excited states of complex atoms. The following articles are representative of the basic theoretical and experimental efforts required to support the development of isotopic and nonisotopic laser-driven applications.

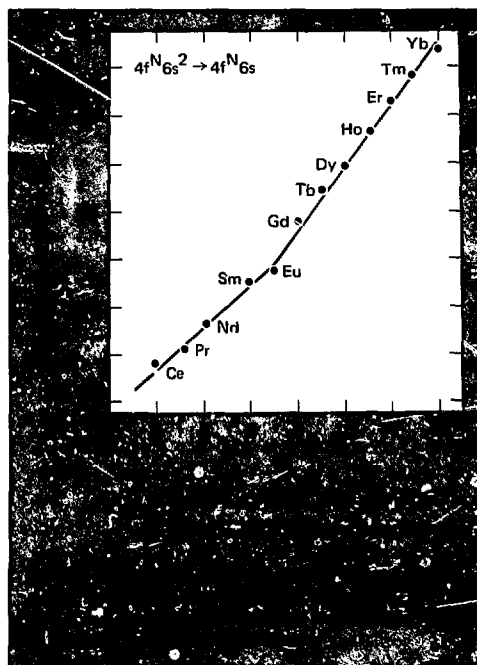
**Author**

**J. Davis**

## 9.2 Atomic Vapor Lanthanide Spectroscopy with Lasers

In the 1976 Laser Program Annual Report (UCRL-50021-76), we described how lasers could be employed to obtain a number of atomic parameters for very complex atoms.<sup>1</sup> Data such as level energies, J-values, level lifetime, and level branching ratios, transition strengths, ionization threshold, and Rydberg series (the latter two yield the ionization potential) can be obtained for elements whose spectra are so complex that conventional spectroscopic methods fail. The lanthanides are such a group of elements. Lanthanide elements are of special interest because of their similarities in chemical properties, resulting from the fact that electrons are added to the inner 4f shell rather than to the valence shell as the series is ascended. Regularities in these elements, such as ionic radius and energies of electronic configurations, have long been of interest.

We have determined accurate first ionization potentials of 10 lanthanide elements by laser techniques. These accurate values have enabled us to ascertain that the change in ionization potential with atomic number is very regular across the lanthanide series.<sup>2</sup> The ionization process  $fN_s^2$



$\rightarrow fN_s$  is well fitted to two straight lines that are joined at the half-filled shell (Fig. 9-1). Subsequently, we found that this connected, two-straight-line behavior can be observed in any row of the periodic table when the ionization limit can be normalized to an ionization mechanism of the type  $\ell N_s^2 \rightarrow \ell N_s$  or  $\ell N_s \rightarrow \ell N$ . This behavior holds true for any stage of ionization, enabling interpolation or calculation of ionization potentials when a value is missing in a row or when data are sparse (e.g., as for the actinide elements). The theoretical explanation for the connected, two-straight-line behavior has been presented in detail by Rajnak and Shore.<sup>3</sup>

Here, we briefly describe the methods used to obtain accurate ionization potentials for the lanthanides. We provide the simple physical explanation for the connected, two-straight-line behavior. The results obtained by application of the theoretical model to extrapolate ionization potentials for ionized species of the lanthanides and for the actinides also are given.

### 9.2.1 Lanthanide First Ionization Potentials

The lanthanide ionization potentials were determined, using multistep laser excitation and

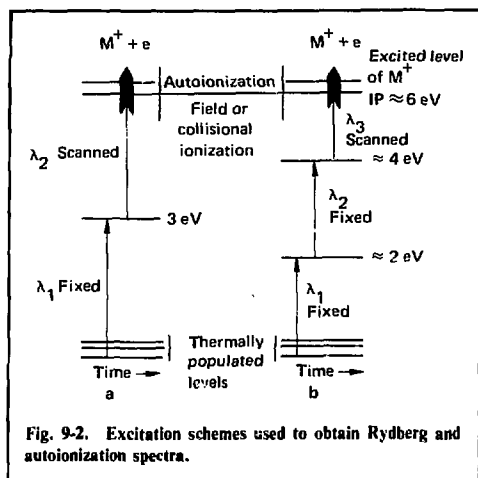


Fig. 9-2. Excitation schemes used to obtain Rydberg and autoionization spectra.

photo, field, or collisional ionization (Fig. 9-2). The experimental apparatus is described in Refs. 1 and 2. In these experiments, a beam of atoms of the element under investigation is irradiated by two or more synchronous pulse dye lasers. This irradiation populates the high bound Rydberg levels that are eventually field- or photo-ionized. The ions are then mass filtered and detected by a channeltron ion detector. All spectra are given as ion signal vs scan laser wavelength.

Ionization limits accurate to  $\pm 30 \text{ cm}^{-1}$  (0.003 eV) can be determined from photoionization threshold scans. Ionization potentials accurate to  $\pm 5 \text{ cm}^{-1}$  (0.0006 eV) are then determined from Rydberg series observations that yield the convergence limit. The photoionization threshold usually is observed first, using the two-step method (Fig. 9-2a). This method involves scanning a considerable range of wavelengths estimated from the available literature ionization potential values<sup>4,5</sup> with quoted uncertainties as large as  $\pm 800 \text{ cm}^{-1}$ . The most recent compilation of values based on spectroscopic data<sup>4</sup> quotes uncertainties of about  $\pm 200 \text{ cm}^{-1}$  and, in most cases, the thresholds are found within the wavelength ranges estimated from these values. Thresholds also are observed using the three-step method (Fig. 9-2b) to confirm and improve some of the two-step results. We obtain the photoionization threshold limit to an accuracy of about  $\pm 30 \text{ cm}^{-1}$  for an element. Then, we estimate wavelength ranges in which we must search for bound Rydberg series with field ionization or collisional ionization, or for autoionizing series converging to excited states of the ion for various

parent levels that could be conveniently populated by one- or two-step excitation. Scans are made from various parent levels until the complete series is obtained.

In most cases (e.g., for Nd, Sm, Eu, Dy, and Er), we obtain autoionizing Rydberg series converging to an excited state of the ion. For lanthanides where the autoionizing Rydberg series are obscured by the high density of autoionizing valence states, we had to use field ionization (e.g., for Ce, Gd, and Tm). The ionizing field is applied 2 to 5  $\mu\text{s}$  after the populating laser  $\lambda_2$  or  $\lambda_3$ . This time resolution allows for radiative decay of some of the shorter-lived valence levels, facilitating preferential detection of the longer-lived Rydberg levels. Collisional ionization is used to observe a series in holmium. For holmium, the oven temperature is increased until the atomic vapor is dense enough so that the bound Rydberg levels are collisionally ionized and a long series is obtained.

**Results.** A photoionization spectrum for neodymium, obtained by the two-step process, is shown in Fig. 9-3. The neodymium excitation sequence also is shown in this figure. The thresholds are marked by the onset of very strong autoionizing levels. In addition, weak background resulting from continuum ionization is present. In contrast to the neodymium spectra where the density of well-

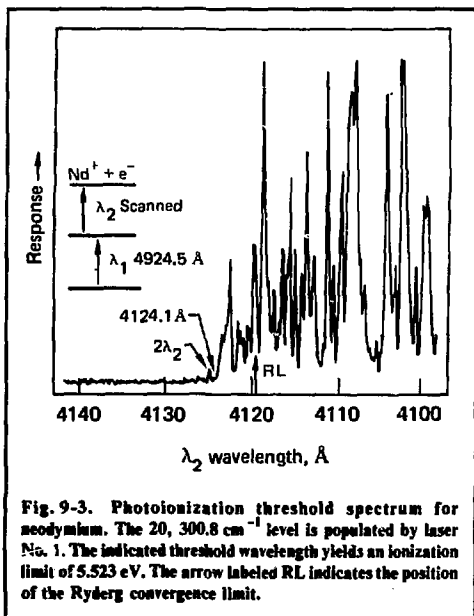


Fig. 9-3. Photoionization threshold spectrum for neodymium. The 20,300.8  $\text{cm}^{-1}$  level is populated by laser No. 1. The indicated threshold wavelength yields an ionization limit of 5.523 eV. The arrow labeled RL indicates the position of the Rydberg convergence limit.

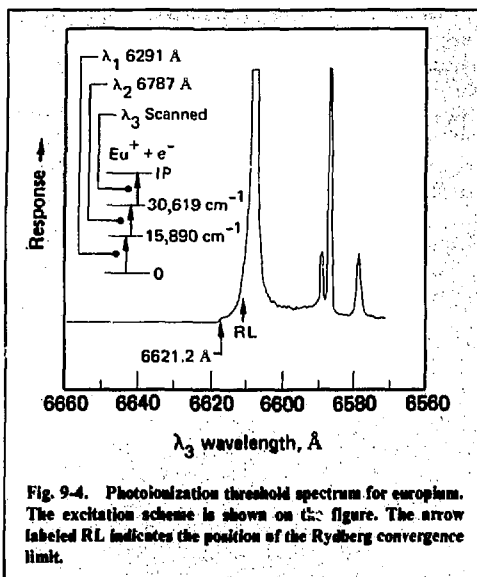


Fig. 9-4. Photoionization threshold spectrum for europium. The excitation scheme is shown on the figure. The arrow labeled RL indicates the position of the Rydberg convergence limit.

defined autoionization peaks approaches instrumental resolution, the spectrum for europium (Fig. 9-4) exhibits very few autoionization peaks and the threshold is identified by the weak continuous photoionization background. The density of autoionizing transitions of each element follows roughly the complexity of the level structure as revealed by the analysis of the emission spectra.<sup>6</sup> Except for europium, the lanthanides that we investigated all exhibited autoionization spectra near the threshold similar to that shown by neodymium. The ionization potentials determined from the photoionization spectra are given in the fourth column of Table 9-1.

The autoionizing Rydberg spectrum for dysprosium (Fig. 9-5) is a double series that converges to the  $4f^{10}6s^4I_{15/2}$  limit,  $828.31 \text{ cm}^{-1}$  above the ground level of the ion. The dysprosium spectrum is relatively free from perturbing and obscuring autoionizing levels. Similarly well-developed autoionizing Rydberg series also are obtained for Eu, Nd, Sm, and Er.

For the cerium Rydberg series (Fig. 9-6), we

Table 9-1. Summary of lanthanide first ionization potentials from LLL laser spectroscopy work and from Refs. 4, 5, 7, and 8 (values in parentheses indicate that the last digits are in error to the amount indicated; values in brackets indicate an interpolated value).

Element	Electron impact <sup>a</sup>	Spectroscopic techniques <sup>b</sup>	LLL Laser Spectroscopic Techniques		Non-LLL Rydberg convergence
			Photoionization threshold	Rydberg convergence	
Ce	5.44(10)	5.466(20)	5.537(5)	5.5387(4)	ND
Pr	5.37(10)	5.422(20)	5.464(+12,-2)	[5.473(10)]	ND
Nd	5.49(10)	5.489(20)	5.523(2)	5.5250(6)	ND
Pm	ND <sup>c</sup>	5.554(20)	ND	[5.582(10)]	ND
Sm	5.58(10)	5.531(20)	5.639(2)	5.6437(6)	ND
Eu	5.68(10)	5.666(7)	5.666(4)	5.6704(3)	5.670 45(3) <sup>d</sup>
Gd	6.24(10)	5.141(20)	ND	6.1502(6)	ND
Tb	5.84(10)	5.852(20)	ND	5.8639(6)	ND
Dy	5.90(10)	5.927(8)	5.936(3)	5.9390(6)	ND
Ho	5.99(10)	6.018(20)	6.017(3)	6.0216(6)	ND
Er	5.93(10)	6.101(20)	6.104(2)	6.1077(10)	ND
Tm	6.11(10)	6.18(2)	ND	ND	6.184 36(6) <sup>e</sup>
Yb	6.21(10)	6.25(2)	ND	ND	6.253 94(25) <sup>e</sup>

<sup>a</sup>Ref. 5. This reference also contains a collection of limits determined by other techniques up to 1975.

<sup>b</sup>Ref. 4. This reference is a collections of the best available limits derived by spectroscopic techniques up to the date of publication in 1974.

<sup>c</sup>Not determined.

<sup>d</sup>Ref. 7.

<sup>e</sup>Ref. 8.

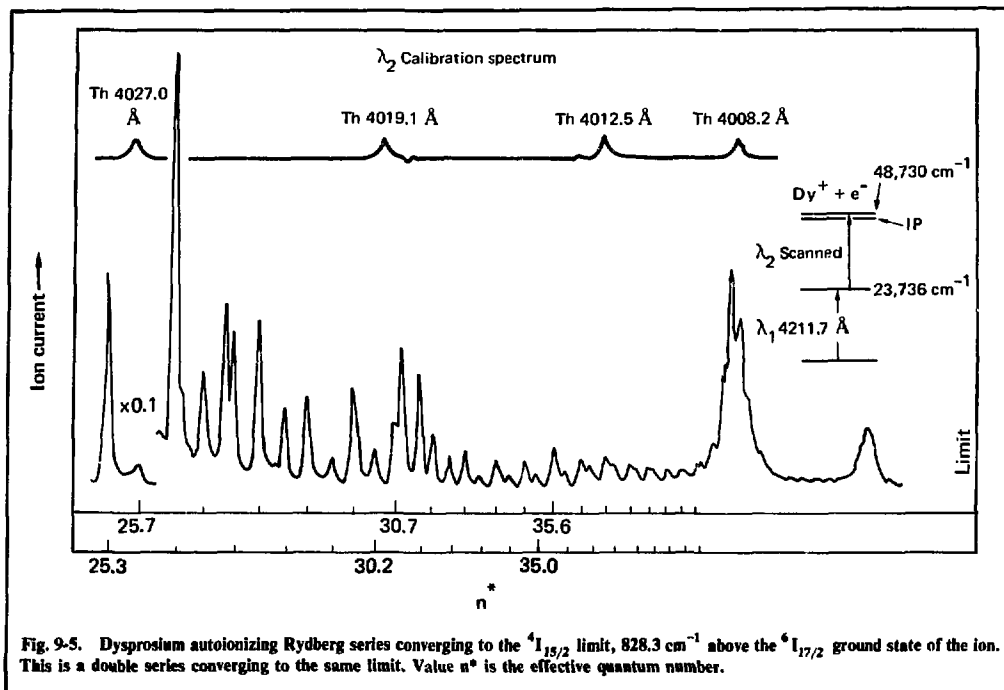


Fig. 9-5. Dysprosium autoionizing Rydberg series converging to the  $^4I_{15/2}$  limit,  $828.3\text{ cm}^{-1}$  above the  $^6I_{7/2}$  ground state of the ion. This is a double series converging to the same limit. Value  $n^*$  is the effective quantum number.

used field ionization with a field strength of 100 V/cm and the pulse delayed by 4  $\mu$ s from the populating laser  $\lambda_2$ .

The variation in quantum defect ( $n - n^*$ ) vs  $n$  with change in the assumed limit value for cerium is shown in Fig. 9-7. The  $n$  value is not necessarily the principal quantum number but is an integer chosen close to  $n^*$  to evaluate the variation in quantum defect. The effective quantum number  $n^*$  is obtained from  $n^* = [R/(\text{assumed limit} - \text{level value})]^{1/2}$ , where  $R$  is the Rydberg constant. The selected ionization limit of the element is that which gives the smoothest and most constant value of the quantum defect as a function of  $n$  for the high quantum number Rydberg levels.

**Discussion.** A summary of the lanthanide ionization limits that we obtained, together with those obtained by various methods, is given in Table 9-1. Except for erbium, the latest electron impact values<sup>5</sup> agree with our accurate Rydberg convergence limits within the quoted uncertainties. The spectroscopic values by Martin et al.,<sup>4</sup> are in excellent agreement with our Rydberg convergence limits for Sm through Er, but their Ce, Pr, and Nd values are lower than ours.

A comparison of our threshold limits with the Rydberg convergence limits reveals that, in every case, the threshold limits are lower by approximately 0.002 to 0.005 eV (15 to 40  $\text{cm}^{-1}$ ). The Rydberg convergence limits for neodymium and europium are indicated in Figs. 9-3 and 9-4 by an arrow labeled RL in the photoionization threshold spectra. As is the case in the neodymium scans (Fig. 9-3), the Rydberg convergence limit generally occurs above the first apparent autoionization peak or peaks for all cases except europium. However, the first very strong autoionization peak always occurs at or above the Rydberg convergence limit. In our uranium investigation,<sup>1</sup> a similar difference between the limits was seen; however, it remains an unexplained experimental discrepancy. Stray electric fields, the effect of intense laser radiation, and collisional effects are all possible explanations. Thus for all lanthanides, we believe that the Rydberg convergence limit values are the more precise and thus they are the preferred values.

In Table 9-1 we include interpolated values for praseodymium and promethium. We believe these are currently the most accurate values for the ionization potentials of the two elements.

With the exception of cerium and gadolinium,

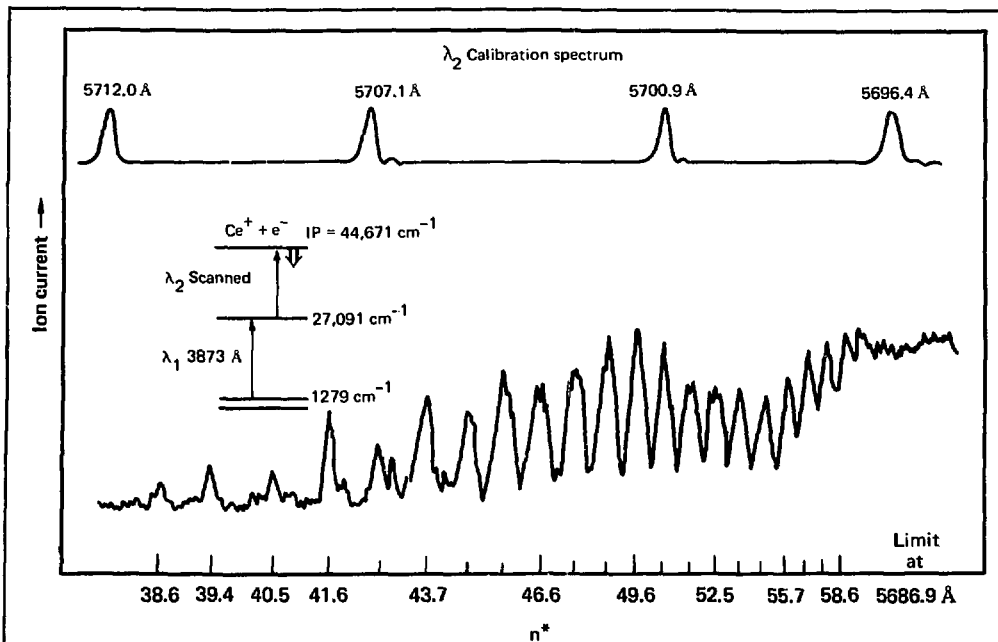
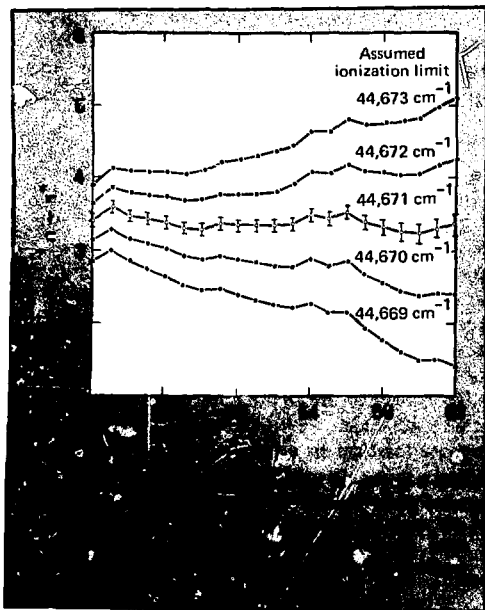


Fig. 9-6. Cerium series converging to the ground state of the ion obtained by pulsed field ionization (indicated by double arrow) of the bound Rydberg levels. The pulsed field of 100 V/cm was delayed 4  $\mu\text{s}$  from the populating laser pulse.



the ionization process in the lanthanides involves the removal of an  $s$  electron from the  $4f^N 6s^2$  configuration with  $N$  equal to 2 through 14. The ionization potential is the energy required to remove an  $s$  electron from an atom in the lowest level of the  $f^N s^2$  configuration of the neutral state and produce an ion that is in the lowest level of the  $f^N s$  configuration. The ionization processes in cerium ( $N = 2$ ) and gadolinium ( $N = 8$ ) correspond to  $f^N - 1d s^2 \rightarrow f^N - 1d$  and  $f^N - 1d s^2 \rightarrow f^N - 1d s$ , respectively. However, these ionization limits can be corrected to correspond to the  $f^N s^2 \rightarrow f^N s$  ionization process by using the very accurately known positions of the lowest levels of the  $f^N s^2$  and  $f^N s$  configurations in the neutral and singly ionized atoms of cerium and gadolinium.<sup>6</sup> Thus, all these ionization potentials can be normalized to correspond to the removal of an  $s$  electron from the lowest level of the  $f^N s^2$  configuration. The resulting normalized ionization limits are plotted as a function of  $N$  in Fig. 9-1 and clearly show a connected, two-straight-line behavior with a change in slope at the half-filled shell ( $N = 7$ ). The limits for thulium and ytterbium are taken from Camus.<sup>8</sup> The solid line in

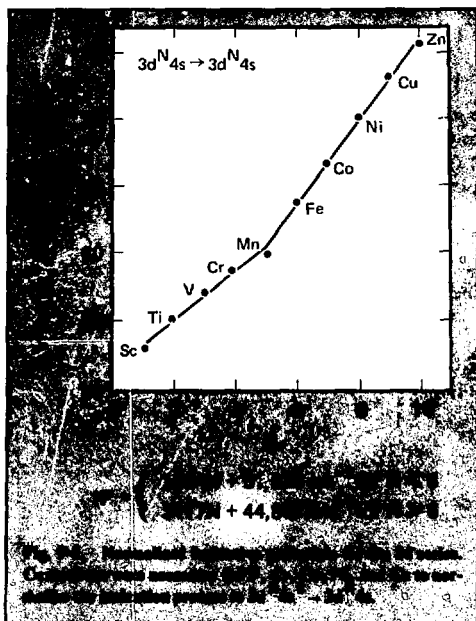


Fig. 9-1 is an unweighted least squares fit to the experimental data, using a connected, two-straight-line equation; the resulting numerical fit is shown at the bottom of the figure. The experimental normalized ionization values have a standard deviation of  $\pm 84 \text{ cm}^{-1}$  from this solid line.

A theoretical explanation of the behavior of the  $\ell N_s^2 \rightarrow \ell N_s$  and the  $\ell N_s - \ell$  ionization potentials is given in Ref. 3, where it is shown that the change in slope at the half-filled shell is equal to  $G_f^{\text{ion}}(\ell, s)$ . The difference in slope between the two lines in Fig. 9-1 is  $220 \pm 23 \text{ cm}^{-1}$ . This is in good agreement with the average experimental value of  $G_f(s) = 205 \pm 6 \text{ cm}^{-1}$  for the lanthanides.

The linear dependence of the  $\ell N_s^2 \rightarrow \ell N_s$  ionization process on  $N$  with a slope break at the half-filled shell is not confined to the lanthanide series; we see the same behavior for the 3d and 4d series elements and for the  $s^2 \ell N \rightarrow s \ell N$  ionization process for the 2p and 3p series elements. The plot for the 3d or iron series is shown in Fig. 9-8. Again, the connected, two-straight-line behavior with a slope change at the half-filled shell is shown. This behavior can be found for any stage of ionization, in any row of the periodic table, when ionization limits are normalized to correspond to ionization mechanisms of the type  $\ell N_s^2 \rightarrow \ell N_s \rightarrow \ell N_s - \ell$ .

A simple physical explanation can be given in terms of the Pauli principle and Hund's rule. For an ionization process of the type  $\ell N_s^2 \rightarrow \ell N_s$  and in the absence of electron correlations, as one moves across a given row of the periodic table, the ionization limit increases monotonically and linearly with  $N$  as a result of incomplete shielding of the added electrons. However, the exclusion principle requires that the various electronic motions be correlated. As a result, Coulomb repulsion between electrons is least energetic and binding energies are greatest when the spatial wavefunction is completely antisymmetric with all electronic spins parallel. From Hund's rule, the term of highest multiplicity has the lowest energy within a given configuration. Thus, the ion ground state experiences a substantial correlation energy between the aligned spins of the  $f$  shell and the single  $s$  electron; this correlation does not exist in the neutral atom where the  $s$  shell is filled with two antiparallel electrons. The greater the number of  $f$  electrons, the greater the correlation term or binding energy of the electrons in the ion. This is the reason for the linearly increasing deviation of ionization limits from the behavior in the absence of electron correlations (or the increasing difference of binding energies in the lowest level of the ionic  $\ell N_s$  and the neutral  $\ell N_s^2$  configurations) as one moves toward the half-filled shell. At



the half-filled shell, additional electrons begin pairing spins and the deviation diminishes linearly with the number of paired electrons.

Elementary application of the Slater-Condon semiempirical methods to calculate the ionization potential  $IP_N$  for the process  $\ell N_s^2 \rightarrow \ell N_s$  suggests that the pattern in ionization limits should be

$$IP_N \begin{cases} = A + NB, & N \leq 2\ell + 1 \\ = A + N[B + G_f(\ell, s)], & N \geq 2 + 1. \end{cases}$$

That is, the ionization limits are piecewise linear with a change in slope occurring at the half-filled shell. The constants  $A$  and  $B$  are combinations of Slater parameters. The important point is that the change of slope at the half-filled shell is simply the Slater exchange integral of the ion,  $G_f(\ell, s)$ . More elaborate ab initio Hartree-Fock calculations confirm this interpretation.<sup>3</sup> Consequently, knowledge of any two ionization limits plus an exchange integral within a row, or alternatively knowledge of three ionization limits, allows interpolation of any other ionization limit within that row. We have applied this method to obtain values for the ionization limits of the neutral actinides as well as of the doubly and triply ionized lanthanides.

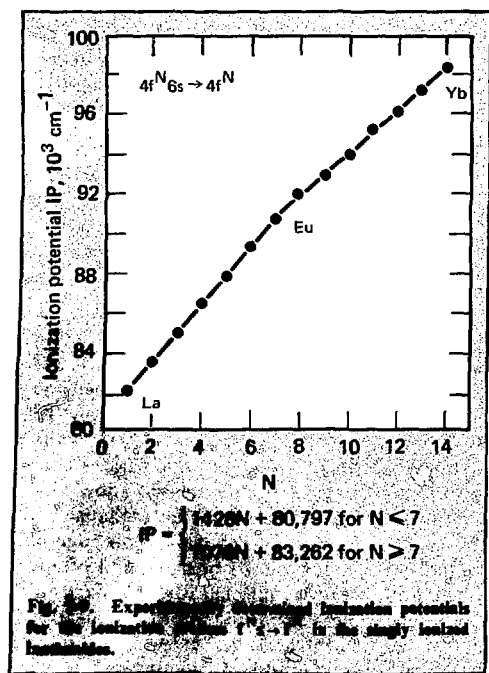
## 9.2.2 Ionization Potentials Of Singly, Doubly, and Triply Ionized Lanthanides

The singly ionized lanthanide ionization potentials are known to 0.1 eV or better.<sup>8</sup> The values form two connected straight lines (Fig. 9-9) and are well fitted by the equation given below the figure. For the doubly and triply ionized lanthanides, there are few experimental values. The equations derived by semiempirical methods (involving both theoretical and experimental parameters) and explained in detail in Ref. 3 are

$$IP_N \begin{cases} = 1688N + 145,449, & N \leq 7 \\ = 2261N + 141,438, & N \geq 7 \end{cases}$$

for doubly ionized species and

$$IP_N \begin{cases} = 3182N + 211,656, & N \leq 7 \\ = 2347N + 217,236, & N \geq 7 \end{cases}$$



for triply ionized species. In all cases, the ionization potentials given thus are for the process  $f^N s \rightarrow f^{N+1}$ . Because most of these ions have the ground configuration  $f^{N+1}$ , the correction for the  $f^{N+1} \rightarrow f^N s$  energy difference must be made to find the ionization potential of the ion.

## 9.2.3 Actinide First Ionization Potentials

In contrast to the lanthanides, few accurate ionization potentials are available for the actinides. An additional complication arises because the ground state for the first five actinide elements (Ac to Np) is not  $f^N s^2$ . Configuration interactions severely affect the position of this configuration relative to the ground configuration when the energy difference is known. The equations

$$IP_N = \begin{cases} 368N + 45,362, & N \leq 7 \\ 338N + 42,071, & N \geq 7 \end{cases}$$

for the energies of the  $f^N s^2 \rightarrow f^N s$  ionization process were derived by extrapolating experimental and theoretical data for the lanthanides to the actinides.<sup>3</sup> The results are in good agreement with Sugar's values<sup>9</sup> that are based on the  $f^N s^2 \rightarrow f^N s$  interval for the higher actinides (Pu to Es). The value for Np of 47,202 cm<sup>-1</sup> is in agreement with the recently determined value of 47,788 cm<sup>-1</sup> for the  $f^5 s^2 \rightarrow f^5 s$  ionization process in Np. This value was determined from the series convergence for five different Rydberg series in Np observed, using laser spectroscopy techniques at LLL.

The determination of the Am and Cm ionization potentials by laser techniques would allow a much more accurate extrapolation of ionization potentials for the higher actinides in the series.

## References

1. *Laser Program Annual Report - 1976*, Lawrence Livermore Laboratory, Rept. UCRL 50021-76 (1977), pp 8-9 to 8-20.
2. E. F. Worden, R. W. Solarz, J. A. Paisner, and J. G. Conway, "First Ionization Potentials of Lanthanides by Laser Spectroscopy," *J. Opt. Soc. Amer.* **68**, 52 (1978).
3. K. Rajnak and B. W. Shore, "Regularities in s-Electron Binding Energies in  $f^N s^M$  Configurations," *J. Opt. Soc. Amer.* **68**, 360 (1978).
4. W. C. Martin, L. Hagan, J. Reader, and J. Sugar, "Ground Levels and Ionization Potentials for Lanthanide and Actinide Atoms and Ions," *J. Phys. Chem. Ref. Data* **3**, 771 (1974).
5. R. J. Ackermann, E. G. Rauh, and R. J. Thorn, "The Thermodynamics of Ionization of Gaseous Oxides; the First Ionization Potentials of the Lanthanide Metals and Monoxides," *J. Chem Phys.* **65**, 1027 (1976).
6. J. Blaise, P. Camus, and J. F. Wyart, "Sellenerdelements, Sc,

La, and Lanthanide," in *Gmelin Handbuch der Anorganischen Chemie No. System 39* (Springer, Berlin, 1976).

7. G. Smith and F. S. Tomkins, "The Absorption Spectrum of Europium," *Philos. Trans. R. Soc. A283*, 345 (1976).
8. P. Camus, "Etude des spectres absorption de l'ytterbium du lutecium et du thulium entre 2700 Å et 1900 Å," Ph. D. Thesis, University of Paris, Orsay, France (1971) pp. 126-334 (unpublished).
9. J. Sugar, "Revised Ionization Potentials of the Neutral Actinides," *J. Chem. Phys.* **60**, 4103 (1974).

#### Author

E. F. Worden

#### Major Contributors

J. G. Conway

J. A. Paisner

K. Rajnak

B. W. Shore

R. W. Solarz

### 9.3 Measuring Absolute Elastic Scattering Cross Sections in the Uranium-Krypton System

In support of the existing photophysical and potential photochemical LIS processes, we have initiated a program to measure the scattering and chemical reactions of ground and excited state uranium atoms under single collision conditions. The most basic question we must answer is: "What is the hard sphere diameter of the atom?" This measurement would yield the scaling factor, which then could be used to estimate all gas-phase uranium atom properties with greater confidence. The value for the atomic radius of uranium is derived from experiments on the scattering of uranium from krypton. In effect, we are using modern technology to measure a transport property.

This year we completed our study of the uranium-krypton system by calibrating absolutely the scattering of a uranium beam. The molecular beam machine, with the gas catcher installed for absolute calibration measurements, is described elsewhere.<sup>10</sup>

The use of crossed beams for absolute scattering measurements is a new technique for which we derived the necessary theory. The working formula relating the center-of-mass differential cross section  $d^2\sigma/d\omega^2$  to the uranium beam scattered at laboratory angle  $\theta$ ,  $I(\theta)$ , and the straight-through uranium beam  $I_0$  is

$$K_F \theta \left( \frac{d^2\sigma(\theta)}{d\omega^2} \right)_F + K_B(\theta) \left( \frac{d^2\sigma(\theta)}{d\omega^2} \right)_B$$

$$= \frac{I(\theta)}{I_0} \left[ \frac{1}{n_2 V} \frac{A_D \bar{A}_{SD}}{A_{SV} A_{DV}} \frac{R_{SV}^2 R_{VD}^2}{R_{SD}^2} \right]$$

The subscripts S, V, and D denote the source, scattering volume, and detector, respectively. The forward F and backward B center-of-mass angles  $\theta$  that scatter to one laboratory angle are defined in Fig. 9-10. Also, K is the kinematic weight (i.e., the scattering observed at  $\theta$  if  $d^2\sigma/d\omega^2$  were constant), A is an aperture area, R is a distance, and V is the size of the scattering volume. The krypton atom number density in the scattering volume is measured with the gas catcher as

$$n_2 = 2.37 \times 10^{11} \text{ cm}^{-3}.$$

All quantities on the right-hand side of the working formula are either measured or geometric properties of the apparatus. The kinematic weights are calculated from first principles.

The overlapping contributions from forward and backward scattering can be sorted out at large  $\theta$ , corresponding to large  $\theta$  where  $d^2\sigma/d\omega^2$  is constant and  $\theta_F \approx \theta_B$  (Fig. 9-10). The absolute center-of-mass cross section is then unrolled to smaller  $\theta$  (see Fig. 9-11). Integrating this cross section

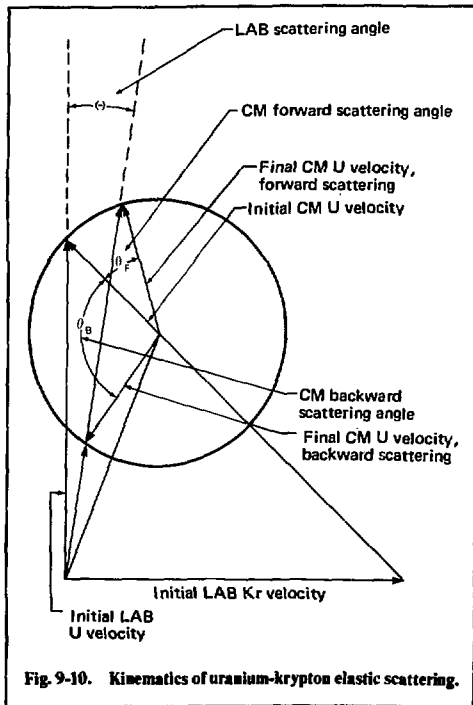


Fig. 9-10. Kinematics of uranium-krypton elastic scattering.

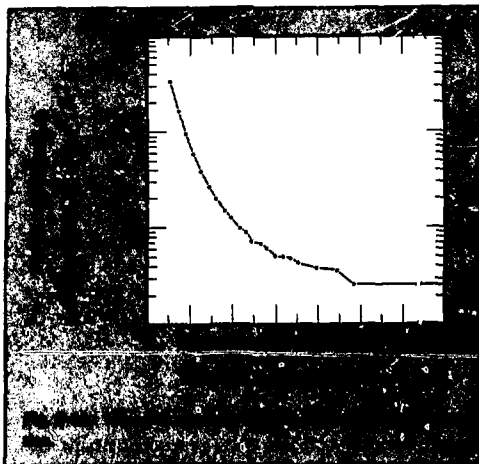


Table 9-2. Effective atomic radii for metal and rare-gas scattering from krypton.

Element	Radius, A
Ne	1.40
Ar	1.60
Kr	1.79
Li	2.40
U	2.43
Na	2.49
K	2.80
Rb	2.92
Cs	3.06

weighted by  $(1 - \cos \theta)$ , we determine that the absolute uranium-krypton momentum transfer cross section, at the experimental energy of 0.10 eV, is

$$\sigma_m(U - Kr) = 46.5^{+4.4}_{-8.7} \text{ \AA}^2.$$

Previous crossed beam experiments on alkali atom/rare gas and rare gas/rare gas scattering<sup>11</sup> enable us to estimate the krypton atom radius and the Van der Waals attractive potential well depth for the uranium-krypton system. Then, the classical theory of transport cross sections<sup>12</sup> can be applied to generate a zero-energy uranium atom repulsive wall radius of 2.43 Å. This value is compared in Table 9-2 with similarly derived radii for alkali scattering and rare-gas scattering from krypton. The uranium atom is found to be smaller than is naively expected.

## References

10. R. C. Stern and N. C. Lang, *Measurement of the U-Kr Momentum Transfer Cross Section Using Crossed Molecular*

*Beams*, Lawrence Livermore Laboratory, Preprint UCRL-81209 (1978).

11. U. Buck, *Adv. Chem. Phys.* XXX, 313 (1975).
12. J. O. Hirschfelder, C. F. Curtiss, and R. B. Bird, *Molecular Theory of Gases and Liquids* (Wiley, New York, 1954), p. 552 ff.

## Authors

N. Lang

R. Stern

## 9.4 Laser Photochemistry

### 9.4.1 Reactions of Excited State Alkaline Earth Elements

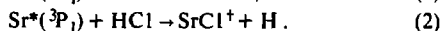
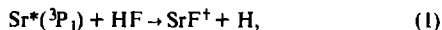
The central principle of laser photochemistry is the ability to drive chemical reactions through the selective irradiation of one or more reactants to states that favor the ensuing reaction. Often, such states are inaccessible at modest temperatures; laser excitation, however, opens up new synthetic routes for making bulk or fine chemicals. However, applications in practical synthesis must first be preceded by studies on the reactivity of specific laser-prepared states in simple systems. Accordingly, we initiated a series of studies to further our understanding of the dynamics of chemical reactions that proceed from excited electronic states where a multiplicity of potential surfaces can influence the outcome of the reaction. In particular, we concentrated on the reactions of the alkaline earth metals with halogenated methanes and hydrogen halides. These reactions are well suited to experimental study and are amenable to limited theoretical interpretation. The reactions of ground and excited state alkaline earth atoms with halogenated methanes offer unique opportunities for studying the behavior of various excited state reaction surfaces that are highly exoergic. The reactions of alkaline earths with hydrogen halides are reported here to illustrate the effect of the reactant state on the energy disposal in the reaction products.

These reactions have been conducted under molecular beam conditions. The atomic beam is excited to a reactive state with either a parametric oscillator or a flashlamp-pumped dye laser. The product molecules are detected, after a suitable delay time to allow for completion of the reaction, using another tunable laser as a probe by laser-induced fluorescence (LIF).<sup>13</sup> In LIF, the product molecules and their internal state distributions are identified by fluorescence induced by the probe laser at wavelength  $\lambda$ . This serves as an unambiguous fingerprint of the presence of specific

product molecules of well-specified internal energy. The LIF method is limited in that only those molecular products having fluorescent states accessible with currently available tunable lasers can be studied. These same states also must possess well-studied spectroscopic features. However, the great attractions of LIF are its simplicity and sensitivity (see Refs. 13-16 for details).

The experimental arrangement for these studies consists of a differentially pumped molecular beam apparatus, interfaced with a nitrogen-laser-pumped, tunable probe dye laser and with a narrow band ( $0.2\text{ cm}^{-1}$ ) flashlamp-pumped dye laser, to energize the atoms to their excited states (Fig. 9-12). Typically, the experimental procedure involves exciting the alkaline earth atoms and then detecting the product, some microseconds later, with the tunable probe laser. A fluorescence detection photomultiplier, placed a few centimeters from the reaction zone, is gated on approximately  $1\text{ }\mu\text{s}$  before the probe pulse. The atomic oven is operated at about  $1000\text{ K}$  in a chamber held at  $2 \times 10^{-6}\text{ Torr}$ . The atoms, collimated by an approximate  $3\text{-mm-by-10-mm}$  slot, enter the reaction chamber which is filled with reactant gas at pressures between  $5 \times 10^{-5}$  and  $1 \times 10^{-3}\text{ Torr}$ . Pressures are measured with a single-sided MKS Baratron, which is attached directly to the interaction chamber, and by calibrated ion gauges in the chamber. Boxcar integration is performed on the laser-induced fluorescence signal. The experimental data consist of records of fluorescence intensity as a function of exciting laser wavelength and reactant quantum state. The resulting spectra are interpreted to identify the products and the manner in which the energy available from the chemical reaction is partitioned. This information furnishes important clues to the mechanism of the reaction.

Consider the reactions



Reactions (1) and (2) are slightly endothermic when both reagents are in their ground states. Excitation of the strontium to the  $^3\text{P}_1$  state is energetically insufficient to give rise to an electronically excited SrX product. The complete product spectrum can thus be detected by LIF.

Figure 9-13 shows the LIF spectrum for the product SrF of reaction (1). From the published spectroscopic constants for the relevant electronic states of SrF, the distribution of internal energy in

the SrF product can be obtained from this spectrum. The spectrum exhibits LIF of the SrF product formed in vibrational states ranging from  $V'' = 0$  to  $V''$  near 15. The fluorescence bandhead intensities only need to be corrected for the Franck-Condon factors and for the calculated relative velocities of the product molecules in each internal state, before the bandhead intensities can be converted to the true relative internal state populations. From these manipulations, we find that the SrF formed in reaction (1) consumes 40% of the energy available from the chemical reaction by releasing this energy as vibrational excitation. The SrCl formed in reaction (2) consumes 70% of the available energy by releasing the energy as vibrational excitation.

This large fraction of reaction exothermicity consumed in vibrational excitation of the products is in contrast to the reactions of ground state alkaline earth atoms with hydrogen halides. For example, when ground state barium collides with HF, only 12% of its exothermicity is deposited into vibration; BaCl is produced with 33% of reaction energy used in vibration (Table 9-3). A simple explanation for the difference in behavior between ground state and excited state alkaline earth atoms is based on the expected qualitative differences between the singlet and triplet surfaces that correlate with the ground state products (see Fig. 9-14). In going from reactants to products, the alkaline earth atom trades its covalent character for a highly ionic character by adiabatically mixing in contributions from either a singlet-coupled or triplet-coupled ionic state growing out of the  $\text{Sr}^+(^5\text{S}) \otimes \text{F}^-(^1\text{S}) \otimes \text{H}(^2\text{S})$  asymptotic limit. Because the excited state surface is initially closer to the energy of the ionic state, it feels the influence of this attractive configuration more rapidly than does the ground state. This effect is further enhanced by the fact that the triplet state is more attractive than the singlet state. These two effects combine to give the lowest adiabatic triplet surface an earlier release of energy than the ground state singlet, implying that the excited state reaction will channel more of its exothermicity into vibration.

We also have completed a series of experiments on the reactivity of halogenated methanes with the ground and excited states of barium and strontium. An unusual aspect of these systems is that although they are generally characterized by substantial exothermicity, large barriers in the reaction channels often prohibit the reactions from taking place on the lowest potential energy surface. With photochemistry, however, it is possible to overcome this topographical feature by placing the reactants on a potential energy surface with a smaller or nonexistent

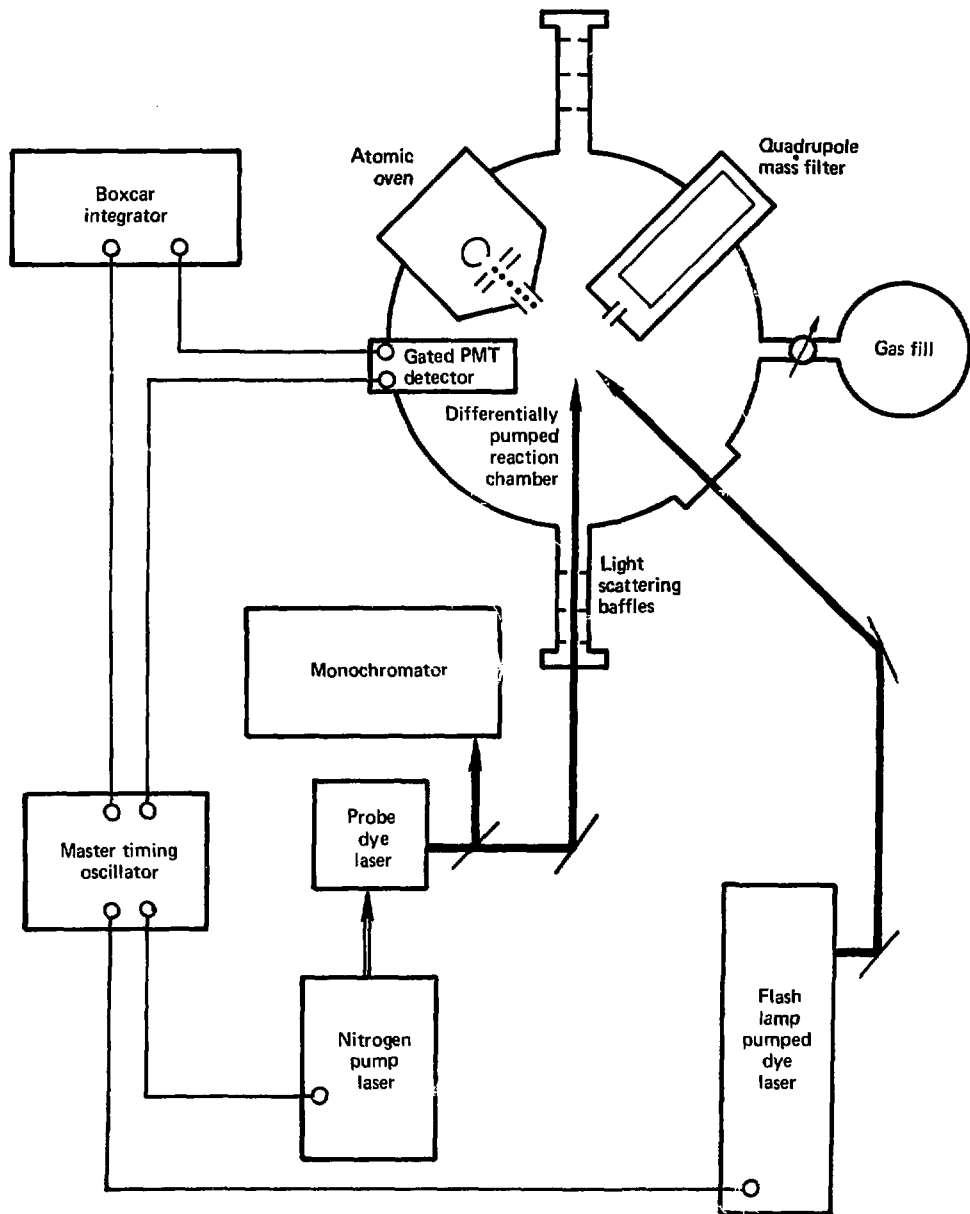


Fig. 9-12. Laser-induced fluorescence detection apparatus.

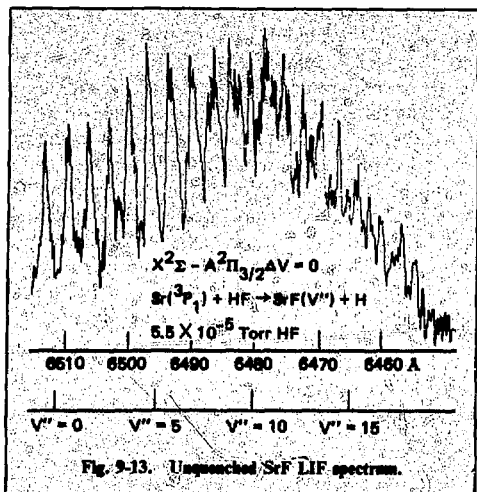


Fig. 9-13. Unquenched SrF LIF spectrum.

tent barrier. Using experimental methods similar to those outlined for the hydrogen halide studies, we obtained the data in Tables 9-4 and 9-5. Several features of interest emerge. First, in each case where more than one type of halogen molecule is bonded to the carbon atom, it is always the bond of the

Table 9-3. Energy deposition in alkaline earth-hydrogen halide reactions.

Reaction	Fractional disposal of energy as vibration, $F_V$	Exoergicity, eV
$\text{Ba}(^1\text{S}) + \text{HF}$	0.12	0.55
$\text{Ba}(^1\text{S}) + \text{HCl}$	0.28	0.48
$\text{Ba}(^1\text{S}) + \text{HCl}$	0.29	0.42
$\text{Ba}(^1\text{S}) + \text{HBr}$	0.36	0.61
$\text{Ba}(^1\text{S}) + \text{HI}$	0.18	1.26
$\text{Sr}(^3\text{P}) + \text{HF}$	0.40	1.49
$\text{Sr}(^3\text{P}) + \text{HCl}$	0.70	1.39

heavier halogen that is broken. The carbon-fluorine bond has proven to be an especially difficult bond to break by metal atom attack. Second, and most important for reactions with  $\text{CF}_3\text{Cl}$  and  $\text{CH}_3\text{Cl}$  where a substantial barrier prevents reaction along the lowest potential energy surface, reactions from the excited triplet states are sometimes observed.

Note that the methyl- and trifluoro-leaving radicals give rise to two distinct groups of

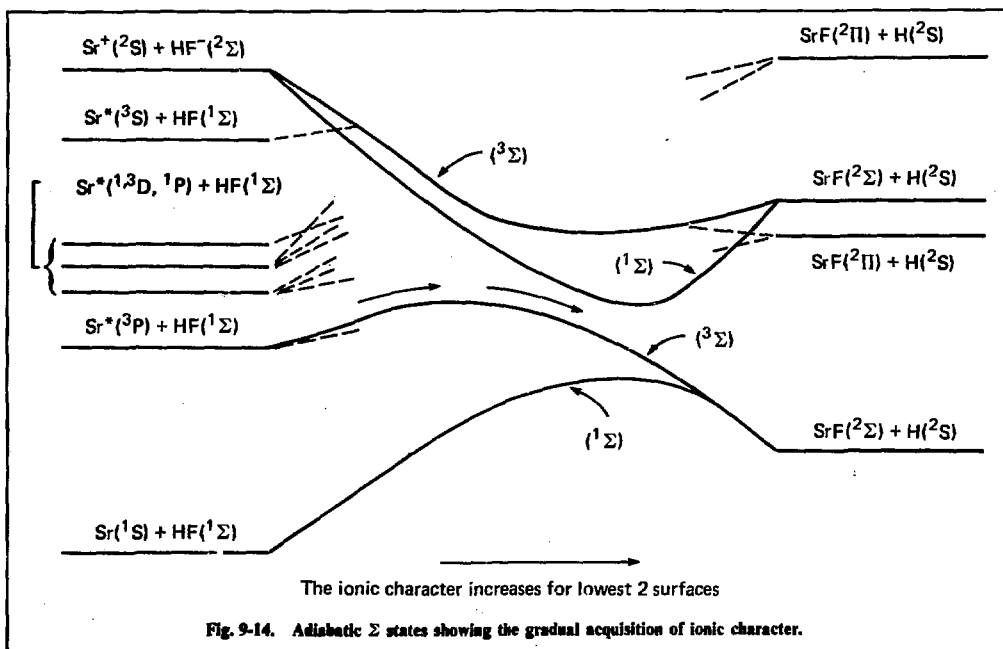


Fig. 9-14. Adiabatic  $\Sigma$  states showing the gradual acquisition of ionic character.

vibrational energy distributions in the diatomic halide products, regardless of whether the reaction was initiated on the ground surface or on the excited triplet surface. This indicates that the pyramidal trifluoro-leaving radical and the planar methyl-leaving group are dominant factors in the reaction dynamics. The methyl group departs with considerable internal energy because it changes from pyramidal to planar geometry during the chemical reaction. The trifluoro radical, on the other hand, does not undergo such a change. Thus, much of the energy available from the chemical reaction with the methyl halides is absorbed by the methyl-leaving

radical, whereas the internally cold trifluoro radical permits the diatomic halide product to attain much higher vibrational temperatures.

Experiments are now in progress to determine the reactivity differences of the various excited-spin-orbit reactions with bromochloro methanes in the singlet and triplet reaction surfaces. We have also found that it is possible to determine the reaction cross section of the laser-prepared species or the ground state species by measuring the relative number density of the reactant state of interest, as a function of the reactant gas pressure as it is titrated into the chamber. Relative density is determined as

Table 9-4. Reactions of Ba(<sup>1</sup>S) and Ba(<sup>3</sup>D) with halogenated methanes.

Halogenated methane	Ba( <sup>1</sup> S)	Ba( <sup>3</sup> D)
CH <sub>3</sub> F	nr <sup>a</sup>	nr
CH <sub>3</sub> Cl	nr	$\bar{V} \approx 23$ , $F_V \approx 0.3$
CH <sub>3</sub> Br	$\bar{V} \approx 11$ , $F_V \approx 0.3$	ns <sup>b</sup>
CH <sub>3</sub> I	$\bar{V} \approx 21$ , $F_V \approx 0.4$	ns
CH <sub>2</sub> Cl <sub>2</sub>	$\bar{V} \approx 39$ , $F_V \approx 0.6$	ns
CCl <sub>3</sub> F	$\bar{V} \approx 30$ , $F_V \approx 0.6$	ns
CCl <sub>4</sub>	$\bar{V} \approx 45$ , $F_V \approx 0.8$	ns
CF <sub>4</sub>	nr	nr
CF <sub>3</sub> Cl	nr	$\bar{V} \approx 60$ , $F_V \approx 0.7$
CF <sub>3</sub> Br	$\bar{V} \approx 30$ , $F_V \approx 0.8$	ns
CF <sub>3</sub> I	$\bar{V} \approx 27.52$ , $F_V \approx 0.7$	ns

<sup>a</sup>No reaction.

<sup>b</sup>Not studied.

Table 9-5. Reactions of barium and strontium with halogenated methanes. In the far left column, the values in parentheses are the carbon-halide bond energies (kcal); in the other four columns, the values in parentheses denote the reaction exoergicity.

Halogenated methane	Ba( <sup>1</sup> S)	Ba( <sup>3</sup> D)	Sr( <sup>1</sup> S)	Sr( <sup>3</sup> P)
CH <sub>3</sub> F (108)	nr <sup>a</sup> (31.5)	nr (58.9)	nr (20.7)	nr (62.2)
CH <sub>3</sub> Cl (81)	nr (23.4)	BaCl (30.8)	nr (14.9)	nr (56.4)
CH <sub>3</sub> Br (67)	BaBr (18.5)	ns <sup>b</sup>	SrBr (11.7)	ns
CH <sub>3</sub> I (54)	BaI (17.6)	ns	SrI (11.6)	ns
CH <sub>2</sub> Cl <sub>2</sub> (76)	BaCl (28.4)	ns	ns	ns
CCl <sub>3</sub> F (~70)	BaCl (~34.4)	ns	ns	ns
CCl <sub>4</sub> (123)	BaCl (34.4)	ns	SrCl (25.9)	ns
CF <sub>3</sub> Cl (80)	nr (16.5)	nr (43.9)	nr (5.7)	nr (47.2)
CF <sub>3</sub> Br (80)	nr (24.4)	BaBr (51.8)	nr (15.9)	nr (57.4)
CF <sub>3</sub> I (68)	BaBr (17.5)	ns	SrBr (10.7)	ns
CF <sub>3</sub> I (54)	BaI (17.6)	ns	SrI (11.6)	ns

<sup>a</sup>No reaction.

<sup>b</sup>Not studied.



a function of pressure, simply by probing the reactant state population through the measurement of the laser-induced atomic fluorescence of this state with a separate probe laser and detector. Sample data obtained from a cross-section measurement of this type are shown in Fig. 9-15. The laser-prepared  $^3P_1$  state of strontium reacts so quickly that relaxation via collisions into the  $^3P_0$  and  $^3P_2$  states is an insignificant mechanism for the quenching of the  $^3P_1$  level population. It will be extremely interesting to measure the relative reactivity of the various laser prepared, spin orbit  $^3D$  states of barium.

The reactions of metal atoms with halogenated methanes are ideal for synthetic laser photochemistry. The reaction rate can be enormously accelerated by single-photon excitation of the metal atom. In fact, the reaction cross section changes from zero to roughly  $100 \text{ \AA}^2$ . Also, with single-photon excitation (rather than with multistep excitation schemes), the available population of reactant states is maximized. Finally, as has been shown for strontium  $^3P_1$  states, the ratio of  $\sigma_{\text{reaction}}$  to  $\sigma_{\text{relaxation}}$  is large, probably greater than 20. This situation is favorable for efficient photon utilization. Thus, we hope that future studies of this type will continue to advance our understanding of ex-

cited state photochemistry and may lead eventually to the discovery of photochemical pathways of commercial significance.

## References

13. H. W. Cruse, P. J. Dagdigan, and R. N. Zare, "Crossed-Beam Reactions of Barium with Hydrogen Halides," *Faraday Disc. Chem. Soc.* **55**, 277 (1973).
14. W. Schmidt, A. Siegel, and A. Schultz, "Laser-Induced Fluorescence of the Reaction  $\text{Ba} + \text{CCl}_4 \rightarrow \text{BaCl} + \text{CCl}_3$ ," *Chem. Phys.* **16**, 161 (1976).
15. G. P. Smith, J. C. Whitehead, and R. N. Zare, "Binodal Distribution of Bal Vibrational States from the Reaction  $\text{Ba} + \text{CF}_3\text{I}$ ," *J. Chem. Phys.* **67**, 912 (1977).
16. R. W. Solarz, S. A. Johnson, and R. K. Preston, "Reactive Collisions of  $\text{Ba}(^1S_0, ^3D_2, ^3D_1)$  and  $\text{Sr}(^1S_0, ^3P_1)$  with Halogenated Methanes," to be published in *J. Chem. Phys.*

## Authors

S. Johnson

R. Solarz

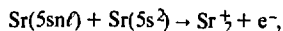
## 9.4.2 Associative Ionization Reactions of Strontium

We describe some initial experiments on the chemistry and kinetics of high Rydberg states in atomic systems. The motivations for these studies include:

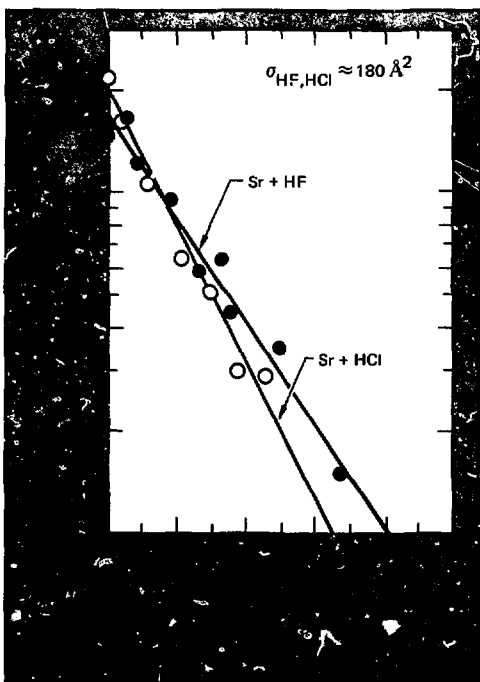
- Multiphoton ionization experiments.<sup>17</sup>
- Observation of superelastic collisional heating of electrons.<sup>18</sup>
- New applications of infrared lasers and detectors.
- Advances in Rydberg state chemistry.

To date, our experiments have involved studying the collisional and associative ionization behavior of laser-excited Rydberg states in atomic strontium vapor. We studied strontium because its excited state Rydberg spectra have been extensively analyzed.

The production of dimer ions by homonuclear associative ionization (HAI) of atomic Rydberg states is known to occur for the noble gases<sup>19,20</sup> and for the alkali metals.<sup>21</sup> Although HAI has been assumed to occur for the alkaline earths, no systematic study or product identification has been reported.<sup>22</sup> We, however, have observed the HAI process,



for laser-populated Rydberg states of atomic strontium. The energy to produce the ion is provided by the binding energy of the molecular ion. The



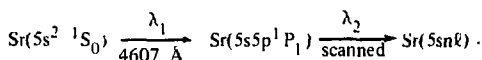
production of dimer ions by this reaction was confirmed by mass spectrometry. We studied this reaction under conditions of low- and high-excitation density ( $<10^{12}$  and  $>10^{12}$  Rydberg atoms/cm<sup>3</sup>, respectively). We find strong evidence that electrons, initially produced by photoionization, play an important role in the ionization of laser-populated high Rydberg states through an avalanche mechanism. This avalanche mechanism strongly influences the chemistry of these Rydberg states at high-excitation density.

With some minor modifications, the experimental technique we use here is identical to that employed in our previous multistep photoionization experiments on heavy atoms (see Fig. 9-16).<sup>23</sup> Briefly, the stream of atoms in the vacuum chamber is irradiated by the output of two or three dye lasers tuned to excite the atoms to high Rydberg states through resonant transitions. The source of the strontium vapor is a resistively heated tungsten oven containing a tantalum crucible loaded with strontium metal. The vapor issues through a 2-by-10-mm slit into the photoionization volume, 2 cm away. The oven is operated at the high temperatures necessary to obtain strontium vapor densities in the interaction zone in excess of  $10^{14}$  atoms/cm<sup>3</sup>. The background pressure is typically less than  $10^{-6}$  Torr. Under these conditions, ionization collisions can

take place on a time scale comparable to the radiative lifetimes of the low-*n* Rydberg states.<sup>24</sup>

Ion products, resulting from photo, collisional, and associative ionization, are then electrostatically focused onto the quadrupole mass analyzer used at a resolution of about 2 amu. The mass-filtered ion current is detected and amplified by a channeltron particle multiplier; the output is processed by a boxcar integrator. The tunable pulsed dye lasers are pumped by separate, synchronous nitrogen lasers. The dye lasers provide unpolarized peak-power outputs of about 10 kW, 10 ns in duration, and with a  $2\text{-cm}^{-1}$  linewidth.

Rydberg states in the  $5sns^1S_0$  and  $5snd^1,^3D$  series are populated by the two-step process,



This excitation sequence is shown in Fig. 9-17. The Rydberg states accessible by this technique have been observed and characterized previously by laser spectroscopy.<sup>25</sup> All experiments entail measuring either the atomic ion signal at mass 88 or the dimer ion signal at mass 176 as a function of the scanned laser wavelength (see Fig. 9-18 for results).<sup>26</sup>

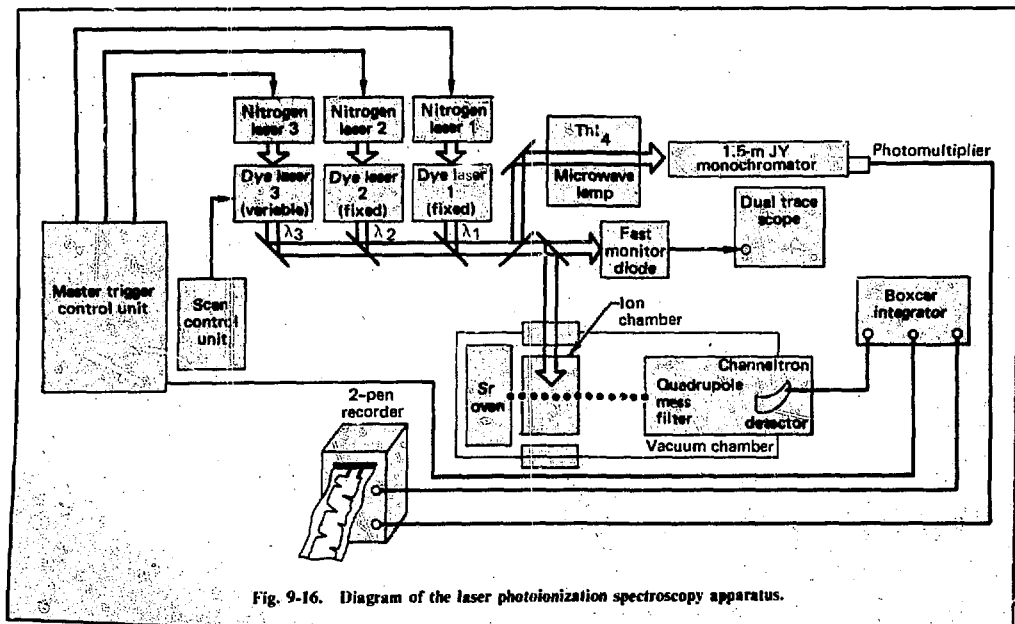
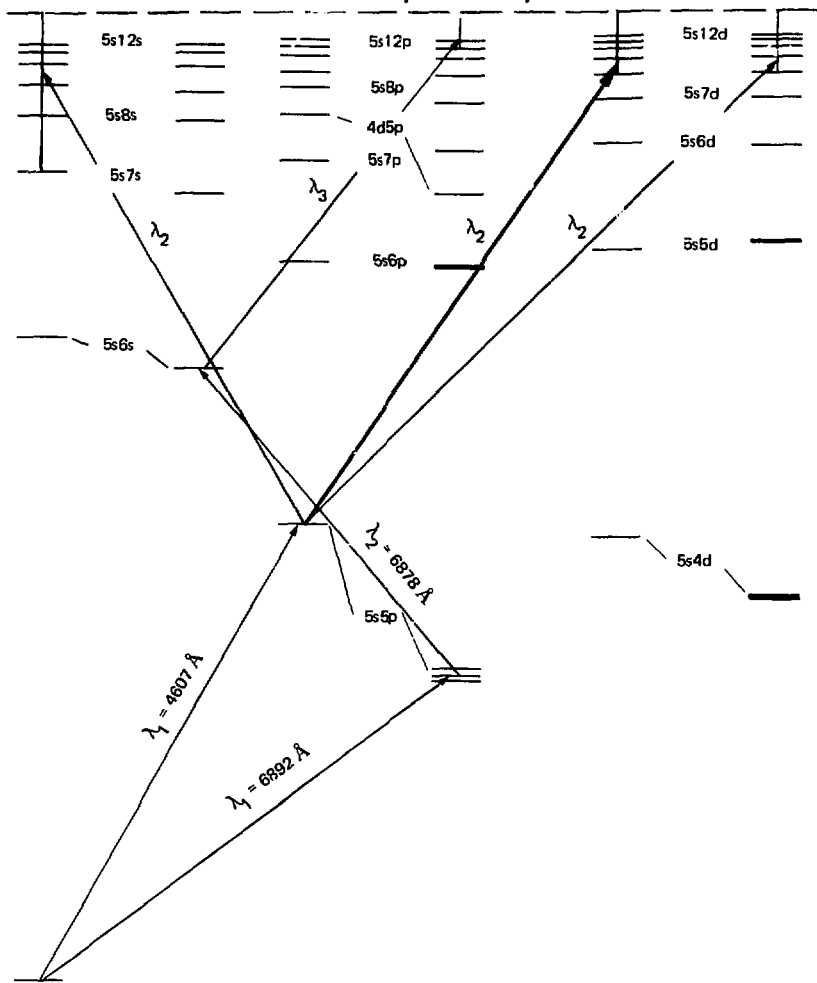
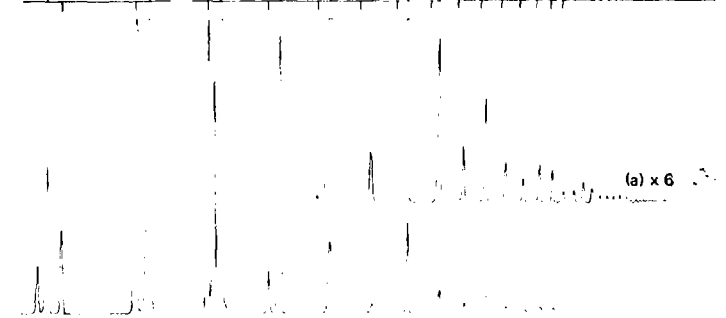
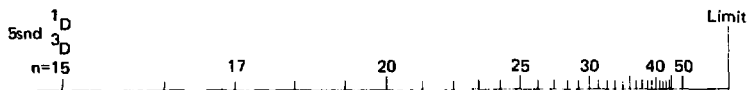
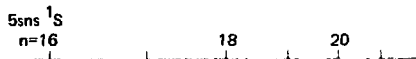


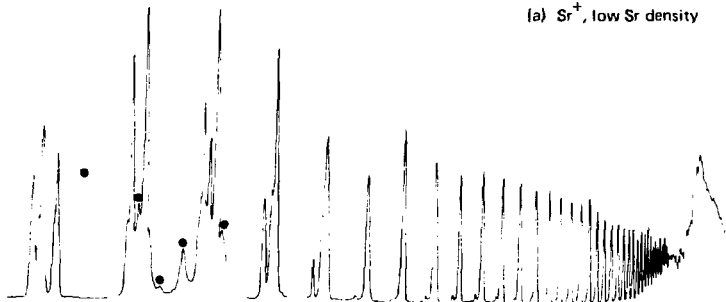
Fig. 9-16. Diagram of the laser photoionization spectroscopy apparatus.

# Strontium ionization potential 45,932 cm<sup>-1</sup>

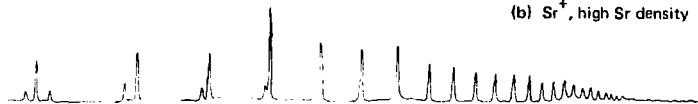




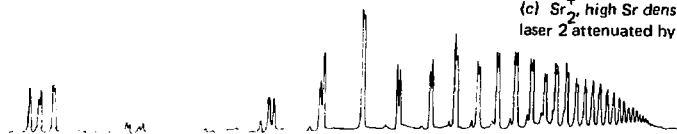
(a)  $Sr^+$ , low Sr density



(b)  $Sr^+$ , high Sr density



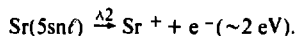
(c)  $Sr_2^+$ , high Sr density,  
laser 2 attenuated by  $\times 0.1$



(d)  $Sr_2^+$ , high Sr density,  
laser 2 unattenuated

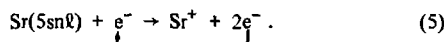
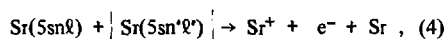
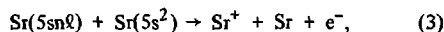
A: the highest vapor densities ( $\sim 10^{14}$  atoms/cm<sup>3</sup>), associative ionization is observed down to  $n = 8$  at 41,052.5 cm<sup>-1</sup> for series members 5sns<sup>1</sup>S<sub>0</sub> and down to  $n = 6$  at 39,685.9 cm<sup>-1</sup> for series members 5snd<sup>1,3</sup>D. Because the ionization potential of strontium is known<sup>25</sup> to be 45,932.2 cm<sup>-1</sup>, the dissociation energy of the dimer ion D<sub>0</sub>(Sr<sub>2</sub><sup>+</sup>) must be at least 0.77 eV. This can be compared with the theoretically calculated value of 1.04 eV for Ca<sub>2</sub>.<sup>27</sup> No reaction is observed for the 5s7s<sup>1</sup>S<sub>0</sub> level at 38,444 cm<sup>-1</sup> or for the 5s7s<sup>3</sup>S<sub>1</sub> level at 37,424 cm<sup>-1</sup> (0.53 and 1.05 eV below the strontium limit, respectively). However, it is difficult to observe associative ionization of states of low  $n$  value because of their short radiative lifetimes.<sup>24</sup> In addition, although energetically allowed, we did not observe<sup>25</sup> associative ionization of the interloping valence levels 4d<sup>2</sup> <sup>3</sup>P<sub>0,1,2</sub>. These valence levels occur between the 11s and 13s Rydberg levels and yield very strong Sr<sup>+</sup> signals.

The Sr<sup>+</sup> signal from high members of the 5sns and 5snd Rydberg series, obtained at low vapor density ( $\sim 10^{10}$  atoms/cm<sup>3</sup>), is shown in Fig. 9-18a. Strontium ions are produced by direct photoionization of the Rydberg levels by the scanning laser:



The Sr<sup>+</sup> signal depends (1) on the cross section for population of the Rydberg level ( $\sim n^{-3}$  dependence), and (2) on the photoionization cross section from the populated level. The second cross section is responsible for the large intensity variations in this spectrum.<sup>28</sup>

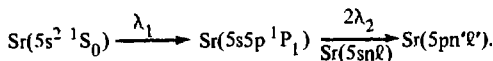
In Fig. 9-18b, we show the spectrum for high members of the 5sns and 5snd Rydberg series, taken at a significantly higher strontium vapor density ( $\sim 10^{13}$  atoms/cm<sup>3</sup>). Here, the production of the Sr<sup>+</sup> signal is dominated by the collisional processes,



Reaction (3) is most important at high  $n$ , whereas reaction (5) is more important at  $14 < n < 35$ . The seed electrons for reaction (5) can be generated by reaction (3) or (4).

The peaks in scan b of Fig. 9-18, indicated by dots between  $n = 16$  and 20, represent newly ob-

served phenomena: near-resonant, two-photon transitions to core-excited autoionizing Rydberg states:<sup>28</sup>



Consequently, these resonances do not appear in the associative ionization collision scans.

Scans c and d of Fig. 9-18 reveal the associative ion production for the laser-populated bound Rydberg states. Scan c was taken at a strontium vapor density of approximately  $10^{13}$  atoms/cm<sup>3</sup>. The nominal 10-kW intensity of the populating laser was reduced tenfold. Under these conditions, the transitions to the lower  $n$  Rydberg states are still close to saturation. At full laser intensity and at the same initial ground state vapor density (scan d), the molecular ion signal for the series numbers  $14 < n < 35$  exhibits a spectral line reversal. These dips in the centers of the lines increase dramatically with laser intensity and strontium vapor density. A comparison of scans a and d reveals that the magnitude of the dip correlates directly with the photoion signal. The molecular ion signal nearly disappears for the 18s <sup>1</sup>S and 17d <sup>1,3</sup>D levels. This effect is not observed for the atomic ion signal (compare scans b and d).

We believe that the primary mechanism responsible for this photoion signal effect is an avalanche of electrons produced by electron impact ionization of the high Rydberg states (reaction 5). The initial electrons are provided by photoionization (reaction 2). The Rydberg states are destroyed, producing even more electrons by electron impact ionization before an associative ionization collision can occur. This effect increases nonlinearly with the number of electrons produced by photoionization. The observed lineshapes and the near disappearance of the signal near  $n = 17$  can be thus explained.

We can estimate the cross section of electron impact ionization from the work of Percival.<sup>29</sup> The cross section scales geometrically with radius; for  $n = 20$  and 2-eV photoelectrons, the cross section is  $1.4 \times 10^{-12}$  cm<sup>2</sup>. With the laser intensities used to obtain scan d in Fig. 9-18, we expect a photoelectron density of 0.1 to 10% of the strontium ground state density, or  $10^{10}$  to  $10^{12}$  electrons/cm<sup>3</sup> when the ground state density is  $10^{13}$  atoms/cm<sup>3</sup>. If this were a steady state electron density, an electron impact ionization collision would occur every 0.01 to 1  $\mu$ s. [With a cross section of  $\sigma_{\text{ai}}(20) = 10^{-13}$  cm<sup>2</sup>, associative ionization collisions occur every 25  $\mu$ s.] The radiative lifetimes of Rydberg states with  $n > 15$  are probably longer than 1  $\mu$ s.<sup>24</sup> Undoubt-

edly, the radiative lifetimes are lengthened significantly by electron impact  $\ell$  changing collisions whose cross sections can be an order of magnitude larger than  $\sigma_{\text{air}}$ .<sup>30</sup>

A rate equation model that assumes an initial electron density, and includes only two competing collisional channels (associative and electron impact ionization), can reproduce the spectral line dip in the dimer ion signal. Certainly, other processes such as  $n$  and  $\ell$  changing collisions with electrons,<sup>31</sup> excited state and ground state atoms,<sup>32</sup> and super-radiance,<sup>33</sup> can redistribute the population among the high Rydberg states. These processes must be considered in any full treatment of the problem. However, from our experimental observations, the general flow of the high Rydberg state population at high excitation densities is seen to proceed to atomic ionization via electron impact collisions. In some cases, *complete ionization* can occur (see scan a near  $N = 17$ ), limiting the excited state density that can be achieved for these Rydberg states, either for chemistry or device applications.<sup>34</sup>

At a high initial ground state density ( $\sim 10^{14}$  atoms/cm<sup>3</sup>), we also observed associative ions from pumping the  $5s5p\ ^1P_1$  state. These ions could arise either directly from  $^1P_1 - ^1P_1$  collisions, or indirectly from collisionally populated Rydberg states that subsequently ionize associatively. (The  $5s8d$ ,  $5s9p$ , and  $5s18s$  states are near resonance with twice the  $5s5p\ ^1P_1$  energy.) We have planned experiments for the near future to elucidate this mechanism.

## References

- J. A. Armstrong, P. Esherick, and J. J. Wynne, "Bound Even Parity  $J = 0$  and 2 Spectra of Ca: A Multichannel Quantum Defect Theory, Analysis," *Phys. Rev. A* **15**, 180 (1977).
- T. J. McIlrath and T. B. Lucatorto, "Laser Excitation and Ionization in a Dense Li Vapor: Observation of the Even-Parity Core-Excited Autoionizing States," *Phys. Rev. Lett.* **38**, 1390 (1977).
- F. L. Arnot and M. B. M'Ewen, "The Formation of Helium Molecules," *Proc. Roy. Soc. (London)* **A166**, 543 (1938); "The Formation of Helium Molecules II," *Proc. Roy. Soc. (London)* **A171**, 106 (1939).
- J. A. Hornbeck and J. P. Molnar, "Mass Spectrometric Studies of Molecular Ions in the Noble Gases," *Phys. Rev.* **84**, 621 (1951).
- F. L. Mohler and C. Boeckner, "Photoionization of Cesium by Line Absorption," *J. Res. NBS (US)* **5**, 51 (1930).
- A. Fontijn, "Recent Progress in Chemi-Ionization Kinetics," *Pure Appl. Chem.* **39**, 287 (1974); AeroChem Research Laboratories, P.O. Box 12, Princeton, NJ, private communication (1977).
- R. W. Solarz, C. A. May, L. R. Carlson, E. F. Worden, S. A. Johnson, J. A. Paisner, and L. J. Radziemski, "Detection of Rydberg States in Uranium Using Time-Resolved Stepwise Laser Photoionization," *Phys. Rev. A* **14**, 1129 (1976); E. F. Worden, R. W. Solarz, J. A. Paisner, and J. G. Conway, "First Ionization Potentials of Lanthanides by Laser Spectroscopy," *J. Opt. Soc. Amer.* **68**, 52 (1978).
- W. Gornik, "Lifetime Measurements of Highly Excited Levels of Sr Using Stepwise Excitation by Two Pulsed Dye Lasers," *Z. Phys.* **A283**, 231 (1977).
- P. Esherick, "Bound, Even Parity  $J = 0$  and  $J = 2$  Spectra of Sr," *Phys. Rev. A* **15**, 1920 (1977); Sandia Laboratory, Albuquerque, NM, private communication (1977).
- We also have observed associative ionization for the  $5snp\ ^1P_1$  series using the three-step excitation process
 
$$\text{Sr}(5s\ ^2S_{1/2}) \xrightarrow{A1} \text{Sr}(5s5p\ ^3P_1) \xrightarrow{A2} \text{Sr}(5s6s\ ^3S_1) \xrightarrow{A3} \text{Sr}(5snp\ ^1P_1).$$
 The investigation was less extensive than for the  $ns$  and  $nd$  series.
- B. Liu and R. E. Olson, "Potential Energies and Scattering Cross Sections for  $\text{Ca}^+ + \text{Ca}$ ," to be published in *Phys. Rev. A* (1978).
- W. E. Cooke, T. F. Gallagher, S. A. Edelstein, and R. M. Hill, "Doubly Excited Autoionizing Rydberg States of Sr," *Phys. Rev. Lett.* **40**, 178 (1978).
- I. C. Percival, "Cross Sections for Collisions of Electrons with Hydrogen Atoms and Hydrogen-Like Ions," *Nucl. Fus.* **6**, 182 (1966).
- J. A. Schiavone, D. E. Donohue, D. R. Herrick, and R. S. Freund, "Electron-Impact Excitation of Helium: Cross Sections,  $n$ , and Distributions of High Rydberg States," *Phys. Rev. A* **16**, 48 (1977).
- J. F. Delpach, J. Boulmer, and F. Devos, "Transitions Between Rydberg Levels of Helium Induced by Electron Collisions," *Phys. Rev. Lett.* **39**, 1400 (1977).
- J. S. Deech, R. Luybaert, L. R. Pendril, and G. W. Series, "Lifetimes, Depopulating Cross Sections, and Hyperfine Structures of Some Rydberg S and D States of  $^{133}\text{Cs}$ ," *J. Phys.* **B10**, L137 (1977).
- W. E. Cooke, Stanford Research Institute, International, Menlo Park, CA, private communication (May 1978).
- See, for example, J. Reif and H. Walther, "Generation of Tunable  $16\mu\text{m}$  Radiation by Stimulated Hyper-Raman Effect in Strontium Vapor," *Appl. Phys.* **15**, 361 (1978); J. J. Wynne and P. P. Sorokin, "Optically Pumped Stimulated Emission and Stimulated Electronic Raman Scattering from K atoms," *J. Phys.* **B8**, L37 (1975); A.M.F. Lau, W. K. Bischel, C. K. Rhodes, and R. M. Hill, "Optical Frequency Conversion Processes in Atomic Rydberg States," *Appl. Phys. Lett.* **24**, 245 (1976); and T. W. Ducas, M. G. Littman, R. R. Freeman, and D. Kleppner, "Sark Ionization of High-Lying States of Sodium," *Phys. Rev. Lett.* **35**, 366 (1975).

## Authors.

J. A. Paisner  
E. F. Worden

### 9.4.3 Facility for Laser-Molecular Beam Photochemistry

A facility for high-resolution beam spectroscopy and the measurement of elastic scattering and chemical reactions of laser-excited species was completed last year with the addition of a pair of dye lasers to the molecular beam machine. A diagram of the beam machine as configured for high-resolution elastic scattering is given in Fig. 9-19. The main chamber, detector system, and gas source designs are all based on a molecular beam machine constructed by Professor Y. T. Lee of the University of California, Berkeley.

In this configuration, collimated molecular beams from each source intersect in a well-defined region (the scattering center) in the main chamber. The detector rotates about the intersection region, and the intensity of either of the scattered beams or of a reaction product is monitored. In the case of

reactive scattering, such angular scans yield information about reaction pathways, limits on reaction exothermicities and bond strengths of simple molecular fragments, and the dynamics of the reaction itself. This information is required for evaluating potential reagents for photochemical separation schemes and for interpreting measurements of reactions of laser-excited reagents. Angular distributions for nonreactive scattering can be analyzed to yield the integral cross sections for scattering as well as the transport properties of the reagents.

Most of our experiments have been conducted in support of the LIS program and involve measurements on atomic uranium. The uranium source, a 2600-K oven, is placed as close as possible to the scattering center. The uranium is contained in a thick walled, lidded, tungsten crucible that is supported from below. The crucible is surrounded by a

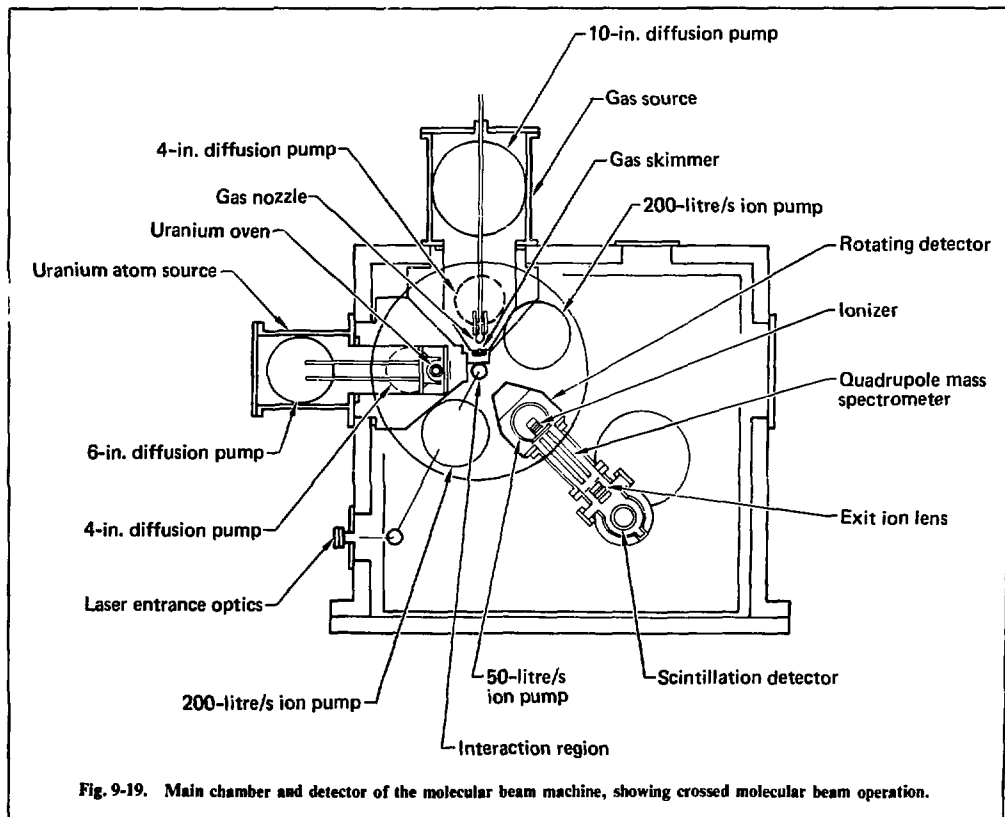


Fig. 9-19. Main chamber and detector of the molecular beam machine, showing crossed molecular beam operation.

cylindrical, tungsten-mesh indirect heater that hangs from the rear on its electrodes. The mesh heater is directly wrapped with several layers of tungsten foil. No oxide insulators are used in the hot zone because they are attacked by uranium to form comparatively volatile uranium oxide. The oven is contained in a water-cooled copper enclosure that is lined with tungsten and tantalum foil heat shields; the copper enclosure forms the front of the plug-in source chamber. Separating the uranium containment and heating functions minimizes the effects of corrosion by liquid and gaseous uranium and of creep of the liquid uranium. The oven has been operated as high as 2800 K and routinely runs above 2500 K. Temperatures, monitored by an automatic optical pyrometer that views the rear of the crucible, are corrected for the emissivity of tungsten.

For the gas source, we use either a differentially pumped, high-flux, supersonic free-expansion nozzle (used for elastic scattering) or a small effusive source located in the main chamber. With the small source, we can obtain a significant ( $> 10$ ) increase in the apparatus sensitivity; this source has been used for studies of ground and excited state chemistry.

In 1977, the major addition to the molecular beam machine was a pair of tunable cw lasers to pump successive transitions in uranium atoms. The decision to use cw rather than pulsed lasers was dictated by signal-to-noise considerations. A typical pulsed laser is on for  $\leq 1 \mu\text{s}$ , although the mean transit time for the product molecules to reach the detector (and thus the time the detector must be gated open) is about 1 ms. If cw lasers can saturate the uranium transitions, the signal-to-background noise ratio is increased more than 1000-fold. The calculations that predicted saturation with the available cw lasers have been verified experimentally.

The most significant problem encountered in the use of cw dye lasers is that they are too monochromatic. The Doppler width of the uranium atomic beam is about 35 MHz with the present (wide) slits. The laser fills less than 1 MHz in  $1 \mu\text{s}$ , the atomic transit time across the light beam. In an attempt to address more of the uranium atoms, we have angle-tuned the lasers into the interaction volume by matching the convergence angle of the light to the divergence of the atomic beam.

The Coherent Radiation (Model 599) dye lasers

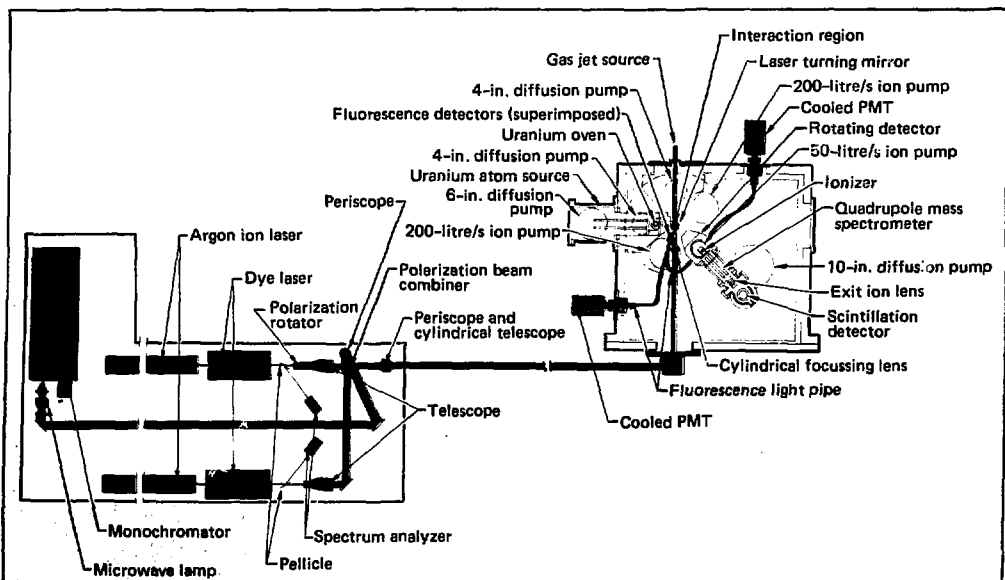


Fig. 9-20. Molecular beam apparatus with gas jet source, lasers, and optical train in the configuration for uranium atom photochemistry.



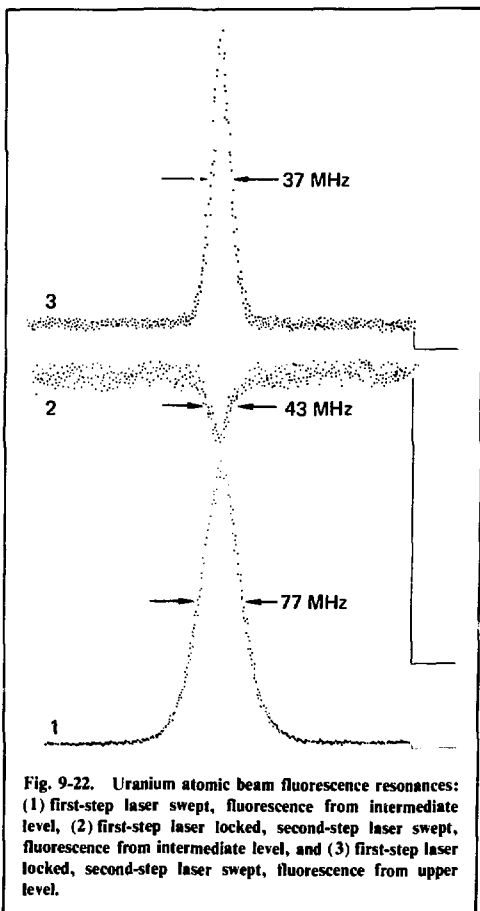
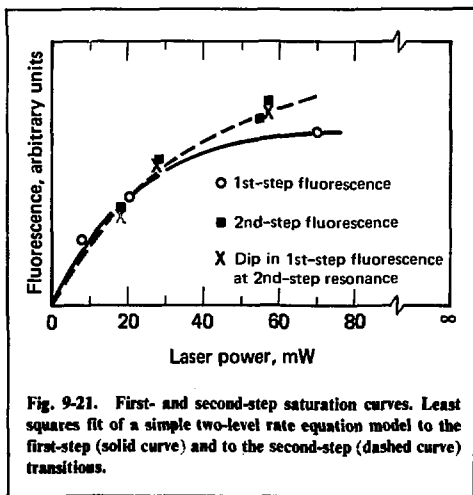
are designed for single-mode output, internally locked to an oven-stabilized reference cavity; these lasers sweep this mode over 30 GHz with level output. Outputs of over 100 mW at 600 nm (Rhodamine 6G) are routinely maintained for about 10 h without a mode hop.

The laser optical train is shown in Fig. 9-20. The polarization rotator and polarization beam combiner superimpose the two laser beams with low loss (<15%). The loss is directed through a uranium microwave lamp to match the optical characteristics of the laser and lamp radiation and then focused on the entrance of a 1.5-m double-pass monochromator. The combination of the uranium lamp spectrum for absolute calibration, the 3-GHz effective linewidth of the spectrometer, the 30-GHz laser tuning range, and sensitive fluorescence detection makes the tuning of the laser to a uranium atomic beam absorption a simple process. The superimposed laser beams are cylindrically focused independently in two dimensions: in depth, to match the depth of the scattering volume, and in width, to angle-tune the frequencies.

The mode-stabilized dye lasers drift freely off the atomic beamline centers in about 1 min. However, a single measurement of a laser-induced reaction requires 30 min of data acquisition. Fortunately, we recognized from the start the need for an active control loop to hold each laser on the atomic frequency. The key elements in this control system are a pair of fluorescence detectors. Each detector consists of a 100-Å bandpass interference filter and a lens to image the scattering volume through a set of tight baffles and into a light pipe

that feeds a cooled photomultiplier. The detectors can be position-tuned even when the beam machine is under vacuum. Typical fluorescence signals are  $2 \times 10^5$  Hz on a background of  $10^2$  to  $10^3$  Hz. The backgrounds compare favorably with the  $10^{17}$  oven-light photons and the  $5 \times 10^{17}$  laser photons passing through the scattering volume each second.

The two dye lasers are frequency-modulated to a depth of approximately 3 MHz at 51 and 111 Hz, respectively. The fluorescence amplitude modulation is detected with a phase-sensitive lock-in amplifier to generate a derivative error signal. The integrated and amplified error signal drives a Brewster plate in the reference cavity of the dye laser. Time constants are chosen so that the internal (mode holding) control loops are 10 times faster than the external loops and so that the second-step



loop is 10 times faster than the first loop (on which it rides). This control system has operated more successfully than we expected. With periodic, on-line, and manual adjustments, the lasers can be held to within a few megahertz of their respective line centers for more than 12 h.

Saturation curves for a typical two-step atomic excitation scheme are shown in Fig. 9-21 along with the best fit of a simple two-level rate model. In terms of the conventional saturation parameters  $\chi$ , the transitions appear to be several times saturated. The first- and second-step resonances, as observed in fluorescence, are shown in Fig. 9-22 to illustrate the high signal-to-background noise ratio and the narrow fluorescence linewidths. The middle curve in Fig. 9-22 shows the dip in the first-step fluorescence when the second-step laser is swept through resonance. Depletions of the intermediate level population, measured from these dips, range from 22 to 29%; this range of experimental values compares favorably with the 28% depletion calculated from a rate equation model.

#### Authors

N. Lang  
R. Stern

## 9.5 Multiphoton Dynamics

In the 1976 Laser Program Annual Report (UCRL-50021-76), we detailed our work to design efficient isotope separation facilities based on isotopically selective laser excitation and subsequent ionization of the atomic vapor. In 1977, we concentrated our efforts on clarifying the relationships between the characteristics of vapors and lasers, and the desired ionization. This section summarizes our advances in theoretical and computational skills.

Excitation of atoms or molecules by laser irradiation can differ appreciably from excitation by particle impact, broadband radiation, or thermal energy sources. Whereas an adequate description of thermal excitation requires only a specification of the time dependence of the excitation population (or probabilities), the sharply definable frequency of laser fields permits the maintenance of temporal phase relationships among probability amplitudes. This situation persists until relaxation mechanisms sufficiently alter the system behavior to mask any evidence of coherent excitation. Relaxation may originate in laser phase fluctuations, amplitude fluctuations, collisional phase interruptions of the atoms, or spontaneous decay. To exploit effectively

the potential for practical application of laser-induced excitation (e.g., for laser isotope separation or laser-induced chemical reactions), we must understand the basic physics of coherent excitation. This understanding and the computational skills thus developed make possible the modeling of practical laser excitation devices and the subsequent optimization of their operation.

### 9.5.1 Excitation Equations

The basic microscopic dynamic equation is the time-dependent Schrödinger equation,

$$i(d/dt)\Psi = H\Psi.$$

To reduce this equation to a tractable form, we introduce a succession of idealizations. First, we consider only a finite set of discrete energy levels, say  $N$  in number, that are linked by near-resonant radiative transitions. These energy levels serve as the basic states for the problem. The expansion coefficient  $C_n$  of  $\Psi$ , when squared, yields the probability  $P_n$  of finding the atom excited into level  $n$ :  $P_n = |C_n|^2$ . The  $N$ -level truncation restricts us to treating laser fields whose interaction energy with the atom is significantly less than the binding energy: the  $N$ -level truncation does not admit the continuum states needed to describe strong distortion in the laser field. More importantly, the truncation eliminates many degrees of freedom. We replace the many separate (though interacting) atoms of an ensemble by an average  $N$ -level atom, whose interaction with the remaining universe appears in appropriate equations of motion. In its simplest form, this equation consists of a Schrödinger equation with a possibly non-Hermitian effective Hamiltonian  $W$ ,

$$i(d/dt)\underline{C} = W\underline{C}.$$

The operator  $W$  can account for irreversible probability loss from levels of the  $N$ -level atom, thereby modeling ionization or decay to nonexcited levels. (See Refs. 35-37 for a discussion of specialized solutions to these equations.) After transforming to the rotating-wave picture, the basic mathematical parameters of this equation are the Rabi frequencies (i.e., the off-diagonal elements of  $W$  expressing the interaction energy between atomic dipole-transition moments and the laser electric field vector), the cumulative detunings of sequences of lasers away from the corresponding sum of Bohr resonance frequencies, and the various probability loss rates.

By averaging solutions to such models over an

appropriate distribution of excitation conditions, we can incorporate the effects of "inhomogeneous" relaxation,<sup>38</sup> which occurs with thermal Doppler shifts<sup>39</sup> or magnetic sublevel degeneracy.<sup>40</sup> However, to treat fully the possible "homogeneous" relaxation, such as spontaneous emission or phase interruptions, we must work with a probability density matrix  $\rho_{nm}$  rather than with the probability amplitudes  $C_n$  with probabilities obtained as diagonal elements  $P_n = \rho_{nn}$ . The Bloch equation for the N-level density matrix has the form<sup>41</sup>

$$i(d/dt) \rho = W\rho - \rho W - i\Gamma\rho.$$

The operator  $W$  is the Schrödinger effective Hamiltonian operator. The linear operator  $\Gamma$  represents the effects of homogeneous relaxation and hence its parameters are defined by the relaxation rate coefficients.

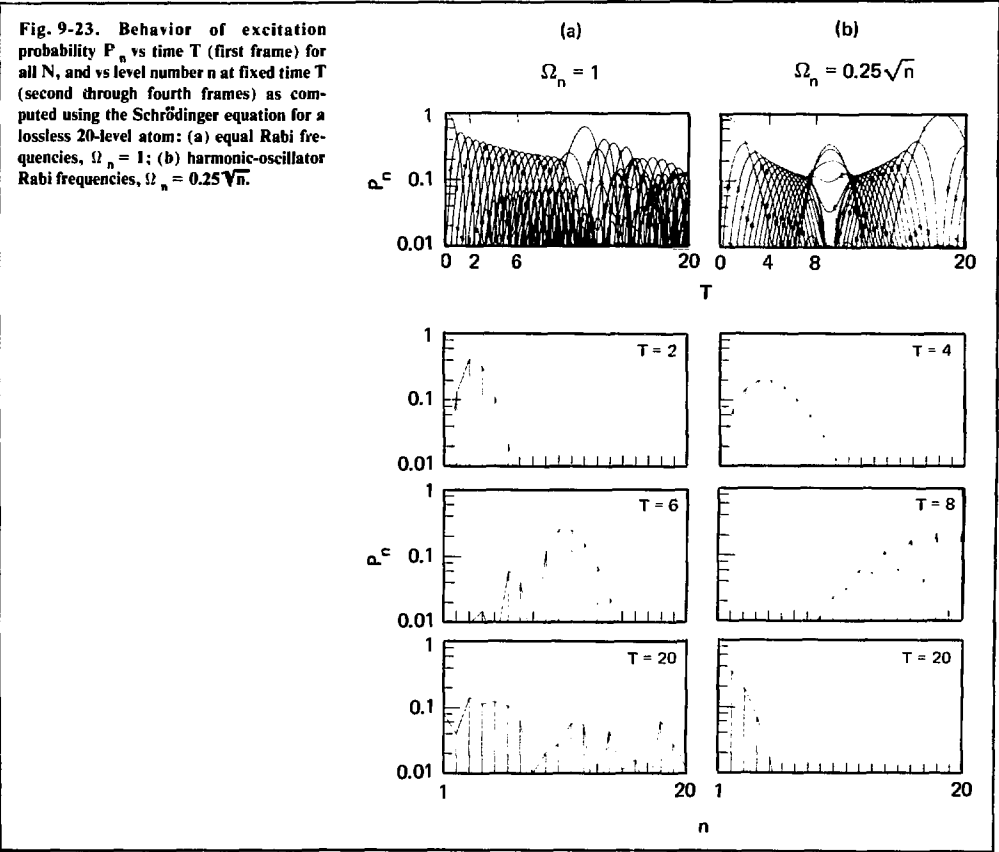
Continuing with the progression of in-

creasingly dominant homogeneous relaxation, we can derive an excitation equation with complete incoherence dealing only with probabilities  $P_n$ , rather than with phase-sensitive quantities such as probability amplitudes. The simplest traditional derivation balances gains and losses to yield an equation of the form

$$(d/dt) \underline{P} = M \underline{P}.$$

Here,  $M$  is a matrix of rate coefficients.

The preceding linear equations represent different, although nonexclusive, physical regimes, ranging from complete coherence (Schrödinger equation) to complete incoherence (rate equation). As noted previously, exact analytic solutions have been obtained for time dependence in a number of interesting and highly idealized examples of the Schrödinger equation.<sup>37,42</sup> At the opposite rate-equation extreme, we can readily obtain steady state

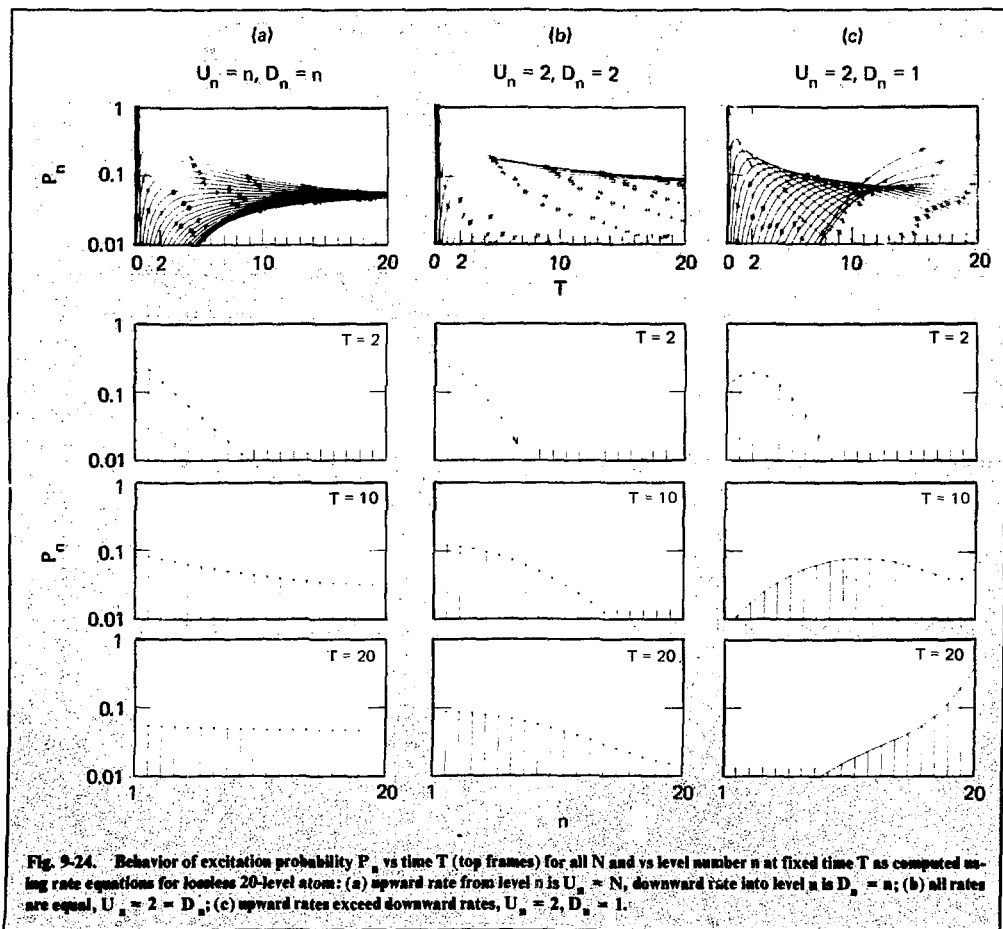


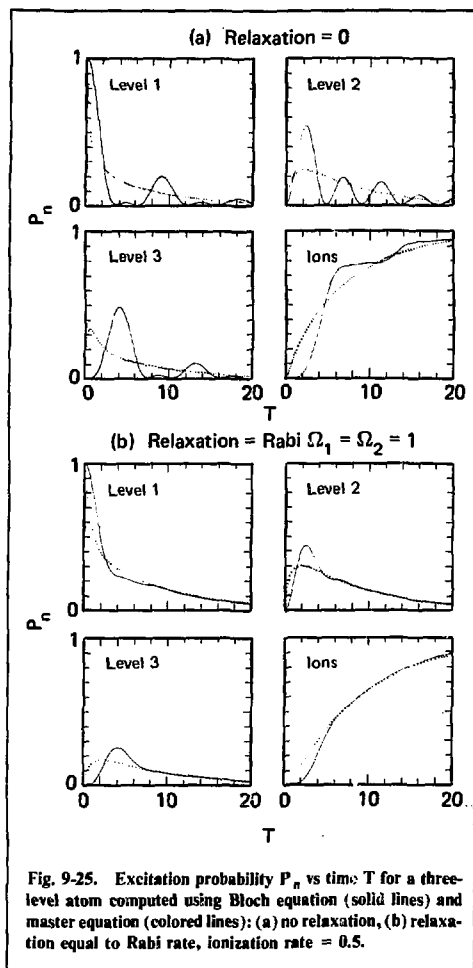
solutions in simple lossless examples. In more general cases, we have employed straightforward numerical integration routines to study the interrelationship of solution behavior and equation parameters. We also have studied partially coherent systems via the  $N$ -level Bloch equations.<sup>41</sup>

It is instructive to compare elementary examples of solutions to the various equations, to appreciate their effects on the populations of varying the physical parameters and the degree of coherence. In Fig. 9-23, we illustrate the excitation predicted by the (completely coherent) Schrödinger equation for a 10-level lossless "atom." These solutions, although not periodic, are marked during the time interval shown here by a "sloshing" flow of probability that never permits a quiescent steady

state. In contrast, rate equation solutions (Fig. 9-24) follow a monotonic approach to steady state. Moreover, the Schrödinger equation solutions reveal frequent brief population inversions, whereas the rate equation solutions show inversion only if upward rate coefficients from level  $n$  exceed downward coefficients into level  $n$ .

Although the population oscillations that mark coherent solutions are absent in rate equation solutions, often we can derive a rate equation that describes the evolution of effectively time-averaged populations. A successful application of this technique to a resonantly excited three-level atom with an appreciable probability loss from level 3 (here, the loss rate equals half the common Rabi frequency) is shown in Fig. 9-25. In Fig. 9-25a, the





description of some excitation processes, there are many regimes in which simple rate equations are not adequate.

We have explored several graphical display techniques for visualizing the complicated time dependence of the (complex-valued) probability amplitudes and density matrices. Some of these computer-generated diagrams have been assembled as an instructive movie,<sup>43</sup> which we have shown at several conferences.

### 9.5.2 Multiphoton Resonances

In an  $N$ -level atom or molecule excited by a single laser, mismatching between Bohr resonance frequencies and the laser frequencies can inhibit excitation; this phenomenon is called detuning. In Fig. 9-26, we have displayed the excitation probability in a lossless system of 15 sequentially linked levels with successive Rabi frequencies increasing in the ratio  $1, \sqrt{2}, \sqrt{3}, \dots, \sqrt{15}$ , as applicable to a harmonic oscillator. The first frame shows how, when the energy levels are equidistant and the laser is tuned to the common resonance frequency, excitation flows up to the final 15th level, after which it returns to lower excitation in a quasi-periodic fashion. (The markedly low probability of the next to last level is a prominent characteristic of the truncated harmonic oscillator.<sup>36</sup>) Succeeding frames show the effects on this probability flow of introducing anharmonicity into the energy level spacing, while retaining the first-step resonance condition as well as the Rabi frequencies. We see that as anharmonicity increases, the excitation becomes more closely confined to the lower levels. As a rule of thumb, we find that excitation can proceed up the  $N$ -level ladder until it reaches a level at which the cumulative detuning balances the Rabi frequency for the next transition. Thus, by increasing laser power (and thereby Rabi frequency), we can excite higher lying levels—an example of power broadening.

black curves represent populations obtained from the Schrödinger equation and the colored curves show solutions of a derived rate equation.<sup>41</sup> We see that, although the incoherent rate equation results fail to reproduce the Rabi oscillations of the coherent excitation, the results do yield a satisfactory portrayal of average populations. In Fig. 9-25b, we have replaced the completely coherent Schrödinger equation with a partially coherent Bloch equation (relaxation rates equal to Rabi frequencies). The closer agreement of black and colored curves illustrates the tendency toward rate equation behavior as inhomogeneous relaxation dominates coherent interactions. Although rate equations do provide a satisfactory time-average

To achieve single-laser excitation of high lying levels, we need not rely on high intensity. We can retune the laser so that, instead of establishing resonance with the fundamental frequency, we achieve resonance condition only after a few steps, i.e., we rely on an  $N$ -photon resonance. In Fig. 9-27, we demonstrate schematically the energy matching in one-, two-, and three-photon resonances. Figure 9-28 presents the time dependence of excitation in a four-photon resonance with large anharmonicity. Because the first step is now off-resonance, the first frame in Fig. 9-28 reveals that little excitation rises initially out of level 1.

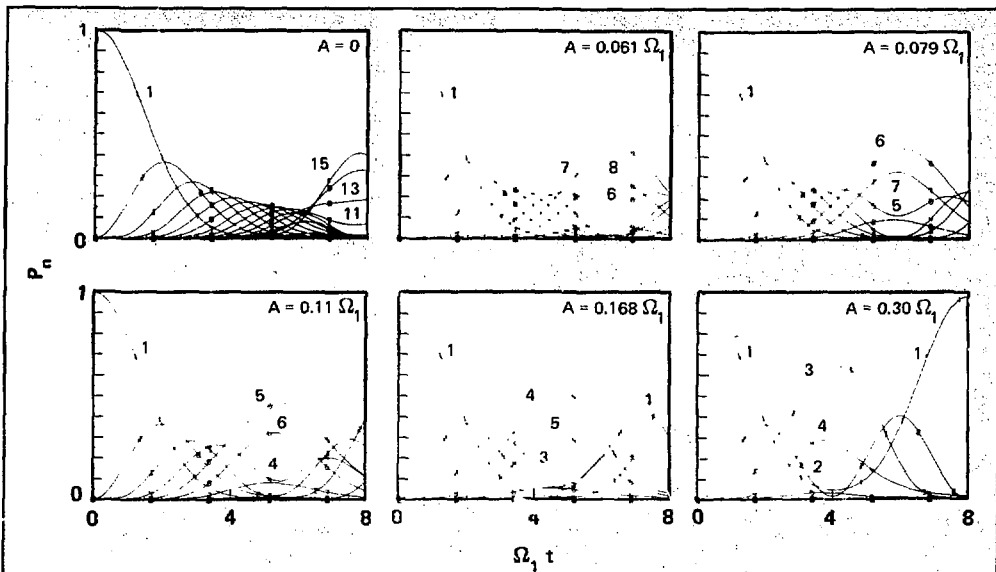


Fig. 9-26. Excitation probability vs  $\Omega_1$  for lossless 15-level system whose Rabi frequencies are those of harmonic oscillator,  $\Omega_n = \Omega_1 \sqrt{n}$ , and whose energy levels are anharmonically spaced. Laser is resonant with fundamental frequency. Successive frames show results with varying anharmonicity.

However, over a longer time, there is a gradual flow of probability from level 1 into level 5 without appreciable population in the intermediate off-resonance (virtual) levels. The long time required to complete the multiphoton transition complements very sharp frequency selection. The long-time average excitation probability is shown in Fig. 9-29

as a function of laser tuning. At sharply defined values, we see a highly enhanced probability of excitation—the multiphoton resonances. It is possible to obtain simple analytic expressions for the widths of these resonances and for the time required to complete a multiphoton transition.

### 9.5.3 Additional Studies Related to Multiphoton Dynamics

The elementary N-level, ladder-linkage, coherent-excitation system described in the 1976 Laser Program Annual Report continues to serve as a valuable reference model. However, real atoms have several properties that require extension of this elementary model. An obvious requirement is that the mathematical description include the consequences of the thermal distribution of vapor velocities along the laser beam direction. The consequent Doppler shifts appear in the mathematical description as a distribution of detunings: the solutions of Hamiltonians with a distribution of diagonal elements must be averaged. We have continued our studies on the effectiveness of various techniques for exciting and ionizing the bulk of the Doppler distribution.

A second similar extension of the elementary

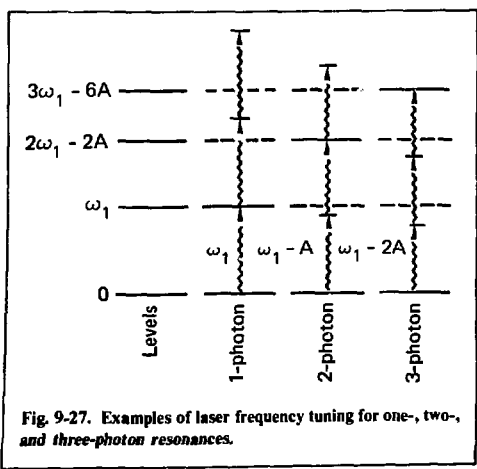


Fig. 9-27. Examples of laser frequency tuning for one-, two-, and three-photon resonances.

N-level ladder occurs because an atom that exists in an energy level characterized by angular momentum quantum number  $J$  has  $2J + 1$  distinguishable and discrete possible orientations with respect to a reference axis, such as the laser electric field vector.<sup>40</sup> Each such orientation, characterized by magnetic quantum number  $m$ , yields a different value of the angle between the dipole moment  $\mathbf{d}$  and the electric vector  $\mathbf{E}$  in the expression for interaction energy  $\mathbf{d} \cdot \mathbf{E}$ . If we continue to neglect spontaneous emission (i.e., optical pumping) and deal with polarized light, the N-level excitation ladder becomes a set of  $2J + 1$  independent N-level ladders, differing in Rabi-frequency sequences that must be averaged. These averages tend to dampen the appearance of population oscillations (see Fig. 9-30). This damping, an example of inhomogeneous relaxation, is similar to the damping caused by Doppler shifts (also by inhomogeneous

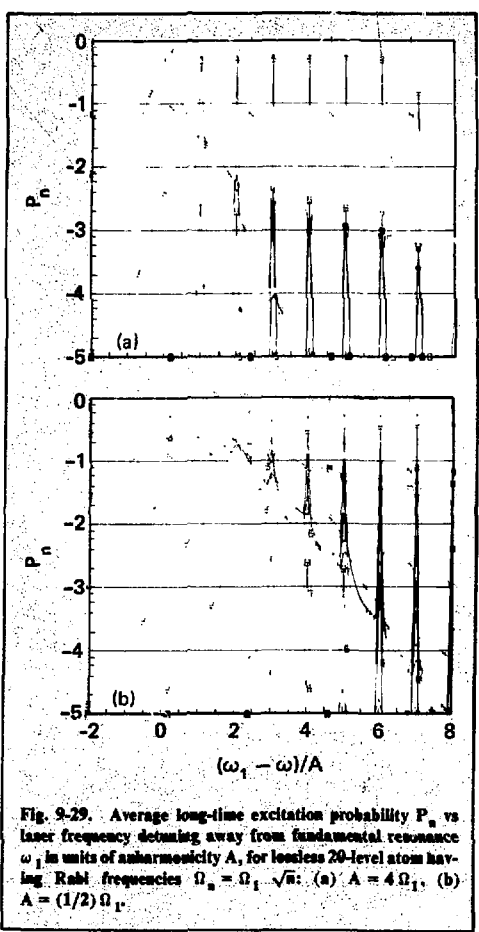
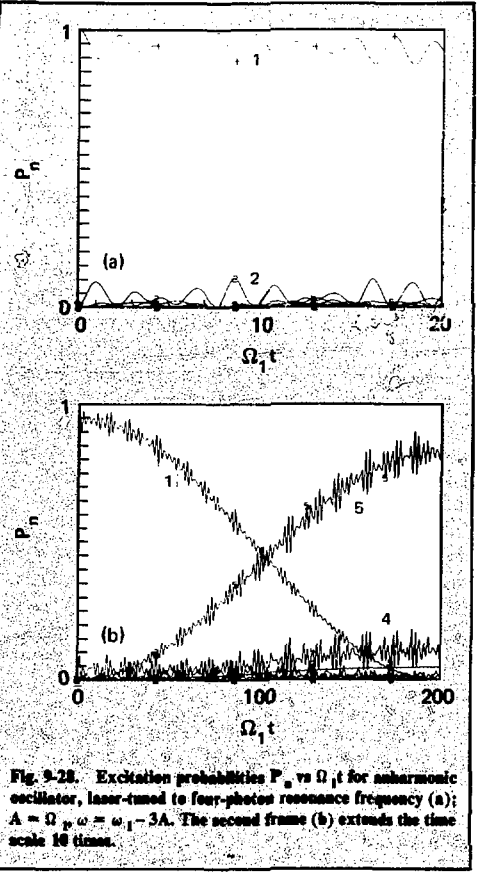


Fig. 9-29. Average long-time excitation probability  $P_n$  vs laser frequency detuning away from fundamental resonance  $\omega_1$  in units of anharmonicity  $A$ , for lossless 20-level atom having Rabi frequencies  $\Omega_n = \Omega_1 \sqrt{n}$ : (a)  $A = 4 \Omega_1$ , (b)  $A = (1/2) \Omega_1$ .

relaxation), although the exact details differ (Fig. 9-31).

When a two-level atom is excited by intense near-resonant radiation, the induced Rabi population oscillations alter the nature of both the fluorescence and the absorption spectrum. For example, if we probe the excited level with a weak tunable ionizing laser, a sweep in frequency of the probe laser reveals a splitting of the low-field absorption peak into two peaks, separated by the Rabi frequency. This splitting, caused by an alternating electric field, is known as the ac Stark effect. The presence of angular momentum, with consequent orientation averages, tends to broaden the individual peaks, even though the two components may remain visible. The pattern, illustrated for resonant excitation in Fig. 9-32, changes with time.

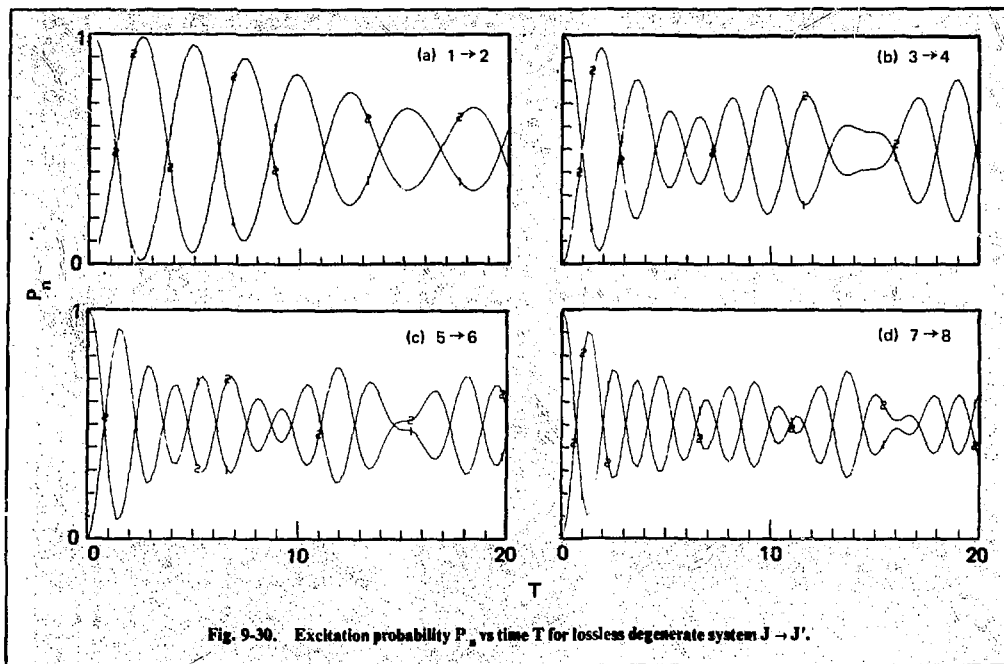


Fig. 9-30. Excitation probability  $P_n$  vs time  $T$  for lossless degenerate system  $J \rightarrow J'$ .

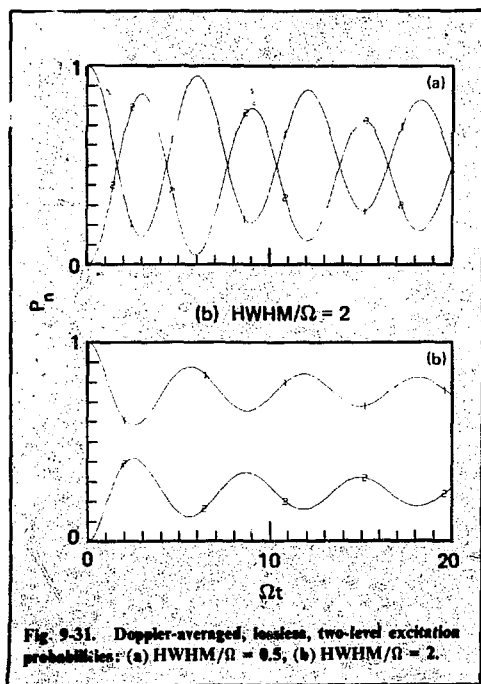


Fig. 9-31. Doppler-averaged, lossless, two-level excitation probabilities: (a)  $\text{HWHM}/\Omega = 0.5$ , (b)  $\text{HWHM}/\Omega = 2$ .

We have published a discussion of these effects<sup>40</sup> and are continuing to study examples of the ac Stark effect both theoretically and experimentally.

The occurrence of nuclear spin  $I$  and atomic angular momentum  $J$  makes possible the hyperfine interaction of nuclear magnetic-dipole and electric-quadrupole moments with the electronic field and gradient. In the presence of the interaction, an individual  $J$  level splits into, at most,  $2I + 1$  levels, each characterized by quantum number  $F$ . Although the energy splitting is small, the new angular momentum quantum number follows selection rules  $\Delta F = \pm 1, 0$  (but not  $0 \rightarrow 0$ ), and hence the linkage pattern becomes much more complicated. For example, Fig. 9-33 illustrates the added linkage complexity that occurs when a two-step sequence (with each  $J > 3$ ) extends to include hyperfine structure for  $I = 1$ . We are currently studying the effects of hyperfine structure on excitation and ionization.

#### 9.5.4 Numerical Modeling

Predictions of excitation and ionization behavior in uranium vapor are now made routinely with two general codes. The more sophisticated code, SHUX, integrates the time-dependent Schrödinger equation after automatically computing the hyperfine-structure energies and linkages



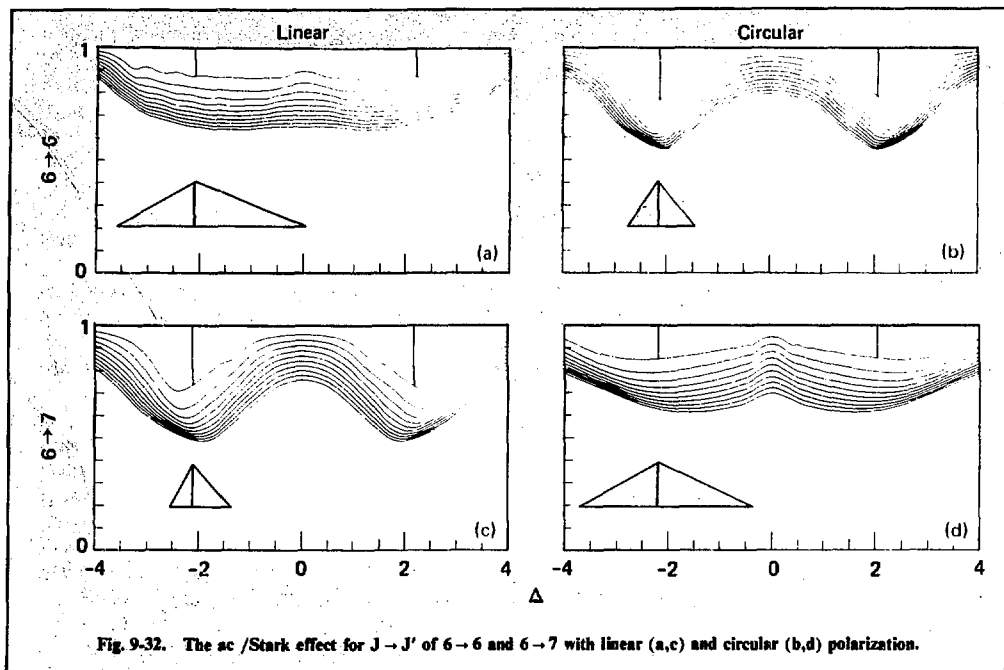


Fig. 9-32. The ac /Stark effect for  $J \rightarrow J'$  of  $6 \rightarrow 6$  and  $6 \rightarrow 7$  with linear (a,c) and circular (b,d) polarization.

(given the hyperfine splitting parameters  $A$  and  $B$ ) and averages these solutions over magnetic sublevels and Doppler shifts. The code permits nearly arbitrary specification of phase and amplitude modulation, thereby enabling realistic descriptions of experimental conditions. The alternative code, BLOCHB, treats more idealized models and per-

mits the use of either Bloch or rate equations. In each code, graphical display of the level populations or the ionized fraction as a function of time or of detuning is the primary output format for results.

Although analytic solutions are most tractable for monochromatic excitation, numerical modeling permits a variety of pulse shapes. In particular, we have investigated the effects of pulse modulation on the excitation and ionization efficiency.<sup>44</sup> Our results revealed that the efficiency of excitation could be significantly improved by modulation. This enhancement can be viewed as a redistribution of power into sidebands, thereby broadening the effective laser bandwidth and avoiding saturation.

All of our modeling assumes that ionization can be incorporated into the Schrödinger equation as a non-Hermitian effective Hamiltonian. We have investigated the validity of this assumption by studying numerical solutions of the time-dependent Schrödinger equation in position representation for a one-dimensional square well potential.<sup>45</sup> This model idealizes the photoionization or dissociation of a system possessing a single bound state. Our results reveal cases for near-threshold excitation where population oscillations into the continuum

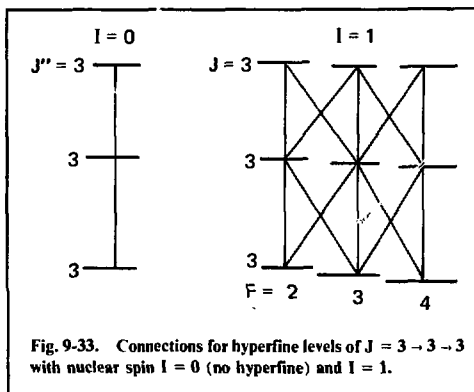


Fig. 9-33. Connections for hyperfine levels of  $J = 3 \rightarrow 3 \rightarrow 3$  with nuclear spin  $I = 0$  (no hyperfine) and  $I = 1$ .

negate the conventional assumptions of incoherent loss.

## References

35. B. W. Shore and J. Ackerhalt, "Dynamics of Multilevel Laser Excitation: Three-Level Atoms," *Phys. Rev. A* **15**, 1640 (1977).
36. J. H. Eberly, B. W. Shore, Z. Bialynicka-Birula, and I. Bialynicki-Birula, "Coherent Dynamics of N-level Atoms and Molecules. I. Numerical Experiments," *Phys. Rev. A* **16**, 2038 (1977).
37. Z. Bialynicka-Birula, I. Bialynicki-Birula, J. H. Eberly, and B. W. Shore, "Coherent Dynamics of N-level Atoms and Molecules. II. Analytic Solutions," *Phys. Rev. A* **16**, 2048 (1977).
38. B. W. Shore and M. A. Johnson, "Coherence vs. Incoherence in Stepwise Laser Excitation," *J. Chem. Phys.* **68**, 5631 (1978).
39. J. R. Ackerbald, J. H. Eberly, and B. W. Shore, "Statistical Broadening and Population Loss in a Strongly Excited Three-Level System," *Phys. Rev. A* (in press).
40. B. W. Shore, "Effects of Magnetic Sublevel Degeneracy on Rabi Oscillations," *Phys. Rev. A* **17**, 1739 (1978).
41. J. R. Ackerhalt and B. W. Shore, "Rate Equations Versus Bloch Equations in Multiphoton Ionization," *Phys. Rev. A* **16**, 277 (1977).
42. B. W. Shore and J. H. Eberly, "Analytic Approximations in Multilevel Excitation Theory," *Optics Commun.* **24**, 83 (1978).
43. B. W. Shore and J. H. Eberly, "The Density Matrix of a Ten-Level System," Lawrence Livermore Laboratory animated film (1977).
44. A. Goldberg and B. W. Shore, "Effects of Pulse Modulation on Multistep Laser Excitation," *Optical and Quantum Electronics* **10**, 331 (1978).
45. A. Goldberg and B. W. Shore, "Modeling Laser Ionization," *J. Phys. B* (in press).

## Author

B. W. Shore

## 9.6 Relaxation Kinetics of Metastable Excited States

The efficiency and selectivity of an LIS process or a laser-derived chemical reaction often are controlled by two important parameters: the ratio of the reactive to the nonreactive collisional cross sections, and the ratio of the density of the excited atoms or molecules populated by lasers to the initial density of excited species prepared from the reactant source. It is commonly recognized that a detailed knowledge of the distribution of the excited state population and its relaxation processes must be obtained before any practical laser chemical or LIS process can be developed.<sup>46</sup>

To obtain information on the initial distribution of the excited state population of metallic vapor produced by electron beam heating, and to gain a basic understanding on the relaxation mechanisms of the excited population, we have made some systematic measurements on the population and on the relaxation rate of electronically excited neodymium vapor during the evaporation process. We chose atomic neodymium as the test sample because of its spectroscopic and kinetic simplicities.

The experimental system used in this work consists of three major components: the atomic source generator, the surface temperature and vaporation rate monitors, and the cw laser-absorption apparatus. A diagram of this system is given in Fig. 9-34.

The atomic vapor is produced through the surface evaporation of metallic neodymium by impact with high-energy electrons. The electron beam is generated from a cw thermionic spot gun. Electron energy, current, and heating spot size are continuously adjustable. Electron energy and current are typically in the 20-to-25-kV and 10-to-50-mA ranges; a typical heating spot size is about 8 mm in diameter. The electron beam strikes the sample surface at an angle of 24 deg from vertical. The debris produced by the primary beam consists of a swarm of electrons and ions, together with excited and ground state atoms. The typical degree of ionization is about  $10^{-3}$ .

We made quantitative measurements of the angular distribution of neodymium vapor by depositing metal vapor on platinum witness pieces. The pieces were mounted on an arched stainless steel fixture, placed 20 cm from the source, which was located behind 1.6-cm-diameter holes. After each evaporation experiment, the weight gain of each witness piece was determined. We found that, at moderate vaporization rates, evaporation becomes more directional: about 20% more vapor is emitted toward the vertical direction than is predicted from Lambert's cosine law.

Transient evaporation rates were monitored with a pair of quartz crystal, deposition rate, thin-film monitors located approximately 27 cm from the source at 0 deg and 14.5 deg from vertical. A metal collector was used to collect the vapor emitted from the source. Averaged total evaporation rates were determined by measuring the target weight loss and the weight gain of the collector, both before and after the evaporation experiment. We found that, at moderate evaporation conditions, the transient and average deposition rates measured by the two monitors were in good agreement (within  $\pm 10\%$ ).

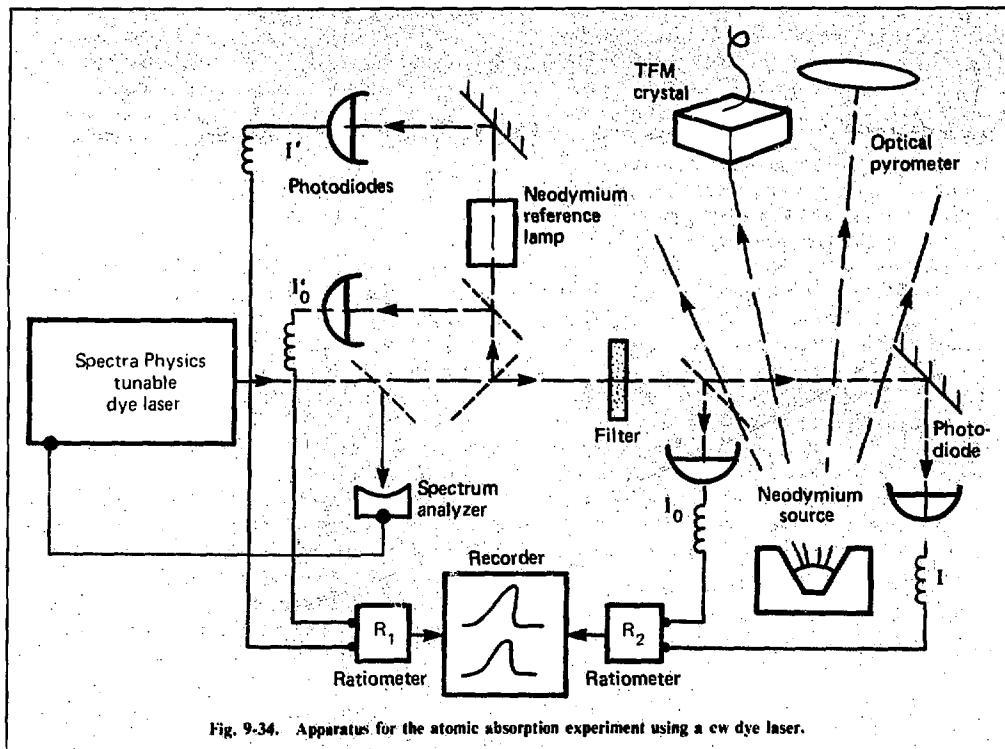


Fig. 9-34. Apparatus for the atomic absorption experiment using a cw dye laser.

with the total vaporization rates, assuming a cosine distribution. The sticking coefficient of neodymium on a precoated neodymium collector was found to be near unity. Assuming that atoms leave the target surface with a velocity related to its spot temperature, we can calculate the initial vapor density from the measured evaporation rates.

Temperature measurements were made with an automatic optical pyrometer located directly above the source. The pyrometer was calibrated to the International Practical Temperature Scale of 1968 by comparison with an NBS reference lamp. Window absorption and emissivity correction factors were determined before the experiments.

The populations of neodymium atoms at the ground state ( $4f^4 6s^2$ ,  $J = 4$ ) and at the  $1128\text{-cm}^{-1}$  ( $J = 5$ ),  $2367\text{-cm}^{-1}$  ( $J = 6$ ), and  $3682\text{-cm}^{-1}$  ( $J = 7$ ) metastable levels,<sup>47</sup> were determined by a laser resonance absorption technique. Figure 9-34 includes a diagram of this optical setup. We used a Spectra Physics tunable dye laser for both linewidth

and percentage absorption measurements. The laser has a frequency bandwidth of about 30 MHz and an output power of 40 mW. For the experiment, the laser radiation was split into two beams. One beam was fed to a spectrum analyzer to monitor the laser bandwidth. The other beam was split again, with 50% sent to a reference photodiode and 50% directed through the vapor chamber onto another photodiode. We used neutral density filters to attenuate the laser beam to avoid saturation or optical pumping effects. Signals from both diodes were then fed to a ratiometer, monitored on an oscilloscope, and recorded on a chart recorder.

During the evaporation experiment, the cw dye laser was tuned to sweep across the  $5620\text{-Å}$  region to monitor the ground state, and to  $5676\text{ Å}$ ,  $5785\text{ Å}$ , and  $5827\text{ Å}$  to sweep the  $1128\text{-cm}^{-1}$ ,  $2367\text{-cm}^{-1}$ , and  $3682\text{-cm}^{-1}$  levels, respectively. Linewidths and percentage absorptions for each transition were measured at various distances from the evaporation source. We calculated the absolute density of

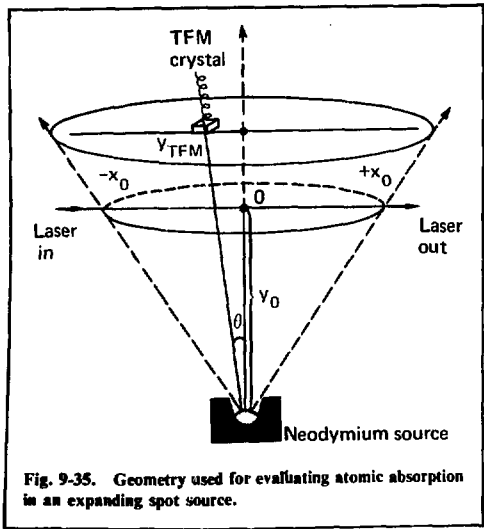
neodymium at each state, using published gA values.<sup>48</sup> The total particle density of neodymium at the absorption position was calculated from the flux and the average velocity. The flux is derived from deposition rate measurements and the calculated velocity.

To determine the absolute population of neodymium in its various electronic levels, the absolute absorption cross section of the probed transition and the total particle density must be accurately known. Uncertainties in branching ratios and radiative lifetimes of reported transitions<sup>48</sup> introduce a large uncertainty in the desired absolute populations. The total particle density of neodymium at the absorption position is determined from both evaporation rate and surface temperature data. As shown in Fig. 9-35, the thin-film monitor located at  $y_{TFM}$  and  $\theta \cong 14.5$  deg records the total particle flux (ground state, excited states, and ions) from a source for the solid angle subtended by the detector. The relationship between the thin-film monitor data and the particle density at  $y_0, \theta = 0$  deg can be written as

$$N_t(y_0, \theta = 0) = \frac{\text{TFM rate}}{\cos \theta} \times \frac{1}{V} \times \left( \frac{y_{TFM}}{y_0} \right)^2, \quad (6)$$

where  $V$  is the stream velocity of evaporant at  $y_{TFM}$  and  $y_0$ . The stream velocity can be calculated from

$$V_{\text{stream}}^2 = \frac{2KT_0}{m} \left( 1 + \frac{\gamma - 1}{2} M^2 \right)^{-1} \frac{\gamma M^2}{2}, \quad (7)$$



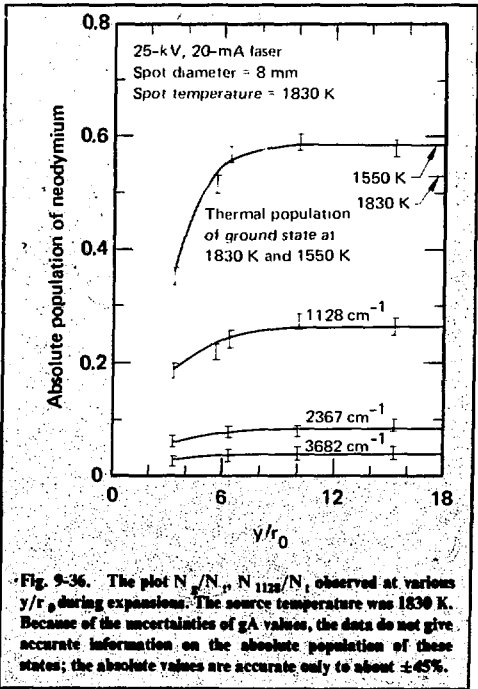
where  $\gamma$  is the heat capacity ratio of neodymium gas,  $T_0$  is the surface temperature, the  $M$  terms are the Mach numbers,  $K$  is the Boltzmann constant, and  $m$  is the atomic weight of neodymium.

The relationship between the Mach numbers at two distances from the source is taken to be<sup>49</sup>

$$\frac{M_0}{M_{TFM}} = \left( \frac{y_0}{y_{TFM}} \right)^{2/3},$$

and  $M = 2(y_0/r_0)^{2/3}$ , where  $y_0$  is the distance from the source and  $r_0$  is the source radius. As shown in Eq. (7), the stream line velocity  $V_{\text{stream}}$  becomes insensitive to the Mach number at  $M > 3$  or 4, i.e., the stream line velocity is no longer changing at  $M > 3$  or 4. Thus, by measuring the surface temperature  $T_0$ , the stream velocity at  $y_0$  can be determined. The total particle density  $N_t(y_0, 0 \text{ deg})$  is then calculated from Eq. (6).

Figure 9-36 shows the measured population ratio of  $N_g/N_t$  employing Corliss's gA values<sup>48</sup> for 5620.54 Å. Using the published gA values for the 5675.97-Å, 5784.96-Å, and 5826.74-Å transitions, we also determined the  $N_{1128}/N_t$ ,  $N_{2367}/N_t$ , and  $N_{3682}/N_t$  ratios. The experimental data indicate



significant increases in relative population during expansion for the ground and  $1128\text{-cm}^{-1}$  levels. There is very little change in population after  $(y/r_0) > 6$ . The final population of neodymium appears to be frozen at about  $1600\text{ K}$ , which is lower than the surface temperature of the melt. As a result of uncertainties of vapor angular distribution, stream line velocity, hyperfine structures, and absorption cross sections, the absolute populations shown in Fig. 9-36 are only accurate to about  $\pm 45\%$ . The changes of relative populations are not likely to be affected by any systematic errors introduced through either the absolute magnitude of the absorption cross sections or the precise angular distribution and velocity of vapor. Thus, our data clearly demonstrate that relaxation of electronically excited neodymium atoms in a weakly ionized plasma does take place during vapor expansion into the vacuum.

To gain an initial understanding of the mechanism of metastable excited state relaxation in the expanding plasma, we derived simple kinetics models. As atoms evaporate from the liquid surface, they can be electronically excited by inelastic collisions with high-energy impinging electrons, expanding secondary electrons, and ions. Radiative lifetimes of most excited electronic states are very short,<sup>48</sup> but because the branching ratios for cascading to the ground state are small, high populations in metastable excited states can build up after excitation. The relaxation of these metastable excited states during expansion can proceed by two different processes: relaxation by collisions with other neodymium atoms, or relaxation by collisions with the coexpanding electrons.

The relaxation of the excited state neodymium atoms by atom-atom collisions from an expanding spot source can be described<sup>50</sup> by

$$\frac{\text{Nd}^m(y)}{\text{Nd}^m(r_0)} = \exp \left\{ -\sigma_{E-T} \text{Nd}(r_0) \frac{r_0}{y} \left[ 1 - \left( \frac{r_0}{y} \right)^{\gamma} \right] \right\},$$

where  $\gamma$  is the heat capacity ratio of neodymium gas,  $\text{Nd}(r_0)$  is the initial neodymium atom density, and  $\sigma_{E-T}$  is the energy transfer cross section and a function of a kinetic temperature of the gas. For simplicity, we assume that  $\sigma_{E-T}$  is roughly a constant. A plot of  $\text{Nd}^m(y)/\text{Nd}^m(r_0)$  vs  $(y/r_0)$  is shown in Fig. 9-37 for an initial vapor density at the surface of  $10^{15}\text{ atoms/cm}^3$  and for two distinct energy transfer cross sections. Cross sections for relaxation processes with  $\Delta E = 1128\text{ cm}^{-1}$  and  $3682\text{ cm}^{-1}$  were estimated from collective data<sup>51</sup> on alkali atoms. The spot radius  $r_0$  and the  $\gamma$  value were

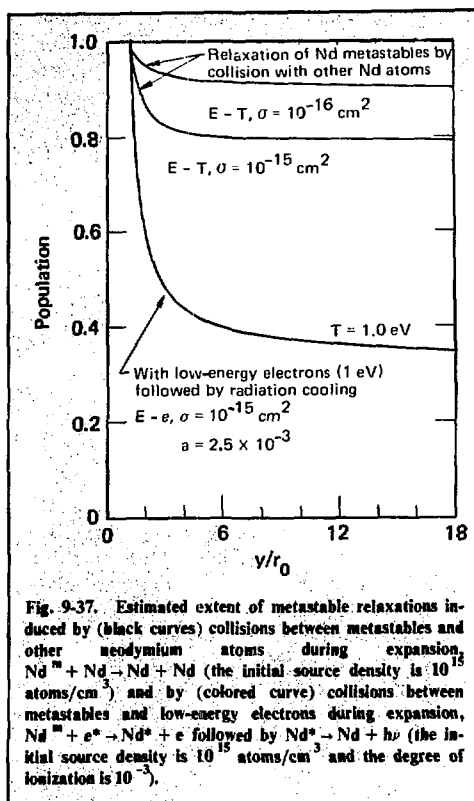
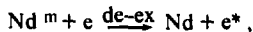


Fig. 9-37. Estimated extent of metastable relaxations induced by (black curves) collisions between metastables and other neodymium atoms during expansion,  $\text{Nd}^m + \text{Nd} \rightarrow \text{Nd} + \text{Nd}$  (the initial source density is  $10^{15}\text{ atoms/cm}^3$ ) and by (colored curve) collisions between metastables and low-energy electrons during expansion,  $\text{Nd}^m + e^- \rightarrow \text{Nd}^* + e^-$  followed by  $\text{Nd}^* \rightarrow \text{Nd} + h\nu$  (the initial source density is  $10^{15}\text{ atoms/cm}^3$  and the degree of ionization is  $10^{-3}$ ).

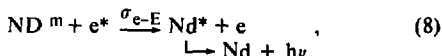
assumed to be  $0.4\text{ cm}$  and  $1.67$ , respectively. During the gas expansion, very little depopulation of the  $3682\text{-cm}^{-1}$  level because of E-T energy transfer is expected. However, collisional relaxation of  $1128\text{ cm}^{-1}$  to the ground state, or energy transfer between adjacent high lying metastable states, might still be possible.

As shown in Fig. 9-37, heavy particle collisional relaxation ceases quite early at about  $y = (2\text{ or }3)r_0$  for an initial vapor density of  $10^{15}\text{ atoms/cm}^3$ . The expected terminal Mach number  $M_T$  of the expanding vapor is about 3 or 4. Thus, further relaxation can only be achieved by other mechanisms, such as collisions with expanding electrons if their kinetic temperature is lower than the electronic temperature of the metastables. The two temperatures will be essentially decoupled as the electron and neutral densities drop during expansion. Because the degree of ionization in vapor is about  $10^{-3}$  and a large fraction of the neodymium atom is at its excited states, there are roughly  $10^3$  times more metastables than

electrons in the vapor. Cooling of the metastable-electron bath will have to depend on an effective electron-electron cooling process and on metastable-electron energy transfer mechanisms. The cross sections for superlastic collisions<sup>52</sup> between metastable neodymium and low energy electrons,



are probably too small for efficient relaxation of metastables at low electron densities. One possible relaxation process of neodymium metastables can be described as



where collisions between metastable neodymium atoms and electrons excite the neodymium atoms into some nearby excited states of different parity. Because radiation from these states is optically allowed, relaxation of metastables by radiation can be accomplished. Thus, during the expansion process, the electrons also can be cooled by reaction (8). Assuming that electrons retain constant kinetic energy as they expand into vacuum, the relaxation rate for  $\text{Nd}^m$  induced by electron metastable collisions can be calculated by

$$\frac{\text{Nd}^m(y)}{\text{Nd}^m(r_0)} = \exp \left\{ -\sigma_{e-E} a \text{Nd}(r_0) \frac{V_{eo}}{V_d} t_0 \left[ 1 - \left( \frac{r_0}{y} \right) \right] \right\},$$

where  $a$  is the ratio of  $\text{Nd}^+$  to  $\text{Nd}$  (estimated to be about  $10^{-3}$ ),  $V_{eo}$  is the thermal velocity of electrons, which is a function of average electron temperature,  $V_d$  is the directional velocity during expansion, and  $\sigma_{e-E}$  is the excitation cross section of neodymium covered by electron impacts. For simplicity, we have assumed that  $\sigma_{e-E}$  is roughly  $10^{-15} \text{ cm}^2$ , and similar values are found for other atomic transitions.<sup>52</sup> A plot of  $\text{Nd}^m(y)/\text{Nd}^m(r_0)$  vs  $(y/r_0)$  is also provided in Fig. 9-37 for an initial vapor density of  $10^{15} \text{ atoms/cm}^3$  at an electron temperature of 1 eV. We note that the collisions with low-energy electrons in the expanding plasma might provide an effective channel for the relaxation of neodymium

metastables that result from electron impact excitation near the source.

We observed increases of population in both the ground and the  $1128\text{-cm}^{-1}$  levels but few changes in either the  $2367\text{-cm}^{-1}$  or the  $3682\text{-cm}^{-1}$  levels (see Fig. 9-36). This clearly indicates that relaxation of higher metastables ( $>0.5 \text{ eV}$ ), such as  $4f^4 5d 6s$  levels, is involved. Because we found very little change in the populations of the  $2367\text{-cm}^{-1}$  and  $3682\text{-cm}^{-1}$  levels, the feeding of these levels from higher levels must be as fast as the removing rates. It is clearly evident from our analysis that relaxation of high lying metastables ( $>0.5 \text{ eV}$ ) by collisions with other neodymium atoms through the E-T process freezes out quite early in expansion. The E-T processes are partially responsible for the feeding of adjacent levels from nearby metastable states. Feeding of the  $1128\text{-cm}^{-1}$  and ground levels most likely occurs from relaxation of high lying levels by collisions with low-energy electrons followed by radiations.

## References

46. A. V. Elotskii, Y. K. Zemtsov, A. V. Rodin, and A. N. Starostin, *Sov. Phys. Dokl.* **20**, 42, (1975).
47. G.E.M.A. Hassa, *Physica* **29**, 678, 1133 (1963).
48. C. H. Corliss and W. R. Bozman, *NBS Monograph* **53** (1962).
49. P. P. Wegener, *Molecular Beams and Low Density Gasdynamics* (Marcel Dekker, New York, 1974).
50. Equation obtained by integrating the kinetic equation derived for collisional relaxation of atoms from an expanding spot source:

$$\frac{\text{Nd}^m(y)}{\text{Nd}^m(r_0)} = \exp \left\{ \int_{-r_0}^y \sigma_{E-T} \text{Nd}(y) \frac{V(y)}{V_d} dy \right\},$$

where  $\sigma_{E-T}$  is the energy transfer cross section. The density of neodymium at distance  $y$  is related to  $r_0$  by

$$\text{Nd}(y) = \text{Nd}(r_0) \left( \frac{r_0}{y} \right)^2.$$

The relative velocity of colliding atoms at  $y$  is related to the velocity  $V_0$  at  $r_0$  by

$$V(y) = V_0 \left( \frac{r_0}{y} \right)^{\gamma-1} \text{ and } \gamma = C_p/C_v;$$

$V_d$  is the directional velocity during expansion.

51. I. Krause, *Ann. Rev. Phys. Chem.* **27**, 267 (1976).
52. W. Williams and S. Trajmar, *J. Phys. B: Atom. Molec. Phys.* **8**, L50 and L96 (1975).

## Author

H. L. Chen